Transactions of the ASME®

Technical Editor, **LEON M. KEER (1993)**

The Technological Institute
Northwestern University
Evanston, IL 60201

APPLIED MECHANICS DIVISION

Chairman, **THOMAS L. GEERS**
Secretary, **S. LEIBOVICH**
Associate Editors,
R. M. CHRISTENSEN (1990)
S. K. DATTA (1993)
G. J. DVORAK (1993)
C. O. HORGAN (1992)
R. L. HUSTON (1991)
D. J. INMAN (1992)
W. G. KNAUSS (1991)
F. A. LECKIE (1991)
J. T. C. LIU (1993)
R. M. McMEEKING (1991)
A. K. NOOR (1991)
J. W. NUNZIATO (1992)
J. W. RUDNICKI (1992)
C. F. SHIH (1993)
J. G. SIMMONDS (1992)
P. D. SPANOS (1992)
K. R. SREENIVASAN (1992)
Z. WARHAFT (1992)
L. T. WHEELER (1991)

BOARD ON COMMUNICATIONS
Chairman and Vice-President
R. E. NICKELL

Members-at-Large
W. BEGELL, T. F. CONRY, M. FRANKE, R. L. KASTOR, M. KUTZ, R. MATES, T. C. MIN, E. M. PATTON, R. E. REDER, R. D. ROCKE, W. O. WINER, A. J. WENNERSTROM, B. ZIELS

President, **C. O. VELZY**
Exec. Dir.
D. L. BELDEN
Treasurer, **ROBERT A. BENNETT**

PUBLISHING STAFF
Mng. Dir., Publ.,
CHARLES W. BEARDSLEY
Managing Editor,
CORNELIA MONAHAN
Production Editor, **JUDY SIERANT**
Prod. Asst., **MARISOL ANDINO**

Transactions of the ASME, Journal of Applied Mechanics (ISSN 0021-8936) is published quarterly (Mar., June, Sept., Dec.) for $120 per year by The American Society of Mechanical Engineers, 345 East 47th Street, New York, NY 10017. Second class postage paid at New York, NY and additional mailing offices. POSTMASTER: Send address changes to Transactions of the ASME, Journal of Applied Mechanics, c/o THE AMERICAN SOCIETY OF MECHANICAL ENGINEERS, 22 Law Drive, Box 2300, Fairfield, NJ 07007-2300.

CHANGES OF ADDRESS must be received at Society headquarters seven weeks before they are to be effective. Please send old label and new address.

PRICES: To members, $29.00, annually; to nonmembers, $120.00. Add $15.00 for postage to countries outside the United States and Canada.

STATEMENT from By-Laws. The Society shall not be responsible for statements or opinions advanced in papers or . . . printed in its publications (B7.1, Par. 3).

COPYRIGHT © 1989 by the American Society of Mechanical Engineers. Reprints from this publication may be made on condition that full credit be given the TRANSACTIONS OF THE ASME, JOURNAL OF APPLIED MECHANICS, and the author, and date of publication be stated.

INDEXED by Applied Mechanics Reviews and Engineering Information, Inc.

Journal of Applied Mechanics

Published Quarterly by The American Society of Mechanical Engineers

VOLUME 56 • NUMBER 4 • DECEMBER 1989

TECHNICAL PAPERS

737 **Large Deflections of an Elastoplastic Strain-Hardening Cantilever**
J. H. Liu, W. J. Stronge, and T. X. Xu

744 **Wave Propagation Through Elastically-Anisotropic Fluid-Saturated Porous Rocks**
P. J. Digby and K. Walton

751 **Nonlinear Analysis of Elastomeric Keyboard Domes**
J. H. Lau and A. H. Jeans

756 **Relaxation of Thermal Stress Singularities in Bonded Viscoelastic Quarter Planes** (89-WA/APM-25)
J. P. Blanchard and N. M. Ghoniem

763 **Elastic-Plastic Analysis of Cracks on Bimaterial Interfaces: Part II—Structure of Small-Scale Yielding Fields**
C. F. Shih and R. J. Asaro

780 **Representations of Stress Intensity Factors by Path-Independent Integrals** (89-WA/APM-34)
K.-C. Wu

786 **Cavities *vis-à-vis* Rigid Inclusions and Some Related General Results in Plane Elasticity** (89-WA/APM-22)
J. Dundurs

791 **An Inverse Transient Thermoelastic Problem for a Transversely-Isotropic Body**
N. Noda, F. Ashida, and T. Tsuji

798 **Some Axisymmetric Problems for Layered Elastic Media: Part I—Multiple Region Contact Solutions for Simply-Connected Indenters** (89-WA/APM-30)
T. W. Shield and D. B. Bogy

807 **Some Axisymmetric Problems for Layered Elastic Media: Part II—Solutions for Annual Indenters and Cracks** (89-WA/APM-31)
T. W. Shield and D. B. Bogy

814 **Rolling Contact With Friction and Non-Hertzian Pressure Distribution** (89-WA/APM-23)
C. Liu and B. Paul

821 **Viscoelastic Winding Mechanics** (89-WA/APM-18)
J. Y. Lin and R. A. Westmann

828 **A First-Order Perturbation Analysis of Crack Trapping by Arrays of Obstacles** (89-WA/APM-36)
H. Gao and J. R. Rice

837 **Crack Fronts Trapped by Arrays of Obstacles: Numerical Solutions Based on Surface Integral Representation**
N. Fares

844 **Analysis of Branched Interface Cracks Between Dissimilar Anisotropic Media**
G. R. Miller and W. L. Stock

850 **Three-Dimensional Analysis of Cracking Through the Boundary of a Two-Phase Material** (89-WA/APM-33)
M. T. Hanson, W. Lin, and L. M. Keer

858 **Branched Cracks in Anisotropic Elastic Solids**
M. Obata, S. Nemat-Nasser, and Y. Goto

865 **On the Approximation of a Deflection Curve by Force Actuators With Variable Spacing**
K. Natarajan, G. A. Dumont, and M. S. Davies

868 **The Anomalous Response of an Elastic-Plastic Structural Model to Impulsive Loading**
T. X. Yu and Y. Xu

874 **Dynamic Analysis of Flexible Structures Using Component Mode Synthesis**
M. De Smet, C. Liefooghe, P. Sas, and R. Snoeys

881 **Free Wave Propagation in Plates of General Anisotropic Media** (89-WA/APM-28)
A. H. Nayfeh and D. E. Chimenti

887 **Dynamics of a Plate in Large Overall Motion**
A. K. Banerjee and T. R. Kane

893 **A Comprehensive Study of the Free Vibration of Rectangular Plates Resting on Symmetrically-Distributed Uniform Elastic Edge Supports** (89-WA/APM-21)
D. J. Gorman

900 **Inelastic Response of an Infinite Cylindrical Shell to Transient Acoustic Waves**
T. L. Geers and C.-L. Yen

910 **Effects of Lateral Surface Conditions in Time-Harmonic Nonsymmetric Wave Propagation in a Cylinder** (89-WA/APM-35)
Y. Y. Kim and C. R. Steele

918 **An Indirect Boundary Integral Equation Applied to Nonshallow Spherical Shell Problems With Arbitrary Boundary Constraints** (89-WA/APM-29)
N. Simos and A. M. Sadegh

926 **Stability of a Semi-Active Impact Damper: Part 1—Global Behavior**
M. P. Karyeaclis and T. K. Caughey

930 **Stability of a Semi-Active Impact Damper: Part II—Periodic Solutions**
M. P. Karyeaclis and T. K. Caughey

(Contents continued on Inside Back Cover)

Downloaded 04 May 2010 to 171.66.16.49. Redistribution subject to ASME license or copyright; see http://www.asme.org/terms/Terms_Use.cfm

941 **Optimal, Coupled-Modal Control of Distributed Parameter Systems With Discrete Actuators** (89-WA/APM-20)
I. G. Tadjbakhsh and Y.-a. Su

947 **Period Doubling and Chaos in Unsymmetric Structures Under Parametric Excitation**
W. Szemplińska-Stupnicka, R. H. Plaut, and J.-C. Hsieh

953 **Probabilistic Torsional Vibration Analysis of a Marine Diesel Engine Shafting System: The Level Crossing Problem** (89-WA/APM-27)
E. Nikolaidis, A. N. Perakis, and M. G. Parsons

960 **An Experimental Investigation of Complicated Responses of a Two-Degree-of-Freedom Structure** (89-WA/APM-24)
A. H. Nayfeh, B. Balechandran, M. A. Colbert, and M. A. Nayfeh

968 **The Oscillation of Slender Elliptical Inviscid and Newtonian Jets: Effects of Surface Tension, Inertia, Viscosity, and Gravity** (89-WA/APM-32)
S. E. Bechtel

BRIEF NOTES

Deflection and Stress in a Curved Shaft Due to Torque
C. W. Bert 975

Mode III Crack Tip Plastic Zone Solution for Work Hardening Solid Using Dislocation Motion
J. Weertan 976

The Singularity at the Apex of a Rigid Wedge After Partial Separation
J. M. Duva 977

979 Effect of the Coupling Between the Longitudinal and Transverse Displacements on the Dynamics of Rotating Curves Beams
D.-c. Chen and A. A. Shabana

981 The Cylindrical Crack
T. N. Farris, K. Kokini, and I. Demir

983 A Note on Microbuckling in Unidirectional Fibrous Composites
T. M. Minahen and W. G. Knauss

BOOK REVIEWS

986 ***Continuum Mechanics of Electromagnetic Solids*, by G. A. Maugin** . . . Reviewed by **A. C. Eringen**

986 ***The Nonlinear Theory of Elastic Solids*, by A. Libai and J. G. Simmonds** . . . Reviewed by **J. L. Sanders, Jr.**

987 Books Received by the Office of the Technical Editor

988 Author Index

990 Worldwide Mechanics Meetings List

843 Change of Address Form

820 Call for Papers—1990 Fluid Machinery Forum

892 Call for Papers—Symposium on Interfacial Phenomena in Fluid Mechanics

899 Call for Award Nominations—Bioengineering Division

Downloaded 04 May 2010 to 171.66.16.49. Redistribution subject to ASME license or copyright; see http://www.asme.org/terms/Terms_Use.cfm

J. H. Liu[1]
Research Assistant.

W. J. Stronge

T. X. Yu[2]

Department of Engineering,
University of Cambridge,
Cambridge, U.K. CB2 1PZ

Large Deflections of an Elastoplastic Strain-Hardening Cantilever

This theoretical analysis of an elastoplastic cantilever examines the effects of linear strain-hardening and the development of partial elastic unloading when deflections become large. For a vertical force at the tip, unloading modifies the distribution of curvature in a substantial internal segment after the deflections become very large, but it has a negligible effect on the tip displacement. The analysis uses a bilinear stress-strain constitutive relation that results in slightly better agreement with previous experiments than a corresponding bilinear approximation for the moment-curvature relation.

1 Introduction

Large deflection solutions for *elastic* cantilevers were summarized by Frisch-Fay (1962). The effect of large deflections on the development of *plastic* deformations was studied by Reid and Reddy (1978) for a rigid, linear-hardening moment-curvature relation. They showed that a cantilever with a tip force acting in a fixed direction had a limited length for the plastically deformed region that extended from the root. As the force F increased, the length of the plastically deformed region increased for $F<F_{cr}$; however, when $F>F_{cr}$ large deflections caused the moment at some plastically deformed sections to decrease with increasing force (unloading). Changes in the distribution of curvature in a cantilever, as a consequence of unloading at large deflections, were considered by Wu and Yu (1986) for a material with an elastic perfectly-plastic stress-strain relation.

The present paper examines the development of large deflections in an *elastoplastic cantilever with linear strain-hardening*, as shown in Fig. 1. The cantilever has a rectangular cross-section with depth H and width B; there is a force at the tip which acts normal to the undeformed beam. Based on assumptions that cross-sections of the cantilever remain plane and axial stretching is negligible, the strain distribution $\epsilon(S,z)$ at any section S is a linear function of distance z from the neutral axis and local curvature $\kappa'(S)$,

$$\epsilon = z\,\kappa'. \tag{1}$$

The curvature is related to the rotation $\theta(S)$ of the cross-section,

$$\kappa' = \frac{d\theta}{dS}. \tag{2}$$

The bending moment distribution in a cantilever of length L is

$$m = (1-\delta-x)f = (x_l - x)f, \tag{3a}$$

where $m=M/M_e$, $f=FL/M_e$, $\delta=\Delta/L$, $x=X/L$, $x_l=X_l/L$, $y=Y/L$ and $s=S/L$. Here, forces and bending moments have been nondimensionalised with respect to the largest elastic moment $M_e=BH^2\sigma_y/6$ where σ_y is the yield stress. In addition, geometric relations yield.

$$\frac{dx}{ds} = \cos\theta \tag{3b}$$

$$\frac{dy}{ds} = \sin\theta \tag{3c}$$

2 Theoretical Analysis

The elastoplastic cantilever has three different distributions

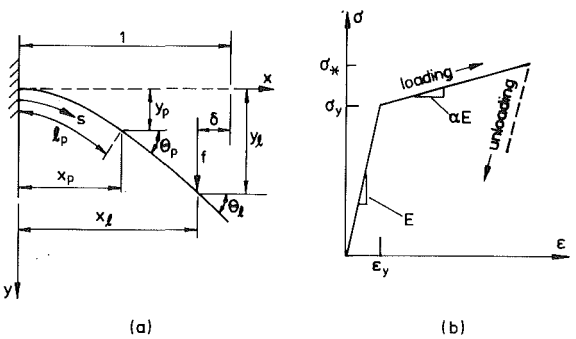


Fig. 1 (a) Cantilever subjected to load at tip; (b) stress-strain relation for beam material

[1]On leave from Huazhong University of Science and Technology, Wuhan, People's Republic of China.

[2]On Leave from the Department of Mechanics, Peking University, Beijing, People's Republic of China.

Contributed by the Applied Mechanics Division of THE AMERICAN SOCIETY OF MECHANICAL ENGINEERS for publication in the JOURNAL OF APPLIED MECHANICS.

Discussion on this paper should be addressed to the Editorial Department, ASME, United Engineering Center, 345 East 47th Street, New York, N.Y. 10017, and will be accepted until two months after final publication of the paper itself in the JOURNAL OF APPLIED MECHANICS. Manuscript received by the ASME Applied Mechanics Division, November 8, 1988; final revision, February 14, 1989.

Copyright © 1989 by ASME

Downloaded 03 May 2010 to 171.66.16.31. Redistribution subject to ASME license or copyright; see http://www.asme.org/terms/Terms_Use.cfm

of plastic deformation corresponding to three ranges of load. When the load is small, $f<f_e$, the entire beam is elastic. The maximum force f_e for fully elastic deformation corresponds to the elastic yield moment at the root $m(0)=1$. When $f>f_e$, the length of the plastic region l_p, increases with f until it reaches a maximum value l_{pm}. The corresponding force at this maximum extent of the plastic region is defined as a critical force f_{cr}, where elastic unloading begins in the plastically deformed segment. When $f>f_{cr}$, the increase in deflection associated with any increase in force causes unloading at some sections so there is a reduction in the length of the plastic loading region.

Unloading of a section is caused by a decrease in the distance of the section from the line of action of the applied force; this distance is $(1-\delta-x)=(x_l-x)$ where x_l is the horizontal coordinate at the tip shown in Fig. 1(*a*). The unloading state expands from the tip and enters the plastically deforming regions when $f=f_{cr}$.

2.1 Elastic Deformation, $0<f<f_e$. The Elastica equation for a vertical force at the tip is (Frisch-Fay, 1962)

$$\kappa=\sqrt{2f\beta(\sin\theta_l-\sin\theta)}. \tag{4a}$$

The bending moment $m(s)$ is linearly related to the nondimensional curvature κ

$$m(s)=\kappa/\beta \tag{4b}$$

where $\kappa'=d\theta/dS$ is the curvature, $\kappa=L\kappa'=d\theta/ds$ and θ_l is the angle of rotation at the tip shown in Fig. 1(*a*). For a cantilever with rectangular cross-section the largest nondimensional elastic curvature is $\beta=M_eL/EI=2\sigma_yL/EH$, where E is the elastic modulus. The solution of equation (4) can be found in Frisch-Fay (1962).

The elastic response ends when the bending moment at the root reaches the elastic limit, $m=1$. The elastic solution is valid only when $\kappa<\beta$ for $0<s<1$, so the applied force f, is limited,

$$f<f_e=\frac{\beta}{2\sin\theta_l}. \tag{5}$$

2.2 Elastoplastic Deformation With Extending Plastic Region, $f_e<f<f_{cr}$. When the load f increases above f_e, a plastic region expands from the root towards the tip. In the plastic region $0<s<l_p$, the stress distribution at a cross-section has an elastic core and is plastic near the top and bottom surfaces. For a rectangular section with bilinear material properties, the relation between the bending moment and the curvature of the neutral axis is

$$m=0.5(3-\rho^2)(1-\alpha)+\alpha/\rho \tag{6}$$

where $\rho=\beta/\kappa$ is the ratio of the radius of curvature to the radius of curvature at the elastic limit and α is the nondimensional plastic strain-hardening modulus.

Equations (3) and (6) give

$$f\cos\theta=\beta^2(1-\alpha)\frac{d^2s}{d\theta^2}+\frac{\alpha}{\beta}\kappa^3\frac{d^2s}{d\theta^2}, \tag{7a}$$

since $$\frac{dm}{d\theta}=\frac{\rho}{\beta}\frac{dm}{ds}=-f\frac{\rho}{\beta}\cos\theta. \tag{7b}$$

Integrating equation (7*a*) and using continuity with the elastic solution at $s=l_p$ gives

Nomenclature

B = width of the cantilever
E = Young's modulus
$E(p)$, $E(p,\phi)$ = complete and incomplete elliptic functions of second kind
F = force
$F(p,\phi)$ = incomplete elliptic function of first kind
H = depth of the cantilever
$K(p)$ = complete elliptic function of first kind
L = length of the cantilever
M = bending moment
M_e = $(BH^2\sigma_y/6)$ bending moment at elastic limit
S = intrinsic coordinate of section from root
X = horizontal coordinate
X_l = horizontal coordinate at tip
Y = vertical coordinate
Y_l = vertical coordinate at tip
f = (FL/M_e) nondimensional tip force
f_e, f_{cr} = forces at elastic limit and beginning of plastic unloading
l_p, l_u, l_{pm} = positions of elastic-plastic interface, loading-unloading interface, and maximum extent of the plastic region, respectively
m = (M/M_e) nondimensional moment at any section
$m^*(s)$ = moment when unloading begins in plastic region
m_u = moment at plastic loading-unloading interface l_u $(m_u=m^*(l_u))$
n = number of calculation steps for plastic unloading stage
q = $\sqrt{f\beta}$
s = (S/L) nondimensional intrinsic coordinate
x = (X/L) nondimensional horizontal coordinate
x_l, x_u, x_p = horizontal coordinate at tip, plastic loading-unloading interface, and elastic plastic interface, respectively
y = (Y/L) nondimensional vertical coordinate
y_l, y_u, y_p = vertical displacements at $s=1$, $s=l_u$, and $s=l_p$, respectively
z = intrinsic coordinate transverse to neutral axis
Δ = $(L-X_l)$ horizontal tip displacement
α = ratio of plastic modulus to elastic Young's modulus
β = (M_eL/EI) nondimensional curvature at yield
δ = (Δ/L) nondimensional horizontal tip deflection
ϵ = strain
$\theta(s)$ = rotation angle
$\theta_l, \theta_p, \theta_u$ = rotation angle at $s=1$, $s=l_p$ and $s=l_u$, respectively
κ = $(d\theta/ds)$ nondimensional curvature
$\kappa^*(s)$ = curvature when unloading begins in plastic region
κ_u = curvature at plastic loading-unloading interface
ρ = $(\beta\,\kappa^{-1})$ radius ratio of curvature to radius of curvature at yield
σ = stress
σ_y = yield stress

Downloaded 03 May 2010 to 171.66.16.31. Redistribution subject to ASME license or copyright; see http://www.asme.org/terms/Terms_Use.cfm

$$\rho^3 - [f(\sin\theta - \sin\theta_p)/\beta + (1-3\alpha/2)]\frac{1}{(1-\alpha)}\rho^2 - \frac{1}{2}\frac{\alpha}{(1-\alpha)} = 0 \tag{7c}$$

since $m=1$, $\kappa=\beta$ and $\theta=\theta_p$ at $s=l_p$.

Solving the cubic equation (7c), we obtain

$$\rho = \begin{cases} \dfrac{\eta}{3(1-\alpha)} + \sqrt[3]{A+\sqrt{C}} + \sqrt[3]{A-\sqrt{C}} & \text{for } \eta^3 > -\dfrac{27}{8}\alpha(1-\alpha)^2 \quad (8a) \\ \dfrac{\eta}{3(1-\alpha)} - 2\gamma\cos\psi & \text{for } \eta^3 < -\dfrac{27}{8}\alpha(1-\alpha)^2 \quad (8b) \end{cases}$$

where $\eta = f(\sin\theta - \sin\theta_\rho)/\beta + (1-3\alpha/2)$,

$$A = \frac{\eta^3}{27(1-\alpha)^3} + \frac{\alpha}{4(1-\alpha)}, \tag{8c}$$

$$C = \frac{\alpha\eta^3}{54(1-\alpha)^4} + \frac{\alpha^2}{16(1-\alpha)^2}, \tag{8d}$$

$$\gamma = \frac{\eta}{3(1-\alpha)}, \tag{8e}$$

and

$$\psi = \frac{1}{3}\cos^{-1}\left[-1 - \frac{27\,\alpha(1-\alpha)^2}{4\eta^3}\right]. \tag{8f}$$

For this case, equation (4a) gives

$$\sin\theta_l = \sin\theta_p + \beta/2f. \tag{9a}$$

For a unit length cantilever with a plastic and an elastic segment,

$$1 - \int_0^{\theta_p} \rho\beta^{-1}d\theta = \int_{\theta_p}^{\theta_l} [2f\beta(\sin\theta_l - \sin\theta)]^{-1/2}d\theta, \tag{9b}$$

where ρ is defined by equations (8). The length of the plastic segment l_p is

$$l_p = \int_0^{\theta_p} \rho\beta^{-1}d\theta. \tag{9c}$$

Equation (9b) can be written in the form of elliptic functions,

$$q(1-l_p) = K(p) - F(p,\phi_2), \tag{10a}$$

where

$$q = \sqrt{f\beta},\ p^2 = 0.5\,(1+\sin\theta_l),\ \phi_2 = \sin^{-1}\sqrt{(1+\sin\theta_p)/2p^2} \tag{10b-d}$$

and K and F are complete and incomplete elliptic functions of first kind, respectively.

Now, we can obtain θ_p, θ_l, and l_p from equations (10) with equations (8) and (9a). Therefore, with the aid of equation (9a) we obtain

$$x_l = x_p + [2(\sin\theta_l - \sin\theta_p)]^{1/2}/q = x_p + 1/f, \tag{11a}$$

$$y_l = y_p + [K(p) - 2E(p) - F(p,\phi_2) + 2E(p,\phi_2)]/q \tag{11b}$$

and

$$\delta = 1 - x_l = 1 - x_p - 1/f, \tag{11c}$$

where

$$x_p = \int_0^{\theta_p} \rho\beta^{-1}\cos\theta\,d\theta \text{ and } y_p = \int_0^{\theta_p} \rho\beta^{-1}\sin\theta\,d\theta \tag{11d,e}$$

are the horizontal and vertical coordinates of the point $s=l_p$, ρ is defined by equations (8), and $E(p)$ and $E(p,\phi_2)$ are complete and incomplete elliptic functions of second kind, respectively.

For a given value of s, the rotation angle in the elastoplastic region can be obtained from equations (8), while in the elastic region equation (4a) applies. Hence, the coordinates of any point s are

$$x = \begin{cases} \displaystyle\int_0^{\theta} \rho\beta^{-1}\cos\theta\,d\theta & \text{for } 0<s<l_p \\ x_p - \sqrt{2}[(\sin\theta_l - \sin\theta)^{1/2} - (\sin\theta_l - \sin\theta_p)^{1/2}]/q & \text{for } l_p<s<1 \end{cases} \tag{12a}$$

$$y = \begin{cases} \displaystyle\int_0^{\theta} \rho\beta^{-1}\sin\theta\,d\theta & \text{for } 0<s<l_p \\ y_p + [F(p,\phi) - 2E(p,\phi) - F(p,\phi_2) + 2E(p,\phi_2)]/q & \text{for } l_p<s<1 \end{cases} \tag{12b}$$

where

$$\phi = \sin^{-1}\sqrt{(1+\sin\theta)/2p^2}. \tag{12c}$$

Extension of the plastically deforming region is limited by large deflection effects. The critical force, f_{cr}, where unloading begins in some plastically deformed sections as the force continues to increase, can be obtained from $dl_p/df=0$. The solution for f_{cr} is given in the Appendix.

2.3 Elastoplastic Deformation With Partial Unloading, $f>f_{cr}$. The plastic region reaches a maximum length l_{pm} at $f=f_{cr}$. For $f>f_{cr}$, the unloading response which originates at the tip extends into the plastic region. Therefore, with increasing force f, the change in bending moment increases in $0<s<l_u$ and decreases in $l_u<s<1$ where $l_u<l_{pm}$. The plastically-deforming region $0<s<l_u$ shrinks as the load f increases.

The bending moment and curvature in the plastic unloading segment are reduced from maximum values m^* and κ^* which occurred at a smaller load. The relation between the bending moment and curvature in this segment is

$$m = m^* + \Delta\kappa/\beta, \tag{13}$$

where the accumulated reduced curvature during unloading is $\Delta\kappa = \kappa - \kappa^*$.

Differentiating equations (3) and (13), with respect to s, we obtain

$$\frac{1}{\beta}\frac{d^2\theta}{ds^2} + f\cos\theta = -\frac{d\mu}{ds}, \tag{14a}$$

where

$$\mu = m^* - \kappa^*/\beta \tag{14b}$$

since $\dfrac{dm}{ds} = -f\cos\theta$.

Therefore, with continuity conditions for curvature and rotation angle, the plastica and elastica equations for this range of applied load are as follows.

Plastic Loading Region, $0<s<l_u$.

Downloaded 03 May 2010 to 171.66.16.31. Redistribution subject to ASME license or copyright; see http://www.asme.org/terms/Terms_Use.cfm

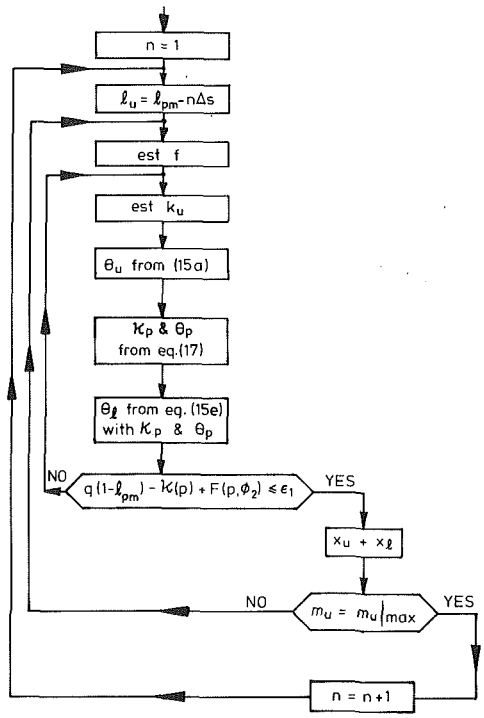


Fig. 2 Flow diagram for loads resulting in partial plastic unloading ($f > f_{cr}$)

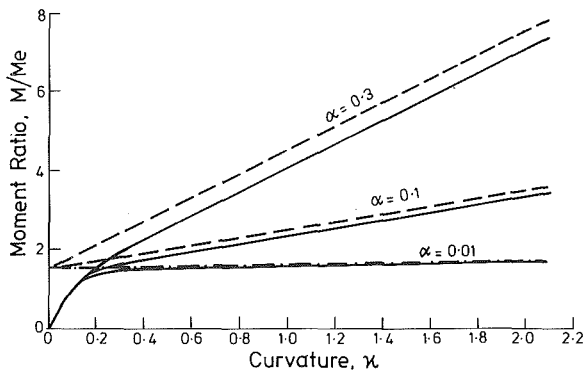


Fig. 3 Bending moment as a function of curvature ($\beta = 0.1$): ——— elastic, linear hardening stress-strain relation; — — — rigid, linear hardening moment-curvature relation

$$\left.\frac{d\theta}{ds}\right|_{s+\Delta s} = -\beta\left[f\cos\theta_s + \frac{\mu(s+\Delta s)-\mu(s)}{\Delta s}\right]\Delta s + \left.\frac{d\theta}{ds}\right|_s \tag{17a}$$

and

$$\theta_{s+\Delta s} = -\beta\left[f\cos\theta_s + \frac{\mu(s+\Delta s)-\mu(s-\Delta s)}{2\Delta s}\right]\Delta s^2 + 2\theta_s - \theta_{s-\Delta s} \tag{17b}$$

$$\rho = \begin{cases} \dfrac{\eta_u}{3(1-\alpha)} + \sqrt[3]{A_u+\sqrt{C_u}} + \sqrt[3]{A_u-\sqrt{C_u}} & \text{when } \eta_u^3 > -\dfrac{27}{8}\alpha(1-\alpha)^2 \quad (15a) \\ \dfrac{\eta_u}{3(1-\alpha)} - 2\gamma_u\cos\psi & \text{when } \eta_u^3 < -\dfrac{27}{8}\alpha(1-\alpha)^2 \quad (15b) \end{cases}$$

where $\eta_u = f\beta^{-1}(\sin\theta - \sin\theta_u) + (1-\alpha)\rho_u - \alpha/2\rho_u^2$,

θ_u and ρ_u are the rotation angle and radius of curvature at $s = l_u$, respectively. A_u, C_u, γ_u, and ψ are defined by equations (8c), (8d), (8e), and (8f), respectively, with η replaced by η_u.

Plastic Unloading Region, $l_u < s < l_{pm}$.

$$\frac{1}{\beta}\frac{d^2\theta}{ds^2} + f\cos\theta = -\frac{d\mu}{ds} \tag{15c}$$

where

$$\mu = \left(\frac{3}{2} - \frac{\beta^2}{2\kappa^{*2}} - \frac{\kappa^*}{\beta}\right)(1-\alpha). \tag{15d}$$

The function μ satisfies continuity of m and κ at the interface between the plastic loading and plastic unloading region with the relation between m^* and κ^* defined by equation (6).

Elastic Region, $l_{pm} < s < 1$.

$$\kappa = \sqrt{2f\beta\,(\sin\theta_l - \sin\theta)} \tag{15e}$$

2.4 Numerical Solution for Elastoplastic Unloading Stage. For any load $f > f_{cr}$, the loading-unloading interface l_u is within the plastically deformed region $0 < l_u < l_{pm}$. The bending moment, m_u, is present at the interface section, l_u,

$$m_u = (x_l - x_u)f. \tag{16}$$

This is the maximum moment for any section in the unloading region and it determines the final distribution of plastic deformation. This local maximum moment can be determined from equation (15), using a finite difference method to evaluate equation (15c),

where $\Delta s = l_{pm}/n$ is the step length, n is the number of steps, and $l_u < s < l_{pm}$.

The solution for $f > f_{cr}$ is obtained step-by-step as the plastic loading region decreases, $l_u = l_{pm} - n\Delta s$. When searching for the section with a maximum value of bending moment m_u as load f varies, the value of m_u for a given f is obtained by solving the elastica and plastica equations (15a), (15e), and (17). Simultaneously, the elastica and plastica equations must be solved by finding ρ_u (or θ_u) which satisfies equations (15) when l_p is replaced by l_{pm}. Standard NAG optimization programs were used for finding the maximum value of m_u as the load f varied and for finding ρ_u which satisfies the elastica and plastica equations (15). The flow diagram for this calculation is illustrated in Fig. 2.

3 Discussion

The moment-curvature relation (6) that results from the bilinear stress-strain relation in a rectangular cross-section is shown in Fig. 3 for three values of the strain-hardening modulus. These curves are compared with the rigid-linear strain-hardening moment-curvature approximation. There is a significant difference for small curvature only when the modulus ratio α is small. When α is large, however, there is a significant difference between these two curves even when the curvature κ is large. This difference increases with β.

Typical deformation profiles and bending moment distributions for an elastoplastic cantilever with vertical force at the tip are shown in Figs. 4(a) and 4(b), respectively. For a slender cantilever with $\beta = \alpha = 0.1$, a plastic region extends from the root towards the tip when $1.0007 < f < f_{cr} = 9.441$. The length of the plastically-deforming segment increases with

Downloaded 03 May 2010 to 171.66.16.31. Redistribution subject to ASME license or copyright; see http://www.asme.org/terms/Terms_Use.cfm

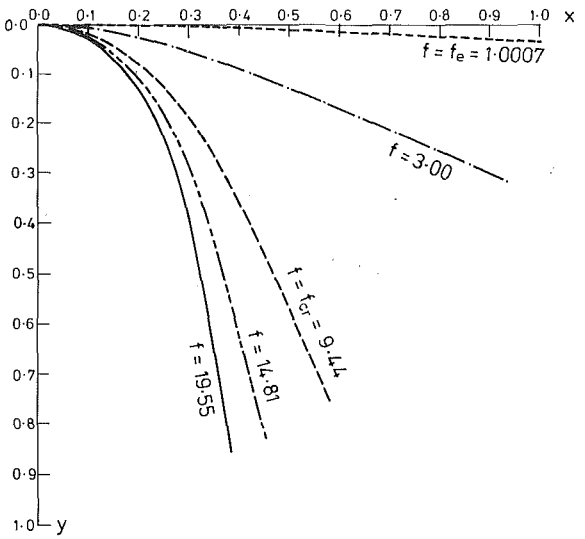


Fig. 4(a)

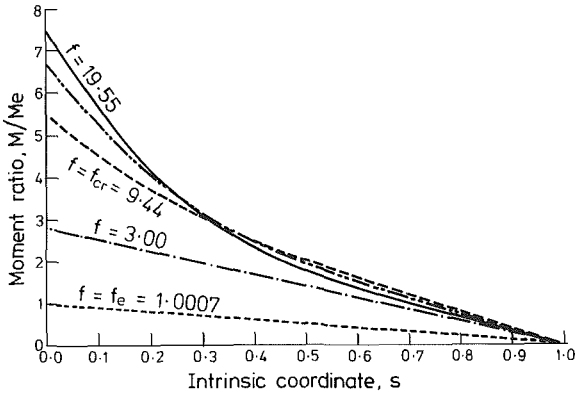


Fig. 4(b)

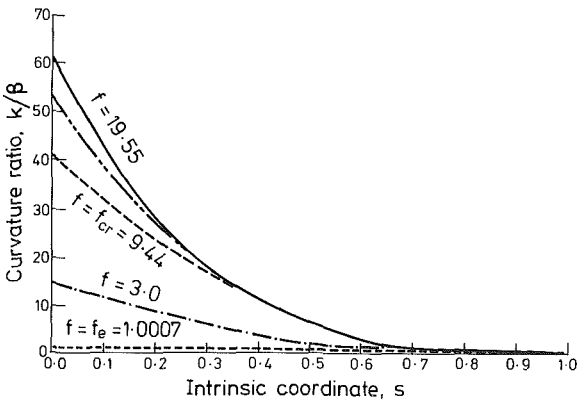


Fig. 4(c)

Fig. 4 Deformed configuration, moment distribution, and curvature distribution ($\alpha = 0.1$, $\beta = 0.1$)

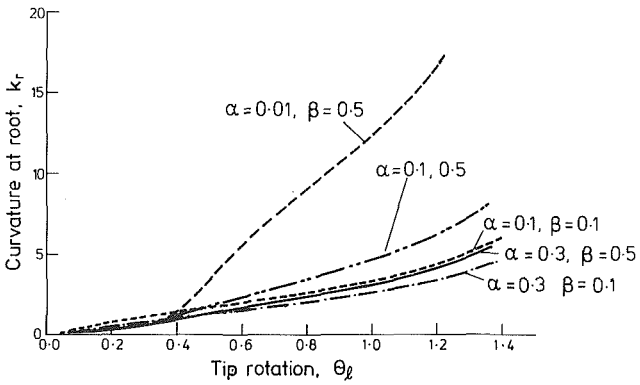


Fig. 5 Curvature at root κ_r as the tip rotates θ_l

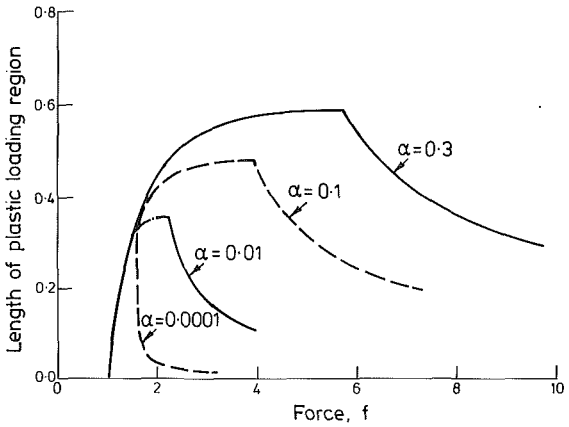


Fig. 6 Length of plastic loading segment ($\beta = 0.5$)

f until f_{cr} when unloading of plastically deforming sections begins at the furthest extent of this region, $l_{pm} = 0.74$. As the force increases to $f = 14.813$, the plastically deforming segment shrinks from 0.74 to 0.296; beyond this loading segment the bending moment at every section decreases elastically as the force increases (Fig. 4*b*). When $f = 19.546$, the plastically deforming segment has length $l_u = 0.222$. Although the bending moment in the unloading segment decreases with increasing force, elastic unloading from a plastically deformed state results in insignificant changes in the curvature (4*c*). The effects of unloading for the deformation are very small because the increasing force and tip rotation combine to cause only a small decrease in the bending moment at unloading sections.

Calculations of the tip deflection at maximum extent of plastic deformation are listed in Table 1, for elastic flexibility $\beta = 0.1$, 0.5, and strain-hardening modulus ratios $0 < \alpha < 0.3$. For $\alpha = 0$, the material is elastic-perfectly plastic, while $\alpha = 1.0$ corresponding to elastic materials. Sections with the same elastic flexibility β have a critical load f_{cr} that increases with the modulus ratio α. The maximum extent of the plastically deforming segment l_{pm} is larger for thick sections (small β) and for more strain-hardening. Slender cantilevers (larger β) with small strain-hardening have deformation more localized near the root since, for the same rotation of the tip, the curvature κ at the root increases with the increase of β and with the decrease of α, as shown in Fig. 5. The variation of the length of the plastically deforming segment with the load f is shown in Fig. 6. As the load f increases above f_{cr}, there is a very rapid expansion of the segment that is elastically unloading from a plastically deformed state.

The transverse displacement at the tip for $\beta = 0.5$ and different values of strain-hardening α are plotted in Fig. 7 as a function of load f. The tip displacement y_l is not significantly affected by unloading, although the bending moment distribution varies slightly.

This calculation was stopped when the tip rotation was larger than 1.4 radian. Wu and Yu (1986) have shown that reverse yielding can occur for larger rotations. Also, with very large rotations, the effects of axial force may become significant.

A comparison between the elastoplastic theory and available experimental data of Reid and Reddy (1978) for cold-drawn mild steel cantilevers is given in Fig. 8. Good agreement is achieved for the deflection when a revised

Downloaded 03 May 2010 to 171.66.16.31. Redistribution subject to ASME license or copyright; see http://www.asme.org/terms/Terms_Use.cfm

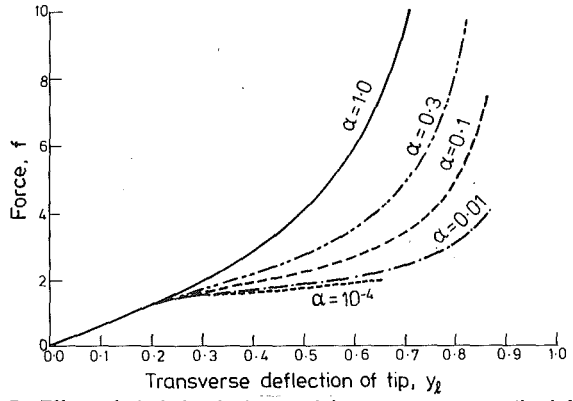


Fig. 7 Effect of strain-hardening modulus α on transverse tip deflection y_l ($\beta = 0.5$)

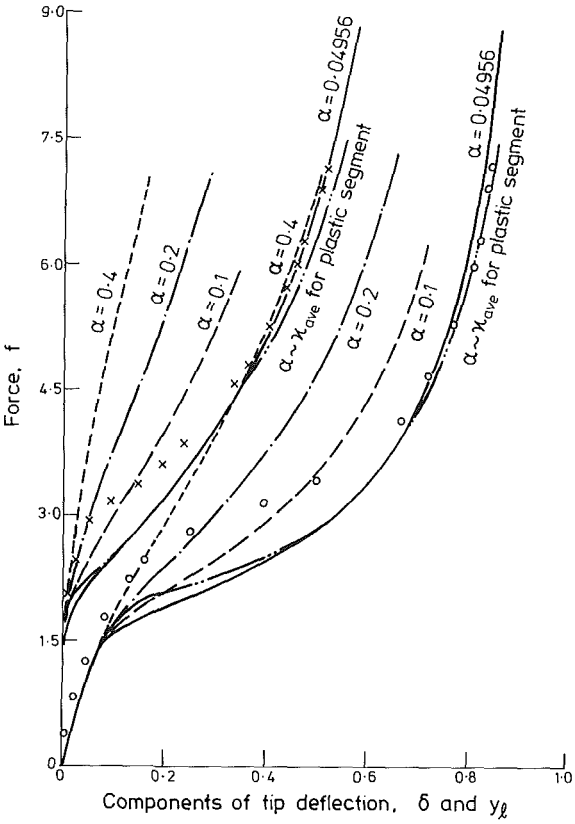


Fig. 8 Comparison between elastoplastic theory and experimental results ($\beta = 0.1475$); experimental results [2]: o transverse displacement, x horizontal displacement; (1) transverse deflection at tip y_l and (2) horizontal deflection at tip δ

modulus ratio α is used[3]. However, our calculated length of the plastically deformed segment $l_{pm} = 0.6$ is larger than the measurements of residual deformed length, $l_{pm} = 0.43$. This discrepency between the theory and experimental measurement may occur because the change in curvature in this region is too small to be detected.

With increasing load, the final tip deflection rapidly increases at $f = 2.5$ in Fig. 8 due to the development of a plastically deforming segment near the root; at this load the plastic segment encompasses almost 40 percent of the cantilever length. Within this segment the variation in the bending moment is relatively small, and the curvature is near the elastic limit β; hence, this is the load where the load-deflection curve is most sensitive to the bilinear approximation for the stress-strain relation. The experimental stress-strain curve for this segment of the mild steel cantilever has a modulus in the range $0.04 < \alpha < 1.0$, while the best fit to the experimental curve corresponding to the average curvature in the plastic segment is $\alpha = 0.04956$.

Acknowledgment

The authors wish to thank Prof. S. R. Reid and Dr. T. Yella Reddy for additional data from their 1978 experiments.

References

Frisch-Fay, R., 1962, *Flexible Bars*, Butterworths, Washington, D.C.

Reddy, T. Y., 1988, Personal Communication, July.

Reid, S. R., and Reddy, T. Y., 1978, "Effect of Strain Hardening on the Large Plastic Deformation of a Cantilever," ASME JOURNAL OF APPLIED MECHANICS, Vol. 45, pp. 953-955.

Wu, S., and Yu, T. X., 1986, "The Complete Process of Large Elastic-Plastic Deflection of a Cantilever," *Acta Mech. Sinica*, Vol. 2, pp. 333-347.

APPENDIX

Critical force f_{cr} corresponding to maximum plastic loading length l_{pm}

The length of the plastic loading segment is a maximum when

$$\frac{dl_p}{df} = \frac{\partial l_p}{\partial f} + \frac{\partial l_p}{\partial \theta_p}\frac{d\theta_p}{df} = 0 \qquad (A1a)$$

where

$$\frac{\partial l_p}{\partial f} = \int_o^{\theta_p} \beta^{-1}\frac{\partial \rho}{\partial f}\, d\theta, \qquad (A1b)$$

$$\frac{\partial l_p}{\partial \theta_p} = \int_o^{\theta_p} \beta^{-1}\frac{\partial \rho}{\partial \theta_p}\, d\theta + \frac{1}{\beta} \qquad (A1c)$$

and ρ is defined by equations (8), since $\rho_p = 1$.

Differentiating equations (8) gives

$$\frac{\partial \rho}{\partial \lambda} = \begin{cases} \dfrac{1}{3(1-\alpha)}\dfrac{\partial \eta}{\partial \lambda} - \dfrac{2}{3(1-\alpha)}\left[\dfrac{\partial \eta}{\partial \lambda}\cos\psi - \eta \sin\psi \dfrac{\partial \psi}{\partial \lambda}\right] & \text{for } C<0 \\ \dfrac{1}{3(1-\alpha)}\dfrac{\partial \eta}{\partial \lambda} + \left(\dfrac{\partial A}{\partial \lambda} + \dfrac{1}{2\sqrt{C}}\dfrac{\partial C}{\partial \lambda}\right)(A+\sqrt{C})^{-2/3}/3 + & \\ \quad + \left(\dfrac{\partial A}{\partial \lambda} - \dfrac{1}{2\sqrt{C}}\dfrac{\partial C}{\partial \lambda}\right)(A-\sqrt{C})^{-2/3}/3 & \text{for } C>0 \end{cases} \qquad (A2a)$$

where λ represents either f or θ_p, and

$$\frac{\partial \eta}{\partial \lambda} = \begin{cases} (\sin\theta - \sin\theta_p)/\beta & \text{if } \lambda = f \\ -f\beta^{-1}\cos\theta_p & \text{if } \lambda = \theta_p \end{cases} \qquad (A2b)$$

[3] The average strain in the plastic region was estimated and the corresponding modulus ratio α was obtained from the stress-strain curve for the experimental specimens (Reddy, 1988).

Downloaded 03 May 2010 to 171.66.16.31. Redistribution subject to ASME license or copyright; see http://www.asme.org/terms/Terms_Use.cfm

$$\frac{\partial \psi}{\partial \lambda} = -\frac{1}{3\sqrt{1-\xi^2}} \frac{\partial \xi}{\partial \lambda}, \quad \frac{\partial \xi}{\partial \lambda} = \frac{81\alpha\,(1-\alpha)^2}{4\eta^4} \frac{\partial \eta}{\partial \lambda}, \tag{A2c,d}$$

$$\xi = \cos 3\psi = -1 - \frac{27\alpha\,(1-\alpha)^2}{4\eta^3}, \quad \frac{\partial A}{\partial \lambda} = \frac{\eta^2}{9\,(1-\alpha)^3} \frac{\partial \eta}{\partial \lambda} \tag{A2e,f}$$

and

$$\frac{\partial C}{\partial \lambda} = \frac{\alpha}{2(1-\alpha)} \frac{\partial A}{\partial \lambda}. \tag{A2g}$$

Equations (9*a*) and (10*c*) give

$$\theta_p = \arcsin\,(2p^2 - 1 - \beta/2f) \tag{A3a}$$

or

$$\frac{d\theta_p}{df} = \frac{1}{\cos\theta_p}\left(\frac{\beta}{2f^2} + 4p\frac{dp}{df}\right), \tag{A3b}$$

since

$$\frac{d\theta_p}{df} = \frac{\partial \theta_p}{\partial f} + \frac{\partial \theta_p}{\partial p}\frac{dp}{df}. \tag{A3c}$$

Substituting equations (*A*2) and (*A*3) into equations (*A*1) with θ_p given by equation (*A*3*a*), we obtain

$$\mu_1\left(\frac{dp}{df}, p, f\right) = 0. \tag{A4}$$

Equations (10) also give

$$l_p = 1 - \frac{1}{\sqrt{f\beta}}\,[K(p) - F(p,\phi_2)]$$

or

$$\frac{dl_p}{df} = \frac{1}{2f\sqrt{f\beta}}\,[K(p) - F(p,\phi_2)] - \frac{1}{\sqrt{f\beta}}\frac{d}{df}\,[K(p) - F(p,\phi_2], \tag{A5a}$$

where

$$\frac{d}{df}\,[K(p) - F(p,\phi_2)] = \frac{dK(p)}{dp}\frac{dp}{df} - \left[\frac{\partial F(p,\phi_2)}{\partial p}\frac{dp}{df} + \frac{\partial F(p,\phi_2)}{\partial \phi_2}\frac{d\phi_2}{df}\right]. \tag{A5b}$$

It can be shown that

$$\frac{dK(p)}{dp} = \frac{E(p) - (1-p^2)K(p)}{p(1-p^2)}, \tag{A6a}$$

$$\frac{\partial F(p,\phi_2)}{\partial p} = \frac{E(p,\phi_2) - (1-p^2)F(p,\phi_2)}{p(1-p^2)} - \frac{p\,\sin\phi_2\,\cos\phi_2}{(1-p^2)\sqrt{1-p^2\sin^2\phi_2}}, \tag{A6b}$$

$$\frac{\partial F(p,\,\phi_2)}{\partial \phi_2} = \frac{1}{\sqrt{1-p^2\sin^2\phi_2}} \tag{A6c}$$

and

$$\frac{d\phi_2}{df} = \left(\frac{1}{p}\frac{dp}{df} + \frac{1}{2f}\right)/\sqrt{4p^2f/\beta - 1}, \tag{A6d}$$

since

$$\phi_2 = \arcsin\sqrt{1 - \beta/4p^2f}. \tag{A6e}$$

Substituting equations (*A*6) into (*A*5) with $dl_p/df = 0$, we obtain

$$\frac{dp}{df} = p(1-p^2)\{D[K(p) - F(p,\phi_2)] + 1\}/2fD_1, \tag{A7a}$$

where

$$D = \sqrt{(1 - p^2 + \beta/4f)\,(4p^2f/\beta - 1)}. \tag{A7b}$$

$$D_1 = \{E(p) - E(p,\phi_2) - (1-p^2)[K(p) - F(p,\phi_2)]\}D + (2p^2 - 1 - \beta/4f) \tag{A7c}$$

Therefore, the critical plastic loading force f_{cr} can be obtained from equations (*A*4) and (*A*7).

Downloaded 03 May 2010 to 171.66.16.31. Redistribution subject to ASME license or copyright; see http://www.asme.org/terms/Terms_Use.cfm

Wave Propagation Through Elastically-Anisotropic Fluid-Saturated Porous Rocks

P. J. Digby
Division of Rock Mechanics,
University of Luleå,
S-951 87 Luleå, Sweden

K. Walton
School of Mathematical Sciences,
University of Bath,
Claverton Down,
Bath BA2 7AY, U.K.

An elastically-anisotropic sedimentary rock is modeled by a simple cubic packing of identical, contacting spherical particles. The connected pore space is filled with an inviscid, compressible fluid. A set of averaged equations is derived to relate the constitutive and dynamic coupling coefficients, and hence also the effective wave speeds in any given direction explicitly to the microstructural properties of the rock considered. Simple, explicit results are obtained when the propagation of either a purely longitudinal or a purely transverse wave is considered.

1 Introduction

Walton and Digby (1987) studied the basic equations for wave propagation in a fluid-saturated granular rock. Here, a sedimentary rock, assumed to be elastically isotropic and homogeneous over lengths large compared with a typical grain diameter, was modeled by a random packing of identical, contacting spherical particles. A low frequency expansion technique was used to relate all of the coefficients appearing in Biot's equations (1956) explicitly to the microstructural properties of the rock considered. To our knowledge, this exercise has been performed successfully for the important case of fluid-saturated elastically-anisotropic granular rocks in only a very limited number of special cases. Walton (1977), for example, considered purely longitudinal wave propagation through a fluid-saturated granular rock, whose framework is modeled by a simple cubic packing of identical, contacting spherical particles. The connected pore space was filled with an inviscid, compressible fluid. In the present paper, we consider an identical regular packing model for a fluid-saturated elastically-anisotropic sedimentary rock. We then generalize Walton's original treatment, (1977), by deriving a set of equations directly applicable to the study of wave propagation in any given direction. In particular, this set of averaged equations may be used to calculate wave speeds in any given direction explicitly in terms of the microstructural properties of the rock considered. Although the effect of the pore fluid viscosity plays an important role in applications of Biot's equations, this has not been considered in the present paper. However, the effect of both the pore fluid pressure and the initial confining pressure to which the rock is subjected can be included in our calculations.

In this paper, we show how the results originally obtained by Walton (1977) for the purely longitudinal wave speeds through a fluid-saturated simple cubic packing model of a porous rock may be obtained directly as a special case from the equations obtained in the present paper. The corresponding simple closed-form expression (not previously obtained) for the purely transverse wave speed will also be presented.

2 The Low Frequency Expansion Technique, the Averaging Procedure, and Some Preliminary Definitions

(a) The Governing Microstructural Equations. With the $e^{-i\omega t}$ time-dependence suppressed (steady-state disturbance of frequency ω), the equations of motion governing vibrations about an equilibrium state are

$$\left.\begin{aligned} &\sigma_{ij,j} = -\rho_s \omega^2 u_i \\ &\sigma_{ij} = \lambda \delta_{ij} u_{k,k} + \mu(u_{i,j} + u_{j,i}) \end{aligned}\right\} \quad \text{in the solid grains} \qquad (1)$$

and

$$\left.\begin{aligned} &p_{,i} = \rho_f \omega^2 v_i \\ &p = -\kappa_f \, v_{k,k} \end{aligned}\right\} \quad \text{in the inviscid pore fluid} \,. \qquad (2)$$

The standard suffix notation is used throughout this paper. δ_{ij} denotes the usual Kronecker delta symbol. ρ_s, λ, and μ denote the density and Lamé coefficients of the solid grains (assumed to be elastically isotropic and homogeneous). ρ_f and κ_f denote the density and bulk modulus of the homogeneous pore fluid component (assumed to be inviscid and compressible). σ_{ij} and u_i denote the increments in the cartesian components of the Cauchy stress tensor and displacement vector, respectively, for the solid component. Similar remarks apply to the fluid displacement vector $\mathbf{v}$ and the fluid pressure p for the fluid component. Across the solid-fluid boundaries we also require continuity of the normal displacements and the traction, that is

$$n_k u_k = n_k v_k$$

and (3)

Contributed by the Applied Mechanical Division of THE AMERICAN SOCIETY OF MECHANICAL ENGINEERS for publication in the JOURNAL OF APPLIED MECHANICS.

Discussion on this paper should be addressed to the Editorial Department, ASME, United Engineering Center, 345 East 47th Street, New York, N.Y. 10017, and will be accepted until two months after final publication of the paper itself in the JOURNAL OF APPLIED MECHANICS. Manuscript received by the ASME Applied Mechanics Division June 10, 1988; final revision, January 19, 1989.

Copyright © 1989 by ASME

Downloaded 03 May 2010 to 171.66.16.31. Redistribution subject to ASME license or copyright; see http://www.asme.org/terms/Terms_Use.cfm

$$\sigma_{ij}n_j = -pn_i$$

where, in equation (3), n_i denotes a component of the unit normal to the fluid-solid boundary pointing out of the solid, that is, into the pore fluid.

(b) The Low Frequency Power Series Expansion. We use the technique developed in Walton and Digby (1987). Thus each field quantity appearing in equations (1)–(3), for example, σ_{ij}, is written in the form

$$\sigma_{ij} = \sigma_{ij}^{(0)} + \omega\sigma_{ij}^{(1)} + \omega^2\sigma_{ij}^{(2)} + . \tag{4}$$

The superscripts in equation (4) denote the order of approximation used. As in our earlier work, all our equations will be expressed in terms of the physical frequency, ω, for convenience. The power series above (equation (4)) is supposed to be valid only for those frequencies ω for which the effective wavelength of a wave propagation through an infinite medium made of the fluid saturated granular material would be much larger than the grain radius R.

(c) Definitions of the Averaged Field Quantities. The average of the stress component $\sigma_{ij}(\mathbf{x})$, for example, denoted by $<\sigma_{ij}> = <\sigma_{ij}>(\mathbf{X})$ is defined by

$$<\sigma_{ij}> = \frac{1}{V}\int_{V_s} \sigma_{ij}(\mathbf{x})\, dV_x. \tag{5}$$

The integral in equation (5) is taken over the volume of solid V_s contained in the averaging volume (the so-called "representative volume element"), of total volume V. Formally, therefore, our definitions for the averaged field quantities are identical to those adopted in our earlier work. Our representative volume element, however, is defined by a cube of side $2R$ (the grain diameter) always having its sides parallel to the line of centers of adjacent, contacting spheres and centered on $\mathbf{X}$, where $\mathbf{X}$ is any point in the medium we are considering. Definitions similar to these are also adopted for those field quantities defined only over the volume V_f of the fluid contained in our averaging cube. Throughout this paper, differentiation of averaged field quantities is taken with respect to the components of the position vector $\mathbf{X}$ of the centroid. For example, equations of the type

$$<\sigma_{ij}>_{,j} = \frac{\partial<\sigma_{ij}>}{\partial X_j} = \frac{1}{V}\int_{S_s} \sigma_{ij}n_j dS_x \tag{6}$$

which arise frequently in later sections of this paper, follow directly from equations (5). Here, S_s denotes the external bounding surface of our representative volume element intersected by the solid grains, having a unit normal n_j and an element of area dS_x. As in our earlier work, we now present two basic equations (see equations (10) and (11) of Walton and Digby (1987)) which will be used in later sections of this paper. These equations may be written in the form

$$\frac{<\sigma_{kk}>}{3\kappa_s} - \frac{<p>}{\kappa_f} = <u_j>_{,j} + <v_j>_{,j} \tag{7}$$

and

$$<\sigma_{ij}>_{,j} - <p>_{,i} = -\rho_s\omega^2<u_i> - \rho_f\omega^2<v_i>. \tag{8}$$

Both of these equations are obtained by application of the boundary conditions (3) to equations (1) and (2). They are valid at all orders of approximation in the power series representation (4). Identical equations hold no matter what packing is used to model the rock we are considering.

3 Some Basic Results Derived From the Low Frequency Expansion Technique

These are all obtained by first substituting the power series expansion of the type (4) into the basic microstructural equations (1)–(3) and then equating coefficients of like powers of ω. Full details are given in Walton and Digby (1987). We therefore present only the essential results here. All of these are, in fact, valid for any choice of representative volume. They may be summarized as follows:

Zeroth-Order Fluid Motion: There exists a displacement potential $\phi^{(0)}$ such that

$$\mathbf{v}^{(0)} = \nabla\phi^{(0)}. \tag{9}$$

Furthermore, $\phi^{(0)}$ is harmonic, that is,

$$\nabla^2\phi^{(0)} = 0 \tag{10}$$

and on the inner boundaries (the solid-fluid interface),

$$u_k^{(0)}n_k = v_k^{(0)}n_k. \tag{11}$$

Also, it can be shown that throughout the fluid,

$$p^{(0)} = 0. \tag{12}$$

Zeroth-Order Solid Motion: It can be shown that the zeroth-order displacement vector $\mathbf{u}^{(0)}$ corresponds to a rigid body translation, that is

$$\mathbf{u}^{(0)} = \text{constant (throughout the solid)}. \tag{13}$$

First-Order Fluid Motion: It can be shown that throughout the fluid,

$$p^{(1)} = \text{constant}. \tag{14}$$

First-Order Solid Motion: Throughout the solid, we have,

$$\sigma_{ij\ j}^{(1)} = 0$$

$$\sigma_{ij}^{(1)} = \mu(u_{i,j}^{(1)} + u_{j,i}^{(1)}) + \lambda\delta_{ij}u_{k,k}^{(1)} \tag{15}$$

and on the inner boundaries,

$$n_k u_k^{(1)} = n_k v_k^{(1)} \tag{16}$$

and

$$\sigma_{ij}^{(1)}n_j = -n_i p^{(1)}.$$

Second-Order Fluid Motion:

$$p^{(2)} = \rho_f\phi^{(0)} + \text{constant} \tag{17}$$

where $\phi^{(0)}$ satisfies equation (10).

4 Derivation of the Equations for the Fluid Motion From the Low Frequency Expansion Technique

(a) Description of the Problem. As in Walton and Digby (1987), the second equation of motion (corresponding to equation (35) of Walton and Digby (1987)) is obtained by considering the zeroth-order fluid motion which is completely determined by the function $\phi^{(0)}$. However, equations (9)–(11) are insufficient to determine $\phi^{(0)}$ uniquely. The remaining conditions are obtained by using the fact that the zeroth-order motion is that in which the respective motions are, on average, constant. Since the granular rock is modeled by a simple cubic packing of identical contacting spherical particles, each of radius R, the medium is periodic, of period $2R$, in each of the coordinate directions and, hence, the zeroth-order fluid velocity, $\mathbf{v}^{(0)}$, must also be periodic and with the same period. To determine $\phi^{(0)}$, consider the particular averaging cube containing one complete spherical grain and take the origin at the center of this sphere. The periodicity conditions may be written in the form

$$\begin{aligned}
&\mathbf{v}^{(0)}(x_1,x_2,R) = \mathbf{v}^{(0)}(x_1,x_2,-R)\\
&\mathbf{v}^{(0)}(x_1,R,x_3) = \mathbf{v}^{(0)}(x_1,-R,x_3), -R \le x_1,x_2,x_3 \le R\\
&\mathbf{v}^{(0)}(R,x_2,x_3) = \mathbf{v}^{(0)}(-R,x_2,x_3).
\end{aligned} \tag{18}$$

It is worth noting that, for example, the first of these implies that $\phi^{(0)}(x_1,x_2,R) - \phi^{(0)}(x_1,x_2,-R) = \text{constant}$ and

Downloaded 03 May 2010 to 171.66.16.31. Redistribution subject to ASME license or copyright; see http://www.asme.org/terms/Terms_Use.cfm

$\phi^{(0)}{}_{,3}(x_1,x_2,R) = \phi^{(0)}{}_{,3}(x_1,x_2,-R)$ and similarly for the other two equations.

(b) **Method of Solution.** We must now determine the form of solution for the fluid displacement potential $\phi^{(0)}$ in the flow problem previously described. To make use of the geometrical symmetries involved, we first introduce the notation f_{EEo} to denote any function of the three variables x_1, x_2, and x_3 which is even in both x_1 and x_2 but odd in x_3. Any other three subscripts to the symbol f, formed from the letters E and o (for example f_{ooo} or f_{Eoo}) will define other functions of x_1, x_2, and x_3 having analogous properties. We can then write $\phi^{(0)}$ as a linear combination of odd and even functions of this type. Thus, we write

$$\phi^{(0)} = \phi_{EEE} + \phi_{EEo} + \phi_{EoE} + \phi_{oEE} + \phi_{Eoo} + \phi_{oEo} + \phi_{ooE} + \phi_{ooo}. \tag{19}$$

Each one of these eight functions satisfies Laplace's equation in the fluid region V_f. We also impose the boundary conditions (11)–(13), together with the periodicity conditions (18) on the flow defined by each of the eight functions on the right-hand side of equation (19). For ϕ_{ooo} these reduce to $(\hat{n}\cdot\nabla)\phi_{ooo} = 0$ on the inner boundary and $\phi_{ooo} = 0$ on the sides, which imply that ϕ_{ooo} is identically zero. Similarly, it is possible to show that each of the functions ϕ_{ooE}, ϕ_{oEo}, and ϕ_{Eoo} vanishes throughout the fluid, and ϕ_{EEE} is also, at most, a constant throughout the fluid. We can also show that the three remaining potential functions, ϕ_{oEE}, ϕ_{EoE}, and ϕ_{EEo} in equation (19) take constant values on each of the surfaces $x_i = \pm R$ for $i = 1$, 2, and 3, respectively. The fluid displacement potential $\phi^{(0)}$ may now, therefore, be written in the form

$$\begin{aligned}\phi^{(0)} &= \text{constant} + \phi_{oEE} + \phi_{EoE} + \phi_{EEo} \\ &= \mathbf{u}^{(0)}\cdot\mathbf{r} + K + (\boldsymbol{\Phi} - \mathbf{u}^{(0)})\cdot\boldsymbol{\psi}\,(x_1,x_2,x_3).\end{aligned} \tag{20}$$

In equations (20), $\mathbf{u}^{(0)}$ (equation (13)), and $\boldsymbol{\Phi} = (\Phi_1,\Phi_2,\Phi_3)$ are constant vectors, $\mathbf{r} = (x_1,x_2,x_3)$, and K is a constant scalar. $\boldsymbol{\psi}$, in equation (20), is also a vector potential function of the type

$$\begin{aligned}\boldsymbol{\psi} &= (\psi_1,\psi_2,\psi_3) \\ &= (\psi_{oEE}, \psi_{EoE}, \psi_{EEo})\end{aligned} \tag{21}$$

where

$$\begin{aligned}\psi_i &= \pm R \text{ on } x_i = \pm R \\ \psi_{i,j} &= 0 \text{ on } x_j = \pm R \text{ for } i \neq j\end{aligned} \qquad (i,j = 1,2,3) \tag{22}$$

and

$$(\hat{n}\cdot\nabla)\boldsymbol{\psi} = \mathbf{0} \text{ on the solid-fluid interface.} \tag{23}$$

The general flow problem we have considered in equations (21)–(23) corresponds to the flow generated by the rigid body translation $\mathbf{u}^{(0)}$ of a spherical grain in any given direction. In equations (20), we also see that $\phi^{(0)}$ is written as a linear combination of three fluid displacement potentials ϕ_{oEE}, ϕ_{EoE}, and ϕ_{EEo} corresponding to the flow generated by rigid body translations $u_1{}^{(0)}$, $u_2{}^{(0)}$, and $u_3{}^{(0)}$ of a spherical grain in the three orthogonal directions x_1, x_2, and x_3, respectively. In addition to the properties expressed by equations (21), it then also follows that the functions ψ_1, ψ_2, and ψ_3 also possess the following symmetries:

$$\begin{aligned}\psi_2(x_1,x_2,x_3) &= \psi_1(x_2,x_3,x_1) \\ \psi_3(x_1,x_2,x_3) &= \psi_1(x_3,x_1,x_2).\end{aligned} \tag{24}$$

We now also see from equations (20)–(23) that the potential $\phi^{(0)}$ for the general flow problem may be written as a linear combination of potential functions ψ_j $(j = 1,2,3)$ which depend only on the geometry of the problem considered, and, furthermore, these functions may be determined by standard numerical techniques.

(c) **The Averaged Equations.** We apply our definitions of averaged field quantities (equations (5) and (6)) to equations (17) and (20). One then obtains the following equations:

$$<p^{(2)}>_{,i} = \frac{\rho_f <u_i^{(0)}>}{(1-\eta)} + \rho_f(\phi_j - u_j^{(0)})I_{ij} \tag{25}$$

and

$$\rho_f <v_i^{(0)}> = < \frac{\partial p^{(2)}}{\partial x_i} > = \frac{\rho_f \eta <u_i^{(0)}>}{(1-\eta)} + \eta\rho_f\,(\Phi_j - u_j^{(0)})K_{ij}. \tag{26}$$

In equations (25) and (26) $(i, j = 1, 2, 3)$, and throughout this paper, the volume porosity η is defined by the ratio V_f/V, whose value is constant and equal to $1 - (\pi/6)$ independently of the position of our averaging cube. The quantities I_{ij} and K_{ij} $(i, j = 1, 2, 3)$ are defined as follows:

$$\begin{aligned}I_{ij} &= \frac{1}{V}\int_{S_f} \psi_j \eta_i \, dS_x \\ &= \delta_{ij}\end{aligned} \tag{27}$$

$$\begin{aligned}\eta K_{ij} &= \frac{1}{V}\int_{V_f} \frac{\partial \psi_j}{\partial x_i}\, dV \\ &= \frac{1}{V}\int_{S_f} x_i(\hat{\mathbf{n}}\cdot\nabla)\psi_j dS_x \\ &= \eta K \delta_{ij}\end{aligned} \tag{28}$$

and

$$\begin{aligned}\eta K &= \frac{2R}{V}\int \frac{\partial \psi_i}{\partial x_i}\, dS_x \qquad \text{(No summation over } i\text{!)} \\ &\quad x_i = R \\ &= \hat{Q}, \text{ say.}\end{aligned} \tag{29}$$

We first note that the leading term in equations (25) above differs by a factor η from that in the corresponding equations (30) in Walton and Digby (1987). The final simple expressions for the coefficients I_{ij} and K_{ij} in equations (27) and (28) follow from the special properties of the potential functions ψ_j $(j = 1, 2, 3)$ given in equations (21), (22), and (24). By elimination of the arbitrary constants $(\Phi_j - u_j^{(0)})$ $(j = 1, 2, 3)$ from equations (25) and (26), we easily obtain the following equations for the fluid motion

$$<p^{(2)}>_{,i} = \rho_f \left\{ \frac{<v_i^{(0)}>}{\hat{Q}} + \frac{\left(1 - \dfrac{\eta}{\hat{Q}}\right)}{(1-\eta)} <u_i^{(0)}> \right\}. \tag{30}$$

The quantity $\hat{Q}$ appearing in equations (29) and (30) can, in fact, also be shown to be identical to the $\hat{Q}$ used in Walton's work (1977) and so has the value 0.24. Equation (30) is the analogue of equation (34) of Walton and Digby (1987). However, it should be emphasized that this applies only when the averaging cube contains a complete sphere.

(d) **The Final Form of the Equation for the Fluid Motion.** In equation (20), the potential $\phi^{(0)}$ is expressed as a linear combination of a linear function and a variable periodic function. Although the derivation of this result made use of the fact that the averaging cube under consideration contained a complete spherical grain, because of the periodicity conditions, this form of solution for $\phi^{(0)}$ will, in fact, be valid for any choice of averaging cube. It then follows that the corresponding zeroth-order averaged fluid displacement vector, $<\mathbf{v}^{(0)}> = <\nabla\phi^{(0)}>$ will be a constant vector, independent of the position of our averaging cube. Furthermore, it follows

Downloaded 03 May 2010 to 171.66.16.31. Redistribution subject to ASME license or copyright; see http://www.asme.org/terms/Terms_Use.cfm

from equations (17) and (20) that the fluid pressure $p^{(2)}$ may be written in the forms

$$\begin{aligned} p^{(2)} &= \rho_f\{u_k^{(0)}x_k + (\Phi_j - u_j^{(0)})\psi_j\} \\ &= \rho_f\Phi_k x_k + \text{periodic function} \end{aligned} \tag{31}$$

and these forms are also valid for any choice of averaging cube. From equation (31) we have

$$<p^{(2)}> = \rho_f\Phi_k\eta X_k + \tilde{p}\ (\mathbf{X}) \tag{32}$$

where $\tilde{p}\ (\mathbf{X})$ is a variable periodic function of the position $\mathbf{X}$ of the centroid of our representative volume element. From equation (32) we then find

$$<p^{(2)}>_{,i} = \rho_f\Phi_i\eta + \frac{\partial\tilde{p}}{\partial X_i}. \tag{33}$$

This equation differs from the corresponding equation in Walton and Digby (1987). There, $<p^{(2)}>_{,i}$ was found to be a constant whereas here it is a variable periodic function. Moreover, since $<\mathbf{v}^{(0)}>$ and $<\mathbf{u}^{(0)}>$ are constant, independent of the averaging cube, it follows that equation (30) is valid *only* when this averaging cube is centered on a sphere. To obtain equations valid for *any* averaging volume, we must obtain equations not involving periodic functions but rather their mean values which are defined, for example, by equations of the type

$$<\overline{p^{(2)}}> = \frac{1}{V}\int_V <p^{(2)}>\ (\mathbf{X})dV_x$$

where the volume integration is taken over all possible positions $\mathbf{X}$ of the centroid of the averaging cube within a similar cube. It then follows that

$$<\overline{p^{(2)}}>_{,i} = <\overline{p^{(2)}>_{,i}} = \rho_f\Phi_i\eta. \tag{34}$$

The interchangeability of differentiation and averaging here and in later sections follows because we are dealing only with linear or periodic functions of $\mathbf{X}$. It also follows from equations (31), however, that

$$\begin{aligned} <p^{(2)}>_{,i} &= \frac{\rho_f\phi_k}{V}\int_{S_f} n_i x_k\, dS_x \\ &= \rho_f\Phi_i \end{aligned} \tag{35}$$

and so $<p^{(2)}>_{,i} = <\overline{p^{(2)}}>_{,i}/\eta$. Thus, from (35) and (34), we see that (30) may now be written entirely in terms of the means of averaged field quantities which, to the order of approximation used here (see for example equation (34)), may be regarded as constant. It then follows that correct to order ω^2, our desired averaged equations for the fluid motion may then be written in the form

$$\overline{<p>}_{,i} = \eta\rho_f\omega^2\left\{\frac{<\bar{v}_i>}{\hat{Q}} + \frac{\left(1-\frac{\eta}{\hat{Q}}\right)}{(1-\eta)}\overline{<u_i>}\right\} \tag{36}$$

and, moreover, this equation is valid at all points within the effective medium.

5 Derivation of Equations for the Solid Motion

(a) Description of the Problem. As in Section 4(*a*) of this paper where we considered the lowest-order fluid motion, we consider the first-order solid motion and, in this case, it is the stresses σ_{ij} or, equivalently, $u_{i,j}$, the derivatives of the displacements that must be periodic. Again, we consider first the case in which our averaging cube contains one complete spherical grain. Let $w_i^{(1)}$ and $\tau_{ij}^{(1)}$ $(i,j = 1, 2, 3)$ denote the displacement field $u_i^{(1)} + (p^{(1)}x_i/3\kappa_s)$ and the associated stress field $\sigma_{ij}^{(1)} + \delta_{ij}\,p^{(1)}$, respectively, where, from equation (14), $p^{(1)}$ is constant. The displacement $\mathbf{w}$ satisfies the following boundary value problem:

$$\begin{aligned} &(\lambda+\mu)\ \nabla\ (\nabla\cdot\mathbf{w}^{(1)}) + \mu\nabla^2\mathbf{w}^{(1)} = \mathbf{0} \\ &\tau_{ij} = \lambda\delta_{ij}w_{k,k}^{(1)} + \mu(w_{i,j}^{(1)} + w_{j,i}^{(1)}) \\ &\qquad (i,j = 1, 2, 3) \end{aligned} \tag{37}$$

in the solid grains, subject to the boundary conditions $\tau_{ij}^{(1)}\,n_j = 0$ on the inner boundaries, and periodicity of the derivatives of $\mathbf{w}$ on the outer boundaries $x_i = \pm R$ $(i = 1, 2, 3)$. For example,

$$w_{i,j}^{(1)}(R,x_2,x_3) = w_{i,j}^{(1)}(-R,x_2,x_3) \tag{38}$$

for $(i, j = 1, 2, 3)$. We note that the problem defined by equations (37) and (38) corresponds to that obtained when we calculate the effective elastic moduli for a simple cubic packing model of a *dry* elastically-anisotropic granular rock. A similar observation was made in Walton and Digby (1987).

(b) Constraints on the Form of Solution Obtained. We again follow our treatment of the lowest-order fluid motion (given in Section 4(*b*) of this paper). Thus, we treat the solid motion by first resolving the displacement field $w^{(1)}$ into odd and even parts. We therefore first write, for $\mathbf{w}^{(1)}$,

$$\begin{aligned} &\mathbf{w}^{(1)} = (w_1^{(1)}, w_2^{(1)}, w_3^{(1)}) \\ &= (w_{1EEE}^{(1)},\ w_{2ooE}^{(1)},\ w_{3oEo}^{(1)}) + (w_{1EEo}^{(1)},\ w_{2ooo}^{(1)},\ w_{3oEE}^{(1)}) \\ &+ (w_{1EoE}^{(1)},\ w_{2oEE}^{(1)},\ w_{3ooo}^{(1)}) + (w_{1oEE}^{(1)},\ w_{2EoE}^{(1)},\ w_{3EEo}^{(1)}) \\ &+ (w_{1ooE}^{(1)},\ w_{2EEE}^{(1)},\ w_{3Eoo}^{(1)}) + (w_{1oEo}^{(1)},\ w_{2Eoo}^{(1)},\ w_{3EEE}^{(1)}) \\ &+ (w_{1Eoo}^{(1)},\ w_{2oEo}^{(1)},\ w_{3ooE}^{(1)}) + (w_{1ooo}^{(1)},\ w_{2EEo}^{(1)},\ w_{3EoE}^{(1)}). \end{aligned} \tag{39}$$

These particular groupings follow from the governing differential equation (37) for the displacement vector $\mathbf{w}^{(1)}$. The boundary conditions in equations (38) are now imposed on each of the eight terms on the right-hand side of equation (39). For example, the following boundary conditions are then satisfied by the displacement vector $(w_{1EEE}^{(1)},\ w_{2ooE}^{(1)},\ w_{3oEo}^{(1)})$ and its associated stress field τ_{ij},

$$\begin{aligned} \tau_{11} &= 0,\ w_{2ooE}^{(1)} = w_{3oEo}^{(1)} = 0 \text{ on } x_1 = \pm R \\ w_{2ooE}^{(1)} &= 0,\ \tau_{12} = \tau_{23} = 0 \text{ on } x_2 = \pm R \\ w_{3oEo}^{(1)} &= 0,\ \tau_{13} = \tau_{23} = 0 \text{ on } x_3 = \pm R \end{aligned} \tag{40}$$

and

$$\tau_{ij}n_j = 0 \text{ for } i = 1, 2, 3 \text{ on the solid-fluid interface.} \tag{41}$$

The only solution satisfying equation (37), and all of the boundary conditions (40) and (41), is given by

$$(w_{1EEE}^{(1)},\ w_{2ooE}^{(1)},\ w_{3oEo}^{(1)}) = (\text{constant},0,0). \tag{42}$$

By a similar argument, we may then also show that

$$\begin{aligned} (w_{1ooE}^{(1)},\ w_{2EEE}^{(1)},\ w_{3Eoo}^{(1)}) &= (0,\text{constant},0) \\ (w_{1oEo}^{(1)},\ w_{2Eoo}^{(1)},\ w_{3EEE}^{(1)}) &= (0,0,\text{constant}) \end{aligned} \tag{43}$$

and, finally,

$$(w_{1Eoo}^{(1)},\ w_{2oEo}^{(1)},\ w_{3ooE}^{(1)}) = \mathbf{0}.$$

Each of the displacement vectors in equations (42) and (43) corresponds to a rigid body translation and, hence, gives rise to zero stresses. They may, therefore, be omitted from equation (39).

(c) The Final Form of Solution Obtained. The remaining terms in equation (39) are now treated in a similar manner. For example, $(w_{1ooo}^{(1)},\ w_{2EEo}^{(1)},\ w_{3EoE}^{(1)})$ satisfies the following boundary conditions:

Downloaded 03 May 2010 to 171.66.16.31. Redistribution subject to ASME license or copyright; see http://www.asme.org/terms/Terms_Use.cfm

$$
\begin{aligned}
w^{(1)}{}_{1ooo} &= 0, \qquad \tau_{12}=\tau_{13}=0 \text{ on } x_1=\pm R\\
\tau_{22} &= 0 \text{ on } x_2=\pm R\\
w^{(1)}{}_{1ooo} &= 0 \text{ on } x_2=\pm R,\\
w^{(1)}{}_{3EoE} &= \text{constant}=+D \text{ say on } x_2=+R\\
&\quad =-D \text{ on } x_2=-R\\
\tau_{33} &= 0 \text{ on } x_3=\pm R\\
w^{(1)}{}_{1ooo} &= 0 \text{ on } x_3=\pm R,\\
w^{(1)}{}_{2EEo} &= \text{constant}=+E \text{ say on } x_3=+R\\
&\quad =-E \text{ on } x_3=-R.
\end{aligned} \tag{44}
$$

Each part of this solution (that corresponding to D and that corresponding to E) represents a pure shear on the four faces $x_2 = \pm R, x_3 = \pm R$, together with a rigid rotation. The terms $(w^{(1)}_{1EEo}, w^{(1)}_{2ooo}, w^{(1)}_{3oEE})$ and $(w^{(1)}_{1EoE}, w^{(1)}_{2oEE}, w^{(1)}_{3ooo})$ have a similar physical interpretation. Finally, each part of the term $(w^{(1)}_{1oEE}, w^{(1)}_{2EoE}, w^{(1)}_{3EEo})$ corresponds to a pure compression. Here, in fact, the following boundary conditions are satisfied:

$$
\begin{aligned}
&\tau_{12}=\tau_{13}=0 \text{ on } x_1=\pm R\\
&\qquad w^{(1)}_{1oEE} = +F \text{ say on } x_1=+R\\
&\qquad\quad = -F \text{ on } x_1=-R\\
&\tau_{12}=\tau_{23}=0 \text{ on } x_2=+R\\
&\qquad w^{(1)}_{2EoE} = +G \text{ say on } x_2=+R\\
&\qquad\quad = -G \text{ on } x_2=-R\\
&\tau_{13}=\tau_{23}=0 \text{ on } x_3=\pm R\\
&\qquad w^{(1)}_{3EEo} = +H \text{ say on } x_3=+R\\
&\qquad\quad = -H \text{ on } x_3=-R
\end{aligned} \tag{45}
$$

where, in equations (45), F, G, and H are constants.

***(d)* The Averaged Equations.** For the special position of our averaging cube (see sections 4(*a*), 5(*a*), we must now first relate the $<\tau_{ij}^{(1)}>$ to the $<w_i^{(1)}>_{,j}$, or, equivalently, we must relate the $<\sigma_{ij}^{(1)}>$ to the $<u_i^{(1)}>_{,j}$.

In sections 5b and 5c we have shown that

$$
\begin{aligned}
\mathbf{w}^{(1)} &= (w^{(1)}_{1ooo}, w^{(1)}_{2EEo}, w^{(1)}_{3EoE})\\
&+ (w^{(1)}_{1EEo}, w^{(1)}_{2ooo}, w^{(1)}_{3oEE})\\
&+ (w^{(1)}_{1EoE}, w^{(1)}_{2oEE}, w^{(1)}_{3ooo})\\
&+ (w^{(1)}_{1oEE}, w^{(1)}_{2EoE}, w^{(1)}_{3EEo})
\end{aligned} \tag{46}
$$

and, for this displacement field, we may derive the following general results:

$$
<\sigma_{ij}^{(1)}> + \left(\frac{1-\eta}{\eta}\right)<p^{(1)}>\delta_{ij} = <\tau_{ij}^{(1)}> = \frac{1}{8R^3}\int_{S_s} x_j \tau_{ik}{}^{(1)} n_k dS \tag{47}
$$

and

$$
<u_i^{(1)}>_{,j} + \frac{1}{12R^2\kappa_s}\frac{<p^{(1)}>}{\eta}\delta_{ij} = \frac{1}{8R^3}\int_{S_s} w_i{}^{(1)} n_j dS = <w_i^{(1)}>_{,j}. \tag{48}
$$

We must evaluate the integrals in equations (47) and (48) for all values of i and j ($i, j = 1, 2, 3$). We consider the symmetries of each term in equation (47). In the case $i = 2, j = 3$, for example, we then find, after tedious but straightforward evaluation of the integrals in equations (47) and (48), that the only nonvanishing integrals are the following:

$$
\begin{aligned}
\int_{S_s} x_3 \tau_{2k} n_k dS &= 2R\int_{x_3=R} \tau_{23} dS\\
\int_{S_s} x_2 \tau_{3k} n_k dS &= 2R\int_{x_2=R} \tau_{32} dS
\end{aligned} \tag{49}
$$

and, from equations (44), we also have

$$
\begin{aligned}
\int_{S_s} w_2 n_3 dS &= 2\int_{x_3=R} w_2 dS = 2EA\\
\int_{S_s} w_3 n_2 dS &= 2\int_{x_2=R} w_3 dS = 2DA
\end{aligned} \tag{50}
$$

where $A = \pi a^2$ is the contact area, assumed to be same on each face. We must now relate the forces and displacements acting at the contact areas. Still restricting our attention to the special case $i = 2, j = 3$, the appopriate displacements are $D = 1/2\ (D+E) + 1/2\ (D-E)$ and $E = 1/2\ (D+E) - 1/2\ (D-E)$, and from equations (49) the corresponding forces acting are $\int_{x_3=R} \tau_{23} dS$ and $\int_{x_2=R} \tau_{32} dS$, respectively. If the sphere is to be in equilibrium, these two integrals must have the same value and each must correspond to the displacement $1/2\ (E+D)$ of the contact area. The remaining part of each displacement, $\pm\ 1/2\ (D-E)$, corresponds to a rigid rotation which gives rise to no stresses. By using the results of Walton (1987), we can now show that

$$
\int_{x_3=R} \tau_{23} dS = \int_{x_2=R} \tau_{32} dS = \frac{2a\ (E+D)}{\pi(2B+C)} \tag{51}
$$

where $B = (\lambda+2\mu)/4\pi\mu(\lambda+\mu)$ and $C = \lambda/4\pi\mu(\lambda+\mu)$.

Since $A = \pi a^2$, it then follows from equations (47)–(51) that

$$
\begin{aligned}
<\sigma_{23}{}^{(1)}> &= <\sigma_{32}{}^{(1)}>\\
&= \frac{1}{4\pi^2 R^2 a(2B+C)}\left(\int_{S_s}(w_2 n_3 + w_3 n_2) dS\right)\\
&= \frac{2R}{\pi^2 a(2B+C)}\left(<u_2{}^{(1)}>_{,3} + <u_3{}^{(1)}>_{,2}\right).
\end{aligned} \tag{52}
$$

The case of all other unequal values of i and j, and also the case of normal compression (equal values of i and j), are treated in a similar manner. We then find that our averaged equations take the form

$$
<\sigma_{ij}^{(1)}> = \frac{2R}{\pi^2 a(2B+C)}\left(<u_i^{(1)}>_{,j} + <u_j^{(1)}>_{,i}\right) \tag{53}
$$

(for $i \neq j$)

$$
\begin{aligned}
<\sigma_{ij}^{(1)}> &= \frac{2R}{\pi^2 Ba}<u_i^{(1)}>_{,j} - \left(\frac{1-\eta}{\eta}\right)<p^{(1)}> + \frac{a<p^{(1)}>}{6\pi RB\kappa_s\eta}\\
&\simeq \frac{2R}{\pi^2 Ba}<u_i^{(1)}>_{,j} - \left(\frac{1-\eta}{\eta}\right)<p^{(1)}>
\end{aligned} \tag{54}
$$

(for $i = j$)

where, in equations (53) and (54) ($i, j = 1, 2, 3$), and we suppose that $R >> a$.

***(e)* The Final Form of the Averaged Equations.** Again,

Downloaded 03 May 2010 to 171.66.16.31. Redistribution subject to ASME license or copyright; see http://www.asme.org/terms/Terms_Use.cfm

as explained in Section 4(d) of this paper, our averaged equations must be expressed in terms of low-order approximations to the means of averaged quantities of the type $\overline{<u_i^{(1)}>}$, rather than those of the type $<u_i^{(1)}>$ (equations (54)), since derivatives of the former are uniform, but those of the latter are periodic. Now the first-order motion of the solid corresponds to an equilibrium solution in which the stresses in the solid, $<\sigma_{ij}^{(1)}>$, are periodic. The associated displacements are therefore a combination of a linear and a variable periodic part, that is,

$$u_i^{(1)} = \gamma_{ij} x_j + \tilde{u}_i(\mathbf{x}) \tag{55}$$

in which γ_{ij} ($i, j = 1, 2, 3$) is constant and $\tilde{u}_i$ is periodic in $\mathbf{x}$. Averaging this equation yields (for a general position $\mathbf{X}$ of our averaging cube)

$$<u_i^{(1)}> = \gamma_{ij} <x_j> + \text{constant}. \tag{56}$$

Now, in general, $<x_j> \neq X_j$, but is of the form $(1-\eta) X_j$ plus a periodic function of X_j (η is the volume porosity). Hence,

$$\begin{aligned} <u_i^{(1)}> &= (1-\eta)\gamma_{ij} X_j + \tilde{g}_i(\mathbf{X}) \\ &= (1-\eta)\gamma_{ij} X_j + \text{periodic function}. \end{aligned} \tag{57}$$

Then,

$$\begin{aligned} <u_i^{(1)}>_{,j} &= \frac{\partial <u_i^{(1)}>}{\partial X_j} \\ &= (1-\eta)\gamma_{ij} + \frac{\partial \tilde{g}_i}{\partial X_j} \\ &= \text{constant} + \text{periodic function}. \end{aligned} \tag{58}$$

Then, from equation (58),

$$\begin{aligned} \overline{<u_i^{(1)}>_{,j}} &= (1-\eta)\gamma_{ij} + \frac{1}{V}\int_V \frac{\partial \tilde{g}_i}{\partial X_j}\, dV \\ &= (1-\eta)\gamma_{ij} + \frac{1}{V}\int_S \tilde{g}_i n_j dS \\ &= (1-\eta)\gamma_{ij}\ (\text{constant}), \end{aligned} \tag{59}$$

since $1/V \int_S \tilde{g}_i n_j dS = 0$ by the periodicity of $\tilde{g}_i$. But, for the particular averaging cube we have selected, which contains just *one* sphere, we have

$$\begin{aligned} <u_i^{(1)}>_{,j} &= \frac{1}{V}\int_{S_s} u_i^{(1)} n_j dS \\ &= \frac{1}{V}\int_{S_s} (\gamma_{ik} x_k + \tilde{u}_i) n_j dS \\ &= \frac{\pi a^2}{4R^2}\gamma_{ij}. \end{aligned} \tag{60}$$

From equations (59) and (60) it then follows that

$$<u_i^{(1)}>_{,j} = \frac{\overline{<u_i^{(1)}>_{,j}}}{(1-\eta)} \frac{\pi a^2}{4R^2}. \tag{61}$$

Now $p^{(1)}$ is constant (see equation (14)). Also, from the periodicity of $<\sigma_{ij}^{(1)}>$, it follows that $\overline{<\sigma_{ij}^{(1)}>}$ is constant. From this and equation (61) it now follows that equations (53) and (54) may be written entirely in terms of the means of averaged field quantities which, to the order of approximation used here, may be regarded as constant. It then follows that our desired averaged equations may be written, correct to the lowest order in ω, (for $i, j = 1, 2, 3$)

$$\begin{aligned} \overline{<\sigma_{ij}>} &= \frac{3a}{\pi^2 R(2B+C)} (\overline{<u_i>}_{,j} + \overline{<u_j>}_{,i}) \text{ for } i \neq j \\ &= \frac{3a}{\pi^2 RB} \overline{<u_i>}_{,j} - \left(\frac{1-\eta}{\eta}\right) \overline{<p>} \text{ for } i = j. \end{aligned} \tag{62}$$

6 Some Further Basic Equations and Summary of the Full System of Averaged Equations

(*a*) Further Basic Equations. The basic equations (7) and (8) derived in Section 2(c) of this paper hold for any choice of averaging volume no matter what packing model of a granular rock is considered. Hence, we may take means of equations (7) and (8) and obtain

$$\frac{\overline{<\sigma_{kk}>}}{3\kappa_s} - \frac{\overline{<p>}}{\kappa_f} = \overline{<u_j>}_{,j} + \overline{<v_j>}_{,j} \tag{63}$$

$$\overline{<\sigma_{ij}>}_{,j} - \overline{<p>}_{,i} = -\rho_s \omega^2 \overline{<u_i>} - \rho_f \omega^2 \overline{<v_i>}. \tag{64}$$

(*b*) Summary of the Full System of Averaged Equations. Collecting together equations (36), (62), (63), and (64) we now have our desired full system of averaged equations, which, for convenience, may be listed as follows:

$$\overline{<p>}_{,i} = \eta \rho_f \omega^2 \left\{ \frac{\overline{<v_i>}}{\hat{Q}} + \frac{\left(1 - \frac{\eta}{\hat{Q}}\right)}{(1-\eta)} \overline{<u_i>} \right\} \tag{65}$$

$$\begin{aligned} \overline{<\sigma_{ij}>} &= \frac{3a}{\pi^2 R(2B+C)} (\overline{<u_i>}_{,j} + \overline{<u_j>}_{,i}) \text{ for } i \neq j \\ &= \frac{3a}{\pi^2 RB} \overline{<u_i>}_{,j} - \left(\frac{1-\eta}{\eta}\right) \overline{<p>} \text{ for } i = j \end{aligned} \tag{66}$$

$$\frac{\overline{<\sigma_{kk}>}}{3\kappa_s} - \frac{\overline{<p>}}{\kappa_f} = \overline{<u_j>}_{,j} + \overline{<v_j>}_{,j} \tag{67}$$

$$\overline{<\sigma_{ij}>}_{,j} - \overline{<p>}_{,i} = -\rho_s \omega^2 \overline{<u_i>} - \rho_f \omega^2 \overline{<v_i>}. \tag{68}$$

The above equations may be used to relate the various coefficients appearing in Biot's equations (Biot, 1956, 1962) to the microstructural properties of the rock we are considering. In the following sections, we show how the above equations may be used to derive a number of simple but physically interesting results concerning wave propagation through a simple cubic packing model of a granular rock.

7 Results Obtained

Our full system of basic equations (65)–(68) summarized in the preceeding section are, in fact, sufficient for the study of wave propagation in any given direction through a simple cubic packing model of a granular rock. However, we shall now restrict our attention to a special case in which simple closed-form results may be obtained. Here, we shall consider the case in which we have either a purely longitudinal wave or a purely transverse wave propagating parallel to a line joining the centers of adjacent contacting spheres.

(*a*) Purely Longitudinal Waves. We consider first the case in which a purely longitudinal wave propagates parallel to the line joining the centers of contacting spheres, in the x_3-direction, say.

In equations (65)–(68) we then have

$$\begin{aligned} \overline{<u_3>} &= U_3\, e^{ikx_3} \\ \overline{<v_3>} &= V_3\, e^{ikx_3} \end{aligned} \tag{69}$$

and

$$\overline{<u_1>}_{,1} = \overline{<u_2>}_{,2} = 0$$

from which it follows that

Downloaded 03 May 2010 to 171.66.16.31. Redistribution subject to ASME license or copyright; see http://www.asme.org/terms/Terms_Use.cfm

$$<\overline{\sigma_{33}}> = \frac{3a}{\pi^2 BR} <\overline{u_3}>_{,3} - \frac{1-\eta}{\eta} <\bar{p}>$$

$$\frac{1}{\eta}<\bar{p}>_{,3} = \frac{\rho_f \omega^2}{\hat{Q}} <\overline{v_3}> + \frac{\rho_f \omega^2}{(1-\eta)} \left(1 - \frac{\eta}{\hat{Q}}\right) <\overline{u_3}>$$

$$<\overline{\sigma_{11}}> = <\overline{\sigma_{22}}> = -\frac{1-\eta}{\eta} <\bar{p}> \tag{70}$$

$$\frac{<\overline{\sigma_{kk}}>}{3\kappa_s} - \frac{<\bar{p}>}{\kappa_f} = <\overline{u_3}>_{,3} + <\overline{v_3}>_{,3}$$

$$<\overline{\sigma_{33}}>_{,3} - <\bar{p}>_{,3} = -\rho_s \omega^2 <\overline{u_3}> - \rho_f \omega^2 <\overline{v_3}>.$$

After some tedious but straightforward algebra, we then find, for the purely longitudinal wave speeds, α,

$$\hat{Q} - \alpha^2 \left\{ \left(\frac{6-\pi}{6\kappa_f} \right) \rho_f + \frac{\pi B}{6\theta_o} (2\pi \hat{Q}(\rho_s - \rho_f + 12\rho_f(1-\hat{Q})) \right\} \tag{71}$$

$$+ \frac{\pi B \rho_f \alpha^4}{6\theta_o} \left\{ \left(\frac{6-\pi}{3\kappa_f} \right) + \frac{\pi}{(3\lambda + 2\mu)} \right\} \{ \pi(\rho_s - \rho_f) + 6(1-\hat{Q})\rho_f \}$$

$$= 0$$

where, in this equation, we have taken $\theta_o = (a/R) << 1$.

It is therefore found in this case that there are exactly two real wave speeds for the purely longitudinal wave. Equation (71) is, in fact, identical to the one obtained by Walton (1977) by a different method.

***(b)* Purely Transverse Wave.** We now obtain the corresponding result (not previously obtained) for the wave speed of a purely transverse wave, propagating in the x_1-direction. In equations (65)–(68), we now take

$$<\overline{u_3}> = U_3 e^{ikx_1}$$
$$<\overline{u_1}>_{,1} = <\overline{u_2}>_{,2} = <\overline{u_3}>_{,3} = 0. \tag{72}$$

Then, from equations (66) and (67),

$$<\bar{p}> = 0. \tag{73}$$

Hence, from equations (65) and (73),

$$<\overline{v_3}> = -\left(\frac{\hat{Q} - \eta}{1-\eta} \right) <\overline{u_3}>. \tag{74}$$

We then find for the propagation speed β of the purely transverse wave

$$\beta^2 = \frac{(3a/\pi^2 R\ (2B+C))}{\left(\rho_s - \dfrac{\hat{Q}-\eta}{1-\eta}\rho_f\right)} \tag{75}$$

$$= \frac{(3a(1-\eta)/\pi^2 R(2B+C))}{\left(\rho_s(1-\eta) + \dfrac{\eta\rho_f(\chi-1)}{\chi}\right)}$$

where, from equation (29), $\hat{Q} = \eta K = \eta/\chi$ say.

Equation (75) for the purely transverse wave speed through a fluid saturated simple cubic packing model of a granular rock has exactly the same form as that obtained for the transverse wave speed through a fluid-saturated random packing model of a granular rock given in equation (60) of Walton and Digby (1987).

8 Discussion

In this paper we have studied wave propagation through a fluid-saturated elastically-anisotropic granular rock. The connected pore space was filled with an inviscid compressible fluid. The rock framework was modeled by a simple cubic packing of identical, contacting spherical particles. In Section 6 (equations (65)–(68) of this paper) we have derived a set of averaged equations from which the constitutive coefficients and the dynamic coupling coefficients (also defined by Biot, 1956, 1962) may be related explicitly to the microstructural properties of the rock considered. The effective wave speeds in any given direction may therefore also be related explicitly to the microstructural properties of the rock considered. The grain contact radius a, appearing in equation (66) and assumed to be the same for all contacting particles, may be related to both the pore fluid pressure and the initial confining pressure by methods similar to those used in our earlier work (Digby, 1981; Walton, 1987). The effect of the pore fluid pressure and the initial confining pressure to which the rock is subjected (of importance in practical applications) may therefore also be included in our calculations. In Sections 7(a) and 7(b) we show how simple explicit results may be obtained when the propagation of either purely longitudinal or purely transverse waves are considered.

The effect of pore fluid viscosity, of importance in applications of Biot's equations, has not been considered in the present paper. It would therefore be of interest to extend our work by considering also the effect of pore fluid viscosity in our calculations. For the case in which the pore fluid is only slightly viscous, it would again be possible to compare the results obtained with those obtained by Walton (1977), again for the special case of purely longitudinal wave propagation. For large values of the dimensionless viscosity of the pore fluid, it might also be possible to determine whether the constitutive equations obtained would characterize a fluid-saturated granular medium as a viscoelastic solid in agreement with the suggestion of Cleary (1978).

We believe that the analysis presented in this paper will also provide a useful basis for the study of wave propagation through other regular packing models of fluid-saturated elastically-anisotropic granular rocks.

Acknowledgments

One of the authors, (P. J. Digby), would like to thank the Swedish Natural Research Foundation (NFR) for their financial support for the work described in this paper.

References

Biot, M. A., 1956, "The Theory of Elastic Waves in a Fluid Saturated Porous Rock – I. – Low-Frequency Range," *J. Acous. Soc. Am.*, Vol. 28, pp. 168–178.

Biot, M. A., 1962, "Mechanics of Deformation and Acoustic Propagation in Porous Media," *J. Apply. Phys.*, Vol. 33, pp. 1482–1498.

Clearly, M. P., 1978, "Elastic and Dynamic Regimes of Fluid-Impregnated Solids with Diverse Microstructres," *Int. J. Solids. Struct.*, Vol. 14, pp. 795–819.

Digby, P. J., 1981, "The Effective Elastic Moduli of Porous Granular Rocks," ASME JOURNAL OF APPLIED MECHANICS, Vol. 48, pp. 803–808.

Walton, K., 1977, "Elastic Wave Propagation in Model Sediments – I," *Geophysical Journal of the Royal Astronomical Society*, Vol. 48, pp. 461–478.

Walton, K., 1987, "The Effective Elastic Moduli of a Random Packing of Spheres," *J. Mech. Phys. Solids*, Vol. 35, pp. 213–225.

Walton, K., and Digby, P. J., 1987, "Wave Propagation through Fluid Saturated Porous Rocks," ASME JOURNAL OF APPLIED MECHANICS, Vol. 54, pp. 788–793.

Downloaded 03 May 2010 to 171.66.16.31. Redistribution subject to ASME license or copyright; see http://www.asme.org/terms/Terms_Use.cfm

Nonlinear Analysis of Elastomeric Keyboard Domes

John H. Lau

Albert H. Jeans

Hewlett-Packard Laboratories,
Palo Alto, CA 94304

The large deflection of an elastomeric dome is studied using the finite element method. The material properties of the elastomer are described by a hyperelastic model in order to capture the strain energy stored in the dome during deformation. The nonlinear responses are determined by the modified Riks procedure, and the calculated load-deflection curve agrees well with experimental results. In addition, a pressurized thick-walled spherical hyperelastic shell is analyzed and the stress results obtained by the finite element method are in excellent agreement with the closed-form solutions. The results provide a better understanding of the mechanical behavior of elastomeric keyboard domes and demonstrate the feasibility of using the finite element method to design such structures.

Introduction

Many electronic keyboards use elastomeric domes which undergo very large deformations as switching elements. These domes usually consist of rubberlike materials which, in large deformation applications, generally do not obey a linear stress-strain law and are governed by hyperelastic models. The determination of a closed-form solution for this class of boundary value problems is very difficult, if not impossible. Consequently, the general purpose finite element program ABAQUS (ABAQUS, 1987b) with the modified Riks method was used to obtain the nonlinear load-deflection curve and the stresses in these hyperelastic structures.

In order to build up confidence in and verify the accuracy of the method, a pressurized hyperelastic spherical thick shell was analyzed and the stress results compared with closed-form solutions.

A hyperelastic material is characterized by the existence of a strain energy W, measured per unit volume of the undeformed state, which is a function of the deformation gradient. The form of the strain energy as a function of the strain components is restricted by any symmetry properties that the material may possess in the undeformed state (Green and Adkins, 1960; Green and Zerna, 1968; Shield, 1983; Smith and Rivlin, 1958).

For an isotropic material (no preferred directions) the form of W does not depend on the orientation of the coordinate system used to describe the initial locations of the particles and depends only on the strain components through I_1, I_2, and I_3, i.e., $W = W(I_1, I_2, I_3)$. The quantities I_i are the three independent strain invariants.

For materials such as rubber, which undergo little change in volume at stress levels that cause severe deformations, the material can be treated as incompressible, i.e., $I_3 = 1$ (Green and Zerna, 1968), and the strain energy becomes $W = W(I_1, I_2)$.

Based on shearing experiments with rubber blocks, Mooney (1940) suggested that $W = C_1(I_1 - 3) + C_2(I_2 - 3)$, where C_1 and C_2 are constants. The Mooney form can be regarded as the first two terms in the expansion of W as a double power series about the values $I_1 = 3$ and $I_2 = 3$ for the undeformed state (Shield, 1983). It has been found to adequately represent rubberlike materials over a moderate range of strain (Ogden, 1982, Treloar, 1958, Treloar, 1973). For strains larger than 450 to 500 percent, however, experiments on natural rubbers indicate a departure from the Mooney law (Alexander, 1968; Oden, 1973; Hart-Smith and Crisp, 1967). In those cases some higher-order terms in the expansion of W are necessary (Alexander, 1968; Hart-Smith and Crisp, 1967). In the present study, the constitutive relation used was based on Mooney's strain energy function.

Nonlinear Analysis of a Pressurized Hyperelastic Sphere

Figure 1 shows a thick-walled spherical shell. The shell material was assumed to be of the Mooney type with material constants C_1 and C_2 of 0.334 and 0.074 MPa, respectively. The internal and external radii of the shell in the unstrained and strained states are denoted by r_1, r_2 and R_1, R_2, respectively, with $r_1 = 25.4$ mm and $r_2 = 38.1$ mm.

The finite element model of the sphere is shown in Fig. 2. It consisted of 144 axisymmetric solid elements. Each element had eight nodal points, each of which had two degrees-of-freedom. The sphere was subjected to an internal pressure, Π_1, and an external pressure, Π_2. These pressures were increased at a constant ratio to final values of 1.24 Mpa and 0.69 Mpa, respectively.

The deformed shapes of the finite element model for various values of pressures are also shown in Fig. 2. It can be seen that the thickness of the shell shrank from 12.7 mm to approximately 1.4 mm. Furthermore, when the applied external

Contributed by the Applied Mechanics Division of THE AMERICAN SOCIETY OF MECHANICAL ENGINEERS for publication in the JOURNAL OF APPLIED MECHANICS.

Discussion on this paper should be addressed to the Editorial Department, ASME, United Engineering Center, 345 East 47th Street, New York, N.Y. 10017, and will be accepted until two months after final publication of the paper itself in the JOURNAL OF APPLIED MECHANICS. Manuscript received by the ASME Applied Mechanics Division, August 19, 1988; final revision, February 13, 1989.

Copyright © 1989 by ASME

Downloaded 03 May 2010 to 171.66.16.31. Redistribution subject to ASME license or copyright; see http://www.asme.org/terms/Terms_Use.cfm

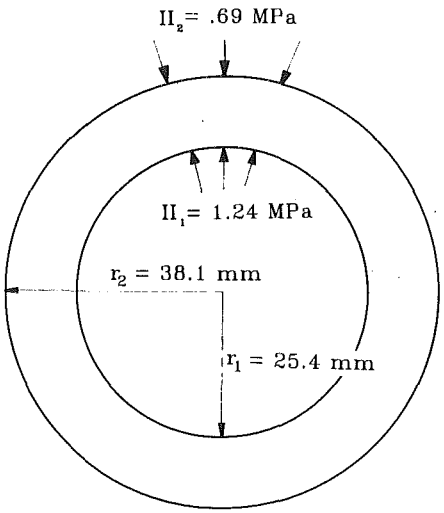


Fig. 1 Hyperelastic thick spherical shell subjected to internal and external pressures

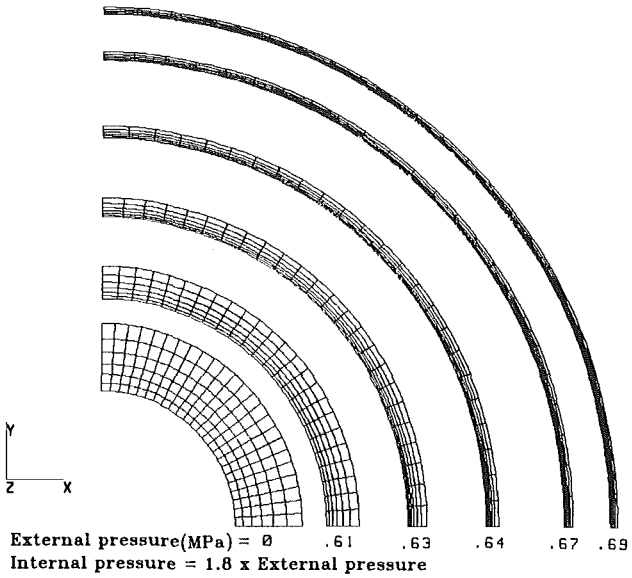


Fig. 2 Deformed shapes of the shell for various values of pressures

pressure was larger than 0.61 MPa, the deflection of the sphere was very sensitive to pressure changes, and Riks algorithm allowed ABAQUS to model large changes in displacements for small changes in the applied pressure (ABAQUS, 1987a). This behavior is more obvious by viewing the calculated nonlinear load-deflection curve shown in Fig. 3. Figure 4 shows the hoop stress (which is the same as the meridian stress) acting through the deformed wall thickness when the internal and external pressures were equal to 1.24 and 0.69 MPa, respectively. It can be seen that the maximum hoop (or meridian) stress occurred at the inner surface of the sphere and decreased to a minimum at the outer surface. The radial stress acting through the deformed wall thickness is shown in Fig. 5.

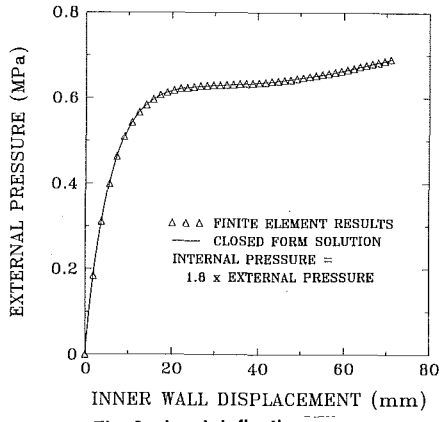


Fig. 3 Load deflection curve

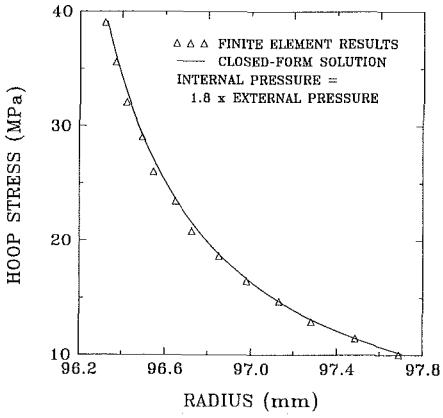


Fig. 4 Hoop stress through-the-wall thickness at external pressure = 0.69 MPa

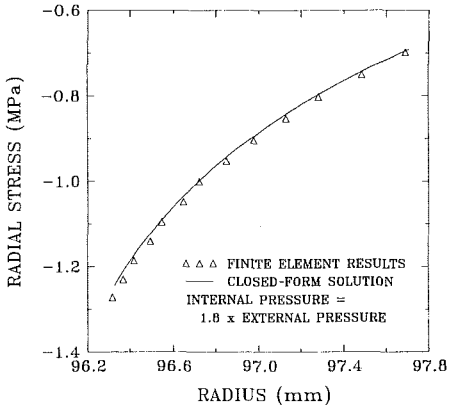


Fig. 5 Radius stress through-the-wall thickness at external pressure = 0.69 MPa

As expected, all the stresses were compressive and the magnitudes were negligibly small compared with the hoop (or meridian) stresses when the wall thickness became very small.

It can be shown that the closed-form solutions of the foregoing problem can be represented by the following equations (Green and Adkins, 1960, Green and Zerna, 1968):

Nomenclature

C_1, C_2 = material constants
I_1, I_2, I_3 = strain invariants
N = number of intervals for integration
Q, Q_1, Q_2 = equations (3)-(5)
r_1 = internal radius of unstrained shell
r_2 = external radius of unstrained shell
R_1 = internal radius of strained shell
R_2 = external radius of strained shell
W = strain energy
W_1, W_2 = equations (6), (7)
λ_1 = normal extension ratio of internal radius of shell
Π_1 = internal pressure
Π_2 = external pressure
σ_{radial} = radial stress in shell
σ_{hoop} = hoop stress in shell
σ_{merid} = meridian stress in shell

Downloaded 03 May 2010 to 171.66.16.31. Redistribution subject to ASME license or copyright; see http://www.asme.org/terms/Terms_Use.cfm

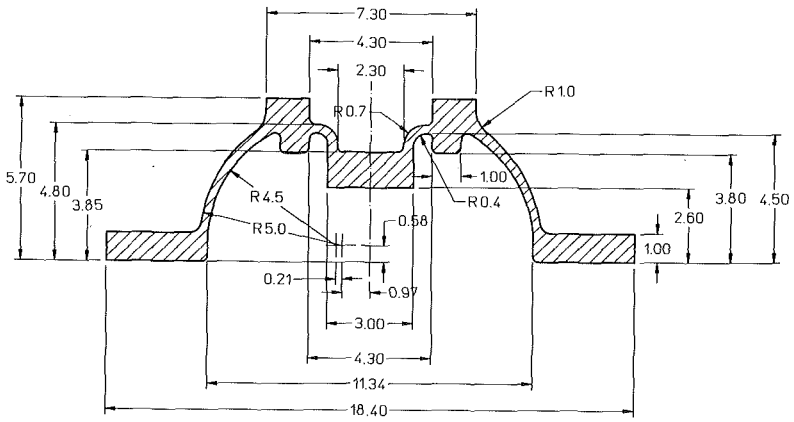


Fig. 6 Cross-sectional view of the dome

$$(R_1^3 - r_1^3)\Pi_1 - (R_2^3 - r_2^3)\Pi_2 = r_1^3 W_1 - r_2^3 W_2 + 3\Big\{ -(C_1 + C_2)(R_2^3 - R_1^3) + C_1 \int_{R_1}^{R_2} \left(Q^4 + \frac{2}{Q^2}\right) R^2 dR + C_2 \int_{R_1}^{R_2} \left(2Q^2 + \frac{1}{Q^4}\right) R^2 dR \Big\} \quad (1)$$

where

$$R_2^3 = r_2^3 - r_1^3 + R_1^3 \quad (2)$$

$$Q^3 = 1 + \frac{(1 - \lambda_1^3) r_1^3}{R^3} \quad (3)$$

$$Q_1 = \frac{r_1}{R_1} = \frac{1}{\lambda_1} \quad (4)$$

$$Q_2^3 = 1 + \frac{(r_1^3 - R_1^3)}{R_2^3} \quad (5)$$

$$W_1 = C_1 \left(Q_1^4 + \frac{2}{Q_1^2} - 3\right) + C_2 \left(2Q_1^2 + \frac{1}{Q_1^4} - 3\right) \quad (6)$$

$$W_2 = C_1 \left(Q_2^4 + \frac{2}{Q_2^2} - 3\right) + C_2 \left(2Q_2^2 + \frac{1}{Q_2^4} - 3\right), \quad (7)$$

and

$$\sigma_{\text{radial}} = C_1(Q^4 + 4Q) + 2C_2\left(Q^2 - \frac{2}{Q}\right) - C_1\left(\frac{1}{\lambda_1^4} + \frac{4}{\lambda_1}\right) - 2C_2\left(\frac{1}{\lambda_1^2} - 2\lambda_1\right) - \Pi_1 \quad (8)$$

$$\sigma_{\text{hoop}} = \sigma_{\text{merid}} = C_1\left(\frac{2}{Q^2} + 4Q - Q^4\right) + 2C_2\left(\frac{1}{Q^4} - \frac{2}{Q}\right) - C_1\left(\frac{1}{\lambda_1^4} + \frac{4}{\lambda_1}\right) - 2C_2\left(\frac{1}{\lambda_1^2} - 2\lambda_1\right) - \Pi_1. \quad (9)$$

In the present study, the previous equations for the shell displacements and stresses were solved numerically as follows:

(1) Substitute equations (2)-(7) into equation (1) with $r_1 = 25.4$ mm, $r_2 = 38.1$ mm, $C_1 = 0.334$ MPa, and $C_2 = 0.074$ MPa. This yields an equation where R_1 is the only unknown if Π_1 and Π_2 are specified.

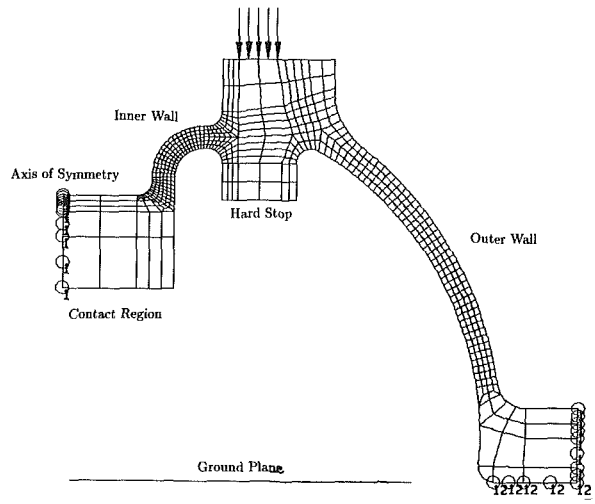


Fig. 7 Finite element model of the dome, load shown by arrows and displacement by circles

(2) For a given Π_1 and Π_2, search for an R_1 (the internal radius of the shell in the strained state) which satisfies equation (1). The integrals in equation (1) were carried out using Simpson's 1/3 Rule with $N = 100$ (Hildebrand, 1976).

(3) Once R_1 has been found, R_2 (the external radius of the shell in the strained state) can be calculated from equation (2) and the nonzero physical components of stresses can be obtained by equations (8)-(9).

Results for the load-deflection curve and the stresses were obtained and are shown in Figs. 3 through 5 in solid lines. It can be seen that the finite element results and the closed-form solutions are in excellent agreement.

Nonlinear Analysis of an Elastomeric Keyboard Dome

Figure 6 shows a cross-sectional view, taken through the axis of symmetry, of the dome under consideration. The inner center portion of the dome is used to make the electrical contact.

The finite element model of the dome is shown in Fig. 7. Because of symmetry, only half of the cross-section was modeled. The mesh shown was refined in order to capture the localized stress gradients, particularly in the inner wall, where deformations were more severe. The final model consisted of 534 axisymmetric solid elements. The element type and the analysis procedures were exactly the same as those used in the previous problem. Furthermore, the dome material was assumed to be of the Mooney type with material constants $C_1 = 0.50$ and $C_2 = 0.11$ Mpa.

The load was applied from above and is shown by the ar-

Downloaded 03 May 2010 to 171.66.16.31. Redistribution subject to ASME license or copyright; see http://www.asme.org/terms/Terms_Use.cfm

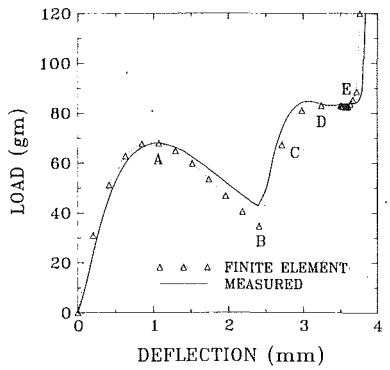


Fig. 8 Finite element and experimental load deflection curves for the dome

rows. The displacement boundary conditions needed to enforce symmetry and fasten the dome to a ground plane are shown by the circles: A "1" represents a restraint in the horizontal direction, while a "2" represents a restraint in the vertical direction.

Figure 8 shows the calculated load-deflection curve (dotted line). It consists of 39 load increments. Each load increment is represented by a triangle and consists of several iterations.

Actual load-deflection curves were measured on a standard uniaxial tester (running in compression) equipped with a load cell capable of resolving 1 gm (force) and an LVDT with a resolution of 0.01 mm. Ten domes were tested. Each was depressed at a speed of 0.02 mm/s. The curve in Fig. 8 is the average of ten measurements. The standard deviation at each point was approximately 2 gm or less. The measured curve is in reasonable agreement with the finite element results.

The highly nonlinear character of problems of this type, as demonstrated by Fig. 8, is worth noting. Figures 9(a) through 9(e) show the dome at various stages of deflection. Reference is made to various points (A,B,C,D,E) along the load-deflection curve shown in Fig. 8.

Figure 9(a) shows the dome just as the outer spherical wall is beginning to buckle. It can be seen from Fig. 8 (point A) that the buckling load is 68 gm. This buckling load introduces a set of internal axial forces and bending moments near the neck of the strained outer wall leading to a maximum compressive principal stress of 0.81 MPa and a maximum tensile principal stress of 0.48 MPa (Fig. 9(a)). The principal stresses acting in the extreme fibers near the middle portion of the strained outer wall are 0.45 Mpa in tension and 0.57 Mpa in compression. The principal stresses acting in the strained inner wall are small compared with those acting in the strained outer wall.

In Fig. 9(b), the outer spherical wall has buckled and the center contact region is about to make contact with the ground plane. At this stage (point B in Fig. 8) the applied load is 35 gm, which is about half of the buckling load. The principal stresses acting in the strained inner wall have not changed very much; however, the principal stresses acting in the strained outer wall have increased by a factor of two or more. This is due to excessive bending of the strained outer wall and the downward movement of the inner center portion of the dome.

Figures 9(c) and 9(d) show the inner spherical wall deforming after contact has been made. By this time (points C and D of Fig. 8), the dome has become stiffer because of the contact. Comparing the values of stresses between reference point B (Fig. 9(b)) and reference points C and D (Figs. 9(c) and 9(d)) it can be seen that the principal stresses acting in the strained inner wall have increased by as much as a factor of ten. This is due to contact of the inner center contact region with the ground plane. The increases in the principal stresses acting in the strained outer wall have become smaller than the increases in the strained inner wall.

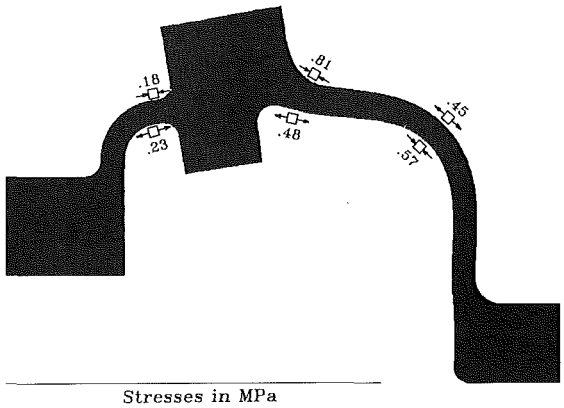


Fig. 9(a) Point A on the load deflection curve, Fig. 8

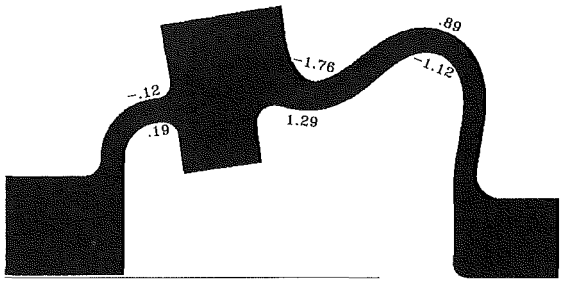


Fig. 9(b) Point B on the load deflection curve, Fig. 8

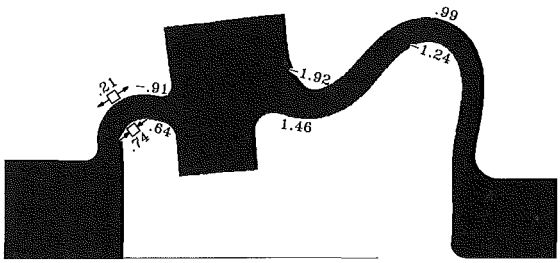


Fig. 9(c) Point C on the load deflection curve, Fig. 8

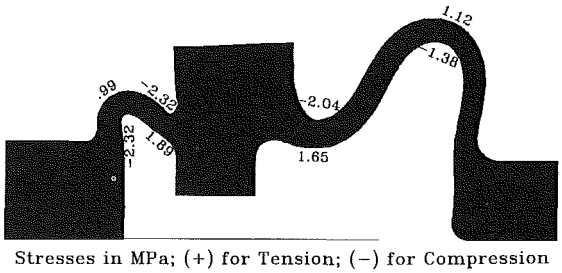


Fig. 9(d) Point D on the load deflection curve, Fig. 8

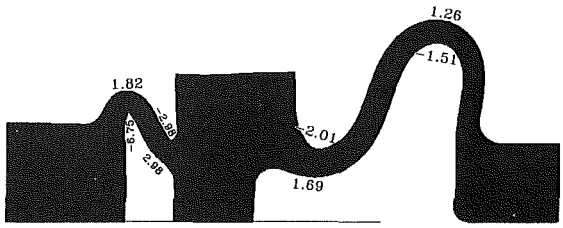


Fig. 9(e) Point E on the load deflection curve, Fig. 8

Fig. 9 Deformed shape of the dome

Downloaded 03 May 2010 to 171.66.16.31. Redistribution subject to ASME license or copyright; see http://www.asme.org/terms/Terms_Use.cfm

Finally, Fig. 9(*e*) shows the final position of the dome, when further loading simply compresses the hard-stop material. At this stage the principal stresses in the strained outer wall are not changing much. However, some of the calculated principal stresses in the strained inner wall are invalid (e.g., 6.75 Mpa) due to excessive distortion of some of the finite elements.

Conclusions

A finite elasticity analysis of an elastomeric dome by the finite element method was performed. Whole-field deformations and stress contours for five load increments were examined to better understand the mechanical behavior of keyboard domes. The calculated nonlinear load-deflection curve agreed well with the measured result.

In addition, a pressurized thick-walled spherical hyperelastic shell was analyzed. The stress results through the strained wall thickness obtained by the finite element method were in excellent agreement with the closed-form solutions, thus providing greater confidence in the ability of the finite element code to solve this class of problems.

Acknowledgments

We wish to thank Dr. C. H. Chao of Hewlett-Packard Laboratories for his help in accessing the computer resources. The keyboard dome dimensions and initial motivation for this work were provided by Mr. Y. N. Chan of Hewlett-Packard, Singapore (now with Northern Telecom, Ottawa) who first performed an axisymmetric linear buckling analysis using ANSYS. Mr. Chan also supplied us with actual parts to test. Finally, we wish to thank Mr. Graeme Burward of Hewlett-Packard Laboratories for making the load deflection measurements on the keyboard domes.

References

ABAQUS Theory Manual, 1987a, Hibbitt, Karlsson and Sorensen, Inc., Providence, R. I.

ABAQUS User's Manual, 1987b, Hibbitt, Karlsson and Sorensen, Inc., Providence, R. I.

Alexander, H., 1968, "A Constitutive Relation for Rubber-Like Materials," *International Journal of Engineering Science*, Vol. 6, pp. 549–563.

Green, A. E., and Adkins, J. E., 1960, *Large Elastic Deformations*, Oxford University Press, London.

Green, A. E., and Zerna, W., 1968, *Theoretical Elasticity*, 2nd ed., Oxford University Press, London.

Hart-Smith, L. J., and Crisp, J. D. C., 1967, "Large Elastic Deformations of Thin Rubber Membranes," *International Journal of Engineering Science*, Vol. 5, pp. 1–24.

Hildebrand, F. B., 1976, *Advanced Calculus for Applications*, 2nd ed., Prentice-Hall, Englewood Cliffs, N.J.

Mooney, M., 1940, "Theory of Large Elastic Deformation," *Journal of Applied Physics*, Vol. 11, pp. 582–592.

Oden, J. T., 1973, *Finite Elements of Nonlinear Continua*, McGraw-Hill, New York.

Ogden, R. W., 1982, "Elastic Deformations of Rubberlike Solids," *Mechanics of Solids*, H. G. Hopkins and M. J. Sewell, eds., Pergamon Press, Oxford U.K., pp. 499–537.

Shield, R. T., 1983, "Equilibrium Solution in Finite Elasticity," ASME JOURNAL OF APPLIED MECHANICS, Vol. 50, pp. 1171–1180.

Smith, G. F., and Rivlin, R. S., 1958, "The Strain-Energy Function for Anisotropic Elastic Materials," *Transactions of the American Mathematical Society*, Vol. 88, pp. 175–193.

Treloar, L. R. G., 1958, *The Physics of Rubber Elasticity*, 2nd ed., Oxford University Press, London.

Treloar, L. R. G., 1973, "The Elasticity and Related Properties of Rubbers," *Reports on Progress in Physics*, Vol. 36, pp. 755–826.

Downloaded 03 May 2010 to 171.66.16.31. Redistribution subject to ASME license or copyright; see http://www.asme.org/terms/Terms_Use.cfm

James P. Blanchard
Department of Nuclear Engineering
and Engineering Physics,
University of Wisconsin-Madison,
Madison, Wis. 53706
Mem. ASME

Nasr M. Ghoniem
School of Engineering and Applied Science,
University of California, Los Angeles,
Los Angeles, Calif. 90024

Relaxation of Thermal Stress Singularities in Bonded Viscoelastic Quarter Planes

Singular thermal stress fields in bonded viscoelastic quarter planes are studied with the use of the viscoelastic analogy. The order of the singularity is shown to depend on the material properties, indicating that it will vary with time in viscoelastic materials. This is studied in detail for Maxwell materials, and it is shown that the order of the singularity generally increases with time. This evolution of the singularity can, for certain combinations of material properties, lead to initial increases in the stress levels near the edge of the interface before relaxation occurs.

1 Introduction

Engineering components often feature disssimilar materials bonded along planar surfaces. Elastic analyses of such configurations generally exhibit stress singularities of various types depending on the loadings, geometry, and materials. Bogy (1968, 1970), for instance, studied stresses in bonded elastic quarter planes under applied surface tractions and found, under certain conditions, stress singularities of the order $r^{-\lambda}$, where $0 \leq \lambda \leq 0.41$. Depending on the loadings and the material combinations, Bogy (1970) also identified situations in which the edge singularities either were logarithmic or nonexistent. Two studies (Hein and Erdogan (1971) and Dempsey and Sinclair (1981)) consider bimaterial wedges and show that geometries other than quarter planes can lead to oscillatory stresses near the edge of the interface. In all cases, the singularity depends on the elastic properties of the two materials.

In many applications, including energy conversion and space technology, high temperature operation of bonded structures is necessary, so time-dependent deformation often occurs in at least one of the materials. In other applications, a viscoelastic adhesive is used to bond two elastic materials, thus forming a pair of interfaces in which one material is elastic and the other is viscoelastic. The latter problem has been studied by Delale and Erdogan (1981), who consider a lap joint composed of two plates bonded by a thin viscoelastic adhesive. The results exhibit a redistribution of the peak shear stresses near the edge of the interface, but no singularities are encountered because of the assumptions associated with plate theory.

Because elastic stress singularities in crack-free bonded structures are a function of the material properties, the order of the singularity in viscoelastic materials is time-dependent and the relaxation of the near-edge stress fields depends on its evolution. In this paper, thermal stress singularities in bonded quarter planes are analyzed using the viscoelastic analogy. A rather simple thermal field, consisting of a semicircular disk in which the temperature changes uniformly, is considered in order to allow the study to focus on the effects of viscoelastic behavior on the singular stress field. The elastic thermal stresses are derived, following Bogy, with the use of the Mellin transform and the asymptotic solutions for the near-edge stresses are obtained by application of the residue theorem to the inversion integral. This result is then used as the Laplace transform of the time-dependent viscoelastic solution (with appropriately transformed material properties), whereupon numerical inversion of this transform leads to the desired result for the relaxation of singularities in viscoelastic bonded quarter planes.

This procedure is outlined in Sections 2 and 3, while some examples of viscoelastic relaxation of the singular fields near the edge of the interface are given in Section 4. Conclusions follow in Section 5.

2 Elastic Solution

The model to be studied herein features two quarter planes bonded along one surface, as shown in Fig. 1. The layers are assumed to be in perfect contact, with no defects or cracks anywhere in the structure. Slipping or debonding at the interface is not allowed. The elastic and viscoelastic properties in the lower quarter plane are referred to with a single prime (e.g., μ', ν', and α'), while those of the upper quarter plane are denoted by a double prime (μ'', ν'', and α''). The materials are assumed to be homogeneous, isotropic, and linear viscoelastic. The free surfaces of the model (at $x = 0$) are assumed to be traction-free and the thermal field provides the only loading.

The well-known equations of small strain elasticity are solved by way of the Airy stress function Φ, which is governed by the following equation:

Contributed by the Applied Mechanics Division of THE AMERICAN SOCIETY OF MECHANICAL ENGINEERS for presentation at the Winter Annual Meeting, San Francisco, Calif., December 10-15, 1989.

Discussion on this paper should be addressed to the Editorial Department, ASME, United Engineering Center, 345 East 47th Street, New York, N.Y. 10017, and will be accepted until two months after final publication of the paper itself in the JOURNAL OF APPLIED MECHANICS. Manuscript received and accepted by the ASME Applied Mechanics Division, October 21, 1988.

Paper No. 89-WA/APM-25.

Copyright © 1989 by ASME

Downloaded 03 May 2010 to 171.66.16.31. Redistribution subject to ASME license or copyright; see http://www.asme.org/terms/Terms_Use.cfm

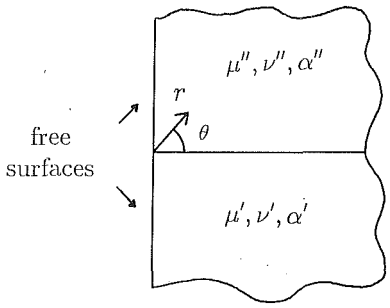


Fig. 1 Model for determination of thermal stresses in bonded quarter planes

$$\nabla^4\Phi + q\alpha E\nabla^2 T = 0, \tag{1}$$

where T is the temperature change from the stress-free reference temperature, α is the thermal expansion coefficient, and

$$q = \begin{cases} 1 & \text{for plane stress} \\ 1/(1-\nu) & \text{for plane strain} \end{cases}. \tag{2}$$

By definition, the stresses are found from the stress function Φ in the following manner:

$$\sigma_{rr} = \frac{1}{r}\Phi_{,r} + \frac{1}{r^2}\Phi_{,\theta\theta}$$
$$\sigma_{\theta\theta} = \Phi_{,rr}$$
$$\sigma_{r\theta} = \frac{1}{r^2}\Phi_{,\theta} - \frac{1}{r}\Phi_{,r\theta} \tag{3}$$

and the displacements can be shown to be given by

$$u_{r,r} = \frac{1}{2\mu}\left[\frac{1}{r}\Phi_{,r} + \frac{1}{r^2}\Phi_{,\theta\theta} - \left(1 - \frac{m}{4}\right)\nabla^2\Phi\right] + n\alpha T$$

$$u_{\theta,r} - \frac{u_\theta}{r} + \frac{1}{r}u_{r,\theta} = \frac{1}{\mu}\left(\frac{1}{r^2}\Phi_{,\theta} - \frac{1}{r}\Phi_{,r\theta}\right), \tag{4}$$

where

$$m = \begin{cases} 4/(1+\nu) & \text{for plane stress} \\ 4(1-\nu) & \text{for plane strain} \end{cases} \tag{5}$$

and

$$n = \begin{cases} 1 & \text{for plane stress} \\ (1+\nu) & \text{for plane strain} \end{cases}. \tag{6}$$

Combining these equations with the traction-free boundary conditions (at $\theta = \pm\pi/2$)

$$\sigma_{\theta\theta} = \sigma_{r\theta} = 0, \tag{7}$$

and the interface conditions (at $\theta = 0$)

$$\sigma'_{\theta\theta} = \sigma''_{\theta\theta}$$
$$\sigma'_{r\theta} = \sigma''_{r\theta}$$
$$u'_r = u''_r$$
$$u'_\theta = u''_\theta, \tag{8}$$

one can solve the problem. Solving for the stress function Φ, subject to the appropriate traction or displacement boundary conditions, provides a means for computing the steady-state thermal stresses, strains, and displacements in a planar medium.

The solution of this problem is facilitated by the Mellin transform, defined as

$$\hat{\Phi}(s,\theta) = \int_0^\infty \Phi(r,\theta) r^{s-1} dr, \tag{9}$$

where $\hat{\Phi}$ denotes the Mellin transform of Φ and s is the transform parameter. Similar transforms are defined for the stresses, displacements, and the temperature field, according to:

$$\hat{\sigma}_{ij}(s,\theta) = \int_0^\infty \sigma_{ij}(r,\theta) r^{s+1} dr,$$

$$\hat{u}_i(s,\theta) = \int_0^\infty u_i(r,\theta) r^s dr,$$

$$\hat{T}(s,\theta) = qE\alpha\int_0^\infty T(r,\theta) r^{s+1} dr. \tag{10}$$

For this study, the thermal field is assumed to consist of a uniform temperature change T_0 over a semicircle of radius R_0. This field can be thought of as an initial temperature distribution that has not yet had a chance to diffuse to a steady field. By assuming this temperature distribution to be steady, one can isolate the effects of the viscoelastic relaxation from the effects of the transient temperature. Also, this simple thermal field avoids the need to derive complicated solutions for steady temperature distributions in bonded structures. Inserting this thermal field into equation (10) leads to a transformed field of the form:

$$\hat{T} = \frac{qE\alpha T_0}{s+2} R_0^{s+2}. \tag{11}$$

Under the Mellin transformation the equation for the stress function (equation (1)) becomes

$$\left(\frac{d^2}{d\theta^2} + s^2\right)\left(\frac{d^2}{d\theta^2} + (s+2)^2\right)\hat{\Phi} + \left(\frac{d^2}{d\theta^2} + (s+2)^2\right)\hat{T} = 0 \tag{12}$$

and the stresses and displacements are conveniently written as:

$$\sigma_{r\theta} + i\sigma_{\theta\theta} + (s+1)\left(\frac{d}{d\theta} + is\right)\hat{\Phi} \tag{13}$$

and

$$2\mu(u_r + iu_\theta) = -i\left(\frac{d}{d\theta} + is\right)$$
$$\left\{1 + \frac{m\left(\frac{d}{d\theta} - is\right)\left[\frac{d}{d\theta} - i(s+2)\right]}{4(s+1)(s+2)}\right\}\hat{\Phi} - \frac{m\hat{T}}{4(s+1)}. \tag{14}$$

The solution to equation (12), for $\hat{T}$ independent of θ, is:

$$\hat{\Phi} = Ae^{is\theta} + \bar{A}e^{-is\theta} + Be^{i(s+2)\theta} + \bar{B}e^{-i(s+2)\theta} - \frac{\hat{T}}{s^2} \tag{15}$$

where A and B are unknown complex constants and $\bar{A}$ and $\bar{B}$ denote their complex conjugates. The complex notation is used in order to reduce the algebra involved in the problem, as demonstrated by Hein and Erdogan (1971).

Given a solution for the stress function in each quarter plane of the model, the full solution is obtained by using the boundary and interface conditions to determine A', B', A'', and B''. The traction-free conditions on the free surfaces can be used to determine the A's in terms of the B's, giving

$$A's = B'(s+1) - \bar{B}'e^{is\pi} + \frac{\hat{T}'}{2s}e^{is\frac{\pi}{2}} \tag{16}$$

and

$$A''s = B''(s+1) - \bar{B}''e^{-is\pi} + \frac{\hat{T}''}{2s}e^{-is\frac{\pi}{2}}. \tag{17}$$

This allows determination of the stresses in terms of the complex constant B

$$\hat{\sigma}'_{r\theta} + i\hat{\sigma}'_{\theta\theta} = 2i(s+1)\Big\{(s+1)(e^{is\theta} + e^{i(s+2)\theta})B' -$$
$$(e^{is(\theta+\pi)} + e^{-i(s+2)\theta})\bar{B}' + (e^{is(\theta+\pi/2)} - 1)\frac{\hat{T}'}{2s}\Big\}$$

Downloaded 03 May 2010 to 171.66.16.31. Redistribution subject to ASME license or copyright; see http://www.asme.org/terms/Terms_Use.cfm

$$\hat{\sigma}''_{r\theta} + i\hat{\sigma}''_{\theta\theta} = 2i(s+1)\Big\{(s+1)(e^{is\theta} + e^{i(s+2)\theta})B'' -$$

$$(e^{is(\theta-\pi)} + e^{-i(s+2)\theta})\bar{B}'' + (e^{is(\theta-\pi/2)} - 1)\frac{\hat{T}''}{2s}\Big\}. \quad (18)$$

Using the interface conditions, which require continuous displacements and shear and normal stresses across the interface, and breaking B' and B'' into real and imaginary parts according to:

$$B' = 2E + 2iF \quad (19)$$

and

$$B'' = 2G + 2iH, \quad (20)$$

the following linear system of four equations is obtained

$$\begin{bmatrix} \gamma & \eta & -\gamma & \eta \\ \eta & \lambda & \eta & -\lambda \\ \gamma+m' & \eta & -k(\gamma+m'') & k\eta \\ \eta & \lambda-m' & k\eta & -k(\lambda-m'') \end{bmatrix} \begin{Bmatrix} E \\ F \\ G \\ H \end{Bmatrix} = \begin{Bmatrix} R_1 \\ R_2 \\ R_3 \\ R_4 \end{Bmatrix} \quad (21)$$

where

$$k = \frac{\mu'}{\mu''}$$

$$\gamma = 2[(s+1) - \cos^2\xi],$$

$$\eta = -2\sin\xi\cos\xi,$$

$$\lambda = 2[(s+1) + \cos^2\xi],$$

$$\xi = \frac{s\pi}{2},$$

$$R_1 = (1-\cos\xi)\left(\frac{\hat{T}' - \hat{T}''}{4s}\right),$$

$$R_2 = -\sin\xi\left(\frac{\hat{T}' + \hat{T}''}{4s}\right),$$

$$R_3 = (1-\cos\xi)\left(\frac{\hat{T}' - k\hat{T}''}{4s}\right),$$

$$R_4 = -\sin\xi\left(\frac{\hat{T}' + k\hat{T}''}{4s}\right). \quad (22)$$

The solution of the steady-state problem now reduces to the inversion of the matrix in equation (21).

The system represented by equation (21) is similar to previous solutions for different loadings. Hein and Erdogan (1971), for instance, considered the same geometric model with a dislocation at the interface, and came up with the same matrix on the left side and a different loading vector on the right side. Bogy (1968), on the other hand, used a different notation and developed an 8×8 system, but the determinant of the coefficient matrix was identical to that of equation (21).

After extensive algebra, the transformed stresses can be found by solving equation (21) for the constants E, F, G, and H and substituting them into equation (18). The resulting interface stresses are given by

$$\hat{\sigma}_{r\theta}(\theta=0) = \frac{-(s+1)}{s\|\mathbf{X}\|}[Q_1 m' \hat{T}' + Q_2 k m'' \hat{T}''] \quad (23)$$

and

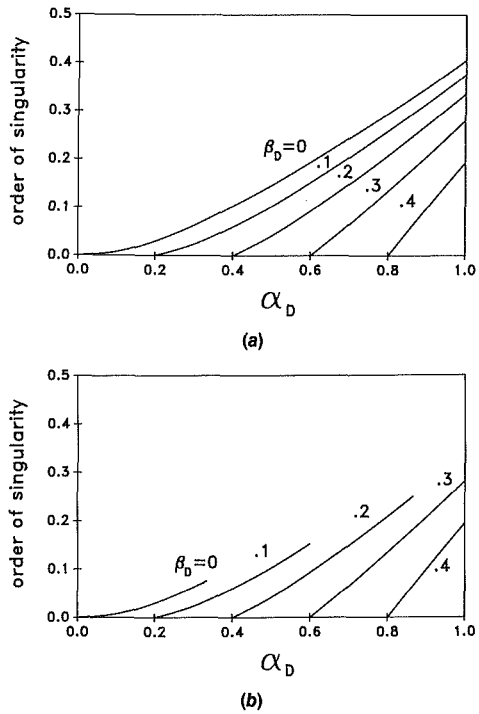


Fig. 2 Order of the singularity for various values of Dundurs' parameters under (a) plane-strain and (b) plane-stress conditions

$$\hat{\sigma}_{\theta\theta}(\theta=0) = \frac{-(s+1)}{s\|\mathbf{X}\|}[Q_3 m' \hat{T}' + Q_4 k m'' \hat{T}''], \quad (24)$$

where the four functions Q_i are given by

$$Q_1 = \eta(1-\cos\xi)[(1/2)k_1(\gamma\lambda-\eta^2) + 2k\lambda m''] + \sin\xi[(1/2)k_1\gamma(\gamma\lambda-\eta^2) + k_2\gamma\lambda + k_3\eta^2],$$

$$Q_2 = \eta(1-\cos\xi)[(1/2)k_1(\gamma\lambda-\eta^2) - 2\lambda m'] + \sin\xi[(1/2)k_1\gamma(\gamma\lambda-\eta^2) + k_2\gamma\lambda - k_3\eta^2],$$

$$Q_3 = (1-\cos\xi)[-(1/2)k_1\lambda(\gamma\lambda-\eta^2) + k_2\gamma\lambda + k_3\eta^2] + \eta\sin\xi[-(1/2)k_1(\gamma\lambda-\eta^2) + 2km''\gamma],$$

$$Q_4 = (1-\cos\xi)[(1/2)k_1\lambda(\gamma\lambda-\eta^2) - k_2\gamma\lambda + k_3\eta^2] + \eta\sin\xi[(1/2)k_1(\gamma\lambda-\eta^2) + 2m'\gamma], \quad (25)$$

where

$$k_1 = 2(k-1)$$

$$k_2 = km' - m'$$

$$k_3 = km'' + m'. \quad (26)$$

Also, $\|\mathbf{X}\|$, the determinant of the matrix in equation (21), is given by

$$\|\mathbf{X}\| = k_3^2\eta^2 + (k-1)^2(\gamma\lambda-\eta^2)^2 - k_2^2\gamma\lambda + k_2(k-1)(\lambda-\gamma)(\gamma\lambda-\eta^2). \quad (27)$$

This determinant has a profound effect on the solution of the problem because its zeroes locate the poles of the transformed stresses in the Mellin domain, so it warrants further investigation.

Both the number and location of the zeroes of the determinant in equation (27) depend on a parameter P, defined by

$$P = k_2[2k_1 - k_2]. \quad (28)$$

In order for the transforms of the stresses to exist, the real part of the transform parameter s must be less than -1, so the Mellin inversion depends only on the zeroes of the determinant for $\mathrm{Re}(s) < -1$. For all k_1, k_2, and k_3 (i.e., for any combination of materials), $s = -1$ and $s = -2$ are always zeroes. Hence, we concern ourselves with roots of the determinant

Downloaded 03 May 2010 to 171.66.16.31. Redistribution subject to ASME license or copyright; see http://www.asme.org/terms/Terms_Use.cfm

that lie between -2 and -1. For $P>0$, there is exactly one zero on the interval $-2 < s < -1$, and it is a simple zero. For all admissible values of the material constants (i.e., $0 < \nu < \frac{1}{2}$), this zero occurs between -1.59 and -2.0. As P approaches zero, the zero of the determinant moves closer to $s=-2$ until, when $P=0$, there are no zeroes on $-2 < s < -1$ and the zero at $s=-2$ becomes a double root. Finally, for $P<0$, there are no zeroes on $-2 < s < -1$ and the zero at $s=-2$ is simple; there is also a simple zero between -2.4 and -2.0. In this paper, only those material combinations which lead to algebraic singularities (i.e., only those for which P is positive) will be considered.

As shown by Dundurs (1969), calculation of the roots of the determinant actually can be reduced to two material parameters, one possible set of which is:

$$\alpha_D = \frac{k_2}{k_3} \text{ and } \beta_D = \frac{k_2 - k_1}{k_3}. \tag{29}$$

By confining Poisson's ratios to $0 < \nu < 0.5$, one limits Dundurs' parameters to $-1 < \alpha_D < 1$ and $(\alpha_D - 1)/4 < \beta_D < (\alpha_D + 1)/4$ for plane strain and $(3\alpha_D - 1)/8 < \beta_D < (3\alpha_D + 1)/8$ for plane stress. Typical plots of the order of singularity for various values of these parameters are shown in Fig. 2. (See Bogy (1970) for a more detailed discussion of the roots of this determinant.)

The recovery of the stresses in real space from the transformed stresses involves inversion of the Mellin transform, using the following complex integral:

$$\sigma_{ij}(r,\theta) = \frac{1}{2\pi i}\int_{c-i\infty}^{c+i\infty} \hat{\sigma}_{ij}(s,\theta) r^{-(s+2)} ds, \tag{30}$$

where c lies in a strip of regularity of the integrand. As mentioned previously, we are concerned only with $s < -1$, so c lies between $\mathrm{Re}(s) = -1$ and the first pole of the integrand associated with the inversion of the transformed stresses. In order to obtain the leading terms in the asymptotic expansions for the stresses, one can perform the inversion using contour integration and the residue theorem. It can be shown that for an appropriately chosen contour, the inversion integral of equation (30) is asymptotic to the residue as r approaches zero. Once s_1, the first pole of the integrand is found, the asymptotic solution follows directly. The form of the stress thus depends on the nature of the pole and is quite different for the three types of determinant mentioned earlier in this section.

For the assumed thermal field and for cases where there is an algebraic singularity, the shear and normal stresses in the interface are given by

$$\begin{aligned} \sigma_{r\theta}(\theta=0) &= F(r;s)[Q_1 m' q' E' \alpha' + Q_2 k m'' q'' E'' \alpha''] \\ \sigma_{\theta\theta}(\theta=0) &= F(r;s)[Q_3 m' q' E' \alpha' + Q_4 k m'' q'' E'' \alpha''], \end{aligned} \tag{31}$$

where

$$F(r;s) = \frac{-(s_1+1)}{s_1(s_1+2)} \frac{T_0}{\dfrac{d}{ds}(\|\mathbf{X}\|)\big|_{s=s_1}} \left(\frac{R_0}{r}\right)^{(s_1+2)}. \tag{32}$$

This elastic solution provides a tool for determining the response of viscoelastic materials via the viscoelastic analogy.

3 Viscoelastic Solution

In order to determine the stresses and strains in a viscoelastic body, the constitutive relations must be modified to account for the time-dependent deformations. In general, these relations are written as

$$P_1(D) s_{ij} = P_2(D) e_{ij} \tag{33}$$

and

$$P_3(D)\sigma_{ii} = P_4(D)(\epsilon_{ij} - 3\alpha T), \tag{34}$$

where

$$P_k(D) = \sum_{n=1}^{N} C_{kn} \frac{\partial^n}{\partial t^n}. \tag{35}$$

The operator $P_k(D)$ is a general, linear, differential operator of order N, and C_{kn} are appropriate coefficients representing the material behavior of a viscoelastic solid. A common solution method for these types of problems is to take the Laplace transform of the viscoelastic equations and compare the resulting set of equations to the steady-state formulation (see, for instance, Lee (1955)). Because the bulk behavior is often different from the shear behavior in viscoelastic materials, the stress-strain relations are usually written in terms of the stress and strain deviators, s_{ij} and e_{ij}, defined as

$$s_{ij} = \sigma_{ij} - \frac{\sigma_{ll}}{3} \tag{36}$$

and

$$e_{ij} = \epsilon_{ij} - \frac{\epsilon_{ll}}{3}. \tag{37}$$

In terms of these quantities, the elastic stress-strain relations are

$$s_{ij} = 2\mu e_{ij} \tag{38}$$

and

$$\sigma_{ll} = 3\kappa(\epsilon_{ll} - 3\alpha T), \tag{39}$$

where κ is the bulk modulus, i.e.,

$$\kappa = \frac{E}{3(1-2\nu)} = \frac{2\mu(1+\nu)}{3(1-2\nu)}. \tag{40}$$

Transforming equations (33) and (34) gives

$$\tilde{s}_{ij} = \frac{P_2(p)}{P_1(p)} \tilde{e}_{ij} \tag{41}$$

and

$$\tilde{\sigma}_{ii} = \frac{P_4(p)}{P_3(p)} (\tilde{\epsilon}_{ii} - 3\alpha\tilde{T}), \tag{42}$$

where the Laplace transform of a function f is denoted by $\tilde{f}$, and p is the independent variable in the Laplace domain. By comparing the elastic and viscoelastic constitutive equations, it is apparent that the solution of the viscoelastic problem in the Laplace domain is equivalent to the solution of the steady-state problem, with the elastic properties 2μ and 3κ replaced by $P_2(p)/P_1(p)$ and $P_4(p)/P_3(p)$, respectively. The time-dependent behavior of the viscoelastic problem is thus recovered by substituting the equivalent transformed properties into the steady-state elastic solution and inverting the Laplace transform.

The analysis of bonded structures composed of viscoelastic materials is difficult, even with the use of the analogy described in the previous section. The substitution of functions of the Laplace parameter p for the material properties in elastic solutions such as those represented by equation (31) leads to very complicated expressions for the stresses in the Laplace domain and analytical inversion is not possible. The primary difficulty is the fact that the eigenvalues s_k, which are functions of the Laplace parameter p, are not known explicitly because these are determined by solving a transcendental equation. Hence, numerical inversion is necessary. Unfortunately, numerical inversion of the Laplace transform is difficult because the operator's inherent unboundedness prevents explicit error control. Because a small change in the transformed function can lead to an arbitrarily large change in the real function, high precision is needed to obtain accurate results.

The method adopted for this study solves the Laplace

Downloaded 03 May 2010 to 171.66.16.31. Redistribution subject to ASME license or copyright; see http://www.asme.org/terms/Terms_Use.cfm

transform integral definition as an integral equation, with $f(t)$ as the unknown, using Gaussian quadrature (Bellman (1966, p. 32)). Other methods, such as those suggested by Miller and Guy (1966), Papoulis (1957), and Piessens (1972) may be used if the accuracy of the quadrature method is insufficient. Each of these methods are useful because they do not require evaluation of the transformed function for complex values of the Laplace parameter p.

The first step is to transform the integral into one with finite limits, then approximate the integral as a finite sum, using Nth-order Gaussian quadrature. This can be evaluated for N arbitrary values of the Laplace parameter p, giving a linear system represented by

$$\tilde{f}(p_k)=\frac{1}{2}\sum_{i=0}^{N} w_i\left(\frac{1+\tau_i}{2}\right)^{p_k-1} g(\tau_i). \tag{43}$$

This gives a system of N equations for the N unknowns $g(\tau_i)$, which represent values of the unknown function $g(\tau)$ at discrete locations τ_i. The solution from this point is trivial. For this study, order 15 quadrature ($N=15$) was used because it was found to be the most reliable for problems associated with exponential decay. This is useful for the present study because the relaxation of stresses in Maxwell materials tends to be exponential.

As an example of one type of viscoelastic material, the rest of this paper will consider Maxwell materials. For these materials, the stress-strain equations are

$$\frac{\partial s_{ij}}{\partial t}+\frac{s_{ij}}{\tau_0}=2\mu\frac{\partial \epsilon_{ij}}{\partial t} \tag{44}$$

and

$$\sigma_{ii}=3\kappa(\epsilon_{ii}-3\alpha T). \tag{45}$$

Hence, by comparison with equations (33) and (34),

$$P_1(D)=\frac{\partial}{\partial t}+\frac{1}{\tau_0}$$

$$P_2(D)=2\mu\frac{\partial}{\partial t}$$

$$P_3(D)=1$$

$$P_4(D)=3\kappa. \tag{46}$$

Taking the Laplace transform of these operators and substituting into equation (41) yields the following equivalencies between the elastic materials properties and the viscoelastic "properties" in the Laplace domain:

$$2\mu\rightarrow\frac{2\mu p}{p+\dfrac{1}{\tau_0}} \tag{47}$$

and

$$\kappa\rightarrow\kappa. \tag{48}$$

This represents a material for which the bulk behavior is elastic, and the stress decays exponentially (with a decay constant of τ_0) for a uniaxial fixed-grip test. Substituting equations (47) and (48) into the elastic stress solutions represented by equations (31) yields expressions for the stresses in the Laplace domain. This is then inverted numerically to obtain the time-dependent behavior of duplex structures.

Using these equivalent properties in the elastic solution for the interface stresses near the edge of the interface of bonded quarter planes, one finds transformed viscoelastic solutions of the form:

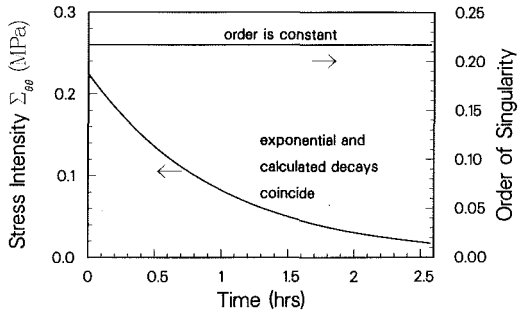


Fig. 3 Relaxation of the boundary layer stress intensity for constant order of the singularity

$$\sigma_{r\theta}(\theta=0)=\frac{1}{p}F(r;s_1)[Q_1 m' q' E' \alpha' + Q_2 \tilde{k} m'' q'' E'' \alpha'']$$

$$\sigma_{\theta\theta}(\theta=0)=\frac{1}{p}F(r;s_1)[Q_3 m' q' E' \alpha' + Q_4 \tilde{k} m'' q'' E'' \alpha''] \tag{49}$$

If the decay constants are equal (i.e., $\tau_0' = \tau_0''$), and for plane stress conditions these equations simplify to:

$$\sigma_{r\theta}(\theta=0)=8F(r;s_1)[Q_1\alpha' + Q_2\alpha'']\frac{\mu'}{p+1/\tau}$$

$$\sigma_{r\theta}(\theta=0)=8F(r;s_1)[Q_3\alpha' + Q_4\alpha'']\frac{\mu'}{p+1/\tau} \tag{50}$$

If the order of the singularity for this problem were independent of time, then the transformed stresses could be inverted analytically, leading to a time dependence of the form:

$$\sigma_{ij}=C_{ij}e^{-t/\tau_0}, \tag{51}$$

where C_{ij} is the initial value of the stress σ_{ij}. In reality, though, the order of the singularity must be determined from the roots of the determinant given in equation (27), which becomes a function of the Laplace transform parameter p when the effective material properties are used. Hence, the order of singularity is time-dependent and numerical inversion of the transformed stresses is required. As an example, the transform of one of the material parameters, k, can be written:

$$\tilde{k}=\frac{\mu'}{\mu''}\left(\frac{p+\dfrac{1}{\tau_0''}}{p+\dfrac{1}{\tau_0'}}\right). \tag{52}$$

As the Laplace parameter p ranges from 0 to ∞, $\tilde{k}$ can take on virtually any value, depending on the creep constants of the two materials. This can be shown with the use of the limit theorems of the Laplace transform, giving the final value of $\tilde{k}$ (at $t\rightarrow\infty$) as:

$$\tilde{k}_\infty=\frac{\mu'\tau_0'}{\mu''\tau_0''}. \tag{53}$$

Therefore, depending on the ratios of the creep constants of the two materials, $\tilde{k}$ can take on any value during the life of the component, thus leading to numerous possibilities for the final order of singularity. For Maxwell materials, the final value for the effective Poisson's ratio is 0.5 for any finite decay rate τ. Hence, the material parameter m as defined in equation (5) has the following limiting values:

$$\tilde{m}_\infty=\begin{cases}8/3 & \text{for plane stress}\\ 2 & \text{for plane strain}\end{cases}. \tag{54}$$

Given these limiting values for the material properties $\tilde{k}$, $\tilde{m}'$, and $\tilde{m}''$, one can determine the limiting value for $\tilde{P}$ =

Downloaded 03 May 2010 to 171.66.16.31. Redistribution subject to ASME license or copyright; see http://www.asme.org/terms/Terms_Use.cfm

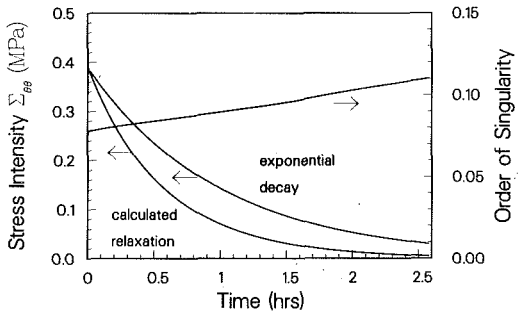


Fig. 4 Relaxation of the boundary layer stress intensity for a time-dependent order of the singularity

$\tilde{k}_2(2\tilde{k}_1 - \tilde{k}_2)$, which determines whether or not there will be a singularity for a given set of material properties. This limiting value is

$$\tilde{P}_\infty = \tilde{m}_\infty(4-\tilde{m}_\infty)(\tilde{k}_\infty - 1)^2 \tag{55}$$

which is non-negative. Therefore, regardless of whether there is an initial singularity, there will always be a singularity at $t=\infty$, unless the limiting value of the shear modulus ratio $\tilde{k}_\infty$ is 1.

4 Results

The singular stress fields in this study can be characterized by two parameters: the order of the singularity and the associated "boundary layer stress intensity factor." This latter quantity, as defined by Wang and Choi (1982), is given by

$$K_{ij} = \lim_{r\to 0} r^{s_1+2}\sigma_{ij}(\theta=0). \tag{56}$$

For this paper, this stress intensity is normalized by the quantity $R_0^{-(s_1+2)}$, giving it stress units. Hence, results are presented for a new parameter Σ_{ij}, given by:

$$\Sigma_{ij} = \lim_{r\to 0}\left(\frac{r}{R_0}\right)^{s_1+2}\sigma_{ij}(\theta=0). \tag{57}$$

In addition, only those results for the normal stress at the interface $\sigma_{\theta\theta}$ ($\theta = 0$) will be presented, because it is generally the largest of the four interface stresses (σ'_{rr}, σ''_{rr}, $\sigma_{r\theta}$, and $\sigma_{\theta\theta}$).

As is evident from the previous section, choosing $\tau' = \tau''$ and $\nu' = \nu''$ provides a situation in which the order of the singularity is independent of time. Figure 3 shows the decay of the stress intensity factor for such a case, where

$$\begin{aligned}
&\tau' = \tau'' = 1 \text{ hr}\\
&\nu' = \nu'' = 0.5\\
&\mu' = 10 \text{ GPa}\\
&\mu'' = 100 \text{ GPa}\\
&\alpha' = 1\times 10^{-6}\,^\circ\text{C}^{-1}\\
&\alpha'' = 2\times 10^{-6}\,^\circ\text{C}^{-1}\\
&T_0 = 100^\circ\text{C}
\end{aligned} \tag{58}$$

and plane stress conditions were assumed. As discussed previously, the relaxation of the stresses for a constant order should be exponential. This is verified in this figure where the comparison between the calculated relaxation, from numerical Laplace transform inversion and a purely exponential decay, is shown to be excellent. This result provides some verification of the numerical transform inversion.

Figure 4 shows the results for the relaxation of the stresses in a case where the order is varying. The properties used in this case were identical to those given above, except $\nu' = 0.1$ and $\nu'' = 0.3$. This figure shows that the order of singularity more than doubles from its initial value of 0.065. The relaxation of the stress intensity, in this case, is faster than exponential decay. It is unclear how these competing effects (decreasing stress intensity and increasing order) will effect failure or delamination.

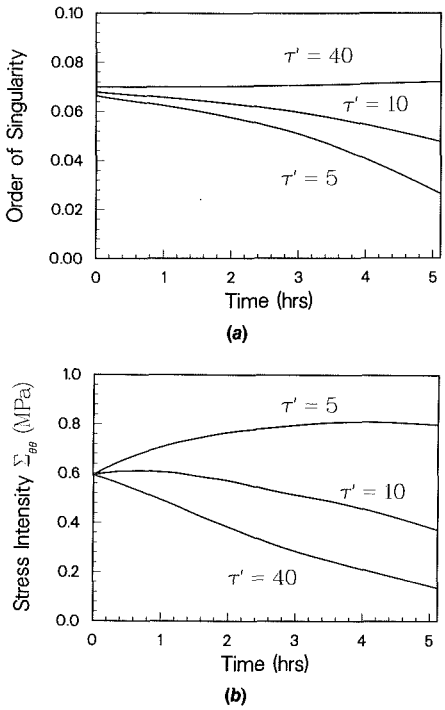


Fig. 5 Order of the (*a*) singularity and (*b*) boundary layer stress intensity factor for different ratios of the relaxation constant

In some cases the order of singularity can decrease before increasing. This behavior is accompanied by a stress intensity which increases before relaxing. This was explored using the following properties:

$$\begin{aligned}
&\tau'' = 1 \text{ hr}\\
&\nu' = 0.3\\
&\nu'' = 0.5\\
&\mu' = 10 \text{ GPa}\\
&\mu'' = 100 \text{ GPa}\\
&\alpha' = 1\times 10^{-6}\,^\circ\text{C}^{-1}\\
&\alpha'' = 2\times 10^{-6}\,^\circ\text{C}^{-1}\\
&T_0 = 100^\circ\text{C}
\end{aligned} \tag{59}$$

with a varying relaxation constant τ' in the lower quarter plane and assuming plane-strain conditions. These properties indicate that the shear modulus in the upper plane is greater than that in the lower plane, giving $k = 0.1$ initially, but if the softer material has a higher relaxation constant ($\tau' > \tau''$), the final value for the shear moduli ratio will be greater than one. Hence, for some time this ratio will be near one and the singularity will disappear. As shown in Fig. 5(*a*), the order of the singularity decreases faster for increasing τ' (i.e., for slower relaxation in the lower quarter plane). The subsequent increase in the order is not shown here. The companion Fig., 5(*b*), shows the corresponding relaxation of the boundary layer stress intensities. As the relaxation constant in the softer material is increased (and the order of the singularity drops at an increasing rate), the stress intensity tends to relax more slowly. In fact, it increases in some cases. Again, there is competition between the relaxation of the stress intensity and the increase (or decrease) of the order of the singularity.

Downloaded 03 May 2010 to 171.66.16.31. Redistribution subject to ASME license or copyright; see http://www.asme.org/terms/Terms_Use.cfm

5 Conclusions

Thermal stresses in perfectly-bonded dissimilar quarter planes are often singular, depending on the loading and the material properties. Because the order of this singularity is material-dependent, it tends to change with time in viscoelastic materials. It is apparent from the results in the previous section that as the order increases with time, the relaxation of the boundary layer stress intensity factor tends to be faster than exponential decay, while the relaxation is relatively slow when the order decreases. Experimental evidence is required to assess the impact that this phenomenon has on the onset of failure in crack-free structures.

6 Acknowledgment

This research was performed under appointment to the Magnetic Fusion Energy Technology Fellowship Program administered at Oak Ridge Associated Universities for the United States Department of Energy. Financial support for Professor Ghoniem was provided by the Office of Fusion Energy, U.S. Department of Energy, Grant # DE-FG03-86ER52126.

7 References

Bellman, R., Kalaba, R., and Lockett, J., 1966, *Numerical Inversion of the Laplace Transform*, Elsevier, New York.

Bogy, D. B., 1968, "Edge-Bonded Dissimilar Orthogonal Elastic Wedges Under Normal and Shear Loading," ASME JOURNAL OF APPLIED MECHANICS, Vol. 35, pp. 460–466.

Bogy, D. B., 1970, "On the Problem of Edge-Bonded Elastic Quarter-Planes Loaded at the Boundary," *International Journal of Solids and Structures*, Vol. 6, pp. 1287–1313.

Delale, F., and Erdogan, F., 1981, "Viscoelastic Analysis of Adhesively Bonded Structures," ASME JOURNAL OF APPLIED MECHANICS, Vol. 48, pp. 331–338.

Dempsey, J. P., and Sinclair, G. B., 1981, "On the Singular Behavior at the Vertex of a Bi-Material Wedge," *Journal of Elasticity*, Vol. 11, pp. 317–327.

Dundurs, J., 1969, discussion, ASME JOURNAL OF APPLIED MECHANICS, Vol. 36, pp. 650.

Hein, V. L., and Erdogan, F., 1971, "Stress Singularities in a Two-Material Wedge," *International Journal of Fracture Mechanics*, Vol. 7, pp. 317–330.

Lee, E. H., 1955, "Stress Analysis in Viscoelastic Bodies," *Quarterly of Applied Mathematics*, Vol. 13, pp. 183–190.

Miller, M. K., and Guy, W. T., 1966, "Numerical Inversion of the Laplace Transform by Use of the Jacobi Polynomials," *SIAM Journal of Numerical Analysis*, Vol. 3, pp. 624–635.

Papoulis, A., 1957, "A New Method of Inversion of the Laplace Transform," *Quarterly of Applied Mathematics*, Vol. 14, pp. 405–414.

Piessens, R., 1972, "A New Numerical Method for the Inversion of the Laplace Transform," *Journal of the Institute of Mathematics and its Applications*, Vol. 10, pp. 185–192.

Wang, S. S., and Choi, I., 1982, "Boundary-Layer Effects in Composite Laminates: Part 2–Free-Edge Stress Solutions and Basic Characteristics," ASME JOURNAL OF APPLIED MECHANICS, Vol. 49, pp. 549.

Downloaded 03 May 2010 to 171.66.16.31. Redistribution subject to ASME license or copyright; see http://www.asme.org/terms/Terms_Use.cfm

Elastic-Plastic Analysis of Cracks on Bimaterial Interfaces: Part II—Structure of Small-Scale Yielding Fields

C. F. Shih

R. J. Asaro

Division of Engineering,
Brown University,
Providence, R. I. 02912

In Part I we found that although the near tip fields of cracks on bimaterial interfaces do not have a separable form of the HRR type, they appear to be nearly separable in an annular zone within the plastic zone. Furthermore, the fields bear strong similarities to mixed mode HRR fields for homogeneous medium. Based on our numerical results, we have been able to identify a clear mathematical structure. We found that the small-scale yielding crack tip fields are members of a family parameterized by a near tip phase angle ξ, and that the fields nearly scale with the value of the J-integral. In Part II, the original derivation of the mathematical structure of the small-scale yielding fields is elaborated upon. The issue of crack face contact is addressed and the phenomenology is described in terms of the phase parameter ξ. Crack tip plastic deformation results in an open *crack for a range of ξ which is nearly symmetric about the state corresponding to pure remote tension. Plane-strain plastic zones and crack tip fields for the complete range of ξ are presented. Over distances comparable to the size of the dominant plastic zone, the stress levels that can be achieved are limited by the yield stress of the weaker (lower yield strength) material. On the other hand, the stresses well within the plastic zone are governed by the strain-hardening behavior of the more plastically compliant (lower strain-hardening) material. We observe that the extent of the annular zone where the fields are nearly separable (i.e., of the HRR form) is dependent on the remote load combinations and the material combination. When the tractions on the interface are predominantly tensile, there are no indications of crack face contact over any length scale of physical relevance. Instead, the crack tip opens smoothly and crack tip fields as well as the crack opening displacement are scaled by the J-integral. The paper concludes with a discussion on the range of load combinations which could be applied to two fracture test specimen geometries to obtain valid fracture toughness data.*

1 Introduction

In Part I of this article (Shih and Asaro, 1988), numerical solutions were presented for the elastic-plastic fields of a crack on the interface between a nonlinear power-law hardening material and a rigid substrate. Specifically, the problem of an infinite crack embedded in an infinite bimaterial body (see Fig. 1) subject to combinations of remote tension and shear was analyzed under loading conditions that caused small-scale yielding. The calculations were performed for a material described by a small strain, isotropic J_2 deformation theory. This facilitated making the connection between the interface crack solutions, the existing framework for nonlinear fracture mechanics, and specific solutions for crack tip fields in homogeneous media (e.g., Hutchinson, 1983). In one sense the work complimented analyses such as that of Knowles and Sternberg (1983) who studied the behavior of an interface crack between two neo-Hookean sheets. In these analytic asymptotic solutions, as well as the numerical solutions of Part I, it was shown that pathological features of the linear elastic solutions, such as the near tip oscillations in stresses and displacements are strongly mitigated by nonlinear kinematics or material behavior. The linear elastic asymptotic solutions, which provided the point of departure for our numerical analyses, were discussed in Part I.

The numerical analyses described in Part I also provided clarification of the structure of the small-scale yielding fields. In particular, it was found that the interface crack small-scale

Contributed by the Applied Mechanics Division of THE AMERICAN SOCIETY OF MECHANICAL ENGINEERS for publication in the JOURNAL OF APPLIED MECHANICS.

Discussion on this paper should be addressed to the Editorial Department, ASME, United Engineering Center, 345 East 47th Street, New York, N. Y. 10017, and will be accepted until two months after final publication of the paper itself in the JOURNAL OF APPLIED MECHANICS. Manuscript received by ASME Applied Mechanics Division, April 25, 1988; final revision, February 1, 1989.

Copyright © 1989 by ASME

Downloaded 03 May 2010 to 171.66.16.31. Redistribution subject to ASME license or copyright; see http://www.asme.org/terms/Terms_Use.cfm

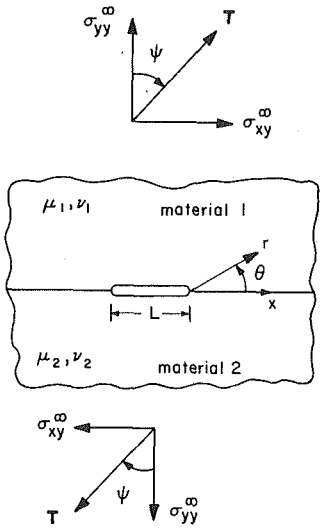


Fig. 1 Crack on bimaterial interface

yielding fields are members of a family parameterized by a near-tip *phase angle*, ξ, defined as $\xi \equiv \phi + \epsilon \ln (\mathbf{Q}\bar{\mathbf{Q}}/\sigma_0^2 L)$. $\mathbf{Q}$ is a complex stress intensity factor defined by the linear elastic asymptotic solution, ϕ is its phase angle, L is a characteristic crack dimension, σ_0 is the yield stress of the weaker material, and ϵ is a elastic bimaterial constant. We found that the dependence of the crack tip fields on radial distance is nearly of the HRR form for asymptotic fields in homogeneous media (Hutchinson, 1968; Rice and Rosengren, 1968) and that the small-scale yielding fields nearly scale with the value of the J-integral (Rice, 1968). This structure is reviewed in Section 2 of this paper.

In the present paper we describe the small-scale yielding fields in more detail and also demonstrate how the phenomenology of crack face contact can be described in terms of ξ. In the absence of plastic deformation, the range of ξ for which the crack is *open* is skewed about the state corresponding to pure remote tension. In contrast, crack tip plastic deformation results in an *open* crack range, which is more nearly symmetrical about the state corresponding to pure remote tension. We make contact with a dimensional analysis by Rice (1988) and a subsequent study by Zywicz and Parks (1988), which contain results which are consistent with our general framework.

The plan of the paper is as follows. In the next section the structure of the small-scale yielding fields is described. Numerical methods and the finite element boundary problems are described in Section 3. Results of plane-strain crack tip fields for two material combinations involving an elastic-plastic solid bonded onto an elastic substrate and, secondly, to an elastic-plastic material with different material properties, are presented in Section 4. The range of validity of linear elasticity and small-scale yielding solutions as they pertain to two fracture test specimens are discussed in Section 5.

2 Structure of Fields Under Small-Scale Yielding

2.1 Linear Elasticity Solutions. Solutions to specific problems of cracks lying along bimaterial interfaces of isotropic media have been given by Cherepanov (1962), England (1965), Erdogan (1965), and Rice and Sih (1965). More recently, Ting (1986) has presented a framework for determining the degree of singularity and the nature of the asymptotic fields for the general interfacial crack between two elastic anisotropic materials. Park and Earmme (1986), Hutchinson, Mear, and Rice (1987), and Suo and Hutchinson (1988) have obtained solutions for several elastic interfacial crack problems, and Rice (1988) has reexamined elastic fracture mechanics concepts for interface cracks.

A crack of total length L lying on the interface between two semi-infinite slabs of isotropic elastic solids with differing material moduli is shown in Fig. 1. The shear moduli and Poisson's ratios are μ_1, μ_2, and ν_1, ν_2, and r and θ are polar coordinates centered at the crack tip. There are three independent nondimensional material parameters but, as has been shown by Dundurs (1969), the solution for this class of problems depends on only two parameters. In plane strain they are

$$\beta_1 = [\mu_1(1-\nu_2) - \mu_2(1-\nu_1)]/[\mu_1(1-\nu_2) + \mu_2(1-\nu_1)] \quad (1)$$

$$\beta_2 = [\mu_1(1-2\nu_2) - \mu_2(1-2\nu_1)]/[\mu_1(1-\nu_2) + \mu_2(1-\nu_1)]. \quad (2)$$

These parameters vanish for identical materials across the interface and change sign when the materials are interchanged.

At small distances from the crack tip, the in-plane stresses have the singular form

$$\sigma_{ij} = \mathrm{Re}\left\{\frac{\mathbf{Q}}{\sqrt{2\pi r}}\left(\frac{r}{L}\right)^{i\epsilon}\tilde{\sigma}_{ij}(\theta;\epsilon)\right\} \quad (3)$$

where $i = \sqrt{-1}$, $\mathbf{Q}$ is the complex stress intensity factor, $|(r/L)^{i\epsilon}| = 1$, and $\tilde{\sigma}_{ij}(\theta;\epsilon)$ is the universal complex dimensionless angular function which depends on the bimaterial constant ϵ defined by (Williams, 1959) as

$$\epsilon = \frac{1}{2\pi}\ln\left(\frac{1-\beta_2}{1+\beta_2}\right). \quad (4)$$

In (3), L is a characteristic dimension of the crack geometry. As an example, L is identified as the crack length of the geometry depicted in Fig. 1. It is convenient to write $\mathbf{Q}$ as

$$\mathbf{Q} = Q_1 + iQ_2 = |\mathbf{Q}|e^{i\phi} \quad (5)$$

where $|\mathbf{Q}|$ and ϕ are the amplitude and phase of $\mathbf{Q}$. Thus, tractions on the bond line are

$$\mathbf{t} = (\sigma_{yy} + i\sigma_{xy})_{\theta=0} = \frac{\mathbf{Q}}{\sqrt{2\pi r}}\left(\frac{r}{L}\right)^{i\epsilon} = \frac{|\mathbf{Q}|}{\sqrt{2\pi r}}e^{i(\phi + \epsilon\ln(r/L))} \quad (6)$$

and displacement jumps across crack faces take the form

$$\Delta\mathbf{u} = \Delta u_y + i\Delta u_x = (u_y + iu_x)_{\theta=\pi} - (u_y + iu_x)_{\theta=-\pi}$$

$$= \frac{8\Lambda}{\sqrt{(1+4\epsilon^2)}}\frac{|\mathbf{Q}|\sqrt{r}}{\sqrt{2\pi}}e^{i(-\Theta+\phi+\epsilon\ln(r/L))} \quad (7)$$

where $\Theta = \tan^{-1}2\epsilon$, and for plane strain $\Lambda = [(1-\nu_1)/\mu_1 + (1-\nu_2)/\mu_2]/(4\cosh^2\pi\epsilon)$.

Different normalizations of the singular crack tip fields which result in stress intensity factors that differ by phase angles and scaling constants involving ϵ have appeared in the literature on interface cracks. Rice (1988) introduced the stress intensity factor $\mathbf{K}$ which is related to $\mathbf{Q}$ by

$$\mathbf{K} = \mathbf{Q}L^{-i\epsilon},\ |\mathbf{K}| = |\mathbf{Q}|,\ \mathbf{K}\bar{\mathbf{K}} = \mathbf{Q}\bar{\mathbf{Q}} \text{ and } \varphi = \phi - \epsilon\ln L \quad (8)$$

where φ is the phase of $\mathbf{K}$. It is clear from (3) that $\mathbf{K}$ or $\mathbf{Q}L^{-i\epsilon}$ uniquely characterizes the crack tip fields. In other words, $\mathbf{K}$ fully accounts for the effects of both load and geometry on the crack tip field whereas $\mathbf{Q}$ and a characteristic length L are required for the same purpose. The merits of various definitions of stress intensity factors and possible approaches for recording and using fracture toughness data have been discussed by Rice (1988).

For the geometry depicted in Fig. 1 and stressed by remote traction $\mathbf{T}(\mathbf{T} = |\mathbf{T}|e^{i\psi} = \sigma_{yy}^{\infty} + i\sigma_{xy}^{\infty})$, $\mathbf{Q} = (1+i2\epsilon)\mathbf{T}\sqrt{\pi L/2}$ (Rice and Sih, 1965). The connection between the phase of $\mathbf{Q}$ and $\mathbf{T}$ is $\phi = \psi + \tan^{-1}2\epsilon$. Thus, changes in crack length at fixed

Downloaded 03 May 2010 to 171.66.16.31. Redistribution subject to ASME license or copyright; see http://www.asme.org/terms/Terms_Use.cfm

ψ($|\mathbf{T}|$ is free to vary) do not change the phase of $\mathbf{Q}$. For later use, we note that $\varphi = -\epsilon \ln L + \psi + \tan^{-1} 2\epsilon$ for the geometry of Fig. 1.

A relation which will be of use later in the analysis is the energy release rate for the crack advancing along the interface (Malyshev and Salganik, 1965; Willis, 1971)

$$\mathcal{G} = \Lambda \mathbf{Q}\bar{\mathbf{Q}} = \Lambda \mathbf{K}\bar{\mathbf{K}} \tag{9}$$

where Λ is the parameter defined for (7).

The linear elasticity solution for the displacement jumps (7) predicts that overlapping of crack faces always occurs, though the zone of overlapping crack faces is very small compared to L for load states in the range -45 deg $\leq \phi \leq 45$ deg, i.e., $Q_1 > |Q_2|$. To redress this physically objectionable behavior, investigators have proposed various models and approaches. Comninou (1977a, b) and Comninou and Schmueser (1978) reformulated the linear elasticity boundary value problem to allow a zone of contact to develop at the crack tip. Solutions for a range of remote load combinations were obtained. Achenbach et al. (1979) introduced a Dugdale-Barenblatt strip yield zone at the crack tip which eliminated crack face overlapping as well as stress singularities altogether. Ortiz and Blume (1988) have obtained an inner solution, based on a zone of decohesion (and sliding) at the crack tip, which does not lead to interpenetrating crack faces in the region of dominance of this inner solution. Along similar lines of inquiry, Needleman (1987) has implemented a decohesion model in a finite element study of (rigid) inclusion debonding which takes account of finite geometry changes.

We take the view that while the elasticity solutions are invalid on the scale of the contact zone, they still provide an accurate description of the fields in an annular region surrounding the contact zone, as long as the size of the contact zone and plastic zone (if any) is small compared to the zone of dominance of the elastic fields given by (3). In this sense, crack face contact on a size scale which is much smaller than the crack length (or the relevant crack dimension) can be treated as a small-scale nonlinearity. Along this line of argument, Atkinson (1982) had used (3) as the outer solution and matched asymptotic expansions to derive an analytic contact zone solution for the Comninou (1977a) model. We will return to the issue of crack face contact following the discussion on the structure of the small-scale yielding fields.

2.2 Small-Scale Yielding Formulation. In the small-scale yielding formulation, the actual crack problem is replaced by a semi-infinite crack in an infinite media with the asymptotic boundary condition that at large r the field approaches that given by (3). The original derivation of the results to be discussed here is contained in an earlier publication (Shih and Asaro, 1988). It is elaborated upon here and contact is made with subsequent studies (and alternative approaches) which lead to results which are in agreement with our main conclusions.

Let σ_{01} and σ_{02} be the yield strengths of materials 1 and 2. It is convenient to designate the yield strength of the weaker solid by σ_0, i.e., $\sigma_0 = \min(\sigma_{01}, \sigma_{02})$. Within the boundary layer formulation, the stresses depend on $\mathbf{Q}L^{-i\epsilon}$ and σ_0, and on dimensionless material parameters, e.g., σ_{02}/σ_0, β_1, β_2, etc. By dimensional analysis,

$$\sigma_{ij} = \sigma_0 f_{ij}\left(\frac{r\sigma_0^2}{\mathbf{Q}\bar{\mathbf{Q}}},\ \theta,\ \text{phase}\left\{\mathbf{Q}\left(\frac{r}{L}\right)^{i\epsilon}\right\};\ \text{dimensionless material parameters}\right). \tag{10}$$

Here, f_{ij} is a dimensionless function of the dimensionless arguments and it may be noted that $\mathbf{Q}\bar{\mathbf{Q}}$ has dimensions of *square of stress* times *length*. Henceforth we will assume that the implicit dependence of f_{ij} on material parameters is understood.

Directing our attention to the dependence on σ_{ij} on $\mathbf{Q}$, L and distance from the crack tip we write

$$\sigma_{ij} = \sigma_0 f_{ij}\left(\frac{r\sigma_0^2}{\mathbf{Q}\bar{\mathbf{Q}}},\theta,\phi + \epsilon \ln\left(\frac{r}{L}\right)\right) \tag{11}$$

where $\phi + \epsilon \ln(r/L)$ is the phase of $\mathbf{Q}(r/L)^{i\epsilon}$. To reveal the structure of f_{ij}, it is advantageous to express the third argument as the sum of a constant phase angle and a variable phase angle which depends on distance r. To this end, the third argument is modified by incorporating a dependence on the first argument, viz.,

$$\phi + \epsilon \ln\left[\left(\frac{r}{L}\right)\left(\frac{\mathbf{Q}\bar{\mathbf{Q}}}{r\sigma_0^2}\right)^m\right] = \phi + \epsilon \ln\left(\frac{\mathbf{Q}\bar{\mathbf{Q}}}{L\sigma_0^2}\right) + (m-1)\epsilon \ln\left(\frac{\mathbf{Q}\bar{\mathbf{Q}}}{r\sigma_0^2}\right). \tag{12}$$

We should point out that the phase can depend on $\ln r$ in a manner which is more complex than that suggested by the last term in (12). In Part I we introduced a near-tip phase parameter, ξ, defined by

$$\xi = \phi + \epsilon \ln\left(\frac{\mathbf{Q}\bar{\mathbf{Q}}}{L\sigma_0^2}\right). \tag{13}$$

ξ varies linearly with ϕ, depends weakly on $\mathbf{Q}\bar{\mathbf{Q}}$ and L, and does not involve r. Making use of (13), the right-hand side of (12) can be written as

$$\xi + \text{phase}\left\{\left(\frac{r\sigma_0^2}{\mathbf{Q}\bar{\mathbf{Q}}}\right)^{i\Sigma}\right\} \tag{14}$$

where Σ is a dimensionless combination of material parameters yet to be determined. We use the latter result to restate (11) as

$$\sigma_{ij} = \sigma_0 f_{ij}\left(\frac{r\sigma_0^2}{\mathbf{Q}\bar{\mathbf{Q}}},\ \theta,\ \text{phase}\left\{\left(\frac{r\sigma_0^2}{\mathbf{Q}\bar{\mathbf{Q}}}\right)^{i\Sigma}\right\};\xi\right). \tag{15}$$

For the small-scale yielding analysis, it is convenient to phrase the remote load in terms of $|\mathbf{K}|$ (or $\mathbf{K}\bar{\mathbf{K}}/\sigma_0^2$) and its phase φ. Use (8) in (13) to obtain

$$\xi = \varphi + \epsilon \ln\left(\frac{\mathbf{K}\bar{\mathbf{K}}}{\sigma_0^2}\right). \tag{16}$$

The characteristic crack dimension, L, does not appear explicitly in the equation (16) for ξ, but has been absorbed in the phase of $\mathbf{K}$. Now, the general result in (15) has the alternative representation:

$$\sigma_{ij} = \sigma_0 f_{ij}\left(\frac{r\sigma_0^2}{\mathbf{K}\bar{\mathbf{K}}},\ \theta,\ \text{phase}\left\{\left(\frac{r\sigma_0^2}{\mathbf{K}\bar{\mathbf{K}}}\right)^{i\Sigma}\right\};\xi\right). \tag{17}$$

Since ξ is the phase angle of a complex quantity, f_{ij} has a periodicity of 2π with respect to the argument ξ, i.e.,

$$f_{ij}(\ldots\ldots;\ \xi) = f_{ij}(\ldots\ldots;\ \xi + m\pi) \qquad m = 2,4,6. \tag{18}$$

Furthermore, due to the linearity of the equilibrium and strain-displacement equations

$$f_{ij}(\ldots\ldots;\ \xi) = -f_{ij}(\ldots\ldots;\ \xi + m\pi) \qquad m = 1,3,5. \tag{19}$$

Thus, ξ serves as the phase parameter of the fields in the small-scale yielding formulation just as φ (or $\phi - \epsilon \ln L$) is the phase angle of the linear elastic singular fields. Using a different approach, Zywicz and Parks (1988) introduced a phase parameter ζ_0 which differs inconsequentially from (16) by a constant involving ϵ.

The mathematical structure of the fields expressed by (15), and (17)–(19) was derived without regard to contact between the crack faces. In fact, displacement jumps across the crack faces must have the form,

Downloaded 03 May 2010 to 171.66.16.31. Redistribution subject to ASME license or copyright; see http://www.asme.org/terms/Terms_Use.cfm

$$\Delta u_i = \epsilon_0 \frac{\mathbf{K}\bar{\mathbf{K}}}{\sigma_0^2} g_i\left(\frac{r\sigma_0^2}{\mathbf{K}\bar{\mathbf{K}}}, \text{phase}\left\{\left(\frac{r\sigma_0^2}{\mathbf{K}\bar{\mathbf{K}}}\right)^{i\Sigma}\right\}; \xi\right) \tag{20}$$

where ϵ_0 is a reference yield strain and the dimensionless function g_i has the periodic structure expressed by (18) and (19). In this paper our interest is restricted to the range of ξ where the crack faces are not in *contact*. The definition of an *open* crack will be introduced shortly and the validity of the proposed fields will be established in Section 4 in terms of the range of ξ. For the present, it is useful to examine the mathematical structure of the fields under the fictitious assumption that crack faces may overlap.

The effective stress σ_e ($\sigma_e^2 = 3s_{ij}s_{ij}/2$, where s_{ij} is the deviatoric stress), has the form

$$\sigma_e = \sigma_0 f_e\left(\frac{r\sigma_0^2}{\mathbf{K}\bar{\mathbf{K}}}, \theta, \text{phase}\left\{\left(\frac{r\sigma_0^2}{\mathbf{K}\bar{\mathbf{K}}}\right)^{i\Sigma}\right\}; \xi\right). \tag{21}$$

The elastic-plastic boundary in the weaker material is the locus of points where σ_e equals σ_0. Substituting these values in (21) and rearranging leads immediately to the following results for the plastic zone (Shih and Asaro, 1988):

$$r_p(\theta) = \frac{\mathbf{K}\bar{\mathbf{K}}}{\sigma_0^2} R(\theta;\xi)\ . \tag{22}$$

Here, $R(\theta; \xi)$ is a dimensionless angular function which depends on ξ and on dimensionless material parameters. Since σ_e is quadratic in the stress components which have periodicity expressed by (18) and (19), the angular function R has a periodicity of π with respect to ξ,

$$R(\theta;\xi) = R(\theta;\xi + m\pi) \quad m = 1,2,3, \ldots\ldots \tag{23}$$

Rice (1988) has derived the relation,

$$r_p = \frac{\mathbf{K}\bar{\mathbf{K}}}{\sigma_0^2} \tilde{R}(\phi - \epsilon \ln(L/r_p)) \tag{24}$$

by a similar dimensional analysis. In (24), r_p is a characteristic dimension of the plastic zone; for example, r_p can be taken to be the maximum extent of the plastic zone. Rice's implicit equation for r_p can be made explicit by replacing r_p in the argument by $\mathbf{K}\bar{\mathbf{K}}/\sigma_0^2$, whereupon a result similar to (22) is recovered.

The function $R(\theta; \xi)$ can be determined directly from plots of small-scale yielding plastic zones. This has been carried out for a range of phase angles ξ in Part I (Shih and Asaro, 1988) and for several material systems in this paper. Alternatively, an estimate of $R(\theta; \xi)$ can be obtained by approximating f_e in (21) by using the linear elasticity fields in (3). The latter procedure has been adopted by Zywicz and Parks (1988) to estimate plastic zone sizes and shapes.

2.3 Plausible Form of Asymptotic Fields. The size of the dominant plastic zone (which develops in the weaker material) is controlled by the yield strength of the weaker material σ_0 (see (22)). Over length scales which are comparable to the dominant plastic zone, the stress levels that can be achieved in both materials are set by σ_0. On the other hand, we will argue that the form of the asymptotic crack tip fields is governed by the hardening characteristics of the material with the least hardening capacity.

We assume that each material of the material pair is characterized by a Ramberg-Osgood stress-strain relation where the uniaxial plastic strain is related to the stress by $\epsilon^p/\epsilon_0 = \alpha(\sigma/\sigma_0)^n$ where $\epsilon_0 = \sigma_0/E$. The plastic properties of material 1 (top material) are designated by α_1, σ_{01}, and n_1 and those for material 2 are designated by α_2, σ_{02}, and n_2. The reference strains are defined by $\epsilon_{01} = \sigma_{01}/E_1$ and $\epsilon_{02} = \sigma_{02}/E_2$. We designate the larger of n_1 and n_2 by n, i.e., $n = \max(n_1, n_2)$. To avoid ambiguity in the discussions to follow, material 1 will be taken to be the lower hardening material and its elastic and plastic properties are designated by ν, E, α, σ_0, ϵ_0, and n.

Let E_{t1} and E_{t2} designate the tangent moduli of material 1 and 2, respectively. As $r \to 0$, and assuming that the stresses are singular, $E_{t1}/E_{t2} \to 0$. This suggests that, as $r \to 0$, the material system behaves increasingly like that of a plastically deforming material which is bonded to a rigid substrate. We will now argue that the form of the asymptotic fields is governed by the strain-hardening characteristics of material 1.

We assume that the response of the plastically deforming material is described by a J_2 deformation theory of plasticity. Path independence of the J-integral (Rice, 1968) is easily demonstrated for the interface crack once it is recognized that the contribution to the J-integral from the upper interface, $x_2 = 0^+$, is negated by the contribution from the lower interface, $x_2 = 0^-$. Now, take a circular contour centered at the tip and use path independence to shrink the contour onto the crack tip. Since J is nonzero, as it must be for a deformation theory solid (in this case the J-integral is precisely the energy release rate), we conclude that the strain energy density $W \sim 0(1/r)$ as $r \to 0$. This requires the product of stress and strain to have a $1/r$ singularity. If it is further assumed that the fields have a product dependence on the first argument of f_{ij} (17), then singular solutions, if they exist, would have the form

$$\sigma_{ij} = \sigma_0\left(\frac{\mathbf{K}\bar{\mathbf{K}}}{\sigma_0^2 r}\right)^{1/(n+1)} \tilde{h}_{ij}(\theta, \text{phase}\{\hat{r}^{\,i\Sigma}\}\ ;\ \xi) \tag{25}$$

where $\hat{r} = r/(\mathbf{K}\bar{\mathbf{K}}/\sigma_0^2)$, and the implicit dependence of $\tilde{h}_{ij}$ on material parameters is understood.

The dimensionless function $\tilde{h}_{ij}$ has a periodic dependence (with period 2π) on ξ, and the arguments leading to (25) require that $\tilde{h}_{ij}$ be bounded. Though $\tilde{h}_{ij}$ is a bounded function, it can nevertheless oscillate rapidly as $\hat{r} \to 0$. Under small-scale yielding, $J = \mathcal{G}$ (Rice, 1968) and noting the relation between $\mathcal{G}$ and $\mathbf{K}\bar{\mathbf{K}}$ (9), the singular fields can be arranged in the form

$$\sigma_{ij} = \sigma_0\left(\frac{J}{\alpha\sigma_0\epsilon_0 r}\right)^{1/(n+1)} h_{ij}(\theta, \text{phase}\ \{\hat{r}^{\,i\Sigma}\}\ ;\ \xi)\ . \tag{26}$$

where $h_{ij} = (\alpha/\Lambda E)^{1/(n+1)}\tilde{h}_{ij}$ and Λ has been defined in connection with (7). It may be noted that (26) is consistent with the product form of the linear elastic fields (3) involving a bounded $\tilde{h}_{ij}$ which depends on the phase $\{(r/L)^{i\epsilon}\}$.

It is instructive to examine the dependence of h_{ij} on r for two special cases. Suppose that both materials are elastic and $\epsilon \neq 0$. At fixed θ, the stresses have the form $\sigma_{ij} \alpha\ r^{-1/2}h_{ij}(\hat{r}; \xi, n)$. Comparing this form with (3), we conclude that the variation of h_{ij} with r is bounded but rapidly oscillatory as $r \to 0$. Now suppose that one material is rigid-perfectly plastic. Then, h_{ij} is again bounded and the term multiplying it, $r^{-1/(n+1)}$ ($n \to \infty$), is also bounded.

As a third example, we take materials 1 and 2 to be strain-hardening materials with $n_1 > n_2$. Then by (26), the stresses above the bond line ($\theta = 0^+$) are of the form $\sigma_{ij} \sim r^{-1/(n_1+1)}h_{ij}\ (\hat{r}; n_1)$. For the moment, suppose that the stresses below the bond line ($\theta = 0^-$) have the form $\sigma_{ij} \sim r^{-1/(n_2+1)}h_{ij}$ $(\hat{r}; n_2)$. Continuity of traction across the bond line requires that $r^{-1/(n_1+1)}h_{2j}(\hat{r}; n_1) = r^{-1/(n_2+1)}h_{2j}(\hat{r}; n_2) = O(r^\lambda)$. For $n_1 \neq n_2$, the equality can be met only if h_{2j} is singular as $r \to 0$, which contradicts the original assumption that h_{ij} is bounded. In fact, if the stresses are assumed to have a power dependence on r such that traction is continuous across the bond line, i.e., $\sigma_{ij} \sim r^\lambda h_{ij}$ for both materials 1 and 2, then continuity of displacements across the bond line cannot be satisfied. Similarly, if the displacements are continuous across the bond line and are of the form $u_i \sim r^p\tilde{u}_i$ for materials 1 and 2, then continuity of traction cannot be satisfied. However, if we assume that as $r \to 0$ the material system behaves like that of a plastically-deforming material bonded to a rigid substrate, then (26) proves to be an admissible form.

Downloaded 03 May 2010 to 171.66.16.31. Redistribution subject to ASME license or copyright; see http://www.asme.org/terms/Terms_Use.cfm

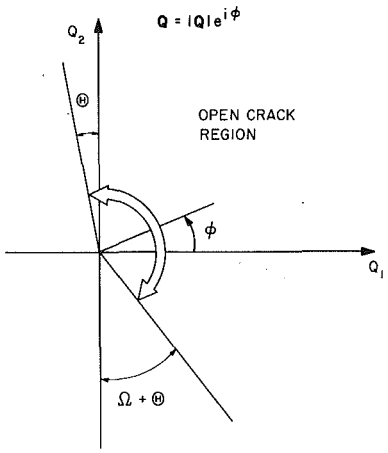


Fig. 2 Open crack domain in Q plane

It is convenient to write (26) in the form

$$\sigma_{ij} = \sigma_0 \left(\frac{J}{\alpha \sigma_0 \epsilon_0 r} \right)^{1/(n+1)} h_{ij}(\theta, \hat{r}; \xi, n) \tag{27}$$

where h_{ij} is a bounded function with respect to $\hat{r}$ and

$$\xi = \phi + \epsilon \ln \left(\frac{\mathbf{Q}\bar{\mathbf{Q}}}{\sigma_0^2 L} \right) = \varphi + \epsilon \ln \left(\frac{\mathbf{K}\bar{\mathbf{K}}}{\sigma_0^2} \right) = \phi + \epsilon \ln \left(\frac{J}{\Lambda \sigma_0^2} \right). \tag{28}$$

The form of the fields (27) has been corroborated by the numerical solutions of Section 4. These full field solutions also show that for load states in the range $-\pi/6 \le \xi \le \pi/6$, h_{ij} is a slowly varying function of $\hat{r}$ over all physically-relevant length scales. Thus, the near tip fields nearly scale with $J^{1/(n+1)}$, since h_{ij} is only weakly dependent on J through the phase parameter ξ. Moreover, these near tip fields of an interface crack display strong similarities to mixed mode HRR fields.

When the plane ahead of the crack is stressed by tension and shear, the HRR singularity (Hutchinson, 1968; Rice and Rosengren, 1968) for homogeneous media has the form (Shih, 1974)

$$\sigma_{ij} = \sigma_0 \left(\frac{J}{\alpha \sigma_0 \epsilon_0 r} \right)^{1/(n+1)} \tilde{\sigma}_{ij}(\theta; M^p, n) \ . \tag{29}$$

Here, M^p is the mixity of the plastic singular fields defined by the relative magnitudes of $\sigma_{\theta\theta}$ and $\sigma_{r\theta}$ along the radial line $\theta = 0$ as $r \to 0$. The angular functions $\tilde{\sigma}_{ij}$ for several values of M^p have been tabulated by Symington et al. (1988). Under small-scale yielding, the effects of load and geometry on the crack tip field of homogeneous media are characterized by J and M^p. The structure of the near tip fields (27) suggests that J and ξ are the characterization parameters of the near tip fields of cracks on bimaterial interfaces.

2.4 Range of ξ for an Open Crack. According to the linear elasticity solution, overlapping of crack faces will occur at some distance for all values of ϕ if $\epsilon \neq 0$. Nevertheless, for a range of ϕ the zone of interpenetration is confined to a distance from the crack tip that is smaller than physically relevant length scales. For this reason, we define a crack to be *open* if

$$\Delta u_2 \ge 0 \text{ for } r_c \le r \le L \tag{30}$$

where r_c is small compared to L. The size of the contact zone can be estimated by using the elasticity solution (7). From (7), the opening gap between the crack faces, Δu_2 is positive over distances r/L which satisfy

$$-\pi/2 \le \phi + \epsilon \ln(r/L) - \Theta \le \pi/2. \tag{31}$$

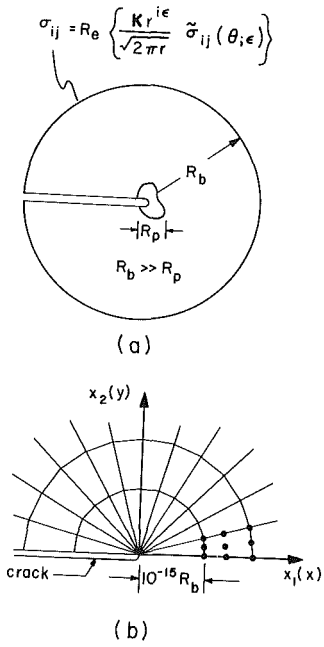


Fig. 3 (*a*) Small-scale yielding formulation and (*b*) finite element mesh of upper half of crack tip region and crack tip conventions

Table 1

ϵ	Θ(deg)	r/L	Ω(deg)
0.025	2.86	10^{-2}	6.6
		10^{-3}	9.89
		10^{-4}	13.2
		10^{-6}	19.8
0.050	5.71	10^{-2}	13.2
		10^{-3}	19.8
		10^{-4}	26.4
		10^{-6}	39.6
0.100	11.3	10^{-2}	26.4
		10^{-3}	39.6
		10^{-4}	52.8
		10^{-6}	79.2
0.175	19.3	10^{-2}	46.2
		10^{-3}	69.3
		10^{-4}	92.3
		10^{-6}	139.0

For the case $\epsilon = 0$, (31) states that the crack is open as long as the Mode I stress intensity factor is positive. Let $\Omega = -\epsilon \ln(r_c/L)$ and recall that $\Theta = \tan^{-1} 2\epsilon$. Then, by combining (30) and (31), the *open* crack range in terms of ϕ is

$$-\pi/2 + \Omega + \Theta \le \phi \le \pi/2 + \Theta. \tag{32}$$

Figure 2 depicts the *open* crack region in the **Q** plane. Values of Ω and Θ for four values of ϵ and four values of r_c/L are tabulated in Table 1. Since $\phi = \psi + \Theta$ for the geometry in Fig. 1, the range of phase angles of the remote load for an *open* right crack tip is

$$-\pi/2 + \Omega \le \psi \le \pi/2. \tag{33}$$

The characteristic length in the small-scale yielding formulation is $\mathbf{K}\bar{\mathbf{K}}/\sigma_0^2$ (or $\mathbf{Q}\bar{\mathbf{Q}}/\sigma_0^2$). Therefore, crack face contact under small-scale yielding must be phrased in terms of the normalized distance $\hat{r}$ ($\equiv r/(\mathbf{K}\bar{\mathbf{K}}/\sigma_0^2 = r/(\mathbf{Q}\bar{\mathbf{Q}}/\sigma_0^2)$). The form of the desired result can be obtained with the help of the elasticity result (31). Using the plastic phase angle ξ, defined by (13), we rewrite (31) as

$$-\pi/2 \le \xi + \epsilon \ln \hat{r} - \Theta \le \pi/2. \tag{34}$$

Under small-scale yielding, the crack is *open* crack if

$$\Delta u_2 \ge 0 \text{ for } c_1 \le \hat{r} \le c_2 \tag{35}$$

Downloaded 03 May 2010 to 171.66.16.31. Redistribution subject to ASME license or copyright; see http://www.asme.org/terms/Terms_Use.cfm

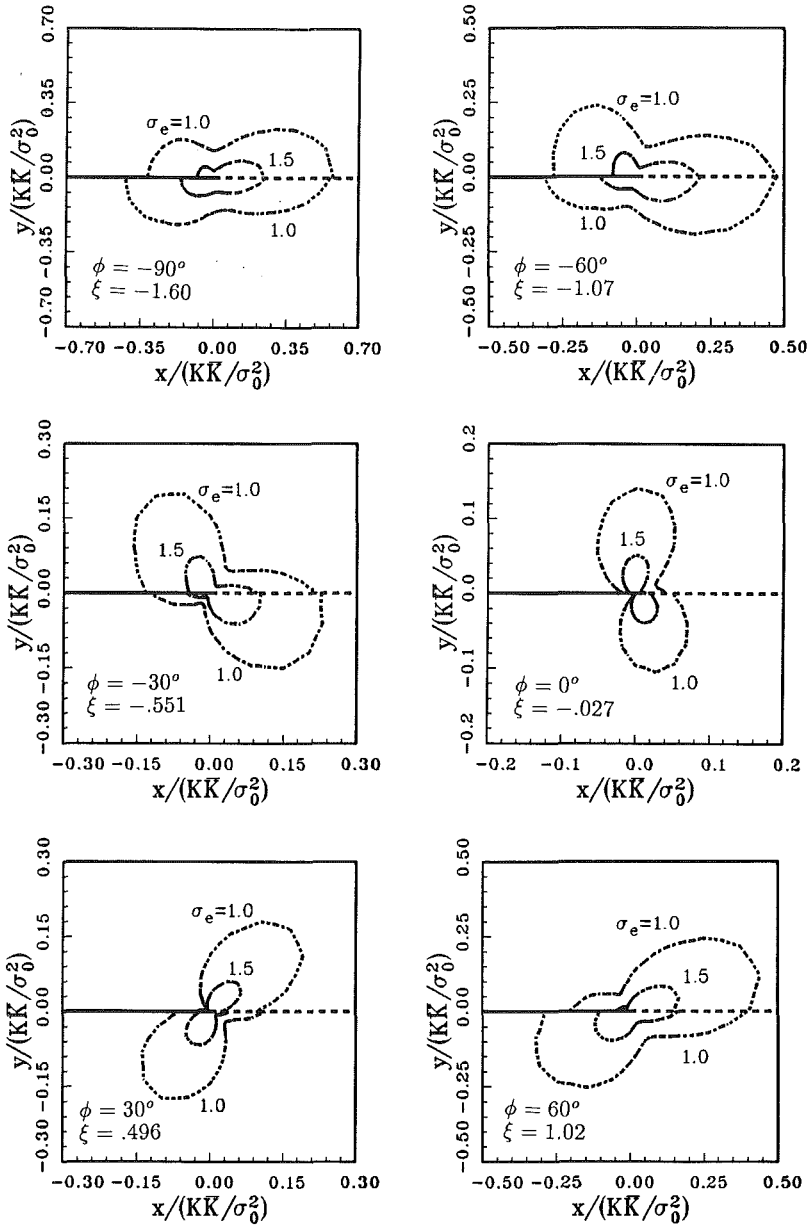


Fig. 4 Elastic-plastic material bonded onto elastic substrate—effective stress contours and plastic zones of six load states

where $c_1 \ll 1$ and $c_2 \gg 1$. Combining (34) and (35) and approximating Θ by 2ϵ, the range of ξ for an *open* crack is

$$-\pi/2+\epsilon(2-\ln c_1)\leq\xi\leq\pi/2+\epsilon(2-\ln c_2). \tag{36}$$

Suppose $\ln c_1 = -2$ and $\ln c_2 = 2$ ($c_2 = 1/c_1 = 7.5$), then (36) reduces to $-\pi/2 + 4\epsilon \leq \xi \leq \pi/2$. If $\ln c_1 = -4$ and $\ln c_2 = 4$ ($c_2 = 1/c_1 = 55$), the range is decreased by 4ϵ, $-\pi/2 + 6\epsilon \leq \xi \leq \pi/2 - 2\epsilon$. A more accurate estimate of the *open* crack range based on the small-scale yielding solutions is discussed in Section 4.

3 Problem Description and Numerical Procedures

3.1 Boundary Conditions and Mesh Design. Computations were performed in Part I for a full boundary value problem involving an interface crack lying on a bimaterial interface of the center-cracked-panel geometry, and for small-scale yielding fields produced by loading the crack tip with a *remote* **K** stress field which is referred to as the boundary layer formulation. The calculations to be discussed in Section 4 are all of the latter type, although contact will be made with the full boundary value problem presented in Part I. Loading is prescribed by imposing the stresses of the asymptotic linear elastic field, given by (3),

$$\sigma_{ij}=\mathrm{Re}\left\{\frac{\mathbf{K}r^{i\epsilon}}{\sqrt{2\pi r}}\tilde{\sigma}_{ij}(\theta;\epsilon)\right\}, \tag{37}$$

on the remote boundary, R_b as depicted in Fig. 3(*a*).

The finite element mesh is constructed with 9-node biquadratic Lagrangian elements. An arrangement of wedge-shaped elements is employed at the crack tip; this innermost ring of elements has dimensions of $10^{-15}R_b$. The upper half of the crack tip mesh and the spatial coordinates are shown in Fig. 3(*b*). Accommodating the 15 orders of magnitude in element size while still preserving the aspect ratio of the element is accomplished by exponential scaling of element size in the

Downloaded 03 May 2010 to 171.66.16.31. Redistribution subject to ASME license or copyright; see http://www.asme.org/terms/Terms_Use.cfm

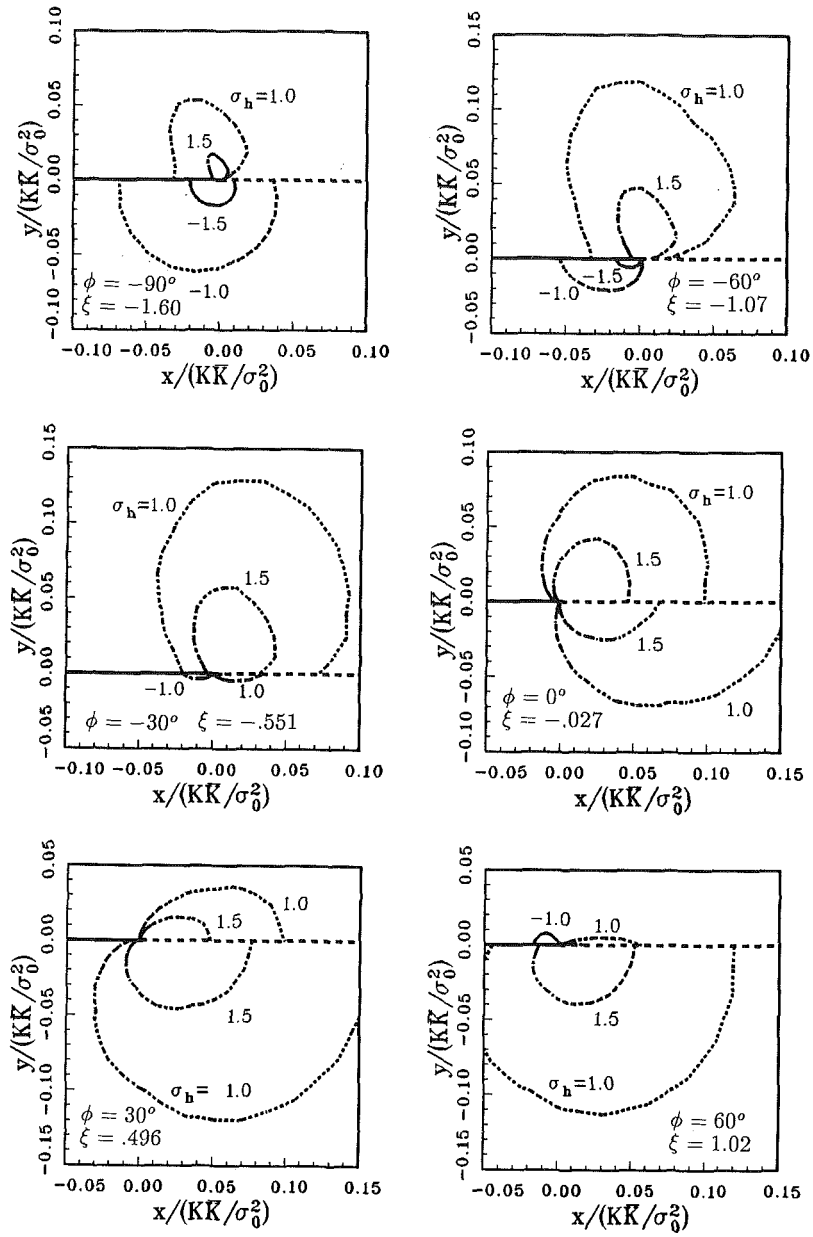


Fig. 5 Elastic-plastic material bonded onto elastic substrate—hydrostatic stress contours of six load states

radial direction. Each decade of radial distance is spanned by four annular strips of elements. In this manner, the domain between $10^{-15}\ R_b$ and R_b is spanned by 60 strips of elements. Within each strip, twelve equally-sized elements span the interval $-\pi \le \theta \le 0$ (the bottom material), and another twelve elements span the interval $0 \le \theta \le \pi$ (the top material). The mesh has a total of 1464 elements and 5980 nodes. A more complete description of a similar finite element mesh and the element arrangements has been given in Part I.

3.2 Material Laws. The deformable media are described by a J_2 deformation theory with a Ramberg-Osgood stress-strain behavior. In uniaxial tension the material deforms according to

$$\epsilon/\epsilon_0 = \sigma/\sigma_0 + \alpha(\sigma/\sigma_0)^n, \tag{38}$$

where σ_0 and ϵ_0 are the yield stress and strain, α is a material constant (taken to be 0.1), and n is the *power-law* strain-hardening exponent. Under multi-axial stress states the strain is given by

$$\epsilon_{ij} = \frac{1+\nu}{E}\, s_{ij} + \frac{1-2\nu}{3E}\, \sigma_{kk}\delta_{ij} + \frac{3}{2}\,\alpha\left(\frac{\sigma_e}{\sigma_0}\right)^{n-1}\frac{s_{ij}}{E}. \tag{39}$$

Here s_{ij} is the stress deviator, $\sigma_e = (3s_{ij}\, s_{ij}/2)^{1/2}$ is the effective stress, and ν and E are the isotropic elastic constants. In (38) the connection $\sigma_0 = E\epsilon_0$ was used. Numerical solutions for $n = 2$ through $n = 10$ have been obtained; in the present paper, however, only results for $n = 5$ and selected results for $n = 10$ are presented.

3.3 Numerical Procedure. The numerical procedure employed in this study is discussed in Part I. Only a summary of the procedures will be provided in this section. As noted in Section 3.2, the cracked body is modeled by 9-node Lagrangian quadrilateral elements. To avoid numerical difficulties which arise from nearly incompressible plastic deformation, the strain-displacement matrix, **B**, is formed using the *B*-bar method (Hughes, 1980). The deviatoric part of **B**, $\mathbf{B}^{\text{dev}}$, is evaluated at a 3 × 3 array of quadrature points, while the volumetric part,

Downloaded 03 May 2010 to 171.66.16.31. Redistribution subject to ASME license or copyright; see http://www.asme.org/terms/Terms_Use.cfm

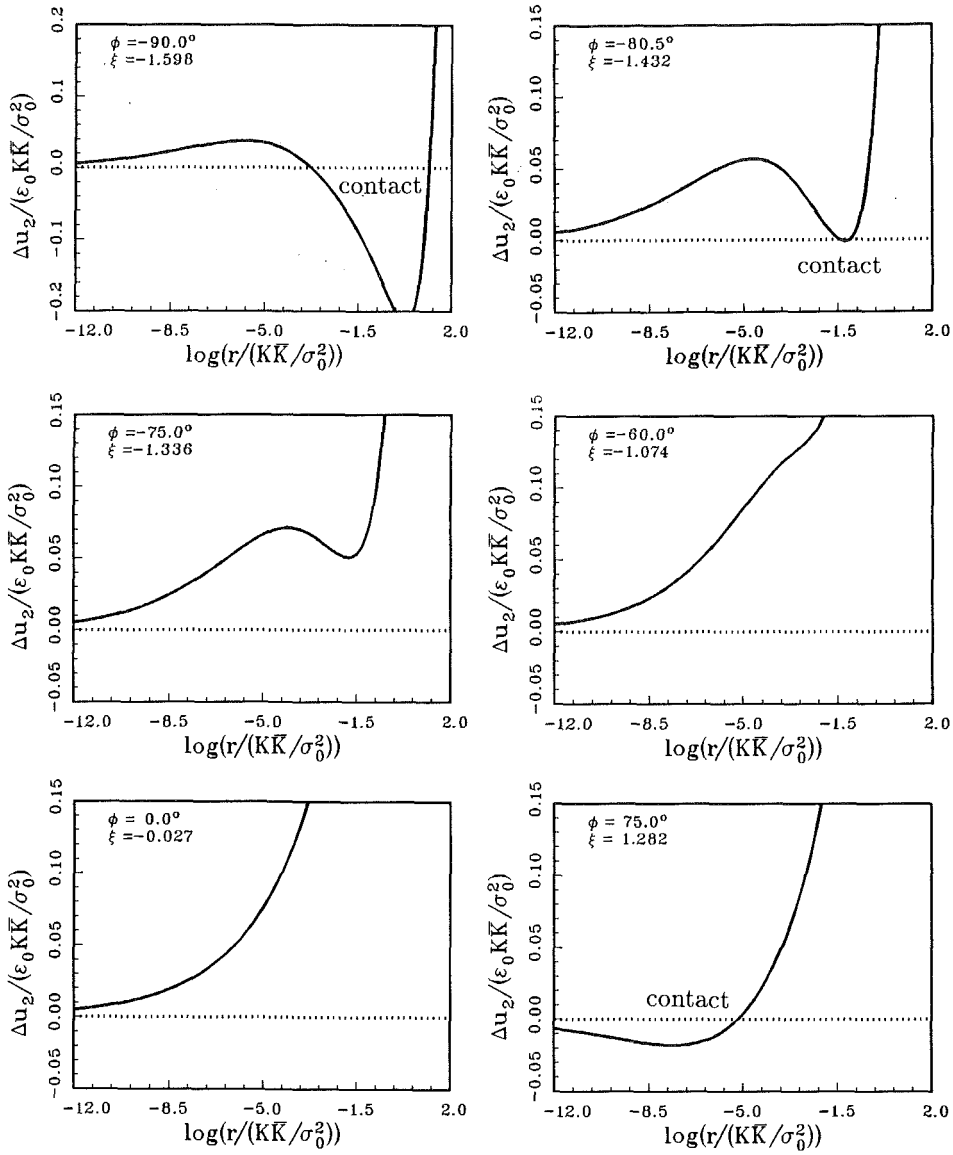


Fig. 6 Elastic-plastic material bonded onto elastic substrate—normal displacement jumps of six load states. Crack face contact (if any) is indicated.

$\mathbf{B}^{vol}$, is evaluated at a reduced array of 2 × 2 quadrature points. The desired matrix is given by

$$\bar{\mathbf{B}} = \mathbf{B}^{dev} + \bar{\mathbf{B}}^{vol} \tag{40}$$

where $\bar{\mathbf{B}}^{vol}$ is associated with the 3 × 3 quadrature points by a bilinear interpolation/extrapolation. The tangent stiffness matrix for an element is given by the sum of the inner products at each Gauss point, viz.,

$$\mathbf{k}^e = \sum_{p=1}^{9} (\bar{\mathbf{B}}\mathbf{D}\bar{\mathbf{B}}) w_p \tag{41}$$

where $\mathbf{D}$ is the matrix of material moduli evaluated at the 3 × 3 quadrature points and w_p is the appropriate weight.

The solution to the nonlinear boundary value problem is obtained by the Newton-Raphson method which is second-order convergent if a close initial estimate of the solution is available. Such an estimate is generated by parameter tracking (Shih and Needleman, 1984).

It is advantageous to work with area/domain integrals in finite element computations. In this regard it may be noted that with the help of a weighting function, a contour integral (path-independent or not) can be restated as an area/domain integral (e.g., Moran and Shih, 1987). To this end consider the path-independent J-integral defined as in Eshelby (1956), or specifically for cracks as in Rice (1968), by

$$J = \int_\Gamma \left[W\delta_{1j} - \sigma_{ij} \frac{\partial u_i}{\partial x_1} \right] n_j d\Gamma. \tag{42}$$

Here, W is the strain energy density, σ_{ij} and $(\partial u_i/\partial x_j)$ are the stresses and displacement gradients, respectively, Γ is a contour beginning at the bottom crack face and ending on the top crack face, and $\mathbf{n}$ is the outward pointing normal to Γ. A weighting function $q_1(x_1, x_2)$ is assigned a value of unity on the inner contour Γ, a value of zero on the outer contour C_0 and is a smooth (C^0) function in the domain bounded by Γ, C_0, and the crack faces C_+ and C_- (these contours are shown in Fig. 4 of Part I). The integral in (42) can then be restated as an integral over a closed contour C, viz.,

$$J = \int_C \left[\sigma_{ij} \frac{\partial u_i}{\partial x_1} - W\delta_{1j} \right] m_j q_1 dC. \tag{43}$$

Here, $\mathbf{m}$ is the unit normal to C pointing away from the en-

Downloaded 03 May 2010 to 171.66.16.31. Redistribution subject to ASME license or copyright; see http://www.asme.org/terms/Terms_Use.cfm

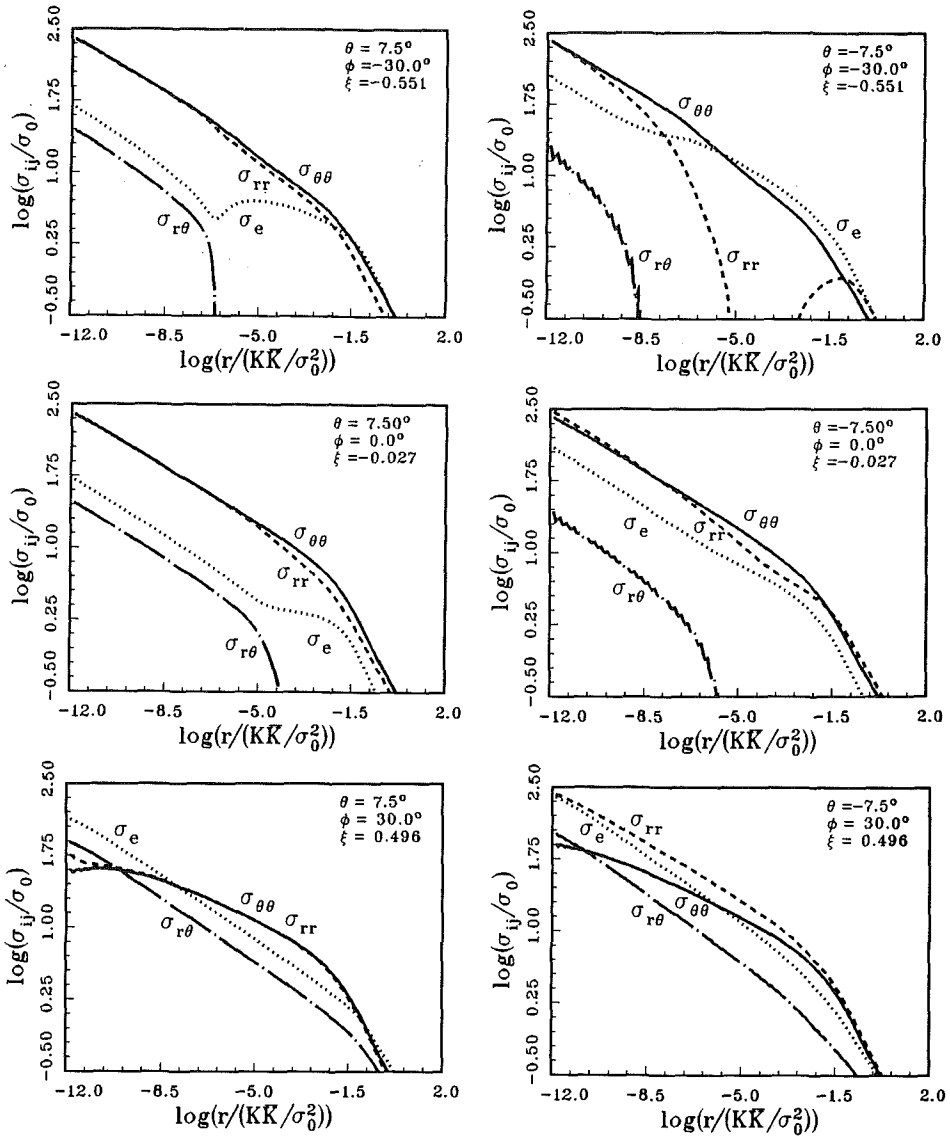


Fig. 7 Variation of normalized stresses with log of normalized distance in elastic-plastic material (θ = 7.5 deg) and in elastic substrate (θ = −7.5 deg) for three load states

closed area; on the contour, Γ, **m** points opposite to **n**. The derivation assumes that the crack faces are traction-free. Applying the divergence theorem to the integral in (43), and using the equations of equilibrium, the equivalent domain representation of (42) is

$$J = \int_A \left[\sigma_{ij} \frac{\partial u_i}{\partial x_1} - W\delta_{1j} \right] \frac{\partial q_1}{\partial x_j} \, dA \tag{44}$$

where A is the area enclosed by C.The finite element form of (44) is given in Part I.

4 Numerical Solutions for Small-Scale Yielding

Full field numerical solutions under plane-strain assumptions have been obtained for a range of bimaterial constants and different combinations of plastic properties for materials 1 and 2. In the interest of length, only two material combinations are discussed in this section.

4.1 Elastic-Plastic Material on Elastic Substrate. Material 1 is elastic-plastic while material 2 is linear elastic. The elastic properties are $\nu_1 = \nu_2 = 0.3$ and $E_2/E_1 = 2.5$; the values of the Dundur's parameters are then $\beta_1 = -0.429$ and $\beta_2 = -0.122$, whereas $\epsilon = 0.039$. Plastic properties of the top material are characterized by yield stress σ_0, strain-hardening exponent n which is equal to 5, and α which has a value of 0.1.

Numerical solutions are presented for seven states of remote load as defined by $K\bar{K}/\sigma_0^2 L = 0.5$, and the elastic phase parameter $\phi = -90$ deg, -60 deg, -30 deg, 0 deg, 30 deg, 60 deg, 90 deg. The small-scale yielding phase parameter, ξ, defined by (13), has these values: -1.60, -1.07, -0.551, -0.027, 0.496, 1.02, and 1.54. Under small-scale yielding conditions,

$$J = \mathcal{G} = \Lambda Q\bar{Q} = \Lambda K\bar{K} \tag{45}$$

where for plane strain, $\Lambda = [(1-\nu_1)/\mu_1 + (1-\nu_2)/\mu_2]/(4\cosh^2 \pi\epsilon)$. The value of J was computed using (44) and a "plateau" weighting function. The J values, which were extracted from annular domains with mean radii that differed by up to fifteen orders of magnitude (10^{-15}), agreed to better than two significant digits with the exact result given by (45). The essentially exact path-independence of the numerically determined J and the excellent agreement with (45) is indicative of the quality of the numerical solutions.

Downloaded 03 May 2010 to 171.66.16.31. Redistribution subject to ASME license or copyright; see http://www.asme.org/terms/Terms_Use.cfm

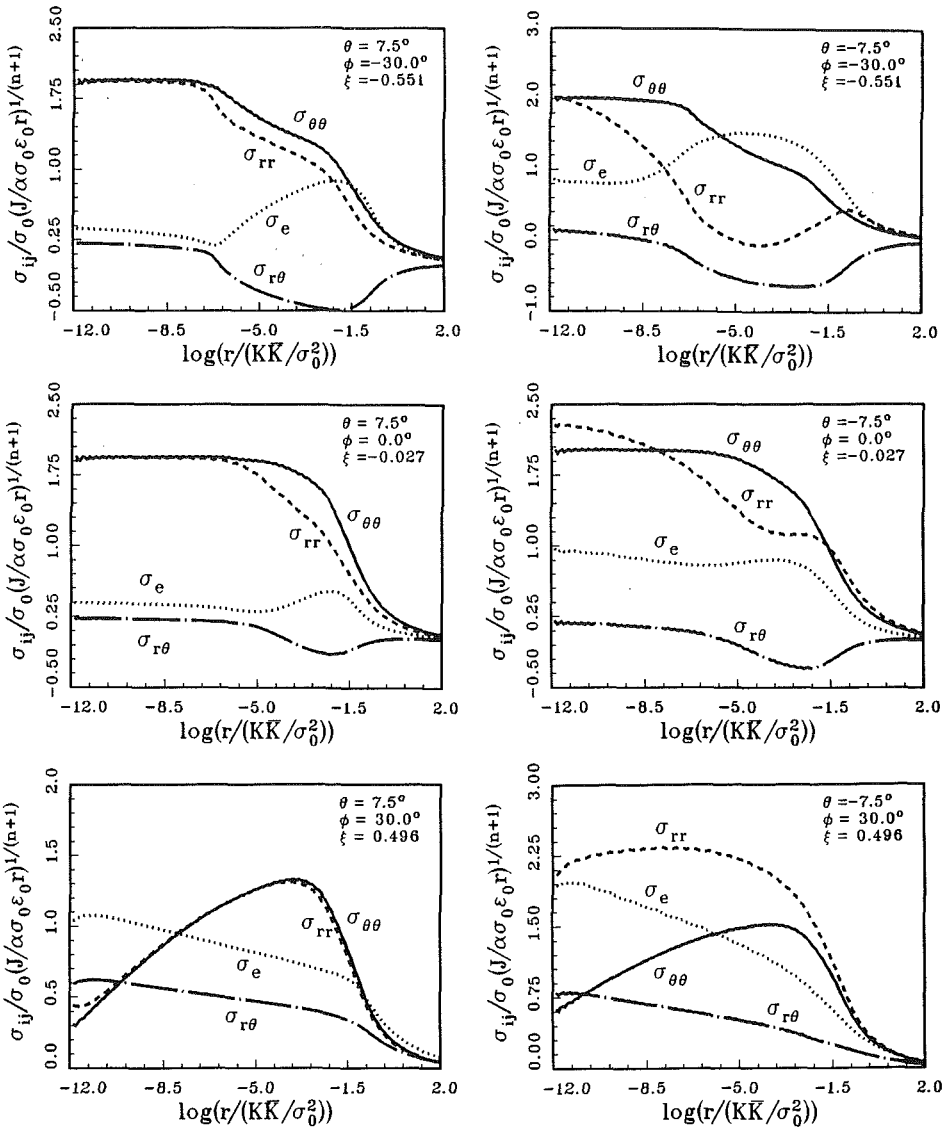


Fig. 8 Variation of stresses normalized by HRR form with log of normalized distance in elastic-plastic material (θ = 7.5 deg) and in elastic substrate (θ = −7.5 deg) for three load states

Plastic zones for six of the loading states, $\xi = -1.60, -1.07, -0.551, -0.027, 0.496, 1.02$ ($\mathbf{K}\bar{\mathbf{K}}/\sigma_0^2 L = 0.5$, $\phi = -90$ deg, -60 deg, -30 deg, 0 deg, 30 deg, 60 deg) are shown in Fig. 4. Distances are normalized by $\mathbf{K}\bar{\mathbf{K}}/\sigma_0^2$ in accordance with (22), and the stress levels indicated in the plots are normalized by σ_0. The computed plastic zone for $\xi = -1.60$ is identical to that determined for $\xi = 1.54$ (as demanded by (23)) and the latter is therefore not shown. The material above the bond line is elastic-plastic and thus the contour labeled by $\sigma_e = 1.0$ is the elastic-plastic boundary; the contour labeled by $\sigma_e = 1.5$ is the contour for $\sigma_e = 1.5\sigma_0$. Maximum extent of the plastic zone, R_p, varies between $0.15\mathbf{K}\bar{\mathbf{K}}/\sigma_0^2$ (for $\xi \approx 0$) and $0.6\mathbf{K}\bar{\mathbf{K}}/\sigma_0^2$ (for $\xi \approx \pm 1.5$). Contours in the elastic substrate has no physical significance other than being indicative of the effective stress levels. It is noteworthy that despite the significant difference in the asymptotic linear elastic fields of cracks on bimaterial interfaces and cracks in homogeneous media, the overall size and shape of the plastic zones are similar to those found for the homogeneous medium subject to combined K_I and K_{II} loading (see Shih, 1974, for a discussion of these latter fields).

Hydrostatic stress contours for the six load states just discussed are shown in Fig. 5. The stress levels indicated in the plots are normalized by σ_0. Positive values correspond to hydrostatic tension while negative values correspond to hydrostatic compression. The stress contours for $\xi = -1.60$ are identical to those for $\xi = 1.54$; however, the sign of the stress levels have to be changed as required by (19). It may be noted that the hydrostatic stress in materials 1 and 2 are very dependent on the load phase even in the vicinity of $\xi = 0$. For $\xi = -0.551$, the top material endures high hydrostatic tension. The top and bottom materials are subjected to high hydrostatic tension for the cases $\xi = -0.027, 0.496$.

The solutions being discussed were obtained without taking into consideration contact of the crack faces if this should occur. In Section 2, the case was made that there is a range of load states where crack face contact does not occur over any physically-significant length scale. Within that range of load combinations we have explained that the bimaterial crack problem can be analyzed as an *open* crack. Based on the elasticity solution, the range of ξ for an *open* crack (36) was determined. An estimate of the *open* crack range based on the small-scale yielding solution is now given. The displacement jump, Δu_2, normalized by $\epsilon_0\mathbf{K}\bar{\mathbf{K}}/\sigma_0^2$, is plotted against $\log\hat{r}$, ($\hat{r} \equiv r/(\mathbf{K}\bar{\mathbf{K}}/\sigma_0^2)$), in Fig. 6. Six load states, $\xi = -1.60, -1.43, -1.34, -1.07, -0.027, 1.28$ ($\mathbf{K}\bar{\mathbf{K}}/\sigma_0^2 L = 0.5$, $\phi = -90$ deg,

Downloaded 03 May 2010 to 171.66.16.31. Redistribution subject to ASME license or copyright; see http://www.asme.org/terms/Terms_Use.cfm

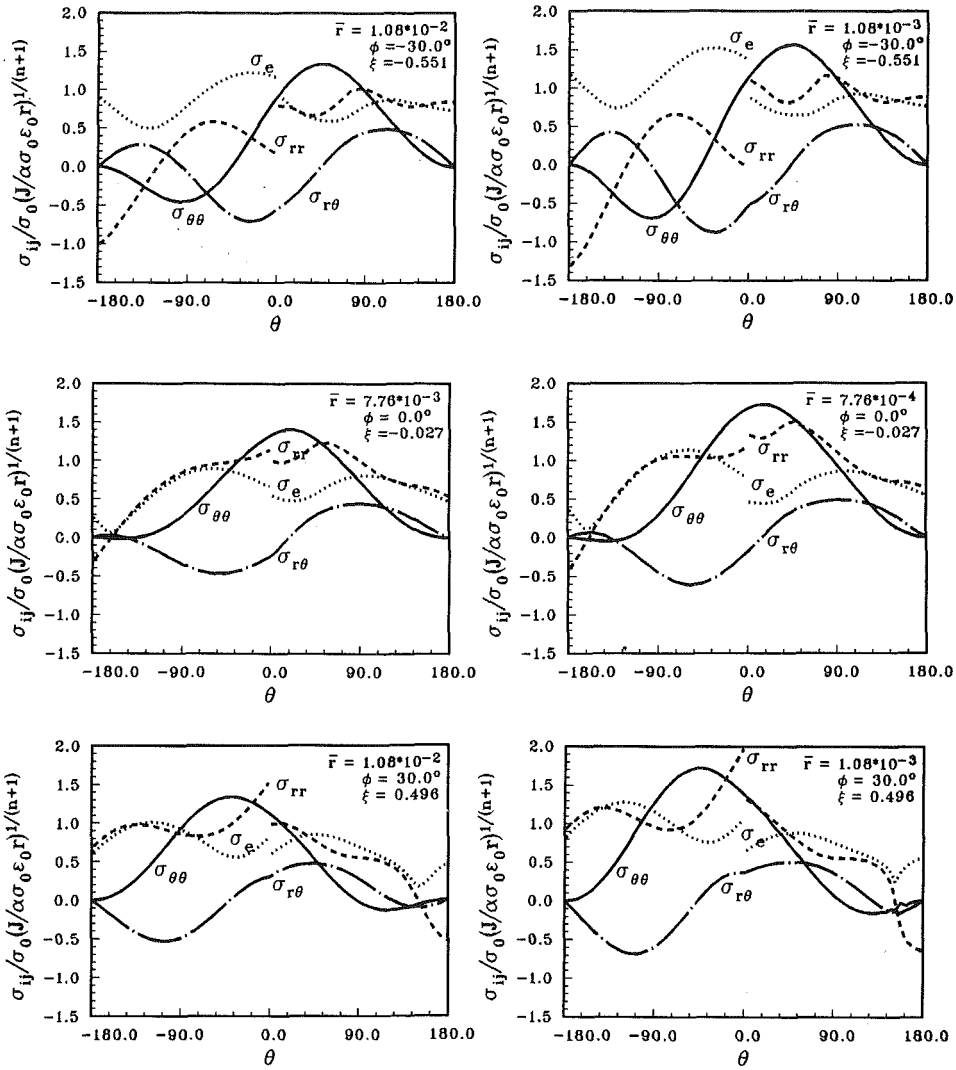


Fig. 9 Angular variation of stresses normalized by HRR form in elastic substrate (-180 deg $\le \theta \le 0$ deg) and in elastic-plastic material (0 deg $\le \theta \le$ 180 deg) for three load states. For each load state, the radial distances correspond to 5 percent and 0.5 percent of the maximum plastic zone size.

-80.5 deg, -75 deg, -60 deg, 0 deg, 75 deg) are shown, and the zone of crack face contact (if any) is indicated.

In Section 2.4 a practical definition for an open crack (35) was introduced; however, values of c_1 and c_2 were not given. Appropriate values for c_1 and c_2 can be determined from plots of the plastic zone in Fig. 4. The maximum extent of the plastic zone, $R_p/(\mathbf{K}\bar{\mathbf{K}}/\sigma_0^2)$, varies between 0.15 to 0.6, depending on the phase ξ. Thus, a reasonable value for c_1 is 10^{-3} (this corresponds to a distance which is less than 10^{-2} of the plastic zone size), while c_2 is assigned a value much larger than unity. We examine the displacement jumps in Fig. 6. The range of ξ for which the crack is opened for distances $\hat{r} \ge 10^{-3}$ is estimated to be

$$-1.3 \le \xi \le 1.3. \tag{46}$$

The aforementioned estimate of the *open* crack range pertains to the particular material combination being investigated. However, crack face profiles for other material combinations have shown that the *open* crack range, when phrased in terms of ξ, is not strongly dependent on material combinations. We have completed a detailed study of an elastic-plastic material bonded onto a rigid foundation ($\epsilon \approx 0.1$). Materials characterized by $n = 3$, 5, and 10 were considered. The *open* crack range differed from the range given in (46) by less than ten percent.

We have previously stated that for the present, our interest is restricted to the range of ξ in which the crack faces are not in contact. Hence, our examination of detailed behavior of the stresses is directed to load states where the crack is *open*. Stresses near the bond line are especially of interest because of the likelihood of crack propagation along the interface. The variation of stresses with radial distance from the crack tip in the elastic-plastic material (along $\theta = 7.5$ deg) and in the elastic material (along $\theta = -7.5$ deg) is detailed. In Fig. 7 log (σ_{ij}/σ_0) is plotted against log$\hat{r}$ for three states of remote loads, $\xi = -0.551$, -0.027, 0.496 ($\mathbf{K}\bar{\mathbf{K}}/\sigma_0^2 L = 0.5$, $\phi = -30$ deg, 0 deg, 30 deg). Within distances that can be resolved by our mesh, $10^{-12} \le \hat{r} \le 10^3$, the crack faces are not in contact. The stresses in material 1 are shown in the left column of plots; two distinct slopes can be seen, a higher slope in the elastic region and a lower slope in the plastic region with the change in slope occurring near the elastic-plastic boundary. Plots on the right column show the stresses in material 2—similar trends are observed and it is apparent that the stress levels in the elastic material is limited by the stress levels achievable in the

Downloaded 03 May 2010 to 171.66.16.31. Redistribution subject to ASME license or copyright; see http://www.asme.org/terms/Terms_Use.cfm

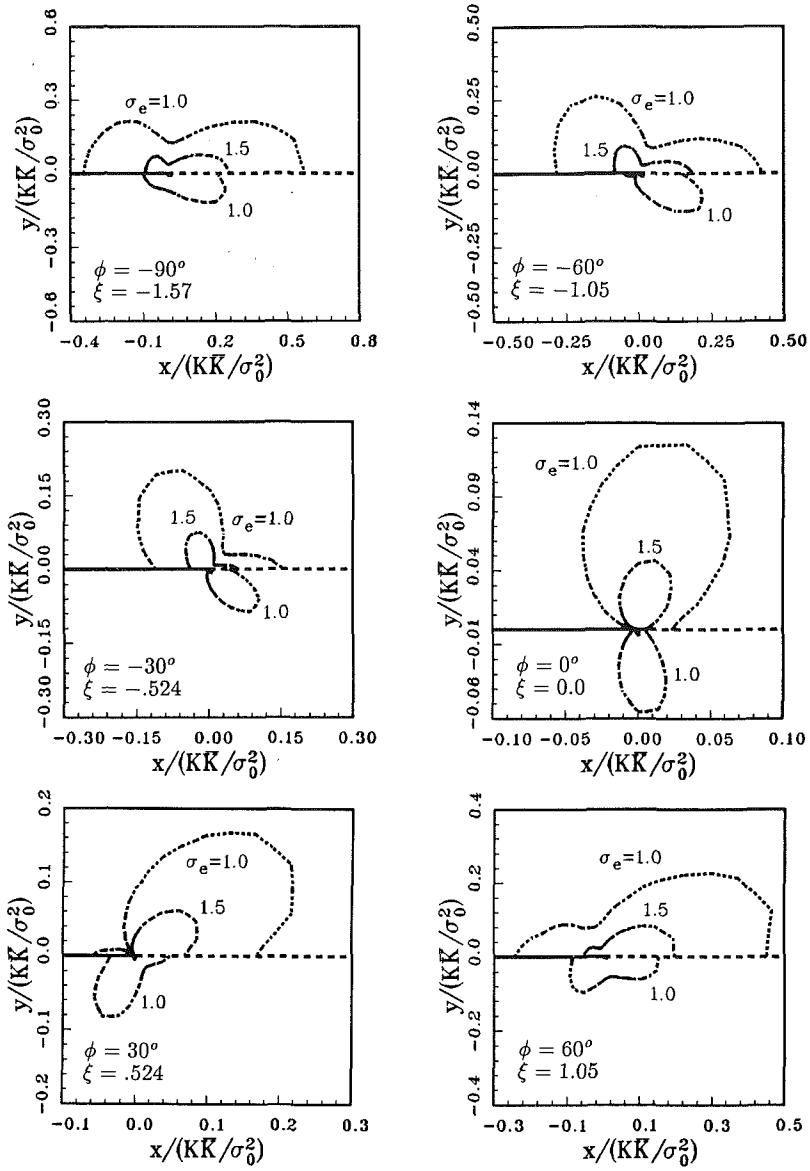


Fig. 10 (Weak) elastic-plastic material bonded onto (strong) elastic-plastic material—effective stress contours and plastic zones of six load states. Distances in the upper and lower half-planes are normalized by $K\bar{K}/\sigma_{01}^2$ and $K\bar{K}/\sigma_{02}^2$, respectively.

elastic-plastic material. It may be noted that the behavior of the stresses along radial distances with other orientations (e.g., $\theta = \pm 67.7$ deg, ± 97.5 deg) are similar to those observed in Fig. 7. We should point out that the plotted stresses are the actual values evaluated at the Gauss points—no smoothing was applied to the data points in our plots of the numerically determined fields.

To examine if the actual fields are amenable to the representation given by (27), the numerically determined stresses are normalized as follows:

$$\hat{\sigma}_{ij} = \frac{\sigma_{ij}/\sigma_0}{(J/\alpha\sigma_0\epsilon_0 r)^{1/(n+1)}}. \tag{47}$$

The plastic properties for the normalization pertain to material 1 (recall that material 2 is elastic). The variation of the normalized stresses, $\hat{\sigma}_{ij}$, with $\log\hat{r}$ is plotted in Fig. 8 for the three load states, $\xi = -0.551, -0.027, 0.496$ ($\mathbf{K}\bar{\mathbf{K}}/\sigma_0^2 L = 0.5$, $\phi = -30$ deg, 0 deg, 30 deg). For the load states, $\xi = -0.551$ and -0.027, the normalized stresses, $\hat{\sigma}_{ij}$, well within the plastic zone do not seem to vary with distance, i.e., the actual field support the proposed form (27) and the observation that h_{ij} depends very weakly on distance. Consider the case $\xi = 0.496$ which displays the "strongest" variation with distance (bottom plots in Fig. 8). From Fig. 4, the maximum length of its plastic zone R_p is $0.2\mathbf{K}\bar{\mathbf{K}}/\sigma_0^2$. Over the distances $10^{-4} < r/R_p < 10^{-1}$, which include all physically-relevant length scales, the deviation of $\hat{\sigma}_{ij}$ from its mean value is less than eight percent. It can also be seen that in every case the stress levels in the elastic substrate are set by the stresses in the elastic-plastic material (as they must by continuity of traction).

Angular variation of $\hat{\sigma}_{ij}$ at fixed radial distances equal to 5 and 0.5 percent of the maximum plastic zone size are shown in Fig. 9 for the three remote load states discussed previously. In the range -180 deg $\leq \theta \leq 0$ deg the material is elastic, while the material is elastic-plastic in the range 0 deg $\leq \theta \leq$ 180 deg. For the case, $\xi = -0.551$, the hoop stress reaches its maximum in material 1. On the other hand, for $\xi = 0.496$, the hoop stress attains its maximum in material 2. In all cases, the stresses in both materials are comparable in magnitude and the normalized values are of order unity. More importantly, we point to the strong similarity of the stresses in the elastic-plastic material to the mixed-mode HRR fields for a homo-

Downloaded 03 May 2010 to 171.66.16.31. Redistribution subject to ASME license or copyright; see http://www.asme.org/terms/Terms_Use.cfm

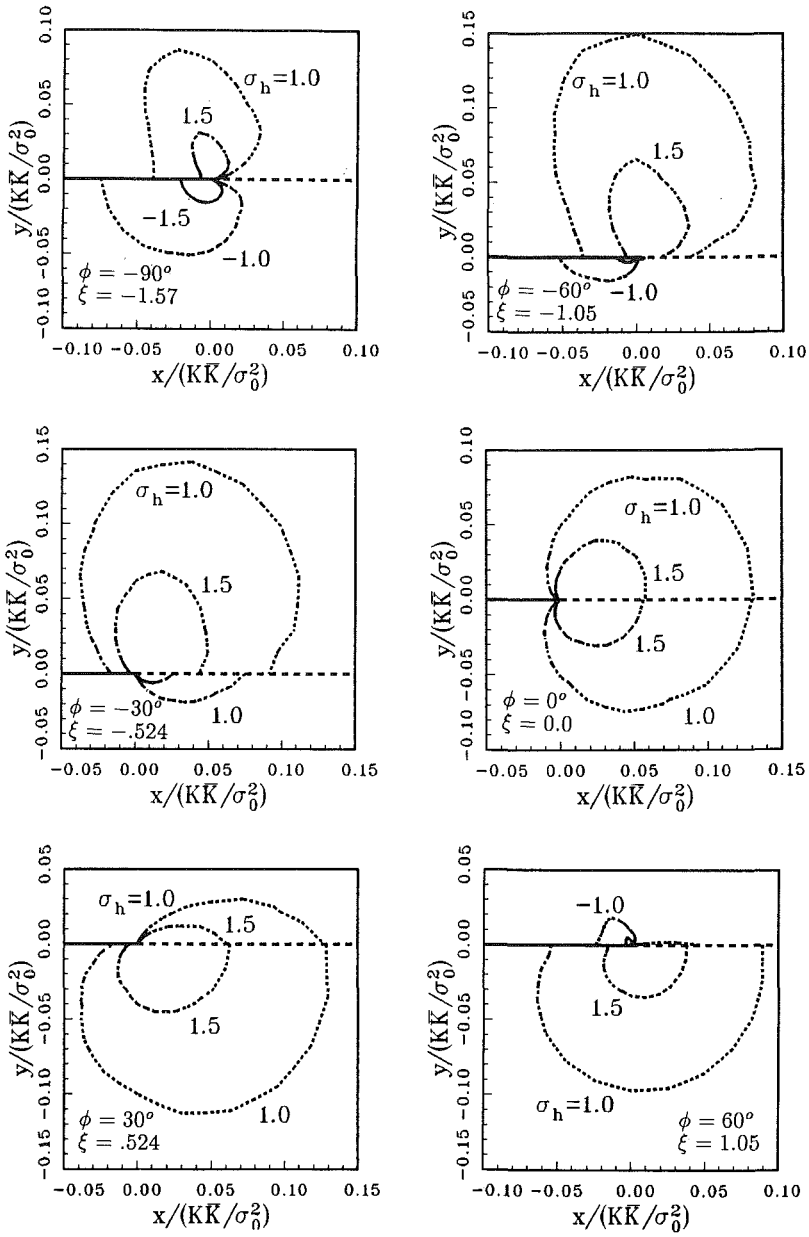


Fig. 11 (Weak) elastic-plastic material bonded onto (strong) elastic-plastic material—hydrostatic stress contours of six load states. Distances in the upper and lower half-planes are normalized by $K\bar{K}/\sigma_{01}^2$.

geneous medium characterized by the plastic properties of material 1. In fact, the radial and angular stress distributions in material 1 for $\xi = -0.027$ agreed closely with those for Mode I HRR fields. Stress distributions for $\xi = -0.551$ and $\xi = 0.496$ are in agreement with the mixed-mode HRR fields for $M^p = -0.95$ and $M^p = 0.78$, respectively (Symington et al., 1988). We defer the more detailed comparisons to Part III where the full field solutions in the small and finite strain regions are presented.

4.2 Two Bonded Elastic-Plastic Materials. For this analysis both materials are elastic-plastic. The elastic properties of materials 1 and 2 are identical, $E_2 = E_1$ and ν_1 and $\nu_2 = 0.3$. Thus, Dundur's parameters $\beta_1 = \beta_2 = 0$ and ϵ also vanishes. The plastic properties of material 1 are characterized by yield stress σ_0, strain-hardening exponent n of 5, and the material constant α equal to 0.1. Material 2 yields at σ_{02}, which is four times higher than the yield stress of material 1. The strain-hardening exponent of material 2, n_2, is 10 and α_2 is 0.1. The remote elastic fields are given by the standard K_I and K_{II} fields and $\xi = \phi$.

Numerical solutions were obtained for seven values of the elastic phase parameter, $\phi = -90$ deg, -60 deg, -30 deg, 0 deg, 30 deg, 60 deg, 90 deg; the values of ξ are -1.57, -1.05, -0.524, 0.0, 0.524, 1.05, and 1.57. J values were extracted from numerical fields using domains in which the mean radii differed by as much as nine orders of magnitude. These values agreed to better than two significant digits with the exact result (45).

Since the yield stress of material 2 is four times higher than the yield stress of material 1, the plastic zone in the (stronger) bottom material is small compared to the plastic zone in the top material. To facilitate the comparison of plastic zones in both materials, distances within material 2 are normalized by $K\bar{K}/\sigma_{02}^2$ while distances within material 1 are normalized by $K\bar{K}/\sigma_{01}^2$. Plastic zones for six load states, $\xi = -1.57$, -1.05,

Downloaded 03 May 2010 to 171.66.16.31. Redistribution subject to ASME license or copyright; see http://www.asme.org/terms/Terms_Use.cfm

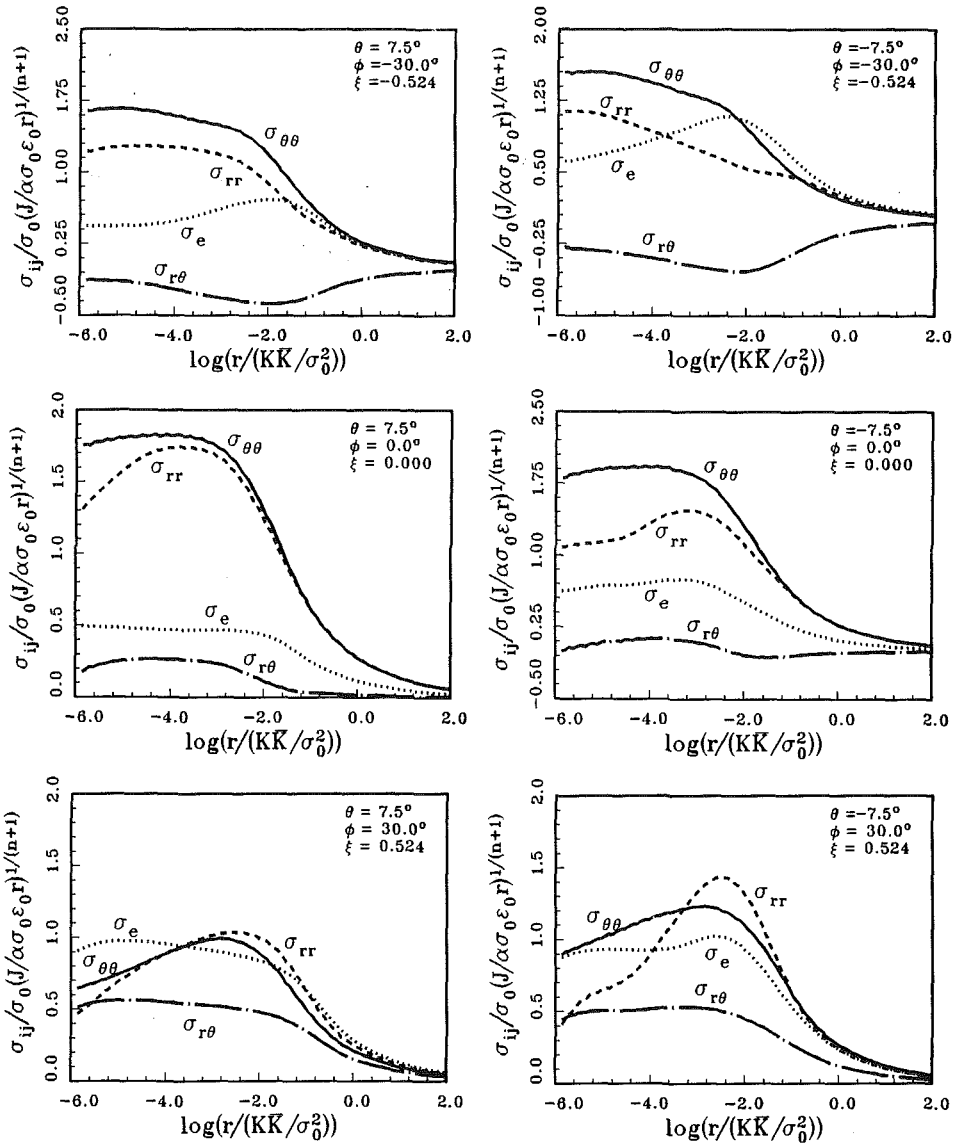


Fig. 12 Variation of normalized stresses with log of normalized distance in (weak) elastic-plastic material (θ = 7.5 deg) and in (strong) elastic-plastic material (θ = −7.5 deg) for three load states

−0.524, 0.0, 0.524, 1.05, (ϕ = −90 deg, −60 deg, −30 deg, 0 deg, 30 deg, 60 deg) are shown in Fig. 10. (The computed plastic zone for ξ = −1.57 is identical to that for ξ = 1.57 and is not known.) The elastic-plastic boundaries in materials 1 and 2 are defined by the locii of $\sigma_e = \sigma_{01}$ and $\sigma_e = \sigma_{02}$, respectively. Since the stress levels in material 1 are normalized by σ_{01}, while those in material 2 are normalized by σ_{02}, contours labeled by σ_e = 1.0 are the elastic-plastic boundaries. The normalized plastic zone size, $R_{p1}/(\mathbf{K}\bar{\mathbf{K}}/\sigma_{01}^2)$, for the weaker material varies between 0.15 and 0.6 and these values are rather similar to those found for the homogeneous medium subject to combined K_I and K_{II} loading (Shih, 1974). For the stronger material, $R_{p2}/(\mathbf{K}\bar{\mathbf{K}}/\sigma_{02}^2)$ varies between 0.06 and 0.25. Thus the length of the plastic zone in the stronger material is about only 1/30 of that in the weaker material, i.e., the relative size of the plastic zones does not obey the ratio $(\sigma_{01}/\sigma_{02})^2$.

Hydrostatic stress contours for the six load states just discussed are plotted in Fig. 11. To permit a direct comparison of the stresses in both materials, the stress levels indicated in materials 1 and 2 are normalized by the same yield stress σ_{01}, and distances in both materials are normalized by the same length $\mathbf{K}\bar{\mathbf{K}}/\sigma_{01}^2$. The stress contours for ξ = −1.57 are identical to those for ξ = 1.57; however, the sign of the stress levels have to be changed in accordance with (19). It is apparent that the magnitude of the hydrostatic stress in both materials vary with the load phase for moderate departures from ξ = 0 (compare plots for ξ = −0.524, 0, 0.524).

Because the plastic properties of materials 1 and 2 are different, the crack tip fields do not have a separable form of the HRR type (see discussion in Section 2). For remote load combinations in the vicinity of $\xi = \phi = \pm\pi/2$, (note that ϵ = 0) our numerical results show crack face contact zones which are comparable to the size of the plastic zone. Subsequent discussions are therefore restricted to those cases where the crack faces are clearly not in contact.

Variation of the normalized stresses, $\hat{\sigma}_{ij}$, with log $(r/(\mathbf{K}\bar{\mathbf{K}}/\sigma_0^2))$ along θ = ±7.5 deg, for ξ = −0.524, 0.0, 0.524 (ϕ = −30 deg, 0 deg, 30 deg) is plotted in Fig. 12. The stresses in both materials are normalized by the yield stress and the hardening exponent for material 1 (the weaker material). It can be seen that the normalized stresses, $\hat{\sigma}_{ij}$, for the two states, ξ = −0.524, 0, are only slightly dependent on radial distance indicating that a form of the type (27) is a suitable representation over the radial distances considered in the figure. By contrast,

Downloaded 03 May 2010 to 171.66.16.31. Redistribution subject to ASME license or copyright; see http://www.asme.org/terms/Terms_Use.cfm

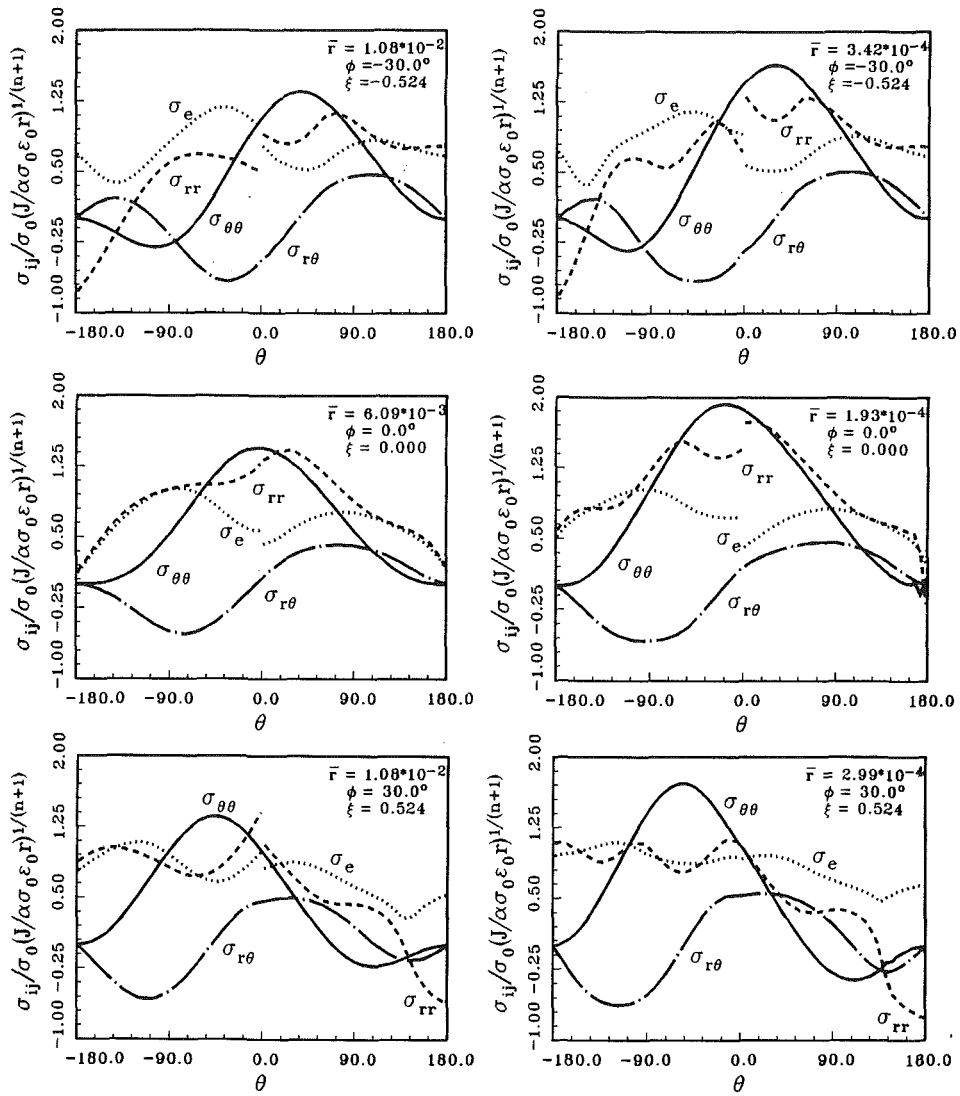


Fig. 13 Angular variation of normalized stresses in (strong) elastic-plastic material (-180 deg $\le \theta \le 0$ deg) and in (weak) elastic-plastic material (0 deg $\le \theta \le$ 180 deg) for three load states. For each load state, the radial distances correspond to five percent of the maximum plastic zone size in the weak and in the strong elastic-plastic materials, respectively.

stresses normalized by the yield stress and hardening exponent for material 2 (the lower-hardening material) display stronger variation with $\hat{r}$ over the distances considered in Fig. 12. However, over vanishingly small distances, $10^{-12} < \hat{r} < 10^{-4}$ (not shown in Fig. 12), these (latter) normalized stresses are nearly independent of $\hat{r}$. Such behavior is consistent with our observation that as $r \to 0$, the stresses are governed by the strain-hardening behavior of the lower-hardening material, namely, material 2 for the material system being considered. These aspects have been discussed by Shih and Asaro (1989).

The angular distribution of $\hat{\sigma}_{ij}$ (normalization based on the plastic properties of the $n = 5$ material) is plotted at two fixed radial distances for each of the load states, $\xi = -0.524$, 0.0, 0.524 ($\phi = -30$ deg, 0 deg, 30 deg). The first distance is chosen to equal five percent of the maximum extent of the plastic zone in the (weaker) top material, and the other distance is chosen to equal five percent of the maximum extent of the plastic zone in the (stronger) bottom material. These angular distributions are shown in Fig. 13. For the case $\xi = -0.524$, the hoop stress reaches its maximum in material 1; it is at its maximum in material 2 for $\xi = 0.524$. It is noteworthy that the magnitude of $\hat{\sigma}_{ij}$ of both materials is of order unity. The similarity between the angular variation of the stresses with the mixed-mode HRR fields for homogeneous medium is discussed in Part III.

5 Open Crack Range for Two Fracture Test Geometries

For arbitrary load histories, the validity of the solutions presented in this paper hinges, in part, on whether or not the crack faces make contact; if contact develops over physically-significant size scales, the solutions are invalid. We have shown that load states, where contact between the crack faces is excluded over sensible distances near and away from the crack tip, can be expressed by a range of ξ. We extend the discussion to the center-cracked-panel and confine attention to the case where the total crack length, L, is small compared to the width of the panel. Using the relation $\phi = \psi + \Theta$ in the linear elasticity prediction for an *open* crack (32), we observe that the right crack tip is *open* if ψ is in the range,

$$-\pi/2+\Omega \le \psi \le \pi/2. \tag{48}$$

Both tips are *open* if

$$-\pi/2+\Omega \le \psi \le \pi/2-\Omega. \tag{49}$$

Downloaded 03 May 2010 to 171.66.16.31. Redistribution subject to ASME license or copyright; see http://www.asme.org/terms/Terms_Use.cfm

The open crack range under small-scale yielding is given by (46). Noting the connections $\phi = \psi + \Theta$ and $\mathbf{QQ} = \mathbf{K}\bar{\mathbf{K}}$, approximating Θ by 2ϵ, and using the relation for ξ (13) in (46), we obtain

$$-1.3-\epsilon\left(2+\ln\frac{\mathbf{K}\bar{\mathbf{K}}}{\sigma_0^2 L}\right)\leq\psi\leq 1.3-\epsilon\left(2+\ln\frac{\mathbf{K}\bar{\mathbf{K}}}{\sigma_0^2 L}\right). \quad (50)$$

The *open* crack range given by (50) takes into consideration the effects of small-scale plasticity. The maximum radial extent of the plastic zone is

$$R_p=\left(\frac{1}{\gamma}\right)\frac{\mathbf{K}\bar{\mathbf{K}}}{\sigma_0^2} \quad (51)$$

where γ varies between 6.5 (for $\xi \approx 0$) and 1.5 (for $\xi \approx \pm\pi/2$). Using (51) in (50) leads immediately to

$$-1.3-\epsilon\left(2+\ln\frac{\gamma R_p}{L}\right)\leq\psi\leq 1.3-\epsilon\left(2+\ln\frac{\gamma R_p}{L}\right). \quad (52)$$

Suppose the plastic zone in the center-cracked-panel is confined to a fraction of L, say, $\gamma R_p/L \approx 0.1$. According to (52), the crack tips are *open* if $-1.3 \leq \psi \leq 1.3$. On the other hand, the *open* crack range as determined by the linear elasticity solution is given by (48). Suppose that r_c/L is of order 10^{-3} and $\epsilon \approx 0.05$, then Ω ($\equiv -\epsilon \ln(r_c/L)$) is approximately 0.3. For these values the predicted *open* crack range by linear elasticity is $-1.27 \leq \psi \leq \pi/2$, which is skewed about the state corresponding to purè remote tension. By contrast, crack tip plasticity results in an *open* crack range which is nearly symmetric about the pure tension state. Alternatively, our results indicate that states of loading corresponding to nearly remote shear may produce contact over a physically-significant size scale even with significant amounts of plastic yielding at the crack tip.

The aforementioned analysis can be extended to other specimen geometries. As an example, consider the specimen proposed by Charalambides et al. (1988) which has been analyzed by Suo and Hutchinson (1988). The beam-like specimen consists of a slender strip of thickness h which is partially bonded onto a thicker substrate. As shown by the latter authors, the specimen design is such that for a broad range of remote moment and axial loads, the loading mode at the crack tip corresponds to $\phi \approx \pi/4$ (note that the strip thickness h is the characteristic crack dimension designated by L in our formulation). To assess if the crack tip in this specimen would remain *open* under small-scale yielding, we use (46) in conjunction with (13) and (51) to get the following condition for an *open* crack:

$$-1.3-\epsilon\ln\frac{\gamma R_p}{h}\leq\phi\leq 1.3-\epsilon\ln\frac{\gamma R_p}{h}. \quad (53)$$

For the specimen under consideration, $\phi \approx \pi/4$, so that the condition for the crack to remain *open* is

$$-1.3-\epsilon\ln\frac{\gamma R_p}{h}\leq\pi/4\leq 1.3-\epsilon\ln\frac{\gamma R_p}{h}. \quad (54)$$

This condition suggests that for nearly all physically reasonable values of interface fracture toughness, the crack tip would be *open*. For example, if $\epsilon = 0.04$ as in the case presented in Section 4.1, (54) would be violated only if $\gamma R_p/h \approx 4 \times 10^5$!

6 Concluding Remarks

In Part I, full field solutions for a complete boundary value problem were presented from which the near tip fields of interface cracks were extracted and characterized. The extent of validity of the small-scale yielding solutions in terms of the intensity of loading and resulting plastic zone size was identified for a center-cracked-panel geometry. For the most part our results were obtained numerically, but they led nonetheless to a clear mathematical structure. In particular, it was found that a plastic phase angle, ξ defined by (28), characterizes the family of solutions for the small-scale yielding fields. In the present paper the structure of the crack tip fields under conditions of small-scale yielding was explored in more detail using a *boundary layer* formulation.

Our numerical results show that the size of the dominant plastic zone is controlled by the yield strength of the weaker (lower yield strength) material and that over length scales comparable to the dominant plastic zone, the stress levels in both materials are set by σ_0, the yield strength of the weaker material. Our results also show that the overall size and shape of the dominant plastic zones are similar to those found for the homogeneous medium subject to similar combined K_I and K_{II} loading (Shih, 1974).

We have observed that the form of the near tip fields is governed by the hardening characteristics of the material with the least hardening capacity. With the stress-strain behavior of both materials being given by piecewise linear elastic/power law plastic relations, our numerical solutions support an observation that as $r \to 0$, the asymptotic stress and strain fields in the lower hardening material approach those for the same material which is bonded to a rigid substrate. Indeed, the near-tip fields for the elastic-plastic material bonded to an elastic substrate (see Figs. 7, 8, and 9) are very similar to the fields presented in Part I for the same elastic-plastic material bonded to a rigid substrate. Furthermore, the present small-scale yielding solutions agreed remarkably well with the center-cracked-panel, small-scale plasticity solutions for the identical values of ξ.

For a range of ξ, the actual numerical fields appear to be nearly separable in an annular region well within the plastic zone. These near-tip fields closely resemble mixed-mode HRR fields and corroborate a proposed representation for the near-tip fields (27). Our results also show that the stresses in the higher hardening material are limited to those levels that can be attained in the lower hardening material. These aspects and the asymptotic form of near tip stress fields are elaborated upon in another publication (Shih and Asaro, 1989).

For selected geometries and three material characterizations, ($n = 5, 10, \infty$), solutions based on a small strain J_2 flow theory have recently been obtained. The plastic zones for the $n = 5$ and $n = 10$ materials and the hydrostatic stress fields are practically identical to those obtained for the corresponding deformation theory solutions. Near the interface, we did find small differences between the deformation and flow theory solutions. Away from the interface, the deformation and flow theory solutions are hardly distinguishable from one another.

Solutions which take into account finite geometry changes associated with blunting at the crack tip have also been obtained. In this case, an important length scale is the crack tip opening displacement δ_t. Within a distance of several δ_t's ahead of the crack tip, the shear stresses near the interface are comparable to those determined by the small strain solutions, but are much smaller than the values predicted by the linear elasticity fields; in the finite strain region, the shear stresses rise slightly due to the asymmetrical blunting of the plastically deforming material. We find remarkable agreement between the full field numerical solutions and the Mode I HRR stresses over the distance $3\delta_t < r < 6\delta_t$ for tension-dominated load states, $-\pi/12 \leq \xi \leq \pi/12$. For remote load states which include moderate amounts of shear, there is good agreement between the full field solutions and the mixed-mode HRR fields, i.e., there is a range of load combinations in which the crack tip fields can be said to be characterized by J and ξ (or M^p). Furthermore, for load states in which $\sigma_{yy}^{\infty} > |\sigma_{xy}^{\infty}|$, the crack tip opens smoothly and the amount of opening scales nearly linearly with the J-integral. These aspects are discussed in Part III (Shih, Asaro, O'Dowd, 1989).

Downloaded 03 May 2010 to 171.66.16.31. Redistribution subject to ASME license or copyright; see http://www.asme.org/terms/Terms_Use.cfm

Acknowledgments

This investigation is supported by the Office of Naval Research through ONR Grant "Mechanics of Interface Cracks." The computations reported were performed on the CRAY-XMP at the Supercomputer Facility of the U.S. Naval Research Laboratory and on the Alliant Computer at the Computational Mechanics Facility of Brown University. The acquisition of the Alliant was made possible by grants from the U.S. National Science Foundation (Grant DMR-8714665), and the Office of Naval Research (Grant N00014-88-K-0119) and matching funds from Brown University.

References

Achenbach, J. D., Keer, L. M., Khetan, R. P., and Chen, S. H., 1979, "Loss of Adhesion at the Tip of an Interface Crack," *Journal of Elasticity*, Vol. 9, pp. 397-409.

Atkinson, C., 1981, "The Interface Crack with a Contact Zone (The Crack of Finite Length)," *International Journal of Fracture*, Vol. 19, pp. 131-138.

Charalambides, P. G., Lund, J., Evans, A. G., and McMeeking, R. M., 1988, "A Test Specimen for Determining the Fracture Resistance of Bimaterial Interfaces," in press.

Cherepanov, G. P., 1962, "The Stress State in a Heterogeneous Plate with Slits," (in Russian), *Izvestia AN SSSR, OTN, Mekhan. i Mashin.*, Vol. 1, pp. 131-137.

Comninou, M., 1977a, "The Interface Crack," ASME JOURNAL OF APPLIED MECHANICS, Vol. 44, pp. 631-636.

Comninou, M., 1977b, "Interface Crack with Friction in the Contact Zone," ASME JOURNAL OF APPLIED MECHANICS, Vol. 44, pp. 780-781.

Comninou, M., and Schmueser, D., 1978, "The Interface Crack in a Combined Tension-Compression and Shear Field," ASME JOURNAL OF APPLIED MECHANICS, Vol. 46, pp. 345-348.

Dundurs, J., 1969, "Edge-bonded Dissimilar Orthogonal Elastic Wedges Under Normal and Shear Loading," ASME JOURNAL OF APPLIED MECHANICS, Vol. 36, pp. 650-652.

England, A. H., 1965, "A Crack Between Dissimilar Media," ASME JOURNAL OF APPLIED MECHANICS, Vol. 32, pp. 400-402.

Erdogan, F., 1965, "Stress Distribution in Bonded Dissimilar Materials with Cracks," ASME JOURNAL OF APPLIED MECHANICS, Vol. 32, pp. 403-410.

Eshelby, J. D., 1965, "The Continuum Theory of Lattice Defects," *Solid State Physics*, Vol. 3, Seitz and Turnbull, eds., pp. 79-144.

Hughes, T. J. R., 1980, "Generalization of Selective Integration Procedures to Anisotropic and Nonlinear Materials," *International Journal for Numerical Methods in Engineering*, Vol. 15, pp. 1413-1418.

Hutchinson, J. W., 1968, "Singular Behavior at the End of a Tensile Crack in a Hardening Material," *Journal of the Mechanics and Physics of Solids*, Vol. 16, pp. 13-31.

Hutchinson, J. W., 1983, "Fundamentals of the Phenomenological Theory of Nonlinear Fracture Mechanics," ASME JOURNAL OF APPLIED MECHANICS, Vol. 50, pp. 1042-1051.

Hutchinson, J. W., Mear, M., and Rice, J. R., 1987, "Crack Paralleling an Interface between Dissimilar Materials," ASME JOURNAL OF APPLIED MECHANICS, Vol. 54, pp. 828-832.

Knowles, J. K., and Sternberg, E., 1983, "Large Deformations Near a Tip of an Interface-Crack Between Two Neo-Hookean Sheets," *Journal of Elasticity*, Vol. 13, pp. 257-293.

Malyshev, B. M., and Salganik, R. L., 1965, "The Strength of Adhesive Joints using the Theory of Cracks," *International Journal of Fracture Mechanics*, Vol. 1, pp. 114-128.

Moran, B., and Shih, C. F., 1987, "Crack Tip and Associated Domain Integrals from Momentum and Energy Balance," *Engineering Fracture Mechanics*, Vol. 27, pp. 615-642.

Needleman, A., 1987, "A Continuum Model for Void Nucleation by Inclusion Debonding," ASME JOURNAL OF APPLIED MECHANICS, Vol. 54, pp. 525-531.

Ortiz, M., and Blume, J. A., 1988, "Effect of Decohesion and Sliding on Bimaterial Crack-Tip Fields," Brown University Report, submitted for publication.

Park, J. H., and Earmme, Y. Y., 1986, "Application of Conservation Integrals to Interfacial Crack Problems," *Mechanics of Materials*, Vol. 5, pp. 261-276.

Rice, J. R., 1968, "A Path Independent Integral and the Approximate Analysis of Strain Concentration by Notches and Cracks," ASME JOURNAL OF APPLIED MECHANICS, Vol. 35, pp. 379-386.

Rice, J. R., 1988, "Elastic Fracture Mechanics Concepts for Interfacial Cracks," ASME JOURNAL OF APPLIED MECHANICS, Vol. 55, pp. 98-103.

Rice, J. R., and Rosengren, G. F., 1968, "Plane Strain Deformation Near a Crack Tip in a Power Law Hardening Material," *Journal of the Mechanics and Physics of Solids*, Vol. 16, pp. 1-12.

Rice, J. R., and Sih, G. C., 1965, "Plane Problems of Cracks in Dissimilar Media," ASME JOURNAL OF APPLIED MECHANICS, Vol. 32, pp. 418-423.

Shih, C. F., 1974, "Small-Scale Yielding Analysis of Mixed Plane-Strain Crack Problems," in Fracture Analysis, ASTM STP 560, pp. 187-210.

Shih, C. F., and Needleman, A., 1984, "Fully Plastic Crack Problems: Part I—Solutions by a Penalty Method," ASME JOURNAL OF APPLIED MECHANICS, Vol. 51, pp. 48-56.

Shih, C. F., and Asaro, R. J., 1988, "Elastic-Plastic Analysis of Cracks on Bimaterial Interfaces: Part I—Small Scale Yielding," ASME JOURNAL OF APPLIED MECHANICS, Vol. 55, pp. 299-316.

Shih, C. F., and Asaro, R. J., 1989, "Elastic-Plastic and Asymptotic Fields of Interface Cracks," *International Journal of Fracture*, in press.

Shih, C. F., Asaro, R. J., and O'Dowd, N. P., 1989, "Elastic-Plastic Analysis of Cracks on Bimaterial Interfaces: Part III—Finite Deformation and Large Scale Yielding Studies," in preparation.

Symington, M., Shih, C. F., and Ortiz, M., 1988, "Tables of Plane Strain Mixed-Mode Plastic Crack Tip Fields," Brown University Report, MRG/DMR-8714665/1.

Suo, Z., and Hutchinson, J. W., 1988, "Interface Crack between two Elastic Layers," Harvard University Report, Mech-118, to be published.

Ting, T. C., 1986, "Explicit Solution and Invariance of the Singularities at an Interface Crack in Anisotropic Composites," *International Journal of Solids and Structures*, Vol. 22, pp. 965-983.

Williams, M. L., 1959, "The Stresses Around a Fault or Crack in Dissimilar Media," *Bulletin of the Seismological Society of America*, Vol. 49, pp. 199-204.

Willis, J. R., 1971, "Fracture Mechanics of Interfacial Cracks," *Journal of the Mechanics and Physics of Solids*, Vol. 19, pp. 353-368.

Zywicz, E., and Parks, D. M., 1989, "Elastic Yield Zone around an Interfacial Crack Tip," ASME JOURNAL OF APPLIED MECHANICS, Vol. 56, pp. 577-584.

Downloaded 03 May 2010 to 171.66.16.31. Redistribution subject to ASME license or copyright; see http://www.asme.org/terms/Terms_Use.cfm

Representations of Stress Intensity Factors by Path-Independent Integrals

Kuang-Chong Wu
Associate Professor,
Institute of Applied Mechanics,
National Taiwan University,
Taipei, Taiwan 10764

Stress intensity factors are represented by path independent integrals for linear elastic materials. Two types of representation are given. The first type of integrals are expressed by integration over contours surrounding a crack tip. Those of the second type are integrated over contours enclosing a finite crack. The path independent integrals are applied to determine the stress intensity factors due to a body force and a dislocation for a finite crack in an infinite anisotropic body.

1 Introduction

It is well known that the stress fields near the tip of a crack in a linear elastic material exhibit a square-root singularity. The amplitudes of the singular stress fields are characterized by the stress intensity factors (SIFs). In linear elastic fracture mechanics, the SIFs are usually used as the parameters in fracture criteria. It is therefore an important task to determine the SIFs in the analyses of elastic bodies containing cracks.

As analytical solutions of SIFs are limited to a few idealized cases for practical problems involving finite geometries and complex loadings, numerical methods such as finite element methods or boundary element methods must be employed to compute the SIFs. An alternative method is to use the path-independent J-integral, proposed by Rice (1968), which is related to SIFs for linear elastic materials. By the J-integral method, SIFs can be calculated using data that are far removed from the crack tip and higher accuracy can be achieved. The J-integral method, however, can not be applied to problems where mixed-mode SIFs are present since the value of the integral only gives the sum of SIFs. A method to extract SIF corresponding to each fracture mode is to examine the interaction energy between the elastic state of interest and an auxiliary state. By choosing appropriate auxiliary states, SIFs can be computed via path-independent contour integrals. The general concept of this methods was discussed by Chen and Shield (1977). The method has been used by Stern et al. (1976) and Yau et al. (1980) for isotropic homogeneous materials. Hong and Stern (1978) and Sih and Asaro (1988) have also applied the method to treat interfacial crack problems for isotropic bimaterials. In the works of Stern et al. (1976) and Hong and Stern (1978), Betti's reciprocal work theorem was used to obtain representations of the SIFs by integrals involving displacements and tractions in the problem of interest and those in the particular auxiliary states. The particular states were so chosen that the displacement and the stress fields possess $\sqrt{r}$ and $r^{3/2}$ singularity at the crack tip, respectively. Here r is the distance from the crack tip. Yau et al. (1980) and Sih and Asaro (1988) gave line integrals for SIFs based on the interaction energy release rate. The line integrals were expressed in terms of stresses (or strains), and displacement gradients in the crack line direction in both the state of interest and the auxiliary states. Sih and Asaro (1988) have employed the singular fields for isotropic bimaterial interfacial cracks as the auxiliary state in their analysis. Both types of integrals are limited to contours that enclose only one crack tip.

In this paper, we show that the line integrals proposed by Yau et al. (1980) and Sih and Asaro (1988) can be simplified. The simplified integrals require only the tangential derivatives and tractions along the contour in the state of interest and the stresses σ_{i2} and displacement gradients in the crack line direction for the auxiliary states. Explicit expressions for the contour integrals are given with the elastic crack-tip fields chosen as the auxiliary state. The connection is also established between the seemingly different integrals obtained by Stern et al. (1976) and Hong and Stern (1978) and those given by Yau et al. (1980) and Sih and Asaro (1988). Furthermore, by choosing an appropriate auxiliary state, another type of line integrals is obtained. The new integrals can be evaluated along paths that completely surround a finite crack to yield the SIFs associated with either one of the crack tips. As an interesting application, the new integrals are utilized to find the SIFs induced by a body force and a dislocation in an unbounded anisotropic solid containing a finite crack without actually solving any boundary value problem. Both the isotropic and anisotropic materials are considered in the analysis. In the treatment of anisotropic materials, results obtained by a method due to Stroh (1956) will be used. Stroh's method will be introduced in the next section.

2 Stroh's Formulation

Throughout this paper, all indices range from 1 to 3 and the

Contributed by the Applied Mechanics Division of THE AMERICAN SOCIETY OF MECHANICAL ENGINEERS for presentation at the Winter Annual Meeting, San Francisco, Calif., December 10–15, 1989.

Discussion on this paper should be addressed to the Editorial Department, ASME, United Engineering Center, 345 East 47th Street, New York, N.Y. 10017, and will be accepted until two months after final publication of the paper itself in the JOURNAL OF APPLIED MECHANICS. Manuscript received by the ASME Applied Mechanics Division, December 6, 1988; final revision, March 10, 1989.
Paper No. 89-WA/APM-34.

Copyright © 1989 by ASME

Downloaded 03 May 2010 to 171.66.16.31. Redistribution subject to ASME license or copyright; see http://www.asme.org/terms/Terms_Use.cfm

convention of summation over a repeated Latin index is adopted unless otherwise noted. Summation over Greek indices is expressed explicitly. Boldfaced symbols are used to represent matrices or vectors. Comma denotes differentiation.

With respect to a fixed Cartesian coordinate system (x_1, x_2, x_3), the stresses σ_{ij} are related to the displacements by the generalized Hooke's law:

$$\sigma_{ij} = c_{ijkl} u_{k,l}, \tag{1}$$

where **c** is the elastic moduli. Substituting equation (1) in the equilibrium equations,

$$\sigma_{ij,j} = 0, \tag{2}$$

one obtains

$$c_{ijkl} u_{k,lj} = 0. \tag{3}$$

For problems in which **u** is independent of x_3, it is assumed that

$$u_k = A_k f(x_1 + p x_2). \tag{4}$$

Substituting equation (4) into equation (3) yields

$$[c_{i1k1} + p(c_{i1k2} + c_{i2k1}) + p^2 c_{i2k2}] A_k = 0. \tag{5}$$

For nontrivial solutions of A_k, it follows that

$$\det[c_{i1k1} + p(c_{i1k2} + c_{i2k1}) + p^2 c_{i2k2}] = 0. \tag{6}$$

Equation (6) is a sextic equation of p. It can be shown that equation (6) has no real roots, so that the roots must appear in complex conjugate pairs. The three roots with positive imaginary part will be denoted by $p_\alpha (\alpha = 1,2,3,)$; the corresponding values of A_k obtained from equation (5) are $A_{k\alpha}$. A general expression for the displacement can then be written as

$$u_k = \sum_\alpha A_{k\alpha} f_\alpha(z_\alpha) + \sum_\alpha \bar{A}_{k\alpha} \overline{f_\alpha(z_\alpha)}, \tag{7}$$

where an overline denotes complex conjugate. From equation (1) and equation (4), the stresses can be expressed as

$$\sigma_{k1} = -\sum_\alpha p_\alpha B_{k\alpha} g_\alpha(z_\alpha) - \sum_\alpha \bar{p}_\alpha \bar{B}_{k\alpha} \overline{g_\alpha(z_\alpha)}, \tag{8}$$

$$\sigma_{k2} = \sum_\alpha B_{k\alpha} g_\alpha(z_\alpha) + \sum_\alpha \bar{B}_{k\alpha} \overline{g_\alpha(z_\alpha)}, \tag{9}$$

where

$$B_{k\alpha} = (c_{i1k2} + p_\alpha c_{i2k2}) A_{i\alpha}, \tag{10}$$

$$g_\alpha(z_\alpha) = \frac{df_\alpha(z_\alpha)}{dz_\alpha}. \tag{11}$$

The displacement gradients, with respect x_1, are given by

$$u_{k,1} = \sum_\alpha A_{k\alpha} g_\alpha(z_\alpha) + \sum_\alpha \bar{A}_{k\alpha} \overline{g_\alpha(z_\alpha)}. \tag{12}$$

In the method of Stroh, the task of solving anisotropic elasticity problems is simplified to find appropriate functions of $g_\alpha(z_\alpha)$ that satisfy the boundary conditions.

For future reference, some properties of matrices **A** and **B** are listed next (Ting, 1986):

$$\mathbf{L} = -2i\mathbf{B}\mathbf{B}^T \tag{13}$$

$$\mathbf{A}\mathbf{B}^T = \frac{1}{2}(\mathbf{I} - i\mathbf{S}) \tag{14}$$

where **L** is a real symmetric positive definite matrix, **I** is the identity matrix, and **S** is real.

In general, Stroh's method can not be directly applied to isotropic materials for which equation (6) gives triple roots of i. However, if the final solution requires only **L** and **S**, then the solution also holds for isotropic materials (Barnett and Lothe, 1973). The expressions of **L** and **S** for isotropic materials are given as follows (Bacon, et al., 1978):

$$\mathbf{L} = \mu \begin{pmatrix} \frac{1}{1-\nu} & 0 & 0 \\ 0 & \frac{1}{1-\nu} & 0 \\ 0 & 0 & 1 \end{pmatrix} \tag{15}$$

$$\mathbf{S} = \frac{1-2\nu}{2(1-\nu)} \begin{pmatrix} 0 & -1 & 0 \\ 1 & 0 & 0 \\ 0 & 0 & 0 \end{pmatrix} \tag{16}$$

where μ and ν are the shear modulus and Poisson's ratio, respectively.

3 Path-Independent Integrals of SIF

In this section representations of SIF by path-independent integrals are derived.

Consider the path independent J-integrals of Rice (1968) given by

$$J = \int_\Gamma (W n_1 - u_{i,1} t_i) dl \tag{17}$$

where Γ is the contour of integration, W is the strain energy density, n_1 is the x_1-component of the unit outward normal to Γ, u_i is the displacement, t_i is the traction, and dl is the element of arc length. If the contour Γ is chosen to trace from the lower crack face to the upper crack face so that the tip of a crack lying on the x_1-axis is surrounded by Γ (see Fig. 1), Rice (1968) showed that in absence of body forces and dislocations the value of J is equal to the energy release rate, $\mathcal{G}$, due to crack extension. The expression of $\mathcal{G}$ for linear elastic materials is given by Barnett and Asaro (1972) as

$$\mathcal{G} = \frac{1}{2} L_{pq}^{-1} k_p k_q^1 \tag{18}$$

where **L** is given by equation (13) and **k** is the SIF defined by

$$k_p = \lim_{x_1 \to 0} \sqrt{2\pi x_1}\, \sigma_{p2}(x_1, 0)^2. \tag{19}$$

Thus

$$\frac{1}{2} L_{pq}^{-1} k_p k_q = \int_\Gamma \left(\frac{1}{2} \sigma_{ij} u_{i,j} n_1 - u_{i,1} t_i \right) dl \tag{20}$$

where the expression of W for linear elastic materials has been substituted. Let σ', $\mathbf{u}'$, and $\mathbf{k}'$ be the stress, displacement, and SIF of another elastic state in the same cracked body. Then

$$\frac{1}{2} L_{pq}^{-1} k_p' k_q' = \int_\Gamma \left(\frac{1}{2} \sigma_{ij}' u_{i,j}' n_1 - u_{i,1}' t_i' \right) dl. \tag{21}$$

Now let the primed state be superimposed on the unprimed state. By linearity of the material, the stress, displacement, and the SIF are simply the sums of those of the primed and unprimed states. Application of the J-integral to this combined state leads to

$$\frac{1}{2} L_{pq}^{-1} (k_p + k_p')(k_q + k_q') = \int_\Gamma \left[\frac{1}{2} (\sigma_{ij} + \sigma_{ij}')(u_{i,j} + u_{i,j}') n_1 - (u_{i,1} + u_{i,1}')(t_i + t_i') \right] dl. \tag{22}$$

[1] **L** is equal to $4\pi\mathbf{K}$ in Barnett's work.

[2] k_1 here is the mode II SIF while k_2 is the mode I SIF.

Downloaded 03 May 2010 to 171.66.16.31. Redistribution subject to ASME license or copyright; see http://www.asme.org/terms/Terms_Use.cfm

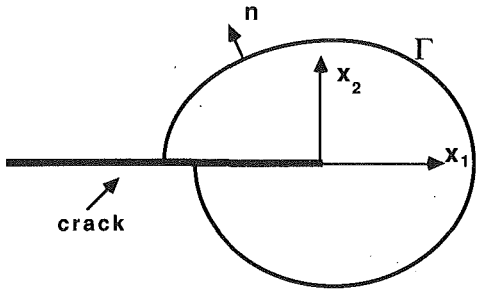


Fig. 1 Contour Γ surrounding a crack tip

Substracting equations (20) and (21) from (22), one has

$$L_{pq}^{-1}k_p k_q' = \int_\Gamma (\sigma_{ij}' u_{i,j} n_1 - u_{i,1}' t_i - u_{i,1} t_i')\, dl. \tag{23}$$

The derivation so far has been given by Yau et al. (1980) and Sih and Asaro (1988). The integrals in equation (23) can be further simplified by noting the following identity:

$$\begin{aligned}\sigma_{ij}' u_{i,j} n_1 - u_{i,1} t_i' &= \sigma_{i2}'(-u_{i,1} n_2 + u_{i,2} n_1) \\ &= \sigma_{i2}' \frac{\partial u_i}{\partial l}\end{aligned} \tag{24}$$

where $\partial u_i/\partial l$ is the tangential derivative of the displacement u_i along Γ. With the equation (24), equation (23) can be rewritten as

$$L_{pq}^{-1}k_p k_q' = \int_\Gamma \left(\sigma_{i2}' \frac{\partial u_i}{\partial l} - u_{i,1}' t_i\right) dl. \tag{25}$$

Since the primed state can be any state that may exist in the cracked body, one can take the primed state to be the crack-tip fields given by

$$\sigma_{ij}' = \hat{\sigma}_{ijq} k_q' \tag{26}$$

$$u_i' = \hat{u}_{iq} k_q' \tag{27}$$

where $\hat{\sigma}_{ijq}$ and $\hat{u}_{iq}$ are the universal inverse square-root singular stress and corresponding displacement fields for k_q. The idea of using the crack-tip fields as the auxiliary state has been applied by Sih and Asaro (1988) for isotropic interfacial cracks. The expressions of $\hat{\sigma}_{ijq}$ and $\hat{u}_{iq}$ for isotropic and anisotropic materials will be given in the next section. In equation (26) and equation (27), $\mathbf{k}'$ is an arbitrary constant vector. Substitution of equation (26) and equation (27) into equation (25) yields

$$\left[L_{pq}^{-1}k_p - \int_\Gamma \left(\hat{\sigma}_{i2q} \frac{\partial u_i}{\partial l} - \hat{u}_{i,1} t_i\right) dl\right] k_q' = 0. \tag{28}$$

As $\mathbf{k}'$ is arbitrary, it follows that

$$L_{pq}^{-1}k_p = \int_\Gamma \left(\hat{\sigma}_{i2q} \frac{\partial u_i}{\partial l} - \hat{u}_{iq,1} t_i\right) dl \tag{29}$$

or, mutiplying both sides by $\mathbf{L}$,

$$k_p = \int_\Gamma \left(G_{pi} \frac{\partial u_i}{\partial l} - H_{pi} t_i\right) dl \tag{30}$$

where

$$G_{pi} = L_{pq}\hat{\sigma}_{i2q} \tag{31}$$

$$H_{pi} = L_{pq}\hat{u}_{iq,1}. \tag{32}$$

Equation (30) is the main result of this section. With equation (30), the SIF of each mode can be calculated separately by tangential derivatives of the displacements and tractions on an arbitrary contour surrounding the crack tip.

The relation between the integrals of equation (30) and those given by Stern et al. (1976) can be obtained by integrating the first term on the r.h.s. of equation (30) by parts. The result is

$$k_p = \int_\Gamma \left[\left(-\frac{\partial G_{pi}}{\partial l}\right) u_i - H_{pi} t_i\right] dl. \tag{33}$$

Equation (33) would be the same as the integrals of Stern et al. (1976) if it can be shown that

$$-\frac{\partial G_{pi}}{\partial l} = T_{pi} \tag{34}$$

$$H_{pi} = U_{pi} \tag{35}$$

where T_{pi} and U_{pi} are the traction and displacement corresponding to the auxiliary state employed by Stern et al. (1976) for the SIF associated with k_p. This is indeed so since H_{pi} as given by equation (32) can be regarded as an admissible displacement field which possesses a square root singularity at the crack tip. The stresses S_{ijp} corresponding to the displacement U_{pi} are given by

$$S_{ijp} = L_{pq} \frac{\partial \hat{\sigma}_{ijq}}{\partial x_1}. \tag{36}$$

The traction T_{pi} on the contour Γ is thus

$$\begin{aligned}T_{pi} &= S_{ijp} n_j \\ &= L_{pq}\left(\frac{\partial \hat{\sigma}_{i1q}}{\partial x_1} n_1 + \frac{\partial \hat{\sigma}_{i2q}}{\partial x_1} n_2\right) \\ &= L_{pq}\left(-\frac{\partial \hat{\sigma}_{i2q}}{\partial x_2} n_1 + \frac{\partial \hat{\sigma}_{i2q}}{\partial x_1} n_2\right) \\ &= -L_{pq}\frac{\partial \hat{\sigma}_{i2q}}{\partial l} \\ &= -\frac{\partial G_{pi}}{\partial l}.\end{aligned}$$

In equation (36), the equilibrium equations of $\hat{\sigma}_{ijq}$ have been used. The integrals obtained by Stern et al. are therefore equivalent to the ones presented here and the auxiliary fields they used are derivable from the crack-tip fields.

4 Expressions for G and H

Explicit expressions for the matrix functions $\mathbf{G}$ and $\mathbf{H}$ for anisotropic and isotropic materials are given in this section.

4.1 Anisotropic Materials. The crack-tip fields for anisotropic materials are obtained by letting (Wu, 1989)

$$g_\alpha(z_\alpha) = B_{\alpha q}^{-1} \frac{1}{2\sqrt{2\pi z_\alpha}}$$

in equation (9) and equation (12). The resulting expressions of $\hat{\sigma}_{i2q}$ and $\hat{u}_{iq}$ are given by

$$\hat{\sigma}_{i2q} = \frac{1}{\sqrt{2\pi}} \sum_{\alpha=1}^{3} \Re\left[B_{i\alpha} B_{\alpha q}^{-1} \frac{1}{\sqrt{z_\alpha}}\right] \tag{37}$$

$$\hat{u}_{iq,1} = \frac{1}{\sqrt{2\pi}} \sum_{\alpha=1}^{3} \Re\left[A_{i\alpha} B_{\alpha q}^{-1} \frac{1}{\sqrt{z_\alpha}}\right] \tag{38}$$

where $\Re$ denotes real part. Substitution of equation (37), (38), and (13) into (31) and (32) yields

$$G_{pi} = \sqrt{\frac{2}{\pi}} \sum_{\alpha=1}^{3} \Im\left[B_{p\alpha} B_{i\alpha} \frac{1}{\sqrt{z_\alpha}}\right] \tag{39}$$

$$H_{pi} = \sqrt{\frac{2}{\pi}} \sum_{\alpha=1}^{3} \Im\left[B_{p\alpha} B_{i\alpha} \frac{1}{\sqrt{z_\alpha}}\right] \tag{40}$$

where $\Im$ denotes imaginary part.

Downloaded 03 May 2010 to 171.66.16.31. Redistribution subject to ASME license or copyright; see http://www.asme.org/terms/Terms_Use.cfm

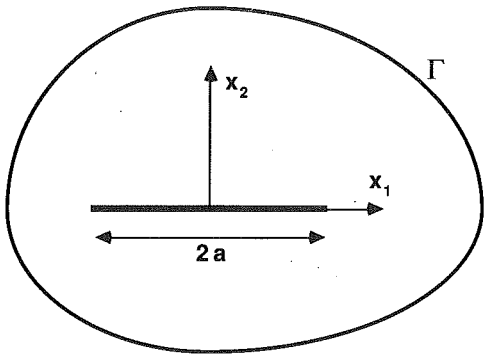


Fig. 2 Contour Γ surrounding a crack

As mentioned in Section 2, these expressions are not valid (except as an appropriate limit) for isotropic materials. **G** and **H** for isotropic materials will be given separately in the following section.

4.2 Isotropic Materials. For isotropic plane-strain cracks, it is more convenient to express equation (30) as

$$k_p = \Re\left[\int \left(G_p \frac{\partial \bar{u}}{\partial l} - H_p \bar{t}\right) dl\right] \tag{41}$$

where $\bar{u} = u_1 - iu_2$, $\bar{t} = t_1 - it_2$ and

$$G_p = \frac{\mu}{1-\nu}\,(\hat{\sigma}_{12p} + i\hat{\sigma}_{22p}) \tag{42}$$

$$H_p = \frac{\mu}{1-\nu}\,(\hat{u}_{1p} + i\hat{u}_{2p})_{,1} \tag{43}$$

where equation (15) has been used. The crack-tip fields of an isotropic crack are well known. For the case of plane strain, they can be obtained by the method of Muskhelishvili (1963) as

$$\hat{\sigma}_{121} + i\hat{\sigma}_{221} = \phi(z) + \phi(\bar{z}) - (z-\bar{z})\overline{\phi'(z)} \tag{44}$$

$$\hat{\sigma}_{122} + i\hat{\sigma}_{222} = i(\phi(z) + \phi(\bar{z}) + (z-\bar{z})\overline{\phi'(z)}) \tag{45}$$

$$(\hat{u}_{11} + i\hat{u}_{21})_{,1} = \frac{-i}{2\mu}\,((3-4\nu)\phi(z) - \phi(\bar{z}) + (z-\bar{z})\overline{\phi'(z)}) \tag{46}$$

$$(\hat{u}_{12} + i\hat{u}_{22})_{,1} = \frac{1}{2\mu}\,((3-4\nu)\phi(z) - \phi(\bar{z}) - (z-\bar{z})\overline{\phi'(z)}) \tag{47}$$

where $z = x_1 + ix_2$ and $\phi(z)$ is given by

$$\phi(z) = \frac{1}{2\sqrt{2\pi z}}\,. \tag{48}$$

G_p and H_p can be obtained by substituting the crack tip fields into equation (42) and (43).

5 Another Form of Path-Independent Integrals

In equation (30), countour Γ is assumed to start from the lower crack face and terminate at the upper crack face. In this section, another form of path-independent integrals for SIF which can be evaluated along a closed contour completely surrounding a crack will be derived.

Consider a body containing an internal crack of length $2a$ under loading. Let Γ be a closed contour completely surrounding the crack as shown in Fig. 2. The J-integral evaluated on Γ can be shown to be

$$J = \frac{1}{2}\,L_{pq}^{-1}(k_p^+ k_q^+ - k_p^- k_q^-) \tag{49}$$

where $\mathbf{k}^+$ is the SIF of the tip at $x_1 = a$ and $\mathbf{k}^-$ is the SIF of the tip at $x_1 = -a$. Let σ' and $\mathbf{u}'$ be another state in the same cracked body. Following arguments similar to those presented in Section 3, one can show that

$$L_{pq}^{-1}(k_p^+ k_q'^+ - k_p^- k_q'^-) = \int_\Gamma \left(\sigma_{i2}' \frac{\partial u_i}{\partial l} - u_{i,1}' t_i\right) dl. \tag{50}$$

Let σ_{i2}' and u_i' be given by

$$\sigma_{i2}' = \tilde{\sigma}_{i2q}' k_q' \tag{51}$$

$$\frac{\partial u_i'}{\partial x_1} = \frac{\partial \tilde{u}_{iq}'}{\partial x_1}\,k_q' \tag{52}$$

where k_q' is an arbitrary constant, $\tilde{\sigma}_{i2q}$ and $\tilde{u}_{iq}$ are chosen such that as the crack tip at $x_1 = a$ is approached

$$\tilde{\sigma}_{i2q}' \to \hat{\sigma}_{i2q}$$

$$\tilde{u}_{iq,1}' \to \hat{u}_{iq,1}, \tag{53}$$

and, as the crack tip at $x_1 = -a$ is approached,

$$\tilde{\sigma}_{i2q}' \to 0$$

$$\tilde{u}_{iq}' \to 0. \tag{54}$$

The SIFs for the primed state can be shown to be

$$k_q'^+ = k_q',\ k_q'^- = 0.$$

With this choice of the primed state, equation (50) becomes

$$\left[L_{pq}^{-1} k_p \int_\Gamma \left(\tilde{\sigma}_{i2q} \frac{\partial u_i}{\partial l} - \tilde{u}_{i,1} t_i\right) dl\right] k_q' = 0. \tag{55}$$

Since k_q' is arbitrary, equation (55) implies

$$k_p = \int_\Gamma \left(\tilde{G}_{pi} \frac{\partial u_i}{\partial l} - \tilde{H}_{pi} t_i\right) dl \tag{56}$$

where

$$\tilde{G}_{pi} = L_{pq}\tilde{\sigma}_{i2q} \tag{57}$$

$$\tilde{H}_{pi} = L_{pq}\tilde{u}_{iq,1}. \tag{58}$$

For anisotropic materials, choices for equation (51) and (52) that satisfy (53) and (54) can be obtained by taking

$$g_\alpha(z_\alpha) = \frac{1}{4\sqrt{\pi a}}\,B_{\alpha q}^{-1}\sqrt{\frac{z_\alpha + a}{z_\alpha - a}}\,k_q'$$

in Stroh's respresentations, (9) and (12). The branch cut for g_α is taken to coincide with the crack. The corresponding expressions of $\tilde{\sigma}_{i2q}$ and $\tilde{u}_{iq,1}$ can be shown to be

$$\tilde{\sigma}_{i2q} = \frac{1}{2\sqrt{\pi a}} \sum_{\alpha=1}^{3} \Re\left[B_{i\alpha} B_{\alpha q}^{-1} \sqrt{\frac{z_\alpha + a}{z_\alpha - a}}\right] \tag{59}$$

$$\tilde{u}_{iq,1} = \frac{1}{2\sqrt{\pi a}} \sum_{\alpha=1}^{3} \Re\left[A_{i\alpha} B_{\alpha q}^{-1} \sqrt{\frac{z_\alpha + a}{z_\alpha - a}}\right]. \tag{60}$$

Substitution of equations (59) and (13) into (57) and (58) yields

$$\tilde{G}_{pi} = \frac{1}{\sqrt{\pi a}} \sum_{\alpha=1}^{3} \Im\left[B_{p\alpha} B_{i\alpha} \sqrt{\frac{z_\alpha + a}{z_\alpha - a}}\right] \tag{61}$$

$$\tilde{H}_{pi} = \frac{1}{\sqrt{\pi a}} \sum_{\alpha=1}^{3} \Im\left[B_{p\alpha} A_{i\alpha} \sqrt{\frac{z_\alpha + a}{z_\alpha - a}}\right]. \tag{62}$$

For isotropic materials, equation (41) is also valid in the present case provided that ϕ in equation (48) is replaced by

$$\phi(z) = \frac{1}{4\sqrt{\pi a}} \sqrt{\frac{z+a}{z-a}}\,. \tag{63}$$

Path-independent integrals for SIF's of the crack tip at $x_1 = -a$ can be derived in a similar procedure. The final results can also be expressed by equations (30) and (41) with

Downloaded 03 May 2010 to 171.66.16.31. Redistribution subject to ASME license or copyright; see http://www.asme.org/terms/Terms_Use.cfm

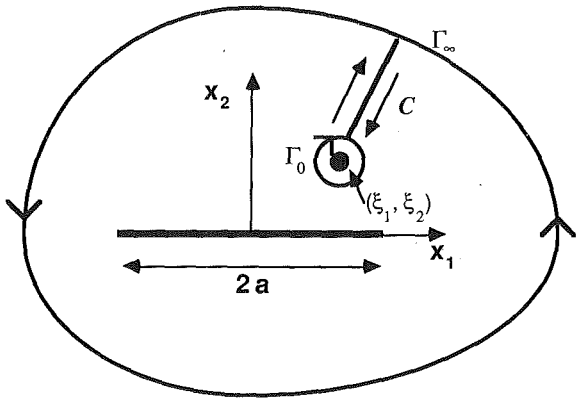


Fig. 3 Contour for evaluation of the SIF's due to a body force and a dislocation located at (ξ_1, ξ_2)

$$-\sqrt{2a}\sqrt{\frac{z_\alpha + a}{z_\alpha - a}},$$

replacing $\sqrt{z_\alpha}$ in (39) and (40) for anisotropic materials, and with

$$-\sqrt{2a}\sqrt{\frac{z + a}{z - a}},$$

replacing $\sqrt{z}$ in (48) for isotropic materials.

6 SIF Due to a Body Force and a Dislocation

In this section, the SIF's due to a body force and a dislocation in an unbounded anisotropic solid containing a crack of length $2a$ are derived. In the following discussion, only the crack tip at $x_1 = a$ is considered as the SIF's for the tip at $x_1 = -a$ can be determined easily by the same procedure.

Let a body force **f** and a dislocation of Burger's vector **b** be located at (ξ_1, ξ_2) as shown in Fig. 3. The dislocated plane for the dislocation is assumed to extend from (ξ_1, ξ_2) to infinity. One may question the validity of this choice of the branch cut, as in reality the dislocations are usually emanated from the crack tip where there is high stress concentration and the branch cut is in the form of a finite length cut. However, a finite dislocated plane (or branch cut) can be envisioned as consisting of two dislocations with infinite branch cuts at the ends of the finite cut. The two dislocations at the ends have Burger's vectors equal in magnitude but opposite in sign. Thus, SIFs for a finite dislocated plane can be obtained as the sum of those due to a single dislocation considered here.

The SIFs induced by the body force and the dislocation can be calculated by the path-independent integrals of equation (56) integrated over the path Γ shown in Fig. 3. The path Γ consists of three parts: (*a*) a contour Γ_0 centered at (ξ_1, ξ_2) with a vanishingly small radius, (*b*) an infinite contour Γ_∞, and (*c*) a line C connecting Γ_0 and Γ_∞. Since $\partial u_i/\partial l$ and t_i are continuous across C, calculation of the integral along C cancels. The integral therefore need only be evaluated over Γ_0 and Γ_∞.

The contribution to the SIF's from Γ_0 can be shown to be

$$\int_{\Gamma_0} \left(\tilde{G}_{pi} \frac{\partial u_i}{\partial l} - \tilde{H}_{pi} t_i\right) dl = -\tilde{G}_{pi}(\zeta_\alpha) b_i - \tilde{H}_{pi}(\zeta_\alpha) f_i \qquad (64)$$

where $\zeta_\alpha = \xi_1 + p_\alpha \xi_2$. In deriving the equation (64), the following equations have been used:

$$\int_{\Gamma_0} \frac{\partial u_i}{\partial l} dl = -b_i \qquad (65)$$

$$\int_{\Gamma_0} t_i dl = f_i. \qquad (66)$$

Equation (65) states that the displacements around a dislocation suffer jumps given by Burger's vector. A negative sign on the r.h.s. of (65) appears as the direction of the circuit Γ_0 is clockwise. Equation (66) expresses equilibrium of the body force and the surrounding tractions on Γ_0 according to the normal pointing toward (ξ_1, ξ_2).

The contribution from Γ_∞ is calculated as follows

$$\int_{\Gamma_\infty} \left(\tilde{G}_{pi} \frac{\partial u_i}{\partial l} - \tilde{H}_{pi} t_i\right) dl = \lim_{z_\alpha \to \infty} \tilde{G}_{pi}(\xi_\alpha) \int_{\Gamma_\infty} \frac{\partial u_i}{\partial l} dl - \lim_{z_\alpha \to \infty} \tilde{H}_{pi}(\xi_\alpha) \int_{\Gamma_\infty} t_i dl \qquad (67)$$

From (61) and (62), it can be shown that

$$\lim_{z_\alpha \to \infty} \tilde{G}_{pi}(z_\alpha) = \Im[B_{p\alpha} B_{i\alpha}] \qquad (68)$$

$$\lim_{z_\alpha \to \infty} \tilde{H}_{pi}(z_\alpha) = \Im[B_{p\alpha} A_{i\alpha}]. \qquad (69)$$

Equation (67) thus becomes

$$\int_{\Gamma_\infty} \left(\tilde{G}_{pi} \frac{\partial u_i}{\partial l} - \tilde{H}_{pi} t_i\right) dl = \Im[B_{p\alpha} B_{i\alpha}] b_i + \Im[B_{p\alpha} A_{i\alpha}] f_i, \qquad (70)$$

where the following relations have been used

$$\int_{\Gamma_\infty} \frac{\partial u_i}{\partial l} dl = b_i$$

$$\int_{\Gamma_\infty} t_i dl = -f_i.$$

The above equations differ in sign from (65) and (66) since the direction of the contour is counterclockwise and the normal vector of the contour points outwards.

The induced SIF's are the sum of (64) and (70). The final result is given by

$$k_p^+ = \frac{1}{\sqrt{\pi a}} \Im\left[B_{p\alpha} B_{i\alpha} \left(1 - \sqrt{\frac{\zeta_\alpha + a}{\zeta_\alpha - a}}\right)\right] b_i + \frac{1}{\sqrt{\pi a}} \Im\left[B_{p\alpha} A_{i\alpha} \left(1 - \sqrt{\frac{\zeta_\alpha + a}{\zeta_\alpha - a}}\right)\right] f_i. \qquad (71)$$

Note that for a dislocated plane in the form of a finite line segment, the constant term on the r.h.s. of (71) would be absent. Note also that for a dislocated plane (finite or infinite) extending from the crack tip, the SIF's are unbounded. The fact indicates that the stress singularity at the crack tip is stronger than the square root.

For the special case where the body force and the dislocation are near the crack tip, the above result reduces to

$$k_p^+ = -\sqrt{\frac{2}{\pi}} \Im\left[B_{p\alpha} B_{i\alpha} \frac{1}{\sqrt{\zeta_\alpha - a}}\right] b_i - \sqrt{\frac{2}{\pi}} \Im\left[B_{p\alpha} A_{i\alpha} \frac{1}{\sqrt{\zeta_\alpha - a}}\right] f_i. \qquad (72)$$

Equation (72) agrees with that obtained by Wu (1988) who considered the situation in which a body force and dislocation are present near the tip of an extending crack. Rice (1985) has proposed an alternative method for deriving the stress intensity factors due to a dislocation and has given an explicit result as the dislocation is close to the crack tip. The method proposed by Rice (1985) is also based on conservation of energy. In Rice's method, however, use is made of reciprocity between the energetic forces exerted on the crack tip and the dislocation. In contrast, the approach presented here basically utilizes the fact that the sum of all energetic forces in the x_1-direction must vanish.

Downloaded 03 May 2010 to 171.66.16.31. Redistribution subject to ASME license or copyright; see http://www.asme.org/terms/Terms_Use.cfm

For a point force **T** applied on the upper crack face at $x_1 = c$, $x_2 = 0^+$, equation (71) becomes

$$\mathbf{k}^+ = \frac{-1}{2\sqrt{\pi a}} \mathbf{S}^T \mathbf{T} + \frac{1}{2\sqrt{\pi a}} \sqrt{\frac{a+c}{a-c}}\, \mathbf{T} \tag{73}$$

where (14) has been used. It is interesting to note that the first term on the r.h.s. of (73) is independent of the point of force application c while the second term is independent of the material constants. Thus, for a system of self-equilibrating forces applied on the crack faces, the first term would drop out and the SIF's would be independent of the material constants. Similarly, if a pair of identical forces are applied on $x_1 = c$, $x_2 = 0^+$ and $x_1 = c$, $x_2 = 0^-$, the resulting SIF's would be independent of c. Equation (73) is also valid for isotropic materials since it contains only matrix **S**. Substituting the expression of **S**, (16), the result for isotropic materials is given by

$$k_1^+ = -\frac{1-2\nu}{4(1-\nu)} \frac{T_2}{\sqrt{\pi a}} + \frac{1}{2} \sqrt{\frac{a+c}{a-c}} \frac{T_1}{\sqrt{\pi a}}$$

$$k_2^+ = \frac{1-2\nu}{4(1-\nu)} \frac{T_1}{\sqrt{\pi a}} + \frac{1}{2} \sqrt{\frac{a+c}{a-c}} \frac{T_2}{\sqrt{\pi a}}$$

$$k_3^+ = \frac{1}{2} \sqrt{\frac{a+c}{a-c}} \frac{T_3}{\sqrt{\pi a}}$$

The solutions of k_1 and k_2 agree with those obtained by Sih (1962).

7 Conclusion

Stress intensity factors have been represented by path-independent integrals in this paper. The integrals have been derived by the path independent J-integral with the use of the crack-tip fields characteristic to linear elastic materials. Integrals that can be computed over contours surrounding a crack tip or an internal crack were given. The integrals were expressed in terms of the tangential derivatives of the displacements and the tractions convoluted by kernel functions appropriate to each fracture mode. The treatment can be easily extended to obtain path-independent integrals with contours enclosing n collinear cracks for each crack tip. The derivation is similar to that given in Section 5 and will not be repeated here. Let the cracks line on the x_1-axis and the positions of the crack tips be $x_1 = a_m$, $m = 1,2, \ldots, 2n$ where $a_1 < a_2 < \ldots < a_{2n}$. The kernel functions in (30) for the tip at $x_1 = a_m$ can be shown to be

$$\tilde{G}_{pi} = (-1)^m \sqrt{\frac{2}{\pi |F_m(a_m)|}} \sum_{\alpha=1}^{3} \Im\left[B_{p\alpha} B_{i\alpha} \sqrt{\frac{F_m(z_\alpha)}{z_\alpha - a_m}} \right]$$

$$\tilde{H}_{pi} = (-1)^m \sqrt{\frac{2}{\pi |F_m(a_m)|}} \sum_{\alpha=1}^{3} \Im\left[B_{p\alpha} A_{i\alpha} \sqrt{\frac{F_m(z_\alpha)}{z_\alpha - a_m}} \right]$$

where

$$F_m(z_\alpha) = \prod_{i=1, i\neq m}^{2n} (z_\alpha - a_i).$$

References

Bacon, D. J., Barnett, D. M., and Scattergood, R. O., 1978, "Anisotropic continuum theory of lattice defects," *Prog. Mater. Sci.*, Vol. 23, pp. 51–262.

Barnett, D. M., and Asaro, R. J., 1972, "The fracture mechanics of Slit-like cracks in anisotropic elastic media.," *J. Mech. Phys. Solids*, Vol. 20, pp. 353–366.

Barnett, D. M., and Lothe, J., 1973, "Synthesis of the sextic and the integral formalism for dislocations, Greens functions and surface waves in anisotropic elastic solids," *Phys. Norv.*, Vol. 7, pp. 13–19.

Chen, F. H. K., and Shield, R. T., 1977, "Conservation laws in Elasticity of the J-integral type," *Z. Angw. Math. Phys.*, Vol. 28, pp. 1–22.

Hong, C. C., and Stern, M., 1978, "The computation of stress intensity factors in dissimilar materials," *J. Elasticity*, Vol. 8, pp. 21–34.

Muskhelishvili, I. N., 1963, "Some basic problems of the mathematical theory of elasticity," J. R. M. Radok, trans., Noordhoff Groningen, The Netherlands.

Rice, J. R., 1968, "A path-independent intergral and the approximate analysis of strain concentration by notches and cracks," ASME JOURNAL OF APPLIED MECHANICS, Vol. 35, pp. 379–386.

Rice, J. R., 1985, "Conserved integrals and energetic forces," *Fundamentals of Deformation and Fracture* (*Eshelby Memorial Symposium*), B. A. Bilby, K. J. Miller and J. R. Willis, eds., Cambridge Univ. Press.

Sih, C. F., and Asaro, R. J., 1988, "Elastic-plastic analysis of cracks on Bimaterial interfaces: Part I – small scale yielding," ASME JOURNAL OF APPLIED MECHANICS, Vol. 55, pp. 299–316.

Sih, G. C., 1962, "Application of Muskhelishvili's method to fracture mechanics," *The Chinese Assn. for Advanced Studies*, p. 25.

Stern, M., Becker, E. B., and Dunham, R. S., 1976, "A contour integral computation of mixed-mode stress intensity factors," *Int. Journ. of Fracture*, Vol. 12, pp. 359–368.

Stroh, A. N., 1958, "Dislocations and cracks in anisotropic elasticity," *Philos. Mag.*, Vol. 7, pp. 625–646.

Ting, T. C. T., 1986, "Explicit solution and in variance of the singularities at an interface crack in anisotropic composite," *Int. J. Solids Structures*, Vol. 22, No. 9, pp. 965–983.

Wu, K. C., 1989, "On the crack tip fields of a dynamically propagating crack in an anisotropic elastic solid," *Int. Journ. of Fracture*, in press.

Wu, K. C., 1988, "Stress intensity factors due to nonelastic strains and body forces for steady dynamic crack extension in an anisotropic elastic material," *Int. J. Solids Structure*, Vol. 24, No. 8, pp. 805–811.

Yau, J. F., Wang, S. S., and Corten, H. T., 1980, "A mixed mode crack analysis of isotropic solids using conservation laws of elasticity," ASME JOURNAL OF APPLIED MECHANICS, Vol. 47, pp. 335–341.

Downloaded 03 May 2010 to 171.66.16.31. Redistribution subject to ASME license or copyright; see http://www.asme.org/terms/Terms_Use.cfm

John Dundurs
Professor,
Departments of Civil Engineering and Mechanical Engineering,
Northwestern University,
Evanston, Ill. 60208
Fellow ASME

Cavities *vis-à-vis* Rigid Inclusions and Some Related General Results in Plane Elasticity

There is a strange feature of plane elasticity that seems to have gone unnoticed: The stresses in a body that contains rigid inclusions and is loaded by specified surface tractions depend on the Poisson ratio of the material. If the Poisson ratio in this stress field is set equal to +1 for plane strain, or $+\infty$ for plane stress, the rigid inclusions become cavities for elastic constants within the physical range. The paper pursues this circumstance, and in doing so also produces several useful by-products that are connected with the stretching and curvature change of a boundary.

1 Introduction

The investigation reported in this article is prompted by a casual observation: The stresses in an elastic body that contains rigid inclusions and is loaded by given surface tractions depend on the Poisson ratio of the material. Suppose that the Poisson ratio in this stress field is set equal to +1 for plane strain, or $+\infty$ for plane stress.[1] Then the resulting stresses, more often than not, correspond to cavities that are free of surface tractions. Hence, a natural question to ask is why is this so. The subsequent discussion also produces several useful by-products. Among them is a relation in terms of strains for the change in curvature of the boundary curve, and the boundary conditions for rigid inclusions that are expressed in terms of stresses.

It is instructive to consider immediately a simple example, such as provided by a circular rigid inclusion in a field of uniform tension (see Fig. 1). The Airy stress function for this problem is

$$U=\frac{1}{4}T\left(r^2-r^2\cos 2\theta+Aa^2\log r+Ba^2\cos 2\theta+Ca^4\frac{\cos 2\theta}{r^2}\right) \tag{1}$$

where the first two terms correspond to the field of uniform tension, and the last three terms constitute the disturbance caused by the inclusion. For a bonded interface (Goodier 1933; Muskhelishvili, 1953)

$$A=k-1 \qquad B=-2/k \qquad C=1/k \tag{2}$$

and, for a frictionless slipping interface,

$$A=k-1 \qquad B=-4/(3k+1) \qquad C=-(k-1)/(3k+1), \tag{3}$$

where $k=3-4\nu$ for plane strain and $k=(3-\nu)/(1+\nu)$ for plane stress, with ν denoting Poisson's ratio. It may be recalled that for a cavity (Timoshenko and Goodier, 1970),

$$A=-2, \qquad B=2, \qquad C=-1. \tag{4}$$

Since the stress components are simply the derivatives of the Airy stress function, their structure in the elastic constants is the same as that of the latter. It is seen now that both (2) and (3) give (4) upon setting $k=-1$, which corresponds to $\nu=+1$ for plane strain, and $\nu=+\infty$ for plane stress. It is interesting to note that the stresses induced by the rigid inclusion are singular at some values of k that fall outside the physical range of $1\le k\le 3$ ($0\le\nu\le 1/2$). For the bonded interface, the stresses are singular at $k=0$ ($\nu=3/4$ for plane strain, $\nu=3$ for plane stress). For the slipping interface, this happens at $k=-1/3$ ($\nu=5/6$ for plane strain, $\nu=5$ for plane stress). However, in both cases, the stresses remain defined at $k=-1$ and correspond to a cavity. The displacement and stress fields for the bonded inclusion and the cavity are written in full, and further observations are made in Appendix B.

This example shows that a stress field, while satisfying the given boundary conditions for all elastic constants that fall within the physical range, somehow assumes a life of its own outside the physical range and for specific values of the elastic constants satisfies different boundary conditions that are back in the physical realm.

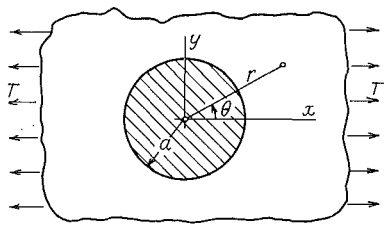


Fig. 1 Circular inclusion in a field of uniform tension

[1] These are precisely the values for which elasticity loses its Green's tensor function—plane strain, in this sense, being the same as three dimensions.

Contributed by the Applied Mechanics Division of THE AMERICAN SOCIETY OF MECHANICAL ENGINEERS for presentation at the Winter Annual Meeting, San Francisco, Calif., December 10–15, 1989.

Discussion on this paper should be addressed to the Editorial Department, ASME, United Engineering Center, 345 East 47th Street, New York, N.Y., 10017, and will be accepted until two months after final publication of the paper itself in the JOURNAL OF APPLIED MECHANICS. Manuscript received by the ASME Applied Mechanics Division, April 26, 1988; final revision, March 28, 1989.

Paper No. 89-WA/APM-22.

Copyright © 1989 by ASME

Downloaded 03 May 2010 to 171.66.16.31. Redistribution subject to ASME license or copyright; see http://www.asme.org/terms/Terms_Use.cfm

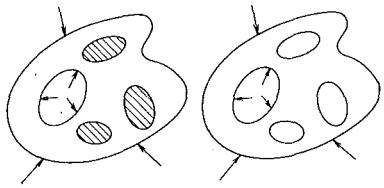


Fig. 2 Body with rigid inclusions *vis-à-vis* cavities

2 Comparison of the Two Problems

In order to fix ideas, consider the two situations shown in Fig. 2. One of them pertains to an elastic body that contains some rigid inclusions and is loaded by given surface tractions on the other boundaries. The other is the same body loaded by identical surface tractions, but in which the inclusions have been replaced by cavities that are free of tractions. In both problems, the stress components must satisfy the field equations

$$\partial_j \sigma_{ji} = 0, \qquad i,j, \ldots = 1,2 \tag{5}$$

$$\partial_i \partial_i \sigma_{jj} = 0 \tag{6}$$

which ensure equilibrium and local compatibility. In addition, the stresses in both cases must satisfy on each of the internal boundaries the Michell integral conditions for global compatibility (Michell, 1900; Mindlin and Salvadori, 1950):

$$\oint \frac{\partial \Sigma}{\partial n}\, ds = 0 \tag{7}$$

$$\oint \left(x_1 \frac{\partial \Sigma}{\partial n} + x_2 \frac{\partial \Sigma}{\partial s} \right) ds = 0 \tag{8}$$

$$\oint \left(x_2 \frac{\partial \Sigma}{\partial n} - x_1 \frac{\partial \Sigma}{\partial s} \right) ds = 0 \tag{9}$$

where

$$\Sigma = \sigma_{ii}. \tag{10}$$

To simplify the discussion from the outset, the Michell integrals have been set equal to zero, meaning that the loaded boundaries in neither problem transmit a net force. Similarly, no net forces are applied to the rigid inclusions, but there is no immediate reason to exclude the possibility of couples being applied to the inclusions. The boundary conditions on the loaded boundaries are identical in both problems:

$$\sigma_{ij} n_j = t_i(s) \tag{11}$$

where n_i is the unit outer normal and s the arc length of the boundary curve used as a parameter. The traction functions t_i specify the loading.

The only difference between the two problems is in the boundary conditions of cavities versus rigid inclusions. For cavities they are

$$\sigma_{ij} n_j = 0. \tag{12}$$

A rigid inclusion with a bonded interface restricts the displacements on the boundary to a rigid body motion, and the conventional boundary condition is

$$u_i = a_i + \epsilon_{i3j} \omega_3 x_j \tag{13}$$

where the constants a_i and ω_3 are determined by the three equilibrium conditions for the inclusion. For a rigid inclusion with a frictionless slipping interface, the boundary conditions are

$$\sigma_{ji} n_j = \lambda n_i \tag{14}$$

$$u_i n_i = a_i n_i + \epsilon_{i3j} n_i \omega_3 x_j. \tag{15}$$

The first of these, with λ a free constant, expresses the requirement that the shear tractions vanish, or that $\sigma_{ns} = 0$ on the interface. The second condition restricts the normal displacements to be compatible with the motion of a rigid body. Again the constraints a_i and ω_3 are determined by the equilibrium conditions of the inclusion.

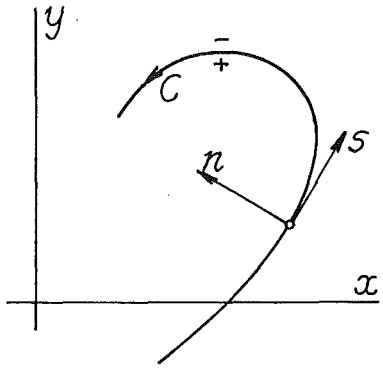


Fig. 3 Tangential and normal directions on a curve

The boundary conditions (13) and (15) involving the displacements reveal nothing of value for making a comparison between cavities and rigid inclusions.[2] However, it is shown in the next section that these boundary conditions can be replaced by conditions involving stresses which then are open to interpretations.

3 Boundary Conditions for Rigid Inclusions That Are in Terms of Stresses

The boundary conditions for a rigid inclusion with a bonded interface can also be taken as the requirements that a line element at the interface neither stretches nor changes its curvature, or

$$\epsilon_{ss} = 0, \qquad \Delta\kappa = 0 \tag{16a,b}$$

where ϵ_{ss} denotes the tangential normal strain, and $\Delta\kappa$ is the change in curvature. For a rigid inclusion with a frictionless slipping interface, the boundary conditions are

$$\sigma_{ns} = 0, \qquad \Delta\kappa = 0. \tag{17a,b}$$

It is shown in Appendix A that the curvature change of a boundary curve in terms of strains is

$$\Delta\kappa = 2 \frac{\partial \epsilon_{ns}}{\partial s} - \frac{\partial \epsilon_{ss}}{\partial n} - \kappa \epsilon_{nn}, \tag{18}$$

where the strain components are referred to the normal and tangential directions, and κ is the original curvature of the boundary. The sign convention for the formula (18) is as follows (see Fig. 3): Assign the curve C a direction. The arc coordinate s points in the direction of the curve, and the normal n points to the left when moving along C in the assigned direction. The curvature κ is taken as positive when the center of curvature is on the side in which n points. The sign convention for the strain components ϵ_{nn}, ϵ_{ns}, and ϵ_{ss} is the customary one applied to the n, s-system.

Hooke's law for plane elasticity is

$$2\mu \epsilon_{ij} = \sigma_{ij} - \frac{1}{4}(3-k)\sigma_{kk}\delta_{ij}, \quad i,j,k = 1,2 \tag{19}$$

where μ denotes the shear modulus. Substituting the strains from (19) into (18), the result is

[2] It may be noted that the boundary conditions of specified displacements and specified tractions are closely related in formulations using complex potentials. The transformation is, in effect, $k = -1$, but there is an essential constant in the condition for zero tractions, and unloaded inclusions inject also a term proportional to z. The transformation can be found in books (Sokolnikoff, 1956; England, 1971), but not much seems to be made of this connection.

Downloaded 03 May 2010 to 171.66.16.31. Redistribution subject to ASME license or copyright; see http://www.asme.org/terms/Terms_Use.cfm

$$8\mu\Delta\kappa = 8\frac{\partial\sigma_{ns}}{\partial s} - (k+1)\frac{\partial\sigma_{ss}}{\partial n} + (3-k)\frac{\partial\sigma_{nn}}{\partial n} + \kappa[(3-k)\sigma_{ss} - (k+1)\sigma_{nn}]. \quad (20)$$

The last expression can be simplified by using the equilibrium condition

$$\frac{\partial\sigma_{nn}}{\partial n} + \frac{\partial\sigma_{ns}}{\partial s} + \kappa(\sigma_{ss} - \sigma_{nn}) = 0. \quad (21)$$

Thus,

$$8\mu\Delta\kappa = (5+k)\frac{\partial\sigma_{ns}}{\partial s} - (k+1)\frac{\partial\sigma_{ss}}{\partial n} - 2\kappa(k-1)\sigma_{nn}. \quad (22)$$

The boundary conditions (16) for a rigid inclusion with a bonded interface now reduce to

$$(3-k)\sigma_{nn} - (k+1)\sigma_{ss} = 0 \quad (23)$$

$$(5+k)\frac{\partial\sigma_{ns}}{\partial s} - (k+1)\frac{\partial\sigma_{ss}}{\partial n} - 2\kappa(k-1)\sigma_{nn} = 0. \quad (24)$$

Similarly, the boundary conditions (17) for a rigid inclusion with a slipping interface become

$$\sigma_{ns} = 0 \quad (25)$$

$$(k+1)\frac{\partial\sigma_{ss}}{\partial n} + 2\kappa(k-1)\sigma_{nn} = 0. \quad (26)$$

Special considerations may be required if the inclusions had sharp corners.

4 Relation of Cavities to Rigid Inclusions

Setting $k=-1$ in (23) and (24) under the assumption that σ_{nn}, σ_{ss} and $\partial\sigma_{ss}/\partial n$ are finite, the boundary conditions for a bonded inclusion become

$$\sigma_{nn} = 0, \qquad \sigma_{ns} = \sigma^0 = \text{const.} \quad (27)$$

The boundary conditions, (25) and (26), for a slipping inclusion with $k=-1$ yield

$$\sigma_{nn} = 0, \qquad \sigma_{ns} = 0 \quad (28)$$

when the special case $\kappa = 0$ is excluded. These will be called the k-transformed boundary conditions.

The principal question at this point is whether the stresses obtained for rigid inclusions with k in the physically admissible range $(1 \le k \le 3)$ remain defined at $k=-1$. Known solutions suggest this is connected with the inclusion possibly being in equilibrium under the k-transformed boundary conditions.

For instance, consider an anticrack (rigid lamellar inclusion with negligible thickness that is bonded to the surrounding elastic material) in an infinitely extended material. If the anticrack is loaded by a couple with the moment M (see Fig. 4), the resulting stresses in the plane of the anticrack are (Dundurs and Markenscoff, 1989)

$$\sigma_{xx}(x, 0\pm) = \mp\frac{M(3-k)}{\pi(k+1)a^2}\frac{x\,H(a-|x|)}{(a^2-x^2)^{1/2}}, \quad |x| < \infty \quad (29)$$

$$\sigma_{xy}(x, 0) = \frac{M(k-1)}{\pi(k+1)a^2}\left\{1 - \frac{|x|H(|x|-a)}{(x^2-a^2)^{1/2}}\right\}, \quad |x| < \infty \quad (30)$$

$$\sigma_{yy}(x, 0\pm) = \mp\frac{M}{\pi a^2}\frac{x\,H(a-|x|)}{(a^2-x^2)^{1/2}}, \quad |x| < a. \quad (31)$$

It is clear that the k-transformed boundary conditions (27) cannot provide equilibrium in this problem, which then is reflected in the stresses being singular at $k=-1$ (it can be shown that the boundary conditions (23) and (24) are satisfied for all $k \neq -1$). If, in contrast, the couple were applied through a circular inclusion, equilibrium is possible under the k-transformed boundary conditions, and the resulting stresses

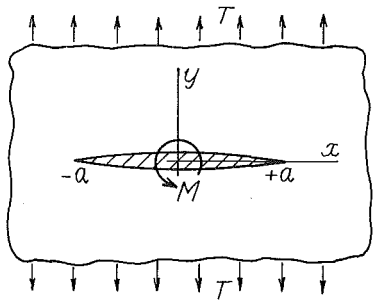


Fig. 4 Anticrack disturbing a field of uniform tension, or being loaded by a couple

$$\sigma_{r\theta} = M/2\pi r^2, \quad \sigma_{rr} = \sigma_{\theta\theta} = 0 \quad (32)$$

are defined for all k. Similarly, it may be noted that the singular nature of the stresses at $k=-1$ in the first example has evidently nothing to do with the singular geometry of the anticrack. If the anticrack is placed in a field uniform tension (see Fig. 4), the stresses in its plane are (Dundurs and Markenscoff, 1989):

$$\sigma_{xx}(x, 0) = \frac{T(9-k^2)}{8k}\left\{1 - \frac{|x|H(|x|-a)}{(x^2-a^2)^{1/2}}\right\}, \quad |x| < \infty \quad (33)$$

$$\sigma_{xy}(x, 0\pm) = \mp\frac{T(k+1)(3-k)}{8k}\frac{x\,H(a-|x|)}{(a^2-x^2)^{1/2}}, \quad |x| < \infty \quad (34)$$

$$\sigma_{yy}(x, 0) = \frac{T}{8k}\left\{(k=1)(3+k) + (k-1)(3-k)\frac{|x|H(|x|-a)}{(x^2-a^2)^{1/2}}\right\}, \quad |x| < \infty. \quad (35)$$

Now the stresses are singular at $k=0$, but remain defined and give the results for the Griffith crack at $k=-1$.

If the stresses in the inclusion problem are not singular at $k=-1$, they satisfy the k-transformed boundary conditions (27) and (28), and we can reach the following conclusions.

Inclusions With Bonded Interfaces. Setting $k=-1$ in the stresses of the inclusion problem yields cavities that are free of normal tractions, but that may be subjected to *uniformly* distributed shear tractions σ^0. The result of these uniform shear tractions is a couple with the moment

$$M = 2A\sigma^0 \quad (36)$$

where A is the enclosed area of the cavity. It is clear that $\sigma^0 \neq 0$, when the inclusion is loaded by a couple, but one should not infer that $\sigma^0 = 0$ when no couple is applied. An example is again provided by the anticrack. An anticrack placed in a field of uniform shear stresses

$$\sigma_{xy} = S = \text{const}, \qquad \sigma_{xx} = \sigma_{yy} = 0 \quad (37)$$

causes no disturbance, and (37) is also the stress field in the presence of the anticrack. Setting $k=-1$ in (37) changes nothing, and one is left with a cavity (crack) that is loaded by uniform shear tractions. In most other known solutions, however, $k=-1$ yields $\sigma^0 = 0$, and the cavity is completely free of tractions.

Inclusions With Slipping Interfaces. It follows from (28) that setting $k=-1$ in the stress fields for inclusions gives cavities that are completely free of tractions. If the boundary of an inclusion has flat parts ($\kappa = 0$), however, there may and probably will be some normal tractions left on the corresponding flat parts of the cavity. This is seen going back to (26).

Downloaded 03 May 2010 to 171.66.16.31. Redistribution subject to ASME license or copyright; see http://www.asme.org/terms/Terms_Use.cfm

5 Extensions

The relation of cavities versus rigid inclusions has so far been discussed on the basis that the source of stresses is applied tractions. It is easy to reach similar conclusions also for other sources of stress that involve no net forces, such as various nuclei of strain, concentrated couples, dislocations and disclinations, and finite domains undergoing transformation strains. To keep the discussion from becoming too tedious, only the edge dislocation is mentioned, since the situation with all other sources of stress is quite similar.

The singular part of the stress field for an edge dislocation is of the form (Mura 1982):

$$\sigma_{ij}^{S} = \frac{2\mu b}{\pi(k+1)} f_{ij}(x_1,x_2) \tag{38}$$

where b is the Burgers vector of the dislocation. If the edge dislocation is placed in a body that has finite unloaded boundaries and contains some rigid inclusions, the resulting stresses are of the form

$$\sigma_{ij}^{I} = \frac{2\mu b}{\pi(k+1)} g_{ij}(x_1,x_2;k). \tag{39}$$

Now, the k-transformation to go from inclusions to cavities is: (1) leave the multiplier in (39) involving $(k+1)$ in the denominator as is and (2) set $k=-1$ inside the function g_{ij}. This gives the stresses in the body with cavities as

$$\sigma_{ij}^{C} = \frac{2\mu b}{\pi(k+1)} g_{ij}(x_1,x_2;-1).$$

The various stipulations mentioned before apply, but it can be confirmed that for circular inclusions with bonded or slipping interfaces (Dundurs and Mura, 1964; Dundurs and Gangadharan, 1969) one gets cavities that are completely free of tractions. The same applies for anticracks (Dundurs and Markenscoff, 1989).

An extension of a different kind pertains to the situation when a part of the outer boundary of the body is supported by imposing zero displacements (clamping) or providing a frictionless base. In such a case, the boundary conditions (23) to (26) also apply at the supports, although one can generally expect singularities at the transition points in the boundary conditions. If the loading on the rest of the boundaries is such that overall equilibrium cannot exist under the k-transformed boundary conditions (27) or (28) (including $\sigma_{nn}\neq 0$ for a frictionless base with $\kappa=0$), the stresses will be singular at $k=-1$. If, however, equilibrium is possible under the k-transformed boundary conditions, the situation becomes completely analogous with that for inclusions, and setting $k=-1$ will yield stresses that satisfy (27) or (28). An example of this type when $\kappa=0$ and, hence, $\sigma_{nn}\neq 0$, is provided by the Sadowsky (1928) solution of a rigid frictionless punch with a flat bottom indenting an elastic half space.

6 Conclusion

The curvature formulas (18) and (22) derived here have various other applications. For instance, they can be used to replace boundary conditions of specified displacements with conditions on stresses, and to establish the jump conditions in the stresses and their derivatives that occur at an interface between two different materials. However, the discussion of these topics falls outside the scope of the present article.

Acknowledgment

I am indebted to Richard T. Shield at the University of Illinois for interesting and valuable discussions of the curvature formula.

References

Dundurs, J., and Mura, T., 1964, "Interfaction Between an Edge Dislocation and a Circular Inclusion," *Journal of the Mechanics and Physics of Solids*, Vol. 12, pp. 177–189.

Dundurs, J., and Gangadharan, A. C., 1969, "Edge Dislocation Near an Inclusion With a Slipping Interface," *Journal of the Mechanics and Physics of Solids*, Vol. 17, pp. 459–471.

Dundurs, J., and Markenscoff, X., 1989, "A Green's Function Formulation of Anticracks and Their Interaction with Load-induced Singularities," ASME Journal of Applied Mechanics, Vol. 56, pp. 550–555.

England, A. H., 1971, *Complex Variable Methods in Elasticity*, John Wiley and Sons, New York.

Goodier, J. N., 1933, "Concentration of Stress Around Spherical and Cylindrical Inclusions and Flaws," *Transactions of the ASME*, No. APM-55-7, Vol. 55, pp. 39–44.

Michell, J. H., 1900, "On the Direct Determination of Stress in an Elastic Solid, With Application to the Theory of Plates," *Proceedings of the London Mathematical Society*, Vol. 31, pp. 100–124.

Mindlin, R. D., and Salvadori, M. G., 1950, "Analogies," *Handbook of Experimental Stress Analysis*, M. Hetényi ed., John Wiley and Sons, New York.

Mura, T., 1982, *Micromechanics of Defects in Solids*, Martinus Nijhoff Publishers.

Muskhelishvili, N. I., 1953, *Some Basic Problems of the Mathematical Theory of Elasticity*, translated by J. R. M. Radok, P. Noordhoff.

Sadowsky, M., 1928, "Zweidimensionale Probleme der Elastizitätstheorie," *Zeitschrift für angewandte Mathematik und Mechanik*, Vol. 8, pp. 107–121.

Sokolnikoff, I. S., 1956, *Mathematical Theory of Elasticity*, McGraw-Hill Book Co., New York.

Timoshenko, S. P., and Goodier, J. N., 1970, *Theory of Elasticity*, 3rd ed., McGraw-Hill Book Co., New York.

APPENDIX A

Curvature Change of a Strained Curve

Consider a plane curve C drawn on a deformable sheet. The parametric representation of the curve is

$$x=x(t), \qquad y=y(t) \tag{A1a,b}$$

and its original curvature is

$$\kappa = \frac{\dot{x}\,\ddot{y}-\dot{y}\,\ddot{x}}{(\dot{x}^2+\dot{y}^2)^{3/2}}. \tag{A2}$$

Suppose now that the sheet is strained. The imposed strains are compatible and, hence, correspond to displacements with the cartesian components u and v. Then the new curvature of the curve is

$$K = \frac{(\dot{x}+\dot{u})(\ddot{y}+\ddot{v})-(\dot{y}+\dot{v})(\ddot{x}+\ddot{u})}{[(\dot{x}+\dot{u})^2+(\dot{y}+\dot{v})^2]^{3/2}}. \tag{A3}$$

By chain rule of differentiation,

$$\dot{u} = \dot{x}\frac{\partial u}{\partial x} + \dot{y}\frac{\partial u}{\partial y} \tag{A4}$$

$$\dot{v} = \dot{x}\frac{\partial v}{\partial x} + \dot{y}\frac{\partial v}{\partial y} \tag{A5}$$

$$\ddot{u} = \ddot{x}\frac{\partial u}{\partial x} + \ddot{y}\frac{\partial u}{\partial y} + \dot{x}^2\frac{\partial^2 u}{\partial x^2} + 2\dot{x}\dot{y}\frac{\partial^2 u}{\partial x\partial y} + \dot{y}^2\frac{\partial^2 u}{\partial y^2} \tag{A6}$$

$$\ddot{v} = \ddot{x}\frac{\partial v}{\partial x} + \ddot{y}\frac{\partial v}{\partial y} + \dot{x}^2\frac{\partial^2 v}{\partial x^2} + 2\dot{x}\dot{y}\frac{\partial^2 v}{\partial x\partial y} + \dot{y}^2\frac{\partial^2 v}{\partial y^2}. \tag{A7}$$

The first-order approximations for small strains yield

$$(\dot{x}+\dot{u})(\ddot{y}+\ddot{v})-(\dot{y}+\dot{v})(\ddot{x}+\ddot{u}) = (\dot{x}\,\ddot{y}-\dot{y}\,\ddot{x})(1+\epsilon_{xx}+\epsilon_{yy}) + \dot{x}^3\left(2\frac{\partial \epsilon_{xy}}{\partial x} - \frac{\partial \epsilon_{xx}}{\partial y}\right)$$

Downloaded 03 May 2010 to 171.66.16.31. Redistribution subject to ASME license or copyright; see http://www.asme.org/terms/Terms_Use.cfm

$$+\dot{x}^2\dot{y}\left(2\frac{\partial\epsilon_{yy}}{\partial x}-\frac{\partial\epsilon_{xx}}{\partial x}\right)$$

$$+\dot{x}\dot{y}^2\left(\frac{\partial\epsilon_{yy}}{\partial y}-2\frac{\partial\epsilon_{xx}}{\partial y}\right)+\dot{y}^3\left(\frac{\partial\epsilon_{yy}}{\partial x}-2\frac{\partial\epsilon_{xy}}{\partial y}\right) \quad (A8)$$

$$(\dot{x}+\dot{y})^2+(\dot{y}+\dot{v})^2=\dot{x}^2+\dot{y}^2+2(\dot{x}^2\epsilon_{xx}+2\dot{x}\dot{y}\epsilon_{xy}+\dot{y}^2\epsilon_{yy}). \quad (A9)$$

Finally, using the first two terms in the expansion for $[\ ]^{-3/2}$ in (A3), the change in curvature $\Delta\kappa=K-\kappa$ is seen to be

$$\Delta\kappa=\kappa\{\epsilon_{xx}+\epsilon_{yy}-3R^{-2}(\dot{x}^2\epsilon_{xx}+2\dot{x}\dot{y}\epsilon_{xy}+\dot{y}^2\epsilon_{yy})\}$$
$$+R^{-3}\left\{\dot{x}^3\left(2\frac{\partial\epsilon_{xy}}{\partial x}-\frac{\partial\epsilon_{xx}}{\partial y}\right)+\dot{x}^2\dot{y}\left(2\frac{\partial\epsilon_{yy}}{\partial x}-\frac{\partial\epsilon_{xx}}{\partial x}\right)\right.$$
$$\left.+\dot{x}\dot{y}^2\left(\frac{\partial\epsilon_{yy}}{\partial y}-2\frac{\partial\epsilon_{xx}}{\partial y}\right)+\dot{y}^3\left(\frac{\partial\epsilon_{yy}}{\partial x}-2\frac{\partial\epsilon_{xy}}{\partial y}\right)\right\} \quad (A10)$$

where

$$R=(\dot{x}^2+\dot{y}^2)^{1/2}. \quad (A11)$$

At a point on the curve where the tangent is parallel to the x-axis, (A10) simplifies to

$$\Delta\kappa=2\frac{\partial\epsilon_{xy}}{\partial x}-\frac{\partial\epsilon_{xx}}{\partial y}+\kappa(\epsilon_{yy}-2\epsilon_{xx}). \quad (A12)$$

The expression (A10) for the change in curvature also simplifies when the natural coordinates n and s indicated in Fig. 3 are used. At this point it is possible to use the arc length s instead of t as the parameter, which makes $R=1$. Then using

$$\frac{\partial}{\partial x}=\dot{y}\frac{\partial}{\partial n}+\dot{x}\frac{\partial}{\partial s},\quad \frac{\partial}{\partial y}=-\dot{x}\frac{\partial}{\partial n}+\dot{y}\frac{\partial}{\partial s} \quad (A13a,b)$$

($\partial/\partial n$ is to be viewed as a directional derivative so that $\partial\dot{x}/\partial n=\partial\dot{y}/\partial n=0$) and transforming the strains in (A10) to their n and s components, the result is

$$\Delta\kappa=2\frac{\partial\epsilon_{ns}}{\partial s}-\frac{\partial\epsilon_{ss}}{\partial n}-\kappa\epsilon_{nn}. \quad (A14)$$

APPENDIX B

Bonded Rigid Inclusion

$$4\mu u_r^I(r,\theta;k)=Ta\left(\frac{r}{a}-\frac{a}{r}\right)\left\{\frac{1}{2}(k-1)+\left(1-\frac{1}{k}\frac{a^2}{r^2}\right)\cos 2\theta\right\} \quad (B1)$$

$$4\mu u_\theta^I(r,\theta;k)=-Ta\left(\frac{r}{a}-\frac{a}{r}\right)\left(1+\frac{1}{k}\frac{a^2}{r^2}\right)\sin 2\theta \quad (B2)$$

$$\sigma_{rr}^I(r,\theta;k)=\frac{1}{2}T\left\{1+\frac{1}{2}(k-1)\frac{a^2}{r^2}+\left[1+\frac{4}{k}\frac{a^2}{r^2}-\frac{3}{k}\frac{a^4}{r^4}\right]\cos 2\theta\right\} \quad (B3)$$

$$\sigma_{r\theta}^I(r,\theta;k)=\frac{1}{2}T\left[-1+\frac{2}{k}\frac{a^2}{r^2}-\frac{3}{k}\frac{a^4}{r^4}\right]\sin 2\theta \quad (B4)$$

$$\sigma_{\theta\theta}^I(r,\theta;k)=\frac{1}{2}T\left\{1-\frac{1}{2}(k-1)\frac{a^2}{r^2}-\left[1-\frac{3}{k}\frac{a^4}{r^4}\right]\cos 2\theta\right\} \quad (B5)$$

Cavity

$$4\mu u_r^C(r,\theta;k)=Ta\left\{\frac{1}{2}(k-1)\frac{r}{a}+\frac{a}{r}+\left[\frac{r}{a}+(k+1)\frac{a}{r}-\frac{a^3}{r^3}\right]\cos 2\theta\right\} \quad (B6)$$

$$4\mu u_\theta^C(r,\theta;k)=Ta\left[\frac{r}{a}+(k-1)\frac{a}{r}+\frac{a^3}{r^3}\right]\sin 2\theta \quad (B7)$$

$$\sigma_{rr}^C(r,\theta)=\frac{1}{2}T\left(1-\frac{a^2}{r^2}\right)\left\{1+\left[1-3\frac{a^2}{r^2}\right]\cos 2\theta\right\} \quad (B8)$$

$$\sigma_{r\theta}^C(r,\theta)=-\frac{1}{2}T\left(1-\frac{a^2}{r^2}\right)\left(1+3\frac{a^2}{r^2}\right)\sin 2\theta \quad (B9)$$

$$\sigma_{\theta\theta}^C(r,\theta)=\frac{1}{2}T\left\{1+\frac{a^2}{r^2}-\left[1+3\frac{a^4}{r^4}\right]\cos 2\theta\right\} \quad (B10)$$

Observations

$$u_r^I(a,\theta;k)=u_\theta^I(a,\theta;k)=0,\quad \forall\ k\neq 0 \quad (B11)$$

$$u_r^C(a,\theta;-1)=u_\theta^C(a,\theta;-1)=0 \quad (B12)$$

$$u_i^I(r,\theta;-1)=u_i^C(r,\theta;-1) \quad (B13)$$

$$\sigma_{rr}^I(a,\theta;-1)=\sigma_{r\theta}^I(a,\theta;-1)=0 \quad (B14)$$

$$\sigma_{ij}^I(r,\theta;-1)=\sigma_{ij}^C(r,\theta) \quad (B15)$$

It can be reasoned that the counterparts of these observations about the displacements are true in the general case, except at values of k for which the fields are singular.

Downloaded 03 May 2010 to 171.66.16.31. Redistribution subject to ASME license or copyright; see http://www.asme.org/terms/Terms_Use.cfm

An Inverse Transient Thermoelastic Problem for a Transversely-Isotropic Body

Naotake Noda
Professor,
Department of Mechanical Engineering,
Faculty of Engineering,
Shizuoka University,
Jyohuku 3, Hamamatsu,
Shizuoka 432, Japan

Fumihiro Ashida
Assistant Professor,
Department of Mechanical Engineering,
Tsuyama National College of Technology,
Tsuyama, Okayama 708, Japan

Tomoaki Tsuji
Associate Professor,
Department of Mechanical Engineering,
Shizuoka University,
Hamamatsu, Shizuoka, 432, Japan

The present paper discusses an analytical method for an inverse problem of three-dimensional transient thermoelasticity in a transversely-isotropic solid. The inverse thermoelastic problem consists of the determination of the condition of heating when the conditions of displacements and stresses are given at some points of the solid considered. Applying the Laplace and Fourier transforms as well as the new potential function method, the temperature, displacements, and stresses are represented by the potential functions alone, and they are determined from the prescribed conditions. The heating condition is obtained from the boundary condition for the temperature field. As a practical example of an inverse problem, the heating temperature of a transversely-isotropic infinite circular cylinder is determined in the case where the radial displacement is given at an arbitrary cylindrical section and the radial and shear stresses are free on the lateral surface of the cylinder. Numerical calculations are carried out to illustrate the heating temperature of the cylinder as well as the temperature and stresses on the lateral surface of the cylinder.

1 Introduction

In a great number of papers on thermoelasticity, an approach was taken to derive the temperature, displacement, and stress distributions in various types of solid due to heating. However, the thermoelastic problems called "inverse problems" have begun to atrract a great deal of attention in the recent literature. The inverse thermoelastic problem consists of the determination of either the temperature of the heating medium, the heat flux on the boundary surface, or the Biot's number of the solid when the conditions of the displacements and stresses are known at some points of the solid considered. This inverse problem is very important in view of its relevance to various industrial machines subjected to heating, such as the main shaft of lathe and turbine and the role of rolling mill. The inverse problems, however, have been treated only in a few papers. Cialkowski and Grysa (1980), Grysa, Cialkowski, and Kaminski (1981), Grysa and Kozlowski (1982), and Kozlowski and Grysa (1982) investigated one-dimensional transient thermoelastic problems, and derived the heating temperature and heat flux on the surface of an isotropic infinite slab.

The present paper concerns with an analytical method for the inverse problem of three-dimensional transient thermoelasticity in a transversely-isotropic solid. The first section discusses the general treatise on the inverse thermoelastic problem and describes a procedure for the determination of the condition of heating when the conditions of displacements and stresses are given at some points of the solid. Applying the Laplace and Fourier transforms as well as the new transversely isotropic potential function method, the temperature, displacements, and stresses are represented by the potential functions alone, and their distributions are determined from the prescribed conditions. (One among the heating temperature, the heat flux, and the Biot's number is prescribed as the boundary condition for the temperature.)

The second section illustrates a practical example, namely, the inverse problem of axisymmetric transient thermoelasticity in a transversely-isotropic circular cylinder. The heating temperature of the surrounding medium is determined in the case where the radial and shear stresses are free on the lateral surface of the cylinder and the radial displacement in the cylinder is given as the function of time and position variables. It is also assumed that the cylinder is initially in natural conditions.

For a numerical example, the time variation of the heating temperature of the surrounding medium, the temperature and stresses on the lateral surface of the cylinder are calculated for a graphite which possesses transverse isotropy. The results are compared with those derived under isotropic conditions. The effects of the Biot's number and the anisotropies of transversely-isotropic material constants on the heating temperature are also investigated.

2 General Treatise on Inverse Thermoelastic Problem in Transverse Isotropy

We consider an inverse problem for three-dimensional tran-

Contributed by the Applied Mechanics Division of THE AMERICAN SOCIETY OF MECHANICAL ENGINEERS for publication in the JOURNAL OF APPLIED MECHANICS.

Discussion on this paper should be addressed to the Editorial Department, ASME, United Engineering Center, 345 East 47th Street, New York, N.Y. 10017, and will be accepted until two months after final publication of the paper itself in the JOURNAL OF APPLIED MECHANICS. Manuscript received by the ASME Applied Mechanics Division, June 30, 1988; final revision, December 15, 1988.

Copyright © 1989 by ASME

Downloaded 03 May 2010 to 171.66.16.31. Redistribution subject to ASME license or copyright; see http://www.asme.org/terms/Terms_Use.cfm

sient thermoelasticity in a transversely-isotropic solid. The heating condition of the solid is determined according to the prescribed conditions of displacements and stresses. It is assumed that the solid is initially in natural conditions. In order to analyze this inverse problem, we improve the modified transversely-isotropic potential function method proposed by Takeuti and Noda (1978).

In the cylindrical coordinate system (r, θ, z) the stress-strain relations (Nowinski, 1978) are

$$\left.\begin{aligned} &\sigma_{rr}=c_{11}\epsilon_{rr}+c_{12}\epsilon_{\theta\theta}+c_{13}\epsilon_{zz}-\bar{\beta}_1 T, \qquad \sigma_{r\theta}=\frac{c_{11}-c_{12}}{2}\epsilon_{r\theta},\\ &\sigma_{\theta\theta}=c_{12}\epsilon_{rr}+c_{11}\epsilon_{\theta\theta}+c_{13}\epsilon_{zz}-\bar{\beta}_1 T, \qquad \sigma_{\theta z}=c_{44}\epsilon_{\theta z},\\ &\sigma_{zz}=c_{13}\epsilon_{rr}+c_{13}\epsilon_{\theta\theta}+c_{33}\epsilon_{zz}-\bar{\beta}_3 T, \qquad \sigma_{zr}=c_{44}\epsilon_{zr} \end{aligned}\right\} \tag{1}$$

where σ_{ij} are the stress components and ϵ_{ij} are the strain components, T is the temperature change, and c_{ij} and $\bar{\beta}_i$ are the material constants.

The governing equations for the temperature and displacement fields consist of the two partial differential equations (Nowinski, 1978), which are the heat conduction equation

$$\Delta_1 T+\lambda^2 T_{,zz}=\frac{1}{\kappa_r}T_{,t} \tag{2}$$

and the equilibrium equations.

$$\left.\begin{aligned} &c_{11}\left(u_{r,rr}+\frac{1}{r}u_{r,r}-\frac{1}{r^2}u_r\right)+\frac{c_{11}-c_{12}}{2r^2}u_{r,\theta\theta}+c_{44}u_{r,zz}\\ &\quad+\frac{c_{11}+c_{12}}{2r}u_{\theta,r\theta}-\frac{3c_{11}-c_{12}}{2r^2}u_{\theta,\theta}\\ &\quad+(c_{13}+c_{44})u_{z,rz}-\bar{\beta}_1 T_{,r}=0,\\ &\frac{c_{11}-c_{12}}{2}\left(u_{\theta,rr}+\frac{1}{r}u_{\theta,r}-\frac{1}{r^2}u_\theta\right)+\frac{c_{11}}{r^2}u_{\theta,\theta\theta}+c_{44}u_{\theta,zz}\\ &\quad+\frac{c_{11}+c_{12}}{2r}u_{r,r\theta}+\frac{3c_{11}-c_{12}}{2r^2}u_{r,\theta}\\ &\quad+\frac{c_{13}+c_{44}}{r}u_{z,z\theta}-\frac{\bar{\beta}_1}{r}T_{,\theta}=0,\\ &c_{44}\left(u_{z,rr}+\frac{1}{r}u_{z,r}+\frac{1}{r^2}u_{z,\theta\theta}\right)+c_{33}u_{z,zz}\\ &\quad+(c_{13}+c_{44})\left(u_{r,rz}+\frac{1}{r}u_{r,z}+\frac{1}{r}u_{\theta,\theta z}\right)-\bar{\beta}_3 T_{,z}=0 \end{aligned}\right\} \tag{3}$$

where $\Delta_1 T=T_{,rr}+r^{-1}T_{,r}+r^{-2}T_{,\theta\theta}$, $T_{,r}=\partial T/\partial r$, $\lambda^2=\lambda_z/\lambda_r$ is the ratio of the coefficient of thermal conductivity in the axial and radial direction, κ_r is the thermal diffusivity, t is the time variable, and u_i are the displacement components.

To solve the partial differential equations (2) and (3), we introduce the potential functions which relate to the displacements as follows (Takeuti and Noda, 1978):

$$\left.\begin{aligned} &u_r=\Omega_{,r}+k_1\phi_{,r}+\frac{1}{r}\psi_{,\theta},\\ &u_\theta=\frac{1}{r}\Omega_{,\theta}+k_1\frac{1}{r}\phi_{,\theta}-\psi_{,r},\\ &u_z=-\Omega_{,z}+k_2\phi_{,z} \end{aligned}\right\} \tag{4}$$

and the Laplace and Fourier transforms defined as follows:

$$\left.\begin{aligned} &\hat{u}_r=\int_0^\infty u_r\cdot\exp(-st)dt,\\ &u_r^*=\int_{-\infty}^\infty u_r\cdot\exp(-ipz)dz \end{aligned}\right\} \tag{5}$$

where s and p are the Laplace and Fourier parameters, and $i^2=-1$. Applying the foregoing transforms to equations (2) to (4), and substituting equations (4) into equations (3), the potential functions $\hat{\Omega}^*$, $\hat{\phi}^*$, and $\hat{\psi}^*$ must satisfy the following differential equations:

$$\left.\begin{aligned} &\Delta_1\hat{\Omega}^*-\nu_1 p^2\hat{\Omega}^*=\eta_1\hat{T}^*,\\ &\Delta_1\hat{\phi}^*-\nu_2 p^2\hat{\phi}^*=-\mu p^2\hat{\Omega}^*+\eta_1\xi\hat{T}^*,\\ &\Delta_1\hat{\psi}^*-\nu_3 p^2\hat{\psi}^*=0 \end{aligned}\right\} \tag{6}$$

where

$$\left.\begin{aligned} &\eta_1=\frac{\bar{\beta}_1}{c_{11}}-\frac{(c_{13}+c_{44})(c_{11}\bar{\beta}_3-c_{13}\bar{\beta}_1)}{c_{11}c_{44}(c_{11}\nu_2+c_{13})}, \quad \nu_3=\frac{2c_{44}}{c_{11}-c_{12}},\\ &\xi=\frac{c_{11}\bar{\beta}_3-c_{13}\bar{\beta}_1}{\eta_1 c_{11}c_{44}}, \quad \mu=\frac{c_{11}c_{33}-c_{13}^2}{c_{11}c_{44}} \end{aligned}\right\} \tag{7}$$

and where $\nu_i\,(i=1, 2)$ and k_i $(i=1, 2)$ are the roots of the following equations:

$$\left.\begin{aligned} &c_{11}c_{44}\nu^2+(2c_{13}c_{44}+c_{13}^2-c_{11}c_{33})\nu+c_{33}c_{44}=0,\\ &(c_{11}c_{33}-c_{13}^2)k^2-(c_{11}c_{33}-c_{13}^2)k+c_{44}(c_{13}+c_{44})=0 \end{aligned}\right\}. \tag{8}$$

To analyze the inverse thermoelastic problem, we may divide the potential functions $\hat{\Omega}^*$ and $\hat{\phi}^*$ as follows:

$$\left.\begin{aligned} &\hat{\Omega}^*=\hat{\omega}^*+\hat{\phi}_1^*,\\ &\hat{\phi}^*=\hat{\chi}^*+\hat{\phi}_2^* \end{aligned}\right\}. \tag{9}$$

Rearranging this potential function method by use of equations (2) and (9), we can find the following relations:

$$\hat{T}^*=\frac{1}{\eta_1}\{\Delta_1\hat{\omega}^*-\nu_1 p^2\hat{\omega}^*\} \tag{10}$$

$$\left.\begin{aligned} &\hat{u}_r^*=\{\hat{\omega}^*+j_1\hat{\phi}_1^*+k_1(\hat{\chi}^*+\hat{\phi}_2^*)\}_{,r}+\frac{1}{r}\hat{\psi}^*_{,\theta},\\ &\hat{u}_\theta^*=\frac{1}{r}\{\hat{\omega}^*+j_1\hat{\phi}_1^*+k_1(\hat{\chi}^*+\hat{\phi}_2^*)\}_{,\theta}-\hat{\psi}^*_{,r},\\ &\hat{u}_z^*=-ip\{\hat{\omega}^*+j_2\hat{\phi}^*{}_1-k_2(\hat{\chi}^*+\hat{\phi}_2^*)\} \end{aligned}\right\} \tag{11}$$

where

$$j_0=\frac{\mu}{\nu_1-\nu_2}, \quad j_1=1+k_1 j_0, \quad j_2=1-k_2 j_0. \tag{12}$$

The fundamental equations for the potential functions $\hat{\omega}^*$, $\hat{\chi}^*$, $\hat{\phi}_1^*$, $\hat{\phi}_2^*$ and $\hat{\psi}^*$ are given by

$$\left.\begin{aligned} &\Delta_1\hat{\omega}^*-q^2\hat{\omega}^*=0,\\ &\Delta_1\hat{\chi}^*-\nu_2 p^2\hat{\chi}^*=(\xi q^2-\eta_2 p^2)\hat{\omega}^*,\\ &\Delta_1\hat{\phi}_1^*-\nu_1 p^2\hat{\phi}_1^*=0,\\ &\Delta_1\hat{\phi}_2^*-\nu_2 p^2\hat{\phi}_2^*=0,\\ &\Delta_1\hat{\psi}^*-\nu_3 p^2\hat{\psi}^*=0 \end{aligned}\right\} \tag{13}$$

Downloaded 03 May 2010 to 171.66.16.31. Redistribution subject to ASME license or copyright; see http://www.asme.org/terms/Terms_Use.cfm

where $q^2=\lambda^2 p^2+\frac{s}{\kappa_r}$, $\eta_2=\mu+\xi\,\nu_1$. (14)

The general solutions for the potential functions $\hat{\omega}^*$, $\hat{\phi}_1^*$, $\hat{\phi}_2^*$ and $\hat{\psi}^*$ may be given by the following expressions:

$$(\hat{\omega}^*,\ \hat{\phi}_1^*,\ \hat{\phi}_2^*,\ \hat{\psi}^*)=\begin{pmatrix}\cos(m\theta)\\ \sin(m\theta)\end{pmatrix}\begin{pmatrix}J_m(\upsilon_1 r)\\ Y_m(\upsilon_1 r)\end{pmatrix},\ \begin{pmatrix}\cos(m\theta)\\ \sin(m\theta)\end{pmatrix}\begin{pmatrix}I_m(\upsilon_2 r)\\ K_m(\upsilon_2 r)\end{pmatrix} \tag{15}$$

where $J_m(r)$, $Y_m(r)$, $I_m(r)$, and $K_m(r)$ are the Bessel functions of order m, and the coefficients υ_i are determined from the fundamental equations (13). It is clear from the second of equations (13) that the potential function $\hat{\chi}^*$ is the particular solutoin for $\hat{\omega}^*$. Therefore, $\hat{\chi}^*$ may be expressed by the same form as $\hat{\omega}^*$ given by equation (15).

Applying the Laplace and Fourier transforms to equations (1) and substituting equations (10) and (11) into those equations, the thermal stress components are represented by the only potential functions as follows:

$$\begin{aligned}
\hat{\sigma}_{rr}^* =& -(c_{11}-c_{12})\Big[\frac{1}{r}\Big\{(\hat{\omega}^*+k_1\hat{\chi}^*)_{,r}\\
&+\frac{1}{r}(\hat{\omega}^*+k_1\hat{\chi}^*)_{,\theta\theta}\Big\}-\frac{c_{44}}{c_{11}-c_{12}}p^2\hat{\chi}^*\\
&+\frac{j_1}{r}\Big\{\hat{\phi}_{1,r}^*+\frac{1}{r}\hat{\phi}_{1,\theta\theta}^*\Big\}-\frac{j_0 c_{44}}{c_{11}-c_{12}}p^2\hat{\phi}_1^*\\
&+\frac{k_1}{r}\Big\{\hat{\phi}_{2,r}^*+\frac{1}{r}\hat{\phi}_{2,\theta\theta}^*\Big\}-\frac{c_{44}}{c_{11}-c_{12}}p^2\hat{\phi}_2^*\\
&-\Big(\frac{1}{r}\hat{\psi}^*{}_{,\theta}\Big)_{,r}\Big],\\
\hat{\sigma}_{\theta\theta}^* =& (c_{11}-c_{12})\Big[\frac{1}{r}\Big\{(\hat{\omega}^*+k_1\hat{\chi}^*)_{,r}+\frac{1}{r}(\hat{\omega}^*+k_1\hat{\chi}^*)_{,\theta\theta}\Big\}\\
&+\frac{c_{13}\bar{\beta}_3-c_{33}\bar{\beta}_1}{\eta_1\mu c_{11}c_{44}}(q^2-\nu_1 p^2)\hat{\omega}^*\\
&-\frac{1}{\mu c_{11}}\Big\{c_{13}\Delta_1\hat{\chi}^*+\frac{c_{13}{}^2-c_{12}c_{33}}{c_{11}-c_{12}}p^2\hat{\chi}^*\Big\}\\
&+\frac{j_1}{r}\Big\{\hat{\phi}_{1,r}^*+\frac{1}{r}\hat{\phi}_{1,\theta\theta}^*\Big\}\\
&-\frac{j_0}{\mu c_{11}}\Big\{c_{13}\Delta_1\hat{\phi}_1^*+\frac{c_{13}{}^2-c_{12}c_{33}}{c_{11}-c_{12}}p^2\hat{\phi}_1^*\Big)\Big\}\\
&+\frac{k_1}{r}\Big\{\hat{\phi}_{2,r}^*+\frac{1}{r}\hat{\phi}_{2,\theta\theta}^*\Big\}\\
&-\frac{1}{\mu c_{11}}\Big\{c_{13}\Delta_1\hat{\phi}_2^*+\frac{c_{13}{}^2-c_{12}c_{33}}{c_{11}-c_{12}}p^2\hat{\phi}_2^*\Big)\Big\}\\
&-\Big(\frac{1}{r}\hat{\psi}^*{}_{,\theta}\Big)_{,r}\Big],\\
\hat{\sigma}_{zz}^* =& -c_{44}[\Delta_1\hat{\chi}^*+j_0\Delta_1\hat{\phi}_1^*+\Delta_1\hat{\phi}_2^*],\\
\hat{\sigma}_{r\theta}^* =& (c_{11}-c_{12})\Big[\Big\{\frac{1}{r}(\hat{\omega}^*+k_1\hat{\chi}^*)_{,\theta}\Big\}_{,r}\\
&+j_1\Big(\frac{1}{r}\hat{\phi}_{1,\theta}^*\Big)_{,r}+k_1\Big(\frac{1}{r}\hat{\phi}_{2,\theta}^*\Big)_{,r}\\
&-\frac{1}{2}\Big\{\hat{\psi}^*{}_{,rr}-\frac{1}{r}\hat{\psi}^*{}_{,r}-\frac{1}{r^2}\hat{\psi}^*{}_{,\theta\theta}\Big\}\Big],\\
\hat{\sigma}_{\theta z}^* =& c_{44}ip\Big[\frac{1}{r}\chi^*{}_{,\theta}+j_0\hat{\phi}_{1,\theta}^*+\hat{\phi}_{2,\theta}^*-\hat{\psi}^*{}_{,r}\Big],\\
\hat{\sigma}_{zr}^* =& c_{44}ip\Big[\hat{\chi}^*{}_{,r}+j_0\hat{\phi}_{1,r}^*+\hat{\phi}_{2,r}^*+\frac{1}{r}\hat{\psi}^*{}_{,\theta}\Big]
\end{aligned} \tag{16}$$

The unknowns, which may be included in the potential functions $\hat{\omega}^*$, $\hat{\chi}^*$, $\hat{\phi}_1^*$, $\hat{\phi}_2^*$, and $\hat{\psi}^*$, can be determined according to the boundary conditions. Subsequently, the temperature, displacements, and stresses are obtained.

Our task in the inverse thermoelastic problem is to determine the heating condition which can be expressed in terms of either the heat flux from the boundary surface Q, the heating temperature of the surrounding medium Θ or the coefficient of relative heat transfer on the boundary surface h_n. For that, we consider the following boundary condition for the temperature field:

$$-T_{,n}+\frac{Q}{\lambda_n}=h_n(T-\Theta)\quad\text{on the boundary surface} \tag{17}$$

where n denotes the normal direction on the boundary surface. Applying the Laplace and Fourier transforms to equation (17), the heating condition can be determined from the temperature T.

Taking the inverse Fourier and Laplace transforms, the heating condition of the solid, and the temperature, displacements and stresses in the solid can be obtained.

3 Inverse Thermoelastic Problem in a Transversely Isotropic, Infinite Circular Cylinder

As an application of our method described in the preceding section, we consider an inverse problem of axisymmetric three-dimensional transient thermoelasticity in a transversely-isotropic infinite circular cylinder of radius a. The heating temperature of the surrounding medium is determined for the case where the radial displacement is given at arbitrary radius b in the cylinder as follows:

$$u_r=u_0 f(z)g(t)\quad\text{at}\quad r=b\ \ (0<b\leqq a) \tag{18}$$

where u_0 is the constant displacement. It is assumed that $f(z)$ is symmetric with respect to z. The traction-free boundary conditions are given by

$$\sigma_{rr}=\sigma_{zr}=0\quad\text{on}\quad r=a. \tag{19}$$

In this case, the Fourier transform defined by the second of equations (5) reduces to

$$u_r^*=\int_0^\infty u_r\cdot\cos(pz)\,dz. \tag{20}$$

Let us assume the following admissible solutions for the potential functions $\hat{\omega}^*$, $\hat{\chi}^*$, $\hat{\phi}_1^*$, and $\hat{\phi}_2^*$:

$$\hat{\omega}^*=\frac{1}{p^2}\hat{D}^* I_0(qr) \tag{21}$$

$$\hat{\chi}^*=\frac{1}{p^2}\hat{F}^* I_0(qr) \tag{22}$$

$$\hat{\phi}_i^*=\frac{1}{p^2}\hat{A}_i^* I_0(\sqrt{\nu_i}pr),\quad (i=1,\ 2) \tag{23}$$

where $\hat{D}^*$, $\hat{F}^*$, $\hat{A}_1^*$, and $\hat{A}_2^*$ are the unknowns. The potential function $\hat{\psi}^*$, which is the component of rotation, may not be required in the axisymmetric problem. Substitution of equations (21) and (22) into the second of equations (13) yields

$$\hat{F}^*=\frac{\xi\,q^2-\eta_2 p^2}{q^2-\nu_2 p^2}\hat{D}^*. \tag{24}$$

Substituting equations (21) to (23) into equations (11) and (16), the radial displacement and the radial and shear stresses are expressed as follows:

Downloaded 03 May 2010 to 171.66.16.31. Redistribution subject to ASME license or copyright; see http://www.asme.org/terms/Terms_Use.cfm

$$\hat{u}_r^* = \frac{1}{p}\left[(\hat{D}^* + k_1\hat{F}^*)\frac{qI_1(qr)}{p} + j_1\hat{A}_1^*\sqrt{\nu_1}I_1(\sqrt{\nu_1}pr) + k_1\hat{A}_2^*\sqrt{\nu_2}I_1(\sqrt{\nu_2}pr)\right] \tag{25}$$

$$\begin{aligned}\hat{\sigma}_{rr}^* = & -(c_{11}-c_{12})\left[\hat{D}^*\frac{qI_1(qr)}{p^2r}\right. \\ & + \hat{F}^*\left\{\frac{k_1qI_1(qr)}{p^2r} - \delta_4 I_0(qr)\right\} \\ & - \hat{A}_1^*\left\{j_0\delta_3 I_0(\sqrt{\nu_1}pr) - \frac{j_1\sqrt{\nu_1}I_1(\sqrt{\nu_1}pr)}{pr}\right\} \\ & \left. - \hat{A}_2^*\left\{\delta_3 I_0(\sqrt{\nu_2}pr) - \frac{k_1\sqrt{\nu_2}I_1(\sqrt{\nu_2}pr)}{pr}\right\}\right]\end{aligned} \tag{26}$$

$$\hat{\sigma}_{rz}^* = -c_{44}\left[\hat{F}^*\frac{qI_1(qr)}{p} + j_0\hat{A}_1^*\sqrt{\nu_1}I_1(\sqrt{\nu_1}pr) + \hat{A}_2^*\sqrt{\nu_2}I_1(\sqrt{\nu_2}pr)\right]. \tag{27}$$

Applying the Laplace and Fourier transforms to equations (18) and (19) and substituting equations (25) to (27) into those equations, the unknowns are determined as follows:

$$\left.\begin{aligned}&\hat{D}^* = u_0(q^2-\nu_2p^2)pf^*(p)\hat{g}(s) \\ &\Big/\left[(\delta_1q^2-\delta_2p^2)\frac{qI_1(qb)}{p} - \delta_3\Omega_5(\xi\, q^2-\eta_2p^2)I_0(qa)\right. \\ &\left. + \{\Omega_5(\delta_1q^2-\delta_2p^2) - \Omega_6(\xi\, q^2-\eta_2p^2)\}\frac{qI_1(qa)}{p}\right], \\ &\hat{A}_1^* = \frac{1}{(q^2-\nu_2p^2)}\left[\delta_3\Omega_2pa(\xi\, q^2-\eta_2p^2)I_0(qa)\right. \\ &\left. - \left\{\frac{\Omega_2(\delta_1q^2-\delta_2p^2)}{pa} - \Omega_4(\xi\, q^2-\eta_2p^2)\right\}\frac{qI_1(qa)}{p}\right]\hat{D}^*, \\ &\hat{A}_2^* = \frac{1}{(q^2-\nu_2p^2)}\left[\delta_3\Omega_1pa(\xi\, q^2-\eta_2p^2)I_0(qa)\right. \\ &\left. - \left\{\frac{\Omega_1(\delta_1q^2-\delta_2p^2)}{pa} - \Omega_3(\xi\, q^2-\eta_2p^2)\right\}\frac{qI_1(qa)}{p}\right]\hat{D}^*\end{aligned}\right\} \tag{28}$$

where

$$\left.\begin{aligned}&\Lambda_1 = j_0\sqrt{\nu_1}I_1(\sqrt{\nu_1}pa), \quad \Lambda_2 = \sqrt{\nu_2}I_0(\sqrt{\nu_2}pa), \\ &\Lambda_3 = \frac{j_1\sqrt{\nu_1}I_1(\sqrt{\nu_1}pa)}{pa} - j_0\delta_3 I_0(\sqrt{\nu_1}pa), \\ &\Lambda_4 = \frac{k_1\sqrt{\nu_2}I_1(\sqrt{\nu_2}pa)}{pa} - \delta_3 I_0(\sqrt{\nu_2}pa), \\ &\Lambda_5 = j_1\sqrt{\nu_1}I_1(\sqrt{\nu_1}pb), \quad \Lambda_6 = k_1\sqrt{\nu_2}I_1(\sqrt{\nu_2}pb), \\ &\{\Omega_1,\Omega_2,\Omega_3,\Omega_4\} = \frac{\{\Lambda_1,\Lambda_2,\Lambda_3,\Lambda_4\}}{\Lambda_2\Lambda_3-\Lambda_1\Lambda_4}, \\ &\{\Omega_5,\Omega_6\} = \frac{\{(\Lambda_1\Lambda_6-\Lambda_2\Lambda_5),(\Lambda_3\Lambda_6-\Lambda_4\Lambda_5)\}}{\Lambda_2\Lambda_3-\Lambda_1\Lambda_4}\end{aligned}\right\} \tag{29}$$

$$\delta_1 = k_1\xi + 1, \quad \delta_2 = k_1\eta_2 + \nu_2, \quad \delta_3 = \frac{c_{44}}{c_{11}-c_{12}}. \tag{30}$$

Substituting equation (21) into equation (10), we find the temperature as follows:

$$\hat{T}^* = \frac{q^2-\nu_1p^2}{\eta_1p^2}\hat{D}^*I_0(qr). \tag{31}$$

We assume that the heat flux does not act on the cylinder and the Biot's number is known, so the boundary condition for the temperature field given by equation (17) reduces to

$$T_{,r} + h_r(T-\Theta) = 0 \quad \text{on} \quad r=a. \tag{32}$$

Application of the Laplace and Fourier transforms to equation (32) yields

$$\hat{T}^*_{,r} + h_r(\hat{T}^* - \hat{\Theta}^*) = 0 \quad \text{on} \quad r=a. \tag{33}$$

Substituting equation (31) into equation (33), $\hat{\Theta}^*$ is determined as follows:

$$\hat{\Theta}^* = \frac{q^2-\nu_1p^2}{\eta_1p^2}\hat{D}^*\left\{I_0(qr) + \frac{qI_1(qr)}{h_r}\right\}. \tag{34}$$

From the foregoing, the unknowns are determined completely, and the heating temperature $\hat{\Theta}^*$ can be obtained.

For example, we assume the function of heating temperature, with respect to a time variable, as follows:

$$g(t) = 1 - \exp\left(-\frac{\gamma\kappa_r t}{a^2}\right) \tag{35}$$

where, γ is the known constant. Application of the Laplace transform to equation (35) yields

$$\hat{g}(s) = \frac{\gamma\kappa_r/a^2}{s(s+\gamma\kappa_r/a^2)}. \tag{36}$$

Moreover, taking the inverse Fourier and Laplace transforms, the heating temperature of the surrounding medium, as well as the temperature, radial displacement and hoop stress in the cylinder are expressed by

$$\begin{aligned}\Theta = \frac{u_0}{\eta_1}\int_0^\infty \frac{f^*(p)}{p}\Big[&(\lambda^2-\nu_1)(\lambda^2-\nu_2)p^4\Psi_{00} \\ &\times\left\{I_0(\lambda pr) + \frac{\lambda pI_1(\lambda pr)}{h_r}\right\} \\ &+ (\tau_1{}^2-\nu_1p^2)(\tau_1{}^2-\nu_2p^2)\left(\Psi_{01}\left\{I_0(\tau_1r) + \frac{\tau_1I_1(\tau_1r)}{h_r}\right\}\right. \\ &\left. + \Psi_{02}\left\{J_0(\tau_2r) - \frac{\tau_2J_1(\tau_2r)}{h_r}\right\}\right) \\ &+ \sum_{m=1}^{\infty}\Psi_m(\lambda^2\beta_m{}^2+\nu_1p^2)(\beta_m{}^2+\nu_2p^2) \\ &\times\left\{J_0(\lambda\beta_mr) - \frac{\lambda\beta_mJ_1(\lambda\beta_mr)}{h_r}\right\}\Big]\cos(pz)\,dp\end{aligned} \tag{37}$$

Downloaded 03 May 2010 to 171.66.16.31. Redistribution subject to ASME license or copyright; see http://www.asme.org/terms/Terms_Use.cfm

$$T = \frac{u_0}{\eta_1}\int_0^\infty \frac{f^*(p)}{p}\Big[(\lambda^2-\nu_1)(\lambda^2-\nu_2)p^4\Psi_{00}I_0(\lambda pr)$$
$$-(\tau_1{}^2-\nu_1p^2)(\tau_1{}^2-\nu_2p^2)\{\Psi_{01}I_0(\tau_1 r)+\Psi_{02}J_0(\tau_2 r)\}$$
$$+\sum_{m=1}^{\infty}\Psi_m(\lambda^2\beta_m{}^2+\nu_1p^2)(\lambda^2\beta_m{}^2+\nu_2p^2)J_0(\lambda\beta_m r)\Big]$$
$$\times\cos(pz)\,dp \tag{38}$$

$$u_r = u_0\int_0^\infty \frac{f^*(p)}{p}\Big[(\delta_1\lambda^2-\delta_2)\lambda p^3\Psi_{00}I_1(\lambda pr)$$
$$+\Psi_{01}(\delta_1\tau_1{}^2-\delta_2p^2)\tau_1I_1(\tau_1 r)+\Psi_{02}(\delta_1\tau_2{}^2+\delta_2p^2)\tau_2J_1(\tau_2 r)$$
$$+\sum_{m=1}^{\infty}\Psi_m(\delta_1\lambda^2\beta_m{}^2+\delta_2p^2)\lambda\beta_mJ_1(\lambda\beta_m r)$$
$$+j_1\bar{A}_1\sqrt{\nu_1}I_1(\sqrt{\nu_1}pr)+k_1\bar{A}_2\sqrt{\nu_2}I_1(\sqrt{\nu_2}pr)\Big]\cos(pz)\,dp \tag{39}$$

$$\sigma_{\theta\theta} = u_0(c_{11}-c_{12})\int_0^\infty \frac{f^*(p)}{p}\Big[p^4\Psi_{00}\Big(\{\delta_6(\lambda^2-\nu_1)(\lambda^2-\nu_2)$$
$$-(\xi\lambda^2-\eta_2)(\delta_4\lambda^2+\delta_5)\}I_0(\lambda pr)$$
$$+\{\lambda^2-\nu_2+k_1(\xi\lambda^2-\eta_2)\}\frac{\lambda I_1(\lambda pr)}{pr}\Big)$$
$$-\Psi_{01}\Big(\{(\xi\tau_1{}^2-\eta_2p^2)(\delta_4\tau_1{}^2+\delta_5p^2)$$
$$-\delta_6(\tau_1{}^2-\nu_1p^2)(\tau_1{}^2-\nu_2p^2)\}I_0(\tau_1 r)$$
$$-\{\tau_1{}^2-\nu_2p^2+k_1(\xi\tau_1{}^2-\eta_2p^2)\}\frac{\tau_1I_1(\tau_1 r)}{r}\Big)$$
$$-\Psi_{02}\Big(\{(\xi\tau_2{}^2+\eta_2p^2)(\delta_4\tau_2{}^2-\delta_5p^2)$$
$$-\delta_6(\tau_2{}^2+\nu_1p^2)(\tau_2{}^2+\nu_2p^2)\}J_0(\tau_2 r)$$
$$-\{\tau_2{}^2+\nu_2p^2+k_1(\xi\tau_2{}^2+\eta_2p^2)\}\frac{\tau_2J_1(\tau_2 r)}{r}\Big)$$
$$-\sum_{m=1}^{\infty}\Psi_m\Big(\{(\xi\lambda^2\beta_m{}^2+\eta_2p^2)(\delta_4\lambda^2\beta_m{}^2-\delta_5p^2)$$
$$+\delta_6(\lambda^2\beta_m{}^2+\nu_1p^2)(\lambda^2\beta_m{}^2+\nu_2p^2)\}J_0(\lambda\beta_m r)$$
$$-\{\lambda^2\beta_m{}^2+\nu_2p^2+k_1(\xi\lambda^2\beta_m{}^2+\eta_2p^2)\}\frac{\lambda\beta_mJ_1(\lambda\beta_m r)}{r}\Big)$$
$$-\bar{A}_1p\Big(j_0(\delta_4\nu_1+\delta_5)I_0(\sqrt{\nu_1}pr)-\frac{j_1\sqrt{\nu_1}I_1(\sqrt{\nu_1}pr)}{pr}\Big)$$
$$-\bar{A}_2p\Big((\delta_4\nu_2+\delta_5)prI_0(\sqrt{\nu_2}pr)-\frac{\sqrt{\nu_2}I_1(\sqrt{\nu_2}pr)}{pr}\Big)\Big]$$
$$\times\cos(pz)\,dp \tag{40}$$

where

$$f^*(p) = \frac{1}{2\pi}\int_0^\infty f(z)\cos(pz)\,dz \tag{41}$$

$$\delta_4 = \frac{c_{13}}{\mu c_{11}},\quad \delta_5 = \frac{c_{13}{}^2-c_{12}c_{33}}{\mu c_{11}(c_{11}-c_{12})},\quad \delta_6 = \frac{c_{13}\bar{\beta}_3-c_{33}\bar{\beta}_1}{\mu\eta_1c_{11}c_{44}} \tag{42}$$

$$\tau_1 = p^2\lambda^2-\frac{\gamma}{a^2},\quad \tau_2 = \frac{\gamma}{a^2}-p^2\lambda^2 \tag{43}$$

$$\Psi_{00} = 1/[p^2\{(\delta_1\lambda^2-\delta_2)\lambda I_1(\lambda pb)-\delta_3\Omega_5(\xi\lambda^2-\eta_2)I_0(\lambda pa)$$
$$+\{(\delta_1\Omega_5-\xi\Omega_6)\lambda^2-(\delta_2\Omega_5-\eta_2\Omega_6)\}\lambda I_1(\lambda pa)\}],$$
$$\Psi_{01} = -H(\tau_1{}^2)\exp\Big(-\frac{\gamma\kappa_r t}{a^2}\Big)\Big/\Big[(\delta_1\tau_1{}^2-\delta_2p^2)\frac{\tau_1I_1(\tau_1 b)}{p}$$
$$-\delta_3\Omega_5(\xi\tau_1{}^2-\eta_2p^2)I_0(\tau_1 a)$$
$$+\{(\delta_1\Omega_5-\xi\Omega_6)\tau_1{}^2-(\delta_2\Omega_5-\eta_2\Omega_6)p^2\}\frac{\tau_1I_1(\tau_1 a)}{p}\Big],$$
$$\Psi_{02} = -H(\tau_2{}^2)\exp\Big(-\frac{\gamma\kappa_r t}{a^2}\Big)\Big/\Big[(\delta_1\tau_2{}^2+\delta_2p^2)\frac{\tau_2J_1(\tau_2 b)}{p}$$
$$+\delta_3\Omega_5(\xi\tau_2{}^2+\eta_2p^2)J_0(\tau_2 a)$$
$$+\{(\delta_1\Omega_5-\xi\Omega_6)\tau_2{}^2+(\delta_2\Omega_5-\eta_2\Omega_6)p^2\}\frac{\tau_2J_1(\tau_2 a)}{p}\Big],$$
$$\Psi_m = \frac{2\gamma}{a^2}\exp\{-\kappa_r\lambda^2(\beta_m{}^2+p^2)t\}$$
$$\Big/\Big[\lambda^2a(\beta_m{}^2+p^2)\Big(\lambda^2\beta_m{}^2+\lambda^2p^2-\frac{\gamma}{a^2}\Big)$$
$$\times\Big((\delta_1\lambda^2\beta_m{}^2+\delta_2p^2)\frac{J_0(\lambda\beta_m b)}{p}+\frac{2\delta_1\lambda\beta_mJ_1(\lambda\beta_m b)}{pa}$$
$$+\Big\{(\delta_1\Omega_5-\xi\Omega_6)\lambda^2\beta_m{}^2+(\delta_2\Omega_5-\eta_2\Omega_6)p^2$$
$$+2\xi\delta_3\Omega_5\frac{p}{a}\Big\}\frac{J_0(\lambda\beta_m a)}{p}$$
$$-\Big\{2(\delta_1\Omega_5-\xi\Omega_6)\frac{\beta_m{}^2\lambda^2}{pa}$$
$$+\delta_3\Omega_5(\xi\beta_m{}^2\lambda^2+\eta_2p^2)\Big\}J_1(\lambda\beta_m a)\Big)\Big] \tag{44}$$

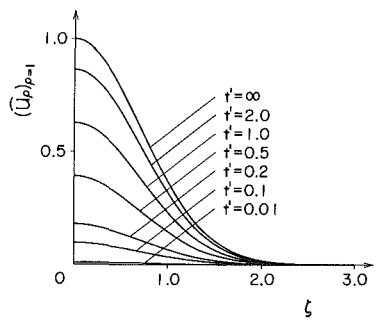


Fig. 1 Time variations of prescribed radial displacement on the lateral surface of cylinder

Downloaded 03 May 2010 to 171.66.16.31. Redistribution subject to ASME license or copyright; see http://www.asme.org/terms/Terms_Use.cfm

$$A_1 = u_0 f^*(p)\bar{A}_1,$$

$$\bar{A}_1 = \Psi_{00} p^3 \Big(\delta_3\Omega_2(\xi\lambda^2-\eta_2)I_0(\lambda pa) - \Big\{\frac{\Omega_2(\delta_1\lambda^2-\delta_2)}{pa} - \Omega_4(\xi\lambda^2-\eta_2)\Big\}\lambda I_1(\lambda pa)\Big)$$
$$+\Psi_{01}\Big(\delta_3\Omega_2(\xi\tau_1^2-\eta_2p^2)pI_0(\tau_1 a) - \Big\{\frac{\Omega_2}{pa}(\delta_1\tau_1^2-\delta_2p^2) - \Omega_4(\xi\tau_1^2-\eta_2p^2)\Big\}\tau_1 I_1(\tau_1 a)\Big)$$
$$-\Psi_{02}\Big(\delta_3\Omega_2(\xi\tau_2^2+\eta_2p^2)pJ_0(\tau_2 a) + \Big\{\frac{\Omega_2}{pa}(\delta_1\tau_2^2+\delta_2p^2) - \Omega_4(\xi\tau_2^2+\eta_2p^2)\Big\}\tau_2 J_1(\tau_2 a)\Big)$$
$$-\sum_{m=1}^{\infty}\Psi_m\Big(\delta_3\Omega_2(\xi\lambda^2\beta_m^2+\eta_2p^2)pJ_0(\lambda\beta_m a) + \Big\{\frac{\Omega_2}{pa}(\delta_1\lambda^2\beta_m^2+\delta_2p^2) - \Omega_4(\xi\lambda^2\beta_m^2+\eta_2p^2)\Big\}\lambda\beta_m J_1(\lambda\beta_m a)\Big),$$

$$A_2 = u_0 f^*(p)\bar{A}_2,$$

$$\bar{A}_2 = -\Psi_{00} p^3 \Big(\delta_3\Omega_1(\xi\lambda^2-\eta_2)I_0(\lambda pa) - \Big\{\frac{\Omega_1(\delta_1\lambda^2-\delta_2)}{pa} - \Omega_3(\xi\lambda^2-\eta_2)\Big\}\lambda I_1(\lambda pa)\Big)$$
$$-\Psi_{01}\Big(\delta_3\Omega_1(\xi\tau_1^2-\eta_2p^2)pI_0(\tau_1 a) - \Big\{\frac{\Omega_1}{pa}(\delta_1\tau_1^2-\delta_2p^2) - \Omega_3(\xi\tau_1^2-\eta_2p^2)\Big\}\tau_1 I_1(\tau_1 a)\Big)$$
$$+\Psi_{02}\Big(\delta_3\Omega_1(\xi\tau_2^2+\eta_2p^2)pJ_0(\tau_2 a) + \Big\{\frac{\Omega_1}{pa}(\delta_1\tau_2^2+\delta_2p^2) - \Omega_3(\xi\tau_2^2+\eta_2p^2)\Big\}\tau_2 J_1(\tau_2 a)\Big)$$
$$+\sum_{m=1}^{\infty}\Psi_m\Big(\delta_3\Omega_1(\xi\lambda^2\beta_m^2+\eta_2p^2)pJ_0(\lambda\beta_m a) + \Big\{\frac{\Omega_1}{pa}(\delta_1\lambda^2\beta_m^2+\delta_2p^2) - \Omega_1(\xi\lambda^2\beta_m^2+\eta_2p^2)\Big\}\lambda\beta_m J_1(\lambda\beta_m a)\Big) \quad (45)$$

and where $H(r)$ is the Heaviside's unit step function and β_m are the roots of equation:

$$(\delta_1\lambda^2\beta^2+\delta_2p^2)\lambda\beta J_1(\lambda\beta b) + \delta_3\Omega_5(\xi\lambda^2\beta^2+\eta_2p^2)pJ_0(\lambda\beta a) + \{(\Omega_5\delta_1-\xi\Omega_6)\lambda^2\beta^2 + (\delta_2\Omega_5-\eta_2\Omega_6)p^2\}\lambda\beta J_1(\lambda\beta a) = 0. \quad (46)$$

(The axial displacement and radial and shear stresses are omitted here.)

4 Numerical Examples and Discussions

Owing to the convenience of numerical calculations, the following dimensionless quantities are introduced.

$$\rho = \frac{r}{a},\ \zeta = \frac{z}{a},\ t' = \frac{\kappa_r t}{a^2},\ \rho_1 = \frac{b}{a},\ B_i = ah_r,$$

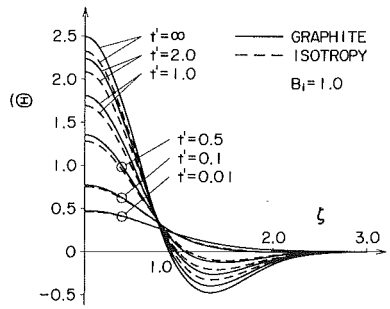


Fig. 2 Time variations of heating temperature of surrounding medium for graphite and under isotropic conditions

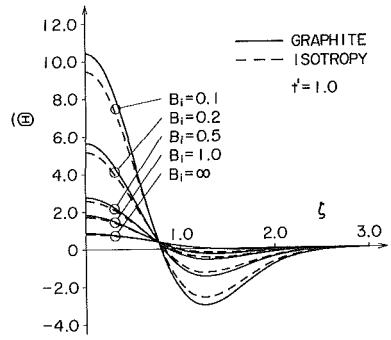


Fig. 3 Effect of Biot's number on heating temperature of surrounding medium for graphite and under isotropic conditions

$$(\hat{\Theta}, \hat{T}) = \frac{\alpha_r a(\Theta, T)}{u_0},\ \hat{u_\rho} = \frac{u_r}{u_0},\ (\widehat{\theta\theta}, \widehat{\zeta\zeta}) = \frac{a(\sigma_{\theta\theta}, \sigma_{zz})}{E_r u_0},$$

$$E = \frac{E_z}{E_r},\ G = \frac{G_{rz}}{E_r},\ \alpha = \frac{\alpha_z}{\alpha_r}$$

where E_r, E_z, and G_{rz} are the moduli of elasticity, α_r and α_z are the coefficients of linear thermal expansion.

The material constants are taken as for a graphite which possesses transverse isotropy

$\lambda_r = 1.172$ W/mK, $\lambda_z = 1.340$ W/mK,
$E_r = 10.4$ GPa, $E_z = 11.8$ GPa, $G_{rz} = 4.14$ GPa,
$\alpha_r = 3.9\times10^{-6}$ K^{-1}, $\alpha_z = 3.5\times10^{-6}$ K^{-1}, $\nu_{r\theta} = \nu_{rz} = 0.11$

and for isotropic conditions

$$\lambda^2 = E = \alpha = 1,\quad G = \frac{E}{2(1+\nu_{rz})},\quad \nu_{r\theta} = \nu_{rz} = 0.11$$

where $\nu_{r\theta}$ and ν_{rz} are the Poisson's ratios.

Numerical calculations are carried out for the following conditions of prescribed radial displacement:

$$\rho_1 = 1,\quad \gamma = 1,\quad f(\zeta) = \exp(-\zeta^2).$$

Figure 1 illustrates the time variations of radial displacement prescribed on the lateral surface of the cylinder.

Figures 2 and 3 illustrate the time variations of the heating temperature of the surrounding medium $\hat{\Theta}$ for $B_i = 1$ and the effect of B_i on $\hat{\Theta}$ for $t' = 1$. The solid and broken lines represent the resulting $\hat{\Theta}$ for a graphite and under isotropic conditions, respectively. The figures show that $\hat{\Theta}$ for a graphite is higher than $\hat{\Theta}$ under isotropic conditions and that $\hat{\Theta}$ changes with the time variations of radial displacement prescribed in Fig. 1. The heating temperature $\hat{\Theta}$ increases with decreasing B_i, and cooling regions appear for $t' > 0.1$. It may be noted that the gradient of the prescribed radial displacement, with respect to axial direction, is considerably large around the region where $\zeta = 1$. Figures 4–7 illustrate the influences of the anisotropies of material constants on $\hat{\Theta}$ when only one among the material constants such as λ^2, E, G, and α exhibits various anisotropies, while the other material constants are kept equal

Downloaded 03 May 2010 to 171.66.16.31. Redistribution subject to ASME license or copyright; see http://www.asme.org/terms/Terms_Use.cfm

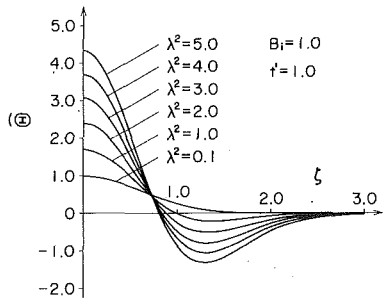


Fig. 4 Effect of anisotropy of material constant λ^2 on heating temperature of surrounding medium

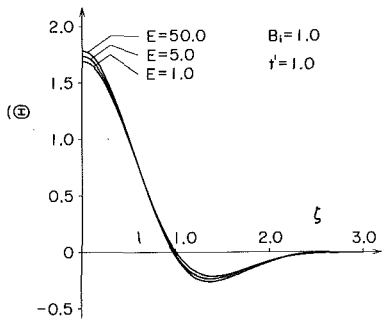


Fig. 5 Effect of anisotropy of material constant *E* on heating temperature of surrounding medium

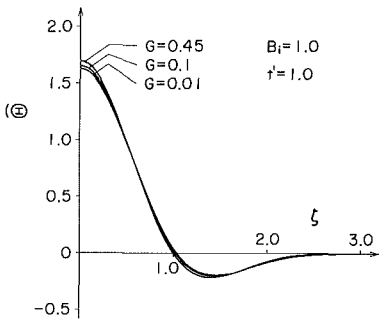


Fig. 6 Effect of anisotropy of material constant *G* on heating temperature of surrounding medium

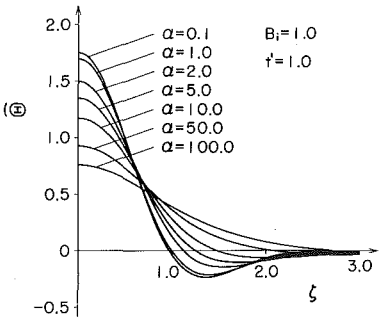


Fig. 7 Effect of anisotropy of material constant α on heating temperature of surrounding medium

the material constants such as λ^2, E, G, and α exhibits various anisotropies, while the other material constants are kept equal to those of isotropic conditions. These figures clearly show that the influences of the anisotropies of thermal material constants such as λ^2 and α on $\widehat{\Theta}$ are quite significant while the anisotropies of elastic material constants such as E and G do not reflect much on $\widehat{\Theta}$.

Figures 8–10 illustrate the time variations of temperature and hoop and axial stresses for a graphite and those obtained under isotropic conditions on the lateral surface of the cylinder. The temperature and hoop and axial stresses for a graphite are somewhat larger than those under isotropic conditions.

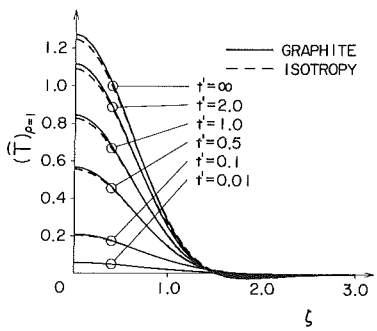


Fig. 8 Time variations of temperature on lateral surface of cylinder for graphite and under isotropic conditions

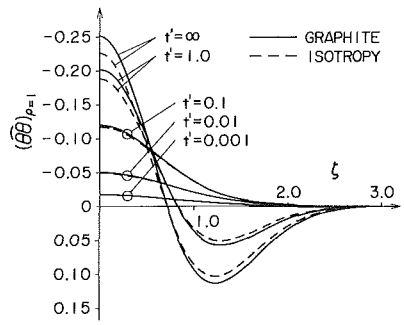


Fig. 9 Time variations of hoop stress on lateral surface of cylinder for graphite and under isotropic conditions

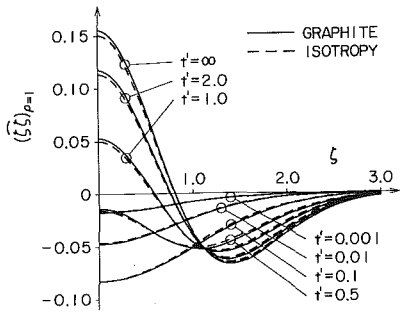


Fig. 10 Time variations of axial stress on lateral surface of cylinder for graphite and under isotropic conditions

References

Cialkowski, M. J., and Grysa, K. W., 1980, "On a Certain Inverse Problem of Temperature and Thermal Stress Fields," *Acta Mechanica*, Vol. 36, pp. 169–185.

Grysa, K., Cialkowski, M. J., and Kaminski, H., 1981, "An Inverse Temperature Field Problem of the Theory of Thermal Stresses," *Nuclear Engineering and Design*, Vol. 64, pp. 169–184.

Grysa, K., and Kozlowski, Z., 1982, "One-Dimensional Problems of Temperature and Heat Flux Determination at the Surfaces of a Thermoelastic Slab, Part I: The Analytical Solutions," *Nuclear Engineering and Design*, Vol. 74, pp. 1–14.

Kozłowski, Z., and Grysa, K., 1982, "One-Dimensional Problems of Temperature and Heat Flux Determination at the Surfaces of a Thermoelastic Slab, Part II: Numerical Analysis," *Nuclear Engineering and Design*, Vol. 74, pp. 15–24.

Nowinski, J. L., 1978, *Theory of Thermoelasticity with Applications*, Sijthoff and Noordhoff, p. 104, p. 396.

Takeuti, Y., and Noda, N., 1978, "A General Treatise on the Three-Dimensional Thermoelasticity of Curvilinear Aeolotropic Solids," *Journal of Thermal Stresses*, Vol. 1, pp. 25–39.

Downloaded 03 May 2010 to 171.66.16.31. Redistribution subject to ASME license or copyright; see http://www.asme.org/terms/Terms_Use.cfm

Some Axisymmetric Problems for Layered Elastic Media: Part I—Multiple Region Contact Solutions for Simply-Connected Indenters

T. W. Shield[1]

D. B. Bogy
Mem. ASME

University of California,
Berkeley, Calif. 94720

The contact of a flat, simply-connected axisymmetric indenter with a layered elastic half space is examined. The problem is mathematically formulated using integral transforms to derive singular integral equations for the contact pressure. The solution of these equations is obtained by expansion in orthogonal polynomials. The solution predicts complete contact between the indenter and the surface of the layered half space only for a restricted range of the material and geometrical parameters. Outside of this range, solutions exist with multiple contact regions. A parameter space is divided into zones for single and multiple contact solutions and comparisons are made with the solutions for the analogous plane-strain problem.

1 Introduction

In this paper, Part I, we consider axisymmetric elastic contact problems for a flat simply-connected indenter. The solutions obtained predict annular and/or circular contact regions. The extent of the contact region is determined by two factors: the modulus of the top layer relative to the substrate and the ratio of layer thickness to indenter radius. The study of the effects of the layered structure for an axisymmetric indenter presented here is a continuation of the plane-strain study by Shield and Bogy (1989). The results presented in Shield and Bogy (1989) will be used extensively in the interest of brevity. As noted in Shield and Bogy (1989), this problem is one of stationary receding contact as defined by Dundurs and Stippes (see Gladwell (1980), page 183).

The problem is considered in the context of linear elasticity. The elastic material consists of multiple layers bonded to each other and to the underlying substrate. The layers and the substrate are assumed to be isotropic and homogeneous. The indenter is rigid with a perfectly-plane face and sharp corners. The interfaces between the layers and the surface of the top layer are perfectly flat. No surface roughness effects are considered and frictional forces are assumed absent between the indenter and the top layer. The layers and substrate are assumed to be of infinite extent, that is, the structure is a layered half space.

With these assumptions the problem is solved by the use of integral transforms. In axisymmetric geometry, where cylindrical polar coordinates are employed, the Hankel transform is used. After the transformed field equations are solved and the boundary conditions applied, the inverse transform leads to a singular integral equation for the pressure under the indenter. The equations kernel has a logarithmic singularity which must be converted, by differentiation, to a Cauchy-type singularity. The equation is then solved by the technique of expansion in the orthogonal polynomials that are appropriate to the characteristic behavior of the solution. A set of linear equations is obtained for the unknown coefficients in the expansion, and these equations are then solved numerically.

The solution of the contact problem that assumes the indenter contacts the surface of the top layer over the entire face of the indenter is not the physically relevant one when it predicts tension in some portion of the contact region. Thus, other solutions must be sought. Indeed, solutions with one, two, or three contact regions between the indenter and the layer surface are found. These are called the one, "two," and "three" contact region configurations because of the similarity to the plane-strain solutions presented in Shield and Bogy (1989). The "two" contact region solution actually has a single annular contact region. These solutions exist only for certain combinations of the material and geometrical parameters for the layered media. In the case of a single layer, the number of contact regions in the solution depends on the elastic moduli and the layer thickness. Underlying layers have the effect of changing the effective modulus of the substrate

[1] Currently at the Department of Theoretical and Applied Mechanics, University of Illinois, Urbana, Ill. 61801.

Contributed by the Applied Mechanics Division of THE AMERICAN SOCIETY OF MECHANICAL ENGINEERS for presentation at the Winter Annual Meeting, San Francisco, Calif., December 10–15, 1989.

Discussion on this paper should be addressed to the Editorial Department, ASME, United Engineering Center, 345 East 47th Street, New York, N.Y. 10017, and will be accepted until two months after final publication of the paper itself in the JOURNAL OF APPLIED MECHANICS. Manuscript received and accepted by the ASME Applied Mechanics Division, August 8, 1988.

Paper No. 89-WA/APM-30.

Copyright © 1989 by ASME

Downloaded 03 May 2010 to 171.66.16.31. Redistribution subject to ASME license or copyright; see http://www.asme.org/terms/Terms_Use.cfm

under the top layer. After the solution is obtained, the modulus-thickness parameter space is divided into zones where the solution has one, two, or three contact regions. It was argued in Shield and Bogy (1989) that these are the only possibilities and the same holds true here.

The two contact region solution will also be used in Part II to solve the problems of an annular indenter and an annular crack. In this case the contact region is determined by the shape of the indenter and/or the layer properties.

2 The Problem Formulation

The following equations give the relevant displacements and stresses, in terms of two unknown harmonic potential functions, $\phi(r, z)$ and $\Psi(r, z)$. The radial component of the displacement is denoted by u and the axial one by w, while the stress components contain double subscripts, corresponding to the appropriate coordinates.

$$2\mu u = -\frac{\partial}{\partial r}(z\Psi + \phi), \tag{1}$$

$$2\mu w = \kappa\Psi - z\frac{\partial\Psi}{\partial z} - \frac{\partial\phi}{\partial z}, \tag{2}$$

$$\tau_{rr} = 2\nu\frac{\partial\phi}{\partial z} - z\frac{\partial^2\Psi}{\partial r^2} - \frac{\partial^2\phi}{\partial r^2}, \tag{3}$$

$$\tau_{rz} = (1-2\nu)\frac{\partial\Psi}{\partial r} - z\frac{\partial^2\Psi}{\partial r\partial z} - \frac{\partial^2\phi}{\partial r\partial z}, \tag{4}$$

$$\tau_{zz} = 2(1-\nu)\frac{\partial\Psi}{\partial z} - z\frac{\partial^2\Psi}{\partial z^2} - \frac{\partial^2\phi}{\partial z^2}. \tag{5}$$

The shear modulus is μ and κ is defined in terms of Poisson's ratio ν by

$$\kappa = 3 - 4\nu. \tag{6}$$

We are considering axisymmetric contact problems, where a smooth, rigid indenter is pressed into the surface of an elastic half space, $z \geq 0$, with one or more layers. The layers are perfectly bonded to each other and to the half space. We use the notation that a numerical superscript on a dependent variable denotes the number of the layer in which the quantity is defined, with 1 being the top layer. Quantities in the substrate are denoted with a superscript s. Parameters and other quantities carry this information with use of a subscript. The boundary conditions for this problem are:

$$\begin{aligned} w^1(r, 0) &= \delta \quad , \ r \in A_c \\ \tau^1_{zz}(r, 0) &= 0 \quad , \ r \in \tilde{A}_c, \\ \tau^1_{rz}(r, 0) &= 0 \quad , \ \text{all } r \end{aligned} \tag{7}$$

where δ is the indentation, A_c and $\tilde{A}_c$ are the contact region and its complement, respectively.

Since the layers are bonded to each other and to the substrate (half space), the displacements and stress components involved in the tractions are continuous across these interfaces. The number of layers is N_l. Thus, the boundary conditions at the interfaces are

$$\begin{aligned} u^i(r, z_i) &= u^{i+1}(r, z_i) \\ w^i(r, z_i) &= w^{i+1}(r, z_i), \ i = 1, 2, \ldots, N_l, \\ \tau^i_{rz}(r, z_i) &= \tau^{i+1}_{rz}(r, z_i) \\ \tau^i_{zz}(r, z_i) &= \tau^{i+1}_{zz}(r, z_i) \end{aligned} \tag{8}$$

where z_i is the z coordinate of the interface between the ith and $(i+1)$th layer, and the equations hold for all values of the coordinate r. An index value of $N_l + 1$ denotes quantities in the substrate. The layer thicknesses are given by

$$h_i = z_i - z_{i-1}, \ i = 1, 2, \ldots, N_l, \tag{9}$$

where z_0 is zero.

Overall equilibrium requires that the integral of the pressure over the contact region must equal the total load, L, applied to the indenter. This condition is

$$L = 2\pi\int_{A_c} \tau^1_{zz}(r, 0) r\, dr. \tag{10}$$

2.1 Application of Integral Transforms. The method of solution of the Laplace equations, supplemented by the boundary conditions (7) and (8), employs a Hankel transform in the coordinate r to reduce the problem to a singular integral equation. The transformed field equations can then be solved analytically in terms of exponentials and unknown functions of the transform variable, which are determined by the transformed boundary conditions. The inverse transform is then applied to recover the dependence on the r coordinate in the form of an integral equation. This is a well-known technique (see Gladwell (1980), for example). The application of the boundary conditions can be simplified by a judicious ordering of the calculations. Brekhovskikh (1980) provides a useful method for this ordering in the context of the elastic wave solutions for layered media.

The use of the Hankel (or Bessel Fourier) transform differs little from the use of the Fourier transform. The forward transform is

$$\bar{g}^\nu(\xi) = \int_0^{+\infty} g(r) J_\nu(r\xi) r\, dr, \tag{11}$$

where J_ν is the Bessel function of the first kind of order ν. The Hankel transform is its own inverse. The transform of a gradient, with respect to r, is given by

$$\int_0^{+\infty} \frac{\partial g(r)}{\partial r} J_1(r\xi) r\, dr = -\xi\bar{g}^0(\xi). \tag{12}$$

The form of Laplace's equation in polar coordinates dictates that the zeroth-order Hankel transform is the proper one to use on both ϕ and Ψ. The transforms of the general solutions are

$$\bar{\Psi}^0 = A(\xi)e^{z\xi} + B(\xi)e^{-z\xi} \tag{13}$$

and

$$\bar{\phi}^0 = C(\xi)e^{z\xi} + D(\xi)e^{-z\xi}. \tag{14}$$

The transforms of u, w, τ_{rz}, and τ_{zz} are needed in order to apply the boundary conditions (7) and (8). These are written in tems of the four unknown functions $A(\xi)$, $B(\xi)$, $C(\xi)$, and $D(\xi)$, by substituting equations (13) and (14) into the transforms of equations (1), (2), (4), and (5). The result of these operations can be written as

$$\mathbf{f}(\xi, z) = \mathbf{T}(\xi, z)\mathbf{a}(\xi), \tag{15}$$

where

$$\mathbf{f}(\xi, z) = \begin{Bmatrix} \bar{u}^1(\xi, z) \\ \bar{w}^0(\xi, z) \\ \bar{\tau}^1_{xz}(\xi, z) \\ \bar{\tau}^0_{zz}(\xi, z) \end{Bmatrix}, \quad \mathbf{a}(\xi) = \begin{Bmatrix} A(\xi) \\ B(\xi) \\ C(\xi) \\ D(\xi) \end{Bmatrix} \tag{16}$$

and

Downloaded 03 May 2010 to 171.66.16.31. Redistribution subject to ASME license or copyright; see http://www.asme.org/terms/Terms_Use.cfm

$$\mathbf{T}(\xi,z)=\begin{bmatrix} \frac{\xi}{2\mu}e^{z\xi} & \frac{\xi}{2\mu}e^{-z\xi} & \frac{\xi z}{2\mu}e^{z\xi} & \frac{\xi z}{2\mu}e^{-z\xi} \\ \frac{-\xi}{2\mu}e^{z\xi} & \frac{\xi}{2\mu}e^{-z\xi} & \frac{(\kappa-z\xi)}{2\mu}e^{z\xi} & \frac{(\kappa+z\xi)}{2\mu}e^{-z\xi} \\ \xi^2 e^{z\xi} & -\xi^2 e^{-z\xi} & -\xi((1-2\nu)-z\xi)e^{z\xi} & -\xi((1-2\nu)+z\xi)e^{-z\xi} \\ -\xi^2 e^{z\xi} & -\xi^2 e^{-z\xi} & (2(1-\nu)\xi-z\xi^2)e^{z\xi} & -(2(1-\nu)\xi+z\xi^2)e^{-z\xi} \end{bmatrix} \quad (17)$$

The overall equilibrium requires that $A_s(\xi)=C_s(\xi)=0$.

2.2 Transfer Matrix Approach. In order to apply the boundary conditions (7) and (8), we use the transfer matrix approach given in Brehovshikh (1980). The idea is to eliminate the unknown functions of ξ in the layers and write the surface values of the physical quantities directly in terms of the substrate functions $B_s(\xi)$ and $D_s(\xi)$. Then the boundary conditions (7) can be used to determine these two remaining functions. This procedure is outlined in Shield and Bogy (1989) for the plane-strain case and it is similar for the axisymmetric problem. Only the range of the transform variable and the inverse transform differ.

If $G(\xi)$ represents the transform of the Green's function that relates the surface normal displacement to the applied surface pressure by

$$\bar{w}^0(\xi,0)=G(\xi)\bar{\tau}^0_{zz}(\xi,0), \quad (18)$$

then for the case of a single layer

$$G(\xi)=\frac{\alpha_1+e^{-2h_1\xi}(\alpha_2(h_1\xi)+\alpha_3 e^{-2h_1\xi})}{2\mu_1[\beta_1+e^{-2h_1\xi}(\beta_2(h_1\xi)^2+\beta_3+\beta_4 e^{-2h_1\xi})]\,|\xi|} \quad (19)$$

where the constants α_i and β_i depend only on the four material parameters as given in the Appendix.

When more than one layer is present, the computation of $G(\xi)$ becomes too complicated for an algebraic manipulation program on a main-frame computer. Then it is necessary to calculate the values of $G(\xi)$ numerically from its definition. This is also outlined in Shield and Bogy (1989) and the procedure is identical here when more than one layer is present.

2.3 Reduction to a Singular Integral Equation. In this section the two remaining equations in the boundary conditions (7) are used to derive the singular integral equation for the contact problems.

The inverse transform of (18) and the first of (7) give

$$\delta=\int_0^{+\infty} G(\xi)P(\xi)J_0(r\xi)\xi d\xi,\ r\in A_c, \quad (20)$$

where $P(\xi)$ is the transform of the pressure,

$$P(\xi)=\int_{A_c} p(r)J_0(r\,\xi)r\,dr. \quad (21)$$

Using both of these equations, we can eliminate $P(\xi)$ to give

$$\delta=\int_{A_c} p(t)\int_0^{+\infty} G(\xi)J_0(r\,\xi)J_0(t\,\xi)\xi d\xi t\,dt\ ,\ r\in A_c, \quad (22)$$

where the interchange of the order of integration is formal. We can rewrite equation (22) as

$$\delta=\frac{1-\nu_1}{\mu_1}\int_{A_c} t\,p(t)g(r,t)dt, \quad (23)$$

where

$$g(r,t)=K(r,t)+\int_0^{+\infty} N(\xi)J_0(r\xi)J_0(t\xi)d\xi \quad (24)$$

and

$$K(r,t)=\int_0^{+\infty} J_0(r\xi)J_0(t\xi)d\xi. \quad (25)$$

The kernel $N(\xi)$ is given by

$$N(\xi)=\frac{\mu_1}{1-\nu_1}\xi G(\xi)-1. \quad (26)$$

This function is bounded and decays exponentially to zero as $|\xi|\to\infty$, making its inverse Hankel transform well defined.

The kernel $K(r,t)$ has a logarithmic singularity at $r=t$. This can best be seen when $K(r,t)$ is expressed in terms of elliptic integrals as (Gradshteyn and Ryzhik, (1980)),

$$K(r,t)=\begin{cases}\frac{2}{\pi r}\mathbf{K}(t/r) & r>t \\ \frac{2}{\pi t}\mathbf{K}(r/t) & r<t\end{cases} \quad (27)$$

where $\mathbf{K}(k)$ is the complete elliptic integral of the first kind. It is well known that $\mathbf{K}(k)$ has a logarithmic singularity at $k=1$.

It is possible to solve (23) with its logarithmic kernel for the case of a rigid simply-connected circular punch (see Popov (1962)). The analogous plane-strain equations have Gauchy singularities, and better numerical methods exist for this type of equation. For this reason and ones that will be apparent, it is desirable to convert equation (23) to an equation with a Cauchy singularity. After differentiation with respect to r, equation (23) becomes

$$0=\frac{1-\nu_1}{\pi\mu_1}\int_{A_c} p(t)g'(r,t)dt,\ r\in A_c, \quad (28)$$

where

$$g'(r,t)=K'(r,t)-\pi t\int_0^{+\infty} N(\xi)J_1(r\xi)J_0(t\xi)\xi d\xi, \quad (29)$$

and

$$K'(r,t)=\frac{\partial K(r,t)}{\partial r}=\frac{2t}{t^2-r^2}\begin{cases}\mathbf{E}(t/r) & r>t \\ \frac{t}{r}\mathbf{E}(r/t)-\frac{t^2-r^2}{r\,t}\mathbf{K}(r/t) & r<t\end{cases}. \quad (30)$$

The relation (Gradshteyn and Ryzhik (1980))

$$\frac{\partial\mathbf{K}(k)}{\partial k}=\frac{\mathbf{E}(k)}{k(1-k^2)}-\frac{\mathbf{K}(k)}{k} \quad (31)$$

has been used, and $\mathbf{E}(k)$ is the complete elliptic integral of the second kind. The kernel K' has a Cauchy and a logarithmic singular term. They can be displayed explicitly by writing k' as

$$K'(r,t)=\frac{2r}{t^2-r^2}+k(r,t), \quad (32)$$

Downloaded 03 May 2010 to 171.66.16.31. Redistribution subject to ASME license or copyright; see http://www.asme.org/terms/Terms_Use.cfm

where

$$k(r,t)=2r\left[\frac{h(r,t)-1}{t^2-r^2}\right] \tag{33}$$

and

$$h(r,t)=\begin{cases}\dfrac{t}{r}\,\mathbf{E}(t/r) & r\geq t\\[2ex] \dfrac{t^2}{r^2}\,\mathbf{E}(r/t)-\dfrac{t^2-r^2}{r^2}\,\mathbf{K}(r/t) & r<t\end{cases}, \tag{34}$$

which has only a logarithmic singularity since $h(r,r)=1$.

It is useful in the following analysis to extend the range of the independent variable to negative values. By extending $p(r)$ as an even function and $\partial w/\partial r$ as an odd function for negative values of r, and using the fact that

$$\frac{2r}{t^2-r^2}=\frac{1}{t-r}-\frac{1}{t+r}, \tag{35}$$

we obtain from equation (28)

$$0=\frac{1-\nu_1}{\pi\mu_1}\left[\int_{A_c}p(t)\left(\frac{1}{t-r}+K_1(r,t)\right)dt + \int_{A_c}p(t)\left(\frac{-1}{t+r}+K_1(r,t)\right)dt\right]. \tag{36}$$

The variable t in the second integral in equation (36) can be changed to $-t$ to make the integrands of the two integrals identical. They can then be combined to give

$$0=\frac{1-\nu_1}{\pi\mu_1}\int_{A_c\cup -A_c}p(t)\left(\frac{1}{t-r}+K_1(r,t)\right)dt, \tag{37}$$

where the notation $-A_c$ denotes the reflection of the contact region about $r=0$. The kernel $K_1(r,t)$, defined as an even function of t and an odd function of r to agree with the extensions of $p(t)$ and $\partial w/\partial r$, is then given by

$$K_1(r,t)=\frac{h(|r|,|t|)-1}{t-r} - \frac{\pi\,\mathrm{sgn}(r)\,|t|}{2}\int_0^{+\infty}N(\xi)J_1(|r|\xi)J_0(|t|\xi)\xi\,d\xi. \tag{38}$$

It can be shown (Erdogan, 1969), that the function $K_1(r,t)$ has only a logarithmic singularity at $r=t$, since

$$\text{for } r\approx t\quad k(r,t)=\frac{1}{2|r|}\log|t-r|+O(1). \tag{39}$$

This result will be used later when the numerical problems associated with this singularity are discussed.

3 Numerical Solution of the Singular Integral Equations

The method of solution of an equation of the form of (37) is given by Erdogan and Gupta (1972) and outlined in (Shield and Bogy, 1989). This method leads to a set of linear equations for the unknown coefficients g_n in a polynomial expansion for the nonsingular part of the pressure. These equations can be written as

$$0=\sum_{n=0}^{N-1}g_n\left[\frac{\pi}{N}\sum_{i=1}^{N}T_n(s_i)\,\frac{1}{s_i-y_k} + \int_{-1}^{+1}\frac{T_n(t)K_1(y_k,t)}{\sqrt{1-t^2}}\,dt\right],\quad k=1,\ldots,N-1, \tag{40}$$

for the case of $-A_c\cup A_c=[-1,\,1]$, where the s_i and y_k are given in (7.56) of Erdogan, Gupta, and Cook (1973). The polynomials $T_n(x)$ are the Chebyshev polynomials of the first kind. The Nth equation is the load equation (10) approximated with a suitable integration scheme.

The kernel K_1 has a logarithmic singularity. Thus, use of the Gauss-Chebyshev integrator in Abramowitz and Stegun (1965) to evaluate the second integral in (40) is not correct, and its use could lead to errors in the computed solution. Erdogan (1969) provides a technique for treating this problem. The logarithmic singularity given in equation (39) is isolated from $K_1(r,t)$ by defining

$$K_2(r,t)=K_1(r,t)-\frac{1}{2|r|}\log|t-r|. \tag{41}$$

The kernel $K_2(r,t)$ is bounded, thus, the Gauss-Chebyshev integrator can be used on this term and equation (40) becomes

$$0=\sum_{n=0}^{N/2-1}g_n\left[\frac{\pi}{N}\sum_{i=1}^{N}T_{2n}(s_i)\left(\frac{1}{s_i-y_k}+K_2(y_k,s_i)\right) + \frac{1}{2|y_k|}\int_{-1}^{+1}\frac{T_{2n}(t)\log|t-y_k|}{\sqrt{1-t^2}}\,dt\right],\quad k=1,\ldots,N/2-1, \tag{42}$$

where only the even coefficients are calculated since the solution is symmetric. The last integral, which we denote by $W_n(y_k)$, can be evaluated analytically (Erdogan (1969) has a misprint here), to be

$$W_n(r)=\int_{-1}^{+1}\frac{T_n(t)\log|t-r|}{\sqrt{1-t^2}}\,dt =\begin{cases}-\pi\log 2 & n=0\\[1ex] \dfrac{\pi}{n}\,T_n(r) & n=1,\,3,\ldots.\\[2ex] -\dfrac{\pi}{n}\,T_n(r) & n=2,\,4,\ldots\end{cases} \tag{43}$$

Using this result, we obtain for the unknowns g_n the set of equations

$$0=\sum_{n=0}^{N/2-1}g_n\left[\frac{\pi}{N}\sum_{i=1}^{N}T_{2n}(s_i)\left(\frac{1}{s_i-y_k}+K_2(y_k,s_i)\right) + \frac{1}{2|y_k|}W_{2n}(y_k)\right]\quad k=1,\ldots,N/2-1. \tag{44}$$

When considering multiple contact region solutions, as we do in what follows, the integral of the corresponding logarithmic kernel will not have the same form as in equation (40), and it will not be possible to use the analytic result presented. However, this integral can be evaluated numerically using an integrator that is better suited to the logarithmic singularity in K_1. This will also allow the integrator for the logarithmic term to be of higher order than the integrators used elsewhere. In order to avoid the square root behavior at the end points of the integral, we use the map $t=\cos\theta$, which leads to the transformation

$$\int_{-1}^{+1}\frac{T_n(t)K_1(y_k,t)}{\sqrt{1-t^2}}\,dt=\int_0^{\pi}\cos(n\theta)K_1(y_k,\cos\theta)\,d\theta, \tag{45}$$

where the trigonometric representation of T_n has also been used. This integral can be easily evaluated using a trapezoidal integrator. The need to consider the logarithmic singularity will be examined when the solutions obtained by the various methods are compared in Section 5.

In order to solve the equations, it is necessary to calculate the values of the kernel K_1, which contains a term due to the presence of the layer. This term is

Downloaded 03 May 2010 to 171.66.16.31. Redistribution subject to ASME license or copyright; see http://www.asme.org/terms/Terms_Use.cfm

$$n'(r,t) = -t\int_0^{+\infty} N(\xi)J_1(r\xi)J_0(t\xi)\xi d\xi. \tag{46}$$

The integrator that is used for this term is discussed in Shield and Bogy (1989) for the plane-strain analog of equation (46).

4 The Solution for Specific A_c

In this section, we follow the procedure of Shield and Bogy (1989) and specialize the problems to three specific cases of A_c. First, we consider the single contact region case, in which there is contact over the entire face of the indenter, $r \le 1$. Next, we examine the two contact region solutions, which involve contact of the indenter with the surface of the top layer only over the region $c \le r \le 1$. Even though the contact region is annular and therefore connected, it is referred to as a "two contact region" solution because of its similarity with the plane-strain problem. Similar designations are used for other multiple contact region solutions in the sequel. Finally, the "three contact region" solution is presented, in which the indenter contacts the top layer surface for $r \le d$ and $c \le r \le 1$, with $d < c$.

We discussed in Shield and Bogy (1989) the effect of layers on the number of contact regions for the case of plane strain. It is possible to have any of these three contact region geometries. The same is true here for the axisymmetric indenter.

4.1 One Contact Region Solution. The one contact region solution has the form

$$p(t) = \frac{1}{\sqrt{1-t^2}} \sum_{n=0}^{N/2-1} g_n T_{2n}(t), \quad t \in [-1,1]. \tag{47}$$

The contact region A_c is [0,1] in this case. The set of algebraic linear equations for this case is given by (40) specialized to the symmetric form of the pressure given in (47). We write this set of linear equations as $A\mathbf{g} = \mathbf{b}$, where

$$\mathbf{g} = \begin{Bmatrix} g_0 \\ g_1 \\ \cdots \\ g_{N/2-1} \end{Bmatrix}, \quad \mathbf{b} = \begin{Bmatrix} 0 \\ \cdots \\ 0 \\ 1 \end{Bmatrix}, \tag{48}$$

and the first $N/2-1$ rows of the matrix A are determined by equation (40) to be

$${}^1_1A_{kn} = \frac{\pi}{N} \sum_{i=1}^{N} T_{2n}(s_i)\left(\frac{1}{s_i - y_k} + K_1(y_k, s_i)\right), \quad k = 1, \ldots, N/2-1, \quad n = 0, \ldots, N/2-1 \tag{49}$$

The points s_i and the y_k are given by (7.56) of Erdogan, Gupta, and Cook (1973). The $(N/2)$th row of the matrix A is given by the coefficients of g_n in the load equation,

$$1 = \frac{2\pi^2}{N} \sum_{n=0}^{N/2-1} g_n \sum_{i=1}^{2N} T_{2n}(s_i)\,|s_i|. \tag{50}$$

The nondimensional load has the value of one, without loss of generality, because the problems considered here are linear in the load. The notation used on the matrix in (49) denotes the method of solution and the number of contact regions. The presuperscript refers to the number of contact regions. The presubscript refers the method of solution. The first method of solution is the Erodgan and Gupta method (1972) ignoring the logarithmic singularity in K_1.

The second method of solving the axisymmetric problem with one contact region takes into account the logarithmic singularity in $K_1(r,t)$. The components of $\frac{1}{2}A$, as determined by equation (44), are

$${}^1_2A_{kn} = \frac{\pi}{N} \sum_{i=1}^{N} T_{2n}(s_i)\left(\frac{1}{s_i - y_k} + K_2(y_k, s_i)\right) + \frac{1}{2|y_k|} W_{2n}(y_k), \quad n = 0, \ldots, N/2-1, \quad k = 1, \ldots, N/2-1. \tag{51}$$

The last row of this matrix is given by equation (50).

The integral of the logarithmic singularity can also be evaluated by using a trapezoidal integrator to evaluate equation (45). The coefficient matrix for this method of solution is

$${}^1_3A_{kn} = \frac{\pi}{N} \sum_{i=1}^{N} T_{2n}(s_i) \frac{1}{s_i - y_k} + I_n(y_k), \quad k = 1, \ldots, N/2-1, \quad n = 0, \ldots, N/2-1 \tag{52}$$

The term $I_n(y_k)$ is obtained by evaluating the right-hand side of equation (45) with a trapezoidal integrator. The load equation remains (50).

All valid solutions must satisfy the condition that the pressure is non-negative over the entire contact region. Thus, if we define a function that is $+1$ when $p(t) > 0$ for all $t \in [-1,1]$ and -1 otherwise, a simple bisection root-finding routine can be used to determine the parameter values such that $p(t) = 0$ for some t. The parameters that determine this root are the layer thicknesses h_i and the material constants μ_i and ν_i. The root-finding routine varies one parameter, usually the top layer modulus μ_1, while all the others are fixed. The curve found (a surface in the $3N_l + 2$ parameter space) is the boundary of the zone of validity of the one contact region solution.

4.2 Two Contact Region Solution. If the pressure predicted by the one contact region solution is negative in some symmetric region about $t = 0$, then the solution is not valid. The correct solution has contact between the indenter and the surface only over the region $c \le r \le 1$ for some unknown value of c. In order to solve the problem under these conditions, we must consider the solution of the integral equation before it has been extended to $r < 0$. Thus,

$$0 = \frac{1}{\pi}\int_c^{+1} \left(\frac{2r}{t^2 - r^2} + K_1^*(r,t)\right)p(t)dt, \quad r \in [c,1] \tag{53}$$

is the equation to solve where

$$K_1^*(r,t) = k(r,t) - \pi t\int_0^{+\infty} N(\xi)J_1(r\xi)J_0(t\xi)\xi d\xi. \tag{54}$$

The term $k(r,t)$ is defined by equation (33). The pressure for the two contact region solution is zero at $r = c$ and has a square root singularity at $r = 1$. Thus, we assume that

$$p(t) = \sqrt{\frac{t^2 - c^2}{1 - t^2}}\, tg(s), \tag{55}$$

where the function $g(s)$ is given by

$$g(s) = \sigma^{-1} \sum_{n=0}^{N-1} g_n T_{2n+1}(\sigma), \tag{56}$$

where

$$\sigma = \sqrt{\frac{s+1}{2}}. \tag{57}$$

The variable s is related to the variable t through the relation

Downloaded 03 May 2010 to 171.66.16.31. Redistribution subject to ASME license or copyright; see http://www.asme.org/terms/Terms_Use.cfm

$$s = \frac{2t^2 - 1 - c^2}{1 - c^2}. \tag{58}$$

The solution method outlined in Shield and Bogy (1989) results in the numerical approximation of equation (53) as

$$0 = \frac{\pi}{2N+1} \sum_{n=0}^{N-1} g_n {}^2A_{kn},\ k = 1, \ldots, N, \tag{59}$$

where

$$ {}^2A_{kn} = \sum_{i=1}^{N} (1+s_i)\sigma_i^{-1} T_{2n+1}(\sigma_i) \left(\frac{r_k}{s_i - y_k} + \frac{1-c^2}{4} K_1^*(r_k, t_i) \right) $$

$$n = 0, \ldots, N-1,\ k = 1, \ldots, N. \tag{60}$$

The load equation (10) is approximated by

$$1 = \frac{\pi^2(1-c^2)}{2N+1} \sum_{n=0}^{N-1} g_n \sum_{i=1}^{N} (1+s_i) t_i \sigma_i^{-1} T_{2n+1}(\sigma_i). \tag{61}$$

The approximation in (59) ignores the singular nature of $K_1^*(r,t)$. Since the layer effects dominate in the region of validity for the two contact region solution, it is not necessary to treat the logarithmic singularity separately in the two and three contact region problems.

We have found $N+1$ equations involving the N unknowns g_n. Equation (59) provides N equations and the load equation (61) gives the other one. The number of equations is not excessive because there is another unknown, c, the inner contact dimension, that must be determined as part of the solution. In order for a unique nontrivial solution to be found, the rank of the $N+1$ equations must be N. Because the load equation is not related to the other N equations, we must find a value of c such that one of the equations in (59) is redundant. That is, we require

$$\det({}^2A) = 0. \tag{62}$$

This is a nonlinear equation giving c as a function of the material and geometrical parameters of the problem. As discussed in Shield and Bogy (1989), the two contact region solution is valid when (62) has a single root. This defines the zone of validity in the parameter space for the two contact region solution. This zone is bounded by the set of values of the parameters for which the number of roots of equation (62) changes from one to zero or two. After the value of c is found as in Shield and Bogy (1989) and one row of ${}^2A$ is replaced by the load equation, then these equations can be solved for the coefficients in the expansion for the pressure.

4.3 Three Contact Region Solution. The three contact region geometry has $A_c = [0,d] \cup [c,1]$. It was observed that the one contact region solution can predict negative pressure over a region that does not include the origin. This occurs for top layers with thicknesses that are less than necessary for the two contact region solution to exist. Therefore, there is a zone in the parameter space in which neither the one nor the two contact region solution is valid. This is the zone where the three contact region solutions exist. Again, we use the results from Shield and Bogy (1989).

The pressure, $p_1(t)$, defined in the region $[c,1]$ is the same as in the two contact region solution, and is given by equations (55) and (56). The pressure $p_2(t)$ defined in $[-d,d]$, has a square root zero at the points $\pm d$,

$$p_2(t) = \sqrt{d^2 - t^2}\, g_2(s'), \tag{63}$$

where the function $g_2(s')$ is given by

$$g_2(s') = (\sigma')^{-1} \sum_{n=0}^{N-1} g'_n T_{2n+1}(\sigma'). \tag{64}$$

The variable s' is related to t by

$$s' = \frac{2t^2 - d^2}{d^2}, \tag{65}$$

and σ' is given by equation (57) evaluated at s'. The prime is used on subscripted variables to denote quantities associated with the region $[-d,d]$.

The four submatrices given in Shield and Bogy (1989) make up the complete set of equations to solve, whose coefficient matrix is

$$ {}^3A = \begin{bmatrix} {}^3A^{11} & {}^3A^{12} \\ {}^3A^{21} & {}^3A^{22} \end{bmatrix}. \tag{66}$$

The matrix ${}^3A$ has $2N$ nonzero rows. The number of unknowns in this problem is $2N+2$. There are $2N$ entries in $\mathbf{g}$, and the two contact region dimensions c and d must also be determined as part of the solution. The extra equations are the resultant load equation for the indenter, involving the sum of the integrals of p_1 and p_2, and a consistency condition. The consistency condition is a mathematical statement that there is only one indenter, that is, that the normal displacement in each region must be the same. This condition is necessary because the integral equations are formulated in terms of the slope. It is

$$\int_d^c \frac{\partial w(r)}{\partial r}\, dr = 0, \tag{67}$$

that is, $w(c) = w(d)$. The coefficients of the g_n and g'_n in the numerical approximation to (67) form the row of the matrix ${}^3A$ for the consistency equation.

We now have $2N+2$ linear equations ((66), (67), and the load equation) for the $2N$ unknowns $(g_1, \ldots, g_N, g'_1, \ldots, g'_N)$, however, they include implicit nonlinear equations for the two contact dimensions. For the correct values of c and d there must be a unique nontrivial solution $\mathbf{g}$ to these $2N+2$ equations. Thus, these $2N+2$ equations must have rank $2N$ at the correct values of c and d. This suggests that the proper conditions to determine c and d are

$$\det({}^3A) = 0 \tag{68}$$

and

$$\det({}^3_dA) = 0, \tag{69}$$

where ${}^3_dA$ is the matrix ${}^3A$ with one row replaced by the numerical approximation to (67). After the simultaneous root of these two equations is found, one row of ${}^3_dA$ can be replaced by the load equation to solve for pressures. This load equation is

$$1 = L_1 + L_2, \tag{70}$$

where L_1 is given by the right-hand side of equation (61). The contribution to the load by $p_2(t)$ is given by

$$L_2 = \frac{\pi d^2}{2(2N+1)} \sum_{n=0}^{N-1} g'_n \sum_{i=1}^{N} (1+s'_i) t'_i (\sigma'_i)^{-1} T_{2n+1}(\sigma'_i). \tag{71}$$

The integration abscissas, s'_i, are given in 25.4.43 of Abramowitz and Stegun (1965).

4.4 Calculation of Other Quantities of Interest. After the coefficients in the pressure expansion and the contact dimensions have been obtained using the procedures given, several other quantities can be calculated. Given the pressure under the punch, the stress intensity factors at the corners of the in-

Downloaded 03 May 2010 to 171.66.16.31. Redistribution subject to ASME license or copyright; see http://www.asme.org/terms/Terms_Use.cfm

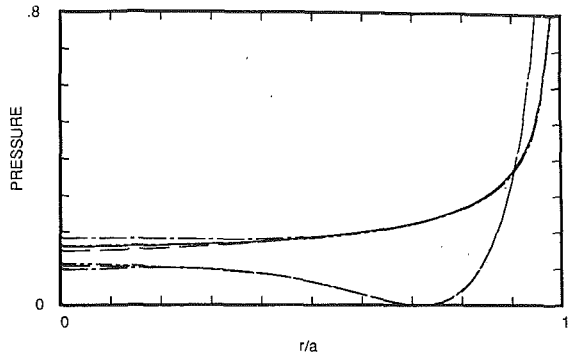


Fig. 1 Solution of the axisymmetric half-space problem (upper set of curves) using the three methods of solution: (1) Erdogan and Gupta (1972), ignoring the log term (dot-dashed), (2) analytic treatment of the log term (dashed), and (3) special integrator for the log term (dot-dot-dashed), compared to the analytic solution (solid). Solution to the axisymmetric problem for $h = .25$, $\mu = 9.2$ using the three methods (lower set of curves), there is no analytical solution in this case.

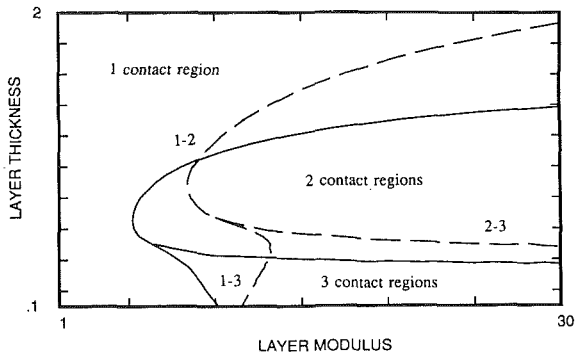


Fig. 2 The parameter space for a single layer showing the zones of existence of the three types of solutions; axisymmetric (solid) and plane-strain (dashed) results are shown. In both cases $\nu = \nu_s = 1/3$.

denter are given by the values of $g(t)$ at ± 1. It is also possible to calculate the surface displacements. In the axisymmetric problem the displacements are globally defined and the total displacement of the indenter can be found.

The surface displacement is given directly by the right-hand side of equation (23). Thus, we have

$$w(r) = \frac{1-\nu_1}{\mu_1}\int_{A_c} g(r,t)p(t)t\,dt, \tag{72}$$

which is a nonsingular integral for r outside the contact region. This integral will also be evaluated using a Gauss-Chebyshev integrator suitable for the form of the pressure. The total indentation of the punch, referenced to zero displacement at infinity, is

$$\delta = w(1). \tag{73}$$

The compliance of the surface is proportional to δ for constant load.

The stress intensity factor at the corner of the indenter is given by

$$K_I = \lim_{t\to 1}(1-t)^{1/2}p(t). \tag{74}$$

The stress intensities for the half-space solution are easily calculated analytically to be 0.1125. The stress intensity at the point $r = c$ is zero.

5 Results

In this section we present the results of the calculations. First, we evaluate the accuracy of the methods used to treat the logarithmic singularity. Next, we determine the zones in the parameter space in which each solution is valid. To reduce the number of combinations, the values of all Poisson's ratios are fixed at 1/3. The behavior of the solutions is examined for the case of a single layer, but in the two-layer case, only the parameter space divisions for selected two-layer examples are presented. Then, the contact dimensions and other quantities of interest are calculated.

5.1 Numerical Accuracy. The parameters needed for convergence of the numerical solution were determined in Shield and Bogy (1989). The only numerical parameter discussed here was the order of the polynomial expansion, it was found that $N = 10$ is suitable for all calculations.

The numerical accuracy of the axisymmetric solution is also affected by the method of treatment of the logarithmic singularity in the kernel of the integral equation. In Section 3 three techniques were presented for dealing with this term. The first technique ignores the logarithmic term, resulting in the matrix of coefficients ${}_1^1A$. The second technique uses equation (43), to give the matrix ${}_2^1A$. The third method uses an integrator better suited to the behavior of the integrand to give ${}_3^1A$. The contact pressures obtained using these three methods are compared in Fig. 1 for a homogeneous half space and a layered half space with one choice of the layer parameters. The monotonic curves in Fig. 1 compare the exact homogeneous half-space solution with the numerical results obtained from the layered half-space solution when the layer modulus is unity. When the logarithmic singularity is ignored, the solution shows the largest error. The other set of curves in Fig. 1 are for a layered half space. For the parameter values used, the differences between the various numerical solutions are much less than they are for the homogeneous half-space case. Since the errors for the solutions in the presence of layers are relatively small and method one is the most economical (recall that the second method cannot be applied to the multiple contact region solutions), the logarithmic singularity will be ignored in the calculations that follow.

5.2 Parameter Space Division According to the Number of Contact Regions. In the case of a single layer, the two parameters are the layer modulus ratio, μ, and thickness, h. The subscripts will be omitted when only one layer is involved. The most important issue is the type of solution, as regards the number of contact regions for given layer properties. In Section 4 the conditions for each of the three types of solutions were stated. A more detailed discussion of the behaviors of the solutions is given in Shield and Bogy (1989). Figure 2 shows the zones in the (μ,h) plane for both the plane-strain and axisymmetric geometries. The boundary curves for both geometries are similar and all of the discussions pertaining to one geometry generally apply to the other as well. We observe that a curve separates the zone of lower modulus from the rest of the plane. It divides the plane into the domains of low-modulus, single contact region solutions and the high-modulus, multiple contact region solutions. The curve that is almost parallel to the modulus axis in the high-modulus, multiple contact region zone separates the zones for the two and the three contact region solutions.

The high-modulus, low-modulus separation curve on which $p(t) = 0$ for some isolated t, can be divided into two parts. If, as μ increases for fixed h, zero pressure occurs first for $t = 0$, then crossing the curve in the direction of increasing modulus changes the type of solution from one to two contact regions. This curve is labeled as the 1-2 boundary in Fig. 2. If in this process of increasing μ for fixed h the zero in pressure occurs first for $t \neq 0$, then further increasing the modulus causes the solution to change from a one to a three contact region solution. This curve is labeled the 1-3 boundary. The 1-3 boundary occurs for thinner layers than the 1-2 boundary. The point at which the 1-2 and 1-3 boundary curves meet is also the in-

Downloaded 03 May 2010 to 171.66.16.31. Redistribution subject to ASME license or copyright; see http://www.asme.org/terms/Terms_Use.cfm

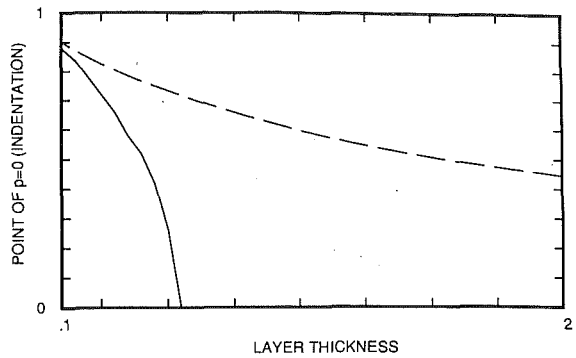


Fig. 3 The value of $c = d$ along the 1-3 boundary (solid) and the relative indentation for a single layer with a modulus of 4.0 (dashed)

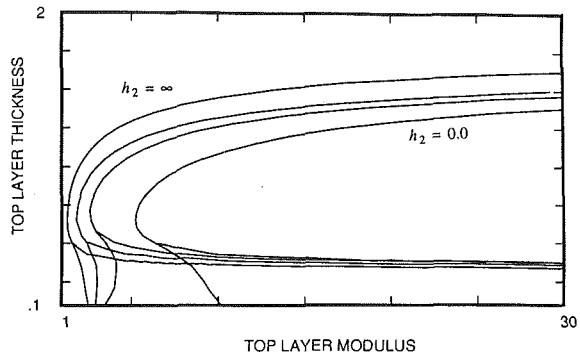


Fig. 5 Axisymmetric goemetry parameter space divisions for a midlayer modulus of 0.25 and thicknesses of ∞, 1.0, 0.5, and 0.0

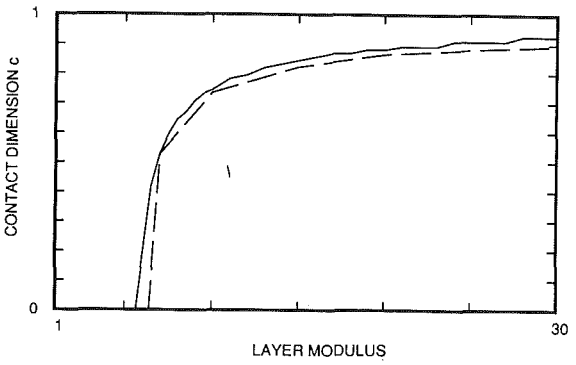


Fig. 4 The contact dimension c versus modulus along the 2-3 boundary (solid) and along the $h = 0.5$ line (dashed)

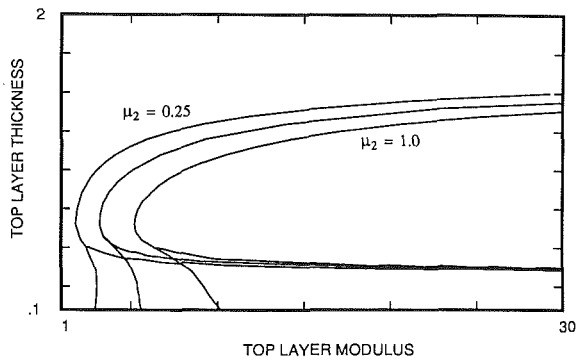


Fig. 6 Axisymmetric geometry parameter space divisions for a midlayer thickness of 1.0 and moduli of 0.25, 0.5, and 1.0.

tersection point with the 2-3 boundary curve, which is defined as the curve across which the number of roots of (62) changes from one to two. At exactly this triple point all three solutions exist for the contact dimensions of $c = d = 0$.

5.2.1 Dependence of Contact Regions on the Physical Parameters of the Layered Structure. Obtaining the two and three contact region solutions involves finding the contact region as well as the pressure distributions. The contact dimensions are easiest to determine on the boundaries of the zones in the (μ,h) plane. At points on the 1-2 boundary the value of c is zero, and this determines the edge of contact in the outer contact region. The parameter d determines the edge of contact in the inner contact region of the three contact region solution. On the 1-3 boundary, c is equal to d and the common value can be determined by finding the point at which the pressure first becomes zero as the modulus is increased for fixed h. Along the 2-3 boundary the value of c must be determined by finding the root of (62), and the value of d is zero. The dependence of c and d on the layer properties will be discussed next.

The solid curve in Fig. 3 shows the common value of $c = d$ as a function of the layer thickness along the 1-3 boundary. As the layer thickness approaches zero, the value of $c = d$ approaches unity. The behavior of the solution as the layer thickness approaches zero was discussed in detail in Shield and Bogy (1989).

At points on the 2-3 boundary in the (μ,h) plane, the contact dimension, d, is zero. Figure 4 shows the value of c versus layer modulus for points along the 2-3 boundary as well as along the line $h = 0.5$. In both cases, as the layer modulus increases, c approaches 1, that is, the extent of the contact goes to a ring at the outer corner of the indenter. On the basis of Fig. 2, this also the case for any fixed value of h as $\mu \to \infty$, not just along the 2-3 boundary. This means that regardless of the values of h, the contact can be forced to the limiting case of only contact at the outer edge of the indenter if the layered modulus is made sufficiently large.

5.2.2 The Effect of Second Layer. The previous sections considered one layer bonded to a substrate. In this section the (μ,h) parameter space divisions for two layers are examined. We only consider middle layers with moduli less than one. The top layer must be stiffer than the effective modulus of the midlayer substrate combination for multiple contact region solutions to exist, however, the minimum top layer modulus necessary for multiple contacts decreases for increasing middle-layer thickness. In the limit of an infinitely-thick middle layer, this minimum modulus is reduced, compared to the case of no middle layer, by a factor equal to the midlayer modulus. This can be seen in Fig. 5, which presents the results for a middle layer with $\mu_2 = 0.25$. The right-most curves show the results for a single layer ($h_2 = 0$). The left-most curves are for an infinitely-thick midlayer, and they agree with the one layer results with the modulus reduced by a factor of 0.25. The intermediate curves are for midlayer thicknesses of 1.0 and 0.5. The results for all intermediate thicknesses lie between the curves for zero and infinite thickness. The shape of the curves in Fig. 5 and the behavior of the solution for a given top layer are similar to those for the one layer case.

If the thickness of the midlayer is fixed and the parameter space curves are found for various moduli of the midlayer, the results obtained are as shown in Fig. 6. The right-most curve is the single layer result, since the midlayer has a modulus of one. As the modulus of the midlayer is reduced from one, the top layer modulus at which multiple contact region solutions exist is decreased. The division between the low-modulus, single contact zone and the high-modulus, multiple contact zone in the limit of zero midlayer modulus evidently moves to the straight line $\mu_1 = 0.0$ for thin layers. For thicker layers the separation will occur for some positive modulus. Plate theory also predicts the behavior for the thinner layers.

Downloaded 03 May 2010 to 171.66.16.31. Redistribution subject to ASME license or copyright; see http://www.asme.org/terms/Terms_Use.cfm

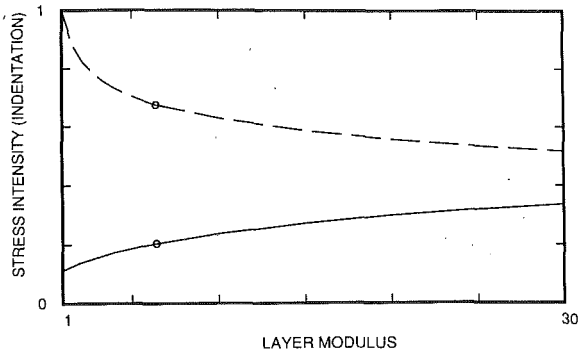


Fig. 7 The stress intensity factor at the corner of the indenter (solid) and the indentation (dashed) for a single layer with a thickness of 0.5; the circle marks the 1-2 boundary in Fig. 2

5.3 Stress Intensity Factor. The stress intensity factor defined in equation (74) is a measure of the strength of the pressure singularity at the corners of the indenter. Figure 7 shows the stress intensity factor versus layer modulus for a single layer of thickness 0.5. As the layer modulus is increased, the stress intensity increases. The circular symbol is for the parameter values at the 1-2 boundary in the (μ,h) parameter space of Fig. 2. Since the contact dimension c approaches one as the layer modulus increases for fixed-layer thickness, the increase in stress intensity factor is to be expected.

5.4 Indentation. It was mentioned previously that the displacements in the axisymmetric case are globally defined, thus the displacement caused by the fixed load on the indenter can be found. The indentation is inversely related to the effective modulus of the layered media. For comparison purposes, we normalize the indentation to the half-space result, thus an indentation of 1.0 means the effective modulus of the layered media is the same as the modulus of a half space of the substrate material. The indentation results are presented here only for the single layer case. For a top layer with modulus of 4.0, the indentation caused by the indenter is shown by the dashed line of Fig. 3 for a range of top layer thicknesses. The limiting values of the indentation are 1.0 at zero top-layer thickness and 0.25 for an infinitely-thick top layer. These values are all in the parameter zone where a single contact solution is valid. The indentation for a layer thickness of 0.5 as a function of the modulus is given by the dashed line in Fig. 7. For a top layer of unit modulus the indentation is one, and as the top layer modulus increases the indentation decreases to zero in the limit of an infinitely-stiff top layer.

6 Summary and Conclusions

A method for direct application of the technique of Erdogan and Gupta (1972) for the solution of a Cauchy-type singular integral equation was presented for annular regions. This solution was applied to the axisymmetric contact problem. The geometry of the contact region arose from the effects of the layered structure of the elastic material.

In the case of the simply-connected indenter, the layer properties determine the extent of the contact regions. This led to the consideration of a (μ,h) parameter space. The parameter space for a single layer is divided into three zones. In each zone the contact configuration is different. For low moduli layers there is only one contact configuration; the layer surface contacts the entire face of the indenter. Depending on the layer thickness, two contact configurations are possible for stiffer layers. Here, for thicker layers the two contact region solution is valid, for thinner layers the three contact region solution exists. In Shield and Bogy (1989) it was deduced that these are the only possible configurations.

In the axisymmetric geometry the presence of a logarithmic singularity in the kernel made special treatment of this term necessary. If the layer effects were large, the error induced by ignoring the logarithmic singularity was found to be small.

In Part II of this paper, the solutions presented here will be applied to the cases of annular indenters and cracks. These results will be compared to published results in the case of a homogeneous half space. The effect of the layered structure on the contact region(s) under the annular indenter will also be considered.

Acknowledgment

The first author, T.W.S., would like to thank the National Science Foundation and the University of California at Berkeley for fellowship support during the course of this research.

References

Abramowitz, M., and Stegun, I. A., 1965, *Handbook of Mathematical Functions*, Dover, New York.

Brekhovshikh, L. M., 1980, *Waves in Layered Media*, Academic Press, New York.

Erdogan, F., 1969, "Approximate Solutions of Systems of Singular Integral Equations," *SIAM Journal of Applied Mathematics*, Vol. 17, No. 6, pp. 1041–1059.

Erdogan, F., and Gupta, G. D., 1972, "On the Numerical Solution of Singular Integral Equations," ASME JOURNAL OF APPLIED MECHANICS, Vol. 29, pp. 525–534.

Erdogan, F., Gupta, G. D., and Cook, T. S., 1973, "Numerical Solutions of Singular Integral Equations," *Methods of Analysis and Solutions of Crack Problems*, Vol. 1, G. C. Sih, ed., Noordhoff Int. Publ., Leyden, pp. 368–425.

Gladwell, G. M., L., 1980, *Contact Problems in the Theory of Elasticity*, Sijthoff and Noordhoff, Maryland.

Gradshteyn, I. S., and Ryzhik, I. M., 1980, *Table of Integrals, Series, and Products*, Academic Press, New York.

Popov, G. Ia., 1962, "The Contact Problem of the Theory of Elasticity for the Case of a Circular Area of Contact," *PMM*, Vol. 26, No. 1, pp. 207–225.

Shield, T. W., and Bogy, D. B., 1989, "Multiple Contact Region Solutions for a Flat Indenter on a Layered Elastic Half Space: Plane-Strain Case," ASME JOURNAL OF APPLIED MECHANICS, Vol. 56, pp. 251–262.

APPENDIX

Listed here are the coefficients in the analytical solution for the Green's function for a single layer on a half space. The modulus ratio for the single layer is α, where

$$\alpha = \frac{\mu_s}{\mu_1}. \tag{A1}$$

$$\alpha_1 = 2(-4\alpha^2\nu^2 + 7\alpha^2\nu - 3\alpha^2 + 16\alpha\nu^2\nu_s - 12\alpha\nu^2 - 28\alpha\nu\nu_s + 22\alpha\nu + 12\alpha\nu_s - 10\alpha - 4\nu\nu_s + 3\nu + 4\nu_s - 3) \tag{A2}$$

$$\alpha_2 = 8(-\alpha^2\nu + \alpha^2 + 4\alpha\nu\nu_s - 2\alpha\nu - 4\alpha\nu_s + 2\alpha - 4\nu\nu_s + 3\nu + 4\nu_s - 3) \tag{A3}$$

$$\alpha_3 = 2(4\alpha^2\nu^2 - 7\alpha^2\nu + 3\alpha^2 - 4\alpha\nu^2 - 4\alpha\nu\nu_s + 10\alpha\nu + 4\alpha\nu_s - 6\alpha + 4\nu\nu_s - 3\nu - 4\nu_s + 3) \tag{A4}$$

$$\beta_1 = (4\alpha^2\nu - 3\alpha^2 - 16\alpha\nu\nu_s + 12\alpha\nu + 12\alpha\nu_s - 10\alpha + 4\nu_s - 3) \tag{A5}$$

$$\beta_2 = 4(-\alpha^2 + 4\alpha\nu_s - 2\alpha - 4\nu_s + 3) \tag{A6}$$

$$\beta_3 = 2(-8\alpha^2\nu^2 + 12\alpha^2\nu - 5\alpha^2 + 8\alpha\nu\nu_s - 4\alpha\nu - 4\alpha\nu_s + 2\alpha - 4\nu_s + 3) \tag{A7}$$

$$\beta_4 = (4\alpha^2\nu - 3\alpha^2 - 4\alpha\nu - 4\alpha\nu_s + 6\alpha + 4\nu_s - 3) \tag{A8}$$

Downloaded 03 May 2010 to 171.66.16.31. Redistribution subject to ASME license or copyright; see http://www.asme.org/terms/Terms_Use.cfm

Some Axisymmetric Problems for Layered Elastic Media: Part II—Solutions for Annular Indenters and Cracks

T. W. Shield[1]

D. B. Bogy
Mem. ASME

University of California,
Berkeley, Calif. 94720

In Part I, the multiple contact region solutions for an axisymmetric indenter were presented. The solution technique utilized integral transforms and singular integral equations. The emphasis there was the study of the conditions of contact as a function of the physical parameters of the indenter and the layered elastic half space. The method and results were similar to those for the analogous plane-strain problem that was studied in Shield and Bogy (1989). However, several differences in detail were required for the analysis of the axisymmetric geometry. In this Part II, the solution of Part I is used to study some related problems that have been considered previously in the literature for homogeneous half spaces. First we solve the problem of the axisymmetric annular indenter for the layered half space. Multiple contact region solutions are studied and the problem of an axisymmetric punch with internal pressure is solved for the layered half space and also for the special case of a layer with a traction-free lower surface. Finally, the problem of an annular crack in a homogeneous or layered structure is solved.

1 Introduction

The contact of an axisymmetric annular indenter with a homogeneous elastic half space was considered by Gladwell and Gupta (1979). They employed an approximate method that is valid for small values of the inner radius of the indenter. The leading term in their expansion is the solution for a simply-connected circular indenter. They employed two methods of calculating the coefficients in their expansion to approximate the stress-free boundary condition on the surface outside the indenter. The solution obtained here will be compared to these results, which were compared in Gladwell and Gupta (1979) with other approximate solutions in the literature.

The technique used here for treating the problem of an annular indenter on a layered half space takes advantage of the solution presented in Part I. This solution is based on the Erdogan and Gupta (1972) method of solution of Cauchy singular integral equations using an expansion in orthogonal polynomials. Before this method can be applied to the integral equations for the present problem, the equations must be transformed to the form of the equations treated in Erdogan and Gupta (1972). In Part I, the axisymmetric indenter was simply connected and the extent of contact was determined by the layered structure. It was found that three different contact region configurations are possible. These were called the one, "two," and "three" contact region configurations because of the similarity to the plane-strain solutions presented in Shield and Bogy (1989), the "two" contact region solution actually has a single annular contact region. It is clear that the solutions for an annular and a simply-connected indenter are the same in the "two" contact region case of the latter if the inner radius of the annular indenter is smaller than that of the noncontact region. For the case of a homogeneous half space, the results obtained here are compared to those presented in Gladwell and Gupta (1979).

The problem of an axisymmetric annular indenter with internal suction on an elastic layer was discussed by Theret et al. (1988). Their solution technique employed a method of alternating regions that starts with the solution for a homogeneous half space. The technique is an iterative one that utilizes a sequence of overlapping half spaces, each solution in the sequence removes from the boundary the undesired tractions of the previous partial sum. Here the problem of an axisymmetric annular indenter on a layered half sapce with internal pressure or suction is solved by application of the solution presented in Part I. The analogous solution for a single layer is obtained from this solution by taking the limit of vanishing shear modulus of the substrate. This solution is presented and numerical results are discussed for both positive and negative internal pressure.

[1] Currently at the Department of Theoretical and Applied Mechanics, University of Illinois, Urbana, Ill. 61801.

Contributed by the Applied Mechanics Division of THE AMERICAN SOCIETY OF MECHANICAL ENGINEERS for presentation at the Winter Annual Meeting, San Francisco, Calif., December 10–15, 1989.

Discussion on this paper should be addressed to the Editorial Department, ASME, United Engineering Center, 345 East 47th Street, New York, N.Y. 10017, and will be accepted until two months after final publication of the paper itself in the JOURNAL OF APPLIED MECHANICS. Manuscript received and accepted by the ASME Applied Mechanics Division, August 8, 1988.

Paper No. 89-WA/APM-31.

Copyright © 1989 by ASME

Downloaded 03 May 2010 to 171.66.16.31. Redistribution subject to ASME license or copyright; see http://www.asme.org/terms/Terms_Use.cfm

The problem of an annular crack in a homogeneous elastic space has been considered by Choi and Shield (1982). They used Betti's reciprocal theorem to derive the integral equations for the problem, which were then solved numerically. To improve the convergence of the value of the stress intensity factor at the inner crack tip, they used the M-integral to relate the two stress intensities to an integral over the crack surface.

Here the annular crack solution for a layered structure is obtained from the solution in Part I. However, numerical results are only presented for the case of a homogeneous medium and they are compared with those in Choi and Shield (1982).

2 The Problem Formulation

The formulation from Part I can be used directly for the problems considered here. Only the differences from Part I will be exhibited. Equations from Part I will be referred to here by (I.1), for example, to mean equation (1) of Part I.

In the crack problems, the first two of (I.7) are replaced by

$$\begin{aligned} \tau^1_{zz}(r,0) &= P, \quad r \in A_c \\ w^1(r,0) &= 0, \quad r \in \tilde{A}_c \end{aligned}, \tag{1}$$

where P is the internal pressure in the crack and A_c refers to the crack surface. We only consider cracks where the geometry is symmetric with respect to the $z=0$ plane, thus the last condition in (I.7) still applies.

Since the surfaces of the crack must meet at both tips, we require the slope of the crack surface, $\lambda(r)$, to satisfy,

$$0 = \int_{A_c} \lambda(r)\,dr. \tag{2}$$

This equation plays the role of the load equation (I.10) for the crack problem.

In the annular indenter problem, suction can be applied to the interior of the annular indenter to make the resultant load on the surface of the layered half space zero. This is a self-equilibrated solution, which is of interest for the case of a single layer with no tractions applied to the bottom surface $z=h$. Since the constants given in the Appendix of Part I are written in terms of the ratio μ_s/μ_1, only a simple limit is needed to evaluate $G(\xi)$ for $\mu_s = 0$ and the same solution method can be used for the layer as for the layered half space.

2.1 Reduction to a Singular Integral Equation: Crack Problems. For a penny-shaped or annular crack, the roles of the pressure and the surface slope in Part I must be reversed. The pressure is the known quantity, either from loading at infinity or from internal pressurization of the crack. The crack opening displacement, or the crack surface slope, $\lambda(r)$, are found by solving the appropriate singular integral equation. We only consider crack problems that are symmetric with respect to $z=0$, that is, either a crack in a homogeneous body or a crack centered in a layer that is bonded between identical half spaces. In these cases the surface $z=0$ outside of the cracked region experiences no normal displacement or shear traction. Thus, the Green's function given in Part I is applicable.

The analogous equation to (I.22) is

$$P = \int_{A_c} \lambda(t) \int_0^{+\infty} \frac{-1}{\xi G(\xi)} J_0(r\xi) J_1(t\xi)\xi\, d\xi t\, dt, \; r \in A_c, \tag{3}$$

and now A_c denotes the crack surfaces. We can rewrite equation (3) as

$$P = \frac{\mu_1}{\pi(1-\nu_1)} \int_{A_c} \lambda(t) g'_c(r,t)\,dt, \tag{4}$$

where

$$g'_c(r,t) = K'_c(r,t) - \pi t \int_0^{+\infty} N_c(\xi) J_0(r\xi) J_1(t\xi)\,d\xi \tag{5}$$

and

$$K'_c(r,t) = -\pi t \int_0^{+\infty} J_0(r\xi) J_1(t\xi)\xi\, d\xi. \tag{6}$$

The kernel $N_c(\xi)$ is given by

$$N_c(\xi) = \frac{1-\nu_1}{\mu_1 \xi G(\xi)} - 1, \tag{7}$$

where $G(\xi)$ is given by (I.19). This function is bounded and decays exponentially to zero as $\xi \to \infty$, making its inverse Hankel transform well defined.

To evaluate (6), consider $\partial/\partial t\, K(r,t)$, where $K(r,t)$ is given by (I.27), thus

$$K'_c(r,t) = \frac{\partial K(r,t)}{\partial t} = \frac{-2t}{t^2 - r^2}$$

$$\begin{cases} \mathbf{E}(r/t) & t > r \\ \dfrac{r}{t}\,\mathbf{E}(t/r) + \dfrac{t^2 - r^2}{rt}\,\mathbf{K}(t/r) & t < r \end{cases} \tag{8}$$

Following the same approach as in Part I we obtain

$$K'_c(r,t) = \frac{-2r}{t^2 - r^2} + k_c(r,t), \tag{9}$$

where

$$k_c(r,t) = 2r\left[\frac{h_c(r,t)+1}{t^2 - r^2}\right] \tag{10}$$

and

$$h_c(r,t) = -\begin{cases} \dfrac{t}{r}\,\mathbf{E}(r/t) & t \geq r \\ \mathbf{E}(t/r) + \dfrac{t^2 - r^2}{r^2}\,\mathbf{K}(t/r) & t < r \end{cases} \tag{11}$$

Again we define

$$K^*_{Ic}(r,t) = k_c(r,t) - \pi t \int_0^{+\infty} N_c(\xi) J_0(r\xi) J_1(t\xi)\,d\xi. \tag{12}$$

Equation (4) can be extended to negative values of r as in Part I, however, since we will only consider annular cracks, this is not necessary.

3 The Solution for Specific A_c

The numerical methods given in Part I and Shield and Bogy (1989) will be used directly in the following and, hence, will not be repeated here.

There are two factors that influence the number of contact regions: the geometry of the indenter and the presence of layers on the half space. An annular indenter can, at most, have contact over $c \leq r \leq 1$. It is also possible for an annular indenter to have incomplete contact due to the presence of a layer. This can produce a "four" or "six" contact region geometry that involves contact at both the inner and outer radii of the annular indenter but has annular separation region(s). These solutions will not be presented here; however, the parameter values for which they exist will be discussed when the results of the calculations are presented.

3.1 The Solution for an Annular Indenter: Complete Contact. In Part I the contact region was determined by the properties of the layer, and the "two contact region" solution resulted from separation over the central disk of the indenter. It is also clearly possible to have a two contact region solution if the indenter has an annular plan form. The method of solu-

Downloaded 03 May 2010 to 171.66.16.31. Redistribution subject to ASME license or copyright; see http://www.asme.org/terms/Terms_Use.cfm

tion used in Part I, Section 4.2 can be used here as well; only the form of the pressure is different. For the complete contact problem for the annular indenter, the extent of the contact is known *a priori*. The contact dimension c is determined by the size of the indenter not by the layer properties. The indenter has sharp corners at the inner and outer radii, making the pressure singular at these two points. Therefore, the form of the pressure for this case is

$$p(t)=\frac{t}{\sqrt{1-t^2}\sqrt{t^2-c^2}}\sum_{n=0}^{N-1} g_n T_n(s), \tag{13}$$

or in terms of s,

$$p(t)=\frac{2}{1-c^2}\frac{t}{\sqrt{1-s^2}}\sum_{n=0}^{N-1} g_n T_n(s), \tag{14}$$

where s is given by (I.58). Following the procedure in Section 4.2 of Part I, we find that the set of equations for the pressure under an annular punch is

$$0=\frac{2(1-\nu_1)}{\pi\mu_1(1-c^2)}\sum_{n=0}^{N-1} g_n\left[\frac{\pi}{N}\sum_{i=1}^{N} T_n(s_i)\frac{1}{s_i-y_k}\right.$$

$$\left.+\frac{1-c^2}{4}\int_{-1}^{+1}\frac{T_n(s)K_1^*(r_k,t)}{\sqrt{1-s^2}}\,ds\right],\ k=1,\ \ldots,\ N-1. \tag{15}$$

The remaining integral can be evaluated either with a Gaussian scheme suitable for the behavior of the integrand at the end points of the interval or with a trapezoidal integrator. This was discussed in detail in section on the treatment of the logarithmic singularities in the kernel $K_1^*(r, t)$. The additional equation needed is the load equation (I.10) approximated with the proper Gaussian quadrature method from Abramowitz and Stegun (1965).

Equations (15) give a valid solution for the half space case because the contact region is determined by the shape of the indenter and not the layer properties. The solution found for the annular punch agrees with the two contact region solution for a solid punch when the layer properties cause the annular punch solution to have zero pressure at the inner corner. This is one of the limits of the validity of the annular solution presented here. It is also possible for the pressure under the annular punch to vanish on a circle away from a corner due to the layered structure. These possibilities are discussed when the results are presented.

3.2 The Solution for an Internally Pressurized Annular Indenter. A simple addition to the solution of the previous section is a uniform pressure over the region $r\le c$. This pressure can be positive or negative to correspond to a pressure or suction on the inside of the annular indenter. The case of suction has application to biological problems as discussed by Theret et al. (1988).

The singular integral equation for the problem is still (I.28) but now the contribution to the known pressure over the region $r\le c$ must be included. The suitably modified equation is

$$0=\frac{1-\nu_1}{\pi\mu_1}\int_{A_c} p(t)g'(r,t)dt+\frac{1-\nu_1}{\pi\mu_1}\int_0^c P_i K'(r,t)dt$$

$$-\frac{1-\nu_1}{\mu_1}\int_0^c P_i t\int_0^{+\infty} N(\xi)J_1(r\xi)J_0(t\xi)\xi\,d\xi dt,\ r\in[c,\ 1], \tag{16}$$

where P_i is the internal pressure. The contribution to the surface slope due to the uniform pressure P_i has been broken into two parts. The second term in (16) is the solution for a uniform pressure over the region $r\le c$ on a half space of modulus μ_1 and Poisson's ratio ν_1. The third term is the effect of the finite thickness of the layer(s). The second integral can be evaluated analytically by considering the displacement for the half space solution, which is

$$w_2(r)=\frac{2(1-\nu_1)P_i c}{\pi\mu_1}$$

$$\begin{cases}\mathbf{E}(r/c) & r\le c\\ \dfrac{r}{c}\left[\mathbf{E}(c/r)-\left(1-\dfrac{c^2}{r^2}\right)\mathbf{K}(c/r)\right] & r>c\end{cases} \tag{17}$$

Differentiation with respect to r gives the surface slope for $r>c$ as

$$w_2'(r)=\frac{2(1-\nu_1)P_i}{\pi\mu_1}\left[\mathbf{E}(c/r)-\mathbf{K}(c/r)\right]\quad r>c. \tag{18}$$

Using this result in (16) and then applying the method of solution just presented, we find the set of linear equations for the unknown coefficients in the pressure expansion to be

$$0=\frac{2}{\pi(1-c^2)}\sum_{n=0}^{N-1} g_n\left[\frac{\pi}{N}\sum_{i=1}^{N} T_n(s_i)\frac{1}{s_i-y_k}\right.$$

$$\left.+\frac{1-c^2}{4}\int_{-1}^{+1}\frac{T_n(s)K_1^*(r_k,t)}{\sqrt{1-s^2}}\,ds\right]+P_i\left\{\frac{2}{\pi}\left[\mathbf{E}(c/r_k)\right.\right.$$

$$\left.\left.-\mathbf{K}(c/r_k)\right]-\int_0^c t\int_0^{+\infty} N(\xi)J_1(r_k\xi)J_0(t\xi)\xi\,d\xi dt\right\}$$

$$,k=1,\ \ldots,\ N-1. \tag{19}$$

The integral in the last term of (19) is evaluated with the sixteenth-order Gaussian scheme given in 25.4.30 of Abramowitz and Stegun (1965).

Again, this must be supplemented with the load equation (I.10) approximated numerically. This problem is not linear in the load, but is linear in the ratio of the load to $P_i\pi c^2$. If the load on the annular indenter is fixed at the value of one, then there is no resultant load on the surface of the layer if

$$P_i=\frac{-1}{\pi c^2}. \tag{20}$$

To calculate the surface displacements due to the internally-pressurized annular indenter, the surface displacement due to the internal pressure is added to the results of evaluating (I.72). Thus we find

$$w(r)=w_2(r)+\frac{1-\nu_1}{\mu_1}\left\{\int_c^{+1} g(r,t)p(t)t\,dt\right.$$

$$\left.+P_i\int_0^c t\int_0^{+\infty} N(\xi)J_0(r\xi)J_0(t\xi)d\xi dt\right\}, \tag{21}$$

where $w_2(r)$ is given by (17).

3.3 The Solution for an Annular Crack. The method of solution of the indentation integral equation can be directly applied to the integral equation for a crack (4) with only minor changes. Instead of the expanding the pressure, (13) is used to represent the crack surface slope as

$$\lambda(t)=\frac{t}{\sqrt{1-t^2}\sqrt{t^2-c^2}}\sum_{n=0}^{N-1} g_n T_n(s). \tag{22}$$

The approximation to (4) is then taken from (15), and is

$$P=\frac{2\mu_1}{\pi(1-\nu_1)(1-c^2)}\sum_{n=0}^{N-1} g_n\left[\frac{\pi}{N}\sum_{i=1}^{N} T_n(s_i)\frac{1}{s_i-y_k}\right.$$

Downloaded 03 May 2010 to 171.66.16.31. Redistribution subject to ASME license or copyright; see http://www.asme.org/terms/Terms_Use.cfm

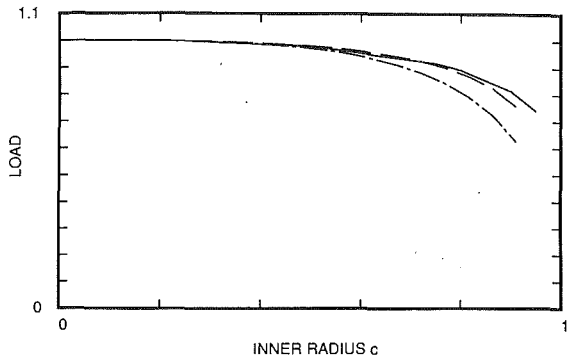


Fig. 1 The load necessary for a unit indentation versus the inner radius of the annular indenter: present solution (solid), Gladwell and Gupta (1979) moment method (dashed), and coefficient method (dot-dashed)

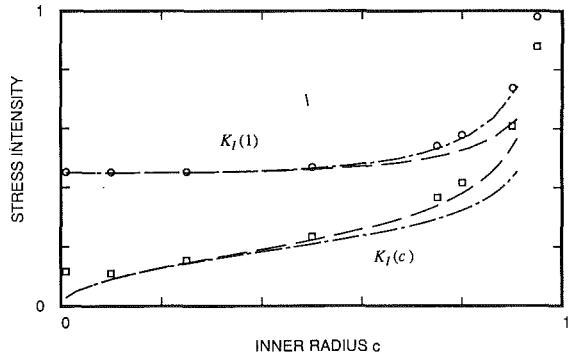


Fig. 2 The stress intensity factors at the inner $r = c$ and outer $r = 1$ corners of the annular indenter: present solution (symbols), Gladwell and Gupta (1979) moment method (dashed), and coefficient method (dot-dashed). The stress intensity at the inner corner is less than that at the outer corner.

$$+\frac{1-c^2}{4}\int_{-1}^{+1}\frac{T_n(s)K_{Ic}^*(r_k,t)}{\sqrt{1-s^2}}\,ds\Bigg], \quad k=1,\ldots,N-1. \quad (23)$$

The load equation is replaced by the condition that the crack must be closed at both ends, equation (2), whose approximation is

$$g_0 = 0. \quad (24)$$

3.4 Calculation of Other Quantities of Interest. The stress intensity at the point $r=c$ is zero for the simply-connected punch, but the annular punch has a sharp corner at $r=c$ with a nonzero stress intensity there. The stress intensity factor at this corner is given by

$$K_I(c) = \lim_{t\to c}\ (t-c)^{1/2}p(t). \quad (25)$$

The limiting value of $K_I(c)$ are 0 for $c\to 0$ and $K_I(1)$ as $c\to 1$. The stress intensity factor at $r=1$ is still given by (I.74).

In the case of an annular crack, the solution yields the surface slope of the crack face. The stress intensity factors at the crack tips are directly proportional to the singularity in the crack surface slope; thus, the previous equations also give the stress intensity factors for the annular crack solution if we replace $p(t)$ by $\lambda(t)$ in (I.74) and (25).

4 Results

The annular indenter solution will be compared with the approximation of Gladwell and Gupta (1979) for the half space case. Then the effect of a layered structure on the annular solution is found and a discussion of this behavior in the limits of $c=0$ and $c=1$ is presented. Finally, the stress intensities at the tips of an annular crack are determined.

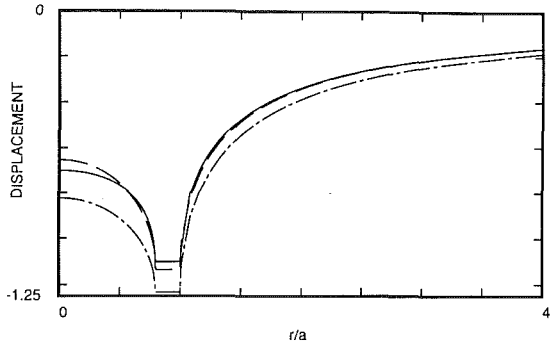


Fig. 3 The surface displacements due to an annular indenter of inner radius $c = 0.8$: present solution (solid), Gladwell and Gupta (1979) moment method (dashed), and coefficient method (dot-dashed)

4.1 Results for an Annular Indenter. A comparison of the pressure profiles obtained here with those of Gladwell and Gupta (1979) shows good agreement for small c. Because the indentation is proportional to the load, the reciprocal of the indentation for $L=1$ is the load needed to produce a unit indentation. Figure 1 shows the load required for a unit indentation as a function of the inner radius, c, and the results in Gladwell and Gupta (1979). These results are normalized to the case of a simply-connected circular punch ($c=0$). The values of stress intensity factor at the edges of the punch are plotted against the inner radius in Fig. 2. The lower curves are the stress intensity, $K_I(c)$, and the upper curves are $K_I(1)$, the values given by the present solution are marked by symbols. The lack of agreement in $K_I(c)$ for small c is due to the slow convergence of our method for small c. The surface displacement calculated using equation (I.72) is compared to the result in Gladwell and Gupta (1979) in Fig. 3 for $c=0.8$, where the agreement is poor. Good agreement is found for $c \le 0.5$. This is not unexpected since the solution in Gladwell and Gupta (1979) is an approximation for small c.

If an annular indenter contacts a layered structure, stationary receding contact as defined by Dundurs and Stippes (see Gladwell, 1980, p. 183) can occur and the contact region can be different from $[c, 1]$. Several possibilities exist. The simplest is separation around the corner $r=c$ so that the contact region becomes $[c', 1]$ with $c' \ge c$. This solution is similar to the two contact region solution for the simply-connected indenter and agrees exactly with that solution if the displacement of the surface for $r < c'$ is greater than the total indentation of the indenter. This type of annular solution is denoted as the incomplete contact annular solution in contrast to the complete contact annular solution characterized by positive pressure over the entire face of the indenter. The boundary of the zone of existence of this type of solution in the parameter plane is the set of points (μ, h) for which $K_I(c) = 0$ and the pressure is positive everywhere else.

It is also possible for separation to occur on a concentric annular region away from both corners, and then the contact region is $[c, d'] \cup [c', 1]$. For small values of c this contact region configuration is similar to the three contact regions of the simply-connected indenter as the notation c' and d' suggests. This solution is also similar to the two contact region solution for the plane-strain indenter if each "side" ($r < 0$ and $r > 0$) of the annular indenter is considered separately. Thus, this type of annular solution is called a "four contact region" solution. The boundary for the zone of existence of this type of solution is defined by the set of points in the (μ, h) parameter space where $p(t) = 0$ for $c < t < 1$.

For $c \approx 1$ and layers that are thin compared to $1-c$, a "six

Downloaded 03 May 2010 to 171.66.16.31. Redistribution subject to ASME license or copyright; see http://www.asme.org/terms/Terms_Use.cfm

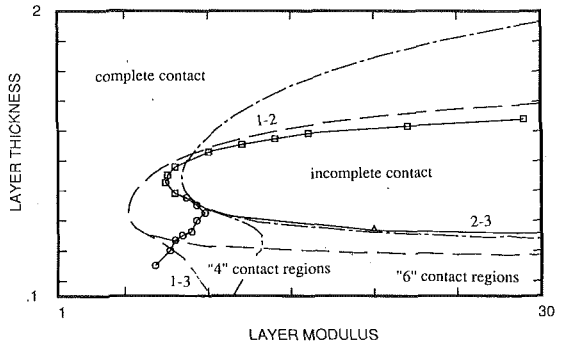


Fig. 4 The parameter space for an annular indenter of $c = 0.2$ contacting a single layer bonded to a half space showing the zones of existence of the types of solutions. The results for an axisymmetric simply-connected indenter (dashed) and plane-strain indenter (double-dashed) are also shown. In all cases $\nu = \nu_s = 1/3$. The symbols are discussed in the text.

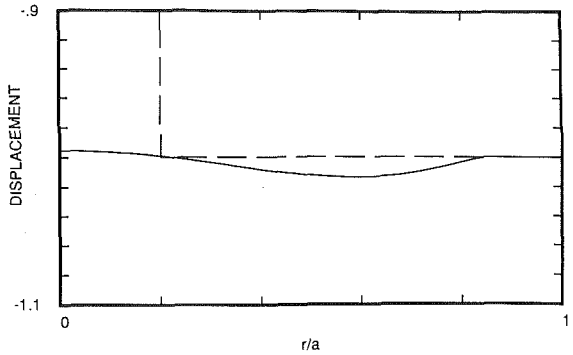


Fig. 5 The surface displacement under an annular indenter of inner radius $c = 0.2$ contacting a layer of modulus $\mu = 20.0$ and thickness $h = 0.535$. Here $c' = 0.845$ and $d' = 0.2$.

contact region'' solution is possible. In this case the contact region on each ''side'' of the annular indenter is similar to the three contact region solution for the plane-strain indenter and the contact region has the form $[c, c'] \cup [d', d''] \cup [c'', 1]$.

For an annular indenter of $c = 0.2$, the points on the boundary mentioned previously are marked by the symbols connected by solid lines in Fig. 4. The square symbols correspond to the points at which the stress intensity at $r = c$ vanishes. The circles mark the points at which the pressure vanishes on a circle away from the edges of the indenter. The single triangle marks a point where the incomplete and four contact solutions exists simultaneously. At this point $d' = c$ and $K_I(c) = 0$. The surface displacement for this case is shown in Fig. 5, where $c' = 0.845$ and $c = d' = 0.2$. The boundary of the zone of existence in Fig. 4 for the six contact region solution was not computed, but by limiting arguments (to follow) it can be deduced that it must lie in the zone of high modulus and very thin layers to the right of the circles and below the triangle. The results presented are only for one value of c, but since the results for the limits of $c = 0$ and $c = 1$ correspond to the simply-connected indenter (dashed curves in Fig. 4) and the plane-strain results (double-dashed curves in Fig. 4), respectively, the general behavior for all values of c may be deduced.

In the limit as $c \to 0$ the results for a simply-connected indenter become valid. The incomplete contact solution becomes the two contact solution of the simply-connected indenter and the four contact region solution becomes the three contact region, simply-connected indenter solution. Thus, the square symbols in Fig. 4 for this case correspond to the 1–2 curve for the simply-connected indenter, the circular symbols to the 1–3 curve and the triangular symbol to the 2–3 curve. In this limit the contact dimensions c' and d' become c and d of the simply-connected indenter solutions, respectively. Using the arguments presented in Shield and Bogy (1989), it can be concluded that there is no zone of existence for the six contact region solution in this limit.

The limit as $c \to 1$ is slightly more complicated since the scaling on h must be changed. Presently, the layer thickness is measured relative to the radius of the indenter. However, if for large c the annular indenter is to be regarded as two plane-strain indenters, h must be measured relative to the half-width of the indenters $(1 - c)/2$. For $c \approx 1$ this is small compared to a, thus the indenters can be treated individually. This rescaling of h means that the layer thickness must also be small compared to a before separation occurs. If this rescaling is performed and the limit taken, the results will correspond to the plane-strain results of Fig. 4 as follows. In the limit as $c \to 1$, the zone of existence of the incomplete solution becomes smaller, moves to larger moduli and thicker layers, and vanishes off the top-right edge of Fig. 4. The circles move to the 1–2 and 1–3 curves of the plane-strain results because the four contact region annular solution becomes the two contact region plane-strain solution and the six contact region solution becomes the three contact region solution. Part of the boundary of the zone of existence of the six contact region solution (which is not shown on Fig. 4) merges with part of the curve formed by the circles to form the 1–3 curve and the remainder of this boundary becomes the 2–3 curve. The merging of part of the circles with part of the boundary of the zone for the six contact region solution to form the 1–3 curve can be explained as follows: For any value of c slightly less than one, the solution for one ''side'' of the annular indenter can not be symmetric due to the presence of the ''other'' indenter. Thus, the transition from a one to a three contact region solution directly is not possible, a two contact region solution must be intermediate. But in the limit, where a 1–3 transition is possible, the curves coincide. This determined the nomenclature for the endpoints of the six region solution. In the limit of $c = 1$ we have $c' = -c''$ and $d' = -d''$ which correspond to c and d, respectively (if we map $[c,1]$ onto $[-1,1]$).

4.2 Results for an Internally Pressurized Annular Indenter. Figures 6–9 present the results of the calculations for an internally-pressurized annular indenter. Figure 6 shows the contact pressure and the surface displacement for the annular indenter on a homogeneous half space for three values of the internal pressure with $c = 0.5$. The solid lines are the zero internal pressure solution, which is the annular indenter solution of the previous section. The other two values of the internal pressure, one positive and one negative, where chosen such that the stress intensity factor at the inner and outer edges of the indenter vanish, respectively. The solution for the case of a layered half space is given in Fig. 7; only two curves are shown because the effect of the layer is to unload the inner edge of the indenter. Thus, the internal pressure needed to give $K_I(c) = 0$ is small, and this solution is practically the same as the solution for $P_i = 0$.

Figure 8 presents the internal pressure needed to unload the inner and outer edges of the indenter as a function of the inner radius. The circular and square symbols are for a homogeneous half space, the triangular symbols are for a layered structure. The circles and inverted triangles correspond to the values of P_i needed for $K_I(1) = 0$. The squares and upright triangles are at the values of internal pressure for $K_I(c) = 0$. The dashed line corresponds to the internal pressure for the self-equilibrated problem given by equation (20). For the values of $c = 0.2$ and 0.3 the upright triangles are at negative values of P_i, this is due to the layer effects unloading the inner edge of the indenter. Suction is necessary to keep the surface in complete contact with the indenter. For pressure outside of the range of values between the symbols in Fig. 8, separation will occur at one of the edges of the annular

Downloaded 03 May 2010 to 171.66.16.31. Redistribution subject to ASME license or copyright; see http://www.asme.org/terms/Terms_Use.cfm

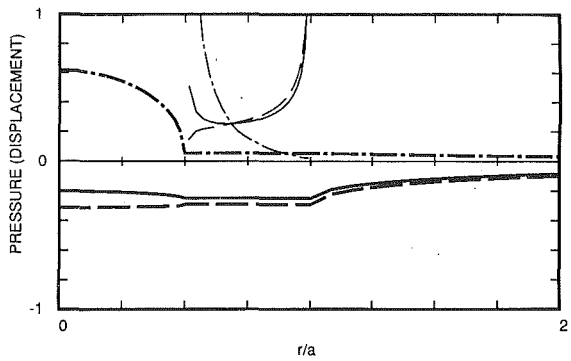


Fig. 6 The solution for an internally-pressurized annular indenter of inner radius $c = 0.5$ for the case of a homogeneous half space with $\nu = 1/3$ and internal pressure $P_i = 0.0$ (solid), 0.24 (dashed), and -1.80 (dot-dashed). The thicker curves are the displacement and the thinner curves are the pressure.

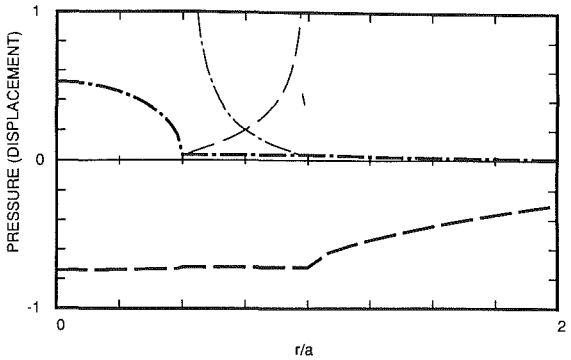


Fig. 7 The solution for an internally-pressurized annular indenter of inner radius $c = 0.5$ for the case of a layered half space with $\mu_1 = 10.0$, $h_1 = 1.0$, $\nu_1 = \nu_s = 1/3$ and internal pressure $P_i = 0.0293$ (dashed) and -1.34 (dot-dashed). The thicker curves are the displacement and the thinner curves are the pressure.

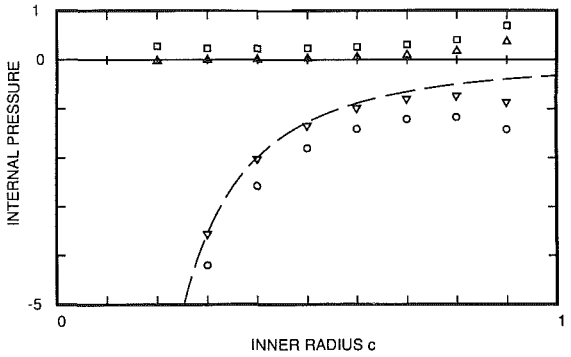


Fig. 8 The internal pressure needed to unload the inner edge (squares and upright triangles) or the outer edge (circles and inverted triangles) of an annular indenter of radius c. The circles and squares are for a homogeneous half space and the triangles are for a single layer on a half space with $\mu_1/\mu_s = 10.0$, $h_1/a = 1.0$ and $\nu_1 = \nu_s = 1/3$. The dashed line is the pressure necessary for self-equilibrium as given by (20).

indenter and the solution found here assuming complete contact is no longer valid. The techniques presented in Part I and Shield and Bogy (1989) could then be used to determine the extent of contact in these cases.

If an unsupported layer is considered, the applied tractions must be self-equilibrated or the assumption that the stresses decay to zero from the contact region will be violated. This problem can be solved by using the layered half-space equations with $\mu_s = 0$. The pressure and displacement results for an unsupported layer of thickness $h = 1.0$ are shown in Fig. 9 along with the results for the self-equilibrated problem on a homogeneous half space. The solution for this layer thickness

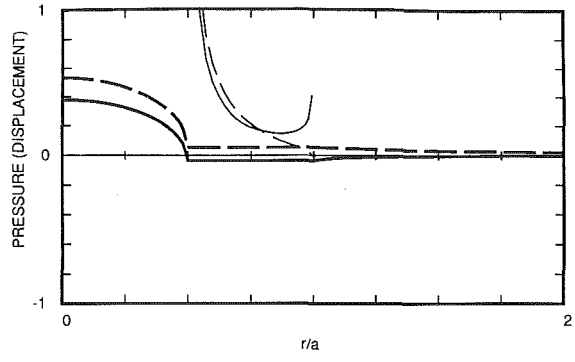


Fig. 9 A comparison of the self-equilibrated solutions for an internally-pressurized annular indenter ($c = 0.5$) for the case of a homogeneous half space (solid) and a layer of thickness $h = 1.0$ with a traction-free lower surface (dashed). The thicker curves are the displacement and the thinner curves are the pressure.

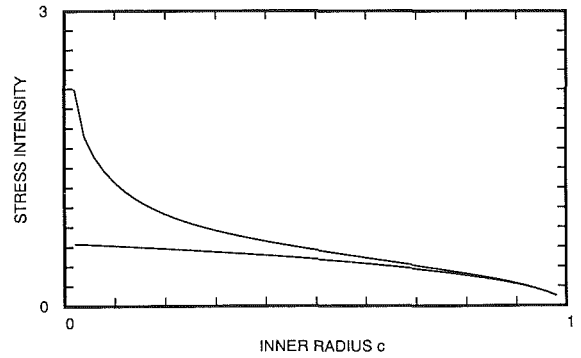


Fig. 10 The stress intensity at the tips of an annular crack versus the inner radius of the crack

has $K_I(1) \approx 0$, thus if the layer is thinner than $h = 1.0$, separation will occur at the outer edge for this value of c. The solutions for layer thicknesses greater than 1.0 will lie between the two shown in Fig. 9, because the half space solution corresponds to the case of $h = \infty$.

4.3 Results for an Annular Crack. The problem of an annular crack in an infinite homogeneous medium was also solved. Only the stress intensities at the tips of the annular crack are presented. These results are shown in Fig. 10 for the entire range of inner radius c. These results agree well with those of Choi and Shield (1982). The stress intensity at the inner tip is unbounded as $c \to 0$ due to the singular nature of the problem. As Choi and Shield note, since the stress intensity at the inner tip is always greater than that at the outer (for the case of internal pressure or axial tension at infinity) an annular crack will first grow to a penny-shaped crack before its outer radius can increase.

5 Summary and Conclusions

In this continuation of Part I, which extends the plane-strain results of Shield and Bogy (1989) to axisymmetry, we treated the problems involving contact of an annular indenter with a layered elastic half space. The effect of internal pressure on the annular indenter solution was also considered. The self-equilibrated problem for suction inside an annular indenter was found for a layer with a traction-free lower surface. Finally, the solutions found were applied to the case of an annular crack in a homogeneous body.

The results for an annular indenter contacting an elastic half

Downloaded 03 May 2010 to 171.66.16.31. Redistribution subject to ASME license or copyright; see http://www.asme.org/terms/Terms_Use.cfm

space showed good agreement with the results of Gladwell and Gupta (1979) for small c. The pressure distributions agreed well over a large range of the inner radius dimension. However, quantities such as stress intensity factors and displacements showed greater discrepancies at larger values of the inner radius. On the other hand, our calculation of the stress intensity factor at the inner corner for very small values of the inner radius converged slowly. The contact of an annular indenter on a layered structure was also considered and the zones in a (μ, h) parameter space of existence of the various possible contact region configurations were discussed. The limiting behavior of these zones was related to the results for the solid indenter of Part I and the plane-strain geometry of Shield and Bogy (1989).

The internal pressure needed to unload the inner and outer edges of an annular indenter was found for a homogeneous body and one layered structure. Beyond these values separation occurs, and the extent of contact must be determined.

The stress intensity factors at the tips of an annular crack in a homogeneous body were found to agree well with those of Choi and Shield (1982). The solution for an annular crack symmetrically placed in a layered structure was presented but no results were given.

Acknowledgment

The first author, TWS, would like to thank the National Science Foundation and the University of California at Berkeley for fellowship support during the course of this research.

References

Abramowitz, M., and Stegun, I. A., 1965, *Handbook of Mathematical Functions*, Dover, New York.

Choi, I., and Shield, R. T., 1982, "A Note on a Flat Toroidal Crack in an Elastic Isotropic Body," *Int. J. Solids Structures*, Vol. 18, No. 6, pp. 479–486.

Erdogan, F., and Gupta, G. D., 1972, "On the Numerical Solutions of Singular Integral Equations," ASME JOURNAL OF APPLIED MECHANICS, Vol. 29, pp. 525–534.

Gladwell, G. M. L., 1980, *Contact Problems in the Theory of Elasticity*, Sijthoff and Noordhoff, Maryland.

Gladwell, G. M. L., and Gupta, O. P., 1979, "On the Approximate Solution of Elastic Contact Problems for a Circular Annulus," *J. Elast.*, Vol. 9, pp. 335–348.

Shield, T. W., and Bogy, D. B., 1989, "Multiple Contact Region Solutions for a Flat Indenter on a Layered Elastic Half Space: Plane-Strain Case," ASME JOURNAL OF APPLIED MECHANICS, Vol. 56, pp. 251–262.

Theret, D. P., Levesque, M. J., Sato, M., Nerem, R. M., and Wheeler, L., 1988, "The Application of a Homogeneous Half-Space Model in the Analysis of Endothelial Cell Micropipette Measurements," *J. Biomech. Engrg.*, Vol. 110, No. 3, pp. 190–199.

Downloaded 03 May 2010 to 171.66.16.31. Redistribution subject to ASME license or copyright; see http://www.asme.org/terms/Terms_Use.cfm

C. Liu
Associate Professor of Mechanical Engineering,
Tamkang University,
Tamsui, Tapei
Taiwan

B. Paul
Asa Whitney Professor of Dynamical Engineering,
Department of Mechanical Engineering and Applied Mechanics,
University of Pennsylvania,
Philadelphia, Penna. 19104
Fellow, ASME.

Rolling Contact With Friction and Non-Hertzian Pressure Distribution

A numerical technique has been developed to deal with three-dimensional rolling contact problems with an arbitrary contact region under an arbitrary pressure. Results of this technique are checked against existing solutions for cases of Hertzian contact. A solution for a case of non-Hertzian contact is also presented. This numerical technique works satisfactorily for cases with small spin creepage. For cases of large spin creepage, we utilize a recent work (by the authors) for the limiting case of fully developed sliding contact.

1 Introduction

Figure 1 shows two elastically identical bodies in rolling contact. A normal compressive force N presses the two bodies together, and a contact region Ω develops as a result of this force. In this work, only cases of counterformal contact regions are studied. By definition, the contact surfaces in this case are essentially plane, and a set of Cartesian Coordinates x, y, and z may be chosen so that the x and y axes are in the plane of contact. The x axis coincides with the direction of rolling, the z axis points into the upper body of contact, and the y axis is chosen such that the x, y, z axes are right-handed.

The problem of determining the size and shape of the contact region Ω, and the normal contact pressure distribution has been studied extensively since the fundamental work of Hertz (1882). (See, for example, Love (1944, pp. 193–198), Timoshenko and Goodier (1970, pp. 409–420), Paul and Hashemi (1977, 1981), and Johnson (1985, pp. 84–152)).

If tangential forces (F_x, F_y) and twisting moment M_z are applied on the upper body, tangential tractions T_x, T_y develop in Ω. If the two bodies in contact are elastically identical, it has been shown (de Pater, 1962, p. 33; Kalker, 1967, pp. 9–11; Johnson, 1985, pp. 203–204) that the normal pressure between the two bodies are not influenced by the presence of tangential tractions. Throughout this paper, the two bodies in contact are assumed to be elastically identical.

2 Problem Formulation

As a result of the tangential forces F_x, F_y and the twisting moment M_z, the contact region Ω may be divided into two subregions. At a point (x, y) in the *slipped region* Ω_S, the upper body slips over the lower body. At a point (x, y) in the *locked region* Ω_L, there is no relative motion between the two bodies in contact. The boundary between these two regions is called the *separatrix*. According to Coulomb's law of friction, the surface tractions (T_x, T_y) must satisfy

$$(T_x^L)^2 + (T_y^L)^2 < (\mu p)^2, \text{ if } (x,y) \in \Omega_L \tag{1}$$

$$(T_x^S)^2 + (T_y^S)^2 < (\mu p)^2, \text{ if } (x,y) \in \Omega_S \tag{2}$$

where μ is the coefficient of friction, p is normal pressure, and indices S and L are used to denote variables associated with the slipped and locked regions, respectively.

The governing equations for a three-dimensional rolling contact problem were formulated by Johnson (1958). Kalker (1967, 1979) dealt with rolling contact problems with Hertzian pressure distributions by minimizing functionals. He extended his study to some non-Hertzian problems (Kalker, 1982).

The governing integral equations, for steady-state nominal rolling velocity V in the x direction, are conveniently expressed

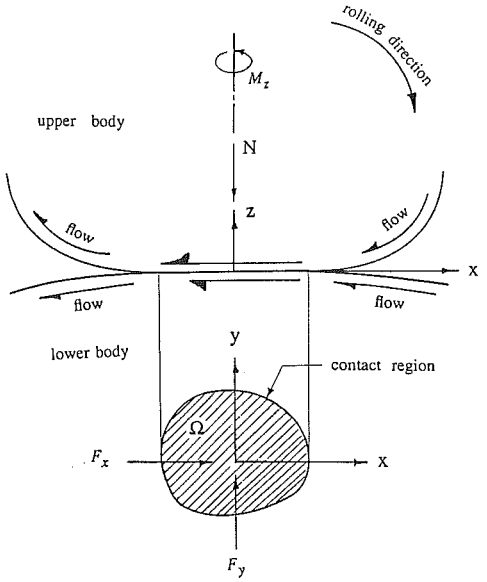


Fig. 1 Two bodies rolling over each other

Contributed by the Applied Mechanics Division of THE AMERICAN SOCIETY OF MECHANICAL ENGINEERS for presentation at the Winter Annual Meeting, San Francisco, Calif., December 10–15, 1989.

Discussion on this paper should be addressed to the Editorial Department, ASME, United Engineering Center, 345 East 47th Street, New York, N.Y. 10017, and will be accepted until two months after final publication of the paper itself in the JOURNAL OF APPLIED MECHANICS. Manuscript received by the ASME Applied Mechanics Division, June 23, 1988; final revision, November 22, 1988.

Paper No. 89-WA/APM-23.

Copyright © 1989 by ASME

Downloaded 03 May 2010 to 171.66.16.31. Redistribution subject to ASME license or copyright; see http://www.asme.org/terms/Terms_Use.cfm

using Eulerian (spatial) coordinates in the form (Kalker, 1967, p. 78; also see Liu, 1988):

$$s_x = v_x - \phi y + 2\frac{\partial}{\partial x}\int\int_{\Omega_L} [f_{xx}(x,y,\alpha,\beta)T_x^L(\alpha,\beta) + f_{xy}(x,y,\alpha,\beta)T_y^L(\alpha,\beta)]d\alpha d\beta + 2\frac{\partial}{\partial x}\int\int_{\Omega_S} [f_{xx}(x,y,\alpha,\beta)T_x^S(\alpha,\beta) + f_{xy}(x,y,\alpha,\beta)T_y^S(\alpha,\beta)]d\alpha d\beta \quad (3a)$$

$$s_y = v_y + \phi x + 2\frac{\partial}{\partial x}\int\int_{\Omega_L} [f_{yx}(x,y,\alpha,\beta)T_x^L(\alpha,\beta) + f_{yy}(x,y,\alpha,\beta)T_y^L(\alpha,\beta)]d\alpha d\beta + 2\frac{\partial}{\partial x}\int\int_{\Omega_S} [f_{yx}(x,y,\alpha,\beta)T_x^S(\alpha,\beta) + f_{yy}(x,y,\alpha,\beta)T_y^S(\alpha,\beta)]d\alpha d\beta \quad (3b)$$

where

$(s_x,s_y)V$ = relative velocity of upper surface with respect to lower surface at the point (x, y).
$(v_x,v_y)V$ = relative translational velocity of point (0,0) on the surface in the absence of elastic deformation.
ϕV = angular velocity of the upper surface relative to the lower surface in the absence of elastic deformation.
f_{ij} = tangential elastic displacement, in direction i, of lower body, at point (x,y) due to a unit tangential force in direction j at point (α, β): $(i,j = x \text{ or } y)$.

The quantities v_x, v_y, and ϕ are called the *longitudinal*, *lateral*, and *spin creepages*, respectively; and the vector $\mathbf{s} = (s_x,s_y)$ is called the *slip vector*.

Explicit expressions for the influence functions, f_{ij}, due to Cerruti, may be found in classical texts on the theory of elasticity, for example, Love (1944, p. 243), and in Johnson (1985, p. 69). A detailed derivation of equations (3*a*) and (3*b*) is given in Liu (1988) from which this paper has been abstracted.

The surface traction vector at a point in Ω on the lower body acts in the direction of the relative velocity vector of the point which is sliding over it. That is:

$$s_x T_y - s_y T_x = 0 \quad (4)$$

$$s_x T_x + s_y T_y > 0. \quad (5)$$

For a given contact patch, normal pressure distribution, creepage, and spin, the stresses and slippages are unknowns to be determined. The existence and uniqueness of solutions to equations and inequalities (1)–(5) have been established by Duvaut and Lions (1976) and Kalker (1977).

Cain (1950) (also see Ollerton (1963–1964)) has shown that the locked region must adjoin the leading edge of rolling. But the boundary (separatrix) between the locked region and the slipped region is, in general, unknown, and has to be determined in the process of solving the problem. The problem of determining the stresses and slippages given by equations (2)–(4), based on an assumed location of the separatrix, we call the *inner problem*. Based on a solution of the inner problem, we use expressions (1) and (5) to adjust the location of the separatrix; this we call the *outer problem*.

In the following section we describe numerical algorithms for solving the problem posed. These algorithms have been incorporated into a computer program named ROLCREEP.[1]

Recently, Kalker (1987) described a very powerful computer program called CONTACT, which is capable of solving the problem just described. CONTACT is based on a mathematical programming technique. Our program, ROLCREEP, is based on a direct solution technique. We offer our program as an alternative. A complete comparison of the relative advantages of the two programs is beyond the scope of this paper.

3 Inner Problem

Discretization. The most obvious way to deal with the partial derivatives on the right-hand sides of equations (3*a*) and (3*b*) is to differentiate under the integral signs. The stress profiles so obtained were found, for pure longitudinal creepage, (Singh, S., 1982) to be saw-tooth shaped rather than smooth as found experimentally (Haines and Ollerton, 1963). Therefore, instead of differentiating under the integral sign, Singh *integrated* with respect to x on both sides of equations (3*a*) and (3*b*) (treating y as a constant). We shall utilize this approach for the general case of rolling with spin. For a point $(x, y) \in \Omega_L$, the integration is from the point (x, y) to the leading edge (x_L, y) (i.e., x is the lower limit of integration and x_L is the upper limit).

$$\begin{Bmatrix} 0 \\ 0 \end{Bmatrix} = \begin{Bmatrix} v_x(x_L - x) - \phi(x_L - x)y \\ v_y(x_L - x) + \frac{1}{2}\phi(x_L^2 - x^2) \end{Bmatrix} + 2\int\int_{\Omega_L} \begin{bmatrix} g_{xx} & g_{xy} \\ g_{yx} & g_{yy} \end{bmatrix} \begin{Bmatrix} T_x^L \\ T_y^L \end{Bmatrix} d\alpha \; d\beta + 2\int\int_{\Omega_S} \begin{bmatrix} h_{xx} & h_{xy} \\ h_{yx} & h_{yy} \end{bmatrix} \begin{Bmatrix} T_x^S \\ T_y^S \end{Bmatrix} d\alpha \; d\beta, \quad (x,y) \in \Omega_L \quad (6a)$$

If $(x, y) \in \Omega_S$, the integration is from (x, y) to the separatix (x_S, y), i.e.,

$$\int_x^{x_S} \begin{Bmatrix} s_x \\ s_y \end{Bmatrix} dx = \begin{Bmatrix} v_x(x_S - x) - \phi(x_S - x)y \\ v_y(x_S - x) + \frac{1}{2}\phi(x_S^2 - x^2) \end{Bmatrix} + 2\int\int_{\Omega_L} \begin{bmatrix} g_{xx} & g_{xy} \\ g_{yx} & g_{yy} \end{bmatrix} \begin{Bmatrix} T_x^L \\ T_y^L \end{Bmatrix} d\alpha \; d\beta + 2\int\int_{\Omega_S} \begin{bmatrix} h_{xx} & h_{xy} \\ h_{yx} & h_{yy} \end{bmatrix} \begin{Bmatrix} T_x^S \\ T_y^S \end{Bmatrix} d\alpha \; d\beta \quad (x,y) \in \Omega_L \quad (6b)$$

where the functions g and h represent differences between Cerruti influence functions evaluated at the upper and lower limits. Typical expressions for these functions are

$$g_{xx}(x,y,\alpha,\beta) = f_{xx}(x_L,y,\alpha,\beta) - f_{xx}(x,y,\alpha,\beta) \quad (7a)$$

$$h_{xx}(x,y,\alpha,\beta) = f_{xx}(x_S,y,\alpha,\beta) - f_{xx}(x,y,\alpha,\beta). \quad (7b)$$

[1] The FORTRAN code for ROLCREEP is available from B. Paul.

Downloaded 03 May 2010 to 171.66.16.31. Redistribution subject to ASME license or copyright; see http://www.asme.org/terms/Terms_Use.cfm

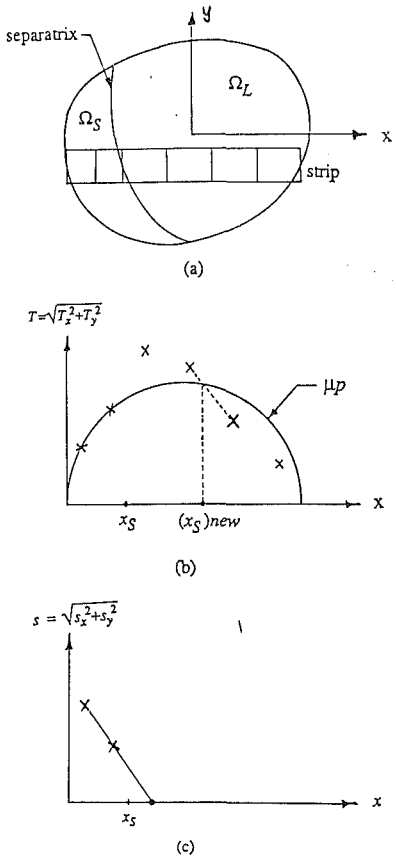


Fig. 2 (a) The current separatrix and a strip of a contact patch, (b) new x coordinate of the separatrix predicted by criterion 1, and (c) the point s = 0 obtained by linear extrapolation

To evaluate the double quadratures shown in equations (6*a*) and (6*b*), the contact patch is divided into horizontal strips. Each strip is further divided into rectangular cells (a typical strip is shown in Fig. 2(*a*)). The tractions and slippages are assumed to be uniform within each cell and may be placed outside of the integral sign. The remaining integrals may be evaluated analytically (Kalker 1979, p. 1306).

Each of the integrals in equations (6*a*) and (6*b*) reduces to a linear combination of the unknowns (T's and T's). Each coefficient of T_x and T_y in these linear combinations is found from a double quadrature over a cell. If one generates N_S (N_L) cells in the slipped (locked) region, the discritization of equations (6*a*) and equations (6*b*) leads to $2N_S + 2N_L$ linear algebraic equations. If the analytical results of double quadratures are arranged in matrices **A**, **B**, **C**, and **D**, then these linear equations may be written as

$$\mathbf{0} = \mathbf{e} + \mathbf{A}\,\mathbf{t}^L + \mathbf{B}\,\mathbf{t}^S \tag{8a}$$

$$\mathbf{W}\,\mathbf{s} = \mathbf{q} + \mathbf{C}\,\mathbf{t}^L + \mathbf{D}\,\mathbf{t}^S \tag{8b}$$

where **e** and **q** represent the terms containing creepages and spins shown on the right-hand sides of equations (6*a*) and (6*b*), **s** is the slippage vector, $\mathbf{t}^L$ and $\mathbf{t}^S$ are traction vectors, and **W** is a matrix containing functions of the width of cells in Ω_S.

For a suitable discretization scheme, the number of unknowns should be equal to the number of equations. For a cell in the locked region, there are two unknown tractions $T_x{}^L$, and $T_y{}^L$ to be determined. For a cell in the slipped region, the unknowns are $T_x{}^S$, $T_y{}^S$, s_x, and s_y. If N_S and N_L denote the number of cells in Ω_S and Ω_L, respectively, then the total number of unknowns is $4N_S + 2N_L$. We have already seen that $2N_S + 2N_L$ linear equations, given by equations (8*a*) and (8*b*), are available. For every cell in the slipped region, there are two additional equations; viz. equations (2) and (4). Hence, the total number of equations is also $4N_S + 2N_L$.

Iterative Technique to Solve Equations (2) and (4). Equation (8*a*) may be expressed in the form

$$\mathbf{t}^L = -\mathbf{A}^{-1}\mathbf{e} - \mathbf{A}^{-1}\mathbf{B}\mathbf{t}^S. \tag{9}$$

Using equation (9), one may show that equation (8*b*) reduces to

$$\mathbf{s} = \mathbf{W}^{-1}[\mathbf{q} - \mathbf{C}\mathbf{A}^{-1}\mathbf{e} + (\mathbf{D} - \mathbf{C}\mathbf{A}^{-1}\mathbf{B})\mathbf{t}^S] \equiv \mathbf{h} + \mathbf{G}\mathbf{t}^S \tag{10}$$

where **h** and **G** are defined implicitly by equation (10). Equations (9) and (10) show that if $\mathbf{t}^S$ is known, then all other unknowns may be found. Therefore, one may treat $\mathbf{t}^S$ as a vector of primary unknowns.

In order to solve for the primary unknowns $\mathbf{t}^S$, we have to make use of the nonlinear equations (2) and (4). We have shown that the slippages in equations (2) may be expressed in terms of $\mathbf{t}^S$ (see equation (10)). Therefore, $\mathbf{t}^S$ may be obtained by solving (2), (4), and (10).

The nonlinearities shown in equations (2) and (4) suggest that an iterative procedure is required. The Newton-Raphson technique has been utilized to solve these equations. It is described in most textbooks on numerical methods. (We refer to Dählquist and Björck (1974, pp. 219–215) and Paul (1979, pp. 609–615) for descriptions of this standard technique).

If **p** is the pressure vector, its first N_L elements are for cells in Ω_L, and the remaining N_S elements are for cells in Ω_S. Also, if $\mathbf{t}^S$ and **s** are partitioned such that their first N_S elements are x components of tractions and slippages, respectively, and the second N_S elements are y components, then equations (4) and (2) may be rewritten as

$$f_i(T_i^S, T_{i+N_S}^S, s_i, s_{i+N_S}) = s_i T_{i+N_S}^S - s_{i+N_S} T_i^S = 0 \qquad i = 1,2,\ldots,N_S \tag{11}$$

$$f_{i+N_S}(T_i^S, T_{i+N_S}^S) = (T_i^S)^2 + (T_{i+N_S}^S)^2 - (\mu p_{i+N_L})^2 = 0 \qquad i = 1,2,\ldots,N_S. \tag{12}$$

In the Newton-Raphson procedure we must start from an assumed solution for $\mathbf{t}^S$, which is systematically updated in each iteration of the process. At any stage, $\mathbf{t}^S$ will be called the current $\mathbf{t}^S$. To update $\mathbf{t}^S$, we must solve the matrix equation

$$\mathbf{J}\Delta\mathbf{t}^S = -\mathbf{f} \tag{13}$$

where $\Delta\mathbf{t}^S$ is the required increment of $\mathbf{t}^S$, **f** is the vector containing the current values of the functions defined by the equality sign in (11) and (12) and **J** is the current Jacobian matrix given by

$$\mathbf{J} = \frac{\partial(f_1, f_2, \ldots, f_{2N_S})}{\partial(T_1^S, T_2^S, \ldots, T_{2N_S}^S)} = \begin{bmatrix} \frac{\partial f_1}{\partial T_1^S} & \frac{\partial f_1}{\partial T_2^S} & \cdots & \frac{\partial f_1}{\partial T_{2N_S}^S} \\ \frac{\partial f_2}{\partial T_1^S} & \frac{\partial f_2}{\partial T_2^S} & \cdots & \frac{\partial f_2}{\partial T_{2N_S}^S} \\ \vdots & \vdots & \cdots & \vdots \\ \frac{\partial f_{2N_S}}{\partial T_1^S} & \frac{\partial f_{2N_S}}{\partial T_2^S} & \cdots & \frac{\partial f_{2N_S}}{\partial T_{2N_S}^S} \end{bmatrix}. \tag{14}$$

To evaluate the partial derivatives in the Jacobian matrix, it is convenient to rewrite equation (10) in the following form

$$s_i = h_i + \sum_{k=1}^{2N_S} G_{ik} T_k^S, \quad i = 1,2,\ldots,N_S. \tag{15}$$

Downloaded 03 May 2010 to 171.66.16.31. Redistribution subject to ASME license or copyright; see http://www.asme.org/terms/Terms_Use.cfm

By taking partial derivatives with respect to T_j^S, one may show that

$$\frac{\partial s_i}{\partial T_j^S} = \frac{\partial}{\partial T_j^S} \sum_{k=1}^{2N_S} G_{ik} T_k^S = G_{ij}, \quad i = 1,2, \ldots, N_S. \tag{16}$$

From equations (11), (12), and (16), we find the partial derivatives needed in equation (14) to be

$$\frac{\partial f_i}{\partial T_j^S} = G_{ij} T_{i+N_S} + s_i \delta_{(i+N_S)j} - G_{(i+N_S)j} - s_{i+N_S} - s_{i+N_S} \delta_{ij},$$

$$i = 1,2, \ldots, N_S \tag{17}$$

$$\frac{\partial f_{i+N_S}}{\partial T_j^S} = 2\delta_{ij} T_i^S + 2\delta_{(i+N_S)j} T_{i+N_S}^S, \quad i = 1,2, \ldots, N_S \tag{18}$$

where repeated subscripts do not imply summation, and δ_{ij} is the Kronecker delta defined by

$$\delta_{ij} = \begin{cases} 0 \text{ if } i \neq j \\ 1 \text{ if } i = j \end{cases}. \tag{19}$$

Within every step of iteration (utilizing the current $\mathbf{t}^S$), one may calculate current values of $\mathbf{s}$ by using equation (10) or equation (15), $\mathbf{f}$ from equations (11) and (12), $\mathbf{J}$ from equations (17) and (18), and then obtain $\Delta \mathbf{t}^S$ by solving equation (13).

It is known that a suitable initial guess is crucial for the success of the Newton-Raphson technique. We may begin with the following traction, which corresponds to a rigid body translation:

$$(T_x^S, T_y^S) = (1/\nu)(v_x, v_y)\mu p \tag{20}$$

where

$$\nu = \sqrt{v_x^2 + v_y^2}. \tag{21}$$

This initial traction may be used at every point in Ω_S. Equation (20) represents a suitable initial estimate only for cases where the spin creepage ϕ is relatively small. For larger values of ϕ, equation (20) could be modified appropriately. We have confined out attention in this paper to such cases of small ϕ.

For large values of ϕ, the spin moment M_z approaches the values associated with fully developed sliding. A means of finding this limiting value, which depends upon F_x and F_y, is given in Liu and Paul (1988).

4 Outer Problem

Given the location of the separatrix, the corresponding stresses and slippages may be obtained by solving the inner problem. We shall next describe an iterative procedure which permits us to adjust the shape and location of the separatrix, when necessary.

Initial Guess for the Location of Separatrix. Extending an idea introduced by Kalker (1973), for the case of pure longitudinal creepage in the direction of rolling (x axis), the initial candidate separatrix is assumed (Liu 1988) to be the trailing edge shifted forward by a distance $\bar{x}_S$ which is proportional to the quantity $G\bar{a}\nu/(\mu p_m)$, where $\bar{a}$ is the half width of the contact patch in the x direction through the point of maximum pressure (for an elliptic contact patch, $\bar{a}$ is one of the semi-axes of the ellipse), and ν is defined by equation (21). In the algorithm, we use the following value of $\bar{x}_S$ as initial guess

$$\bar{x}_S = \frac{G\bar{a}\nu}{3\mu p_m}. \tag{22}$$

Adjusting the Location of Separatrix. For an arbitrary cell in the locked region, we require the traction to be less than the limiting friction; i.e., to satisfy inequality (1). In the slipped region, the tractions must satisfy inequality (5). Finally, the slippage is required to be zero along the separatrix. These three requirements are used to iteratively adjust the shape and location of the separatrix, as will be described next.

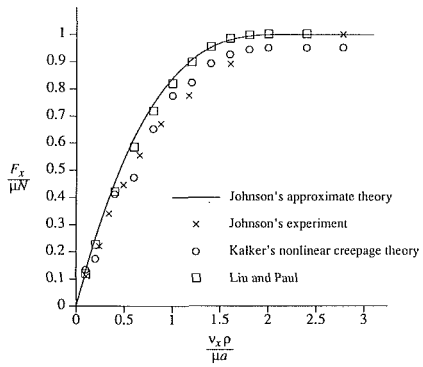


Fig. 3 Longitudinal creepage curve for rolling contact of two elastically identical bodies with circular contact patch

Criterion 1. When the tractions (T_x^L, T_y^L) are higher than μp (i.e., inequality (1) is violated), we must adjust the location of the separatrix for the next iteration. We find that such high tractions always first appear in the cells adjacent to the separatrix. Therefore, we move the separatrix toward the leading edge so that condition (1) is satisfied everywhere in the current locked region. By linear interpolations, locations where tractions are equal to μp are found and chosen to be the new location of the separatrix (see Fig. 2(b)). If tractions are found to be above the limiting values in every cell of a given strip, it is likely that there is no locked region in this strip, i.e., the separatrix is located at the leading edge.

Criterion 2. Beginning with cells adjacent to the separatrix, one may move toward the trailing edge to check if the condition (5) is fulfilled. Generally, we find that condition (5) is first violated in cells adjacent to the separatrix. Therefore, we chose the midpoint between the center of the last cell in which the condition is violated and the center of the first cell in which it is satisfied to be the new x coordinate of the separatrix.

Criterion 3. Since $s = \sqrt{s_x^2 + s_y^2}$ must vanish everywhere in the locked region, $s = 0$ along the separatrix. We therefore examine the current distribution of s along each strip in the neighborhood of the current separatrix. In particular, (see Fig. 2(c)), we find the point where $s = 0$ by linear extrapolation of the current values of s at the two cells in each strip closest to the current separatrix, but still within the slipped region. This adjustment to the separatrix is made only if the required change exceeds the cell width in the slipped region.

5 Results and Discussion

We now check the solutions obtained by our numerical technique against some known numerical results, as well as for a non-Hertzian contact case for which no prior solutions exist.

For longitudinal creepages with a circular contact patch, we show creepage curves in Fig. 3, along with data from experiments and from an approximate theory by Johnson (1958), and from a computer program of Kalker (see Goree, 1978) based upon a nonlinear creepage theory. In Fig. 3, the variable ρ is defined by

$$1/\rho = (1/4)(1/R_1 + 1/R_1' + 1/R_2 + 1/R_2') \tag{23}$$

where (R_1, R_1') and (R_2, R_2') are principal radii of curvature of the two bodies in contact. In Fig. 4, we show longitudinal stress distributions for a case of longitudinal creepage over a

Downloaded 03 May 2010 to 171.66.16.31. Redistribution subject to ASME license or copyright; see http://www.asme.org/terms/Terms_Use.cfm

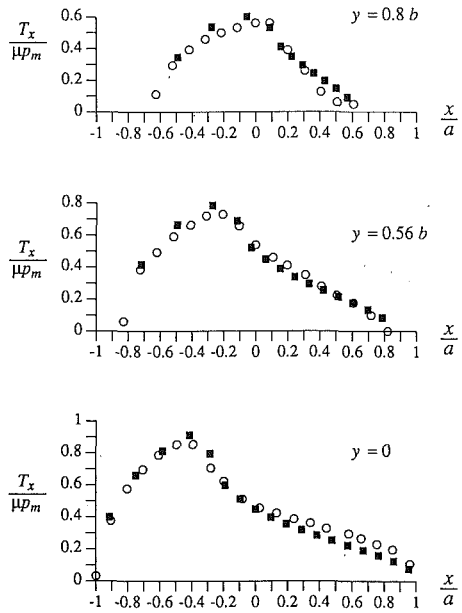


Fig. 4 Comparison with Haines and Ollerton's photoelastic results. Solid box—Liu and Paul; circle—Haines and Ollerton's experiment. $a = b = 1.237 \times 10^{-2} m$ (0.487 in.), $\mu = 0.2$, $\nu_x = 0.01$

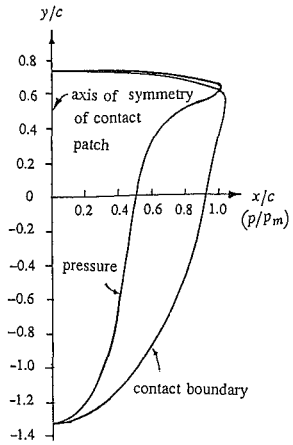


Fig. 5 Shape of a non-Hertzian contact patch (for a wheel-rail interaction, see Paul and Hashemi, 1977, p. 26). The origin has been moved to the centroid of pressure. $c = \sqrt{A/\pi} = 7.681 \times 10^{-3} m$ (0.3024 in.), where A is area of contact patch. Also shown is the pressure distribution along the y axis, $p_m = 2.102 \times 10^6$ Pa (3.048×10^5 psi).

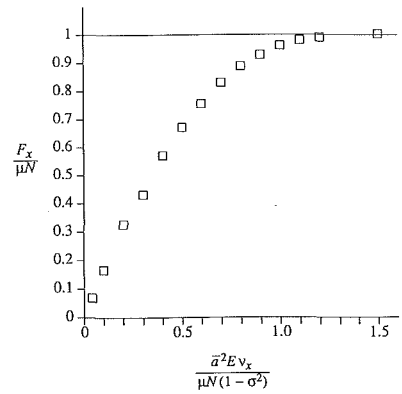


Fig. 6 Longitudinal force versus creepage for longitudinal rolling contact of two elastically identical bodies with contact patch shown in Fig. 5. $\bar{a}$ is the half width in the x direction through the point of maximum pressure p_m. $\bar{a} = 7.53 \times 10^{-3}$ m (0.2965 in.)

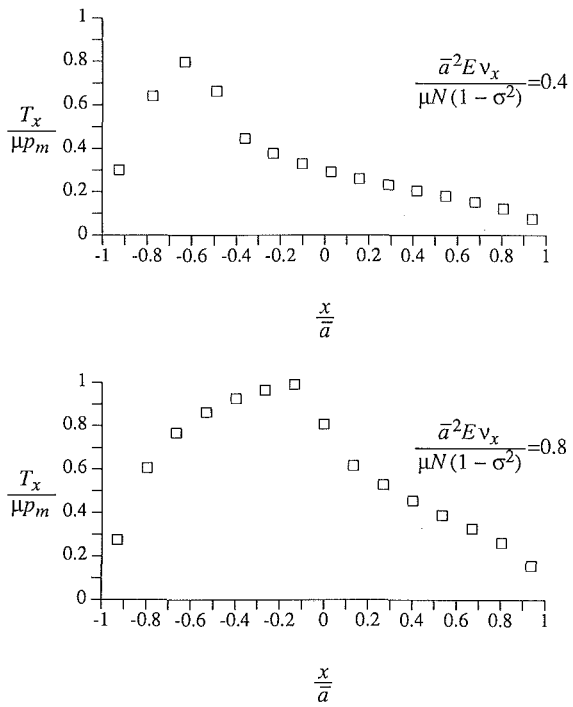


Fig. 7 Longitudinal traction along the strip of maximum pressure for the contact patch shown in Fig. 5. The half length of this strip is $\bar{a}$. $\nu_y = \phi = 0$.

circular contact patch, along with data from photoelastic experiments of Haines and Ollerton (1963).

We now proceed to show the results of a non-Hertzian contact. The contact patch and pressure along the y axis shown in Fig. 5 correspond to a counterformal contact between a wheel and rail determined by Paul and Hashemi (1977). The curve of longitudinal force F_x versus longitudinal creepage ν_x is shown in Fig. 6. Traction distributions in the x direction through the point of maximum pressure are shown in Fig. 7, for different values of the creepages ν_x. In Figs. 8–10, we show results for longitudinal creepage with spin. The separatrices for different values of spin are shown in Fig. 8; longitudinal and lateral tractions are shown in Figs. 9 and 10. The separatrices shown in Fig. 8 have been smoothed (by eye) within the resolution of the computed points, which is known to be one cell width.

In all the creepage curves shown, the relationship between the force and creepage is linear when creepage is small. This also true for computed values of M_z versus ϕ, with fixed values of F_x and F_y (see Fig. 11). For larger values of ϕ, it is more difficult to make reasonable initial guesses for either the inner or the outer iterations. For the case of a circular contact patch, Kalker (1967, p. 132) has shown that the locked region may not even be connected. Because the initial guess (in the iteration procedure) given by equation (20) corresponds to a rigid body translation without rotation, the chosen procedure converged only for the case of small spin. Although we have suggested how this initial guess may be improved, we have not yet implemented that improvement.

By comparing with the creepage curves (without spin) shown before (e.g., Fig. 6), we expect to see the curves become nonlinear as ϕ increases, and approach upper limits on M_z. Unlike the case of pure creepage without spin, the upper limits are not known *a priori*. Therefore we use the recently obtained results for gross sliding (i.e., fully developed slippage with no locked region) between two bodies in contact (Liu and Paul, 1988) to bracket all cases between known solutions for small and large spins.

Downloaded 03 May 2010 to 171.66.16.31. Redistribution subject to ASME license or copyright; see http://www.asme.org/terms/Terms_Use.cfm

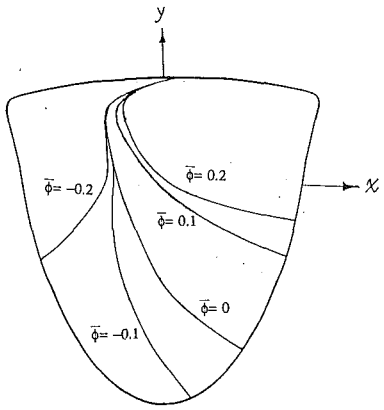


Fig. 8 Locations of separatrices for various values of $\bar{\phi}$ for the contact patch shown in Fig. 5, with longitudinal creepage ($\bar{V}_x = \bar{a}^2 E\nu_x/[\mu N(1-\sigma^2)] = 0.6$, $\nu_y = 0$). $\bar{\phi} = \bar{a}^3 E\phi/[\mu N(1-\sigma^2)]$

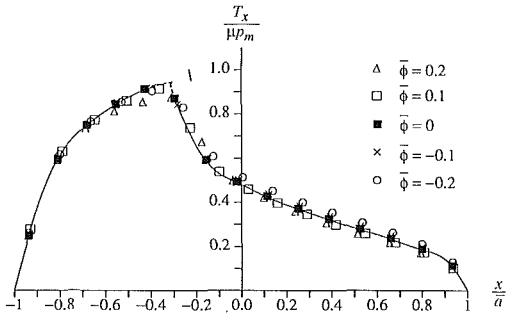


Fig. 9 Longitudinal tractions for various values of $\bar{\phi}$ along the strip of maximum pressure for the contact patch shown in Fig. 5, with longitudinal creepage ($\nu_y = 0$, $\bar{\nu}_x = \bar{a}^2 E\nu_x/\mu N(1-\sigma^2) = 0.6$). The half length of this strip is $\bar{a}$. $\bar{\phi} = \bar{a}^3 E\gamma/\mu N(1-\sigma^2)$.

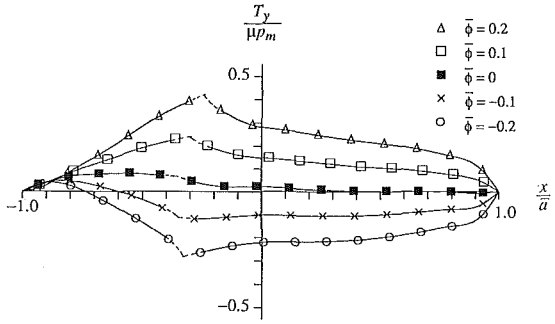


Fig. 10 Lateral tractions for various values of $\bar{\phi}$ along with the strip of maximum pressure for the contact patch shown in Fig. 5, with longitudinal creepage ($\nu_y = 0$, $\bar{\nu}_x = \bar{a}^2 E\nu_x/\mu N(1-\sigma^2) = 0.6$). The half length of this strip is $\bar{a}$. $\bar{\phi} = a^3 E\phi/\mu N(1-\sigma^2)$.

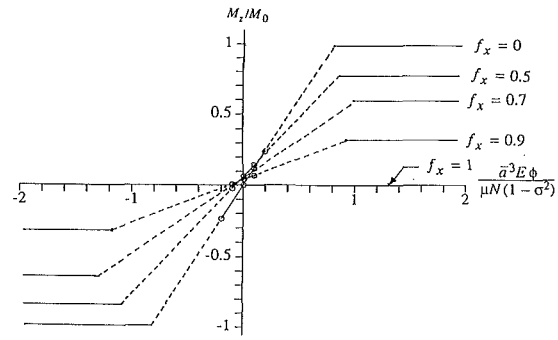


Fig. 11 Moment versus spin for rolling contact of two elastically identical bodies with contact patch shown in Fig. 5. $f_x = F_x/(\mu N)$, $F_y = 0$, $M_0/[(\mu N\bar{a}) = 0.633$. Small circles indicate numerical calculations via program ROLCREEP. Horizontal lines are calculated via program SLIDFORC (Liu and Paul, 1988). Dashed lines are extrapolations.

The numerical solution just developed, together with the limiting values of M_z for fully developed sliding (Liu and Paul, 1988), permit us to establish reasonable upper bounds on the spin moment for an arbitrary degree of spin as indicated by the dashed lines in Fig. 11 for a specific non-Hertzian example. The variable M_z in Fig. 11 is the moment of tractions (T_x, T_y) about the centroid of pressure. M_0, the maximum attainable value of M_z, was found to be

$$M_0 = 0.633\mu N\bar{a}. \tag{24}$$

Comments on Numerical Accuracy and Stability. Although we have not, as yet, made a systematic study of the numerical accuracy and stability of our algorithm, we have found that the method provides good accuracy when the mesh contains 15–20 cells across the x diameter (in direction of rolling) of the contact patch. The number of cells in the y direction is determined by an adaptive mesh generation scheme which maintains an aspect ratio close to one for each cell. In the absence of spin creepage, no convergence problems have arisen when the spin creepage parameter $\bar{\phi}$ (defined in the caption of Fig. 9) is less than 0.2. We can raise this limit somewhat by tracking the initial estimate of the separatrix; however, we have not yet fully explored this approach.

6 Conclusions

In this paper, a numerical technique has been developed to solve rolling contact problems for arbitrary contact patches under arbitrary pressure distributions. The inputs to the computer program (called ROLCREEP) are contact patch, pressure distribution, elastic moduli, creepages, and spin. The algorithm determines the location of separatrix and tangential stress distributions within the contact region. This technique works satisfactorily for the case of pure creepages and cases of creepage plus small spin.

Acknowledgment

We gratefully acknowledge that this research was partially supported by the National Science Foundation under Grant No. MEA81-15806.

Reference

Cain, 1950, Discussion of the paper by H. Poritsky, "Stress and Deflections of Cylindrical Bodies in Contact With Applications to Contact Gears and of Locomotive Wheels," ASME JOURNAL OF APPLIED MECHANICS, Series E, Dec., p. 465.

Carter, F. W., 1926, "On the Action of a Locomotive Driving Wheel," *Proceedings, Royal Society*, Vol. A112, pp. 151–157.

Dählquist, G., and Björck, A., 1974, *Numerical Methods*, Prentice-Hall, Englewood Cliffs, N.J., pp. 249–251.

Duvaut, G., and Lions, J. L., 1976, *Inequalities in Mechanics and Physics*, Springer-Verlag, New York, pp. 134–142.

Goree, J. G., 1978, "User's Manual for Kalker's 'Exact' Nonlinear Creep Theory," Report No. FRA/ORD-78/50, Contract DOT-OS-40018, U.S. Department of Transportation, Federal Railroad Administration, Office of R&D, Washington, D.C.

Haines, D. J., Ollerton, E., 1963, "Contact Stress Distributions on Elliptical Contact Surface Subjected to Radial and Tangential Forces," *Proceedings, Institution of Mechanical Engineers*, Vol. 177, pp. 95–114.

Hashemi, J., and Paul, B., 1979, "Contact Stresses on Bodies with Arbitrary Geometry, Applications to Wheel and Rails," Technical Report No. 7, FRA-ORD-79/23, Contract DOT-OS-60144, pp. 101–102.

Hertz, H., 1882, "Über die Berührung fester elastischer Körper," *J. reine und angewandte Mathematik*, Vol. 92, pp. 156–171.

Johnson, K. L., 1958, "The Effect of a Tangential Contact Force upon the Rolling Motion of an Elastic Sphere on a Plane," ASME JOURNAL OF APPLIED MECHANICS, Vol. 25, pp. 330–346.

Downloaded 03 May 2010 to 171.66.16.31. Redistribution subject to ASME license or copyright; see http://www.asme.org/terms/Terms_Use.cfm

Johnson, K. L., 1985, *Contact Mechanics*, Cambridge University Press.

Kalker, J. J. 1967, "On the Rolling Contact of Two Elastic Bodies in the Presence of Dry Friction," Ph.D. Thesis, Delft University, pp. 95–100.

Kalker, J. J., 1973, "Simplified Theory of Rolling Contact," Delft Progress Report, Series C, pp. 1–10.

Kalker, J. J., 1977, "Variational Principles of Contact Elastostatics," *J. Inst. Maths. Applic.*, Vol. 20, pp. 207–208.

Kalker, J. J., 1979, "The Computation of Three-Dimensional Rolling Contact With Dry Friction," *International Journal For Numerical Methods in Engineering*, Vol. 14, pp. 1293–1307.

Kalker, J. J., 1982, "Introduction to the Fortran IV Programs DUVOROL and CONTACT for the Solution of 3D Elastostic Half-space Contact Problems with and without Friction," *Report of the Department of Mathematics and Informatics*, No. 82–89, Delft University, The Netherlands.

Kalker, J. J., 1987, "Wheel-Rail Wear Calculations With The Program CONTACT," *Contact Mechanics and Wear of Rail/Wheel Systems II. Proc. Int. Symposium*, University of Waterloo Press, Waterloo, Ontario, pp. 3–26.

Liu, C., 1988, "Rolling Contact with Friction and non-Hertzian Pressure Distributions," Ph.D. Thesis, Department of Mechanical Engineering and Applied Mechanics, University of Pennsylvania, Philadelphia.

Liu, C., and Paul, B., 1988, "Fully Developed Sliding of Rough Surfaces," to be published in *Journal of Tribology* and in *Proceedings of the Symposium on Applications of Applied Mechanics to Railway Engineering Problems*, 1988 ASME Winter Annual Meeting, Chicago, Ill.

Love, A. E. H., 1944, *A Treatise on the Mathematical Theory of Elasticity*, Dover, New York, p. 196.

Ollerton, E., 1963–1964, "Stresses in the Contact Zone," *Proceedings, Institution of Mechanical Engineers*, Vol. 178, pp. 161–171.

dePater, A. D., 1962, "On the Reciprocal Pressure Between Two Bodies," *Proc. Symp. Rolling Contact Phenomena*, J. B. Bidwill, ed., Elsevier, New York, pp. 29–75.

Paul, B., 1979, *Kinematics and Dynamics of Planar Machinery*, Prentice-Hall, Englewood Cliffs, N.J., p. 609.

Paul, B., and Hashemi, J., 1977, "User's Manual for Program COUNTACT (COUNTerformal contACT stress problems)," Technical Report No. 4, FRA-ORD-78-27, (PB 286097/AS, available from National Technical Information Service, Springfield, Va. 22151.)

Paul, B., and Hashemi, J., 1981, "Contact Pressures on Closely Conforming Elastic Bodies," ASME JOURNAL OF APPLIED MECHANICS, Vol. 48, pp. 543–548.

Singh, S., 1982, private communications.

Timoshenko, S. P., and Goodier, J. N., 1970, *Theory of Elasticity*, McGraw-Hill, New York.

Downloaded 03 May 2010 to 171.66.16.31. Redistribution subject to ASME license or copyright; see http://www.asme.org/terms/Terms_Use.cfm

J. Y. Lin
Mechanical Industry Research Laboratories,
Industrial Technology Research Institute,
Taiwan, Republic of China

R. A. Westmann
Mechanical, Aerospace and Nuclear Engineering Department,
University of California,
Los Angeles, Calif. 90024
Mem. ASME

Viscoelastic Winding Mechanics

The viscoelastic analysis of tape systems composed of rate-dependent materials is presented. Histories for winding, winding-pause, and winding-pause-unwinding are considered. The winding problem is reduced to determining the appropriate Green's function by numerical solution of a Volterra integral equation of the second kind. This Green's function and integral superposition permits the evaluation of the stress and displacement fields in the tape system for any winding history. Viscoelastic unwinding is treated by the superposition of two-states – one determined from the initial condition of the tape when unwinding begins and the second state given in terms of an arbitrary external pressure evaluated by solving an integral equation. Numerical results are presented for several histories and representative material properties.

1 Introduction

Storage of paper and plastic sheets in the form of rolls is common practice. It is anticipated that during the winding, storage/handling, and unwinding phases, the rolls remain intact and the materials undamaged. To preclude slipping between layers or buckling of sections of the tape it is necessary to know the stress and displacement fields induced in the roll by the winding process.

Another related application is in the field of magnetic tapes. In this case the Mylar tapes are wound/unwound many times in addition to being stored for lengthy periods. The need for high quality reproduction of information stored on such tapes requires the dimensions of the tape to be virtually unchanged during and between read/write operations. Knowledge of the stress and displacement fields is useful in evaluating those operating conditions which may lead to relatively poor tape performance.

In some of the above applications the materials are rate dependent and subject to creep deformations. Such behavior needs to be accounted for in any analysis if the stress and displacement fields are to be meaningful. Altmann (1968) and later Yagoda (1980) presented the solution for the problem of winding under constant tension for elastic, anisotropic materials. Tramposch (1965, 1967) considered the viscoelastic relaxation of the internal stress field arising from an initial elastic stress state in the completed roll. Willett and Poesch (1988) present an excellent summary of the research literature in the area of winding mechanics.

In the actual winding process the sheet is initially stretched and applied one layer at a time, beginning as the first layer is placed over the compliant hub or core. As each subsequent layer is added it alters the stress state in the hub and layers present at that time. This accretion process continues until the final roll radius is attained, the final stress state being the sum of the effects of adding all of the layers.

Should the layers be composed of a viscoelastic material, the stress state at the end of the winding phase will depend upon the winding speed. Storage or pausing at this point will result in stress redistribution. If the roll is unwound or cycled, this will induce additional changes in the stress field. In the viscoelastic case, the stress state at any time depends upon the entire winding history of the roll up to that point.

In this paper a viscoelastic analysis of the winding/unwinding process is presented. Results from such an analysis will show the effects of different winding rates and what speeds might lead to undesirable creep and relaxation in the magnetic tape.

2 Elastic Winding/Unwinding

The elastic case is first reviewed in preparation for the solution of the viscoelastic problem. This treatment is essentially the same as presented in Altmann (1968). The roll of tape is considered to be in a state of plane stress and the solution obtained using the two-dimensional theory of classical elastostatics. The tape material is assumed to be homogeneous and isotropic with elastic constants E, ν.

A polar coodinate system r, θ with origin at the hub center is employed (Fig. 1). The hub radius is taken to be unity[1] while the current outer radius of the reel is denoted by R. During the winding/unwinding process the outer radius varies attaining a maximum value of R_0. Hence, $1 \leq r \leq R \leq R_0$.

The winding/unwinding process proceeds with the tape under initial tension σ_0 (taken to be constant). The torque about the hub center induced by the winding tension is assumed to be small and, hence, is neglected. Furthermore, the winding process is treated as the placement of one layer of stretched tape at a time upon the roll already in place, thus leading to an incremental increase in the roll radius. This is a

Contributed by the Applied Mechanics Division of THE AMERICAN SOCIETY OF MECHANICAL ENGINEERS for presentation at the Winter Annual Meeting, San Francisco, Calif., December 10–15, 1989.

Discussion on this paper should be addressed to the Editorial Department, ASME, United Engineering Center, 345 East 47th Street, New York, N.Y. 10017, and will be accepted until two months after final publication of the paper itself in the JOURNAL OF APPLIED MECHANICS. Manuscript received by the ASME Applied Mechanics Division, January 8, 1988; final revision, November 9, 1988.

Paper No. 89-WA/APM-18.

[1] This is equivalent to normalizing the spatial variables by the hub radius. Accordingly, the spatial dimensions and coordinates are dimensionless.

Copyright © 1989 by ASME

Downloaded 03 May 2010 to 171.66.16.31. Redistribution subject to ASME license or copyright; see http://www.asme.org/terms/Terms_Use.cfm

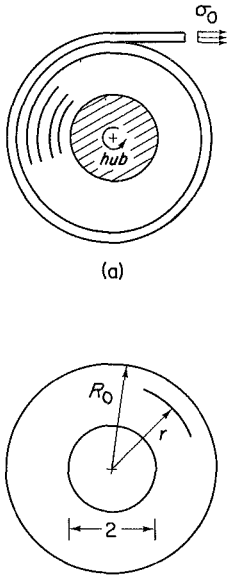


Fig. 1 Problem geometry

form of an accretion problem in solid mechanics discussed by Brown and Goodman (1963).

Let σ_r^*, σ_θ^* denote the incremental components of the torsionless axisymmetric stress state induced by the addition of the stretched layer. The corresponding incremental strains and displacement are ϵ_r^*, ϵ_θ^*, and u^* which depend only upon the radial coordinate.

The governing field equations for this incremental state are

$$\text{equilibrium} \quad \frac{d\sigma_r^*}{dr} + (\sigma_r^* - \sigma_\theta^*)\frac{1}{r} = 0 \qquad r\epsilon(1, R) \quad (1)$$

$$\text{stress-strain} \quad E\epsilon_r^* = \sigma_r^* - \nu\sigma_\theta^* \qquad r\epsilon(1, R) \quad (2a)$$

$$E\epsilon_\theta^* = \sigma_\theta^* - \nu\sigma_r^* \qquad r\epsilon(1, R) \quad (2b)$$

$$\text{strain-displacement} \quad \epsilon_r^* = \frac{du^*}{dr} \qquad r\epsilon(1, R) \quad (3a)$$

$$\epsilon_\theta^* = \frac{u^*}{r} \qquad r\epsilon(1, R). \quad (3b)$$

The associated boundary conditions follow from the requirement of displacement and traction continuity at the hub-tape interface

$$\sigma_r^*(1) = E' u^*(1), \quad (4a)$$

and the application of the prestressed hoop at the current outer radius

$$\sigma_r^*(R) = -\sigma_0 \frac{dR}{R}. \quad (4b)$$

In (4*a*) E' is the effective modulus of the hub while in (4*b*) the thickness of the tape, h, is set equal to the differential dR. Note that in typical applications $h/R \simeq 10^{-3}$ justifying this latter approximation.

The preceding system of equations and boundary conditions is readily solved yielding the following expressions for the incremental stress and displacement fields.

$$\sigma_r^* = \sigma_0 \frac{R}{(DR^2 - 1)}\left(\frac{1}{r^2} - D\right) dR\, H(R - r) \quad (5a)$$

$$\sigma_\theta^* = -\sigma_0 \frac{R}{(DR^2 - 1)}\left(\frac{1}{r^2} + D\right) dR\, H(R - r) \quad (5b)$$

$$u^* = \frac{-\sigma_0}{E}\frac{R}{(DR^2 - 1)}\left[\frac{1+\nu}{r} + (1-\nu)rD\right] dR\, H(R - r) \quad (6)$$

where

$$D = \frac{E/E' + \nu + 1}{E/E' + \nu - 1}$$

and the Heaviside operator $H(R-r)$ has been included to indicate the range of applicability of the expressions.

The total stress and displacement fields are obtained through the integral superposition of the relevant incremental solutions as follows:

$$\sigma_r = \int_r^{R_0} \sigma_r^* = \left(\frac{1}{r^2} - D\right)\frac{1}{2D} \ln\left(\frac{R_0^2 D - 1}{r^2 D - 1}\right)\sigma_0 \quad (7a)$$

$$\sigma_\theta = \sigma_0 + \int_r^{R_0} \sigma_\theta^* = \sigma_0 - \left(\frac{1}{r^2} + D\right)\frac{1}{2D} \ln\left(\frac{R_0^2 D - 1}{r^2 D - 1}\right)\sigma_0 \quad (7b)$$

$$u = \int_r^{R_0} u^* = -\left[\frac{1+\nu}{r} + (1+\nu)rD\right]\frac{1}{2D} \ln\left(\frac{R_0^2 D - 1}{r^2 D - 1}\right)\frac{\sigma_0}{E}. \quad (8)$$

The term σ_0 in (7*b*) is included to account for the prestress present in each incremental hoop as it is added to the roll.

It is interesting to note from equation (8) that $u(R_0) = 0$. This arises from the incremental process wherein it is assumed that $u(r) = 0$ for $r \geq R$. A more meaningful expression for the displacement is given by

$$u = \frac{\sigma_r(1)}{E'} + \int_1^r \epsilon_r(\xi)\, d\xi, \quad \epsilon_r = \int_r^{R_0} \epsilon_r^* \quad (9)$$

where ϵ_r^* is evaluated by substituting from (5*a*), (5*b*) into equation (2*a*). The displacement defined by equation (9) gives the radial movement of the material point from the position it would have occupied if the roll had been wound with zero tension ($\sigma_0 = 0$).

Equations (7*a*), (7*b*) may be used in conjunction with the stress-strain relations to evaluate the components of the strain state. One may verify that the resulting strain state does not satisfy the compatibility equation. This is due to the incremental process wherein the addition of each prestretched different layer leads to a final strain field that is incompatible.

Unwinding of the elastic tape system may be treated in a manner similar to the winding case. If the unwinding tension σ_0 is the same as the winding tension, it results that the elastic stress and strain states then depend only upon the current radius and not the history. And so equations (7), (8) may be used.

3 Viscoelastic Winding and Pause

The solution procedure for the viscoelastic case parallels the method used for the elastic winding problem. The winding process is treated as the placement of a sequence of pretensioned layers starting with the hub. In the case of viscoelastic material properties, the timing of the placement is important so as to be consistent with the winding history.

If $v = v(t)$ is the speed the tape is wound on the roll and h is the tape thickness (width 1), then

$$d(\text{Vol}) = 2\pi R\, dR = v(t)\, dt\, h. \quad (10)$$

Knowledge of $v(t)$ permits integration of (10) and therefore determination of $R(t)$. As two special cases consider

$v(t) = v_0$ (constant tape velocity):

$$\pi(R^2 - 1) = v_0 th \quad (11a)$$

$v(t) = R\omega_0$ (constant hub angular velocity):

$$2\pi(R - 1) = \omega_0 th \quad (11b)$$

In this way one may establish the relationship between the current roll radius and time, $R = R(t)$.

To begin, the solution is obtained for the incremental stress and displacement fields due to the application of a prestressed

Downloaded 03 May 2010 to 171.66.16.31. Redistribution subject to ASME license or copyright; see http://www.asme.org/terms/Terms_Use.cfm

layer at time $t = \tau$ to a roll of current radius R. The governing equilibrium equations and strain-displacement relations presented in (1), (3*a*), and (3*b*) are still valid. However, the stress-strain relations must be extended to account for the rate dependence of the viscoelastic material.

Let $J(t)$, $Y(t)$ denote the creep and relaxation functions of the material in uniaxial tension. Then, as the reel is taken to be in a state of plane stress,

$$Y^*\dot{\epsilon}_r^* = \sigma_r^* - \nu\sigma_\theta^* \tag{12a}$$

$$Y^*\dot{\epsilon}_\theta^* = \sigma_\theta^* - \nu\sigma_r^* \tag{12b}$$

where

$$Y^*\dot{\epsilon} \equiv \int_{0^-}^{t} Y(t-\tau)\,\frac{\partial \epsilon(\tau)}{\partial \tau}\,d\tau.$$

In equations (12*a*), (12*b*) it has been assumed that Poisson's ratio is constant. The associated side conditions are given by the two boundary conditions (4*a*) and (4*b*) and the initial conditions

$$u^*(r,t) = \sigma_r^*(r,t) = \sigma_\theta^*(r,t) = \epsilon_r^*(r,t) = \epsilon_\theta^*(r,t) = 0$$
$$t < \tau,\ r\epsilon(1,R). \tag{13}$$

It is convenient to obtain the solution to this system of equations by employing the Laplace Transform (L.T.). Let the L.T. of $\sigma(r,t)$ be denoted by $\bar{\sigma}(r,s)$ where s is the L.T. parameter. Then, application of the L.T. to equations (1), (3*a*), (3*b*), (4*a*), (4*b*), (12*a*), and (12*b*) and enforcing the initial conditions (13) leads to the following associated boundary value problem

$$\frac{d\bar{\sigma}_r^*(r,s)}{dr} + \left[\frac{\bar{\sigma}_r^*(r,s) - \bar{\sigma}_\theta^*(r,s)}{r}\right] = 0 \quad r\epsilon(1,R) \tag{14}$$

$$\bar{Y}(s)s\bar{\epsilon}_r^* = \bar{\sigma}_r^* - \nu\bar{\sigma}_\theta^* \qquad r\epsilon(1,R) \tag{15a}$$

$$\bar{Y}(s)s\bar{\epsilon}_\theta^* = \bar{\sigma}_\theta^* - \nu\bar{\sigma}_r^* \qquad r\epsilon(1,R) \tag{15b}$$

$$\bar{\epsilon}_r^* = \frac{d\bar{u}^*}{dr} \qquad r\epsilon(1,R) \tag{16a}$$

$$\bar{\epsilon}_\theta^* = \frac{\bar{u}^*}{r} \qquad r\epsilon(1,R) \tag{16b}$$

$$\bar{\sigma}_r^*(1,s) = E'\bar{u}^*(1,s) \tag{17a}$$

$$\bar{\sigma}_r^*(R,s) = -\frac{\sigma_0 dR}{sR}\,e^{-s\tau}. \tag{17b}$$

Solving this system of equations, employing the relation

$$s\bar{Y}(s) = \frac{1}{s\bar{J}(s)}, \tag{18}$$

and inverting the L.T. leads to the following solution

$$\sigma_r^* = \left\{\frac{\Psi(t-\tau)}{1+\nu}\left(\frac{1}{R^2} - \frac{1}{r^2}\right) - \frac{\sigma_0}{R}\right\}dR\,H(t-\tau) \tag{19a}$$

$$\sigma_\theta^* = \left\{\frac{\Psi(t-\tau)}{(1+\nu)}\left(\frac{1}{R^2} + \frac{1}{r^2}\right) - \frac{\sigma_0}{R}\right\}dR\,H(t-\tau) \tag{19b}$$

$$\epsilon_r^* = \left\{-(1-\nu)J(t-\tau)\frac{\sigma_0}{R} + \int_{0^-}^{t-\tau}\left[\frac{1-\nu}{(1+\nu)R^2} - \frac{1}{r^2}\right]\Psi(\xi)\,\frac{dJ(t-\tau-\xi)}{d(t-\tau-\xi)}\,d\xi\right\}dR\,H(t-\tau). \tag{20}$$

In equations (19*a*), (19*b*), and (20) (which represent the Green's function for the winding problem), the function $\Psi(t)$ is the solution of the following Volterra integral equation of second kind

$$\Psi(t) = \left\{\left[\frac{(1+\nu)}{E'} - (1-\nu^2)J(t)\right]R\sigma_0 + \int_0^t [1-\nu+(1+\nu)R^2]\,\frac{dJ(t-\xi)}{d(t-\xi)}\,\Psi(\xi)d\xi\right\} \cdot \frac{1}{\left[\frac{1}{E'} - J(0)(1-\nu)\right] - \left[\frac{1}{E'} + (1+\nu)J(0)\right]R^2}. \tag{21}$$

The total stress and displacement fields then follow upon integral superposition with the following result;

$$\sigma_r = \sigma_0 \int_r^{R_0} \frac{\Psi(t-\tau)}{(1+\nu)}\left(\frac{1}{R^2} - \frac{1}{r^2}\right)dR - \sigma_0 \ln\frac{R_0}{r} \tag{22a}$$

$$\sigma_\theta = \sigma_0 + \sigma_0 \int_r^{R_0} \frac{\Psi(t-\tau)}{(1+\nu)}\left(\frac{1}{R^2} + \frac{1}{r^2}\right)dR - \sigma_0 \ln\frac{R_0}{r} \tag{22b}$$

$$u = \frac{\sigma_r(1)}{E'} + \int_1^r \int_\xi^{R_0} \left\{-(1-\nu)J(t-\tau)\,\frac{\sigma_0}{R} + \int_{0^-}^{t-\tau}\left[\frac{(1-\nu)}{(1+\nu)R^2} - \frac{1}{\xi^2}\right]\frac{\Psi(\eta)dJ(t-\tau-\eta)}{d(t-\tau-\eta)}\,d\eta\right\}dR\,d\xi. \tag{23}$$

In the evaluation of the integral in equations (22*a*), (22*b*), and (23), one must observe the constraint between the current roll radius and time, $R(t)$. For example, if the roll radius at time t is R_0, while R is the radius at time τ, then one determines from equation (11*a*) that

$$t = \frac{\pi}{v_0 h}\,(R_0^2 - 1), \quad \tau = \frac{\pi}{v_0 h}\,(R^2 - 1)$$

and

$$t - \tau = \frac{\pi}{v_0 h}\,(R_0^2 - R^2) \quad \text{(constant tape velocity)}. \tag{24a}$$

In a similar manner, it follows from equation (11*b*) that

$$t - \tau = \frac{2\pi}{\omega_0 h}\,(R_0 - R) \quad \text{(constant hub angular velocity)}. \tag{24b}$$

Once the creep function $J(t)$ and the winding history are stated, $\Psi(\tau)$ is evaluated for $R\epsilon(1,R_0)$ and then the stress and displacement fields follow by substituting from equation (24*a*) or (24*b*) into equation (22*a*), (22*b*), (23) and completing the indicated integrations.

In order to consider the winding problem followed by a period of pausing (R_0 constant), several minor changes are required in the procedure. The relationship between $t-\tau$ and R_0, R must be changed to reflect the fact that once the final R_0 is attained, say at $t = t_0$, the reel radius remains fixed for subsequent time ($t > t_0$). Appropriate expressions then for the cases of constant velocity and constant hub angular velocity are given by equations (25*a*) and (25*b*).

$$t - \tau = \frac{\pi(R_0^2 - R^2)}{v_0 h}\,H(R_0 - R) + tH(t - t_0),\ t_0 \equiv \frac{\pi(R_0^2 - 1)}{v_0 h} \tag{25a}$$

$$t - \tau = \frac{2\pi(R_0 - R)}{\omega_0 h}\,H(R_0 - R) + tH(t - t_1),\ t_1 \equiv \frac{2\pi(R_0 - 1)}{\omega_0 h} \tag{25b}$$

The evaluation of stress and displacement fields is essentially the same as in the viscoplastic winding case except that the time history given by equation (25*a*) or (25*b*) is employed when evaluating equations (22*a*), (22*b*), and (23).

Downloaded 03 May 2010 to 171.66.16.31. Redistribution subject to ASME license or copyright; see http://www.asme.org/terms/Terms_Use.cfm

Table 1 Material properties

$1/E_0$	0.35871×10^{-5} (1/psi)
$1/E_1$	0.19453×10^{-5}
τ_1	0.1×10^{5} (sec)
	(*a*) $N=1$
$1/E_0$	0.35871×10^{-5} (1/psi)
$1/E_1$	0.90823×10^{-9}
$1/E_2$	0.16903×10^{-7}
$1/E_3$	0.10489×10^{-6}
$1/E_4$	0.17270×10^{-6}
$1/E_5$	0.39090×10^{-6}
$1/E_6$	0.62461×10^{-6}
$1/E_7$	0.64518×10^{-6}
τ_1	0.1×10^{0} (sec)
τ_2	0.1×10^{1}
τ_3	0.1×10^{2}
τ_4	0.1×10^{3}
τ_5	0.1×10^{4}
τ_6	0.1×10^{5}
τ_7	0.1×10^{6}
	(*b*) $N=7$
ν	$=0.3$
E'	$=0.30851\times10^{6}$ (psi)
E_G	$=0.61244\times10^{6}$
E_R	$=0.27878\times10^{6}$

4 Viscoelastic Unwinding

Unwinding of the viscoelastic tape system may be treated by superposing two time-dependent states, an initial, and a correction state. This solution scheme is similar to that presented by Lee, Radok and Woodward (1959). The initial state σ_r^i, σ_θ^i, u^i is the result of the viscoelastic winding process, equations (22*a*), (22*b*), (23) including both the winding and pause periods.[2]

The correction state, σ_r^c, σ_θ^c, u^c, is determined so that the sum of the initial and correction states satisfies the traction-free condition for the current unwinding radius R_1. The correction state is determined by first solving the problem of a reel with a fixed radius, R_0, subjected to an arbitrary external pressure history $P(\tilde{t})$ where $\tilde{t}=0$ denotes the time when unwinding begins.

Let $\tilde{\sigma}_r$, $\tilde{\sigma}_\theta$, $\tilde{u}$ denote the Green's functions for a unit pressure applied at R_0 and $\tilde{t}=0$. These Green's functions may be directly obtained from equations (19)–(21) by setting $\sigma_0 dR/R = 1$ and $R=R_0$. Then the correction state is obtained by integral superposition of the Green's function; for example

$$\sigma_r^c=\tilde{\sigma}_r(r,R_0,0)P(\tilde{t})+\int_0^{\tilde{t}}P(\tau)\,\frac{\partial\tilde{\sigma}_r(r,R_0,\tilde{t}-\tau)}{\partial(\tilde{t}-\tau)}\,d\tau \tag{26}$$

$$u^c=\tilde{u}_r(r,R_0,0)P(\tilde{t})+\int_0^{\tilde{t}}P(\tau)\,\frac{\partial\tilde{u}(r,R_0,\tilde{t}-\tau)}{\partial(\tilde{t}-\tau)}\,d\tau. \tag{27}$$

The history of the unknown external pressure $P(\tilde{t})$ is now determined by enforcing the traction-free condition at the current unwinding radius R_1 for the sum of the initial and correction states;

$$\sigma_r(R_1,R_0,t)=\sigma_r^i(R_1,R_0,t)+\sigma_r^c(R_1,R_0,\tilde{t})=0 \tag{28}$$

leading to a Volterra integral equation of the second kind for $P(\tilde{t})$

$$P(\tilde{t})=\frac{-1}{\sigma_r(R_1,R_0,0)}\left[\sigma_r^i(R_1,R_0,t)+\int_0^{\tilde{t}}P(\tau)\,\frac{\partial\tilde{\sigma}_r(R_1,R_0,\tilde{t}-\tau)}{\partial(\tilde{t}-\tau)}\,d\tau\right]. \tag{29}$$

The current stress and displacement fields are then the sum of the initial and correction states, where the correction state is evaluated for the external pressures $P(\tilde{t})$ determined from equation (29)

$$\sigma_r=\sigma_r^i+\sigma_r^c \tag{30a}$$

$$\sigma_\theta=\sigma_\theta^i+\sigma_\theta^c \tag{30b}$$

$$u=u^i+u^c. \tag{31}$$

[2]For the initial state, the pause phase is maintained for values of time greater than the time at which unwinding begins.

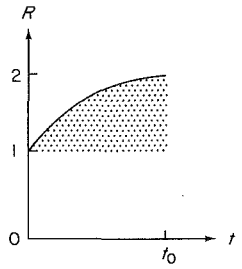


Fig. 2 Integration scheme mesh points

5 Numerical Solutions and Results

In the numerical examples presented here, a generalized Maxwell model for creep is employed so that

$$J(t)=\frac{1}{E_0}-\sum_{n=1}^{N}\frac{1}{E_n}e^{-t/\tau_n}. \tag{32}$$

Representative values for the elastic moduli, E_n, and retardation times, τ_n, are presented in Table 1 for Mylar tape at room temperature for the two cases of $N=1$ and 7. Glassy (E_G, $t\to0+$) and rubbery (E_R, $t\to\infty$) moduli are also listed. In all of the numerical results, Poisson's ratio of the tape is taken to be $\nu=0.3$ while the effective modulus of the elastic hub is $E'=3.085\times10^5$ psi.

In the case of the winding and winding/pause problems, the solution procedure begins with the numerical solution of the Volterra integral equation of the second kind (21) for a suitable range of R and t, Fig. 2. Subsequent numerical integrations of equations (22) and (23) leads to the stress and displacement components. To achieve the desired accuracy, a modified version of the standard numerical method for solving Volterra integral equations was employed (see Appendix).

The special case of $N=1$ was first considered to establish the numerical accuracy of the procedure. For $N=1$, equation (21) can be solved analytically thereby determining $\Psi(t)$ in closed form; the stress and displacement components follow upon numerically completing the integrals in (22) and (23). These semianalytical results were compared with values obtained by a totally numerical solution ($N=1$) with excellent agreement between the two methods.

Figures 3–5 present results for σ_r, σ_θ, u for viscoelastic winding and $N=7$. A dimensionless (constant) tape velocity $V=v_0\tau_6/1$ is employed, and results presented for $R_o=2$, and a range of values V. Elastic solutions, equations (7) and (9), are included for the glassy and rubbery limiting response for reference purposes. Figures 3–5 show the expected transition from rubbery response for relatively low values of V to glassy response for relatively high values of the dimensionless velocity. The results presented in Figs. 3–5 show that if V is equal to or larger than 3×10^7, then the elastic results for the glassy limit are applicable.

The numerical results presented in Figs. 6–8 are for a typical winding-pause problem. In this example, it is assumed that the tape is wound with dimensionless constant tape velocity $V=3\times10^5$ during a period t_o. The winding process is then stopped and the stress and displacement fields evaluated for subsequent values of time $t=t_o, 2t_0 \ldots 11t_0$. It is observed, as expected, that as the pause time increases, the stress and

Downloaded 03 May 2010 to 171.66.16.31. Redistribution subject to ASME license or copyright; see http://www.asme.org/terms/Terms_Use.cfm

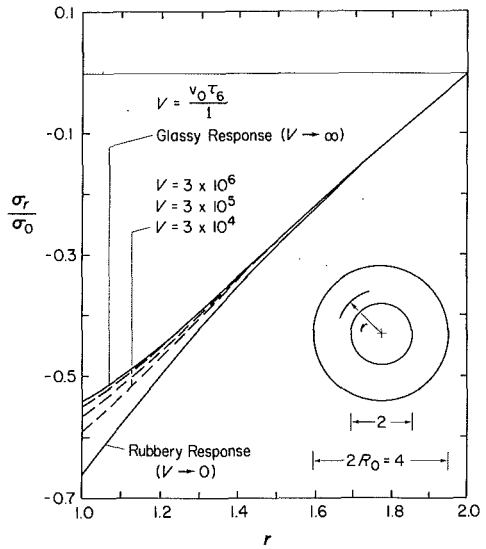


Fig. 3 Distribution of radial stress for winding problem ($N = 7$)

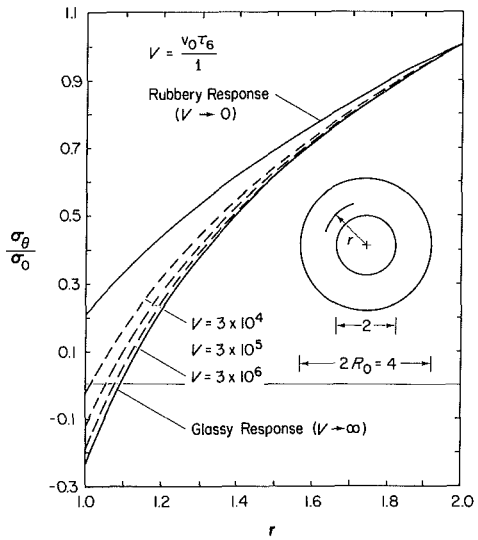


Fig. 4 Distribution of hoop stress for winding problem ($N = 7$)

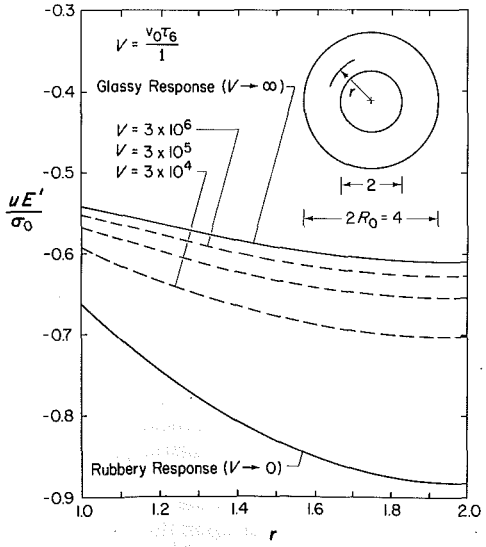


Fig. 5 Displacement for winding problem ($N = 7$)

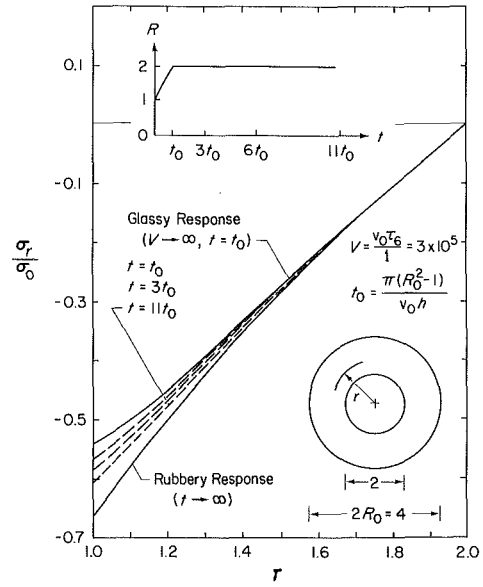


Fig. 6 Distribution of radial stress for winding-pause problem ($N = 7$)

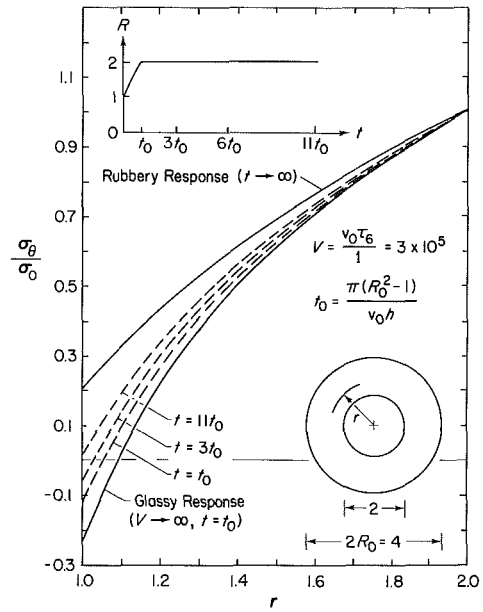


Fig. 7 Distribution of hoop stress for winding-pause problem ($N = 7$)

displacement fields relax and tend toward the rubbery response.

As a representative example of the unwinding problem, the following history was considered. The tape was first wound with dimensionless tape velocity $V = v_0\tau_1/1$ in time t_0 to a radius of $R_0 = 2$. The radius was then held constant (pause phase) for a period of 0.5 t_0 at which time the tape was unwound (with dimensionless velocity V) to a radius of $R = 1.7$. The resulting stress and displacement fields are presented in Figs. 9–11 for the case of $N = 1$. The dashed lines represent the results obtained by the semianalytical approach, while the triangles represent the solution for the same problem obtained by numerically solving equations (19)–(21) and (29).

Again, the close agreement between the two solution methods (for $N=1$) indicates that the accuracy of the numerical scheme is adequate. Other results for the case of $N = 7$ have been obtained numerically, but as they indicate, the same general trends are not presented. The results presented in Figs. 9–11 indicate for this simple material model that if V is greater than or equal to 3×10^6 then the response is essentially elastic and the glassy limit is applicable.

Downloaded 03 May 2010 to 171.66.16.31. Redistribution subject to ASME license or copyright; see http://www.asme.org/terms/Terms_Use.cfm

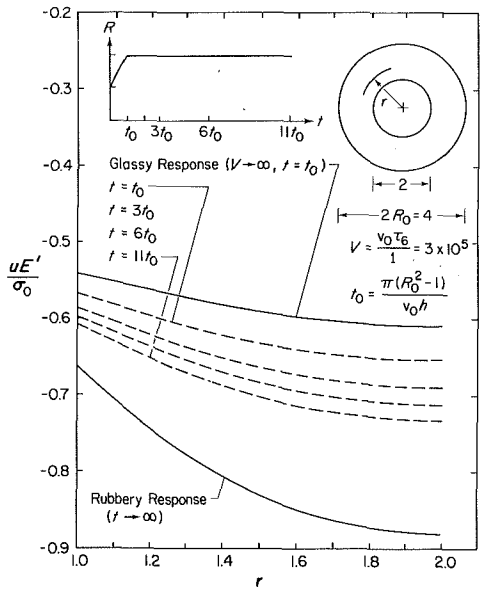


Fig. 8 Displacement for winding-pause problem ($N = 7$)

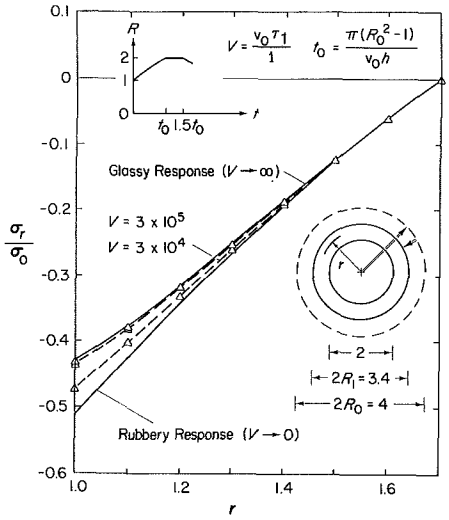


Fig. 9 Distribution of radial stress for unwinding problem ($N = 1$)

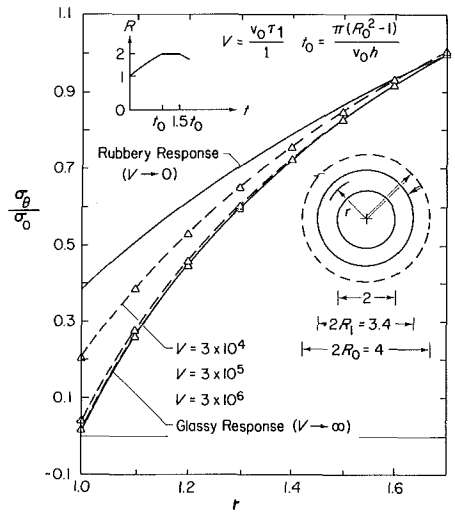


Fig. 10 Distribution of hoop stress for unwinding problem ($N = 1$)

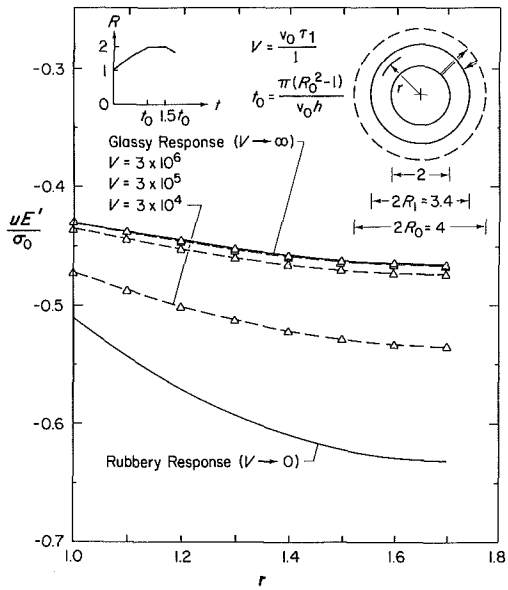


Fig. 11 Displacement for unwinding problem ($N = 1$)

6 Final Remarks

The analysis presented in the preceding sections provides a methodology for analyzing viscoelastic winding problems. Three specific cases have been addressed (winding, winding-pause, and unwinding) which are the basic components of a general history. While only a selected set of representative histories have been examined numerically and presented here, more general and extensive winding-unwinding profiles are treated by adapting these methods and completing the necessary numerical calculation.

As demonstrated by the examples of winding, the reel response is essentially elastic for the dimensionless velocity $V \geq 3 \times 10^7$. Taking a typical hub radius to be 1 in., and noting that $\tau_6 = 10^4$ sec, shows that for elastic response, the tape velocity must satisfy the requirement $v_0 \geq 3 \times 10^3$ in./sec. Such a speed is higher than encountered in most magnetic tape systems. On the other hand, the rubbery response might be achieved if $V < 3 \times 10^2$ requiring $v_0 < 0.03$ in./sec. Of course, such a slow tape speed is impractical.

As shown in the winding-pause problem, if the tape is wound rapidly and then stopped (pause phase), the stress and displacement fields are relaxed. The amount of relaxation depends upon the length of the pause and relative difference between the glassy and rubbery moduli of the tape materials. An upper bound on this relaxation is readily obtained by evaluating the difference between the glassy and rubbery response.

It is interesting to note that for example problems, compressive values of σ_θ are initially induced by high winding speeds (Fig. 4). During the pause phase the tangential stress relaxes approaching a tensile value predicted by the rubbery response (Fig. 7). This time response of the stress state is bounded by the elastic results corresponding to the glassy and rubbery elastic moduli and the value of the hub modulus E'.

The mathematical model presented here is for a linear, isotropic tape material. Actual tape properties are orthotropic and as demonstrated in Willet and Poesch (1967) the effective value of the radial modulus is nonlinear. Incorporation of such features will provide more realistic predictions of the stress state in the reel.

It remains to assess the effects of the viscoelastic changes in the stress and displacement fields upon the performance of the tape system. Should the viscoelastic response prove

Downloaded 03 May 2010 to 171.66.16.31. Redistribution subject to ASME license or copyright; see http://www.asme.org/terms/Terms_Use.cfm

deleterious, it would be necessary to select an appropriate set of material properties, tape speeds, and histories to achieve the desired tape performance.

Acknowledgments

The research reported in this paper was supported by a grant from IBM, General Products Division, Tucson, Ariz. The authors gratefully acknowledge the support and the assistance provided by Dr. Derry Connolly of IBM. Thanks are also due to Mr. Erdogan Madenci for providing valuable assistance in the early phases of this work.

References

Altmann, H. C., 1968, "Formulas for Computing the Stresses in Center-Wound Rolls," *Journal of the Technical Association of the Pulp and Paper Industry* (*TAPPI*), Vol. 51, pp. 176–179.

Brown, C. B., and Goodman, L. E., 1963, "Gravitational Stresses in Accreted Bodies," *Proceedings of the Royal Society, London*, Vol. A276, pp. 571–576.

Lee, E. H., Radok, J. R. M., and Woodward, W. B., (1959), "Stress Analysis for Linear Viscoelastic Material," *Trans. of the Society of Rheology*, Vol. 3, pp. 41–59.

Tramposch, H., 1965, "Relaxation of Internal Forces in a Wound Reel of Magnetic Tape," ASME JOURNAL OF APPLIED MECHANICS, Vol. 32, pp. 865–873.

Tramposch, H., 1967, "Anisotropic Relaxation of Internal Forces in a Wound Reel of Magnetic Tape," ASME JOURNAL OF APPLIED MECHANICS, Vol. 34, pp. 888–894.

Willett, M. S., and Poesch, W. L., 1988, "Determining the Stress Distributions in Wound Reels of Magnetic Tape Using a Nonlinear Finite-Difference Approach," ASME JOURNAL OF APPLIED MECHANICS, Vol. 55, pp. 365–371.

Yagoda, H. P., 1980, "Resolution of a Core Problem in Wound Rolls," ASME JOURNAL OF APPLIED MECHANICS, Vol. 47, pp. 847–854.

APPENDIX

In developing the results presented in this paper, it was necessary to numerically solve several Volterra integral equations of the second kind

$$\phi(t) = f(t) + \int_0^t K(t,\xi)\phi(\xi)d\xi \tag{A1}$$

for the unknown $\phi(t)$. Normally, conventional numerical quadrature using the trapezoidal rule is satisfactory for equations of the type (A1). For example, for a uniform partition (h) of the t- and ξ-coordinate axes, (A1) reduces to

$$\phi(t_n) = f(t_n) + \int_0^{t_n} K(t_n, \xi)\phi(\xi)d\xi$$

$$\doteq f(t_n) + \sum_{m=0}^{N} K(t_n,\xi_m)\phi(\xi_m)W_m \quad \begin{matrix} t_n = nh \\ \xi_m = mh \end{matrix} \tag{A2}$$

where $W_m = \dfrac{h}{2} \quad m = 0,n$

$= h \quad m = 1, 2, \ldots n-1.$

The resulting triangular system of equations is then sequentially solved for $\phi(t_n)$ $n = 1, 2, \ldots$ providing the desired numerical solution.

Unfortunately, this procedure does not lead to the desired accuracy and numerical stability for the Volterra integral equations encountered in this paper. To overcome this difficulty, a higher-order integration scheme is employed.

If n is even then a Simpson's rule integration scheme is employed and the weights W_m are given by

$$\begin{aligned} W_m &= \frac{4h}{3} && m = 3, 5, \ldots n-1 \\ &= \frac{2h}{3} && m = 2, 4, \ldots n-2 \\ &= \frac{h}{3} && m = 1, n \end{aligned} \tag{A3}$$

When n is odd and greater than one, then Simpson's ⅜ rule is used for the last three intervals, $((n-3)h, nh)$, and the weights (A3) are modified to be

$$\begin{aligned} W_m &= \frac{h}{3} + \frac{3}{8}h && m = n-3 \\ W_m &= \frac{9}{8}h && m = n-2, n-1 \\ W_m &= \frac{3}{8}h && m = n. \end{aligned} \tag{A4}$$

For the case $n = 1$, the interval is refined by a factor of 10 and the conventional trapezoidal rule is employed. In this way the integral in (A1) is evaluated with an error of order h^4, instead of an error of order h^2 associated with the trapezoidal rule.

Use of this higher-order integration scheme results in an efficient, numerically stable, and accurate solution of the integral equations arising in this paper.

Downloaded 03 May 2010 to 171.66.16.31. Redistribution subject to ASME license or copyright; see http://www.asme.org/terms/Terms_Use.cfm

A First-Order Perturbation Analysis of Crack Trapping by Arrays of Obstacles

Huajian Gao
Division of Applied Mechanics,
Stanford University,
Stanford, CA 94305

James R. Rice
Division of Applied Sciences,
Harvard University,
Cambridge, MA 02138

A first-order perturbation analysis is presented for the configuration of an initially straight crack front which is trapped against forward advance by contact with an array of obstacles (i.e., regions of higher fracture toughness than their surroundings). The problem is important to the micromechanics of crack advance in brittle, locally heterogeneous solids. The formulation is based on a linear perturbation result for the stress intensity factor distribution along the front of a half-plane crack when the location of that front differs moderately from a straight line. The trapping solutions for a periodic array of blocking rectangular obstacles are given using an analogy to the plane stress Dugdale/BCS elastic-plastic crack model. For a periodic array of obstacles with a given spacing and size in the direction parallel to the crack front, the obstacle shape may affect the limit load at which the crack breaks through the array. When such effects are examined within the range of validity of the linear perturbation theory, it is found that obstacles whose cross-sections fully envelop a critical reference area give the maximum limit load while others are broken through at lower load levels. We also formulate a numerical procedure using the FFT technique and adopting a "viscoplastic" crack growth model which, in an appropriate limit, simulates crack growth at a critical stress intensity factor. This is applied to show how a crack front begins to surround and penetrate into various arrays of round obstacles (with a toughness ratio of 2) as the applied load is gradually increased. The limitations of the first-order analysis restrict its validity to obstacles only slightly tougher than the surrounding elastic medium. Recently, Fares (1988) analyzed the crack trapping problem by a Boundary Element Method (BEM) with results indicating that the first-order linear analysis is acceptable when the fracture of toughness of the obstacles differs by a moderate amount from that of their surroundings (e.g., the toughness ratio can be as large as 2 for circular obstacles spaced by 2 diameters). However, the first-order theory is not only quantitatively inaccurate, but can make qualitatively wrong predictions when applied to very tough obstacles.

Introduction

The micromechanics of crack advance through brittle, locally heterogeneous materials is of fundamental interest. In general, the fracture resistance (local fracture toughness) varies along the front of an advancing macroscopic crack due to microlevel heterogeneities, such as second-phase tough particles which can cause macroscopic toughening of a brittle matrix. This is associated with a process referred to as the "crack trapping," in which the crack front advances nonuniformly and has segments which are trapped, at least temporarily, by contact with tough particles whose fracture toughness value exceeds the local stress intensity. The problems involved are of three-dimensional character and often lack a theoretical treatment due to mathematical difficulties. Solution procedures based on finite element and boundary element analyses can be devised (see Fares, 1988) and they involve heavy numerical computations. This paper gives a simplified analysis, of limited validity, based on linear perturbation theory for the configuration of an initially straight crack front which is trapped against forward advance by contact with arrays of obstacles. The obstacles are modeled as having the same elastic properties as the rest of the elastic medium, but with slightly higher fracture toughness, so that the material considered here is treated as elastically homogeneous. We assume that the crack grows whenever the local stress intensity factor reaches the local fracture toughness at some point along the crack front. As the applied load increases, the crack front penetrates between and partially into the blocking obstacles and reaches new equilibrium

Contributed by the Applied Mechanics Division of THE AMERICAN SOCIETY OF MECHANICAL ENGINEERS for presentation at the Winter Annual Meeting, San Francisco, Calif., December 10–15, 1989.

Discussion on this paper should be addressed to the Editorial Department, ASME, United Engineering Center, 345 East 47th Street, New York, N.Y. 10017, and will be accepted until two months after final publication of the paper itself in the JOURNAL OF APPLIED MECHANICS. Manuscript received by the ASME Applied Mechanics Division, November 22, 1988; final revision, March 20, 1989.

Paper No. 89-WA/APM-36.

Copyright © 1989 by ASME

Downloaded 03 May 2010 to 171.66.16.31. Redistribution subject to ASME license or copyright; see http://www.asme.org/terms/Terms_Use.cfm

states in which the intensity factor equals the fracture toughness value along the penetrating portions of the crack front. The distribution of stress intensity factors is calculated based on the linear perturbation result, developed earlier in Rice (1985a, 1988), for a half-plane tensile crack with a slightly curved front. The half-plane crack result models finite-sized cracks, assuming the lengths of the cracks are large compared to other parameters such as obstacle spacing along the crack front.

The trapping solutions for a periodic array of rectangular blocking obstacles are obtained using an analogy, following Rice (1988), to the two-dimensional plane stress Dugdale/BCS (for Bilby-Cottrell-Swinden) type of elastic-plastic crack model. The effects of the shape and size of the blocking obstacles on the limit load at which the crack breaks through the obstacles are discussed within the range of validity of the linear perturbation theory, although those concepts can be extended to a broader context.

The limitations of the linear perturbation theory are emphasized here, in that it is accurate only to the first-order in crack front perturbations. This restricts the validity of the present first-order analysis to obstacles only slightly tougher than their elastic surroundings, i.e., the fracture toughness ratio (of the obstacles to surroundings) must be near unity. It will be discussed in the text that when applied to very tough obstacles, the first-order theory is not only quantitatively inaccurate, but can also be qualitatively wrong. Fares (1988) recently performed a BEM (Boundary Element Method) analysis on crack trapping configurations, based on a fundamental solution developed by Rice (1985b), for a prismatic opening dislocation source ahead of a half-plane crack with a straight front. By comparing the BEM results with those obtained by the first-order theory, Fares showed that, for simple cosine wave form perturbations of the crack front, the first-order theory gives quantitatively acceptable results for the stress intensity factor distribution (within 7 percent error) when the wave amplitude is within roughly 0.1 times the wavelength. For the case of periodically emplaced circular obstacles spaced by 2 diameters (Figs. 7, 8), which is analyzed both by Fares (1988) and the present authors, the first-order theory can be applied to obstacles that are up to approximately twice as tough as the surrounding material.

Based on the linear perturbation theory, we formulate a numerical procedure for crack penetration of a periodic array of blocking obstacles by using the Fast Fourier Transform (FFT) technique and adopting a "visco-plastic" crack growth model. In that model, once the stress intensity factor exceeds the local fracture toughness, the rate of the crack growth is taken to be proportional to the difference between them at the same location along the crack front. The crack then continues to grow until the new equilibrium state is reached. By controlling the rate term in such a viscoplastic formulation, the procedure may be made to simulate crack growth with the intensity factor equal, effectively, to the local fracture toughness. We give several examples of applications of the numerical model to show how a crack begins to surround and penetrate into arrays of round obstacles as the applied load is gradually increased.

Formulation of Crack Trapping and Penetration

Following Rice (1988) in formulating the crack trapping problem, we consider a half-plane crack in a linear, isotropic elastic solid. Assume that the crack lies on the plane $y=0$ with a straight tip along $x=a_0$ parallel to the z-axis (Fig. 1(a)), and is subjected to fixed applied tensile loadings which induce mode 1 tensile stress intensity factor

$$K=K^0[z;a_0] \tag{1}$$

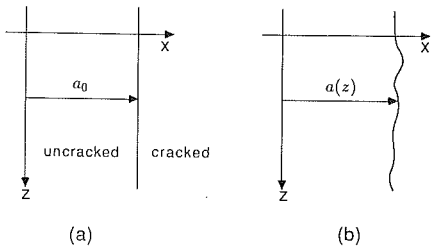


Fig. 1 A half-plane crack in homogeneous, isotropic elastic medium with a (a) straight crack front; (b) slightly-curved crack front

along the crack front. The following linear perturbation result was developed by Rice (1985a) to calculate the distribution of stress intensity factor K along a slightly perturbed crack front, along the arc $x=a(z)$ in the plane $y=0$ (Fig. 1(b))

$$K(z)=K^0[z;a(z)] + (1/2\pi)PV\int_{-\infty}^{+\infty}\frac{K^0[z';a(z)][a(z')-a(z)]}{(z'-z)^2}\,dz' \tag{2}$$

to the first-order accuracy in the deviation of $a(z')$ from constancy; PV denotes principal value. In writing equation (2) for any chosen z, we have chosen a reference straight crack with tip along $x=a(z)$.

We will use these half-plane crack results to model the trapping problems of a finite-sized crack, a_0 now being the crack length in the x-dimension (e.g., half of the length of a tunnel crack). We assume that the real intensity factor distribution along the reference straight crack front varies negligibly with z and also that the representative perturbation wavelength of the actual crack front is much smaller than the overall crack length. Thus the aforementioned half-plane crack result can be used with K^0 regarded as uniform along the crack front and independent of the crack length over the small perturbations to be considered. Note that the representative wavelength of the perturbation of the crack front must be consistent with that of the variation of the nonuniform fracture toughness along the crack front. Using an integration by part in equation (2), one can show that

$$\frac{K(z)-K^0}{K^0}=(1/2\pi)PV\int_{-\infty}^{+\infty}\frac{da(z')/dz'}{z'-z}\,dz'. \tag{3}$$

Let K_c and $\hat{K}_c$ denote the fracture toughness, or the critical K's, for the obstacle-free material and the obstacles, respectively. Now imagine a crack front that is trapped by obstacles of some given distribution. The crack penetrates between and partially into the obstacles so that we may assume the $K=K_c$ on the portions of the front between the obstacles and $K=\hat{K}_c$ on the portions where the obstacles are being partially penetrated. However, the penetration depth $a(z)$ is unknown in those penetrated zones. Yet, $a(z)$ is known but $K(z)$ is unknown where the crack front just contacts the obstacles. One then needs to solve the singular integral equation (3) for $a(z)$ and $K(z)$ with the values of either $a(z)$ or $K(z)$ given along complementary portions of the z-axis. The special solution to equation (3) with $K(z)=K^0=K_c$ and $a(z)=a_0=\text{const}$, corresponds to the initial state when crack penetration is imminent.

Clearly, equation (3) is strictly valid only if $|da(z)/dz|\ll 1$ over the whole crack front ($-\infty<z<\infty$). This is equivalent to $[K(z)-K^0]/K^0\ll 1$. Crack penetration into the obstacles starts when the applied K^0 is increased from K_c. Hence, during a penetration process one always has $[K(z)-K^0]/K^0\le[\hat{K}_c-K_c]/K_c$ so that the condition $|da(z)/dz|\ll 1$ can be guaranteed by having $[\hat{K}_c-K_c]/K_c\ll 1$. In practical terms it appears that our results are still approximately valid when $[\hat{K}_c-K_c]/K_c$ is near unity.

Downloaded 03 May 2010 to 171.66.16.31. Redistribution subject to ASME license or copyright; see http://www.asme.org/terms/Terms_Use.cfm

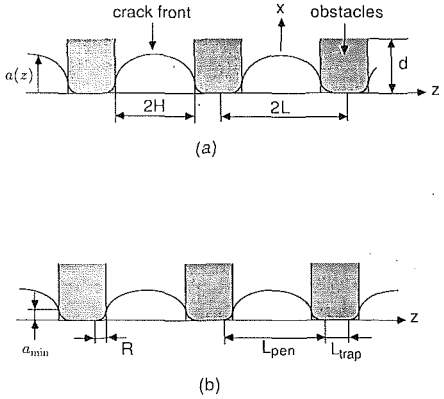


Fig. 2 (a) A crack front trapped by a periodic array of rectangular obstacles and (b) regions L_{trap}, L_{pen}, and R along the trapped crack front

Analogy to Elastic-Plastic Plane Stress Crack Model

Let us consider the two-dimensional plane stress problem in the y, z-plane, with an array of cracks along the z-axis on $y=0$ which can be represented by a continuous distribution of prismatic opening (edge) dislocations. A remotely applied uniform stress $\sigma_{yy}=\sigma^0$ generates an opening gap $\delta=\delta(z)$ (i.e., net y-direction displacement) between $y=0^+$ and $y=0^-$. The stress σ_{yy} along the $z-$axis, denoted by $\sigma(z)$, is the sum of σ^0 and the effect of a continuous distribution of edge dislocations representing the opening gap between the crack faces. Hence, we write the following,

$$\frac{2[\sigma(z)-\sigma^0]}{E}=\frac{1}{2\pi}\,PV\int_{-\infty}^{+\infty}\frac{d\delta(z')/dz'}{z'-z}\,dz'. \tag{4}$$

Equation (4) may be rearranged to coincide exactly with (3) provided that one makes the identifications (Rice, 1988)

$$2[\sigma(z)-\sigma^0]/E\rightarrow[K(z)-K^0]/K^0;\quad \delta(z)\rightarrow a(z). \tag{5}$$

Thus, the three-dimensional linearized perturbation problem of a crack trapped by, penetrating between, and partially into an array of blocking obstacles has the following two-dimensional plane stress analog: The z-axis is divided into the following two parts, L_{trap} and L_{pen}, analogous to the contact and penetration regions along the crack front (see Fig. 2(b)). Along L_{trap} the plane stress opening gap is prescribed, i.e., as a given distribution of prismatic opening dislocation corresponding to $\delta(z)=a(z)$. Along the portions of L_{pen} between the obstacles, conditions correspond to an array of plane stress cracks with the stress sustained along the crack faces prescribed as $\sigma(z)=\sigma^0+E(K_c-K^0)/2K^0$. The region denoted as R in Fig. 2(b), as a part of L_{pen}, is analogous to a Dugdale/BCS line plastic zone in plane stress, along which $\sigma(z)=\sigma^0+E(\hat{K}_c-K^0)/2K^0$. The region L_{trap} reduces, and R increases, with increase of the "applied" stress intensity K^0, as the crack front gradually penetrates into the obstacles. The size of the zones R must be determined as part of the solution by imposing the condition that $K(z)$ be finite (equal to $\hat{K}_c$) as the border between L_{trap} and R is approached from within L_{trap}. A special case when $\hat{K}_c\rightarrow\infty$, corresponding to impenetrable obstacles, has the analogy of purely-elastic plane stress cracks without plastic regions.

The plastic flow in the aforementioned analogous two-dimensional plane stress problem, of an array of cracks in an elastic-plastic sheet, is confined to line plastic zones along the z-axis. Thus $\sigma(z)=\hat{\sigma}_c(>\sigma^0)$ along the plastic zones R, where the Dugdale/BCS tensile yield strength $\hat{\sigma}_c$ is identified as $\sigma^0+E(\hat{K}_c-K^0)/2K^0$. The portions of L_{pen} complementary to R correspond to loaded crack faces on which $\sigma(z)=\sigma_c(<\sigma^0)$ ($\sigma_c=\sigma^0+E(K_c-K^0)/2K^0$).

Hence, the solutions for the three-dimensional problem of crack trapping by obstacles can be simply extracted from the known two-dimensional Dugdale/BCS plane stress crack model solutions, or from new solutions that can be generated by solving the integral equation or, perhaps, by solving an alternative numerical model of the two-dimensional plane stress problem.

Gradual Penetration of a Periodic Array of Obstacles

Figure 2 shows a periodic array of obstacles with center-to-center spacing of $2L$ and a gap $2H$ between them. The obstacles have flat edges, parallel to the z-axis, and are aligned so that the crack front encounters them simultaneously. Thus they could represent aligned rectangular-shaped obstacles of sufficiently large (see the following) extent d in the x-direction. As remarked, the trapping solution may be developed directly from the analogy to the two-dimensional solution of plane stress Dugdale/BCS model. The Dugdale/BCS model for a periodic crack array has been solved by Bilby and Swinden (1965) and Smith (1966). In particular, the parameters R and a_{min}, characterizing spread of the crack into the obstacles as defined in Fig. 2(b), are given by:

$$\mathrm{R}=\mathrm{H}\{(1/\epsilon)\arcsin[\sin\epsilon/\sin\mu]-1\}$$

$$a_{min}=\frac{2H}{\pi}\,\frac{\omega\sin\alpha}{\epsilon}\int_{\mu}^{\pi/2}\times\frac{\cos\phi}{(1-\sin^2\alpha\sin^2\phi)^{1/2}}\ln\left[\frac{\sin(\phi+\mu)}{\sin(\phi-\mu)}\right]d\phi \tag{6}$$

where

$$\mu=\pi(\hat{K}_c-K^0)/2(\hat{K}_c-K_c),\quad \omega=(\hat{K}_c-K_c)/K^0,$$

$$\epsilon=\pi H/2L,\quad \alpha=\pi(H+R)/2L. \tag{7}$$

These results are meaningful for the range

$$K_c\le K^0\le K_c+f(\hat{K}_c-K_c) \tag{8}$$

where $f=(L-H)/L$ is the line fraction of contact zones. The crack front is predicted, within the linear perturbation formulation, to completely penetrate the obstacles (i.e., L_{trap} shrinks to zero in Fig. 2(b)) at the upper limit. Of course, the linear perturbation procedures themselves are rigorously valid only for K^0 slightly greater than the lower limit K_c. Note that $\mu=\pi/2$ corresponds to the lower limit and $\mu=\epsilon$ to the upper limit.

The upper limit in (8) gives the limit load at which the crack front just breaks through the array of obstacles,

$$K^0=K_c+f(\hat{K}_c-K_c). \tag{9}$$

This predicts the maximum load that the crack obstacle system can sustain within the range of validity of the linear perturbation theory.

However, the limit load K^0 can be calculated exactly (Rice, 1988) if $K(z)$ is known everywhere along the crack front when the final failure of the crack obstacle system occurs. This would be true if the obstacles are fully penetrated prior to the final failure, so that the local $K(z)$ is everywhere equal to the local toughness. Since it is assumed here that the straight-crack-front value K^0 of equation (1) can be regarded as constant, it is necessary that

$$(K^0)^2=<[K(z)]^2> \tag{10}$$

be satisfied for any crack front configuration $a(z)$ in Fig. 1(b). Here the brackets denote an average along the entire z-axis. Equation (10) can be proved by considering the energy release in a unit translation of the crack front in the x-direction

Downloaded 03 May 2010 to 171.66.16.31. Redistribution subject to ASME license or copyright; see http://www.asme.org/terms/Terms_Use.cfm

without any change of the crack front shape. If no instabilities occur, $K(z)$ is known everywhere at final breakthrough, i.e., $K(z)=K_c$ on regions between the obstacles and $K(z)=\hat{K}_c$ within the obstacles. Hence, equation (10) gives the exact value of the limit load K^0 as

$$K^0=[K_c{}^2+f(\hat{K}_c{}^2-K_c{}^2)]^{1/2}. \tag{11}$$

This agrees with equation (9) to first-order in $(\hat{K}_c-K_c)$ and a table comparing the results over a range of parameters is given by Rice (1988).

However, crack obstacle systems can also fail by mechanisms involving instabilities that occur before the crack front has fully penetrated the blocking obstacles, in which case (11) does not apply. The BEM analysis of Fares (1988) showed that for a crack trapped by sufficiently tough obstacles, there is a maximum local $K(z)=WK_c$ which can be generated at the crack front prior to final instability. When the obstacle toughness $\hat{K}_c$ is more than WK_c, the penetrating crack front segments coalesce with one another and the crack front bypasses the still-intact obstacles. This mechanism of the final instability is completely different from anything explainable within the first-order theory. In fact, the first-order theory predicts that failure always occurs by having the crack front break through the obstacles, and the K^0 at breakthrough increases linearly with the obstacle toughness. The first-order theory also implies that an arbitrarily large local $K(z)$ can be developed where a crack is blocked by a sufficiently tough array of obstacles. Therefore, the first-order theory can be even qualitatively, as well as quantitatively, wrong when applied to tough obstacles.

Hence, W is defined as a critical parameter which sets the upper limit of the obstacle toughness value $\hat{K}_c=WK_c$ for having a breakthrough mechanism as predicted by the first-order theory. In other words, W sets the boundary between the breakthrough mechanism in which case the first-order theory is at least qualitatively correct and the bypass mechanism (coalescence of penetrating crack front segments beyond an unbroken particle) which is completely beyond the scope of the first-order theory. This W can only be determined through more accurate formulations such as the BEM analysis of Fares (1988). Since the maximum local $K(z)=\mathrm{WK_c}$, when the penetrating crack front segments start to coalesce unstably, would be determined solely by the configuration of the obstacles, W is dependent on that configuration. For a given center-to-center spacing and obstacle size measured in the z-direction, parallel to the crack front, W is sensitive to the obstacle size d in the x-direction. As a limiting case, W approaches infinity when $d\to\infty$, as in the case of straight-edge obstacles with semi-infinite extent in the x-direction. The toughness ratio $\hat{K}_c/K_c$ should be significantly smaller than W to get quantitatively acceptable results from linear analysis.

Even if the breakthrough mechanism is guaranteed by having $\hat{K}_c/K_c<W$, there exists another type of instability which leads to final failure before the state of full penetration of the obstacles is attained. In these cases $K(z)$ is not known everywhere at breakthrough (unknown along the unpenetrated portion of the obstacle). For convenience we will refer to such breakthrough processes that become unstable prior to the full penetration of obstacles as "irregular" processes, and others for which $K(z)$ is known everywhere at breakthrough as "regular" processes. In the next section we explore the critical parameters associated with irregular processes within the first-order theory. It will be shown that for rectangular obstacles of given L and H as shown in Fig. 2, a critical length d^L can be defined so that the penetration process is regular if $d>d^L$ and irregular if $d<d^L$.

Therefore, the failure processes of a crack trapped by blocking obstacles fall into three categories. Taking rectangular obstacles of given L and H as in Fig. 2(*a*) as a demonstration, there are two critical parameters W, d^L. If the toughness ratio $\hat{K}_c/K_c>W$, the crack will bypass the obstacles without breaking them (category 1). When $\hat{K}_c/K_c<W$, the crack will break the obstacles by penetration. The penetration process will be regular (category 2) if $d<d^L$ and irregular (category 3) if $d>d^L$. The first category involves the mechanism of crack bypassing the unbroken obstacles, which is completely beyond the scope of the first-order theory. We will restrict our attention to the latter categories (2 and 3) of breakthrough mechanism.

For regular processes the obstacles are gradually penetrated by the crack until final breakthrough. The argument leading to equation (11) for rectangular obstacles can be readily extended to arbitrarily-shaped, but symmetric (about the x-direction), blocking obstacles in a periodic array. Let us define $f(x_0)$ as the line fraction of the obstacles on a straight line located at $x=x_0$ parallel to the original crack front. (For rectangular obstacles of Fig. 2, the line fraction $f(x_0)$ is a constant which takes the value of $(L-H)/L$). Equation (11) then gives the exact value of the limit load K^0, provided that f now represents the maximum line fraction, i.e., $f=\max_{x_0} f(x_0)$. In fact, this is also the upper bound for limit load for irregular penetration processes in the third category. For general, possibly asymmetric blocking obstacles, the limit load for regular processes can still be calculated from (11), but the line fraction f now depends on the crack front profile at final breakthrough. Again considering the energy release in a unit rigid translation of the crack front in the x-direction at the final breakthrough, one easily concludes that $f=S/2L$ where S represents the projection in the z-direction of all the crack front segments within the obstacles in one period. This is even true for mulitrow systems of periodic arrays of obstacles (see later examples), in which case the bowing-out crack front will encounter obstacles in different rows.

Assuming $[\hat{K}_c-K_c]/K_c$ is sufficiently small, both regular and irregular crack penetration processes can be studied by first-order perturbation theory. In particular, the irregular processes deserves special attention. We next report a quantitative study on the role of the shape and size of the obstacles in crack penetration processes and discuss the limit load for irregular processes. The case discussed previously, for crack trapping by periodic array of rectangular obstacles with large x-dimension shown in Fig. 2, is important in the following discussions. For convenience we will refer to it as the "model" case.

Irregular Processes in Crack Penetration of an Array of Obstacles

The problem is addressed on the assumption that $[\hat{K}_c-K_c]/K_c$ is within a range suitable for linear perturbation theory. Referring to the model case shown in Fig. 2, we denote the value of $a_{\min}$ at the complete penetration of the obstacles (i.e., $R=L-H$) by a^L, and define the area between the line $x=a^L$ and the crack front within an obstacle by A^L(Fig. 3(*a*)). Taking the upper limit $\mu=\epsilon=(1-f)\pi/2$ in equations (6), one obtains

$$\frac{a^L}{L}=\frac{4}{\pi^2}\,\frac{\hat{K}_c-K_c}{K_c+f(\hat{K}_c-K_c)}\int_0^{f\pi/2}\ln\left[\frac{\sin(f\pi/2+\phi)}{\sin(f\pi/2-\phi)}\right]d\phi. \tag{12}$$

Hence, a^L/L is expressed as a function of the line fraction f of the obstacles and the toughness ratio $\hat{K}_c/K_c$. Now imagine an array of arbitrarily-shaped, but symmetric (about the x-direction), obstacles spaced by $2L$ with a minimum gap of $2H$ in the z-direction. We choose a model case with parameters H, L for reference. If an obstacle can fully contain the area A^L associated with the chosen reference (Fig. 3(*b*)), then at breakthrough the crack is undergoing exactly the same state as

Downloaded 03 May 2010 to 171.66.16.31. Redistribution subject to ASME license or copyright; see http://www.asme.org/terms/Terms_Use.cfm

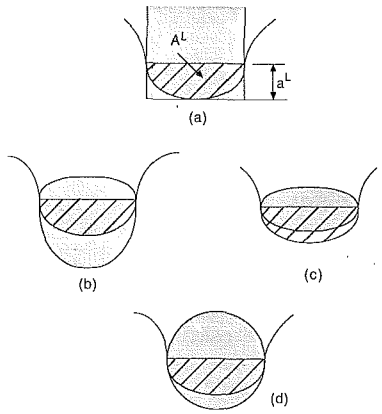


Fig. 3 (*a*) Area A^L distinguishing between regular and irregular penetration processes; shapes of obstacles that cause (*b*) regular and (*c*) irregular processes; (*d*) round obstacles

the reference model case. Therefore, the penetration process is a regular one so that equation (9) applies to give the limit load based on the maximum line fraction f of the obstacles in the z-direction. For example, it can be proved that $a^L < L-H$ (the proof can be achieved by choosing a variable $u=(L-H)/L$, then forming a function $g(u)=a^L/L-u$ and proving that $g(u)$ is monotonously decreasing from zero over the interval [0, 1]). Therefore, the crack penetration of an array of round obstacles with radius equal to $L-H$ is a regular process (Fig. 3(*d*)), in which case the limit load is predicted by equation (9) for maximum line fraction $f=(L-H)/L$.

However, if the shape of the obstacle can not fully envelop the area A^L of the reference state, but rather is contained (below its maximum width line) fully within A^L (Fig. 3(*c*)), the full penetration of the obstacle will not be possible at the moment of final breakthrough. That is, an instability will lead to breakthrough prior to the full penetration and the penetration is irregular. Therefore, the area A^L is the critical parameter that distinguishes between the regular and irregular processes. The actual breakthrough loads for irregular processes are smaller than those predicted by equation (9) using the maximum line fraction f.

Usually the calculation of limit loads for irregular processes requires numerical search for the occurrence of instability. However, there are some some cases for which direct analysis suffices. For example, consider a periodic array of obstacles with shape shown in Fig. 4(*a*). Apparently the penetration would be a regular one if the height d of the base portion of the obstacles is greater than a^L, i.e., $d>a^L$. When $d<a^L$, the process is an irregular one if the angle $\psi<\pi/2$. Let us look at a moment at which the crack has penetrated into the obstacle an amount characterized by the parameter p shown in Fig. 4(*a*). It can be argued that the shown state, if in equilibrium with the imposed load, is the same as another model case with parameter H' defined by $H'=H+p$. It follows from equations (6) that

$$d+p\tan\psi=\frac{4L}{\pi^2}\,\omega\sin\epsilon\int_{\mu}^{\pi/2}\times\frac{\cos\phi}{(\sin^2\mu-\sin^2\epsilon\sin^2\phi)^{1/2}}\ln\left[\frac{\sin(\phi+\mu)}{\sin(\phi-\mu)}\right]d\phi \qquad (13)$$

where $\epsilon=\pi H'/2L$ and μ, ω are as defined in equations (7). If we take the derivative of both sides of equation (13), with respect to p, keeping other parameters constant, we can solve for the quantity dK^0/dp for any p. If $dK^0/dp>0$ the current state is a stable one, in the sense that the load K^0 needs to be increased to increase the penetration p. Instability (failure) occurs when $dK^0/dp\le 0$ with the critical point reached when the

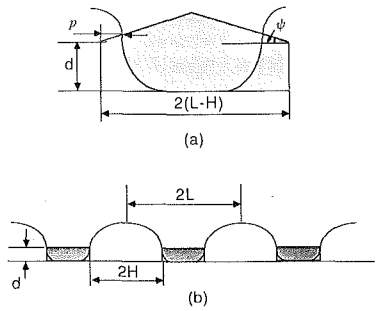


Fig. 4 (*a*) A special shape of the blocking obstacles; parameter p describing the crack penetration into the obstacles and (*b*) an example of an irregular penetration process caused by rectangular obstacles

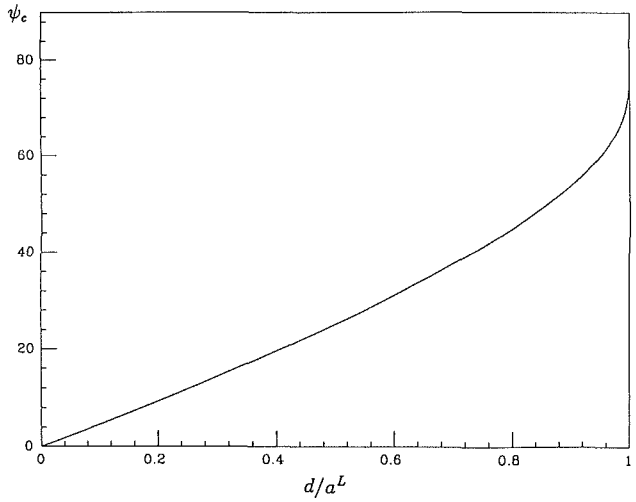


Fig. 5 Critical angle ψ_c for the obstacle shape shown in Fig. 4

equal sign is taken. An important case is $dK^0/dp\,|_{p=0}=0$, which determine a critical angle ψ_c below which the instability occurs instantly when $p=0$. After some algebraic manipulations, it can be shown that

$$\tan\psi_c=\frac{2}{\pi}\,\omega\int_{\mu}^{\pi/2}\times\frac{\cos\epsilon\cos\phi\sin^2\mu}{(\sin^2\mu-\sin^2\epsilon\sin^2\phi)^{3/2}}\ln\left[\frac{\sin(\phi+\mu)}{\sin(\phi-\mu)}\right]d\phi \qquad (14)$$

where $\epsilon=\pi H/2L$ at $p=0$ and ω, μ are determined further by solving (13) for K_0 using $p=0$. That is

$$d=\frac{4L}{\pi^2}\,\omega\sin\epsilon\int_{\mu}^{\pi/2}\times\frac{\cos\phi}{(\sin^2\mu-\sin^2\epsilon\sin^2\phi)^{1/2}}\ln\left[\frac{\sin(\phi+\mu)}{\sin(\phi-\mu)}\right]d\phi. \qquad (15)$$

When the geometrical angle ψ is less than ψ_c, the limit load K^0 at which the crack breaks the obstacles is then determined directly by equation (15). We observe that $\psi_c=\pi/2$ for $\mu=\epsilon$ corresponding to the upper limit in (8), so that at that limit the crack breaks through the obstacles with any ψ, up to $\psi=90$ deg (corresponding to the model case). As $d\to 0$, as for a very thin obstacle, $\mu\to\pi/2$ and $\psi_c\to 0$. Usually $0<\psi_c<\pi/2$. The value of ψ_c is plotted in Fig. 5 against d/a^L, the height of the obstacle nondimensionalized by a^L, for $H/L=0.5$ and $\hat{K}_c/K_c=2$. It is shown that ψ_c is increasing in a rather linear fashion with d/a^L until $d/a^L\simeq 0.9$, after which a sharp increase toward 90 deg is then observed. A rectangular obstacle with $\psi=0$ and $d<a^L$ can then be always categorized as $\psi<\psi_c$ (Fig. 4(*b*)), and the limit load at which a crack breaks through an array of rectangular-shaped obstacles is deter-

Downloaded 03 May 2010 to 171.66.16.31. Redistribution subject to ASME license or copyright; see http://www.asme.org/terms/Terms_Use.cfm

mined by the equation (15) when $d<a^L$. Hence, one can define a critical length $d^L(=a^L)$ for rectangular obstacles so that the crack penetration process is regular if $d>d^L$ and irregular if $d<d^L$.

Finally, if $\psi>\psi_c$, instability will occur at some $p>0$ and a similar critical location can be determined by the condition $dK^0/dp=0$. We do not present the details of the analysis.

Numerical Formulation of Crack Penetration of Periodic Arrays of Obstacles

Within the range of validity of the linear perturbation theory, we have discussed the problem of crack trapping by a single array of obstacles based on an analogy to the two-dimensional Dugdale/BCS plane stress crack model. The solutions are given for characteristic quantities such as the penetration depths and the limiting K value at which the final breakthrough occurs. In the following we formulate the trapping problem by an alternative, more powerful numerical procedure. The results are compared to those previously derived as well as applied to other cases for which analytical solutions are not know.

General Numerical Formulation. For the general formulation consider that the fracture toughness varies in space so that on the crack plane, $K_c=K_c(x, z)$. The crack will grow at the positions along the crack front where the stress intensity factor exceeds the fracture toughness K_c. We adopt the following "viscoplastic" model for the crack growth

$$\frac{\partial a(z,t)}{\partial t}=\begin{cases}\rho[K(z,t)-K_c(a(z,t),z)] & K<K_c\\ 0 & \text{otherwise}\end{cases} \tag{16}$$

where t is a time parameter in this model and ρ is a coefficient that represents the "viscosity" of the system. By making ρ sufficiently large, or else (as we do) by waiting a sufficiently long time for a new equilibrium configuration of the crack front to be approached after each small increase of load K^0 in a "staircase" load versus time history, we can make (stable) growth occur arbitrarily close to the condition that $K=K_c$ during growth. Mastrojannis et al. (1980) have used a similar (but higher order) criteria in analyzing planar crack growth induced by hydraulic fracturing.

Note that in equation (16), $K=K(z,t)$ is related to $a(z,t)$ by equation (3) at a time t. In principle one can solve the coupled equations (3) and (16) for $K(z,t)$ and $a(z,t)$. Apparently $a(z)=a(z,\infty)$, after step increase to the K^0 of interest, is the final equilibrium crack profile, corresponding to the sort of solution for crack penetration discussed in the previous sections. While it is often impossible to solve the coupled equations analytically, numerical procedures can be designed by discretizing the equation (16) into small time steps, and for each step updating $a(z,t)$ and $K(z,t)$ according to (3). The time step Δt for any given value of ρ can be adjusted to speed up the convergence of the solution. We will apply this procedure to the periodic array of blocking obstacles in the following.

Tunnel Cracks With Periodic Arrays of Obstacles. Consider a tunnel crack lying in a homogeneous, isotropic elastic solid, having length $2a$ along the x-axis, and subjected to a remote tensile stress σ that induces

$$K^0=K^0[a]=\sigma\sqrt{\pi a} \tag{17}$$

along the crack front. The crack advance is blocked by an array of obstacles. Assuming the half-size of the tunnel crack is initially equal to a_i, crack growth will be imminent once the load σ reaches a point that condition $K^0=\sigma\sqrt{\pi a_i}=K_c$ is satisfied, where here K_c is the minimum fracture toughness of the elastic medium along $x=a_i$. With further increase of the load, the crack will grow into a new equilibrium state having a slightly curved front. Now expand $a(z,t)$ and $K(z,t)$ in Fourier series,

$$a(z,t)=\sum_{n=-\infty}^{\infty}A_n e^{in\pi z/L},\qquad K(z,t)=\sum_{n=-\infty}^{\infty}K_n e^{in\pi z/L}, \tag{18}$$

where we recall that $2L$ is the obstacle spacing. Here $A_n=A_{-n}$, $K_n=K_{-n}$ are necessary for $a(z,t)$, $K(z,t)$ to be real valued. Substituting equations (18) into equation (3), and carrying out the principal value integrations, one finds (Rice, 1985a),

$K_0=K^0[A_0]=\sigma\sqrt{\pi A_0}$ and, for $n\neq 0$,

$$K_n=\left\{\frac{dK^0[A_0]}{dA_0}-\frac{n\pi}{2L}K^0[A_0]\right\}A_n=\frac{K_0}{2}\left\{\frac{1}{A_0}-\frac{n\pi}{L}\right\}A_n. \tag{19}$$

Equations (19) replace equation (3) in the case of periodic array of obstacles. Since equation (3) is for a half-plane crack and valid only to the first order in da/dz (or $\partial a(z,t)/\partial z$)), equations (19) are only valid when L/A_0, $|A_n|/A_0\ll 1$.

For a single cosine wave perturbation assume that $A_n=0$ for $|n|>1$ so that $a(z)=A_0+2A_1\cos(\pi z/L)$. In this case, it follows from (19) that

$$K(z)=K_0\left[1+\left(1-\frac{\pi A_0}{L}\right)\frac{A_1}{A_0}\cos(\pi z/L)\right]. \tag{20}$$

Fares (1988) has shown that the error of (20), when $A_1/A_0\ll 1$, is within seven percent for $A_1=0.1L$ but can be as large as 20 percent for $A_1=0.2L$. It is seen from (20) that $K(z)$ is predicted to be linear with A_1, and when A_1/L exceeds $1/\pi$, $K(z)$ is predicted to be negative at the most protruding parts of the crack front, e.g., $z=0$. This is why the first-order theory can be qualitatively wrong when applied to tough obstacles in which case large crack front perturbations might occur. By contrast, the BEM results of Fares (1988) show that $K(z)$ attains the smallest, but always positive, value at the most protruding parts along the crack front.

The fast Fourier transform (FFT) method is used to carry out the expansion and inversion of the Fourier series in equations (18). The numerical procedure of solving for the equilibrium profile $a(z)$ at a given load σ is then formulated as follows: The initial shape function $a(z,0)$ (e.g., a constant at the start of the procedure) is expanded into a Fourier series by the FFT method, and the coefficients K_n in the second of equations (18) are calculated by equations (19). A FFT inversion (or summation) by equation (18) gives the distribution of $K(z,0)$. Equation (16) is then used, for a chosen time interval Δt (sufficiently small for numerical convergence) and constant (arbitrary) ρ, to calculate the amount of growth $\Delta a(z,0)$ for one period $0<z<2L$, therefore updating $a(z,\Delta t)$ as $a(z,0)+\Delta a(z,0)$. This procedure is repeated to calculate the subsequent growth until the final equilibrium state is achieved in which $a(z,t)$ no longer increases by any substantial amount (e.g., less than $10^{-6}L$), indicating that conditions $K(z)=K_c$, $K(z)=\hat{K}_c$ are satisfied to the accuracy required along the corresponding portions of penetration. Then the applied stress may be increased by another step and the same sequence of steps followed. We have found that this procedure is a rapidly convergent process for properly chosen time steps (scaling inversely with the constant ρ).

In order to compare the numerical solution to the previously derived results, we consider again the model case of crack penetration into a periodic array of semi-infinite obstacles spaced at gaps of $2L$ as shown in Fig. 2. Figure 6 depicts the obstacles (as lightly-shaded regions) with $H=0.5L$ and the trapped crack front profiles in one period $-1<z/L<1$. The initial crack length a_i is assumed to be 10 times L for the solid

Downloaded 03 May 2010 to 171.66.16.31. Redistribution subject to ASME license or copyright; see http://www.asme.org/terms/Terms_Use.cfm

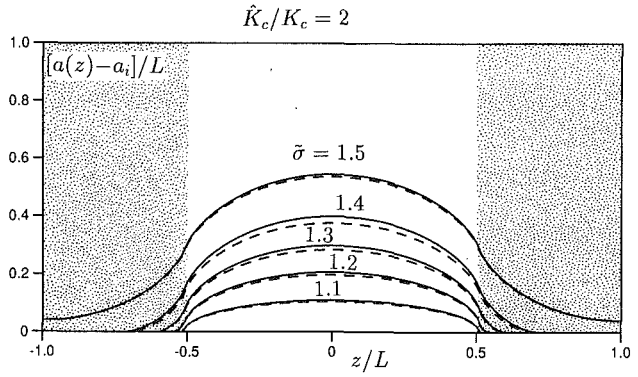


Fig. 6 Crack penetrating a periodic array of straight-edged obstacles aligned in front of a crack with toughness ratio $\hat{K}_c/K_c = 2$. For solid line curves $a_i = 10L$ and for dashed line curves $a_i = 100L$.

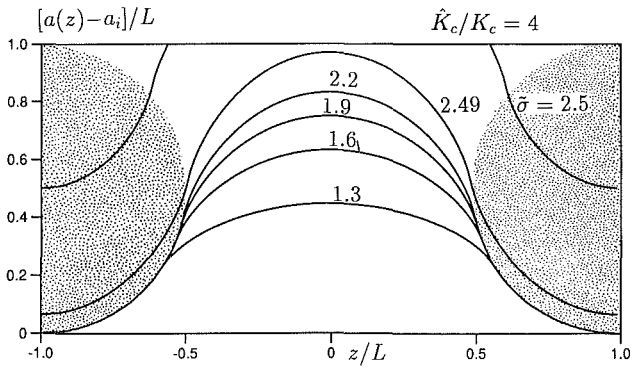


Fig. 7 An array of round obstacles spaced by 2 diameters and the crack trapping profiles when toughness ratio $\hat{K}_c/K_c = 4$ (note that the first-order theory gives qualitatively wrong predictions at the higher $\tilde{\sigma}$ values in this case, see text)

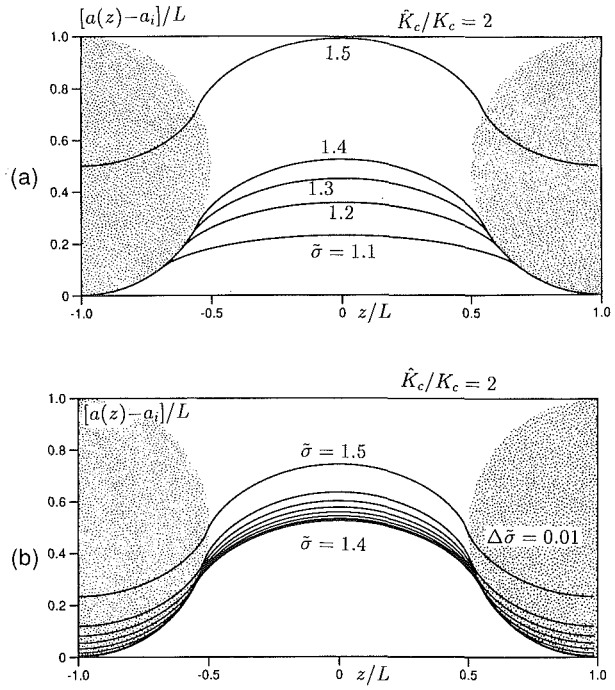


Fig. 8 Crack trapping profiles for round obstacles with toughness ratio $\hat{K}_c/K_c = 2$, when the load σ is increased (*a*) from 1.1 to 1.5 with a step increment of 0.1 and (*b*) from 1.4 to 1.5 with a step increment of 0.01

line curves. The load σ_i for penetration to start and the initial crack length a_i are related by

$$\sigma_i\sqrt{\pi a_i} = K_c. \tag{21}$$

We define a nondimensional load parameter as $\hat{\sigma} = \sigma/\sigma_i$. The fracture toughness $\hat{K}_c$ of the obstacles is taken as twice the value of K_c. The crack front trapping configurations are shown in solid lines in Fig. 6. The full penetration, which is also the final breakthrough in this special case, occurs when $\hat{\sigma}$ reaches 1.5, as predicted in equation (9). Also shown in Fig. 6 in dashed lines are the corresponding curves when $a_i = 100L$, in which case the half-plane crack is better approximated. We see that the curves for $a_i = 10L$ are very close to those at $a_i = 100L$. The penetration curves also match closely the previously derived $a_{\min}$ and R of equations (6).

Before concluding this section, we further consider a crack penetrating an array of round, circular-shaped obstacles spaced by 2 diameters (Fig. 7). To examine the validity range of the first-order theory, let us first assume a toughness ratio $(\hat{K}_c/K_c)$ of 4. The trapping configurations are shown in Fig. 7 and the final breakthrough occurs at $\hat{\sigma} = 2.5$. Fares (1988) calculated the stress intensity factor distribution corresponding to these first-order-accurate trapping configurations. His results show that only the first profile, corresponding to $\tilde{\sigma} = 1.3$, gives the correct $K(z)$ distribution, i.e., $K(z) = K_c$ along the penetrating portion of the crack front. As shown in Fig. 7, the maximum perturbation for the first trapping profile is slightly greater than $0.4L$, which is reasonably consistent with the BEM results on the single cosine wave perturbation shown before. Fares (1988) also pointed out that in this case the maximum local $K(z)$ which can be generated along the crack front is only $3.52K_c$, i.e., $W = 3.52$. The final failure occurs at $\tilde{\sigma} = 2.35$, by having the crack front bypass the still-intact obstacles. The first-order-accurate trappings configurations at the higher $\tilde{\sigma}$ values in Fig. 7 are, hence, even qualitatively wrong.

This indicates that it is necessary to reduce the toughness ratio substantially in order to apply the first-order theory. The maximum perturbation of the crack front should be kept within a reasonable range. Figure 8(*a*) depicts the trapping profiles when the toughness ratio is reduced to 2. In this case the maximum perturbation is below $0.6L$ and the linear perturbation theory can be regarded as an acceptable approximation. In Fig. 8(*b*) a more detailed picture of the crack penetrating the round obstacles is shown as the applied load is gradually increased from 1.4 to 1.5 with a step increment of 0.01. The complete breakthrough of the whole array of obstacles occurs when $\tilde{\sigma} = 1.5$. This confirms the previous conclusions that the penetration of round obstacles is a regular process when the toughness ratio is low enough for analysis within the first-order theory. The penetration of the obstacle starts at a load level lower than but close to the final breakthrough load (in our case $\tilde{\sigma}_{\text{pen}} = 1.44$). One may see in Fig. 8(*a*), (*b*) that the crack initially grows by following closely the outer curvature of the obstacles and starts penetrating the obstacle when $\tilde{\sigma} = 1.44$. Shortly after the start of penetration the final breakthrough occurs. This occurs because the circular boundary of the obstacles is close to the bounding curve of A^L. A limiting case is when the shape of the blocking obstacles exactly coincides with the contour of A^L. Then no partial penetration of the obstacles will occur before the final breakthrough.

Some Further Case Studies

Here we give several examples of using the viscoplastic/FFT numerical model to show how a crack starts to penetrate and surround round obstacles, emplaced in the form of multirow periodic arrays, as the applied load is gradually increased. A toughness ratio of two is assumed for each crack obstacle system. The obstacles are shown as lightly-shaded regions in Figs. 9-12.

Downloaded 03 May 2010 to 171.66.16.31. Redistribution subject to ASME license or copyright; see http://www.asme.org/terms/Terms_Use.cfm

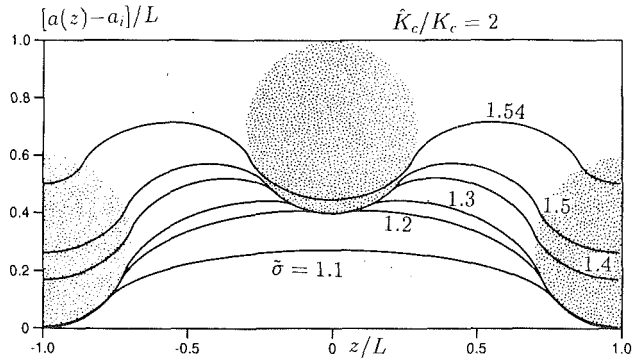


Fig. 9 Case 1: a crack penetrating two rows of periodic arrays of round obstacles with diameter equal to 0.3 times the obstacle spacing

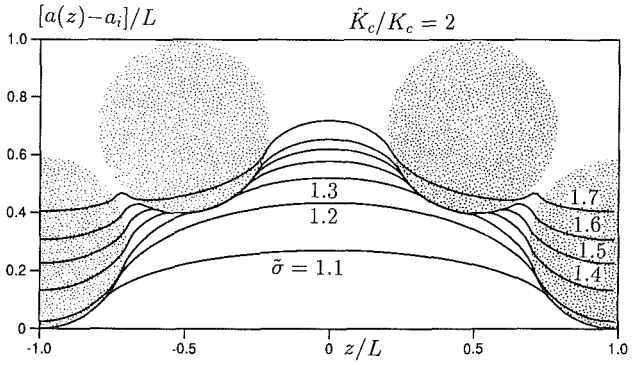


Fig. 10 Case 2: a crack penetrating two rows of periodic arrays of round obstacles with diameter equal to 0.3 times the obstacle spacing

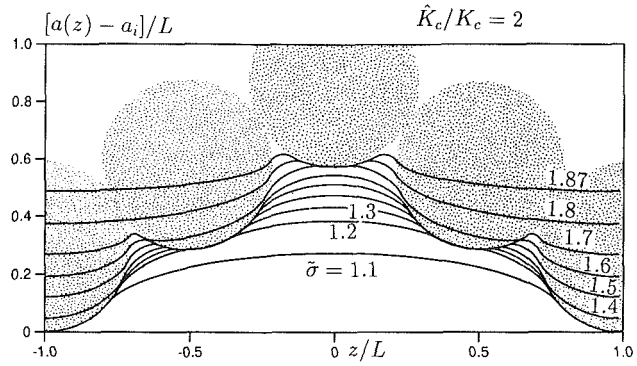


Fig. 11 Case 3: a crack penetrating three rows of periodic arrays of round obstacles with diameter equal to $1/2\sqrt{3}$ times the obstacle spacing

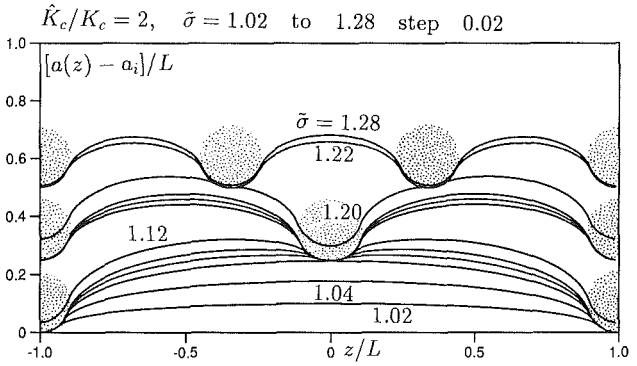


Fig. 12 Case 4: a crack penetrating three rows of periodic arrays of round obstacles with diameter equal to 0.1 times the obstacle spacing

Case 1. Figure 9 shows a two-row periodic array of round obstacles (lightly-shaded circular regions) in one period $-1 < z/L < 1$. The radius of the obstacles is taken as $0.3L$. As can be observed from the resulting crack front trapping configurations, the crack penetration starts by following the circular boundary of the round obstacles in the first row. When load $\tilde{\sigma}$ is increased to 1.2, the central part of the penetrating crack front touches the second row of obstacles, and at $\tilde{\sigma} = 1.4$, the first row of the obstacles is fully penetrated. The final breakthrough occurs at $\tilde{\sigma} = 1.55$.

Case 2. We consider in the second case two rows of round obstacles, still with radius $0.3L$, but with one more obstacle in the second row as shown in Fig. 10. The trapping profiles display more complicated features when the applied load $\tilde{\sigma}$ is increased by step increments of 0.1. The first row gets penetrated at $\tilde{\sigma} = 1.3$ and the final breakthrough occurs at $\tilde{\sigma} = 1.71$.

Case 3. In Fig. 11 three rows of blocking round obstacles are shown, each with radius equal to $L/2\sqrt{3}$. The lines that join the centers of neighboring obstacles are inclined by 30 deg relative to the z-axis (horizontal line). The final breakthrough occurs at $\tilde{\sigma} = 1.87$. This obstacle arrangement is interesting, in that a toughening ratio (K^0/K_c) of 1.87 is achieved with the area fraction of the obstacles less than 0.5. This occurs because at final breakthrough a large portion of the crack front lies within the obstacle region. Hence, this type of obstacle arrangement is quite efficient in toughening the elastic matrix material. This suggests an interesting problem to find the optimum arrangement for the obstacles at a given volume fraction such that the maximum toughening can be achieved. We leave it as future work to address such issue.

Case 4. Finally, we give a simulation of a crack penetrating smaller particles (with radius taken as $0.1L$) as shown in Fig. 12. Again, three rows of blocking round obstacles are shown, each row contains one more obstacle such that it is harder to break than the previous row. As the obstacles in the first row have a large spacing, part of the crack front contacts the second row and the interaction effect results in stronger resistance to crack penetration. Such interaction becomes smaller between the second and third row and the final breakthrough occurs at $\tilde{\sigma} = 1.30$.

These case studies clearly show that significant toughening of a brittle matrix can be achieved through crack trapping by obstacles (e.g., second-phase particles, inclusions, etc.) by having the obstacles emplaced in a "good arrangement" such that the bowing out crack front encounters the maximum number of obstacles in final breakthrough. In these discussions we have excluded the possibility of having crack bypass tough obstacles (see previous discussions in the text). That mechanism gives rise to unbroken ligaments behind the crack front, which cause an additional toughening effect, referred to as the "bridging effect" in the literature, by reducing the effective crack front stress intensity factor. One expects that, in reality, these mechanisms will have a combined toughening effect on a brittle matrix containing tough second-phase inhomogeneities.

While our considerations here are for tensile (mode I) cracks, the corresponding equations of the first-order perturbation theory are of closely similar form for those loaded in mode II or mode III shear (Gao and Rice, 1986). Thus, to the extent that a shear crack adequately models a tectonic fault, the present considerations may be of interest for faulting in regions of heterogeneous shear toughness.

Acknowledgments

The work reported was supported by subagreement POAVB38639-0 with Harvard University from the University

Downloaded 03 May 2010 to 171.66.16.31. Redistribution subject to ASME license or copyright; see http://www.asme.org/terms/Terms_Use.cfm

of California at Santa Barbara, based on ONR contract N00014-86-K-0753, and by the U.S. Geological Survey under grant 14-08-0001-G1367 to Harvard. We are grateful to Dr. Nabil Fares for valuable discussions.

References

Bilby, B. A., and Swinden, K. H., 1965, "Representation of Plasticity at Notches by Linear Dislocation Arrays," *Proc. Roy. Soc.*, Vol. 285A, pp. 23-33.

Fares, N., 1988, "Crack Front Trapped by Arrays of Obstacles: Numerical Solutions Based on Surface Integral Representation," ASME JOURNAL OF APPLIED MECHANICS, Vol. 56.

Gao, H., and Rice, J. R., 1986, "Shear Stress Intensity Factors for a Planar Crack With Slightly Curved Front," ASME JOURNAL OF APPLIED MECHANICS, Vol. 53, pp. 774-778.

Mastrojannis, E. N., Keer, L. M., and Mura, T., 1980, "Growth of Planar Cracks Induced by Hydraulic Fracturing," *International Journal of Numerical Methods in Engineering*, Vol. 15, pp. 41-54.

Rice, J. R., 1988, "Crack Fronts Trapped by Arrays of Obstacles: Solutions Based on Linear Perturbation Theory," *Proceedings of Symposium on Analytical, Numerical and Experimental Aspects of Three-Dimensional Fracture Processes*, ASME-AMD Vol. 91, A. Rosakis, K. RaviChandar, and Y. Rajapakse, eds., pp. 175-184.

Rice, J. R., 1985a, "First Order Variations in Elastic Fields Due to Variation in Location of a Planar Crack Front," ASME JOURNAL OF APPLIED MECHANICS, Vol. 52, pp. 571-579.

Rice, J. R., 1985b, "Three-Dimensional Elastic Crack Tip Interactions with Transformation Strains and Dislocations," *International Journal of Solids and Structures*, Vol. 21, pp. 781-791.

Smith, E., 1966, *Proceedings of the 1st International Conference of Fracture*, Vol. 1, T. Yokobori et al., eds., Japanese Society for Strength and Fracture of Materials, Tokyo, pp. 133-152.

Downloaded 03 May 2010 to 171.66.16.31. Redistribution subject to ASME license or copyright; see http://www.asme.org/terms/Terms_Use.cfm

Crack Fronts Trapped by Arrays of Obstacles: Numerical Solutions Based on Surface Integral Representation

Nabil Fares[1]
Civil Engineering,
Rensselaer Polytechnic Institute,
Troy, NY 12181

This paper addresses the trapping of the front of a planar crack as it impinges upon a row of periodically-emplaced tough obstacles. The initial penetration of the crack between obstacles, under increasing load, as well as the ultimate unstable joining of penetrating segments so as to surround and by-pass the obstacles, are analyzed. The formulation used for the associated three-dimensional elasticity problems of half-plane cracks with nonuniform, curved fronts is a Boundary Element Method (BEM). This incorporates a specialized fundamental solution for an opening (prismatic) dislocation source ahead of a half-plane crack with a straight front (Rice, 1985a). The implementation of this BEM and associated mesh moving with the front is first discussed after which a series of case studies are carried out. The first two case studies evaluate the accuracy of previously obtained linear perturbation results (Rice (1985b), Gao and Rice (1988)). The last study is a crack growth simulation around a periodic array of circular obstacles with a particle size to spacing ratio of 0.5. The simulation shows in that case that crack trapping achieves an effective toughening ratio of 2.35 when the particle-to-matrix-toughness ratio (K_{cp}/K_c) is greater than 3.52. The simulation also gives lower bounds on the net toughening when $K_{cp}/K_c < 3.52$.

Introduction

The object of this paper is to study crack trapping. Crack trapping is a specific micromechanism of toughening in a brittle matrix containing second-phase inclusions (Lange (1970)). Two related toughening micromechanisms of crack front interaction with second-phase inclusions have been recognized in the literature. These are the bridging and the trapping effect. Unbroken ligaments surrounding second-phase inclusions or fibers can sometimes lag behind a main crack front. These ligaments would then serve as bridges forming a process zone and reducing the effective crack front stress intensity factor. This mechanism of toughening is referred to as the bridging effect and has been extensively studied (e.g., Krstic, 1983; Rose, 1987a; Budiansky et al., 1988). On the other hand, crack trapping addresses the process by which tough second-phase inclusions get surrounded or cracked by an advancing crack front. The crack-trapping effect was first studied by Lange (1970, 1971) who (based on experimental observations) suggested an analogous mechanism in crack front movement to that of dislocations bowing between obstacles. Lange attempted to quantify this possible source of toughening on the basis of a line tension associated with the crack front. Evans (1972) further considered this idea and noted that toughening cannot be simply related to the increase in length of a crack front due to bowing. Evans also noted that toughening should depend on the ratio of inclusion-size-to-spacing and not solely on the spacing as was predicted by Lange's line tension model. Finally, Rose (1987b) developed a model which assumed the two effects identified here as crack trapping and crack bridging to be multiplicatively reinforcing. However, Rose circumvented the trapping studies by assuming a simple rule of mixtures as the crack-trapping toughening effect.

In contrast to the bridging effect, the trapping effect requires explicit three-dimensional modeling in order to be effectively discussed. That is because the Stress Intensity Factor (SIF) variations along the crack front have to be accounted for explicitly in crack-trapping studies whereas smearing of the "bridges" along the direction parallel to the macrocrack in order to obtain a two-dimensional mechanical model plausibly retains the essence of the bridging effect. The development of three-dimensional weight function theory (Rice (1985a,b)) provided a means of effectively studying SIF variations along a crack front. In particular, the theory of first-order variation of SIF due to variation in location of a planar crack front (Rice 1985b) made the preliminary analysis of the crack-

[1]Formerly in the Division of Applied Sciences, Harvard University.

Contributed by the Applied Mechanics Division of THE AMERICAN SOCIETY OF MECHANICAL ENGINEERS for publication in the JOURNAL OF APPLIED MECHANICS.

Discussion on this paper should be addressed to the Editorial Department, ASME, United Engineering Center, 345 East 47th Street, New York, N.Y. 10017, and will be accepted until two months after final publication of the paper itself in the JOURNAL OF APPLIED MECHANICS. Manuscript received by the ASME Applied Mechanics Division, December 1, 1988; final revision, February 28, 1989.

Copyright © 1989 by ASME

Downloaded 03 May 2010 to 171.66.16.31. Redistribution subject to ASME license or copyright; see http://www.asme.org/terms/Terms_Use.cfm

trapping problem possible. In a first study (Rice (1988)), a methodology of obtaining the configuration of the front of a planar crack which is trapped against forward advance by contact with an array of obstacles was presented. The method was then used to obtain an analytic solution to a periodic array of long rectangular obstacles. Gao and Rice (1988) further developed the first-order perturbation, crack-trapping analysis and included discussions concerning the effect of obstacle shape. Gao and Rice also implemented a numerical procedure (based on the linear perturbation theory) having a "viscoplastic" crack growth model which, in the limit they considered, simulates growth with the intensity factor equal to the local fracture toughness. They simulated the evolution of a crack front encountering an array of round obstacles as the applied load was quasi-statically increased. The present study evaluates the accuracy of the first-order perturbation studies and performs an analogous crack growth simulation without the linearization assumptions. It analyzes the finite penetration of crack segments between obstacles and the ultimate joining of segments so as to by-pass particles. These problems are well beyond the scope of the linear perturbation theory.

Formulation

In order to study the trapping effect, a specific mechanical model has to be considered. Following Gao and Rice (1988), the present model is a half-plane tensile crack with an arbitrarily shaped but symmetric and periodic crack front in an elastic medium. The nonstraightness of a crack front could be ascribed to the trapping effect of periodic second-phase inclusions. Thus, by having the capability to evaluate the SIF values along a nonstraight crack front, investigation of the accuracy of the first-order perturbation results as well as crack growth simulations could be performed. However, there are several limitations to the present model. For example, the half-plane crack idealization applies to finite-sized cracks only when the cracks are long compared to the micromechanical length parameters (such as second-phase size and spacing). The model also assumes that the elastic moduli of the inclusions are identical to those of the matrix. Some of the limitations in this study (such as periodicity of the crack front) are due to a specific implementation of the weight function theory while others (such as homogeneity of elastic properties) require much more extensive numerical and/or theoretical developments to be overcome. The limitations of homogeneous elastic properties will next be discussed.

The effect of having particles with elastic moduli different from the matrix could be (qualitatively) compared to the homogeneous moduli model as follows. Under the same load, relatively stiffer particles will tend to deform less. To induce the same matrix deformation in a homogeneous model, local compressive elastic fields have to be introduced to replace the stiffer particles. The higher load thereby carried by the particles could be structurally identified with larger particles in the homogeneous model. Hence, stiffer particles will qualitatively behave as larger more compliant inclusions. In a similar manner, it can be argued that more compliant particles will qualitatively behave as smaller stiffer inclusions. The mathematical formulation of the homogeneous elastic moduli model will be described next.

In order to effectively model nonuniform three-dimensional crack growth of an initially straight-edged semi-infinite planar crack, its elastic interaction with opening dislocation distributions ahead of the initial crack front is required. That is because by analytically accounting for the interaction of the initial crack surface with such dislocations, the half-infinite initial crack surface can be excluded from the discretization requirements in a surface integral formulation of the problem. Fortunately, the interaction of a semi-infinite planar crack with arbitrary opening-point dislocations (nuclei of strain) has been obtained by Rice (1985a). Consequently, the mathematical formulation of the present model of a semi-infinite crack with a wavy crack front and the associated numerical method rely on equation (54) of Rice (1985a) with an additional term (the applied load) added. Specifically, referring to the coordinate system shown in Fig. 1, where $y=0$ is the plane of the crack, and σ_{yy} and Δu_y are the tensile stress and crack opening in the y-direction, respectively, we have:

$$\sigma_{yy}(x,0,z)=\sigma^0_{yy}(x,0,z)+\frac{K^o}{\sqrt{2\pi x}}+\frac{\mu}{2\pi^2(1-\nu)}\int_{-\infty}^{\infty}\int_0^{\infty}\frac{1}{D^3}\left[\frac{D}{2\sqrt{xx'}}-\arctan\frac{D}{2\sqrt{xx'}}\right]\cdot\Delta u_y(x',z')\cdot dx'dz' \quad (1)$$

where

$$D=\sqrt{(x-x')^2+(z-z')^2} \quad (2)$$

and μ, ν are the shear modulus and Poisson's ratio, respectively. The expression σ^o_{yy} is for the stress which a dislocation on $x>0$ with the same opening Δu_y induces in an infinite uncracked body, while K^o is the amplitude of a macrolevel applied crack-tip stress field. σ^o_{yy} can be expressed in various ways (e.g., equation (57) of Rice (1985a)). However, the implemented representation is given by:

$$\sigma^o_{yy}(x,0,z)=\frac{\mu}{4\pi(1-\nu)}FV\int_{-\infty}^{\infty}\int_0^{\infty}\frac{\Delta u_y(x',z')}{D^3}\cdot dx'dz' \quad (3)$$

where FV in front of the integral denotes an appropriately defined "finite part" integral in the Hadamard sense, and is discussed by Fares and Li (1988) and Murakami and Nemat-Nasser (1983). The representation (3) does not require obtaining partial derivatives of Δu_y and affords significant flexibility in choosing shape functions (to be described later).

Assuming that the crack front is symmetric (with respect to the x-axis) and periodic (with a period $2L$ in the z-direction), and noting that Δu_y is nonzero only on the crack surface makes it possible to reduce the integration region in equation (1) to a representative sector. An example of a representative sector is shown shaded in Fig. 1. Thus, the integral appearing in (1) can be rewritten as:

$$\int_S G^*(x,z;x',z')\cdot\Delta u_y(x',z')\cdot dx'dz' \quad (4)$$

where

$$G^*(x,z;x',z')=\sum_{n=-\infty}^{\infty}[G(x,z;x',z'+2nL)+G(x,z;x',-z'+2nL)] \quad (5)$$

and $G(x,z;x',z')$ denotes the kernel of the integrand in equation (1). In equations (4) and (5), $2L$ (see Fig. 1) is the period of the crack front and S is the area of a representative sector. The kernel in the integral representation of the expression for σ^o_{yy} is similarly treated to account for periodicity and symmetry. Now, the crack surface is assumed to be traction-free and hence $\sigma_{yy}=0$ on the representative sector. The previous condition leads to the following singular integral equation in $\Delta u_y(x,z)$:

$$\sigma^o_{yy}(x,0,z)+\frac{\mu}{2\pi^2(1-\nu)}\cdot\int_S G^*(x,z;x',z')\cdot\Delta u_y(x',z')\cdot dx'dz'+\frac{K^o}{\sqrt{2\pi x}}=0 \qquad \{\text{on } S\}. \quad (6)$$

Once Δu_y is determined on "S", the SIF at any point along the crack front can be determined using plane-strain asymptotic relations involving the opening Δu_y. In general, equation

Downloaded 03 May 2010 to 171.66.16.31. Redistribution subject to ASME license or copyright; see http://www.asme.org/terms/Terms_Use.cfm

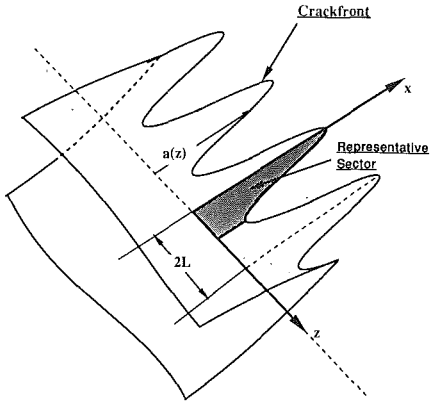


Fig. 1 Shows a wavy crack front of the type analyzed using the BEM. Only a representative sector (shown shaded) needs to be discretized.

(6) has to be numerically solved for each specific crack front configuration. The numerical method used to solve equation (6) will next be described.

Numerical Formulation

In order to solve (6) numerically, a representation of Δu_y on "S" has to be chosen. Since the geometry of a representative sector can vary widely, a piecewise description of Δu_y would be most suitable. The surface "S" (defined in (6)) is first divided into straight-edged triangular subregions forming a mesh. For example, Fig. 2 is a mesh of a representative sector. A local coordinate system is then associated with each triangle and functional variations in terms of the local coordinates are chosen and are multiplied by parameters to be determined by approximately satisfying the governing equation (6). Following boundary element terminology, specific functional variations with the corresponding parameters when associated with a particular triangular region will be called an element. Two types of elements have been used in the case studies to follow, and will be referred to as normal and crack front elements. The normal elements have a linear variation of opening. Consequently, each normal element used contributes three unknown parameters to the representation of Δu_y over "S". The crack front elements have a linear multiplied by a square root (as measured by a local Cartesian coordinate normal to the crack front) opening variation and are used whenever an element has an edge or vertex lying along a crack front. The use of crack front elements incorporate the asymptotic functional variation of crack opening near a crack front. Furthermore, the coefficients of such an expansion can easily be used to obtain the SIF along the crack front. Again, each crack front element used contributes three unknown parameters to the representation of Δu_y over "S". It is to be noted that the representation chosen allows Δu_y to be discontinuous along the edges of triangles. The elements in such a representation are described in finite and boundary element analysis as being incompatible. However, incompatible elements have been extensively and successfully used in boundary element analysis (e.g., Brebbia (1984)).

Once a discrete representation of Δu_y has been specified, the parameters corresponding to the amplitudes of the functional variation within each element have to be determined. In order to approximately satisfy the governing equation (6), the equality is enforced (apart from numerical errors) at Gaussian integration points of order 3 within each triangle. (Specifically those points in a triangle having area coordinates a permutation of (1/6,1/6,2/3).) This method of approximation is called a collocation procedure. Moreover, the method of representation and approximation described previously could be classified as a boundary element method with a highly-specialized fundamental solution. Thus, the current method

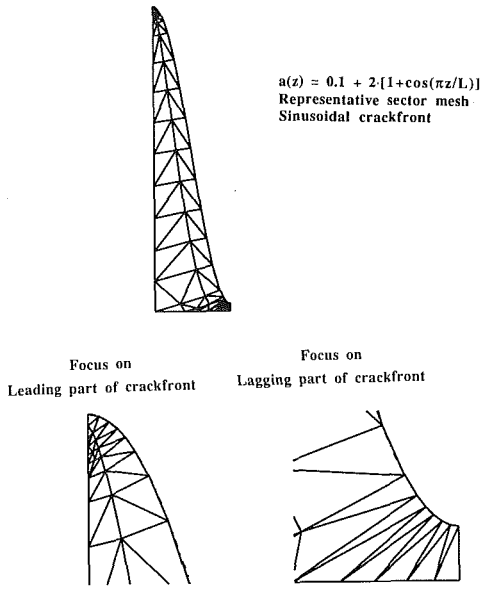


Fig. 2 Shows a mesh of a representative sector whose crack front shape is sinusoidal with the amplitude to wavelength ratio being 1.0

will be referred to as a Boundary Element Method (BEM). Some of the difficulties involved in the implementation of this BEM are in evaluating the infinite sum in (5) and in evaluating the singular integrals required in equation (6) and will next be discussed.

A closed form of the summation of (5) is not available. The direct alternative of summing a large number of terms would be highly inefficient since the evaluation of $G^*(x,z;x',z')$ is repeatedly needed to obtain the integrals in (6). The first few terms in an asymptotic expansion of the error in evaluating (5) from $-N$ to N can be shown to be expressible as a power series in "$1/N$". This makes the use of Richardson's extrapolation appropriate (e.g., see Bender and Orszag, 1978). The accuracy of implementing Richardson's extrapolation to obtain G^* in (5) is numerically verified by comparing with the direct alternative method of obtaining G^* (i.e., summing a large number of terms in (5)). Sufficient accuracy (greater than four significant digits) was obtained by an extrapolation using $n=2$ to $n=5$ in (5). The next difficulty to be addressed is the evaluation of singular integrals.

Two types of singular integrals are involved in (6). The first is evident in the integral representation of σ^o_{yy} (i.e., (3)). The numerical evaluation of (3) follows that given by Fares and Li (1988). The other is present in $G^*(x,z;x',z')$ and occurs in the kernel of equation (1), namely:

$$\frac{1}{D^3}\cdot\left[\frac{D}{2\sqrt{xx'}}-\arctan\frac{D}{2\sqrt{xx'}}\right]. \tag{7}$$

The expression (7) can be shown to be bounded as $(x,z)\to(x',z')$, and that the only singularity is along $x=0$ with $\sqrt{x'}$ type behavior. The numerical evaluation of integrals with singular kernels of the type given in (7) can be alleviated by using the transformations:

$$t=(z'-z)/(x'+x) \tag{8a}$$

$$r=\sqrt{x'/x}. \tag{8b}$$

The transformation of coordinates (8) (with the implied Jacobean) removes the singularity and smooths the integrand for a wide range of functional variations of Δu_y. After using (8), integrals with kernels of type (7) can be numerically evaluated using standard quadrature formulas (assuming $x\neq 0$).

Once this BEM is implemented, it is numerically verified that a uniform translation of the crack front gives SIF along the shifted crack front equal (within a small tolerance) to the applied SIF. This is the only verification case problem in

Downloaded 03 May 2010 to 171.66.16.31. Redistribution subject to ASME license or copyright; see http://www.asme.org/terms/Terms_Use.cfm

Table 1 $\Delta K_I/K^o$ **(the normalized difference between the actual and the macro SIF) versus** $A/2L$ **(half the crack front amplitude divided by crack front wavelength) as determined by both linear perturbation theory and the present BEM**

	$\Delta K_I/K^o$ at $z/L=0.0$		$\Delta K_I/K^o$ at $z/L=1.0$	
Amplitude/2L	(First Order)	(BEM)	(First Order)	(BEM)
0.005	−0.015708	−0.015164	0.015708	0.016595
0.01	−0.031416	−0.030358	0.031416	0.032329
0.05	−0.15708	−0.15585	0.15708	0.15257
0.1	−0.31416	−0.29769	0.31416	0.29317
0.2	−0.62832	−0.51872	0.62832	0.52875
0.3	−0.94248	−0.65664	0.94248	0.71397
0.4	−1.2566	−0.74330	1.2566	0.85852
0.5	−1.5708	−0.79793	1.5708	0.99231
0.6	−1.8850	−0.83465	1.8850	1.1125
0.7	−2.1991	−0.86085	2.1991	1.2330
0.8	−2.5133	−0.87982	2.5133	1.3364
0.9	−2.8274	−0.89389	2.8274	1.4291
1.0	−3.1416	−0.90547	3.1416	1.4730

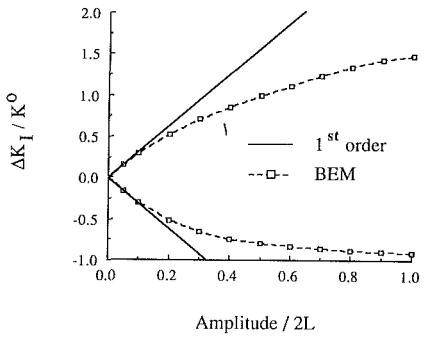


Fig. 3 $\Delta K_I/K^o$ **(the normalized difference between the actual and the macro SIF) versus** $A/2L$ **(half the crack front amplitude divided by crack front wavelength) as determined by both the linear perturbation theory and the present BEM. These comparisons are shown at the leading (negative** $\Delta K_I/K^o$**) and lagging (positive** $\Delta K_I/K^o$**) tips of the crack front.**

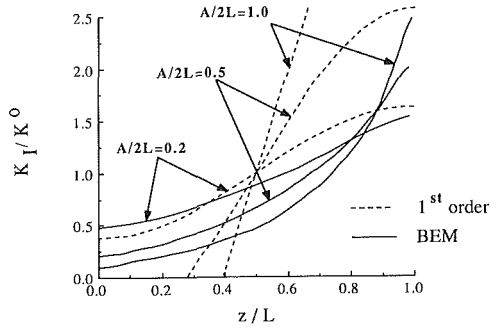


Fig. 4 The normalized SIF versus the location along the crack front as determined by both the linear perturbation theory and the present BEM at various amplitude to wavelength ratios

which the exact SIF variation is known. However, approximate crack front SIF of a wavy crack front are available which are obtained from a first-order theory (Rice (1985b)). Comparisons with the first-order results as well as other SIF solutions of nonstraight crack fronts will be presented next.

Case Studies

Three case studies will be discussed. The first is a comparison of first-order theory (Rice, 1985b) with BEM results of SIF along a sinusoidal crack front. The second is an evaluation of SIF along crack fronts obtained from crack growth simulations based on the linear perturbation theory. The last is a crack growth simulation using the BEM.

(1) Sinusoidal Crack Front. Referring to Fig. 1, we consider a crack front where:

$$a(z) = A \cdot [1 + \cos(\pi z/L)] + a_o. \tag{9}$$

The SIF variation along such a crack front due to an applied macrolevel crack-tip stress field of amplitude K^o which is correct to first order in $(A/2L)$ is given as (Rice, 1985b):

$$K_I/K^o = 1 - (\pi A/2L) \cdot \cos(\pi z/L). \tag{10}$$

The discretization of a representative sector of a crack front of form (9) where $(A/2L) = 1.0$ is shown in Fig. 2. The number of straight-line segments (edges of triangular elements) discretizing the crack front are chosen as a fixed fraction of the local radius of curvature. The parameters controlling the accuracy of the numerical integrations (e.g., quadrature integration orders and region subdivision specifications) and infinite sums extrapolation are chosen so that the errors in SIF along a straight crack front are less than 0.01 percent. In the other case studies, this tolerance value is increased to 0.1 percent. In addition, extra care in the meshing procedure was taken with the sinusoidal crack fronts in order to gain experience in the use of the method. Specifically, the SIF results of a given mesh are considered acceptable only when the maximum discontinuity in SIF values at coincident edges of adjacent triangles lying along the crack front is less than 1 percent. Otherwise a finer mesh is chosen. CPU time needed to obtain results of sinusoidal crack fronts ranged between 5 and 20 minutes on a VAX 8600 depending on the specific crack front. A comparison of BEM with the first-order results for sinusoidal crack fronts will next be discussed.

A comparison of $\Delta K_I/K^o = (K_I - K^o)/K^o$ versus $A/2L$ at the leading $(z=0)$ and lagging $(z=L)$ edges of the crack front are shown in Fig. 3 and Table 1. At small values of $A/2L$ $(A/2L < 0.1)$, the first-order and BEM results agree closely (errors at the leading and lagging edges when $A/2L = 0.1$ are around 7 percent and 5 percent, respectively). This agreement could be considered as further verification of the BEM. The comparisons in Fig. 3 also show that the errors in the first-order results are tolerable up to $A/2L = 0.2$ where the errors at the leading and lagging edges are around 21 percent and 19 percent, respectively. Note that (unlike the first-order results) the BEM predicts that the SIF at the leading edge never goes negative $(\Delta K_I/K^o > -1)$ as is intuitively expected of a crack loaded in tension. A further comparison of K_I/K^o versus z/L (position along the crack front) is shown in Fig. 4 at $A/2L = 0.2$, 0.5, and 1.0. It is interesting to note the qualitative change in the variation of SIF along the crack front at successively larger values of $A/2L$. It appears that the part of the crack front at which the SIF exceeds K^o localizes at a successively narrower region near the lagging edge of the crack front.

(2) First-Order Crack Growth Profiles. In the next two cases, crack growth simulations through or around a periodic array of circular obstacles (Fig. 5) are studied. The ratio H/L in Fig. 5 equals 0.5 in both of the next two case studies. Defin-

Downloaded 03 May 2010 to 171.66.16.31. Redistribution subject to ASME license or copyright; see http://www.asme.org/terms/Terms_Use.cfm

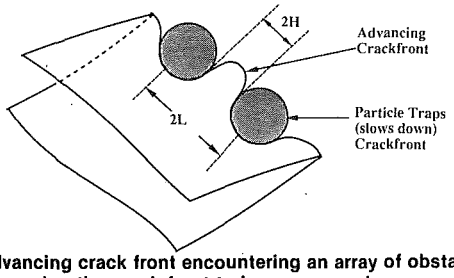


Fig. 5 An advancing crack front encountering an array of obstacles is trapped thus causing the crack front to have a wavy shape

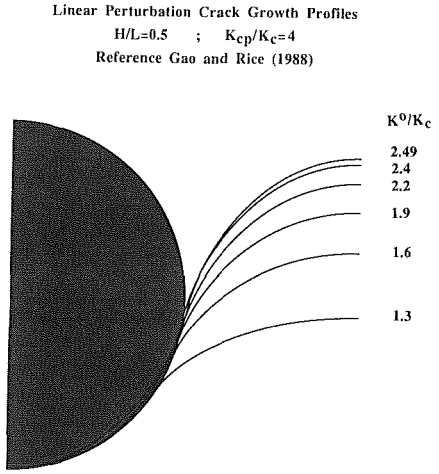


Fig. 6 The crack growth profiles based on the linear perturbation theory are shown with the corresponding macro normalized stress intensity factor (K^o/K_c) required to reach that profile

ing the matrix and particle toughness by K_c and K_{cp}, respectively, a particular linear perturbation simulation (Gao and Rice (1988)) assumed $K_{cp}/K_c = 4$. They use the "viscoplastic" crack growth model (Mastrojannis et al. (1980)):

$$\frac{\partial a(z,t)}{\partial t} = \begin{cases} \rho(K_I - K_c) & K_I > K_c \text{ (or } K_{cp} \text{ when the crack is in the particle)} \\ 0 & \text{otherwise} \end{cases} \quad (11)$$

where "t" is a time parameter, ρ is a "viscosity" coefficient of the system, and K_I is the SIF value at points along the crack front. The details of the numerical implementation of the crack growth studies using the linear perturbation theory are discussed in Gao and Rice (1988). Essentially, by making ρ large enough, they simulate growth at $K_I = K_c$. Crack growth profiles at various K^o/K_c values from Gao and Rice's simulations are shown in Fig. 6. These crack front configurations are then discretized and the SIF along the crack fronts are determined using the BEM. A typical mesh used in these discretizations is shown in Fig. 7 and corresponds to the curve with $K^o/K_c = 2.4$ in Fig. 6.

The SIF along the crack fronts shown in Fig. 6 as determined by the BEM are shown in Fig. 8. In order to more easily discuss the results of Fig. 8, the crack front will be divided into two parts. The part which touches the particle will be called CF_{trap} and that which doesn't will be called CF_{pen}. The linear perturbation results would predict that $K_I/K_c = 1$ along CF_{pen} and that when $K^o/K_c = 2.5$ then $K_I/K_c \approx 4$ along CF_{trap}. The BEM results show that the linear perturbation predictions are correct only for the first profile ($K^o/K_c = 1.3$). At subsequent profiles, the linear perturbation theory underestimates K_I/K_c along CF_{pen}. In addition, when $K^o/K_c \approx 2.5$, the linear perturbation results overestimate K_I/K_c along CF_{trap}. Both the previous observations would imply that crack growth would have to proceed deeper into the matrix before particle rupture occurs. This observation is borne out in the next simulation.

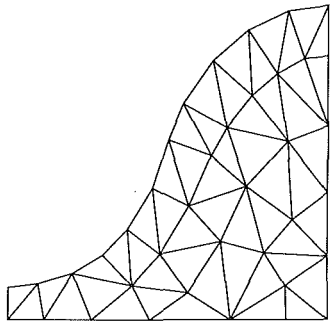


Fig. 7 A typical mesh used to discretize the crack growth profiles based on the linear perturbation theory shown in Fig. 6

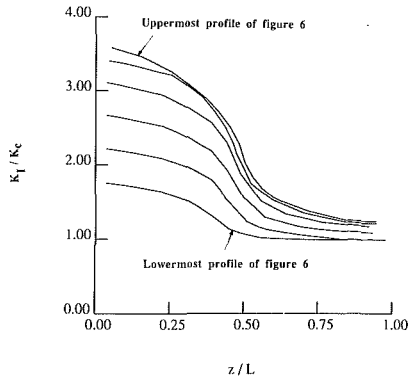


Fig. 8 The SIF along the crack growth shown in Fig. 6 as determined by the BEM discussed in the text

(3) Crack Growth Simulation Using BEM. The last case study performs a crack growth simulation using the BEM. In these simulations, the "viscoplastic" crack growth model (equation (11)) will again be used but with the following modifications. First, $da(z,t)$ will be replaced by $da^*(s,t)$ where "s" is the arc length along the crack front and da^* is an increment of crack advance measured in the direction normal to the crack front. This modification is necessary since $a(z,t)$ would be multivalued when the crack front wraps around the obstacles. Finally, in order to force the crack front to wrap around instead of breaking the obstacles, K_{cp}/K_c will be allowed to be as large as necessary. Fortunately, the simulations show that the obstacle toughness K_{cp} needs only to satisfy $K_{cp} \geq 3.52K_c$ for the obstacles to remain unpenetrated as the protruding crack fronts begin to unstably grow towards one another and surround the obstacles. Some of the implementation details of the crack growth simulation will next be described.

The crack growth simulations require forming a new mesh (re-meshing) whenever the crack advances. A sample mesh at a particular crack front advance is shown in Fig. 9. The procedure for crack growth is therefore as follows. The SIF along the current crack front is obtained using the BEM. Based on the SIF values a new crack front is calculated. Re-meshing is performed with the new crack front which is consequently considered as being the current one. Thereupon, the cycle of BEM analysis and crack growth is repeated. The time step taken in equation (11) while growing the crack is periodically readjusted to satisfy the following constraint. The maximum deviation of K_I/K_c from 1 along CF_{pen} should not exceed ± 6 percent. When the constraint is violated, the time step increment is decreased. When the constraint is again satisfied, larger time steps are again taken. Sample crack front profiles from the crack growth simulations which satisfy the aforementioned constraint are shown in Fig. 10. Further remarks on crack trapping and the deductions that can be made from Fig. 10 will next be discussed.

Downloaded 03 May 2010 to 171.66.16.31. Redistribution subject to ASME license or copyright; see http://www.asme.org/terms/Terms_Use.cfm

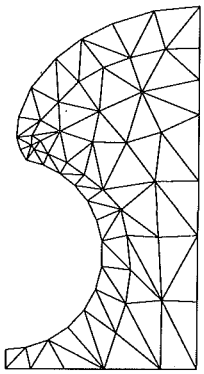


Fig. 9 A typical mesh used to discretize the crack growth profiles based on a full numerical simulation using the BEM discussed in the text

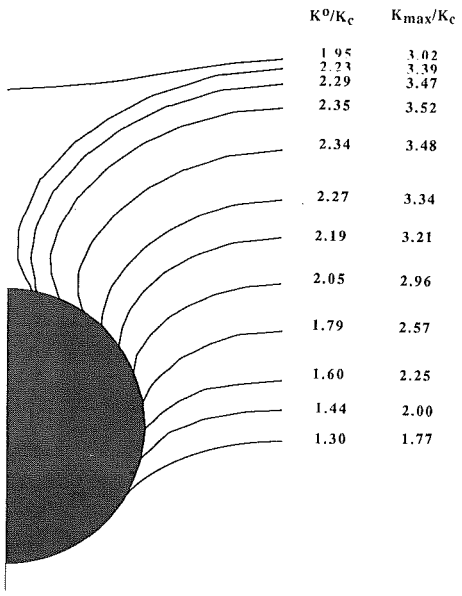


Fig. 10 Crack growth profiles based on a full numerical simulation are shown with the corresponding macro-normalized SIF (K^o/K_c) required to reach that profile as well as the associated normalized maximum SIF (K_{max}/K_c) along the particle

The toughening effect of crack trapping will be defined as the maximum of K^o/K_c that is to be applied in order to move the crack front ahead of the first array of obstacles (particles) lying parallel to the crack front. The crack front can either move in such a way as to break the obstacles or to circumvent them by surrounding them.

When the particles break, then the value of K^o/K_c at breakthrough is the net toughening achieved by introducing the particles or second phase inclusions. The simulation shown in Fig. 10 gives lower bounds (since the particles' toughness may not be fully mobilized) on the net toughening when $K_{cp}/K_c < 3.52$ with $H/L = 0.5$. An upper bound is obtained from the rule of mixtures (Rose, 1987b). The exact level depends on the shape of the particles where a (possible) full mobilization of the particles' toughness may require partial crack growth (not considered in the present simulation) into the particles as discussed by Gao and Rice (1988). For example, based on the first curve values of K^o/K_c and K_{max}/K_c (the maximum SIF acting on the particle), an upper and lower bound for the net toughness when $K_{cp}/K_c = 1.77$ is 1.44 and 1.30, respectively.

When the obstacles are circumvented, the unbroken particles (perhaps several arrays of unbroken circumvented particles) act as bridges and lead to the bridging effect discussed in the introduction. The net toughening achieved in this case is due to both the bridging and the crack trapping effect. A simplified account of the toughening achieved under the combined effect of crack trapping and crack bridging is as follows. Due to crack bridging, the macro-applied K decreases to a lower effective K^o applied at the crack front. Crack trapping then requires K^o to reach a value several times K_c in order to circumvent the obstructing array of particles at the crack front. The amplification factor achieved by crack trapping in the present simulation will be discussed next.

Figure 10 suggests that at least the first array of obstacles might be circumvented when $K_{cp}/K_c \geq 3.52$ (with $H/L = 0.5$) and that the crack trapping toughening contribution (amplification factor) is then $K^o/K_c = 2.35$. The actual K_{cp}/K_c value required to circumvent the first array of obstacles with a realistic loading situation depends on the location of the next array of obstacles. That is because with a realistic loading situation, there would be no way to suddenly reduce K^o/K_c from 2.35 after the penetrating crack segments begin to join unstably with one another. For example, if the crack front is considered retrapped at the most advanced configuration shown in Fig. 10, and K^o/K_c remains at 2.35, then a lower bound on the K_{cp}/K_c required to circumvent the first array of obstacles is 3.64 (i.e., $2.35 \times 3.02/1.95$). In any case, the crack trapping toughening contribution is independent of K_{cp}/K_c when $K_{cp}/K_c \geq 3.52$ (i.e., irrespective of whether the first array of obstacles are circumvented). However, the toughening contribution of crack trapping would depend on H/L and in a more general situation on obstacle elastic moduli, shape, and configuration within the brittle matrix. Further case studies have to be performed in order to determine the dependence of the crack trapping toughening contribution on H/L ($(1-H/L)$ is the ratio of particle size to particle spacing).

Conclusion

A BEM was formulated and implemented for the case of a semi-infinite crack having a wavy crack front. Using the BEM, the linear perturbation theory of wavy crack fronts was evaluated in two case studies. In general, the linear perturbation theory underestimates the SIF along the lagging part of a crack front and overestimates them along the leading part. In the case of a sinusoidal crack front, the linear perturbation theory gives acceptable agreement with the BEM when the amplitude-to-wavelength ratio is less than around 0.2. A crack growth simulation around obstacles using the BEM yields lower bounds on the toughness of the matrix-particles system when a crack front breaks through the particles. The simulation also gives the toughening contribution of crack trapping when the particle to matrix toughness is above a critical ratio allowing the crack front to circumvent the obstacles by surrounding them. Further studies have to be carried out in order to quantify the effect of particle size to spacing on crack trapping.

Acknowledgments

The work reported was supported by subagreement POAVB38639-0 with Harvard University from the University California based on ONR contract N00014-86-K-0753. I am grateful to Prof. J. R. Rice for having supervised this work. I am also grateful for discussions with Dr. Huajian Gao. Finally, I would also like to thank two unidentified reviewers and Prof. J. W. Rudnicki for helpful comments and suggestions.

References

Bender, C. M., and Orszag, S. A., 1978, *Advanced Mathematical Methods for Scientists and Engineers*, McGraw-Hill, New York.

Brebbia, C. A., 1984, *Boundary Element Techniques: Theory and Applications in Engineering*, Springer-Verlag, New York.

Budiansky, B., Amazigo, J. C., and Evans, A. G., 1988, "Small-scale Crack Bridging and the Fracture Toughness of Particulate Reinforced Ceramics," *J. Mech. Phys. Solids*, in press.

Downloaded 03 May 2010 to 171.66.16.31. Redistribution subject to ASME license or copyright; see http://www.asme.org/terms/Terms_Use.cfm

Evans, A. G., 1972, "The Strength of Brittle Materials Containing Second Phase Dispersions," *Phil. Mag. A*, Vol. 26, pp. 1327–1344.

Fares, N., 1988, "Green's Functions for Plane-Layered Elastostatic and Viscoelastic Regions with Application to 3-D Crack Analysis," Ph.D. Thesis, Massachusetts Institute of Technology, 1987.

Fares, N., and Li, V. C., 1988, "Boundary Element Method for 3-D Cracks in a Plate," *Proceedings of Symposium in Analytical, Numerical and Experimental Aspects of Three-Dimensional Fracture Processes*, ASME AMD Vol. 91 (ASME Book No. G00427), A. Rosakis, K. Ravi-Chandar, and Y. Rajapakse, eds., pp. 113–124.

Gao, H., and Rice, J. R., 1988, "A First Order Perturbation Analysis on Crack-Trapping by Arrays of Obstacles," to be submitted for publication.

Hadamard, J., 1923, "Lectures on Cauchy's Problem in Linear Partial Differential Equations," Yale University Press.

Krstic, V. D., 1983, "On the Fracture of Brittle-matrix/Ductile-particle Composites," *Phil. Mag. A*, Vol. 48, No. 5, pp. 695–708.

Lange, F. F., 1970, "The Interaction of a Crack Front with a Second-phase Dispersion," *Phil. Mag.*, Vol. 22, pp. 983–992.

Lange, F. F., 1971, "Fracture Energy and Strength Behavior of a Sodium Borosilicate Glass-Al_2O_3 Composite System," *J. Ceramic Soc. Amer.*, Vol. 54, No. 12, pp. 614–620.

Mastrojannis, E. N., Keer, L. M., and Mura, T., 1980, "Growth of Planar Cracks Induced by Hydraulic Fracturing," *Intl. J. for Num. Meth. Eng.*, Vol. 15, pp. 41–54.

Murakami, Y., and Nemat-Nasser, S., 1983, "Growth and Stability of Interacting Surface Flaws of Arbitrary Shape," *Eng. Fract. Mech.*, Vol. 17, No. 3, pp. 193–210.

Rice, J. R., 1985a, "Three-dimensional Elastic Crack Tip Interactions with Transformation Strains and Dislocations," *Int. J. Solids Struct.*, Vol. 21, No. 7, pp. 781–791.

Rice, J. R., 1985b, "First Order Variations in Elastic Fields Due to Variation in Location of a Planar Crack Front," ASME JOURNAL OF APPLIED MECHANICS, Vol. 52, pp. 571–579.

Rice, J. R., 1988, "Crack Front Trapped by Arrays of Obstacles: Solutions Based on Linear Perturbation Theory," *Proceedings of Symposium in Analytical, Numerical, and Experimental Aspects of Three-Dimensional Fracture Processes*, ASME AMD Vol. 91 (ASME Book No. G00427), A. Rosakis, K. Ravi-Chandar, and Y. Rajapakse, eds., pp. 175–184.

Rose, L. R. F., 1987a, "Crack Reinforcement by Distributed Springs," *J. Mech. Phys. Solids*, Vol. 35, No. 4, pp. 383–405.

Rose, L. R. F., 1987b, "Toughening Due to Crack-front Interaction with a Second-phase Dispersion," *Mech. of Mat.*, Vol. 6, pp. 11–15.

Downloaded 03 May 2010 to 171.66.16.31. Redistribution subject to ASME license or copyright; see http://www.asme.org/terms/Terms_Use.cfm

Analysis of Branched Interface Cracks Between Dissimilar Anisotropic Media

G. R. Miller
Associate Professor,
Department of Civil Engineering,
University of Washington,
Seattle, WA 98195
Assoc. Mem. ASME

W. L. Stock
McDonnell-Douglas, Inc.
San Diego, CA

A solution is presented for the problem of a crack branching off the interface between two dissimilar anisotropic materials. A Green's function solution is developed using the complex potentials of Lekhnitskii (1981) allowing the branched crack problem to be expressed in terms of coupled singular integral equations. Numerical results for the stress intensity factors at the branch crack tip are presented for some special cases, including the no-interface case which is compared to the isotropic no-interface results of Lo (1978).

1 Introduction

Interfaces between materials are ubiquitous both in nature and in technological applications. This, coupled with the fact that the overall performance of a given component frequently is governed by the behavior of such interfaces, has caused researchers to devote a great deal of attention to the study of interface failure mechanics. Recent papers by Rice (1988), Shih and Asaro (1988), Gautesen and Dundurs (1987, 1988), He and Hutchinson (1988), Mukai et al. (1989), and Delale and Erdogan (1988) are indicative of this interest and provide good overviews of recent developments in the topic.

This paper analyzes the problem of the branching of a crack at the interface between two anisotropic materials, thereby providing additional tools for examining the conditions under which failure will occur either at the interface itself or in one of the neighboring materials. Similar analyses have been carried out recently for isotropic materials by He and Hutchinson (1988) for the case of semi-infinite cracks and by Mukai et al. (1989) for the case of finite length cracks. The basic background of branch analyses and the interpretation of results for isotropic materials are discussed in these papers.

With respect to anisotropic materials, Wang and Choi (1983) have presented a good review of the interface crack problem in a paper applying Comninou's (Comninou, 1977) crack tip closure model to anisotropic media. Their discussion focused on the oscillating singularity at the crack tip and the resulting anomaly of material overlap, which they corrected by introducing crack tip contact zones. Their intent was to provide a means of characterizing delamination type failure in composite materials. In this paper the intent is to provide a means for characterizing failures in anisotropic materials in which an interlaminar crack branches away from the interface. By introducing a branch off the interface the material overlap problem is avoided, and standard techniques may be used at the tip of the branch. By examining the stress intensity factors at the tip of the branched crack it is possible to make some conjectures concerning the liklihood of branching and the expected branch direction. The analysis can be used both in an "after-the-fact" manner to treat relatively long, existing branch extensions, and in a quasi-asymptotic manner by considering very short branch lengths. The latter case could be considered in a truly asymptotic fashion by using a semi-infinite main crack as He and Hutchinson (1988) have done for isotropic materials.

The analysis presented here is similar to that of Lo (1978) treating branched cracks in isotropic media. Using Lekhnitskii's (Lekhnitskii, 1981) complex potentials for anisotropic materials, a Green's function is obtained for the interface problem. The crack branch is then modeled using singular integral equations, which are solved numerically. Numerical results for some special cases are presented, including the no-interface case, where comparisons are made with Lo's no-interface results for isotropic materials (Lo, 1978).

2 Problem Formulation

As shown by Lekhnitskii (1981), the stresses and displacements in an anisotropic body subjected to loading with no variation along the z-axis (i.e., generalized plane strain) may be expressed in terms of complex potentials as follows:

$$\sigma_{yy} = \sum_{k=1}^{3} \left\{ \phi_k(z_k) + \overline{\phi_k(z_k)} \right\} \tag{1a}$$

$$\sigma_{xx} = \sum_{k=1}^{3} \left\{ \mu_k^2 \phi_k(z_k) + \overline{\mu_k^2 \phi_k(z_k)} \right\} \tag{1b}$$

$$\tau_{xy} = -\sum_{k=1}^{3} \left\{ \mu_k \phi_k(z_k) + \overline{\mu_k \phi_k(z_k)} \right\} \tag{1c}$$

Contributed by the Applied Mechanics Division of THE AMERICAN SOCIETY OF MECHANICAL ENGINEERS for publication in the JOURNAL OF APPLIED MECHANICS.

Discussion on this paper should be addressed to the Editorial Department, ASME, United Engineering Center, 345 East 47th Street, New York, N.Y. 10017, and will be accepted until two months after final publication of the paper itself in the JOURNAL OF APPLIED MECHANICS. Manuscript received by ASME Applied Mechanics Division, October 24, 1988; final revision, February 22, 1989.

Copyright © 1989 by ASME

Downloaded 03 May 2010 to 171.66.16.31. Redistribution subject to ASME license or copyright; see http://www.asme.org/terms/Terms_Use.cfm

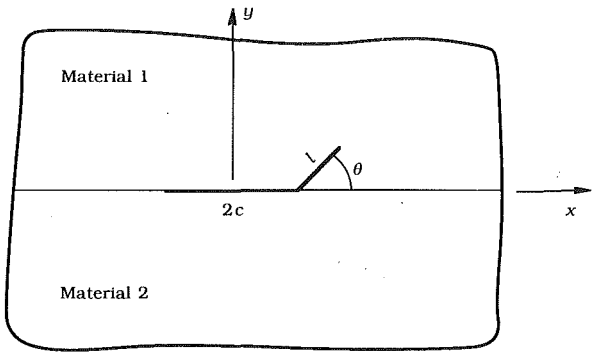


Fig. 1 A branched interface crack

$$\tau_{yz} = -\sum_{k=1}^{3}\left\{\eta_k\phi_k(z_k) + \overline{\eta_k\phi_k(z_k)}\right\} \tag{1d}$$

$$\tau_{xz} = \sum_{k=1}^{3}\left\{\eta_k\mu_k\phi_k(z_k) + \overline{\eta_k\mu_k\phi_k(z_k)}\right\} \tag{1e}$$

and

$$u' = \sum_{k=1}^{3}\left\{p_k\phi_k(z_k) + \overline{p_k\phi_k(z_k)}\right\} \tag{2a}$$

$$v' = \sum_{k=1}^{3}\left\{q_k\phi_k(z_k) + \overline{q_k\phi_k(z_k)}\right\} \tag{2b}$$

$$w' = \sum_{k=1}^{3}\left\{t_k\phi_k(z_k) + \overline{t_k\phi_k(z_k)}\right\} \tag{2c}$$

in which the ϕ_k are functions of the generalized complex variables, z_k, defined by $z_k = x + \mu_k y$. The multipliers in equations (2) depend on the elastic constants in the following manner for the case of generalized plane strain:

$$p_k = \tilde{S}_{11}\mu_k^2 + \tilde{S}_{12} - \tilde{S}_{14}\eta_k + \tilde{S}_{15}\eta_k\mu_k - \tilde{S}_{16}\mu_k \tag{3a}$$

$$q_k = \tilde{S}_{12}\mu_k + \tilde{S}_{22}/\mu_k - \tilde{S}_{24}\eta_k/\mu_k + \tilde{S}_{25}\eta_k - \tilde{S}_{26} \tag{3b}$$

$$t_k = \tilde{S}_{14}\mu_k + \tilde{S}_{24}/\mu_k - \tilde{S}_{44}\eta_k/\mu_k + \tilde{S}_{45}\eta_k - \tilde{S}_{46} \tag{3c}$$

while the quantities μ_k are given by the roots of the following characteristic equation:

$$F_4(\mu)F_2(\mu) - F^2{}_3(\mu) = 0 \tag{4}$$

in which

$$F_2(\mu_k) = \tilde{S}_{55}\mu_k^2 - 2\tilde{S}_{45}\mu_k + \tilde{S}_{44} \tag{5a}$$

$$F_3(\mu_k) = \tilde{S}_{15}\mu_k^3 - (\tilde{S}_{14} + \tilde{S}_{56})\mu_k^2 + (\tilde{S}_{25} + \tilde{S}_{46})\mu_k - \tilde{S}_{24} \tag{5b}$$

$$F_4(\mu_k) = \tilde{S}_{11}\mu_k^4 - 2\tilde{S}_{16}\mu_k^3 + (2\tilde{S}_{12} + \tilde{S}_{66})\mu_k^2 - \tilde{S}_{26}\mu_k - \tilde{S}_{22} \tag{5c}$$

and

$$\eta_k = \begin{cases} -F_3(\mu_k)/F_2(\mu_k) & k = 1,2 \\ -F_4(\mu_3)/F_3(\mu_3) & k = 3. \end{cases} \tag{5d}$$

For the case of generalized plane-strain, the elastic compliances $\tilde{S}_{ij}$ are given by

$$\tilde{S}_{ij} = S_{ij} - \frac{S_{i3}S_{j3}}{S_{33}} \qquad (i, j) \neq 3 \tag{6}$$

where the S_{ij} are defined in terms of the generalized Hooke's Law as:

$$\epsilon_i = S_{ij}\sigma_j \qquad (i, j = 1,2,3, \ldots, 6). \tag{7}$$

The geometrical configuration of the problem to be solved is depicted in Fig. 1. A main crack is shown lying along the interface between materials 1 and 2, with a crack branch extending into material 1. The corresponding boundary conditions to be satisfied are as follows:

On $y = 0$:

$$\left.\begin{aligned} \sigma_{yy}^{(1)} = \tau_{xy}^{(1)} = \tau_{yz}^{(1)} = 0 \\ \sigma_{yy}^{(2)} = \tau_{xy}^{(2)} = \tau_{yz}^{(2)} = 0 \end{aligned}\right\} \quad |x| < c \tag{8}$$

$$\left.\begin{aligned} u^{(1)} = u^{(2)},\ v^{(1)} = v^{(2)},\ w^{(1)} = w^{(2)} \\ \sigma_{yy}^{(1)} = \sigma_{yy}^{(2)},\ \tau_{xy}^{(1)} = \tau_{xy}^{(2)},\ \tau_{yz}^{(1)} = \tau_{yz}^{(2)} \end{aligned}\right\} \quad |x| > c. \tag{9}$$

Along the branch:

$$\sigma_{\theta\theta} = \tau_{\rho\theta} = \tau_{z\theta} = 0 \qquad \rho < l. \tag{10}$$

At infinity:

$$\sigma_{yy} = \sigma_{yy}^{\infty},\ \tau_{xy} = \tau_{xy}^{\infty},\ \tau_{yz} = \tau_{yz}^{\infty} \tag{11}$$

in which σ_{ij}^{∞} represent the applied external loads as a far-field uniform stress field, and ρ, θ, and z represent a local cylindrical coordinate system located at the root of the branch and oriented along it. At this point it is important to note that for interface problems in general, it is not possible to specify the far-field stresses independently of the stress components parallel to the interface (i.e., σ_{xx} in the present case). Although these parallel stresses are not important for cracks lying along the interface, they are certainly important for cracks branching off the interface. As discussed by Rice and Sih (1968), a jump in the parallel stresses across the interface is required in general, and so these stresses can not be made to vanish in both the upper and lower materials. To pin down the resulting arbitrary σ_{xx} values in materials 1 and 2, it will be assumed here that these stresses are equal and opposite. This is consistent with simple equilibrium concepts and with finite element studies of bonded, finite-width strips (Ballarini (1988)). The details of calculating the parallel stresses in terms of the material constants for two anisotropic materials are presented in Miller (1989).

Given this formulation, the problem now consists of determining a set of potentials σ_k which satisfy the conditions (8)–(11) through the relations (1) and (2).

3 Method of Solution

To solve the branched crack problem, an approach analogous to that of Lo (1978) will be used. In particular, a singular solution corresponding to a dislocation interacting with an interface crack will be developed analytically. Replacing the discrete singularity by a distribution will make it possible to satisfy the conditions along the branch (10) by numerically solving a system of coupled singular integral equations. The difficulty of the oscillating singularity is handled in the same manner as in Miller and Keer (1982): At the root of the branch the singularity is considered to be less than 1/2, which can be modeled approximately in the numerical scheme by essentially ignoring the point. This assumption concerning the singularity appears to be consistent with the in-depth studies of similar geometries by Bogy (1971, 1972).

3.1 Singular Solution. To develop the required singular solution, the formulation in Clements (1971) will be used along with some of his results and those of Wang and Choi (1983). First, the following piecewise analytical potentials are introduced to account for stress or displacement discontinuities across the interface between materials 1 and 2:

Downloaded 03 May 2010 to 171.66.16.31. Redistribution subject to ASME license or copyright; see http://www.asme.org/terms/Terms_Use.cfm

$$\Omega_j(z) = \begin{cases} \sum_{k=1}^{3}\left\{m_{jk}^{(1)}\phi_k^{(1)}(z) - \overline{m}_{jk}^{(2)}\overline{\phi}_k^{(2)}(z)\right\} & z\epsilon S^+ \\ & j=1,2,3,\ldots,6 \\ \sum_{k=1}^{3}\left\{m_{jk}^{(2)}\phi_k^{(2)}(z) - \overline{m}_{jk}^{(1)}\overline{\phi}_k^{(1)}(z)\right\} & z\epsilon S^- \end{cases} \tag{12}$$

in which the notation $\bar{f}(z) = \overline{f(\bar{z})}$ is used, and the $m_{jk}^{(\alpha)}(\alpha = 1, 2)$ have been introduced for brevity:

$$m_{1k}^{(\alpha)} = p_k^{(\alpha)} \qquad (u') \tag{13a}$$

$$m_{2k}^{(\alpha)} = q_k^{(\alpha)} \qquad (v') \tag{13b}$$

$$m_{3k}^{(\alpha)} = t_k^{(\alpha)} \qquad (w') \tag{13c}$$

$$m_{4k}^{\alpha} = 1 \qquad (\sigma_{yy}) \tag{13d}$$

$$m_{5k}^{(\alpha)} = -\eta_k^{(\alpha)} \qquad (\tau_{yz}) \tag{13e}$$

$$m_{6k}^{(\alpha)} = -\mu_k^{(\alpha)} \qquad (\tau_{xy}). \tag{13f}$$

Each of the six potentials Ω_j are defined such that $\Omega_j^+(x) - \Omega_j^-(x)$ represents the jump in the corresponding quantity given in the parenthesis in each of the equations (13). For the interface crack problem as expressed by equations (8), (9) and (11), the tractions are continuous across the interface, and thus $\Omega_4 = \Omega_5 = \Omega_6 = 0$.

Equations (13) may be inverted to express the original potentials ϕ_k in terms of the new potentials:

Im {z} > *0:*

$$\phi_k^{(1)}(z) = b_{kj}\Omega_j(z) \qquad (k=1,2,3) \tag{14a}$$

$$\overline{\phi}_k^{(1)}(\bar{z}) = -\overline{b}_{kj}\Omega_j(\bar{z}) \qquad (k=1,2,3) \tag{14b}$$

(14c)

Im {z} < *0:* (14d)

$$\phi_k^{(2)}(z) = b_{(k+3)j}\Omega_j(z) \qquad (k=1,2,3)$$

$$\overline{\phi}_k^{(2)}(\bar{z}) = -\overline{b}_{(k+3)j}\Omega_j(\bar{z}) \qquad (k=1,2,3)$$

in which the b_{kj} are inverse constants related to the $m_{jk}^{(\alpha)}$. Substituting equations (14) into the boundary conditions (8) and (11) leads to the following coupled Hilbert problem for the potentials $\Omega_j(z)$:

$$d_{ij}\Omega_j^+(x) - \bar{d}_{ij}\bar{\Omega}_j^-(x) = h_i(x). \tag{15}$$

The constants d_{ij} are algebraic combinations of the μ_k, η_k, and b_{ij}, while the $h_i(x)$ are known functions determined from the crack face loading. Decoupling equations (15), followed by the application of the well-known Hilbert problem solution of Muskhelishvili (Muskhelishvili, 1954), leads to the following expressions for the $\Omega_j(z)$:

$$C_{\gamma j}\Omega_j(z) = \frac{X_\gamma(z)}{2\pi i}\int_{-c}^{c}\frac{N_{\gamma i}h_i(t)}{X_\gamma^+(t)(t-z)}\,dt + P_\gamma^n(z)X_\gamma(z). \tag{16}$$

The constants $C_{\gamma k}$ arise during the decoupling process (see Wang and Choi, 1983; or Clements, 1971), while the functions $X_\gamma(z)$ provide the branch cut necessary to model the crack:

$$X_\gamma(z) = (z-c)^{\delta\gamma-1}(z+c)^{-\delta\gamma}$$

$$\delta_\gamma = \frac{1}{2\pi i}\ln\lambda_\gamma. \tag{17}$$

The constants λ_γ are also determined as part of the decoupling process (Clements, 1971; Wang and Choi, 1983).

The final term in equation (16) gives the homogeneous solution, with $P^n{}_\gamma(z)$ representing a polynomial or order n chosen to ensure the proper behavior at infinity. In particular, for the conditions (8) and (11), $h_i(x) = 0$, and the solution to (15) may be written:

$$\Omega_j(z) = \sum_\gamma C_{j\gamma}^{-1}\frac{N_{\gamma i}\hat{h}_i(t)}{1-\lambda_\gamma}\{1 + [c(1-2\delta_\gamma) - z]X_\gamma(z)\} \tag{18}$$

in which the $\hat{h}_i$ are constants related to σ_{yy}^∞, τ_{yz}^∞, and τ_{yx}^∞. This solution has been presented both in Clements (1971) and Wang and Choi (1983). Although the potentials in equation (18) satisfy the required boundary conditions, the nature of the singularity characterized by δ_γ (equation (17)) is such that the physically inadmissible phenomenon of material overlap occurs. This anomaly will be circumvented later in this analysis through the introduction of the crack branch.

It is now necessary to introduce the singular terms modeling a discrete dislocation near an interface between two anisotropic media. As shown by Miller (1989), the corresponding potentials are

$$\phi_k(\hat{z}) = \frac{B_k}{z-\hat{z}_k} - \sum_{j=1}^{6}b_{kj}\sum_{i=1}^{3}\overline{m}_{ji}\frac{\overline{B}_i}{z-z_i} \tag{19}$$

in which the $\hat{z}_k$ represent a specified point $(\hat{x}_k, \hat{y}_k)$ locating the singularity $\hat{z}_k = \hat{x}_k + \mu_k\hat{y}_k$. The constants B_i are related to the net force and displacement jump components obtained upon circling the singularity. In particular (see Lekhnitskii, 1981), we have:

$$\mathrm{Im}\{B_1 + B_2 + B_3\} = -\frac{Y}{4\pi} \tag{20a}$$

$$\mathrm{Im}\{\mu_1B_1 + \mu_2B_2 + \mu_3B_3\} = \frac{X}{4\pi} \tag{20b}$$

$$\mathrm{Im}\{\eta_1B_1 + \eta_2B_2 + \eta_3B_3\} = 0 \tag{20c}$$

$$\mathrm{Im}\{p_1B_1 + p_2B_2 + p_3B_3\} = -\frac{[u]}{4\pi} \tag{20d}$$

$$\mathrm{Im}\{q_1B_1 + q_2B_2 + q_3B_3\} = -\frac{[v]}{4\pi} \tag{20e}$$

$$\mathrm{Im}\{t_1B_1 + t_2B_2 + t_3B_3\} = -\frac{[w]}{4\pi} \tag{20f}$$

where X and Y represent the x and y-components of the net force, and $[u]$, $[v]$, and $[w]$ give the displacement jump components. Equations (20) can be solved for the B_i such that any type of dislocation or concentrated force singularity can be handled. For the case at hand we take $X = Y = 0$, thereby obtaining the required dislocation singularity.

The next step in the analysis involves the determination of the interaction effects between the singular solution (19) and the interface crack. This is accomplished by evaluating the tractions on the crack face due to the singularity and introducing appropriate potentials to cancel these tractions. Using equations (1*a*), (*c*), (1*d*), (1*e*), (16), and (19), and evaluating the resulting integrals using contour integration leads to the following expressions for the crack/dislocation interaction potentials:

$${}_I\Omega_j(z) = \sum_{\gamma=1}^{3}C_{j\gamma}^{-1}\left\{\sum_{i=1}^{3}\omega_{i\gamma}(z;\hat{z})\frac{N_{\gamma i}}{1-\lambda_\gamma}\right\} \tag{21a}$$

in which

$$\omega_{i\gamma}(z;\hat{z}) = \sum_{j=1}^{3}(d_{ij} - \bar{d}_{ij})\sum_{k=1}^{3}\left\{m_{jk}^{(1)}B_kF_\gamma(z;\hat{z}) - \overline{m}_{jk}^{(1)}\overline{B}_kF_\gamma(z;z)\right\} \tag{21b}$$

and

Downloaded 03 May 2010 to 171.66.16.31. Redistribution subject to ASME license or copyright; see http://www.asme.org/terms/Terms_Use.cfm

$$F_\gamma(z;\zeta)=\frac{1}{z-\zeta}\left\{1-\frac{X_\gamma(z)}{X_\gamma(\zeta)}\right\}. \tag{21c}$$

The potentials defined in equations (19) and (21) together provide a Green's function solution for the interface crack problem: The singularity is contained in (19) and the main crack interactions are accounted for by (21).

3.2 Branch Analysis. The remaining boundary conditions, equations (10), can be satisfied by redefining the discrete B_k in terms of dislocation densities, $B_k(\xi)$ defined along a line, $z = c + \xi e^{i\theta}$ emanating from the main crack tip. Assuming a crack branch length of l, the potentials $\phi_k(z)$ and ${}_I\Omega_j(z)$ as defined in relations (19) and (21) can now be expressed as integral expressions in terms of the unknown densities, $B_k(\xi)$:

$$\phi_k(\hat{z})=\int_0^l \frac{B_k(\xi)d\xi}{z-\hat{z}_k(\xi)} - \sum_{j=1}^{6} b_{kj} \sum_{i=1}^{3} \overline{m}_{ji} \int_0^l \frac{\overline{B}_i(\xi)d\xi}{z-\hat{\bar{z}}_i(\xi)} \tag{22}$$

with an analogous expression for ${}_I\Omega_j(z)$. Substituting these integral potentials, along with the $\Omega_j(z)$ from equation (18) into expressions for the tractions $(\sigma_{\theta\theta}, \tau_{\rho\theta}, \tau_{z\theta})$ along the branch, and enforcing the branch conditions (10), leads to a system of singular integral equations of the form:

$$\int_0^l \frac{M_{ik}B_k(\xi)+\overline{M}_{ik}\overline{B}_k(\xi)}{\xi-\eta}\,d\xi + \int_0^l L_{ik}B_k(\xi) + \overline{L}_{ik}\overline{B}_k(\xi)d\xi = f_i(\eta) \tag{23}$$

for $0 < \xi, \zeta < l$. The M_{ik} and L_{ik} are known constants and kernel terms, while the f_i are known functions corresponding to the stress field induced by the main crack and the applied stresses on the branched crack. The solution of this type of system of equations generally requires auxiliary conditions to render the solution unique. The normal "crack-closed" condition has been satisfied already in equations (18), (19), and (21) by eliminating any net dislocation terms, and so the required auxiliary condition is sought in terms of the singular behavior allowed at the ends of the crack branch. As mentioned earlier, we assume the singularity at the main crack/branch intersection is of order less than 1/2. As will be seen shortly, this provides a unique, albeit approximate, solution.

Equation (23) can be solved numerically in straightforward fashion. The calculations to be presented here were performed using the piecewise polynomial method of Gerasoulis (Gerasoulis, 1982), which is essentially a modified Simpson's quadrature rule. First, the singularity is incorporated *a priori* into the unknown functions, $B_k(\xi)$, by defining regular unknown functions $\hat{B}_k(\xi)$, as follows:

$$B_k(\xi)=\frac{\hat{B}_k(\xi)}{\sqrt{\xi(l-\xi)}}. \tag{24}$$

Approximating the $\hat{B}_k$ by piecewise quadratic functions and carrying out the shape function integrations then enables the system of equation (23) to be written as a system of $3n$ linear algebraic equations for the $3n + 3$ unknowns, $\hat{B}_k(\xi_i)$ (although the $\hat{B}_k(\xi)$ are complex numbers, equations (20*a–c*) show that they are not fully independent). The algebraic equations are evaluated at n collocation points between each pair of $n + 1$ internal end points, thus giving the imbalance of equations and unknowns. This difficulty is removed by noting from equation (24) that if the singularity at the main crack/branch crack intersection point is to be of order less than 1/2, then $\hat{B}_k(0) = 0$. This effectively reduces the number of unknowns to $3n$, and thus the solution is rendered unique. Clearly this assumption only remains valid for loads, extension angles, and material properties such that the crack faces are not brought into contact. This final condition can be checked by integrating the numerically-determined dislocation distribution and looking for material overlap.

The quantities of interest are the stress intensity factors K_I, K_{II}, and K_{III} at the tip of the crack branch. These may be expressed directly in terms of the B_k evaluated at the endpoints $\xi = l$ by noting that for each stress intensity factor, there is an equation of the form:

$$K=\lim_{\xi\to l+}\sqrt{2\pi(\xi-l)}\;\sigma(\xi). \tag{25}$$

These limits may be evaluated from equation (23) with $i = 1$, 2, 3, corresponding to K_I, K_{II}, and K_{III}, respectively. The result is

$$K_i=\sqrt{2}(\pi l)^{3/2}\mathrm{Re}\{M_{ik}B_k(l)\}. \tag{26}$$

4 Numerical Results and Discussion

In this section sample calculations are presented for some special cases. For simplicity, we assume material alignments such that the z-axis is an axis of material symmetry. This essentially decouples the mode III behavior from the mode I/mode II response, and we will henceforth ignore the mode III problem. To further pin down the number of parameters, the materials 1 and 2 are taken as identical, and interface effects are introduced by varying the material orientations in the upper and lower half planes. The principal compliances are taken to correspond to those of a typical wood: $E_1 = 9.79 \times 10^6$ MPa, $E_2 = E_3 = 4.07 \times 10^5$ MPa, $G_{21} = 7.31 \times 10^5$, and $\nu_{21} = \nu_{23} = \nu_{31} = 0.01$. The angle β_α defines the angle between the material x_1 axis and the coordinate x axis in each body, $\alpha = 1, 2$. The geometric parameters are the branch length relative to the main crack length, l/c, and the extension angle θ, as shown in Fig. 1. The applied load is taken to be uniaxial tension σ^∞_{yy}.

Figures 2–5 show numerical results for the case in which the material orientations in the upper and lower planes are identical, i.e., the no-interface case. These results are shown plotted along with those of Lo (1978) for crack branching in isotropic media. Figures 2–5 depict the variation in Mode I and Mode II stress intensity factor values as functions of c/l, the ratio of the main crack length to the branch length, for extension angles of 15 deg and 75 deg. The anisotropic material axes were taken as $\beta_1 = \beta_2 = \pm 45$ deg. It can be seen in Fig. 2 that for relatively low extension angles, the behavior is not greatly influenced by the material properties. Figures 3 and 4, on the other hand, show the somewhat strong influence of material properties for large extension angles. These results are further illustrated in Fig. 5, which shows the stress intensity factors for a range of extensions angles for a constant branch length ratio. Here the well-known independence of the stress intensity factors on the material properties behavior at zero degrees can be seen (Sih, Paris, and Irwin, 1965).

In Figs. 6–10, similar results are presented for the case of interface cracks. As shown, the material configuration is taken as $\beta_1 = 0$ deg, $\beta_2 = -30$ deg. For the chosen material constants, this choice of material orientations maximizes the mismatch stresses, σ_{xx} (Miller, 1989). For the case shown the mismatch stress is 0.39148 σ^∞_{yy}, with tension in the upper material and compression in the lower material. Comparing Figs. 6 and 7 to their counterparts, Figs. 2–4, it is clear that an increased sensitivity to material properties arises when the interface exists, even for small angles. For larger extension angles, the influence of the mismatch stresses becomes particularly important. The clearest illustration of the extension angle behavior is provided by Figs. 8–10, which are analogous to Fig. 5. In particular, it can be seen that there are clear maximum values of K_I, with respect to extension angle, and that at these angles K_{II} tends to be near zero. Under these conditions it is often possible to predict experimental extension angles using the calculated angle giving maximum K_I (see, e.g., Nemat-

Downloaded 03 May 2010 to 171.66.16.31. Redistribution subject to ASME license or copyright; see http://www.asme.org/terms/Terms_Use.cfm

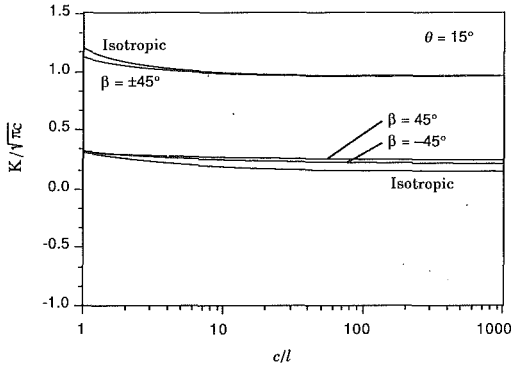


Fig. 2 Stress intensity factors versus *c/l* for θ = 15 deg; no interface: upper curves show Mode I, lower curves Mode II. Isotropic results are from Lo (1978).

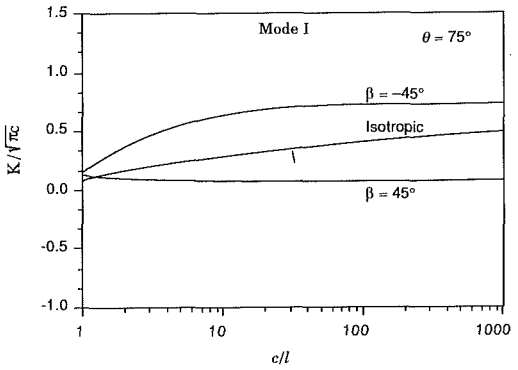


Fig. 3 Mode I stress intensity factors versus *c/l* for θ = 75 deg; no interface

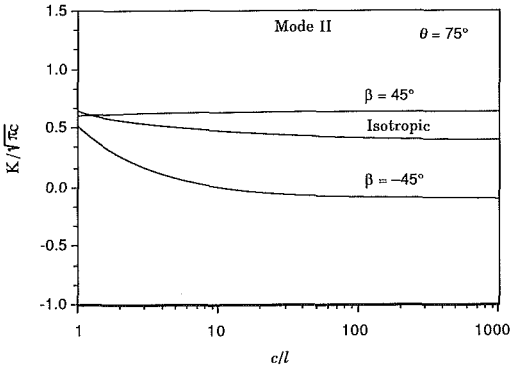


Fig. 4 Mode II stress intensity factors versus *c/l* for θ = 75 deg; no interface

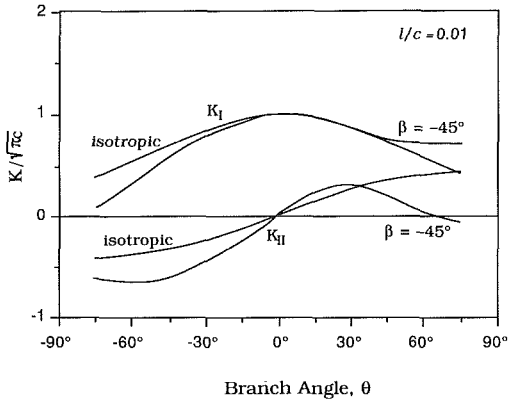


Fig. 5 Stress intensity factors versus extension angle for *l/c* = 0.01; no interface

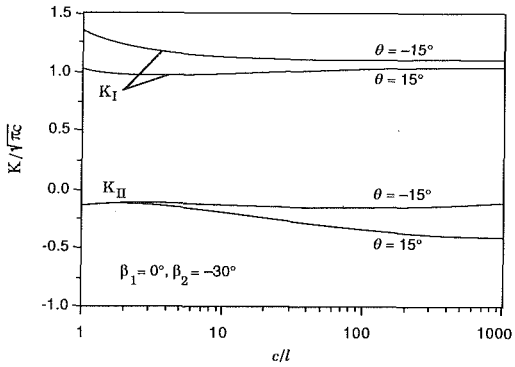


Fig. 6 Stress intensity factors versus *c/l* for θ = 15 deg; with interface

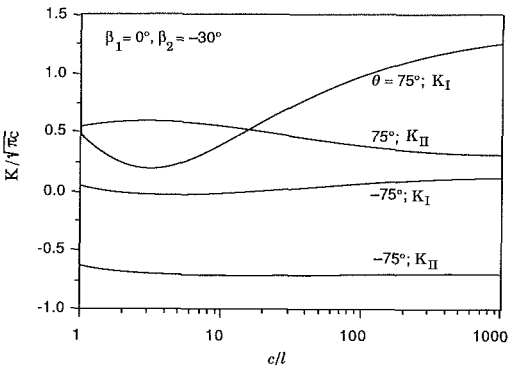


Fig. 7 Stress intensity factors versus *c/l* for θ = 75 deg; with interface

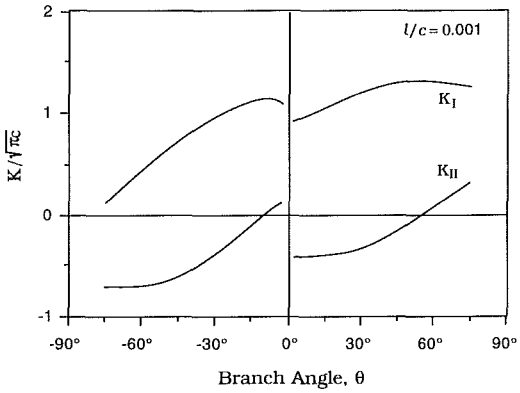


Fig. 8 Stress intensity factors versus extension angles for *l/c* = 0.001; with interface

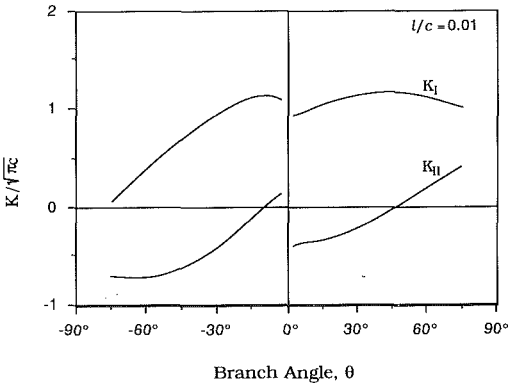


Fig. 9 Stress intensity factors versus extension angles for *l/c* = 0.01; with interface

Downloaded 03 May 2010 to 171.66.16.31. Redistribution subject to ASME license or copyright; see http://www.asme.org/terms/Terms_Use.cfm

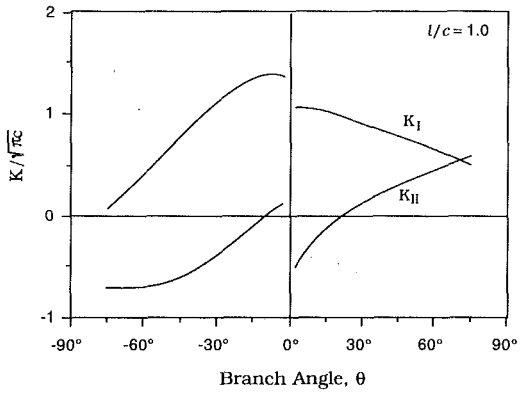


Fig. 10 Stress intensity factors versus extension angles for *l/c* = 1.0; with interface

Nasser and Horii, 1984). To the degree this type of prediction is valid here, the results in Figs. 8–10 would indicate that off-interface growth could be the preferred growth mode, and that a crack branching into the upper material would tend to start out around 50 deg and flatten out as the branch grows, since the maximum K_I/minimum K_{II} angle decreases as the branch length increases. On the other hand, for branching into the lower material, the extension angle would tend to remain constant at around 10 deg. These conclusions, however, must be considered tentative, since fracture depends not only the driving force in terms of stress distributions, but also on the generally anisotropic material resistance.

An additional phenomenon of interest in Figs. 8–10 is the discontinuity in the stress intensity factors across the 0 deg extension angle. This is not surprising in light of the complex singularity associated with 0 deg, and in fact these results can be viewed as providing an additional perspective on the overlap/contact zone phenomenon.

5 Conclusions

An analysis of branched interface cracks in anisotropic media has been presented, making it possible to characterize the crack branch tip within the confines of linear elastic fracture mechanics. The calculations presented here allow an overview comparison between the crack branch tip conditions for no-interface isotropic and anisotropic case, and for anisotropic interface cases. In particular, the no-interface cases were similar for small extension angles, with increasing variations for larger extension angles. Introducing the interface increases the range of variation of all angles, and gives indications of a possible propensity for off-interface growth.

Acknowledgments

This material is based upon work supported by the National Science Foundation under Grant No. MSM-8657628.

References

Ballarini, R., 1988, private communication.

Bogy, D. B., 1971, "Two Edge-Bonded Elastic Wedges on Different Materials and Wedge Angles Under Surface Tractions," ASME JOURNAL OF APPLIED MECHANICS, Vol. 38, pp. 377–386.

Bogy, D. B., 1972, "The Plane Solution for Anisotropic Elastic Wedges Under Normal and Shear Loading," ASME JOURNAL OF APPLIED MECHANICS, Vol. 39, pp. 1103–1109.

Clements, D. L., 1971, "A Crack Between Dissimilar Anisotropic Media," *International Journal of Engineering Science*, No. 1, Vol. 9, pp. 257–265.

Comninou, M., 1977, "The Interface Crack," ASME JOURNAL OF APPLIED MECHANICS, Vol. 44, pp. 631–636.

Delale, F., and Erdogan, F., 1988, "On the Mechanical Modeling of the Interfacial Region in Bonded Half-Planes," ASME JOURNAL OF APPLIED MECHANICS, Vol. 55, pp. 317–324.

Gautesen, A. K., and Dundurs, John, 1987, "The Interface Crack in a Tension Field," ASME JOURNAL OF APPLIED MECHANICS, Vol. 54, pp. 93–98.

Gautesen, A. K., and Dundurs, John, 1988, "The Interface Crack Under Combined Loading," ASME JOURNAL OF APPLIED MECHANICS, Vol. 55, pp. 580–586.

Gerasoulis, A., 1982, "The Use of Piecewise Quadratic Polynomials for the Solution of Singular Integral Equations of Cauchy Type," *Computational Mathematics with Applications*, Vol. 8, pp. 15–22.

He, M. Y., and Hutchinson, J. W., 1988, "Kinking of a Crack Out of an Interface," Harvard Report MECH-13, Cambridge, Mass.

Keer, L. M., and Miller, G. R., 1982, "Approximate Analytical Model of Anchor Pull-Out Test," ASME JOURNAL OF APPLIED MECHANICS, Vol. 49, pp. 768–772.

Lekhnitskii, S. G., 1981, *Theory of Elasticity of an Anisotropic Body*, MIR Publishers, Moscow.

Lo, K. K., 1978, "Analysis of Branched Cracks," ASME JOURNAL OF APPLIED MECHANICS, Vol. 45, pp. 797–802.

Miller, G. R., 1989, "Analysis of Cracks Near Interfaces Between Dissimilar Anisotropic Materials," *International Journal of Engineering Sciences*, in press.

Mukai, D. J., Ballarini, R., and Miller, G. R., 1989, "Analysis of Branched Interface Cracks," ASME JOURNAL OF APPLIED MECHANICS, submitted for publication.

Muskhelishvili, N. I., 1953, *Singular Integral Equations*, Noordhoff, Groningen.

Nemat-Nasser, S., and Horii, H., 1982, "Compression-Induced Nonplanar Crack Extension With Application to Splitting, Exfoliation, and Rockburst," *Journal of Geophysical Research*, Vol. 87, pp. 6805–6821.

Rice, J. R., 1988, "Elastic Fracture Mechanics Concepts for Interfacial Cracks," ASME JOURNAL OF APPLIED MECHANICS, Vol. 55, pp. 98–103.

Shih, C. F., and Asaro, R. J., 1988, "Elastic-Plastic Analysis of Cracks on Bimaterial Interfaces: Part 1—Small Scale Yielding," ASME JOURNAL OF APPLIED MECHANICS, Vol. 55, pp. 299–316.

Sih, G. C., Paris, P. C., and Irwin, G. R., 1965, "On Cracks in Rectilinearly Anisotropic Bodies," *International Journal of Fracture*, Vol. 1, pp. 189–203.

Wang, S. S., and Choi, I., 1983, "The Interface Crack Between Dissimilar Anisotropic Composite Materials," ASME JOURNAL OF APPLIED MECHANICS, Vol. 50, pp. 169–178.

Downloaded 03 May 2010 to 171.66.16.31. Redistribution subject to ASME license or copyright; see http://www.asme.org/terms/Terms_Use.cfm

M. T. Hanson

W. Lin

L. M. Keer
Fellow, ASME

Department of Civil Engineering,
Northwestern University,
Evanston, IL 60208

Three-Dimensional Analysis of Cracking Through the Boundary of a Two-Phase Material

The penetration through a two-phase boundary by a biplanar (kinked) crack of arbitrary shape is considered in this paper. The two-phase boundary is modeled as the interface between two perfectly-bonded elastic, isotropic, homogeneous half spaces with different elastic constants. The planar crack on either side of the interface may be arbitrarily orientated with respect to the interface boundary. The body-force method is used to derive a set of coupled two-dimensional singular integral equations which are solved numerically. The solution yields the three crack opening displacements as well as the three modes of stress intensity factors along the crack contour. Numerical results are given for a penny-shaped crack symmetrically oriented with respect to the interface. Mode I stress intensity factors are given for the biplanar crack that experiences a kink when passing through the interface.

Introduction

Considerable research effort has been directed towards analyzing flaws (idealized as cracks) near phase boundaries. This is largely because of the increasing interest in composites over bulk materials as components of structural systems, as well as the use of large-scale hydraulic fracturing to access fossil fuels. Since the flaws may be idealized as cracks, a fracture mechanics approach has been introduced in order to quantify under what conditions and in what directions a crack may extend.

Because of its relative simplicity, research into fractures near phase boundaries has consisted predominantly of two-dimensional analyses. A wide class of problems have been treated including the interface crack, kinked interface cracks, cracks near or terminating at an interface of a two or multiphase material, as well as straight or kinked cracks penetrating through an interface, among others. A good review of this literature is given by Murakami (1987) and Sih and Chen (1981).

The more realistic three-dimensional analysis of fracture near interfaces has, however, received less attention. The analysis of a penny-shaped crack contained within a single phase of a multiphase material is reviewed by Murakami (1987). Lee and Keer (1986), by extending the body-force method developed for three-dimensional fracture analysis by Murakami and Nemat-Nasser (1982, 1983) and Murakami (1985), considered cases of constrained crack growth for cracks perpendicular to and terminating at an interface under uniform internal pressure. This analysis was later extended by Lee et al. (1987) to analyze a planar crack terminating at an interface under general loading and crack orientation conditions. Lin and Keer (1988) considered perpendicular crack penetration through an interface under internal pressure loading.

The purpose of the present analysis is to study three-dimensional crack penetration through a phase boundary under general crack geometry, orientation, and loading conditions. In particular, it is desired to determine the stress intensity factors around the crack contour as a measure for quantifying the magnitude and direction of crack growth. The solution to this problem is quite complex since, in addition to the square-root stress singularity along the contour of the crack embedded in each body, a line singularity in the stress field will be present where the crack plane intersects the interface (Bogy (1971)) and a point singularity where the crack front intersects the interface, (Benthem (1977), Bazant and Estenssoro (1979)). The inclusion of these interfacial singularities and intersection of lines of singularities is beyond the scope of the present analysis and only the square root behavior will be explicitly accounted for. It is felt that the present analysis gives a good approximation to overall behavior but the three-dimensional singularity will have to be analyzed to further investigate the crack growth characteristics of the more complex singularities that occur in the vicinity of the interface.

In the following, by utilizing the body-force method, a set of singular boundary integral equations is derived over the crack domain in each body. The numerical solution of these equations yields the crack opening displacements and stress intensity factors. The planar domains of the crack in each body may have an arbitrary shape; however, the only geometrical requirement is that the two domains intersect the interface along a common line. Numerical results are given for a penny-shaped crack symmetrically oriented with respect to the inter-

Contributed by the Applied Mechanics Division of THE AMERICAN SOCIETY OF MECHANICAL ENGINEERS for presentation at the Winter Annual Meeting, San Francisco, Calif., December 10-15, 1989.

Discussion of this paper should be addressed to the Editorial Department, ASME, United Engineering Center, 345 East 47th Street, New York, N.Y. 10017, and will be accepted until two months after final publication of the paper it itself in the JOURNAL OF APPLIED MECHANICS. Manuscript received by the ASME Applied Mechanics Division, August 10, 1988; final revision, January 19, 1989.

Paper No. 89-WA/APM-33.

Copyright © 1989 by ASME

Downloaded 03 May 2010 to 171.66.16.31. Redistribution subject to ASME license or copyright; see http://www.asme.org/terms/Terms_Use.cfm

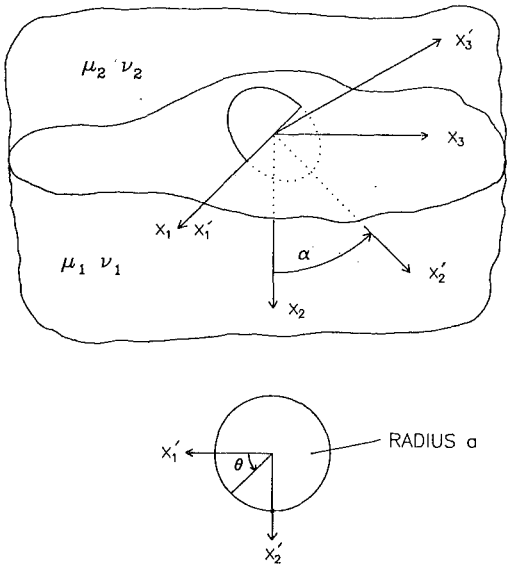


Fig. 1 Geometry and coordinate system for three-dimensional planar crack penetration through an interface

face under internal pressure and farfield tensile loading. Numerical results for planar crack penetration with directional change through the interface are also given.

Derivation of the Integral Equations

Planar Crack Penetration. It will be temporarily assumed that the crack penetrates the interface while remaining in its original plane, although the crack plane may be arbitrarily oriented with respect to the plane of the interface. The geometry and coordinate system are shown in Fig. 1. The lower body is described by the shear modulus and Poisson's ratio μ_1 and ν_1, respectively, while the upper body has elastic constants μ_2 and ν_2. Two rectangular cartesian coordinate systems are introduced, one for the interface (x_1, x_2, x_3) and one for the planar crack (x_1', x_2', x_3'). The interface is the $x_2 = 0$ plane, while $x_3' = 0$ is the plane of the crack. The primed and unprimed coordinates are related to each other through the rotations

$$x_i' = e_{is}x_s, \quad x_i = e_{si}x_s', \quad i = 1, 2, 3. \tag{1}$$

here, and subsequently, the summation convention is used on repeated subscripts and derivatives, and e_{is} is defined by

$$e_{is} = \begin{bmatrix} 1 & 0 & 0 \\ 0 & c & s \\ 0 & -s & c \end{bmatrix}, \tag{2}$$

where $c = \cos(\alpha)$, $s = \sin(\alpha)$, and α is the angle between the crack plane and the x_2 axis (Fig. 1).

Using the superscripts 1 and 2 to refer to the corresponding regions, the boundary conditions are given next. Considering perfect bonding, matching of the displacements and tractions at the interface requires

$$u_i^1(x_1, 0, x_3) = u_i^2(x_1, 0, x_3), \ -\infty < x_1, x_3 < \infty, \tag{3}$$

$$\sigma_{2i}^1(x_1, 0, x_3) = \sigma_{2i}^2(x_1, 0, x_3), \ -\infty < x_1, x_3 < \infty, \tag{4}$$

while over the crack domain

$$\sigma_{3i}'^k(x_1', x_2', 0) = T_i'^k(x_1', x_2'), \quad x_1', x_2' \epsilon D_k, \tag{5}$$

where $i = 1, 2, 3$ with $k = 1, 2$ referring to bodies 1 and 2. Here, D_k is the planar domain of the crack in body k and the quantities $T_i'^k(x_1', x_2')$ are the known tractions exerted on the crack faces. For external loadings, they are found from the uncracked solution.

The basis of the body force method is to model the stress disturbance caused by the crack with a fictitious distribution of eigenstrains ϵ_{ij}^*. In the present analysis the eigenstrains are distributed in volumes Ω_1 and Ω_2 for each body. A limiting procedure is applied to shrink the volumes to a planar crack domain; i.e., $\Omega_1 \to D_1$ and $\Omega_2 \to D_2$. Appropriate representations of the displacement fields in each body outside of the domains, Ω_k, which satisfy boundary conditions (3,4) can be given as

$$u_i^k(\mathbf{x}) = \int_{\Omega_1} C_{jpmn}^1 \epsilon_{mn}^{*1} \frac{\partial G_{ij}^{k1}(\mathbf{x}, \xi)}{\partial \xi_p} d\xi + \int_{\Omega_2} C_{jpmn}^2 \epsilon_{mn}^{*2} \frac{\partial G_{ij}^{k2}(\mathbf{x}, \xi)}{\partial \xi_p} d\xi. \tag{6}$$

Here, $\mathbf{x}$ represents the vector (x_1, x_2, x_3) and ϵ_{mn}^{*k} are the distributed eigenstrains in Ω_k. The elastic constants for body k are C_{jpmn}^k which are given by

$$C_{jpmn}^k = \lambda_k \delta_{jp}\delta_{mn} + \mu_k(\delta_{jm}\delta_{pn} + \delta_{jn}\delta_{pm}), \tag{7}$$

where λ_k and μ_k are the Lamé constants. The Green's function $G_{ij}^{kl}(\mathbf{x}, \xi)$ represents the x_i coordinate direction displacement in body k at point $\mathbf{x}$ caused by a unit body force in the x_j direction in body l at point ξ. Use is made of the Rongved (1955) Green's function for two perfectly-bonded half spaces in the form given by Dundurs and Hetenyi (1965) and notation by Mura (1982).

Using the stress-displacement relations outside the volumes Ω_k,

$$\sigma_{ij}^k(\mathbf{x}) = C_{ijml}^k u_{m,l}^k(\mathbf{x}), \tag{8}$$

the corresponding stress field in each body is given by

$$\sigma_{ij}^k(\mathbf{x}) = C_{ijsl}^k \int_{\Omega_1} C_{qpmn}^1 \epsilon_{mn}^{*1} \frac{\partial G_{sq}^{k1}(\mathbf{x}, \xi)}{\partial x_l \partial \xi_p} d\xi + C_{ijsl}^k \int_{\Omega_2} C_{qpmn}^2 \epsilon_{mn}^{*2} \frac{\partial G_{sq}^{k2}(\mathbf{x}, \xi)}{\partial x_l \partial \xi_p} d\xi. \tag{9}$$

The Green's function is given in terms of the Papkovich-Neuber displacement potentials Φ_{ij}^{kl} and ψ_j^{kl} through the relation

$$G_{ij}^{kl} = \frac{1}{2\mu_k}\left[(\kappa_k + 1)\Phi_{ij}^{kl} - \frac{\partial}{\partial x_i}(\bar{x}_p \Phi_{pj}^{kl} + \psi_j^{kl})\right]. \tag{10}$$

Here, $\kappa_k = 3 - 4\nu_k$ and $\bar{x}_p$ is defined by

$$\bar{x}_1 = x_1 - \xi_1, \quad \bar{x}_2 = x_2, \quad \bar{x}_3 = x_3 - \xi_3. \tag{11}$$

For the geometry and coordinate system used here, the potentials are given in Appendix A.

Equation (9) represents the stress field outside the volume Ω_k in body k caused by the distributed eigenstrains. To obtain a limiting form for the crack it is appropriate to first rotate the eigenstrains to the primed system through the relation

$$\epsilon_{ij}^{*k} = e_{qi}e_{pj}\epsilon_{pq}'^{*k}, \tag{12}$$

noting that

$$\epsilon_{11}'^{*k} = \epsilon_{22}'^{*k} = \epsilon_{21}'^{*k} = 0. \tag{13}$$

Subsequently, the stresses in the primed system may be determined by

$$\sigma_{3i}'^k = e_{3p}e_{iq}\sigma_{pq}^k. \tag{14}$$

Equations (12)–(13) are substituted into equation (9); then

Downloaded 03 May 2010 to 171.66.16.31. Redistribution subject to ASME license or copyright; see http://www.asme.org/terms/Terms_Use.cfm

equation (9) is substituted into equation (14). Subsequently, the field variable $\mathbf{x}$ and integration variable $\boldsymbol{\xi}$ are rotated to the primed coordinates through (1).

To obtain the limiting form as $\Omega_k \to D_k$, define the distance to the surface of Ω_k in the $\pm\xi_3'$ direction as $\pm g^k(\xi_1', \xi_2')$. As $g^k \to 0$, the crack opening displacements in the limit can be extracted as

$$b_1'^k(\xi_1', \xi_2') = 2\int_{-g^k}^{g^k} \epsilon_{31}'^{*k}(\xi_1', \xi_2', \xi_3')d\xi_3', \tag{15}$$

$$b_2'^k(\xi_1', \xi_2') = 2\int_{-g^k}^{g^k} \epsilon_{32}'^{*k}(\xi_1', \xi_2', \xi_3')d\xi_3', \tag{16}$$

$$b_3'^k(\xi_1', \xi_2') = \int_{-g^k}^{g^k} \epsilon_{33}'^{*k}(\xi_1', \xi_2', \xi_3')d\xi_3', \tag{17}$$

with the force doublets distributed on the $\xi_3' = 0$ plane. By evaluating the field point $\mathbf{x}'$ on the crack plane within the crack and enforcing the boundary conditions, the following set of coupled two-dimensional singular integral equations is obtained

$$T_i'^k(x_1', x_2') = \int_{D_1} b_m'^1(\xi_1', \xi_2')K_{im}^{k1}(x_1', x_2', \xi_1', \xi_2')d\xi_1'd\xi_2' + \int_{D_2} b_m'^2(\xi_1', \xi_2')K_{im}^{k2}(x_1', x_2', \xi_1', \xi_2')d\xi_1'd\xi_2', \quad \mathbf{x}' \epsilon D_k. \tag{18}$$

Equation (18) represents six equations, one set for each body k with three per set for each direction x_i'. The set of kernels K_{im}^{11} and K_{im}^{22} contain both singular and regular terms while K_{im}^{12} and K_{im}^{21} are regular. The set of kernels K_{im}^{11} was derived from the Φ_{ij}^{11} and ψ_j^{11} potentials and is given by Lee et al. (1987) with the singular and regular terms separated. This set of kernels contains a parameter h that represents the translation perpendicular to the interface in the coordinate transformation, which is taken as $h = 0$ as applied here. The singular terms are identified with the Kelvin Green's function for the full space while the regular terms represent corrections for the interface effects. The singular terms cause the integrals to be divergent and their contribution to the integral equations are as the finite part of the divergent integrals.

It remains to determine the additional three sets of kernels. Using the potentials Φ_{ij}^{21} and ψ_j^{21}, the kernels K_{im}^{21} were derived in a similar manner. This set of kernels is given in Appendix B. The kernels K_{im}^{12} and K_{im}^{22} can be obtained from K_{im}^{21} and K_{im}^{11}, respectively, by interchanging the elastic constants and substituting $\mathbf{x}' \to -\mathbf{x}'$, $\boldsymbol{\xi}' \to -\boldsymbol{\xi}'$.

Planar Crack Penetration With Directional Change Through the Interface. Equations (18) and the four sets of kernels are derived for crack penetration without a planar directional change through the interface. This restriction is now relaxed and the equations are modified to allow the crack to penetrate the interface and exit in a different planar direction. Hence the crack is now biplanar with a kink at the interface.

The procedure is analogous to the preceeding with suitable modifications outlined below. An additional set of coordinates $\mathbf{x}''$ is now introduced to describe the planar crack in body 2 while $\mathbf{x}'$ is retained for the planar crack in body 1. The angle α is replaced by α_1 and α_2 is defined as the angle between the x_2 and x_2'' axis. Equation (1) holds with e_{is}, c, and s in equation (2) replaced by e_{is}^1, $c_1 = \cos(\alpha_1)$ and $s_1 = \sin(\alpha_1)$. The additional rotations are given by

$$x_i'' = e_{is}^2 x_s, \quad x_i = e_{si}^2 x_s'', \quad i = 1, 2, 3, \tag{19}$$

$$e_{is}^2 = e_{is}^1(c_1 \to c_2, s_1 \to s_2). \tag{20}$$

The integral equations may now be derived as before with differing stress, eigenstrain, and coordinate rotations for the two different planar crack domains. The integral equations can be given as

$$T_i'^1(x_1', x_2') = \int_{D_1} b_m'^1(\xi_1', \xi_2')K_{im}^{11}(x_1', x_2', \xi_1', \xi_2')d\xi_1'd\xi_2' + \int_{D_2} b_m''^2(\xi_1'', \xi_2'')K_{im}^{12}(x_1', x_2', \xi_1'', \xi_2'')d\xi_1''d\xi_2'', \mathbf{x}' \epsilon D_1, \tag{21}$$

$$T_i''^2(x_1'', x_2'') = \int_{D_1} b_m'^1(\xi_1', \xi_2')K_{im}^{21}(x_1'', x_2'', \xi_1', \xi_2')d\xi_1', \xi_2') + \int_{D_2} b_m''^2(\xi_1'', \xi_2'')K_{im}^{22}(x_1'', x_2'', \xi_1'', \xi_2'')d\xi_1''d\xi_2'', \mathbf{x}'' \epsilon D_2, \tag{22}$$

and it remains to determine the four sets of kernels. The kernels K_{im}^{11} are obtained simply from the set K_{im}^{11} of (18) with α replaced by α_1. Similarily, K_{im}^{22} is obtained from K_{im}^{22} of (18) with $\alpha \to \alpha_2$, $\mathbf{x}' \to \mathbf{x}''$, and $\boldsymbol{\xi}' \to \boldsymbol{\xi}''$. The set K_{im}^{21} is given as

$$K_{im}^{21}(x_1'', x_2'', \xi_1', \xi_2') = \frac{\mu_1}{4\pi(\kappa_1 + 1)} K_i^m(x_1'', c_2x_2'', s_2x_2'', \xi_1', c_1\xi_2', s_1\xi_2'), \tag{23}$$

with

$$K_i^m(x_1, x_2, x_3, \xi_1, \xi_2, \xi_3) = 2\pi(\kappa_1 + 1)e_{3p}^2 e_{iq}^2(e_{mj}^1 e_{3n}^1 + e_{3j}^1 e_{mn}^1)B_{pqjn}, \quad m = 1, 2, \tag{24}$$

$$K_i^3(x_1, x_2, x_3, \xi_1, \xi_2, \xi_3) = 4\pi(\kappa_1 + 1)e_{3p}^2 e_{iq}^2(A_{pq} + e_{3j}^1 e_{3n}^1 B_{pqjn}), \tag{25}$$

where A_{ij} and B_{ijmn} are defined in Appendix B. The kernels K_{im}^{12} can be obtained from K_{im}^{21} defined by (23)–(25), by interchanging the elastic constants, the angles α_1 and α_2, and substituting $\mathbf{x}'' \to -\mathbf{x}'$ and $\boldsymbol{\xi}' \to -\boldsymbol{\xi}''$.

Numerical Procedure

The basis of the numerical solution of equation (18) and, hence, (21)–(22) is analogous to that used by Lee et al. (1987). The crack front contour ∂D_k in body k is replaced with a straight line segment polygon ∂D_k^o and the domain D_k is replaced by D_k^o, the domain interior to ∂D_k^o. It is well known that for a smooth crack front embedded in a homogeneous material, the crack opening displacement vanishes in a square root fashion as the crack front is approached. Hence, accurate results near the crack front are obtained when the crack opening displacements are represented as

$$b_i'^k(\xi_1', \xi_2') = \sqrt{2a\epsilon - \epsilon^2} f_i'^k(\xi_1', \xi_2'), \; i = 1, 2, 3, \tag{26}$$

where ϵ represents the shortest distance from the integration point (ξ_1', ξ_2') in D_k^o to the crack boundary ∂D_k^o (Mastrojannis et al. (1979)), and "a" is a characteristic crack length, (Murakami and Nemat-Nasser (1983)). The crack domain D_k^o is subdivided into N_k triangular elements D_k^{op}, $p = 1, 2, \ldots, N_k$ over which the unknown function $f_i'^k(\xi_1', \xi_2')$ is taken to be constant. The integral equations are thus reduced to a set of algebraic equations given as

Downloaded 03 May 2010 to 171.66.16.31. Redistribution subject to ASME license or copyright; see http://www.asme.org/terms/Terms_Use.cfm

$$\sum_{p=1}^{N_1} K^{11}_{impr\tau_1} f'^{1}_{mp} + \sum_{p=1}^{N_2} K^{12}_{impr\tau_1} f'^{2}_{mp} = T'^{1}_{i}(x'^{\tau_1}_1, x'^{\tau_1}_2),$$

$$i = 1, 2, 3, \tau_1 = 1, 2, \ldots, N_1, \quad (27)$$

$$\sum_{p=1}^{N_1} K^{21}_{impr\tau_2} f'^{1}_{mp} + \sum_{p=1}^{N_2} K^{22}_{impr\tau_2} f'^{2}_{mp} = T'^{2}_{i}(x'^{\tau_2}_1, x'^{\tau_2}_2),$$

$$i = 1, 2, 3, \tau_2 = 1, 2, \ldots, N_2. \quad (28)$$

The coefficients are given as

$$K^{11}_{impr\tau_1} = \int_{D^{qp}_1} \sqrt{2a\epsilon - \epsilon^2} K^{11}_{im}(x'^{\tau_1}_1, x'^{\tau_1}_2, \xi'_1, \xi'_2) d\xi'_1 d\xi'_2, \quad (29)$$

$$K^{12}_{impr\tau_1} = \int_{D^{qp}_2} \sqrt{2a\epsilon - \epsilon^2} K^{12}_{im}(x'^{\tau_1}_1, x'^{\tau_1}_2, \xi'_1, \xi'_2) d\xi'_1 d\xi'_2, \quad (30)$$

$$K^{21}_{impr\tau_2} = \int_{D^{qp}_1} \sqrt{2a\epsilon - \epsilon^2} K^{21}_{im}(x'^{\tau_2}_1, x'^{\tau_2}_2, \xi'_1, \xi'_2) d\xi'_1 d\xi'_2, \quad (31)$$

$$K^{22}_{impr\tau_2} = \int_{D^{qp}_2} \sqrt{2a\epsilon - \epsilon^2} K^{22}_{im}(x'^{\tau_2}_1, x'^{\tau_2}_2, \xi'_1, \xi'_2) d\xi'_1 d\xi'_2, \quad (32)$$

with $(x'^{\tau_k}_1, x'^{\tau_k}_2)$ being the locations of the collocation points in the set of triangles D^{qp}_k.

It was noted earlier that K^{11}_{im} and K^{22}_{im} contain both singular and regular terms while K^{12}_{im} and K^{21}_{im} are regular. For the singular and regular terms associated with K^{11}_{im}, the details of the numerical integrations are given by Lee et al. (1987) and may also be applied to K^{22}_{im}. For K^{21}_{im}, Gaussian double integration is applied directly to each triangle and good convergence is obtained if $r_1 > 5\sqrt{\text{Area } D^{qp}_1}$ where

$$r_1^2 = (x'^{\tau_2}_1 - \xi'^{p}_1)^2 + (x'^{\tau_2}_2 - \xi'^{p}_2)^2, \quad (33)$$

with $(x'^{\tau_2}_1, x'^{\tau_2}_2)$ being a collocation point in D^{q}_2 and (ξ'^{p}_1, ξ'^{p}_2) being the center of gravity of triangle D^{qp}_1. A similar requirement is utilized for the K^{12}_{im} set of kernels.

Numerical Results

The critical quantities of interest in studying crack growth are the stress intensity factors. They depend on loading, crack and body geometry, and material properties when a crack is near a phase boundary. In particular, for the present analysis of three-dimensional crack penetration through an interface, the stress intensity factor variation along the crack front contour will depend on the crack geometry in each phase. In order to closely analyze the interfacial effect, the crack geometry on each side of the interface is taken to be symmetric. A semicircular crack geometry is used since this eliminates the stress intensity factor variation caused by a variation in crack front curvature.

In the following figures, the mode I, II, and III stress intensity factors along the crack front contour are given. Points along the crack front are located by the angle θ, Fig. 1, where $\theta = -90$ deg is the deepest point of the crack in body 2, $\theta = 0$ deg is the interface, and $\theta = 90$ deg is the deepest point in body 1. In order to study the interfacial effects, various values of the stiffness ratio $\Gamma = \mu_2/\mu_1$ are considered as well as various crack inclination angles α. For all cases considered $\nu_1 = \nu_2 = 0.3$.

Figures 2–8 are for planar (nonkinked) crack penetration and they show the variation in the mode I, II, and III stress intensity factors for $\Gamma = 2$, 4, and 10, and crack angles of $\alpha = 0$,

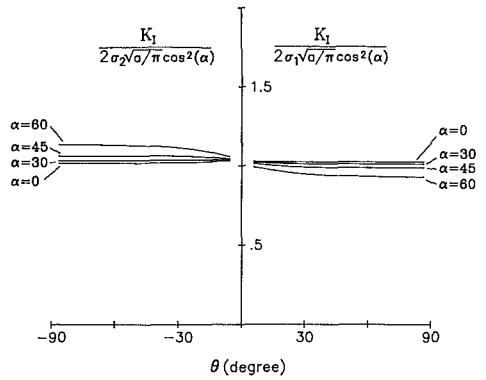


Fig. 2 Mode I stress intensity factors for a penny-shaped crack located symmetrically across the interface, $\Gamma = 2$, $\nu_1 = \nu_2 = 0.3$, farfield tensile loading, $\sigma^1_{33} = \sigma_1$, $\sigma^2_{33} = \sigma_2$, $x_3 \to \mp\infty$

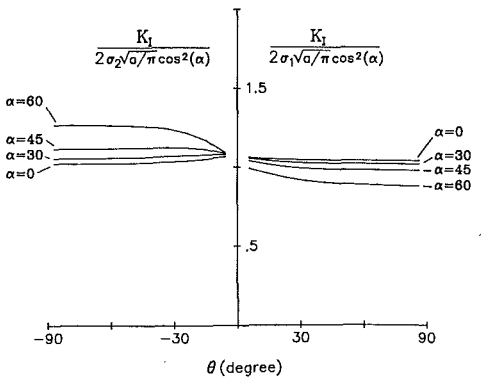


Fig. 3 Mode I stress intensity factors for a penny-shaped crack located symmetrically across the interface, $\Gamma = 4$, $\nu_1 = \nu_2 = 0.3$, farfield tensile loading, $\sigma^1_{33} = \sigma_1$, $\sigma^2_{33} = \sigma_2$, $x_3 \to \mp\infty$

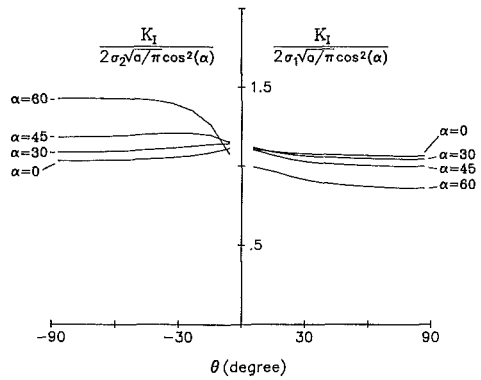


Fig. 4 Mode I stress intensity factors for a penny-shaped crack located symmetrically across the interface, $\Gamma = 10$, $\nu_1 = \nu_2 = 0.3$, farfield tensile loading, $\sigma^1_{33} = \sigma_1$, $\sigma^2_{33} = \sigma_2$, $x_3 \to \mp\infty$

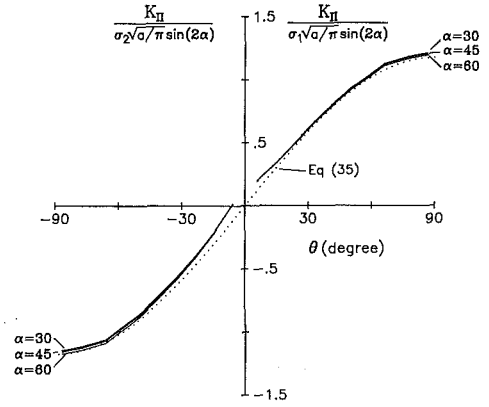


Fig. 5 Mode II stress intensity factors for a penny-shaped crack located symmetrically across the interface, $\Gamma = 2$, $\nu_1 = \nu_2 = 0.3$, farfield tensile loading, $\sigma^1_{33} = \sigma_1$, $\sigma^2_{33} = \sigma_2$, $x_3 \to \mp\infty$

Downloaded 03 May 2010 to 171.66.16.31. Redistribution subject to ASME license or copyright; see http://www.asme.org/terms/Terms_Use.cfm

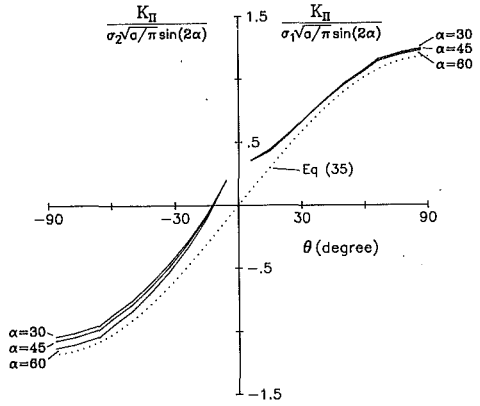


Fig. 6 Mode II stress intensity factors for a penny-shaped crack located symmetrically across the interface, $\Gamma = 10$, $\nu_1 = \nu_2 = 0.3$, fairfield tensile loading, $\sigma^1_{33} = \sigma_1$, $\sigma^2_{33} = \sigma_2$, $x_3 \to \mp\infty$

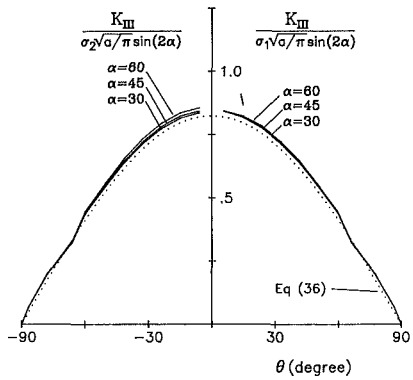


Fig. 7 Mode III stress intensity factors for a penny-shaped crack located symmetrically across the interface, $\Gamma = 2$, $\nu_1 = \nu_2 = 0.3$, farfield tensile loading, $\sigma^1_{33} = \sigma_1$, $\sigma^2_{33} = \sigma_2$, $x_3 \to \mp\infty$

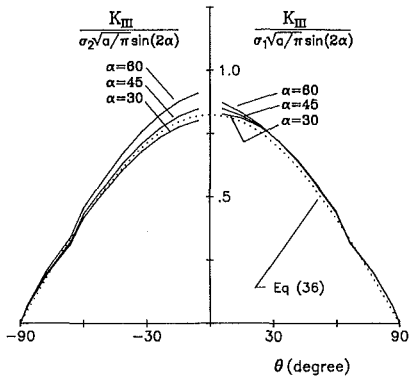


Fig. 8 Mode III stress intensity factors for a penny-shaped crack located symmetrically across the interface, $\Gamma = 10$, $\nu_1 = \nu_2 = 0.3$, farfield tensile loading, $\sigma^1_{33} = \sigma_1$, $\sigma^2_{33} = \sigma_2$, $x_3 \to \mp\infty$

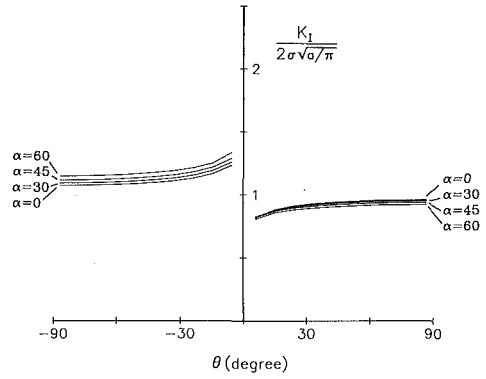


Fig. 9 Mode I stress intensity factors for a penny-shaped crack located symmetrically across the interface, $\Gamma = 2$, $\nu_1 = \nu_2 = 0.3$, uniform internal pressure σ

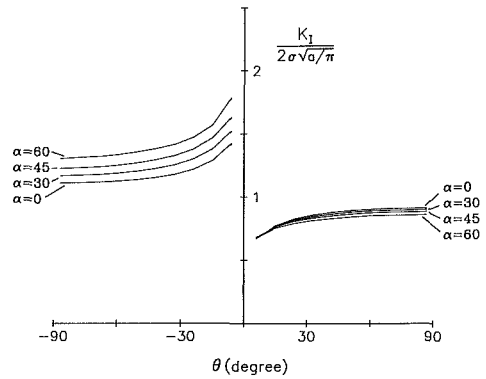


Fig. 10 Mode I stress intensity factors for a penny-shaped crack located symmetrically across the interface, $\Gamma = 4$, $\nu_1 = \nu_2 = 0.3$, uniform internal pressure σ

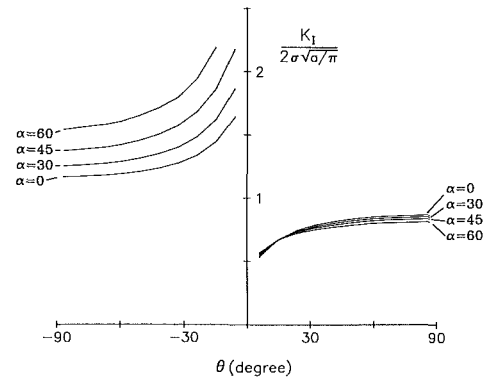


Fig. 11 Mode I stress intensity factors for a penny-shaped crack located symmetrically across the interface, $\Gamma = 10$, $\nu_1 = \nu_2 = 0.3$, uniform internal pressure σ

30, 45, and 60 deg. The loading, which is chosen to produce identical strains within each phase, is uniform tension at infinity parallel to the interface; therefore, $\sigma^1_{33} = \sigma_1$, $\sigma^2{}_{33} = \sigma_2$, $x_3 \to \mp\infty$. In order to match the interface displacements, the uniform stresses in each body are related through

$$\sigma_2 = \Gamma \frac{\kappa_1 + 1}{\kappa_2 + 1} \sigma_1. \tag{34}$$

The mode I stress intensity factor in each body is nondimensionalized by the normal traction across the crack faces in the form for a penny-shaped crack in an infinite body. The mode II and III are nondimensionalized in the same manner except the shear stress on the crack plane is used.

Figures 2–4 display the mode I stress intensity factor for $\Gamma = 2$, 4 and 10, respectively. There are several interesting features in these figures. First, the stress intensity factors are virtually constant away from the interface except for high stiffness ratios combined with large crack angles α. The stress intensity factors are close to one for $\Gamma = 2$, but the deviation increases with the stiffness ratio. In general, as the crack angle α increases, the K_I curves decrease in the more compliant body and increase in the stiffer body. For a given crack angle α, the K_I curves for the stiffer body increase significantly with Γ while in the weaker body the change is less.

Figure 5–6 show the mode II stress intensity factors for $\Gamma = 2$ and 10 while Figs. 7–8 are for mode III. For comparison, the results for identical materials ($\Gamma = 1$)

Downloaded 03 May 2010 to 171.66.16.31. Redistribution subject to ASME license or copyright; see http://www.asme.org/terms/Terms_Use.cfm

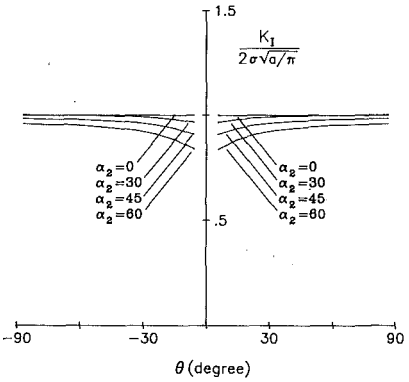


Fig. 12 Mode I stress intensity factors for a kinked penny-shaped crack located symmetrically across the interface, $\alpha_1 = 0$, $\Gamma = 1$, $\nu_1 = \nu_2 = 0.3$, uniform internal pressure σ

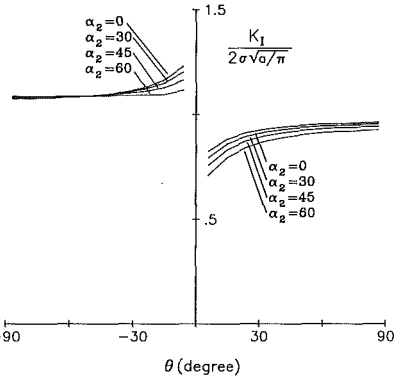


Fig. 13 Mode I stress intensity factors for a kinked penny-shaped crack located symmetrically across the interface, $\alpha_1 = 0$, $\Gamma = 2$, $\nu_1 = \nu_2 = 0.3$, uniform internal pressure σ

$$K_{II} = \left(\frac{2}{2-\nu}\sin(\theta)\right)\sigma\sqrt{a/\pi}\sin(2\alpha), \tag{35}$$

$$K_{III} = \left(2\frac{1-\nu}{2-\nu}\cos(\theta)\sigma\sqrt{a/\pi}\sin(2\alpha)\right), \tag{36}$$

are also plotted. For a stiffness ratio of $\Gamma = 2$, the results are very close to the homogeneous value except near the interface where the deviation increases. For $\Gamma = 10$ the difference is more pronounced around the entire crack front and, in the stiffer body, the dependence on the orientation angle increases.

Figures 9–11 display the mode I stress intensity factors for $\Gamma = 2$, 4, and 10 under a uniform hydraulic pressure σ. Again the values are essentially constant away from the interface, however, the behavior as the interface is approached is different. By approaching the interface from the more compliant body, the stress intensity factors decrease and increase coming from the stiffer side. Since uniform pressure is exerted over the entire crack, the crack opening displacement in the stiffer body is smaller than in the more compliant body. Again the same dependence on the angle α and stiffness ratio Γ are noted. The mode I stress intensity factors in body 1 are lower than for identical materials because of the stiffening effect of material 2; the stress intensity factors are higher in body 2 since material 1 is weaker.

Figures 12–13 show the mode I stress intensity factors for a crack that experiences a directional change through the interface, where the crack in each body is semicircular and internally loaded by a pressure σ. In Fig. 12, $\Gamma = 1$ (homogeneous case), the results represent a three-dimensional kinked crack. The angle $\alpha_1 = 0$ and α_2 is varied as shown. The presence of the kink produces a confining effect that reduces the K_I values as the kink is approached along the crack front. In Fig. 13, $\Gamma = 2$ and $\alpha_1 = 0$. Here, the effect of the mismatch in elastic constants dominates the behavior causing the K_I curves to increase as the interface is approached from the stiffer body; in the more compliant body the decrease is greater.

Acknowledgment

The authors are grateful to support from the Amoco Production Company, in particular to Drs. R. W. Veatch and Z. Moschovidis. Support is also gratefully acknowledged from the Center for Engineering Tribology jointly supported by the National Science Foundation and the industrial consortium at Northwestern University.

References

Bazant, Z. B., and Estenssoro, L. F., 1979, "Surface Singularity and Crack Propagation," *International Journal of Solids and Structures*, Vol. 15, pp. 405–426.

Benthem, J. P., 1977, "State of Stress at the Vertex of a Quarter-Infinite Crack in a Half-Space," *International Journal of Solids and Structures*, Vol. 13, pp. 479–492.

Bogy, D. B., 1971, "Two Edge-Bonded Elastic Wedges of Different Materials and Wedge Angles Under Surface Tractions," ASME JOURNAL OF APPLIED MECHANICS, Vol. 35, pp. 377–386.

Dundurs, J., and Hetényi, M., 1965, "Transmission of Force Between Two Semi-Infinite Solids," ASME JOURNAL OF APPLIED MECHANICS, Vol. 32, pp. 671–674.

Lee, J. C., and Keer, L. M., 1986, "Study of a Three-Dimensional Crack Terminating at an Interface," ASME JOURNAL OF APPLIED MECHANICS, Vol. 53, pp. 311–316.

Lee, J. C., Farris, T. N., and Keer, L. M., 1987, "Stress Intensity Factors for Cracks of Arbitrary Shape Near an Interfacial Boundary," *Engineering Fracture Mechanics*, Vol. 27, pp. 27–41.

Lin, W., and Keer, L. M., 1988, "Growth of a Hydraulically Pressurized Fracture," *Engineering Fracture Mechanics*, Vol. 29, pp. 473–481.

Mura, T., 1982, *Micromechanics of Defects in Solids*, 1st ed., Martinus Nijhoff, pp. 105–106.

Murakami, Y., and Nemat-Nasser, S., 1982, "Interacting Dissimilar Semi-elliptical Surface Flaws Under Tension and Bending," *Engineering Fracture Mechanics*, Vol. 16, pp. 373–386.

Murakami, Y., and Nemat-Nasser, S., 1983, "Growth and Stability of Interacting Surface Flaws of Arbitrary Shape," *Engineering Fracture Mechanics*, Vol. 17, No. 3, pp. 193–210.

Murakami, Y., 1985, "Analysis of Stress Intensity Factors of Modes I, II, and III for Inclined Surface Cracks of Arbitrary Shape," *Engineering Fracture Mechanics*, Vol. 17, pp. 101–114.

Murakami, Y., 1987, *Stress Intensity Factors Handbook*, Vol. 1, Y. Murakami, ed., Pergamon, pp. 429–640.

Mastrojannis, E. N., Keer, L. M., and Mura, T., 1979, "Stress Intensity Factor for a Plane Crack Under Normal Pressure," *International Journal of Fracture*, Vol. 15, pp. 247–258.

Rongved, L., 1955, "Force Interior to One of Two Joined Semi-Infinite Solids," *Proceedings of the Second Midwestern Conference on Solid Mechanics*, pp. 1–13.

Sih, G. C., and Chen, E. P., 1981, *Cracks in Composite Materials; Mechanics of Fracture*, Vol. 6, G. C. Sih, ed., Martinus Nijhoff.

APPENDIX A

The potentials Φ_{ij}^{11} and ψ_j^{11} are given with suppressed superscripts as

$$\Phi_{11} = \Phi_{33} = \frac{1}{2\pi(\kappa_1+1)}\left[\frac{1}{R_1} + \frac{S}{R_2}\right], \tag{A1}$$

$$\Phi_{12} = \Phi_{13} = \Phi_{31} = \Phi_{32} = 0, \tag{A2}$$

$$\Phi_{2i} = \frac{1}{2\pi(\kappa_1+1)}\left[\frac{(A\kappa_1 - S)(x_i - \xi_i)}{R_2(R_2 + x_2 + \xi_2)} - \frac{2A\xi_2(x_i - \xi_i)}{R_2^3}\right], \quad i = 1, 3 \tag{A3}$$

$$\Phi_{22} = \frac{1}{2\pi(\kappa_1+1)}\left[\frac{1}{R_1} + \frac{A\kappa_1}{R_2} + \frac{2A\xi_2(x_2+\xi_2)}{R_2^3}\right], \tag{A4}$$

Downloaded 03 May 2010 to 171.66.16.31. Redistribution subject to ASME license or copyright; see http://www.asme.org/terms/Terms_Use.cfm

$$\psi_i = \frac{1}{2\pi(\kappa_1+1)}\left[-\frac{(A\kappa_1^2+B-2S\kappa_1)(x_i-\xi_i)}{2(R_2+x_2+\xi_2)} + \frac{(A\kappa_1-S)\xi_2(x_i-\xi_i)}{R_2(R_2+x_2+\xi_2)}\right],\ i=1,\ 3 \tag{A5}$$

$$\psi_2 = \frac{1}{2\pi(\kappa_1+1)}\left[-\frac{\xi_2}{R_1} - \frac{A\kappa_1\xi_2}{R_2} + \frac{(A\kappa_1^2-B)}{2}\ln(R_2+x_2+\xi_2)\right], \tag{A6}$$

where

$$R_1 = \sqrt{(x_1-\xi_1)^2+(x_2-\xi_2)^2+(x_3-\xi_3)^2}, \tag{A7}$$

$$R_2 = \sqrt{(x_1-\xi_1)^2+(x_2+\xi_2)^2+(x_3-\xi_3)^2}, \tag{A8}$$

$$A=\frac{1-\Gamma}{1+\kappa_1\Gamma},\ B=\frac{\kappa_2-\kappa_1\Gamma}{\kappa_2+\Gamma},\ S=\frac{1-\Gamma}{1+\Gamma},\ \Gamma=\frac{\mu_2}{\mu_1}. \tag{A9}$$

The potentials Φ_{ij}^{21} and ψ_j^{21} are given as

$$\Phi_{11}=\Phi_{33}=\frac{1}{2\pi(\kappa_1+1)}\left[\frac{T}{R_1}\right], \tag{A10}$$

$$\Phi_{12}=\Phi_{13}=\Phi_{31}=\Phi_{32}=0, \tag{A11}$$

$$\Phi_{2i}=\frac{1}{2\pi(\kappa_1+1)}\left[-\frac{(1-B-T)(x_i-\xi_i)}{R_1(R_1-x_2+\xi_2)}\right],\ i=1,\ 3 \tag{A12}$$

$$\Phi_{22}=\frac{1}{2\pi(\kappa_1+1)}\left[\frac{1-B}{R_1}\right], \tag{A13}$$

$$\psi_i = \frac{1}{2\pi(\kappa_1+1)}\left[-\frac{V(x_i-\xi_i)}{2(R_1-x_2+\xi_2)} + \frac{(1-A-T)\xi_2(x_i-\xi_i)}{R_1(R_1-x_2+\xi_2)}\right],\ i=1,\ 3 \tag{A14}$$

$$\psi_2 = \frac{1}{2\pi(\kappa_1+1)}\left[-\frac{(1-A)\xi_2}{R_1}+\frac{W}{2}\ln(R_1-x_2+\xi_2)\right], \tag{A15}$$

and

$$T=\frac{2(\kappa_1+1)\Gamma}{(\kappa_2+1)(1+\Gamma)},\quad W=(1-A)\kappa_1-(1-B)\kappa_2, \tag{A16}$$

$$V=(1-A)\kappa_1+(1-B-2T)\kappa_2. \tag{A17}$$

The reciprocal potentials can be obtained from the relations

$$\Phi_{ij}^{12}(\mathbf{x},\boldsymbol{\xi})=\bar{\Phi}_{ij}^{21}(-\mathbf{x},-\boldsymbol{\xi}), \tag{A18}$$

$$\psi_j^{12}(\mathbf{x},-\boldsymbol{\xi})=-\bar{\psi}_j^{21}(-\mathbf{x},-\boldsymbol{\xi}), \tag{A19}$$

$$\Phi_{ij}^{22}(\mathbf{x},\boldsymbol{\xi})=\bar{\Phi}_{ij}^{11}(-\mathbf{x},-\boldsymbol{\xi}), \tag{A20}$$

$$\psi_j^{22}(\mathbf{x},\boldsymbol{\xi})=-\bar{\psi}_j^{11}(-\mathbf{x},-\boldsymbol{\xi}), \tag{A21}$$

where an overbar in (A18–A21) implies interchanging subscripts on the elastic constants.

APPENDIX B

The set of kernels K_{im}^{21} are given by the relations

$$K_{im}^{21}(x_1', x_2', \xi_1', \xi_2') = \frac{\mu_1}{4\pi(\kappa_1+1)}K_i^m(x_1',\ cx_2',\ sx_2',\ \xi_1',\ c\xi_2',\ s\xi_2'). \tag{B1}$$

The functions K_i^m are known in terms of a second and fourth-order tensor function through

$$K_i^m(x_1,x_2,x_3,\xi_1,\xi_2,\xi_3) = 2\pi(\kappa_1+1)e_{3p}e_{iq}(e_{mj}e_{3n}+e_{3j}e_{mn})B_{pqjn},\quad m=1,\ 2, \tag{B2}$$

$$K_i^3(x_1,x_2,x_3,\xi_1,\xi_2,\xi_3) = 4\pi(\kappa_1+1)e_{3p}e_{iq}(A_{pq}+e_{3j}e_{3n}B_{pqjn}), \tag{B3}$$

with e_{ij}, c and s defined in equation (2). The tensor functions are

$$A_{ij}=\frac{2\nu_1}{(\kappa_1-1)}\left\{\frac{6T-2(1-A)(\kappa_1-1)}{2\pi(\kappa_1+1)}F_{,ij}+2a_{11}\bar{x}_lF_{,lij}\right\}, \tag{B4}$$

and

$$\begin{aligned}B_{ijmn} = &-4\nu_2a_{22}\delta_{ij}F_{,mn}-(\kappa_2-1)(a_{im}F_{,jn}\\ &+a_{jm}F_{,in})+2(\delta_{1n}\delta_{1m}a_{11}-\delta_{2m}\delta_{2n}d\\ &+\delta_{3m}\delta_{3n}a_{11})F_{,ij}+2[\delta_{1m}a_{11}\bar{x}_1\\ &+\delta_{2m}(a_{22}x_2+\xi_2d)+\delta_{3m}a_{11}\bar{x}_3]F_{,ijn}\\ &-(\kappa_2-1)b_2(\delta_{i2}I_{m,jn}+\delta_{j2}I_{m,in})\\ &+2(x_2b_2+\beta\xi_2)I_{m,ijn}-2(-\gamma H_{m,ijn}\\ &+\beta\delta_{n2}I_{m,ij}-g\delta_{2m}Q_{2,ijn}).\end{aligned} \tag{B5}$$

Here, δ_{ij} is the Kronecker delta and the material constants are given by

$$a_{ij}=0,\ i\neq j,\ a_{11}=a_{33}=\frac{T}{2\pi(\kappa_1+1)},\quad a_{22}=\frac{1-B}{2\pi(\kappa_1+1)}, \tag{B6}$$

$$b_2=-\frac{(1-B-T)}{2\pi(\kappa_1+1)},\quad d=-\frac{1-A}{2\pi(\kappa_1+1)},\quad \beta=\frac{(1-A-T)}{2\pi(\kappa_1+1)}, \tag{B7}$$

$$\gamma=-\frac{V}{4\pi(\kappa_1+1)},\quad g=\frac{W}{4\pi(\kappa_1+1)}. \tag{B8}$$

with T, B, A, V, and W defined in Appendix A.

The functions are defined as

$$\bar{x}_m=x_m-\xi_m, \tag{B9}$$

$$F=\frac{1}{R_1}, \tag{B10}$$

$$I_m=\frac{\bar{x}_m}{R_1\bar{R}_1}(m\neq 2)\quad I_2=0, \tag{B11}$$

$$H_m=\frac{\bar{x}_m}{\bar{R}_1}(m\neq 2)\quad H_2=0, \tag{B12}$$

$$Q_2=\ln\bar{R}_1, \tag{B13}$$

with R_1 defined in Appendix A and $\bar{R}_1=R_1-\bar{x}_2$. In (B4)–(B5) a comma denotes differentiation with respect to a component of the vector $\mathbf{x}$ and the results for F are

$$F_{,ij}=-\frac{\delta_{ij}}{R_1^3}+3\frac{\bar{x}_i\bar{x}_j}{R_1^5}, \tag{B14}$$

$$F_{,ijk}=\frac{3(\delta_{ij}\bar{x}_k+\delta_{ki}\bar{x}_j+\delta_{kj}\bar{x}_i)}{R_1^5}-15\frac{\bar{x}_i\bar{x}_j\bar{x}_k}{R_1^7}. \tag{B15}$$

Downloaded 03 May 2010 to 171.66.16.31. Redistribution subject to ASME license or copyright; see http://www.asme.org/terms/Terms_Use.cfm

For the function I_m $(m \neq 2)$,

$$I_{m,i} = \frac{\delta_{mi}}{R_1 \bar{R}_1} - \bar{x}_m \bar{x}_i \left(\frac{1}{R_1^2 \bar{R}_1^2} + \frac{1}{R_1^3 \bar{R}_1} \right), \quad (i \neq 2), \tag{B16}$$

$$I_{m,2} = -F_{,m}, \tag{B17}$$

$$I_{m,ij} = (\delta_{mi}\bar{x}_j + \delta_{ij}\bar{x}_m + \delta_{mj}\bar{x}_i)\left(-\frac{1}{R_1^3 \bar{R}_1} - \frac{1}{R_1^2 \bar{R}_1^2} \right) + \bar{x}_i \bar{x}_j \bar{x}_m \left(\frac{3}{R_1^5 \bar{R}_1} + \frac{3}{R_1^4 \bar{R}_1^2} + \frac{2}{R_1^3 \bar{R}_1^3} \right), \quad (i, j \neq 2), \tag{B18}$$

$$I_{m,ijk} = (\delta_{mi}\delta_{kj} + \delta_{jm}\delta_{ik} + \delta_{ij}\delta_{km})\left(-\frac{1}{R_1^3 \bar{R}_1} - \frac{1}{R_1^2 \bar{R}_1^2} \right) + (\delta_{mi}\bar{x}_k\bar{x}_j + \delta_{jm}\bar{x}_k\bar{x}_i + \delta_{ij}\bar{x}_k\bar{x}_m + \delta_{ik}\bar{x}_j\bar{x}_m + \delta_{kj}\bar{x}_i\bar{x}_m + \delta_{km}\bar{x}_i\bar{x}_j)\left(\frac{3}{R_1^5 \bar{R}_1} + \frac{3}{R_1^4 \bar{R}_1^2} + \frac{2}{R_1^3 \bar{R}_1^3} \right) - \bar{x}_i\bar{x}_j\bar{x}_m\bar{x}_k \left(\frac{15}{R_1^7 \bar{R}_1} + \frac{15}{R_1^6 \bar{R}_1^2} + \frac{12}{R_1^5 \bar{R}_1^3} + \frac{6}{R_1^4 \bar{R}_1^4} \right), \quad (i, j, k \neq 2). \tag{B19}$$

For the function Q_2,

$$Q_{2,i} = I_i \ (i \neq 2), \qquad Q_{2,2} = -F, \tag{B20}$$

hence, further derivatives can be found from the previous expressions.

Finally, the derivatives of $H_m (m \neq 2)$ may be expressed as

$$H_{m,i} = \frac{\delta_{im}}{\bar{R}_1} - \frac{\bar{x}_i \bar{x}_m}{R_1 \bar{R}_1^2}, \quad (i \neq 2), \tag{B21}$$

$$H_{m,2} = I_m, \tag{B22}$$

$$H_{m,ij} = -(\delta_{ij}\bar{x}_m + \delta_{jm}\bar{x}_i + \delta_{im}\bar{x}_j)\left(\frac{1}{R_1 \bar{R}_1^2} \right) + \bar{x}_i \bar{x}_j \bar{x}_m \left(\frac{1}{R_1^3 \bar{R}_1^2} + \frac{2}{R_1^2 \bar{R}_1^3} \right), \quad (i, j \neq 2), \tag{B23}$$

$$H_{m,ijk} = -(\delta_{ij}\delta_{mk} + \delta_{jm}\delta_{ik} + \delta_{im}\delta_{jk})\left(\frac{1}{R_1 \bar{R}_1^2} \right) + (\delta_{ij}\bar{x}_m\bar{x}_k + \delta_{jm}\bar{x}_k\bar{x}_i + \delta_{im}\bar{x}_j\bar{x}_k + \delta_{ik}\bar{x}_j\bar{x}_m + \delta_{kj}\bar{x}_i\bar{x}_m + \delta_{km}\bar{x}_i\bar{x}_j)\left(\frac{1}{R_1^3 \bar{R}_1^2} + \frac{2}{R_1^2 \bar{R}_1^3} \right) - \bar{x}_i\bar{x}_j\bar{x}_m\bar{x}_k \left(\frac{3}{R_1^5 \bar{R}_1^2} + \frac{6}{R_1^4 \bar{R}_1^3} + \frac{6}{R_1^3 \bar{R}_1^4} \right), \quad (i, j, k \neq 2). \tag{B24}$$

Downloaded 03 May 2010 to 171.66.16.31. Redistribution subject to ASME license or copyright; see http://www.asme.org/terms/Terms_Use.cfm

Makoto Obata
Research Associate,
Department of Civil Engineering,
Nagoya Institute of Technology,
Gokiso-cho, Showa-ku,
Nagoya, 466, Japan

Siavouche Nemat-Nasser
Professor of Applied Mechanics and Engineering Sciences
and Director of Center of Excellence for Advanced Materials,
The University of California, San Diego,
La Jolla, Calif. 92093
Fellow ASME

Yoshiaki Goto
Associate Professor,
Department of Civil Engineering,
Nagoya Institute of Technology,
Gokiso-Cho, Showa-Ku,
Nagoya, 466, Japan

Branched Cracks in Anisotropic Elastic Solids

Branched crack problems are analyzed in two-dimensional, anisotropically elastic homogeneous solids. The method of analysis is based on the complex variable approach of Savin and Lekhnitskii. The Hilbert problem in an anisotropic body is defined, and a pair of singular integral equations are derived for dislocation density functions associated with a branched crack. For both symmetric and nonsymmetric geometries, and under symmetric and antisymmetric loads, the stress intensity factors and the energy release rate are computed numerically by extrapolation for infinitesimally small lengths of branched cracks. The results are compared with those of the isotropic case given in the literature and the effects of anisotropy are discussed.

1 Introduction

Branched or kinked cracks are of considerable importance in the field of fracture mechanics. For isotropic materials, this problem has been extensively investigated both theoretically and experimentally (Erdogan and Sih (1963), Sih (1972), Hussain et al. (1974), Bilby and Cardew (1975), Lo (1978), Palaniswamy and Knauss (1978), Wu (1979), Karihaloo et al. (1980), and Hayashi and Nemat-Nasser (1981)). On the other hand, the analysis of cracks in anisotropic solids has received relatively little attention. Early work began with Stroh (1958), who investigated cracks in terms of dislocation theory in anisotropic elastic solids. (See also Eshelby et al. (1953) and Willis (1966) for related works.) Later, this problem received limited interest in conjunction with the application of fracture mechanics to composites which are often fibrous or laminar and therefore highly anisotropic (Sih et al. (1965) and Tsai and Wu (1971)).

In the present work, we analyze a branched crack in an anisotropic elastic solid. We aim to give the essential information on the nature of the stress field just after crack branching. The method of analysis is based on the complex variable approach outlined by Savin (1961) and Lekhnitiskii (1963). Following Muskhelishvili (1953), we express a plane crack problem in terms of the Hilbert problem, and study the branched crack using the method proposed by Lo (1978). The stress intensity factors are computed at the tip of the branched crack by extrapolation. Also, the energy release rate for infinitesimally small branched crack lengths is computed. This provides some of the basic information necessary for the analysis of crack branching in terms of the field quantities prior to branching.

2 Formulation

Consider a class of plane problems in anisotropic elasticity, where the stress-strain relations are

$$\begin{aligned} \epsilon_{xx} &= c_{11}\sigma_{xx} + c_{12}\sigma_{yy} + c_{16}\sigma_{xy}, \\ \epsilon_{yy} &= c_{12}\sigma_{xx} + c_{22}\sigma_{yy} + c_{26}\sigma_{xy}, \\ 2\epsilon_{xy} &= c_{16}\sigma_{xx} + c_{26}\sigma_{yy} + c_{66}\sigma_{xy}, \end{aligned} \tag{1a-c}$$

and where a fixed rectangular Cartesian coordinate system, (x, y), is used. Problems of this kind have been successfully analyzed using a complex variable approach, similar to the case of isotropic elasticity (see Savin (1961) and Lekhnitskii (1963) and also Green and Zerna (1954)). In fact, as will be shown, the formulas for anisotropic elasticity are sometimes more systematic and simpler, in a certain sense, than those for the isotropic case. The stress and displacement fields can be expressed in terms of two independent analytic functions as

$$\begin{aligned} \sigma_{xx} &= 2\mathrm{Re}\{s_1^2\Phi(z_1) + s_2^2\Psi(z_2)\}, \\ \sigma_{yy} &= 2\mathrm{Re}\{\Phi(z_1) + \Psi(z_2)\}, \\ \sigma_{xy} &= -2\mathrm{Re}\{s_1\Phi(z_1) + s_2\Psi(z_2)\}, \\ u_x &= 2\mathrm{Re}\{p_1\phi(z_1) + p_2\psi(z_2)\}, \\ u_y &= 2\mathrm{Re}\{q_1\phi(z_1) + q_2\psi(z_2)\}, \\ \Phi(z) &= \phi'(z), \quad \Psi(z) = \psi'(z), \end{aligned} \tag{2a-g}$$

Contributed by the Applied Mechanics Division of THE AMERICAN SOCIETY OF MECHANICAL ENGINEERS for publication in the JOURNAL OF APPLIED MECHANICS.

Discussion on this paper should be addressed to the Editorial Department, ASME, United Engineering Center, 345 East 47th Street, New York, N.Y. 10017, and will be accepted until two months after final publication of the paper itself in the JOURNAL OF APPLIED MECHANICS. Manuscript received by the ASME Applied Mechanics Division, July 20, 1988; final revision, December 6, 1988.

Copyright © 1989 by ASME

Downloaded 03 May 2010 to 171.66.16.31. Redistribution subject to ASME license or copyright; see http://www.asme.org/terms/Terms_Use.cfm

where

$$z_1 = x + s_1 y, \quad z_2 = x + s_2 y,$$
$$p_1 = c_{11}s_1^2 - c_{16}s_1 + c_{12}, \quad p_2 = c_{11}s_2^2 - c_{16}s_2 + c_{12} \qquad (2h\text{-}m)$$
$$q_1 = \frac{c_{12}s_1^2 - c_{26}s_1 + c_{22}}{s_1}, \quad q_2 = \frac{c_{12}s_2^2 - c_{26}s_2 + c_{22}}{s_2}.$$

Here, u_x and u_y denote the displacements in the x and y-direction, respectively, prime denotes differentiation with respect to the corresponding argument, and $s_i (i = 1, 2)$ are the roots of the characteristic equation,

$$c_{11}s^4 - 2c_{16}s^3 + (2c_{12} + c_{66})s^2 - 2c_{26}s^2 + c_{22} = 0. \qquad (3)$$

The positiveness of the elastic energy density ensures that no real roots exist for this equation (Eshelby et al. (1953) and Lekhnitskii (1963)). Then, since two of the roots are the complex conjugate of the other two, we choose s_1 and s_2 such that their imaginary parts are positive. If s_1 equals s_2, equations (2) cease to be valid. In this case, however, the field quantities can be formulated in terms of the biharmonic Airy stress function by an easy change of the variables, and, therefore, can be treated in the same way as in isotropic elasticity (Mikhlin (1936)). In what follows, we will assume that s_1 and s_2 are distinct. Note that the isotropic case may be regarded as the limiting case when s_1 and s_2 equal $i = \sqrt{-1}$.

For isotropic elasticity, Muskhelishvili (1953) has formulated the boundary value problems for a plane containing straight cuts in terms of the Hilbert problem. A similar approach to these problems in anisotropic solids does seem to exist. It turns out that even in the case of an anisotropic solid, Muskhelishvili's approach provides a simple and powerful technique.

Consider the functions defined by

$$\Omega(z) = \bar{\Phi}(z) + \lambda\bar{\Psi}(z), \quad \Theta(z) = \Phi(z) + \mu\Psi(z), \qquad (4a,b)$$

where an overbar denotes the complex conjugate, and where λ and μ are constants given in Appendix A. These functions are holomorphic as long as Φ and Ψ are holomorphic. From equations (2) and (4), the stress and displacement fields can be expressed as

$$\sigma_{yy} - \alpha\sigma_{xy} = (1 + \alpha s_1)\Theta(z_1) + (1 + \alpha s_3)\Omega(\bar{z}_1) + (1 + \alpha s_2)\{\Psi(z_2) - \Psi(z_1)\} + (1 + \alpha s_4)\{\bar{\Psi}(\bar{z}_2) - \bar{\Psi}(\bar{z}_1)\}, \qquad (5a)$$

$$u_x + \alpha u_y = (p_1 + \alpha q_1)\theta(z_1) + (p_3 + \alpha q_3)\omega(\bar{z}_1) + (p_2 + \alpha q_2)\{\psi(z_2) - \psi(z_1)\} + (p_4 + \alpha q_4)\{\bar{\psi}(\bar{z}_2) - \bar{\psi}(\bar{z}_1)\}, \qquad (5b)$$

where α is a constant (see Appendix A) and

$$\Theta(z) = \theta'(z), \quad \Omega(z) = \omega'(z). \qquad (5c,d)$$

It is shown in Appendix A that α is not real and that λ cannot be equal to μ. Hence, equations (4) always determine a unique set of Φ and Ψ in terms of Ω and Θ.

On the x-axis, these expressions take on the form

$$\sigma_{yy}^{+} - \alpha\sigma_{xy}^{+} = (1 + \alpha s_1)\Theta^{+}(x) + (1 + \alpha s_3)\Omega^{-}(x),$$
$$\sigma_{yy}^{-} - \alpha\sigma_{xy}^{-} = (1 + \alpha s_1)\Theta^{-}(x) + (1 + \alpha s_3)\Omega^{+}(x). \qquad (6a,b)$$

Note that both $(\Psi(z_2) - \Psi(z_1))$ and $(\psi(z_2) - \psi(z_1))$ vanish when y goes to zero from either side of the x-axis since the imaginary parts of s_1 and s_2 have the same sign. Expressions (6) yield some important and interesting results for the stress singularities associated with the problem of straight cuts in anisotropic solids. One is the well-known fact that the stress singularity at the tip of a cut is the same square root as in the isotropic case.

Consider the branched crack shown in Fig. 1. The main crack of length $2a$ lies on the x-axis between $(-a, 0)$ and $(a, 0)$.

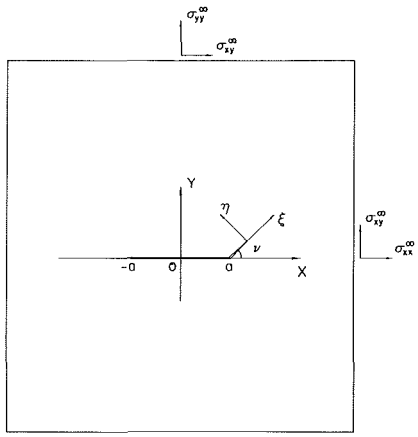


Fig. 1 A branched crack

Crack branching is assumed to occur at an angle ν as shown. In what follows, we concentrate attention on the case when the surfaces of the main crack are traction-free. If the main crack is closed, we can still follow the formulation given next, and obtain the final results summarized in Appendix B.

The boundary conditions are:

$$\sigma_{yy} = \sigma_{xy} = 0 \text{ on the main crack},$$
$$\sigma_{\eta\eta} = \sigma_{\xi\eta} = 0 \text{ on the branched crack}, \qquad (7a,b)$$

with the constant stress components prescribed at infinity. A branched crack is modeled by a continuous distribution of dislocations. As a first step, we seek the singular solution which satisfies the boundary condition (7a) when an isolated edge dislocation exists in the presence of the unbranched crack. This solution is formally decomposed as

$$\Phi(z_1) = \Phi_D(z_1) + \Phi_M(z_1) + \Phi_H(z_1),$$
$$\Psi(z_2) = \Psi_D(z_2) + \Psi_M(z_2) + \Psi_H(z_2). \qquad (8a,b)$$

The terms with subscript D are associated with the edge dislocation at (x_0, y_0) and are given by

$$\Phi_D(z_1, z_{01}) = \frac{1}{2\pi i}\frac{1}{c_{11}}\frac{s_1B_x - B_y}{(s_1 - s_2)(s_1 - s_3)(s_1 - s_4)}\frac{1}{z_1 - z_{01}}, \qquad (9a,b)$$
$$\Psi_D(z_2, z_{02}) = \frac{1}{2\pi i}\frac{1}{c_{11}}\frac{s_2B_x - B_y}{(s_2 - s_1)(s_2 - s_3)(s_2 - s_4)}\frac{1}{z_2 - z_{02}},$$
$$z_{0i} = x_0 + s_i y_0, \quad s_3 = \bar{s}_1, s_4 = \bar{s}_2, \qquad (9c\text{-}e)$$

where B_x and B_y are the displacement discontinuities in the x and y-direction, respectively, across the dislocation line. These functions are obtained in the same way as in the isotropic case; e.g., Stroh (1958). Substitution of equations (9) into equations (2) yields the corresponding stress distribution along the main crack surface. Using equations (6) and the results of Muskhelishvili (1953), we can determine the potential functions Φ_M and Ψ_M such that the main crack surface remains traction-free:

$$\Phi_M(z_1) = \frac{1}{4\pi i}\frac{1}{c_{11}}\frac{1}{s_1 - s_2}\left\{\frac{s_1B_x - B_y}{(s_1 - s_3)(s_1 - s_4)}\frac{1}{z_1 - z_{01}}\left(\frac{X(z_{01})}{X(z_1)} - 1\right) - \frac{s_3B_x - B_y}{(s_3 - s_1)(s_3 - s_4)}\frac{1}{z_1 - z_{03}}\left(\frac{X(z_{03})}{X(z_1)} - 1\right) - \frac{s_4B_x - B_y}{(s_4 - s_1)(s_4 - s_3)}\frac{1}{z_1 - z_{04}}\left(\frac{X(z_{04})}{X(z_1)} - 1\right)\right\}, \qquad (10a)$$

Downloaded 03 May 2010 to 171.66.16.31. Redistribution subject to ASME license or copyright; see http://www.asme.org/terms/Terms_Use.cfm

$$\Psi_M(z_2)=\frac{1}{4\pi i}\frac{1}{c_{11}}\frac{1}{s_2-s_1}\left\{\frac{s_2B_x-B_y}{(s_2-s_3)(s_2-s_4)}\frac{1}{z_2-z_{02}}\left(\frac{X(z_{02})}{X(z_2)}-1\right)-\frac{s_3B_x-B_y}{(s_3-s_2)(s_3-s_4)}\frac{1}{z_2-z_{03}}\left(\frac{X(z_{03})}{X(z_2)}-1\right)-\frac{s_4B_x-B_y}{(s_4-s_2)(s_4-s_3)}\frac{1}{z_2-z_{04}}\left(\frac{X(z_{04})}{X(z_2)}-1\right)\right\}, \tag{10b}$$

$$X(z)=\sqrt{z^2-a^2}. \tag{10c}$$

To obtain these, the condition of the single-valuedness of the displacement at infinity is also imposed. The branch of $X(z)$ is chosen such that $z/X(z)\approx 1$ at infinity. The last terms in equations (8*a*, *b*) express the field where a single crack exists under the applied uniform stresses at infinity. They can be obtained by the use of equations (6) (and also from the solution of an elliptical hole in an infinite plane, Savin, 1961):

$$\Phi_H(z_1)=-\frac{1}{2}\frac{s_2\sigma_{yy}^{\infty}+\sigma_{xy}^{\infty}}{s_1-s_2}\frac{z_1}{X(z_1)}, \tag{11a}$$

$$\Psi_H(z_2)=-\frac{1}{2}\frac{s_1\sigma_{yy}^{\infty}+\sigma_{xy}^{\infty}}{s_2-s_1}\frac{z_2}{X(z_2)}, \tag{11b}$$

where superposed ∞ denotes a quantity prescribed at infinity.

The boundary condition (7*b*) is now considered. Substituting equations (9), (10), and (11) into equations (2) and, after some manipulation, the following pair of singular integral equations for the dislocation density is obtained:

$$\sigma_{\eta\eta}=\int_0^l\frac{M_{11}B_x(\zeta)+M_{12}B_y(\zeta)}{t-\zeta}d\zeta+\int_0^l 2\mathrm{Re}\{(\cos\nu+s_1\sin\nu)^2\Phi_M(z_1)+(\cos\nu+s_2\sin\nu)^2\Psi_M(z_2)\}d\zeta+2\mathrm{Re}\{(\cos\nu+s_1\sin\nu)^2\Phi_H(z_1)+(\cos\nu+s_2\sin\nu)^2\Psi_H(z_2)\}=0, \tag{12a}$$

$$\sigma_{\xi\eta}=\int_0^l\frac{M_{21}B_x(\zeta)+M_{22}B_y(\zeta)}{t-\zeta}d\zeta+\int_0^l 2\mathrm{Re}[\{(1-s_1^2)\cos\nu\sin\nu-s_1\cos2\nu)\}\Phi_M(z_1)+\{(1-s_2^2)\cos\nu\sin\nu-s_2\cos2\nu)\}\Psi_M(z_2)]d\zeta+2\mathrm{Re}[\{(1-s_1^2)\cos\nu\sin\nu-s_1\cos2\nu)\}\Phi_H(z_1)+\{(1-s_2^2)\cos\nu\sin\nu-s_2\cos2\nu)\}\Psi_H(z_2)]=0, \tag{12b}$$

where

$$z_1=a+t(\cos\nu+s_1\sin\nu),\quad z_{01}=a+\zeta(\cos\nu+s_1\sin\nu),\quad z_2=a+t(\cos\nu+s_2\sin\nu),\quad z_{02}=a+\zeta(\cos\nu+s_2\sin\nu). \tag{12c-f}$$

The detailed expressions for the constants M_{ij} are given in Appendix A.

The pair of singular integral equations can be solved numerically with the condition that the stress has a singularity of less than one half at the knee of the kinked crack. Once the dislocation density functions are known, we can compute the stress intensity factors at the tip of the branched crack according to the same definitions as for the isotropic case:

$$K_I=\pi\sqrt{(2\pi/l)}\{M_{11}B_x(l)+M_{12}B_y(l)\},\quad K_{II}=\pi\sqrt{(2\pi/l)}\{M_{21}B_x(l)+M_{22}B_y(l)\}. \tag{13a,b}$$

With these stress intensity factors, the asymptotic field around the branched crack tip is completely determined:

$$\sigma_{\eta\eta}=\frac{1}{\sqrt{2\pi r}}\mathrm{Re}\left[\frac{1}{s_1'-s_2'}\left\{\frac{s_1'K_I+K_{II}}{\gamma_2}-\frac{s_2'K_I+K_{II}}{\gamma_1}\right\}\right],$$

$$\sigma_{\xi\xi}=\frac{1}{\sqrt{2\pi r}}\mathrm{Re}\left[\frac{1}{s_1'-s_2'}\left\{\frac{s_2'^2(s_1'K_I+K_{II})}{\gamma_2}-\frac{s_1'^2(s_2'K_I+K_{II})}{\gamma_1}\right\}\right],$$

$$\sigma_{\xi\eta}=\frac{1}{\sqrt{2\pi r}}\mathrm{Re}\left[\frac{1}{s_1'-s_2'}\left\{\frac{s_1'(s_2'K_I+K_{II})}{\gamma_1}-\frac{s_2'(s_1'K_I+K_{II})}{\gamma_2}\right\}\right], \tag{14a-c}$$

$$u_\xi=\sqrt{\frac{2r}{\pi}}\mathrm{Re}\left[\frac{1}{s_1'-s_2'}\{(s_1'K_I+K_{II})p_2'\gamma_2-(s_2'K_I+K_{II})p_1'\gamma_1\}\right],$$

$$u_\eta=\sqrt{\frac{2r}{\pi}}\mathrm{Re}\left[\frac{1}{s_1'-s_2'}\{(s_1'K_I+K_{II})q_2'\gamma_2-(s_2'K_I+K_{II})q_1'\gamma_1\}\right], \tag{14d,e}$$

$$\gamma_1=\sqrt{\cos\theta+s_1'\sin\theta},\quad \gamma_2=\sqrt{\cos\theta+s_2'\sin\theta}, \tag{14f,g}$$

$$r=\sqrt{\xi^2+\eta^2},\quad \theta=\tan^{-1}(\eta/\xi), \tag{14h,i}$$

$$s_1'=\frac{s_i\cos\nu-\sin\nu}{\cos\nu+s_i\sin\nu}. \tag{14j}$$

Quantities with prime are associated with the (ξ,η) coordinate system shown in Fig. 1. Equation (14*j*) is a transformation formula for the characteristic roots with respect to the rotation of the coordinate system. If necessary, the suffixes of s_i' must be renumbered such that the imaginary parts of s_1' and s_2' are positive. Following Irwin's method for the isotropic case, in terms of these asymptotic quantities, the energy release rate G associated with the growth of the branched crack is calculated:

$$G=-\frac{c_{11}}{2}\mathrm{Im}\{K_I^2(s_1'+s_2')\bar{s}_1'\bar{s}_2'+2K_IK_{II}\bar{s}_1'\bar{s}_2'-K_{II}^2(s_1'+s_2')\}; \tag{15}$$

e.g., Sih et al. (1965).

3 Results and Discussion

An interesting aspect of crack branching is the limiting case of an infinitesimally small branch length. All the results given here are for this particular limiting case. They are obtained by extrapolation. Although the foregoing formulation applies to anisotropic solids with six independent elastic constants, we limit the numerical results to orthotropic solids. The corresponding nonzero elastic constants in equations (1) then are c_{11}, c_{22}, c_{12}, and $c_{66}=2(c_{11}-c_{12})$, when proper coordinate axes are chosen. Even with this restricted anisotropy, the results are significantly different from those for the isotropic case.

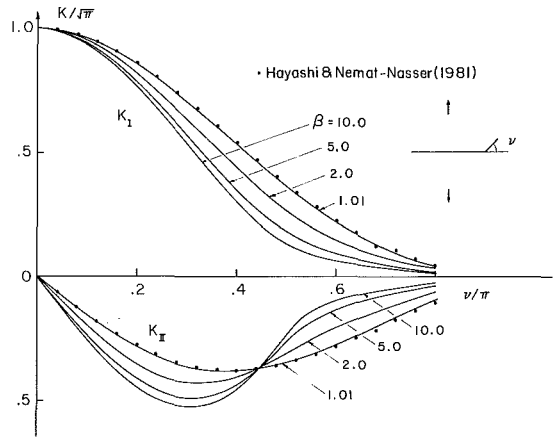


Fig. 2 Stress intensity factors at the tip of a branched crack

Downloaded 03 May 2010 to 171.66.16.31. Redistribution subject to ASME license or copyright; see http://www.asme.org/terms/Terms_Use.cfm

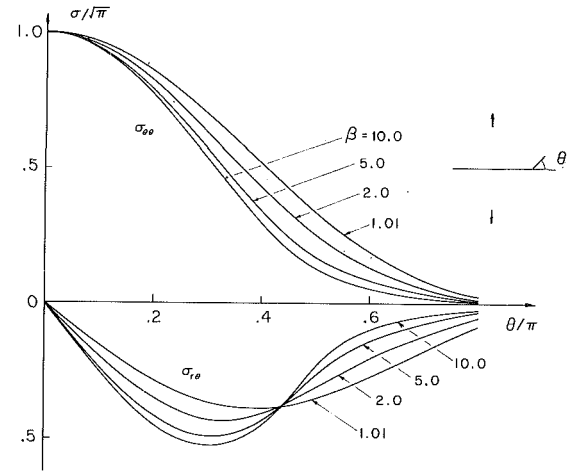


Fig. 3 Asymptotic stress field at the tip of the main crack before branching

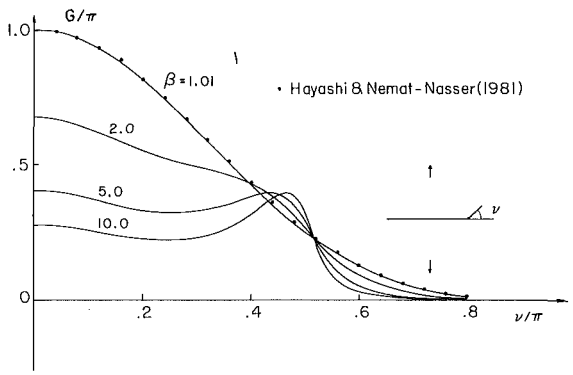


Fig. 4 Energy release rate for branched cracks

In what follows, c_{12}/c_{11} is fixed at -0.25. The degree of anisotropy is defined by $\beta = c_{11}/c_{22}$. The material is isotropic when $\beta = 1$. $\beta = 10 \sim 20$ for typical graphite epoxy composite materials. All quantities are nondimensionalized using the half-length of the main crack a and one of the stress components σ^{∞}_{yy} or σ^{∞}_{xy} prescribed at infinity. Figure 2 shows the resulting stress intensity factors for various degrees of anisotropy. In this case, the main crack lies parallel to the x-axis which is the weaker material axis. Uniform tension is applied at infinity perpendicular to the main crack. The present solution converges to the one by Hayashi and Nemat-Nasser (1981) as the degree of anisotropy becomes small. Figure 3 illustrates the variation of the dominant asymptotic stress field prior to crack branching. As for the isotropic case, the variations of the asymptotic stress components and that of the stress intensity factors are very similar regardless of the degree of anisotropy. However, the energy release rate G shows quite an unexpected variation with respect to the orientation of the branch; Fig. 4. When the material is isotropic or close to isotropic, the stress intensity factor K_I, the asymptotic hoop stress, and the energy release rate G all have similar angular variations. However, with a high degree of anisotropy, G does not follow the same pattern. When $\beta = 10.0$, G has a maximum at $\nu = 83.5$ deg. Even under symmetric loading and with a symmetric geometry, asymmetric crack growth may be expected to occur if the criterion of the maximum energy release rate governs fracturing. This is, however, not the case if one of the criteria: (1) maximum K_I, (2) zero K_{II}, or (3) maximum hoop stress is employed. We hasten to add, however, that the possible anisotropic variation in the material resistance, e.g., in critical value of the energy release rate, G_c, should also be considered in estimating the actual kink angle.

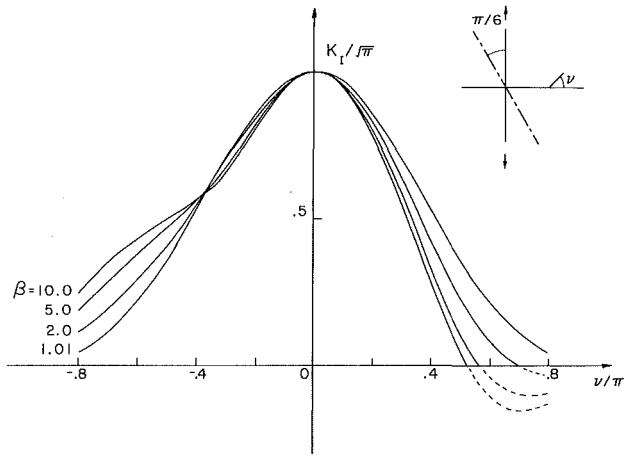


Fig. 5 Stress intensity factor K_I at the tip of a branched crack

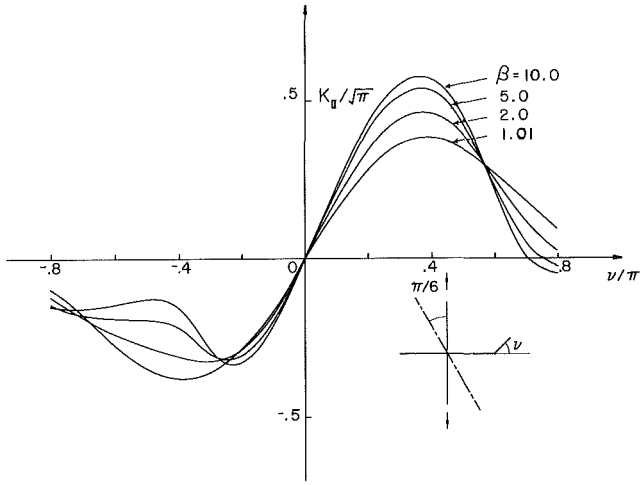


Fig. 6 Stress intensity factor K_{II} at the tip of a branched crack

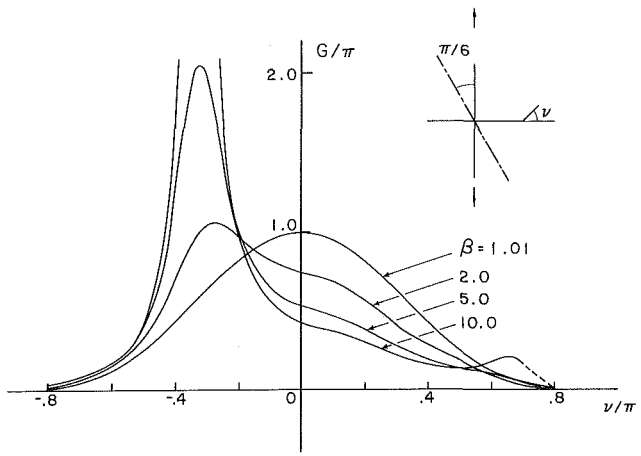


Fig. 7 Energy release rate for branched cracks

For the same symmetric loading condition, but with an asymmetric geometry, the results are given in Figs. 5, 6, and 7. As shown in these figures, the normal of the main crack makes an angle of $\pi/6$ with the stiffer axis. In the figures, the dotted part of the curves corresponds to the regime where K_I is negative. The ν_c that maximizes G is given in Table 1. The effects of anisotropy is more evident than the previous cases especially in the behavior of the energy release rate G. Table 1 suggests that G has a maximum at the orientation close to the

Downloaded 03 May 2010 to 171.66.16.31. Redistribution subject to ASME license or copyright; see http://www.asme.org/terms/Terms_Use.cfm

stiffer axis. This behavior of G is interesting because, in fiber-reinforced composites, cracks are often expected to grow parallel to fibers, or to the stiffer axis; e.g., Nemat-Nasser and Hori (1987).

In Figs. 8(*a*) and 9(*a*), the results are given for purely antisymmetric loads. The geometry of the main crack is the same as in the previous case. With this geometry and loading condition, the surface of the main crack remains traction-free. It can be seen that both stress intensity factors, K_I and K_{II}, are relatively less sensitive to the degree of anisotropy in this case. G, however, varies in a complicated manner with the degree of anisotropy (Fig. 10(*a*)). Table 2 shows the values of the branch angle ν_c which maximize K_I and G. The difference between the value that maximizes K_I and the one that maximizes G becomes larger with an increasing degree of anisotropy. Note that the maximum K_I occurs essentially at the orientation where K_{II} is zero. Hence, the two criteria, maximum K_I and zero K_{II}, yield essentially the same branch orientation.

Figures 8(*b*), 9(*b*), and 10(*b*) are the results when the reversed antisymmetric loading is applied to the same geometry of the main crack. ν_c is given in Table 2. Unlike the isotropic case, this loading leads to a boundary value problem different from the previous case. The surface of the main crack is closed and not traction free. Therefore, the functions Φ_M and Ψ_M of equations (9) and also Φ_H and Ψ_H of equations (10) must be recalculated for this particular case, as given in Appendix B. Here we have assumed that the surface of the main crack is frictionless. As expected, strong anisotropy yields results appreciably different from those of the previous case. Although not given here, the angular variations of the stress intensity factors and the asymptotic stress field are fairly similar regardless of anisotropy, whether the main crack is open or closed. It should be added that also in the cases shown in Figs. 8, 9, and 10, the branch angles ν_c that maximize G are close to the stiffer axis with strong anisotropy.

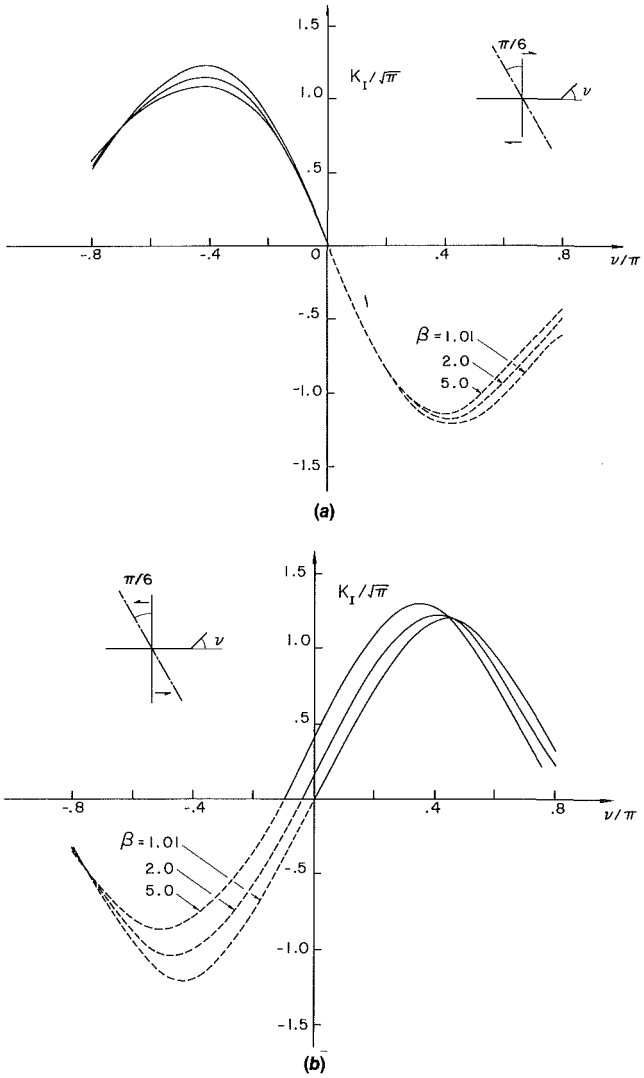


Fig. 8 Stress intensity factor K_I at the tip of a branched crack under pure shear loading: (*a*) main crack open and (*b*) main crack closed

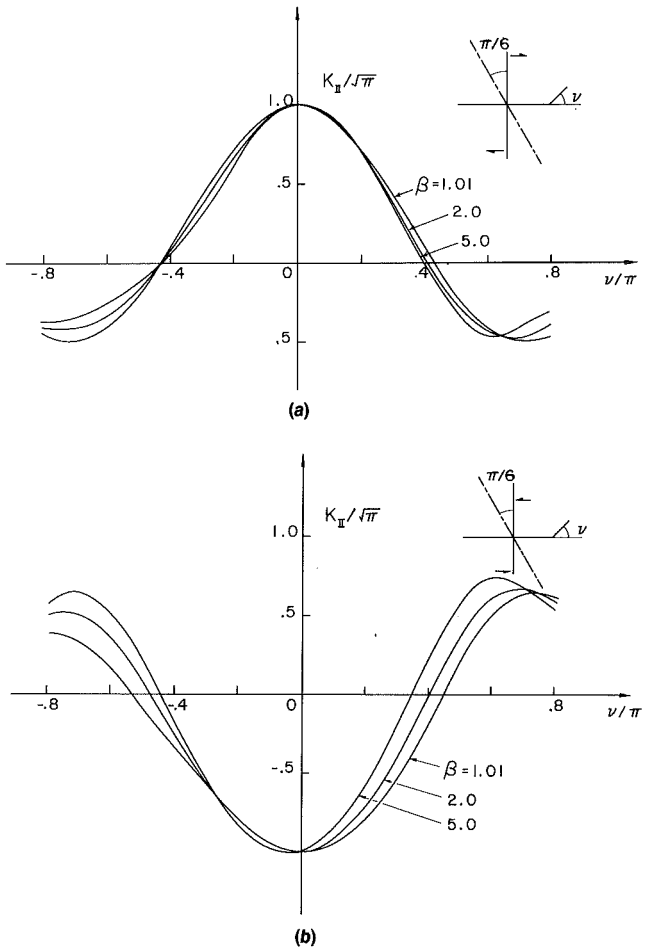


Fig. 9 Stress intensity factor K_{II} at the tip of a branched crack under pure shear loading: (*a*) main crack open and (*b*) main crack closed

Table 1 Peak values of G

β	ν_c/π	G/π
1.01	0.003	0.996
2.00	−0.273	1.059
5.00	−0.320	2.074
10.00	−0.328	3.671

Table 2 Peak values of K_I and G

Main Crack	Open				Closed			
β	ν_c/π	$K_I/\sqrt{\pi}$	ν_c/π	G/π	ν_c/π	$K_I/\sqrt{\pi}$	ν_c/π	G/π
1.01	−0.424	1.23	−0.414	1.52	0.442	1.20	0.400	1.46
2.00	−0.421	1.15	−0.343	2.48	0.404	1.23	0.585	1.69
5.00	−0.427	1.09	−0.337	5.23	0.352	1.30	0.636	2.36

Downloaded 03 May 2010 to 171.66.16.31. Redistribution subject to ASME license or copyright; see http://www.asme.org/terms/Terms_Use.cfm

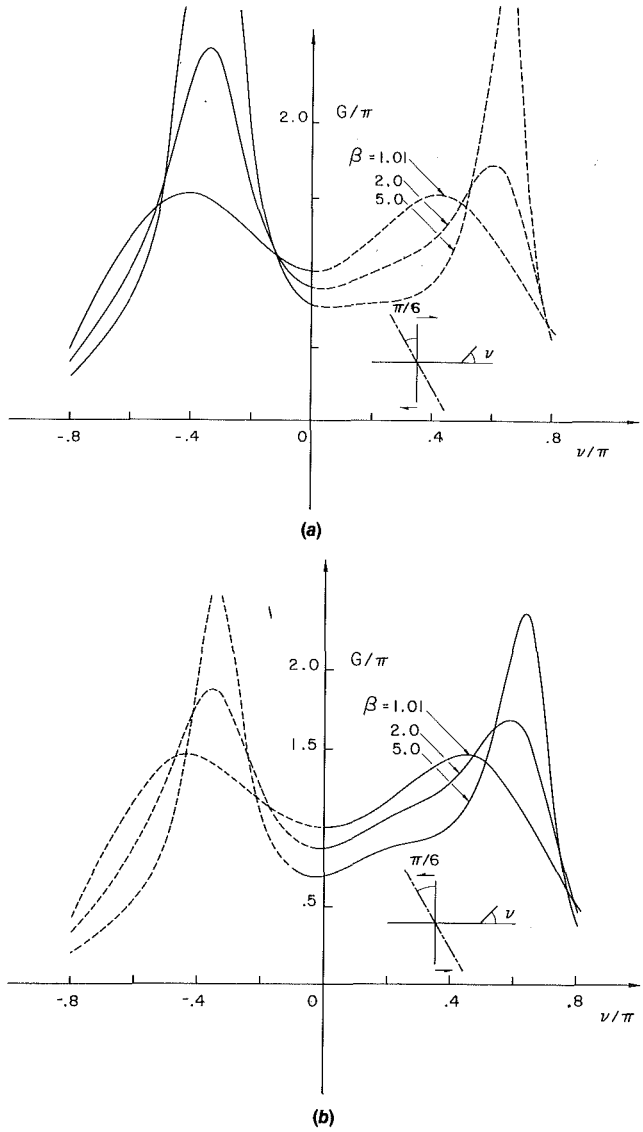


Fig. 10 Energy release rate for a branched crack under pure shear loading: (a) main crack open and (b) main crack closed

These results show the complex features of cracks in anisotropic solids. With regard to fracture under general loading conditions, all the criteria: (1) maximum K_I, (2) zero K_{II}, (3) maximum hoop stress, and (4) maximum energy release rate, lead to similar results when the material is isotropic. This is not always the case in the presence of anisotropy. Actually, the angular variation of the energy release rate cannot be easily predicted intuitively based on the field quantities prior to branching. It may be added, however, that the fields after branching can be *practically* predicted on the basis of the similarity in the variations of the stress intensity factor and the asymptotic stress field.

One of the reasons for these complexities may stem from the definition of the stress intensity factors, which is the same as for the isotropic case. Stress intensity factors should be considered in two different ways. They are the mathematical parameters which determine the asymptotic field around a crack tip. At the same time they are, to a certain extent, also the physical parameters which connect the asymptotic field around the crack tip with engineering parameters such as the fracture toughness, and therefore should have good correspondence to our observation and intuition. For example, for symmetric loading, often only K_I is used independently of anisotropy. The corresponding asymptotic stress field, however, is not always symmetric for anisotropic solids, while it is symmetric for isotropic ones. As far as general anisotropic solids are concerned, the current definition of stress intensity factors does not seem closely related to the material resistance to fracturing which is also expected to be an anisotropic quantity. More adequate fracture parameters need to be defined for a better understanding of anisotropic fracture.

References

Bilby, B. A., and Cardew, G. E., 1975, "The crack with a kinked tip," *Int. J. Fract.*, Vol. 11, pp. 708–712.

Erdogan, F., and Sih, G. C., 1963, "On the crack extension in plates under plane loading and transverse shear," *J. Basic Engrg.*, Vol. 85, pp. 519–527.

Eshelby, J. D., Read, W. T., and Shockley, W., 1953, "Anisotropic elasticity with applications to dislocation theory," *Acta Metall.*, Vol. 1, pp. 251–259.

Green, A. E., and Zerna, W., 1954, *Theoretical Elasticity*, Clarendon Press, Oxford.

Hayashi, K., and Nemat-Nasser, S., 1981, "Energy-Release Rate and Crack Kinking Under Combined Loading," ASME JOURNAL OF APPLIED MECHANICS, Vol. 48, pp. 520–524.

Hussain, M. A., Pu, S. L., and Underwood, J., 1974, "Strain energy release rate for a crack under combined mode I and mode II," ASTM STP560, pp. 2–28.

Karihaloo, B. L., Keer, L. M., and Nemat-Nasser, S., 1980, "Crack kinking under nonsymmetric loading," *Engrg. Frac. Mech.*, Vol. 13, pp. 879–888.

Lekhnitskii, S. G., 1963, *Theory of elasticity of an anisotropic elastic body*, Holden-Day, San Francisco, Calif.

Lo, K. K., 1978, "Analysis of Branched Cracks," ASME JOURNAL OF APPLIED MECHANICS, Vol. 45, pp. 797–802.

Mikhlin, S. G., 1936, "Two-dimensional deformation in anisotropic media," *Trudy seismol. inst. Adad. Nauk. SSSR.*, Vol. 76.

Muskhelishvili, N. I., 1953, *Some basic problems of the mathematical theory of elasticity*, Noordhoff, Groningen.

Nemat-Nasser, S., and Hori, M., 1987, "Toughening by partial or full bridging of cracks in ceramics and fiber reinforced composites," *Mechanics of Materials*, Vol. 6, pp. 245–269.

Palaniswamy, K., and Knauss, W. G., 1978, "On the problem of crack extension in brittle solids under general loading," *Mechanics Today*, S. Nemat-Nasser, ed., Pergamon Press, Oxford.

Savin, G. N., 1961, *Stress concentration around holes*, Pergamon Press, Oxford.

Sih, G. C., Paris, P. C., and Irwin, G. R., 1965, "On cracks in rectilinearly anisotropic bodies," *Int. J. Fract. Mech.*, Vol. 1, pp. 189–203.

Sih, G. C., 1973, "A special theory of crack propagation," *Mechanics of Fracture*, G. C. Sih, ed., Noordhoff, Leyden.

Sih, G. C., Chen, E. P., Huang, S. L., and McQuillen, E. J., 1975, "Material characterization on the fracture of filament-reinforced composites," *J. Composite Materials*, Vol. 9, pp. 167–186.

Stroh, A. N., 1958, "Dislocations and cracks in anisotropic elasticity," *Phil. Mag.*, Ser. 8, No. 3, pp. 625–646.

Tsai, S. W., and Wu, E. M., 1971, "A general theory of strength for anisotropic materials," *J. Composite Materials*, Vol. 5, pp. 58–81.

Willis, J. R., 1966, "Hertzian contact of anisotropic bodies," *J. Mech. Phys. Solids*, Vol. 14, pp. 163–176.

Wu, C. H., 1978, "Fracture under combined loads by maximum-energy-release-rate criterion," ASME JOURNAL OF APPLIED MECHANICS, Vol. 46, pp. 553–558.

APPENDIX A

$$\alpha = -\frac{s_1 s_2 - s_3 s_4 \pm \sqrt{\Delta}}{s_1 s_2 (s_3 + s_4) - s_3 s_4 (s_1 + s_2)}, \tag{A1}$$

where

$$\Delta = (s_1 - s_3)(s_1 - s_4)(s_2 - s_3)(s_2 - s_4)$$
$$= -(s_1 - \bar{s}_1)(s_2 - \bar{s}_2)(s_1 - \bar{s}_2)(s_2 - \bar{s}_1) > 0. \tag{A2}$$

Because s_3 and s_4 are, by definition, the complex conjugates of s_1 and s_2, respectively, α is not a real number.

$$\lambda = \frac{s_1 s_2 (s_3 + s_4) - s_3 s_4 (s_1 + s_2) - s_2 (s_1 s_2 - s_3 s_4 \pm \sqrt{\Delta})}{s_1 s_2 (s_3 + s_4) - s_3 s_4 (s_1 + s_2) - s_1 (s_1 s_2 - s_3 s_4 \pm \sqrt{\Delta})}, \tag{A3}$$

$$\mu = \frac{s_1 s_2 (s_3 + s_4) - s_3 s_4 (s_1 + s_2) - s_4 (s_1 s_2 - s_3 s_4 \pm \sqrt{\Delta})}{s_1 s_2 (s_3 + s_4) - s_3 s_4 (s_1 + s_2) - s_3 (s_1 s_2 - s_3 s_4 \pm \sqrt{\Delta})}. \tag{A4}$$

The choice of the sign + or − must be consistent in all of the previous definitions. Since $\Delta > 0$, λ cannot be equal to μ.

Downloaded 03 May 2010 to 171.66.16.31. Redistribution subject to ASME license or copyright; see http://www.asme.org/terms/Terms_Use.cfm

M_{ij} in equations (12) are given as follows:

$$M_{11}=2\mathrm{Re}\left[\frac{1}{2\pi i}\frac{1}{c_{11}}\left\{\frac{s_1}{(s_1-s_2)(s_1-s_3)(s_1-s_4)}(\cos\nu+s_1\sin\nu)+\frac{s_2}{(s_2-s_1)(s_2-s_3)(s_2-s_4)}(\cos\nu+s_2\sin\nu)\right\}\right], \quad (A5a)$$

$$M_{12}=-2\mathrm{Re}\left[\frac{1}{2\pi i}\frac{1}{c_{11}}\left\{\frac{1}{(s_1-s_2)(s_1-s_3)(s_1-s_4)}(\cos\nu+s_1\sin\nu)+\frac{1}{(s_2-s_1)(s_2-s_3)(s_2-s_4)}(\cos\nu+s_2\sin\nu)\right\}\right], \quad (A5b)$$

$$M_{21}=2\mathrm{Re}\left[\frac{1}{2\pi i}\frac{1}{c_{11}}\left\{\frac{s_1}{(s_1-s_2)(s_1-s_3)(s_1-s_4)}\frac{(1-s_1^2)\cos\nu\sin\nu-s_1\cos 2\nu}{\cos\nu+s_1\sin\nu}+\frac{s_2}{(s_2-s_1)(s_2-s_3)(s_2-s_4)}\frac{(1-s_2^2)\cos\nu\sin\nu-s_2\cos 2\nu}{\cos\nu+s_2\sin\nu}\right\}\right], \quad (A5c)$$

$$M_{22}=-2\mathrm{Re}\left[\frac{1}{2\pi i}\frac{1}{c_{11}}\left\{\frac{1}{(s_1-s_2)(s_1-s_3)(s_1-s_4)}\frac{(1-s_1^2)\cos\nu\sin\nu-s_1\cos 2\nu}{\cos\nu+s_1\sin\nu}+\frac{1}{(s_2-s_1)(s_2-s_3)(s_2-s_4)}\frac{(1-s_2^2)\cos\nu\sin\nu-s_2\cos 2\nu}{\cos\nu+s_2\sin\nu}\right\}\right]. \quad (A5d)$$

APPENDIX B

When the main crack is closed, but frictionless sliding is permitted, $\Phi_M(z_1)$ and $\Psi_M(z_2)$ in equations (10) and $\Phi_H(z_1)$ and $\Psi_H(z_2)$ in equations (11) are given by

$$\Phi_M(z_1)=-\frac{1}{4\pi i}\frac{1}{c_{11}}\frac{s_1}{s_1-s_2}\frac{(s_2-s_3)(s_2-s_4)}{s_1s_3(s_2-s_4)+s_2s_4(s_1-s_3)}\times\left\{s_1\frac{s_1B_x-B_y}{(s_1-s_2)(s_1-s_3)(s_1-s_4)}\frac{1}{z_1-z_{01}}\left(\frac{X(z_{01})}{X(z_1)}-1\right)-s_3\frac{s_3B_x-B_y}{(s_3-s_4)(s_3-s_1)(s_3-s_2)}\frac{1}{z_1-z_{03}}\left(\frac{X(z_{03})}{X(z_1)}-1\right)+s_2\frac{s_2B_x-B_y}{(s_2-s_1)(s_2-s_3)(s_2-s_4)}\frac{1}{z_1-z_{02}}\left(\frac{X(z_{02})}{X(z_1)}-1\right)-s_4\frac{s_4B_x-B_y}{(s_4-s_3)(s_4-s_1)(s_4-s_2)}\frac{1}{z_1-z_{04}}\left(\frac{X(z_{04})}{X(z_1)}-1\right)\right\}, \quad (B1a)$$

$$\Psi_M(z_2)=-\frac{1}{4\pi i}\frac{1}{c_{11}}\frac{s_2}{s_2-s_1}\frac{(s_1-s_3)(s_1-s_4)}{s_1s_3(s_2-s_4)+s_2s_4(s_1-s_3)}\times\left\{s_1\frac{s_1B_x-B_y}{(s_1-s_2)(s_1-s_3)(s_1-s_4)}\frac{1}{z_2-z_{01}}\left(\frac{X(z_{01})}{X(z_2)}-1\right)-s_3\frac{s_3B_x-B_y}{(s_3-s_4)(s_3-s_1)(s_3-s_2)}\frac{1}{z_2-z_{03}}\left(\frac{X(z_{03})}{X(z_2)}-1\right)+s_2\frac{s_2B_x-B_y}{(s_2-s_1)(s_2-s_3)(s_2-s_4)}\frac{1}{z_2-z_{02}}\left(\frac{X(z_{02})}{X(z_2)}-1\right)-s_4\frac{s_4B_x-B_y}{(s_4-s_3)(s_4-s_1)(s_4-s_2)}\frac{1}{z_2-z_{04}}\left(\frac{X(z_{04})}{X(z_2)}-1\right)\right\}, \quad (B1b)$$

$$\Phi_H(z_1)=\frac{\sigma_{xy}^{\infty}}{2}\frac{s_1}{s_1-s_2}\frac{(s_2-s_3)(s_2-s_4)}{s_1s_3(s_2-s_4)+s_2s_4(s_1-s_3)}\frac{z_1}{X(z_1)}, \quad (B1c)$$

$$\Psi_H(z_2)=\frac{\sigma_{xy}^{\infty}}{2}\frac{s_2}{s_2-s_1}\frac{(s_1-s_3)(s_1-s_4)}{s_1s_3(s_2-s_4)+s_2s_4(s_1-s_3)}\frac{z_2}{X(z_2)}. \quad (B1d)$$

Downloaded 03 May 2010 to 171.66.16.31. Redistribution subject to ASME license or copyright; see http://www.asme.org/terms/Terms_Use.cfm

K. Natarajan[1]
Department of Electrical Engineering,
Lakehead University,
Thunder Bay, ON, Canada

G. A. Dumont
Pulp and Paper Research Institute of
Canada and Department of Electrical
Engineering,
University of British Columbia,
Pulp and Paper Centre,
Vancouver, BC V6T 1W5, Canada

M. S. Davies
Department of Electrical Engineering,
University of British Columbia,
Vancouver, BC, Canada

On the Approximation of a Deflection Curve by Force Actuators With Variable Spacing

In this paper we discuss a suboptimal method of approximating a desired deflection curve of a simple beam by a given number of force actuators. The spacing between the actuators is allowed to vary as a function of the deflection curve. The method is applied to an example of approximation of a deflection curve of the slice lip on a paper machine headbox for the control of the basis weight profile of paper. The approximation error with variable spacing is compared with that obtained when the spacing is not varied (uniformly-spaced actuators). Significant reduction in error is observed.

1 Introduction

The problem discussed in this paper arose out of a study on the manipulation of the slice lip of a headbox on a paper machine for the cross-directional (CD) control of basis weight (Natarajan et al., 1988). Basis weight of paper is its weight per unit area. The basis weight profile is controlled as paper is being made by a set of N force actuators positioned on the lip (currently at a fixed uniform spacing). Vertical movement of the slice lip, by developing adequate force in the actuators, causes a change in the opening between the lip and the apron of the headbox causing a change in basis weight profile. As shown experimentally by Balakrishnan and McFarlin (1985), a simple Euler-Bernoulli beam model adequately predicts the actual lip deflection curve. Because of the small amplitude of the deflections and the small section moduli of the lip, the shearing deformation due to the large number of actuators seems to have a negligible effect on the deflection curve. The reduction algorithm is therefore worked out here for such a model.

Basis weight is measured at N_m equispaced points along the width of the paper by a scanning sensor. From the measurements, the deflections at the corresponding N_m points on the lip can be specified. If there were N_m actuators located on the lip, then the desired deflections can be exactly achieved. The continuous deflection curve of the lip, achieved when N_m actuators are available, is termed the desired deflection curve. In Section 2, we obtain this curve and the corresponding bending moments on the lip at the N_m locations by cubic B-splines.

The number of actuators, N, is usually less than the number of measurement points, N_m. With N actuators, the deflection of the lip can be made to match the desired curve at N locations on the lip under the actuators. At other points there will be an error. The reduction of this error, when the spacing between the N actuators is allowed to vary as a function of the desired deflection curve, is the main theme of the paper. The method developed for this purpose is detailed in Section 3. The overall approach is to assume that there are N_m actuators to begin with and iteratively reduce at each stage by one actuator to the desired number N. The reduction at each stage is done ensuring minimal error of approximation.

In Section 4 of the paper we apply this method to an example and compare the improvements achieved over uniform spacing. The contributions of this paper are the use of cubic B-splines to solve for the deflection curve, and the actuator reduction algorithm.

2 B-Spline Method of Computing Deflection Curve and Bending Moment

As mentioned in the previous section, our objective is not to derive a new lip model, but to study the approximation of the desired deflection curve by nonuniformly-spaced actuators. Because actual data has shown the Euler-Bernoulli beam model of the lip to be satisfactory (Balakrishnan and McFarlin, 1985), it shall be used in this work. The slice lip is modeled as a simple beam with uniform cross-section. The forces acting on the lip are assumed to act in a plane containing the neutral axis and perpendicular to the breadth of the lip. With the sign conventions, notations, and frame of reference of Popov (1978), the deflection of the lip is assumed to be governed by equation (1).

$$EI\frac{d^2y}{dx^2} = M(x) \tag{1}$$

The actuators are capable of only applying force (no moment). It is assumed that the lip is always supported by an ac-

[1]Previously with the Pulp and Paper Centre, University of British Columbia, Vancouver, BC, Canada.

Contributed by the Applied Mechanics Division of THE AMERICAN SOCIETY OF MECHANICAL ENGINEERS for publication in the JOURNAL OF APPLIED MECHANICS.

Discussion on this paper should be addressed to the Editorial Department, ASME, United Engineering Center, 345 East 47th Street, New York, N.Y. 10017, and will be accepted until two months after final publication of the paper itself in the JOURNAL OF APPLIED MECHANICS. Manuscript received by the ASME Applied Mechanics Division, September 8, 1988; final revision, January 30, 1989.

Copyright © 1989 by ASME

Downloaded 03 May 2010 to 171.66.16.31. Redistribution subject to ASME license or copyright; see http://www.asme.org/terms/Terms_Use.cfm

tuator at either end. This assumption can be relaxed. The assumption of end support and the equilibrium of the lip imply that (L is the length of the lip)

$$M(0)=M(L)=0. \tag{2}$$

If (x_i, M_i), $i=0,1, \ldots ,(N_m-1)$ are N_m values of position of the actuator and corresponding bending moment with the x_i such that $0=x_0<x_1< \ldots <x_{(N_m-1)}=L$, then the deflection of the lip y at a point x on the lip can be expressed by

$$y(x)=\sum_{k=1}^{N_m-1} V_k\langle x-x_{k-1}\rangle^3-\sum_{k=1}^{N_m-1} V_k\langle x-x_k\rangle^3+C_1x+C_2 \tag{3}$$

where $\langle\theta\rangle$ is the singularity function of the argument θ and evaluates to θ if $\theta>0$, else to 0.

V_k is the negative of the shear force (with the sign conventions of Popov (1978)) in the section of the beam between x_{k-1} and x_k and is given by (4). The shear force is a piecewise constant curve.

$$V_k=(M_k-M_{k-1})/\{6EI(x_k-x_{k-1})\} \tag{4}$$

C_1, C_2 are constants of the homogeneous solution of (1) and can be determined using (3) and the values of $y(0)$ and $y(L)$.

The deflection curve expressed in (3) is cubic in x. A cubic curve passing through N_m points and satisfying (2) can be (uniquely) expressed as a series in N_m+2 cubic B-splines (De Boor, 1978) by (5),

$$y(x)=\sum_{i=-1}^{N_m} \alpha_i B_i(x-ih), \tag{5}$$

where $y(x)$ is the deflection at position $x(0\le x\le L)$ and $B_i(x-ih)$ denotes the cubic B-spline with knots at intervals of h and centered at $x=ih$. α_i is the real coefficient scaling the corresponding cubic B-spline.

From the uniqueness of the solution of a differential equation satisfying boundary conditions, the two cubic curves obtained from (3), (5), passing through the specified deflections at the N_m points, are identical. The method for determining the coefficients α is available, in general, in De Boor (1978), and for the particular problem being considered in Natarajan et al. (1988).

The bending moments at the N_m actuators at intervals of h are given in (6).

$$M_i=0.25EIh(\alpha_{i-1}-2\alpha_i+\alpha_{i+1}) \quad (i=0,1, \ldots ,N_m-1). \tag{6}$$

From the moments, the forces in the actuators are readily computed. This method of computing requires an operation count linear in N_m in comparison to the superposition method (Popov, 1978) used by Balakrishnan and McFarlin (1985) which requires a count quadratic in N_m. Details of the B-spline method and its operations count are available in Natarajan et al. (1988).

3 Reduction Algorithm

It is assumed that the stress in the slice lip and the actuators is within allowable stress limits. The principle of reduction is first discussed and thereafter an iterative algorithm for progressively reducing the number of actuators by one is described.

3.1 Principle of Reduction. Consider a $zone_i$ comprised of four consecutive values of actuator position and corresponding bending moment, vis. (x_i,M_i), (x_{i+1},M_{i+1}), (x_{i+2},M_{i+2}), (x_{i+3},M_{i+3}). We seek to replace this $zone_i$ by three values of actuator position and corresponding bending moment (x_i,M_i), (x',M'), (x_{i+3},M_{i+3}).

In this section, let $y(x)$ denote the particular solution of (1) (i.e., in (3), C_1, $C_2=0$) associated with the original $zone_i$ (four actuators). Let $y'(x)$ denote the particular solution with the reduced $zone_i$ (three actuators). From (3) and (4), we observe that the deflections $y(x)$ and $y'(x)$ match $\forall x$ such that $0\le x\le x_i$. We now demand, as the condition of reduction, that $y(x)$ and $y'(x)$ match $\forall x$ such that $x_{i+3}\le x\le L$. Thus, after a successful reduction, $y(x)$ and $y'(x)$ differ only in the region $x_i<x<x_{i+3}$, i.e., within the $zone_i$. The remainder of the lip is not disturbed.

If this criterion is satisfied, then the two particular solutions match each other at $x=0$ and $x=L$. It follows then that the homogenous solution constants to be added to the particular solutions, to obtain the actual deflection curves, will be the same for both deflections. These constants play no part in the reduction algorithm and are therefore not considered further in this section.

Imposing the condition of reduction on (3) and using (4), we require (7) to hold $\forall x\ge x_{i+3}$ (with the common factor $(1/6EI)$ omitted on both sides).

$$\begin{aligned}&\sum_{k=i}^{i+2}\left(\frac{M_{k+1}-M_k}{x_{k+1}-x_k}\right)(x-x_k)^3\\&-\sum_{k=i}^{i+2}\left(\frac{M_{k+1}-M_k}{x_{k+1}-x_k}\right)(x-x_{k+1})^3\\&=\left(\frac{M'-M_i}{x'-x_i}\right)\{(x-x_i)^3-(x-x')^3\}\\&+\left(\frac{M_{i+3}-M'}{x_{i+3}-x'}\right)\{(x-x')^3-(x-x_{i+3})^3\}\end{aligned} \tag{7}$$

equation (7) can hold $\forall x\ge x_{i+3}$ if the corresponding coefficients of all the powers of x are equal on both sides. Expanding both sides of (7) and collecting coefficients of the powers of x, we find that the coefficients of x^3 and x^2 are the same on both sides. Equating the coefficients of x^1 and x^0 and simplifying we obtain x' and M' in terms of γ and δ, the coefficients of x^1 and x^0 on the left-hand side of (7).

$$x'=\frac{(M_{i+3}-M_i)x_{i+3}x_i-\gamma(x_{i+3}+x_i)+\delta}{\gamma-(M_{i+3}-M_i)(x_{i+3}+x_i)} \tag{8}$$

$$M'=\frac{\gamma x'+M_{i+3}x_{i+3}^2-M_ix_i^2-\delta}{x_{i+3}^2-x_i^2} \tag{9}$$

A solution for x' fails to exist if

$$\gamma=(M_{i+3}-M_i)(x_{i+3}+x_i). \tag{10}$$

Using the expression for γ, a solution does not exist if

$$\frac{M_{i+3}-M_{i+1}}{x_{i+3}-x_{i+1}}=\frac{M_{i+2}-M_i}{x_{i+2}-x_i}. \tag{11}$$

When the four actuator points being considered are in a straight line in the (x,M) plane, then (11) is satisfied. When this occurs it implies that $zone_i$ has just two actuators at (x_i,M_i) and (x_{i+3},M_{i+3}), and therefore can be so reduced. We shall assume hereafter that each *zone* is not colinear. In all other cases when the solution does not exist, we deem $zone_i$ irreducible. Let h_m denote the smallest allowable spacing between any pair of actuators, then a solution for x' in $zone_i$ is acceptable if $x_i+h_m\le x'\le x_{i+3}-h_m$. If the solution does not satisfy this inequality, we deem $zone_i$ irreducible.

3.2 Iterative Algorithm. The algorithm for reduction concentrates on reducible *zones*. We consider as candidates for reduction reducible *zones* in which the deflections before reduction (with 4 actuators) and deflections after reduction (with 3 actuators) match well. Assuming we are at a stage with p actuators on the slice lip, at the end of the iteration, we reduce by one actuator to $(p-1)$ actuators. In each iteration, we find the $zone_k$ in which z of (12) lies and replace the four

Downloaded 03 May 2010 to 171.66.16.31. Redistribution subject to ASME license or copyright; see http://www.asme.org/terms/Terms_Use.cfm

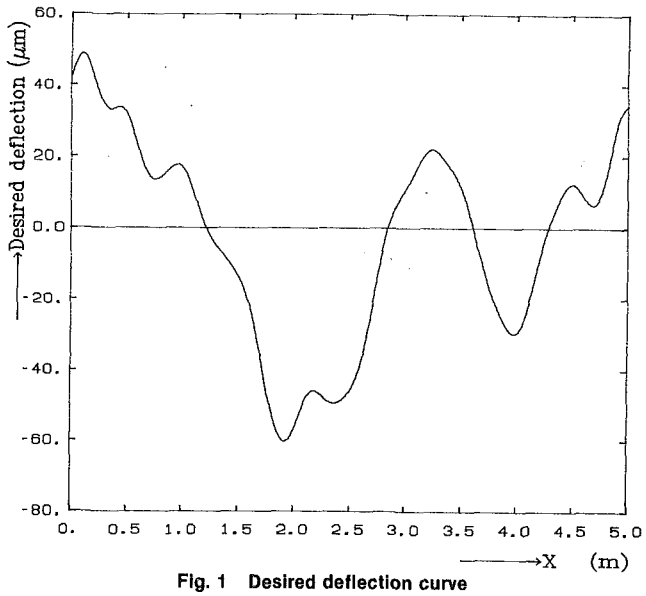


Fig. 1 Desired deflection curve

actuators in $zone_k$ by three using (8), (9), effecting the overall reduction from p to $p-1$ actuators. We repeat the procedure until the desired number of actuators is reached.

$$z = \min_{i\in[0,1,\ldots,p-4]} \left\{ \max_{x\in \text{ reducible } zone_i} |y(x)-y'(x)| \right\}. \tag{12}$$

In (12), $y(x)$ refers to the deflection curve (particular solution) with p actuators. In numerical simulation of the algorithm, it is found that the results of reduction are almost the same when $y(x)$ referred to the deflection curve with N_m actuators instead of the curve with p actuators. Also, the computation of the maximum referred to in (12) is achieved using a finite number (q) of equally-spaced points in each *zone* and choosing the maximum of the error $|y(x)-y'(x)|$ at these points. In the simulations the value of q is 10. An upper bound on the number of operations (all operations being considered equivalent) for this algorithm using q points, starting with N_m actuators and reducing to N actuators, is given by $35q(N_m-N)(N_m+N+1)$.

Pathologies where the algorithm fails to reduce by one actuator can arise when every *zone* is irreducible. In our experience with this algorithm applied to slice lip deflection curves, such cases do not seem to occur. If they occur, then it is possible to evolve formulae which allow graceful degradation in the error between $y(x)$ and $y'(x)$ outside the *zones*. Since this case has not yet been met, we have not developed such formulae.

4 Example

From actual basis weight measurements a filtered CD profile was obtained at 58 points across a 5-m width. From the profile deviation, the deflection of the lip at the corresponding 58 points is obtained using a simple proportionality constant (1 mil change at a point on the lip produces 0.25 lb/1000 sq ft change in basis weight). A deflection curve passing through the obtained points creates stress in the lip in excess of the allowable limit. The curve is therefore low pass-filtered to produce a deflection curve which keeps the stress within allowable limit. This filtered curve is chosen as the desired deflection curve and is shown in Fig. 1. The spacing between the measurement points is assumed to be the smallest spacing between two actuators (h_m). Using the cubic B-spline method of Section 2, the bending moments with N_m (58) uniformly-spaced actuators are computed. The number of actuators available on the lip is assumed to be $N=29$ so that a 2:1 reduction is needed. The reduction algorithm is applied to determine the spacing of the N actuators. The error between the resultant deflection curve and the desired curve is summarized in Table 1. In Table 1, $\|e\|_\infty$ denotes the maximum absolute value of the error and $\|e\|_2$ denotes the square root of the integral over the length of the lip of the square of the error between the desired and approximate deflection curves. The results are compared with that obtained by minimizing the integral over the length of the lip of the square of the approximation error when the N actuators are uniformly spaced on the lip. Details of the optimal method for the case of uniform spacing subject to the integral squared error criterion are available in Natarajan et al. (1988) and will be a subject matter of another communication. From Table 1, a 3:1 improvement is seen by the use of nonuniform spacing over uniform spacing.

Table 1 Summary of errors between desired and approximate deflections

Type of Spacing	$\|e\|_\infty$ $\times 10^{-6}$	factor of improvement in $\|e\|_\infty$	$\|e\|_2$ $\times 10^{-6}$	factor of improvement in $\|e\|_2$
Non-uniform	1.5961		0.6730	
Uniform	3.7105	2.3247	2.2082	3.2811

5 Conclusion

In this paper, we considered the role of spacing of force actuators on a beam to approximate a desired deflection curve. From the example worked out in this paper, it is seen that the suboptimal algorithm developed here gives a greatly reduced approximation error in comparison with an optimal algorithm for uniformly-spaced actuators. Considerable practical problems remain to be tackled to translate the results to an industrial situation. A complete redesign of the lip and actuators (and the method of coupling them) may be needed. Also, the spreading of the material on the web due to the water wave effect (Wahren, 1986) has not been taken into account in this work. However, the preliminary results reported in this paper show the value of the idea and encourage further consideration to realise the results in an industrial situation.

A topic of further research would be to develop models of the lip to account for non-negligible shearing deformations due to closely-spaced actuators on the lip and for the water wave effect causing the spreading of material on the web. The encouraging results of this paper could then be tested on this more complex model.

References

Balakrishnan R., and McFarlin, D., 1985, "The Application of a Model of the Slice Lip as an Elastic Beam for Weight Profile Control," TAPPI Process Control Symposium, pp. 105–109.

De Boor, C., 1978, *A Practical Guide to Splines*, Springer Verlag, New York.

Natarajan, K., Dumont, G. A., and Davies, M. S., 1988, "On the Manipulation of the Slice Lip for the Control of Basis Weight," PGRL Report 409. Pulp and Paper Research Institute of Canada, St. John's Boulevard, Pointe Claire, P.Q., Canada, H9R 3J9.

Popov, E. P., 1978, Introduction to Mechanics of Solids, Prentice-Hall, Englewood Cliffs, New Jersey.

Wahren, D., 1986, "Recent Highlights in Paper Technology," *TAPPI Journal*, Vol. 69, No. 3, pp. 36-45.

Downloaded 03 May 2010 to 171.66.16.31. Redistribution subject to ASME license or copyright; see http://www.asme.org/terms/Terms_Use.cfm

The Anomalous Response of an Elastic-Plastic Structural Model to Impulsive Loading

T. X. Yu
Professor of Mechanics.

Y. Xu
Research Student.

Department of Mechanics,
Peking University,
Beijing 100871 China

To simulate the response of a pin-ended elastic-plastic beam, a nonlinear structural model, i.e., a double-tier-spring model is analyzed to follow its deformation process after it is subjected to impulsive loading. After examining the first integral of the equation of motion, in the final elastic vibration, combined with other conditions, a region in the parameter's map is found in which the anomalous behavior (i.e., a negative-negative vibration) appears. This model is proved to be equivalent to the Shanley-type model adopted in previous analyses, but the present approach provides new results in a more complete way.

Introduction

In studying the effect of pulse shape upon the dynamic response of elastic-plastic beams, Symonds and Yu (1985) surprisingly explored a counterintuitive behavior in a particular example of short pulse loading on a pin-ended beam, that is, the permanent deflection predicted by a numerical solution using finite element code ABAQUS is in the direction opposite to that of load. Further calculations by other established numerical codes have also confirmed the existence of the anomalous behavior and indicated the high sensitivity of the solution to the algorithm and details of programs.

To explain this counterintuitive behavior, Symonds and Yu analyzed a Shanley-type model, as shown in Fig. 1, which represents the most essentially physical behaviors concerned, and obtained $\phi_{max}-\phi_0$ and $\phi_{min}-\phi_0$ curves for the case of $\eta=0.0271$ as shown in Fig. 2, where $\eta=h'/l$ is a geometrical parameter of the model, ϕ_0 is the initial "release" angle corresponding to the peak displacement in the loading process, ϕ_{max} and ϕ_{min} denote maximum and minimum deflection angles in the final steady elastic vibration, respectively. This diagram is called characteristic diagram and it illustrates vividly that in a small range of ϕ_0, between two discontinuous transitions approximately at 0.0082 and 0.0092, there is a notable "slot" in $\phi_{max}-\phi_0$ curve, in which the pulse loading leads to a vibration between negative extreme values. This is the result of a complex interplay between effects of bending moments, axial thrusts and inertia forces and exchanges between kinetic energy, elastic strain energy, and plastic dissipation.

Following the original work mentioned above, Symonds, McNamara and Genna (1985) made a detailed study to the case of $\eta=0.0271$ for the Shanley-type model. Genna and Symonds (1987) also determined the displacement-time history for the Shanley-type model by applying both a standard step-by-step numerical integration scheme of Newmark type and exact integration of the equation of motion, and showed that covergence with decreasing time step may fail, near critical values. Using numerical scheme, Genna and Symonds (1988) explored the effects of slenderness ratio (i.e., parameter $\eta=h'/l$) and damping. The anomalous response behavior is found to occur for a narrow window of η, i.e., $0<\eta<0.0283$. They also showed that as another source of energy dissipation, damping in the system may alter the anomalous behaviors of the Shanley-type model, both in the position and in the numbers of discontinuous transitions. For some cases, more than one "slot" are observed, and this strongly suggests

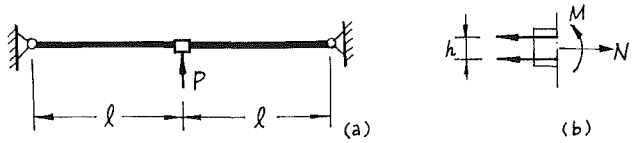


Fig. 1 The Shanley-type model adopted in previous papers

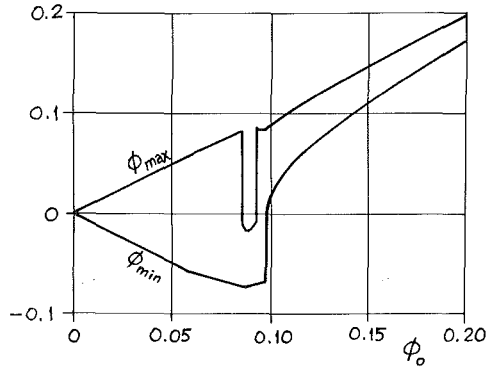


Fig. 2 A typical characteristic diagram obtained by the Shanley-type model with $\mu=400$ and $\eta=0.0271$

Contributed by the Applied Mechanics Division of THE AMERICAN SOCIETY OF MECHANICAL ENGINEERS for publication in the JOURNAL OF APPLIED MECHANICS.

Discussion on this paper should be addressed to the Editorial Department, ASME, United Engineering Center, 345 East 47th Street, New York, N.Y. 10017, and will be accepted until two months after final publication of the paper itself in the JOURNAL OF APPLIED MECHANICS. Manuscript received by the ASME Applied Mechanics Division, March 7, 1988; final revision, December 6, 1988.

Copyright © 1989 by ASME

Downloaded 03 May 2010 to 171.66.16.31. Redistribution subject to ASME license or copyright; see http://www.asme.org/terms/Terms_Use.cfm

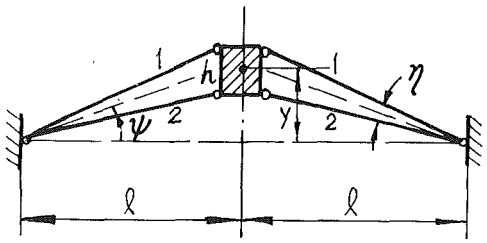


Fig. 3 The double-tier-spring model (DTS model)

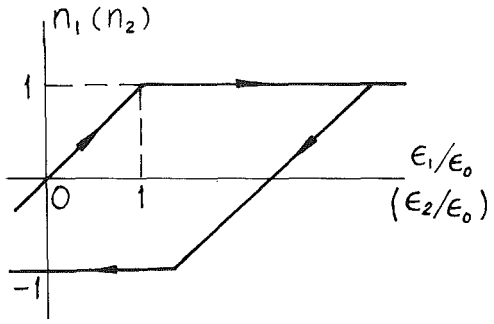


Fig. 4 The axial force-strain relationship of springs

chaotic behavior, which has been further studied by Poddar, Moon and Mukherjee (1988).

The approaches of Shanley-type model in these papers are aimed to find the discontinuous transition points mainly by using numerical integration scheme. When the exact integration is carried out, it only serves as a comparison for the numerical integration scheme used. These previous investigations have not given a systematic presentation or mathematical criterion to the condition under which discontinuous transitions do occur.

In the present paper, a new model, i.e., a double-tier-spring model (DTS model) is introduced and analyzed to follow its entire process of elastic-plastic deformation, after it is subjected to impulsive loading. Our major aim is to clarify the background of the anomalous behavior in the DTS model from the viewpoint of mathematics and mechanics. The deformation history of the model depends upon two parameters, i.e., parameter $\beta(=1/\sqrt{2\epsilon_0}\cdot h/2l)$, which characterizes the model itself, and parameter ω, which is the non-dimensional initial angular velocity. After analyzing this dependency, the conditions, under which the model possesses anomalous behavior, can be shown as some regions in the $\beta-\omega$ map, or alternatively in the $\beta-\theta_0$ map, where θ_0 is the initial "release" angle (see below). Finally, the equivalency of the present double-tier-spring model to Shanely-type model analyzed previously is proved, and the comparison of the present results with the previous ones is also presented.

The Double-Tier-Spring Model

The double-tier-spring model consists of a rigid concentrated mass m and two tiers of elastic-plastic springs which connect the mass to fixed pin ends, with the geometrical parameters shown in Fig. 3.

As an one-degree-of-freedom system, the deformation of the DTS model is indicated by angle ψ. The nonlinear relation between the elongation of springs and angle ψ simulates the effect of axial forces in the real beam problem; and the configuration of two tiers of springs simulate the fibers in the cross-section of a beam with different deformation histories. Clearly, parameter $\eta=h/l$ expresses the inherent geometrical characteristic of the model. It is assumed that at $t=0$, $\psi=0$; but the rigid mass has an initial velocity, as a result of impulsive loading.

By referring to Fig. 3, the equation of motion for the rigid mass can be set up as

$$m\frac{d^2y}{dt^2}+2\left[N_2\sin\left(\psi-\frac{\eta}{2}\right)+N_1\sin\left(\psi+\frac{\eta}{2}\right)\right]=0 \qquad (1)$$

where y is the displacement of the mass, N_1 and N_2 denote the axial forces in the first tier and the second tier of springs, respectively. By noting that ψ and η are small in comparison with unit, the nondimensionalization of equation (1) leads to

$$\ddot{\theta}+\frac{n_1+n_2}{2}\theta+\frac{n_1-n_2}{2}\beta=0 \qquad (2)$$

where

$$\theta=\psi/\sqrt{2\epsilon_0},\ \beta=\frac{1}{\sqrt{2\epsilon_0}}\cdot\frac{\eta}{2}=\frac{1}{\sqrt{2\epsilon_0}}\cdot\frac{h}{2l},$$

$$n_1=N_1/N_0,\ n_2=N_2/N_0,$$

ϵ_0 and N_0 are the strain and the force, respectively, for the springs when they reach the initial yield point, the dot denotes the differentiation with respect to τ, and $\tau=\sqrt{(4N_0/ml)}\cdot t$.

It is further assumed that all the springs are elastic-perfectly plastic, then the nondimensional relationships between axial forces and strains for spring 1 and spring 2 are as shown in Fig. 4.

From the configuration of the model, the strains of spring 1 and spring 2 are related to angle θ as

$$\epsilon_1/\epsilon_0=(\theta+\beta)^2-\beta^2,\ \epsilon_2/\epsilon_0=(\theta-\beta)^2-\beta^2. \qquad (3)$$

The initial condition due to impulse loading can be expressed as

$$\theta=0,\qquad \dot{\theta}=\omega. \qquad (4)$$

Therefore, the mathematical problem is to solve $\theta=\theta(\tau)$ from equation (2) under initial condition (4), while n_1 and n_2 are associated with θ through ϵ_1 and ϵ_2 by Fig. 4 and expression (3).

Governing Equations for Various Stages of Motion

In order to establish the characteristic diagram (see 'Introduction' for its meaning) of the DTS model, we have to analyze not only its final elastic vibration but also previous elastic-plastic deformation history.

Due to the elastic-perfectly plastic property of the springs (see Fig. 4), the deformation history of the DTS model can be divided into several stages. The transitions from one stage to the next one happens when one tier of springs change their state from elastic one to plastic one of vice versa. Stages 1, 2, 3, 4, . . . are numbered in succession. The state variables at the end of one stage constitute the initial conditions for the next state. Based on this clue, we set up equations of motion and their first integrals, stage by stage, according to the following procedure.

i) For a certain stage of motion, spring 1 and spring 2 are in certain sections of their force-strain diagrams, then the combination of Fig. 4 and expression (3) will give their constitutive relations as

$$\left.\begin{aligned} n_1 &= g_1(\theta;\beta,\omega),\\ n_2 &= g_2(\theta;\beta,\omega) \end{aligned}\right\}. \qquad (5)$$

For instance, for Stage 1, in which all springs are deforming elastically, it is easily shown that

$$\left.\begin{aligned} n_1 &= (\theta+\beta)^2-\beta^2,\\ n_2 &= (\theta-\beta)^2-\beta^2 \end{aligned}\right\}. \qquad (5a)$$

Downloaded 03 May 2010 to 171.66.16.31. Redistribution subject to ASME license or copyright; see http://www.asme.org/terms/Terms_Use.cfm

For Stage 2, spring 1 is in plastic state while spring 2 is still elastic, then

$$\left.\begin{aligned} n_1 &= 1, \\ n_2 &= (\theta-\beta)^2-\beta^2 \end{aligned}\right\}. \tag{5b}$$

In Stage 3, all springs are in plastic state, then

$$n_1=1 \quad \text{and} \quad n_2=1 \tag{5c}$$

will hold.

ii) Substituting (5) into (2) results in a concrete form of the equation of motion for a certain stage of deformation, i.e.,

$$\ddot{\theta}-f(\theta;\beta,\omega)=0. \tag{6}$$

For instance, (5*a*) (5*b*) and (5*c*) lead to

$$\ddot{\theta}+\theta^3+2\beta^2\theta=0, \tag{6a}$$

$$\ddot{\theta}+\frac{1}{2}(\theta+\beta)+\frac{1}{2}[(\theta-\beta)^2-\beta^2](\theta-\beta)=0 \tag{6b}$$

and

$$\ddot{\theta}+\theta=0, \tag{6c}$$

respectively. By doing so, it is confirmed that function f in equation (6) is a third-order polynomial of θ for all stages, except the stages in which both spring 1 and spring 2 are in plastic state. For the latter f in (6) is a linear function of θ, as seen in (6*c*).

iii) The first integral of equation (6) gives

$$\dot{\theta}^2-F(\theta;\beta,\omega)=0. \tag{7}$$

Since function F comes from the integration of f with respect to θ, F is a second-order polynomial of θ, if springs 1 and 2 both are in plastic state; otherwise F is a fourth-order polynomial of θ.

To determine function F for a certain stage, the variables at the end of the previous stage serve as the initial conditions in integrating equation (6).

For instance, the first integral of (6*a*) for Stage 1 leads to

$$\dot{\theta}^2+\frac{1}{2}\theta^4+2\beta^2\theta^2=\omega^2. \tag{8}$$

By recalling (5*a*), it is known that spring 1 will reach its elastic limit ($n_1=1$) when

$$\theta=(1+\beta^2)^{1/2}-\beta. \tag{9}$$

Substituting (9) into (8) yields

$$\dot{\theta}^2\Big|_{\theta=(1+\beta^2)^{1/2}-\beta}=\omega^2-\frac{1}{2}-6\beta^2-8\beta^4+2\beta(1+\beta^2)^{1/2}(1+4\beta^2). \tag{10}$$

Hence, the transition from Stage 1 and Stage 2 will happen if the calculation of the r.h.s. of (10) gives

$$\dot{\theta}^2\Big|_{\theta=(1+\beta^2)^{1/2}-\beta}>0. \tag{11}$$

In this case, the value of $\dot{\theta}$ at $\theta=(1+\beta^2)^{1/2}-\beta$ calculated from (10) can serve as the initial condition to integrate the equation of motion for Stage 2, i.e., equation (6*b*), and results in

$$\dot{\theta}^2+\frac{1}{2}(\theta+\beta)^2+\frac{1}{4}(\theta-\beta)^4-\frac{1}{2}\beta^2(\theta-\beta)^2 = \omega^2+\frac{1}{4}+\frac{1}{2}\beta^2-\frac{1}{4}\beta^4. \tag{12}$$

Stage 2 will end when $n_2=1$, i.e., when

$$\theta=(1+\beta^2)^{1/2}+\beta. \tag{13}$$

Repeating the aforementioned procedure, we find that the first integral of equation (6*c*) for Stage 3 is

$$\dot{\theta}^2+\theta^2=\omega^2+\frac{1}{2}. \tag{14}$$

The loading process for the DTS model will end when the velocity of the mass m vanishes, i.e., $\dot{\theta}=0$. This may happen in Stage 1, 2, or 3, depending on the values of ω and β given. Let θ_0 denote the value of θ when $\dot{\theta}=0$, then it is known by putting $\dot{\theta}=0$ into (14) that

$$\theta_0=\left(\omega^2+\frac{1}{2}\right)^{1/2}, \tag{15}$$

if the loading process continues until Stage 3. If the loading process finishes in Stage 1 or Stage 2, then θ_0 can be determined by putting $\dot{\theta}=0$ into (8) and (12), respectively, provided ω and β are specified. Instead of ω and β, therefore, we may adopt θ_0 and β as two independent parameters, which entirely govern the following deformation history of the DTS model.

The transition from one stage to the next stage happens if (*i*) one tier of springs changes their state from elastic one to plastic one (loading); and (*ii*) one tier of springs changes their state from plastic one to elastic one (unloading). The former cases can be easily detected by $|n_1|=1$ or $|n_2|=1$, as shown above. The latter cases include that (*a*) the velocity of the model vanishes (i.e., $\dot{\theta}=0$, so that all springs will start their springback); (*b*) one tier of springs passes through the straight configuration (i.e., $\theta=-\beta$ or $\theta=+\beta$, so that $d\epsilon$ will change its sign accordingly).

Finally, it should be noticed that if θ^* denotes the value of θ at a transitions from one stage to the next, then a necessary conditions for completing this transition is

$$\dot{\theta}\,|_{\theta=\theta^*}>0; \tag{16}$$

and the critical condition for reaching this transition point is given by

$$\dot{\theta}\,|_{\theta=\theta^*}=0. \tag{17}$$

In (16) and (17), $\dot{\theta}$ is calculated by the corresponding first integral shown in (7).

The Final Elastic Vibration

After a certain number of deformation stages, if there is no more energy can be plastically dissipated by the springs, then the DTS model comes to its final elastic vibration stage. Similar to that for the previous stages, a first integral of the equation of motion can be found in this final stage is also in the form of equation (7), that is,

$$\dot{\theta}^2-F_{ev}(\theta;\beta,\theta_0)=0, \tag{18}$$

where (β, θ_0) is used to replace (β, ω) in (7), and the subscript ev for F_{ev} denotes the final elastic vibration. By recalling the discussion on equation (7), it is known that function F_{ev} must a fourth-order polynomial of θ.

The extreme values of θ in the final elastic vibration, $\theta_{\max}$ and $\theta_{\min}$, are given by the solutions of equation (18) when $\dot{\theta}=0$ is taken. In other words, $\theta_{\max}$ and $\theta_{\min}$ must be the roots of function $F_{ev}(\theta;\ \beta,\ \theta_0)$. In the phase plane, i.e., in the $\theta-\dot{\theta}$ plane, these are the intersecting points of phase locus with the θ-axis.

In general, the phase locus determined by equation (18) may have three forms, as shown in Fig. 5. If the phase locus varies from the form in Fig. 5(*a*) to the form in Fig. 5(*c*) due to the variation of parameters β and θ_0, then the values of $\theta_{\max}$ or $\theta_{\min}$ must have a jump. Because the form in Fig. 5(*b*) is the transition's state between the form in Fig. 5(*a*) and that in

Downloaded 03 May 2010 to 171.66.16.31. Redistribution subject to ASME license or copyright; see http://www.asme.org/terms/Terms_Use.cfm

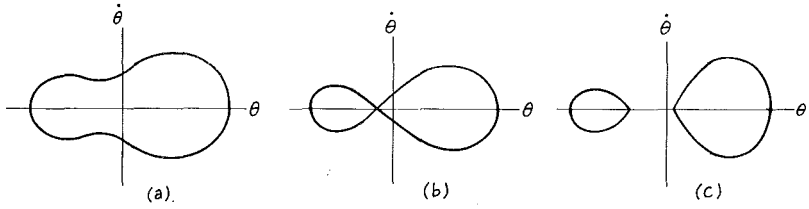


Fig. 5 Three possible forms of phase locus

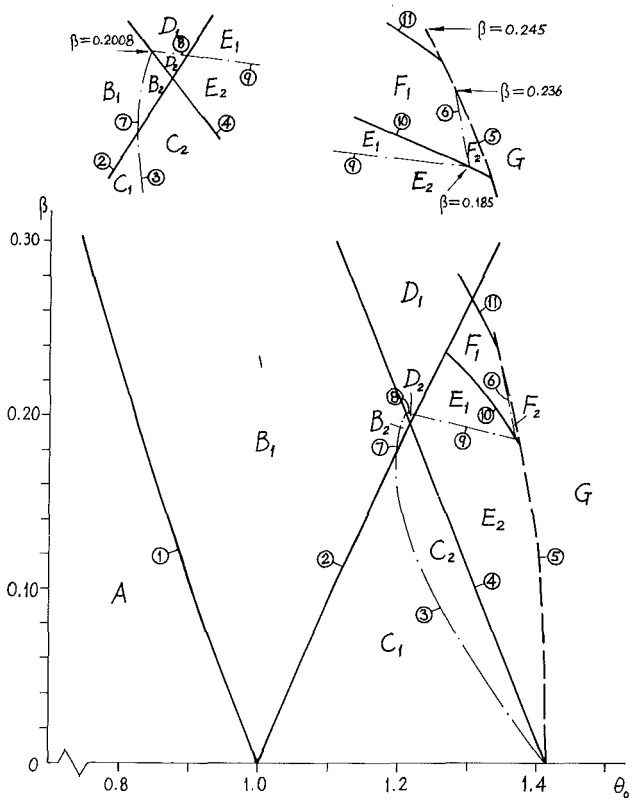


Fig. 6 A map in the $\beta-\theta_0$ plane

Fig. 5(*c*), it provides the condition for the jump in θ_{max} or θ_{min}. As a matter of fact, the phase locus of form in Fig. 5(*b*) is corresponding to the case that equation

$$F_{ev}(\theta;\beta,\theta_0)=0 \tag{19}$$

has a multiple root.

Map in the $\beta-\theta_0$ Plane

In order to condense the previous discussions and to show the dependence of the behaviors of the DTS model upon parameters β and θ_0, we use the $\beta-\theta_0$ plane to construct a map.

First, as discussed previously (see (17)), only a certain combination of β and θ_0 may make it possible for the DTS model to reach a certain stage of motion, and accordingly this will construct a curve in the $\beta-\theta_0$ plane, called a "stage transition curve."

As far as the final elastic vibration is concerned, it is known from algebra that if F_{ev} has the form of

$$F_{ev}(\theta;\beta,\theta_0)=\theta^4+a\theta^2+b\theta+c, \tag{20}$$

then $F_{ev}=0$ will have multiple root under the condition

$$16a^4c-4a^3b^2-128a^2c^2+144ab^2c-27b^4+256c^3=0. \tag{21}$$

Therefore, after a, b, and c are found from F_{ev}, the condition

Table 1 Property of regions in Fig. 6

region	θ_{min}	θ_{max}	property of motion
A	−	+	elastic vibration in beam mode
B_1,C_1,D_1,E_1,F_1	−	+	elastic-plastic vibration in beam mode
B_2,C_2,D_2,E_2,F_2	−	−	anomalous behavior in the final phase
G	+	+	elastic-plastic vibration in arch mode

(21) is indicated by a certain curve in the $\beta-\theta_0$ map, called a "multiple root curve," at which θ_{max} or θ_{min} displays a jump.

Apart from the case of "multiple root" of F_{ev} $(\theta;\beta,\theta_0)$ in the final stage, the jump in θ_{max} or θ_{min} may also be caused by similar cases in the early stages. In particular, if this occurs at a stage in which spring 2 passes through its straight configuration (i.e., $\theta=-\beta$), it may cause sign changes and jumps both in θ_{min} and θ_{max}. This case may refer to dynamic snap-through of the model, while the corresponding condition may be plotted as a "snap-through curve" in the $\beta-\theta_0$ map.

Thus, these three kinds of curves for the DTS model can be calculated and then plotted in the $\beta-\theta_0$ map, as shown in Fig. 6. There, curves ①, ②, ④, ⑩, and ⑪ are "stage transition curves," ⑤ is a "snap-through curve," and the others are "multiple root curves," among which ③, ⑥, and ⑦ pertain to a jump in θ_{max} from positive to negative, while ⑧ and ⑨ pertain to a jump in θ_{max} from negative to positive.

These curves intersect to each other and separate the $\beta-\theta_0$ map into regions, which are labeled by capital letters, e.g., region A, region B, etc., in Fig. 6. The properties of these regions are summarized in Table 1.

It is known from Fig. 6 and Table 1 that regions B_2, C_2, D_2, E_2, and F_2 merge into a single region, in which the motion of the DTS model has anomalous behavior, that is, its final elastic vibration takes place between a negative θ_{min} and a negative θ_{max}. This is our answer to the question raised in the Introduction, that is, which combination of parameters β and θ_0 will lead to the anomalous behavior.

When parameter β is specified, the feature of the characteristic diagram, i.e., that of $\theta_{max}-\theta_0$ and $\theta_{min}-\theta_0$ curves can be easily observed by drawing a horizontal straight line $\beta=$ const across Fig. 6. As a result, the characteristic diagrams for various β may be sketched as Fig. 7, from which it is seen that

(*i*) in case of $0<\beta<0.185$, a notable slot in the $\theta_{max}-\theta_0$ curve is found, the width of the slot is determined by the distance from curve ③ to curve ⑤ in Fig. 6, and it reaches maximum at $\beta\simeq 0.15$;

(*ii*) in the case of $0.185<\beta<0.2008$, two slots in the $\theta_{max}-\theta_0$ curve are found, and the second one was failed to be detected in previous approaches;

(*iii*) in case of $0.2008<\beta<0.236$, only a very narrow slot is found in the $\theta_{max}-\theta_0$ curve;

(*iv*) in case of $0.236<\beta<0.245$, there is no slot in the $\theta_{max}-\theta_0$ curve, but the jump in θ_{min} from negative to positive still exists; and finally,

(*v*) in the case $\beta>0.245$, neither slot nor jump can be observed.

As a typical example, Fig. 8 shows the calculated

Downloaded 03 May 2010 to 171.66.16.31. Redistribution subject to ASME license or copyright; see http://www.asme.org/terms/Terms_Use.cfm

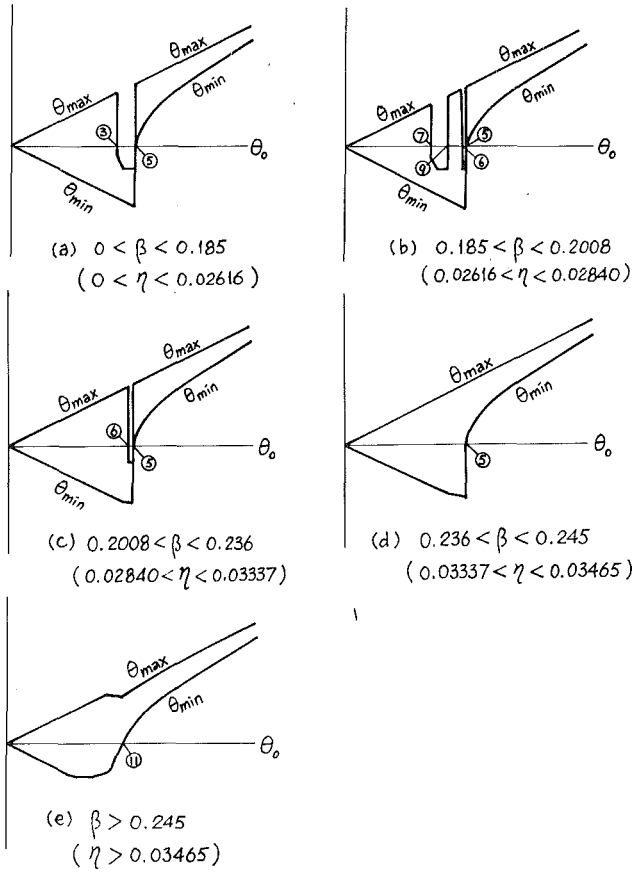


Fig. 7 Sketches of characteristic diagrams for various ranges of β

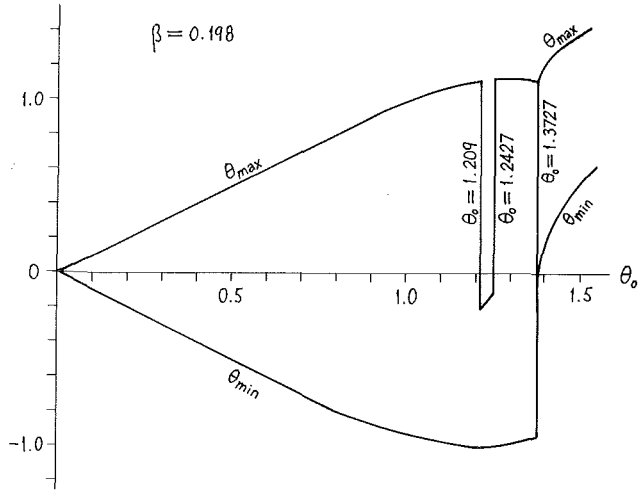


Fig. 8 Characteristic diagram for $\beta = 0.198$ (i.e., $\eta = 0.0280$ and $\mu = 400$)

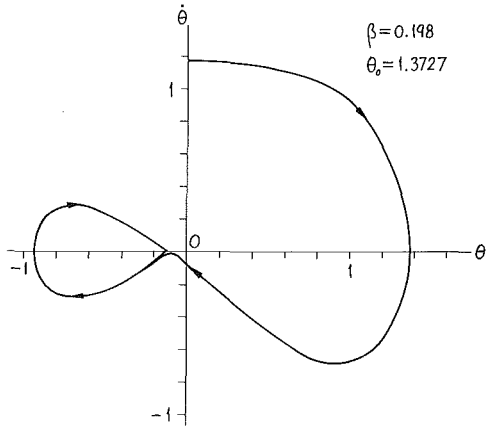


Fig. 9 The phase locus for $\beta = 0.198$ and $\theta_0 = 1.3727$

characteristic diagram for $\beta = 0.198$, which belongs to case (*ii*). The corresponding phase locus for specified θ_0 in the range of the second slot is given in Fig. 9.

A Comparison With the Shanley-Type Model

In the Appendix, a proof is given on the equivalency of our DTS model to the Shanley-type model used in the previous papers. In fact, the present results on the DTS model may be directly transferred to a Shanley-type model, provided

$$\phi = \sqrt{\frac{2}{\mu}}\theta \quad \text{and} \quad \eta = \sqrt{\frac{8}{\mu}}\beta \tag{22}$$

are taken. Here, θ and β pertain to our DTS model, while ϕ, μ, and η are the notations used in the previous papers.

The characteristic diagrams given in Genna and Symonds (1988) for $\eta = 0$, 0.001, 0.01, 0.0271, 0.03 and 0.04 are all in good agreement with our sketches in Fig. 7, which may easily be obtained from Fig. 6.

In the previous papers, a typical example with $\mu = 400$ and $\eta = 0.0271$ was discussed in detail. Noting (22), we take $\beta = \sqrt{\mu/8}\,\eta = 0.191626$ in our DTS model and then obtained its numerical results. A good agreement is also found for the discontinuous transitions in the characteristic diagram.

In addition to this, the analysis of our DTS model with $\beta = 0.191626$ reveals the second slot, with the endpoints being $\theta_0 = 1.376130$ and 1.376139 in the $\theta_{\max} - \theta_0$ curve (or $\phi_0 = 0.973071$ and 0.0973077 in the $\phi_{\max} - \phi_0$ curve, as recently calculated by Symonds and his collaboraters), which was missing in the previous analyses to the Shanley-type model. Although the second slot is very narrow, it indicates an important feature of the DTS model (indeed, of the Shanley-type model, too). That is, if $\theta_{\max}$ ($\phi_{\max}$) has jumps in the characteristic diagram, then its last jump (the rightest one) must be accompanied by a jump of $\theta_{\min}$ ($\phi_{\min}$) from negative to positive.

Conclusions

The present analysis introduces a structural model, i.e., the double-tier-spring (DTS) model, which is essentially equivalent to the Shanley-type model adopted previously, provided a proper transference in parameter is taken. However, we have shown that only one structural parameter, i.e., $\beta = 1/\sqrt{2\epsilon_0} \cdot h/2l = \sqrt{\mu/8}\eta$ needs to specified, instead of two (η and μ) in the previous analyses on the Shanley-type model.

By adopting this DTS model, the jumps in the characteristic diagram are related to the conditions, under which function $F_{ev}(\theta; \beta, \theta_0)$ in the first integral of the equation of motion in the final elastic vibration stage has a multiple root, or the motion involves snap-through of the springs. In the $\beta - \theta_0$ map, the jumps in $\theta_{\max}$ or $\theta_{\min}$ occur at some curves obtained from the above consideration, while a region enveloped by these curves indicates the combination of parameters β and θ_0, in which the so-called anomalous behaviors in the dynamic response of the model appear. In this way, we have shown all types of behaviors that can be expected over full range of values of β, and done this algebraically and essentially exactly.

In the case of $0.185 < \beta < 0.2008$, e.g., for $\beta = 0.191626$ (i.e., $\mu = 400$ and $\eta = 0.0271$ in the Shanley-type model), the present approach predicts the existence of the second narrow slot in the characteristic diagram, which was missing in the previous analyses but has been confirmed by precise calculation.

Due to the complexity of theoretical treatment, the present

Downloaded 03 May 2010 to 171.66.16.31. Redistribution subject to ASME license or copyright; see http://www.asme.org/terms/Terms_Use.cfm

analysis of the DTS model has been completely carried out only for a certain range of parameters β and θ_0. However, the theoretical method adopted in the present paper can also be applied to the analysis for other ranges of parameters.

Acknowledgment

The authors would like to thank G. S. Tong for helpful discussion on the modal.

References

Genna, F., and Symonds, P. S., 1987, "Induced Vibrations and Dynamic Instabilities of a Nonlinear Structural Model due to Pulse Loading," *Mecanica*, Vol. 22, pp. 144–149.

Genna, F., and Symonds, P. S., 1988, "Dynamic Plastic Instabilities in Response to Short Pulse Excitation—Effects of Slenderness Ratio and Damping," *Proc. Royal Society*, Vol. 417, pp. 31–44.

Poddar, B., Moon, F. C., and Mukherjee, S., 1988, "Chaotic Motion of an Elastic-Plastic Beam," ASME JOURNAL OF APPLIED MECHANICS, Vol. 55, pp. 185–189.

Symonds, P. S., McNamara, J. F., and Genna, F., 1985, "Vibration and Permanent Displacements of a Pin-ended Beam Deformed Plastically by Short Pulse Excitation," *Int. J. Impact Engineering*, Vol. 4, pp. 73–82.

Symonds, P. S., and Yu, T. X., 1985, "Counterintuitive Behavior in a Problem of Elastic-Plastic Beam Dynamics," ASME JOURNAL OF APPLIED MECHANICS, Vol. 52, pp. 517–522.

APPENDIX

A Proof on the Equivalency of the DTS Model to the Shanley-Type Model

The equation of motion for the Shanley-type model is (see Symonds and Yu (1985))

$$\frac{A'}{2}\phi(\sigma_1+\sigma_2)+\frac{h'}{4l}(\sigma_1-\sigma_2)A'+\frac{1}{3}\bar{\rho}l^2\ddot{\phi}=0. \tag{A1}$$

Only the release process from $\phi=\phi_0$ is concerned, so that the external load is zero, and the strains are

$$\left.\begin{aligned}\epsilon_1 &= \frac{1}{2}\left[\left(\phi+\frac{h'}{2l}\right)^2-\left(\frac{h'}{2l}\right)^2\right],\\ \epsilon_2 &= \frac{1}{2}\left[\left(\phi-\frac{h'}{2l}\right)^2-\left(\frac{h'}{2l}\right)^2\right]\end{aligned}\right\}. \tag{A2}$$

The strain at the initial yield point $\epsilon^*=\sigma_0/E=1/\mu$. Therefore, introducing

$$\theta=\sqrt{\frac{\mu}{2}}\phi \quad \text{and} \quad \beta=\sqrt{\frac{\mu}{2}}\frac{h'}{2l}=\sqrt{\frac{\mu}{8}}\eta \tag{A3}$$

we have

$$\left.\begin{aligned}\epsilon_1/\epsilon^* &= (\theta+\beta)^2-\beta^2,\\ \epsilon_2/\epsilon^* &= (\theta-\beta)^2-\beta^2\end{aligned}\right\}. \tag{A4}$$

Then the equation (A1) can be simplified as

$$\frac{d^2\theta}{d\tau^2}+\frac{1}{2}(\sigma_1'+\sigma_2')\theta+\frac{1}{2}(\sigma_1'-\sigma_2')\beta=0, \tag{A5}$$

where

$$\sigma_1'=\sigma_1/\sigma_0,\ \sigma_2'=\sigma_2/\sigma_0,\ \tau=t/\sqrt{\frac{1}{3}\frac{\bar{\rho}l^2}{\sigma_0 A'}}.$$

The relationships between σ_1' and ϵ_1/ϵ^*, σ_2' and ϵ_z/ϵ^* obviously are the same as that shown in Fig. 4, since the material is assumed to be elastic-perfectly plastic. By comparing equation (A5) and equation (2), it is confirmed that two models are equivalent to each other, if the parameters' transference (22) is applied.

Downloaded 03 May 2010 to 171.66.16.31. Redistribution subject to ASME license or copyright; see http://www.asme.org/terms/Terms_Use.cfm

M. De Smet
NFWO Research Assistant.

C. Liefooghe
Research Assistant.

P. Sas
Professor, NFWO Research Associate.

R. Snoeys
Professor,
Mem. ASME

Katholieke Universiteit Leuven,
Department of Mechanical Engineering,
Celestijnenlaan 300B
B-3030 Heverlee, Belgium

Dynamic Analysis of Flexible Structures Using Component Mode Synthesis

In this paper a dynamic model of a flexible robot is built out of a finite element model of each of its links. The number of degrees-of-freedom of these models is strongly reduced by applying the Component Mode Synthesis technique which involves the preliminary calculation of a limited number of mode shapes of the separate links. As can be seen from examples, the type of boundary conditions thereby imposed in the nodes in which one link is connected to the others, strongly determines the accuracy of the calculated resonance frequencies of the robot. The method is applied to an industrial manipulator. The reduced finite element model of the robot is changed in order to match the numerically and experimentally (modal analysis) determined resonance data. Further, the influence of the position of the robot on its resonance frequencies is studied using the optimized numerical model.

1 Introduction

The demand for higher industrial productivity has led to an increasing use of processor-controlled robot manipulators. In order to fully exploit the potentials of modern digital controllers, the control algorithms should not be limited to dynamic models based on rigid links and joints. Up to now, the control system's bandwidth is deliberately limited to avoid excitation of the first resonance frequencies of the robot. If this limitation could be shifted beyond the first resonance frequencies of the manipulator, faster and lighter robots with increased accuracy and payload could become feasible. To realize this, the robot control system should take the dynamic effects of joint and link flexibilities into account, in order to ensure sufficient end-effector positional accuracy, even when the speed is increased (Iida, Oono, Tamura, and Ono, 1986; Book, Maizza-Neto, and Whitney, 1975; Alberts, Dickerson, and Book, 1985). Therefore, numerical techniques must be developed to determine the dynamic behavior of high-speed, light-weight robots (Sunada, 1980; Sunada, and Dubowsky, 1981; Sunada, and Dubowsky, 1983; Usoro, Nadira, and Mahil, 1986; Shabana, and Wehage, 1983).

In this paper an efficient method is proposed to calculate the dynamic characteristics of a robotic manipulator in different fixed positions. Its links may be complexly shaped and the proposed method may take the flexibility of the joints into account.

The structure to be analyzed is therefore divided into different components. For each component a finite element model is built. The large number of degrees-of-freedom of these models is reduced by means of a Component Mode Synthesis technique (Ookuma and Nagamatsu, 1984a, 1984b, 1985; Nagamatsu and Ookuma, 1981), that makes use of a limited number of natural mode shapes of each of the components. Finally, the reduced link models are combined into a dynamic model of the complete flexible manipulator, using compatibility matrices.

In order to verify the accuracy of the CMS technique, this method has been applied to a one-side-clamped beam and a fictive robot with three links. In addition the method has been applied to an industrial robot, where the results of the CMS technique have been compared with modal analysis test results. A study has been made of the influence of the position of the manipulator on its dynamic behavior.

2 Numerical Method

2.1 Dynamic Model of a Separate Link. Using a general finite element code, a finite element model of each separate link is built, i.e., its mass matrix $[m_i]$ and stiffness matrix $[k_i]$ are extracted. The dynamic equation of link i can be written as:

$$\begin{bmatrix} [m_i^{II}] & [m_i^{IF}] \\ [m_i^{FI}] & [m_i^{FF}] \end{bmatrix} \begin{Bmatrix} \{\ddot{p}_i^I\} \\ \{\ddot{p}_i^F\} \end{Bmatrix} + \begin{bmatrix} [k_i^{II}] & [k_i^{IF}] \\ [k_i^{FI}] & [k_i^{FF}] \end{bmatrix} \begin{Bmatrix} \{p_i^I\} \\ \{p_i^F\} \end{Bmatrix} = \begin{Bmatrix} \{f_i^I\} \\ \{f_i^F\} \end{Bmatrix} \quad (1)$$

with $\{p_i\}$ being the vector containing the displacements and rotations with respect to local x, y, and z axes, and $\{f_i\}$ a force vector. Because equation (1) may already represent a rather large set of equations for detailed finite element models, the model's order needs to be reduced before all link equations are assembled into a model of the whole structure. In view of this

Contributed by the Applied Mechanics Division of THE AMERICAN SOCIETY OF MECHANICAL ENGINEERS for publication in the JOURNAL OF APPLIED MECHANICS.

Discussion on this paper should be addressed to the Editorial Department, ASME, United Engineering Center, 345 East 47th Street, New York, NY 10017, and will be accepted until two months after final publication of the paper itself in the JOURNAL OF APPLIED MECHANICS. Manuscript received by the ASME Applied Mechanics Division, May 10, 1988; final revision, January 25, 1989.

Copyright © 1989 by ASME

Downloaded 03 May 2010 to 171.66.16.31. Redistribution subject to ASME license or copyright; see http://www.asme.org/terms/Terms_Use.cfm

reduction, distinction has been made in equation (1) between "interface nodes" $\{p_i^I\}$ and "free nodes" $\{p_i^F\}$. In the former, link i is connected to the other links of the system, whereas in the latter, no connections with other links exist.

2.2 Component Mode Synthesis. Applying the Component Mode Synthesis technique consists of eliminating the degrees-of-freedom corresponding to the free nodes, $\{p_i^F\}$, according to:

$$\{p_i^F\} = -[k_i^{FF}]^{-1}[k_i^{FI}]\{p_i^I\} + [\Phi_i]\{\eta_i\}. \tag{2}$$

The right-hand sum consists of two terms. The first term resembles the displacements of the free nodes when only static behavior is taken into account and the forces on the free nodes $\{f_i^F\}$ are set equal to zero. The second term consists of a linear combination of mode shapes Φ_i calculated with clamped interface nodes (fixed-fixed modes).

By taking into account only a limited number of eigenvectors based on a frequency criterion, the dynamic link-equation's order is seriously reduced. The reduction of the set of eigenvectors is the fundamental approximation of the Component Mode Synthesis method. When no modes are selected, the reduction corresponds to the Guyan reduction with respect to the interface nodes (Guyan, 1965).

Considering mode shapes with clamped interface nodes does not exclude the degrees-of-freedom of these nodes, because they are explicitly included in the list of remaining coordinates $\{a_i\}$ for link i. Examples will show that the results are not so accurate when free-free modes instead of fixed-fixed modes are taken into account.

The resulting transformation can now be written as follows:

$$\begin{Bmatrix} \{p_i^I\} \\ \{p_i^F\} \end{Bmatrix} = \begin{bmatrix} [I] & [0] \\ -[k_i^{FF}]^{-1}.[k_i^{FI}] & [\Phi_i] \end{bmatrix} \begin{Bmatrix} \{p_i^I\} \\ \{\eta_i\} \end{Bmatrix} = [A_i]\{a_i\}. \tag{3}$$

2.3 Transformation to a Global Frame. The reduced link models are formed in a local frame, a different frame for each link. In order to simplify the assembling procedure of the links, the local coordinates are transformed to a general global frame using the Denavit-Hartenberg transformation (Denavit and Hartenberg, 1955; Simons and Van Brussel, 1983). Symbolically, the transformation of the vector $\{a_i\}$ of link i to the global frame can be written as:

$$\{a_i\} = [\tau_i]\{a_i^0\} \tag{4}$$

with $[\tau_i]$ the transformation matrix.

2.4 Assemblage of the Link Models into a Model of the Global Structure. The link models, each expressed in terms of a few interface degrees-of-freedom and some modal coordinates η_i, have to be assembled into a model of the whole structure. The degrees-of-freedom of this global model are represented in a so-called "system vector" $\{q^0\}$. This vector consists of two parts: the displacements of the interface nodes of all the links and the modal coordinates of the different links. Because all displacement components are transformed to one and the same global frame, it is straightforward to define the relation between $\{q^0\}$ and the vector $\{a_i^0\}$ using a compatibility matrix $[B_i]$ which consists only of 0's and 1's:

$$\{a_i^0\} = [B_i]\{q^0\}. \tag{5}$$

The displacements of nodes in which different links have to be rigidly connected (e.g., nodes a and b in Fig. 1) are set equal to the same set of system coordinates. Consequently, these nodes will have the same displacements. So, equation (5) incorporates relationships as (see Fig. 1):

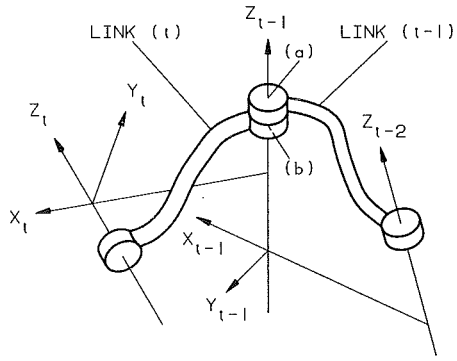


Fig. 1 Connection of link i and link $i-1$ with a hinge

$$\{p_i^0\}_b = [I]\{p_{i-1}^0\}_a. \tag{6}$$

If two links are connected by a hinge, an extra system coordinate is added to the "system vector" $\{q^0\}$ for the second link, corresponding with the degree-of-freedom of the hinge. The displacements of node a on link $i-1$ are then represented by an ordinary set of system coordinates in $\{q^0\}$. The displacements of node b on link i, however, can be expressed in terms of the same set of system coordinates plus the extra created system coordinate. This is extensively explained in (De Smet and Liefooghe, 1987).

The flexibility of joints can also be taken into account. This is done by defining an element of which the two nodes, a and b, coincide. Node a is connected rigidly to the first link of the joint, node b to the second. Between these two nodes a spring is defined along each degree-of-freedom. The stiffness matrix $[k_i]$ of this element contains only the stiffnesses of the springs, the mass matrix $[m_i]$ is a zero matrix.

The original finite element model of a separate link is transformed three times: first, a reduction of the number of degrees-of-freedom using the Component Mode Synthesis technique, secondly, a transformation to a global frame, and finally, a transformation to system coordinates. These three transformations together are represented by the matrix $[C_i]$:

$$\{p_i\} = [C_i]\{q^0\} = [A_i][\tau_i][B_i]\{q^0\}. \tag{7}$$

Because the structure is analyzed in one specific position, the matrix $[C_i]$ is time independent. Consequently,

$$\{\ddot{p}_i\} = [C_i]\{\ddot{q}^0\}. \tag{8}$$

Substituting equations (7) and (8) into (1), premultiplicating with $[C_i]^T$, and adding over all links results in the dynamic model of the global structure:

$$\sum_{i=1}^{n}[C_i]^T[m_i][C_i]\{\ddot{q}^0\} + \sum_{i=1}^{n}[C_i]^T[k_i][C_i]\{q^0\} = \sum_{i=1}^{n}\{Q_i\}. \tag{9}$$

To calculate the resonance frequencies and mode shapes of the structure, $\Sigma_{i=1}^{n}\{Q_i\}$ is set to zero and the resulting eigenvalue problem has to be solved.

2.5 Computer Software Package. This numerical method has been implemented in a computer software package called FLEX. Figure 2 shows the proposed method in a schematic way. This figure indicates which part of the algorithm is performed by the finite element code SYSTUS (Framatome, 1987) and also shows what is done by the newly-developed program FLEX. The method presented in this paper has several advantages in comparison with the classical finite element modeling of the whole structure:

- The model's order is strongly reduced, which means a reduced calculation time, for the same level of accuracy.

Downloaded 03 May 2010 to 171.66.16.31. Redistribution subject to ASME license or copyright; see http://www.asme.org/terms/Terms_Use.cfm

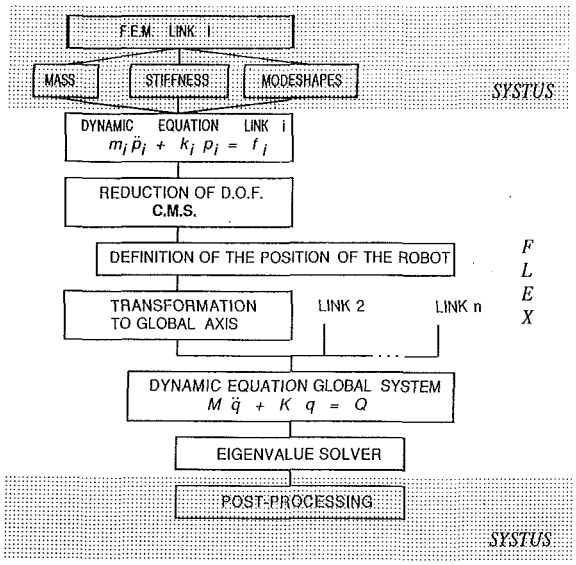


Fig. 2 Scheme of the FLEX method

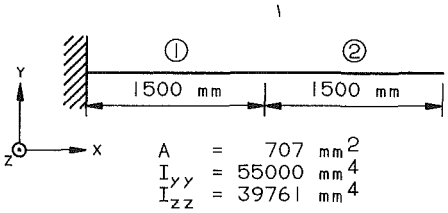


Fig. 3 Geometry of a one-sided-clamped beam

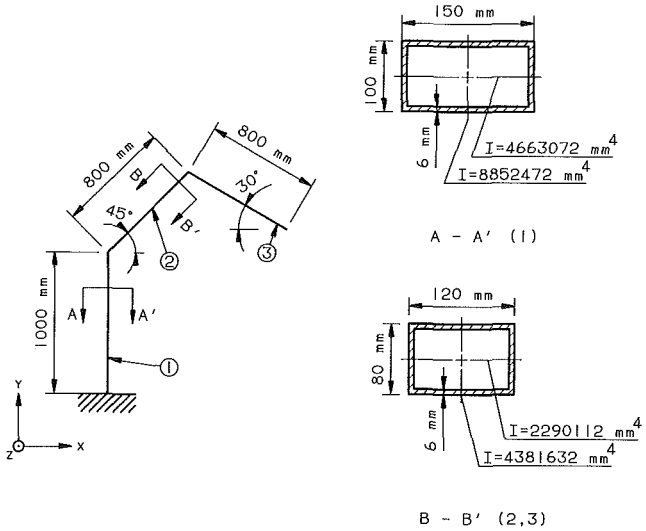


Fig. 4 Geometry of a fictive robot

- A second position of the structure can be analyzed easier and faster: One has to restart the calculation at the definition of the position of the robot (Fig. 2). The reduced link models of the first analysis can be reused.
- The finite element model of a separate link may contain many nodes.
- It is possible to define flexible joints.

3 Examples

For this study the finite element code SYSTUS was applied.

3.1 One-Side-Clamped Beam.

3.1.1 Description of the System. The construction consists of two identical links rigidly connected to each other and oriented along the same axis, so that they form the one-side-clamped beam (Fig. 3).

Table 1 Comparison of the resonance frequencies of the one-side-clamped beam with different types of modes used in CMS

freq. [Hz]	SYSTUS	FLEX-frequencies 6 6 fixed-fixed modes	6 6 rotation-DOF free	6 6 free-free modes	8 6 fixed-free modes
1	2.4	2.4	2.4	2.4	2.4
2	2.8	2.8	2.8	2.8	2.8
3	15.1	15.1	15.1	15.2	15.1
4	17.7	17.7	17.8	17.9	17.7
5	42.1	42.2	43.8	51.3	44.8
6	49.6	49.6	51.4	60.3	52.7
7	82.5	82.6	88.8	144.1	97.9
8	97.0	97.1	104.3	169.4	115.5
9	136.3	136.4	158.1	273.4	159.4
10	160.2	160.3	185.3	311.1	187.4
11	203.5	205.0	271.6	358.1	257.3
12	239.0	240.8	273.4	364.8	270.5
13	266.5	273.4	317.9	420.0	302.1
14	283.9	286.2	326.6	440.8	436.1
15	333.3	336.0	381.8	670.3	468.9

3.1.2 Results. As mentioned before, this paper proposes a CMS method using fixed-fixed modes. From a theoretical point of view it is not evident why this type of mode should be preferred. The following example shows that the accuracy of all other types (free-free, fixed-free) is not satisfying.

In this example the same frequency criterion is used for all types of modes, i.e., the frequency limit f^* for selection is 400 Hz.

The case of fixed-fixed modes means that six modes for each link are taken into account. Table 1 shows that reliable frequencies are obtained up to the fifteenth resonance frequency (333 Hz): The deviation, with respect to the SYSTUS results, is smaller than 1 percent. Thus, the frequency range of reliable results is smaller than the limit f^*. This is true for all the other examples discussed in this paper.

The same frequency criterion is applied to three other cases of constraints. When releasing the rotational degrees-of-freedom of the node the deviations, with respect to the SYSTUS results, exceed 10 percent from the ninth frequency on. Even more substantial deviations are noticed when free-free modes are taken into account. Apart from the four resonance frequencies obtained by the Guyan reduction, no accurate modes are found. To approximate the constraints of the global structure better, modes with one end fixed and the other end completely free are taken into account for the first link. The results appear to be better than those with the free-free conditions, but they are still less accurate than the results with fixed-fixed conditions.

3.2 Robot With Three Links.

3.2.1 Description of the System. The second example considers a beam construction, consisting of three hollow links. The geometric description of the links is indicated in Fig. 4. This construction can be seen as a model of a fictive robot: Link 1 would represent the shoulder, link 2 the upper arm, and link 3 the forearm of the robot.

A finite element model was built for each link, using the finite element code SYSTUS. The link models consist of beam elements and each model has eleven nodes. The resonance frequencies of the separate links were calculated with completely-clamped interface nodes.

3.2.2 Results.

- Influence of the number of selected modes: The influence of the number of selected link modes on the accuracy of the results is analyzed by calculating several times the

Downloaded 03 May 2010 to 171.66.16.31. Redistribution subject to ASME license or copyright; see http://www.asme.org/terms/Terms_Use.cfm

resonance frequencies of the structure, each time with a different selection of modes. The deviations of these frequencies, with respect to those calculated using a global finite element model (SYSTUS), are shown in Fig. 5. As can be seen, the frequency range within which the calculated resonance frequencies are accurate, can be extended by selecting more modes for each link.

• Considerations about the calculation time: As mentioned before, the reduction of calculation time due to the CMS, in comparison with the classical finite element calculation, is an important advantage of the FLEX software. Both the calculations with the FLEX programs and the calculations with the finite element program SYSTUS were performed on a VAX-750 computer. So, it is possible to compare directly the calculation time (CPU time) of both packages. Using the Subspace Method, 20 resonance frequencies were calculated with SYSTUS; the CPU time amounted to 190 seconds. Seven modes for each link are necessary with the FLEX program, to also obtain 20 accurate resonance frequencies. With the FLEX method the total computation time can be divided into the

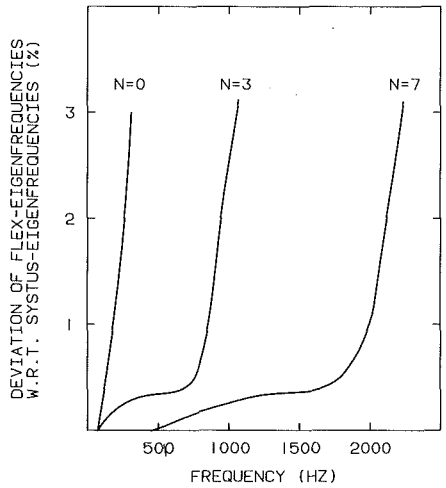


Fig. 5 Influence of the number of selected link mode shapes *N* on the accuracy of the calculated resonance frequencies with respect to the SYSTUS resonance frequencies

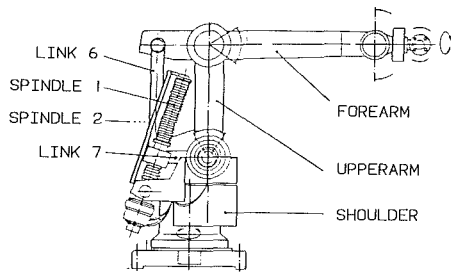


Fig. 6 Links of the ASEA robot IRB-60

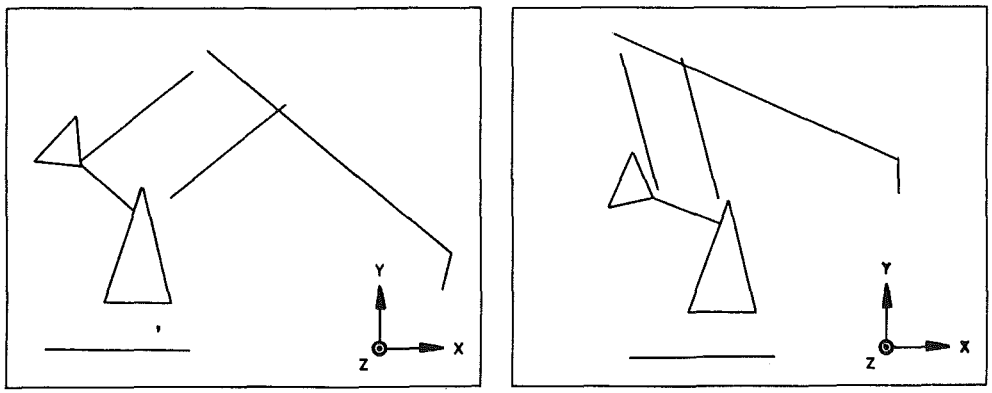


Fig. 7 Two positions of the ASEA robot in which experimental modal analyses were performed

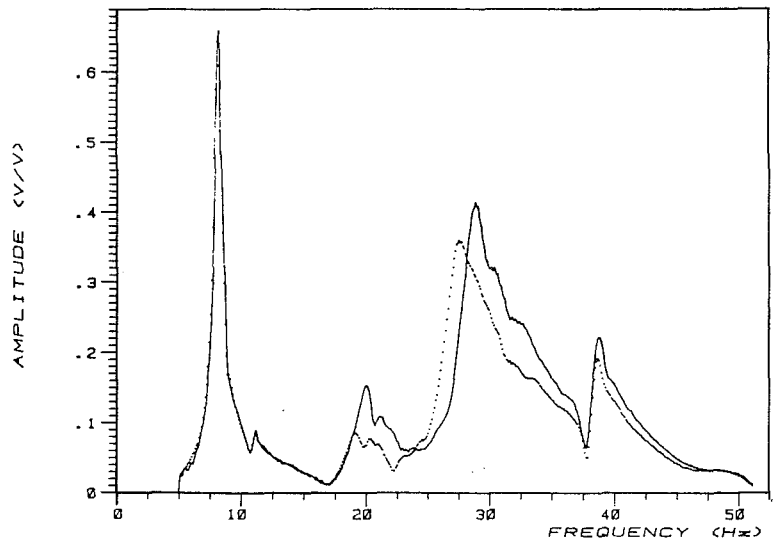


Fig. 8 Frequency response function in a point of the forearm:
—force-amplitude 25 *N*
. . . force-amplitude 50 *N*

Downloaded 03 May 2010 to 171.66.16.31. Redistribution subject to ASME license or copyright; see http://www.asme.org/terms/Terms_Use.cfm

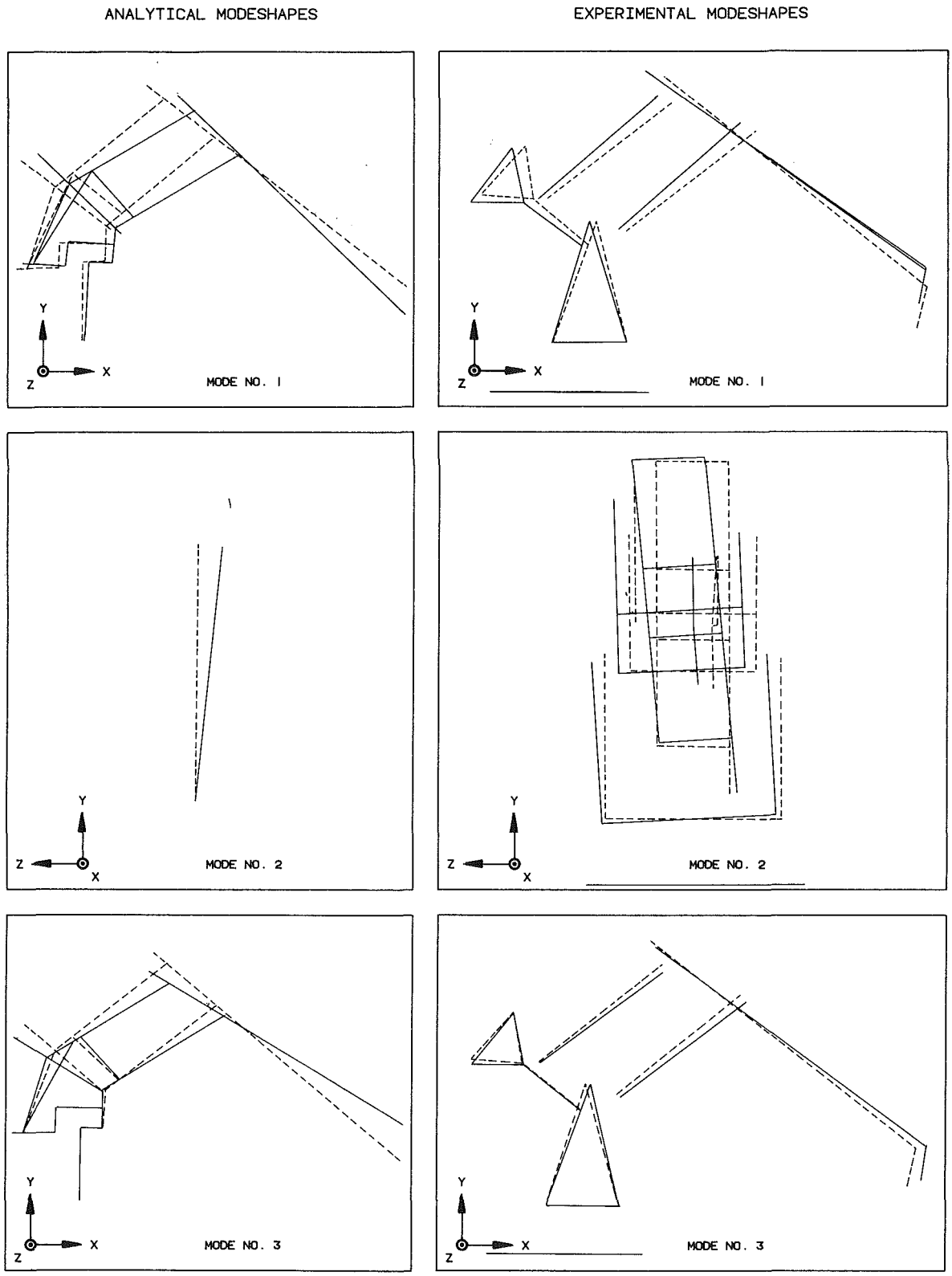


Fig. 9 Comparison between the three lowest experimental and numerical mode shapes

time for the CMS reduction and the time to solve the reduced system. For this example this total time is 243 seconds—195 seconds CPU time for the reduction and 48 seconds for the solution.

The advantage of using this method becomes clear, however, when the construction has to be analyzed in different positions. Indeed, while with the classical finite element code SYSTUS the complete model has to be recalculated, with the FLEX program only the reduced model has to be recomputed and solved (the CMS reduction does not have to be repeated anymore). This means that the resonance frequency calculation for any position after the first one takes only 48 seconds

Downloaded 03 May 2010 to 171.66.16.31. Redistribution subject to ASME license or copyright; see http://www.asme.org/terms/Terms_Use.cfm

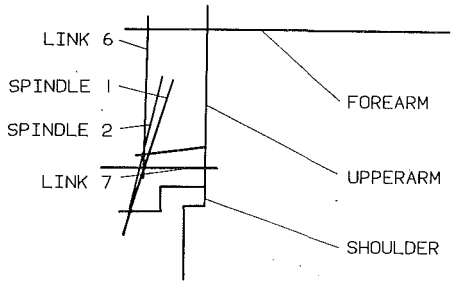


Fig 10 Numerical model of the ASEA robot

with the FLEX program, while it would always take 190 seconds with SYSTUS. Since the level of the authors programming technique is not high, their programs can be much improved. If they are revised by programming specialists, the CPU time for the FLEX programs will be much shorter.

4 Case Study

4.1 Description of the System. The method presented in this paper was also applied to the industrial robot manipulator shown in Fig. 6. This manipulator is an ASEA robot, type IRB-60. The three major links of the manipulator are referred to as the shoulder, the upper arm, and the forearm.

4.2 Experimental Modal Analysis. A modal test was performed on this robot in two different positions (Fig. 7). A typical frequency response function (FRF) in a point of the forearm is shown in Fig. 8. It is clear that the modes are highly damped. In addition, some nonlinearities can be seen from this FRF, i.e., the peaks in the FRF shift to lower frequencies when a higher force level is applied to excite the robot, except for the two lowest resonance frequencies.

Table 2 summarizes the experimentally-determined modal parameters. The three lowest modes for the first position are shown in Fig. 9. The two first modes can be seen as rigid body modes of the robot, with respect to the supports. The third mode corresponds to the tilting of the forearm together with the upper arm, with respect to the shoulder of the robot. This mode is probably due to the flexibility in the coupling between the spindles and the robot arms.

4.3 Numerical Model. For this industrial robot a numerical model is built. On each link, nodes are defined at small distance from each other and between two nodes the section of the robot arm is determined. The dimensions of the sections are needed to define the elements of the finite element model of the links. Because the section of the link changes very much along its axis, many nodes have to be defined. Only in this way a fair estimation of the mass distribution can be obtained. For the whole robot seven links are defined, and they are joined to each other by means of hinges (Fig. 10).

4.4 Tuning of the Numerical Model. The numerical model of the robot has been assembled to simulate the three lowest modes. For the CMS reduction no modes are selected, because the lowest resonance frequency of the components is 83 Hz, and the third resonance frequency of the robot is about 20 Hz. To simulate the two lowest modes of the ASEA robot, a flexible joint between the shoulder of the robot and the environment is defined. A study of the numerical model makes clear that the third mode cannot be simulated very well without defining supplementary flexible joints. It is necessary to define a flexible joint between upper arm and spindle 2, and also between link 6, link 7, and spindle 1. After applying CMS, the resulting numerical model contains only 65 DOF. A comparable classical finite element model would contain 852 DOF.

Table 2 Resonance frequencies and damping ratios of the ASEA robot

order	position 1		position 2	
	frequency [Hz]	damping ratio [%]	frequency [Hz]	damping ratio [%]
1	8.05	3.14	9.32	1.63
2	10.91	1.71	10.01	2.39
3	18.83	7.11	15.93	6.40
4	22.82	2.96	19.66	5.02
5	27.24	4.44	24.42	2.83
6	38.60	1.17	31.26	2.53

Table 3 Resonance frequencies and MAC values of the FLEX model of the ASEA robot

frequencies [Hz]	experiments		FLEX-model		deviations	
	position 1	position 2	position 1	position 2	position 1	position 2
f1	8.05	9.32	8.25	8.96	+2.5 %	-3.9 %
f2	10.91	10.01	11.00	9.97	+0.8 %	-0.4 %
f3	18.83	15.93	16.01	15.35	-15.9 %	-3.6 %

position 1			
exp. / anal.	1	2	3
1	0.96	0.06	0.16
2	0.02	0.84	0.00
3	0.00	0.00	0.89

position 2			
exp. / anal.	1	2	3
1	0.86	0.17	0.03
2	0.13	0.74	0.06
3	0.01	0.02	0.62

The stiffness values of the two flexible joints and the coupling with the environment are iteratively determined. First of all, the three lowest resonance frequencies for the two measuring positions of the robot are taken into account to determine the stiffness values. The correspondence between the experimental modes Φ_e and numerical modes Φ_n, however, is also taken into account; this can be evaluated using the Modal Assurance Criterion:

$$\mathrm{MAC}(\{\Phi_e\},\{\Phi_n\}) = \frac{(\{\Phi_e\}^T\{\Phi_n\})}{(\{\Phi_e\}^T\{\Phi_e\})(\{\Phi_n\}^T\{\Phi_n\})} . \tag{10}$$

The more the MAC value approximates 1, the better is this correspondence. To evaluate this formula, a point correspondence file between measuring points and nodes of the numerical model has to be created. Therefore, nodes are added to the model in the neighborhood of the measuring points. Optimal tuning of the model results in the resonance frequencies and MAC values for the three lowest modes shown in Table 3.

The MAC value of a simple mechanical construction should be at least 0.95 for good correspondence between numerical and experimental modes. The MAC values obtained for the ASEA robot can nevertheless be considered as quite good because this robot is a very complex structure. This appears, for instance, from the highly-damped modes. Figure 9 confirms the good correspondence of the modes. The MAC value of the third resonance frequency in position 2 can be improved, but at the expense of a larger underestimation of the third resonance frequency. The underestimation is probably due to an inaccurate estimation of the mass distribution of the links. Model updating for each separate link would, presumably, make the global model more reliable (Janter, Heylen, Liefooghe, and Sas). On the other hand, the nonlinearity of the third mode of the ASEA robot cannot be neglected. Therefore, a fine tuning of this resonance frequency makes no sense.

4.5 Influence of the Position. The purpose of this study was to verify the influence of the position of the robot on its resonance frequencies. With the FLEX model the robot was analyzed in 11 different positions; these positions are chosen so that the end of the forearm moves along a straight line through the two measuring points. This choice is made to have

Downloaded 03 May 2010 to 171.66.16.31. Redistribution subject to ASME license or copyright; see http://www.asme.org/terms/Terms_Use.cfm

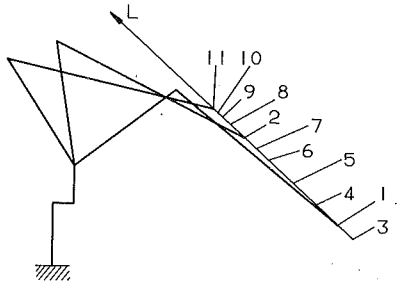


Fig. 11 Positions of the ASEA robot in which the resonance frequencies are analyzed

a meaningful graphical representation of the resonance frequencies with the distance L as parameter (Fig. 11). From Fig. 12 it can be concluded that the variance of the resonance frequencies with the position is limited to about 10 percent for most of the range, but there is no simple linear relationship. When the robot approaches the extreme positions 3 and 11, the variance of the resonance frequencies becomes more than 10 percent.

5 Conclusions

In this paper an efficient method has been proposed to calculate the dynamic characteristics of a flexible structure. The construction is divided into several components and the dynamic model of each separate link is obtained from a general finite element analysis. These components may be modeled in detail because the Component Mode Synthesis (CMS) strongly reduces the number of degrees-of-freedom. These models are assembled into a global model using compatibility matrices. These compatibility matrices can be composed automatically when the separate link dynamic equations are first transformed to a global frame. This method has been implemented in a program package FLEX. The possibility to define flexible joints between two links is included.

The method was first applied to two examples of flexible structures. From the second example (a fictive robot with three links), it appears that good dynamic accuracy can be achieved despite the reduction of the number of degrees-of-freedom by CMS. To be safe, however, the frequency limit f^* for selection of the modes for each link has to be taken at 1.5 f, with f the limit of the frequency band of interest. An important advantage of the FLEX programs, with respect to general finite element calculations, is the reduction of the effective computation time (CPU time) to obtain the resonance frequencies of the flexible robot in different positions. From the examples it is also clear the CMS with fixed-fixed modes gives the most reliable resonance frequencies.

Finally, the FLEX programs have been applied to an industrial robot manipulator. The numerical model has been tuned, and the results are found to compare well with the experimental data. The study of this robot with the FLEX programs shows that there is a rather strong influence of the position of the robot on its resonance frequencies. The numerical method presented in this paper may provide a useful numerical tool to design relatively light-weight, high-speed manipulators which would be more productive than currently available systems.

Acknowledgments

This research was performed in the framework of the ESPRIT project 1561 SACODY.

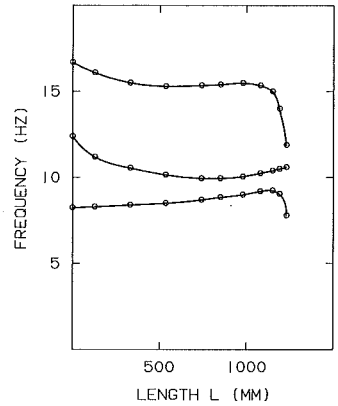


Fig. 12 Influence of the position of the robot on the resonance frequencies

References

Alberts, T. E., Dickerson, S. L., and Book, W. J., 1985, "Modeling of Flexible Manipulators," *Proceedings of ROBOTS9 Conference*, Vol. 1, pp. 59–71.

Book, W. J., Maizza-Neto, O., and Whitney, D. E., 1975, "Feedback Control of Two Beam, Two Joint Systems With Distributed Flexibility," *Journal of Dynamic Systems, Measurement, and Control*, pp. 424–431.

Denavit, J., and Hartenberg, R. S., 1955, "A Kinematic Notation for Lower Pair Mechanisms Based on Matrices," ASME JOURNAL OF APPLIED MECHANICS, Vol. 22, pp. 215–221.

De Smet, M., and Liefooghe, C., 1987, *Dynamische analyse van flexibele robots*, Thesis, Faculty of Applied Sciences, Katholieke Universiteit Leuven, Leuven, Belgium.

Framatome, S. A., 1987, *SYSTUS - Finite Element System: TITUS-Users' Manual*, Vol. I, II, Version 229, Saint-Marcel, France.

Guyan, R. J., 1965, "Reduction of Stiffness and Mass Matrices," *AIAA Journal*, Vol. 3, p. 380.

Iida, H., Oono, T., Tamura, A., and Ono, K., 1986, "High Speed Positioning Control of a Fexible System," *Bulletin of JSME*, Vol. 29, No. 257, pp. 3899–3902.

Janter, T., Heylen, W., Liefooghe, C., and Sas, P., "Model Updating Based on User Acceptance Requirements," *12th Biennual ASME Conference on Mechanical Vibrations and Noise*, 1989, Montreal, Canada, in preparation.

Nagamatsu, M., and Ookuma, M., 1981, "Analysis of Vibration by Component Mode Synthesis Method (Part 1, Natural Frequency and Natural Mode (I))," *Bulletin of the JSME*, Vol. 24, No. 194, pp. 1448–1453.

Ookuma, M., and Nagamatsu, A., 1984a, "Analysis by Vibration by Component Mode Synthesis Method (Part 4, Natural Frequency and Natural Mode (II))," *Bulletin of the JSME*, Vol. 27, No. 225, pp. 529–533.

Ookuma, M., and Nagamatsu, A., 1984b, "Vibration Analysis by Multiple Component Mode Synthesis Methods," *Bulletin of the JSME*, Vol. 27, No. 228, pp. 1288–1293.

Ookuma, M., and Nagamatsu, A., 1985, "Vibration Analysis by Substructure Synthesis Method (Part 4, Calculation of Residual Compliance Matrix)," *Bulletin of the JSME*, Vol. 28, No. 239, pp. 905–910.

Shabana, A., and Wehage, R. A., 1983, "Variable-Degree-of-Freedom Component Mode Analysis of Variant Flexible Mechanical Systems," *Journal of Mechanisms, Transmissions, and Automation in Design*, Vol. 105, pp. 371–378.

Simons, J., and Van Brussel, H., 1983, *Zomercursus Mathematica, Programmatie en Controle van Industrile Robots*, Leuven, Belgium.

Sunada, W., 1980, *Finite Element Dynamic Analysis of Flexible Spatial Mechanisms and Manipulators*, Ph.D. thesis, School of Engineering and Applied Science, University of California, Los Angeles, Calif.

Sunada, W., and Dubowsky, S., 1981, "The Application of Finite Element Methods to the Dynamic Analysis of Flexible Spatial and Coplanar Linkage Systems," *Journal of Mechanical Design*, Vol. 103, pp. 643–651.

Sunada, W., and Dubowksy, S, 1983, "On the Dynamic Analysis and Behavior of Industrial Robotic Manipulators With Elastic Members," *Journal of Mechanisms, Transmissions, and Automation in Design*, Vol. 105, pp. 42–51.

Usoro, P. B., Nadira, R., and Mahil, S. S., 1986, "A Finite Element/Lagrange Approach to Modeling Light-Weight Flexible Manipulators," *Journal of Dynamic Systems, Measurement, and Control*, Vol. 108, pp. 198–205.

Downloaded 03 May 2010 to 171.66.16.31. Redistribution subject to ASME license or copyright; see http://www.asme.org/terms/Terms_Use.cfm

Free Wave Propagation in Plates of General Anisotropic Media

Adnan H. Nayfeh
Aerospace Engineering and Engineering Mechanics, University of Cincinnati, Cincinnati, Ohio 45221
Mem. ASME

D. E. Chimenti
Air Force Materials Laboratory, Wright-Patterson A.F.B., Ohio 45433

We develop the analysis for the propagation of free waves in a general anisotropic plate. We begin with a formal analysis of waves in a plate belonging to the triclinic symmetry group. The calculation is then carried forward for the slightly more specialized case of a monoclinic plate. We derive the secular equation for this case in closed form and isolate the mathematical conditions for symmetric and antisymmetric wave mode propagation in completely separate terms. Material systems of higher symmetry, such as orthotropic, transversely isotropic, cubic, and isotropic are contained implicitly in our analysis. We also demonstrate that the particle motions for Lamb and SH modes uncouple if propagation occurs along an in-plane axis of symmetry. We present numerical free-wave dispersion results drawn from concrete examples of materials belonging to several of these symmetry groups.

Introduction

The propagation of Lamb waves in plates has been the subject of numerous investigations since their postulation by Lamb in 1916. Most of this work deals with various aspects of these guided waves in plates of isotropic materials. Comparatively speaking, however, only a limited number of results has appeared in which Lamb or horizontally-polarized SH wave propagation in anisotropic plates has been considered in any detail. Some of the difficulties in the treatment of wave propagation in anisotropic plates can be illustrated by considering slowness wave surface methods for infinite media (Synge, 1957; Fedorov, 1968; Musgrave, 1970). According to this analysis, the slowness surface of an isotropic material consists of two concentric spherical sheets, an inner one representing the longitudinal wave mode and an outer one representing the two degenerate transverse modes. In the anisotropic case, we find there are three general wave surfaces, one for the so-called quasi-longitudinal wave and two nondegenerate sheets for the quasi-transverse waves. Moreover, the surfaces will no longer be spherical in shape but will reflect the elastic symmetry, or lack of it, of the material. In fact, it has recently been shown (Ledbetter and Kriz, 1982) that for orthorhombic symmetry the wave surfaces interconnect with one another, leading, in restricted cases, to a single topologically interpenetrating wave surface still describing the general anisotropic wave types.

Perhaps the most severe consequence of elastic anisotropy in infinite media is the loss of pure wave modes for general propagation directions. This fact also implies that the direction of energy flow (i.e., group velocity) does not generally coincide with the wave vector, or wave front normal (Fedorov, 1968). Clearly, uncoupled pure potentials (such as are found in the isotropic case) are much simpler to treat than the mixed modes characteristic of anisotropic materials. For wave propagation in directions of symmetry some wave types revert to pure modes, leading to a simpler characteristic equation of lower order.

Compared to the extensive literature on elastic waves in infinite anisotropic media, relatively less work can be found on the wave propagation problem in the presence of interfaces, i.e., guided waves. Here, we mention that several authors (Merkulov, 1963; Merkulov and Yakovlev, 1962; Musgrave, 1960; Gates, 1965; Joel, 1961; Henneke, 1972; Lim and Musgrave, 1970; Johnson, 1970; Chadwick and Currie, 1974; Rokhlin et al., 1986) have discussed, in varying degrees of depth, reflection and refraction of sound waves from interfaces of anisotropic media. The related problem of Rayleigh waves on anisotropic surfaces has received some attention from other workers (Buchwald, 1961; Buchwald and Davis, 1961, 1963; Gazis et al., 1960; Rollins et al., 1968; Lim and Farnell, 1969) since Stoneley (1955) first calculated the secular equations of Rayleigh surface wave propagation on a cubic half space. For Lamb waves, limited theoretical analyses have been reported in plates of cubic (Markus et al., 1985; Nikiforenko et al., 1972), transversely isotropic (Abubakar, 1962; Kosevich and Syrkin, 1985; Baylis and Green, 1986), and orthotropic (Moon, 1972; Solie and Auld, 1973) media. Further work on free waves in piezoelectric plates is reviewed by Auld (1973) and Wagers (1977). When we discuss waves in anisotropic plates the distinction between mode types is somewhat artificial, since the equations for classical Lamb and shear horizontal (SH) modes generally will be coupled. Therefore, we will refer to these modes as free waves in the plate.

In this paper, we develop the analysis for the propagation of

Contributed by the Applied Mechanics Division of THE AMERICAN SOCIETY OF MECHANICAL ENGINEERS for presentation at the Winter Annual Meeting, San Francisco, Calif., December 10–15, 1989.

Discussion on this paper should be addressed to the Editorial Department, ASME, United Engineering Center, 345 East 47th Street, New York, N.Y. 10017, and will be accepted until two months after final publication of the paper itself in the JOURNAL OF APPLIED MECHANICS. Manuscript received by the ASME Applied Mechanics Division, June 2, 1988; final revision, November 10, 1988. Paper No. 89-WA/APM-28.

Copyright © 1989 by ASME

Downloaded 03 May 2010 to 171.66.16.31. Redistribution subject to ASME license or copyright; see http://www.asme.org/terms/Terms_Use.cfm

free waves in a general anisotropic plate and present numerical results for some special cases of interest. We begin with a formal analysis for waves in a plate belonging to the triclinic symmetry group (the most general, with 21 independent elastic constants). The calculation is then carried forward for the slightly more specialized case of a monoclinic plate (13 independent elastic constants), where the surface of the plate is parallel with the single plane of mirror symmetry in this material system. We derive the secular equation for this case in closed form and isolate the mathematical conditions for symmetric and antisymmetric wave mode propagation in completely separate terms. Material systems of higher symmetry, such as orthotropic, transversely isotropic, cubic, and isotropic are contained implicitly in our analysis. The equivalent crystal systems of monoclinic, orthorhombic, hexagonal, and cubic may be substituted for the elastic material systems analyzed here. We demonstrate numerical free wave dispersion results drawn from concrete examples of materials belonging to several of these symmetry groups. For orthotropic and higher symmetry materials where the remaining two principal axes lie in the plane of the plate, the particle motions for Lamb and SH modes uncouple if propagation occurs along either of these in-plane axes.

A key condition which facilitates our subsequent analysis is that at any boundary, all wave vectors must lie in the same plane. This requirement implies that the response of the plate will be independent of the in-plane coordinate normal to the propagation direction (see Henneke (1972) and Jones (1971) for justification). We therefore conduct our analysis in a coordinate system formed by the guided wave vector direction, its in-plane normal, and the plate normal, rather than one determined by material symmetry axes. This choice leads to a significant simplification in our algebraic analysis and computations.

Theoretical Development

Consider an infinite generally-anisotropic plate, having thickness d, whose normal is aligned with the x_3'-axis of a reference cartesian coordinate system $x_i'=(x_1',x_2',x_3')$. The midplane of the plate is chosen to coincide with the x_1'-x_2' plane. With respect to this primed coordinate system, the equations of motion of the plate are given by

$$\frac{\partial \sigma_{ij}'}{\partial x_j'}=\rho'\frac{\partial^2 u_i'}{\partial t^2} \tag{1}$$

and the general constitutive relations

$$\sigma_{ij}'=c_{ijkl}'\,e_{kl}', \quad i,j,k,l,=1,2,3, \tag{2}$$

where σ_{ij}', e_{kl}', and u_i' are the components of stress, strain, and displacement, respectively, ρ' is the material density, and c_{ijkl}' are the elastic material constants. In equations (1) and (2), and in all subsequent analysis, the usual summation convention holds.

In what follows, we study the propagation of harmonic waves in a plate along a direction that makes an arbitrary azimuthal angle ϕ with the x_1'-axis. That is, the direction $\phi=0$ coincides with the reference coordinate x_1'. Since, as was pointed out in the introduction, the response of the plate to such a wave is independent of the in-plane coordinate transverse to the propagation direction, we can conduct our analysis in a transformed coordinate system x_i formed by a rotation of the orthogonal reference axes x_1', x_2' about the x_3' direction through the angle ϕ. This coordinate transformation obeys the relation

$$x_i=\beta_{ij}x_j' \tag{3}$$

where β_{ij} is the cosine of the angle between x_i and x_j'. In the rotated system we note that the elastic wave equations, for a plane wave propagating along x_1, are independent of x_2. Nonetheless, the particle motion can generally have three nonzero spatial components u_1, u_2, and u_3 corresponding to longitudinal waves (along the x_1-axis) and horizontally and vertically polarized transverse waves, respectively. In an anisotropic material, the equations describing these three wave motions will be coupled, complicating the analysis of free waves in the plate. For propagation along in-plane principal material axes, if they exist, the SH modes uncouple, yielding algebraic simplifications. In terms of the rotated coordinate system x_i, equations (1) and (2) transform via (3) to

$$\frac{\partial \sigma_{ij}}{\partial x_j}=\rho\frac{\partial^2 u_i}{\partial t^2}, \tag{4}$$

$$\sigma_{ij} = c_{ijkl}\,e_{kl}, \tag{5a}$$

with the transformed constitutive constants

$$c_{ijkl}=\beta_{im}\beta_{jn}\beta_{ko}\beta_{lp}c_{mnop}'. \tag{5b}$$

Substituting from equation (5) into equation (4) results in a system of three coupled equations for the displacements u_1, u_2, and u_3. Since plane wave propagation along the x_1-direction is independent of x_2, a formal solution for these displacements can be written as

$$u_j=U_j e^{i\xi(x_1+\alpha x_3-ct)}, \quad j=1,2,3, \tag{6}$$

where ξ is the wave number, $i=\sqrt{-1}$, c is the phase velocity $(=\omega/\xi)$, ω is the circular frequency, α is the ratio of the x_3 to x_1 wave numbers which is to be determined, and U_j is the displacement amplitude of u_j. This leads to the three coupled equations

$$K_{mn}(\alpha)U_n=0, \quad m,n=1,2,3 \tag{7}$$

where, again, the summation convention is implied, K_{mn} is symmetric, namely $K_{mn}=K_{nm}$ and

$$\begin{aligned}
K_{11} &= C_{11}-\rho c^2+2C_{15}\alpha+C_{55}\alpha^2\\
K_{12} &= C_{16}+(C_{14}+C_{56})\alpha+C_{45}\alpha^2\\
K_{13} &= C_{15}+(C_{13}+C_{55})\alpha+C_{35}\alpha^2\\
K_{22} &= C_{66}-\rho c^2+2C_{46}\alpha+C_{44}\alpha^2\\
K_{23} &= C_{56}+(C_{36}+C_{45})\alpha+C_{34}\alpha^2\\
K_{33} &= C_{55}-\rho c^2+2C_{35}\alpha+C_{33}\alpha^2.
\end{aligned} \tag{8}$$

In equation (8), we used the standard contracted subscript notations $1\rightarrow11$, $2\rightarrow22$, $3\rightarrow33$, $4\rightarrow23$, $5\rightarrow13$, and $6\rightarrow12$ to replace c_{ijkl} with C_{pq} ($i,j,k,l=1,2,3$ and $p,q=1,2,\ldots,6$). Thus, C_{56} stands for c_{1312}, for example.

The existence of nontrivial solutions for U_1, U_2, and U_3 demands the vanishing of the determinant in equation (7), which yields an algebraic equation relating α to c. We obtain a sixth-degree polynomial equation in α, which can be written formally as

$$\alpha^6+B_1\alpha^5+A_1\alpha^4+B_2\alpha^3+A_2\alpha^2+B_3\alpha+A_3=0. \tag{9}$$

Equation (9) admits six distinct solutions for α which we label as α_q, $q=1,2,\ldots,6$. For each α_q, we can use the relations of equation (7) and express the displacement ratios $V_q=U_{2q}/U_{1q}$ and $W_q=U_{3q}/U_{1q}$ as

$$V_q=\frac{K_{11}(\alpha_q)K_{23}(\alpha_q)-K_{13}(\alpha_q)K_{12}(\alpha_q)}{K_{13}(\alpha_q)K_{22}(\alpha_q)-K_{12}(\alpha_q)K_{23}(\alpha_q)} \tag{10}$$

$$W_q=\frac{K_{11}(\alpha_q)K_{23}(\alpha_q)-K_{12}(\alpha_q)K_{13}(\alpha_q)}{K_{12}(\alpha_q)K_{33}(\alpha_q)-K_{23}(\alpha_q)K_{13}(\alpha_q)}. \tag{11}$$

Combining equations (10) and (11) with the stress-strain relations (5), and using superposition, we write the formal solutions for the displacements and stresses as

Downloaded 03 May 2010 to 171.66.16.31. Redistribution subject to ASME license or copyright; see http://www.asme.org/terms/Terms_Use.cfm

$$(u_1,u_2,u_3)=\sum_{q=1}^{6}(1,V_q,W_q)U_{1q}e^{i\xi(x_1+\alpha_q x_3-ct)} \tag{12}$$

$$(\sigma_{33},\sigma_{13},\sigma_{23})=\sum_{q=1}^{6}i\xi(D_{1q},D_{2q},D_{3q})U_{1q}e^{i\xi(x_1+\alpha_q x_3-ct)} \tag{13}$$

where

$$D_{1q} = [C_{13}+\alpha_q C_{35}+(C_{36}+\alpha_q C_{34})V_q+(C_{35}+\alpha_q C_{33})W_q] \tag{14a}$$

$$D_{2q} = [C_{15}+\alpha_q C_{55}+(C_{56}+\alpha_q C_{45})V_q+(C_{55}+\alpha_q C_{35})W_q] \tag{14b}$$

$$D_{3q} = [C_{14}+\alpha_q C_{45}+(C_{46}+\alpha_q C_{44})V_q+(C_{45}+\alpha_q C_{34})W_q]. \tag{14c}$$

Calculating the stresses σ_{33}, σ_{13}, and σ_{23} of equation (13) at the upper and lower faces $x_3=d/2$ and $x_3=-d/2$, respectively, and setting them equal to zero to invoke the stress-free boundary conditions finally yield the six equations relating the propagation amplitudes U_{11}, U_{12}, . . . , U_{16}, whose determinant of coefficients is

$$\begin{vmatrix} D_{11}E_1 & D_{12}E_2 & D_{13}E_3 & D_{14}E_4 & D_{15}E_5 & D_{16}E_6 \\ D_{21}E_1 & D_{22}E_2 & D_{23}E_3 & D_{24}E_4 & D_{25}E_5 & D_{26}E_6 \\ D_{31}E_1 & D_{32}E_2 & D_{33}E_3 & D_{34}E_4 & D_{35}E_5 & D_{36}E_6 \\ D_{41}\bar{E}_1 & D_{42}\bar{E}_2 & D_{43}\bar{E}_3 & D_{44}\bar{E}_4 & D_{45}\bar{E}_5 & D_{46}\bar{E}_6 \\ D_{51}\bar{E}_1 & D_{52}\bar{E}_2 & D_{53}\bar{E}_3 & D_{54}\bar{E}_4 & D_{55}\bar{E}_5 & D_{56}\bar{E}_6 \\ D_{61}\bar{E}_1 & D_{62}\bar{E}_2 & D_{63}\bar{E}_3 & D_{64}\bar{E}_4 & D_{65}\bar{E}_5 & D_{66}\bar{E}_6 \end{vmatrix} = 0 \tag{15}$$

where

$$\bar{E}_q=E_q^{-1}=e^{-i\xi\alpha_q d/2}, \quad q=1, \ldots, 6. \tag{16}$$

Thus far we have presented only a formal analysis for free waves in a generally anisotropic plate, that is, one belonging to the triclinic symmetry group. With one plane of mirror symmetry, say $x_3=0$, eight property elements vanish by symmetry considerations, leaving thirteen independent constants. Such a material is termed monoclinic. If there are two orthogonal planes of mirror symmetry, the existence of a third mutually-orthogonal symmetry plane is assured. Materials with these characteristics are orthotropic and possess nine elastic constants. If, in addition, there exists a single plane in which all properties are independent of direction, we have a transversely isotropic material which can be described by five elastic constants. Starting again from the orthotropic case, if we now require interchangeability among the three coordinate axes, the material is cubic, and its elastic matrix has only three independent elements. Finally, complete spherical symmetry of mechanical properties implies an isotropic material needing only two independent constants. In the next heading we particularize the foregoing general treatment to a monoclinic material having its plane of mirror symmetry in the plane of the plate, and we derive explicit secular equations for symmetric and antisymmetric wave modes.

The Monoclinic Case

For monoclinic materials having $x_1'-x_2'$ as a plane of mirror symmetry, the following elastic stiffnesses vanish

$$C_{14}', C_{24}', C_{34}', C_{15}', C_{25}', C_{35}', C_{46}', C_{56}'=0. \tag{17}$$

Furthermore, their corresponding unprimed stiffnesses from equation (5*b*) also vanish for all aximuthal angles ϕ. Substituting the restrictions resulting from equation (17) into the general property relations of equations (8)–(14), we obtain considerable algebraic simplifications. Specifically, for a monoclinic material the coefficients of the simultaneous displacement equations in equation (8) can be expressed in simpler form, permitting important properties of the analytical solution of the reduced equation (9) for the α_q. Due to their subsequent importance, we list the $K_{mn}(\alpha)$ coefficients for the monoclinic case

$$\begin{aligned} K_{11} &= C_{11}-\rho c^2+C_{55}\alpha^2 \\ K_{12} &= C_{16}+C_{45}\alpha^2 \\ K_{13} &= (C_{13}+C_{55})\alpha \\ K_{22} &= C_{66}-\rho c^2+C_{44}\alpha^2 \\ K_{23} &= (C_{36}+C_{45})\alpha \\ K_{33} &= C_{55}-\rho c^2+C_{33}\alpha^2. \end{aligned} \tag{18}$$

The reduced complexity of the relations in equation (18) results in the vanishing of the coefficients of the odd powers of α in equation (9) which leaves

$$\alpha^6+A_1\alpha^4+A_2\alpha^2+A_3=0 \tag{19}$$

where, for this monoclinic case, the coefficients A_1, A_2, and A_3, are given in the Appendix. Equation (19) admits six solutions for α (having the properties)

$$\alpha_2=-\alpha_1, \alpha_4=-\alpha_3, \alpha_6=-\alpha_5. \tag{20}$$

Incorporating equations (20) and (17) in equations (10)–(14), and inspecting the resulting relations, we conclude that monoclinic symmetry implies the further restrictions

$$W_{j+1}=-W_j, \quad D_{2j+1}=-D_{2j}, \quad D_{3j+1}=-D_{3j}$$
$$V_{j+1}=V_j, \quad D_{1j+1}=D_{1j}, \quad j=1,3,5 \tag{21}$$

where now

$$D_q = [C_{13}+C_{36}V_q+C_{33}\alpha_q W_q] \tag{22a}$$

$$D_{2q} = [C_{55}(\alpha_q+W_q)+C_{45}\alpha_q V_q] \tag{22b}$$

$$D_{3q} = [C_{45}(\alpha_q+W_q)+C_{44}\alpha_q V_q], \; q=1,2, \ldots, 6. \tag{22c}$$

Substituting from equations (21) and (22) into (15) prepares the way for algebraic manipulations and reductions of the monoclinic determinantal characteristic equation. Due to the complexity of the manipulation procedure, we will list only the various steps taken in their chronological order.

In the first step, we add the second column to the first, the fourth to the third, and the sixth to the fifth. In the second step, we add the original first column to the negative of the second, the third to the negative of the fourth, and the fifth to the negative of the sixth. In the third step, we exchange columns two and five. After these steps, one can easily see by either adding or subtracting various rows that the determinant can be reduced and partitioned to a 2×2 diagonal matrix whose entries comprise 3×3 square matrices. The determinant can therefore be separated, leading to the two uncoupled characteristic equations

$$D_{11}G_1\cot(\gamma\alpha_1)-D_{13}G_3\cot(\gamma\alpha_3)+D_{15}G_5\cot(\gamma\alpha_5)=0 \tag{23a}$$

$$D_{11}G_1\tan(\gamma\alpha_1)-D_{13}G_3\tan(\gamma\alpha_3)+D_{15}G_5\tan(\gamma\alpha_5)=0 \tag{23b}$$

corresponding to symmetric and antisymmetric modes, respectively, with

$$G_1=D_{23}D_{35}-D_{33}D_{25}, \quad G_3=D_{31}D_{25}-D_{21}D_{35}, \tag{24a}$$

$$G_5=D_{21}D_{33}-D_{31}D_{23}, \quad \gamma=\xi d/2=\omega d/2c. \tag{24b}$$

Downloaded 03 May 2010 to 171.66.16.31. Redistribution subject to ASME license or copyright; see http://www.asme.org/terms/Terms_Use.cfm

Table 1

Property (GPa)	Orthotropic Fictitious	Transversely Isotropic Graphite-Epoxy Nayfeh (1988)	Cubic Nickel Farnell (1972)
C'_{11}	128	155.6	261
C'_{12}	7	3.7	151
C'_{13}	6	3.7	151
C'_{22}	72	15.95	261
C'_{23}	5	4.33	151
C'_{33}	32	15.95	261
C'_{44}	18	5.81	130.9
C'_{55}	12.25	7.46	130.9
C'_{66}	8	7.46	130.9
$\rho(g/cm^3)$	2.0	1.6	8.91

Higher Symmetry Materials

The results of equations (23) obtained for the monoclinic case can, under restricted conditions, also hold for higher symmetry classes such as orthotropic, transversely isotropic, and cubic. Recognizing that these classes of materials are different from the monoclinic material in that each can possess two orthogonal principal axes in the plane of the plate, equations (23) apply if the wave propagates along directions other than these axes. This is due to the fact that coupling of the SH wave field equations with those of the classical Lamb wave will persist. Uncoupling of these equations occurs, on the other hand, for propagation along axes of rotational symmetry, resulting in simplified versions of equations (23 *a,b*). Here, we also recognize that results for all symmetry classes higher than orthotropic (which include transversely isotropic, cubic, and isotropic) are contained as special cases of the corresponding solutions for the orthotropic case. Thus, once the characteristic equations for propagation either off or along principal axes are derived for orthotropic symmetry, the corresponding results for the higher symmetry materials can be obtained merely by applying the appropriate restrictions on their properties. For this reason, we now concentrate on deriving results for orthotropic symmetry.

Propagation Off Principal Axes. For off-principal-axis propagation, one needs only to assure that further appropriate reductions in the number of nonzero elastic constants are exploited in equations (23*a*, *b*). If x'_1 and x'_2 of equation (2) are chosen to coincide with the in-plane principal axes for orthotropic symmetry, then besides the vanishing of the constants in equation (17), we have that

$$C'_{16}, C'_{26}, C'_{36}, C'_{45} = 0. \tag{25}$$

These reductions leave nine independent constants $C'_{11}, C'_{12}, C'_{13}, C'_{22}, C'_{23}, C'_{33}, C'_{44}, C'_{55}$, and C'_{66}. Results for material possessing transverse isotropy, whose x'_1 axis is normal to the plane of isotropy, can be easily obtained from equations (23) by noting the additional conditions imposed by symmetry, namely

$$C'_{33} = C'_{22}, \quad C'_{13} = C'_{12}, \quad C'_{55} = C'_{66}, \quad C'_{22} - C'_{23} = 2C'_{44} \tag{26}$$

on the nine constants describing the orthotropic case. Finally, the presence of cubic symmetry requires

$$C'_{11} = C'_{22} = C'_{33}, \quad C'_{12} = C'_{13} = C'_{23}, \quad C'_{44} = C'_{55} = C'_{66}. \tag{27}$$

Propagation Along Axes of Rotational Symmetry. Returning to the case of orthotropic symmetry, we note that the axis x'_1 and x'_2 coincide with the axiumthal angles $\phi = 0$ and $\phi = 90$ deg, respectively. We substitute from equations (17) and (25), which particularize the constitutive relations (2) to orthotropic media, into the coefficients of the Appendix. Inspection of the resulting entries leads to the conclusion that, for propagation along rotational symmetry axes, the matrix elements C_{16}, C_{26}, C_{36}, and C_{45} also vanish. This simplification of the elastic stiffness matrix has implications for the analysis commencing at equation (18). Of greatest importance is the fact that K_{12} and K_{23} in equation (18) vanish. This result means that the SH wave motions uncouple from those of the Lamb type. As a consequence, equation (19) leads for $\phi = 0$ to the simpler solution for the α_k

$$\alpha_{1,3} = \frac{-B \pm [B^2 - 4AC]^{1/2}}{2A}, \quad \alpha_2 = -\alpha_1, \quad \alpha_4 = -\alpha_3 \tag{27}$$

$$\alpha_5 = -\alpha_6 = [(\rho c^2 - C_{66})/C_{44}]^{1/2} \tag{28}$$

with

$$\begin{aligned} A &= C_{33}C_{55} \\ B &= (C_{11} - \rho c^2)C_{33} - (C_{55} - \rho c^2)C_{55} - (C_{13} + C_{55})^2 \\ C &= (C_{11} - \rho c^2)(C_{55} - \rho c^2). \end{aligned} \tag{29}$$

For each α_k, $k = 1,2,3,4$, the displacements and stress amplitudes reduce to

$$\begin{aligned} W_k &= \frac{\rho c^2 - C_{11} - C_{55}\alpha_k^2}{(C_{13} + C_{55})\alpha_k} \\ D_{1k} &= (C_{13} + C_{33}\alpha_k W_k), \\ D_{2k} &= C_{55}(\alpha_k + W_k). \end{aligned} \tag{30}$$

For the SH-type wave, one now has

$$D_{36} = -D_{35} = C_{44}\alpha_5. \tag{31}$$

By employing the new relations (27)–(31), and following the matrix reduction steps used in obtaining the results of equations (23), one gets the reduced uncoupled characteristic equation

$$D_{11}D_{23}\cot(\gamma\alpha_1) - D_{13}D_{21}\cot(\gamma\alpha_3) = 0 \tag{32a}$$

$$D_{11}D_{23}\tan(\gamma\alpha_1) - D_{13}D_{21}\tan(\gamma\alpha_3) = 0, \tag{32b}$$

$$\sin(2\gamma\alpha_5) = 0, \tag{32c}$$

with γ as defined in equation (24*b*).

The results (32*a*, *b*), with their parameters defined in equations (27) and (30), constitute the characteristic equations for symmetric and antisymmetric modes for Lamb waves propagating along an in-plane axis of symmetry of an orthotropic plate. Equation (32*c*), alternatively, is the characteristic equation of a horizontally-polarized SH wave on the same plate. The two wave types uncouple since the wave vector is along the axis of symmetry. Furthermore, the relation (32) implicitly contains corresponding results for materials possessing higher than orthotropic symmetry. These include transversely isotropic, cubic, and isotropic. Here, one needs only to exploit the appropriate restrictions on the elastic properties as described in equations (26) and (27).

Numerical Examples

In this section, we illustrate the analytical results derived in the previous section with a limited selection of numerical examples drawn from the several material symmetry classes we have considered. While the cases we present here are certainly typical, they are by no means exhaustive of the variety of phenomenology contained in our analysis. In each instance we present phase velocity dispersion curves plotted as a function of the product of frequency and plate thickness. These curves have been calculated from expressions based on the dispersion relations in equations (23) and (32), suitably modified according to details of the symmetry class and the propagation direction under study. For the elastic stiffnesses, we have chosen to model materials of interest where values of the C_{pq} were readily available. In the cases of lower symmetry, namely

Downloaded 03 May 2010 to 171.66.16.31. Redistribution subject to ASME license or copyright; see http://www.asme.org/terms/Terms_Use.cfm

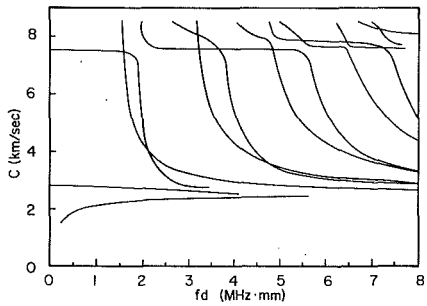


Fig. 1 Dispersion relation curves for a plate having monoclinic material symmetry with propagation along $\phi = 0$ deg

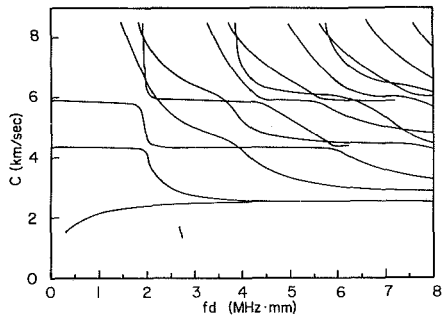


Fig. 2 Dispersion relation curves for an orthotropic plate whose properties are listed in Table 1; propagation is along $\phi = 45$ deg

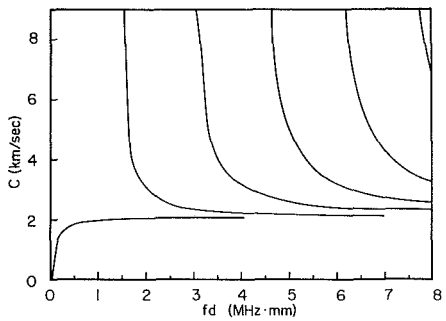


Fig. 3 Dispersion relation curves for a transversely isotropic graphite-epoxy plate with propagation along $\phi = 0$ deg

monoclinic, our approach has been to construct the elastic properties from those of known, higher symmetry material by applying the rotational tensor transformation outlined in the analysis. This transformation yields a covariant, but more fully populated, elastic tensor from which elastic properties are derived. The C_{pq} for the numerical examples considered here are collected in Table 1.

In Fig. 1 are shown dispersion curves for a monoclinic material whose plane of mirror symmetry is coincident with the plate surface. The elastic properties used are constructed from a 20 deg rotation of those listed in Table 1 for the orthotropic symmetry material. Since there is no in-plane principal axis, a propagation direction has been arbitrarily chosen. Beyond the complexity of the curves, an unusual feature is the existence of an additional mode at low fd. Free wave dispersion in an orthotropic material is given in Fig. 2 for propagation at 45 deg to the principal in-plane axes. Here, the behavior is similar in complexity and appearance to the monoclinic case. This result is anticipated since the orthotropic elastic properties for off-principal-axis propagation will have the same number of nonzero elements as in the monoclinic case.

Moving to higher symmetry classes, we now illustrate the case of transverse isotropy. Figure 3 shows free waves in a graphite-epoxy composite, where the propagation direction is normal to the plane of isotropy. We label this direction 0 deg.

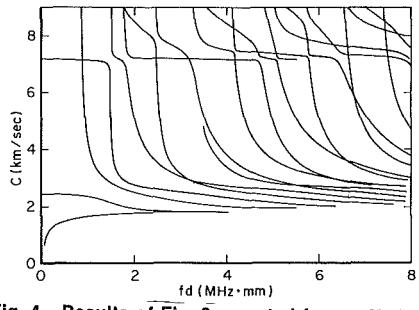


Fig. 4 Results of Fig. 3 repeated for $\phi = 45$ deg

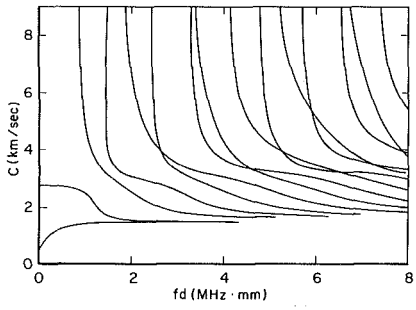


Fig. 5 Results of Fig. 3 repeated for $\phi = 90$ deg

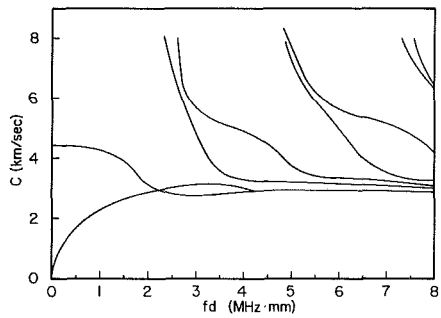


Fig. 6 Dispersion relation curves for a cubic nickel plate with propagation along a principal axis, i.e., $\phi = 0$ deg or 90 deg

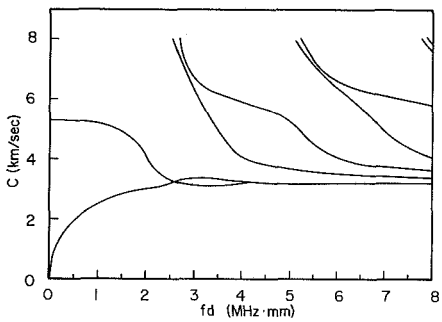


Fig. 7 Results of Fig. 6 repeated for $\phi = 45$ deg

The very high stiffness of the graphite fibers is apparent in the details of the curves in Fig. 3. That is, the turning of the lowest-order symmetric mode curve to approach the C-axis at low fd occurs at such a large value of phase velocity (namely, 9.8 km/s) that it cannot be seen on the figure. For propagation in the 45 deg direction, the transformed elastic properties soften, and the full range of this mode is visible, as shown in Fig. 4. Eventually, in the 90 deg direction, propagation occurs in the plane of isotropy. The dramatic decrease in the values of the material properties, caused by the low transverse fiber modulus and the morphology of the composite, is apparent in the dispersion behavior shown in Fig. 5. The zeroth-order symmetric mode, which is related to Young's modulus at low fd, intersects the vertical axis at a much lower value of phase velocity than in Figs. 3 or 4.

Downloaded 03 May 2010 to 171.66.16.31. Redistribution subject to ASME license or copyright; see http://www.asme.org/terms/Terms_Use.cfm

The last two examples are for the case of cubic symmetry. We have chosen to model a nickel plate, and in Fig. 6 are the dispersion curves for free wave propagation along a principal cubic axis. An interesting feature of the two fundamental modes is that they cross at values of about 2.2 and 4.5 MHz-mm, approaching each other at high fd where the phase velocity tends toward the Rayleigh surface wave speed. Propagation at 45 deg to two orthogonal cubic axes is illustrated in Fig. 7. Similar behavior is observed in this set of mode curves, reflecting the fact that nickel is only moderately anisotropic.

Summary

We have considered the problem of guided elastic wave propagation in free plates exhibiting arbitrary anisotropy. For the most general case, triclinic symmetry, we have provided an exact formal solution for the displacements and stresses in the plate. Moving to the slightly less general case of monoclinic symmetry, we have solved exactly for the dispersion equation of free waves, employing algebraic reductions to express the results in a compact form. It is assumed in this and all other cases that the plate surface contains a material mirror symmetry plane. Exploiting the monoclinic solution as a starting point, we have constructed, or shown how to construct, dispersion relations for plates having orthotropic, transversely isotropic, and cubic symmetry, whereby free waves may propagate in any arbitrary in-plane direction. These analytical results are illustrated by numerical calculations of free wave velocity dispersion in materials representing the symmetry classes considered here and for several in-plane propagation directions.

Acknowledgment

This work has been supported by AFOSR.

References

Abubakar, I., 1962, "Free Vibrations of a Transversely Isotropic Plate," *Quarterly Journal of Mechanics and Applied Mathematics*, Vol. 15, pp. 129–136.

Baylis, E. R., and Green, W. A., 1986, "Flexural Waves in Fiber Reinforced Laminated Plates," *Journal of Sound and Vibration*, Vol. 110, pp. 1–26.

Buchwald, V. T., 1961, "Rayleigh Waves in Anisotropic Media," *Quarterly Journal of Mechanics and Applied Mathematics*, Vol. 14, pp. 461–469.

Buchwald, V. T., and Davis, A., 1961, "Surface Waves in Anisotropic Elastic Media," *Nature* (London), Vol. 191, pp. 899–900.

Buchwald, V. T., and Davis, A., 1963, "Surface Waves in Elastic Media with Cubic Symmetry," *Quarterly Journal of Mechanics and Applied Mathematics*, Vol. 16, pp. 283–294.

Chadwick, P., and Curried, P. K., 1974, "Stoneley Waves at at Interface Between Elastic Crystals," *Quarterly Journal of Mechanics and Applied Mathematics*, Vol. 27, pp. 497–503.

Farnell, G. W., and Adler, E. L., 1972, "Elastic Waves Propagation in Thin Layers," in *Physical Acoustics*, Vol. 9, W. P. Mason and R. N. Thurston, eds., Academic Press, New York, pp. 35–128.

Fedorov, F. I., 1968, *Theory of Elastic Waves in Crystals*, Plenum, New York.

Gates, E., 1965, "Propagation and Oblique Reflection of Slant-Mode Hypersonic Waves in Quartz," *Applied Physics Letters*, Vol. 7, pp. 187–189.

Gazis, D. C., Herman, R., and Wallis, R. F., 1960, "Surface Elastic Waves in Cubic Crystals," *Physical Review*, Vol. 119, pp. 533–544.

Henneke, H. E. G., 1972, "Reflection-Refraction of a Stress Wave at a Plane Boundary Between Anisotropic Media," *Journal of the Acoustical Society of America*, Vol. 51, pp. 210–217.

Joel, N., 1961, "Reflection and Polarization of Elastic Waves in a LiF Crystal: Mode Conversion from Longitudinal to Transverse," *Proc. Physical Society*, Sec. A, Vol. 78, pp. 38–45.

Johnson, W. W., 1970, "The Propagation of Stoneley and Rayleigh Waves in Anisotropic Elastic Media," *Bulletin of the Seismological Society of America*, Vol. 60, pp. 1105–1121.

Jones, A. T., 1971, "Exact Natural Frequencies and Modal Functions for a Thick Off-axis Lamina," *Journal of Composite Materials*, Vol. 5, pp. 504–520.

Kosevich, Yu., A., and Syrkin, E. S., 1985, "Elastic Waves in Plates of Highly Anisotropic Crystals," *Soviet Physics Acoustics*, Vol. 31, pp. 365–367.

Kulkarni, S. V., and Pagano, N. J., 1972, "Dynamic Characteristics of Composite Laminates," *Journal of Sound and Vibration*, Vol. 123, pp. 127–143.

Lamb, H., 1917, "Waves in an Elastic Plate," *Proc. Royal Society*, (London), Ser. A., Vol. 93, pp. 114–128.

Ledbetter, H. M., and Kriz, R. D., 1982, "Elastic-wave Surfaces in Solids," *Physica Status Solidi* (*B*), Vol. 144, pp. 475–480.

Lim, T. C., and Farnell, G. W., 1969, "Character of Pseudo Surface Waves on Anisotropic Crystals," *Journal of the Acoustic Society of America*, Vol. 45, pp. 845–851.

Lim, T. C., and Musgrave, M. J. P., 1970, "Stoneley Waves in Anisotropic Media," *Nature*, Vol. 225, p. 372.

Markus, S. A., Kaplan, M. D., and Veremeenko, S. V., 1985, "Propagation of Normal Waves in Orthotropic Plates," *Soviet Journal of Nondestructive Testing*, Vol. 21, p. 739.

Merkulov, L. G., 1963, "Ultrasonic Waves in Crystals," *Applied Material Res.*, Vol. 2, pp. 231–240.

Merkulov, L. G., and Yakovlev, L. A., 1962, "Propagation and Reflection of Ultrasonic Beams in Crystals," *Soviet Physics Acoustics*, Vol. 8, pp. 72–77.

Moon, F. C., 1972, "Wave Surfaces Due to Impact on Anisotropic Plates," *Journal of Composite Materials*," Vol. 6, pp. 62–79.

Musgrave, M. J. P., 1960, "Reflection and Refraction of Plane Elastic Waves at a Plane Boundary of Aelotropic Media," *Geophysics*, Vol. 3, pp. 406–418.

Musgrave, M. J. P., 1970, *Crystal Acoustics*, Holden Day, San Francisco, Calif.

Nayfeh, A. H., and Chimenti, D. E., 1988a, "Propagation of Guided Waves in Fluid-Coupled Plates of Fiber-Reinforced Composites," *Journal of the Acoustical Society of America*, Vol. 83, p. 1736.

Nayfeh, A. H., and Chimenti, D. E., 1988b, "Ultrasonic Wave Reflection From Liquid-Coupled Orthotropic Plates with Application to Fibrous Composites," ASME JOURNAL OF APPLIED MECHANICS, Vol. 55, pp. 863–870. (Note that C_{11} quoted in Table 1 should read 155.6 GPA).

Nikiforenki, Zh. G., Bobrov, V. T., and Averbukh, I. I., 1972, "Propagation of Lamb Waves in Anisotropic Sheets," *Soviet Journal of Nondestructive Testing*, Vol. 8, p. 543.

Rokhlin, S. I., Bolland, T. K., and Adler, L., 1986, "Reflection and Refraction of Elastic Waves on a Plane Interface between Two Generally Anisotropic Media," *Journal of the Acoustical Society of America*, Vol. 79, pp. 906–918.

Rollins, F. R., Lim, T. C., and Farnell, G. W., 1968, "Ultrasonic Reflectivity and Surface Wave Phenomena on Surfaces of Copper Crystals," *Applied Physics Letters*, Vol. 12, pp. 236–238.

Solie, L. P., and Auld, B. A., 1973, "Elastic Waves in Free Anisotropic Plates," *Journal of the Acoustical Society of America*, Vol. 54, pp. 50–65.

Stoneley, R., 1955, "The Propagation of the Surfaces Elastic Waves in a Cubic Crystal," *Proc. Royal Society of Acoustics*, Vol. 232, pp. 447–448.

Synge, J. L., 1957, "Elastic Waves in Anisotropic Media," *Journal of Mathematical Physics*, Vol. 25, pp. 323–334.

Thompson, R. B., Lee, S. C., and Smith, J. F., 1987, "Relative Anisotropies of Plane Waves and Guided Modes in Thin Orthohombic Plates: Implication for Texture Characterization," *Ultrasonics*, Vol. 25, pp. 133–137.

Viktorov, I. A. M., 1967, *Rayleigh and Lamb Waves*, Plenum, New York.

Wagers, R. S., 1977, "Plate Modes in Surface Acoustic Wave Devices," *Physical Acoustics*, Vol. 14, W. P. Mason and R. N. Thurston, eds., Academic Press, New York, pp. 49–78.

APPENDIX

The coefficients of equation (19) are given by

$$
\begin{aligned}
A_1 &= [C_{11}C_{33}C_{44} - C_{13}^2C_{44} + 2C_{13}C_{36}C_{45} - 2C_{13}C_{44}C_{55} \\
&\quad + C_{13}C_{45}^2 - 2C_{16}C_{33}C_{45} + C_{33}C_{55}C_{66} - C_{36}^2C_{55} \\
&\quad - (C_{33}C_{44} + C_{33}C_{55} + C_{44}C_{55} - C_{45}^2)\rho c^2]/\Delta \\
A_2 &= [C_{11}C_{33}C_{66} - C_{11}C_{36}^2 - 2C_{11}C_{36}C_{45} + C_{11}C_{44}C_{55} \\
&\quad - C_{11}C_{45}^2 + C_{13}^2C_{66} \\
&\quad + 2C_{13}C_{16}C_{36} + 2C_{13}C_{16}C_{45} \\
&\quad - 2C_{13}C_{55}C_{66} - C_{16}^2C_{33} + 2C_{16}C_{36}C_{55} \\
&\quad - (C_{11}C_{33} + C_{11}C_{44} - C_{13}^2 - 2C_{13}C_{55}) - 2C_{16}C_{45}) \\
&\quad + C_{33}C_{66} - C_{36}^2 - 2C_{36}C_{45} + C_{44}C_{55} - C_{45}^2 + C_{55}C_{66})\rho c^2 \\
&\quad + (C_{33} + C_{44} + C_{55})\rho^2c^4]/\Delta \\
A_3 &= [C_{11}C_{55}C_{66} - C_{16}^2C_{55} - (C_{11}C_{55} + C_{11}C_{66} \\
&\quad + C_{16}^2 + C_{55}C_{66})\rho c^2 \\
&\quad + (C_{11} + C_{55} + C_{66})\rho^2c^4 - \rho^3c^6]/\Delta \\
\Delta &= C_{33}C_{44}C_{55} - C_{33}C_{45}^2.
\end{aligned}
$$

Downloaded 03 May 2010 to 171.66.16.31. Redistribution subject to ASME license or copyright; see http://www.asme.org/terms/Terms_Use.cfm

A. K. Banerjee
Senior Staff Engineer,
Lockheed Missiles and Space Co.,
Sunnyvale, CA 94089

T. R. Kane
Professor of Applied Mechanics,
Stanford University,
Stanford, CA 94305
Fellow ASME

Dynamics of a Plate in Large Overall Motion

Equations of motion are formulated for a thin elastic plate that is executing small motions relative to a reference frame undergoing large rigid body motions (three-dimensional rotation and translation) in a Newtonian reference frame. As an illustrative example, a spin-up maneuver for a simply-supported rectangular plate is examined, and the vibration modes of such a plate are used to show that the present theory captures the phenomenon of dynamic stiffening.

1 Introduction

Dynamics of flexible bodies in large overall motion is a subject of considerable current interest because of its relevance to problems encountered in the fields of spaceflight and robotics. Moreover, as was pointed out by Kane, Ryan, and Banerjee (1987) for the case of a beam undergoing such motions, certain rather widely used multibody computer programs intended to deal with problems of this kind can produce erroneous results. The present paper extends the analysis of Kane, Ryan, and Banerjee (1987) to plates.

Figure 1 shows a rectangular plate whose displacements are to be measured with respect to a reference frame R in which orthogonal unit vectors $\mathbf{r}_1$, $\mathbf{r}_2$, $\mathbf{r}_3$ are fixed. Point O designates a particle of the plate fixed in R, and the plate is assumed to be executing small motions in R while R is undergoing large and rapid rigid body motions of rotation and translation in a Newtonian reference frame N; that is, both the orientation of the triad $\mathbf{r}_1$, $\mathbf{r}_2$, $\mathbf{r}_3$ in N and the position of O in N are unrestricted and can change rapidly. Our objective is to produce an algorithm that can be used to simulate motions of the plate when the motion of R in N is given.

Referring to Fig. 1, regard R as a rigid body, and suppose that a 72-in. × 48-in. × 0.1-in. rectangular plate is simply-supported by R along all four edges of the plate, the 72-in.-long edge coinciding with X_1, and the 48-in.-long one coinciding with X_2. Let R undergo a spin-up motion such that X_2 remains fixed in N and ω_2, the $\mathbf{r}_2$ measure number of the angular velocity of R in N, measured in radius per second, is given by

$$\omega_2 = \begin{cases} \dfrac{2\pi t^*}{60\, t^*}\left(t - \dfrac{t^*}{2\pi}\sin\dfrac{2\pi t}{t^*}\right), & t \le t^*; \\ \dfrac{2\pi n^*}{60}, & t > t^*; \end{cases}$$

where n^* is the ultimate spin speed, in revolutions per minute, and t^* is the spin-up time, in seconds. Under these circumstances, Q, the center point of the plate, must experience a deflection, say u_3^Q, parallel to the X_3 axis, and one can predict this deflection in qualitative terms on physical grounds: Initially, u_3^Q is equal to zero. As R begins to rotate, Q must begin to move in the direction of $\mathbf{r}_3$ so that u_3^Q takes on positive values, because, at first the plate cannot keep up with R. But soon restoring forces arising from the elasticity of the plate make themselves felt, and eventually they become sufficiently large not only to arrest the growth of u_3^Q but to cause u_3^Q to decrease. Indeed, sooner or later Q should not only catch up with R, that is, u_3^Q should become equal to zero, but Q should overshoot its original position in R, in which event u_3^Q takes on negative values; and after R has settled down, that is, once ω_2 has reached its maximum value, from which time onward R is rotating with a constant angular speed, it is to be expected that a residual "ringing" will take place, that is, that u_3^Q will have an oscillatory character. Thus, a plot of u_3^Q versus time should have the general appearance of the curve in Fig. 2, which was generated by using the theory set forth in this paper, with $n^* = 12$. Figure 3 deals with the effect of spin speed on steady-state response frequency; that is, the ratio of ω_d, the response frequency when spin-up has been completed, to ω_1, the first natural frequency, is plotted versus the ratio of ω_s, the spin speed, to ω_1. As can be seen, the theory predicts *dynamics stiffening*, that is, an increase in ω_d with increasing ω_s, and this for *all* spin speeds.

In Section 2, we develop the theory underlying a simulation algorithm set forth in detail in Section 3. Conclusions are reported in Section 4, and the Appendix is used to show the relationship between certain integrals arising in the present theory and geometric stiffness coefficients associated with large motion inertia loading.

2 Theory

Referring to Fig. 1, let X_1, X_2, X_3 be mutually perpendicular coordinate axes fixed in R, passing through O, and parallel to $\mathbf{r}_1$, $\mathbf{r}_2$, $\mathbf{r}_3$, respectively; let P' (coordinates x_1, x_2) be the point of R at which a generic material point P of the plate is situated when the plate is undeformed. Then $\mathbf{u}$, the displacement of P, can be expressed in terms of displacement measure numbers u_1, u_2, u_3 as

Contributed by the Applied Mechanics Division of THE AMERICAN SOCIETY OF MECHANICAL ENGINEERS for publication in the JOURNAL OF APPLIED MECHANICS.

Discussion on this paper should be addressed to the Editorial Department, ASME, United Engineering Center, 345 East 47th Street, New York, N.Y. 10017, and will be accepted until two months after final publication of the paper itself in the JOURNAL OF APPLIED MECHANICS. Manuscript received by the ASME Applied Mechanics Division, November 30, 1987; final revision, February 1, 1988.

Copyright © 1989 by ASME

Downloaded 03 May 2010 to 171.66.16.31. Redistribution subject to ASME license or copyright; see http://www.asme.org/terms/Terms_Use.cfm

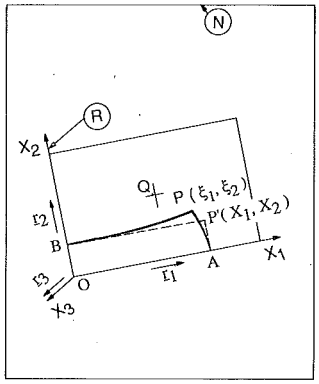


Fig. 1 Plate showing small elastic deformation of line elements in a reference frame R that undergoes large rigid body motion in a Newtonian frame N

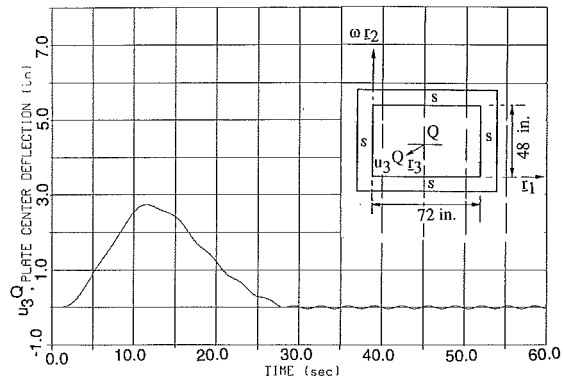


Fig. 2 Transient deflection of the center point of a simply-supported plate (supports indicated by s) spun-up from rest about an edge to a maximum of 12 rpm

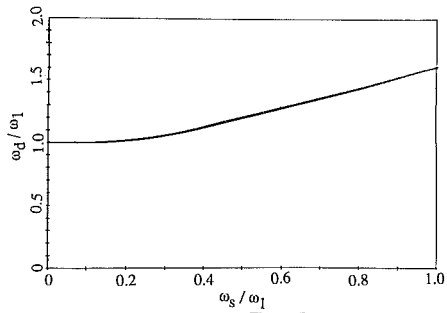


Fig. 3 Ratio of dynamic frequency to first natural frequency, ω_d/ω_1, versus ratio of rotational frequency to first natural frequency, ω_s/ω_1

$$\mathbf{u} = u_1(x_1,x_2,t)\mathbf{r}_1 + u_2(x_1,x_2,t)\mathbf{r}_2 + u_3(x_1,x_2,t)\mathbf{r}_3. \tag{1}$$

Now consider the line elements AP' and BP' (see Fig. 1) which are parallel to x_1 and x_2, respectively, when the plate is undeformed. If we restrict our analysis to a plate whose middle surface is inextensible, then the lengths of these line elements remain constant during deformation of the plate, so that

$$x_1 = \int_0^{\zeta_1} \left\{1 + \left[\frac{\partial u_2}{\partial \sigma}(\sigma,x_2,t)\right]^2 + \left[\frac{\partial u_3}{\partial \sigma}(\sigma,x_2,t)\right]^2\right\}^{1/2} d\sigma \tag{2}$$

$$x_2 = \int_0^{\zeta_2} \left\{1 + \left[\frac{\partial u_1}{\partial \sigma}(x_1,\sigma,t)\right]^2 + \left[\frac{\partial u_3}{\partial \sigma}(x_1,\sigma,t)\right]^2\right\}^{1/2} d\sigma. \tag{3}$$

To save writing, we define J_1 and J_2 as

$$J_1(\sigma,x_2,t) \triangleq 1 + \left[\frac{\partial u_2}{\partial \sigma}(\sigma,x_2,t)\right]^2 + \left[\frac{\partial u_3}{\partial \sigma}(\sigma,x_2,t)\right]^2 \tag{4}$$

$$J_2(x_1,\sigma,t) \triangleq 1 + \left[\frac{\partial u_1}{\partial \sigma}(x_1,\sigma,t)\right]^2 + \left[\frac{\partial u_3}{\partial \sigma}(x_1,\sigma,t)\right]^2 \tag{5}$$

and differentiating equations (2) and (3), with respect to t, obtain

$$0 = \frac{1}{2}\int_0^{\zeta_1} [J_1(\sigma,x_2,t)]^{-1/2} \frac{\partial J_1}{\partial t}(\sigma,x_2,t)d\sigma + \dot{\zeta}_1 [J_1(\zeta_1,x_2,t)]^{1/2} \tag{6}$$

$$0 = \frac{1}{2}\int_0^{\zeta_2} [J_2(x_1,\sigma,t)]^{-1/2} \frac{\partial J_2}{\partial t}(x_1,\sigma,t)d\sigma + \dot{\zeta}_2 [J_1(x_1,\zeta_2,t)]^{1/2}. \tag{7}$$

The coordinates ζ_1, ζ_2 are related to x_1, x_2 and u_1, u_2 as follows:

$$\zeta_1 = x_1 + u_1(x_1,x_2,t) \tag{8}$$

$$\zeta_2 = x_2 + u_2(x_1,x_2,t). \tag{9}$$

Differentiating equations (8) and (9), with respect to t, and using the results in equation (6) and (7) yields

$$\dot{u}_1 = -\frac{1}{2}[J_1(\zeta_1,x_2,t)]^{1/2} \times \int_0^{\zeta_1} [J_1(\sigma,x_2,t)]^{1/2} \frac{\partial J_1}{\partial t}(\sigma,x_2,t)d\sigma \tag{10}$$

$$\dot{u}_2 = -\frac{1}{2}[J_2(x_1,\zeta_2,t)]^{-1/2} \times \int_0^{\zeta_2} [J_2(x_1,\sigma,t)]^{-1/2} \frac{\partial J_2}{\partial t}(x_1,\sigma,t)d\sigma. \tag{11}$$

Considering points on the line element BP', we express u_2, and u_3 as

$$u_2(\sigma,x_2,t) = \sum_{j=1}^{n} \phi_{2j}(\sigma,x_2)q_j(t) \tag{12}$$

$$u_3(\sigma,x_2,t) = \sum_{j=1}^{n} \phi_{3j}(\sigma,x_2)q_j(t). \tag{13}$$

Similarly, for the line element AP', we write

$$u_1(x_1,\sigma,t) = \sum_{j=1}^{n} \phi_{1j}(x_1,\sigma)q_j(t) \tag{14}$$

$$u_3(x_1,\sigma,t) = \sum_{j=1}^{n} \phi_{3j}(x_1,\sigma)q_j(t). \tag{15}$$

The spatial functions ϕ_{1j}, ϕ_{2j}, ϕ_{3j}, $(j=1, \ldots, n)$ introduced in equations (12)–(15) are, as yet, unrestricted; ultimately, we will take them to be vibration mode shapes. The temporal functions $q_j(t)$, $(j=1, \ldots, n)$ play the roles of generalized coordinates in the sense of Lagrange, and n is simply any integer.

Differentiating equations (4) and (5) with respect to t, and then using equations (12)–(15), we arrive at

$$\frac{\partial J_1}{\partial t}(\sigma,x_2,t) = 2\sum_{i=1}^{n}\sum_{j=1}^{n} [\phi'_{2i}(\sigma,x_2)\phi'_{2j}(\sigma,x_2) + \phi'_{3i}(\sigma,x_2)\phi'_{3j}(\sigma,x_2)]\dot{q}_i(t)q_j(t) \tag{16}$$

$$\frac{\partial J_2}{\partial t}(x_1,\sigma,t) = 2\sum_{i=1}^{n}\sum_{j=1}^{n} [\phi'_{1i}(x_1,\sigma)\phi'_{1j}(x_1,\sigma) + \phi'_{3i}(x_1,\sigma)\phi'_{3j}(x_1,\sigma)]\dot{q}_i(t)q_j(t) \tag{17}$$

Downloaded 03 May 2010 to 171.66.16.31. Redistribution subject to ASME license or copyright; see http://www.asme.org/terms/Terms_Use.cfm

where primes denote partial differentiation with respect to σ; and substitution from equations (16) and (17) into equations (10) and (11) gives

$$\dot{u}_1 = -[J_1(\zeta_1,x_2,t)]^{-1/2}\int_0^{\zeta_1}\Big\{[J_1(\sigma,x_2,t)]^{-1/2}\sum_{i=1}^{n}\sum_{j=1}^{n}$$

$$[\phi'_{2i}(\sigma,x_2)\phi'_{2j}(\sigma,x_2)+\phi'_{3i}(\sigma,x_2)\phi'_{3j}(\sigma,x_2)]q_j\dot{q}_i\Big\}d\sigma \qquad (18)$$

$$\dot{u}_2 = -[J_2(x_1,\zeta_2,t)]^{-1/2}\int_0^{\zeta_2}\Big\{[J_2(x_1,\sigma,t)]^{-1/2}\sum_{i=1}^{n}\sum_{j=1}^{n}$$

$$[\phi'_{1i}(x_1,\sigma)\phi'_{1j}(x_1,\sigma)+\phi'_{3i}(x_1,\sigma)\phi'_{3j}(x_1,\sigma)]q_j\dot{q}_i\Big\}d\sigma. \qquad (19)$$

In addition, differentiation of equation (13) or (15) produces

$$\dot{u}_3 = \sum_{i=1}^{n}\phi_{3i}(x_1,x_2)\dot{q}_i. \qquad (20)$$

The velocity of P (Fig. 1) in the Newtonian reference frame N can be written

$$^N\mathbf{v}^P = {}^N\mathbf{v}^O + {}^N\boldsymbol{\omega}^R \times \Big\{\Big[x_1+\sum_{j=1}^{n}\phi_{1j}(x_1,x_2)q_j(t)\Big]\mathbf{r}_1$$

$$+\Big[x_2+\sum_{j=1}^{n}\phi_{2j}(x_1,x_2)q_j(t)\Big]\mathbf{r}_1$$

$$+\sum_{j=1}^{n}\phi_{3j}(x_1,x_2)q_j(t)\mathbf{r}_3\Big\}+\dot{u}_1\mathbf{r}_1+\dot{u}_2\mathbf{r}_2+\dot{u}_3\mathbf{r}_3 \qquad (21)$$

where $^N\mathbf{v}^O$, the velocity of O in N, and $^N\boldsymbol{\omega}^R$, the angular velocity of R in N, can be expressed in terms of specified functions $v_i(t)$ and $\omega_i(t)$ $(i=1,2,3)$ as

$$^N\mathbf{v}^O = v_1(t)\mathbf{r}_1+v_2(t)\mathbf{r}_2+v_3(t)\mathbf{r}_3 \qquad (22)$$

$$^N\tilde{\boldsymbol{\omega}}^R = \omega_1(t)\mathbf{r}_1+\omega_2(t)\mathbf{r}_2+\omega_3(t)\mathbf{r}_3. \qquad (23)$$

Using $\dot{q}_1, \ldots, \dot{q}_n$, as generalized speeds (Kane et al., 1983, p. 40), one can now form $^N\mathbf{v}_i^P$ $(i=1,\ldots,n)$, the associated partial velocities of P in N, by inspection of equations (18)–(21):

$$^N\mathbf{v}_i^P = -\mathbf{r}_1\Big\{[J_1(\zeta_1,x_2,t)]^{-1/2}\int_0^{\zeta_1}\Big\{[J_1(\sigma,x_2,t)]^{-1/2}$$

$$\times\sum_{j=1}^{n}[\phi'_{2i}(\sigma,x_2)\phi'_{2j}(\sigma,x_2)$$

$$+\phi'_{3i}(\sigma,x_2)\phi'_{3j}(\sigma,x_2)]q_j\Big\}d\sigma\Big\}$$

$$-\mathbf{r}_2\Big\{[J_2(x_1,\zeta_2,t)]^{-1/2}\int_0^{\zeta_2}\Big\{[J_2(x_1,\sigma,t)]^{-1/2}$$

$$\times\sum_{j=1}^{n}[\phi'_{1i}(x_1,\sigma)\phi'_{1j}(x_1,\sigma)$$

$$+\phi'_{3i}(x_1,\sigma)\phi'_{3j}(x_1,\sigma)]q_j\Big\}d\sigma\Big\}$$

$$+\mathbf{r}_3\phi_{3i}(x_1,x_2) \qquad (i=1,\ldots,n). \qquad (24)$$

So far, no linearizations have been performed. But now that expressions for partial velocities are in hand, it is appropriate to linearize everywhere in q_j and $\dot{q}_j$ $(j=1,\ldots,n)$ in order to produce a theory good for small motions of the plate relative to R. In the sequel, we perform such linearizations and place a tilde over a quantity linearized in q_j and $\dot{q}_j$ $(j=1,\ldots,n)$. Thus, use of equations (12) and (13) in equation (4) leads to

$$\tilde{J}_1(\sigma,x_2,t)=1; \qquad \tilde{J}_1(\zeta_1,x_2,t)=1. \qquad (25)$$

Similarly, from equations (5), (14), and (15),

$$\tilde{J}_2(x_1,\sigma,t)=1; \qquad \tilde{J}_2(x_1,\zeta_2,t)=1. \qquad (26)$$

Now we introduce the notations

$$\alpha_{ij}(x_1,x_2)\triangleq\int_0^{x_1}[\phi'_{2i}(\sigma,x_2)\phi'_{2j}(\sigma,x_2)+\phi'_{3i}(\sigma,x_2)\phi'_{3j}(\sigma,x_2)]d\sigma$$
$$(i,j=1,\ldots,n) \qquad (27)$$

$$\beta_{ij}(x_1,x_2)\triangleq\int_0^{x_2}[\phi'_{1i}(x_1,\sigma)\phi'_{1j}(x_1,\sigma)+\phi'_{3i}(x_1,\sigma)\phi'_{3j}(x_1,\sigma)]d\sigma$$
$$(i,j=1,\ldots,n). \qquad (28)$$

The linearized partial velocity of P in N then can be written

$$^N\tilde{\mathbf{v}}_i^P = -\mathbf{r}_1\sum_{j=1}^{n}\alpha_{ij}(x_1,x_2)q_j(t)$$

$$-\mathbf{r}_2\sum_{j=1}^{n}\beta_{ij}(x_1,x_2)q_j(t)+\mathbf{r}_3\phi_{3i}(x_1,x_2)$$

$$(i=1,\ldots,n) \qquad (29)$$

and the linearized velocity of P in N becomes

$$^N\tilde{\mathbf{v}}^P = \mathbf{r}_1\Big\{v_1+\omega_2\sum_{j=1}^{n}\phi_{3j}(x_1,x_2)q_j(t)$$

$$-\omega_3\Big[x_2+\sum_{j=1}^{n}\phi_{2j}(x_1,x_2)q_j(t)\Big]\Big\}$$

$$+\mathbf{r}_2\Big\{v_2+\omega_3\Big[x_1+\sum_{j=1}^{n}\phi_{1j}(x_1,x_2)q_j(t)\Big]$$

$$-\omega_1\sum_{j=1}^{n}\phi_{3j}(x_1,x_2)q_j(t)\Big\}$$

$$+\mathbf{r}_3\Big\{v_3+\omega_1\Big[x_2+\sum_{j=1}^{n}\phi_{2j}(x_1,x_2)q_j(t)\Big]$$

$$-\omega_2\Big[x_1+\sum_{j=1}^{n}\phi_{1j}(x_1,x_2)q_j(t)\Big]$$

$$+\sum_{j=1}^{n}\phi_{3j}(x_1,x_2)\dot{q}_j(t)\Big\}. \qquad (30)$$

The acceleration of P in N, linearized in $q_1,\ldots,q_n$, $\dot{q}_1,\ldots,\dot{q}_n$, can be obtained by differentiating $^N\tilde{\mathbf{v}}^P$ in N; that is,

$$^N\tilde{\mathbf{a}}^P = \frac{^Nd}{dt}\,{}^N\tilde{\mathbf{v}}^P = \frac{^Rd}{dt}\,{}^N\tilde{\mathbf{v}}^P + {}^N\tilde{\boldsymbol{\omega}}^R + {}^N\tilde{\mathbf{v}}^P \qquad (31)$$

and the generalized inertia force (Kane et al., 1983, p. 259) corresponding to the ith generalized speed is given by

$$\tilde{F}_i^* = -\int_S {}^N\tilde{\mathbf{v}}_i^P\cdot{}^N\tilde{\mathbf{a}}^P\rho\,dx_1dx_2 \qquad (i=1,\ldots,n) \qquad (32)$$

where S is the domain of the plate.

In expanding equation (32), it is convenient to define the following "modal" integrals:

$$A_i\triangleq\int_S\phi_{3i}\rho dx_1dx_2 \qquad (i=1,\ldots,n) \qquad (33)$$

Downloaded 03 May 2010 to 171.66.16.31. Redistribution subject to ASME license or copyright; see http://www.asme.org/terms/Terms_Use.cfm

$$B_{ki} \triangleq \int_S x_k \phi_{3i} \rho dx_1 dx_2 \qquad (k=1,2; \quad i=1, \ldots, n) \tag{34}$$

$$C_{ij} \triangleq \int_S \alpha_{ij} \rho dx_1 dx_2 \qquad (i,j=1, \ldots, n) \tag{35}$$

$$C_{kij} \triangleq \int_S x_k \alpha_{ij} \rho dx_1 dx_2 \qquad (k=1,2; \quad i,j=1, \ldots, n) \tag{36}$$

$$D_{ij} \triangleq \int_S \beta_{ij} \rho dx_1 dx_2 \qquad (i,j=1, \ldots, n) \tag{37}$$

$$D_{kij} \triangleq \int_S x_k \beta_{ij} \rho dx_1 dx_2 \qquad (k=1,2; \quad i,j=1, \ldots, n) \tag{38}$$

$$E_{kij} \triangleq \int_S \phi_{3i} \phi_{kj} \rho dx_1 dx_2 \qquad (k=1,2,3; \quad i,j=1, \ldots, n). \tag{39}$$

Use of these (again, neglecting all terms nonlinear in $q_1, \ldots, q_n, \dot{q}_1, \ldots, \dot{q}_n$) yields

$$\begin{aligned} \tilde{F}_i^* = & -\sum_{j=1}^{n} E_{3ij} \ddot{q}_j - \sum_{j=1}^{n} (\omega_1 E_{2ij} - \omega_2 E_{1ij}) \dot{q}_j \\ & - \sum_{j=1}^{n} [-(\dot{v}_1 + \omega_2 v_3 - \omega_3 v_2) C_{ij} \\ & - (\omega_1 \omega_2 - \dot{\omega}_3) C_{2ij} + (\omega_2^2 + \omega_3^2) C_{1ij} - (\dot{v}_2 + \omega_3 v_1 \\ & - \omega_1 v_3) D_{ij} - (\dot{\omega}_3 + \omega_1 \omega_2) D_{1ij} \\ & + (\omega_3^2 + \omega_1^2) D_{2ij} + (\dot{\omega}_1 + \omega_2 \omega_3) E_{2ij} \\ & + (\omega_3 \omega_1 - \dot{\omega}_2) E_{1ij} - (\omega_1^2 + \omega_2^2) E_{3ij}] q_j \\ & - (\dot{v}_3 + \omega_1 v_2 - \omega_2 v_1) A_i - (\dot{\omega}_1 + \omega_2 \omega_3) B_{2i} \\ & - (\omega_3 \omega_1 - \dot{\omega}_2) B_{1i}, \quad (i, \ldots, n). \end{aligned} \tag{40}$$

Each coefficient of $q_j (j=1, \ldots, n)$ in equation (40) can be called a "dynamic stiffness coefficient," and terms involving $C_{ij}, C_{1ij}, C_{2ij}, D_{ij}, D_{1ij}, D_{2ij}$, can be related to "geometric stiffness" associated with translational and rotational inertia loads.[1] This topic is discussed further in the Appendix.

The generalized active forces (Kane et al., 1983, p. 247) associated with the elasticity of the plate are given by

$$\tilde{F}_i = -\sum_{j}^{n} \lambda_{ij} q_j \qquad (i=1, \ldots, n) \tag{41}$$

where λ_{ij} is a generic element of the modal stiffness matrix, ($\phi^T K \phi$ in standard matrix notations of structural analysis), which may or may not be diagonal, depending on the type of component modes (Craig, 1981) used to represent the deformation of the plate. Finally, the linearized equations of motion of a plate that is executing small elastic motions in a reference frame undergoing large rigid body motions are obtained by substituting from equations (40) and (41) into (see Kane et al., 1983; p. 275)

$$\tilde{F}_i^* + \tilde{F}_i = 0 \qquad (i=1, \ldots, n). \tag{42}$$

3 Simulation Algorithm

A step-by-step procedure for simulating motions of the plate follows.

(a) Specify base motion temporal functions $v_1, v_2, v_3, \omega_1, \omega_2, \omega_3$ (see equations (22) and (23)).

(b) Specify plate geometry and material constants such as ρ, the mass per unit of area, E, the elastic modulus, and ν, Poisson's ratio.

[1] The authors wish to thank Dr. John Dickens of Lockheed Missiles and Space Co., Sunnyvale, for pointing this out.

(c) Specify the number n of modes to be used.

(d) Determine the vibration mode shapes and frequencies of the plate with at least one point fixed in a Newtonian reference frame. This is standardly done with a finite element code, and yields the eigenfunctions $\phi_{ij}(x_1, x_2)(i=1,2,3; j=1, \ldots, n)$ (see equations (12)–(14)) and the elements of the modal stiffness matrix, $\lambda_{ij}(i,j=1, \ldots, n)$ (see equation (41)).

(e) Select M node points; let ${x_1}^k$, ${x_2}^k (k=1, \ldots, M)$ denote their coordinates; and specify initial displacements $\mathbf{d}({x_1}^k, {x_2}^k)$ and initial velocities $\mathbf{v}({x_1}^k, {x_2}^k) (k=1, \ldots, M)$ by assigning numerical values to $d_i({x_1}^k, {x_2}^k)$ and $v_i({x_1}^k, {x_2}^k) (i=1,2,3; k=1, \ldots, M)$, with

$$\mathbf{d} = d_1({x_1}^k, {x_2}^k)\mathbf{r}_1 + d_2({x_1}^k, {x_2}^k)\mathbf{r}_2 + d_3({x_1}^k, {x_2}^k)\mathbf{r}_3 \tag{43}$$

$$\mathbf{v} = v_1({x_1}^k, {x_2}^k)\mathbf{r}_1 + v_2({x_1}^k, {x_2}^k)\mathbf{r}_2 + v_3({x_1}^k, {x_2}^k)\mathbf{r}_3. \tag{44}$$

To find the associated initial values of q_i and $\dot{q}_i (i=1, \ldots, n)$, denoted by $q_i(0)$ and $\dot{q}_i(0) (i=1, \ldots, n)$, introduce matrices $d, v, \phi, \dot{q}(0)$ as follows:

$$d \triangleq \begin{bmatrix} d_1(x_1^1, x_2^1) \\ d_2(x_1^1, x_2^1) \\ d_3(x_1^1, x_2^1) \\ \vdots \\ d_1(x_1^M, x_2^M) \\ d_2(x_1^M, x_2^M) \\ d_3(x_1^M, x_2^M) \end{bmatrix}, \quad v \triangleq \begin{bmatrix} v_1(x_1^1, x_2^1) \\ v_2(x_1^1, x_2^1) \\ v_3(x_1^1, x_2^1) \\ \vdots \\ v_1(x_1^M, x_2^M) \\ v_2(x_1^M, x_2^M) \\ v_3(x_1^M, x_2^M) \end{bmatrix}, \tag{45}$$

$$\phi \triangleq \begin{bmatrix} \phi_{11}(x_1^1, x_2^1) & \ldots & \phi_{1n}(x_1^1, x_2^1) \\ \phi_{21}(x_1^1, x_2^1) & \ldots & \phi_{2n}(x_1^1, x_2^1) \\ \phi_{31}(x_1^1, x_2^1) & \ldots & \phi_{3n}(x_1^1, x_2^1) \\ \vdots & & \vdots \\ \phi_1(x_1^M, x_2^M) & \ldots & \phi_{1n}(x_1^M, x_2^M) \\ \phi_{21}(x_1^M, x_2^M) & \ldots & \phi_{2n}(x_1^M, x_2^M) \\ \phi_{31}(x_1^M, x_2^M) & \ldots & \phi_{3n}(x_1^M, x_2^M) \end{bmatrix} \tag{46}$$

$$q(0) \triangleq \begin{bmatrix} q_1(0) \\ \vdots \\ q_n(0) \end{bmatrix}, \quad \dot{q}(0) \triangleq \begin{bmatrix} \dot{q}_1(0) \\ \vdots \\ q_n(0) \end{bmatrix}. \tag{47}$$

Then $q_n(0)$ and $\dot{q}_n(0)$ must satisfy (see equations (1) and (12)–(14)) the equations

$$\phi_q(0) = d, \quad \phi \dot{q}(0) = v. \tag{48}$$

Hence, making use of the idea of pseudo-inversion (Penrose, 1956), evaluate $q(0)$ and $\dot{q}(0)$ as

$$q(0) = (\phi^T \phi)^{-1} \phi^T d, \quad \dot{q}(0) = (\phi^T \phi)^{-1} \phi^T v. \tag{49}$$

(f) Evaluate the modal integrals defined in equations (33)–(39), employing integration by parts wherever possible (see the Appendix) and then using finite element interpolation polynomials (Zienkiewicz, 1977, pp. 234, 235).

(g) Substitute the modal integrals from Step (f) into equation (40), and the modal stiffness matrix elements from Step (d) into equation (41).

(h) Form equation (42), expressing them in the matrix form

Downloaded 03 May 2010 to 171.66.16.31. Redistribution subject to ASME license or copyright; see http://www.asme.org/terms/Terms_Use.cfm

$$M\ddot{q}+G\dot{q}+Kq=F$$

where M, G, K are $n\times n$ matrices and q, F are of dimensions $n\times 1$, and integrate these equations numerically.

(i) Evaluate the displacement $\mathbf{d}$ at (x_1,x_2) at time t as

$$\mathbf{d}=\sum_{j=1}^{n}[\phi_{1j}(x_1,x_2)\mathbf{r}_1+\phi_{2j}(x_1,x_2)\mathbf{r}_2+\phi_{3j}(x_1,x_2)\mathbf{r}_3]q_j(t). \quad (50)$$

(We note in passing that all of the numerical results reported in this paper are based on the exact mode shapes of a simply-supported plate, this is, on

$$\phi_{1j}(x_1,x_2)=\phi_{2j}(x_1,x_2)=0 \quad (j=1,\ \ldots,\ n) \quad (51)$$

$$\phi_{3j}(x_1,x_2)=f_j\sin(\alpha_j x_1)\sin(\beta_j x_2) \quad (j=1,\ \ldots,\ n) \quad (52)$$

where f_j is a normalizing factor and α_j, β_j are tabulated in Blevins (1979) for various values of a/b for the plate.)

4 Conclusions

It has been shown that, by retaining nonlinearities up to an appropriate point in the analysis, one can arrive at a theory that captures the phenomenon of *dynamic stiffening*, even though the theory is ultimately linear. As was pointed out by Kane et al. (1987), various widely used multibody codes, working with exactly the same mode shapes as the present theory, lead to *dynamic softening*. The underlying cause is premature linearization.

The present formulation is valid also for boundary conditions other than those of simple support, and it has already been applied to a spinning spacecraft with a cantilever plate (solar panel). However, the formulation does suffer from one limitation, namely, that the plate theory used is essentially that of the strip method (Ugural, p. 80). Incorporation of a plate theory that accounts for shear, membrane, and large deformation effects should yield even greater dynamic stiffening.

References

Blevins, R. D., 1979, *Formulas for Natural Frequency and Mode Shape*, Van Nostrand Reinhold, p. 258.

Bodley, C. S., Devers, A. D., Park, A. C., and Frisch, H. P., 1978, "A Digital Computer Program for the Dynamic Interaction Simulation of Controls and Structure (DISCOS)," Vol. 1, NASA Technical Paper 1219.

Cook, R. D., 1981, *Concepts and Applications of Finite Element Analysis*, 2nd ed., John Wiley and Sons, New York, pp. 338–339.

Craig, Jr., R. R., 1981, *Structural Dynamics*, John Wiley and Sons, New York, pp. 467–492.

Ho, J. Y. L., and Herber, D. R., 1985, "Development of Dynamics and Control Simulation of Large Flexible Space Systems," *AIAA Journal of Guidance, Control, and Dynamics*, Vol. 8, No. 3, pp. 374–383.

Kane, T. R., Ryan, R. R., and Banerjee, A. K., 1987, "Dynamics of a Beam Attached to a Moving Base," *AIAA Journal of Guidance, Control, and Dynamics*, Vol. 10, No. 2, pp. 139–151.

Kane, T. R., Likins, P. W., and Levinson, D. A., 1983, *Spacecraft Dynamics*, McGraw-Hill, New York.

Penrose, R., 1956, "On Best Approximate Solutions of Linear Matrix Equations," *Proceedings of the Cambridge Philosophical Society*, Vol. 52, Part 1, pp. 17–19.

Singh, R. P., van der Voort, R. J., and Likins, P. W., 1985, "Dynamics of Flexible Bodies in Tree Topology—A Computer Oriented Approach," *AIAA Journal of Guidance, Control, and Dynamics*, Vol. 8, No. 5, pp. 584–590.

Ugural, A. C., 1981, *Stresses in Plates and Shells*, McGraw-Hill, New York, p. 80.

Zienkiewicz, O. C., 1977, *The Finite Element Method*, 3rd ed., McGraw-Hill, New York, pp. 518–519.

APPENDIX

The modal integrals in equations (33), (34), and (39) are standard in flexible body dynamics (see, for example, Bodley et al., 1978; Singh et al., 1985; Ho and Herber, 1985). Additional integrals arise in the present theory and are given by equations (35)–(38). Their evaluation is facilitated by employing integration by parts, and the results are listed as follows for a homogeneous rectangular plate of sides of lengths a along the X_1-axis and b along the X_2-axis:

$$C_{ij}=\rho\int_0^b\left\{\int_0^a(a-x_1)\left[\frac{\partial\phi_{2i}}{\partial x_1}\frac{\partial\phi_{2j}}{\partial x_1}+\frac{\partial\phi_{3i}}{\partial x_1}\frac{\partial\phi_{3j}}{\partial x_1}\right]dx_1\right\}dx_2 \quad (53)$$

$$C_{1ij}=\frac{\rho}{2}\int_0^b\left\{\int_0^a(a^2-x_1^2)\left[\frac{\partial\phi_{2i}}{\partial x_1}\frac{\partial\phi_{2j}}{\partial x_1}+\frac{\partial\phi_{3i}}{\partial x_1}\frac{\partial\phi_{3j}}{\partial x_1}\right]dx_1\right\}dx_2 \quad (54)$$

$$C_{2ij}=\rho\int_0^b x_2\left\{\int_0^a(a-x_1)\left[\frac{\partial\phi_{2i}}{\partial x_1}\frac{\partial\phi_{2j}}{\partial x_1}+\frac{\partial\phi_{3i}}{\partial x_1}\frac{\partial\phi_{3j}}{\partial x_1}\right]dx_1\right\}dx_2 \quad (55)$$

$$D_{ij}=\rho\int_0^a\left\{\int_0^b(b-x_2)\left[\frac{\partial\phi_{1i}}{\partial x_2}\frac{\partial\phi_{1j}}{\partial x_2}+\frac{\partial\phi_{3i}}{\partial x_2}\frac{\partial\phi_{3j}}{\partial x_2}\right]dx_2\right\}dx_1 \quad (56)$$

$$D_{1ij}=\frac{\rho}{2}\int_0^a\left\{\int_0^b(b^2-x_2^2)\left[\frac{\partial\phi_{1i}}{\partial x_2}\frac{\partial\phi_{1j}}{\partial x_2}+\frac{\partial\phi_{3i}}{\partial x_2}\frac{\partial\phi_{3j}}{\partial x_2}\right]dx_2\right\}dx_1 \quad (57)$$

$$D_{2ij}=\rho\int_0^a x_1\left\{\int_0^b(b-x_2)\left[\frac{\partial\phi_{1i}}{\partial x_2}\frac{\partial\phi_{1j}}{\partial x_2}+\frac{\partial\phi_{3i}}{\partial x_2}\frac{\partial\phi_{3j}}{\partial x_2}\right]dx_2\right\}dx_1. \quad (58)$$

The terms involving C_{ij}, C_{1ij}, C_{2ij}, D_{ij}, D_{1ij}, D_{2ij}, in equation (40) can be related to *geometric stiffness* due to inertia loading. This is seen as follows. Consider the quantity Q_i defined as

$$Q_i\triangleq\sum_{j=1}^{n}(\dot{v}_1+\omega_2 v_3-\omega_3 v_2)C_{ij}q_j. \quad (59)$$

This is one of the terms in equation (40), and substitution from equation (53) into equation (59) yields

$$Q_i=\rho(\dot{v}_1+\omega_2 v_3-\omega_3 v_2)\int_0^b\int_0^a(a-x_1)\sum_{j=1}^{n}\left[\frac{\partial\phi_{2i}}{\partial x_1}\frac{\partial\phi_{2j}}{\partial x_1}+\frac{\partial\phi_{3i}}{\partial x_1}\frac{\partial\phi_{3j}}{\partial x_1}\right]q_j dx_1 dx_2 \quad (60)$$

or, equivalently,

$$Q_i=\frac{\partial}{\partial q_i}\left\{\rho(\dot{v}_1+\omega_2 v_3-\omega_3 v_2)\int_0^b\int_0^a(a-x_1)(1/2)\sum_{i=1}^{n}\sum_{j=1}^{n}\left[\frac{\partial\phi_{2i}}{\partial x_1}\frac{\partial\phi_{2j}}{\partial x_1}+\frac{\partial\phi_{3i}}{\partial x_1}\frac{\partial\phi_{3j}}{\partial x_1}\right]q_i q_j dx_1 dx_2\right. \quad (61)$$

Now, in view of equations (12) and (13), and with σ_1 defined as

$$\sigma_1(x_1,x_2)\triangleq-\rho(\dot{v}_1+\omega_2 v_3-\omega_3 v_2)(a-x_1), \quad (62)$$

Downloaded 03 May 2010 to 171.66.16.31. Redistribution subject to ASME license or copyright; see http://www.asme.org/terms/Terms_Use.cfm

one can replace equation (61) with

$$Q_i = -\frac{\partial}{\partial q_i}\left\{\int_0^b \int_0^a (\sigma_1/2)\left[\left(\frac{\partial u_2}{\partial x_1}\right)^2 + \left(\frac{\partial u_3}{\partial x_1}\right)^2\right] dx_1 dx_2\right\} \tag{63}$$

and the term within the brace in this equation can be recognized as the geometric stiffness due to σ_1 (Cook, pp. 338–339), provided the contribution of $(\partial u_1/\partial x_1)^2$ to this geometric stiffness be neglected. Moreover, the form of equation (63) shows that Q_i can be thought of as a generalized force derivable from a potential function associated with strain energy. Finally, σ_1 as defined in equation (62) is also the solution of the differential equation

$$\frac{\partial \sigma_1}{\partial x_1} = \rho(\dot{v}_1 + \omega_2 v_3 - \omega_3 v_2) \tag{64}$$

subject to the boundary condition

$$\sigma_1(a, x_2) = 0, \tag{65}$$

and equation (64) has the character of a stress equation of motion, for the quantity $\dot{v}_1 + \omega_2 v_3 - \omega_3 v_2$ is a portion of the $\mathbf{r}_1$ measure number of the inertial acceleration of point P' in Fig. 1. Thus, σ_1 plays the rôle of an acceleration-induced stress; and, proceeding similarly, one finds that C_{1ij}, C_{2ij}, D_{ij}, D_{1ij}, D_{2ij} also are associated with geometric stiffness due to inertia loading.

Downloaded 03 May 2010 to 171.66.16.31. Redistribution subject to ASME license or copyright; see http://www.asme.org/terms/Terms_Use.cfm

A Comprehensive Study of the Free Vibration of Rectangular Plates Resting on Symmetrically-Distributed Uniform Elastic Edge Supports

D. J. Gorman
Professor.
Department of Mechanical Engineering,
University of Ottawa,
Ottawa, Ont. Canada KIN 6N5

An analytical-type solution is developed for the free vibration analysis of rectangular plates with uniform elastic edge support symmetrically distributed about the plate central axes. Both linear elastic rotational and translational support are considered to act simultaneously. Rapid convergence is encountered. Because of the symmetry of the problem, the free vibration modes fall into three distinct families. Eigenvalues are tabulated for the first four modes of vibration of a square plate with identical stiffnesses on each edge and with various ratios of translational to rotational stiffnesses. This represents, to the author's knowledge, the first comprehensive treatment of this problem.

1 Introduction

It is generally accepted that classical edge support conditions employed in the analysis of rectangular plate behavior represent only limiting mathematical conditions. Along any supported edge there will always be some translational and rotational elasticity and simply-supported or clamped edge conditions represent only those limits approached as the elastic constants associated with the edge support approach their natural limits of zero or infinity.

In spite of this situation, a review of the literature quickly reveals that little work of a comprehensive nature has been published to enable the analyst to establish the effects of edge elasticity on the free vibration frequencies and mode shapes of rectangular plates. In his first well-known review of the literature, Leissa reported on the work published up to that time (Leissa, 1969). It is apparent that he found most of the work to have been related to the much simpler family of problems where at least one pair of opposite edges of the plates were given simple support. Furthermore, almost all of the authors considered plates where either rotational or translational elastic support was imposed along an edge, but not both. In his more recent reviews, Leissa has reported little further development in this area.

While one can find numerous papers dealing in some limited fashion with the subject of effects of elastic edge support on plate vibration, the work of Warburton and Edney (Warburton and Edney, 1984) appears to most closely approach the work undertaken here. They utilize beam eigenfunctions and the Rayleigh-Ritz method to perform their analysis. Part of their paper was devoted to the problem of edges involving both types of elastic support. Reference will be made to their findings later. They have also provided a valuable review of the literature in this area, including the publications of Laura and his associates.

In this paper the superposition method as developed by the author for the free vibration analysis of plates with classical edge conditions (Gorman, 1982) is exploited in order to obtain solutions for plates with uniform elastic support along each edge. The sole restriction is that the elastic support must be symmetrically distributed about the plate central axis. In effect, this means that identical elastic coefficients apply along opposite edges. It will be seen that this restriction leads to considerable simplification in the analysis even though it permits accurate solutions for a wide family of practical problems. Furthermore, it is the author's contention that a much better understanding of the general behavior of elastically-supported plates is obtained if solutions to the general problem with no restrictions are preceded by a study of those plates possessing symmetry in their elastic support distribution. Solutions obtained here can also be used as limiting cases for verification of results obtained in future studies related to the general elastically-supported plate problem.

2 Formulation of the Problem

In view of the symmetry which characterizes the distribution

Contributed by the Applied Mechanics Division of THE AMERICAN SOCIETY OF MECHANICAL ENGINEERS for presentation at the Winter Annual Meeting, San Francisco, Calif., December 10–15, 1989.

Discussion on this paper should be addressed to the Editorial Department, ASME, United Engineering Center, 345 East 47th Street, New York, N.Y. 10017, and will be accepted until two months after final publication of the paper itself in the JOURNAL OF APPLIED MECHANICS. Manuscript received by the ASME Applied Mechanics Division, September 21, 1988; final revision, January 27, 1989.

Paper No. 89-WA/APM-21.

Copyright © 1989 by ASME

Downloaded 03 May 2010 to 171.66.16.31. Redistribution subject to ASME license or copyright; see http://www.asme.org/terms/Terms_Use.cfm

of elastic support about the central axes of plates considered in this paper, it will be apparent that all plate free vibration mode shapes will be symmetric or antisymmetric about these axes or symmetric about one axis and antisymmetric about the other. It is, therefore, necessary to analyze only one quarter of the plate, as shown in Fig. 1, provided appropriate boundary conditions are enforced along the coordinate axes. In the analysis reported here, each of these three unique families of mode shapes is considered separately.

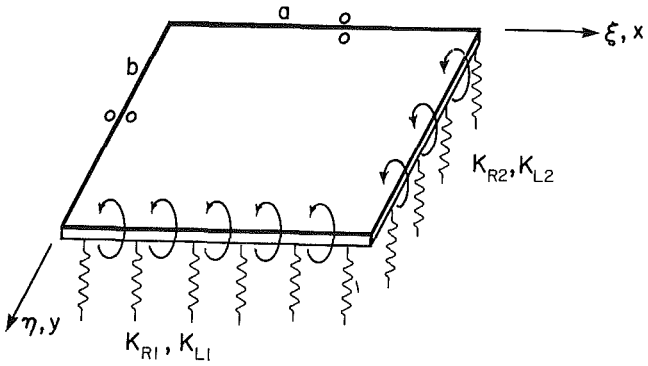


Fig. 1 Quarter segment of rectangular plate with symmetrically-distributed uniform linear and rotational support along the edges (schematic representation)

3 Mathematical Procedure

3.1 The Fully-Symmetric Modes of Vibration. The quarter plate of Fig. 1 is utilized in analyzing this family of modes. The two small circles adjacent to the edges lying along the coordinate axes indicate that there is zero vertical edge reaction along these edges. Slope taken normal to these edges to also zero. Such edge conditions are referred to as slip shear conditions.

A free vibration analysis of this family of modes is readily achieved by the method of superposition on utilizing the building blocks of Fig. 2. Few of the computational details need be given here since the method has been described in detail in earlier publications (Gorman, 1982). A brief description of the analysis of fully-symmetric modes, only, has appeared in the proceedings of the 1988 Conference on Engineering Applications in Industry held at London, Canada (Gorman, 1988). The first building block is driven by a harmonic bending moment and is free of vertical edge reaction. The spatial distribution of this dimensionless moment is represented by series

$$\frac{Mb^2}{aD} = \sum_{m=0,1}^{\infty} E_m \cos m\pi\xi \tag{1}$$

where M is the bending moment, b and a are quarter plate dimensions, and D is the plate flexural rigidity. ξ and η are dimensionless spatial coordinates x/a and y/b, respectively, (see Fig. 1).

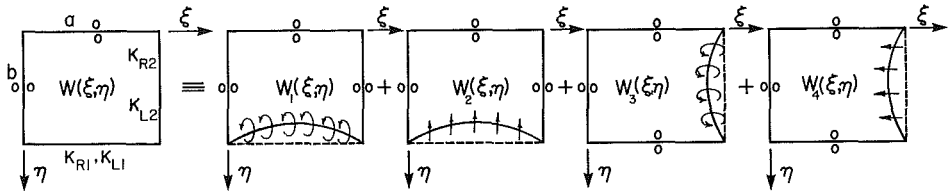


Fig. 2 Building blocks utilized in analyzing symmetric modes of elastically-supported plate

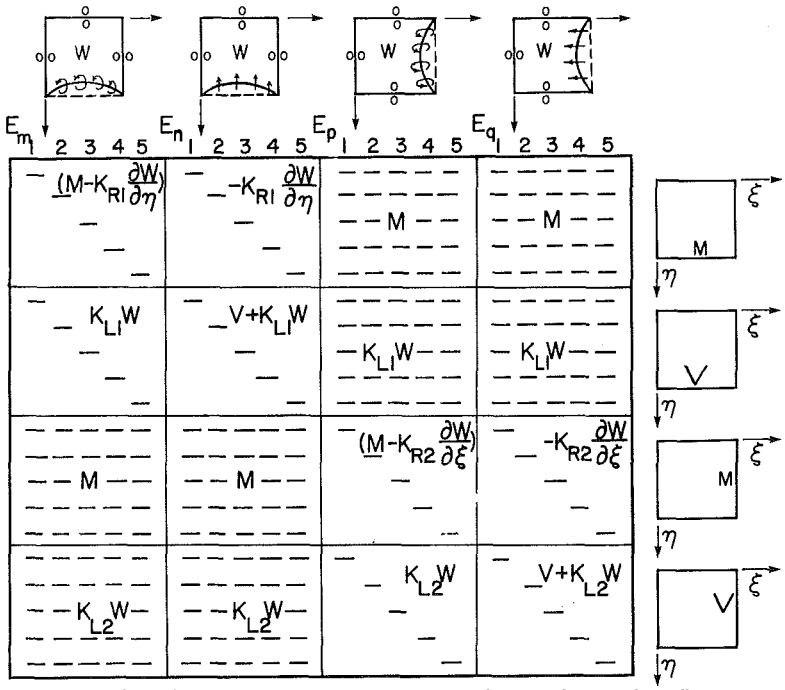


Fig. 3 Schematic representation of eigenvalue matrix based on five-term expansions. Symbols on the right indicate edges where moment or vertical edge reaction equilibrium are enforced.

Downloaded 03 May 2010 to 171.66.16.31. Redistribution subject to ASME license or copyright; see http://www.asme.org/terms/Terms_Use.cfm

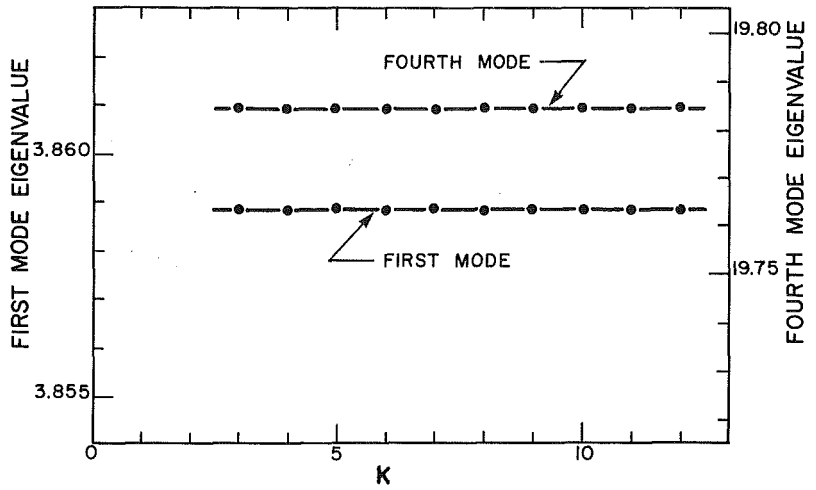


Fig. 4 Results of convergence tests for first and fourth symmetric mode vibration of a square plate. K equals the number of terms in a series. $K_{R1} = K_{R2} = K_{L1} = K_{L2} = 10.0$.

It is known that amplitude of vibration of the first building block can be written in the form proposed by Lévy as

$$W_1(\xi, \eta) = \sum_{m=0,1}^{\infty} Y_m(\eta) \cos m\pi\xi. \tag{2}$$

Following well-established procedures (Gorman, 1982), it is shown that upon substitution in the governing differential equation, one obtains

$$W_1(\xi, \eta) = \sum_{m=0,1}^{K^*} E_m \left\{ \theta_{11m} \frac{\cosh \beta_m \eta}{\sinh \beta_m} + \theta_{13m} \frac{\cos \gamma_m \eta}{\sin \gamma_m} \right\} \cos m\pi\xi + \sum_{m=K^*+1}^{\infty} E_m \left\{ \theta_{22m} \frac{\cosh \beta_m \eta}{\sinh \beta_m} + \theta_{23m} \frac{\cosh \gamma_m \eta}{\sinh \gamma_m} \right\} \cos m\pi\xi \tag{3}$$

where

$$\theta_{11m} = -1/((\beta_m^2 + \gamma_m^2) \cosh \beta_m / \sinh \beta_m)$$

$$\theta_{13m} = 1/((\beta_m^2 + \gamma_m^2) \cosh \gamma_m / \sin \gamma_m)$$

$$\theta_{22m} = -1/((\beta_m^2 - \gamma_m^2) \cosh \beta_m / \sinh \beta_m)$$

$$\theta_{23m} = 1/((\beta_m^2 - \gamma_m^2) \cosh \gamma_m / \sinh \gamma_m)$$

ϕ = plate aspect ratio, b/a

$$\beta_m = \phi\sqrt{\lambda^2 + (m\pi)^2}, \quad \gamma_m = \sqrt{\lambda^2 - (m\pi)^2} \text{ or } \phi\sqrt{(m\pi)^2 - \lambda^2},$$

whichever is real, and the first summation contains only those terms for which $\lambda^2 \geq (m\pi)^2$. λ^2, the eigenvalue $= \omega a^2\sqrt{\rho/D}$, where ω is the circular frequency of vibration and ρ is the mass of the plate per unit area.

The second building block is driven by a harmonic displacement expanded in a series identical to that of equation (1). A condition of zero bending moment is imposed along the driven edge. A solution is obtained for this building block in a manner identical to that described for the first one. Finally, it will be appreciated that solutions for the third and fourth building blocks are easily extracted from those related to the first and second building blocks, respectively. One need only interchange the variables ξ and η and replace the plate aspect ratio with its inverse.

With the building block solutions involving the unknown Fourier coefficients E_m, E_n, E_p, and E_q available, it is now possible to construct the eigenvalue matrix. Such a matrix, based on a five-term expansion, is represented schematically in Fig. 3. The first of the four sets of homogeneous equations arise because of the requirement to satisfy the following moment-slope equation along the edge, $\eta = 1$,

$$\frac{M(\xi)b^2}{aD} - K_R \frac{dW(\xi,\eta)}{d\eta}\bigg|_{\eta=1} = 0 \tag{4}$$

where $K_{R1} = k_1 b/D$, k_1 being the rotational stiffness along the edge, $\eta = 1$.

All moment and slope contributions from the four building blocks which are not available in the form of a cosine series are expanded in a series of this type. With the individual solutions expanded in K terms, we write K-simultaneous homogeneous algebraic equations based on the left-hand side of equation (4). In earlier studies of plates with classical edge conditions, the second term of equation (4) did not appear.

The second set of homogeneous equations, represented schematically in Fig. 3, are based on the requirement of vertical edge force equilibrium along the edge, $\eta = 1$. The third and fourth sets of equations are the counterparts of the first and second set and arise because of the need for moment and transverse force equilibrium along the edge, $\xi = 1$. Additional symbols employed are $K_{L1} = T_1 b^3/D$, where T_1 is the translational stiffness along the edge, $\eta = 1$, and $K_{R2} = k_2\, a/D$, and $K_{L2} = T_2 a^3/D$ where the subscript 2 refers to conditions imposed along the edge, $\xi = 1$.

With the eigenvalue matrix established, one proceeds to obtain the eigenvalues and their associated mode shapes in a manner identical to that described for plates with classical edge support (Gorman, 1982). One must search for those values of the parameter, λ^2, which causes the determinant of the eigenvalue matrix to vanish. It will be obvious that certain known eigenvalues for plates with classical edge support must be approached as the elastic edge coefficients approach their natural limits of zero or infinity.

3.2 The Fully-Antisymmetric Modes of Vibration. Solutions for this family of modes can be obtained by introducing only slight modifications to the building blocks of Fig. 2 and following a computational procedure similar to that described in the previous section for the fully-symmetric modes. A condition of simple support must be enforced along the coordinate axes of each building block. Equation (1) is, therefore, replaced by the following equation

Downloaded 03 May 2010 to 171.66.16.31. Redistribution subject to ASME license or copyright; see http://www.asme.org/terms/Terms_Use.cfm

Table 1 Eigenvalues, $\lambda^2 = \omega\alpha^2\sqrt{\rho/D}$, for fully-symmetric mode vibration of square plates with equal translational and equal rotational stiffnesses along all edges

	$\sqrt{K_{R1}}$												
MODE	0.7	1.0	1.5	2.0	2.5	3.0	3.5	4.0	4.5	5.0	5.5	6.0	7.0
						$\beta = 3.0$							
1	0.534	0.807	1.201	1.587	1.965	2.333	2.689	3.032	3.361	3.674	3.971	4.252	4.765
2	5.934	6.655	7.716	8.496	9.067	9.508	9.873	10.20	10.50	10.79	11.07	11.36	11.95
3	6.757	7.231	8.013	8.656	9.165	9.580	9.939	10.27	10.58	10.89	11.20	11.52	12.18
4	16.15	16.52	17.20	17.84	18.37	18.82	19.19	19.51	19.81	20.09	20.35	20.62	21.15
						$\beta = 2.0$							
1	0.669	0.983	1.456	1.917	2.363	2.792	3.200	3.587	3.951	4.290	4.606	4.899	5.418
2	5.969	6.713	7.817	8.647	9.273	9.776	10.21	10.61	10.99	11.37	11.74	12.12	12.90
3	6.787	7.285	8.114	8.812	9.383	9.868	10.30	10.72	11.13	11.55	11.97	12.40	13.28
4	16.16	16.55	17.27	17.94	18.52	19.01	19.44	19.83	20.20	20.55	20.90	21.26	21.99
						$\beta = 1.5$							
1	0.805	1.128	1.665	2.184	2.680	3.151	3.594	4.007	4.389	4.740	5.062	5.355	5.865
2	6.003	6.771	7.918	8.794	9.473	10.03	10.53	11.00	11.46	11.91	12.36	12.82	13.75
3	6.816	7.338	8.215	8.967	9.599	10.15	10.67	11.17	11.67	12.17	12.68	13.21	14.27
4	16.18	16.58	17.33	18.04	18.66	19.20	19.69	20.14	20.58	21.01	21.44	21.88	22.81
						$\alpha = 1.0$							
1	0.980	1.366	2.001	2.604	3.171	3.697	4.180	4.618	5.014	5.368	5.685	5.968	6.448
2	6.071	6.884	8.113	9.079	9.858	10.53	11.14	11.73	12.31	12.90	13.48	14.07	15.25
3	6.875	7.444	8.414	9.271	10.02	10.71	11.36	12.01	12.66	13.31	13.97	14.64	15.96
4	16.21	16.64	17.45	18.24	18.95	19.59	20.18	20.76	21.33	21.90	22.49	23.10	24.36
						$\alpha = 1.5$							
1	1.188	1.646	2.385	3.071	3.701	4.269	4.776	5.223	5.616	5.960	6.262	6.526	6.962
2	6.171	7.049	8.396	9.487	10.40	11.21	11.98	12.72	13.46	14.19	14.93	15.66	17.10
3	6.963	7.602	8.709	9.716	10.63	11.49	12.32	13.15	13.97	14.79	15.60	16.41	17.96
4	16.26	16.73	17.64	18.53	19.37	20.15	20.91	21.66	22.41	23.19	23.98	24.79	26.48
						$\alpha = 2.0$							
1	1.358	1.870	2.682	3.423	4.088	4.676	5.189	5.633	6.016	6.347	6.632	6.878	7.278
2	6.269	7.210	8.667	9.872	10.90	11.84	12.74	13.61	14.47	15.32	16.16	16.99	18.61
3	7.051	7.758	8.996	10.14	11.20	12.21	13.19	14.15	15.10	16.04	16.95	17.84	19.52
4	16.31	16.82	17.82	18.82	19.78	20.70	21.61	22.52	23.45	24.39	25.36	26.35	28.35
						$\alpha = 3.0$							
1	1.631	2.219	3.128	3.931	4.630	5.229	5.737	6.165	6.526	6.830	7.087	7.305	7.650
2	6.460	7.520	9.179	10.59	11.82	12.97	14.07	15.13	16.17	17.19	18.12	19.14	20.94
3	7.226	8.066	9.549	10.94	12.24	13.48	14.68	15.84	16.96	18.03	19.06	20.04	21.83
4	16.41	17.00	18.18	19.40	20.59	21.77	22.95	24.14	25.35	26.58	27.81	29.04	31.45

$$\frac{Mb^2}{aD} = \sum_{m=1,3,5}^{\infty} E_m \sin\frac{m\pi\xi}{2}. \tag{5}$$

The solution for the vibration amplitude of the first building block is obtained in a form similar to that of equation (3). This solution will, of course, involve the hyperbolic sine and trigonometric sine functions. In generating the eigenvalue matrix, contributions of the building blocks to moment and slope, etc., along the edges are expanded in a sine series as utilized in equation (5).

3.3 Modes Symmetric About the ξ Axis and Antisymmetric About the η Axis. Analysis of this family of modes is achieved by utilizing a set of building blocks, two of which can be extracted from the first set in the previous section, with two more extracted from the second set. One can always orient the coordinate system so that the modes are symmetric about the ξ axis.

4 Presentation of Computed Results

Before examining these results it is appropriate to look at the results of some convergence tests. Typical convergence test curves are plotted in Fig. 4. They pertain to the first and fourth mode fully symmetric vibration of a square plate. All of the dimensionless elastic coefficient are given a value of ten. It is seen that no change in four-digit accuracy is obtained with values of K, the number of terms in the series, exceeding four. Nevertheless, all computed results reported here have been obtained using ten terms in the series. It is reasonable, therefore, to expect all results to have four-digit accuracy.

As indicated earlier, there are numerous verification tests which can be performed by letting the elastic constants approach their natural limits of zero, the infinity. Results of typical tests conducted in conjunction with this study are presented for fully-symmetric mode vibration in Fig. 5. Infinite elastic stiffnesses have been simulated by setting the associated dimensionless elastic coefficients equal to 800. It is easily verified that the correct lower limits of the eigenvalues are approached in this figure. Upper limits of $\pi^2/2$ for the lowest curve (the simply-supported plate) and 8.996 for the other two curves (the fully-clamped plate) are approached as the variable stiffness parameters are increased.

Downloaded 03 May 2010 to 171.66.16.31. Redistribution subject to ASME license or copyright; see http://www.asme.org/terms/Terms_Use.cfm

Table 2 Eigenvalues, $\lambda^2 = \omega a^2 \sqrt{\rho/D}$, for fully-antisymmetric mode vibration of square plates with equal translational and equal rotational stiffnesses along all edges

	$\sqrt{K_{R1}}$												
MODE	0.7	1.0	1.5	2.0	2.5	3.0	3.5	4.0	4.5	5.0	5.5	6.0	7.0
						$\beta = 3.0$							
1	3.678	3.967	4.946	4.474	5.385	5.805	6.220	6.637	7.059	7.487	7.920	8.357	9.237
2	18.09	18.90	20.27	21.42	22.29	22.96	23.47	23.89	24.24	24.54	24.82	25.08	25.56
3	19.78	20.23	21.08	21.89	22.57	23.13	23.58	23.96	24.29	24.59	24.86	25.12	25.62
4	38.34	38.79	38.68	40.56	41.33	41.97	42.49	42.92	43.28	43.58	43.85	44.08	44.51
						$\beta = 2.0$							
1	3.737	4.072	5.243	4.671	5.789	6.321	6.852	7.385	7.922	8.462	9.005	9.544	10.62
2	18.11	18.93	20.33	21.50	22.41	23.12	23.68	24.14	24.54	24.91	25.25	25.57	26.21
3	19.79	20.25	21.13	21.97	22.69	23.29	23.79	24.22	24.61	24.97	25.32	25.65	26.32
4	38.34	38.80	39.71	40.61	41.40	42.06	42.61	43.07	43.46	43.80	44.11	44.39	44.91
						$\beta = 1.5$							
1	3.795	4.175	5.521	4.858	6.161	6.790	7.416	8.043	8.672	9.299	9.922	10.54	11.75
2	18.12	18.96	20.39	21.59	22.54	23.28	23.88	24.39	24.85	25.27	25.67	26.06	26.83
3	19.80	20.28	21.18	22.05	22.81	23.45	24.00	24.49	24.93	25.35	25.77	26.17	27.01
4	38.35	38.82	39.74	40.65	41.46	42.15	42.73	43.22	43.65	44.02	44.37	44.70	45.32
						$\alpha = 1.0$							
1	3.909	4.372	6.031	5.209	6.830	7.617	8.397	9.170	9.936	10.69	11.43	12.15	13.52
2	18.16	19.01	20.50	21.76	22.77	23.59	24.28	24.88	25.44	25.96	26.48	26.99	28.02
3	19.83	20.33	21.28	22.22	23.05	23.77	24.41	25.00	25.56	26.11	26.65	27.20	28.35
4	38.37	38.85	39.80	40.75	41.60	42.34	42.97	43.52	44.01	44.47	44.90	45.32	46.14
						$\alpha = 1.5$							
1	4.072	4.650	5.687	6.705	7.694	8.662	9.609	10.54	11.44	12.31	13.15	13.95	15.43
2	18.20	19.10	20.66	22.02	23.13	24.05	24.86	25.59	26.28	26.95	27.62	28.29	29.64
3	19.87	20.40	21.44	22.46	23.40	24.25	25.03	25.77	26.49	27.21	27.94	28.69	30.24
4	38.39	38.89	39.89	40.89	41.81	42.62	43.33	43.97	44.57	45.14	45.69	46.24	47.36
						$\alpha = 2.0$							
1	4.229	4.909	6.119	7.299	8.438	9.541	10.61	11.63	12.63	13.57	14.60	15.29	16.80
2	18.25	19.19	20.83	22.27	23.47	24.50	25.41	26.26	27.08	27.89	28.69	29.49	31.13
3	19.91	20.47	21.59	22.71	23.76	24.72	25.63	26.51	27.39	28.27	29.17	30.09	31.98
4	38.41	38.93	39.97	41.03	42.02	42.90	43.69	44.43	45.12	45.80	46.48	47.16	48.57
						$\alpha = 3.0$							
1	4.524	5.383	6.880	8.313	9.674	10.96	12.20	13.35	14.43	15.43	16.35	17.20	18.67
2	18.35	19.36	21.15	22.75	24.13	25.35	26.47	27.54	28.58	29.60	30.63	31.66	33.73
3	19.98	20.62	21.89	23.20	24.45	25.65	26.81	27.95	29.10	30.27	31.44	32.63	35.01
4	38.45	39.02	40.15	41.32	42.43	43.46	44.41	45.33	46.23	47.13	48.04	48.97	50.94

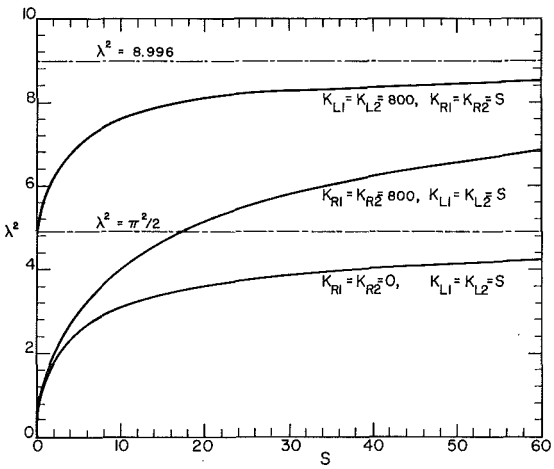


Fig. 5 Plot of eigenvalue versus stiffness coefficients for fundamental mode vibration of a square plate. Correct upper limits shown are approached in all cases.

It will be obvious, in view of the numerous parameters involved, that only a very limited amount of computed data can be presented. This was not the case for plates with classical edge support. The remaining data presented in this paper will be restricted to square plates with uniform translational stiffnesses and uniform rotational stiffnesses around the entire plate. Only the ratio of the dimensionless elastic coefficients will be allowed to vary.

In order to gain insight into the effects of the elastic stiffnesses and their ratios on free vibration eigenvalues, some graphical results related to first-mode fully-symmetric vibration are plotted in Fig. 6. All curves approach the upper limit dictated by the first mode eigenvalue for fully-clamped plates.

The main body of computed digital data related to this paper appears in Tables 1, 2, and 3. Eigenvalues are recorded for the first four modes of each mode family for various stiffnesses and stiffness ratios. Parameters α and β are as defined in Fig. 6. In order to obtain a more favorable distribution of stiffnesses the data is tabulated for approximately even increments in the square root of the parameter K_{R1}. Plots of the

Downloaded 03 May 2010 to 171.66.16.31. Redistribution subject to ASME license or copyright; see http://www.asme.org/terms/Terms_Use.cfm

Table 3 Eigenvalues, $\lambda^2 = \omega\alpha^2\sqrt{\rho/D}$, for modes symmetric about one axis and antisymmetric about the other axis of square plates with equal translational and equal rotational stiffnesses along all edges

	$\sqrt{K_{R1}}$												
MODE	0.7	1.0	1.5	2.0	2.5	3.0	3.5	4.0	4.5	5.0	5.5	6.0	7.0
						$\beta = 3.0$							
1	1.353	1.793	2.401	2.899	3.345	3.770	4.185	4.598	4.985	5.414	5.818	6.216	6.995
2	9.168	9.617	10.37	11.02	11.54	11.97	12.35	12.69	13.02	13.34	13.66	13.99	14.67
3	16.16	16.87	18.12	19.17	19.98	20.59	21.06	21.44	21.76	22.03	22.28	22.51	22.94
4	26.66	27.15	28.07	28.92	29.64	30.22	30.69	31.08	31.41	31.69	31.95	32.19	32.64
						$\beta = 2.0$							
1	1.465	1.955	2.653	3.246	3.790	4.313	4.824	5.327	5.795	6.310	6.787	7.253	8.148
2	9.196	9.668	10.47	11.17	11.76	12.26	12.72	13.15	13.58	14.00	14.43	14.87	15.87
3	16.17	16.90	18.17	19.24	20.08	20.73	21.24	21.66	22.02	22.35	22.65	22.94	23.52
4	26.67	27.17	28.11	28.99	29.73	30.35	30.85	31.28	31.66	31.99	32.31	32.61	33.19
						$\beta = 1.5$							
1	1.569	2.103	2.880	3.554	4.178	4.778	5.363	5.935	6.463	7.038	7.566	8.077	9.043
2	9.223	9.718	10.57	11.32	11.97	12.55	13.08	13.60	14.11	14.63	15.15	15.69	16.79
3	16.18	16.92	18.22	19.32	20.19	20.87	21.42	21.88	22.29	22.67	23.03	23.38	24.08
4	26.68	27.19	28.15	29.05	29.83	30.47	31.02	31.49	31.91	32.29	32.66	33.02	33.74
						$\alpha = 1.0$							
1	1.757	2.370	3.281	4.086	4.837	5.556	6.250	6.920	7.566	8.185	8.776	9.339	10.38
2	9.278	9.818	10.76	11.62	12.39	13.09	13.77	14.44	15.11	15.79	16.47	17.17	18.58
3	16.21	16.97	18.31	19.47	20.48	21.14	21.77	22.31	22.81	23.29	23.76	24.22	25.17
4	26.70	27.23	28.23	29.18	30.01	30.72	31.34	31.89	32.40	32.89	33.37	33.84	34.82
						$\alpha = 1.5$							
1	2.004	2.716	3.787	4.743	5.633	6.476	7.279	8.041	8.762	9.441	10.08	10.67	11.58
2	9.360	9.966	11.04	12.05	12.98	13.87	14.73	15.59	16.46	17.33	18.20	19.07	20.79
3	16.25	17.04	18.45	19.69	20.71	21.55	22.29	22.95	23.58	24.20	24.82	25.44	26.73
4	26.73	27.29	28.35	29.38	30.29	31.10	31.82	32.50	33.14	33.78	34.41	35.06	36.41
						$\alpha = 2.0$							
1	2.222	3.017	4.218	5.290	6.280	7.210	8.083	8.901	9.664	10.37	11.02	11.52	12.67
2	9.441	10.11	11.32	12.47	13.55	14.59	15.62	16.64	17.65	18.67	19.67	20.66	22.56
3	16.29	17.12	18.60	19.91	21.02	21.96	22.79	23.57	24.33	25.07	25.83	26.59	28.17
4	26.76	27.35	28.47	29.57	30.57	31.47	32.30	33.10	33.87	34.65	35.44	36.24	37.93
						$\alpha = 3.0$							
1	2.598	3.528	4.930	6.170	7.299	8.338	9.293	10.16	10.96	11.58	11.58	12.91	13.88
2	9.600	10.40	11.84	13.25	14.60	15.91	17.19	18.45	19.68	20.89	22.05	23.18	25.27
3	16.37	17.27	18.88	20.35	21.62	22.74	23.77	24.77	25.74	26.72	27.71	28.70	30.71
4	26.82	27.47	28.71	29.95	31.12	32.21	33.25	34.28	35.30	36.34	37.40	38.49	40.73

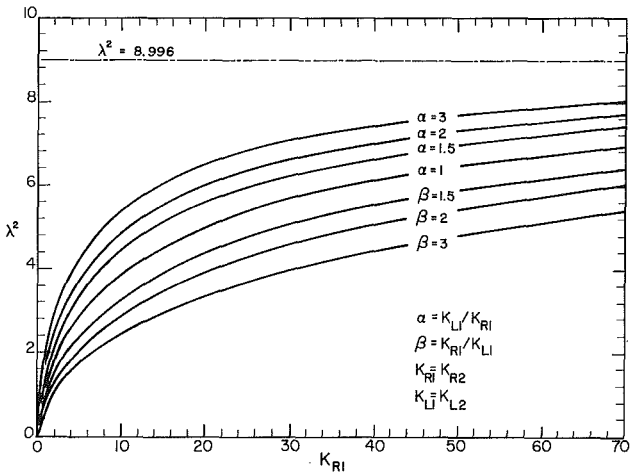


Fig. 6 Plot of eigenvalue versus stiffness coefficients for fundamental mode vibration of a square plate with various ratios of coefficients. Correct upper limit of 8.996 is aproached in all cases.

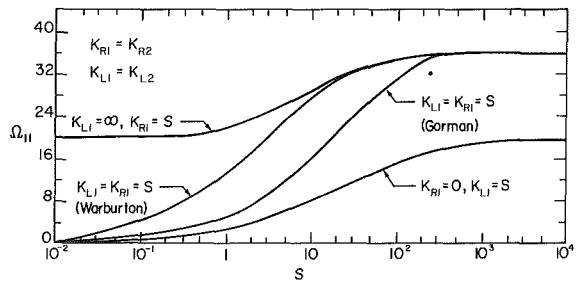


Fig. 7 Comparison of present results with those of Warburton and Edney for first-mode vibration of a square plate. Rotational and displacement elastic coefficients vary simultaneously. Their definition of eigenvalue is utilized.

type provided in Fig. 5 can be prepared from this data.

Finally, in Fig. 7, a comparison is made between data generated by the superposition method described here and corresponding data extracted from the publication of Warburton and Edney (Warburton, 1984). Agreement between the two

Downloaded 03 May 2010 to 171.66.16.31. Redistribution subject to ASME license or copyright; see http://www.asme.org/terms/Terms_Use.cfm

sources for the upper and lower curves is so good that in each case only a single curve can be plotted. For the intermediate curves ($K_{L1} = K_{R1} = S$) there is disparity between data from the two sources even though they approach the same limits. With a value of S equal to ten, for example, it is seen that there is little separation between the upper and intermediate curves of Warburton and Edney. This is equivalent to finding that for this particular value of S, little change is affected by changing the parameter K_{L1} from ten to infinity. This is not in keeping with the findings during the preparation of this paper.

5 Discussion and Conclusions

This represents, to the author's knowledge, the first accurate and comprehensive study of this family of problems. Convergence is found to be rapid. It is pointed out by Warburton and Edney that their Reyleigh-Ritz approach will not handle problems where both rotational and translational elasticity are incorporated into a plate edge if the plate has one or more free corners. No such restrictions apply to the analysis described here.

It is expected that the extensive listing of computed data presented will serve a valuable role in providing other researchers with reference values with which to compare their results. Designers will also find the computed eigenvalues to be useful, provided their problems fall within the range for which results are tabulated. Experimentalists may be able to use this data to infer values for the elastic constants once the frequency of vibration of a plate is measured. It appears that the only practical way to assure the availability of eigenvalues and mode shape information for all possible plate geometries and elastic coefficient combinations is to prepare the necessary digital computer routines following the computational procedures described herein.

References

Gorman, D. J., 1982, *Free Vibration Analysis of Rectangular Plates*, Elsevier North-Holland, Inc., New York.

Gorman, D. J., 1988, "Accurate Free Vibration Analysis of Rectangular Plates Resting on Symmetrically Distributed Uniform Elastic Supports—Symmetric Mode Analysis," *Proceedings of the Ninth Symposium on Eng. Applications of Mechanics*, University of Western Ontario, London, Canada, May 29-31, pp. 152-159.

Leissa, A. H., 1969, "Vibration of Plates," National Aeronautics and Space Administration Report, NASA SP-160.

Warburton, G. B., and Edney, S. L., 1984, "Vibrations of Rectangular Plates with Elastically Restrained Edges," *Journal of Sound and Vibration*, Vol. 95, No. 4, pp. 537-552.

Downloaded 03 May 2010 to 171.66.16.31. Redistribution subject to ASME license or copyright; see http://www.asme.org/terms/Terms_Use.cfm

Inelastic Response of an Infinite Cylindrical Shell to Transient Acoustic Waves

Thomas L. Geers
Department of Mechanical Engineering,
University of Colorado,
Boulder, CO 80309
Fellow ASME

Chi-Lin Yen
Lockheed Missiles and Space Company,
Sunnyvale, CA 94089

The geometrically and constitutively nonlinear response of an infinite, circular, cylindrical shell submerged in an infinite fluid medium to a transverse, transient acoustic wave is analyzed. Circumferential Fourier series solutions are obtained through the numerical integration of coupled ordinary differential equations and convolution integrals. Numerical results are presented in the form of response histories, response snapshots, and iso-damage curves for incident waves of rectangular pressure profile. Response solutions obtained with the first-order doubly asymptotic approximation are compared with their "exact" counterparts. It is found that doubly asymptotic approximations are unsuitable for two-dimensional, shock-response analysis of yielding submerged structures.

Introduction

During the last 15 years, numerous shock response calculations have been performed for submerged structures excited by transient acoustic waves (see, e.g., Ranlet et al., 1977; Neilson et al., 1981). The computer codes employed in these calculations have generally utilized the finite element method (FEM) to model the structure and the boundary element method (BEM) to model the surrounding fluid medium (see, e.g., Everstine, 1976; DeRuntz et al., 1980; DeRuntz and Brogan, 1980; Vasudevan and Ranlet, 1982; Atkatsh et al., 1987). Both linear and nonlinear finite element codes have been used to treat structural response, and boundary element codes based on first and second-order doubly asymptotic approximations (DAA_1 and DAA_2) have been used to treat the fluid-structure interaction (Geers, 1971; Geers, 1978; Felippa, 1980; Geers and Felippa, 1983).

Most of the DAA-based FEM/BEM codes for underwater-shock structural analysis have been tested against analytical solutions to canonical problems. Huang (1969) and Geers (1978) provided generalized Fourier series solutions for the axisymmetric, linear-elastic response of a submerged spherical shell, and Geers (1969, 1972) and Huang (1970) furnished Fourier series solutions for the two-dimensional, linear-elastic response of a submerged, infinite, circular cylindrical shell. Geers and Yen (1981) extended the cylindrical shell analyses by considering geometrically nonlinear shell response in order to examine dynamic instability. Here we extend the cylindrical shell analyses further by considering both geometrically and constitutively nonlinear shell behavior in order to examine dynamically unstable and inelastic shell response.

In this study, the structural analyzer DYNAPLAS (see, e.g., Stricklin et al., 1974) has been used to treat structural response. It is well suited to the task, in that it is based upon circumferential Fourier decomposition of shell response and has been extensively evaluated (Stricklin et al., 1974; Ball et al., 1974). Based on the assumption of small strains, DYNAPLAS accounts for material and geometric nonlinearities through pseudo-force vectors that account for coupling of the Fourier harmonics. For further information, we refer the reader to Stricklin et al., and its extensive reference list.

The fluid-structure interaction is treated rigorously with the residual potential formulation (RPF) of Geers (1969, 1971, 1972). The interaction is subsequently treated with the DAA_1 for evaluation purposes. The formulation used here differs slightly but importantly from that given in Geers and Yen, 1981.

The inelastic-response results obtained in this study exhibit behavior that is quite different from that of elastic shells. They also demonstrate that doubly asymptotic approximations are unsuitable for two-dimensional, underwater-shock analyses of structures undergoing inelastic response.

Governing Equations

Consider the two-dimensional, plane-strain motions of the submerged, infinite, circular cylindrical shell of Fig. 1. The shell is excited by a transient acoustic wave that first contacts the shell at $\theta = \pi$. During the resulting fluid-structure interaction, shell behavior may involve both geometric and constitutive nonlinearity.

Structural Response Equations. For excitation symmetric about the horizontal line through the axis, decomposition of

Contributed by the Applied Mechanics Division of THE AMERICAN SOCIETY OF MECHANICAL ENGINEERS for publication in the JOURNAL OF APPLIED MECHANICS.

Discussion on this paper should be addressed to the Technical Editor, Leon M. Keer, The Technological Institute, Northwestern University, Evanston, IL 60201, and will be accepted until two months after final publication of the paper itself in the JOURNAL OF APPLIED MECHANICS. Manuscript received by the ASME Applied Mechanics Division, September 8, 1988; final revision, June 20, 1989.

Copyright © 1989 by ASME

Downloaded 03 May 2010 to 171.66.16.31. Redistribution subject to ASME license or copyright; see http://www.asme.org/terms/Terms_Use.cfm

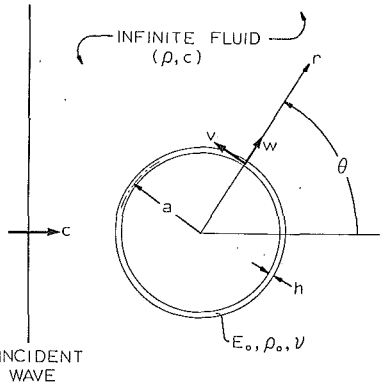


Fig. 1 Geometry of problem

shell and fluid response into circumferential Fourier harmonics yields

$$v(\theta,t)=\sum_{n=1}^{\infty} v_n(t)\,\sin n\theta$$

$$w(\theta,t)=\sum_{n=0}^{\infty} w_n(t)\,\cos n\theta \tag{1}$$

$$\phi(r,\theta,t)=\sum_{n=0}^{\infty}\phi_n(r,t)\,\cos n\theta$$

where $\phi(r,\theta,t)$ is the velocity potential for the acoustic field. Under such a decomposition, it can be shown that the structural equations for the axisymmetric and nth nonaxisymmetric response harmonics are (Stricklin et al., 1974; Geers and Yen, 1981)

$$\rho_o h\,\ddot{w}_o+f_o(v,w)=-[p_o]_{r=a}$$

$$\rho_o h\,\ddot{v}_n+f_{vn}(v,w)=-[p_o]_{r=a}\left(\frac{v_n}{a}+n\frac{w_n}{a}\right),\quad n\geq 1 \tag{2}$$

$$\rho_o h\,\ddot{w}_n+f_{wn}(v,w)=-\left[p_n+p_o\left(n\frac{v_n}{a}+\frac{w_n}{a}\right)+\frac{\partial p_o}{\partial r}w_n\right]_{r=a},\quad n\geq 1$$

where a double-dot denotes a second derivative in time, ρ_o and h are shell density and thickness, respectively, $p_n(r,t)$ is the nth harmonic of fluid pressure, and f_o, f_{wn}, and f_{vn} are stiffness-force harmonics computed within DYNAPLAS that involve linear-elastic, geometrically nonlinear and constitutively nonlinear behavior.

The terms on the right sides of (2) that involve pressure-displacement products are "live-load" terms appropriate to moderate displacements and rotations of the shell surface. They account for the major effect of finite membrane strain and finite rotation of shell normals on shell excitation by a normal pressure loading, as well as the primary effect of finite shell displacement on the loading produced by the spatially varying acoustic field. Note that only the dilatational ($n=0$) component of pressure need be included in the live-load terms (Geers and Yen, 1981). As DYNAPLAS does not possess live-load capability, the live-load terms have been treated as pseudo-forces generated by auxiliary software.

Fluid-Structure Interaction. A residual potential formulation (RPF) of the fluid-structure interaction, which constitutes an exact treatment, may be constructed as follows (Geers, 1969, 1971, 1972). First, fluid pressure and radial fluid-particle velocity are expressed as derivatives of the fluid velocity potential as

$$p=\rho\dot{\phi}$$

$$u=-\frac{\partial\phi}{\partial r}. \tag{3}$$

Second, the total acoustic field is treated as the superposition of the acoustic field for the known *incident wave* and the acoustic field for the unknown *scattered wave*, i.e.,

$$\phi(r,\theta,t)=\phi_I(r,\theta,t)+\phi_S(r,\theta,t). \tag{4}$$

Third, compatibility of radial fluid-particle velocity and radial shell velocity is enforced at the wet surface of the shell as

$$u(a,\theta,t)=\dot{w}(\theta,t). \tag{5}$$

Finally, the wave equation and radiation condition for each circumferential harmonic of the scattered wave are replaced by the equivalent residual-potential equation

$$\frac{\partial\phi_{Sn}}{\partial r}+\frac{1}{c}\dot{\phi}_{Sn}+\frac{1}{2r}\phi_{Sn}=-\frac{1}{r}\phi_{Rn}, \tag{6}$$

in which the residual potential ϕ_{Rn} is given by the convolution relation

$$\phi_{Rn}(r,t)=\int_o^t r_n(r,t-t')\,\phi_{Sn}(r,t')dt', \tag{7}$$

where the $r_n(r,t)$ are characteristic functions that resemble step-exponential functions (Geers, 1969).

Equations (3)–(6) may be utilized to produce, for each circumferential harmonic, the fluid-structure interaction relations

$$p_n^a=\rho(\dot{\phi}_{In}^a+\dot{\phi}_{Sn}^a)$$

$$\frac{\partial p_o^a}{\partial r}=-\rho\ddot{w}_o \tag{8}$$

$$\dot{w}_n-\frac{1}{c}\dot{\phi}_{Sn}^a-\frac{1}{2a}\phi_{Sn}^a=u_{In}^a+\frac{1}{a}\phi_{Rn}^a$$

where $\phi_{Rn}^a=\phi_{Rn}(a,t)$ is obtained from (7).

Coupled-Harmonic Solution Procedure. Coupled-harmonic equations of motion for the submerged shell are now readily obtained as follows. Expressions for the linear loading terms $[p_o]_{r=a}$ and $[p_n]_{r=a}$ in (2) are obtained by eliminating $\dot{\phi}_{Sn}^a$ in the first of (8) with the last of (8). Then, $[p_o]_{r=a}$ and $[\partial p_o/\partial r]_{r=a}$ are eliminated in the live-load terms of (2) with the first and second of (8). The resulting equations are then nondimensionalized in accordance with

$$\hat{p}=p^a/\rho c^2,\quad \hat{w}=w/a,\quad \hat{t}=ct/a. \tag{9}$$

The coupled-harmonic, nondimensional response equations underlying the implementation used for computations are then

$$(\rho_o h/\rho a)\ddot{w}_o+\dot{w}_o+f_o(v,w)=-\dot{\phi}_{Io}+u_{Io}+\frac{1}{2}\phi_{So}+\phi_{Ro}$$

$$(\rho_o h/\rho a)\ddot{v}_n+f_{vn}(v,w)=-(\dot{\phi}_{Io}+\dot{\phi}_{So})(v_n+nw_n),\quad n\geq 1$$

$$(\rho_o h/\rho a)\ddot{w}_n+\dot{w}_n+f_{wn}(v,w)=-\dot{\phi}_{In}+u_{In}+\frac{1}{2}\phi_{Sn}+\phi_{Rn}$$

$$-(\dot{\phi}_{Io}+\dot{\phi}_{So})(nv_n+w_n)+\ddot{w}_o w_n,\quad n\geq 1$$

$$\dot{\phi}_{Sn}+\frac{1}{2}\phi_{Sn}=-u_{In}+\dot{w}_n-\phi_{Rn}$$

$$\phi_{Rn}=r_n*\phi_{Sn} \tag{10}$$

where all circumflexes and a superscripts have been dropped, and the asterisk denotes temporal convolution, as defined in (7). For $n=0$, (10) contains three equations for the three unknowns w_o, ϕ_{So}, and ϕ_{Ro}, while for each $n\geq 1$, (10) contains four equations for the four unknowns v_n, w_n, ϕ_{Sn}, and ϕ_{Rn}. From a computational standpoint, the primary advantage of (10) is that, at early times, the terms involving

Downloaded 03 May 2010 to 171.66.16.31. Redistribution subject to ASME license or copyright; see http://www.asme.org/terms/Terms_Use.cfm

unknowns on the right sides of the first three of (10) are small or slowly varying relative to the acceleration and velocity terms on the left sides.

The combined response equations (10) were solved by step-by-step numerical integration as follows. The first three of (10) were solved with the half-step central-difference algorithm (Dahlquist and Bjork, 1974), which was introduced into DYNAPLAS to improve accuracy. This modification also involved the introduction of structural damping analysis capability into DYNAPLAS to treat the velocity terms on the left sides of the first and third of (10). The fourth of (10) was solved with a fourth-order Runge-Kutta scheme, (Lapidus and Seinfeld, 1971), and the last of (10) was solved with trapezoidal integration. This procedure possessed satisfactory accuracy, stability, and efficiency characteristics.

The coupled equations (10) constitute a simple example of *partitioned analysis* for coupled systems (see, e.g., Felippa and Geers, 1988). Here, the left sides of the first and third of (2) have been modified slightly to produce the left sides of the first and third of (10); such modification is called *augmentation*, and is employed to improve numerical accuracy and stability. The slightly modified structural analyzer, which solves the first three of (10), then operates on its own, responding to prescribed force data and to force data provided by the fluid analyzer at each time step. The fluid analyzer, which solves the last two of (10), also operates on its own, responding at each time step to prescribed displacement data and to displacement data provided by the structural analyzer. Thus the two analyzers operate in tandem, avoiding brute force simultaneous solution.

Calculated Responses. Once (10) have been solved numerically for a suitable number of circumferential harmonics, shell displacement and velocity responses may be calculated in accordance with (1). Often, however, greater physical insight is provided through the examination of other response quantities, as will be seen.

Response quantities that are especially useful for the interpretation of numerical results are the shell's extensional and flexural displacement harmonics $e_n(t)$ and $f_n(t)$. The latter pair is related to the former pair as (Geers and Yen, 1981)

$$e_n(t) = \frac{n}{n^2+1}\left[v_n(t) + \frac{1}{n} w_n(t)\right]$$
$$f_n(t) = \frac{n}{n^2+1}\left[-v_n(t) + n w_n(t)\right]. \tag{11}$$

Additional insight is gained through examination of extensional and flexural strain response, given by (Sanders, 1963),

$$\epsilon_\theta^e(\theta,t) = \sum_{n=0}^{\infty} [n v_n(t) + w_n(t)] \cos n\theta + \frac{1}{2}\left\{\sum_{n=1}^{\infty} [v_n(t) + n w_n(t)] \sin n\theta\right\}^2$$
$$\epsilon_\theta^f(\theta,t) = z \sum_{n=1}^{\infty} n[v_n(t) + n w_n(t)] \cos n\theta, \tag{12}$$

where z is the nondimensional radial distance from the neutral axis to the shell fiber of interest.

Note from (11) and (12) that, if $v_1(t) = -w_1(t)$, i.e., if $e_1(t) = 0$, the $n = 1$ harmonic makes no contribution to either extensional or flexural strain. This response constitutes translational rigid-body motion of the shell; all remaining response is deformational. Deformational response may be examined on its own, therefore, by simply removing the rigid-body harmonic from the Fourier series for total response, as follows. The inversion of (11) yields

$$v_n(t) = n e_n(t) - \frac{1}{n} f_n(t)$$
$$w_n(t) = e_n(t) + f_n(t). \tag{13}$$

The omission of $f_1(t)$ from these expressions when written for $n = 1$, followed by the introduction of the first of (11) for $n = 1$, then gives

$$v_1^*(t) = w_1^*(t) = \frac{1}{2}\left[v_1(t) + w_1(t)\right]. \tag{14}$$

The use of these instead of $v_1(t)$ and $w_1(t)$ in the first two of (1) yields for deformational response

$$v_d(\theta,t) = \frac{1}{2}[v_1(t) + w_1(t)] \sin\theta + \sum_{n=2}^{\infty} v_n(t) \sin n\theta$$
$$w_d(\theta,t) = w_o(t) + \frac{1}{2}[v_1(t) + w_1(t)] \cos\theta + \sum_{n=2}^{\infty} w_n(t) \cos n\theta. \tag{15}$$

Numerical Results

The results of extensive numerical response calculations based on (10) are presented here. The shell parameters are those of a two-dimensional model of a ring-stiffened steel shell, the surrounding fluid is water, and the excitation functions are incident plane waves of rectangular pressure profile.

Shell Model. Consider a thin, ring-stiffened, circular cylindrical shell with average surface density $<\rho_0 h>$, material plate velocity c_0 given by $c_0^2 = E/\rho_0(1-\nu^2)$, material yield stress $\sigma_y = 0.0025 \cdot E$, average membrane stiffness per unit length $<Eh>$, and average circumferential bending stiffness per unit length $<EI>$ equal to one hundred times that of the corresponding unstiffened shell, which is $\rho_0 c_0^2 h^3/12$. For a steel shell in water, appropriate parameter ratios are:

average surface density:	$<\rho_0 h>/\rho a = 0.0772$
material plate velocity:	$c_0/c = 3.53$
material yield stress:	$\sigma_y/\rho c^2 = 0.219$
avg. membrane stiffness:	$<\rho_0 c_0^2 h>/\rho c^2 a = 0.962$
avg. bending stiffness:	$<EI>/\rho c^2 a^3 = 100(\rho_0/\rho)$ $(c_0/c)^2(h/a)^3/12 = 8.02\times10^{-4}$

From these parameters, the following values may be obtained for the nondimensional limits of elastic stability and of hydrostatic elasticity (for the von Mises yield criterion with $\nu = 0.3$):

classical buckling pressure:	$P_c/\rho c^2 = 25(\rho_0/\rho)\ (c_0/c)^2(h/a)^3$ $= 2.41\times10^{-3}$
hydrostatic yield pressure:	$P_o/\rho c^2 = (\sigma_y/\rho c^2)(h/a)$ $= 2.46\times10^{-3}$

A uniform shell model of this ring-stiffened shell may be constructed that reproduces the preceding parameters, as follows:

sheil density:	$\rho_0/\rho = 0.772$
shell thickness:	$h/a = 0.1$
shell plate velocity:	$c_0/c = 3.53$
shell yield stress:	$\sigma_y/\rho c^2 = 0.0219.$

These values yield

surface density:	$\rho_0 h/\rho a = 0.0772$
membrane stiffness:	$\rho_0 c_0^2 h/\rho c^2 a = 0.962$
bending stiffness:	$(\rho_0 c_0^2 h^3/12)/\rho c^2 a^3 = 8.02\times10^{-4}$
buckling pressure:	$0.25\ \rho_0 c_0^2 h^3/\rho c^2 a^3 = 2.41\times10^{-3}$
yield pressure:	$P_o/\rho c^2 = (\sigma_y/\rho c^2)(h/a) = 2.46\times10^{-3}$

Downloaded 03 May 2010 to 171.66.16.31. Redistribution subject to ASME license or copyright; see http://www.asme.org/terms/Terms_Use.cfm

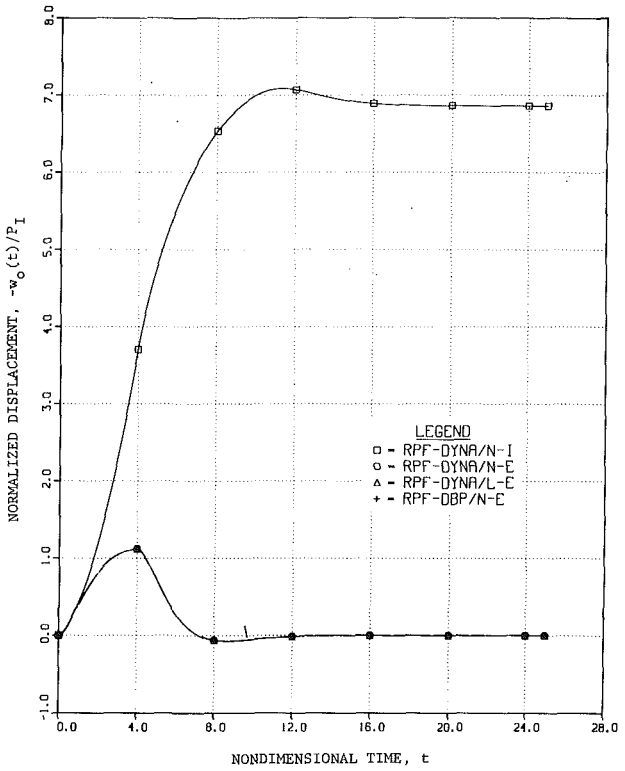


Fig. 2 Representative dilatational ($n=0$) displacement histories (RPF-DYNA and RPF-DBP; $P_I = 4P_c \cong 4\ P_o$, $T_I = 4$)

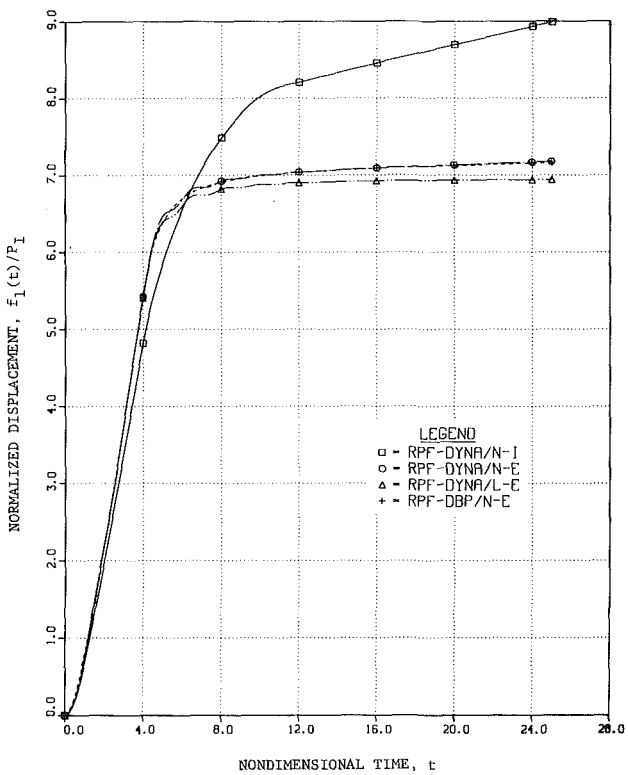


Fig. 3 Representative $n=1$ translational displacement histories (RPF-DYNA and RPF-DBP; $P_I = 4P_c \cong 4\ P_o$, $T_I = 4$)

Hence, the values of average surface density, average membrane stiffness per unit length, average bending stiffness per unit length, classical buckling pressure, and hydrostatic yield pressure for the ring-stiffened shell are reproduced by the uniform shell, which is amenable to two-dimensional analysis. Not reproduced are values for the limit parameters pertaining to circumferential bending: yield moment, yield curvature, and ultimate moment. Such values depend upon details of ring-stiffener geometry, which do not lend themselves to two-dimensional generalization. Fortunately, as will be seen, inelastic flexural response does not figure prominently in overall shell behavior, so this deficiency of the two-dimensional analysis is not serious.

Representative Shock Response Problem. A submerged, infinite, uniform, circular cylindrical shell, with parameters representative of a ring-stiffened shell, responds in plane strain to a transverse, plane, acoustic wave of rectangular pressure profile. The incident wave first contacts the shell at $\theta = \pi$, as pictured in Figure 1. The magnitude of the incident wave, P_I, is equal to four times the shell's elastic critical-buckling pressure, P_c, which, as seen above, is virtually the same as the shell's hydrostatic elastic-limit pressure, P_o. The width of the rectangular wave in the fluid medium is four shell radii ($T_I = 4$); hence the incident wave loading is of moderately long duration.

Figures 2–8 show the results of nonlinear inelastic response calculations produced by software based on (10), hereafter referred to as RFP-DYNA. Six circumferential harmonics ($n = 0$–5) are considered and the nonlinear material behavior of the shell is taken as elastic-perfectly plastic. Also shown are results pertaining to nonlinear elastic shell response, as calculated by the present software and by the small dynamic buckling program RPF-DBP used by Geers and Yen (1981). Good agreement between the RPF-DYNA and RPF-DBP results serve to validate the RPF-DYNA software. Finally, results pertaining to linear elastic shell response are provided for comparison purposes. It is important to remember that displacement and velocity histories are normalized to the magnitude of the incident rectangular wave P_I, which is 9.62×10^{-3} on a nondimensional basis; on a dimensional basis, it is this value times ρc^2, or 3240 psi.

Figure 2 shows $n=0$ displacement histories, which constitute dilatational motion, with inelastic shell behavior both included and excluded. It is seen that the nonlinear elastic (N-E) RPF-DYNA and RPF-DBP histories are coincident with the linear elastic (L-E) RPF-DYNA history. When inelastic shell behavior is included, dilatational response grows rapidly after the $n=0$ elastic-limit displacement $w_{0l} = -0.27$ $P_I = -0.0026$ is reached; the motion slows, however, as the incident wave passes beyond the shell, leaving an $n=0$ set displacement of $w_{0s} = -6.87$ $P_I = -0.0661$. Note the absence of oscillatory behavior in the dilatational response histories; this is the result of the heavy acoustic damping provided by the surrounding fluid (Geers, 1969; Huang, 1970).

As previously mentioned, extensional and flexural response harmonics are superior to radial and circumferential response harmonics for gaining insight into nonaxisymmetric shell behavior. Figure 3 shows $n=1$ flexural displacement histories, which constitute translational motion, for both elastic and inelastic shell response. The coincident nonlinear-elastic RPF-DYNA and RPF-DBP histories follow closely the linear-elastic RPF-DYNA history, while the inelastic RPF-DYNA history deviates significantly from the elastic histories. This deviation is caused by greatly increased $n=1$ extensional response (discussed later), which feeds back through the fluid-structure interaction to affect translational motion. The small late-time velocities exhibited by the nonlinear response histories are due to the pressure gradient term in the second of (2). When this term is omitted, the nonlinear elastic histories coincide with the linear elastic history and the nonlinear inelastic history approaches an asymptotic displacement of $f_1/P_I = 8.0$. Small effects of the pressure gradient term are also found in the $n \geq 2$ response histories.

Appreciable differences among linear elastic, nonlinear elastic, and inelastic histories are exhibited in Fig. 4, which

Downloaded 03 May 2010 to 171.66.16.31. Redistribution subject to ASME license or copyright; see http://www.asme.org/terms/Terms_Use.cfm

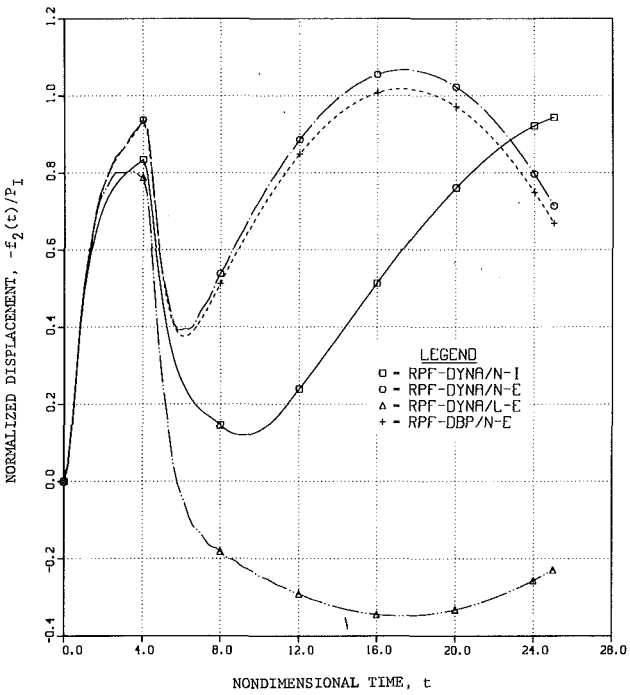


Fig. 4 Representative $n=2$ flexural displacement histories (RPF-FYNA and RPF-DBP; $P_I = 4P_c \cong 4\ P_o$, $T_I = 4$)

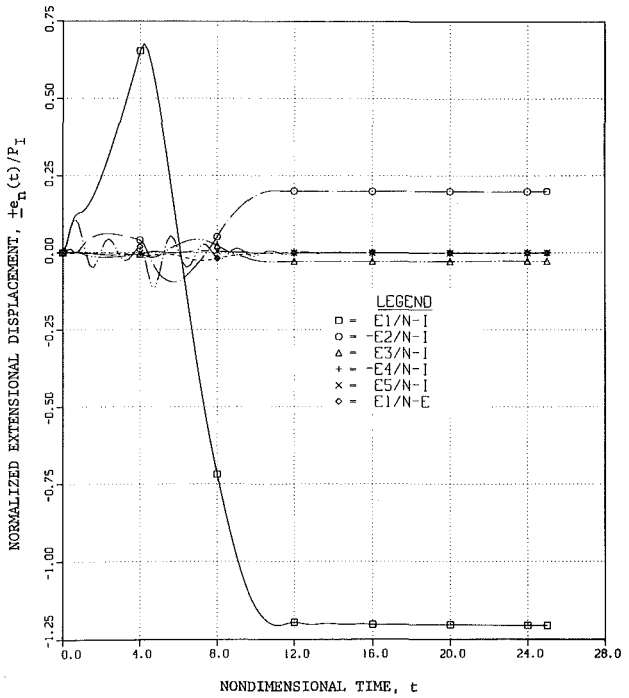


Fig. 5 Representative nonaxisymmetric extensional displacement histories (RPF-DYNA; $P_I = 4P_c \cong 4\ P_o$, $T_I = 4$)

shows $n=2$ flexural displacement response. A small discrepancy between the nonlinear elastic RPF-DYNA and RPF-DBP histories also appears at late times. For $t>11$, inelastic f_2-response consists of lightly damped oscillations about a set displacement whose value cannot be discerned from the figure.

As stated earlier, the response calculations included the $n=3$ through $n=5$ harmonics. These harmonics exhibit elastic response histories that, because of their small magnitudes, differ unimportantly from one another, and inelastic response histories that oscillate at late times about set displacements of $f_{3s}/P_I \cong 0.06$, $f_{4s}/P_I \cong 0.22$, and $f_{5s}/P_I \cong -0.02$.

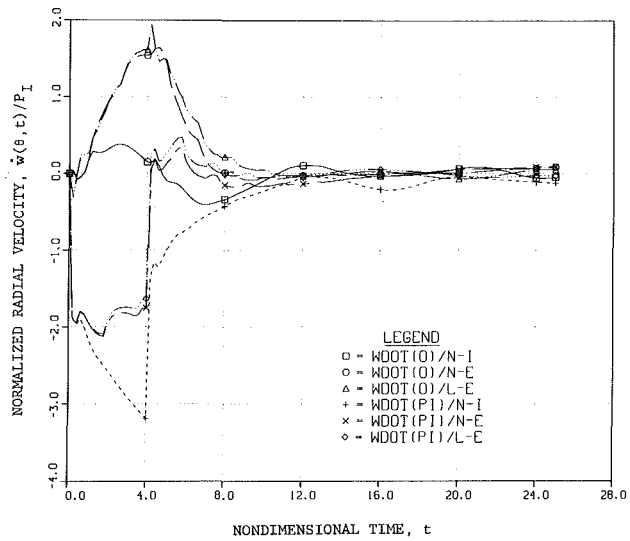


Fig. 6 Representative velocity response histories (RPF-DYNA; $P_I = 4P_c \cong 4\ P_o$, $T_I = 4$)

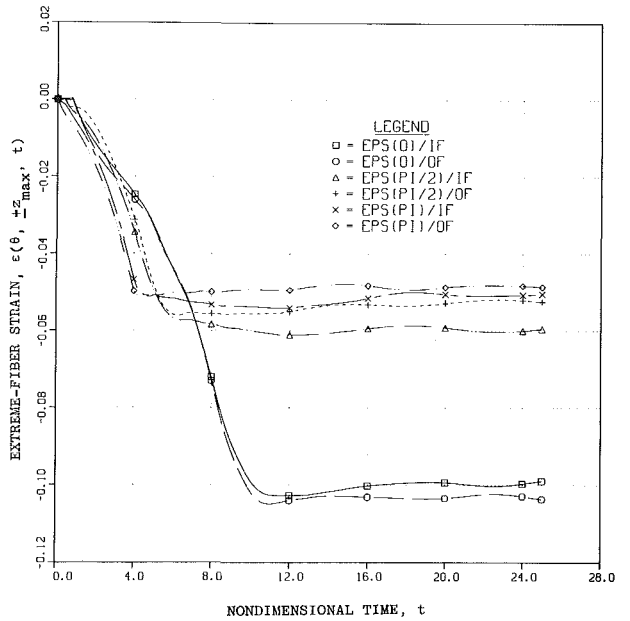


Fig. 7 Representative strain response histories (IF = inner fiber, OF = outer fiber) (RPF-DYNA; $P_I = 4P_c \cong 4\ P_o$, $T_I = 4$)

For elastic shell response, it was shown by Geers and Yen (1981) that nonaxisymmetric extensional displacement is negligible, and the $e_n(t)$ may be ignored. For inelastic shell motion this is not the case, as shown in Fig. 5. The figure shows $n=1-5$ extensional displacement histories for inelastic shell response, as well as the high frequency $n=1$ extensional displacement history for nonlinear elastic shell response; nonlinear elastic extensional displacement for $n \geq 2$ would not be visible in this figure.

Figure 6 shows radial velocity histories at $\theta=0$ and $\theta=\pi$ for inelastic, nonlinear elastic, and linear elastic response. It is seen that the nonlinear elastic histories differ little from their linear elastic counterparts, but that the inelastic histories deviate substantially from the rest. In particular, inelastic response considerably exceeds (in magnitude) elastic response at $\theta=\pi$, where the incident wave first contacts the shell, but is much smaller than elastic response at $\theta=0$, deep in the shadow region.

Downloaded 03 May 2010 to 171.66.16.31. Redistribution subject to ASME license or copyright; see http://www.asme.org/terms/Terms_Use.cfm

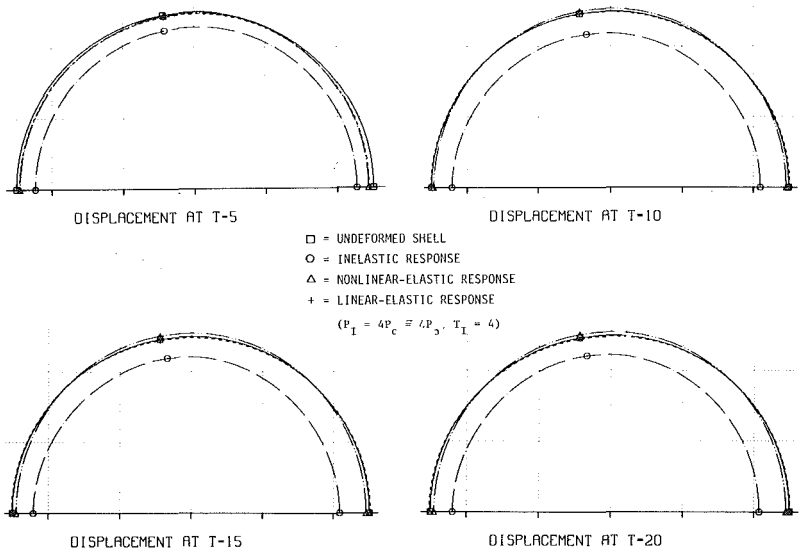


Fig. 8 Representative deformation response snapshots (actual deformations magnified a factor of two)

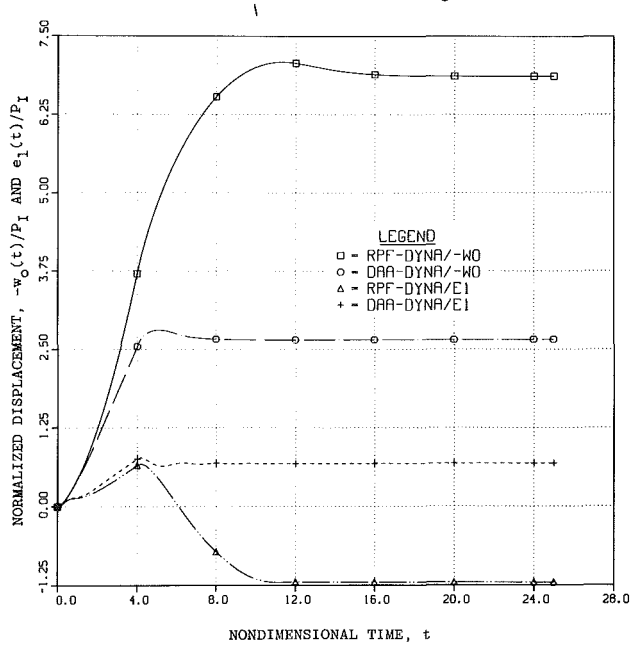


Fig. 9 Representative $n=0$ and $n=1$ extensional displacement histories (RPF-DYNA and DAA-DYNA; $P_I = 4P_c \cong 4\ P_o$, $T_I = 4$)

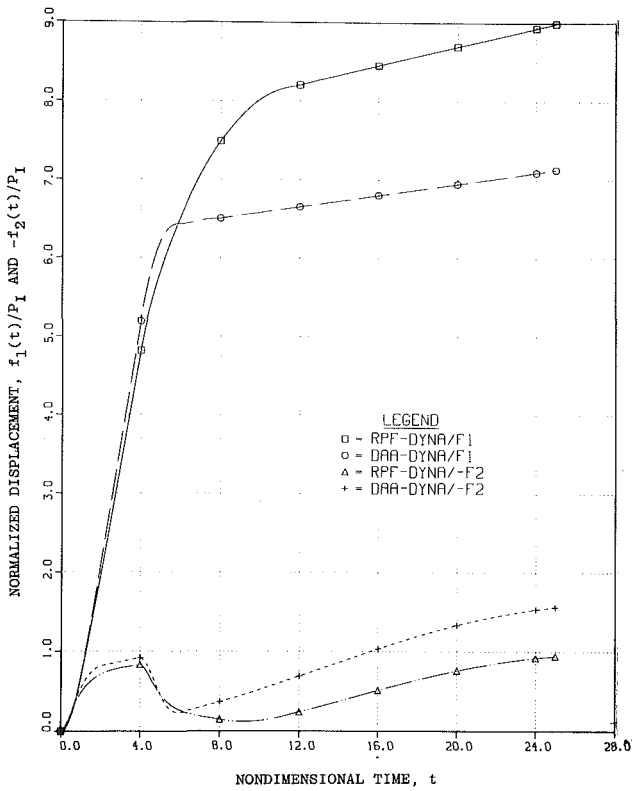


Fig. 10 Representative $n=1$ and $n=2$ flexural displacement histories (RPF-DYNA and DAA-DYNA; $P_I = 4P_c \cong 4\ P_o$, $T_I = 4$)

The substantial $n=1$ and $n=2$ extensional displacement responses of Fig. 5 are manifest in the strain histories of Fig. 7. They are responsible for the largest set strains occurring on the *back* side of the shell, with the maximum occurring at $\theta=0$. The proximity of the inner-fiber and outer-fiber strain histories at each θ-location illustrate the relative unimportance of flexural strain in overall shell response.

Finally, Fig. 8 shows deformation snapshots at $t=5$, 10, 15, and 20 for inelastic, nonlinear elastic and linear elastic shell response. These were obtained by the removal of rigid-body shell motion during Fourier synthesis, as discussed above. The inelastic response snapshots show large axisymmetric deformation; the modest nonaxisymmetric contribution is such that maximum deformation appears at $\theta=0$ when $t=10$, 15, and 20. In comparison, the elastic response snapshots exhibit appreciably smaller deformation dominated by f_2- displacement.

DAA Analysis. Doubly asymptotic approximations are used by all of the FEM/BEM underwater-shock structural analysis codes known to the authors. Hence, it is useful to investigate the accuracy of DAA's when applied to the preceding representative shock response problem. Application of the DAA_1 here involves replacing the last of (10) with $\phi_{Rn}(t) = (n-1/2)\phi_{Sn}(t)$, which is the result of the convolution integral when $\phi_{Sn}(t)$ is slowly varying compared with $r_n(t)$.

Figure 9 shows $n=0$ and $n=1$ extensional displacement histories; large discrepancies between the DAA-based histories and their RPF-based counterparts are observed. Note that the late-time asymptote for DAA $n=1$ response is of opposite sign with respect to its RPF counterpart; the impact of this difference on strain response will be seen shortly. Large

Downloaded 03 May 2010 to 171.66.16.31. Redistribution subject to ASME license or copyright; see http://www.asme.org/terms/Terms_Use.cfm

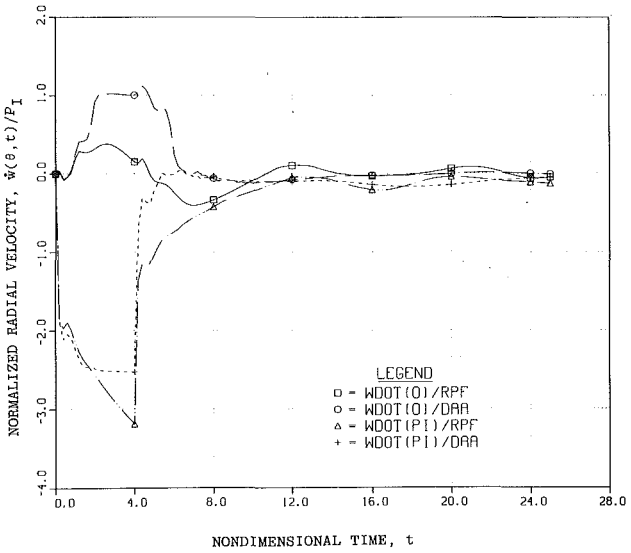


Fig. 11 Representative velocity response histories (RPF-DYNA and DAA-DYNA; $P_I = 4P_c \cong 4\ P_o$, $T_I = 4$)

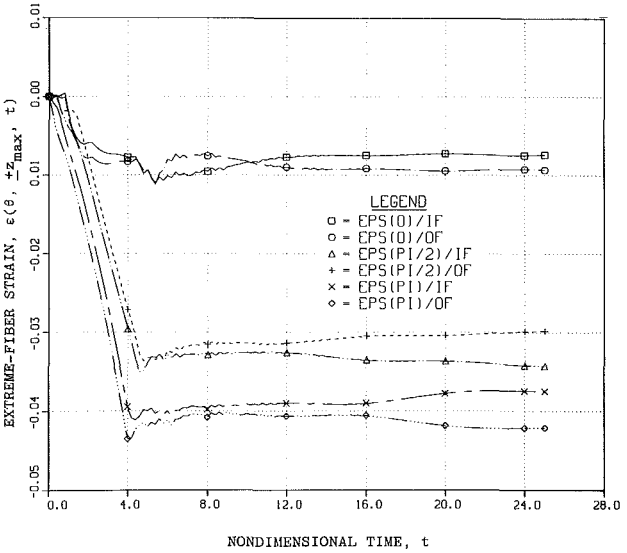


Fig. 12 Representative strain response histories (DAA-DYNA; $P_I = 4P_c \cong 4\ P_o$, $T_I = 4$)

discrepancies also appear between DAA-based and RPF-based flexural displacement histories, as seen in Fig. 10. While flexural responses have little effect on strain response, they play a substantial role in kinematic response.

Radial velocity histories at $\theta = 0$ and $\theta = \pi$ are shown in Fig. 11. It is seen that the DAA-based calculations tend to underestimate (in magnitude) velocity response on the side of the shell facing the incident wave, and to overestimate such response on the back side of the shell.

Finally, Fig. 12 shows DAA-based strain histories at $\theta = 0$, $\pi/2$ and π. A comparison of these histories with their RPF-based counterparts in Fig. 7 is rather startling. Not only is peak strain underestimated by a factor of 2.4, but the location of peak strain occurrence is completely missed, the DAA-based calculations placing it at $\theta = \pi$ and the RPF-based calculations placing it at $\theta = 0$. This is the direct result of the sign differences in the DAA and RPF late-time asymptotes for $n = 1$ *extensional displacement response mentioned above.*

Figures 9–12 clearly demonstrate failure of the DAA_1 as an accurate method for treating the fluid-structure interaction in this representative shock problem. The reason for its failure may be stated as follows. The strain field in the shell, and

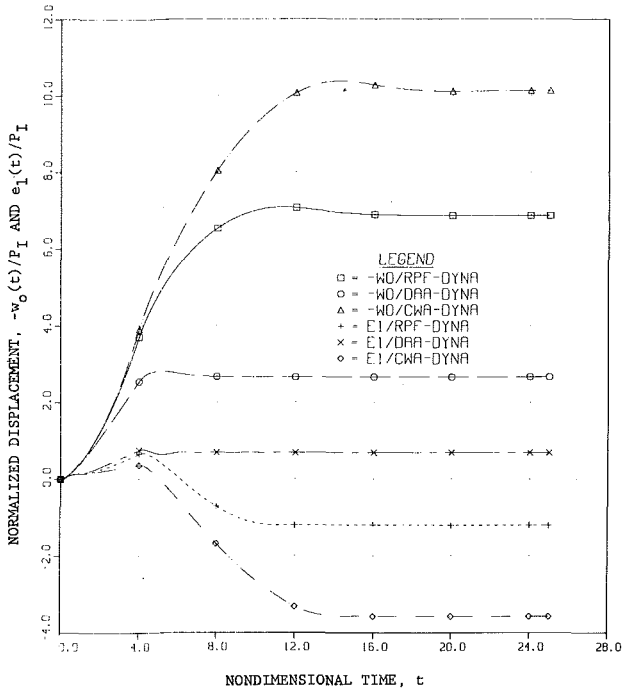


Fig. 13 Representative $n = 0$ and $n = 1$ extensional displacement histories (RPF-DYNA, DAA-DYNA, and CWA-DYNA; $P_I = 4P_c \cong 4\ P_o$, $T_I = 4$)

therefore its inelastic behavior, is dominated by the dilatational ($n = 0$) harmonic. But DAA_1 is *not doubly asymptotic* for dilatational motion of an infinite cylindrical body, because the added mass for such motion is infinite (see, e.g., Whitman, 1972). Hence, DAA_1 reduces in this case to the plane wave approximation (PWA) (see, e.g., Geers, 1975), which is accurate only for high frequency response.

For an *elastic* shell of high-modulus material, such as steel, the reduction of the DAA_1 to the PWA for dilatational shell motion is not harmful, because such motion is high frequency in nature. The motion quickly becomes low frequency, however, if the material yields, and the PWA is no longer valid.

One might seek to improve the situation by moving from DAA_1 to DAA_2. Unfortunately, the lack of an added mass asymptote for low frequency, two-dimensional, dilatational fluid motion is common to both, so prospects are not good. Specifically, the most general DAA_2 relation for dilatational motion is, in dimensional form (Felippa, 1980),

$$(m_o + \rho c q_o m_o^{-1})\ddot{\phi}_{So} + (1 + \kappa c q_o m_o^{-1})\rho c\ \dot{\phi}_{So} + \rho c \omega_o\ \phi_{So} = (m_o + \rho c q_o m_o^{-1}) c\ \dot{u}_{So} + m_o \omega_o c\ u_{So} \tag{16}$$

where the added mass per unit area m_o is initially taken as finite, q_o is a parameter with the dimensions of mass-time per unit area, κ is the curvature of the shell (which is $1/2a$), and ω_o is a frequency parameter. If m_o is allowed to approach infinity, (16) reduces to

$$\ddot{\phi}_{So} = c(\dot{u}_{So} + \omega_o u_{So}). \tag{17}$$

For the DAA_2 formulation based on fluid boundary modes (Geers, 1978), $\omega_o = \rho c m_o^{-1}$, which vanishes as $m_o \to \infty$. The result is just the PWA, which is the same limit that DAA_1 approaches as $m_o \to \infty$. For the DAA_2 formulation based on matching techniques (Felippa, 1980; Geers and Felippa, 1983), $\omega_o = \rho c m_o^{-1} - \kappa c$, which approaches $-\kappa c$ as $m_o \to \infty$. In this case, (17) can be written

$$\dot{u}_{So} - \kappa c\ u_{So} = \frac{1}{c}\ \ddot{\phi}_{So} \tag{18}$$

which yields unbounded solutions for u_{So}. Hence, the DAA_2, in whatever form, does not improve anything.

Downloaded 03 May 2010 to 171.66.16.31. Redistribution subject to ASME license or copyright; see http://www.asme.org/terms/Terms_Use.cfm

Table 1

Format

Maximum Extensional Set Strain Magnitude, $|\epsilon^{set}_{ext}|_{max}$ $\hat{P}_I = P_I/P_c$
Circumferential Location Where Maximum Occurs
Percentage Contribution of n=0 Set Strain to $|\epsilon^{set}_{ext}|_{max}$
Percentage Contribution of n=1 Extensional Set Strain to $|\epsilon^{set}_{ext}|_{max}$
Percentage Contribution of n=2 Extensional Set Strain to $|\epsilon^{set}_{ext}|_{max}$
Approximate Ratio of $|\epsilon^{set}_{flex}|_{max}$ to $|\epsilon^{set}_{ext}|_{max}$

$T_I = 1$, $\hat{P}_I = 1.2$	$T_I = 1$, $\hat{P}_I = 2.0$	$T_I = 1$, $\hat{P}_I = 2.8$
1.823	5.659	11.39
120°	0°	0°
78	66	61
11	9	19
12	16	15
0.06	0.02	0.00
$T_I = 1$, $\hat{P}_I = 3.6$	$T_I = 1$, $\hat{P}_I = 12$	$T_I = 1$, $\hat{P}_I = 18$
1.089	6.159	12.40
0°	0°	70°
41	78	87
16	10	5
20	9	7
0.15	0.01	0.27
$T_I = 2$, $\hat{P}_I = 3$	$T_I = 2$, $\hat{P}_I = 5$	$T_I = 2$, $\hat{P}_I = 9$
1.861	4.801	12.09
0°	0°	0°
55	63	90
24	14	18
12	13	0
0.06	0.03	0.06
$T_I = 4$, $\hat{P}_I = 1.8$	$T_I = 4$, $\hat{P}_I = 3.6$	$T_I = 4$, $\hat{P}_I = 4.2$
1.388	8.305	11.09
60°	0°	0°
69	64	66
7	23	23
8	10	9
0.07	0.02	0.01
$T_I = 6$, $\hat{P}_I = 1.7$	$T_I = 6$, $\hat{P}_I = 2.2$	$T_I = 6$, $\hat{P}_I = 3$
1.890	4.730	11.09
60°	50°	0°
89	73	66
0	20	27
5	2	7
0.04	0.08	0.00
$T_I = 10$, $\hat{P}_I = 1.2$	$T_I = 10$, $\hat{P}_I = 1.8$	$T_I = 10$, $\hat{P}_I = 2.2$
1.182	5.972	12.41
180°	70°	40°
83	89	78
11	3	20
5	8	2
0.10	0.42	0.41

One might next seek to improve the situation by utilizing a more accurate high frequency approximation, namely, the curved wave approximation (CWA) (see, e.g., Geers, 1975). Application of the CWA in this problem merely involves replacing the last of (10) with $\phi_{Rn}(t) = 0$. Extensional displacement response histories for $n = 0$ and $n = 1$ produced by RPF-DYNA, DAA-DYNA, and CWA-DYNA are compared in Fig. 13. It is seen that the RPF-based histories are bounded by their DAA-based and CWA-based counterparts; unfortunately, the bounds are unacceptably large. Similar histories for $n = 1$ and $n = 2$ flexural motion are shown in Fig. 14. Here, the RPF-based histories are bounded by their DAA-based and CWA-based counterparts over most of the time span shown, but these bounds too are unacceptably large. Hence, the CWA does not improve matters.

Damage Behavior. The damage behavior of the shell is now studied through the calculation of numerous transient response histories for an ensemble of incident plane waves with rectangular pressure profile. The response variable chosen for damage assessment is circumferential extensional (or membrane) set strain, because, as demonstrated in the following, the inelastic response of the shell is dominated by extensional motion.

Representative inner-fiber and outer-fiber strain response histories were examined in Fig. 7. In that case, peak extensional set strain was 10.1 percent, while peak flexural set strain was only 0.4 percent. Highly unrepresentative inner-fiber and outer-fiber strain response histories are shown in Fig. 15. In this case, for which $P_I = 1.8\ P_c$ and $T_I = 10$, peak extensional

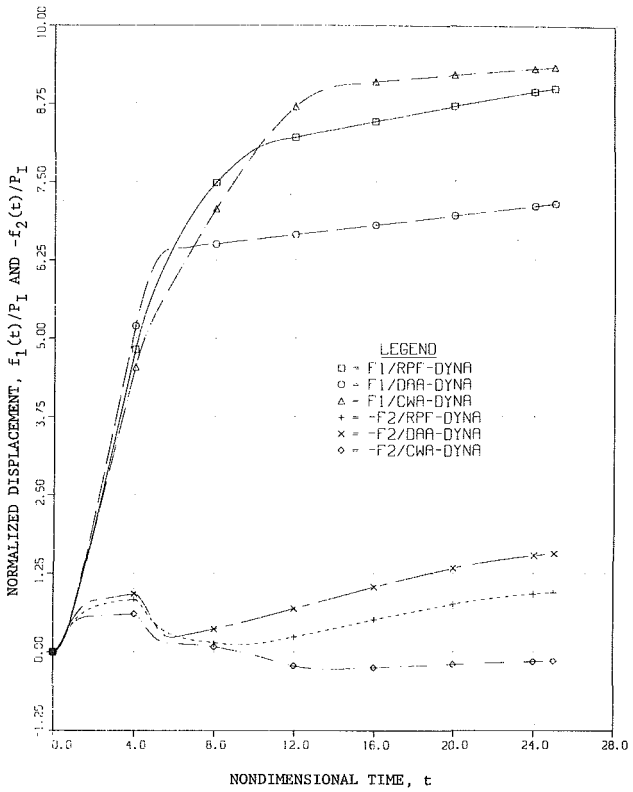


Fig. 14 Representative $n = 1$ and $n = 2$ flexural displacement histories (RPF-DYNA, DAA-DYNA, and CWA-DYNA; $P_I = 4P_c \cong 4\ P_o$, $T_I = 4$)

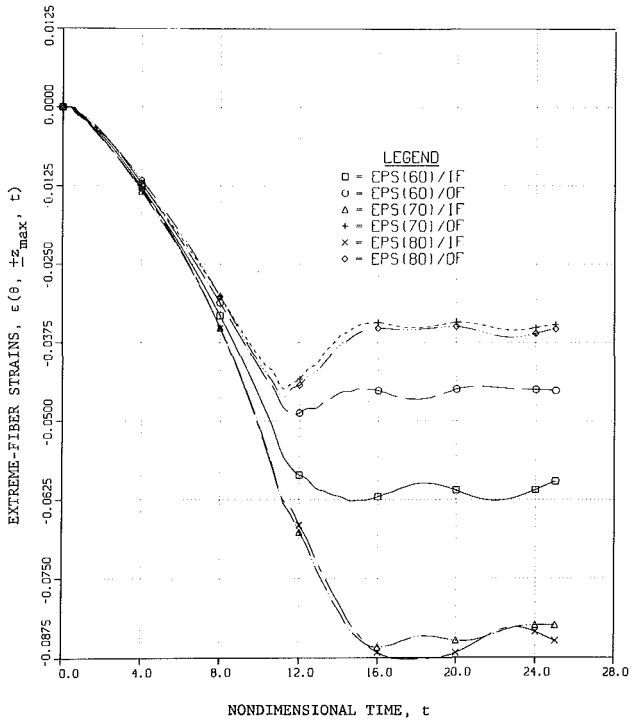


Fig. 15 Unrepresentative strain response histories (RPF-DYNA; $P_I = 1.8P_c \cong 1.8P_o$, $T_I = 10$)

set strain is 6.0 percent, while peak flexural set strain is 2.5 percent.

A more comprehensive picture of the inelastic response results obtained here is provided in Table 1, which summarizes the results obtained in 18 of the more than 50 RPF-DYNA transient response calculations performed. Six quantities are shown for each response calculation, as indicated in the for-

Downloaded 03 May 2010 to 171.66.16.31. Redistribution subject to ASME license or copyright; see http://www.asme.org/terms/Terms_Use.cfm

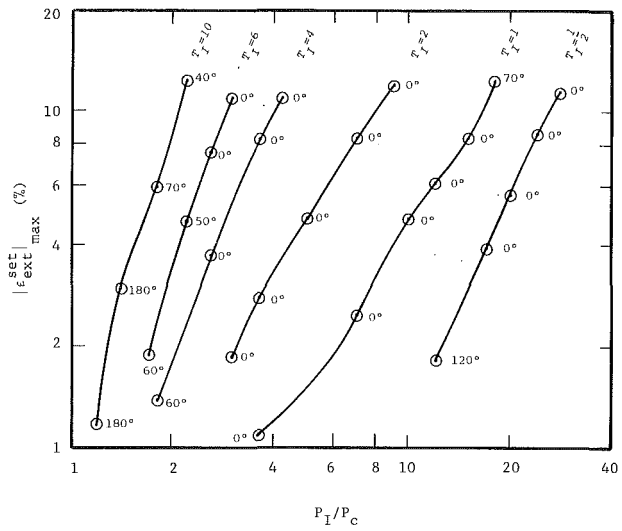


Fig. 16 Peak extensional set strains calculated by RPF-DYNA (angles indicate locations at which peaks are reached)

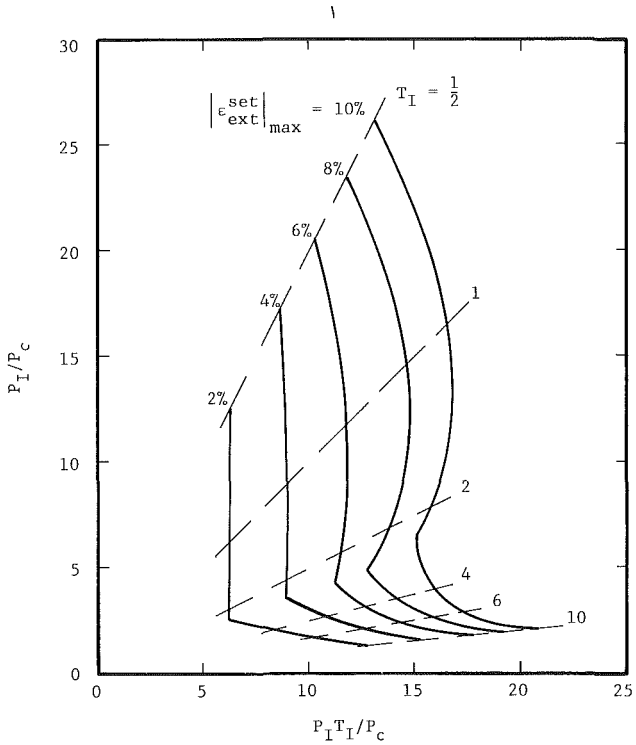


Fig. 17 RPF-DYNA iso-damage curves from the data of Fig. 16

mat statement. The table shows that the set-strain field in the shell is dominated by the $n=0$ harmonic, with the $n=1$ and $n=2$ extensional harmonics making modest contributions and the higher extensional harmonics contributing very little. Flexural set-strain is significant only in a few cases. Maximum extensional set-strain usually occurs on the side of the shell that faces *away* from the incoming wave.

ISO-Damage Curves. Calculated values of peak extensional set strain are shown as circled dots in Fig. 16, plotted as functions of P_I/P_c and T_I; recall that P_c is the elastic-critical-buckling pressure for this shell, which is virtually equal to its hydrostatic elastic-limit pressure. The $T_I=$ constant curves that connect the dots permit the accurate estimation of six combinations of P_I and T_I that yield a prescribed value of peak extensional set strain, which corresponds to a horizontal

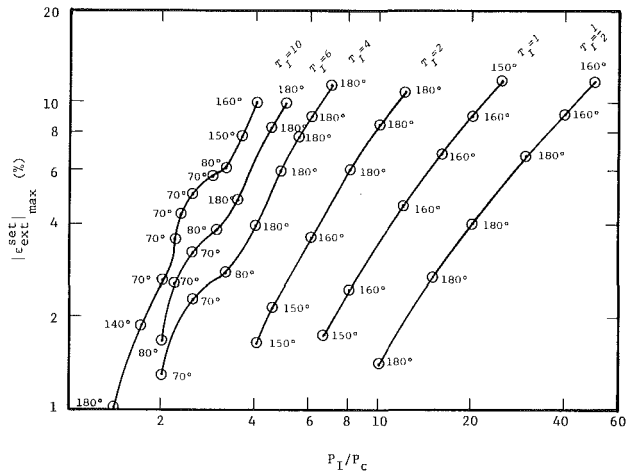


Fig. 18 Peak extensional set strains calculated by DAA-DYNA (angles indicate locations at which peaks are reached)

line across Fig. 16. The selection of five such values then leads to the iso-damage curves of Fig. 17.

Figure 17 shows curves of constant peak extensional set strain plotted in terms of the pressure magnitude and total impulse that completely characterize an incident rectangular wave. Although the curves exhibit the general characteristics of iso-damage curves, i.e., transition from vertical asymptotes for short pulses to horizontal asymptotes for long pulses, they do not possess the simple hyberbolic shapes produced by simple mechanical systems (Abrahamson and Lindberg, 1972).

Each iso-damage curve in Fig. 17 appears to consist of two damage branches, one for pulses with $T_I \leq 3$ and another for pulses with $T_I \geq 3$. The distinctly positive slopes characterizing the high strain branches between $T_I \cong 3$ and $T_I \cong 1.5$ produce an unexpected characteristic, namely, that a decrease in pressure magnitude, P_I, for fixed impulse, $P_I T_I$ (i.e., a downward vertical trajectory in the figure), produces an *increase* in peak extensional set-strain. This is undoubtedly due to a resonance condition where the shell is especially susceptible to pulses with durations comparable to the shell-envelopment period.

In order to gain a global view of the failure of DAA methods for this class of problems, the preceding process was repeated for calculations based on the DAA_1 instead of the RPF. The DAA-based results appear in Figs. 18 and 19, which correspond to the RPF-based results shown in Figs. 16 and 17, respectively. A comparison of Figs. 18 and 16 confirms the previous observation that DAA-based calculations tend to produce peak-strain occurrences on the front half of the shell, whereas the RPF-based calculations tend to produce them on the back half. A comparison of Figs. 19 and 17 supports the previous observation that DAA-based calculations significantly underestimate damage response. For example, a rectangular incident wave of width $T_I=1/2$ and magnitude $P_I/P_c=26$ produces 10 percent peak extensional set-strain in Fig. 17, whereas the same incident wave produces less than 6 percent peak extensional set-strain in Fig. 19.

Conclusion

This paper has examined the geometrically and constitutively nonlinear, plane-strain response of a submerged, infinite, circular cylindrical shell to a transverse acoustic wave. The structural analyzer DYNAPLAS has been used to determine shell response and the residual potential formulation has been used to treat the fluid-structure interaction. In addition, the suitability of doubly asymptotic approximations for solving two-dimensional problems of this type has been evaluated.

Downloaded 03 May 2010 to 171.66.16.31. Redistribution subject to ASME license or copyright; see http://www.asme.org/terms/Terms_Use.cfm

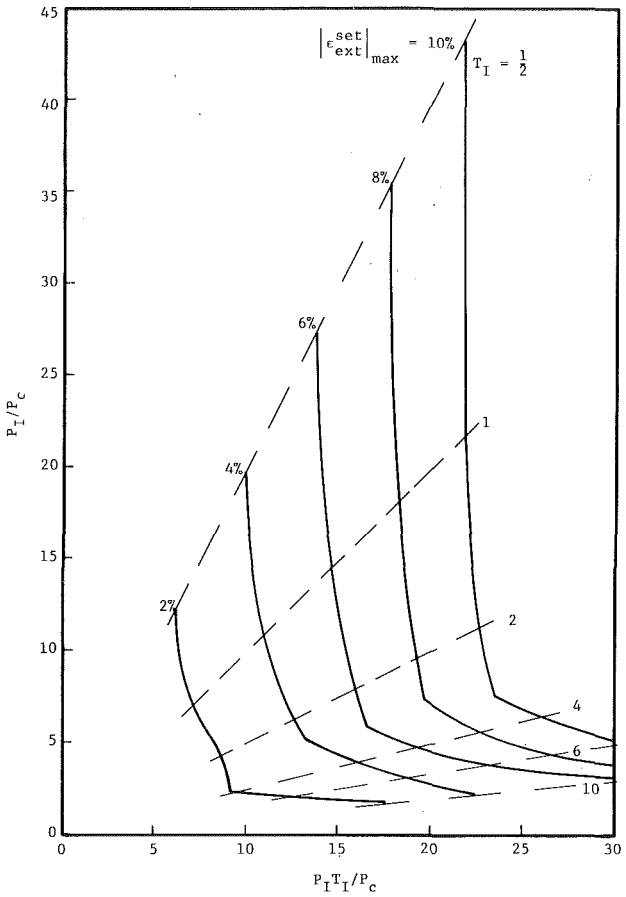


Fig. 19 DAA-DYNA iso-damage curves from the data of Fig. 18

Numerical results have been presented in the form of response histories, response snapshots, and iso-damage curves pertaining to excitation by plane incident waves of rectangular pressure profile. Examination of these results has led to the following observations:

(1) The occurrence of shell inelasticity profoundly affects the nature of both the shell response and fluid-structure interaction.

(2) Dilatational shell response dominates the strain field in the shell, and therefore plays the primary role regarding inelastic shell behavior.

(3) In spite of the dominance of dilatational shell response, nonaxisymmetric extensional response contributes significantly to shell deformation; this is not the case for elastic shell behavior.

(4) The largest set strains tend to occur at locations on the back side of the shell, typically deep in the shadow region.

(5) Due to the absence of an added-mass asymptote for two-dimensional, dilatational fluid flow, doubly asymptotic approximations are unsuitable for two-dimensional, shock response analyses of submerged structures undergoing low frequency motions characteristic of inelastic behavior; high frequency plane wave and curved wave approximations similarly fail.

The last of these observations constitutes a significant limitation to the use of existing computer codes for shock response analysis of submerged structures. For a circular fluid-structure interface, the residual potential formulation may be employed to treat the fluid-structure interaction through Fourier series decomposition of interface pressure and normal velocity. For noncircular interfaces, two-dimensional Kirchhoff or Waterman methods may be attempted (see, e.g., Geers, 1983).

Acknowledgments

This work was sponsored by the Office of Naval Research when both authors were at the Lockheed Palo Alto Research Laboratory. We are grateful to Dr. Nicholas Basdekas of ONR for his participation in many fruitful discussions. We are also indebted to Prof. Walter Haisler of Texas A&M University for his helpful consultation on the DYNAPLAS Code.

References

Atkatsh, R., et al., 1987, "Developments for the EPSA Computer Code," DNA-TR-87-155, Defense Nuclear Agency, Washington, D.C.

Ball, R. E., et al., 1974, "A Comparison of Computer Results for the Dynamic Response of the LMSC Truncated Cone," *International Journal of Computers and Structures*, Vol. 4, pp. 485–498.

Dahlquist, G., and Bjork, A., 1974, *Numerical Methods*, Prentice-Hall, Englewood Cliffs, N.J.

DeRuntz, J. A., et al., 1980, "The Underwater Shock Analysis Code (USA—Version 3)," DNA 5615F, Defense Nuclear Agency, Washington, D.C.

DeRuntz, J. A., and Brogan, F. A., 1980, "Underwater Shock Analysis of Nonlinear Structures, A Reference Manual for the USA-STAGS Code (Version 3)," DNA5545F, Defense Nuclear Agency, Washington, D.C.

Everstine, G. C., 1976, "A NASTRAN Implementation of the Doubly Asymptotic Approximation for Underwater Shock Response," *NASTRAN: Users Experiences*, NASA-TM-X3428, pp. 207–228.

Felippa, C. A., 1980, "Top-Down Derivation of Doubly Asymptotic Approximations for Structure-Fluid Interaction Analysis," *Innovative Numerical Analysis for the Engineering Sciences*, R. P. Shaw, et al., ed., pp. 79–88.

Felippa, C. A., and Geers, T. L., 1988, "Partitioned Analysis for Coupled Mechanical Systems," *Engineering Computation*, Vol. 5, pp. 123–133.

Geers, T. L., 1969, "Excitation of an Elastic Cylindrical Shell by a Transient Acoustic Wave," ASME JOURNAL OF APPLIED MECHANICS, Vol. 36, pp. 459–469.

Geers, T. L., 1971, "Residual Potential and Approximate Methods for Three-Dimensional Fluid-Structure Interaction Problems," *Journal of the Acoustical Society of America*, Vol. 49, pp. 1505–1510.

Geers, T. L., 1972, "Scattering of a Transient Acoustic Wave by an Elastic Cylindrical Shell," *Journal of the Acoustical Society of America*, Vol. 51, pp. 1640–1651.

Geers, T. L., 1975, "Transient Response Analysis of Submerged Structures," *Finite Element Analysis of Transient Nonlinear Behavior*, T. Belytschko, et al., ed., ASME, New York, pp. 59–84.

Geers, T. L., 1978, "Doubly Asymptotic Approximations for Transient Motions of Submerged Structures," *Journal of the Acoustical Society of America*, Vol. 64, pp. 1500–1508.

Geers, T. L., and Yen, C.-L., 1981, "Nonlinear Response of an Elastic Cylindrical Shell to a Transient Acoustic Wave," ASME JOURNAL OF APPLIED MECHANICS, Vol. 48, pp. 15–24.

Geers, T. L., 1983, "Boundary-Element Methods for Transient Response Analysis," *Computational Methods for Transient Analysis*, T. Belytschko and T. J. R. Hughes, eds. North-Holland, Amsterdam, pp. 221–243.

Geers, T. L., and Felippa, C. A., 1983, "Doubly Asymptotic Approximations for Vibration Analysis of Submerged Structures," *Journal of the Acoustical Society of America*, Vol. 73, pp. 1152–1159.

Huang, H., 1969, "Transient Interaction of Plane Acoustic Waves with a Spherical Elastic Shell," *Journal of the Acoustical Society of America*, Vol. 45, pp. 661–670.

Huang, H., 1970, "An Exact Analysis of the Transient Interaction of Acoustic Plane Waves with a Cylindrical Elastic Shell," ASME JOURNAL OF APPLIED MECHANICS, Vol. 37, pp. 1091–1106.

Lapidus, L., and Seinfeld, J. H., 1971, *Numerical Solution of Ordinary Differential Equations*, Academic Press, N.Y.

Neilson, H. C., et al., 1981, "Transient Response of a Submerged, Fluid-Coupled, Double-Walled Shell Structure to a Pressure Pulse," *Journal of the Acoustical Society of America*, Vol. 70, pp. 1776–1782.

Ranlet, D., et al., 1977, "Elastic Response of Submerged Shells with Internally Attached Structures to Shock Loading," *International Journal of Computers and Structures*, Vol. 7, pp. 355–364.

Sanders, J. L., 1963, "Nonlinear Theories for Thin Shells," *Quarterly of Applied Mathematics*, Vol. 21, pp. 21–26.

Stricklin, J. A., et al., 1974, "Large Deflection Elastic-Plastic Dynamic Response of Stiffened Shells of Revolution," *ASME Journal of Pressure Vessel Technology*, Vol. 96, pp. 87–95.

Vasudevan, R., and Ranlet, D., 1982, "Submerged Shock Response of a Linearly Elastic Shell of Revolution Containing Internal Structure—Users Manual for the ELSHOK Code," DNA-TR-81-184, Defense Nuclear Agency, Washington, D.C.

Whitman, A. M., 1972, "Aspect Ratio Effects on the Added-Mass of a Slender Pulsating Cylinder," ASME JOURNAL OF APPLIED MECHANICS, Vol. 39, pp. 1047–1049.

Downloaded 03 May 2010 to 171.66.16.31. Redistribution subject to ASME license or copyright; see http://www.asme.org/terms/Terms_Use.cfm

Effects of Lateral Surface Conditions in Time-Harmonic Nonsymmetric Wave Propagation in a Cylinder

Yoon Young Kim
Research Associate,
Assoc. Mem. ASME

Charles R. Steele
Professor,
Fellow ASME

Division of Applied Mechanics,
Stanford University,
Stanford, CA 94305

The present work is a part of the effort toward the development of an efficient method of solution to handle general nonsymmetric time-harmonic end conditions in a cylinder with a traction-free lateral surface. Previously, Kim and Steele (1989a) develop an approach for the general axisymmetric case, which utilizes the well-known uncoupled wave solutions for a mixed lateral wall condition. For the case of a traction-free lateral wall, the uncoupled wave solutions provide: (1) a convenient set of basis functions and (2) approximations for the relation between end stress and displacement which are asymptotically valid for high mode index numbers. The decay rate with the distance from the end is, however, highly dependent on the lateral wall conditions. The present objective was to demonstrate that the uncoupled solutions of the nonsymmetric waves discussed by Kim (1989), which satisfy certain mixed lateral wall conditions, can be utilized in an analogous manner for the asymptotic analysis of the traction-free case. Results for the end displacement/stress due to various end conditions, computed by the present method and by a more standard collocation method, were compared. The present method was found to reduce the computational effort by orders of magnitude.

1 Introduction

The general solutions for wave propagation in a solid circular cylinder with a traction-free cylindrical surface were obtained by Pochhammer (1876) and again by Chree (1886). Thereafter, numerous investigations on wave propagation in a cylinder followed. Most investigations to date have focused on axisymmetric problems. Armenàkas et al. (1969), Nelson et al. (1971), Zemanek (1972), Huang and Dong (1984), and Kim (1989), among others, studied the dispersion relations for general nonsymmetric cases, but it appears that few attempts have been made to solve for the relation between general conditions of stress and displacement on the end and the solutions along the cylinder, either propagating or evanescent.

For flexural wave propagation, several papers were concerned with the dispersion relation. (See Abramson (1957), Pao and Mindlin (1960), Pao (1962), and Kumar (1972).) Though Timoshenko's approximate theory (1921) can be used for smooth end conditions, it cannot be used to obtain detailed stress and displacement distributions for general end conditions which require many modes. The elasticity solutions were used in some papers to solve a certain class of end problems in flexural wave propagation; Devault and Curtis (1962) study a mixed time-dependent end condition.[1] Shen (1988) uses the modal expansion in order to study transient waves excited by a normal point force applied on the cylindrical surface.

It is known that there is no orthogonality for the displacement and stress components of the eigenfunctions of a cylinder with a traction-free cylindrical surface. The lack of the orthogonality requires solving coupled linear equations for solutions of pure end problems. For mixed end conditions, however, a bi-orthogonality relation can be employed (Frazer (1975) and Gregory (1983)). McKenna and Simpkins (1985) also derive almost identical bi-orthogonality and Wilson (1986) applies it to a specific problem.

In order to develop an efficient solution procedure for pure time-harmonic end problems of longitudinal wave propagation, Kim and Steele (1989a) observe that the solutions at the end are insensitive to cylindrical surface conditions for rapidly varying end conditions. They demonstrate that the solutions of a cylinder with a mixed wall condition corresponding to the well-known uncoupled wave system are not only the convenient

Contributed by the Applied Mechanics Division of THE AMERICAN SOCIETY OF MECHANICAL ENGINEERS for presentation at the Winter Annual Meeting, San Francisco, Calif., December 10-15, 1989.

Discussion on this paper should be addressed to the Editorial Department, ASME, United Engineering Center, 345 East 47th Street, New York, N.Y. 10017, and will be accepted until two months after final publication of the paper itself in the JOURNAL OF APPLIED MECHANICS. Manuscript received by the ASME Applied Mechanics Division, October 21, 1988; final revision, January 18, 1989.
Paper No. 89-WA/APM-35.

[1]For mixed end conditions, either the normal stress and tangential displacements or the normal displacement and the tangential stresses are specified at the end. For pure end conditions, either the three stress components or the three displacement components are specified at the end.

Copyright © 1989 by ASME

Downloaded 03 May 2010 to 171.66.16.31. Redistribution subject to ASME license or copyright; see http://www.asme.org/terms/Terms_Use.cfm

expansions, but also good approximations valid for high mode radial index numbers for the solutions of the traction-free cylinder.

In this paper, the effects of lateral cylindrical surface conditions on the relation between the end stress and displacement are discussed. It is demonstrated that as in the axisymmetric case (see Kim and Steele, 1989a), the solutions of the uncoupled wave system by Kim (1989) are good approximations to the solutions of the nonsymmetric traction-free case for end conditions rapidly varying with high mode radial index numbers. Rapidly varying end conditions typically correspond to end effects, which are difficult to capture by finite or boundary element methods.

New series solutions, which are useful expansions for all variables of the nonsymmetric traction-free case, are obtained from the solutions of the uncoupled wave system. The expansion coefficients can be easily determined by means of so-called "modified" displacement/stress quantities.

Several numerical examples were studied, and the results by the present approach are compared with those by a more standard collocation method, and the substantial computational reduction was made by the present method. For general end conditions, either slowly or rapidly varying, Kim and Steele (1989b) demonstrate a solution procedure in which the present results are utilized.

2 Uncoupled Wave Systems and the Solutions

The general solution to the wave equation for an isotropic elastic solid cylinder can be written (Kim, 1989)

$$\mathbf{u}(r,\theta,z,t) = \tilde{\mathbf{u}}(r)\begin{Bmatrix}\cos n\theta \\ \sin n\theta\end{Bmatrix}\exp[i(\lambda z-\Omega t)]$$
$$\sigma(r,\theta,z,t) = \tilde{\sigma}(r)\begin{Bmatrix}\cos n\theta \\ \sin n\theta\end{Bmatrix}\exp[i(\lambda z-\Omega t)] \quad (1)$$

where

$$\tilde{u}_r(r) = A\frac{dJ_n(hr)}{dr} + B(i\lambda)\frac{dJ_n(kr)}{dr} - C\frac{n}{r}J_n(kr)$$
$$\tilde{u}_\theta(r) = -A\frac{n}{r}J_n(hr) - B(i\lambda)\frac{n}{r}J_n(kr) + C\frac{dJ_n(kr)}{dr}$$
$$\tilde{u}_z(r) = A(i\lambda)J_n(hr) + Bk^2J_n(kr).$$

Displacement $\mathbf{u}$ and stress σ are referred to a, the radius of cylinder, and 2μ, twice the shear modulus, respectively. The dimensionless frequency is denoted by Ω. In equation (1), u_θ, $\sigma_{r\theta}$, and $\sigma_{\theta z}$ take sin $n\theta$, and the other quantities take cos $n\theta$. The parameters h and k, which are defined as $h^2 = \alpha^2\Omega^2-\lambda^2$ and $k^2 = \Omega^2 - \lambda^2$, are the quantities associated with the dilatational and shear waves, respectively. The material parameter α^2 is $(1-2\nu)/2(1-\nu)$ where ν is Poisson's ratio. The unknown constants, A, B, and C will be determined from the boundary conditions. For the detailed notation, refer to Kim (1989).

As pointed out by Kim (1989), there exist two uncoupled wave systems for general nonsymmetric wave propagation. It is shown by Kim (1989) that the asymptotic nature of the Pochhammer frequency equation can be analyzed by means of the uncoupled wave systems. In the present work, we will focus on the use of the uncoupled wave systems to approximate the solutions of the traction-free cylinder and draw some useful conclusions. To this end, we will first consider an uncoupled wave system, for which the cylindrical surface condition is given by

$$u_r = 0 \quad (2a)$$
$$\sigma_{rz} = 0 \quad (2b)$$
$$\sigma_{r\theta} + u_\theta = 0. \quad (2c)$$

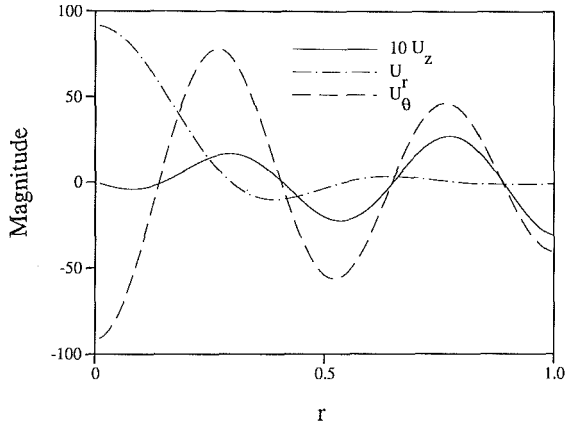


Fig. 1 Displacement components of an eigenfunction of the traction-free cylinder with the wave number $\lambda = 13.13i$ for $n = 1$, $\nu = 0.3317$, and $\Omega = 1$. Axial ($10U_z(r)$), radial ($U_r(r)$), and circumferential ($U_\theta(r)$) displacements are denoted by solid, long dot-dashed, dashed lines, respectively. The eigenfunctions with imaginary wave numbers correspond to end effects.

The solutions for the wave propagating along the positive z-direction can be written

$$u_r = \sum_{m=1}^{\infty}\left\{A_m\frac{dJ_n(\xi_m r)}{dr}\exp[i(\lambda_{dm}z-\Omega t)] + B_m(i\lambda_{sm})\frac{dJ_n(\xi_m r)}{dr}\exp[i(\lambda_{sm}z-\Omega t)] - C_m\frac{n}{r}J_n(\rho_m r)\exp[i(\lambda_{tm}z-\Omega t)]\right\}\cos n\theta \quad (3a)$$

$$u_\theta = \sum_{m=1}^{\infty}\left\{-A_m\frac{n}{r}J_n(\xi_m r)\exp[i(\lambda_{dm}z-\Omega t)] - B_m(i\lambda_{sm})\frac{n}{r}J_n(\xi_m r)\exp[i(\lambda_{sm}z-\Omega t)] + C_m\frac{dJ_n(\rho_m r)}{dr}\exp[i(\lambda_{tm}z-\Omega t)]\right\}\sin n\theta \quad (3b)$$

$$u_z = \sum_{m=1}^{\infty}\{A_m(i\lambda_{dm})J_n(\xi_m r)\exp[i(\lambda_{dm}z-\Omega t)] + B_m\xi_m^2J_n(\xi_m r)\exp[i(\lambda_{sm}z-\Omega t)]\}\cos n\theta \quad (3c)$$

$$\sigma_{rz} = \sum_{m=1}^{\infty}\left\{A_m(i\lambda_{dm})\frac{dJ_n(\xi_m r)}{dr}\exp[i(\lambda_{dm}z-\Omega t)] + B_m\left(\xi_m^2-\frac{\Omega^2}{2}\right)\frac{dJ_n(\xi_m r)}{dr}\exp[i(\lambda_{sm}z-\Omega t)] - C_m\left(\frac{i\lambda_{tm}}{2}\right)\frac{n}{r}J_n(\rho_m r)\exp[i(\lambda_{tm}z-\Omega t)]\right\}\cos n\theta \quad (3d)$$

$$\sigma_{\theta z} = \sum_{m=1}^{\infty}\left\{-A_m(i\lambda_{dm})\frac{n}{r}J_n(\xi_m r)\exp[i(\lambda_{dm}z-\Omega t)] - B_m\left(\xi_m^2-\frac{\Omega^2}{2}\right)\frac{n}{r}J_n(\xi_m r)\exp[i(\lambda_{sm}z-\Omega t)] + C_m(i\lambda_{tm})\frac{dJ_n(\rho_m r)}{dr}\exp[i(\lambda_{tm}z-\Omega t)]\right\}\sin n\theta \quad (3e)$$

$$\sigma_{zz} = \sum_{m=1}^{\infty}\left\{A_m\left(\xi_m^2-\frac{\Omega^2}{2}\right)J_n(\xi_m r)\exp[i(\lambda_{dm}z-\Omega t)] + B_m\xi_m^2(i\lambda_{sm})J_n(\xi_m r)\exp[i(\lambda_{sm}z-\Omega t)]\right\}\cos n\theta \quad (3f)$$

Downloaded 03 May 2010 to 171.66.16.31. Redistribution subject to ASME license or copyright; see http://www.asme.org/terms/Terms_Use.cfm

where ξ and ρ are the zeros of $J_n(r)$ and $dJ_n(r)/dr$, respectively. The wave numbers λ_{dm}, λ_{sm}, and λ_{tm} are defined as

$$\lambda_{dm}^2 = \alpha^2\Omega^2 - \xi_m^2; \quad \lambda_{sm}^2 = \Omega^2 - \xi_m^2; \quad \lambda_{tm}^2 = \Omega^2 - \rho_m^2.$$

For waves propagating along the positive z-direction, $d\Omega/d\lambda > 0$ for real λ and $i\lambda < 0$ for imaginary λ.

For the axisymmetric longitudinal wave propagation (the corresponding boundary condition is equations (2*a*), (2*b*)), it can be seen that the unknowns A_m and B_m can be determined without solving any coupled linear equations, due to the orthogonality of the corresponding eigenfunctions. For the general nonsymmetric wave propagation with the condition (2), however, the eigenfunctions for the stress and displacement are not orthogonal. The lack of the orthogonality seems to require solving systems of coupled linear equations.

To avoid solving the coupled linear equations, we propose to introduce the following modified quantities that can be prescribed at the end:

$$u_I = \frac{1}{r}\frac{\partial}{\partial r}(ru_r) + \frac{1}{r}\frac{\partial}{\partial \theta}(u_\theta)$$

$$u_{II} = \frac{1}{r}\frac{\partial}{\partial r}(ru_\theta) - \frac{1}{r}\frac{\partial}{\partial \theta}(u_r)$$

$$\sigma_I = \frac{1}{r}\frac{\partial}{\partial r}(r\sigma_{rz}) + \frac{1}{r}\frac{\partial}{\partial \theta}(\sigma_{\theta z})$$

$$\sigma_{II} = \frac{1}{r}\frac{\partial}{\partial r}(r\sigma_{\theta z}) - \frac{1}{r}\frac{\partial}{\partial \theta}(\sigma_{rz}).$$

The explicit forms of the modified quantities are

$$u_I(r,\theta,z,t) = [-Ah^2J_n(hr) - B(i\lambda)k^2J_n(kr)] \cos n\theta \exp[i(\lambda z - \Omega t)]$$

$$u_{II}(r,\theta,z,t) = -Ck^2J_n(kr) \sin n\theta \exp[i(\lambda z - \Omega t)]$$

$$\sigma_I(r,\theta,z,t) = \left[-A(i\lambda)h^2J_n(hr) - B\left(\lambda^2 - \frac{\Omega^2}{2}\right)J_n(kr)\right] \cos n\theta \exp[i(\lambda z - \Omega t)]$$

$$\sigma_{II}(r,\theta,z,t) = -C\frac{i\lambda}{2}k^2 J_n(kr) \sin n\theta \exp[i(\lambda z - \Omega t)].$$

From the definition of the modified quantities, one can see that $u_I = \epsilon_{rr} + \epsilon_{\theta\theta}$, the sum of the normal strains in r and θ, and $u_{II} = \omega_z$, the rotation measure about the z-axis. However, the physical interpretation for σ_I and σ_{II} is not obvious. Interestingly, the wave nature can be identified by these quantities; (u_I, u_z) and (σ_I, σ_{zz}) correspond to the coupled motion governed by a dilatational wave and a shear wave and (u_{II}, σ_{II}) is characterized by one shear wave.

We define the quantities that can be prescribed at the end of the cylinder[2]

$$u_r|_{z=0} = U_r(r) \; ; \; u_\theta|_{z=0} = U_\theta(r) \; ; \; u_z|_{z=0} = U_z(r)$$

$$\sigma_{rz}|_{z=0} = S_r(r) \; ; \; \sigma_{\theta z}|_{z=0} = S_\theta(r) \; ; \; \sigma_{zz}|_{z=0} = S_z(r)$$

and

$$u_I|_{z=0} = U_I(r) \; ; \; u_{II}|_{z=0} = U_{II}(r)$$

$$\sigma_I|_{z=0} = S_I(r) \; ; \; \sigma_{II}|_{z=0} = S_{II}(r).$$

For the uncoupled wave system under consideration, the modified quantities have very simple forms at the end such that

$$U_I(r) = -\sum_{m=1}^{\infty}[A_m + (i\lambda_{sm})B_m]\xi_m^2 J_n(\xi_m r) \qquad (4a)$$

$$U_{II}(r) = -\sum_{m=1}^{\infty} C_m \rho_m^2 J_n(\rho_m r) \qquad (4b)$$

[2]The dependence of the stress and displacement on t and θ will be omitted.

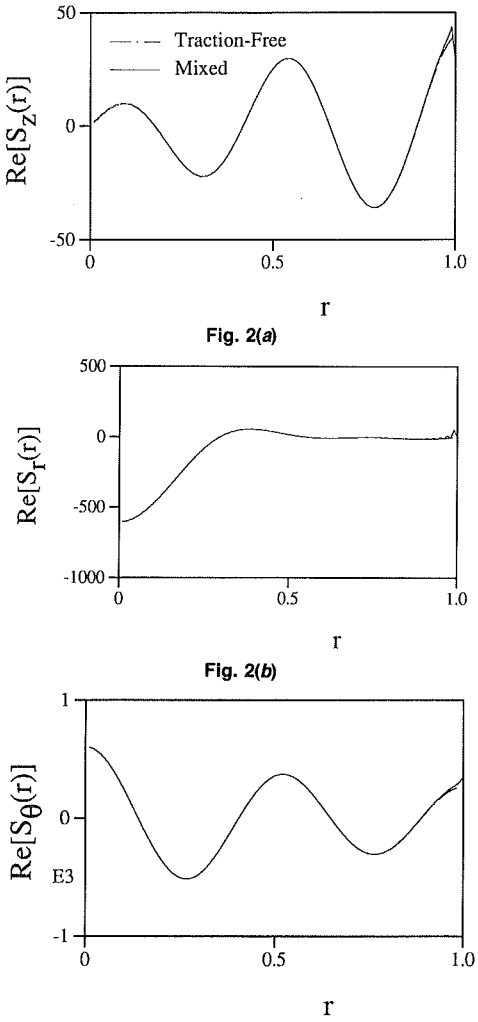


Fig. 2 Stress components (long dot-dashed lines) of the eigenfunction of the traction-free cylinder with the wave number $\lambda = 13.13$ for $n = 1$, $\nu = 0.3317$, and $\Omega = 1$. Taking the displacement components of the eigenfunction for the end condition of the mixed cylinder, the stresses at the end of the mixed cylinder are also shown and the results are obtained by 60 terms in the series expansions; the real parts of (*a*) $S_z(r)$, (*b*) $S_r(r)$, and (*c*) $S_\theta(r)$. The stress components of the eigenfunction of the traction-free cylinder are well approximated by the solutions of the mixed cylinder.

$$S_I(r) = -\sum_{m=1}^{\infty}\left[A_m(i\lambda_{dm}) + B_m\left(\xi_m^2 - \frac{\Omega^2}{2}\right)\right]\xi_m^2 J_n(\xi_m r) \qquad (5a)$$

$$S_{II}(r) = -\sum_{m=1}^{\infty}\frac{i\lambda_{tm}}{2} C_m \rho_m^2 J_n(\rho_m r). \qquad (5b)$$

The usefulness of these modified quantities is apparent; these modified quantities along with $\tilde{\sigma}_{zz}(r)$ and $\tilde{u}_z(r)$ are the Dini series (see Watson (1966)) which are orthogonal and complete. If the usual displacement and stress quantities were used in order to compute the unknowns, solving linear equations would be unavoidable. No systems of linear equations need to be solved when the modified quantities are employed instead. Before we show that the usual quantities can be uniquely determined from the modified quantities, we repeat the well-known facts on the Dini series. For $n \neq 0$, one can expand a function $f(r)$[3] as

[3]For the validity of the expansion, see Watson (1966).

Downloaded 03 May 2010 to 171.66.16.31. Redistribution subject to ASME license or copyright; see http://www.asme.org/terms/Terms_Use.cfm

$$f(r) = \sum_{m=1}^{\infty} a_m J_n(\beta_m r) \quad (0<r<1).$$

The expansion coefficient, a_m, is given by

$$a_m = \eta_m \int_0^1 r f(r) J_n(\beta_m r) dr$$

where

$$\eta_m = \begin{cases} \dfrac{2\xi_m^2}{(\xi_m^2 - n^2) J_n^2(\xi_m)} & \text{if } \beta_m = \xi_m \\ \dfrac{2}{J_{n+1}^2(\rho_m)} & \text{if } \beta_m = \rho_m \end{cases}$$

To prove the uniqueness property of the expansions (4) and (5), one can consider

$$S_I(r) \equiv 0 \quad ; \quad S_{II}(r) \equiv 0. \tag{6}$$

For a nontrivial solution $[S_r(r), S_\theta(r)]$ for (6), one can try

$$S_r(r) = Dr^\alpha \quad ; \quad S_\theta(r) = Er^\beta. \tag{7}$$

Substituting (7) into (6) gives

$$D(\alpha+1)r^{\alpha-1} + Enr^{\beta-1} = 0 \tag{8a}$$

$$Dnr^{\alpha-1} + E(\beta+1)r^{\beta-1} = 0. \tag{8b}$$

The solutions of (8) are

$$\alpha = \beta = n-1 \quad ; \quad E = -D$$

$$\alpha = \beta = -n-1 \quad ; \quad E = D.$$

The general form of the shear stresses $S_r(r)$ and $S_\theta(r)$ can be written as

$$S_r(r) = \hat{S}_r(r) + D_1 r^{n-1} + D_2 r^{-n-1}$$

$$S_\theta(r) = \hat{S}_\theta(r) - D_1 r^{n-1} + D_2 r^{-n-1}$$

where $[\hat{S}_r(r), \hat{S}_\theta(r)]$ denotes the solution solely determined by the modified quantities (5). For nonsymmetric wave propagation in a solid cylinder, the regularity condition at $r = 0$ precludes the D_2 part. In addition, the σ_{rz}-free cylindrical surface condition requires that

$$S_r(r)|_{r=1} = \hat{S}_r(r)|_{r=1} + D_1 \equiv 0. \tag{9}$$

Since $\hat{S}_r(r)|_{r=1} = 0$, equation (9) results in $D_1 = 0$, which concludes that $S_r(r)$ and $S_\theta(r)$ are uniquely determined from $S_I(r)$ and $S_{II}(r)$. Similarly, the displacements are uniquely determined from the modified displacement quantities.

The stresses at the end of the cylinder can be written as

$$S_I(r) = \sum_{m=1} \xi_m S_m J_n(\xi_m r) \tag{10a}$$

$$S_{II}(r) = \sum_{m=1}^{\infty} \rho_m T_m J_n(\rho_m r) \tag{10b}$$

$$S_z(r) = \sum_{m=1}^{\infty} Z_m J_n(\xi_m r). \tag{10c}$$

Note that the expansions (10*a*) and (10*b*) are equivalent to the expansions

$$S_r(r) = \sum_{m=1}^{\infty} \left[-\frac{S_m}{\xi_m} \frac{dJ_n(\xi_m r)}{dr} + \frac{T_m}{\rho_m} \frac{n}{r} J_n(\rho_m r) \right] \tag{11a}$$

$$S_\theta(r) = \sum_{m=1}^{\infty} \left[\frac{S_m}{\xi_m} \frac{n}{r} J_n(\xi_m r) - \frac{T_m}{\rho_m} \frac{dJ_n(\rho_m r)}{dr} \right]. \tag{11b}$$

The unknowns S_m, T_m, and Z_m can be computed by

$$\begin{aligned} \xi_m S_m &= \eta_m \int_0^1 \left\{ \frac{d}{dr} [rS_r(r)] + nS_\theta(r) \right\} J_n(\xi_m r) dr \\ &= \eta_m \Big[S_r(1) J_n(\xi_m) + n \int_0^1 \{S_r(r) + S_\theta(r)\} J_n(\xi_m r) dr \\ &\qquad - \xi_m \int_0^1 S_r(r) J_{n-1}(\xi_m r) r dr \Big] \\ &= \eta_m \Big[n \int_0^1 \{S_r(r) + S_\theta(r)\} J_n(\xi_m r) dr \\ &\qquad - \xi_m \int_0^1 S_r(r) J_{n-1}(\xi_m r) r dr \Big] \end{aligned} \tag{12a}$$

$$\begin{aligned} \rho_m T_m = \eta_m \Big[& n \int_0^1 \{S_\theta(r) + S_r(r)\} J_n(\rho_m r) dr \\ & - \rho_m \int_0^1 S_\theta(r) J_{n-1}(\rho_m r) r dr \Big] \end{aligned} \tag{12b}$$

$$Z_m = \eta_m \int_0^1 S_z(r) J_n(\xi_m r) r dr \tag{12c}$$

where $S_r(1) = 0$ is used in (12*a*). Upon evaluating Z_m, S_m, and T_m, the unknowns A_m, B_m, and C_m can be easily determined by (3*f*), (5), and (10).

Similarly, the displacements at the end of the cylinder can be expanded as

$$U_I(r) = \sum_{m=1}^{\infty} \xi_m U_m J_n(\xi_m r) \tag{13a}$$

$$U_{II}(r) = \sum_{m=1}^{\infty} \rho_m V_m J_n(\rho_m r) \tag{13b}$$

$$U_z(r) = \sum_{m=1}^{\infty} W_m J_n(\xi_m r) \tag{13c}$$

where (13*a*) and (13*b*) are equivalent to

$$U_r(r) = \sum_{m=1}^{\infty} \left[-\frac{U_m}{\xi_m} \frac{dJ_n(\xi_m r)}{dr} + \frac{V_m}{\rho_m} \frac{n}{r} J_n(\rho_m r) \right] \tag{14a}$$

$$U_\theta(r) = \sum_{m=1}^{\infty} \left[\frac{U_m}{\xi_m} \frac{n}{r} J_n(\xi_m r) - \frac{V_m}{\rho_m} \frac{dJ_n(\rho_m r)}{dr} \right] \tag{14b}$$

and U_m, V_m, and W_m may be computed as in (12).

From the solutions of the uncoupled wave system, new series expansions are found. Unlike most series expansions, two sets of eigenvalues appear in the expansions (see equation (11)). The present expansions may be used in various problems. In fact, Kim and Steele (1989b) employ the present expansions as the proper expansions for all variables in order to solve general nonsymmetric end problems of a cylinder with a traction-free cylindrical surface condition.

3 Traction-Free Case

This section is concerned with some known facts on wave propagation in a cylinder with a traction-free cylindrical surface, which will be needed for further analysis. The Pochhammer frequency equation, which is the relation of wave numbers and frequencies, is obtained by applying the cylindrical surface condition

$$\sigma_{rr}|_{r=1} = \sigma_{rz}|_{r=1} = \sigma_{\theta z}|_{r=1} = 0.$$

From the frequency equation, wave numbers and the relative ratios B/A and C/A are determined for a given frequency Ω. The general solution form of displacement and stress can be expressed by summing up all possible modes. For instance, σ_{zz} can be written as

Downloaded 03 May 2010 to 171.66.16.31. Redistribution subject to ASME license or copyright; see http://www.asme.org/terms/Terms_Use.cfm

$$\sigma_{zz}(r,\theta,z,t) = \sum_{p=1}^{\infty} E^p \tilde{\sigma}_{zz}^p(r)\exp[i(\lambda^p z - \Omega t)] \qquad (15)$$

where the superscripted quantities with p are associated with the pth wave number, and E^p denotes the corresponding expansion coefficient. For convenience, the cylinder with the mixed lateral surface condition (2) will be called "the mixed cylinder," whereas the cylinder with the traction-free lateral surface condition will be called "the traction-free cylinder."

It is known that there is no orthogonality condition for the components of the eigenfunctions for the traction-free cylinder. However, there exists the *bi-orthogonality* relation such that (Frazer (1975), and Gregory (1983))

$$\int_0^1 [\tilde{\sigma}_{zz}^p(r)\tilde{u}_z^q(r) - \tilde{u}_r^p(r)\tilde{\sigma}_{rz}^q(r) - \tilde{u}_\theta^p(r)\tilde{\sigma}_{r\theta}^q(r)]rdr = 0 \qquad (16)$$

$$\text{for } p \neq q.$$

Thus bi-orthogonality condition is most useful when $[U_z(r), S_r(r), S_\theta(r)]$ or $[S_z(r), U_r(r), U_\theta(r)]$ is prescribed at the end of the cylinder. For example, if $[U_z(r), S_r(r), S_\theta(r)]$ is prescribed at $z = 0$ for a given frequency, the expansion coefficients can be computed without solving coupled systems of linear equations:

$$E^p = \frac{\int_0^1 [\tilde{\sigma}_{zz}^p(r)U_z(r) - \tilde{u}_r^p(r)S_r(r) - \tilde{u}_\theta^p(r)S_\theta(r)]rdr}{\int_0^1 [\tilde{\sigma}_{zz}^p(r)\tilde{u}_z^p(r) - \tilde{u}_r^p(r)\tilde{\sigma}_{rz}^p(r) - \tilde{u}_\theta^p(r)\tilde{\sigma}_{\theta z}^p(r)]rdr}$$

$$\equiv \frac{N^p}{D^p} \qquad (17)$$

where the denominator D^p can be obtained in a closed-form.

If the mixed end conditions are given in the form of ((10a), (10b), (13c)), the numerator N^p in (17) can be expressed in a closed-form:

$$\begin{aligned} N^p = W_m\Big\{ & A^p\left[(h^p)^2 - \frac{\Omega^2}{2}\right] Q_n(\xi_m,h^p) + B^p(i\lambda^p)(k^p)^2 Q_n(\xi_m,k^p)\Big\} \\ & + S_m\left\{\frac{A^p h^p}{2}[Q_{n-1}(\xi_m,h^p) + Q_{n+1}(\xi_m, h^p)]\right. \\ & + \frac{B^p(i\lambda^p)k^p}{2}[Q_{n-1}(\xi_m,k^p) + Q_{n+1}(\xi_m,k^p)] \\ & \left. - \frac{C^p}{\xi_m} nJ_n(\xi_m)J_n(k^p)\right\} \\ & + T_m \frac{C^p k^p}{2}[Q_{n-1}(\rho_m,k^p) + Q_{n+1}(\rho_m,k^p)]. \end{aligned}$$

The quantity $Q_\nu(\alpha,\beta)$ is defined as

$$Q_\nu(\alpha,\beta) = \int_0^1 J_\nu(\alpha r)J_\nu(\beta r)rdr$$

whose closed-form is available (Watson (1966)). With the end condition ((10c), (13b), (13c), we have

$$\begin{aligned} N^p = {} & Z_m\left[A^p(i\lambda^p)Q_n(\xi_m,h^p) + B^p(k^p)^2 Q_n(\xi_m,k^p)\right] \\ & + U_m\left\{\frac{A^p(i\lambda^p)h^p}{2}[Q_{n-1}(\xi_m, h^p) + Q_{n+1}(\xi_m,h^p)]\right. \\ & + \tfrac{1}{2}B^p k^p[(k^p)^2 - \frac{\Omega^2}{2}][Q_{n-1}(\xi_m,k^p) + Q_{n+1}(\xi_m,k^p)] \\ & \left. - \frac{C^p(i\lambda)}{2\xi_m} nJ_n(\xi_m)J_n(k^p)\right\} \\ & + V_m \frac{C^p(i\lambda)k^p}{4}[Q_{n-1}(\rho_m,k^p) + Q_{n+1}(\rho_m,k^p)]. \end{aligned} \qquad (18)$$

For the solutions of the time-harmonic pure end problems in the traction-free cylinder, the collocation method is perhaps one of the most widely used solution techniques (Miller (1967) and Zemanek (1972)). This method, which requires solving coupled linear equations, is most useful for slowly varying end conditions. However, the collocation method usually converges slowly even for slowly varying end conditions, and becomes less efficient as the end conditions vary more rapidly.

4 Effects of the Cylindrical Wall Conditions and Numerical Examples

First, we examine eigenfunctions of the traction-free cylinder that have imaginary wave numbers for $n = 1$, $\Omega = 1$, and $\nu = 0.3317$. The eigenfunctions with imaginary wave numbers are deliberately chosen, because imaginary wave numbers are associated with end effects. (These eigenfunctions cannot carry any net power away from the end of the cylinder.) The dimensionless imaginary wave numbers for the present case are

$$0.7357i,\ 2.636i,\ 6.621i,\ 9.916i,\ 13.13i,\ 16.32i \ldots .$$

The displacement and stress components of the eigenfunction for the traction-free cylinder with $\lambda = 13.13i$ are shown in Fig. 1 and Fig. 2, respectively.

For the purpose of investigating the effect of the cylindrical wall conditions, the displacement components of the eigenfunction with $\lambda = 13.13i$ is taken as an end condition of the mixed cylinder, where the characterizing radial index number m of the end condition, with respect to the expansions (13) and (14), is 4. Note that for the present choice of n, Ω, and ν, there is no real wave number for the mixed cylinder so that any end conditions correspond to end effects. The solutions of the mixed cylinder at the end are obtained by means of the expansions (10) with 60 terms, and denoted by solid lines in Fig. 2. As seen in Fig. 2, the solutions for the stress components of the mixed cylinder at the end are very close to the stress components (long dot-dashed lines) of the eigenfunction of the traction-free cylinder except very near $r = 1$. This implies that the solutions at the end of the cylinder are insensitive to the cylindrical surface conditions for end conditions corresponding to end effects.

Now, consider a somewhat general end condition with rapid radial variation for $n = 1$, $\nu = 0.3317$, and $\Omega = 1$:

$$S_z(r) = J_1(\xi_m r) \quad ; \quad S_r(r) = S_\theta(r) = 0 \qquad (19)$$

where m (the radial index number) equal to 17 and $\xi_{17} = 52.61$. For given n, ν, and Ω, there is one real wave number (corresponding to a propagating mode) as well as infinite numbers of imaginary and complex wave numbers for the traction-free cylinder (see Zemanek (1972)). We arrange the wave numbers of the traction-free cylinder such that

$$\lambda^1 = (1.41, 0.0),\ \lambda^2 = (0.0, 0.736),\ \lambda^3 = (0.0, 2.64)$$
$$\lambda^4 = -(\lambda^5)^* = (1.50, 4.23),\ \lambda^6 = (0.0, 6.62), \ldots$$

where * denotes the complex conjugate. For the mixed cylinder, there is no real wave number but an infinite number of imaginary wave numbers; there are nonvanishing imaginary parts of the displacements for the traction-free cylinder which account for positive net power input, and no imaginary parts of the displacements for the mixed cylinder are possible.

In Table 1, we present first few expansion coefficients for the traction-free cylinder obtained by collocation with different numbers of wave numbers, in which "n_c" denotes the number of wave numbers used. Table 1 shows the slowly convergent nature of the collocation method. Another problem of the collocation method is that many imaginary and complex wave numbers need to be computed; it is observed that accurate

Downloaded 03 May 2010 to 171.66.16.31. Redistribution subject to ASME license or copyright; see http://www.asme.org/terms/Terms_Use.cfm

Table 1 Expansion coefficients by collocation for the end condition (19)

$\|E^p\|$	$n_e = 300$	$n_e = 600$	$n_e = 900$
$\|E^1\|$	0.107E-3	0.220E-3	0.243E-3
$\|E^2\|$	0.220E-3	0.428E-3	0.473E-3
$\|E^3\|$	0.456E-4	0.492E-2	0.501E-4
$\|E^4\|$	0.586E-4	0.671E-4	0.689E-4

Table 2 Expansion coefficients by collocation and the present asymptotic solutions for the end condition (20) (double precision used)

$\|E^p\|$	Collocation (n_e = 300)	Collocation (n_e = 600)	Collocation (n_e = 900)	Present
$\|E^1\| = \|E^2\|$	0.583E-2	0.576E-2	0.565E-2	0.548E-2
$\|E^3\|$	0.576E-3	0.964E-3	0.945E-3	0.104E-2
$\|E^4\| = \|E^5\|$	0.384E-3	0.381E-3	0.376E-3	0.445E-3

$E^2 = (E^1)^*$, $E^5 = (E^4)^*$

imaginary and complex wave numbers are difficult to obtain numerically, even if asymptotic forms for the imaginary and complex wave numbers (Kim, 1989) may be used as initial guesses.

In order to examine the dependence of the solutions at the end on cylindrical surface conditions, we compare in Fig. 3 the displacement components of the traction-free cylinder and those of the mixed cylinder subject to the end condition (19). The results for the traction-free cylinder are obtained by collocation with 900 unknowns.

Figure 3 shows that the real parts of the normal and circumferential displacements are virtually insensitive to the cylindrical surface conditions. However, the real part of the radial displacement near $r = 1$ appears to be affected by the cylindrical boundary conditions. It is seen that imaginary parts of the solutions of the traction-free cylinder cannot be approximated by the solutions of the uncoupled wave system, but their magnitudes are much smaller than the magnitudes of the real parts of the solutions.

Finally, a non-zero axial displacement end condition for $n = 2$, $\nu = 0.3317$, and $\Omega = 2$ is treated: another end condition with a different Fourier number n. The stresses at the end are determined for the following end condition:

$$U_z(r) = J_2(\xi_m r) \quad ; \quad U_r(r) = U_\theta(r) = 0 \qquad (20)$$

where m (the radial index number) equal to 16 and $\xi_{16} = 51.004$. For the present choice of n, ν, and Ω, the effects of any end conditions will decay exponentially along the z-axis for both the traction-free and mixed cylinders. The corresponding wave numbers for the traction-free cylinder are

$$\lambda^1 = -(\lambda^2)^* = (0.921, 1.14), \ \lambda^3 = (0.0, 3.59)$$

$$\lambda^4 = -(\lambda^5)^* = (1.63, 5.47), \ \lambda^6 = (0.0, 7.87).$$

In Fig. 4 the real parts of the stresses at $z = 0$ for the traction-free cylinder, obtained by collocation with 900 unknowns, are compared with those of the mixed cylinder. For the present end conditions, which can be characterized by rapid radial variation, the solutions of the mixed cylinder appear to be good approximations to those of the traction-free cylinder.

From the approximate solutions, one can compute the expansion coefficient E^p and thus displacement/stress everywhere in the cylinder. To this end, the bi-orthogonality relation (17) can be utilized since $[S_z(r), U_r(r), U_\theta(r)]$ and $[U_z(r), S_r(r) S_\theta(r)]$ (at $z = 0$) are now known. Equation (18) was used for the present example where $U_r(r) = U_\theta(r) = 0$. Table 2 shows the expansion coefficients obtained by both the collocation method with different numbers of unknowns and the present approach.

The slowly convergent nature of the collocation method can be observed again. It is seen in Table 2 that the expansion

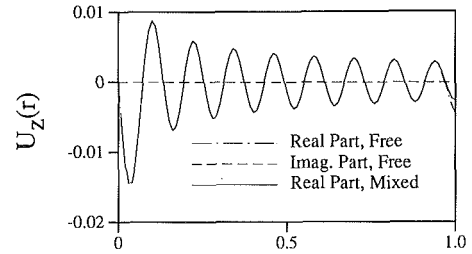


Fig. 3(*a*)

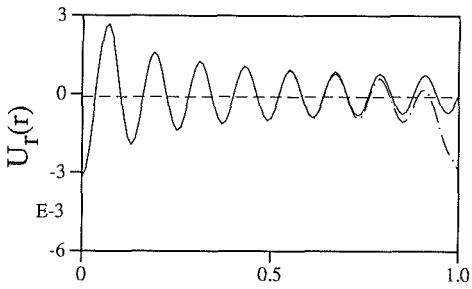


Fig. 3(*b*)

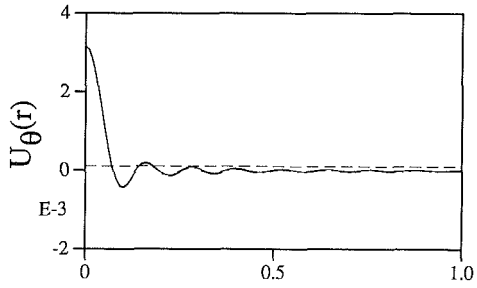


Fig. 3(*c*)

Fig. 3 Comparison of the solutions at the end of the traction-free and mixed cylinders subject to the end condition $S_z(r) = J_1(\xi_{17} r)$ ($\xi_{17} = 52.61$), $S_r(r) = S_\theta(r) = 0$ ($n = 1$, $\nu = 0.3317$, and $\Omega = 1$) for (*a*) $U_z(r)$, (*b*) $U_r(r)$, and (*c*) $U_\theta(r)$. Results are shown for real (long dot-dashed) and imaginary (dashed) parts of the end displacements of the traction-free cylinder obtained by collocation with 900 unknowns and real parts (solid) of the end displacements of the mixed cylinder.

coefficients obtained by the present approximate solutions are comparable with those by collocation. The trend of the results is that E^1 by collocation approaches E^1 by the present approximate solution. It appears that the solutions by collocation with more unknowns would be impractical due to significant numerical errors in obtaining complex and imaginary wave numbers and solving the large system of linear equations; presumably more terms could be computed with quadruple precision.

Figure 5 shows the radial variation of the real part of the normal stress σ_{zz} (in fact, $\sigma_{zz} e^{i\Omega t}/\cos n\theta$) for various z, namely, $z = 0.2$, $z = 0.5$, and $z = 1.0$. The results by collocation for the traction-free cylinder, which are obtained with $n_e = 900$, are denoted by long dot-dashed lines and those by the present approach are represented by solid lines. In Fig. 5, the solutions of the mixed cylinder (dashed lines) are also shown in order to demonstrate different decay rates of the two cylinders along the axial coordinate. Approximately for $z > 0.5$, the solutions of the mixed cylinder are so small in comparison with those of the traction-free cylinder that they are hardly seen in the Figs. 5(*b*), (*c*).

Downloaded 03 May 2010 to 171.66.16.31. Redistribution subject to ASME license or copyright; see http://www.asme.org/terms/Terms_Use.cfm

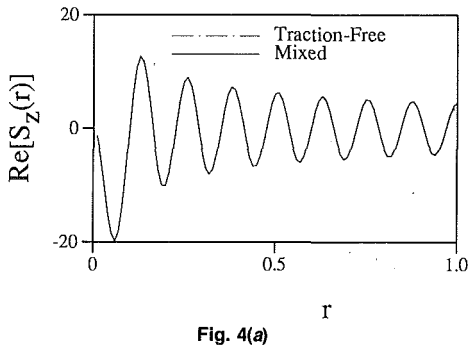


Fig. 4(*a*)

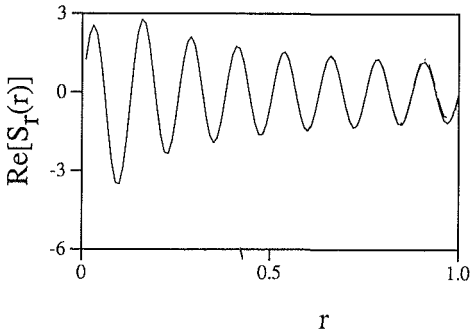


Fig. 4(*b*)

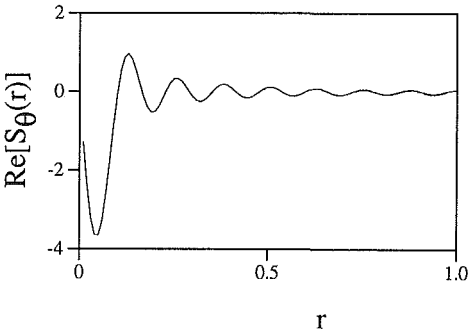


Fig. 4(*c*)

Fig. 4 The solutions of the traction-free cylinder are compared with those of the mixed cylinder at the end, subject to the end condition $U_z(r) = J_2(\xi_{16} r)$ (ξ_{16} = 51.004), $U_r(r) = U_\theta(r) = 0$ for $n = 2$, $\nu = 0.3317$, and $\Omega = 2$; real parts of (*a*) $S_z(r)$, (*b*) $S_r(r)$, and (*c*) $S_\theta(r)$. Results are shown for the traction-free cylinder (long dot-dashed) by collocation with 900 unknowns, and for the mixed cylinder (solid). Good agreement is shown between the present results and the results by collocation.

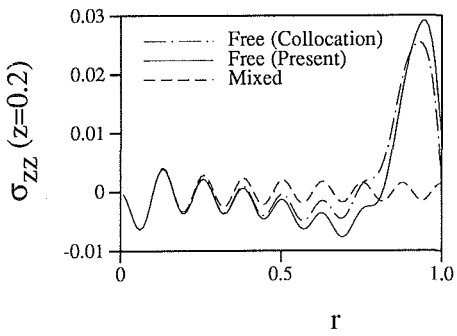


Fig. 5(*a*)

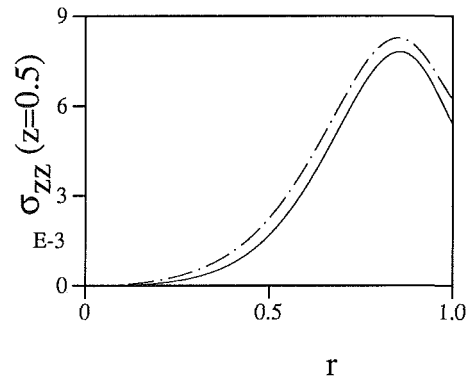


Fig. 5(*b*)

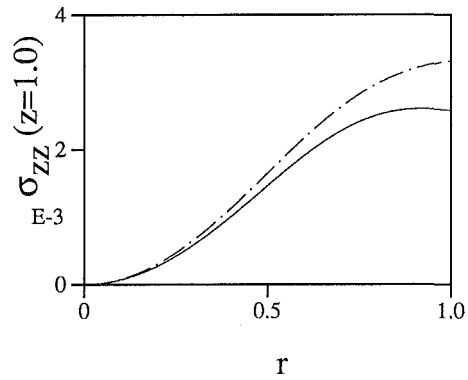


Fig. 5(*c*)

Fig. 5 Radial variation of the normal stress σ_{zz} at (*a*) $z = 0.2$, (*b*) $z = 0.5$, and (*c*) $z = 1.0$ for the end condition used for Fig. 4. Results for the traction-free cylinder by collocation with 900 unknowns (long dot-dashed), and the present approach (solid), where the solutions at the end of the mixed cylinder are used as approximate solutions for the traction-free cylinder. The solutions of the mixed cylinder (dashed) are also shown. The present solutions are comparable with the results by collocation. The decay rate of the mixed cylinder is substantially different from that of the traction-free cylinder.

Table 3 CPU time for the end condition (20) on Convex C-1

Collocation (n_e = 300)	Collocation (n_e = 600)	Collocation (n_e = 900)	Present
1189 sec.	5710 sec.	15561 sec.	66 sec.

Figure 5 also shows how rapidly the first mode becomes dominant as z becomes large. Comparable solutions are obtained by the present solution approach for various z. As seen in Fig. 5, the decay rate of the solutions of the mixed cylinder is substantially different from the counterpart of the traction-free cylinder. Similar behavior was also observed for other components of stress and displacement.

In Table 3, we present the CPU times required in obtaining all the results shown in Figs. 4 and 5. Table 3 demonstrates that the present solution approach is orders of magnitude more efficient than the collocation method.

5 Conclusions

The effects of lateral surface conditions of a semi-infinite cylinder on the solutions at the end were investigated in time-harmonic wave propagation. For end conditions with high mode radial index numbers, which correspond to rapid spatial variation, the solutions at the end are insensitive to the cylindrical surface conditions. It is demonstrated that for such end conditions, the solutions of a cylinder with a traction-free lateral surface condition can be approximated by the solutions of a cylinder with a special mixed lateral surface condition which Kim (1989) studies. However, the decay rate with the

Downloaded 03 May 2010 to 171.66.16.31. Redistribution subject to ASME license or copyright; see http://www.asme.org/terms/Terms_Use.cfm

distance from the end is highly dependent on the lateral wall conditions.

New series solutions, which provide the appropriate expansion sets for the variables of the traction-free cylinder, are obtained from the solutions of the uncoupled wave system. The coefficients of such expansions can be explicitly determined by means of the "modified" stress/displacement quantities.

The present results are incorporated in a recent report by Kim and Steele (1989b) who develop a solution procedure useful for both slowly and rapidly varying end conditions.

Acknowledgment

This work was partially supported by Grant MSM-8814355 from the National Science Foundation and we thank the reviewers for their comments on the earlier version of the manuscript.

References

Abramson, H. N., 1957, "Flexural Waves in Elastic Beams of Circular Cross Section," *J. Acoust. Soc. Am.*, Vol. 29, pp. 42–46.

Armenàkas, A. E., Gazis, D. C., and Herrmann, G., 1969, *Free Vibrations of Circular Cylindrical Shells*, Pergamon Press, Oxford, U.K.

Chree, C., 1886, "Longitudinal Vibrations of a Circular Bar," *Quart. J. Pure and Appl. Math.*, Vol. 21, pp. 287–298.

Devault, G. P., and Curtis, C. W., 1962, "Elastic Cylinder with Free Lateral Surface and Mixed Time-Dependent End Conditions," *J. Acoust. Soc. Am.*, Vol. 34, pp. 421–432.

Gregory, R. D., 1983, "A Note on Bi-Orthogonality Relations for Elastic Cylinders of General Cross Section," *J. Elasticity*, Vol. 13, pp. 351–355.

Frazer, W. B., 1975, "An Orthogonality Relation for the Modes of Wave Propagation in an Elastic Circular Cylinder," *J. Sound Vibration*, Vol. 43, pp. 568–571.

Huang, K. H., and Dong, S. B., 1984, "Propagating Waves and Edge Vibrations in Anisotropic Composite Cylinders," *J. Sound Vibration*, Vol. 96, pp. 8–19.

Kim, Y. Y., 1989, "Uncoupled Wave Systems and Dispersion In an Infinite Solid Cylinder," ASME JOURNAL OF APPLIED MECHANICS, Vol. 56, pp. 347–355.

Kim, Y. Y., and Steele, C. R., 1989a, "End Effects and Time-Harmonic Longitudinal Wave Propagation in a Semi-Infinite Solid Cylinder," ASME JOURNAL OF APPLIED MECHANICS, Vol. 56, pp. 334–346.

Kim, Y. Y., and Steele, C. R., 1989b, "An Analytic-Asymptotic Approach for Time-Harmonic Asymmetric Wave Propagation in a Cylinder," submitted for publication.

Kumar, R., 1972, "The Dispersion Relation of Flexural Waves in an Elastic Circular Cylinder," ASME JOURNAL OF APPLIED MECHANICS, Vol. 39, pp. 817–819.

McKenna, J., and Simpkins, P. G., 1985, "Modal Solutions, Symmetry Properties, and Orthogonality Conditions for Elastic Waves in Cylinders," *J. Acoust. Soc. Am.*, Vol. 78, pp. 1675–1683.

Miller, G. K., 1967, "Axisymmetric Stress-Wave Propagation Across the Plane Interface Between Two Cylindrically-Bounded Media," Elecroacoust. Res. Lab., University of Texas, Austin, Tex., Rep. No. 1-67.

Nelson, R. B., Dong, S. B., and Kalra, R. D., 1971, "Vibrations and Waves in Laminated Orthotropic Circular Cylinders," *J. Sound Vibration*, Vol. 18, pp. 429–444.

Pao, Y.-H., and Mindlin, R. D., 1960, "Dispersion of Flexural Waves in an Elastic, Circular Cylinder," ASME JOURNAL OF APPLIED MECHANICS, Vol. 27, pp. 729–734.

Pao, Y.-H., 1962, "The Dispersion of Flexural Waves in an Elastic, Circular Cylinder—Part 2," ASME JOURNAL OF APPLIED MECHANICS, Vol. 29, pp. 61–64.

Pochhammer, L., 1876, "Ueber die Fortphlanzungsgeschwindigkeiten kleiner Schwingungen in einem unbegrenzten isotropen Kreiscylinder," *J. für reine und angewandte Mathematik*, Vol. 81, pp. 324–336.

Shen, S. Q., 1988, "Transient Elastic Waves in a Circular Cylinder," Ph.D. Thesis, Cornell University, Ithaca, N.Y.

Timoshenko, S., 1921, "On the Correction for Shear of the Differential Equation for Transverse Vibrations of Prismatic Bars," *Philosophical Magazine*, Ser. 6, Vol. 41, pp. 744–746.

Watson, G. N., 1966, *A Treatise on the Theory of Bessel Functions*, 2nd ed., Cambridge University Press, Cambridge, U.K.

Wilson, L. O., 1986, "The Response of a Semi-Infinite Fiber to a Pulse Applied Asymmetrically to Its End," *J. Acoust. Soc. Am.*, Vol. 79, pp. 1798–1810.

Zemanek, J., 1972, "An Experimental and Theoretical Investigation of Elastic Wave Propagation in a Cylinder," *J. Acoust. Soc. Am.*, Vol. 51, pp. 265–283.

Downloaded 03 May 2010 to 171.66.16.31. Redistribution subject to ASME license or copyright; see http://www.asme.org/terms/Terms_Use.cfm

An Indirect Boundary Integral Equation Applied to Nonshallow Spherical Shell Problems With Arbitrary Boundary Constraints

Nikolaos Simos
Postdoctoral Research Associate,
Earthquake Research Center,
Department of Civil Engineering,
Assoc. Mem. ASME

Ali M. Sadegh
Associate Professor,
Department of Mechanical Engineering,
Mem. ASME

The City College of the
City University of New York,
New York, N.Y. 10031

The fundamental singular solutions of a complete elastic spherical shell are utilized and, via the superposition principle, an indirect boundary integral equation is formulated. The singular solutions correspond to the action of normal point loads, concentrated tangential loads, and surface moments which apply in a self-equilibrating fashion over the spherical surface. With singular solutions of such property in hand, an arbitrary spherical shell with surface loading and any set of consistent boundary constraints is embedded onto the complete sphere. A set of fictitious load vectors is introduced along the boundary line which, together with the prescribed surface traction, is required to satisfy the constraints at the boundary. The idea of an auxiliary boundary is also introduced and the solution to a number of representative shell problems is shown as compared to the available analytical and finite element method results.

Introduction

Recent developments in the boundary integral equation method have demonstrated the diverse applicability of such formulation and projected its potential in becoming a significant aid to engineering analysis. However, despite the substantial effort to expand the spectrum of practical problems that can be evaluated by this new idea, the method still remains a second choice to finite element analysis. This is due to the complex nature of its mathematical structure as well as to the widely established FEM procedures. BIM's superior mathematical model, very useful in local analysis (stress concentration or stress intensity in the neighborhood of cracks), and its far more efficient modeling, that results from its ability to reduce the problem dimension by one, constitute the basis upon which such an alternative procedure is being introduced.

The fundamentals of the Boundary Integral Method (BIM) are the validity of either the reciprocal work or the superposition principles and the availability of the singular solutions to the governing differential equations. Further, the ellipticity of the governing equation is highly essential when the direct formulation of the boundary integral equation is desired. It is known that for complex differntial operators, which lead to anything but simple and convenient fundamental solutions, a direct approach would require a far more mathematically sophisticated integral equation. Thus, in the treatment of domains governed by such diffential operators, i.e., shells, an indirect approach would be a better alternative.

In elasticity numerous investigations have focused attention on the analysis of plane-stress and plane-strain problems. A number of papers dealt with plate-bending problems while the incorporation of the bending theory of shells has been very limited. The principles of the boundary integral approach can be found in the works of Altiero (1978) in which the bending of a thin plate is evaluated by embedding the real plate in a fictitious plate for which the Green's function is known. A similar approach was incorporated by Niwa (1974) for the study of a clamped circular plate with a central loading with the introduction of an auxiliary boundary placed away from the real one. Sadegh (1979) also applied the indirect boundary integral approach to solve the problem of a finite plane, linear-elastic region containing an arbitrarily-shaped hole by embedding the region of interest in an infinite plane. The Green's functions and singular solutions used in the present analysis can be found in Simos (1988) and in which a number of works leading to derivation of singular solutions of shells are also cited. Simmonds (1968) and Wilkinson (1966a,b) are some of the investigations in which Green's functions for nonshallow spherical shells were developed.

The aim of this paper is to use the indirect boundary integral equation in the bending analysis of a spherical shell. The fundamental singular solutions of the differential equations of the shell correspond to the action of point loads in the normal and tangential direction and of concentrated surface moments. The singular loads act on the middle surface of a complete spherical shell in a self-equilibrating fashion. Thus, the "in-

Contributed by the Applied Mechanics Division of THE AMERICAN SOCIETY OF MECHANICAL ENGINEERS for presentation at the Winter Annual Meeting, San Francisco, Calif., December 10-15, 1989.

Discussion on this paper should be addressed to the Editorial Department, ASME, United Engineering Center, 345 East 47th Street, New York, N.Y. 10017, and will be accepted until two months after final publication of the paper itself in the JOURNAL OF APPLIED MECHANICS. Manuscript received by the ASME Applied Mechanics Division, June 23, 1988; final revision, February 27, 1989.
Paper No. 89-WA/APM-29.

Copyright © 1989 by ASME

Downloaded 03 May 2010 to 171.66.16.31. Redistribution subject to ASME license or copyright; see http://www.asme.org/terms/Terms_Use.cfm

finite'' domain encountered in plane elasticity and plate theory is now of finite extent, and it in turn demands the satisfaction of the overall equilibrium. Such a basic requirement is satisfied by the unique character of the fundamental solutions. Two different sets of singular solutions are available: one for the classical theory of shells approach and the other for an improved theory which incorporates the effect of transverse shear deformation. While the formulation of the integral equations for both theories is similar, the number of boundary conditions is four in the classical theory and five in the improved. The procedure involves the embedding of a spherical shell domain subject to surface tractions and boundary constraints onto a complete sphere of the same geometric and material properties. Fictitious line-load vectors are introduced along the boundary (equal in number to the specified conditions) such that their effect, combined with that of the prescribed surface traction, ensures the satisfaction of the boundary conditions. The principle of superposition leads to the determination of the intensity of the fictitious load vectors, and finally the solution of any field variable can be obtained at any point of the domain. An alternative approach to the integration of the singularities encountered in almost all the kernels is presented. This approach involves an auxiliary boundary away from the actual one over which the unknown fictitious vectors apply and thus the various integrations are taking place. In the work of Sanders (1970), as well as Tsai and Sanders (1974), integration of kernel singularities was performed on the boundaries of cutouts in shallow shells. As noted in Sander's (1970) analysis, however, the integration by parts used does not eliminate the possibility of a nonconverging integral and thus misrepresentation of the variable intended. Integrated by parts, nevertheless, could be utilized in the direct boundary element approach which, as in Sanders (1970), is also derived from Betti's reciprocal theorem, where two kernel functions integrate against each other. In the indirect method, however, the singular kernel is integrated against a shape function that assumes the distribution of a fictitious load vector over the boundary.

A number of classical shell problems are analyzed in an effort to demonstrate the effectiveness of the new approach. The types of problems that can be solved with this analysis include shells with concentrated or distributed radial and/or tangential loads and surface moments combined with any of the four sets of consistent boundary conditions: fixed, simply-supported, free to move in the normal direction and force-constrained (free). At this stage of the implementation of the approach, especially because of its particular character, the chosen example problems place emphasis on the solution near and on the actual boundaries. Indirect boundary integral approaches suffer in general from inaccuracies of their solution near the domain boundaries. That is due to the discretization of the boundary in a finite number of elements and thus satisfying the solution at a respective number of points. Since the singular solutions in the present analysis DO NOT include the effect of any boundary, while either four or five variables at each boundary point must be satisfied, the performance of the implemented approach near and on the boundary, irrespective of the form of loading (singular or distributed) on the shell surface, should be the proof of its validity.

The results show excellent agreement with the corresponding finite element solutions and also present computational advantages, especially in nonaxisymmetric problems.

Mathematical Statement and Basic Formulation

The equations of equilibrium of the shell element extracted from a spherical shell of middle surface radius R, thickness h, Young's modulus E, and Poisson's ratio μ are reduced to a set of uncoupled differential equations in terms of the transverse displacement function W and an auxiliary stress variable. Since our approach makes explicit use of the action of normal surface traction, q_n, while evaluating the action of tangential loads and surface moments from a limiting procedure that involves no surface load, we record the governing system of equations for such case, i.e., $q_\phi = q_\theta = 0$, $q_n \neq 0$,

Classical Theory:

$$(\nabla^2+2)\left[\nabla^4+2\,\nabla^2+\frac{EhR^2}{R}\right]W=\frac{R^4}{D}\,[\nabla^2+1-\mu]q_n \quad (1)$$

$$(\nabla^2+2)F=\frac{D}{R}\left[\frac{R^4}{D}\,q_n-(\nabla^2+2)^2W\right] \quad (2)$$

Improved Theory:

$$[\nabla^6+p_4\nabla^4+p_2\nabla^2+p_0]W = \frac{R^4}{D}\,(\nabla^2+1-\mu)\left[1-\frac{k_s(1-\mu^2)D}{EhR^2}\,(\nabla^2+1-\mu\right]q_n \quad (3)$$

$$(\nabla^2+2)\left[\nabla^2+2-\frac{1}{\xi k_s^0}\right]\Psi=0 \quad (4)$$

where F and Ψ are the introduced stress variables and ∇^2 is the Laplacian operator in the spherical surface coordinates (ϕ, θ). Further, $D = Eh^3/12(1-\mu^2)$, $\xi = (h^2/12R^2)$ and $k_s^0 = 6/5$ is the transverse shear coefficient equals, while

$$p_4=3-\mu-k_s(1-\mu^2),\quad p_2=\frac{1-\mu^2}{\xi}+2(1-\mu)+k_s(1-\mu^2)(\mu-3)$$

$$p_0=\frac{2(1-\mu^2)}{\xi}-2(1-\mu)(1-\mu^2)k_s,\quad k_s=\frac{2k_s^0}{1-\mu}.$$

The last term in equation (3) represents the contribution of the transverse shear to the governing differential equation for the transverse (radial) displacement.

The fundamental solutions for both sets of equations are constructed so that overall equilibrium of the complete sphere is always satisfied. The main frame of the mathematical derivation for both sets of equations is the same.

The Green's functions for normal surface traction, q_n, are the solutions for each of the two sets of equations with

$$q_n=\frac{1}{R^2}\left[\frac{\delta(\gamma)}{2\,\pi\,\sin\,\gamma}-\frac{3}{4\,\pi}\cos\gamma\right], \quad (5)$$

where $\delta(\gamma)/R^2 2\pi\sin\gamma$ is the Dirac Delta distribution applied at the pole $\gamma = 0$ of a rotated geographical coordinate system (γ, η) and $-\left(\frac{3}{R^2 4\pi}\right)\cos\gamma$ is an axisymmetric distributed surface traction introducing a resultant equal and opposite to that of the Delta function. The relation between the two coordinate systems, (ϕ, θ) and (γ, η), can be viewed through the identity

$$\cos\gamma=\cos\phi\,\cos\phi'+\sin\phi\,\sin\phi'\,\cos(\theta-\theta') \quad (6)$$

Let $\mathbf{x}(\phi, \theta)$ represent an arbitrary surface point and $\mathbf{x}'(\phi', \theta')$ the point where the Delta function applies. Further, we should note that $\cos\gamma$ is the equivalent of $(\mathbf{x} - \mathbf{x}')$ in the Green's functions expressions. The fundamental solutions for W and F for the classical theory set, (1, 2), are derived in the form (Simos 1988),

$$W(\mathbf{x};\mathbf{x}')=2\mathrm{Re}[A\,P_\nu(-\cos\gamma)] - \frac{1+\mu}{4\pi Eh}\,[1+\cos\gamma\,\ln(1-\cos\gamma)+B\,\cos\gamma] \quad (7)$$

$$F(\mathbf{x};\mathbf{x}')=2\mathrm{Re}\{A'P_\nu(-\cos\gamma)\} + C_2[1+\cos\gamma\,\ln(1-\cos\gamma)+B\cos\gamma]+C_1\cos\gamma \quad (8)$$

where $p_\nu(\ldots)$ is the Legendre function of the first kind, while

$$A=\frac{R^2}{D}\,(1-\mu-i\tan\psi)A_2,$$

Downloaded 03 May 2010 to 171.66.16.31. Redistribution subject to ASME license or copyright; see http://www.asme.org/terms/Terms_Use.cfm

$$A' = -\frac{D}{R}[2-\nu(\nu+1)]A, \quad B = \frac{4}{3} - \ln(2)$$

$$A_2 = -[8i\tan\psi(1-i\tan\psi)\sin\nu\pi]^{-1},$$

$$C_1 = -\frac{3D(1+\mu)}{4\pi EhR}, \quad C_2 = \frac{R}{4\pi}$$

$$\nu(\nu+1) = 1 + i\tan\psi, \quad \chi\cos\psi = 1, \quad \chi^2 = \frac{EhR^2}{D}.$$

A similar expression for W is obtained for the improved theory

$$W(\mathbf{x};\mathbf{x}') = 2\mathrm{Re}[AP_\nu(-\cos\gamma)] - T_1[1+\cos\gamma\ln(1-\cos\gamma) + B\cos\gamma] \tag{9}$$

where ν is now derived from one of the complex conjugate roots of the equation, say r_c,

$$r_c^3 + p_4 r_c^2 + p_2 r_c + p_0 = 0 \tag{10}$$

such as $\nu = -(1/2) \pm (1/4 - r_c)^{(1/2)}$, while

$$A = \frac{R^2}{D}\left([1-\mu-\nu(\nu+1)]A_2\left[1 - C_0'[1-\mu-\nu(\nu+1)]\right]\right)$$

$$A_2 = -\left(8[2-\nu(\nu+1)]i\ \mathrm{Im}[\nu(\nu+1)]\right]^{-1}$$

$$T_1 = C_0'\left([\mathrm{Re}\{\nu(\nu+1)-2\}]^2 + [\mathrm{Im}\{\nu(\nu+1)-2\}]^2\right]^{-1}$$

$$C_0' = \frac{3R^2(1+\mu)[1+C_0(1+\mu)]}{4\pi D}, \quad C_0 = \frac{k_s(1-\mu^2)D}{EhR^2},$$

and finally $\Psi = 0$.

The singular solutions of a unit tangential load and a unit concentrated moment have been constructed from the general form of the singular homogeneous solutions of (1, 2, 3, 4), $q_n = q_\phi = q_\theta = 0$,

$$W(\mathbf{x};\mathbf{x}') = \left[2\ \mathrm{Re}[h_1 P_\nu^1(\cos\gamma) + h_2 P_\nu^1(-\cos\gamma)] + C^1 Q_1^1(\cos\gamma)\right]\cos\eta \tag{11}$$

$$F(\mathbf{x};\mathbf{x}') = \left[2\ \mathrm{Re}[H_1 P_\nu^1(\cos\gamma) + H_2 P_\nu^1(-\cos\gamma)] + D^1 Q_1^1(\cos\gamma)\right]\cos\eta \tag{12}$$

where $H_1 = -\frac{D}{R}[2-\nu(\nu+1)]h_1, \quad H_2 = -\frac{D}{R}[2-\nu(\nu+1)]h_2,$

and for the improved theory,

$$W(\mathbf{x};\mathbf{x}') = \left(A_2 Q_1^1(\cos\gamma) + 2\ \mathrm{Re}[B_1 P_\nu^1(\cos\gamma) + B_2 P_\nu^1(-\cos\gamma)]\right)\cos\eta \tag{13}$$

$$\psi(\mathbf{x};\mathbf{x}') = \left(A_2' Q_1^1(\cos\gamma) + B_1' P_\omega^1(\cos\gamma) + B_2' P_\omega^1(-\cos\gamma)\right)\cos\eta \tag{14}$$

$$\omega(\omega+1) = 2 - \frac{1}{\xi k_s^0}, \quad \omega = -\frac{1}{2} - i\rho,$$

$$\rho = \frac{1}{2}\left[1 - 4\left(2 - \frac{12R^2}{k_s^0 h^2}\right)\right]^{\frac{1}{2}}.$$

The evaluation of the arbitrary constants in these expressions, which exhibit singularities at both $\gamma = 0$ and $\gamma = \pi$, defines the following physical loading situations: (*a*) a unit tangential load applied at $\mathbf{x}'(\phi', \theta')$, or at $\gamma = 0$ and along $\eta = 0$ in the rotated geographical system, and equilibrated by a similar load applied at $\gamma = \pi$ together with a concentrated moment $M = 2R$ and (*b*) a unit moment applied at $\gamma = 0$ and equilibrated by a similar moment at $\gamma = \pi$.

The rigorous mathematical analysis, which is not presented here, can be found in (Simos 1988) together with the evaluation of the remaining field variables. However, since the behavior of the kernels as $\gamma \to 0$ is of great importance, the leading term is listed here. The normal load solution of the classical theory leads to

$$W \simeq (\cos\gamma)\ u_\gamma \simeq \sin\gamma\ \log\left(\sin\frac{\gamma}{2}\right)$$

$$[N_{\alpha\beta}, M_{\alpha\beta}] \simeq \log\left(\sin\frac{\gamma}{2}\right) \quad Q_\gamma \simeq \left(\frac{1}{\sin\gamma}\right)$$

while the tangential load and moment solutions lead to

$$W \simeq \sin\gamma\ \log\left(\sin\frac{\gamma}{2}\right) \quad u_\alpha \simeq \log\left(\sin\frac{\gamma}{2}\right)$$

$$[N_{\alpha\beta}, M_{\alpha\beta}] \simeq \left(\frac{1}{\sin\gamma}\right) \quad Q_\alpha \simeq \left(\frac{1}{\sin^2\gamma}\right).$$

From the improved theory standpoint, the only differences with these terms occur in the radial displacement of the normal load solution and in the shear stress resultant, Q_α, of the tangential load or moment solution. Their behavior is

$$W \simeq \log\left(\sin\frac{\gamma}{2}\right) \text{ and } Q_\alpha \simeq \log\left(\sin\frac{\gamma}{2}\right),$$

respectively, while $\alpha = \gamma, \eta$ and $\beta = \gamma, \eta$. Even though the validity of the improved theory in the vicinity of singular points is questionable, its ability to satisfy five independent variables at every point on the boundary makes it a very useful tool in fracture mechanics problems. The use of the classical differential system has failed to represent the stress field near cracks in plate and shell problems while, on the other hand, improved theories were more successful in that respect.

This particular form of singular solutions utilized in the boundary intergal analysis introduces limitations in terms of the size of the domain they can apply. Thus, because of the two singularities involved, only shells of size equal or smaller than a hemisphere can be evaluated.

Indirect Boundary Integral Formulation

Consider a spherical shell problem whose domain D^* is a portion of a complete sphere, of size equal or less than a hemisphere, where its boundary ∂B is an arbitrary closed line on the spherical surface. The domain of interest is subjected to surface traction $q^s(n, \phi, \theta)$ and/or surface moment vector m^s, while over the boundary ∂B, a set of consistent boundary conditions are prescribed. To solve this well-posed problem, we embed D^* onto a complete sphere whose singular solutions are available. The specified surface traction is expressed in the form of an integral effect of unit excitation. According to the nature of the fundamental singularities, overall equilibrium of the image domain, as well as of the complete sphere, are preserved. To create the true deformation and stress fields in the interior of the domain, the boundary constraints must be satisfied. This is accomplished with the introduction of "fictitious" line load vectors of unknown intensity along ∂B. They represent the action of tractions as well as normal and twisting couples. Their number is determined by the shell theory being used. Thus, for the classical theory which requires the satisfaction of four conditions at the boundary, the number of such vectors will also be four; with the improved theory the number increases to five.

To complete the problem specification we let: $\mathbf{x}(\phi, \theta)$ be a field point where dependent variables can be evaluated, $\mathbf{x}'(\phi', \theta')$ be a load point where excitation occurs, $\xi'(\phi', \theta')$ be a load point along ∂B, $\xi(\phi, \theta)$ be a boundary point where dependent variables will be evaluated, $\mathbf{n}_s$ and $\mathbf{n}_l$ be the on-surface

Downloaded 03 May 2010 to 171.66.16.31. Redistribution subject to ASME license or copyright; see http://www.asme.org/terms/Terms_Use.cfm

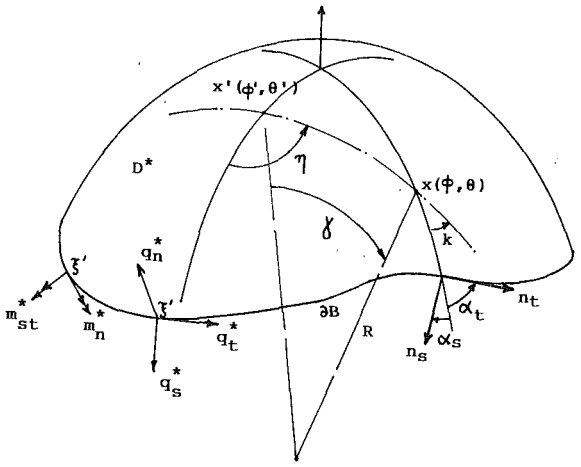


Fig. 1 Surface coordinates and orientation of boundary fictitious loads

unit vectors along the boundary, and α_s, α_t be the surface angles between the surface coordinate ϕ and the directions of the two unit vectors, as shown in Fig. 1.

Using the superposition approach to the boundary integral equations, we can write for the transverse displacement function W at the field point $\mathbf{x}$

$$W(\mathbf{x}) = \int\int_{D^*}\Big[W^n(\mathbf{x};\mathbf{x}')q_n^s(\mathbf{x}') + W_\phi^t(x;x')q_\phi^s(\mathbf{x}') + W_\theta^t(\mathbf{x};\mathbf{x}')q_\theta^s(\mathbf{x}') + W^m(\mathbf{x};\mathbf{x}')m^s(\mathbf{x}')\Big]dR + \int_{2B}\Big[W^m(\mathbf{x};\xi')q_n^*(\xi') + W_\phi^t(\mathbf{x};\xi')q_\phi^*(\xi') + W_\theta^t(\mathbf{x};\xi')q_\theta^*(\xi') + W_s^m(\mathbf{x};\xi')m_s^*(\xi') + W_{st}^m(\mathbf{x};\xi')m_{st}^*(\xi')\Big]dB, \quad (15)$$

where $q^*_{(n,\phi,\theta)}$ and m_s^* and m_{st}^* represent the components of the fictitious boundary line tractions, normal, and twisting line moment vectors, respectively, while W^n, W_ϕ^t, ... , W_{st}^m are the singular solutions due to loads acting along respective directions. Apparently, similar expressions would result for any field variable as long as the appropriate kernels are introduced under the integrals. Thus, we can write in a general format

$$Y(\mathbf{x}) = \int\int_{D^*} Y^i(\mathbf{x};\mathbf{x}')q_s^i d\mathbf{R} + \oint_{\partial B} Y^i[\mathbf{x};\xi']\{q_B^*\}^i d(\partial B) \quad (16)$$

where

$Y(\mathbf{x})$ = a system variable, such as displacement or stress, at a field point $\mathbf{x}(\phi, \theta)$,
$Y^i(\mathbf{x};\mathbf{x}')$ = is the kernel function (fundamental solution) of the variable $Y(\mathbf{x})$ associated with the field point $\mathbf{x}(\phi, \theta)$ and a load point $\mathbf{x}'(\phi', \theta')$,
q_s^i = the surface traction vector,
$\{q_B^*\}^i$ = fictitious load vectors applied along the boundary,
D^* = spherical shell domain,
∂B = boundary of the domain R, and
ξ' = load point at the boundary.

When the field point is brought to the boundary, $[\mathbf{x}(\phi, \theta) \rightarrow \xi(\phi, \theta)]$, the field variable, $Y(\mathbf{x})$, becomes the boundary value that is specified along ∂B. The second integral of (16) is of much concern since it takes the form

$$\oint_{\partial B} Y^i[\mathbf{x};\xi']\{q_B^*\}^i d(\partial B) \quad (17)$$

where $\int$ is an improper integral due to the singular character of the kernel functions as $\xi \rightarrow \xi'$. The singular character of the fundamental singularities is of vital importance and it needs to be addressed properly. In the derivation of the fundamental singularities of the shell equations, the character of their singular behavior was identified. Several of the kernels experience "weak" singularities, such as logarithmic, which are integrable. Stronger singularities of the order $(1/\gamma)$ also appear in several of the expressions. Their integration over the pole is treated in the form of the Cauchy principal value. A graphical representation of such approach is shown in Fig. 3. Thus, for the envelope shown, the integration of a kernel $K(\mathbf{x};\mathbf{x}')$ over a portion of the boundary ΔS_i will be written in the equivalent form,

$$\int_{\Delta S_i} K(\xi;\xi')dS_i = \int_{\Delta S_i} K_S(\xi;\xi')dS_i + \int_{\Delta S_i} K_R(\xi;\xi')dS_i \quad (18)$$

where K_S and K_R are the singular and regular parts of the kernel, respectively. Also,

$$\int_{\Delta S_i} K_S(\xi;\xi')dS_i = \lim_{\epsilon\rightarrow 0}\int_{\gamma_1'}^{\epsilon} K_S(\xi;\xi')dS_i + \lim_{\epsilon\rightarrow 0}\int_0^{2\pi} K_S(\xi;\xi')R\sin\epsilon\, d\eta' + \lim_{\epsilon\rightarrow 0}\int_{\epsilon}^{\gamma_2'} K_S(\xi;\xi')dS_i. \quad (19)$$

For example, the explicit evaluation at ξ of the stress resultant N_s whose corresponding kernels experience such singularity, $(1/\gamma)$, will be of the form

$$N_s(\xi) = \lim_{\epsilon\rightarrow 0}\int_{\xi_1}^{\epsilon}\Big[N_\gamma(\xi;\xi')\cos^2\alpha + N_\eta(\xi;\xi')\sin^2\alpha + 2\,N_{\gamma\eta}(\xi;\xi')\sin\alpha\cos\alpha\Big]dS_j + \lim_{\epsilon\rightarrow 0}\int_{\epsilon}^{2\pi}\Big[N_\gamma(\xi;\xi')\cos^2\beta_0 + N_\eta(\xi;\xi')\sin^2\beta_0 + 2\,N_{\gamma\eta}(\xi;\xi')\sin\beta_0\cos\beta_0\Big]R\,\sin\epsilon\, d\eta' + \lim_{\epsilon\rightarrow 0}\int_{\epsilon}^{\xi_2}\Big[N_\gamma(\xi;\xi')\cos^2\alpha + N_\eta(\xi;\xi')\sin^2\alpha + 2\,N_{\gamma\eta}(\xi;\xi')\sin\alpha\cos\alpha\Big]dS_j \quad (20)$$

where α, β_0 are the surface angles between the great circle connecting ξ and ξ' and the unit vector $\mathbf{n}_s$, while the expressions under the integrals correspond to Mohr-circle transformations of the stress resultants at ξ.

We should further note that according to the classical theory approach, the kernel representing the transverse shear resultant Q, due to a tangential load or a concentrated moment, contain a singularity of the order $(1/\gamma^2)$. Such singularity is not integrable over a surface line and thus special treatment of a shell boundary with such a variable, Q, prescribed over it must be adopted. The difficulty is resolved in the following manner: If one considers an additional fictitious boundary line ∂B_f located away from the actual one, then the fictitious line load vectors can be applied along the new line rather than ∂B. The superposition principle can still hold while the evaluation of singular integrals is no longer necessary. This is because the load and the field points on the boundary will never coincide. Theoretically, the position of the auxiliary boundary line is irrevelant to the formulation for as long as exact integrations are to be performed. However, when numerical integration rather than exact takes place, the choice of the positioning of the auxiliary boundary will be vital to the accuracy of the solution and, for that reason, further reference in the discussion section is presented. Such approach of avoiding singular integration completely has also been used by Niwa (1974).

Downloaded 03 May 2010 to 171.66.16.31. Redistribution subject to ASME license or copyright; see http://www.asme.org/terms/Terms_Use.cfm

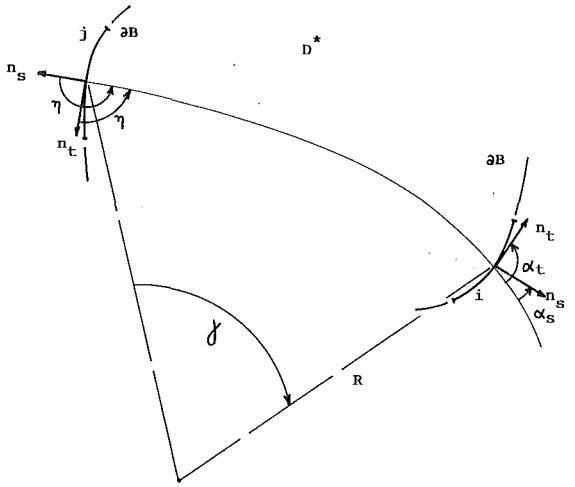


Fig. 2 Orientation of two arbitrary boundary elements

Integration Procedures and Numerical Evaluation

Clearly, if closed-form integrations of the simultaneous integral equations can be performed, the solution of the particular problem would be exact. However, in practical problems, a closed-form solution is almost impossible due to its dependence on the arbitrariness of the boundary geometry and surface traction. Thus, the boundary of the shell is discretized into N line elements and the surface, only in the presence of distributed traction, into M surface elements. The resulting general form of the boundary integral equations will be

$$Y(\mathbf{x}) = \sum_{p=1}^{M}\left[\int_{\Delta A_p} Y^i(\mathbf{x};\mathbf{x}')q_s^i dR_p\right] + \sum_{j=1}^{N}\left[\int_{\Delta S_j} Y^i[\mathbf{x};\xi'][q_B^*]^i dS_j\right] \tag{21}$$

where

M = number of surface elements
N = number of boundary elements.

Special attention is focused onto the discretized, closed boundary integral which is now expressed as the sum of the integrals over each boundary element. The task of the scheme is to effectively integrate the product of the kernel and the load functions over each element. For simplicity, the intensity of the unknown fictitious vectors is assumed to be constant over each element. Furthermore, the effect of each of the constant vectors is replaced by a statically-equivalent system of resultant forces applied at the middle point of each element. This can be viewed in the form

$$\int_{\Delta S} (q_s^* \cdot e)dS = R_n^s + R_s^s + R_t^s \tag{22}$$

where q_s^* is one of the fictitious load vectors, R_n^s, R_s^s, R_t^s are the resultant forces along the normal and the two tangential directions, respectively, and e is the unit vector at the middle point of the element. It is necessary to incorporate such an approach because of the particularities of the kernel functions which are mainly expressed in terms of complex Legendre functions. Such functions are evaluated in terms of their hypergeometric series expansion and, as a result, a closed-form evaluation of the integral

$$\int_{\Delta S_j} Y(\xi;\xi')dS_j \text{ will not be practical.}$$

However, when integrations are to be performed over either the same or neighboring elements, the asymptotic expansions of the Legendre functions may be used instead of the infinite series expansion. Integrations that take place over elements

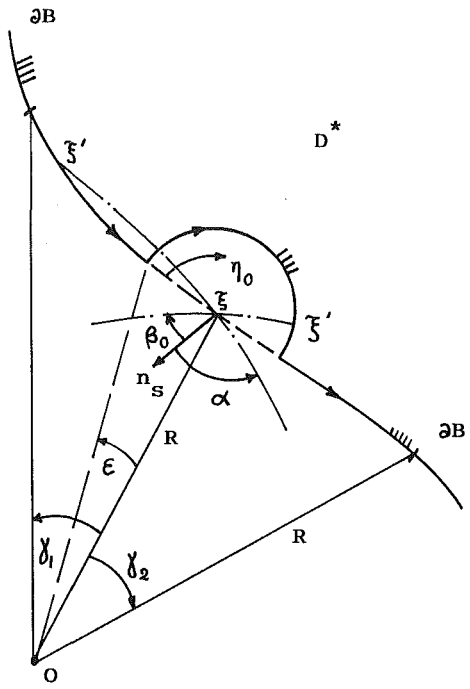


Fig. 3 Integration envelope along the boundary

where both the field and load points coincide, encounter the following singular integrals,

$$I_1 = \int_{\Delta S_B} \frac{1}{\sin\gamma}\, dS_B$$

$$I_2 = \int_{\Delta S_B} \cos\gamma \ln(1-\cos\gamma) dS_B \tag{23}$$

$$I_3 = \int_{\Delta S_B} \ln(1-\cos\gamma) dS_B$$

While I_1 is to be treated as a Cauchy principal value, I_2 and I_3 can be written in closed form. Thus, for a boundary element with surface coordinate θ = constant,

$$I_2 = 2R\left[\{\ln[1-\cos(\Delta\phi)]-1\}\sin(\Delta\phi) + \sin^{-1}[\cos(\Delta\phi)] - \frac{\pi}{2}\right] \tag{24}$$

$$I_3 = 2R\ln(2)\Delta\phi + 8R\left[\ln[\sin(\Delta\phi/2)](\Delta\phi/2) - \sin(\Delta\phi/2) - \sum_{k=1}^{\infty}\frac{(2k-1)!}{2^{2k-1}k!(k-1)!(2k+1)^2}[\sin(\Delta\phi/2)]^{2k+1}\right] \tag{25}$$

where $\Delta\phi = \phi_m - \phi_i$, ϕ_m is the coordinate of the middle point, which is also the pole, and ϕ_i is the coordinate of the end point of the interval.

Obviously, when the auxiliary boundary is being used, the integrals above are eliminated. Further, we should note that when integrations of the kernels are to be performed over surface elements that contain both (the field and the load point) the singularities up to the order $(1/\gamma)$ are all "weak" and can be integrated with no difficulties.

In order to construct the system matrix, we consider two arbitrary boundary elements, i and j, and an interior load point $\mathbf{x}'$, as shown in Fig. 2.

With the discretized form we have reduced the system into the evaluation and, subsequently, satisfaction of the prescribed boundary constraints at N distinct points of the boundary (the nodes of the elements). In Fig. 2, ϕ and θ are the global surface coordinates while γ and η are the surface coordinates of the local system with pole at the load point $\xi'(\phi', \theta')$. Because

Downloaded 03 May 2010 to 171.66.16.31. Redistribution subject to ASME license or copyright; see http://www.asme.org/terms/Terms_Use.cfm

the boundary constraints are expressed along the unit vectors e_S and e_t, and the load vectors, except for the one in the normal direction, are accompanied by directional angles at $\xi'(\phi', \theta')$ and $\mathbf{x}'(\phi', \theta')$, it is necessary to transform stress and displacement vectors from the local to global coordinate systems and vice versa. Such transformations can be deduced by utilizing the angular relationships

$$\cos\eta = \frac{\cos\gamma\cos\phi' - \cos\phi}{\sin\gamma\sin\phi'}, \quad \sin\eta = \frac{\sin\phi\sin(\theta-\theta')}{\sin\gamma}$$

$$\cos k = \frac{\cos\phi' - \cos\phi\cos\gamma}{\sin\phi\sin\gamma}, \quad \sin k = \frac{\sin\phi'\sin(\theta-\theta')}{\sin\gamma} \tag{26}$$

where k represents the angle between θ and η coordinates measured counterclockwise as shown in Fig. 2. When the field point $\mathbf{x}(\phi, \theta)$ is taken to the boundary, ξ, and since the boundary has an orientation described by the angles α_s and α_t, transformations must take place in order for the displacement and stress variables to be expressed along the unit vectors $\mathbf{n}_s$ and $\mathbf{n}_t$. This is necessary due to the fact that prescribed boundary conditions are given along these directions. These transformation relations at the boundary will be of the form:

$$u_s = u_\gamma\cos\alpha_s + u_\eta\sin\alpha_s, \qquad u_t = -u_\gamma\sin\alpha_s + u_\eta\cos\alpha_s$$

$$\beta_s = \beta_\gamma\cos\alpha_s + \beta_\theta\sin\alpha_s, \qquad \beta_t = \beta_\gamma\sin\alpha_s + \beta_\eta\cos\alpha_s$$

$$Q_s = Q_\gamma\cos\alpha_s + Q_\eta\sin\alpha_s \tag{27}$$

and from Mohr-circle transformations,

$$N_s = N_\gamma\cos^2\alpha_s + N_\eta\sin^2\alpha_s + 2N_{\gamma\eta}\sin\alpha_s\cos\alpha_s$$

$$N_{st} = -(N_\gamma - N_\eta)\sin\alpha_s\cos\alpha_s + N_{\gamma\eta}(\cos^2\alpha_s - \sin^2\alpha_s)$$

$$M_s = M_\gamma\cos^2\alpha_s + M_\eta\sin^2\alpha_s + 2M_{\gamma\eta}\sin\alpha_s\cos\alpha_s \tag{28}$$

$$M_{st} = (M_\gamma - M_\eta)\sin\alpha_s\cos\alpha_s + M_{\gamma\eta}(\cos^2\alpha_s - \sin^2\alpha_s).$$

In (27), (28), u_s, u_t are the two components of the surface displacement, β_s, β_t are the components of the angular rotation of the normal, Q_s is the shear stress resultant over the boundary edge, while N_s, N_{st} and M_s, M_{st} are the membrane stress and resultant couples, respectively.

Assembly and Solution of the System of Equations

The first step toward the solution is to effectively assemble a system of linear algebraic equations, which will substitute for the integral equations of the system, incorporating the boundary information for the particular problem. Thus for N discrete boundary elements and n number of specified conditions, we can express the governing system in the form of the matrix relation

$$L\psi^* + S = BC \tag{29}$$

where

- L = $nN \times nN$ fully-populated system matrix associated with the integrations of the fundamental solutions,
- ψ^* = $nN \times 1$ vector of the fictitious boundary loads,
- S = $nN \times 1$ vector whose elements correspond to the accumulated effect of the known surface traction ψ at each node, and
- BC = $nN \times 1$ vector of the specified boundary conditions at the N nodes (the number is four per element for the classical theory and five for the improved theory).

Consider a shell problem bounded by a single clamped boundary ($W = u_s = u_t = \beta_s = \beta_t = 0$). The term $L\,\psi^*$ can be written in the form

$$\begin{array}{c|ccccc|c}
 & \multicolumn{5}{c|}{L} & \psi^* \\
W^n & W^s & W^t & W^m & W^{mt} & (q_n^1)^* \\
 & & & & & \\
(N\times N) & \dots & \dots & \dots & \dots & \vdots \\
 & & & & & (q_n^N)^* \\
\hline
u_s^n & u_s^s & u_s^t & u_s^m & u_s^{mt} & (q_s^1)^* \\
 & & & & & \vdots \\
(N\times N) & \dots & \dots & \dots & \dots & (q_s^N)^* \\
\hline
u_t^n & u_t^s & u_t^t & u_t^m & u_t^{mt} & (q_t^1)^* \\
 & & & & & \vdots \\
(N\times N) & \dots & \dots & \dots & \dots & (q_t^N)^* \\
\hline
\beta_s^n & \beta_s^s & \beta_s^t & \beta_s^m & \beta_s^{mt} & (m_s^1)^* \\
 & & & & & \vdots \\
(N\times N) & \dots & \dots & \dots & \dots & (m_s^N)^* \\
\hline
\beta_t^n & \beta_t^s & \beta_t^t & \beta_t^m & \beta_t^{mt} & (m_{mt}^1)^* \\
 & & & & & \vdots \\
(N\times N) & \dots & \dots & \dots & \dots & (m_{st}^N)^* \\
\hline
\end{array}$$

In equation (30) the superscript in the submatrices denotes the effect of the boundary load vector acting along that direction over an element j, and the subscript identifies the the orientation of the field variable at the node of an element i. Further, $(q_n^j)^*$, $(q_s^j)^*$, $(q_t^j)^*$, $(m)^*_j$, $(m_{st}^j)^*$ represent the fictitious loads over element j with the superscript denoting their orientation with respect to the boundary edge. The formation of the submatricies can be seen in the following sample, i.e.,

$$u_t^t = \begin{bmatrix} u_t^{q_s^*}(1,1) \dots\dots\dots u_t^{q_s^*}(1,N) \\ \dots\dots u_t^{q_s^*}(i,j) \dots\dots \\ \dots\dots\dots\dots\dots u_t^{q_s^*}(N,N) \end{bmatrix} \tag{31}$$

$$u_t^{q_s^*}(i,j) = \int_{\Delta S} u_t(\xi;\xi')q_s^*(\xi')\,dS_j = q_s^*[R_{n,t}u_t^n(i;j) + R^{s,t}u_t^s(i;j) + R_{t,t}u_t^t(i;j)]. \tag{32}$$

The principle of the matrix formulation in (32) can facilitate a number of different boundaries with different prescribed conditions. The computer program that has been written can incorporate clamped boundaries, simply-supported boundaries free to move in the normal to the surface direction, and lastly, boundaries with free-edge conditions.

Downloaded 03 May 2010 to 171.66.16.31. Redistribution subject to ASME license or copyright; see http://www.asme.org/terms/Terms_Use.cfm

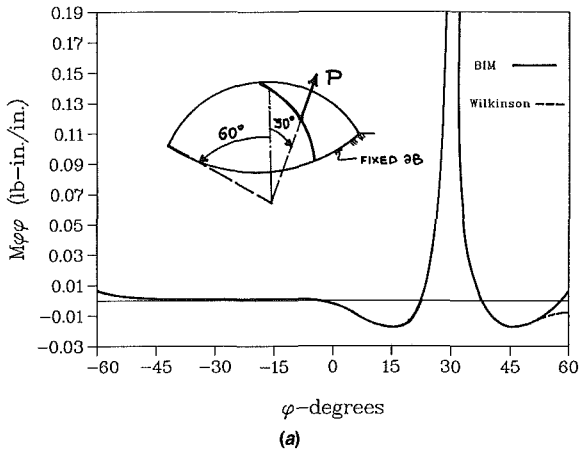
Numerical Results and Discussion

The closed-form singular solutions that have been derived for all the field variables and the ability of the computer program to handle all types of surface tractions as well as boundary constraints, enabled us to investigate in a detailed fashion the effects of such input parameters. Further, we were able to examine and evaluate the transverse shear effect onto the displacement and stress variables. Due to space limitations, only a few of the solved problems will be presented here. Complete evaluation of the different problems can be found in Simos (1988). The results obtained by the boundary integral method were compared against the finite element solutions which utilized the ANSYS code as well as against the available analytical solutions. The agreement was found to be excellent except for the vicinity of concentrated loads. This is due to the singularities experienced by the kernels. Analytical solutions, such as the singular solutions derived, allow for singularities to be present in their expressions. We should note that the singular character of our fundamental solutions fully agrees with all previous studies. On the other hand, finite element analysis introduces finite values of the variables at the point of application of singular loads.

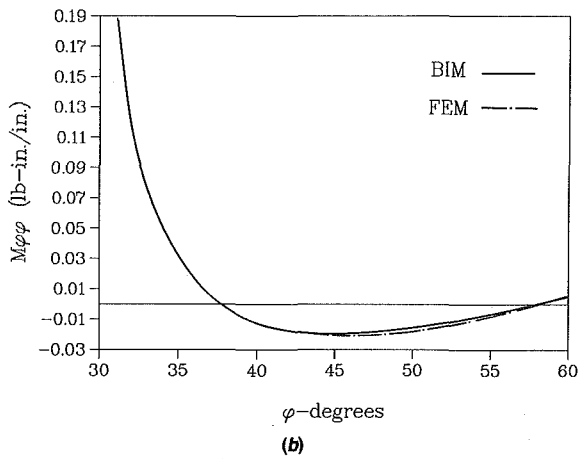
Table 1 Surface displacement comparison between BIM and FEM for a clamped spherical cap of 30 deg opening subjected to a unit moment at the appex.

	$u_\phi \times 10^{-7}$ in (at θ=0°)		$u_\theta \times 10^{-7}$ in (at θ = 90°)	
Degrees	B E M	F E M	B E M	F E M
1	-.2970	-.3026	.3168	.3246
2	-.2854	-.2902	.3180	.3243
3	-.2645	-.2687	.3125	.3177
4	-.2390	-.2429	.3034	.3079
5	-.2114	-.2150	.2921	.2959
6	-.1834	-.1867	.2795	.2827
8	-.1293	-.1323	.2520	.2542
10	-.0820	-.0844	.2233	.2247
12	-.0432	-.0453	.1949	.1958
14	-.0139	-.0155	.1676	.1681
18	.0188	.0179	.1176	.1178
22	.0244	.0242	.0740	.0740
24	.0207	.0206	.0541	.0542
26	.0145	.0145	.0354	.0355
28	.0072	.0072	.0174	.0175
30	.0000	.0000	.0000	.0000

Table 1 contains surface displacement comparison between the boundary element and finite element methods. The solution corresponds to a clamped spherical cap of 30 deg opening subjected to a unit moment at the apex with properties E = 30×10^6 psi, Poisson's ratio $\mu = 0.3$, radius $R = 10$ in., and thickness $h = 0.5$ in. Figure 4 corresponds to a spherical cap of 60 deg opening which is subjected to a point load at 30 deg and has the same properties with the previous example. The solution of the moment resultant $M_{\phi\phi}$ is compared with the analytical result by Wilkinson (1966). While the agreement is excellent throughout, discrepancies arise in the vicinity of the near boundary. Since Wilkinson's solution is subject to the convergence of an infinite series, the same problem was solved with the finite element scheme. The agreement of the boundary element and finite element models is apparent in Fig. 4(*b*). It should be mentioned at this point that, while the same computational effort for this nonaxisymmetric problem was required by the boundary element model as for the previous

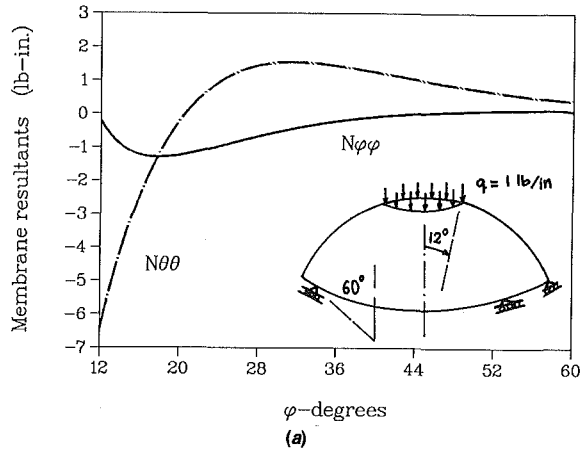


(*a*)

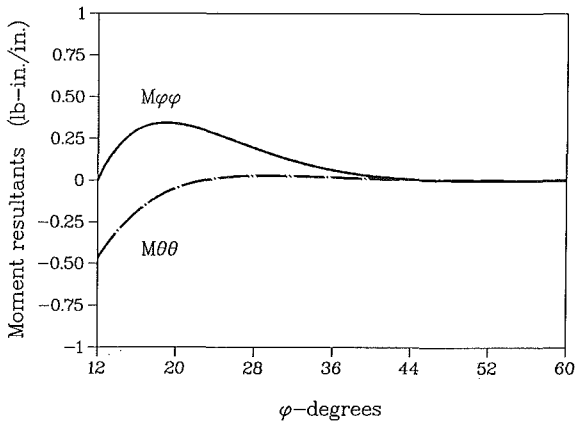


(*b*)

Fig. 4 Moment resultant $M_{\phi\phi}$ solution; (*a*) analytical versus BIM, (*b*) FEM versus BIM



(*a*)



(*b*)

Fig. 5 Variation of the stress resultants in the loaded spherical cap; (*a*) membrane resultants, (*b*) moment resultants

Downloaded 03 May 2010 to 171.66.16.31. Redistribution subject to ASME license or copyright; see http://www.asme.org/terms/Terms_Use.cfm

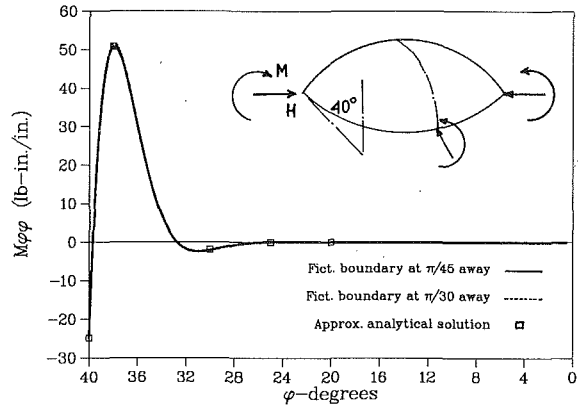


Fig. 6 Comparison of $M_\phi\phi$ with the "exact" solution for a spherical dome reinforced by an edge ring

symmetric one, the respective effort of the finite element model increased dramatically.

The next example problem considered (see Fig. 5) involves a shell problem bounded by two parallel circular boundaries at 12 deg and 60 deg, respectively. While the boundary at 60 deg is allowed to move along the radial direction (it is resting on rollers), the one at 12 deg is subjected to a distributed transverse load $q = 1$ lb/in. Figures 5 (*a*) and 5(*b*) display the membrane and bending resultant variations for the length of the shell.

Finally, a spherical dome with $R = 76.6$ ft, opening angle of 40 deg, and thickness $h = 2.36$ in. is subjected to the action of its own weight. The edge of the shell is constrained by an edge ring. This problem has been solved analytically, but with approximate formulation, (see Timoshenko, pp. 555–558) by reducing the effect of the distributed load to the action of an equivalent force H (lb/in) and a couple M (lb-in/in) acting over the edge, (see Fig. 6). The reason such an example problem was chosen is to study the effect of the positioning of the auxiliary boundary on the solution of a field variable. For this problem the Poisson's ratio for both the ring and the shell is zero, while a load of $q_w = 41$ psf leads to the following values of the edge forces: $M = -24.84$ lb-in/in. and $H = -8.95$ lb/in.

The corresponding values of the bending moment, M_ϕ, for two angular distances of the auxiliary boundary, $\Delta\phi$, and those of the approximate analytical soltuion are presented in Fig. 6. The peak value of the moment resultant for all three evaluations occur at approximate two degrees away from the edge. The numerical value is 50.8 (lb-in/in.) for the analytical approach and 50.68 and 51.45 (lb-in/in.) for the boundary integral method. These results correspond to $\pi/45$ and $\pi/30$ radians of the positioning of the auxiliary boundary away from the real one.

In view of the examples considered, one should note that the discrepancies near the boundary, which are generally experienced by boundary integral approaches, are much smaller in this analysis, thanks to the auxiliary boundary that has been introduced in most of the solved problems.

Since the amount of computer CPU time used by the various methods is of great importance, a comparison on the basis of the simplifications, as well as discretization, scheme used must be made for a fair evaluation. As noted earlier, the boundary integral approach considered curved line elements and fictitious vectors of constant intensity over each element. Indeed, the variation of the number of elements has a drastic effect on the computational time. This is due to the fact that the size of its fully-populated matrix is determined according to the scheme $(4N \times 4N)$ or $(5N \times 5N)$, where N is the number of boundary elements. On the other hand, when the geometry of the problem and the applied loads are of axisymmetric nature the finite element model, which consisted of axisymmetric conical elements, was superior in terms of the computer time, failing though to provide the answer to all the stress variables. However, when axisymmetry is no longer a problem feature, the amount of computer time is far greater than that used by the boundary integral approach. About 32 minutes are required for the evaluation of the problem of a spherical cap subjected to a concentrated lateral force or moment at the appex by using a total of 600 quadrilateral shell elements on a VAX/750 computer. The same problem solved by the boundary element method with 60 boundary elements on an IBM 3090/180 computer required 39.9 seconds of CPU time.

In conclusion, we say that the indirect approach of the boundary integral equation utilized in this analysis was proven to be very accurate in evaluating the stress and displacement fields in a loaded spherical shell. Its flexibility, in terms of the incorporation of the boundary constraints, and its computational efficiency are definitely two of its key characteristics that can effectively be utilized in complex problems.

References

Altiero, N. J., and Sikarskie, D. L., 1978, "A Boundary Integral Method Applied to Plates of Arbitrary Plan Form," *Computers and Structures*, Vol. 9, pp. 163–168.

Banerjee, P. K., and Butterfield, R., 1978, *Boundary Element Methods in Engineering Science*, McGraw-Hill Book Co., New York.

Niwa, Y., Kobayashi, S., and Fukui, T., 1974, "An Application of the Integral Equation Method to Plate Bending," *Faculty of Engineering*, Kyoto University, Japan.

Sadegh, A. M., and Altiero, N. J., 1979, "A Boundary Integral Method Applied to the Problem of an Elastic Region Weakened by an Arbitrarily-Shaped Hole," *Mechanics Research Communications*, Vol. 6, No. 3, pp. 167–175.

Sanders, Jr., J. L., 1970, "Cutouts in Shallow Shells," ASME JOURNAL OF APPLIED MECHANICS, Vol. 37, pp. 374–383.

Simmonds, G. J., 1968, "Green's Functions for Closed Elastic Spherical Shells, Exact, and Accurate Asymptotic Solutions," *Proceedings of the Koninklijke Nederlandse Academie van Wetenschappen*, Series B, Vol. 71, No. 3, pp. 236–249.

Simos, N., 1988, "Singular Solutions and an Indirect Boundary Integral Formulation for Spherical Shells," Ph.D. Thesis, submitted to the Graduate School of The City University of New York.

Timoshenko, S., and Woinowsky-Krieger, S., 1959, *Theory of Plates and Shells*, McGraw-Hill Book Co., New York.

Tsai, C.-J., and Sanders, Jr., J. L., 1975, "Elliptical Cutouts in Cylindrical Shells," ASME JOURNAL OF APPLIED MECHANICS, Vol. 42, pp. 326–334.

Wilkinson, J. P., and Kalnins, A., 1966a, "On Nonsymmetric Dynamic Problem of Elastic Spherical Shells," ASME JOURNAL OF APPLIED MECHANICS, Vol. 87, Series E, pp. 31–38.

Wilkinson, J. P., and Kalnins, A., 1966b, "Deformation of Open Spherical Shells Under Arbitrarily Located Concentrated Loads," ASME JOURNAL OF APPLIED MECHANICS, Series E, pp. 305–312.

Downloaded 03 May 2010 to 171.66.16.31. Redistribution subject to ASME license or copyright; see http://www.asme.org/terms/Terms_Use.cfm

M. P. Karyeaclis
Mem. ASME

T. K. Caughey
Professor of Applied Mechanics.

California Institute of Technology,
Pasadena, Calif. 91125

Stability of a Semi-active Impact Damper: Part I—Global Behavior

A study is made of the general behavior of a semi-active impact damper. The system consists of an undamped forced torsional oscillator, and a flywheel which can be locked to the oscillator through a clutch. The impact which results during clutch engagement is effective in reducing the vibration amplitude level of the oscillator when it is subjected to bounded excitation. All solutions of the system are shown to be bounded when the input is bounded. Periodic solutions are discussed in the following paper, Part II.

1 Introduction

The idea of dissipating energy in a vibrating mechanical system by allowing internal parts to collide with each other is not new, and its development spans the last four decades (Masri, 1965).

Early investigations centered on determining the motion of a particle constrained to move in a container and which collided with the walls of the container. The fundamental assumption was that the motion involved two impacts per cycle and methods for determining such motion were developed. Estimates of the dissipated energy were also made for these undamped, single degree-of-freedom oscillators. Moreover, theoretical investigations were complemented by experiments involving a variety of applications (Masri, 1965). These investigations confirmed the fact that the predominant motion is that which involves two impacts per cycle.

Due to the impacts involved, the equation of motion is only piecewise linear, the resulting solution is piecewise continuous and, as a result, the stability of the periodic solutions was not investigated until 1965, when Masri and Caughey (1965, 1966) developed a suitable method for analyzing a fourth-order model. Their method is based on the idea of determining how initial perturbations evolve between impacts and is applicable not only to impact dampers, but also to any system governed by piecewise linear/nonlinear differential equations as long as the solution between impacts is known.

The objective of this investigation is to introduce a new element in the study of impact dampers, namely, the idea of actively controlling the time of impact and, in addition, to complement earlier studies by providing information on the global behavior of impacting systems. The system studied consists of two rotating masses which are locked together by energizing a fast-acting clutch at selected times, but the idea is not necessarily restricted to rotating masses.

2 System Description

The system under consideration is shown in Fig. 1. It consists of two parts. The primary system is an undamped forced torsional oscillator while the secondary system consists of a flywheel which is free to rotate with respect to the main rotor. The two can be linked together by energizing a fast-acting clutch. It is assumed that there is no slip between the rotors when the clutch is engaged and, as a result, they both have the same angular velocity during and immediately after engagement.

Let I and J be the moments of inertia of the primary and secondary rotors, respectively, and k the stiffness of the torsional spring. Let $F(x, \dot{x}, v)$ represent the torque acting between the rotors when the clutch in engaged and $x(t)$, $y(t)$ be the angular displacements of the two rotors. Then, the equations of motion for the system are:

$$\left.\begin{aligned} I\ddot{x}+kx+F(x,\dot{x},v) &= p(t) \\ J\dot{v}-F(x,\dot{x},v) &= 0 \\ \dot{y} &= v \\ x(0),\ \dot{x}(0),\ v(0) &\text{ given} \end{aligned}\right\}. \tag{1}$$

Assumptions:

(1) The excitation torque $p(t)$ is bounded with zero mean.

(2) The period of time during which the clutch is engaged is very short. During that time, $x(t)$ and $y(t)$ do not change significantly.

(3) Clutch actuation is instantaneous.

Under these assumptions, the functional form of $F(x, \dot{x}, v)$ may be partly determined. The active aspect of the damper refers to the triggering mechanism for the clutch. In a fully-active arrangement, a feedback control law would be deter-

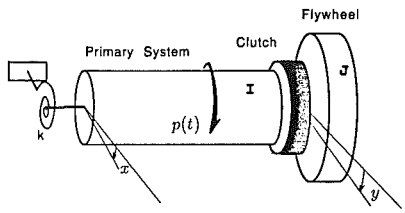


Fig. 1 Schematic representation of the impact damper

Contributed by the Applied Mechanics Division of THE AMERICAN SOCIETY OF MECHANICAL ENGINEERS for publication in the JOURNAL OF APPLIED MECHANICS.

Discussion on this paper should be addressed to the Editorial Department, ASME, United Engineering Center, 345 East 47th Street, New York, N.Y. 10017, and will be accepted until two months after final publication of the paper itself in the JOURNAL OF APPLIED MECHANICS. Manuscript received by ASME Applied Mechanics Division, February 15, 1988; final revision, January 26, 1989.

Copyright © 1989 by ASME

Downloaded 03 May 2010 to 171.66.16.31. Redistribution subject to ASME license or copyright; see http://www.asme.org/terms/Terms_Use.cfm

mined and the clutch would engage accordingly. In this formulation, actuation is determined *a priori* and remains fixed during operation.

The purpose of the mechanism described is to provide damping for the torsional oscillator. To determine what instant in time clutch actuation would be most beneficial, suppose that the primary and secondary rotors are locked and then released. The secondary rotor will continue to rotate with constant angular velocity in a given direction while the primary rotor will reach maximum displacement and then begin to rotate in the opposite direction. It has maximum velocity as it crosses the equilibrium position $x = 0$. Impact time t_i is therefore chosen such that the velocity difference between the two rotors is maximum, i.e., when $x(t_i) = 0$. It follows then that

$$F(x,\dot{x},v)=\delta(x)\dot{x}g(\dot{x},v). \tag{2}$$

Adding the two equations (1) we obtain

$$I\ddot{x}+J\dot{v}+kx=p(t). \tag{3}$$

Let t be the time of impact. Integrating (3) over the infinitesimal time interval during which the clutch is engaged, we get

$$I[\dot{x}(t^+)-\dot{x}(t^-)]+J[v(t^+)-v(t^-)]=0,$$

since both $x(t)$ and $p(t)$ are continuous. Rearranging,

$$I\dot{x}(t^+)+Jv(t^+)=I\dot{x}(t^-)+Jv(t^-), \tag{4}$$

which is simply a statement of conservation of angular momentum.

Moreover, at $t = t^+$ the rotors are locked, and therefore have the same angular velocity. Hence, $v(t^+) = \dot{x}(t^+)$. Using (4) we obtain an expression for the velocity after impact in terms of the velocities just before, as follows:

$$\dot{x}(t^+)=v(t^+)=\frac{I}{I+J}\dot{x}(t^-)+\frac{J}{I+J}v(t^-) \tag{5}$$

or

$$\dot{x}(t^+)=v(t^+)=a\dot{x}(t^-)+bv(t^-),\ t \text{ such that } x(t)=0 \tag{6}$$

where

$$a=\frac{I}{I+J},\ b=\frac{J}{I+J},\ a+b=1. \tag{7}$$

Expression (6) represents the impact condition and will be used extensively in this analysis.

3 Ultimate Boundedness

The main result of this section is that if $p(t)$ is bounded, then so are all solutions of the impact damper. Before proving this, we need some facts concerning the following autonomous auxiliary system:

$$\left.\begin{array}{c} I\ddot{x}+kx+F(x,\dot{x},v)=T\text{sgn}(\dot{x}) \\ J\dot{v}-F(x,\dot{x},v)=0 \\ x(0)=-C_x;\dot{x}(0)=0;v(0^+)=-C_v;C_x>0,C_v>0 \end{array}\right\} \tag{8}$$

where T is a positive constant and $F(x, \dot{x}, v)$ is as before.

Lemma 1. *The auxiliary system (8) possesses a unique limit cycle* $\mathcal{L}(T, \beta)$, *where* $\beta = I/(I + 2J)$.

Proof. We prove the existence of the limit cycle by finding initial conditions C_x and C_v such that the orbit of the system in the $x-\dot{x}$ phase plane is closed. Uniqueness then follows from the fact that the solution of the initial value problem is unique.

A typical limit cycle trajectory is shown in Fig. 2. Due to the symmetry of the system, it sufficies to consider only semi-trajectories.

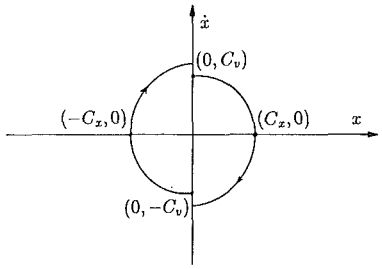


Fig. 2 The limit cycle of auxiliary system (8)

Let t_1 be such that $x(t_1) = 0$ and suppose that $x(t) \le 0$, $\dot{x} \ge 0\ \forall t \in [0, t_1]$. Then, equations (8) become:

$$I\ddot{x}+kx=T \tag{9}$$

$$J\dot{v}=0. \tag{10}$$

Multiplying (9) by $\dot{x}$ and integrating

$$\int I\ddot{x}\dot{x}dt+\int k\dot{x}xdt=\int T\dot{x}dt,$$

$$\Rightarrow H(t)=I\dot{x}^2(t)+kx^2(t)-2Tx(t)=\text{constant}. \tag{11}$$

The constant of integration is evaluated using the initial conditions. Thus,

$$I\dot{x}^2(t)+kx^2(t)-2Tx(t)=kC_x^2+2TC_x;\ t\in[0,t_1). \tag{12}$$

Since at $t=t_1$ $x(t_1) = 0$, equation (12) can be solved for the velocity of the primary mass just prior to impact. Thus,

$$\dot{x}(t_1^-) = \sqrt{\frac{kC_x^2+2TC_x}{I}}. \tag{13}$$

$$v(t_1^-) = -C_v. \tag{14}$$

If the solution is to satisfy the symmetry conditions, then $\dot{x}(t_1^+) = C_v = -v(t_1^-)$. Substituting in the expression for the impact condition, we get

$$\dot{x}(t_1^+)=\frac{I}{I+J}\dot{x}(t_1^-)-\frac{J}{I+J}\dot{x}(t_1^+)\Rightarrow(\dot{x}(t_1^+)=\frac{I}{I+2J}\dot{x}(t_1^-).$$

Using (13) it follows that

$$\dot{x}(t_1^+)=C_v=\beta\sqrt{\frac{kC_x^2+2TC_x}{I}},\ \beta=\frac{I}{I+2J}. \tag{15}$$

To determine C_x, we continue the solution in the interval $t_1 < t \le t_2$ where t_2 is such that $x(t_2) = 0$. From symmetry, $x(t_2) = C_x$. Evaluating the integral of the motion $H(t)$ at t_1^+ and at t_2, we find

$$H(t_1^+)=I\dot{x}^2(t_1^+)+kx^2(t_1^+)-2Tx(t_1^+)=I\beta^2(kC_x^2+2TC_x)$$

$$H(t_2)=I\dot{x}^2(t_2)+kx^2(t_2)-2Tx(t_2)=kC_x^2-2TC_x.$$

Setting these expressions equal, we obtain a relationship which can be solved for C_x. The solution is

$$C_x=0;\ C_x=\frac{2T}{k}\frac{1+\beta^2}{1-\beta^2}.$$

Thus, the initial conditions are

$$C_x=\frac{2T}{k}\frac{1+\beta^2}{1-\beta^2} \tag{16}$$

$$C_v=\beta\sqrt{\frac{kC_x^2+2TC_x}{I}} \tag{17}$$

and they specify the limit cycle which is unique and consists of elliptical arcs passing through the four points $(-C_x, 0)$, $(0, C_v)$, $(C_x, 0)$, and $(0, -C_v)$ as shown in Fig. 2. We denote this limit cycle by $\mathcal{L}(T, \beta)$.

It is evident from expressions (16) and (17) that both C_x and C_v are monotone increasing functions of T and the parameter β. As a result, for $0 < \beta_1 < \beta_2$ the curve $\mathcal{L}(T, \beta_1)$ lies entirely

Downloaded 03 May 2010 to 171.66.16.31. Redistribution subject to ASME license or copyright; see http://www.asme.org/terms/Terms_Use.cfm

inside $\mathcal{L}(T, \beta_2)$. Let $\mathcal{S}(T, \beta)$ be the set enclosed by the limit cycle $\mathcal{L}(T, \beta)$.

The following lemma addresses the question of stability of the limit cycle $\mathcal{L}(T, \beta)$.

Lemma 2. *The limit cycle* $\mathcal{L}(T, \beta)$ *of system (8) is globally asymptotically stable.*

Proof. Clearly we need not consider completely arbitrary initial conditions. For if we do so, after the first impact we will have $\dot{x}(t_0^+)=0$, $\dot{x}(t_0^+)=v(t_0^+)$ where t_0 is the first impact time.

Thus, without loss of generality, we assume that at $t = 0$ $x(0) = 0$ and $\dot{x}(0^+) = v(0^+)$. Now, let $\{t_n\}_{n=1}^{\infty}$ be the sequence of instants in time that impacts occur. Then $t_n < t_{n+1}$ and $x(t_n) = 0$. Let $\dot{x}_n = \dot{x}(t_n^+)$. We will show that $\lim_{n\to\infty} |\dot{x}_n| = C_v$.

Consider a semi-trajectory starting at $(0, \dot{x}(0^+))$ in the $x-\dot{x}$ projection of the phase plane. Suppose that $v(0^+) = \dot{x}(0^+) \neq C_v$. Let t' be such that $\dot{x}(t') = 0$, and suppose that the next impact occurs at $t = t_1 \Rightarrow x(t_1) = 0$. Then

$$H(t)=\begin{cases} I\dot{x}^2(t)+kx^2(t)-2Tx(t)=I\dot{x}^2(0^+)=kx^2(t')-2Tx(t') \text{ for } \dot{x}>0 \\ I\dot{x}^2(t)+kx^2(t)+2Tx(t)=I\dot{x}^2(t_1^-)=kx^2(t')+2Tx(t') \text{ for } \dot{x}<0. \end{cases}$$

Solving for the velocities we find

$$\dot{x}(0^+)=\sqrt{\frac{kx^2(t')-2Tx(t')}{I}} \tag{18}$$

$$\dot{x}(t_1^-)=-\sqrt{\frac{kx^2(t')+2Tx(t')}{I}}. \tag{19}$$

The impact condition (5) at $t = t_1$ gives:

$$\dot{x}(t_1^+)=\frac{I}{I+J}\dot{x}(t_1^-)+\frac{J}{I+J}\dot{x}(0^+)$$

$$\Rightarrow \frac{|\dot{x}(t_1^+)|}{\dot{x}(0^+)}=\frac{I}{I+J}\frac{|\dot{x}(t_1^-)|}{\dot{x}(0^+)}-\frac{J}{I+J}.$$

Let $R = |\dot{x}(t_1^+)|/\dot{x}(0^+)$, and substitute for $\dot{x}(t_1^-)$ and $\dot{x}(0^+)$ in the previous equations to get:

$$R=\frac{I}{I+J}\sqrt{\frac{kx(t')+2T}{kx(t')-2T}}-\frac{J}{I+J}$$

$$=1-\frac{I+J}{I+J}+\frac{I}{I+J}\sqrt{\frac{kx(t')+2T}{kx(t')-2T}}-\frac{J}{I+J}. \tag{20}$$

Let $x(t')=C_x+d$ where C_x is given by (16). Substituting into equation (20) for $x(t')$ and C_x, we obtain, after rearrangement, the following expression for R:

$$R=\frac{|\dot{x}(t_1^+)|}{\dot{x}(0^+)}=1-\left(\frac{I+2J}{I+J}\right)\left[1-\sqrt{\frac{1+\beta^2 qd}{1+qd}}\right] \tag{21}$$

where

$$q=\frac{k}{T}\frac{J(I+J)}{I^2}>0, \quad \beta=\frac{I}{I+2J}\leq 1. \tag{22}$$

Clearly, if $d>0$, then $R<1$ and the trajectory is closer to the limit cycle than it was at 0^+. If $d<0$, i.e., if the trajectory lies in $\mathcal{S}(T, \beta)$, then $R>1$ and $\dot{x}(t_1^+)$ is closer to the limit cycle than $\dot{x}(0^+)$. The same argument holds for the other half of the trajectory. Thus, as $t_n\to\infty$, $d\to 0$ and $R\to 1$ and, therefore, the trajectory approaches the limit cycle asymptotically. If $d=0$, then $R=1$, i.e., the orbit is on the limit cycle. Moreover, this is true for all initial conditions and, therefore, the region of attraction is the entire phase plane except the origin.

The stability characteristics of the limit cycle are shown in Figs. 3 and 4 for the case $T=0.1$, $k=1$, $I=1$, $a=0.9$.

The next lemma makes the connection between the impact damper and the auxiliary system.

Lemma 3. *All solutions of the impact damper (1) which start outside the limit cycle* $\mathcal{L}(T, \beta)$ *are ultimately bounded in the set* $\mathcal{S}(T, \beta)$ *where* $T=\sup_t |p(t)|+\epsilon$, $\epsilon>0$.

Proof. Since the excitation torque $p(t)$ in (1) is bounded, let $T=\sup_t |p(t)|+\epsilon$, $\epsilon>0$. Suppose that $x(0^+)=0$ with $\dot{x}(0^+)=v(0^+)>0$ and outside the limit cycle. Define

$$V(t)=I\dot{x}^2(t)+kx^2(t)-2Tx(t)>0. \tag{23}$$

Differentiating,

$$\dot{V}(t)=2I\dot{x}\ddot{x}+2kx\dot{x}-2T\dot{x}. \tag{24}$$

Using (1), the derivative of $V(t)$ along the trajectories of the impact damper is

$$\dot{V}(T)=2p(t)\dot{x}-2kx\dot{x}+2kx\dot{x}-2T\dot{x}$$

$$=-2(T-p(t))\dot{x}.$$

Therefore,

$$\dot{V}(t)\leq -2\epsilon\dot{x}\leq 0. \tag{25}$$

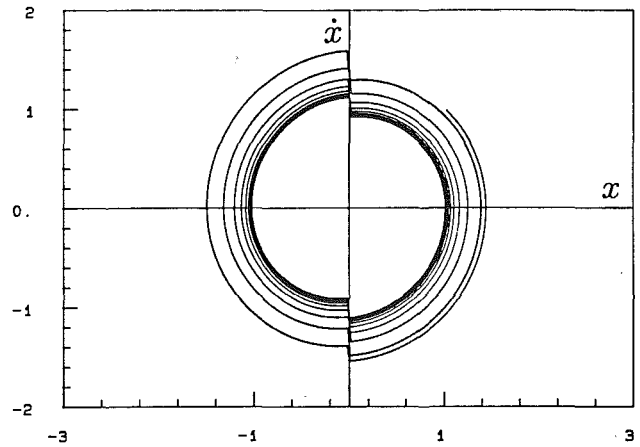


Fig. 3 Convergence to the limit cycle from the outside

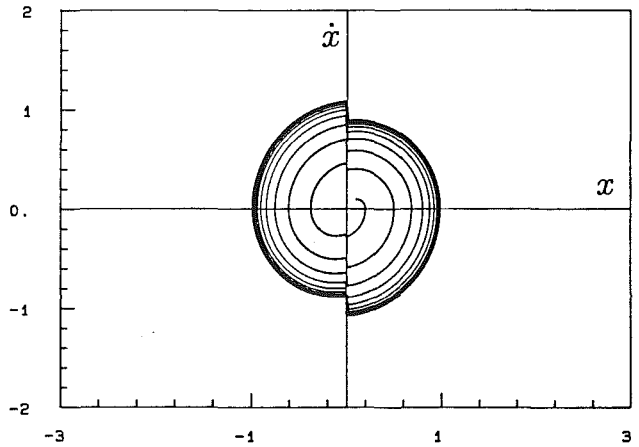


Fig. 4 Convergence to the limit cycle from the inside

Downloaded 03 May 2010 to 171.66.16.31. Redistribution subject to ASME license or copyright; see http://www.asme.org/terms/Terms_Use.cfm

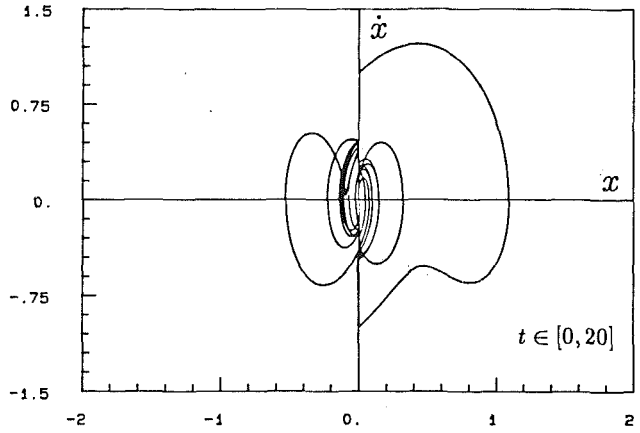


Fig. 5 Ultimate boundedness of solutions; $\omega = 3$, $\omega_0 = 1$, $a = 0.7$

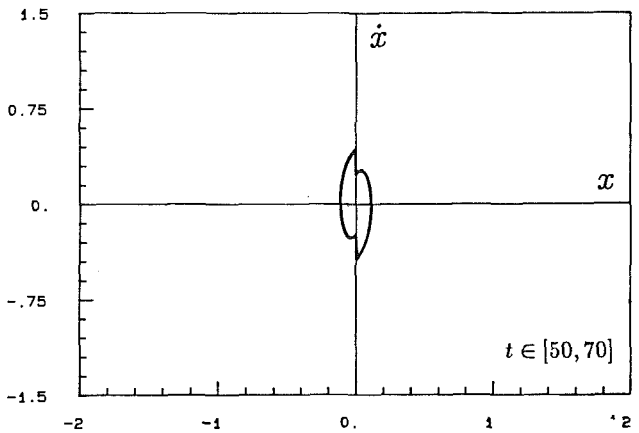


Fig. 6 Ultimate boundedness; $\omega = 3$, $\omega_0 = 1$, $a = 0.7$, $50 \le t \le 70$

Consider the trajectory of the auxiliary system starting with the same initial conditions. Then, along that trajectory, the derivative of the same Lyapunov function is

$$\dot{V}(t) = -\frac{1}{2}(2T - 2T)\dot{x} = 0. \tag{26}$$

Hence, the trajectory of (1) lies closer to the origin than the trajectory of the autonomous system.

Similar arguments apply to each of the other four quadrants. Therefore, the trajectories of the damper must approach the interior of the limit cycle, since by Lemma 2, the autonomous system approaches $\mathcal{L}(T, \beta)$. Moreover, once inside $\mathcal{S}(T, \beta)$ they can never escape.

The ultimate boundedness of solutions of the impact damper is an immediate consequence of the three lemmas. Thus, we have the:

Theorem 3.1 *All solutions of (1) are ultimately bounded in the set* $\mathcal{S}(T, \beta)$, *the interior of the limit cycle* $\mathcal{L}(T, \beta)$.

Proof: Lemma 1 establishes the existence of the limit cycle, lemma 2 proves that the limit cycle is stable, and lemma 3 proves that all solutions of (1) must enter the region bounded by the set $\mathcal{L}(T, \beta)$. Once in $\mathcal{S}(T, \beta)$, the solutions can never escape.

The proof of the theorem also provides weak bounds for the maximum velocity and displacement of the impact damper through the expressions for C_x and C_v. Note that even though the solutions are shown to be bounded, the theorem does *not* guarantee that the response is *always* smaller than that which would be obtained had the damper not been used.

The implications of the theorem are depicted in Figs. 5 and 6 where it is seen that solutions starting far from the origin end up in $\mathcal{S}(T, \beta)$ and remain in that region. In this case $p(t) = \cos(\omega t)$.

4 Summary and Conclusions

The general behavior of the semi-active impact damper is described. Specifically, it was shown that the response of the system to bounded input is bounded. In general, this cannot be proven for passive impact dampers.

Since the response is bounded, the mechanism described is effective for dissipating energy, even though the chosen impact point, $x = 0$, was selected for simplicity and no optimization of any kind was intended. Clearly, because the system undergoes a variety of motions, an impact rule chosen on the basis of simple harmonic motions would not be expected to be optimal. However, for the same reason an *a priori* choice, even optimal in some sense, will only be effective in *some* types of motion and not all.

Acknowledgment

The problem was suggested by Prof. S. F. Masri of USC.

References

Andronov, A. A., Vitt, A. A., and Khaikin, S. E., 1966, *Theory of Oscillators*, Addison-Wesley, New York.

Karyeaclis, M. P., 1988, "Dynamics of a Semi-active Impact Damper: Regular and Chaotic Motions," Ph.D. Thesis, California Institute of Technology, Pasadena, California.

Masri, S. F., and Caughey, T. K., 1966, "On the Stability of the Impact Damper," ASME JOURNAL OF APPLIED MECHANICS, Vol. 33, pp. 586–592.

Masri, S. F., 1965, "Analytical and Experimental Studies of Impact Dampers," Ph.D. Thesis, California Institute of Technology, Pasadena, California.

Downloaded 03 May 2010 to 171.66.16.31. Redistribution subject to ASME license or copyright; see http://www.asme.org/terms/Terms_Use.cfm

M. P. Karyeaclis
Mem. ASME

T. K. Caughey
Professor of Applied Mechanics.

California Institute of Technology,
Pasadena, Calif. 91125

Stability of a Semi-active Impact Damper: Part II—Periodic Solutions

All solutions of the semi-active impact damper described in Part I were shown to be bounded when the excitation is bounded. In this part, the existence of periodic solutions is investigated. Emphasis is placed on two impacts/cycle periodic solutions. Exact symmetric and nonsymmetric harmonic solutions are derived analytically and the region of asymptotic stability is determined.

1 Introduction

Having established the fact that all solutions of the impact damper are bounded, we proceed to find periodic solutions. Experiments and analytical work by Masri (1965, 1966) and Shaw (1985) and Shaw and Holmes (1983) on similar systems systems suggest the existence of 2-impact-per-cycle periodic solutions when the excitation is periodic.

Simulation of the behavior of system (1) also support this behavior as shown in Fig. 6 (Part I). We distinguish between two types of periodic solutions, namely symmetric and nonsymmetric.

For convenience we put the equations of motion in standard form with $\omega_0 = \sqrt{k/I}$ and rewrite the pertinent equations here in a form more suitable to the present analysis. Let the excitation torque

$$p(t) = P\cos(\omega t + \theta).$$

Then, we have

$$\left.\begin{aligned} &\text{Equations of motion:}\\ &\qquad \ddot{x} + \omega_0^2 x = P\cos(\omega t + \theta);\ \dot{v} = 0;\ x(t) \neq 0\\ &\text{Impact condition:}\\ &\qquad \dot{x}(t_1^+) = v(t_1^+) = a\dot{x}(t_1^-) + bv(t_1^-);\ x(t_1) = 0\\ &\qquad a + b = 1 \end{aligned}\right\} \tag{1}$$

2 Periodic Solutions

2.1 Symmetric Solutions. A typical symmetric solution is shown in Fig. 1 and is referred to as such because the $x-\dot{x}$ projection of the trajectory is symmetric with respect to the origin. Solutions which do not satisfy this property are the so-called nonsymmetric.

The construction of solutions is based on the observation that equation (1) is linear in each of the half-planes $x>0$ and $x<0$. We start the solution at point Q_1 where $x(0)=0$ and determine the phase angle θ and initial velocity $\dot{x}(0^+) = v(0^+)$ such that the orbit is closed. Because of symmetry, only one arc of the orbit need be considered.

Let $\dot{x}(0^+) = \dot{x}_0 = v(0^+)$ and $\theta = \theta_0$ at $t=0$. Then, for $x>0$

$$\ddot{x} + \omega_0^2 x = P\cos(\omega t + \theta_0) \tag{2}$$

and the solution for $\omega \neq \omega_0$ is

$$x(t) = \frac{P}{\omega^2 - \omega_0^2}\cos\theta_0\cos\omega_0 t + \left[\frac{\dot{x}_0}{\omega_0} - \frac{P\left(\frac{\omega}{\omega_0}\right)}{\omega^2 - \omega_0^2}\sin\theta_0\right]\sin\omega_0 t - \frac{P}{\omega^2 - \omega_0^2}\cos(\omega t + \theta_0) \tag{3}$$

$$\dot{x}(t) = -\frac{P\omega_0}{\omega^2 - \omega_0^2}\cos\theta_0\sin\omega_0 t + \omega_0\left[\frac{\dot{x}_0}{\omega_0} - \frac{P\left(\frac{\omega}{\omega_0}\right)}{\omega^2 - \omega_0^2}\sin\theta_0\right]\cos\omega_0 t + \frac{P\omega}{\omega^2 - \omega_0^2}\sin(\omega t + \theta_0). \tag{4}$$

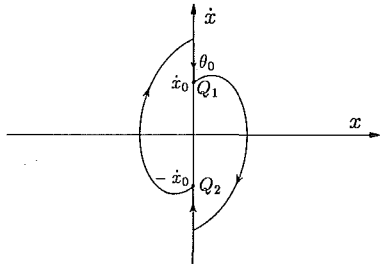


Fig. 1 Symmetric periodic solution

Contributed by the Applied Mechanics Division of THE AMERICAN SOCIETY OF MECHANICAL ENGINEERS for publication in the JOURNAL OF APPLIED MECHANICS.

Discussion on this paper should be addressed to the Editorial Department, ASME, United Engineering Center, 345 East 47th Street, New York, N. Y. 10017, and will be accepted until two months after final publication of the paper itself in the JOURNAL OF APPLIED MECHANICS. Manuscript received by the ASME Applied Mechanics Division, February 15, 1988; final revision, January 26, 1989.

Copyright © 1989 by ASME

Downloaded 03 May 2010 to 171.66.16.31. Redistribution subject to ASME license or copyright; see http://www.asme.org/terms/Terms_Use.cfm

Let t_1 be the time that the first impact occurs, at point Q_2 in Fig. 1. For an harmonic periodic solution, the period of oscillation is $2\pi/\omega$. Due to symmetry, it follows that $t_1 = \pi/\omega$. Thus, at Q_2

$$x\left(\frac{\pi}{\omega}\right) = 0 \tag{5}$$

$$x\left(\frac{\pi^+}{\omega}\right) = v\left(\frac{\pi^+}{\omega}\right) = -\dot{x}_0. \tag{6}$$

Using (6), the impact condition gives

$$-\dot{x}_0 = a\dot{x}\left(\frac{\pi^-}{\omega}\right) + b\dot{x}_0 \Rightarrow$$

$$\Rightarrow -\frac{(1+b)}{a}\dot{x}_0 = \dot{x}\left(\frac{\pi^-}{\omega}\right). \tag{7}$$

The velocity $\dot{x}(\pi^-/\omega)$ is evaluated from (4). Thus, (5) and (7), after rearrangement, are as follows:

$$-\frac{\dot{x}_0}{\omega_0}\sin\left(\frac{\omega_0}{\omega}\pi\right) = \frac{P}{\omega^2-\omega_0^2}\left[1+\cos\left(\frac{\omega_0}{\omega}\pi\right)\right]\cos\theta_0 - \frac{P\left(\frac{\omega}{\omega_0}\right)}{\omega^2-\omega_0^2}\sin\left(\frac{\omega_0}{\omega}\pi\right)\sin\theta_0 \tag{8}$$

$$\frac{\dot{x}_0}{\omega_0}\left[\frac{1+b}{a}+\cos\left(\frac{\omega_0}{\omega}\pi\right)\right] = \frac{P}{\omega^2-\omega_0^2}\sin\left(\frac{\omega_0}{\omega}\pi\right)\cos\theta_0 + \frac{P\left(\frac{\omega}{\omega_0}\right)}{\omega^2-\omega_0^2}\left[1+\cos\left(\frac{\omega_0}{\omega}\pi\right)\right]\sin\theta_0. \tag{9}$$

Equations (8) and (9) are linear in $\sin\theta_0$ and $\cos\theta_0$ and can be solved easily. Substitution in $\sin^2\theta_0 + \cos^2\theta_0 = 1$ then provides an expression which involves only the velocity $\dot{x}_0$ and which can be solved. Once $\dot{x}_0$ is known, expressions for $\cos\theta_0$ and $\sin\theta_0$ give the solution for the phase angle. The case of resonance ($\omega = \omega_0$) must be treated separately because the solution for $x > 0$ in this case is given by:

$$x(t) = \left[\frac{\dot{x}_0}{\omega_0} - \frac{P}{2\omega_0^2}\sin\theta_0\right]\sin\omega_0 t + \frac{1}{2}P\frac{t}{\omega_0}\sin(\omega_0 t + \theta_0) \tag{10}$$

$$\dot{x}(t) = \omega_0\left[\frac{\dot{x}_0}{\omega_0} - \frac{P}{2\omega_0^2}\sin\theta_0\right]\cos\omega_0 t + \frac{1}{2}\frac{P}{\omega_0}\sin(\omega_0 t + \theta_0) + \frac{1}{2}Pt\cos(\omega_0 t + \theta_0). \tag{11}$$

The procedure, however, for solving (5) and (7), in this case, is the same.

To ensure that the system (8)–(9) is nonsingular, special consideration must be given to the cases where the frequency ratio ω_0/ω is such that the coefficients $1+\cos(\omega_0\pi/\omega)$ and $\sin(\omega_0\pi/\omega)$ vanish. This gives rise to two special cases, in addition to resonance: (*i*) $\sin(\omega_0\pi/\omega) = 0$, $\cos(\omega_0\pi/\omega) = 1$, and (*ii*) $\sin(\omega_0\pi/\omega) = 0$, $\cos(\omega_0\pi/\omega) = -1$. In the first case the ratio ω_0/ω is an even integer, while in the second case ω_0/ω is odd. For these two cases the analysis simplifies considerably. It turns out, as might be expected, that the stability characteristics of these special cases differ considerably from those of the generic case.

The solutions of equations (8)–(9) are summarized next for each case separately.

CASE I (Generic):

$$\cos\left(\frac{\omega_0}{\omega}\pi\right) \neq -1, \quad \sin\left(\frac{\omega_0}{\omega}\pi\right) \neq 0.$$

$$\tan\theta_0 = \frac{1+\cos\left(\frac{\omega_0}{\omega}\pi\right)}{b\left(\frac{\omega}{\omega_0}\right)\sin\left(\frac{\omega_0}{\omega}\pi\right)} \tag{12}$$

$$\dot{x}_0 = \frac{Pa\omega}{|\omega^2-\omega_0^2|}\frac{1}{\sqrt{1+\left[\frac{\left(\frac{\omega}{\omega_0}\right)b\sin\left(\frac{\omega_0}{\omega}\pi\right)}{1+\cos\left(\frac{\omega_0}{\omega}\pi\right)}\right]^2}} = \frac{Pa\omega}{|\omega^2-\omega_0^2|}\sin\theta_0 \tag{13}$$

CASE II:

$$\sin\left(\frac{\omega_0}{\omega}\pi\right) = 0, \quad \cos\left(\frac{\omega_0}{\omega}\pi\right) = 1 \Leftrightarrow \frac{\omega_0}{\omega} = 2l, \; l = 1, 2, \ldots$$

$$\theta_0 = -\frac{\pi}{2} \tag{14}$$

$$\dot{x}_0 = \frac{Pa\omega}{\omega_0^2-\omega^2} \tag{15}$$

In this case $x(t)$ simplifies considerably, and we have:

$$x(t) = (1-a)\frac{P\left(\frac{\omega}{\omega_0}\right)}{\omega^2-\omega_0^2}\sin\omega_0 t + \frac{P}{\omega^2-\omega_0^2}\sin\omega t, \; x \geq 0. \tag{16}$$

CASE III:

$$\sin\left(\frac{\omega_0}{\omega}\pi\right) = 0, \quad \cos\left(\frac{\omega_0}{\omega}\pi\right) = -1 \Leftrightarrow \frac{\omega_0}{\omega} = 2l+1, \; l = 1, 2, \ldots$$

$$\theta_0 = -\frac{\pi}{2} \tag{17}$$

$$\dot{x}_0 = 0 \tag{18}$$

and

$$x(t) = \frac{P\left(\frac{\omega}{\omega_0}\right)}{\omega^2-\omega_0^2}\sin\omega_0 t + \frac{P}{\omega^2-\omega_0^2}\sin\omega t, \; x \geq 0. \tag{19}$$

CASE IV (Resonance):

$$\omega = \omega_0.$$

$$\theta_0 = 0 \tag{20}$$

$$\dot{x}_0 = \left(\frac{a}{b}\right)\frac{P\pi}{4\omega_0} \tag{21}$$

The solution is

$$x(t) = \frac{P}{2\omega_0}\left[\left(\frac{a}{b}\right)\frac{\pi}{2\omega_0} + t\right]\sin\omega_0 t, \; x \geq 0. \tag{22}$$

Typical solutions are shown in Figs. 2, 3, and 4. Observe that Case III is singular in the sense that it involves no impacts at all. The secondary rotor remains at rest while the velocity of

Downloaded 03 May 2010 to 171.66.16.31. Redistribution subject to ASME license or copyright; see http://www.asme.org/terms/Terms_Use.cfm

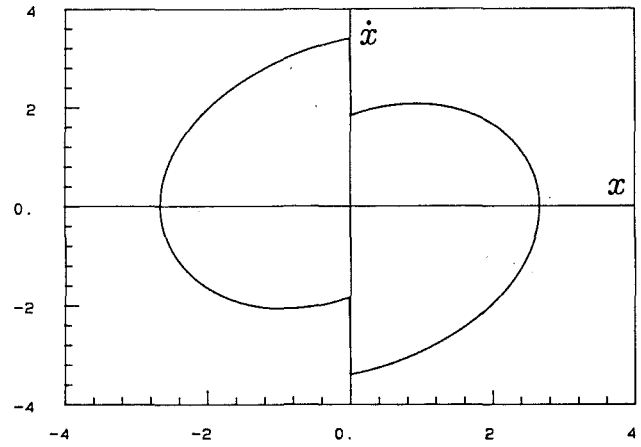


Fig. 2 Periodic solution, resonance, $a = 0.7$, $P = 1$, $\dot{x}_0 = 1.8326$, $\theta_0 = 0$

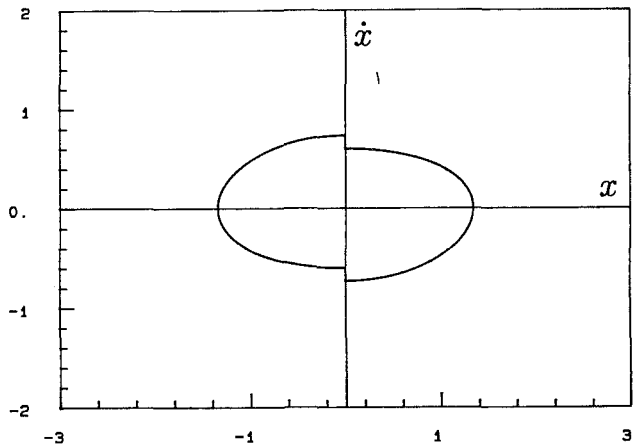


Fig. 3 Periodic solution, $\omega_0/\omega = 2$, $a = 0.9$, $P = 1$, $\dot{x}_0 = 0.6$, $\theta_0 = -\pi/2$

the primary system is zero at the equilibrium position. The impact damper in this case degenerates to a simple harmonic oscillator subjected to periodic excitation. The response of the system is also shown as a function of time in Fig. 5.

As the trajectory crosses the x-axis, $\dot{x} = 0$, and therefore displacement has a stationary value. Typical solutions show only a maximum, while the singular frequency ratios $\omega_0/\omega = 5$, 6, 7, . . . exhibit multiple loops and therefore have multiple crossings of the x-axis. The maximum displacement can be found by setting the velocity to zero and determining the time t of the crossing. However, analytical solution of this transcendental equation is not possible. Rather than solving this equation numerically, the equations of motion are integrated starting at the proper initial conditons and maximum displacement is recorded. Thus, we can plot the maximum displacement as a function of the frequency ratio. The result for $a = 0.9$, $P = 1$ is shown in Fig. 6.

2.2 Nonsymmetric Periodic Solutions. The existence of nonsymmetric periodic solutions is not immediately obvious. In simulation of the system behavior, solutions originating from different initial conditions converge to the symmetric periodic loops. Moreover, the analysis of possible solutions without any symmetry is considerably more complicated than that of the symmetric case.

Consider a possible nonsymmetric periodic solution as shown in Fig. 7. As before, let $t = 0$ be the time at Q_1 and t_1 be the time of impact at Q_3. While in the symmetric case $t_1 = \pi/\omega$, in this case, due to lack of symmetry, there is no reason to expect the same timing for the second impact. As a

Fig. 4 Periodic solution, $\omega_0/\omega = 5$, $a = 0.7$, $P = 1$, $\dot{x}_0 = 0$, $\theta_0 = -\pi/2$

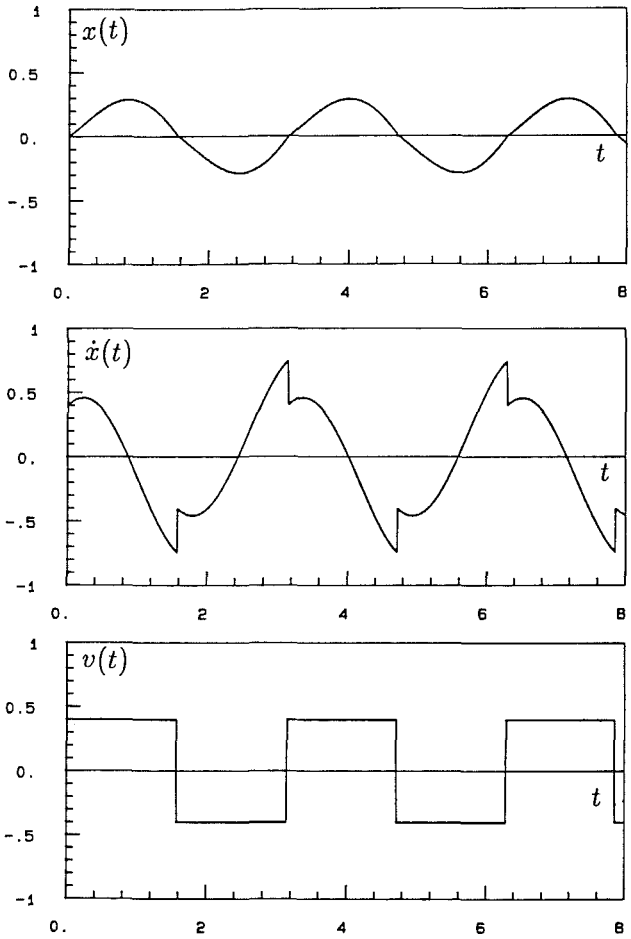


Fig. 5 Periodic solution for $\omega_0/\omega = 0.5$, $a = 0.7$, $P = 1$

result, determination of the initial conditions $\dot{x}_0$ and θ_0 for a closed loop involves the determination of the time of impact as well. Moreover, if $\dot{x}_1 = \dot{x}(t_1^+) = v(t_1^+)$, then $\dot{x}_1 \neq \dot{x}_0$. Thus, the additional complication arises due to the fact that two distinct impacts must be considered in the nonsymmetric case.

For the arc $Q_1Q_2Q_3$ we have the following;
at Q_1:

$$x(0) = 0,\ \dot{x}(0^+) = v(0^+) = \dot{x}_0,\ \theta = \theta_0$$

at Q_3:

$$x(t_1) = 0 \tag{23}$$

Downloaded 03 May 2010 to 171.66.16.31. Redistribution subject to ASME license or copyright; see http://www.asme.org/terms/Terms_Use.cfm

$$\dot{x}(t_1^+) = v(t_1^+) = \dot{x}_1 \tag{24}$$

$$\theta_1 = \theta_0 + \omega t_1. \tag{25}$$

The impact condition at Q_3 gives:

$$\dot{x}_1 = a\dot{x}(t_1^-) + b\dot{x}_0. \tag{26}$$

For the second arc $Q_3Q_4Q_1$ of the trajectory we have; at Q_3:

$$x(0) = 0,\ \dot{x}(0^+) = v(0^+) = \dot{x}_1,\ \theta = \theta_1$$

at Q_1:

$$t_2 = \frac{2\pi}{\omega} - t_1 \tag{27}$$

$$x(t_2) = 0 \tag{28}$$

$$\dot{x}(t_2^+) = v(t_2^+) = \dot{x}_0 \tag{29}$$

and the impact condition,

$$\dot{x}_0 = a\dot{x}(t_2^-) + b\dot{x}_1. \tag{30}$$

In principle, equations (23), (26), (28), and (30) can be solved for the four unknowns $\dot{x}_0, \theta_0, \dot{x}_1$, and t_1. In practice, the most substantial obstacle comes from the solution of the transcendental equation (23).

At first, we investigate the possibility of $t_1 = \pi/\omega \Rightarrow \theta_1 = \theta_0{}^+ + \pi$. Then, for the arc $Q_1Q_2Q_3$ we have that

$$x\left(\frac{\pi}{\omega}\right) = 0.$$

Since the solution is known, we obtain from (3) the following expression for zero displacement at Q_3 ($\omega \neq \omega_0$):

$$\frac{P}{\omega_2 - \omega_0^2}\cos\theta_0\left[1 + \cos\left(\frac{\omega_0}{\omega}\pi\right)\right] + \left[\frac{\dot{x}_0}{\omega_0} - \frac{P\left(\frac{\omega}{\omega_0}\right)}{\omega^2 - \omega_0^2}\sin\theta_0\right]\sin\left(\frac{\omega_0}{\omega}\pi\right) = 0. \tag{31}$$

A similar condition at Q_1 can be obtained for the second arc from (31) by substitution of $\theta_1 = \theta_0 + \pi$ and $\dot{x}_1$ in place of θ_0 and $\dot{x}_0$, respectively. We get

$$-\frac{P}{\omega^2 - \omega_0^2}\cos\theta_0\left[1 + \cos\left(\frac{\omega_0}{\omega}\pi\right)\right] + \left[\frac{\dot{x}_1}{\omega_0} + \frac{P\left(\frac{\omega}{\omega_0}\right)}{\omega^2 - \omega_0^2}\sin\theta_0\right]\sin\left(\frac{\omega_0}{\omega}\pi\right) = 0. \tag{32}$$

Adding (31) and (32)

$$\left[\frac{\dot{x}_0}{\omega_0} - \frac{P\left(\frac{\omega}{\omega_0}\right)}{\omega^2 - \omega_0^2}\sin\theta_0 + \frac{\dot{x}_1}{\omega_0} + \frac{P\left(\frac{\omega}{\omega_0}\right)}{\omega^2 - \omega_0^2}\sin\theta_0\right]\sin\left(\frac{\omega_0}{\omega}\pi\right) = 0$$

$$\Rightarrow \frac{1}{\omega_0}[\dot{x}_1 + \dot{x}_0]\sin\left(\frac{\omega_0}{\omega}\pi\right) = 0. \tag{33}$$

Thus, either $\dot{x}_1 = -\dot{x}_0$ which gives the symmetric solution, or $\sin(\omega_0\pi/\omega) = 0 \Rightarrow \omega_0/\omega = l,\ l = 2, 3, \ldots$.

The case of resonance will be treated below and it will be shown that only the symmetric solution is possible. Thus, the only existing possibilities are those for which the frequency ratio ω_0/ω is an integer.

Consider first $\omega_0/\omega = 2m,\ m = 1, 2, \ldots$. Then, expressions for position and velocity at first impact are as follows:

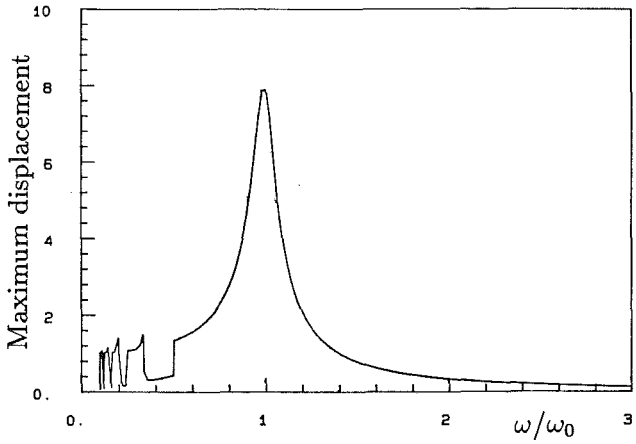


Fig. 6 Frequency response, $a = 0.9$, $P = 1$

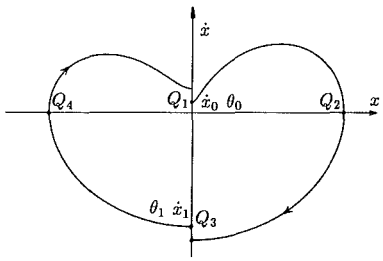


Fig. 7 Nonsymmetric solution

$$x(t_1) = x\left(\frac{\pi}{\omega}\right) = \frac{2P}{\omega^2 - \omega_0^2}\cos\theta_0 = 0 \tag{34}$$

$$\dot{x}(t_1^-) = \dot{x}_0 - \frac{2P\omega}{\omega^2 - \omega_0^2}\sin\theta_0. \tag{35}$$

From (34) we conclude that $\theta_0 = \pm\pi/2$.

Substituting for the velocity in (26) we find

$$\dot{x}_1 = a\left[\dot{x}_0 - \frac{2P\omega}{\omega^2 - \omega_0^2}\sin\theta_0\right] + b\dot{x}_0$$

$$\Rightarrow \dot{x}_1 = \dot{x}_0 - \frac{2Pa\omega}{\omega^2 - \omega_0^2}\sin\theta_0. \tag{36}$$

For the second arc of the trajectory, we again make the substitutions $\theta_0 \to \theta_1 = \theta_0 + \pi$; $\dot{x}_0 \to \dot{x}_1$. Condition (28) is satisfied identically with this choice for the phase angle while

$$\dot{x}(t_2^-) = \dot{x}_1 + \frac{2P\omega}{\omega^2 - \omega_0^2}\sin\theta_0.$$

Substituting in (29) we get

$$\dot{x}_0 = a\left[\dot{x}_1 + \frac{2P\omega}{\omega^2 - \omega_0^2}\sin\theta_0\right] + b\dot{x}_1$$

$$= (a+b)\dot{x}_1 + \frac{2Pa\omega}{\omega^2 - \omega_0^2}\sin\theta_0$$

$$= \dot{x}_0 - \frac{2Pa\omega}{\omega^2 - \omega_0^2}\sin\theta_0 + \frac{2Pa\omega}{\omega^2 - \omega_0^2}\sin\theta_0$$

$$= \dot{x}_0.$$

Thus, the closure conditions are satisfied identically and θ_0 as well as $\dot{x}_0$ have not been determined. Note, however, that $\dot{x}_1$

Downloaded 03 May 2010 to 171.66.16.31. Redistribution subject to ASME license or copyright; see http://www.asme.org/terms/Terms_Use.cfm

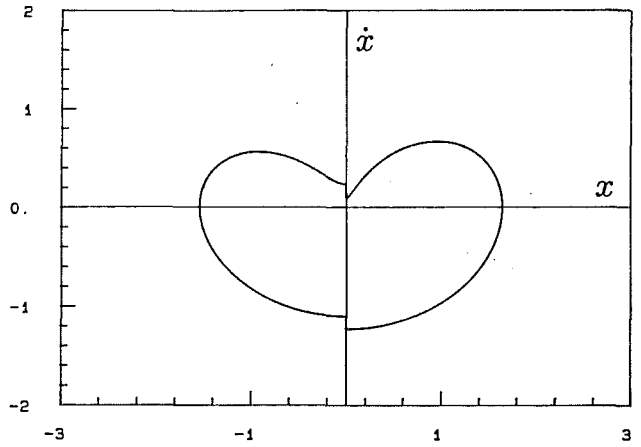


Fig. 8 Nonsymmetric solution, $\omega_0/\omega = 2$, $a = 0.9$, $\dot{x}_0 = 0.1$, $P = 1$

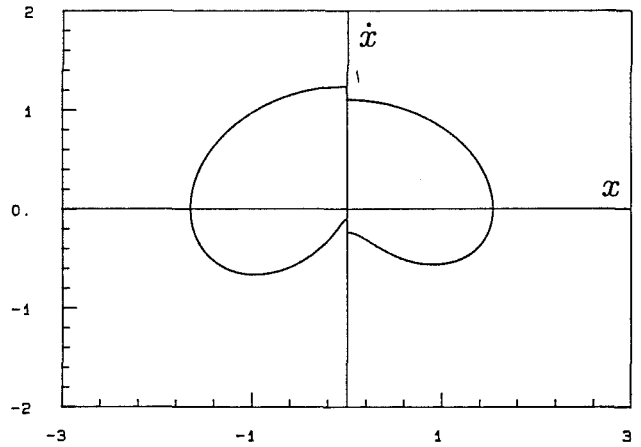


Fig. 9 Nonsymmetric solution, $\omega_0/\omega = 2$, $a = 0.9$, $\dot{x}_0 = 1.1$, $P = 1$

must be negative. Moreover, since $\dot{x}_0 > 0$ and $\omega^2 - \omega_0^2 < 0$, it follows that $\sin\theta_0 < 0$

$$\Rightarrow \theta_0 = -\frac{\pi}{2}. \tag{37}$$

Substituting into (36), we get

$$\dot{x}_1 = \dot{x}_0 - \frac{2Pa\omega}{\omega_0^2 - \omega^2} \leq 0.$$

Hence, the only restriction on the initial velocity of the primary mass is

$$0 \leq \dot{x}_0 \leq \frac{2Pa\omega}{\omega_0^2 - \omega^2}. \tag{38}$$

This inequality indicates that there is an infinity of solutions of this type which lie arbitarily close to each other. Note that the symmetric solution $\dot{x}_0 = Pa\omega/(\omega_0^2 - \omega^2)$ is a special case of equation (38). Specifically, any solution starting in the interval specified by (38) with $\theta_0 = -\pi/2$ is a periodic solution.

Three of the solutions specified are shown in Figs. 3, 8, and 9 for the frequency ratio $\omega_0/\omega = 2$. The one shown in Fig. 3 is the symmetric solution. Note that for each nonsymmetric solution with $\dot{x}_0 \in [0,\ Pa\omega/(\omega_0^2 - \omega^2))$, there is a "conjugate" one which is its symmetric image about the origin and for which $\dot{x}_0 \in (Pa\omega/(\omega_0^2 - \omega^2),\ 2Pa\omega/(\omega_0^2 - \omega^2))$. A pair of these "conjugate" solutions is shown in the other two figures.

In the case $\omega_0/\omega = 2m + 1$, $m = 1, 2, \ldots$, the position is zero at $t_1 = \pi/\omega$ and this is independent of the phase angle θ_0. Moreover, the velocity prior to impact is $\dot{x}(t_1^-) = -\dot{x}_0$. After impact

$$\begin{aligned}\dot{x}_1 &= a\dot{x}(t_1^-) + b\dot{x}_0 \\ &= -a\dot{x}_0 + b\dot{x}_0 \\ &= (b-a)\dot{x}_0. \end{aligned} \tag{39}$$

Repeating for the second arc we find

$$\dot{x}_0 = (b-a)\dot{x}_1. \tag{40}$$

The only possible solution of (39) and (40) is $\dot{x}_0 = \dot{x}_1 = 0$ which is the symmetric solution.

In the case of resonance, clearly $\theta_0 = 0$ and the velocity prior to impact is

$$\dot{x}(t_1^-) = -\left(\dot{x}_0 + \frac{P\pi}{2\omega_0}\right).$$

After impact,

$$\begin{aligned}\dot{x}_1 &= a\dot{x}(t_1^-) + b\dot{x}_0 \\ &= -a\left(\dot{x}_0 + \frac{P\pi}{2\omega_0}\right) + b\dot{x}_0 \\ &= (b-a)\dot{x}_0 - \frac{Pa\pi}{2\omega_0}. \end{aligned} \tag{41}$$

For the second arc, $\theta_1 = \theta_0 + \pi = \pi$ and $x(t_2) = x(\pi) = 0$. The velocity is $\dot{x}(t_2^-) = -\dot{x}_1 + P\pi/2\omega_0$. After impact

$$\begin{aligned}\dot{x}_0 &= a\left(-\dot{x}_1 + \frac{P\pi}{2\omega_0}\right) + b\dot{x}_1 \\ \Rightarrow \dot{x}_0 &= (b-a)\dot{x}_1 + \frac{Pa\pi}{2\omega_0} \\ &= (b-a)\left[(b-a)\dot{x}_0 - \frac{Pa\pi}{2\omega_0}\right] + \frac{Pa\pi}{2\omega_0} \\ &= (b-a)^2\dot{x}_0 + \frac{Pa\pi}{2\omega_0}(1-b+a) \\ &= (b-a)^2\dot{x}_0 + \frac{Pa^2\pi}{\omega_0}. \end{aligned} \tag{42}$$

Solving for $\dot{x}_0$ we find $\dot{x}_0 = (a/b)\ P\pi/4\omega_0$ which is the symmetric solution. In summary, the only nonsymmetric periodic solutions in which the impacts occur at half period are those with ω_0/ω even.

Attempts to solve the system of equations (23), (26), (28), and (30) numerically resulted in two problems. Iterative methods like Newton's method and the iteration method either converged to the symmetric solution or did not converge at all. The bisection method was also applied in order to circumvent this difficulty in the following way: we notice first that an initial guess in $\dot{x}_0$ and θ_0 determines t_1 and $\dot{x}_1$ uniquely through equation $x(t_1) = 0$ and the impact condition at Q_3. As a result, the problem is reduced to finding two unknowns θ_0 and $\dot{x}_0$ such that the trajectory is closed at Q_1. This implies that

$$f(\dot{x}_0,\ \theta_0) = t_1 + t_2 - \frac{2\pi}{\omega} = 0 \tag{43}$$

$$g(\dot{x}_0,\ \theta_0) = \dot{x}_0 - \dot{x}(t_2^+) = 0. \tag{44}$$

Thus, the bisection method was applied to find the zeroes of $f(\dot{x}_0,\ \theta_0)$ and $g(\dot{x}_0,\ \theta_0)$.

To determine the range of values for $\dot{x}_0$ and θ_0 in which to search for possible solutions, the two functions were plotted. It was found that they both have discontinuities from negative to positive values, in effect never crossing the zero axis. Clearly, they both vanish at the point representing the symmetric

Downloaded 03 May 2010 to 171.66.16.31. Redistribution subject to ASME license or copyright; see http://www.asme.org/terms/Terms_Use.cfm

solution, but their unusual behavior makes the search for nonsymmetric solutions impossible.

2.3 Subharmonic Periodic Solutions. Multiple impacts-per-cycle subharmonic solutions would be expected to exist. However, analytical investigation of these solutions is not possible due to the difficulty in solving the transcendental equations $x(t_i)=0$ for the impact times t_i. The only other alternative available, namely numerical solution of these equations, is hindered by problems similar to those encountered in the analysis of the nonsymmetric harmonic solutions. As a result, we investigate only a small subset of these solutions.

Specifically, we look for symmetric, two impacts/cycle periodic solutions whose frequency is equal to the natural frequency of the primary system. The response of the system is given by equations (3) and (4) as before. The time of impact then is $t=t_1=\pi/\omega_0$ and, therefore, at Q_2 (Fig. 1) we have:

$$x\left(\frac{\pi}{\omega_0}\right)=0 \tag{45}$$

$$\dot{x}\left(\frac{\pi^+}{\omega_0}\right)=v\left(\frac{\pi^+}{\omega_0}\right)=-\dot{x}_0$$

where $\dot{x}_0$ is as before. The impact condition gives

$$-\left(\frac{1+b}{a}\right)\dot{x}_0=\dot{x}\left(\frac{\pi^-}{\omega_0}\right). \tag{46}$$

Following the same procedure as in the case of harmonic solutions, (45) and (46) reduce to

$$0=\left[1+\cos\left(\frac{\omega}{\omega_0}\pi\right)\right]\cos\theta_0-\sin\left(\frac{\omega}{\omega_0}\pi\right)\sin\theta_0 \tag{47}$$

$$-2\left(\frac{b}{a}\right)\frac{\dot{x}_0}{\omega_0}=\frac{P\left(\frac{\omega}{\omega_0}\right)}{\omega^2-\omega_0^2}\sin\left(\frac{\omega}{\omega_0}\pi\right)\cos\theta_0+$$

$$+\frac{P\left(\frac{\omega}{\omega_0}\right)}{\omega^2-\omega_0^2}\left[1+\cos\left(\frac{\omega}{\omega_0}\pi\right)\right]\sin\theta_0. \tag{48}$$

In this case additional conditions must be imposed on the forcing term to ensure that the response is symmetric, namely that

$$\cos\left(\frac{\omega}{\omega_0}\pi+\theta_0\right)=-\cos\theta_0 \tag{49}$$

and

$$\sin\left(\frac{\omega}{\omega_0}\pi+\theta_0\right)=-\sin\theta_0. \tag{50}$$

The last two conditions imply that $\omega/\omega_0=2l+1$, $l=1, 2, \ldots$. Thus, (47) is satisfied identically and (48) gives

$$\dot{x}_0=0. \tag{51}$$

This case is, therefore, similar to the harmonic response for $\omega_0/\omega=2l+1$, $l=1, 2, \ldots$. Using similar arguments, we deduce that for this subharmonic solution

$$\theta_0=-\frac{\pi}{2}, \tag{52}$$

also.

Thus, there are subharmonic solutions which involve no impacts at all and are given by (51), (52) and

$$\frac{\omega}{\omega_0}=2l+1,\ l=1, 2, \ldots. \tag{53}$$

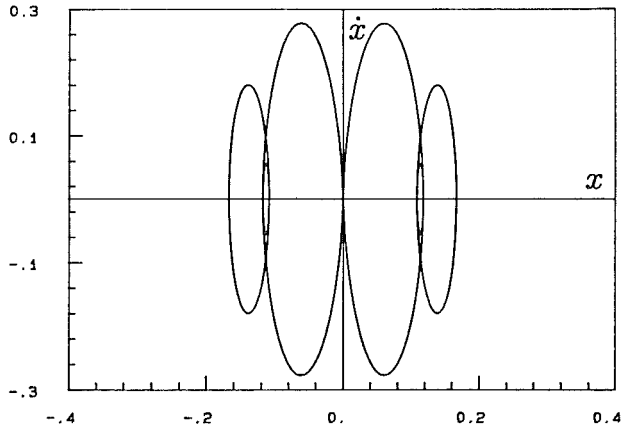


Fig. 10 Subharmonic periodic solution, $\omega/\omega_0=7$, $P=1$

The frequency of the response is the natural frequency of the primary system. The solution for $\omega/\omega_0=7$ is shown in Fig. 10.

3 Stability

We now turn our attention to the stability of the periodic solutions. Specifically, we are interested in the asymptotic behavior of perturbations to the steady-state solution of the impact damper. Because of the discontinuities in the solution of the system, the usual method of investigation does not apply, and we must use an alternative approach developed by Masri and Caughey (1966).

3.1 Method of Analysis. Consider the dynamical system[1]

$$\dot{\mathbf{x}}=\mathbf{f}(\mathbf{x},t),\quad \mathbf{x}\in\mathbb{R}^n,\quad \mathbf{f}\in\mathbb{R}^n \tag{54}$$

with the usual assumptions on $\mathbf{f}(\mathbf{x},t)$. Let $\mathbf{x}=\mathbf{y}(t)$ be a solution of (54) and suppose that this solution is perturbed so that

$$\mathbf{x}(t)=\mathbf{y}(t)+\xi(t).$$

Then, $\mathbf{y}(t)$ is asymptotically stable if it is stable and

$$\lim_{t\to\infty}\|\xi(t)\|=0.$$

To determine the behavior of $\xi(t)$ we substitute in the equations of motion for $\mathbf{x}(t)$ to get

$$\dot{\mathbf{y}}(t)+\dot{\xi}(t)=\mathbf{f}(\mathbf{y}(t)+\xi(t),t)$$

and expand $\mathbf{f}$ in a Taylor series about $\mathbf{y}(t)$ to get the variational equations for the system as

$$\dot{\xi}=F(t)\xi+\mathbf{R}(\xi,t) \tag{55}$$

where $F(t)$ is an $n\times n$ matrix with

$$F_{ij}=\frac{\partial f_i(\mathbf{y}(t),t)}{\partial y_j}.$$

Thus, $\mathbf{y}(t)$ is asymptotically stable if the origin is an asymptotically stable equilibrium point of (55). In the usual method, analysis of the linearized system

$$\dot{\xi}=F(t)\xi(t) \tag{56}$$

is often adequate for determining the stability characteristics of the solution of the complete system (54). Note that if $\mathbf{y}(t)$ is periodic in t, so is $F(t)$ and the Floquet theory applies. However, in the present case as well as in the problem analyzed by Masri and Caughey, the solution is only piecewise continuous with discontinuities at every impact and,

[1] Boldface letters denote vectors. Matrices are denoted with capital letters.

Downloaded 03 May 2010 to 171.66.16.31. Redistribution subject to ASME license or copyright; see http://www.asme.org/terms/Terms_Use.cfm

therefore, the coefficient matrix $F(t)$ cannot be computed in the usual way. We bypass this difficulty by converting the variational equation into a difference equation as follows. The steady-state solution $\mathbf{y}(t)$ is perturbed immediately after impact. These initial perturbations will evolve and their new values after the next impact can be determined. The process can be repeated with the new values for the next half cycle. If the initial perturbations decrease to zero after multiple impacts, the steady-state solution is asymptotically stable. Otherwise it is unstable. Note that between impacts, $\mathbf{f}(\mathbf{x},t)$ is continuous and satisfies the Lipschitz condition. Therefore, the solution of (54) exists and is unique between impacts.

Now, let the initial perturbation vector be ξ_0 so that the initial conditions immediately after impact are

$$\mathbf{x}(\Delta t_0) = \mathbf{x}_0 + \xi_0$$

where $\mathbf{x}_0$ is the vector of initial conditions for steady-state response. Suppose that the steady-state solution is periodic with period $2\pi/\omega$ and involves 2 impacts/cycle. Then the next impact will occur at $\omega t = \pi + \Delta t_0'$ and $\Delta t_0'$ can be determined from

$$\Delta t_0' = h(\mathbf{y}, \xi_0, \Delta t_0)$$

for some function h.

Let the perturbation vector after the next impact be ξ_1. Then

$$\xi_1 = Q\xi_0 + \mathbf{R}(\xi_0) \tag{57}$$

where Q is a constant matrix and $\mathbf{R}$ contains all the terms in ξ_0 of second order or higher. After $m+1$ impacts we get

$$\begin{aligned} \xi_{m+1} &= Q\xi_m + \mathbf{R}(\xi_m) \\ &= Q^{m+1}\xi_0 + \mathbf{R}'(\xi_0). \end{aligned} \tag{58}$$

Consider the linear part of (58) between the mth and $(m+1)$th impacts

$$\begin{aligned} \xi_{m+1} &= Q\xi_m \\ &= Q^{m+1}\xi_0. \end{aligned} \tag{59}$$

If the eigenvalues of Q are distinct, it can be diagonalized using a similarity transformation so that

$$Q = S\Lambda S^{-1} \Rightarrow Q^m = S\Lambda^m S^{-1};\ \Lambda \text{ diagonal.}$$

Let λ_i, $i=1, 2, \ldots, n$ be the eigenvalues of Q. Then, the origin is an asymptotically stable equilibrium point of (59) if and only if the eigenvalues of Q have modulus less than one, i.e.,

$$|\lambda_i| < 1,\ i = 1, 2, \ldots, n. \tag{60}$$

If the eigenvalues of Q are not distinct, it can always be transformed into Jordan canonical form and the condition (60) still applies.

Concerning the stability of (57), we have the following theorem which has been proven by Masri and Caughey (1966).

Theorem 3.1 (*T. K. Caughey, S. Masri*). If

(1) $\|\xi_0\|$ is sufficiently small

(2) $\lim_{\|\xi\|\to 0} \dfrac{\|\mathbf{R}(\xi)\|}{\|\xi\|} = 0$

and if

$$\xi_{m+1} = Q^{m+1}\xi_0 \tag{61}$$

is asymptotically stable, then so is the system

$$\xi_{m+1} = Q^{m+1}\xi_0 + \mathbf{R}'(\xi_0). \tag{62}$$

Thus, the stability problem is reduced to determining the matrix Q and its eigenvalues. However, the theorem allows us to determine the stability characteristics of the nonlinear system only in "the first approximation." As a result, it provides no information at all in the case where one of the eigenvalues of Q has modulus one. To conclude stability or instability in such cases, one must analyze the full nonlinear system.

Table 1 Summary of Initial and final conditions

Steady State	Perturbed
at $\omega t = 0^+$	at $\omega t = (0 + \Delta t_0)^+$
$x = x_0 = 0$	$x = x_0 = 0$
$\dot{x} = \dot{x}_0$	$\dot{x} = \dot{x}_0 + \Delta\dot{x}_0$
$v = v_0 = \dot{x}_0$	$v = v_0 + \Delta v_0 = \dot{x}_0 + \Delta\dot{x}_0$
$\theta = \theta_0$	$\theta = \theta_0 + \Delta\theta_0$
at $\omega t = \pi^+$	at $\omega t = (\pi + \Delta t_0')^+$
$x = x_0 = 0$	$x = x_0 = 0$
$\dot{x} = -\dot{x}_0$	$\dot{x} = -\dot{x}_0 - \Delta\dot{x}_0'$
$v = -v_0 = -\dot{x}_0$	$v = -v_0 - \Delta v_0' = -\dot{x}_0 - \Delta\dot{x}_0'$
$\theta = \theta_0$	$\theta = \theta_0 + \Delta\theta_0'$

3.2 Stability of the Periodic Solutions. To put the equations of motion of the impact damper in the form of (54), let

$$\mathbf{x} = \begin{bmatrix} x \\ \dot{x} \\ y \end{bmatrix}, \quad \mathbf{f}(\mathbf{x},t) = \begin{bmatrix} \dot{x} \\ -\omega_0^2 x + P\cos(\omega t + \theta) \\ v \end{bmatrix} \tag{63}$$

Since the system is third order, the perturbation vector ξ_0 should have three components. Rather than using the position of the primary system and the two velocities, it is convenient because of the way that the solutions have been constructed to choose the phase angle θ as the first component. Moreover, since immediately after impact the two velocities are identical, the perturbations of these velocities from their steady-state value must be equal. Therefore, ξ has only two components, Q is 2×2 and the characteristic equation is quadratic. Let

$$\mathbf{x}_0 = \begin{bmatrix} \theta_0 \\ \dot{x}_0 \\ \hline \omega_0 \end{bmatrix}, \quad \xi_0 = \begin{bmatrix} \Delta\theta_0 \\ \Delta\dot{x}_0 \\ \hline \omega_0 \end{bmatrix}.$$

3.2.1 Symmetric Harmonic Solutions. As before, let the values of the initial conditions for steady-state response be

$$\left.\begin{aligned} x(0) &= x_0 = 0 \\ \dot{x}(0) &= v(0) = \dot{x}_0 \\ \theta &= \theta_0 \end{aligned}\right\}. \tag{64}$$

The conditions at $\omega t = \pi^+$ as well as the perturbations to these values are summarized in Table 1. Primed quantities are those after the second impact (at half cycle). Note that because of the active nature of the system, the position at impact is always zero. Moreover, immediately after impact both rotors assume the same velocity and, therefore,

$$\dot{x}_0 = v_0 \Rightarrow \dot{x}_0 + \Delta\dot{x}_0 = \dot{x}_0 + \Delta v_0 \Rightarrow \Delta\dot{x}_0 = \Delta v_0.$$

As it was shown earlier, depending on the frequency ratio ω_0/ω, there are four classes of symmetric solutions and each must be treated separately. Except for the case of resonance, the solution is

Downloaded 03 May 2010 to 171.66.16.31. Redistribution subject to ASME license or copyright; see http://www.asme.org/terms/Terms_Use.cfm

$$x(t) = A\cos\omega_0 t + B\sin\omega_0 t - \frac{P}{\omega^2-\omega_0^2}\cos(\omega t+\theta_0) \tag{65}$$

$$\dot{x}(t) = -A\omega_0\sin\omega_0 t + B\omega_0\cos\omega_0 t + \frac{P\omega}{\omega^2-\omega_0^2}\sin(\omega t+\theta_0) \tag{66}$$

and the coefficients A and B depend on the initial conditions.

Let A_0 and B_0 denote the values corresponding to periodic solutions, and consider first the generic case where $\cos(\omega_0/\omega)\pi \neq \pm 1$, $\sin((\omega_0/\omega)\pi) \neq 0$.

Then

$$A_0 = A(0) = \frac{P}{\omega^2-\omega_0^2}\cos\theta_0 \tag{67}$$

$$B_0 = B(0) = \frac{\dot{x}_0}{\omega_0} - \frac{P(\omega/\omega_0)}{\omega^2-\omega_0^2}\sin\theta_0. \tag{68}$$

For the perturbed solution $A = A(0+\Delta t_0)$ and $B = B(0+\Delta t_0)$. At $\omega t = \pi + \Delta t_0'$ impact occurs and the displacement is zero:

$$\begin{aligned} 0 &= A(0+\Delta t_0)\cos\omega_0\left(\frac{\pi+\Delta t_0'-\Delta t_0}{\omega}\right) \\ &+ B(0+\Delta t_0)\sin\omega_0\left(\frac{\pi+\Delta t_0'-\Delta t_0}{\omega}\right) \\ &- \frac{P}{\omega^2-\omega_0^2}\cos(\pi+\Delta t_0'-\Delta t_0+\theta_0+\Delta\theta_0) \\ \Rightarrow 0 &= A(0+\Delta t_0)\cos\omega_0\left(\frac{\pi+\Delta T}{\omega}\right) \\ &+ B(0+\Delta t_0)\sin\omega_0\left(\frac{\pi+\Delta T}{\omega}\right) \\ &+ \frac{P}{\omega^2-\omega_0^2}\cos(\Delta T+\theta_0+\Delta\theta_0) \end{aligned} \tag{69}$$

where

$$\Delta T = \Delta t_0' - \Delta t_0 = \Delta\theta_0' - \Delta\theta_0. \tag{70}$$

To first order,

$$A(0+\Delta t_0) = A(0) + \frac{\partial A}{\partial\dot{x}_0}\Delta\dot{x}_0 + \frac{\partial A}{\partial\theta_0}\Delta\theta_0.$$

Since

$$\frac{\partial A}{\partial\dot{x}_0} = \frac{\partial}{\partial\dot{x}_0}\left(\frac{P}{\omega^2-\omega_0^2}\cos\theta_0\right) = 0$$

$$\frac{\partial A}{\partial\theta_0} = -\frac{P}{\omega^2-\omega_0^2}\sin\theta_0,$$

we get

$$A(0+\Delta t_0) = A_0 - \frac{P}{\omega^2-\omega_0^2}\sin\theta_0\Delta\theta_0. \tag{71}$$

Similarly,

$$\begin{aligned} B(0+\Delta t_0) &= B(0) + \frac{\partial B}{\partial\dot{x}_0}\Delta\dot{x}_0 + \frac{\partial B}{\partial\theta_0}\Delta\theta_0 \\ &= B_0 + \frac{1}{\omega_0}\Delta\dot{x}_0 - \frac{P(\omega/\omega_0)}{\omega^2-\omega_0^2}\cos\theta_0\Delta\theta_0. \end{aligned} \tag{72}$$

In addition,

$$\cos\omega_0\left(\frac{\pi+\Delta T}{\omega}\right) \approx \cos\left(\frac{\omega_0}{\omega}\pi\right) - \sin\left(\frac{\omega_0}{\omega}\pi\right)\frac{\omega_0}{\omega}\Delta T \tag{73}$$

$$\sin\omega_0\left(\frac{\pi+\Delta T}{\omega}\right) \approx \sin\left(\frac{\omega_0}{\omega}\pi\right) + \cos\left(\frac{\omega_0}{\omega}\pi\right)\frac{\omega_0}{\omega}\Delta T \tag{74}$$

$$\cos(\Delta T+\theta_0+\Delta\theta_0) \approx \cos\theta_0 - \sin\theta_0(\Delta T+\Delta\theta_0). \tag{75}$$

Note also that from the steady-state solution

$$x\left(\frac{\pi}{\omega}\right) = A_0\cos\left(\frac{\omega_0}{\omega}\pi\right) + B_0\sin\left(\frac{\omega_0}{\omega}\pi\right) + \frac{P}{\omega^2-\omega_0^2}\cos\theta_0 = 0. \tag{76}$$

Substituting into (69) from (71), (72), (73), (74), and (75) and using (76) while keeping only the first-order terms, we obtain, after simplification

$$d_1\Delta T + d_2\Delta\theta_0 + d_3\frac{\Delta\dot{x}_0}{\omega_0} = 0 \tag{77}$$

where the constants d_i, $i=1, 2, 3$ are given in terms of parameters of the problem.

The impact condition (1) at $\omega t = (\pi+\Delta t_0)^+$ gives

$$-(\dot{x}_0+\Delta\dot{x}_0') = a\dot{x}\left(\left(\frac{\pi}{\omega}+\Delta t_0'\right)^-\right) + b(\dot{x}_0+\Delta\dot{x}_0). \tag{78}$$

The velocity $\dot{x}(((\pi/\omega)+\Delta t_0')^-)$ can be evaluated using (66) and (71)–(75). Keeping only first-order terms, we obtain

$$\dot{x}\left(\left(\frac{\pi}{\omega}+\Delta t_0'\right)^-\right) = \dot{x}\left(\frac{\pi^-}{\omega}\right) + \hat{c}_1\Delta T + \hat{c}_2\Delta\dot{x}_0 + \hat{c}_3\Delta\theta_0 \tag{79}$$

where the coefficients $\hat{c}_i$, $i=1, 2, 3$ are given in terms of parameters. The velocity $\dot{x}(\pi/\omega^-)$ is the velocity prior to impact in the steady-state solution and can be evaluated from the known solution. Using (78), (79), and the fact that for the periodic solution $-\dot{x}_0 = a\dot{x}(\pi/\omega^-) + b\dot{x}_0$, we get

$$\frac{\Delta\dot{x}_0'}{\omega_0} = c_1\Delta T + c_2\Delta\theta_0 + c_3\frac{\Delta\dot{x}_0}{\omega_0}. \tag{80}$$

The coefficients c_i, $i=1, 2, 3$ are given in terms of parameters of the problem. Using (70), ΔT can be eliminated from the problem and equations (77) and (80) can be put in matrix form as follows:

$$\begin{bmatrix} \Delta\theta_0' \\ \dfrac{\Delta\dot{x}_0'}{\omega_0} \end{bmatrix} = \begin{bmatrix} 1-\dfrac{d_2}{d_1} & -\dfrac{d_3}{d_1} \\ c_2-c_1\dfrac{d_2}{d_1} & c_3-c_1\dfrac{d_3}{d_1} \end{bmatrix} \begin{bmatrix} \Delta\theta_0 \\ \dfrac{\Delta\dot{x}_0}{\omega_0} \end{bmatrix}. \tag{81}$$

Thus, the transition matrix Q has the above entries for this problem. Let the characteristic polynomial of Q be

$$r(\lambda) = \lambda^2 - \alpha_1\lambda + \alpha_0. \tag{82}$$

Then, the stability of the steady-state solution is determined by the values of the roots of this quadratic. The coefficients α_1 and α_0 are given by:

$$\alpha_1 = \frac{1}{a-2}\left\{\left[(a-1)^2\left(\frac{\omega}{\omega_0}\right)^2 - (a-1)\right] + \left[(a+1) - (a-1)^2\left(\frac{\omega}{\omega_0}\right)^2\right]\cos\left(\frac{\omega_0}{\omega}\pi\right)\right\} \tag{83}$$

Downloaded 03 May 2010 to 171.66.16.31. Redistribution subject to ASME license or copyright; see http://www.asme.org/terms/Terms_Use.cfm

$$\alpha_0 = \frac{1}{a-2}\left\{\left[(a-1)^2\left(\frac{\omega}{\omega_0}\right)^2 - (1-a)\right]\right.$$

$$\left.\times\cos\left(\frac{\omega_0}{\omega}\pi\right) - (1-a)^2\left(\frac{\omega}{\omega_0}\right)^2 + 1 - 2a\right\} \tag{84}$$

and stability of the solution depends on the values of these coefficients.

Although they are for the generic case, the procedure is the same for resonance and the other two special cases. The solutions for $\omega_0/\omega = l$, $l = 2, 3, \ldots$ are simple enough to allow explicit evaluation of the eigenvalues of Q. In fact, for these solutions we can make statements concerning their stability which are not conditional on the values of the system parameters.

Consider first the solution for $\omega_0/\omega = 2l$, $l = 1, 2, 3, \ldots$. We find that

$$\Delta\theta_0' = \frac{a}{a-2}\Delta\theta_0 \tag{85}$$

$$\frac{\Delta\dot{x}_0'}{\omega_0} = -(a+b)\frac{\Delta\dot{x}_0}{\omega_0} = -\frac{\Delta\dot{x}_0}{\omega_0}. \tag{86}$$

Thus, Q is diagonal and the two eigenvalues are

$$|\lambda_1| = \left|\frac{a}{a-2}\right| < 1 \tag{87}$$

$$\lambda_2 = -1. \tag{88}$$

The conclusion from (87) is that perturbations in the phase angle decrease. However, we cannot make any statement concerning perturbations of the velocity because in this case stability is *marginal* and linear theory is not adequate. Note that these solutions belong to the larger class of nonsymmetric solutions and will be discussed later.

For $\omega_0/\omega = 2l+1$, $l = 1, 2, 3, \ldots$ we find that

$$\Delta\theta_0' = \Delta\theta_0 \tag{89}$$

$$\frac{\Delta\dot{x}_0'}{\omega_0} = (a-b)\frac{\Delta\dot{x}_0}{\omega_0}. \tag{90}$$

As a result,

$$\lambda_1 = 1, \quad |\lambda_2| = |a-b| < 1$$

and we have another *marginal* case except that here it is the velocity perturbations that die out.

In the case of resonance we find that

$$\Delta\theta_0' = \frac{a}{1+b}\Delta\theta_0 \tag{91}$$

$$\frac{\Delta\dot{x}_0'}{\omega_0} = (a-b)\frac{\Delta\dot{x}_0}{\omega_0} + \frac{2Pab}{(1+b)\omega_0}\Delta\theta_0. \tag{92}$$

Since

$$|\lambda_1| = \left|\frac{a}{a+b}\right| < 1 \text{ and } |\lambda_2| = |a-b| < 1, \tag{93}$$

the resonance solution is always stable.

While expressions (83) and (84) enable us to compute the eigenvalues of Q for specific cases, it is important to determine the regions in parameter space where solutions are stable. The boundaries of this region can be determined without explicit knowledge of the eigenvalues themselves. Because $r(\lambda)$ is quadratic, there are two possibilities for the roots on the boundary:

(1) λ_1, λ_2 are complex, $\lambda_2 = \bar{\lambda}_1$ and $|\lambda_1| = 1$.
(2) λ_1, λ_2 are real, $|\lambda_1| > |\lambda_2|$ and $|\lambda_1| = 1$.

In the first case,

$$\lambda_1\bar{\lambda}_1 = \alpha_0 = |\lambda_1|^2, \tag{94}$$

so that on the boundary $\alpha_0 = 1$,

$$\Rightarrow \cos\left(\frac{\omega_0}{\omega}\pi\right)\left[(1-a)^2\left(\frac{\omega}{\omega_0}\right)^2 - (1-a)\right] - (1-a)^2\left(\frac{\omega}{\omega_0}\right)^2$$

$$+ 1 - 2a = a - 2.$$

Solving for a we find[2]

$$a = 1 - \frac{\cos\left(\frac{\omega_0}{\omega}\pi\right) - 3}{\left(\frac{\omega}{\omega_0}\right)^2\left[\cos\left(\frac{\omega_0}{\omega}\pi\right) - 1\right]}. \tag{95}$$

When the roots are real and the largest is equal to ± 1 we obtain from (82)

$$1 - \alpha_1\lambda + \alpha_0 = 0 \Rightarrow 1 + \alpha_0 = \pm\alpha_1.$$

Assume first that $\lambda_1 = -1$. Substituting the aforementioned equation for α_1 and α_0 from (83) and (84) we obtain

$$2a\left[1 - \cos\left(\frac{\omega_0}{\omega}\pi\right)\right] = 0.$$

Since the term in the brackets is different from zero, it follows that $a = 0$. However, zero is not in the range of values of a and as a result the possibility that $\lambda = -1$ does not exist. Using the positive sign we obtain

$$\left(\frac{\omega}{\omega_0}\right)^2(a-1)^2\left[\cos\left(\frac{\omega_0}{\omega}\pi\right) - 1\right] = 1 + \cos\left(\frac{\omega_0}{\omega}\pi\right)$$

which does not have any solution because the left-hand side is always negative while the right is always positive. Thus, $\lambda = 1$ is an impossible case. The stability boundary is, therefore, given by (95).

The stability diagram is shown in Fig. 11. The lines $a = 1$ and $a = 0$ are shown as boundary lines but clearly they do not belong to the region of stability. The vertical lines at $\omega/\omega_0 = 1/l$, $l = 2, 3, 4, \ldots$ are meant to indicate that those points represent marginal stability. Near resonance, the region of practical interest, periodic solutions are stable. The right boundary, represented by (95), approaches a horizontal asymptote which can be found from that expression. We get

$$\lim_{n\to\infty} a = 1 - \frac{4}{\pi^2} \approx 0.595. \tag{96}$$

The magnitude of the largest eigenvalue is also plotted as a function of the frequency ratio in Fig. 12. The relative maxima in the region below resonance correspond to the singular frequency ratios $1/l$ and have value one.

3.2.2 Nonsymmetric Solutions. Due to lack of symmetry, the procedure is slightly different in this case. While in analyzing the symmetric type it is necessary to consider only half the cycle, the other half being being identical, here we must consider both halves.

[2]The other root, $a = 1$, is not a possible parameter for the problem.

Downloaded 03 May 2010 to 171.66.16.31. Redistribution subject to ASME license or copyright; see http://www.asme.org/terms/Terms_Use.cfm

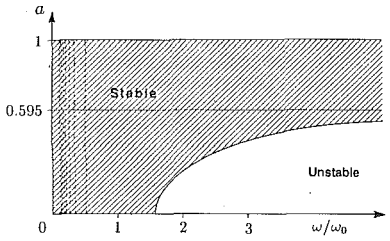


Fig. 11 Stability diagram of symmetric solutions

Recall that nonsymmetric solutions are characterized by

$$\frac{\omega_0}{\omega}=2l,\ l=1,\ 2,\ \ldots;\ \theta_0=-\frac{\pi}{2};\ \dot{x}_0\leq\frac{2Pa\omega}{\omega_0^2-\omega^2} \tag{97}$$

and there are infinitely many. Because these solutions lie infinitely close to each other in phase space, it is evident that they must be neutrally stable. For, if one solution is perturbed slightly, the resulting motion will be on the orbit of a nearby solution and, therefore, stay there, the initial perturbation never decreasing.

More formally, this can be shown as follows. Let the perturbations in phase angle and velocity be as before. Because of (97), the zero-displacement condition (69) yields:

$$\Delta\theta_0'=\left[1-\frac{1}{1-\dfrac{\dot{x}_0(\omega_0^2-\omega^2)}{2P\omega}}\right]\Delta\theta_0.$$

Now, let $\gamma\in[0,\ 1]$ and suppose

$$\dot{x}_0=\gamma\frac{2Pa\omega}{\omega_0^2-\omega^2}.$$

Then

$$\Delta\theta_0'=\left[1-\frac{1}{1-\gamma a}\right]\Delta\theta_0. \tag{98}$$

Let $-\dot{x}_1$ be the initial velocity for the other arc. Then, we get

$$\Delta\theta_0''=\left[1-\frac{1}{1-\dfrac{\dot{x}_1(\omega_0^2-\omega^2)}{2P\omega}}\right]\Delta\theta_0'.$$

But $\dot{x}_0+\dot{x}_1=2Pa\omega/(\omega_0^2-\omega^2)$ and, therefore,

$$\dot{x}_1=(1-\gamma)\frac{2Pa\omega}{\omega_0^2-\omega^2}.$$

Substituting the above for $\dot{x}_1$, we obtain

$$\Delta\theta_0''=\left[1-\frac{1}{1-(1-\gamma)a}\right]\Delta\theta_0'. \tag{99}$$

For the complete cycle we then get

$$\Delta\theta_0''=\left[1-\frac{1}{1-\gamma a}\right]\left[1-\frac{1}{1-(1-\gamma)a}\right]\Delta\theta_0$$

which reduces to

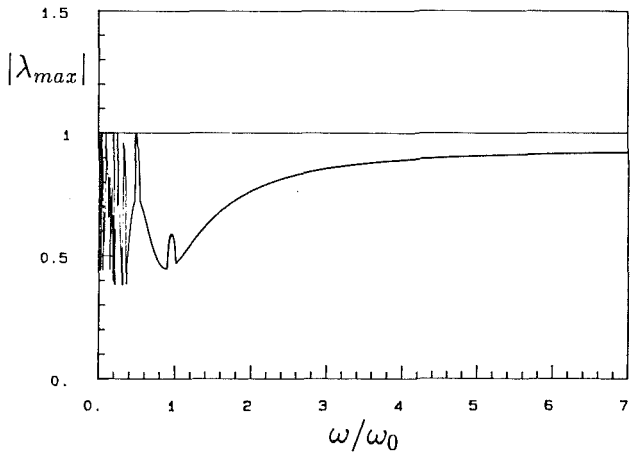


Fig. 12 Magnitude of largest eigenvalue, $a=0.7$

$$\Delta\theta_0''=\frac{1}{1+\dfrac{(1-a)}{\gamma(1-\gamma)a^2}}\Delta\theta_0. \tag{100}$$

Now, $1-a>0$ and $1-\gamma>0\Rightarrow(1-a)/\gamma(1-\gamma)a^2>0$. Hence, $\Delta\theta_0''<\theta_0$ and these solutions are phase stable.

The impact condition (78) for the first arc yields

$$\frac{\Delta\dot{x}_1}{\omega_0}=-(a+b)\frac{\Delta\dot{x}_0}{\omega_0}=-\frac{\Delta\dot{x}_0}{\omega_0}.$$

Similarly, for the other arc

$$\frac{\Delta\dot{x}_0'}{\omega_0}=-(a+b)\frac{\Delta\dot{x}_1}{\omega_0}=-\frac{\Delta\dot{x}_1}{\omega_0}.$$

Hence, $\Delta\dot{x}_0'/\omega_0=\Delta\dot{x}_0/\omega_0$ which confirms the earlier statement, namely that nonsymmetric solutions are *neutrally stable.*

3.2.3 Subharmonic Solutions. The solutions under consideration are only those special cases for which

$$\frac{\omega_0}{\omega}=\frac{1}{2l+1},\ l=1,\ 2,\ \ldots;\ \theta_0=-\frac{\pi}{2};\ \dot{x}_0=x_0=0 \tag{101}$$

and are symmetric with two impacts/cycle. Because of the similarity of these subharmonic solutions to the harmonic orbits with $\omega_0/\omega=2l+1$, one would expect similar stability characteristics, and, indeed, that is the case.

The stability analysis is identical to that of the harmonic case except that here impact occurs at $t_1=\pi/\omega_0\Rightarrow\cos\omega_0 t_1=-1$, $\sin\omega_0 t_1=0$. This results in perturbation equations which are the same as (89) and (90). Thus, subharmonic solutions of this type are *marginally* stable in phase and stable in the initial velocity.

4 Summary and Conclusions

Periodic symmetric and nonsymmetric two impacts/cycle solutions of the semi-active impact damper described in Part I were found and their stability characteristics were determined.

Since the response is bounded, as was found in Part I, the mechanism described is effective for dissipating energy. Moreover, the stability results indicate that even near resonance, symmetric periodic solutions are practically realizable. Actually, this is true for all inertia ratios of practical interest ($a>0.6$) and all frequencies.

In the region where periodic solutions are unstable, preliminary results in the form of time series and Poincaré maps indicate that solutions may be chaotic. This is also sup-

Downloaded 03 May 2010 to 171.66.16.31. Redistribution subject to ASME license or copyright; see http://www.asme.org/terms/Terms_Use.cfm

ported by estimates of the largest Lyapunov exponent which are positive. The dynamics of the system under these conditions need further study.

References

Andronov, A. A., Vitt, A. A., and Khaikin, S. E., 1966, *Theory of Oscillators*, Addison-Wesley, New York.

Karyeaclis, M. P., 1988, "Dynamics of a Semi-active Impact Damper: Regular and Chaotic Motions," Ph.D. Thesis, California Institute of Technology, Pasadena, Calif.

Karyeaclis, M. P., and Caughey, T. K., 1989, "Stability of a Semi-active Impact Damper, Part I: Global Behavior," ASME JOURNAL OF APPLIED MECHANICS, Vol. 56, pp.

Masri, S. F., and Caughey, T. K., 1966, "On the Stability of the Impact Damper," ASME JOURNAL OF APPLIED MECHANICS, Vol. 33, pp. 586–592.

Masri, S. F., 1965, "Analytical and Experimental Studies of Impact Dampers," Ph.D. Thesis, California Institute to Technology, Pasadena, California.

Shaw, S. W., 1985a, "The Dynamics of a Harmonically Excited System Having Rigid Amplitude Constraints, Part 1: Subharmonic Motions and Local Bifurcations," ASME JOURNAL OF APPLIED MECHANICS, Vol. 52, pp. 453–458.

Shaw, S. W., 1985b, "The Dynamics of a Harmonically Excited System Having Rigid Amplitude Constraints, Part 2: Chaotic Motions and Global Bifurcations," ASME JOURNAL OF APPLIED MECHANICS, Vol. 52, pp. 459–464.

Shaw, S. W., and Holmes, P. J., 1983, "A Periodically Forced Impact Oscillator with Large Dissipation," ASME JOURNAL OF APPLIED MECHANICS, Vol. 50, pp. 849–857.

Wolf, A., Swift, J. B., Swinney, H. L., and Vastano, J. A., 1985, "Determining Lyapunov Exponents from a Time Series," *Physica*, Vol. 16D, pp. 285–317.

Downloaded 03 May 2010 to 171.66.16.31. Redistribution subject to ASME license or copyright; see http://www.asme.org/terms/Terms_Use.cfm

Optimal, Coupled-Modal Control of Distributed Parameter Systems With Discrete Actuators

Iradj G. Tadjbakhsh
Fellow ASME

Yuan-an Su

Department of Civil Engineering,
Rensselaer Polytechnic Institute,
Troy, N.Y. 12180-3590

Optimal control of flexible continuous structures subjected to arbitrary time-varying distributed loads is considered. The control is to be implemented by discrete sets of sensors and actuators that monitor the response and apply the necessary forces. The dynamics of the uncontrolled structure is assumed to be governed by a linear, self-adjoint partial differential equation. The control forces at any time are determined on the basis of minimization of the total energy of the system at that time. This leads to a causal optimal algorithm whereby control forces are determined solely on the basis of information available up to the time at which control is being implemented. The effectiveness of the algorithm is demonstrated by applying it to a beam subjected to an impulse.

Introduction

Active control of continuous flexible structures by means of the classical variational theories has been considered by many authors, among them Barnes (1971), Balas (1978), Soong (1982), Leipholz and Abdel-Rohman (1986), and Abdel-Rohman and Nayfeh (1987). For systems governed by self-adjoint partial differential equations the control can be naturally formulated in terms of the spatial modal functions and modal amplitudes. With discrete sets of sensor and actuators these problems become of the category of the coupled-modal control (Meirovitch (1987)).

In a series of papers Meirovitch et al. (1980, 1982, 1983, 1985) have developed the method of independent modal space control (IMSC). In this method each mode of the system is considered independently together with its own control force. The response of each mode is optimized over the time interval of interest by the classical control theory that uses a quadratic performance index. The distributed response of the controlled system and the forces of the actuators are obtained from the controlled mode shapes and the modal control forces using the orthogonal properties of the eigenfunctions.

In this paper a method for the coupled-modal optimal control for continuous self-adjoint structures is developed. It is assumed that a finite number of sensors and actuators are placed on or about the structure that monitor the response and apply the control forces. A primary purpose is that the control algorithm should be causal, i.e., it should depend only on the information available up to the time at which control is being exercised. Yang et al. (1985, 1987) have considered "instantaneous control" of discrete dynamic systems. They consider the discretized state equations of motion and represent the solution in terms of the unknown control forces. Then optimization of the Hamiltonian of the system yields as necessary conditions the optimality algorithm and the response state vector. Komkov (1972) also speaks of "instantly optimal control" algorithms that are obtained by a limiting process from the time optimal law reducing the energy of the system at the maximum possible rate. More generally, Komkov's results are based on the Pontrygin's maximum principle for systems of partial differential equations. The principle characterizes the time optimal solution for a system with prescribed conditions as the solution that reduces the total energy of the system to specified final value at the shortest possible time.

The performance measure used in this paper is the time-dependent, weighted positive sum of the kinetic energy, potential energy, and the energy associated with the expenditure of the control effort. Variational methods determine the feedback control rule with infinite dimensional gain matrices for modal displacements and modal velocities. The behavior of the controlled structure will be governed by a system which is generally nonself-adjoint and with modified damping and stiffness matrices of infinite order. For the system considered the elements of the matrices consist of harmonics with modal periods.

It turns out that the control algorithm that is developed has a limited time interval of applicability about the arbitrary initial point. Outside this interval, negative damping and reduced stiffness may arise. However, the arbitrariness of the initial point allows definition of the end-point of the interval of integration as a new initial point and thus provides a means of continuation of the application of the control. It is likely that the same phenomenon of degradation of control may occur in other optimal algorithms based on an instantaneous perform-

Contributed by the Applied Mechanics Division of THE AMERICAN SOCIETY OF MECHANICAL ENGINEERS for presentation at the Winter Annual Meeting, San Francisco, Calif., December 10-15, 1989.

Discussion on this paper should be addressed to the Editorial Department, ASME, United Engineering Center, 345 East 47th Street, New York, N.Y. 10017, and will be accepted until two months after final publication of the paper itself in the JOURNAL OF APPLIED MECHANICS. Manuscript received by the ASME Applied Mechanics Division, August 1, 1988; final revision, February 28, 1989.

Paper No. 89-WA/APM-20.

Copyright © 1989 by ASME

Downloaded 03 May 2010 to 171.66.16.31. Redistribution subject to ASME license or copyright; see http://www.asme.org/terms/Terms_Use.cfm

ance index, although no specific reference to it was found in prior investigations.

An example of beam vibration is considered. It is the control of vibrations of a concentrated impulse, for which the response decays rapidly to equilibrium.

The Control Problem

Consider a flexible elastic medium such as a plate, a rod, a column, a membrane, or a cable. Let $z(\mathbf{r}, t)$ denote the deflection of the structure with $\mathbf{r}$ and t, respectively, representing the position of a material point in a domain D and the time. Assume n actuators are at locations $\mathbf{r}_i$, $i=1,2,3, \ldots, n$ with control forces $u_i(t)$. Motion of the controlled structure will be described by

$$m(\mathbf{r})\ddot{z}+Lz=f(\mathbf{r},t)+\sum_{i=1}^{n}u_i(t)\delta(\mathbf{r}-\mathbf{r}_i),\mathbf{r}\epsilon D,t>t_O \tag{1}$$

where $m(\mathbf{r})$ is the mass distribution, $f(\mathbf{r}, t)$ is the external excitation, δ is the Dirac delta function, and L is a self-adjoint spatial operator with self-adjoint boundary conditions.

The initial time t_0 is any arbitrary point on the time scale at which the initial conditions

$$z(\mathbf{r},t_O)=z_O(\mathbf{r}),\ \dot{z}(\mathbf{r},t_O)=y_O(\mathbf{r}) \tag{2}$$

are known. In (1) and (2) a dot denotes time derivative.

Associated with the aforementioned system is the positive-definite potential energy, $U(t)$, whose variation, δU, due to a small variation, $\delta z(\mathbf{r},t)$, is given by

$$\delta U=\int_D Lz\ \ \delta z\ \ dD. \tag{3}$$

A positive performance index, J, is defined for the current value of time and consists of the kinetic energy, potential energy, and the control effort

$$J(t)=Q_1\left(\int_D\frac{1}{2}m\dot{z}^2dD\right)+Q_2U+\frac{1}{2}\sum_{i=1}^{n}R_iu_i^2. \tag{4}$$

The positive functions $Q_1(t)$, $Q_2(t)$, and $R_i(t)$ determine the level of the effectiveness of the control criteria and can be assigned arbitrary values by the designer. The control forces, u_i, will be determined such that $J(t)$ is a minimum subject to the constraint of the equations of motion (1)-(2). This minimization implies that the system will acquire a state as near its state of rest $z=\dot{z}=0$ as it is possible with limited control effort.

Using the eigenfunction expansion the displacement z can be represented by an infinite sum of the products of orthonormalized modes $\phi_k(\mathbf{r})$ and the corresponding modal amplitudes $A_k(t)$, $k=1,2,3, \ldots$. When this representation is used in (1) and (2), the following system is obtained

$$\ddot{\mathbf{A}}+\omega^2\mathbf{A}=\mathbf{f}+\mathbf{Bu},\ t>t_O \tag{5}$$

$$\mathbf{A}(t_O)=\mathbf{A}_O,\ \dot{\mathbf{A}}(t_O)=\hat{\mathbf{B}}_O \tag{6}$$

where $\mathbf{A}$, $\mathbf{f}$, $\mathbf{A}_O$, $\hat{B}_O$ are infinite dimensional vectors with their elements given, respectively, by

$$(A_j, A_{Oj}, \hat{B}_{Oj})=\int_D m(z,z_O,y_O)\phi_j(\mathbf{r})dD,$$

$$f_j=\int_D f\phi_j dD,\ j=1,2,3, \ldots, \tag{7}$$

and $\omega=\text{diag}(\omega_j)$, $j=1, 2, 3, \ldots$, where ω_j are the modal frequencies as determined from (see Meirovitch 1967):

$$\omega_j^2=\int_D\phi_jL\phi_jdD,\ j=1,2,3, \ldots. \tag{8}$$

Also, $\mathbf{u}=(u_1, u_2, u_3, \ldots, u_n)^T$ is the vector of actuator forces and $\mathbf{B}$ is a matrix of infinite rows and n columns with the elements of the jth row given by

$$B_{ji}=\phi_j(\mathbf{r}_i),\ i=1,2,3, \ldots n. \tag{9}$$

Solution of (5)-(6), with the aid of the convolution integral, can be represented by

$$\mathbf{A}-\mathbf{C}(t-t_O)\mathbf{A}_O-\mathbf{S}(t-t_O)\hat{\mathbf{B}}O=\mathbf{S}^*(\mathbf{f}+\mathbf{Bu})$$

$$\triangleq\int_{t_O}^{t}S(t-\tau)[f(\tau)+\mathbf{Bu}(\tau)]d\tau \tag{10}$$

where $\mathbf{C}$ and $\mathbf{S}$ are infinite dimensional diagonal matrices of the modal harmonics given by

$$\mathbf{S}=\text{diag}(\omega_j{}^{-1}\sin\omega_jt),\ \mathbf{C}=\dot{\mathbf{S}}=\text{diag}(\cos\omega_jt),$$

$$j=1,2,3, \ldots. \tag{11}$$

Control Algorithm

Introducing the arbitrary variations, $\delta\mathbf{u}$, in the interval, $[t_O,t]$, we have for the variation δA from (10),

$$\delta A=\mathbf{S}^*\mathbf{B}\delta\mathbf{u}. \tag{12}$$

By differentiating (12), one obtains

$$\delta\dot{A}=\mathbf{C}^*\mathbf{B}\delta\mathbf{u}. \tag{13}$$

It is understood that certain modes may be uncontrollable due to coincidence of the actuator locations with nodal points. Also, it may be advantageous to limit the number of modes that participate in the control in order to achieve better controller design. Therefore, variations of these uncontrolled modes will be zero either automatically, $\phi_j(\mathbf{r}_i)=0$, or by choice. In all cases the variations δz and $\delta\dot{z}$ can be written from the eigenfunction representation of z as

$$\delta z=\sum_{j=1}^{\infty}\phi_j\delta A_j,\ \delta\dot{z}=\sum_{j=1}^{\infty}\phi_j\delta\dot{A}_j \tag{14}$$

where it is understood that certain terms in the sums may vanish. Then, from (3)-(4),

$$\delta J=\int_D(Q_1m\dot{z}\delta\dot{z}+Q_2Lz\delta z)dD+\sum_{i=1}^{n}R_iu_i\delta u_i. \tag{15}$$

These, together with the relations defining the eigenfunctions, the frequencies, and the orthogonality conditions

$$L\phi_j=m\omega_j^2\phi_j,\ \int_D m\phi_j\phi_kdD=\delta_{jk},j,k=1,2,3, \ldots \tag{16}$$

yield the modal equivalent of (15)

$$\delta J=Q_1\dot{\mathbf{A}}^T\delta\dot{\mathbf{A}}+Q_2\dot{\mathbf{A}}^T\omega^2\delta\mathbf{A}+\mathbf{u}^T\mathbf{R}\delta\mathbf{u} \tag{17}$$

where $\mathbf{R}=\text{diag}(R_1, R_2, R_3, \ldots R_n)$.

Substitution of (11)-(13) into (17) yields

$$\delta J=Q_1(t)\dot{\mathbf{A}}^T(t)\int_{t_O}^{t}\mathbf{C}(t-\tau)\mathbf{B}\delta\mathbf{u}(\tau)d\tau$$

$$+Q_2(t)\mathbf{A}^T(t)\omega^2\int_{t_O}^{t}\mathbf{S}(t-\tau)\mathbf{B}\delta\mathbf{u}(\tau)d\tau$$

$$+\mathbf{u}^T(t)\mathbf{R}(t)\delta\mathbf{u}(t). \tag{18}$$

By introducing the Heaviside unit step-function, $H(t)$, and the delta function, $\delta(t)$, one can represent (18) as a single integral over the extended interval, $t_O\leq\tau<\infty$. Thus,

$$\delta J=\int_{t_O}^{\infty}\{H(t-\tau)[Q_1(t)\dot{\mathbf{A}}^T(t)\mathbf{C}(t-\tau)$$

$$+Q_2\mathbf{A}^T(t)\omega^2\mathbf{S}(t-\tau)]\mathbf{B}+\delta(t-\tau)\mathbf{u}^T(\tau)\mathbf{R}(\tau)\}\delta\mathbf{u}(\tau)d\tau. \tag{19}$$

Vanishing of δJ for arbitrary $\delta\mathbf{u}$ implies the vanishing of the coefficient of $\delta\mathbf{u}(\tau)$ in the integrand in (19). This condition is

$$H(t-\tau)[Q_1(t)\dot{\mathbf{A}}^T(t)\mathbf{C}(t-\tau)+Q_2(t)\mathbf{A}^T(t)\omega^2\mathbf{S}(t-\tau)]\mathbf{B}$$

$$+\delta(t-\tau)\mathbf{u}^T(\tau)\mathbf{R}(\tau)=0,\quad \text{for } \tau>t_O,\ \tau>t_O. \tag{20}$$

Downloaded 03 May 2010 to 171.66.16.31. Redistribution subject to ASME license or copyright; see http://www.asme.org/terms/Terms_Use.cfm

Integrating this equation with respect to τ, from t_O to t, one obtains

$$\{Q_1\dot{\mathbf{A}}^T\mathbf{S}(t-t_O)+Q_2\mathbf{A}^T[\mathbf{I}-\mathbf{C}(t-t_O)]\}\mathbf{B}+\mathbf{u}^T\mathbf{R}=0,\ t>t_O \quad (21)$$

which determines the control force in the time domain.

Assuming that a certain ordered number Nc of modes are to participate in the control algorithm, we denote them by $\mathbf{A}_c=(A_1,\ A_2,\ \ldots\ A_{N_c})^T$. The remaining modes will be denoted by $\mathbf{A}_r$. In a corresponding manner vectors and matrices will be partitioned

$$\mathbf{A}=\begin{bmatrix}\mathbf{A}_c\\ \mathbf{A}_r\end{bmatrix},\ \mathbf{f}=\begin{bmatrix}\mathbf{f}_c\\ \mathbf{f}_r\end{bmatrix},\ \mathbf{B}=\begin{bmatrix}\mathbf{B}_c\\ \mathbf{B}_r\end{bmatrix},\ \mathbf{S}=\begin{bmatrix}\mathbf{S}_c & \mathbf{0}\\ \mathbf{0} & \mathbf{S}_r\end{bmatrix}$$

$$\mathbf{C}=\begin{bmatrix}\mathbf{C}_c & 0\\ \mathbf{0} & \mathbf{C}_r\end{bmatrix},\ \mathbf{I}=\begin{bmatrix}\mathbf{I}_c & \mathbf{0}\\ \mathbf{0} & \mathbf{I}_r\end{bmatrix},\ \omega=\begin{bmatrix}\omega_c & \mathbf{0}\\ \mathbf{0} & \omega_r\end{bmatrix}. \quad (22)$$

Then (21) can be solved for the control force

$$\mathbf{u}=-Q_1\mathbf{D}\dot{\mathbf{A}}_c-Q_2\mathbf{E}\mathbf{A}_c \quad (23)$$

where

$$\mathbf{D}=\mathbf{R}^{-1}\mathbf{B}_c^T\mathbf{S}_c(t-t_O),\ \mathbf{E}=\mathbf{R}^{-1}\mathbf{B}_c^T[\mathbf{I}_c-\mathbf{C}_c(t-t_O)]. \quad (24)$$

The behavior of the controlled modes are determined, from (5) and (23), to be

$$\ddot{\mathbf{A}}_c+Q_1\mathbf{B}_c\mathbf{D}\dot{\mathbf{A}}_c+(\omega_c^2+Q_2\mathbf{B}_c\mathbf{E})\mathbf{A}_c=\mathbf{f}_c. \quad (25)$$

The residual modes are subject to control spillover and are determined from

$$\ddot{\mathbf{A}}_r+\omega_r^2\mathbf{A}_r=\mathbf{f}_r-Q_1\mathbf{B}_r\mathbf{D}\dot{\mathbf{A}}_c-Q_2\mathbf{B}_r\mathbf{E}\mathbf{A}_c. \quad (26)$$

Implementation

The feedback control algorithm described in (23) requires the modal displacements, $\mathbf{A}_c(t)$, and modal velocities, $\mathbf{A}_c(t)$. These modal states can be estimated from the output of discrete sensors distributed on the system by using the Luenberger observer (see Luenberger, 1971). It is known, however, that in this case observation spillover from the truncated modes will inevitably result. Balas (1971) pointed out that the combination of control and observation spillover may lead to potential instabilities in closed-loop systems. In order to circumvent this problem, one can use the spatial modal filters that were developed by Meirovitch et al. (1985) to reconstruct the required modal states for the implementation of the control algorithm.

The modal filters are based on the orthogonality of the system eigenfunction over the domain of the structure. Therefore, the observation spillover is eliminated by the orthogonality property. However, the accuracy of the modal filters depends on the exactness with which the displacement and velocity field of the structure have been determined from the measurements, i.e., the number of sensors and the accuracy of interpolation procedure. The problems associated with the modal filters were investigated by Meirovitch et al. (1985), and are briefly reconsidered for the closed-loop system of (25) and (26) in the Appendix.

It is evident that the terms corresponding to Q_1, Q_2 in the performance index J, respectively, modify the damping and the stiffness of the system. The gain matrices $\mathbf{E}$, $\mathbf{D}$ are nonsymmetric, nondiagonal infinite dimensional matrices that couple all the modal amplitudes. The governing equations for the controlled system are nonself-adjoint raising the question that in the event of instability, the transition may be through flutter.

The elements of gain matrices consist of modal harmonics $\cos\ \omega_j(t-t_O)$ and $\sin\ \omega_j(t-t_O)$ which initially (i.e., near $t=t_O$) are non-negative. As t increases the higher harmonics begin to change sign, thus creating negative damping and reducing stiffnesses.

It thus becomes clear that the optimal algorithm derived here is valid for a small interval of time during which occurrence of negative damping or reduction in stiffness have not caused amplification of response of those higher modes that participate significantly in the dynamics of the system. This feature of the optimality algorithm, namely its validity in the small neighborhood of the initial time t_O, is plausibly related to the instantaneous definition of the performance index J.

Therefore, the control procedure can not progress too far away from the initial data prescribed at $t=t_O$. This difficulty can simply be overcome when one notes that the initial t_O is arbitrary. Therefore after a finite interval of control, during which the solution is free of modal instabilities, the integration may begin anew with the end-point of the previous interval as the new initial time. If a number N, $N>N_c$, of modes are retained and the remaining modes are truncated, than an upper limit of the interval of integration will be $t-t_O=\pi/\omega_N$.

Example

For illustration we consider control of vibrations of a uniform beam hinged at both ends and controlled by four equally-spaced actuators (Fig. 1). The beam is subjected to an impulse load at the midspan. We assume that the length of the beam is 60 m, its bending stiffness EI is 5×10^5 N-m^2, and its mass per unit length m is 1.0 kg(m). Then the eigenvalues λ_i and orthonormalized eigenfunctions are given by

$$\lambda_i=\omega_i^2=0.039(i\pi)^4,\ \phi_i(x)=0.183\sin(i\pi x/60),i=1,2,3,\ \ldots$$

wherein x denotes the distance along the beam. As mentioned in the previous sections, the control interval depends upon the highest frequency of those modes that are targeted for control. The limitation of the control interval for the first ten modes of this system is listed in Table 1.

In the following analyses, it is assumed that the modal states can properly be reconstructed without observation spillover so that the modal response of the system can be represented by (25) and (26).

The subroutine DVERK of IMSL package, which is based on the Rung Kutta-Verner fifth- and sixth-order methods, was used with 0.001 error tolerance to calculate the response of the controlled system. After some trial, the choice $Q_1=Q_2=5000.0$ and $R_i=1$, $i=1,\ 2,\ 3,\ 4$, proved satisfactory and yielded sufficiently accurate response for the controlled structure.

In order to illustrate the features of the control algorithm, several cases with different controlled modes and varying control intervals are considered as shown in Table 2.

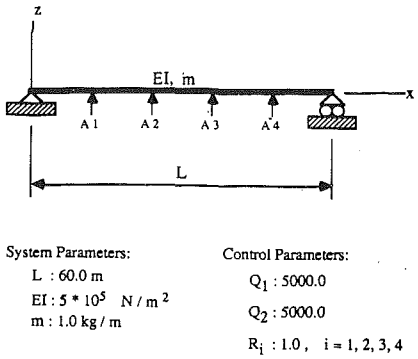
Table 1

Mode	Max.$(t-t_O)$,sec.	Mode	Max.$(t-t_O)$,sec.
1	1.621	6	0.045
2	0.405	7	0.033
3	0.180	8	0.025
4	0.101	9	0.020
5	0.065	10	0.016

Table 2

Case	Controlled modes	Control Interval (sec.)	Modeled modes
1	1,2	0.20	10
2	1,2,3,4	0.05	10
3	1,2,3,4	0.01	10
4	1-10	0.01	10

Downloaded 03 May 2010 to 171.66.16.31. Redistribution subject to ASME license or copyright; see http://www.asme.org/terms/Terms_Use.cfm



System Parameters:
L : 60.0 m
EI : $5 * 10^5$ N / m^2
m : 1.0 kg / m

Control Parameters:
Q_1 : 5000.0
Q_2 : 5000.0
R_i : 1.0, i = 1, 2, 3, 4

Fig. 1 Simply-supported beam with four equally-spaced actuators

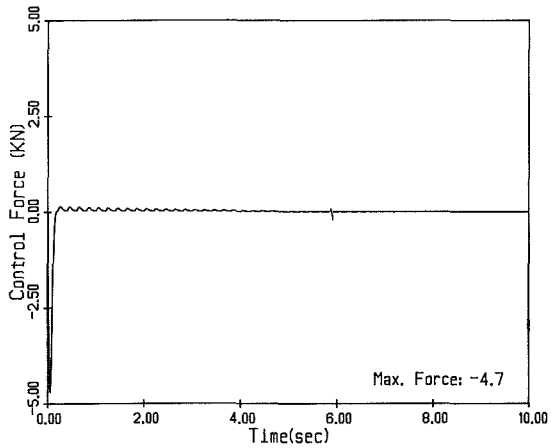


Fig. 2(*a*) Force of middle actuator for a unit impulse load with two controlled modes, $\Delta t = 0.20$ sec

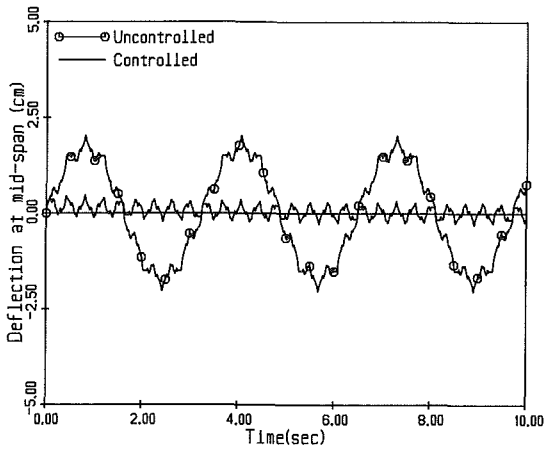


Fig. 2(*b*) Controlled and uncontrolled response under a unit impulse load at midspan with two controlled modes, $\Delta t = 0.20$ sec

The results that are presented refer to the deflection at the midspan of the beam and the commanded force of the actuator No. 2 (Fig. 1) over a time interval of ten seconds. These are shown in Figs. 2(*a-b*), 3(*a-b*), 4(*a-b*), and 5(*a-b*) for the case 1, 2, 3, and 4, respectively.

Figure 2, shows that the control spillover imparts some of the control efforts into the higher modes. The actuators exerted the command force only at the beginning of the time interval and left the structure oscillating for the rest of the time. This control spillover can be mitigated by increasing the number of controlled modes, as shown in Fig. 3, in which the first 4 modes are subjected to control.

The control gain of the algorithm expressed in (24) are characterized as functions of the control interval $t - t_O$. Therefore, the behavior of controlled system varies with the

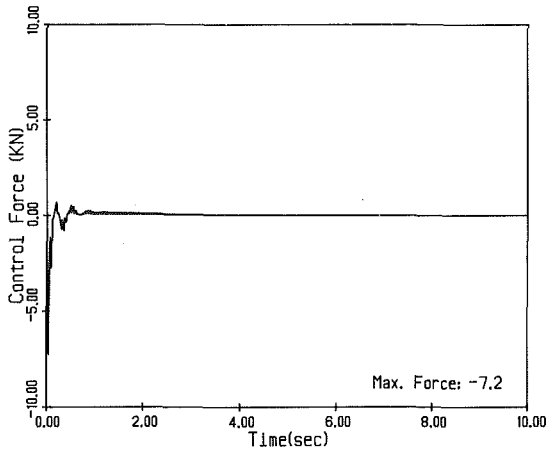


Fig. 3(*a*) Force of middle actuator for a unit impulse load with four controlled modes, $\Delta t = 0.05$ sec

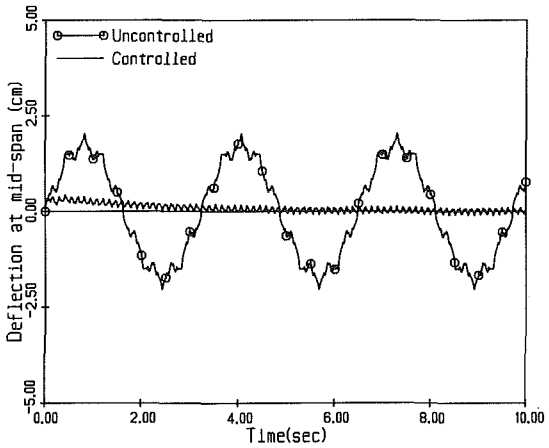


Fig. 3(*b*) Controlled and uncontrolled response under a unit impulse load at midspan with four controlled modes, $\Delta t = 0.05$ sec

changes in the control interval. Figure 4 shows the consequence of change in the control interval from the 0.05 sec. in Case 2 to 0.01 sec. in Case 3. Clearly, the transitory response of the system in the beginning of the period is quite sensitive to the control interval. Comparing Fig. 4 with Fig. 3, we conclude that the behavior of the control algorithm strongly depends on the choice of the control interval.

The effect of increasing the number of modes participating in the coupled control with the same control interval is shown in Fig. 5, in which the controlled modes are increased to ten. The controlled response is practically the same as when only four modes were allowed to participate in the control. This result is due to the actuator spacing that precludes control of the fifth mode and its multiples. The major difference is the rapidly oscillatory behavior of the actuator forces as shown in the same figure. Thus, for this example, it seems advantageous to design the controller on the basis of four mode participation in the control algorithm.

Conclusion

The control algorithm developed here determines the control forces in the time domain explicitly in terms of the coupled model amplitudes and velocities. The algorithm is optimal in that it minimizes the total energy of the system instantly and spatially rather than over a time domain. Consequently, the algorithm is causal and can be implemented on the basis of what has transpired prior to implementation. Additionally, the algorithm allows participation by a limited number of modes with the remainder being subject to spillover. This feature allows for smoothly operating con-

Downloaded 03 May 2010 to 171.66.16.31. Redistribution subject to ASME license or copyright; see http://www.asme.org/terms/Terms_Use.cfm

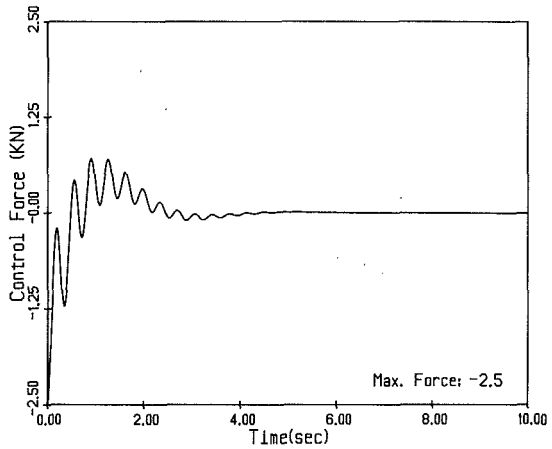


Fig. 4(*a*) Force of a middle actuator for a unit impulse with four controlled modes, $\Delta t = 0.01$ sec

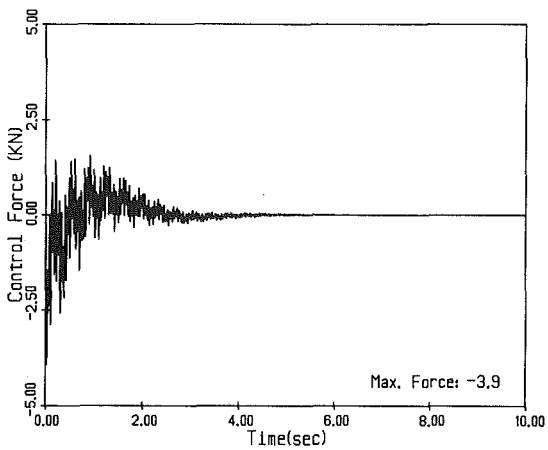


Fig. 5(*a*) Force of a middle actuator for a unit impulse load with ten controlled modes, $\Delta t = 0.01$ sec

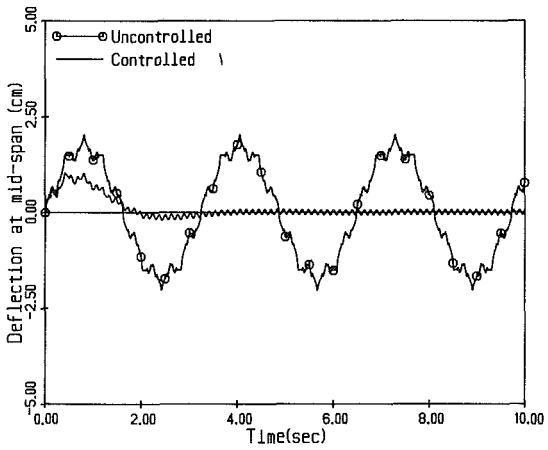


Fig. 4(*b*) Controlled and uncontrolled responses under a unit impulse load at midspan with four controlled modes, $\Delta t = 0.01$ sec

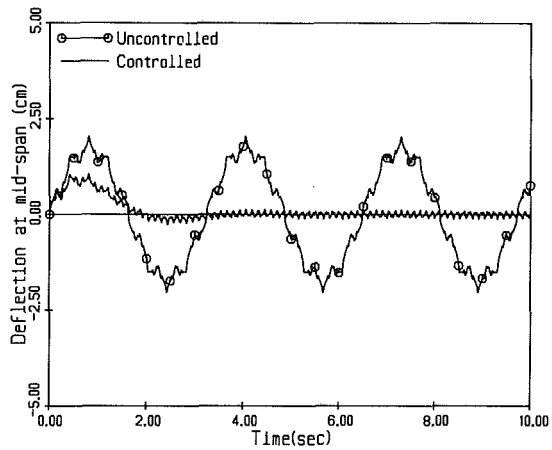


Fig. 5(*b*) Controlled and uncontrolled response under a unit impulse load at midspan with ten controlled modes, $\Delta t = 0.01$ sec

trollers. The instantaneous nature of the algorithm limits its applicability to the small neighborhood of the initial point which, however, is arbitrary. This arbitrariness allows integration over a sequence of intervals whose initial data is determined by the end conditions of the previous interval. Examples considered thus far are free of instabilities and prove the effectiveness of the algorithm.

Acknowledgment

The work presented here was supported by the Army Research office and by the National Center for Earthquake Engineering Research of State University of New York at Buffalo.

References

Abdel-Rohman, M., and Nayfeh, A. H., 1987, "Active Control of Nonlinear Oscillations in Bridges," *ASCE Journal of Engineering Mechanics*, Vol. 113, pp. 335-348.

Balas, M. J., 1978, "Active Control of Flexible Systems," *Journal of Optimization Theory and Applications*, Vol. 25, pp. 415-436.

Balas, M. J., 1978, "Feedback Control of Flexible Systems," *IEEE Transaction on Automatic Control*, Vol. AC-23, pp. 415-436.

Barnes, E. R., 1971, "Necessary and Sufficient Otimality Conditions for a Class of Distributed Parameter Control Systems," *SIAM Journal on Control*, Vol. 9, No. 1, pp. 62-82.

Komkov, V., 1972, *Optimal Control Theory for the Damping of Vibrations of Simple Elastic Systems*, Lecture Notes in Mathematics, No. 253, Springer-Verlag, New York.

Leipholz, H. H. E., and Abdel-Rohman, M., 1986, *Control of Structure*, Martinus Nijhoff Publishers.

Luenberger, D., 1968, "An Introduction to Observers," *IEEE Trans. Automat. Control.*, Vol. AC-16, No. 6, pp. 316-353.

Meirovitch, L., 1969, *Analytical Methods in Vibrations*, Macmillan, New York.

Meirovitch, L., and Oz, H., 1980, "Modal Space Control of Distributed Gyroscopic Systems," *Journal of Guidance and Control*, Vol. 2, No. 3, pp. 140-150.

Meirovitch, L., and Baruh, H., 1982, "Control of Self-Adjoint Distributed Parameter Systems," *Journal of Guidance, Control, and Dynamics*, Vol. 5, No. 1, pp. 60-66.

Meirovitch, L., and Baruh, H., 1983, "Robustness of the Independent Modal Space Control Method," *Journal of Guidance, Control, and Dynamics*, Vol. 6, No. 1, pp. 20-25.

Meirovitch, L., Baruh, H., and Oz, H., 1983, "A Comparison of Control Techniques for Large Flexible Systems," *Journal of Guidance, Control, and Dynamics*, Vol. 6, No. 4, pp. 302-310.

Meirovitch, L., and Baruh, H., 1985, "The Implementation of Modal Filters for Control of Structures," *Journal of Guidance*, Vol. 8, No. 6, pp. 707-716.

Meirovitch, L., 1987, "Some Problems Associated with the Control of Distributed Structures," *Journal of Optimization Theory and Applications*, Vol. 54, No. 1, pp. 1-21.

Soong, T. T., and Chang, J. C. H., 1982, "Active Vibration Control of Large Flexible Structures," *Shock Vibration Bulletin*, Vol. 52, Part IV, pp. 47-54.

Yang, J. N., Akbarpour, A., and Ghaemmaghami, P., 1987, "New Optimal Control Algorithms for Structural Control," *ASCE, Journal of Engineering Mechanics*, Vol. 113, No. 9, pp. 1369-1386.

Yang, J. N., Akbarpour, A., and Ghaemmaghami, P., 1985, "Optimal Control Algorithms for Earthquake-Excited Building," *Proceedings of the Second International Symposium on Structural Control*, H. H. E. Leipholz, ed., University of Waterloo, Waterloo, Canada, July 1985, Martinus Nijhoff, Amsterdam, 1987.

Downloaded 03 May 2010 to 171.66.16.31. Redistribution subject to ASME license or copyright; see http://www.asme.org/terms/Terms_Use.cfm

APPENDIX

The question of implementation of (23) based on data reported by discrete sensors has been previously investigated (see Meirovitch, 1985). Essentially, it is required that continuous displacement and velocity be determined by fitting a Lagrangian or finite element interpolation to discrete data. Then, using the orthogonality of the system eigenfunctions over the domain of the structure, one can design a spatial modal filter to extract the required modal states for implementing the control algorithm.

Due to the fact that the noise of discrete actuators and sensors cannot destabilize the closed-loop systems associated with the controlled or residual modes (Meirovitch and Baruh, 1985), we neglect the effect of the noise on the stability problem in conjunction with the modal filters in closed-loop systems. Using the eigenfunction expansion theorem, the output of the ith sensor, denoted by $\hat{Z}_i(t)$, located at $\mathbf{r}_i$, can be expressed in the form

$$\hat{Z}_i(t) = \sum_{j=i}^{\infty} \phi_j(\mathbf{r}_i) A_j(t), \dot{\hat{Z}}_i(t) = \sum_{j=i}^{\infty} \phi_j(\mathbf{r}_i) \dot{A}_j(t)$$

$$\dot{A}_j(t), i = 1, \ldots N_s \tag{A1}$$

in which, N_s represents the number of sensors.

Let us rewrite (A1) in the matrix form as

$$\hat{\mathbf{Z}}(t) = \mathbf{H}A(t), \dot{\hat{\mathbf{Z}}}(t) = \mathbf{H}\dot{\mathbf{A}}(t) \tag{A2}$$

where $\mathbf{H} = [h_{ij}]$, $i = 1, \ldots N_s$, $j = 1, \ldots \infty$, in which $h_{ij} = \phi_j(\mathbf{r}_i)$. Assuming that the distribution of displacement and velocity of the structure can be reconstructed by introducing the interpolation function $g_i(r)$ for the ith sensor's output, one can express the displacement and velocity as

$$\hat{\mathbf{Z}}(\mathbf{r},t) = \sum_{i=1}^{N_s} g_i(\mathbf{r}) \hat{Z}_i(t), \dot{\hat{\mathbf{Z}}}(\mathbf{r},t) = \sum_{i=1}^{N_s} g_i(\mathbf{r}) \dot{\hat{Z}}_i(t). \tag{A3}$$

Using the second part of the eigenfunction expansion theorem (Meirovitch, 1969), the general form of modal filter displacement can be given by

$$A_i(t) = \int_D \phi_i m(\mathbf{r}) Z(\mathbf{r},t) dD, \quad i = 1,2, \ldots N_c \tag{A4}$$

where N_c is the number of the controlled modes. Therefore, the estimated modal displacement $\hat{A}_i(t)$ is

$$\hat{A}_i(t) = \int_D \phi_i m(\mathbf{r}) \hat{Z}(\mathbf{r},t) dD. \tag{A5}$$

Introducing the first part of (A3) into (A5) leads to

$$\hat{A}_i(t) = \sum_{j=1}^{N_s} G_{ij} \hat{Z}_j(t), \; i = 1,2, \ldots Nc \tag{A6}$$

in which

$$G_{ij} = \int_D \phi_i m(\mathbf{r}) g_j(\mathbf{r}) dD. \tag{A7}$$

Recalling (A2), we can rewrite (A7) in the matrix form

$$\hat{\mathbf{A}}_c(t) = \mathbf{GHA}(t). \tag{A8}$$

Partitioning $\mathbf{H}$ into matrices associated with the controlled and the residual modes, one has

$$\mathbf{H} = [\mathbf{H}_c, \mathbf{H}_r]. \tag{A9}$$

Then (A8) becomes

$$\hat{\mathbf{A}}_c(t) = \mathbf{GH}_c\mathbf{A}_c(t) + \mathbf{GH}_r\mathbf{A}_r(t). \tag{A10}$$

Similarly, the estimated modal velocity can be expressed in the form

$$\dot{\hat{\mathbf{A}}}_c(t) = \mathbf{GH}_c\dot{\mathbf{A}}_c(t) + \mathbf{GH}_r\dot{\mathbf{A}}_r(t). \tag{A11}$$

From (A10) and (A11) it is seen that the measurements are free of interpolation errors, only if $\mathbf{GH}_c = \mathbf{I}$ and $\mathbf{GH}_r = 0$. The $\mathbf{GH}_r$ is the observation spillover of the modal filter which is induced by the interpolation process. To examine the poles of the closed-loop system shown in (5), we first introduce (A10) and (A11) into (23) and obtain the control force

$$\mathbf{u} = -Q_1\mathbf{D}(\mathbf{GH}_c\dot{\mathbf{A}}_c + \mathbf{GH}_r\dot{\mathbf{A}}_r) - Q_2\mathbf{E} \tag{A12}$$
$$(\mathbf{GH}_c\mathbf{A}_c + \mathbf{GH}_r\mathbf{A}_r).$$

Then substituting (A12) into (5) we have

$$\begin{Bmatrix} \ddot{\mathbf{A}}_c \\ \ddot{\mathbf{A}}r \end{Bmatrix} + \begin{bmatrix} Q_1\mathbf{B}_c\mathbf{DGH}_c & Q_1\mathbf{B}_cDGH_r \\ Q_1\mathbf{B}_r\mathbf{DGH}_c & Q_1\mathbf{B}_rDGH_r \end{bmatrix} \begin{Bmatrix} \dot{\mathbf{A}}_c \\ \dot{\mathbf{A}}r \end{Bmatrix}$$

$$+ \begin{bmatrix} \omega_c^2 + Q_2\mathbf{B}_c\mathbf{EGH}_c & Q_2\mathbf{B}_c\mathbf{EGH}_r \\ Q_2\mathbf{B}_r\mathbf{EGH}_c & \omega_r^2 + Q_2\mathbf{B}_r\mathbf{EGH}_r \end{bmatrix} \begin{Bmatrix} \mathbf{A}_c \\ \mathbf{A}r \end{Bmatrix} = \begin{Bmatrix} f_c \\ f_r \end{Bmatrix}. \tag{A13}$$

Clearly, the matrices $Q_1\mathbf{B}_c\mathbf{DGH}_r$ and $Q_2\mathbf{B}_c\mathbf{EGH}_r$ cause coupling of the controlled and the residual modes resulting in observation spillover.

Therefore, when $GH_r \neq 0$, the stability of the closed-loop system associated with the modal filters can be determined by solving the eigenvalue problem of (A13).

Downloaded 03 May 2010 to 171.66.16.31. Redistribution subject to ASME license or copyright; see http://www.asme.org/terms/Terms_Use.cfm

W. Szemplińska-Stupnicka
Professor,
Institute of Fundamental Technological Research,
Polish Academy of Sciences,
Swietokrzyska 21,
PL 00-049 Warsaw, Poland

R. H. Plaut
Professor,
Mem. ASME

J.-C. Hsieh
Research Assistant.

Charles E Via, Jr.
Department of Civil Engineering,
Virginia Polytechnic Institute and State University,
Blacksburg, Va. 24061

Period Doubling and Chaos in Unsymmetric Structures Under Parametric Excitation

Nonlinear oscillations of a single-degree-of-freedom, parametrically-excited system are considered. The stiffness involves quadratic and cubic nonlinearities and models a shallow arch or buckled mechanism. The excitation frequency is assumed to be close to twice the natural frequency of the system. Numerical integration is used to obtain phase plane portraits, power spectra, and Poincaré maps for large-time motions. Period-doubling bifurcations and several types of limit cycles and chaotic behavior are observed. Approximate analytical techniques are applied to analyze some of the limit cycles and transitions of behavior. The results are used to estimate the parameter region in which chaos may occur.

Introduction

Most studies of chaos in mechanical or structural systems have considered external (forcing) excitation (e.g., see Holmes and Moon, 1983). A typical example of the governing equation is Duffing's equation with damping and a harmonic forcing term on the right-hand side. In this paper, however, the excitation appears as a coefficient in the equation of motion (parametric excitation).

A number of earlier studies on chaos in parametrically-excited systems have treated a pendulum subjected to harmonic vertical excitation at its support (e.g., McLaughlin, 1981; Leven and Koch, 1981; Arneodo et al., 1983; Eckmann, 1983; Koch et al., 1983; Koch and Leven, 1985; Leven et al., 1985; Pompe and Leven, 1986). The governing equation in most of those works has the form

$$\ddot{\psi}(t)+k_1\dot{\psi}(t)+(k_2+k_3\cos\Omega t)\sin\psi(t)=0. \quad (1)$$

For example, the first of these references uses $k_1=0$ or 0.2, $k_2=1$, and $\Omega=2$; the second uses $k_1=0.15$, $k_2=1$, and $\Omega=1.56$; and the third uses $k_1=0.18$, $k_2=2$, and $\Omega=2$. Similar equations were analyzed by Gell and Nakach (1986) and Gitterman (1987).

The equation to be examined here is

$$\ddot{u}(t)+2c\dot{u}(t)+(\omega_0{}^2+P\cos\Omega t)u(t)+\alpha u^2(t)+\beta u^3(t)=0 \quad (2)$$

with parameter values

$$c=0.1, \quad \omega_0=1, \quad \alpha=3/2, \quad \beta=1/2 \quad (3)$$

and initial conditions

$$u(0)=0.02, \quad \dot{u}(0)=0. \quad (4)$$

In equation (2), c is the damping coefficient, ω_0 is the natural frequency of the undamped linearized system, P is the excitation amplitude, and Ω is the excitation frequency. This equation is unsymmetric in $u(t)$, due to the quadratic term. It is the equation of motion for a particular shallow arch subjected to horizontal and vertical pulsating loads, and for a two-bar mechanism containing a nonlinear spring (see the Appendix). Equation (2) with different sets of parameters was previously considered by Zavodney et al. (1989).

In the present paper, the parametric frequency Ω is assumed to be in the neighborhood of $2\omega_0$ (principal parametric resonance). Attention is focused on the asymptotic (large-time) behavior of $u(t)$. First, large-time responses are investigated using numerical integration. Examples of phase plane portraits, power spectra, and Poincaré maps are presented. In the (Ω, P) plane, regions associated with different types of resonance are delineated.

Next, some of the transition curves and limit cycles are examined by a perturbation technique and the method of harmonic balance. In particular, period doubling is considered, since it often precedes chaos. In the spirit of work on forced systems by Rudowski and Szemplińska-Stupnicka (1987) and Szemplińska-Stupnicka (1988), simple analytical criteria are obtained which indicate regions in which chaos and other "strange" behavior may occur.

Large-Time Responses

When the parametric excitation is absent, (2) has fixed points (equilibrium states) at $\dot{u}=0$, $u=0$, -1, and -2, which will be called the right, central, and left fixed points, respec-

Contributed by the Applied Mechanics Division of THE AMERICAN SOCIETY OF MECHANICAL ENGINEERS for publication in the JOURNAL OF APPLIED MECHANICS.

Discussion on this paper should be addressed to the Editorial Department, ASME, United Engineering Center, 345 East 47th Street, New York, N.Y. 10017, and will be accepted until two months after final publication of the paper itself in the JOURNAL OF APPLIED MECHANICS. Manuscript received by the ASME Applied Mechanics Division, September 21, 1988; final revision, January 31, 1989.

Copyright © 1989 by ASME

Downloaded 03 May 2010 to 171.66.16.31. Redistribution subject to ASME license or copyright; see http://www.asme.org/terms/Terms_Use.cfm

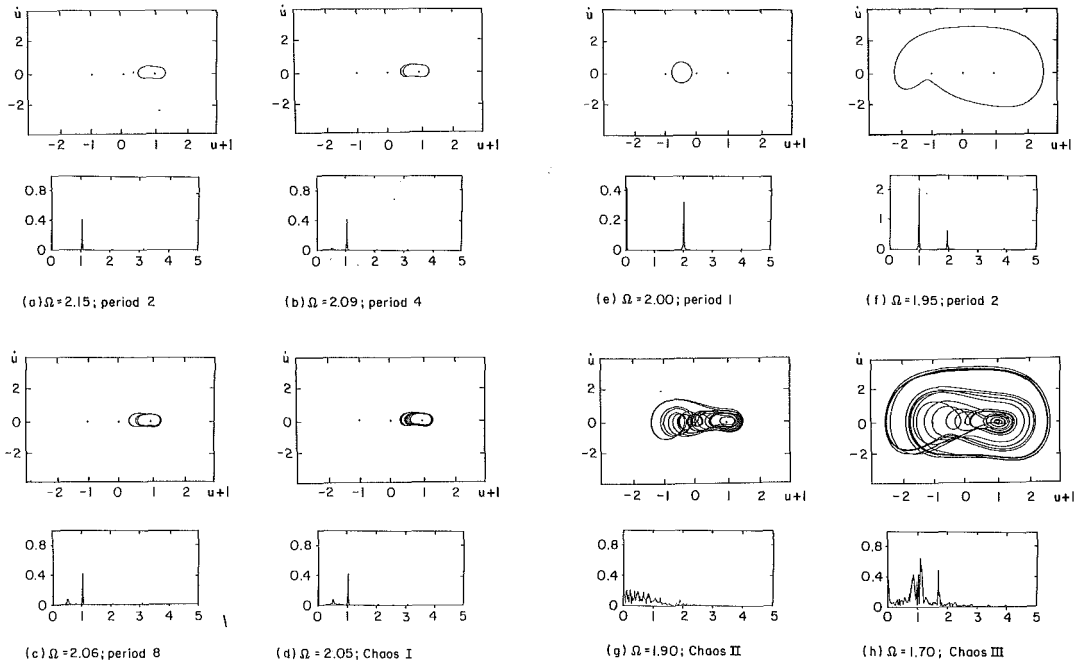


Fig. 1 Phase plane portraits and power spectra for $P = 0.9$ and various values of Ω; $x = u + 1$

tively. The outer ones are stable and the central one is unstable. Defining $x = u + 1$, so $x = 0$ at the central fixed point, (2) with parameters (3) can be written in terms of x as

$$\ddot{x}(t) + 0.2\dot{x}(t) - \frac{1}{2}(1 - 2P\cos\Omega t)x(t) + \frac{1}{2}x^3(t) = P\cos\Omega t. \tag{5}$$

If the parametric excitation term is dropped from (5), the resulting equation has been studied extensively, in part with reference to forced motion of a buckled beam (e.g., see Holmes, 1979; Dowell and Pezeshki, 1986).

Large-time responses are obtained by integrating (5) with initial conditions $x(0) = 1.02$ and $\dot{x}(0) = 0$, which is equivalent to solving (2) with parameters (3) and initial conditions (4). (Starting at $u(0) = \dot{u}(0) = 0$ would simply yield $u(t) \equiv 0$ and, hence, $u(0)$ is given a small initial value.) Some typical phase plane portraits and power spectra are depicted in Fig. 1, where the excitation amplitude is fixed at $P = 0.9$ and eight values of the excitation frequency are considered.

In Fig. 1(*a*), $\Omega = 2.15$ and the response, after transient behavior, settles into a limit cycle encircling the right fixed point ($u = 0$). The frequency of this large-time response is $\Omega/2$, as seen in its power spectrum. It is called a "period-2" motion, since its period is twice that of the excitation. A limit cycle such as that in Fig. 1(*a*) will be called a "right small orbit."

In Fig. 1(*b*), $\Omega = 2.09$ and the limit cycle has two loops and period 4. This change is called a "period-doubling bifurcation." The period is doubled again in Fig. 1(*c*), where $\Omega = 2.06$. When $\Omega = 2.05$, in Fig. 1(*d*), the response is chaotic rather than periodic. The trajectory remains close to the right fixed point, and this type of chaos will be called "Chaos I" here. The corresponding Poincaré map is shown in Fig. 2(*a*), where points are plotted in the phase plane during the large-time response at times nT, $T = 2\pi/\Omega$, for integer values n in a certain range. It indicates that the response is not periodic.

In Fig. 1(*e*), with $\Omega = 2.00$, the phase plane portrait involves a limit cycle lying between the left and central fixed points. Its period is the same as that of the excitation. This unusual limit cycle will be studied in a later section. In Fig. 1(*f*), $\Omega = 1.95$ and there is a large period-2 limit cycle encircling all three

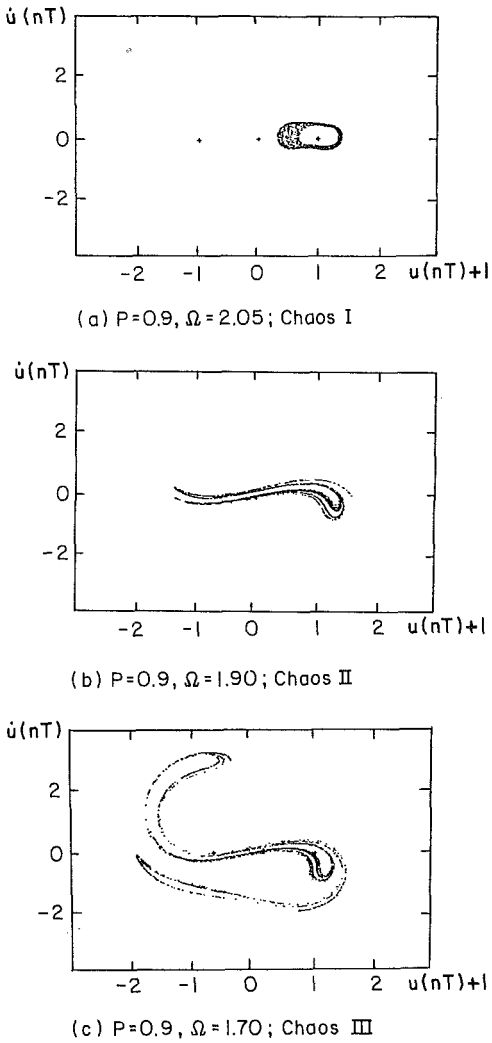


Fig. 2 Poincaré maps corresponding to Fig. 1(*d*), (*g*), and (*h*); $x = u + 1$

Downloaded 03 May 2010 to 171.66.16.31. Redistribution subject to ASME license or copyright; see http://www.asme.org/terms/Terms_Use.cfm

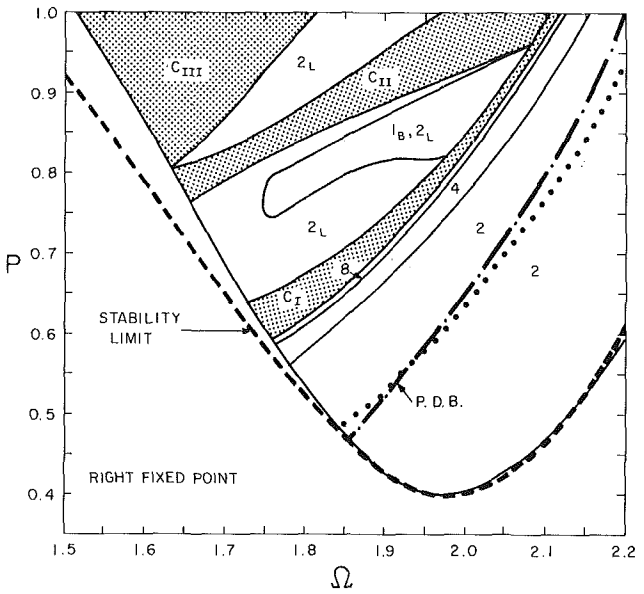


Fig. 3 Regions of different types of large-time response in (Ω, *P*) plane; P.D.B. denotes approximate conditions for period-doubling bifurcation based on (24) (dash-dot curve) and (25) (dotted curve)

fixed points. Chaotic behavior is seen again in Fig. 1(*g*) and Fig. 1(*h*), where $\Omega = 1.90$ and $\Omega = 1.70$, respectively. The corresponding Poincaré maps are presented in Fig. 2(*b*) and Fig. 2(c). The type of chaos in Fig. 1(*g*), which extends beyond the outer fixed points but does not have very large amplitude (e.g., in comparison to the limit cycle in Fig. 1(*f*)), will be called "Chaos II." Large-amplitude chaotic motion, as in Fig. 1(*h*), will be called "Chaos III."

Large-time responses were determined for many combinations of Ω and *P* in the ranges $1.5 \le \Omega \le 2.2$ and $0 < P \le 1.0$. The results are presented in Fig. 3 (where $0.35 \le P \le 1.0$), with solid curves separating regions having different types of behavior. If *P* is sufficiently small, the motion approaches the right fixed point (i.e., $u(t) \to 0$). The boundary of this bottom region has a minimum near $(\Omega, P) = (1.96, 0.40)$. In the regions labeled 2, 4, and 8, the responses are similar to those illustrated in Fig. 1(*a*), (*b*), and (*c*), respectively. The symbols C_I, C_{II}, and C_{III} denote Chaos I, II, and III, respectively, as in Fig. 1(*d*), (*g*), and (*h*). Large motions of period 2, as in Fig. 1(*f*), are indicated by 2_L. Finally, the symbol 1_B refers to a limit cycle of period 1 which lies between the left and central fixed points, as in Fig. 1(*e*). In the region which contains both symbols 2_L and 1_B, these two types of limit cycles are interspersed and a simple boundary separating them was not obtained.

Some comparisons can be made between these results, based on (2), and the previous studies of the parametrically-forced pendulum, based on (1) with $k_1 \ge 0$ and $k_2 > 0$. The fixed points of (1) are at $\dot{\psi} = 0$, $\psi = \pm n\pi$, $n = 0, 1, 2, \ldots$, and "rotating motions" (ψ increasing monotonically) may exist. As k_3 was increased, period-doubling bifurcations occurred, followed by chaos. A local type of chaos was mentioned in Arneodo et al. (1983) and was discussed in Leven et al. (1985) where a Coulomb damping term was added to (1). The nonrotating limit cycles began with period 2 as k_3 was increased from zero, while the rotating motions first appeared with period 1. Small "windows" of periodic solutions were sometimes found in the chaotic regime (e.g., Leven et al., 1985). Due to the rotating motions the response of (1), as described in the references, is quite different from that of (2), although some characteristics (such as the period-doubling route to chaos) are similar.

It would be useful to be able to approximate some of the curves in Fig. 3 by analytical means. In particular, a "lower bound" on the regions of chaos would be of interest. This will be examined in the following sections. In addition, an analysis of the amplitudes of some of the types of limit cycles will be carried out.

Stability of Right Fixed Point

Inside the bottom region of Fig. 3, the right fixed point is asymptotically stable. In order to determine when it loses stability, small motions about it are considered. Writing $u(t) = \xi(t)$, where $\xi(t)$ is small, and linearizing (2), one obtains

$$\ddot{\xi}(t) + 2c\dot{\xi}(t) + (\omega_0^2 + P\cos\Omega t)\xi(t) = 0. \tag{6}$$

From Floquet theory, one expects $\xi(t)$ to have period 2 at the stability limit in the neighborhood of $\Omega = 2\omega_0$. A first approximate solution can be obtained by assuming

$$\xi(t) = e^{\mu t}[b_{1c}\cos(\Omega t/2) + b_{1s}\sin(\Omega t/2)] \tag{7}$$

with $\mu > 0$ in the region of instability. Putting $\mu = 0$ and applying the method of harmonic balance, one obtains the relation

$$\Delta \equiv (\Omega^2 - 4\omega_0^2)^2 + 16c^2\Omega^2 - 4P^2 = 0 \tag{8}$$

to be satisfied at the stability limit, with $\Delta < 0$ when $\mu > 0$ (Hayashi, 1985). Equation (8) is plotted as a dashed curve in Fig. 3 with $\omega_0 = 1$, $c = 0.1$. This approximate stability limit for the right fixed point can be used as an approximate boundary of the region in which the response decays and $u(t) \to 0$.

Right Small Orbit

In this section small period-2 limit cycles, such as the one in Fig. 1(*a*), will be examined. A perturbation technique will be applied to (2) in the neighborhood of $\Omega = 2\omega_0$ to obtain an approximate solution for $u(t)$.

Let

$$(\Omega/2)^2 = \omega_0^2 + \epsilon^2\sigma, \quad c = \epsilon^2\tilde{c}, \quad P = \epsilon^2 R, \quad \alpha = \epsilon\tilde{\alpha}, \quad \beta = \epsilon^2\tilde{\beta}, \tag{9}$$

where ϵ is a small parameter and σ is a detuning parameter. (Alternatively, one could let $u = \epsilon v$ and not define α and β.) Equation (2) becomes

$$\ddot{u} + (\Omega/2)^2 u + \epsilon\tilde{\alpha}u^2 + \epsilon^2(\tilde{\beta}u^3 + Ru\cos\Omega t + 2\tilde{c}\dot{u} - \sigma u) = 0. \tag{10}$$

Next, $u(t)$ is written in the form

$$u(t) = u_0(t) + \epsilon u_1(t) + \epsilon^2 u_2(t) + \ldots. \tag{11}$$

Expansion (11) is substituted into (10) and the coefficients of ϵ^0, ϵ^1, and ϵ^2 are set equal to zero. This yields the equations

$$\ddot{u}_0 + (\Omega/2)^2 u_0 = 0, \tag{12}$$

$$\ddot{u}_1 + (\Omega/2)^2 u_1 = -\tilde{\alpha}u_0^2, \tag{13}$$

$$\ddot{u}_2 + (\Omega/2)^2 u_2 = -2\tilde{\alpha}u_0 u_1 - \tilde{\beta}u_0^3 - Ru_0\cos\Omega t - 2\tilde{c}\dot{u}_0 + \sigma u_0. \tag{14}$$

The solution of (12) can be written as

$$u_0(t) = a\cos\theta(t), \quad \theta(t) = (\Omega/2)t + \phi. \tag{15}$$

Then (13) has the solution

$$u_1(t) = -\alpha a^2[3 - \cos 2\theta(t)]/6. \tag{16}$$

Equations (15) and (16) are substituted into (14), assuming b and ϕ are independent of t. Trigonometric identities are utilized. The coefficients of $\sin\theta$ and $\cos\theta$ on the right-hand side of the resulting equation are then set equal to zero, in order to avoid secular terms. After using the values of α and β from (3), one obtains

$$a^2 = (4 - \Omega^2 \pm 2\sqrt{P^2 - 4c^2\Omega^2})/6, \tag{17}$$

$$\sin 2\phi = 2c\Omega/P, \quad \cos 2\phi = (\Omega^2 + 6a^2 - 4)/(2P), \tag{18}$$

and, from (11), (15), and (16),

$$u(t) = a\cos\theta(t) - (3/4)\epsilon a^2 + (1/4)\epsilon a^2\cos 2\theta(t) + 0(\epsilon^2) \tag{19}$$

Downloaded 03 May 2010 to 171.66.16.31. Redistribution subject to ASME license or copyright; see http://www.asme.org/terms/Terms_Use.cfm

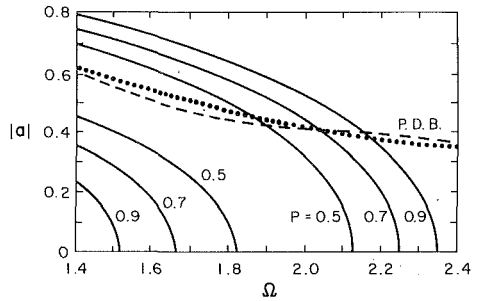


Fig. 4 Amplitude parameter in approximate period-2 response (19); P.D.B. denotes approximate conditions for period-doubling bifurcation based on (24) (dashed curve) and (25) (dotted curve)

where θ is defined in (15). Equation (19) furnishes an approximate solution for the period-2 motion associated with the right small orbit.

The absolute value $|a|$ of the response amplitude parameter in (19) is plotted as a function of the excitation frequency Ω in Fig. 4 for fixed excitation amplitudes $P = 0.5$, 0.7, and 0.9. When $\Omega = 2.15$, the upper branch for $P = 0.9$ yields $|a| = 0.40$, which agrees well with the amplitude 0.41 of the spike on the response spectrum in Fig. 1(*a*) at frequency $\Omega/2$.

The lower branches in Fig. 4 exhibit the classical (first-order) instability which is usually obtained by perturbation methods (Nayfeh and Mook, 1979, p. 347). The upper branch does not exhibit this type of instability. Other types of instability are considered in the following section.

Period-Doubling Bifurcations

In order to study higher-order instabilities, a variation $\eta(t)$ is added to the solution. Let

$$x(t) = 1 + u(t) + \eta(t) \tag{20}$$

where $u(t)$ is given by (19) and $\eta(t)$ is small. This form of $x(t)$ is substituted into (5) and the resulting equation is linearized in $\eta(t)$. One obtains the variational equation

$$\ddot{\eta}(t) + 0.2\dot{\eta}(t) + \left[\lambda_0 + \gamma_2 \sin 2\theta(t) + \sum_{j=1}^{4} \lambda_j \cos j\theta(t)\right]\eta(t) = 0 \tag{21}$$

where

$$\lambda_0 = 1 - (3/2)a^2 + (57/64)a^4, \quad \lambda_1 = 3a - (15/8)a^3,$$
$$\lambda_2 = (3/2)a^2 - (9/16)a^4 + P\cos 2\phi, \quad \lambda_3 = (3/8)a^3, \tag{22}$$
$$\lambda_4 = (3/64)a^4, \quad \gamma_2 = P\sin 2\phi,$$

$\theta(t)$ is defined in (15), and ϕ, a, and P satisfy (17) and (18). Equation (21) is a form of Hill's equation (Hayashi, 1985), and the period of the excitation in (21) is the same as the period of the solution $u(t)$ under investigation, i.e., $2T$ where $T = 2\pi/\Omega$.

To determine a higher-order instability, Floquet theory is applied. A solution of (21) is sought in the form

$$\eta(t) = e^{\mu t}\Phi(t) = e^{\mu t}\Phi(t + 4T)$$
$$= e^{\mu t} \sum_{k=1,3,5,\ldots}^{\infty} d_k \cos[(k\Omega t/4) + \delta_k]. \tag{23}$$

When $\mu > 0$, this type of solution leads to a growth of harmonic components with period $4T$ (i.e., twice the period of the solution u), and thus may lead to period-doubling bifurcation (Hayashi, 1985; Szemplińska-Stupnicka, 1987).

For an approximate solution, at the stability limit ($\mu = 0$), the first two terms of the expansion (23) are considered, written as

$$\eta(t) = d_{1c}\cos(\Omega t/4) + d_{1s}\sin(\Omega t/4) + d_{3c}\cos(3\Omega t/4) + d_{3s}\sin(3\Omega t/4). \tag{24}$$

Equation (24) is substituted into (21) and the method of harmonic balance is applied. This results in combinations of Ω, a, and P which are plotted as curves labeled P.D.B. in Fig. 3 (dash-dot) and Fig. 4 (dashed).

The dash-dot curve in Fig. 3 gives a rough approximation of the solid transition curve from period-2 to period-4 responses which was found from numerical integration of (2) with (3) and (4). Apparently more terms must be used in the expansion (23), leading to greater computational complexity, if a better agreement is desired. On the other hand, one can obtain a simple analytical approximation for the occurrence of period-doubling bifurcations by letting $d_{1s} = d_{3s} = 0$ in (24), which means the damping term in (21) is neglected. The method of harmonic balance then yields

$$\Omega^2 = 4(G \pm \sqrt{G^2 - J}) \tag{25}$$

where

$$G = -(20\lambda_0 + 17\lambda_1 + \lambda_3 + 8\lambda_5)/7$$
$$J = 4[(\lambda_1 + \lambda_5)^2 - (2\lambda_0 + \lambda_1)(2\lambda_0 + \lambda_3)]/7, \tag{26}$$
$$\lambda_5 = (9/2)a^2 - (9/16)a^4 - 2,$$

and λ_0, λ_1, and λ_3 are defined in (22). Equation (25), along with (17), leads to the dotted curves in Figs. 3 and 4. They are quite close to the curves based on the full expression (24).

Consider the V-shaped region in Fig. 3 lying above the dashed curve, obtained from (8), and the dash-dot or dotted curve. It is expected that chaos and other "strange" behavior will not occur below this region. Hence, the "V" formed by these curves furnishes a "lower bound" for chaotic behavior. This is similar to results for systems with external excitation presented by Rudowski and Szemplińska-Stupnicka (1987) and Szemplińska-Stupnicka (1988), although in those cases period-1 motions exist below the V-shaped region.

In Fig. 4, the response amplitude is associated with the approximate response (19). For sufficiently low values of $|a|$, the upper branches in Fig. 4 are stable. The dashed curve and the dotted curve give approximations to values of $|a|$ at which the period-2 motion becomes unstable and bifurcates into a period-4 motion.

Period-1 Limit Cycle

For one-degree-of-freedom systems such as (2), limit cycles usually encircle one or more fixed points in the phase plane. In Fig. 1(*e*), however, the limit cycle lies between the left and central fixed points. This behavior is particularly interesting and will be analyzed now.

The power spectrum in Fig. 1(*e*) exhibits a constant component and a component with the frequency of the excitation. Thus the corresponding motion $x(t)$ can be approximated by the expression

$$x(t) = A_0 + A_1\cos(\Omega t + \zeta) \tag{27}$$

where $-1 < x < 0$ for the responses under consideration. Equation (27) is substituted into (5) and the method of harmonic balance is applied. This results in the three equations

$$0.2\Omega A_1 + P(1 - A_0)\sin\zeta = 0, \tag{28}$$
$$(2A_0^2 + 3A_1^2 - 2)A_0 + 2PA_1\cos\zeta = 0, \tag{29}$$
$$(12A_0^2 + 3A_1^2 - 8\Omega^2 - 4)A_1 + 8P(A_0 - 1)\cos\zeta = 0. \tag{30}$$

For $P = 0.8$, 0.9, and 1.0, solutions of (28)–(30) for A_0 and A_1 are plotted in Fig. 5 as functions of Ω. The amplitude A_0 is negative, and the solid curves give $-A_0$.

For these values of P, one sees in Fig. 5 that solutions of (28)–(30) exist if Ω is larger than 1.76, 1.96, and 2.15, respectively. The first two of these (Ω, P) combinations lie on the up-

Downloaded 03 May 2010 to 171.66.16.31. Redistribution subject to ASME license or copyright; see http://www.asme.org/terms/Terms_Use.cfm

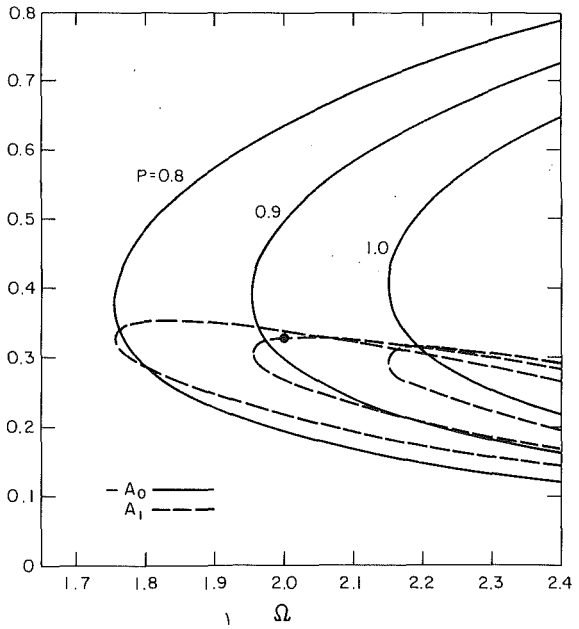


Fig. 5 Amplitudes in approximate period-1 response (27)

per boundary of the region denoted "1_B, 2_L" in Fig. 3. When this type of limit cycle was found in the direct numerical integration of (5), such as in Fig. 1(*e*), its response spectrum possessed amplitudes at frequencies zero and Ω which agree well with values on the upper branches of the $-A_0$ and A_1 curves in Fig. 5. One such value from Fig. 1(*e*), $A_1 = 0.33$ at $P = 0.9$ and $\Omega = 2.00$, is shown as a dot in Fig. 5. (Of course, the existence of such a stable limit cycle solution to (5) does not imply that the motion will approach it; that depends on whether or not the initial conditions are in the domain of attraction of that solution.)

Concluding Remarks

A one-degree-of-freedom system, governed by (2) and (3), has been considered. The equation of motion (2) contains a parametric excitation with amplitude P and frequency Ω which is assumed to be in the neighborhood of $2\omega_0$, where ω_0 is the natural frequency of the system. Linear viscous damping and quadratic and cubic nonlinearities in the stiffness are also included in (2). As described in the Appendix, the system can model a shallow arch or a mechanism subjected to special combinations of axial and transverse loads. These systems have two stable equilibrium states (fixed points) and an intermediate unstable one. Motions beginning near the right fixed point in the phase plane have been investigated here.

Depending on the excitation amplitude and frequency, various types of large-time responses are possible, as illustrated in Figs. 1–3. Three types of chaotic behavior have been described (see Fig. 1(*d*), (*g*), and (*h*), and Fig. 2). In type I, there is no "snap-through" to the left fixed point. In types II and III, the motion passes back and forth between the neighborhoods of the stable fixed points, with much larger amplitudes occurring in type III than in type II.

Approximate analytical methods have been utilized to examine some of the responses and their stability. The stability limit for the right fixed point gives an indication as to when the motions decay (dashed curve in Fig. 3). A theoretical lower bound on chaotic behavior in Fig. 3 is furnished by the V-shaped curve whose left side is the stability limit given by (8) and whose right side is the dash-dot curve (or, for a simple analytical result, the dotted curve determined from (17) and (25)). It is surprising that such a good lower bound can be obtained from such low-order approximations and from such simple analytical formulas as (8), (17), and (25).

Critical dynamic loads for curved or buckled structures are normally defined as the lowest loads at which snap-through occurs. For harmonic loading, the locus of these critical loads in the (Ω, P) plane (Plaut and Hsieh, 1985) tends to give another lower bound for chaos. However, chaos of type I may occur before the system exhibits motions past the central fixed point, and therefore this lower bound may not always be valid.

The type of limit cycle seen in Fig. 1(*e*) and denoted 1_B in Fig. 3 has been analyzed. It is the only period-1 large-time response seen in the numerical integration results in Fig. 3, and is unusual because it does not encircle any fixed point. Other period-1 responses would occur under different initial conditions. For example, if the excitation amplitude P is small and the system begins near the left fixed point, the large-time response is a small orbit encircling that point with period 1. This is understandable since the equation of motion about that point contains both parametric and external excitations, as in (5). Attention here, however, has been focused on the parametrically-excited system (2) with small initial conditions (4). Large motions of this system have not been studied extensively before, and it is seen that they exhibit interesting behavior which can be quite different from that of externally-excited systems.

Acknowledgment

This research was carried out while the first author was a Visiting Professor at Virginia Tech. The second author was supported by the U.S. Army Research Office under Grant No. DAAL03-87-K-0040.

References

Arneodo, A., et al., 1983, "On the Observation of an Uncompleted Cascade in a Rayleigh-Bénard Experiment," *Physica D*, Vol. 6D, pp. 385–392.

Dowell, E. H., and Pezeshki, C., 1986, "On the Understanding of Chaos in Duffing's Equation Including a Comparison with Experiment," ASME Journal of Applied Mechanics, Vol. 53, pp. 5–9.

Eckmann, J.-P., 1983, "Routes to Chaos with Special Emphasis on Period Doubling," *Chaotic Behavior of Deterministic Systems*, G. Iooss, R. H. G. Helleman, and R. Stora, eds., North-Holland, Amsterdam, pp. 453–510.

Fung, Y. C., and Kaplan, A., 1952, "Buckling of Low Arches or Curved Beams of Small Curvature," U.S. National Advisory Committee for Aeronautics, Technical Note 2840.

Gell, Y., and Nakach, R., 1986, "Route to Chaos in a Nonlinear Conservative Oscillatory System," *Physical Review A*, Vol. 34, pp. 4276–4285.

Gitterman, M., 1987, "Parametric Resonance in Magnetically (Electrically) Anisotropic Systems," *Physical Review A*, Vol. 35, pp. 421–424.

Hayashi, C., 1985, *Nonlinear Oscillations in Physical Systems*, Princeton University Press, Princeton, N.J.

Holmes, P., 1979, "A Nonlinear Oscillator with a Strange Attractor," *Philosophical Transactions of the Royal Society of London*, Series A, Vol. 292, pp. 419–448.

Holmes, P., and Moon, F. C., 1983, "Strange Attractors and Chaos in Nonlinear Mechanics," ASME Journal of Applied Mechanics, Vol. 50, pp. 1021–1032.

Koch, B. P., and Leven, R. W., 1985, "Subharmonic and Homoclinic Bifurcations in a Parametrically Forced Pendulum," *Physica D*, Vol. 16D, pp. 1–13.

Koch, B. P., Leven, R. W., Pompe, B., and Wilke, C., 1983, "Experimental Evidence for Chaotic Behaviour of a Parametrically Forced Pendulum," *Physics Letters*, Vol. 96A, pp. 219–224.

Leven, R. W., and Koch, B. P., 1981, "Chaotic Behaviour of a Parametrically Excited Damped Pendulum," *Physics Letters*, Vol. 86A, pp. 71–74.

Leven, R. W., Pompe, B., Wilke, C., and Koch, B. P., 1985, "Experiments on Periodic and Chaotic Motions of a Parametrically Forced Pendulum," *Physica D*, Vol. 16D, pp. 371–384.

McLaughlin, J. B., 1981, "Period-Doubling Bifurcations and Chaotic Motion for a Parametrically Forced Pendulum," *Journal of Statistical Physics*, Vol. 24, pp. 371–388.

Nayfeh, A. H., and Mook, D. T., 1979, *Nonlinear Oscillations*, John Wiley and Sons, New York.

Plaut, R. H., and Hsieh, J.-C., 1985, "Oscillations and Instability of a Shallow Arch Under Two-Frequency Excitation," *Journal of Sound and Vibration*, Vol. 102, pp. 189–201.

Plaut, R. H., and Hsieh, J.-C., 1987, "Chaos in a Mechanism with Time Delays Under Parametric and External Excitation," *Journal of Sound and Vibration*, Vol. 114, pp. 73–90.

Pompe, B., and Leven, R. W., 1986, "Transinformation of Chaotic Systems," *Physica Scripta*, Vol. 34, pp. 8–13.

Downloaded 03 May 2010 to 171.66.16.31. Redistribution subject to ASME license or copyright; see http://www.asme.org/terms/Terms_Use.cfm

Rudowski, J., and Szemplińska-Stupnicka, W., 1987, "On an Approximate Criterion for Chaotic Motion in a Model of a Buckled Beam," *Ingenieur-Archiv*, Vol. 57, pp. 243–255.

Szemplińska-Stupnicka, W., 1987, "Secondary Resonances and Approximate Models of Routes to Chaotic Motion in Non-Linear Oscillators," *Journal of Sound and Vibration*, Vol. 113, pp. 155–172.

Szemplińska-Stupnicka, W., 1988, "The Refined Approximate Criterion for Chaos in a Two-State Mechanical System," *Ingenieur-Archiv*, Vol. 58, pp. 354–366.

Zavodney, L. D., Nayfeh, A. H., and Sanchez, N. E., 1989, "The Response of a Single-Degree-of-Freedom System with Quadratic and Cubic Nonlinearities to a Principal Parametric Resonance," *Journal of Sound and Vibration*, Vol. 129, pp. 417–442.

APPENDIX

First, consider the shallow elastic arch depicted in Fig. 6(*a*). The ends ($X = 0, L$) are simply supported, with the right end attached to a horizontal spring with stiffness coefficient k and allowed to move horizontally. The initial thrust is H_0 and the equilibrium configuration is $Y_0(X)$, while E denotes the modulus of elasticity, A is the cross-sectional area, I is the moment of inertia, r is the radius of gyration $\sqrt{I/A}$, m is the mass per unit length, and C is a damping coefficient.

Two dynamic loads are applied, as shown in Fig. 6(*b*): $\bar{Q}(X, \bar{t})$ is a distributed vertical load and $\bar{P}(\bar{t})$ is a horizontal load at the right support, with $\bar{t}$ denoting time. The configuration at time $\bar{t}$ is $Y(X, \bar{t})$. Define the nondimensional quantities

$$x = X/L,\ y = Y/(2r),\ y_0 = Y_0/(2r),\ t = (\bar{t}/L^2)\sqrt{EI/m},$$
$$h_0 = H_0L^2/(EI),\ p = \bar{P}L^2/(EI),\ q = \bar{Q}L^4/(2EIr),$$
$$c = CL^2/\sqrt{EIm},\ \gamma = k/[k + (EA/L)]. \tag{A1}$$

The equation of motion is given by

$$\frac{\partial^2 y}{\partial t^2} + 2c\frac{\partial y}{\partial t} + \frac{\partial^4 y}{\partial x^4} - \frac{d^4 y_0}{dx^4} + (p + h_0)\frac{\partial^2 y}{\partial x^2} - h_0\frac{d^2 y_0}{dx^2}$$
$$+ 2\gamma\frac{\partial^2 y}{\partial x^2}\int_0^1 \left[\left(\frac{dy_0}{dx}\right)^2 - \left(\frac{\partial y}{\partial x}\right)^2\right]dx = -q \tag{A2}$$

(Fung and Kaplan, 1952).

Assume that

$$y_0(x) = \lambda\sin\pi x,\ q(x,t) = \bar{q}(t)\sin\pi x \tag{A3}$$

and write the motion as

$$y(x,t) = [\lambda + u(t)]\sin\pi x. \tag{A4}$$

Substitution of (*A*3) and (*A*4) into (*A*2) leads to

$$\ddot{u} + 2c\dot{u} + \pi^2(\pi^2 + 2\pi^2\lambda^2\gamma - h_0 - p)u + 3\pi^4\gamma\lambda u^2 + \pi^4\gamma u^3$$
$$= \pi^2\lambda p - \bar{q} \tag{A5}$$

after dividing by $\sin \pi x$. Equation (2) with parameters (3) is then obtained for the special case

$$h_0 = \pi^2,\quad \lambda = 1,\quad \gamma = 1/(2\pi^4),\quad c = 0.1,$$
$$p(t) = -(P/\pi^2)\cos\Omega t,\quad \bar{q}(t) = -P\cos\Omega t. \tag{A6}$$

A second example is provided by the mechanism in Fig. 7. It consists of two rigid bars with length L, a mass M at the central joint, a nonlinear (hardening) spring with linear stiffness coefficient K_1 and cubic coefficient K_3, and a dashpot with damping coefficient C. A horizontal load Q_0, larger than the buckling load $K_1L/2$, is applied, and then horizontal and vertical dynamic loads $\bar{Q}\cos\bar{\Omega}\bar{t}$ and $\bar{P}\cos\bar{\Omega}\bar{t}$ are applied as shown in Fig. 7(*b*). The vertical motion of the mass from the buckled

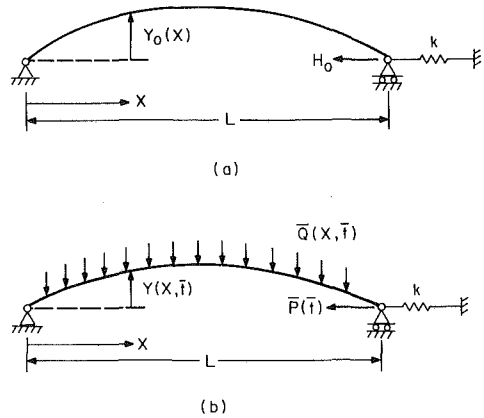


Fig. 6 Geometry of arch

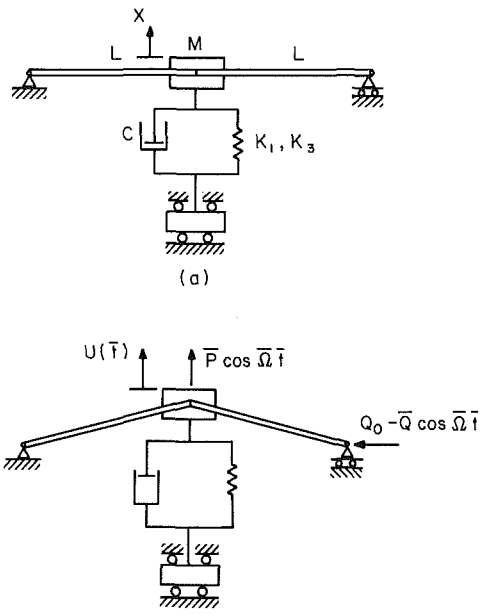


Fig. 7 Geometry of mechanism

equilibrium state is denoted $U(\bar{t})$, and it is assumed that the vertical deflection $X(\bar{t})$ from the unloaded horizontal equilibrium state is small enough so that $L^2 - X^2 \approx L^2$.

Define

$$D^2 = (2Q_0 - K_1L)/(K_3L),\ F^2 = ML/(4Q_0 - 2K_1L) \tag{A7}$$

and the nondimensional quantities

$$u = U/D,\ t = \bar{t}/F,\ c = CF/M,\ P = \bar{P}F^2/(MD),$$
$$Q = 2\bar{Q}F^2/(ML),\ \Omega = \bar{\Omega}F. \tag{A8}$$

If $Q = P$, the nondimensional equation of motion for $u(t)$ is given by (2) with parameters (3) (Plaut and Hsieh, 1987). (If Q and P were not equal, the equation of motion for $u(t)$ would include both parametric and external excitations.)

Downloaded 03 May 2010 to 171.66.16.31. Redistribution subject to ASME license or copyright; see http://www.asme.org/terms/Terms_Use.cfm

Probabilistic Torsional Vibration Analysis of a Marine Diesel Engine Shafting System: The Level Crossing Problem

Efstratios Nikolaidis[1]
Assistant Professor,
Department of Aerospace
and Ocean Engineering,
Virginia Polytechnic Institute
and State University,
Blacksburg, Va. 24061
Assoc. Mem. ASME

Anastassios N. Perakis
Associate Professor.

Michael G. Parsons
Professor and Chairman.

Department of Naval Architecture
and Marine Engineering,
The University of Michigan,
Ann Arbor, Mich. 48109

A probabilistic approach to the torsional vibration problem of a marine diesel engine shafting system has been developed. In this analysis, the shafting shear stress is found to be a Gaussian, harmonizable cyclostationary process with a harmonic series representation consisting of two complex conjugate components. In this paper, the level crossing problem for this stress process is studied. Two methods for estimating the probability that the stress exceeds a specified threshold at least once over a given time interval are presented. In the first method, a local maximum of the process is approximated by the value of the corresponding envelope at the time of occurrence of this maximum. A Markov-type condition is assumed to hold for the local maxima. The second method assumes that the maximum of the process over a reasonable number of cycles is approximately equal to that of the envelope process. The envelope crossings are assumed to constitute a Poisson process. The two methods are applied to estimate the upcrossing probability in various cases. The results of both approaches are found to be in good agreement with those from Monte Carlo simulation.

1 Introduction and Background

In previous works of the authors, a probabilistic torsional vibration analysis of a marine diesel shafting system has been introduced (Nikolaidis et al., 1987, 1985). An important feature of that problem is that the excitation statistics are varying with time. For example, when viewed on a time scale shorter than the combustion cycle time, the mean and the standard deviation of the gas torque are higher at the time of combustion of the air-fuel mixture than at any other time within the combustion cycle. Therefore, the excitation is a nonstationary process. A statistical model for the cylinder excitation has been developed, taking into account the torque variability from cylinder to cylinder and from cycle to cycle. The cylinder gas torques are modeled as amplitude-modulated processes where the amplitudes are jointly Gaussian stationary processes.

With this type of excitation, the vibratory shear stress at a resonance, $r(t)$, will be a Gaussian process of the form:

$$r(t) = X(t)\cos p\omega t + Y(t)\sin p\omega t \tag{1}$$

where $X(t)$ and $Y(t)$ are Gaussian stationary processes with known statistics, ω is the angular frequency of rotation of the shaft, and p is the resonant order of the excitation Fourier representation. The product $p\omega$ is equal to the resonant natural frequency of the shafting system ω_0. Finally, the frequency content of $X(t)$ and $Y(t)$ is low compared to ω_0 (Nikolaidis et al., 1987, 1985).

An important property of process $r(t)$ is the periodic character of its statistics. For example, the moments of $r(t)$ are periodic functions in time with fundamental frequency $p\omega$. In signal processing, the term "cyclostationary" has been adopted to describe processes whose statistics are periodic in time. A number of physical processes are cyclostationary. An example is the response of a structural member, such as a blade of a turbine or a marine propeller, rotating in a nonhomogeneous random field.

A cyclostationary process, when viewed over many cycles, might be approximated as a stationary process. However, some important properties, such as those related with the crossing of a threshold, are significantly different than those of a stationary process. Furthermore, the substitution of a cyclostationary process, with an equivalent stationary one whose second moment equals the temporal average of the

[1]Formerly at The Department of Naval Architecture and Marine Engineering, The University of Michigan, Ann Arbor, Mich. 48109.

Contributed by the Applied Mechanics Division of THE AMERICAN SOCIETY OF MECHANICAL ENGINEERS for presentation at the Winter Annual Meeting, San Francisco, Calif., December 10–15, 1989.

Discussion on this paper should be addressed to the Editorial Department, ASME, United Engineering Center, 345 East 47th Street, New York, N.Y. 10017, and will be accepted until two months after final publication of the paper itself in the JOURNAL OF APPLIED MECHANICS. Manuscript received by the ASME Applied Mechanics Division, November 21, 1986; final revision, November 16, 1988.

Paper No. 89-WA/APM-27.

Copyright © 1989 by ASME

Downloaded 03 May 2010 to 171.66.16.31. Redistribution subject to ASME license or copyright; see http://www.asme.org/terms/Terms_Use.cfm

original process, could lead to serious errors when solving the first passage problem.

A random process is called cyclostationary in the wide sense if its mean and its autocorrelation function, $R(t+\tau,t)$, are periodic in time (Franks, 1969, Gardner and Franks, 1975, Ogura, 1971, and Papoulis, 1983). The autocorrelation function, $R(t_1,t_2)$, is called "harmonizable" if there exists a covariance $\gamma(s,s')$ of bounded variation so that $R(t_1,t_2)$ can be represented as a Riemann-Stieltjes integral (Loeve, 1977),

$$R(t_1,t_2)=\int\int_{-\infty}^{+\infty}\exp\,(2\pi i(st_1-s't_2))dd'\gamma(s,s'). \qquad (2)$$

It can be shown that if the autocorrelation function of a cyclostationary random process, $r(t)$, with period T is harmonizable, the random process itself is called "harmonizable" and admits the harmonic representation,

$$r(t)=\sum_{n=0}^{+\infty}[X_n(t)\cos(\omega_0 nt)+Y_n(t)\sin(\omega_0 nt)], \qquad (3)$$

where $\omega_0=2\pi/T$ and $X_n(t)$ and $Y_n(t)$ are wide-sense jointly stationary (Ogura, 1971).

Process (1) is a special case of a general harmonizable cyclostationary process with $X_n(t)=Y_n(t)=0$ for any $n\neq p$. In the special case that (*a*) the means of $X_n(t)$ and $Y_n(t)$ are zero, (*b*) their autocorrelation functions are equal, and (*c*) the cross-correlation of $X_n(t)$ and $Y_n(t)$ is an odd function, $r(t)$ is stationary (Papoulis, 1983).

The level crossings problem for a general random process remains unsolved. Some results are available for certain classes of random processes. A survey of these widely-scattered level crossing results was published by Blake and Lindsey (1973).

The classical work of Rice (1944–1945) has been used as a starting point for most studies related to the level crossing problem. Efforts have concentrated on determining the statistical character of quantities such as the local maxima and the average crossing rate of a given threshold by the process or its envelope (Rice, 1945; Cramer and Leadbetter, 1967; Ochi, 1973). The probability of an upcrossing in a given time period by a zero-mean, Gaussian stationary process has been estimated under the assumption that the maxima are independent (Ochi, 1973). An alternative approach, using the assumption that the crossings form a Poisson process, has also been employed to estimate the upcrossing probability (Coleman, 1959).

Most of the studies on the statistical prediction of the maxima of a random process assume that the maxima are statistically independent. The validity of this assumption is often questionable. An example is the case of a narrow-band random process, where the envelope of the maxima forms a curve that varies slowly with time. In this case, the maxima are highly correlated. In a number of studies, the correlation of the subsequent maxima is taken into account by assuming that they are subject to the Markov chain condition. This approach was first proposed for stationary processes by Yang and Shinozuka (1971 and 1972). In Ocean Engineering, this approach has been used by Ochi (1979) to evaluate the statistics of the maximum wave height and bending moment that a ship experiences over a given time period. The input random process involved in this problem, that is, the wave elevation at a given location, was assumed to be stationary and Gaussian.

The level crossing problem has also been studied for a few classes of nonstationary processes. Yang (1972a) proposed a definition for the envelope of a nonstationary process possessing an evolutionary power spectrum and developed various approaches to the level crossing problem. He found upper and lower bounds for the upcrossing probability. Among the approaches that Yang (1973) used, he found that one based on the Markov chain assumption for the process of the local maxima produced results in best agreement with those from Monte Carlo simulation. Krenk (1979) defined the notion of narrowbandedness for a nonstationary process; defined the envelope of a narrow-band, nonstationary process; and under this definition derived an approximation for the upcrossing probability for a narrow-band, nonstationary process. Krenk's definitions of the narrowbandedness and the envelope apply to a normalized process, defined as the difference between an arbitrary process and its expected value divided by its standard deviation. An implicit assumption in this definition is that the expected value and the standard deviation of the original process are changing slowly with time.

In this paper, we employ the Markov chain approximation to approach the level crossing problem for a cyclostationary process of the form of equation (1). This process does not possess an evolutionary spectrum. Therefore, the results reported by Yang (1973) cannot be applied directly here. More specifically, since the second moments of $X(t)$ and $Y(t)$ are not equal, the expression for the probability density function of the envelope of equation (1) is different from that of an evolutionary process (Yang, 1973).

Three cases are encountered in solving the level crossing problem for equation (1).

(*a*) The frequency content of the envelope of the process is small compared to the frequency $p\omega$ (the envelope is defined as the square root of the sum of the squares of $X(t)$ and $Y(t)$).

(*b*) $p\omega$ is in the range of the frequency content of the envelope.

(*c*) $p\omega$ is small compared to the frequency content of the envelope.

Here we study the crossing problem for Case (*a*), because the frequency content of the envelope of the shafting stress has been found to be low compared to the natural frequency of the system, $p\omega$ (Nikolaidis et al., 1985). Cases (*b*) and (*c*) are encountered when considering other problems, such as the response of turbine blades to turbulence-induced excitation. Solutions to the crossing problem in the last two cases are briefly discussed in Section 6 of this paper.

The approach developed in this paper enables us to estimate the probability of the event that the shafting stress exceeds a specified threshold within a given time interval. This event is called first excursion failure. Two methods are presented. The first is a Markovian approach to the level crossing problem, based on the approximation of a local maximum by the value of the envelope process at the time it occurs. This approximation is justified by proof that if frequency $p\omega$ is sufficiently large, a local maximum and the corresponding value of the envelope are almost identical with a high degree of certainty. A discrete time process with two states is defined. One state denoted "D" occurs when the value of the envelope is less than the threshold, while state "U" occurs when the value of the envelope exceeds the threshold. The process takes values at times 0, τ, 2τ, . . . where τ is the expected period between subsequent maxima. We derive an expression for the probability of upcrossing the threshold within a given time interval assuming that this discrete-time, two-state process is Markov.

The second approach is based on the assumption that the maximum of the process over a reasonable number of cycles is equal to the maximum of the envelope and that the envelope crossings constitute a Poisson process. This is equivalent to the assumption that the maxima of the envelope process are statistically independent. This is often more realistic than the assumption that the local maxima of the original process are independent. An expression for the expected upcrossing rate of the envelope process is derived and the upcrossing probability is calculated.

Another application area where a random process of the form of equation (1) occurs is underwater signal detection. The sum of signals propagating from the source to the receiver through independent paths subjected to narrow-band noise is

Downloaded 03 May 2010 to 171.66.16.31. Redistribution subject to ASME license or copyright; see http://www.asme.org/terms/Terms_Use.cfm

a narrow-band, multipath process (Mikhalevsky, 1982; Nikolaidis and Perakis, 1985). There is a certain phase relationship between the signals propagating through the independent paths. The narrow-band, multipath process is narrow-band cyclostationary as described by equation (1).

2 The Markov Approach for the Level Crossing Problem

Our problem is to derive an expression for the probability that random process, $r(t)$, exceeds a specified threshold, ρ_0, at least once during a time interval $[0,T_1]$. The assumptions of Section 1 hold for $r(t)$. Furthermore, we assume that $r(t)$ is twice differentiable.

According to Cramer (1967), the envelope $\rho(t)$ of a stationary random process is defined as the square root of the sum of the square of the process and its Hilbert transform. Yang (1972) extended this definition for the case of a process possessing an evolutionary spectrum using the equation:

$$\rho(t) = (r^2(t) + \hat{r}^2(t))^{1/2}, \tag{4}$$

where $\hat{r}(t)$ is the Hilbert transform of $r(t)$. Applying this definition to a cyclostationary process of the form of equation (1), the envelope of $r(t)$ is:

$$\rho(t) = (X^2(t) + Y^2(t))^{1/2}. \tag{5}$$

The local maxima of $r(t)$ can be approximated by the values of this envelope process $\rho(t)$ at the time the maxima occur. This is called the "envelope approximation." The first and second-order statistical properties of the envelope have already been derived (Mikhalevsky, 1982; Nikolaidis and Perakis, 1985).

The Markov approach is based on the envelope approximation. The probability that $r(t)$ exceeds the threshold ρ_0 is equal to the probability that at least one of its local maxima exceeds the threshold ρ_0. Let $t_1, t_2, \ldots$ be the times at which the local maxima of $r(t)$ occur. The upcrossing probability is assumed to equal the probability that at least one of the values of the envelope at the times $t_1, t_2, \ldots$ exceeds the threshold ρ_0. By using the results reported by Mikhalevsky (1982) and Nikolaidis and Perakis (1985) for the envelope statistics at one and two points in time, and by assuming that the local maxima are subject to a Markov-type condition, we can derive an expression for the upcrossing probability. Since $r(t)$ is narrow band, the time interval between two successive, local maxima is approximately constant. We will assume that $\tau = t_{k+1} - t_k$ is constant for all k. The expected period between successive local maxima is

$$\tau = 2\pi/p\omega, \tag{6}$$

and the expected number of maxima in time period T_1 is

$$\nu = T_1/\tau + 1. \tag{7}$$

Define a discrete-time, two-state process taking values at times $0, \tau, 2\tau, \ldots$. The first state is defined to exist when the value of the envelope does not exceed the threshold ρ_0, while the other exists when the value exceeds ρ_0. We assume that this process is Markov. Under these assumptions, the upcrossing probability is,

$$\begin{aligned} &P(\text{upcrossing in } [0,T_1]) \\ &\simeq P(\xi_0 > \rho_0) + P(\xi_1 > \rho_0 \mid \xi_0 \leqq \rho_0) P(\xi_0 \leqq \rho_0) \\ &+ P(\xi_2 > \rho_0 \mid \xi_1 \leqq \rho_0) P(\xi_1 \leqq \rho_0 \mid \xi_0 \leqq \rho_0) P(\xi_0 \leqq \rho_0) + \ldots \\ &+ P(\xi_{\nu-1} > \rho_0 \mid \xi_{\nu-2} \leqq \rho_0) P(\xi_{\nu-2} \leqq \rho_0 \mid \xi_{\nu-3} < \rho_0) \ldots \\ &P(\xi_1 \leqq \rho_0 \mid \xi_0 \leqq \rho_0) P(\xi_0 \leqq \rho_0), \end{aligned} \tag{8}$$

where ξ_i denotes the value of the ith maximum. Assuming that the local maxima are approximately equal to the envelope process evaluated at the time they occur, we obtain:

$$P(\xi_0 > \rho_0) = P(\rho > \rho_0) = 1 - \int_o^{\rho_0} f_{\rho_t}(\rho_1) d\rho_1 \text{ and}$$

$$P(\xi_i < \rho_0 \mid \xi_{i-1} < \rho_0) \simeq P(\rho(i\tau) < \rho_0 \mid \rho((i-1)\tau) < \rho_0) \tag{9}$$

$$= P(\rho(\tau) < \rho_0 \mid \rho(0) < \rho_0) = \frac{\int_o^{\rho_0} \int_o^{\rho_0} f_{\rho_{t+\tau},\rho_t}(\rho_1,\rho_2) d\rho_1 d\rho_2}{\int_o^{\rho_0} f_{\rho_t}(\rho_1) d\rho_1},$$

where $f_{\rho_t}(\rho_1)$ denotes the envelope PDF at ρ_1 and $f_{\rho_{t+\tau},\rho_t}(\rho_1,\rho_2)$ denotes the joint PDF of the envelope at two points in time (t and $t+\tau$). The last equality is true because the envelope process $\rho(t)$ is stationary and, therefore, its first-order PDF is independent of time and the second-order PDF of $\rho(t+\tau)$ and $\rho(t)$ depends on the time difference τ.

Using the following notation,

$$C_1 = \int_o^{\rho_0} f_{\rho_t}(\rho_1) d\rho_1$$

and

$$b_1 = \int_o^{\rho_0} \int_o^{\rho_0} f_{\rho_{t+\tau},\rho_t}(\rho_1,\rho_2) d\rho_1 d\rho_2 / \left(\int_o^{\rho_0} f_{\rho_t}(\rho_1) d\rho_1 \right),$$

equation (8) then gives

$$\begin{aligned} &P(\text{upcrossing in } [0,T_1]) \\ &= 1 - c_1 + (1-b_1)c_1 + (1-b_1)b_1 c_1 + \ldots \\ &+ (1-b_1)b_1^{\nu-2} c_1 = 1 - c_1 b_1^{\nu-1}. \end{aligned} \tag{10}$$

Equation (10) gives an estimate of the probability that random process, $r(t)$, exceeds the threshold, ρ_0, at least once during the time interval $[0,T_1]$.

Unfortunately, the integrations required to evaluate coefficients c_1 and b_1 cannot be performed analytically. Moreover, the first-order PDF of the envelope requires one numerical integration, and the second-order PDF requires two because the second moments of $X(t)$ and $Y(t)$ are not equal (Nikolaidis, 1985). Only in the stationary case, in which these moments are equal and the cross-correlation function of $X(t)$ and $Y(t)$ is odd, can these integrals be performed analytically and the expressions for b_1 and c_1 can be simplified (Yang, 1972a).

3 Expected Upcrossing Rate of a Given Threshold

In this section, an expression for the expected upcrossing rate of a given threshold ρ_0 by the envelope of the stress process $r(t)$ will be derived. For the limiting cases that $r(t)$ is stationary, the expression for the expected upcrossing rate reduces to the corresponding expression already existing in the literature.

The expected upcrossing rate of the threshold ρ_0 is given by:

$$\nu_{\rho_0}^+ = \int_o^{\infty} x f_{\rho,\dot{\rho}}(\rho_0, x) dx, \tag{11}$$

where $f_{\rho,\dot{\rho}}(\cdot,\cdot)$ is the joint PDF of the envelope and its derivative (Rice, 1944-1945). First, the PDF of the envelope and its derivative is derived from the PDF of the Gaussian random vector $(X(t), Y(t), \dot{X}(t), \dot{Y}(t))^T$. Then $\nu_{\rho_0}^+$ can be evaluated using equation (11). The final result is:

$$\nu_{\rho_0}^+ = \int_o^{2\pi} \left(\frac{\rho_0^2}{(2\pi)^{3/2} |\Lambda'|^{1/2} B'^{1/2} L'} \exp\left\{ -\frac{1}{2} F' + \frac{E'^2}{8B'} \right\} - \frac{\rho_0^2 M'}{4\pi |\Lambda'|^{1/2} B'^{1/2} L'^{3/2}} \right.$$

Downloaded 03 May 2010 to 171.66.16.31. Redistribution subject to ASME license or copyright; see http://www.asme.org/terms/Terms_Use.cfm

$$\exp\left\{-\frac{1}{2}F'+\frac{E'^2}{8B'}+\frac{M'^2}{8L'}\right\}\left(1-\Phi\left(\frac{M'}{2L'^{1/2}}\right)\right)d\theta, \tag{12}$$

where

$$B'=\rho_0^2(\lambda'_{33}\sin^2\theta+\lambda'_{44}\cos^2\theta-\lambda'_{34}\sin 2\theta),$$

$$D'=-\lambda'_{33}\rho_0\sin 2\theta+\lambda'_{44}\rho_0\sin 2\theta+2\lambda'_{34}\rho_0\cos 2\theta,$$

$$\begin{aligned}E'=&-\lambda'_{13}\rho_0^2\sin 2\theta+2\lambda'_{13}\mu_x\rho_0\sin\theta\\&+2\lambda'_{14}\rho_0^2\cos^2\theta-2\lambda'_{14}\mu_x\rho_0\cos\theta\\&-2\lambda'_{23}\rho_0^2\sin^2\theta+2\lambda'_{23}\rho_0\mu_y\sin\theta\\&+\lambda'_{24}\rho_0^2\sin 2\theta-2\lambda'_{24}\mu_y\rho_0\cos\theta,\end{aligned}$$

$$\begin{aligned}F'=&\lambda'_{11}(\rho_0\cos\theta-\mu_x)^2+\lambda'_{22}(\rho_0\sin\theta-\mu_y)^2\\&+2\lambda'_{12}(\rho_0\cos\theta-\mu_x)(\rho_0\sin\theta-\mu_y),\end{aligned}$$

$$\begin{aligned}G'=&2\lambda'_{13}\rho_0\cos^2\theta-2\lambda'_{13}\mu_x\cos\theta+\lambda'_{14}\rho_0\sin 2\theta\\&-2\lambda'_{14}\mu_x\sin\theta+\lambda'_{23}\rho_0\sin 2\theta-2\lambda'_{23}\mu_y\cos\theta\\&+2\lambda'_{24}\rho_0\sin^2\theta-2\lambda'_{24}\mu_y\sin\theta,\end{aligned}$$

$$H'=\lambda'_{33}\cos^2\theta+\lambda'_{44}\sin^2\theta+\lambda'_{34}\sin 2\theta,$$

$$L'=H'-D'^2/4B',$$

$$M'=G'-D'E'/2B',$$

and Φ is the probability distribution function of a standard, Gaussian random variable. Here λ'_{ij} denotes the (i, j) entry of the inverse of the covariance matrix of the random vector $(X(t),Y(t),\dot{X}(t),\dot{Y}(t))^T$.

In the limiting case that $X(t)$ and $Y(t)$ are zero-mean, Gaussian processes with identical autocorrelations and an odd cross-correlation function, random process $r(t)$ is stationary. The covariance matrix of the random vector $(X(t), Y(t),\dot{X}(t),\dot{Y}(t))^T$ is then,

$$\Lambda'=\begin{bmatrix}\sigma_X^2 & 0 & 0 & k\\ 0 & \sigma_X^2 & -k & 0\\ 0 & -k & \sigma_{\dot{X}}^2 & 0\\ k & 0 & 0 & \sigma_{\dot{X}}^2\end{bmatrix}, \tag{13}$$

where σ_X^2 is the variance of $X(t)$, $\sigma_{\dot{X}}^2$ is the variance of $\dot{X}(t)$, and k is the covariance of $X(t)$ and $\dot{Y}(t)$. In this limiting case, equation (12) yields,

$$\nu^+_{\rho_0}=\frac{\rho_0(\sigma_X^2\sigma_{\dot{X}}^2-\kappa^2)^{1/2}}{(2\pi)^{1/2}\sigma_X^3}\exp\left\{-\frac{1}{2}\frac{\rho_0^2}{\sigma_X^2}\right\}, \tag{14}$$

which is the expected upcrossing rate of the envelope of a stationary, Guassian random process (Naess, 1982). If $X(t)$ and $Y(t)$ are independent, the expression for the crossing rate reduces to that derived by Lyon (1961).

4 The Poisson Approach to the Level Crossing Problem

The second approach to the level crossing problem exploits the fact that the maximum of $r(t)$, over a reasonable number of cycles, is approximately equal to the maximum of the envelope process. The point process, defined by the upcrossings of the given threshold by the envelope, is assumed to be a Poisson process. This is equivalent to the assumption that the maxima of the envelope are statistically independent. This assumption is often more realistic than assuming that the local maxima of the original process $r(t)$ are independent, since the subsequent local maxima of the envelope are less correlated than the subsequent maxima of $r(t)$.

According to the Poisson assumption, the probability of upcrossing the level ρ_0 within a time interval $[0,T_1]$ is:

$$P(\text{upcrossing in } [0,T_1])=1-\exp(-\nu^+_{\rho_0}T_1). \tag{15}$$

It is clear from equations (12) and (15) that the upcrossing probability as given by the Poisson approach is independent of the frequency $p\omega$, since equation (15) expresses the upcrossing probability of the threshold ρ_0 by the envelope $\rho(t)$, whose definition does not involve the frequency $p\omega$.

5 Numerical Example

We will now compare the two approaches outlined in the previous sections to the level crossing problem using several numerical examples. We will also investigate how the fact that the process $r(t)$ is nonstationary affects the probability of first excursion failure.

As we have mentioned earlier, the stress $r(t)$ is stationary if and only if the following conditions are satisfied:

(*a*) the expected values of $X(t)$ and $Y(t)$ are zero,

(*b*) the autocovariance of $X(t)$, $C_X(\tau)$, equals the autocovariance of $Y(t)$, $C_Y(\tau)$, for any τ, and

(*c*) the cross-covariance of $X(t)$ and $Y(t)$, $C_{XY}(\tau)$, is an odd function of τ.

For this example, let us consider the class of processes for which the autocovariances of $X(t)$ and $Y(t)$ and their cross-covariance are formed by mulitplying the same function with a different scale parameter in each case. Thus,

$$\frac{C_X(\tau)}{C_X(0)}=\frac{C_Y(\tau)}{C_Y(0)}=\frac{C_{XY}(\tau)}{C_{XY}(0)}. \tag{16}$$

For this class of processes, we can define two coefficients η_1 and η_2 that uniquely characterize the features of the crossing problem. Coefficients η_1 and η_2, denoted here as nonstationary coefficients, are defined as follows:

$$\eta_1=\frac{|C_X(0)-C_Y(0)|}{C_X(0)+C_Y(0)}=\frac{|\sigma_X^2-\sigma_Y^2|}{\sigma_X^2+\sigma_Y^2}, \tag{17}$$

and

$$\eta_2=\frac{|C_{XY}(0)|}{\sqrt{C_X(0)C_Y(0)}}=\rho_{XY}, \tag{18}$$

where ρ_{XY} is the correlation coefficient of $X(t)$ and $Y(t)$. These two coefficients express the degree of nonstationary of the process $r(t)$. Consider the case that the means of $X(t)$ and $Y(t)$ are zero. Then for $\eta_1=0$, the autocovariances of $X(t)$ and $Y(t)$ are identical. Furthermore, for $\eta_2=0$, the cross-covariance of $X(t)$ and $Y(t)$ is zero and $r(t)$ is a stationary process. The maximum value of each of the nonstationarity coefficients is one. Table 1 summarizes the properties of $r(t)$ for various values of the nonstationarity coefficients η_1 and η_2 and the means of $X(t)$ and $Y(t)$.

Table 1 Properties of *r(t)* for various values of the nonstationarity coefficients η_1 and η_2 and the means of *X(t)* and *Y(t)*

η_1		η_2	μ_x		μ_y	$r(t)$
0		0	0		0	stationary (Gaussian noise)
0		0	$\neq 0$	or	$\neq 0$	sine wave plus Gaussian noise
1		0	0		0	amplitude modulated process
$\neq 0$	or	$\neq 0$	$\neq 0$	or	$\neq 0$	nonstationary process

Downloaded 03 May 2010 to 171.66.16.31. Redistribution subject to ASME license or copyright; see http://www.asme.org/terms/Terms_Use.cfm

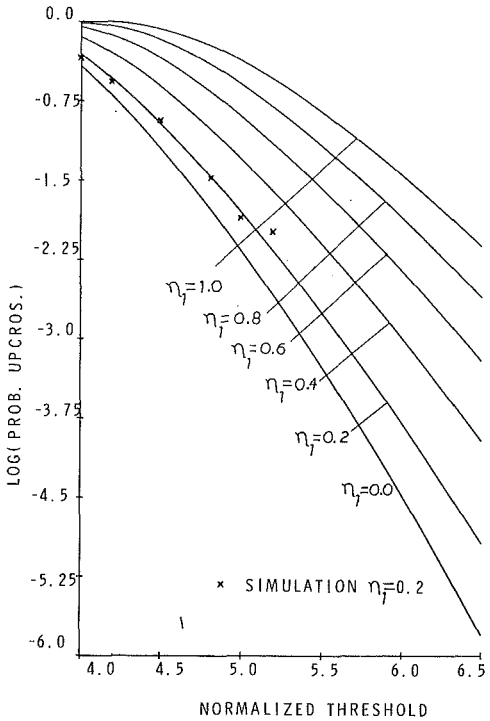


Fig. 1 Influence of the value of nonstationarity coefficient η_1 on the upcrossing probability

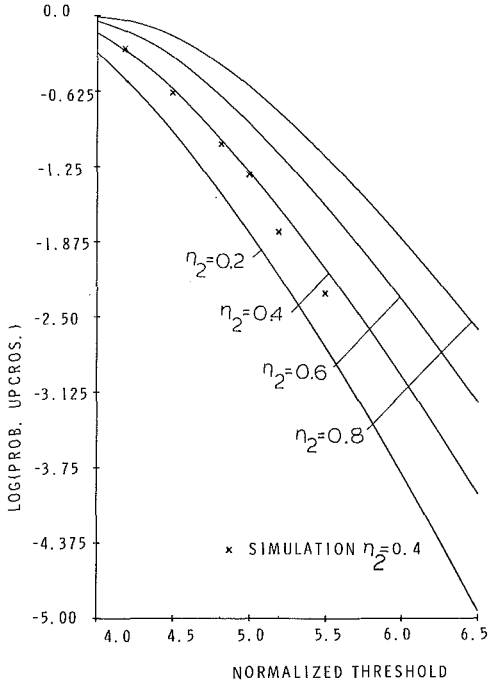


Fig. 2 Influence of the value of nonstationarity coefficient η_2 on the upcrossing probability

The two approaches to the level crossing problem were derived to estimate the probability that the stress process $r(t)$ as presented in equation (1) exceeds a threshold ρ_0 at least once over a time interval $[0,T_1]$. For an example application, the coefficients of the cosine and sine components of the stress $X(t)$ and $Y(t)$ are assumed to be zero-mean, Gaussian processes with autocovariances of the form:

$$C_X(\tau)=C_X(0)e^{-\kappa\tau^2} \text{ and}$$
$$C_Y(\tau)=C_Y(0)e^{-\kappa\tau^2}, \tag{19}$$

and cross-covariance function of the form:

$$C_{XY}(\tau)=C_{XY}(0)e^{-\kappa\tau^2}, \tag{20}$$

where $\kappa=0.1$. The root mean square (RMS) of this stress process is equal to:

$$((C_X(0)+C_Y(0))/2)^{1/2}. \tag{21}$$

Assume that the RMS of the process is equal to 5 ksi, for this example, and assume the frequency $p\omega$ is 314 rad/s. The probability of this process upcrossing a threshold ρ_0 within a 2000-s interval is shown in Fig. 1 and Fig. 2 for various values of the nonstationarity coefficients η_1 and η_2 and for thresholds ranging from 20.0 to 32.5 ksi. In the figures, the threshold has been normalized with respect to the time-average RMS.

The upcrossing probabilities for η_1 taking values from 0 to 1 and for η_2 equal to zero are plotted in Fig. 1. The results of the Markov and the Poisson approach are virtually identical. The upcrossing probability is highly dependent on the value of the nonstationarity coefficient η_1. In this example, where the mean power of the process is kept constant, the upcrossing probability rapidly increases with the value of η_1.

The upcrossing probabilities for η_1 equal to zero and η_2 taking values in the range from 0.2 to 0.8 are plotted in Fig. 2. The upcrossing probability increases with the value of η_2 because for any t, random variables $X(t)$ and $Y(t)$ become more correlated as the value of η_2 increases. Hence, if the amplitude of the cosine component is high, the amplitude of the sine component is also likely to be high. In this case, the amplitude $(X^2(t)+Y^2(t))^{1/2}$ is more likely to exceed the threshold ρ_0 than in the case where $X(t)$ and $Y(t)$ are statistically independent. Therefore, the upcrossing probability for η_2 approaching 1 is higher than that for $\eta_2=0$.

The dependency of the upcrossing probability on the values of η_1 and η_2 can be explained further by considering the variance of the original process $\sigma_r^2(t)$. This is a periodic function in time and can be expressed in terms of the nonstationarity coefficients η_1 and η_2, as follows:

$$\sigma_r^2(t)=MS(1+(\eta_1^2+\eta_2^2-\eta_1^2\eta_2^2)^{1/2}\cos(2p\omega t-\phi)), \tag{22}$$

where MS stands for the time-average mean-square of the process. Note that the variance of $r(t)$ consists of a steady and a fluctuating component. The former is independent of η_1 and η_2, while the amplitude of the latter is an increasing function of these two parameters. Hence, the higher the values of η_1 and η_2, the higher the maximum value of the fluctuating instantaneous power of the process over each cycle. Since the thresholds considered here are higher than three times the RMS of $r(t)$, the upcrossing probability should increase with the nonstationarity coefficients η_1 and η_2.

From the results in Figs. 1 and 2 and the foregoing discussion, we conclude that even if the time-average power of two processes of the form equation (1) are the same, the PDFs of their maxima and the corresponding upcrossing probabilities of some high threshold may be signficantly different. Another interesting conclusion can be drawn by considering a class of cyclostationary processes which have the same time-average RMS and satisfy

$$\frac{C_X(\tau)}{C_X(0)}=\frac{C_Y(\tau)}{C_Y(0)}=\frac{C_{XY}(\tau)}{C_{XY}(0)}=f(\tau) \tag{16'}$$

where $f(\tau)$ is the same for all processes. Among this class of processes, it is the stationary one which yields the lowest upcrossing probability. Consequently, approximating a cyclostationary process by an equivalent stationary process which has the same time-average RMS and satisfies equation (16′) will be nonconservative.

As noted previously, the results of the simpler Poisson ap-

Downloaded 03 May 2010 to 171.66.16.31. Redistribution subject to ASME license or copyright; see http://www.asme.org/terms/Terms_Use.cfm

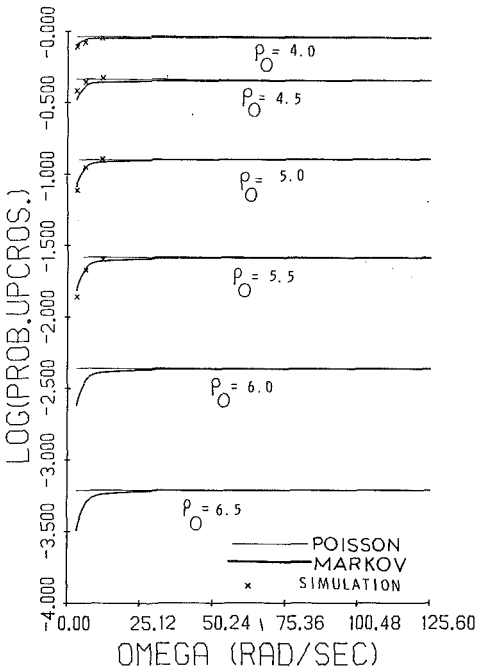


Fig. 3 Upcrossing probability for various frequencies $p\omega$

proach are frequency independent. For comparison, it is of interest to investigate the influnce of $p\omega$ on the Markov upcrossing probability. The upcrossing probability was calculated for various values of $p\omega$ for an example where the autocovariances of $X(t)$ and $Y(t)$ are 10 ksi^2 and 40 ksi^2, respectively, and the cross-covariance of $X(t)$ and $Y(t)$ is equal to zero. The nonstationarity coefficients η_1 and η_2 corresponding to these values of $C_X(0)$, $C_Y(0)$, and $C_{XY}(0)$ are 0.6 and 0, respectively. The results of the calculations using equation (10) and (15) are plotted in Fig. 3.

In order to estimate the power distribution of $X(t)$ and $Y(t)$ in the frequency domain, we have also calculated the percentage of the mean power of $X(t)$ within a frequency interval $[-\omega,\omega]$ for various values. These results are presented in Table 2. For $p\omega$ greater than about 12 rad/s, the upcrossing probability is essentially independent of $p\omega$ (Fig. 3). The upcrossing probability drops rapidly for values of $p\omega$ less than 12 rad/s. The results of the Markov and the Poisson approach are almost identical for $p\omega$ greater than 12 rad/s, but the Poisson approach appears to overpredict the probability at lower frequencies. This discrepancy increases as $p\omega$ decreases. This might be expected, since the envelope approximation is meaningful only if the frequency content of $X(t)$ and $Y(t)$ is low compared with $p\omega$. Since both methods are based on the envelope approximation, either can be expected to yield reliable results for small values of $p\omega$. The upcrossing probability must, however, decrease for lower values of $p\omega$ because the number of local maxima is decreasing. The Markov results are, therefore, more accurate than the Poisson results. The upcrossing probability calculated by the Markov approach becomes constant as $p\omega$ increases (Fig. 3). It appears that as $p\omega$ increases, the transition probability b_1 in equation (10) decreases because the distance between two subsequent local maxima becomes smaller and, hence, the maxima become more and more correlated. On the other hand, the number of maxima ν in the same equation increases. The results of these to opposing trends is that the upcrossing probability is insensitive to $p\omega$ for values greater than 25 rad/s.

The results of the two approaches were also compared with Monte Carlo simulation. The method developed by Shinozuka (1971) was used to simulate random processes $X(t)$ and $Y(t)$

Table 2 Percentage of the power of $X(t)$ within the interval $[-\omega,\omega]$

ω (rad/s)	$\frac{1}{2\pi\sigma_x^2}\int S_x(\omega)d\omega$
0.00	0.0000
0.10	0.1742
0.20	0.3472
0.30	0.4972
0.50	0.7372
0.70	0.8836
1.00	0.9742
1.15	0.9900
1.20	0.9926

and, consequently, the envelope process. This procedure has also been used by Yang (1972b) to simulate the envelope of stationary and nonstationary random processes. These results are shown as crosses in Figs. 1, 2, and 3. The results of both approaches are in good agreement with the Monte Carlo results. The only exception is for low values of $p\omega$, where there is a discrepancy between the Poisson and Monte Carlo results. In this range of frequencies, the Markov and the simulation results are still in good agreement.

6 The Level Crossing Problem in Cases (*B*) and (*C*)

The Poisson approach to the crossing problem in Case (*a*) developed in the previous section is based on the assumption that crossings of a threshold by the envelope are always followed by crossings of the process itself. This assumption becomes weak in Case (*b*), because the time period that the envelope is above the threshold may be small compared to the time between two subsequent maxima of the original process. The likelihood of an upcrossing decreases as the length of time the envelope remains above the threshold level decreases. Therefore, as this length of time decreases, the process may not cross the threshold, even if the envelope does so. The Poisson approach can be modified and used for Cases (*b*) and (*c*) if we account for these "nonqualified" envelope upcrossings. An approach based on these ideas, and also taking into account the possibility of an upcrossing occurring at time zero, was developed by Vanmarcke (1969) for stationary processes. This was generalized by Yang (1972a) for nonstationary processes possessing evolutionary spectra. The crossing problem for Cases (*b*) and (*c*) can be solved by following the same approaches (Yang, 1972a; Vanmarcke, 1969). In our case, the crossing rate of the stationary envelope is already available (equation (12)). On the other hand, the crossing rate of the original process should be averaged in time over the fundamental period of fluctuation of the statistics of the process ($2\pi/p\omega$).

The Markov approach may still be used to evaluate the upcrossing probability for Case (*b*). Indeed, the results in Fig. 3 have shown that its estimates are more accurate than that of the Poisson approach for low frequencies $p\omega$.

7 Concluding Remarks

We have presented two approaches, one Markovian and one Poisson, to the first excursion failure problem for a marine diesel shafting system, where the stress is of the form of equation (1). The Poisson approach, which requires one numerical integration, is computationally more efficient than the Markov approach, which requires four nested numerical integrations.

The accuracy of the results depends on the value of the shaft natural frequency ω_o, which will equal $p\omega$ in equation (1). If this frequency is high, compared with the frequencies for which the power spectra of $X(t)$ and $Y(t)$ are different than zero, the results of the two approaches are almost identical. For low values of the frequency $p\omega$, there is a discrepancy be-

Downloaded 03 May 2010 to 171.66.16.31. Redistribution subject to ASME license or copyright; see http://www.asme.org/terms/Terms_Use.cfm

tween the results of the two methods. The Markov approach yields more accurate results than the Poisson approach for this low frequency range.

Two nonstationarity coefficients were defined for a special class of processes. These coefficients express the degree of "nonstationarity." The influence of the nonstationarity coefficients was studied by numerical examples. The first excursion probability is highly dependent on the values of those two coefficients. The PDFs of the maxima and the upcrossing probabilities of two equal mean-power processes of the form of equation (1) may vary considerably for different values of their nonstationarity coefficients. Therefore, the study of level crossing which replaces the stress $r(t)$ by a stationary process having the same mean power as $r(t)$ may lead in unrealistic estimates, usually not on the safe side.

The first excursion or level crossing analysis presented here, together with the fatigue reliability analysis discussed by Nikolaidis et al. (1985), constitute a complete methodology for estimating the structural reliability of a marine diesel engine propulsion shafting system (Nikolaidis et al., 1987, 1985).

References

Blake, I. F., and Lindsey, C. W., 1973, "Level Crossing Problems for Random Processes," *IEEE Transactions on Information Theory*, pp. 295–315.

Coleman, J. J., 1959, "Reliability of Aircraft Structures Resisting Chance Failure," *Operations Research*, Vol. 7, No. 5, pp. 639–645.

Cramer, H., and Leadbetter, M. R., 1967, *Stationary and Related Stochastic Processes*, John Wiley and Sons, New York.

Franks, L., 1969, *Signal Theory*, Prentice-Hall, Englewood Cliffs, N.J.

Gardner, W., and Franks, L., 1975, "Characterization of Cyclostationary Random Signal Processes," *IEEE Transactions on Information Theory*, Vol. IT21, No. 1, pp. 4–14.

Krenk, S., 1979, "Nonstationary Narrow-Band Response and First-Passage Probability," ASME Journal of Applied Mechanics, Vol. 46, pp. 919–924.

Loeve, M., 1977, *Probability Theory I*, 4th ed., Springer-Verlag, New York.

Lyon, R. H., 1961, "On the Vibration Statistics of a Randomly Excited Hard-Spring Oscillator—II," *The Journal of Acoustical Society of America*, Vol. 33, pp. 1395–1403.

Mikhalevsky, P., 1982, "Envelope Statistics of Partially Saturated Processes," *Journal of Acoustic Society of America*, Vol. 72, pp. 151–158.

Naess, A., 1982, "Extreme Value Estimates Based on the Envelope Concept," *Journal of Applied Ocean Research*, Vol. 4, No. 3, pp. 181–187.

Nikolaidis, E., and Perakis, A. N., 1985, "Second Order Statistics and Discrete-Time Detection Modeling for Partially Saturated Processes," *Journal of the Acoustical Society of America*, Vol. 77, No. 3, pp. 1978–1085.

Nikolaidis, E., Perakis, A. N., and Parsons, M. G., 1985, "Structural Reliability of Marine Diesel Engine Propulsion Shafting Systems," *Transactions of The Society of Naval Architects and Marine Engineers*, Vol. 93, pp. 189–223.

Nikolaidis, E., Perakis, A. N., and Parsons, M. G., 1987, "Probabilistic Torsional Vibration Analysis of a Motor Ship Propulsion Shafting System: The Input-Output Problem," *Journal of Ship Research*, Vol. 31, No. 1, pp. 41–52.

Ochi, M. K., 1973, "On Prediction of Extreme Values," *Journal of Ship Research*, Vol. 17, No. 1, pp. 29–37.

Ochi, M. K., 1979, "Extreme Values of Waves and Ship Responses Subject to the Markov Chain Condition," *Journal of Ship Research*, Vol. 23, No. 3, pp. 188–197.

Ogura, H., 1971, "Spectral Representation of a Period Nonstationary Random Process," *IEEE Transactions on Information Theory*, Vol. IT17, No. 2, pp. 143–149.

Papoulis, A., 1983, "Random Modulation: A Review," *IEEE Transactions on Acoustic, Speech and Signal Processing*, Vol. ASSP-31, No. 1, pp. 96–105.

Rice, S. O., 1944–1945, "The Mathematical Analysis of Random Noise," *Bell System Technical Journal*, Vol. 23, pp. 282–332 and Vol. 24, pp. 46–156.

Shinozuka, M., 1971, "Simulation of Multivariate and Multidimensional Random Processes," *The Journal of Acoustical Society of America*, Vol. 49, No. 1, Part 2, pp. 357–368.

Vanmarcke, E. H., 1969, "First Passage and Other Failure Criteria in Narrow Band Random Vibration: A Discrete State Approach," Ph.D. Dissertation, Department of Civil Engineering, M.I.T., Cambridge, Mass.

Yang, J. N., 1972a, "Nonstationary Envelope Process and First Excursion Failure Probability," *Journal of Structural Mechanics*, Vol. 1, No. 2, ASCE, New York, pp. 231–248.

Yang, J. N., 1972b, "Simulation of Random Envelope Processes," *Journal of Sound and Vibration*, Vol. 21, No. 1, pp. 73–85.

Yang, J. N., 1973, "First Excursion Probability in Non-Stationary Random Vibration," *Journal of Sound and Vibration*, Vol. 27, No. 2, pp. 165–182.

Yang, J. N., and Shinozuka, M., 1971, "On the First Excursion Probability in Stationary Narrow-Band Random Vibration," ASME Journal of Applied Mechanics, Vol. 38, No. 4, pp. 1017–1022.

Yang, J. N., and Shinozuka, M., 1972, "On the First Excursion Probability in Stationary Narrow-Band Random Vibration—II," ASME Journal of Applied Mechanics, Vol. 39, pp. 733–738.

Downloaded 03 May 2010 to 171.66.16.31. Redistribution subject to ASME license or copyright; see http://www.asme.org/terms/Terms_Use.cfm

An Experimental Investigation of Complicated Responses of a Two-Degree-of-Freedom Structure

A. H. Nayfeh

B. Balachandran

M. A. Colbert

M. A. Nayfeh

Department of Engineering Science and Mechanics,
Virginia Polytechnic Institute and State University
Blacksburg, Va. 24061

Recent theoretical studies indicate that whereas large excitation amplitudes are needed to produce chaotic motions in single-degree-of-freedom systems, extremely small excitation levels can produce chaotic motions in multi-degree-of-freedom systems if they possess autoparametric resonances. To verify these results, we conducted an experimental study of the response of a two-degree-of-freedom structure with quadratic nonlinearities and a two-to-one internal resonance to a primary resonant excitation of the second mode. The responses were analyzed using hardware and software developed for performing time-dependent modal decomposition. We observed periodic, quasi-periodic, and chaotic responses, as predicted by theory. Conditions were found under which extremely small excitation levels produced chaotic motions.

1 Introduction

Physical systems are inherently nonlinear. The sources of the nonlinearities may be geometric, or inertial, or material, or damping, or a combination of them. Including the nonlinearities in the governing equations, or the boundary conditions, or both, can lead to the prediction of a whole range of phenomena that are not found in linear mathematical models, but found in the actual systems. In single-degree-of-freedom systems, these phenomena include multiple solutions, jumps, limit cycles, frequency entrainment, natural frequency shift, subharmonic, superharmonic, and ultrasubharmonic resonances, period-multiplying bifurcations, and chaotic motions. The presence of chaotic motions in the response of thin buckled beams was demonstrated experimentally by Moon (1980) and Dowell and Pezeshki (1986). However, large excitation levels are usually needed to produce the period-doubling bifurcations and chaotic motions in single-degree-of-freedom systems. Consequently, many researchers do not consider the importance of period-multiplying bifurcations and chaotic motions in the design and control of structures.

Besides the above phenomena, the response of multi-degree-of freedom systems can exhibit combinational resonances and what is generally referred to as modal interactions; the latter may provide a coupling or an energy exchange among the system's modes. This coupling can dominate the response of systems having some modes that are involved in internal or autoparametric resonances; that is, the linear natural frequencies, ω_i, are commensurable or nearly commensurable. The types of internal resonances depend on the degree of the nonlinearities. When the nonlinearity is cubic, internal resonances may occur if $\omega_n \approx 3\omega_m$, $\omega_n \approx |\pm 2\omega_m \pm \omega_k|$, or $\omega_n \approx |\pm \omega_m \pm \omega_k \pm \omega_l|$. When the nonlinearity is quadratic, besides the above resonances, internal resonances may occur if $\omega_n \approx 2\omega_m$ or $\omega_n \approx \omega_m + \omega_k$.

Autoparametric resonances are responsible for many interesting phenomena (Nayfeh and Mook, 1979). For example, they are responsible for saturation (Nayfeh et al., 1973) in the response of systems with quadratic nonlinearities when $\omega_2 \approx 2\omega_1$ and the second mode is excited by a single-harmonic load of amplitude g and frequency $\Omega \approx \omega_2$. One expects from linear theory that the second mode would be dominant; initially this is so. But as g increases above a threshold value, which can be extremely small, the second mode becomes saturated and the additional energy spills over into the first mode. The saturation phenomenon has been found analytically in the response of ships, elastic pendulums, shells, arches, valves, and beams and plates under static loadings (Nayfeh and Mook, 1979). Haddow et al. (1984) experimentally verified the saturation phenomenon using a model consisting of two lightweight beams and two concentrated masses, similar to the model shown in Fig. 1.

Later, Nayfeh (1988, 1989) analyzed the response of general two-degree-of-freedom systems having quadratic nonlinearities when $\omega_2 \approx 2\omega_1$ and the external excitation frequency $\Omega \approx \omega_2$. He obtained a fourth-order polynomial equation for the eigenvalues determining the stability of the fixed-point or steady-state solutions. He found that these solutions can lose stability through Hopf bifurcations in addition to saddle-node bifurcations. In between the Hopf bifurcation parameters, Nayfeh and Raouf (1987) found conditions under which fixed-point solutions experience a cascade of period-doubling bifurcations, leading to chaos. Whereas large excitation levels are needed to produce chaotic motions in single-degree-of-

Contributed by the Applied Mechanics Division of THE AMERICAN SOCIETY OF MECHANICAL ENGINEERS for presentation at the Winter Annual Meeting, San Francisco, Calif., December 10-15, 1989.

Discussion on this paper should be addressed to the Editorial Department, ASME, United Engineering Center, 345 East 47th Street, New York, N.Y., 10017, and will be accepted until two months after final publication of the paper itself in the JOURNAL OF APPLIED MECHANICS. Manuscript received by the ASME Applied Mechanics Division, July 11, 1988; final revision, January 31, 1989.

Paper No. 89-WA/APM-24.

Copyright © 1989 by ASME

Downloaded 03 May 2010 to 171.66.16.31. Redistribution subject to ASME license or copyright; see http://www.asme.org/terms/Terms_Use.cfm

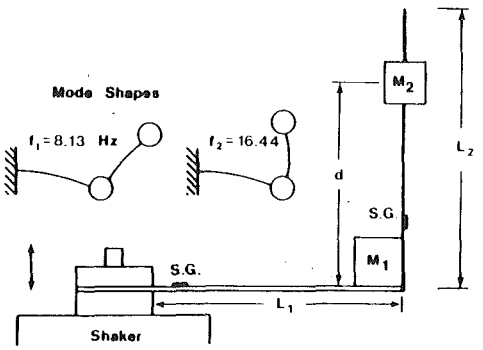


Fig. 1 Two-degree-of-freedom model tuned for a 2:1 internal resonance and accompanying linear mode shapes. Beam 1: 1.676 mm x 12.827 mm x 154.51 mm, $\rho_1 = 0.162$ g/mm, $m_1 = 31.1$ g; Beam 2: 0.559 mm x 12.802 mm x 152.40 mm, $\rho_2 = 0.0498$ g/mm, $m_2 = 40.0$ g; $d = 90.525$ mm.

freedom systems, extremely small excitation levels can produce chaotic motions in multi-degree-of-freedom systems possessing a two-to-one autoparametric resonance. Such systems include ships, arches, elastic pendulums, shells, liquids in containers, valves, and beam and plates under static loadings.

Yamamoto et al. (1977) observed amplitude and phase-modulated motions in their analog computer simulations of two internally resonant oscillators subjected to a primary resonant excitation of the higher mode. Hatwal et al. (1983) reported some numerical and experimental results which demonstrate the existence of chaotic motions in an internally resonant two-degree-of-freedom model when the higher mode is excited by a primary resonance. However, moderately high levels of excitation were used in their study, and hence, they found that "the first-order approximation does not predict the true stability behavior of the steady-state solutions." Consequently, they carried out higher-order approximations and included higher-order nonlinear terms. However, the analytical and numerical studies of Nayfeh (1988, 1989) and Nayfeh and Raouf (1987) show that Hopf bufurcations are possible at extremely small levels of excitation for certain detunings. Inside the Hopf bifurcation region, they found that the response consisted of amplitude and phase-modulated motions, which undergo a sequence of period-doubling bifurcations culminating in chaos. Except for the present experiments, there are no experimental studies that demonstrate the existence of periodically and chaotically modulated motions at very small excitation levels when the excitation frequency is close to the natural frequency of the second mode.

The purpose of the present paper is to experimentally verify the presence of period-doubling bifurcations and chaotic motions in systems with quadratic nonlinearities having a two-to-one autoparametric resonance when the second mode is excited by a very small primary resonant harmonic load. The structure chosen for the experiment is shown in Fig. 1, which is similar to the model used by Haddow et al. (1984) to verify the saturation phenomenon, and by Nayfeh and Zavodney (1988) to observe amplitude and phase-modulated motions when the lower mode is excited by a primary resonant harmonic load.

2 Theory

We consider the nonlinear response of a structure having quadratic nonlinearities and possessing a two-to-one autoparametric resonance to a primary excitation of the higher mode. Since, in the presence of damping, modes that are not directly excited by the load or indirectly excited by the internal or autoparametric resonance die out with time, the response of the structure can be modeled by a two-mode approximation, involving the internally resonant modes. If u_1 and u_2 are the generalized coordinates of these two modes, the governing equations are of the form

$$\ddot{u}_1 + \omega_1^2 u_1 + 2\mu_1 \dot{u}_1 + \delta_1 u_1^2 + \delta_2 u_1 u_2 + \delta_3 u_2^2 + \delta_4 \dot{u}_1^2 + \delta_5 \dot{u}_1 \dot{u}_2 + \delta_6 \dot{u}_2^2 + \delta_7 u_1 \ddot{u}_1 + \delta_8 u_2 \ddot{u}_1 + \delta_9 u_1 \ddot{u}_2 + \delta_{10} u_2 \ddot{u}_2 + (h_{11} u_1 + h_{12} u_2)\cos\Omega t = F\cos\Omega t, \quad (1)$$

$$\ddot{u}_2 + \omega_2^2 u_2 + 2\mu_2 \dot{u}_2 + \alpha_1 u_1^2 + \alpha_2 u_1 u_2 + \alpha_3 u_2^2 + \alpha_4 \dot{u}_1^2 + \alpha_5 \dot{u}_1 \dot{u}_2 + \alpha_6 \dot{u}_2^2 + \alpha_7 u_1 \ddot{u}_1 + \alpha_8 u_2 \ddot{u}_1 + \alpha_9 u_1 \ddot{u}_2 + \alpha_{10} u_2 \ddot{u}_2 + (h_{21} u_1 + h_{22} u_2)\cos\Omega t = G\cos\Omega t, \quad (2)$$

where the highest order of terms retained is quadratic, μ_1 and μ_2 are the modal damping coefficients, and F, G, Ω, ω_n, δ_n, α_n, and h_{mn} are the constants. The equations (1) and (2) are generic and describe the forced response of physical systems such as ships, beams, arches, and shells (Nayfeh and Mook, 1979; Nayfeh, 1989). The structure shown in Fig. 1 is governed by a special form of equations (1) and (2) obtained by putting $\delta_1 = \delta_2 = \delta_3 = \alpha_1 = \alpha_2 = \alpha_3 = 0$. The first three parameters F, G, and Ω and the h_{mn} depend on the excitation, whereas the parameters ω_n, δ_n, and α_n depend on the values of the two masses and the dimensions and properties of the two beams.

Sethna (1965), Nayfeh, Mook, and Marshall (1973), Yamamoto, Yasuda, and Nagasaka (1977), Nayfeh and Mook (1979), Hatwal, Mallik, and Ghosh (1983), Haddow, Barr, and Mook (1984), and Nayfeh (1988) studied theoretically special cases of the present problem using various techniques. The governing equations for the amplitude and phase were derived by Sethna (1965) using the method of averaging, by Yamamoto et al. (1977) using the method of harmonic balance, and by Nayfeh et al. (1973), Haddow et al. (1984), and Nayfeh (1988) using the method of multiple scales (1973, 1981).

To determine an approximate solution of equations (1) and (2) for small but finite amplitudes, we introduce a small dimensionless parameter ϵ, which is the order of the amplitude of the response, as a bookkeeping device and set it equal to unity in the final solution. To quantitatively describe the nearness of the resonances, we introduce the detuning parameters σ_1 and σ_2 defined according to

$$\omega_2 = 2\omega_1 + \epsilon\sigma_1 \quad \text{and} \quad \Omega = \omega_2 + \epsilon\sigma_2. \quad (3)$$

Then, using the method of multiple scales, one finds that to the first approximation, the solutions of equations (1) and (2) are

$$u_1 = a_1\cos\left(\frac{1}{2}\Omega t - \frac{1}{2}\gamma_1 - \frac{1}{2}\gamma_2\right) + \ldots \quad (4)$$

$$u_2 = a_2\cos(\Omega t - \gamma_2) + \ldots \quad (5)$$

where the amplitudes a_n and phases β_n are governed by

$$\dot{a}_1 = -\mu_1 a_1 - \Lambda_1 a_1 a_2 \sin\gamma_1 \quad (6)$$

$$\dot{a}_2 = -\mu_2 a_2 + \Lambda_2 a_1^2 \sin\gamma_1 + g\sin\gamma_2 \quad (7)$$

$$a_1\dot{\beta}_1 = \Lambda_1 a_1 a_2 \cos\gamma_1 \quad (8)$$

$$a_2\dot{\beta}_2 = \Lambda_2 a_1^2 \cos\gamma_1 - g\cos\gamma_2 \quad (9)$$

$$\gamma_1 = \sigma_1 t + \beta_2 - 2\beta_1 \quad \text{and} \quad \gamma_2 = \sigma_2 t - \beta_2 \quad (10)$$

$$4\omega_1\Lambda_1 = \delta_2 + \delta_5\omega_1\omega_2 - \delta_8\omega_1^2 - \delta_9\omega_2^2, \quad (11)$$

$$4\omega_2\Lambda_2 = \alpha_1 - \alpha_4\omega_1^2 - \alpha_7\omega_1^2. \quad (12)$$

Periodic solutions of equations (1) and (2) correspond to the fixed points of equations (6)-(10). They are obtained by setting $\dot{a}_1 = \dot{a}_2 = \dot{\gamma}_1 = \dot{\gamma}_2 = 0$. There are two possibilities. First,

$$a_1 = 0 \quad \text{and} \quad a_2 = \frac{g}{\sqrt{\sigma_2^2 + \mu_2^2}}, \quad g = G/2\omega_2 \quad (13)$$

and to the first approximation, the response is

$$u_1 = 0 \quad \text{and} \quad u_2 = a_2\cos(\Omega t - \gamma_2) + \ldots \quad (14)$$

which is essentially the linear solution. Second,

Downloaded 03 May 2010 to 171.66.16.31. Redistribution subject to ASME license or copyright; see http://www.asme.org/terms/Terms_Use.cfm

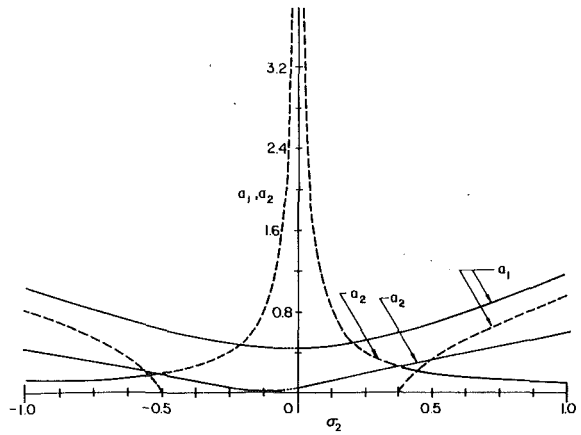


Fig. 2 Theoretically-predicted frequency-response curves for the case $\Lambda_1 = 1.0$, $\Lambda_2 = 0.5$, $\mu_1 = \mu_2 = 0.02$, $\sigma_2 = 0.12$, and $g = 0.1$: —— stable, . . . , — — — unstable

$$a_1 = (\Lambda_1\Lambda_2)^{-1/2}[\chi_1 \pm (g^2\Lambda_1^2 - \chi_2^2)^{1/2}]^{1/2} \tag{15}$$

$$a_2 = a_{2s} = |\Lambda_1|^{-1}\left[\mu_1^2 + \frac{1}{4}(\sigma_1 + \sigma_2)^2\right]^{1/2} \tag{16}$$

where

$$\chi_1 = \frac{1}{2}\sigma_2(\sigma_1 + \sigma_2) - \mu_1\mu_2, \tag{17}$$

$$\chi_2 = \sigma_2\mu_1 + \frac{1}{2}\mu_2(\sigma_1 + \sigma_2). \tag{18}$$

We note that the nonlinear solutions depend on the coefficients of the nonlinearities in the model equations through Λ_1 and Λ_2. Moreover, one can scale the amplitudes of the response and excitation so that the solution is independent of the problem under consideration and the results can be applied to shells, pendulums, ships, and the structure in Fig. 1. The scaling is

$$\hat{a}_1 = a_1\sqrt{\Lambda_1\Lambda_2},\ \hat{a}_2 = |\Lambda_1|a_2,\ \hat{g} = g|\Lambda_1|.$$

To study the stability of the linear solution given by equation (13), we add to it a small disturbance proportional to $\exp(\lambda t)$ and find that

$$\lambda = -\mu_1 \pm \sqrt{\Lambda_1^2 a_2^2 - \frac{1}{4}(\sigma_1 + \sigma_2)^2},\ -\mu_2 \pm i\sigma_2. \tag{19}$$

Hence, the linear solution is stable if and only if

$$\Lambda_1^2 a_2^2 \le \mu_1^2 + \frac{1}{4}(\sigma_1 + \sigma_2)^2 \text{ or } a_2 \le a_{2s}. \tag{20}$$

Similarly, the stability of the nonlinear solution to a disturbance proportional to $\exp(\lambda t)$ is determined by the zeros of

$$\lambda^4 + 2(\mu_1 + \mu_2)\lambda^3 + [\mu_2^2 + 4\mu_1\mu_2 + \sigma_2^2 + 4\Lambda_1\Lambda_2 a_1^2]\lambda^2 + [2\mu_1\mu_2^2 + 2\mu_1\sigma_2^2 + 4\Lambda_1\Lambda_2(\mu_1 + \mu_2)a_1^2]\lambda + 4\Lambda_1\Lambda_2 a_1^2\left[\Lambda_1\Lambda_2 a_1^2 + \mu_1\mu_2 - \frac{1}{2}\sigma_2(\sigma_1 + \sigma_2)\right] = 0. \tag{21}$$

According to the Routh-Hurwitz criterion, at least one root of equation (21) has a positive real part, and hence, a fixed point given by equations (15) and (16) is unstable if all of the following conditions are not satisfied:

$$r_1 r_2 - r_3 > 0,\ r_3(r_1 r_2 - r_3) - r_1^2 r_4 > 0,\ r_4 > 0 \tag{22}$$

where r_1, r_2, r_3, and r_4 are, respectively, the coefficients of λ^3, λ^2, λ^1, and λ^0 in equation (21). The violation of the second condition in equation (22) would imply the existence of a pair of complex conjugate eigenvalues having a positive real part. When $\sigma_2(\sigma_1 + \sigma_2) > 0$, the second condition in (22) is satisfied for all values of μ_n and g. On the other hand, when $\sigma_2(\sigma_1 + \sigma_2) < 0$, the second condition may be violated, depending on the values of μ_n and g. Hence, replacing the inequality by an equality yields the parameters corresponding to Hopf bifurcation.

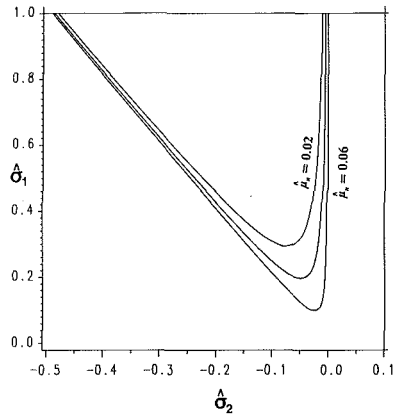


Fig. 3 Transition curves across which real part of a complex conjugate pair of eigenvalues changes sign (it is positive inside the curves) for $\hat{\mu}_n = 0.02$, 0.04 and 0.06, where $\hat{\mu}_n = \mu_n/\sqrt{\Lambda_1 g}$ and $\hat{\sigma}_n = \sigma_n/\sqrt{\Lambda_1 g}$

The theoretically-predicted amplitude-response curve exhibits saturation (Nayfeh et al., 1973). Figure 2 shows theoretically-determined frequency-response curves for the case $\Lambda_1 = 1.0$, $\Lambda_2 = 0.5$, $\mu_1 = \mu_2 = 0.02$, $\sigma_1 = 0.12$, and $g = 0.1$. The solid branches correspond to stable periodic motions, the dashed portions correspond to unstable fixed points with at least one eigenvalue being positive, and the dotted portion ($-0.047 \le \sigma_2 \le -0.0127$) corresponds to unstable fixed points with the real part of a complex conjugate pair of eigenvalues being positive. In the latter case, the amplitudes and phases are not constant but vary with time. The corresponding response is an amplitude- and phase-modulated or chaotic motion. Figure 3 shows theoretically-determined curves corresponding to Hopf bifurcation when $\hat{\mu}_n\,(\mu_n/\sqrt{\Lambda_1 g}) = 0.02$, 0.04 and 0.06. As the parameters $\hat{\sigma}_n\,(\sigma_n/\sqrt{\Lambda_1 g})$ are varied to cross the bifurcation curves, the nontrivial solution loses its stability with a pair of complex eigenvalues crossing the imaginary axis transversally into the right half of the complex plane. The motion is aperiodic in the region included by the bifurcation curves.

Next, we present the results of an experimental investigation of the response of the mechanical model shown in Fig. 1, which is internally tuned for modal interaction, to a primary resonant excitation of the second mode. We verify the existence of periodically and chaotically modulated motions and analyze the modulated motions using Fourier spectra and time-dependent modal decompositions. We describe an experimental procedure to perform the time-dependent modal decomposition. Cilberto and Gollub (1985) used digital imaging methods to obtain the time-dependent modal amplitudes in their study of parametrically-forced surface waves.

3 Experiment

Figure 4 shows the experimental setup. The displacements of the beam ends were measured using strain gages mounted on the beams. The shaker-table acceleration was measured using an accelerometer mounted on the table.

The signal from the strain gage on the vertical beam was used for obtaining the frequency spectrum of the model response and for time-dependent modal decomposition analysis. The displacement at any point on the beam can be written as

$$w(s,t) = \sum_i a_i\phi_i(s)\cos(\Omega_i t + \gamma_i)$$

Downloaded 03 May 2010 to 171.66.16.31. Redistribution subject to ASME license or copyright; see http://www.asme.org/terms/Terms_Use.cfm

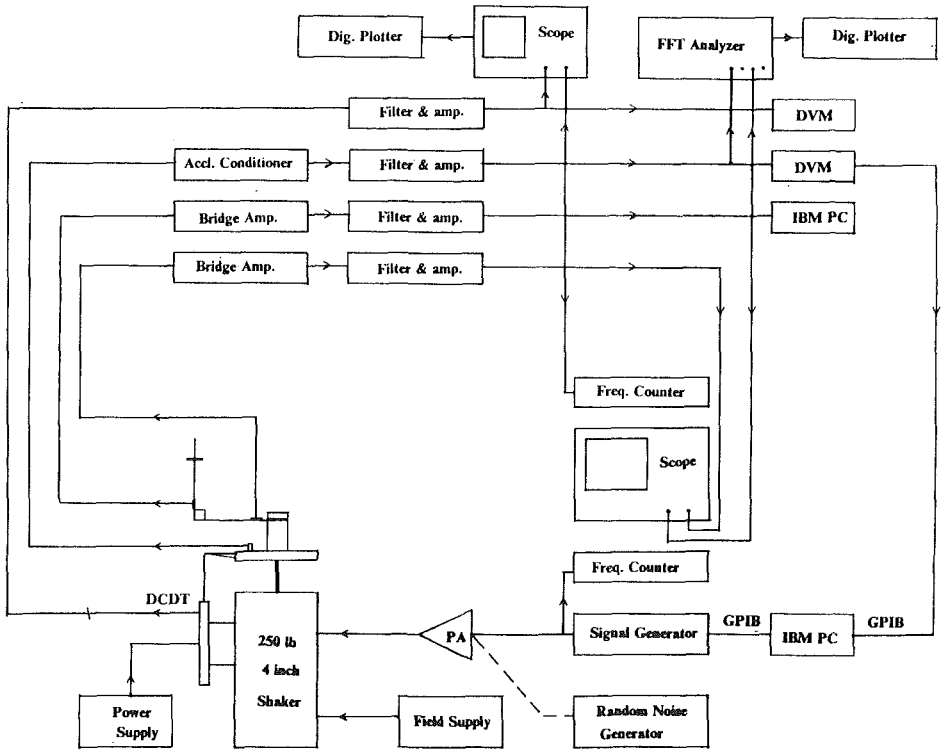


Fig. 4 A schematic of the experimental setup

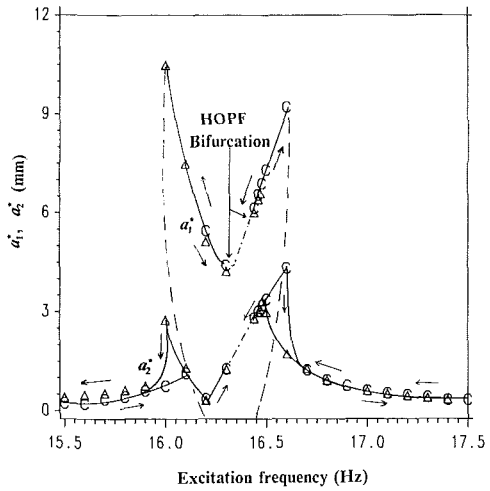


Fig. 5 Experimentally-obtained frequency-response curves when the excitation frequency is close to the higher natural frequency $f_2 = 16.44$ Hz. The table acceleration was 47.14 mili g's: ——— periodic, —·—·— aperiodic.

where the $\phi_i(s)$ are the mode shapes, the Ω_i are the frequencies present, and the γ_i are the phase angles. At the strain-gage location,

$$w(s,t) = \sum_i a_i^* \cos(\Omega_i t + \gamma_i)$$

where

$$a_i^* = a_i \phi_i(s).$$

For periodic motions, the amplitudes a_1^* and a_2^* (proportional to the modal amplitudes a_1 and a_2, respectively) were determined from the frequency spectra.

The cross plot of the two strain-gage signals was used to distinguish a modulated response from a periodic response. The two strain-gage signals were used as the coordinates for the phase plane and the excitation frequency was used as the clock frequency for the Poincaré maps.

The linear resonant frequencies of the structure, determined using a random excitation, were $f_1 = 8.13$ Hz and $f_2 = 16.44$ Hz. From parameter-identification studies carried out with the structure, we found the modal damping coefficients to be very small and so the linear resonant frequencies should be very close to the linear natural frequencies. Figure 1 also shows the associated mode shapes.

The frequency-response curve obtained from sweeping the frequency range up and down at a small constant level of excitation (maintained using a feedback control, see Fig. 4) is shown in Fig. 5. The frequency of excitation f ranged from 15.5 Hz to 17.5 Hz. The circles in the figure correspond to observations obtained during the forward sweep and the triangles correspond to observations obtained during the reverse sweep. The points where periodic motions ceased to exist are labeled Hopf bifurcation in the figure. Aperiodic motions were observed when the driving frequency was in the range $16.3 \le f < 16.44$ Hz. It should be noted that the amplitude and phase-modulated motions were seen only when $\sigma_2\,(\sigma_1 + \sigma_2) < 0$, as predicted by theory. Comparing Figs. 5 and 2, one can see the qualitative agreement between theory and experiment.

Figure 6 shows the experimentally-obtained variation of the response amplitude with excitation amplitude. For this experiment, the driving frequency was held constant at 16.38 Hz, while the excitation amplitude was varied. We observed the saturation phenomenon (Nayfeh et al., 1973; Nayfeh and Mook, 1979). Beyond a certain excitation amplitude, which was very small, the periodic motions ceased to exist, and hence, the saturation phenomenon did not exist anymore. We saw amplitude and phase-modulated motions beyond this excitation amplitude. The circles and triangles shown in the figure correspond to the forward and reverse sweeps of the driving amplitude, respectively. The point at which periodic motions ceased to exist are again labeled Hopf bifurcation. The dashed lines in Figs. 5 and 6 are imaginary and are drawn to show the occurrence of jumps observed in the experiment.

Downloaded 03 May 2010 to 171.66.16.31. Redistribution subject to ASME license or copyright; see http://www.asme.org/terms/Terms_Use.cfm

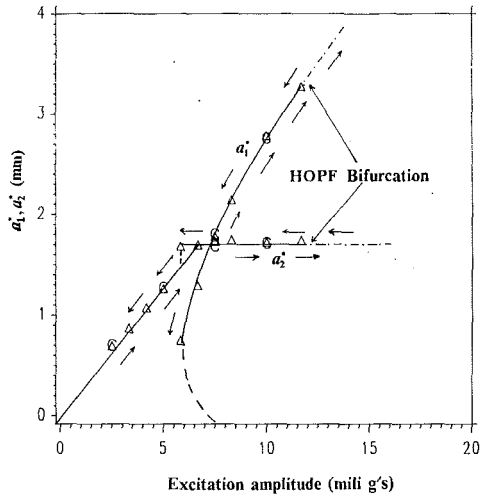


Fig. 6 Experimentally-obtained amplitude-response curves when the excitation frequency is held constant at 16.38 Hz: ——— periodic, —·—·— aperiodic

We note the excitation levels involved are very small and that the amplitude- and phase-modulated motions are not the result of large amplitudes. Moreover, these modulated motions can be predicted using quadratic nonlinearities. When the detunings were adjusted so that $\sigma_2(\sigma_1+\sigma_2)>0$, periodic responses and the saturation phenomenon were observed even at levels of excitation, higher than those shown in Fig. 6, as predicted by theory.

The same mechanical model, with different linear resonant frequencies (8.16 Hz and 16.50 Hz) was used for a few more experimental observations. Figure 7 shows the spectra of the response and the table acceleration and the corresponding cross plots of the two strain-gage signals for a periodic linear response, a periodic nonlinear response, and an aperiodic response. The response spectrum in Fig. 7(*c*) shows discrete spectral lines at $f\pm n\delta f$ and $1/2\ f\pm n\delta f$, where $n=0,1,2,3,\ldots$. The sidebands are due to the amplitude and phase modulations. Also, we note that the table-acceleration spectrum shows sidebands around the exictation frequency, which is indicative of the feedback from the mechanical model to the table. Following this observation, we are considering modeling the mechanical model and the table as a three-degree-of-freedom structure for future work as the feedback control is not effective in case of amplitude and phase-modulated responses in spite of the fact that the model is about 5.5 oz. and the shaker is capable of delivering a 250 lb. excitation force. The implications of the ineffectiveness of the feedback control in such cases (periodically and chaotically-modulated motions) on the control of actual structures need to be ascertained, especially when the structures are much heavier than our model and the actuators in general are not capable of delivering forces as large as our shaker. The cross plot in Fig. 7(*c*) shows an evolving "eight shape" pattern due to the modulation. Amplitude and phase-modulated motions were observed for $16.36\le f<16.50$ Hz.

In order to get a better idea of the aperiodic responses, we took a zoom span (resolution 0.002 Hz) around the excitation frequency. Figures 8(*a*) to 8(*c*) show the spectra of the responses on a log scale for the excitation frequencies 16.36 Hz, 16.37 Hz, and 16.41 Hz. In all cases the sharp peak at the center corresponds to the excitation (carrier) frequency and the peaks surrounding it correspond to the modulation frequencies. When we go from Fig. 8(*a*) to Fig. 8(*b*) we see a distinct peak appearing midway between the carrier frequency peak and the largest other peak. This indicates that the period of modulation has undergone a period doubling. Figure 8(*c*) shows a more prominent peak between the carrier frequency peak and the largest other peak. Figures 8(*d*) and 8(*e*) correspond to an excitation frequency of 16.44 Hz. The spectrum shows a broadband character around the carrier frequencies, indicating that the motion is chaotic at this frequency. These observations are in qualitative agreement with the analytical and numerical results of Nayfeh and Raouf (1987).

In order to see the projection of the attractor in the $a_1^*-a_2^*$ phase plane, we had to do time-dependent modal decomposition to obtain the modal amplitudes. Ciliberto and Gollub (1985) obtained the modal amplitudes at different times from the angular power spectrum. We could not use the power spectrum (see Fig. 7) or the corresponding time series to obtain the time-dependence of the modal amplitudes because the phases were time-dependent. The measured signal is of the form

$$w(t)=a_1^*(t)\cos\left[\frac{1}{2}\Omega t-\frac{1}{2}\gamma_1(t)-\frac{1}{2}\gamma_2(t)\right]+a_2^*(t)\cos[\Omega t-\gamma_2(t)]. \tag{23}$$

The signal was low-pass filtered ($f_c=40$ Hz) to eliminate the line noise, amplified, and sent to an IBM PC which acquired data through an 8-bit analog-to-digital converter. It should be noted that at the time of conducting the experiment, only an 8-bit A/D converter was available. However, in spite of its limitations, we were able to resolve the first period-doubling bifurcation. Probably, with a 16-bit A/D converter, we might be able to resolve some of the subsequent bifurcations in the period-doubling sequence. A quartz clock was used to set the desired sampling rate. We used a sampling frequency of 244.285 Hz and collected 8192 points per frame. Using an FFT algorithm, we transformed the data from the time domain to the frequency domain. From the frequency spectrum the spectral width Δf of the sideband structure was determined. Two band-pass filters centered at f and $f/2$ and each having the width Δf were used for the digital filtering, which separated the two modes. We used this procedure because the two modes were well separated. The separated frequency components were transformed back to the time domain using an inverse FFT (IFFT) algorithm. Using quadrature demodulation on the separated signals, we extracted $a_i^*(t)$ and $\gamma_i(t)$. The process is detailed in the next paragraph.

The separated signal $a(t)\cos[\omega t+\gamma(t)]$ is modulated by the $\sin(\omega t)$ and $\cos(\omega t)$ functions. Each of the resulting signals is made up of a high-frequency component and a low-frequency component; that is,

$$a(t)\cos[\omega t+\gamma(t)]\cos(\omega t)=\frac{1}{2}a(t)\{\cos[2\omega t+\gamma(t)]+\cos[\gamma(t)]\} \tag{24}$$

$$a(t)\cos[\omega t+\gamma(t)]\sin(\omega t)=\frac{1}{2}a(t)\{\sin[2\omega t+\gamma(t)]-\sin[\gamma(t)]\}. \tag{25}$$

Using a low-pass filter to eliminate the 2ω components, we obtain

$$p(t)=\frac{1}{2}a(t)\cos[\gamma(t)]$$

$$\text{and}\quad q(t)=-\frac{1}{2}a(t)\sin[\gamma(t)], \tag{26}$$

from which we calculate $a(t)$ and $\gamma(t)$ according to

$$a=2\sqrt{p^2+q^2},\quad \gamma=\tan^{-1}\left(-\frac{q}{p}\right). \tag{27}$$

Figure 9 illustrates an application of the aforementioned procedure when the excitation frequency was 16.36 Hz. The time traces of the measured strain-gage signal, the two separated modes, and the extracted modal amplitudes are

Downloaded 03 May 2010 to 171.66.16.31. Redistribution subject to ASME license or copyright; see http://www.asme.org/terms/Terms_Use.cfm

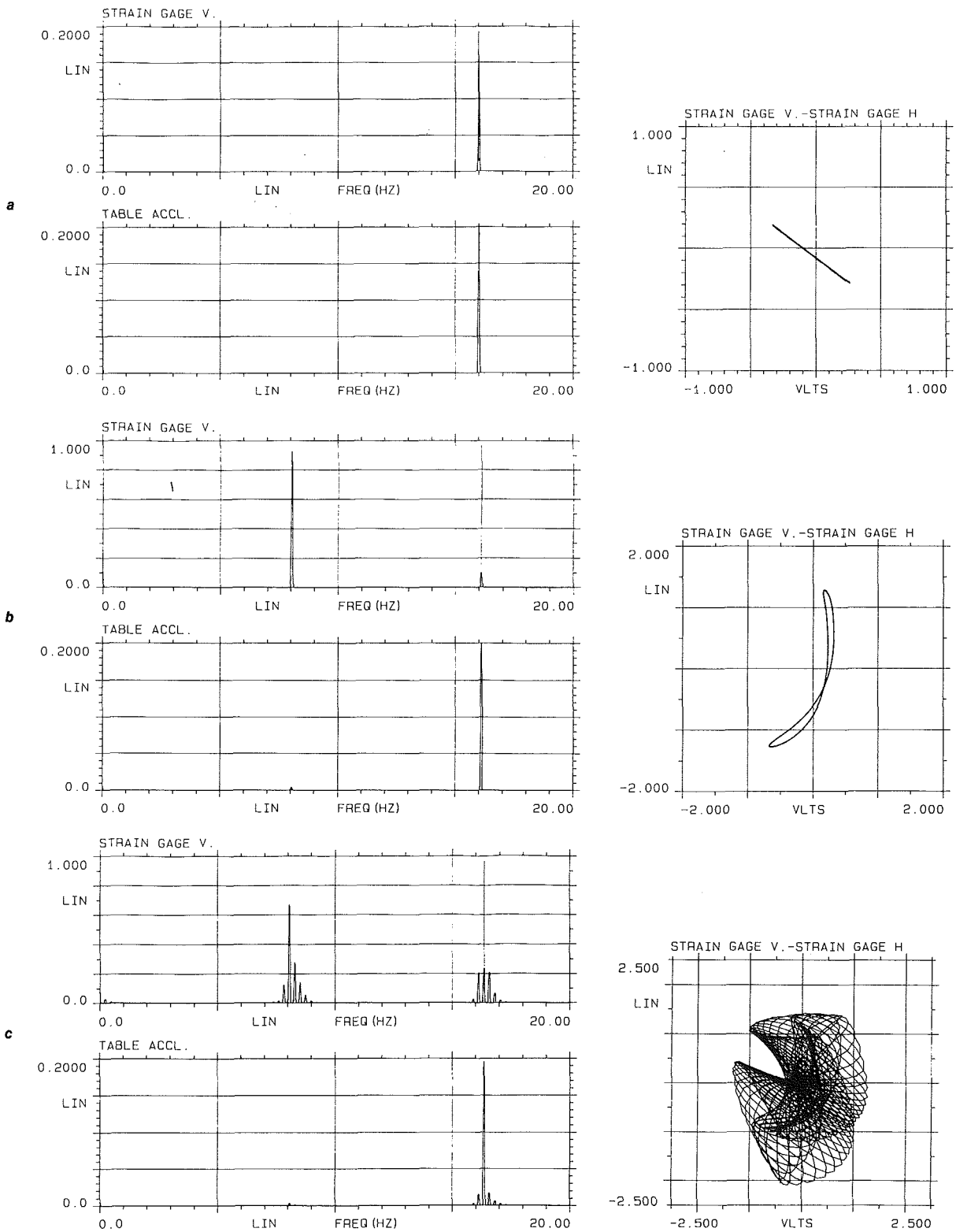


Fig. 7 Spectra of the response, table acceleration, and cross plot of the strain-gage signals: (*a*) $f = 16.00$ Hz, periodic linear response, (*b*) $f = 16.10$ Hz, periodic nonlinear response, and (*c*) $f = 16.36$ Hz, aperiodic response

shown, in that order, in the figure. There is a phase difference of about 90 deg between the two modal amplitudes.

In the region of stable periodic motions, the projection of the attractor was a point in the $a_1^* - a_2^*$ phase plane. Figure 10 shows the projection of the attractor for the excitation frequencies 16.36 Hz, 16.37 Hz, 16.46 Hz, and 16.47 Hz. The projections are limit cycles indicating that the modulated motion is two-period quasi-periodic with the incommensurable frequencies f and δf. The period of the limit cycle doubled as the excitation frequency was increased from 16.36 Hz to 16.37 Hz, consistent with the observations shown in Fig. 8. The motion eventually became chaotic at 16.44 Hz. As the excitation

Downloaded 03 May 2010 to 171.66.16.31. Redistribution subject to ASME license or copyright; see http://www.asme.org/terms/Terms_Use.cfm

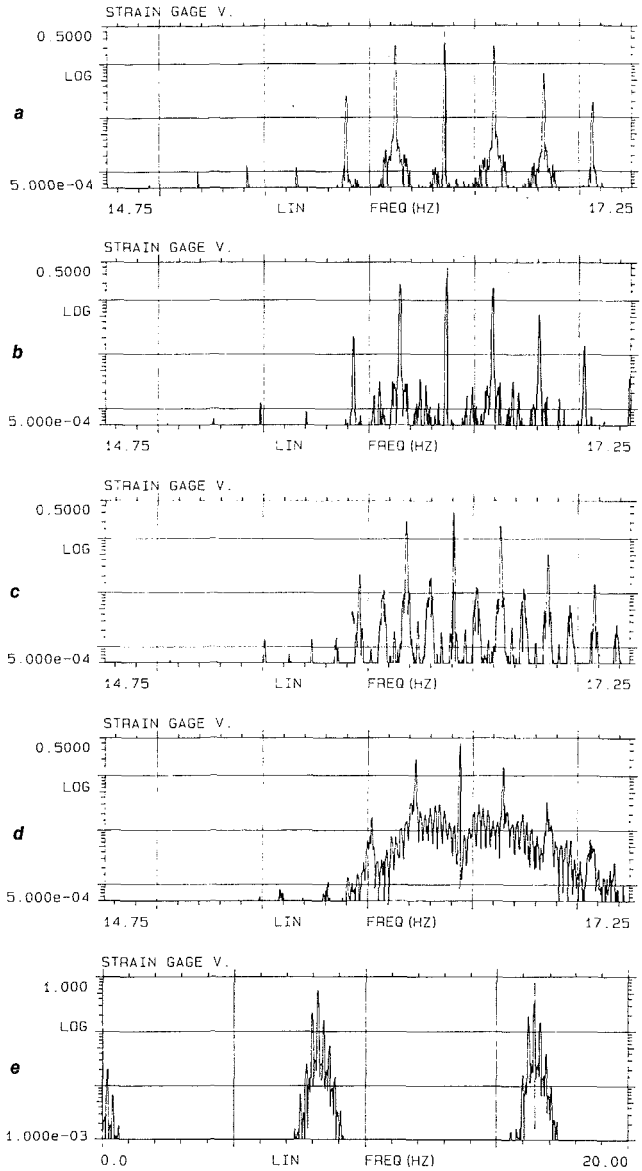


Fig. 8 Spectra of the response on a log scale: (*a*) $f = 16.36$ Hz, (*b*) $f = 16.37$ Hz, (*c*) $f = 16.41$ Hz, (*d*) $f = 16.44$ Hz, and (*e*) $f = 16.44$ Hz. We note the subharmonics of the modulation freqency appearing in the spectrum as we go from (*a*) to (*b*) to (*c*) and broadening around the carrier frequencies in (*d*) and (*e*).

frequency was increased to 16.46 Hz, we saw a two-period quasi-periodic motion. The period of the limit cycle was reduced by one-half as the excitation frequency was increased from 16.46 Hz to 16.47 Hz. Ciliberto and Gollub (1985) observed limit cycles and period-doubling bifurcations in the pseudo-phase plane, which was constructed using the method delays.

The Poincaré maps obtained at the excitation frequencies 16.36 Hz, 16.40 Hz, 16.43 Hz, and 16.44 Hz are shown in Fig. 11. They are consistent with the other observations.

In order to verify that the motion was chaotic at 16.44 Hz, we computed the pointwise dimension (Farmer et al., 1983). We collected 61,440 points at a sampling frequency of 120.00 Hz and a delay of 3.5 seconds was used for embedding. The plot for the pointwise dimension d, Fig. 12, shows the logarithm of the number of points $N(r)$ in an n-dimensional ball of radius r on the y-axis and the logarithm of the radius of the ball on the x-axis. The delay was chosen to give as large a scaling region for $N(r)$ as possible. For an embedding dimension of eight, d_ω as found to be 2.748, confirming the chaotic

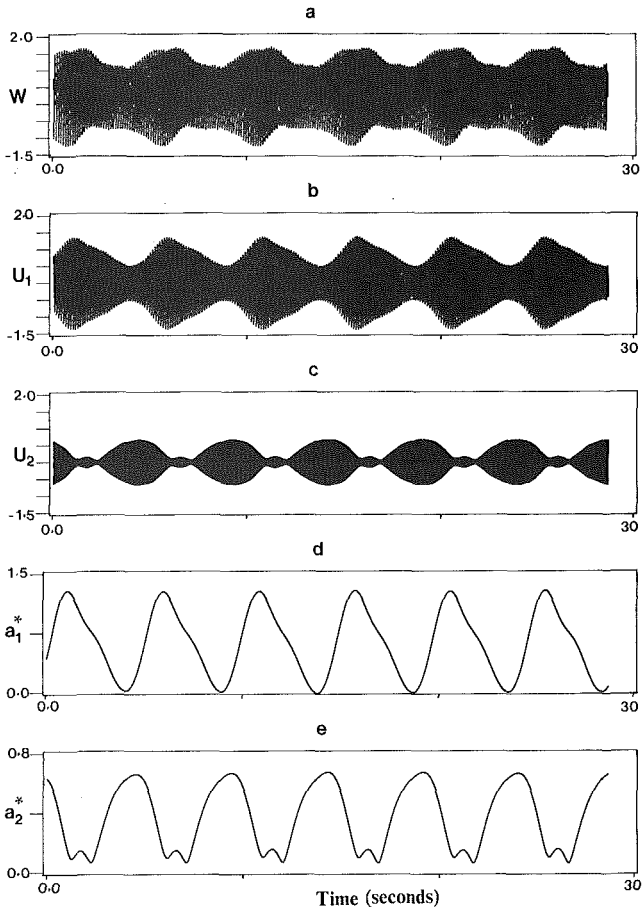


Fig. 9 Time traces: (*a*) measured strain-gage signal, (*b*) first mode, (*c*) second mode, (*d*) modal amplitude a_1^*, and (*e*) modal amplitude a_2^*

character of the motion. The variation of the dimension d, with respect to the delay time, was within a range of ± 0.2.

4 Summary

We conducted an experimental investigation of the response of a two-degree-of-freedom structure tuned for modal interaction to a small primary resonant excitation. The experimentally-obtained frequency-response curves show good qualitative agreement with the theoretical predictions. For certain detuning parameters, the response amplitude of the model showed that the saturation phenomenon breaks down at extremely small levels of excitation giving way to periodically-modulated motions and chaotically-modulated motions. We saw limit cycles in the projection of the attractor onto the phase plane of the amplitudes during periodically-modulated motions. Also, the Fourier spectra and Poincaré maps of the periodically-modulated motions indicate that the motion was two-period quasi-periodic. We saw period-doubling bifurcations in the modulation of the amplitudes and phases during the quasi-periodic motions, leading to the chaotic motions. Also, we described an experimental procedure to perform time-dependent modal decomposition. We believe that this procedure has a wide range of applicability.

Acknowledgment

This work was supported by the Air Force Office of Scientific Research under Grant Nos. AFOSR-86-0090 and F49620-87-C-0088.

References

Ciliberto, S., and Gollub, J. P., 1985, "Chaotic Mode Competition in

Downloaded 03 May 2010 to 171.66.16.31. Redistribution subject to ASME license or copyright; see http://www.asme.org/terms/Terms_Use.cfm

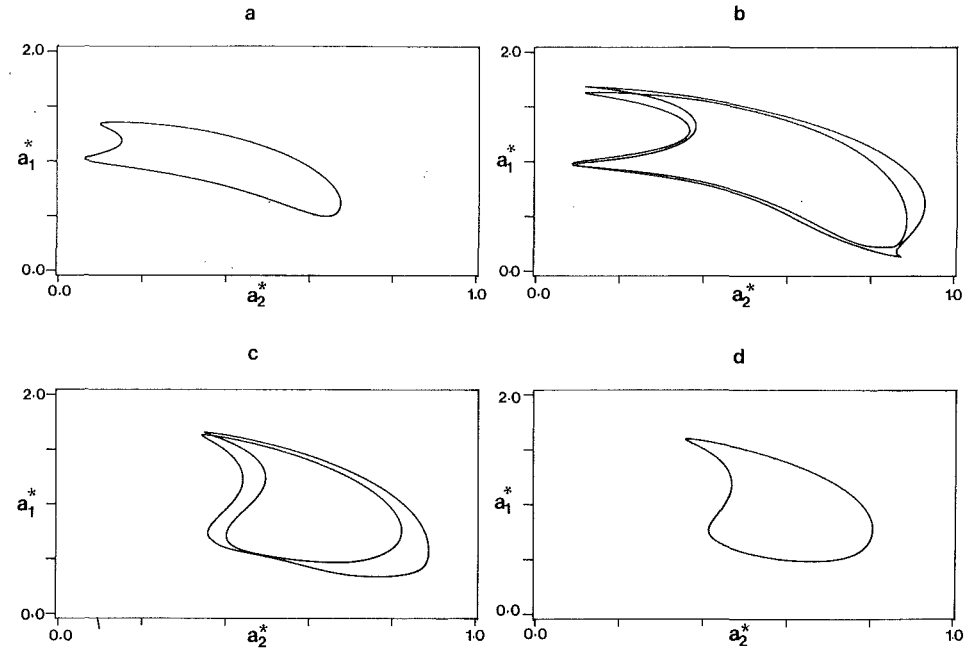


Fig. 10 Projection of the attractor on the $a_1^* - a_2^*$ plane: (a) $f = 16.36$ Hz, (b) $f = 16.37$ Hz, (c) $f = 16.46$ Hz, and (d) $f = 16.47$ Hz

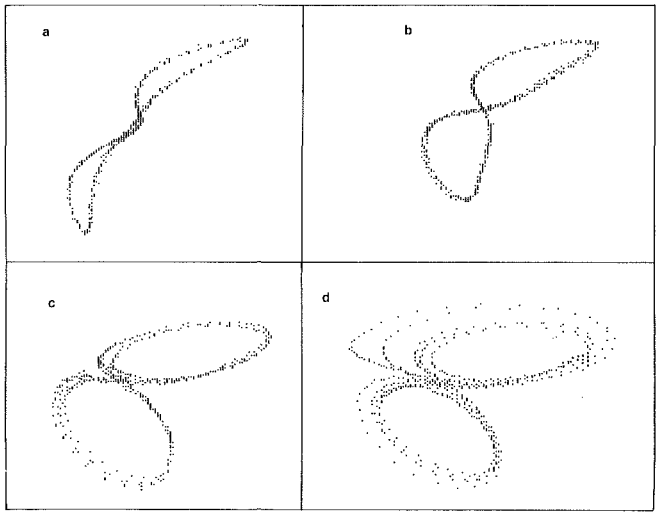


Fig. 11 Poincaré maps: (a) $f = 16.36$ Hz, (b) $f = 16.40$ Hz, (c) $f = 16.43$ Hz, and (d) $f = 16.44$ Hz

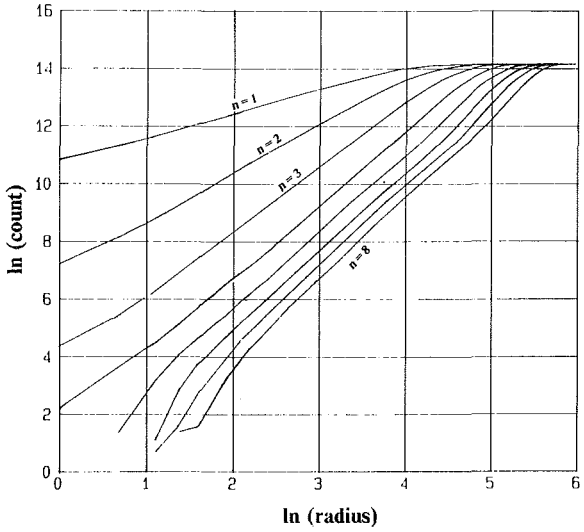


Fig. 12 Plot for pointwise dimension

Parametrically Forced Surface Waves," *Journal of Fluid Mechanics*, Vol. 158, pp. 381–398.

Dowell, E. H., and Pezeshki, C., 1986, "On the Understanding of Chaos in Duffings Equation Including a Comparison with Experiment," ASME JOURNAL OF APPLIED MECHANICS, Vol. 53, pp. 5–9.

Farmer, J. D., Ott, E., and Yorke, J. A., 1983, "The Dimension of Chaotic Attractors," *Physica D*, Vol. 7, pp. 153–180.

Haddow, A. G., Barr, A. D. S., and Mook, D. T., 1984, "Theoretical and Experimental Study of Modal Interaction in a Two-Degree-of-Freedom Structure," *Journal of Sound and Vibration*, Vol. 97, pp. 451–473.

Hatwal, H., Mallik, A. K., and Ghosh, A., 1983, "Forced Nonlinear Oscillations of an Autoparametric System—Part 2: Chaotic Responses," ASME JOURNAL OF APPLIED MECHANICS, Vol. 50, pp. 663–668.

Moon, F. C., 1980, "Experiments on Chaotic Motions of a Forced Nonlinear Oscillators: Strange Attractors," ASME JOURNAL OF APPLIED MECHANICS, Vol. 47, pp. 638–644.

Nayfeh, A. H., 1981, *Introduction to Perturbation Techniques*, John Wiley and Sons, New York.

Nayfeh, A. H., 1988, "On the Undersirable Roll Characteristics of Ships in Regular Sea," *Journal of Ship Research*, Vol. 32, pp. 92–100.

Nayfeh, A. H., 1989, "Application of the Method of Multiple Scales to Nonlinearly Coupled Oscillators," *Lasers, Molecules and Methods*, J. O. Hirschfelder, R. E. Wyatt, and R. D. Coalson, eds., John Wiley and Sons, New York, pp. 137–196.

Nayfeh, A. H., and Mook, D. T., 1979, *Nonlinear Oscillations*, John Wiley and Sons, New York.

Nayfeh, A. H., Mook, D. T., and Marshall, L. R., 1973, "Nonlinear Coupling of Pitch and Roll Modes in Ship Motions," *Journal of Hydronautics*, Vol. 7, pp. 145–152.

Nayfeh, A. H., and Raouf, R. A., 1987, "Nonlinear Forced Response of Infinitely Long Circular Cylindrical Shells," ASME JOURNAL OF APPLIED MECHANICS, Vol. 54, pp. 571–577.

Nayfeh, A. H., and Zavodney, L. D., 1988, "Experimental Observation of Amplitude- and Phase-Modulated Responses of Two Internally Coupled Oscillators to a Harmonic Excitation," ASME JOURNAL OF APPLIED MECHANICS, Vol. 55, pp. 706–710.

Sethna, P. R., 1965, "Vibrations of Dynamical Systems With Quadratic Nonlinearities," ASME JOURNAL OF APPLIED MECHANICS, Vol. 32, pp. 576–582.

Yamamoto, T., Yasuda, K., and Nagasaka, I., 1977, "On the Internal Resonance in a Nonlinear Two-Degree-of-Freedom System (Forced Vibrations Near the Higher Resonance Point When the Natural Frequencies are in the Ratio 1:2)," *Bulletin of the Japanese Society of Mechanical Engineering*, Vol. 20, pp. 1093–1101.

Downloaded 03 May 2010 to 171.66.16.31. Redistribution subject to ASME license or copyright; see http://www.asme.org/terms/Terms_Use.cfm

The Oscillation of Slender Elliptical Inviscid and Newtonian Jets: Effects of Surface Tension, Inertia, Viscosity, and Gravity

S. E. Bechtel
Department of Engineering Mechanics,
The Ohio State University,
Columbus, Ohio 43210
Mem. ASME

The motion of inviscid and Newtonian jets issuing from elliptical orifices is analyzed. The analysis is not confined to small departures of the jet free surface from a circular cylindrical mean surface, but rather is fully nonlinear. Two types of behavior are predicted: (1) In the presence of surface tension the major axis of the elliptical jet cross-section alternates between perpendicular directions with distance down the jet. In this case the system is described as a single-degree-of-freedom nonlinear oscillator, conservative for the inviscid elliptical jet in the absence of gravity, and nonconservative for the Newtonian jet. (2) When surface tension is neglected, the transformation occurs only once, after which the jet flattens into a sheet perpendicular to the major axis of the orifice. The effect of gravity is discussed both for downward flowing jets and fountains.

1 Introduction

In many instances when a fluid exits an elliptical orifice, the free jet behavior is oscillatory: From elliptical the cross-section becomes circular down the jet, then again elliptical but with major axis perpendicular to that of the elliptical orifice, then circular, then elliptical with major axis in the original direction, and so on. The oscillation of the major axis of the free surface elliptical cross-section between perpendicular directions persists until the oscillations are damped or the jet breaks up. In other instances of a jet issuing from an elliptical orifice, the transformation of the major axis of the jet cross-section between perpendicular directions occurs only once, after which the cross-section continues to flatten.

The latter type of behavior is described by Rayleigh for a water jet issuing under large pressure from an elliptical orifice of aspect ratio 24:17: "Near the orifice the sections of the vein are elliptical with major axis horizontal. The ellipticity gradually diminishes until at a distance of 30 lines from the orifice the section is circular. Beyond this point the vertical axis of the section increases, and the horizontal axis decreases, so that the vein reduces itself to a flat vertical sheet, very broad and thin. The sheet preserves its continuity to a distance of 6 feet from the orifice, where the vein is penetrated by air." (Rayleigh, 1879a). The former, oscillatory type of behavior is described by Rayleigh (for an arbitrary noncircular orifice): "In many cases, more especially when the orifices are small and the heads of water low, the extension of the sheets in directions perpendicular to the jet [orifice] reaches a limit. Sections taken at greater distances from the orifice show a gradual shortening of the sheets, until a compact form is attained, similar to that of the first contraction. Beyond this point, if the jet retains its coherence, sheets are gradually thrown out again, but in directions bisecting the angles between the directions of the former sheets. These sheets may, in their turn, reach a limit of development, again contract, and so on."

The first conjecture as to the mechanism of the nonoscillatory, single transformation behavior was provided by Bidone (1829) through reference to the different situation of two meeting streams. As related by Rayleigh (1879a): "If the axes of the jets intersect obliquely, a sheet is formed symmetrically in the plane perpendicular to that of the impinging jets." Taylor (1960) comments that the single transformation behavior occurs in the absence of surface tension, and constructs an approximate representation of the behavior by arranging a sequence of two-dimensional unsteady solutions for impinging inviscid jets along an axis. The only other analytical prediction of this behavior is by Green (1977) in the context of an inviscid one-dimensional director theory, again without surface tension.

The explanation of the oscillatory free surface behavior as due to surface tension was first suggested by Buff (1857) and then clarified by Rayleigh: "Under the operation of this [capillary] force the fluid behaves as if enclosed in an envelope of constant tension, and the recurrent form of the jet is due to vibrations of the fluid column about the circular figures of

Contributed by the Applied Mechanics Division of THE AMERICAN SOCIETY OF MECHANICAL ENGINEERS for presentation at the Winter Annual Meeting, San Francisco, Calif., December 10-15, 1989.

Discussion on this paper should be addressed to the Editorial Department, ASME, United Engineering Center, 345 East 47th Street, New York, N.Y. 10017, and will be accepted until two months after final publication of the paper itself in the JOURNAL OF APPLIED MECHANICS. Manuscript received by the ASME Applied Mechanics Division, September 7, 1988; final revision, March 2, 1989.
Paper No. 89-WA/APM-32.

Copyright © 1989 by ASME

Downloaded 03 May 2010 to 171.66.16.31. Redistribution subject to ASME license or copyright; see http://www.asme.org/terms/Terms_Use.cfm

equilibrium, superposed upon the general progressive motion. Since the phase of vibration depends upon the time elapsed, it is always the same at the same point in space, and thus the motion is *steady* in the hydrodynamical sense, and the boundary of the jet is fixed in space." (Rayleigh, 1879a). Although this behavior has long been understood qualitatively, analysis has been confined to *small* oscillations about a circular cylindrical mean surface of infinite extent (Rayleigh, 1879a, b; Caulk and Naghdi, 1979).

The two sets of elliptical free jet analyses are disjoint: the oscillatory type of behavior has not been connected within a single model to the behavior which leads to the formation of a sheet. (Taylor (1960) and Green (1977) neglect surface tension *a priori*, so that the oscillatory behavior is not possible in their analyses. The analyses of Rayleigh (1879a, b) and Caulk and Naghdi (1979) are restricted to small departures of the jet cross-section from circular, and are invalid as the cross-section flattens to a sheet; also a harmonic behavior along the entire length of the jet is assumed *a priori*.)

In this paper *both* types of behavior are predicted using a single comprehensive, *nonlinear* theory for slender elliptical free jets. A derivation of the theory in its most general and complete form is in Bechtel, Forest, Holm, and Lin (1988a, b). The theory is summarized in Sections 2 and 3 in the form best suited for this application. In Section 4 we use the theory to predict the two aforementioned types of behavior.

2 The Newtonian Free Jet With Elliptical Cross-Section

In this paper, the jet is assumed to be straight and along the direction of gravity. We introduce a system of fixed rectangular Cartesian coordinates $(x_1, x_2, x_3)=(x, y, z)$ and associated base vectors $\mathbf{e}_1, \mathbf{e}_2, \mathbf{e}_3$ such that the z-axis ($\mathbf{e}_3$ direction) is along the centerline of the jet. The free surface of the jet is given by

$$F(x,y,z,t)=\frac{x^2}{\phi_1^2(z,t)}+\frac{y^2}{\phi_2^2(z,t)}-1=0, \tag{1}$$

so that the free jet has elliptical cross-section, with semiaxes of lengths ϕ_1, ϕ_2 in the $\mathbf{e}_1$, $\mathbf{e}_2$ directions. The jet cross-section can change with distance down the jet and time, both in area and aspect ratio, since ϕ_1 and ϕ_2 are functions of z and t. At the boundary (1) we assume a constant surface tension σ. To decouple the outer ambient fluid problem from the free jet problem, we assume that the ambient material exerts a specified constant pressure p_a. (Refer to Joseph et al. (1983) for a study, in the axisymmetric special case, of the effects of entrainment of the ambient fluid.)

In this paper the fluid jet is modeled as inviscid or Newtonian; the oscillation of viscoelastic jets is studied in a later paper (Bechtel, 1989). The three-dimensional field equations in the jet are then

$$\mathrm{div}\mathbf{T}+\rho g\mathbf{e}_3=\rho\left[\frac{\partial}{\partial t}\mathbf{v}+(\mathbf{v}\cdot\nabla)\mathbf{v}\right], \tag{2}$$

$$\mathbf{T}=\hat{\mathbf{T}}-p\mathbf{I}=\mathbf{T}^T,\ \mathrm{div}\mathbf{v}=0,\ \hat{\mathbf{T}}=2\eta\mathbf{D}, \tag{3),(4),(5)}$$

where $\hat{\mathbf{T}}$ is the determinate part of the Cauchy stress tensor $\mathbf{T}$, p is the constraint pressure, ρ is the mass density (assumed constant), and $|g|$ is the acceleration of gravity. The sign of g is positive for a downward flowing jet and negative for a fountain. The constant η is the Newtonian viscosity ($\eta=0$ in the inviscid case) and $\mathbf{D}$ is the symmetric part of the velocity gradient.

3 The Slender Jet Model

The jet is now assumed to have two characteristic length scales: r_o in the transverse directions $\mathbf{e}_1$ and $\mathbf{e}_2$, and z_o in the axial direction $\mathbf{e}_3$. The nondimensional parameter

$$\epsilon=\frac{r_o}{z_o} \tag{6}$$

is called the slenderness ratio; for slender jets $\epsilon\ll 1$. This small parameter is also adopted by Schultz and Davis (1982) in their study of axisymmetric Newtonian jets.

The velocity vector is assumed to be expressible as a power series in the transverse coordinates x and y. Consistent with the form of the free surface (1), reflection symmetry is assumed about the (x, z) and (y, z) planes. The three-dimensional velocity vector is scaled with respect to the transverse and axial length scales r_o and z_o, and a characteristic time scale t_o. The scaled velocity is then

$$\tilde{\mathbf{v}}(\tilde{x},\tilde{y},\tilde{z},\tilde{t})=[\epsilon\tilde{x}\tilde{\zeta}_1(\tilde{z},\tilde{t})+\mathrm{O}(\epsilon^3)]\mathbf{e}_1+[\epsilon\tilde{y}\tilde{\zeta}_2(\tilde{z},\tilde{t})+\mathrm{O}(\epsilon^3)]\mathbf{e}_2$$
$$+[\tilde{v}(\tilde{z},\tilde{t})+\mathrm{O}(\epsilon^2)]\mathbf{e}_3, \tag{7}$$

where the dimensionless velocity $\tilde{\mathbf{v}}$ and dimensionless coordinates $\tilde{x}$, $\tilde{y}$, $\tilde{z}$, and $\tilde{t}$ are defined by

$$\mathbf{v}=\frac{z_o}{t_o}\tilde{\mathbf{v}},\ x=r_o\tilde{x},\ y=r_o\tilde{y},\ z=z_o\tilde{z},\ t=t_o\tilde{t}. \tag{8}$$

(In this paper, only the lowest-order problem in the slender jet asymptotics is discussed. The velocity coefficients involved in the lowest-order problem are ζ_1, ζ_2, and v. As is shown in Bechtel, Forest, and Lin (1989), the slender jet model can be derived to arbitrary order in ϵ by retaining terms beyond $\mathrm{O}(\epsilon)$ in expansion (7). The next order problem involves terms which are parabolic and cubic in the transverse coordinates.)

Insertion of expansion (7) in the incompressibility constraint (4) gives to lowest order in ϵ

$$\tilde{\zeta}_1+\tilde{\zeta}_2+\tilde{v}_{\tilde{z}}=0, \tag{9}$$

where subscript $\tilde{z}$ denotes partial differentiation with respect to the scaled axial coordinate $\tilde{z}$. Similarly, insertion of (1) and (7) into the kinematic free-surface condition yields to lowest order in ϵ

$$\tilde{\phi}_{1\tilde{t}}+\tilde{v}\tilde{\phi}_{1\tilde{z}}-\tilde{\phi}_1\tilde{\zeta}_1=0,\ \tilde{\phi}_{2\tilde{t}}+\tilde{v}\tilde{\phi}_{2\tilde{z}}-\tilde{\phi}_2\tilde{\zeta}_2=0, \tag{10),(11)}$$

where the free surface semiaxes ϕ_1, ϕ_2 have been scaled to the transverse length scale r_o, and subscript $\tilde{t}$ denotes partial differentiation with respect to nondimensional time $\tilde{t}$.

To complete the lowest-order slender jet model, the field equations (2), (5) are integrated over the jet cross-section bounded by the ellipse (1). This integration (*i*) removes the x and y dependence from the equations, and (*ii*) incorporates, through use of the divergence theorem, the surface tension free-surface condition. Importantly, *the technique results in a closed set of one-space one-time p.d.e.'s at each order in the slender jet asymptotics*. For details see Bechtel, Forest, Holm, and Lin (1988a, b) and Bechtel, Forest, and Lin (1989). The integrated equations which lead to the lowest-order slender jet models are, with tildes deleted,

$$B[P-A_{11}+\mathrm{O}(\epsilon^2)]=-\frac{1}{W}[\phi_1\phi_2\chi_c+\mathrm{O}(\epsilon^2)]$$
$$+\frac{1}{4}\phi_1^3\phi_2(\zeta_{1t}+v\zeta_{1z}+\zeta_1^2)+\mathrm{O}(\epsilon^2), \tag{12}$$

$$B[P-A_{22}+\mathrm{O}(\epsilon^2)]=-\frac{1}{W}[\phi_1\phi_2\chi_s+\mathrm{O}(\epsilon^2)]$$
$$+\frac{1}{4}\phi_1\phi_2^3(\zeta_{2t}+v\zeta_{2z}+\zeta_2^2)+\mathrm{O}(\epsilon^2), \tag{13}$$

Downloaded 03 May 2010 to 171.66.16.31. Redistribution subject to ASME license or copyright; see http://www.asme.org/terms/Terms_Use.cfm

$$\epsilon^2 B[A_{33z} - P_z + O(\epsilon^2)] = -\frac{1}{F}[\phi_1\phi_2 + O(\epsilon^2)]$$

$$+\frac{\epsilon^2}{W}[\phi_{1z}\phi_2\chi_c + \phi_1\phi_{2z}\chi_s + O(\epsilon^2)]$$

$$+\phi_1\phi_2(v_t + vv_z) + O(\epsilon^2), \quad (14)$$

$$A_{11} = 2Z\phi_1\phi_2\zeta_1 + O(\epsilon^2), \quad (15)$$

$$A_{22} = 2Z\phi_1\phi_2\zeta_2 + O(\epsilon^2), \quad (16)$$

$$A_{33} = 2Z\phi_1\phi_2 v_z + O(\epsilon^2), \quad (17)$$

where A_{ij} is the integral over the jet cross-section of the component $\hat{T}_{ij}$ of the determinant stress tensor, and P is the integral of the constraint pressure p over the jet cross-section minus $p_a\pi\phi_1\phi_2$ (the ambient pressure times the cross-sectional area). The forces A_{11}, A_{22}, A_{33}, and P are nondimensionalized with respect to a characteristic force scale f_o. The functions χ_c and χ_s are defined by

$$\chi_c = \frac{-\phi_1\phi_2}{\pi}\int_0^{2\pi}\frac{\cos^2\theta d\theta}{(\phi_1^2\sin^2\theta + \phi_2^2\cos^2\theta)^{3/2}}, \quad (18)$$

$$\chi_s = \frac{-\phi_1\phi_2}{\pi}\int_0^{2\pi}\frac{\sin^2\theta d\theta}{(\phi_1^2\sin^2\theta + \phi_2^2\cos^2\theta)^{3/2}}, \quad (19)$$

and the dimensionless groups in (12)–(17) are

$$B = \frac{t_o^2 f_o}{\pi\rho r_o^4},\ W = \frac{\rho r_o^3}{\sigma t_o^2},\ F = \frac{z_o}{g t_o^2},\ Z = \frac{\pi\eta r_o^2}{t_o f_o}. \quad (20a\text{–}d)$$

The parameters W, F, and $(BZ)^{-1}$ are recognized as the Weber, Froude, and Reynolds numbers, respectively.

We cannot produce lowest-order jet models from (9)–(17) until the orders of B, W, F, Z in the slenderness parameter ϵ are known. The scaling of these four quantities in a particular application, called the *regime* of free jet behavior, gives the balance in the application of the physical effects incorporated, namely surface tension, gravity, inertia, and viscosity. Only some of these effects need be leading order.

4 Oscillatory Regimes of Free Jet Behavior

In this paper we only consider free jets for which the dimensionless numbers B and $1/W$ are at most O(1), so that the inertia terms in the equations of transverse motion (12) and (13) are always leading order. It then follows that the forces arising from constitutive and capillary effects are insufficiently large to accelerate the slender jet in the axial direction, since the B and $1/W$ terms in equation (14) are at most $O(\epsilon^2)$, and therefore negligible compared to the O(1) inertia term. Regimes of this type produce an oscillation of the major axis of the elliptical jet cross-section between the $\mathbf{e}_1$ and $\mathbf{e}_2$ directions when surface tension is present. We call this type of regime *oscillatory*.

(The behavior predicted in the other type of regimes, in which the constitutive and surface tension terms are leading order in the axial equation of motion (14), is much different than that discussed in this paper. If B and/or $1/W$ are at least $O(\epsilon^{-2})$, jet behavior is characterized by swelling or contracting of the cross-section in the absence of free surface oscillation. Behavior in these nonoscillatory regimes is discussed in Bechtel, Forest, and Bogy (1986) and Bechtel, Forest, and Lin (1987, 1988). In Bechtel, Forest, Holm, and Lin (1988 a, b) we show that the one-dimensional theories of Matovich and Pearson (1969), Denn, Petrie, and Avenas (1975), Fisher and Denn (1976), Denn and Marrucci (1977), Tanner (1985), Gupta et al. (1986), and Beris and Liu (1988) for axisymmetric Newtonian and viscoelastic jets are the axisymmetric special cases of the lowest-order equations from particular regimes of this type.)

The physical mechanisms which may affect the motion of the jet in our model are surface tension, gravity, viscosity, and inertia. In the most general case, where all possible physical effects are important to leading order, each of the parameters B, W, F, and Z is O(1) in equations (12)–(17) and all four parameters appear in the lowest-order model. In applications for which only some of the physical effects are important, some of B, $1/W$, $1/F$, and Z are $O(\epsilon)$, and their corresponding terms are absent from the lowest-order model. In this paper we discuss solutions to the lowest-order jet model which are steady in time.

4.1 Inviscid Jet With Surface Tension. As a first regime, consider the case where only inertia and surface tension are important to leading order, so that $1/W$ and B are O(1) and $1/F$ and Z are $O(\epsilon)$ in equations (12)–(17). The temporally steady leading-order problem is then, without simplification,

$$v_z + \zeta_1 + \zeta_2 = 0,\ v\phi_{1z} = \phi_1\zeta_1,\ v\phi_{2z} = \phi_2\zeta_2, \quad (21),(22),(23)$$

$$BP = -\frac{1}{W}\phi_1\phi_2\chi_c + \frac{1}{4}\phi_1^3\phi_2(v\zeta_{1z} + \zeta_1^2), \quad (24)$$

$$BP = -\frac{1}{W}\phi_1\phi_2\chi_s + \frac{1}{4}\phi_1\phi_2^3(v\zeta_{2z} + \zeta_2^2),\ \phi_1\phi_2 v v_z = 0. \quad (25),(26)$$

Integration of equations (26) and (21)–(23) gives

$$v = 1,\ \phi_1\phi_2 = 1, \quad (27),(28)$$

where the integration constants have been taken as one by appropriate definition of the characteristic length and time scales. Equations (24) and (25) then reduce, after elimination of P, ζ_1, ζ_2, and ϕ_2, to

$$(1+\phi_1^4)\phi_{1zz} - 2\frac{\phi_{1z}^2}{\phi_1} + \frac{4}{W}\phi_1^3(\chi_s - \chi_c) = 0, \quad (29)$$

which integrates to[1]

$$\frac{1}{8}(1+\phi_1^{-4})\phi_{1z}^2 + \frac{4}{W}\left[\frac{E(1-\phi_1^4)}{\pi\phi_1} - \frac{1}{2}\right] = h, \quad (30)$$

where E is the complete elliptic integral of the second kind. The constant h is the energy level of the jet cross-section; the first term on the left side of equation (30) is the kinetic energy per length and the second term is the potential energy per length. The datum has been chosen so that the energy level h is non-negative, with $h=0$ for the axisymmetric jet. In dimensional quantities:

$$h = \underset{\text{cross-section}}{\iint}\frac{1}{2}\rho\mathbf{v}\cdot\mathbf{v}dA - \frac{1}{2}\rho\frac{z_o^2}{t_o^2}\pi r_o^2 + \underset{\text{cross-sectional boundary}}{\oint}\sigma ds - \sigma 2\pi r_o.$$

From equations (27)–(29) we see that in the absence of gravity the inviscid jet proceeds with constant axial velocity and cross-sectional area, but changing aspect ratio ϕ_2/ϕ_1. The motion predicted is that of a single-degree-of-freedom conservative nonlinear oscillator, with surface tension providing the restoring force. For any assigned energy level h (determined by boundary conditions on ϕ_1 and ϕ_{1z} at $z=0$) and Weber number, the trajectory on the (ϕ_1, ϕ_{1z}) phase plane is a closed curve about the point (1, 0). The parameter for the trajectory in this Eulerian description is axial distance z; in a Lagrangian description the parameter is time t (the two are equivalent since the jet is proceeding with constant axial velocity 1). Figure 1 shows the trajectories for several energy levels at

[1] This corrects an incorrect definition in Bechtel, Forest, and Lin (1988).

Downloaded 03 May 2010 to 171.66.16.31. Redistribution subject to ASME license or copyright; see http://www.asme.org/terms/Terms_Use.cfm

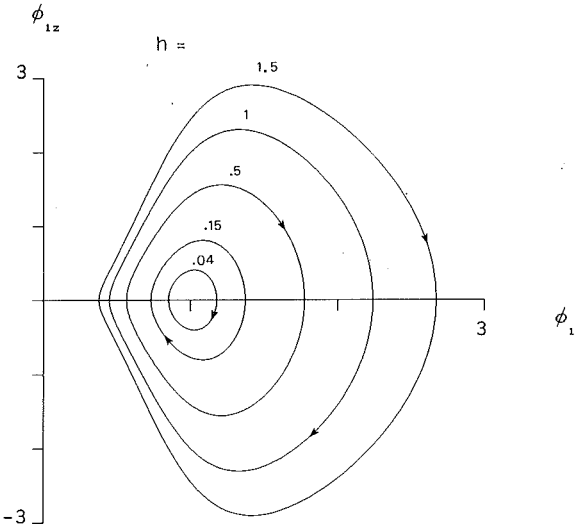


Fig. 1 Phase plane for elliptical inviscid jets with surface tension; $W = 1$, varying energy level

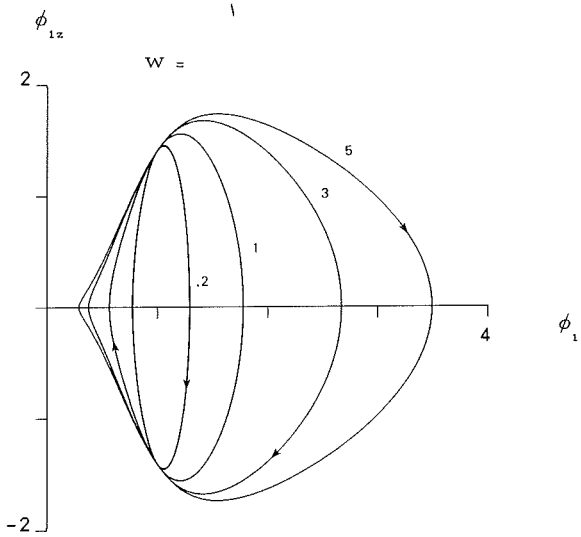


Fig. 2 Phase plane for elliptical inviscid jets with surface tension; $h = .5$, varying Weber number

fixed Weber number; Fig. 2 shows trajectories at fixed energy level for several values of Weber number.

The center (1, 0) on the phase plane corresponds to the trivial solution $v = \phi_1 = \phi_2 = 1$. It is a singular point in the sense that there is no motion in the transverse directions, and the axisymmetric jet has only the constant axial velocity component $v = 1$. The energy level h of the circular cylindrical jet is zero.

At the points of a trajectory directly above and below (1, 0) the jet is passing through the circular cross-section, and the energy due to surface tension is minimal; kinetic energy in the material cross-section at this phase in the cycle is maximal. The pair of intercepts with the $\phi_{1z} = 0$ axis in each trajectory are reciprocals of one another. At these points the ellipticity of the jet cross-section is extreme; from equation (28) we conclude that the maximum distortion of the jet cross-section from a circle in the $\mathbf{e}_1$ direction is equal to the maximum distortion in the $\mathbf{e}_2$ direction. The perpendicular extreme ellipses are separated by one-half wavelength (or one-half period in the Lagrangian description). This is the oscillatory jet behavior discussed by Rayleigh (1879a).

Figure 3 gives profiles and aspect ratios as functions of axial distances for jets with differing energy levels and common Weber number. Figure 4 gives profiles and aspect ratios for

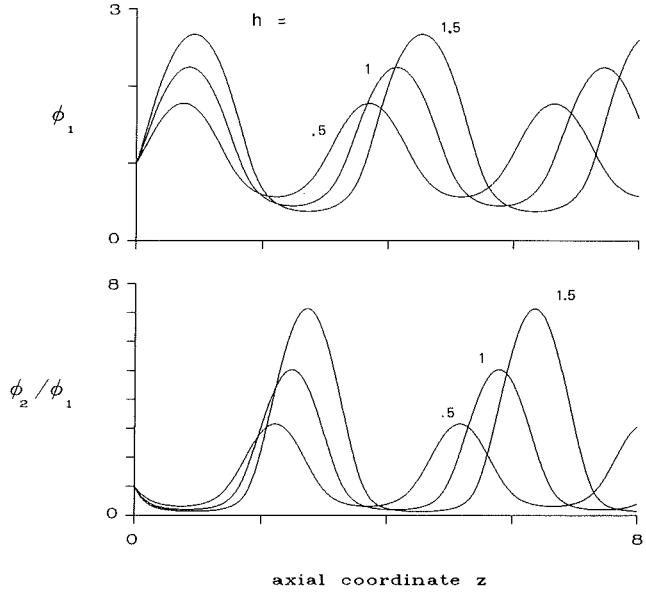


Fig. 3 Profiles and aspect ratios for elliptical invisicid jets with surface tension; $W = 1$, varying energy level

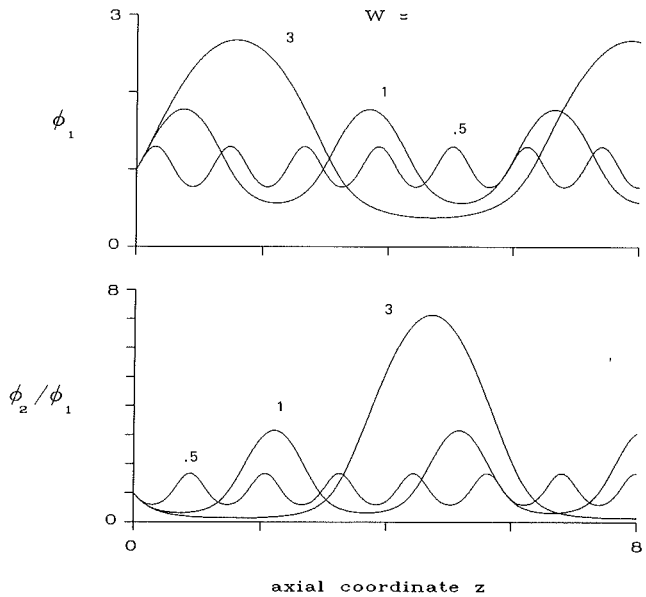


Fig. 4 Profiles and aspect ratios for elliptical invisicid jets with surface tension; $h = .5$, varying Weber number

jets with the same energy level, but different Weber numbers. Note that as the energy level increases or surface tension decreases (i.e., Weber number increases), the amplitude and wavelength of the spatial oscillation of the free surface semiaxes increase.

4.2 Newtonian Jet With Surface Tension. We now include Newtonian viscosity as a leading order physical effect in the elliptical jet model, by considering the case in which $1/W$, B, and Z are O(1) and $1/F$ is $O(\epsilon)$. The leading order equations from (9)–(17) reduce in this regime to

$$v = 1,\ \phi_1\phi_2 = 1,\ \frac{d}{dz}h = -\frac{4\phi_{1z}^2}{R\phi_1^2}, \qquad (31), (32), (33)$$

where now the energy level h defined in equation (30) is no longer constant, but decays with distance down the jet. (Recall BZ is the reciprocal of the Reynolds number.)

The motion is that of a single-degree-of-freedom nonconservative nonlinear oscillator. For any initial energy level h_o and values of W and R, the trajectory in the (ϕ_1, ϕ_{1z}) phase

Downloaded 03 May 2010 to 171.66.16.31. Redistribution subject to ASME license or copyright; see http://www.asme.org/terms/Terms_Use.cfm

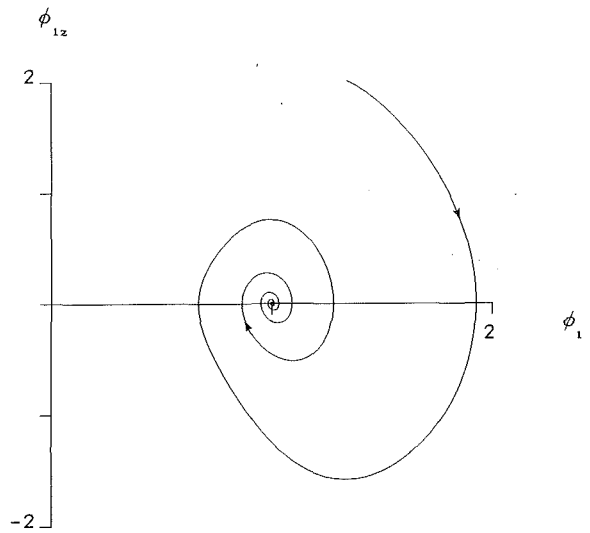


Fig. 5 Phase plane for an elliptical Newtonian jet with surface tension (*underdamped case*); *initial energy level* h_o = Weber number = 1, Reynolds number = 10

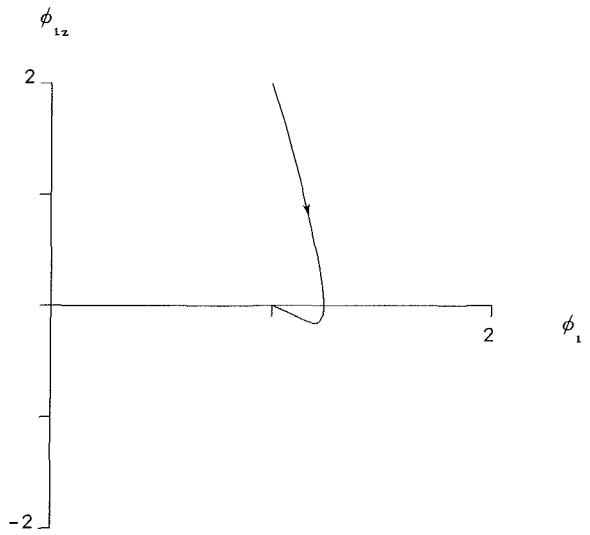


Fig. 6 Phase plane for an elliptical Newtonian jet with surface tension (overdamped case); $h_o = W = R = 1$

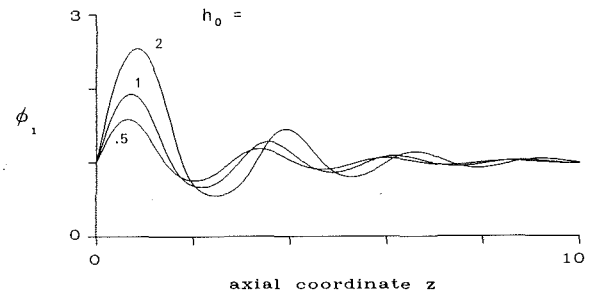


Fig. 7 Profiles for elliptical Newtonian jets with surface tension; $W = 1$, $R = 10$, varying initial energy level

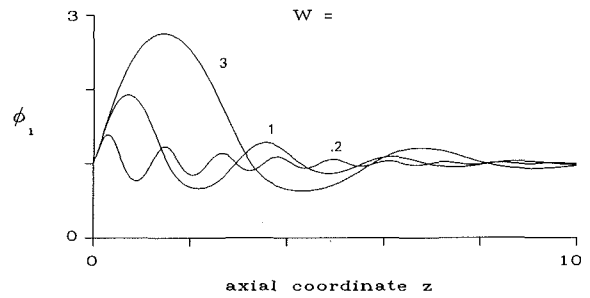


Fig. 8 Profiles for elliptical Newtonian jets with surface tension; $R = 10$, $h_o = 1$, varying Weber number

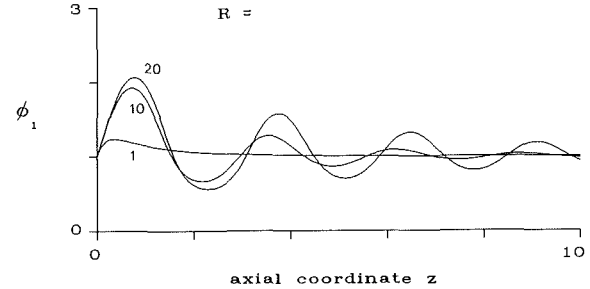


Fig. 9 Profiles for elliptical Newtonian jets with surface tension; $W = h_o = 1$, varying Reynolds number

plane goes to the globally attracting focus (1, 0). Therefore, any noncircular elliptical cross section of a Newtonian jet decays to a circle down the jet. The decay is either with oscillation between perpendicular transverse directions in the under damped case ($R^2/W = \rho r_O \sigma/\eta^2 > 8/3$), or without oscillation in the critically damped or overdamped cases ($R^2/W \leq 8/3$).

Figure 5 shows an underdamped trajectory; Fig. 6 shows an overdamped trajectory. Figures 7–9 give families of jet profiles, in which the initial energy level h_O, Weber number W, and Reynolds number R are varied, in turn, with the other two quantities held fixed.

4.3 Inviscid and Newtonian Jets Under Gravity. When inertia, surface tension, and gravity are the leading-order effects in the elliptical jet model ($1/W$, B, and $1/F$ are O(1) and Z is $O(\epsilon)$ in equations (12)–(17)) equations (9)–(11) and the O(1) equation from the axial equation of motion (14) integrate to

$$v\phi_1\phi_2 = 1, \quad v^2 = \frac{2z}{F} + 1. \qquad (34),(35)$$

The remainder of the lowest-order model in this regime reduces to, through elimination of all unknowns but ϕ_1,

$$\left[1 + \phi_1^4\left(\frac{2z}{F} + 1\right)\right]\phi_{1zz} - \frac{2}{\phi_1}\phi_{1z}^2 + \frac{4}{W}\phi_1^3(\chi_s - \chi_c)$$
$$+ \frac{1}{F}\left[\phi_1^4 - \left(\frac{2z}{F} + 1\right)^{-1}\right]\phi_{1z} - \frac{2}{F^2}\left(\frac{2z}{F} + 1\right)^{-2}\phi_1 = 0, \quad (36)$$

where now the second-order homogeneous integral-differential equation for $\phi_1(z)$ explicitly involves the independent variable z.

In the case of a downward flowing jet ($F > 0$), equations (34) and (35) predict that the axial velocity v increases from its initial value 1 with distance down the jet, and the jet cross-sectional area decreases from its initial value 1. The deformation of the cross-section during this draw-down, governed by equation (36), is oscillatory, with major axis of the ellipse alternating between the $\mathbf{e}_1$ and $\mathbf{e}_2$ directions. The trajectory of this single-degree-of-freedom oscillator spirals, on the positive ϕ_1 half of the (ϕ_1, ϕ_{1z}) phase plane, to the point (0, 0), reflecting that the cross-section contracts to a point at infinity. (See Fig. 10.)

Profiles for positive Froude number and several values of Weber number are shown in Fig. 11. Note that for each case the amplitude of oscillation of the semiaxis length ϕ_1 decays

Downloaded 03 May 2010 to 171.66.16.31. Redistribution subject to ASME license or copyright; see http://www.asme.org/terms/Terms_Use.cfm

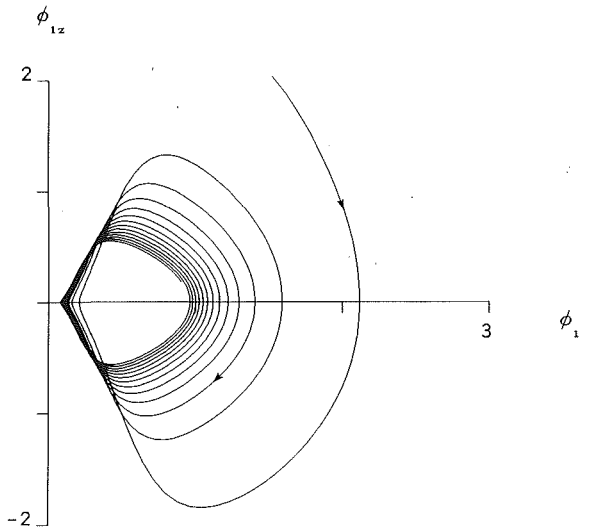


Fig. 10 Phase plane for draw-down under gravity of an elliptical inviscid jet with surface tension; $W = F = \phi_1(0) = 1$, $\phi_{1z}(0) = 2$

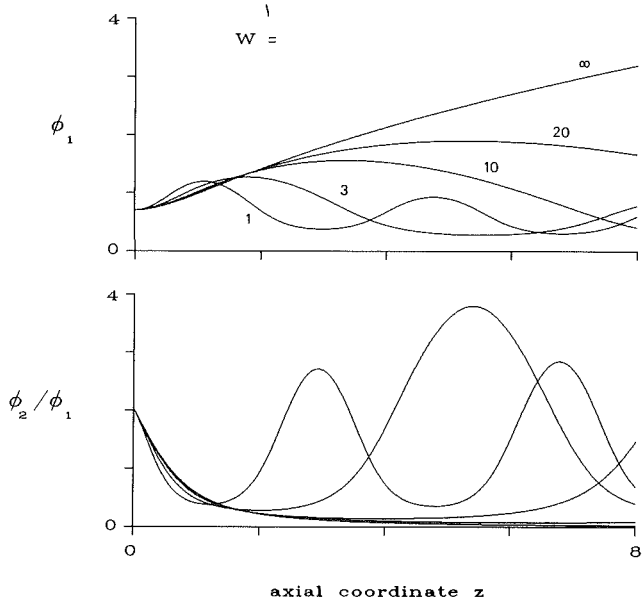


Fig. 11 Profiles and aspect ratios for draw-down under gravity of elliptical inviscid jets; $\phi_1(0) = .7$ (initial aspect ratio = 2), $\phi_{1z}(0) = 0$, $F = 1$, varying Weber number

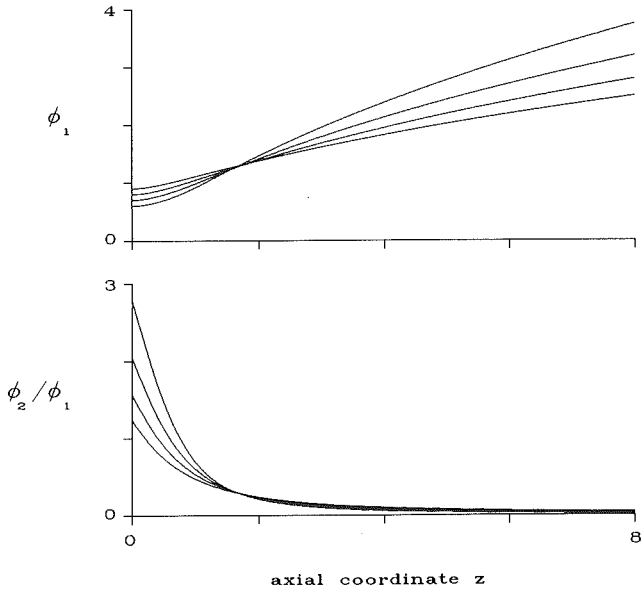


Fig. 12 Profiles of elliiptical inviscid jets under gravity in the absence of surface tension; $F = 1$, $\phi_{1z}(0) = 0$, varying initial aspect ratio

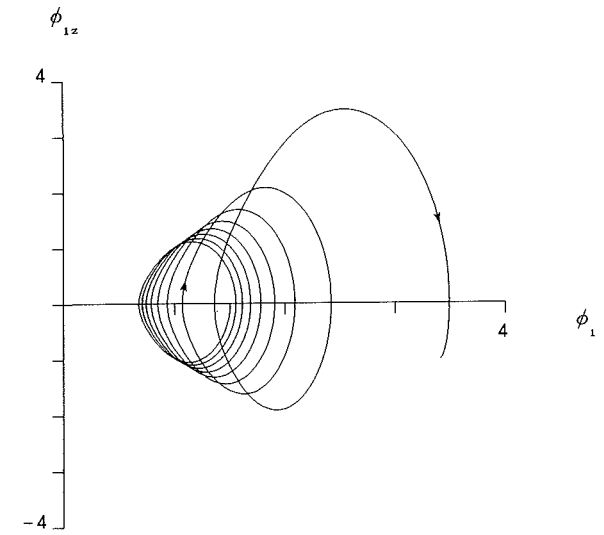


Fig. 13 Phase plane for an elliptical inviscid fountain with surface tension; $F = -40$, $\phi_1(0) = 1.5$, $\phi_{1z}(0) = 0$

with axial distance z, but the wavelength and aspect ratio amplitude of the oscillation increase with z. Also note that as surface tension becomes weaker relative to inertia and gravity (W increases), the rate of lengthening of the wavelength increases.

In the limit as surface tension vanishes from the leading-order model, the wavelength after the first passage through $\phi_1 = 0$ goes to infinity. In this regime (governed by equations (34)–(36) with $1/W$ set to zero), the jet cross-section does not oscillate, but instead contracts into a circle and then flattens into a ribbon in the plane perpendicular to the major axis of the orifice. This is the nonoscillatory jet behavior discussed by Rayleigh (1879a). That it is predicted in the absence of surface tension agrees with the conclusions of Taylor (1960) and Green (1977). Profiles of inviscid jets under gravity in the absence of surface tension are shown in Fig. 12.

In the case of a fountain ($F<0$), equations (34) and (35) predict that the jet attains a finite height $\bar{z} = |F|/2$, where the axial velocity vanishes and the cross-sectional area becomes infinite. The oscillation due to surface tension within the cross-section leading up to this height is governed by equation (35). The trajectory of the oscillation spirals outward in the (ϕ_1, ϕ_{1z}) plane, and shifts down the positive ϕ_1 axis. (See Fig. 13.)

When Newtonian viscosity is included in the regime, the term

$$\frac{16}{R}\left(\frac{2z}{F}+1\right)^{-1/2}\phi_1^2\left[\left(\frac{2z}{F}+1\right)\phi_{1z}+\frac{\phi_1}{2F}\right]$$

is added to the left-hand side of equation (36). Trajectories for a Newtonian downward flowing jet and Newtonian fountain are shown in Figs. 14 and 15, respectively.

Acknowledgment

This paper continues earlier work of the author with Prof. M. G. Forest and K. J. Lin. The author acknowledges the many contributions of these co-workers. This research is supported by the Air Force Office of Scientific Research through Grant AFOSR-87NM472.

Downloaded 03 May 2010 to 171.66.16.31. Redistribution subject to ASME license or copyright; see http://www.asme.org/terms/Terms_Use.cfm

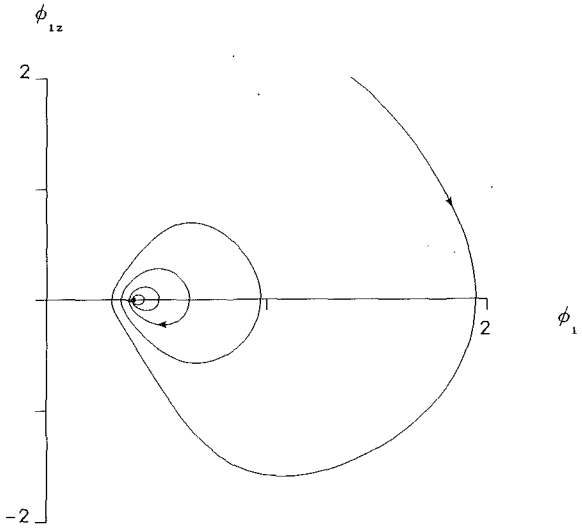


Fig. 14 Phase plane for drawn-down under gravity of an elliptical Newtonian jet with surface tension; $W = F = \phi_1(0) = 1$, $\phi_{1z}(0) = 2$, $R = 20$

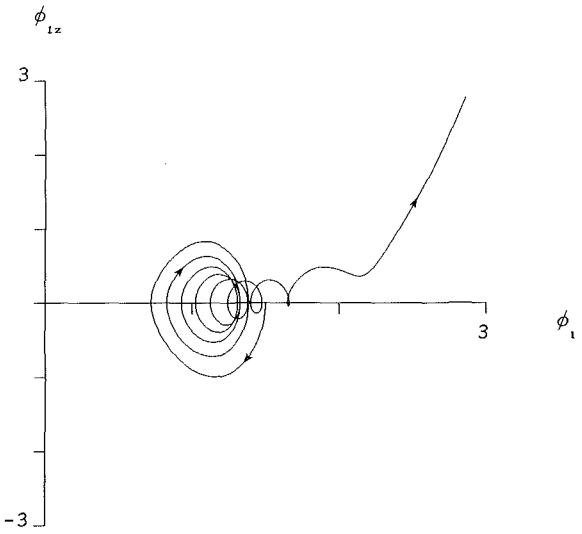


Fig. 15 Phase plane for an elliptical Newtonian fountain with surface tension; $F = -40$, $\phi_1(0) = 1.5$, $\phi_{1z}(0) = 0$, $R = 30$

References

Bechtel, S. E., 1989, "The Oscillation of Elliptical Viscoelastic Free Jets: Effect of Viscoelastic Properties and Nozzle Stresses," to be submitted to ASME JOURNAL OF APPLIED MECHANICS.

Bechtel, S. E., Forest, M. G., and Bogy, D. B., 1986, "A One-Dimensional Theory for Viscoelastic Fluid Jets, with Application to Extrudate Swell and Draw-Down Under Gravity," *J. Non-Newtonian Fluid Mechanics*, Vol. 21, pp. 273-308.

Bechtel, S. E., Forest, M. G., Holm, D. D., and Lin., K. J., 1988a, "One-Dimensional Closure Models for Three-Dimensional Incompressible Viscoelastic Free Jets: von Kármán Flow Geometry and Elliptical Cross-Section," *J. Fluid Mechanics*, Vol. 196, pp. 241-262.

Bechtel, S. E., Forest, M. G., Holm, D. D., and Lin, K. J., 1988b, "1-D Closure Models for Slender 3-D Viscoelastic Free Jets with Elliptical Cross Section," Proceedings of the AIAA/ASME/SIAM/APS 1st National Fluid Dynamics Congress, July 25-28, Cincinnati, Ohio, Part 3, pp. 2062-2069.

Bechtel, S. E., Forest, M. G., and Lin, K. J., 1987, "Effective Stress Rates of Viscoelastic Free Jets," *J. Non-Newtonian Fluid Mechanics*, Vol. 26, pp. 1-41.

Bechtel, S. E., Forest, M. G., and Lin, K. J., 1988, "On the Behavior of Viscoelastic Free Jets with Elliptical Cross Section," *J. Non-Newtonian Fluid Mechanics*, Vol. 27, pp. 87-126.

Bechtel, S. E., Forest, M. G., and Lin, K. J., 1989, "One-Dimensional Closure Models for Three-Dimensional Incompressible Viscoelastic Free Jets: Higher Order Perturbations," submitted to *J. Fluid Mechanics*.

Beris, A. N., and Liu, B., 1988, "Time-Dependent Fiber Spinning Equations. 1. Analysis of the Mathematical Behavior," *J. Non-Newtonian Fluid Mechanics*, Vol. 26, pp. 341-361.

Bidone, G., 1829, *Expériences sur la Forme et sur la Direction des Veines et des Courans d'Eau lancés par diverses Ouvertures*, Turin; also in *Academia delle scienze di Torino*, Vol. 34, 1830, pp. 229-362.

Buff, 1857, "Schreiben an Hrn. Prof. G. Magnus vom Prof. Buff," *Annalen der Physik und Chemie* von J. C. Poggendorff, Vol. 100, pp. 168-171.

Caulk, D. A. and Naghdi, P. M., 1979, "On the Onset of Breakup in Inviscid and Viscous Jets," ASME JOURNAL OF APPLIED MECHANICS, Vol. 46, pp. 291-297.

Denn, M. M., and Marrucci, G., 1977, "Effect of Relaxation Time Spectrum on Mechanics of Polymer Melt Spinning," *J. Non-Newtonian Fluid Mechanics*, Vol. 2, pp. 159-167.

Denn, M. M., Petrie, C. J. S., and Avenas, P., 1975, "Mechanics of Steady Spinning of a Viscoelastic Liquid," *AIChE J.*, Vol. 21, pp. 791-799.

Fisher, R. J., and Denn, M. M., 1976, "A Theory of Isothermal Melt Spinning and Draw Resonance," *AIChE J.*, Vol. 22, pp. 236-246.

Green, A. E., 1977, "On the Steady Motion of Jets with Elliptical Sections," *Acta Mechanica*, Vol. 26, pp. 171-177.

Gupta, R. K., Puszynski, J., and Sridhar, T., 1986, "Steady Spinning of the Oldroyd Fluid B.1. Theory," *J. Non-Newtonian Fluid Mechanics*, Vol. 21, pp. 99-113.

Joseph, D. D., Matta, J. E., and Nguyen, K., 1983, "Jets into Liquid Under Gravity," *J. Fluid Mechanics*, Vol. 128, pp. 443-468.

Matovich, M. A., and Pearson, J. R. A., 1969, "Spinning a Molten Threadline: Steady State Isothermal Viscous Flows," *Ind. Engng. Chem. Fundam.*, Vol. 8, pp. 512-520.

Lord Rayleigh, 1879a, "On the Capillary Phenomena of Jets," *Proceedings of the Royal Society*, London, Vol. 29, pp. 71-97.

Lord Rayleigh, 1879b, "On the Instability of Jets," *Proceedings of the London Mathematical Society*, Vol. 10, pp. 4-13.

Schultz, W. W., and Davis, S. H., 1982, "One-Dimensional Liquid Fibers," *J. Rheol.*, Vol. 26, pp. 331-345.

Tanner, R. I., 1985, *Engineering Rheology*, Clarendon Press.

Taylor, G. I., 1960, "Formation of Thin Flat Sheets of Water," *Journal of Fluid Mechanics*, Vol. 259, pp. 1-17.

Downloaded 03 May 2010 to 171.66.16.31. Redistribution subject to ASME license or copyright; see http://www.asme.org/terms/Terms_Use.cfm

Journal of Applied Mechanics

Brief Notes

A Brief Note is a short paper that presents a specific solution of technical interest in mechanics but which does not necessarily contain new general methods or results. A Brief Note should not exceed 1500 words *or equivalent* (a typical one-column figure or table is equivalent to 250 words; a one line equation to 30 words). Brief Notes will be subject to the usual review procedures prior to publication. After approval such Notes will be published as soon as possible. The Notes should be submitted to the Technical Editor of the JOURNAL OF APPLIED MECHANICS. Discussions on the Brief Notes should be addressed to the Editorial Department, ASME, United Engineering Center, 345 East 47th Street, New York, N. Y. 10017, or to the Technical Editor of the JOURNAL OF APPLIED MECHANICS. Discussions on Brief Notes appearing in this issue will be accepted until two months after publication. Readers who need more time to prepare a Discussion should request an extension of the deadline from the Editorial Department.

Deflection and Stress in a Curved Shaft Due to Torque

C. W. Bert[1]

This problem has been previously treated by Eubanks (1963) and Cheney (1965). The first paper was based on an unwidely approach using the Kirchhoff rod equations and the second used thin-ring theory but obtained an erroneous solution. Both papers were concerned only with pinned ends. Here the problem is formulated directly from thin-ring theory and solved directly. Results are given for both pinned and clamped ends.

The equilibrium equations for out-of-plane bending and twisting of a thin circular arc can be expressed as follows (cf., Volterra, 1952):

$$M_b'' + M_t' = 0;\ -M_b + M_t' = 0 \tag{1}$$

where M_b and M_t are the respective bending and twisting moments at a given circumferential angular position ϕ, and a prime denotes differentiation with respect to ϕ.

Eliminating M_t from equations (1) yields

$$M_b'' + M_b = 0. \tag{2}$$

The constitutive equations for small deflections and rotations are

$$M_b = (EI/R)(\beta - R^{-1}w'') \tag{3}$$

$$M_t = (C_t/R)(\beta + R^{-1}w)' \tag{4}$$

where EI and C_t are the respective flexural and torsional rigidities, R is the center-line radius of the arc, w is the out-of-plane deflection, and β is the twist angle.

Substituting M_b and w' from equations (3) and (4) into equation (2), and assuming that $M_t = T = \text{const.}$, gives the following governing ordinary differential equation

$$\beta^{iv} + 2\beta'' + \beta = 0 \tag{5}$$

which has the general solution

$$\beta(\phi) = C_1\cos\phi + C_2\sin\phi + C_3\phi\sin\phi + C_4\phi\cos\phi \tag{6}$$

where the C's are constants of integration. In view of equation (4), the general solution for the out-of-plane deflection is

$$w(\phi) = B_o - C_1R\cos\phi - C_2R\sin\phi - C_3R\phi\sin\phi - C_4R\phi\cos\phi + (TR^2/C_t)\phi. \tag{7}$$

Choosing the origin for ϕ to be at the midpoint of the arc and using the *antisymmetric* nature of the problem, one may write

$$w(\phi) = -w(-\phi). \tag{8}$$

Thus, B_o, C_1, and C_3 must vanish.

Pinned Ends. The appropriate boundary conditions are

$$M_b(\alpha) = 0,\ w(\alpha) = 0 \tag{9}$$

where α is one half of the total included angle of the arc. Thus

$$w(\phi) = (TR^2/C_t)\left(\phi - \alpha\frac{\sin\phi}{\sin\alpha}\right) \tag{10}$$

and

$$\beta(\phi) = (TR/C_t)(\alpha/\sin\alpha)\sin\phi. \tag{11}$$

It can easily be shown, for these boundary conditions, that M_b is identically zero along the entire length of the arc. As in the work of Cheney, equations (10) and (11) increase without bound at $\alpha = \pi$ only.

Clamped Ends. Here, the boundary conditions are

$$w(\alpha) = 0,\ w'(\alpha) = 0. \tag{12}$$

Thus,

$$w(\phi) = \left[\frac{(\alpha^2\sin\alpha)\sin\phi - (\sin\alpha - \alpha\cos\alpha)\phi\cos\phi}{\sin\alpha\cos\alpha - \alpha} + \phi\right](TR^2/C_t) \tag{13}$$

$$\beta(\phi) = \frac{-(\alpha^2\sin\alpha)\sin\phi + (\sin\alpha - \phi\cos\alpha)\phi\cos\phi}{\sin\alpha\cos\alpha - \alpha}(TR/C_t). \tag{14}$$

Unlike the solutions due to Eubanks and Cheney, equations (13) and (14) do not blow up for any values of α.

The bending moment is

$$M_b(\phi) = 2T(EI/C_t)\frac{\alpha\cos\alpha - \sin\alpha}{\sin\alpha\cos\alpha - \alpha}\sin\phi. \tag{15}$$

The maximum absolute value of M_b occurs at the ends ($\phi = \pm\alpha$) and is given by

[1]Benjamin H. Perkinson Chair Professor of Engineering, School of Aerospace and Mechanical Engineering, University of Oklahoma, Norman, OK 73019. Fellow ASME.

Manuscript received by the ASME Applied Mechanics Division, September 16, 1988; final revision, March 23, 1989.

Copyright © 1989 by ASME

Downloaded 03 May 2010 to 171.66.16.31. Redistribution subject to ASME license or copyright; see http://www.asme.org/terms/Terms_Use.cfm

$$|M_b|_{\max} = 2T(EI/C_t)\frac{\alpha\cos\alpha - \sin\alpha}{\sin\alpha\cos\alpha - \alpha}\sin\alpha. \quad (16)$$

For solid or concentric annular circular cross-sections, $C_t = GJ = 2GI$. Then equation (16) shows that $(M_b)_{\max}$ increases with the arc angle α and the material property ratio E/G. For isotropic materials with Poisson's ratios ≈ 0.3, $E/G \approx 2.6$. However, for certain composite materials with elastomeric matrices, E/G values as low as 0.129 have been reported by Hannibal and Avila (1984). Such material would obviously be very advantageous in reducing the maximum bending moment and, hence, the maximum bending stress.

References

Cheney, J. A., 1965, "Deflection of a Curved Shaft Due to Torque," ASME JOURNAL OF APPLIED MECHANICS, Vol. 32, pp. 215–217.

Eubanks, R. A., 1963, "Nonlinear Deformation of a Curved Shaft Due to Torque," ASME JOURNAL OF APPLIED MECHANICS, Vol. 30, pp. 468–471.

Hannibal, A. J., and Avila, J. A., 1984, "A Torsionally Stiff-Bending Soft Driveshaft," *Proceedings of the 39th Annual Conference*, Reinforced Plastics/Composites Institute, Society of the Plastics Industry, Jan. 16–19, 1984.

Volterra, E., 1952, "Bending of a Circular Beam Resting on an Elastic Foundation," ASME JOURNAL OF APPLIED MECHANICS, Vol. 19, pp. 1–4.

Mode III Crack Tip Plastic Zone Solution for Work Hardening Solid Using Dislocation Motion

J. Weertman[2]

The stress and strain field solutions for the stationary mode III crack in small-scale yielding is obtained from a direct physical picture in which the plastic strain is produced by the motion of infinitesimal dislocations. The analysis is based on a shifting center, cylindrical coordinate system. The nonredundant dislocation density is determined. The ratio of nonredundant to redundant dislocation density within the plastic zone may be a useful measure for placing cracks into a brittle class, a ductile class and semibrittle to semiductile classes.

1 Introduction

Rice obtained a fairly general solution to the stationary mode III crack in a work hardening solid (Rice, 1967). A more physically direct way to this solution uses the motion of infinitesimal screw dislocations and stepped stress-strain curves (Weertman, 1986). A solution is presented here which eliminates the need of a stepped stress-strain curve. The method of solution makes use of the fact that a stress field which satisfies the equilibrium condition contains, except in the elastic case, a dislocation density field. Plastic strain is produced by dislocation motion down the stress trajectories of the stress field. If the stress trajectories, on increasing the applied stress intensity factor, K, remain fixed in space, the strain can be found from an integration down a stress trajectory of the dislocation density.

2 Basic Equations

Let the nonredundant dislocation density be represented by $\mathfrak{B}$, expressed as total Burgers vector of infinitesimal screw dislocations in a unit area. (See Nabarro (1967) for a review of nonredundant dislocations.) The elastic-plastic stress law is assumed to be one which satisfies $d\sigma_{rz}/d\sigma_{\theta z} = d\epsilon_{rz}/d\epsilon_{\theta z}$ and $d\sigma_{xz}/d\sigma_{yz} = d\epsilon_{xz}/d\epsilon_{yz}$, where σ_{ij} and ϵ_{ij} are the usual stress and strain components. In addition, it is assumed that the stress magnitude, which is equal to $\sigma = (\sigma_{rz}^2 + \sigma_{\theta z}^2)^{1/2} = (\sigma_{xz}^2 + \sigma_{yz}^2)^{1/2}$, is a function of only the strain magnitude $\epsilon = (\epsilon_{rz}^2 + \epsilon_{\theta z}^2)^{1/2} = (\epsilon_{xz}^2 + \epsilon_{yz}^2)^{1/2}$.

Let the stress vector be defined to be $\boldsymbol{\sigma} = \sigma_{\theta z}\mathbf{i}_r - \sigma_{rz}\mathbf{i}_\theta = \sigma_{yz}\mathbf{i}_x - \sigma_{xz}\mathbf{i}_y$. *The screw dislocations move in the direction of the stress vector when the stress vector is defined this way.* (The screw dislocations move at right angles to the Rice defined stress vector.) The strain vector is given by $\boldsymbol{\epsilon} = \epsilon_{\theta z}\mathbf{i}_r - \epsilon_{rz}\mathbf{i}_\theta = \epsilon_{yz}\mathbf{i}_x - \epsilon_{xz}\mathbf{i}_y$. The total strain vector $\boldsymbol{\epsilon}$ is the sum of the elastic $\boldsymbol{\epsilon}^e$ and the plastic $\boldsymbol{\epsilon}^p = \boldsymbol{\sigma}/G$ parts (G is the shear modulus). The equation of static equilibrium is $\nabla \times \boldsymbol{\sigma} = 0$.

The dislocation density $\mathfrak{B}$ is given by the equation (Weertman, 1989)

$$\mathfrak{B} = -\nabla \cdot \boldsymbol{\epsilon}^p = (\nabla \cdot \boldsymbol{\sigma})/G. \quad (1)$$

Let a shifting center, cylindrical coordinate system r, θ be used in the analysis that is defined by the equations: $x = r\cos\theta + c(r,\theta)$; $y = r\sin\theta$. The crack tip is at $x = y = 0$. The origin of the shifting center, cylindrical coordinate system is on the crack plane at the point c ahead of the crack tip. In this coordinate system it is possible to show that the ∇ operator is given by (where $c' = \partial c/\partial r$ and $b' = \partial c/\partial\theta$).

$$\nabla = \{1/[r(1 + c'\cos\theta) - b'\sin\theta]\}$$
$$\{[1 + (r - b'\sin\theta)(\partial/\partial r) + c'\cos\theta + c'\sin\theta(\partial/\partial\theta)]\mathbf{i}_r$$
$$+ [(1 + c'\cos\theta)(\partial/\partial\theta) - b'\cos\theta(\partial/\partial r) - c'\sin\theta]\mathbf{i}_\theta\}. \quad (2)$$

3 Solution

It is obvious by inspection that stress vector

$$\boldsymbol{\sigma} = \sigma(r)[\cos(\theta/2)\mathbf{i}_r - \sin(\theta/2)\mathbf{i}_\theta] \quad (3)$$

satisfies the static equilibrium equation ($\nabla \times \boldsymbol{\sigma} = 0$), if $d\sigma/dr = -(\sigma/2r)(1 - c')$. The shifting center coordinate system is used with $c' \neq 0$ and $b' = 0$. (In the elastic region: $\sigma(r) = K/(2\pi r)^{1/2}$. The elastic-plastic boundary occurs at $r = r_0 = K^2/2\pi\sigma_0^2$, where σ_0 is the yield stress. The elastic strain at yield is $\epsilon_0 = \sigma_0 = G$.)

The stress vector field given by equation (3) contains the dislocation density:

$$\mathfrak{B} = \cos(\theta/2)[2r(d\sigma/dr) + \sigma(1 + c')]/[2Gr(1 + c'\cos\theta)]$$
$$= c'\sigma\cos(\theta/2)/Gr(1 + c'\cos\theta). \quad (4)$$

The plastic strain ϵ^p can be found with the aid of Fig. 1 *when the stress and dislocation trajectories in the plastic zone do not shift their positions when the applied stress is increased.* This figure shows two closely-spaced dislocation–stress trajectories. Let ds represent an incremental

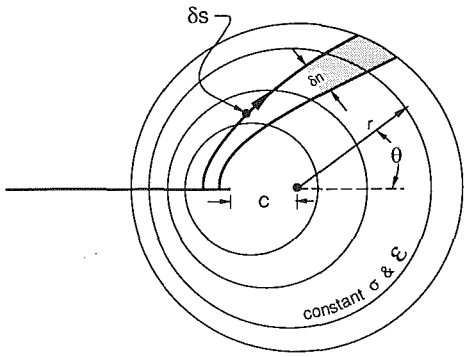


Fig. 1 Closely-spaced dislocation (and stress) trajectories

[2]Department of Materials Science and Engineering, Department of Geological Sciences, Northwestern University, Evanston, IL 60208.

Manuscript received by the ASME Applied Mechanics Division, October 21, 1988; final revision, March 6, 1989.

Downloaded 03 May 2010 to 171.66.16.31. Redistribution subject to ASME license or copyright; see http://www.asme.org/terms/Terms_Use.cfm

$$|M_b|_{\max} = 2T(EI/C_t)\frac{\alpha\cos\alpha - \sin\alpha}{\sin\alpha\cos\alpha - \alpha}\sin\alpha. \quad (16)$$

For solid or concentric annular circular cross-sections, $C_t = GJ = 2GI$. Then equation (16) shows that $(M_b)_{\max}$ increases with the arc angle α and the material property ratio E/G. For isotropic materials with Poisson's ratios ≈ 0.3, $E/G \approx 2.6$. However, for certain composite materials with elastomeric matrices, E/G values as low as 0.129 have been reported by Hannibal and Avila (1984). Such material would obviously be very advantageous in reducing the maximum bending moment and, hence, the maximum bending stress.

References

Cheney, J. A., 1965, "Deflection of a Curved Shaft Due to Torque," ASME JOURNAL OF APPLIED MECHANICS, Vol. 32, pp. 215–217.

Eubanks, R. A., 1963, "Nonlinear Deformation of a Curved Shaft Due to Torque," ASME JOURNAL OF APPLIED MECHANICS, Vol. 30, pp. 468–471.

Hannibal, A. J., and Avila, J. A., 1984, "A Torsionally Stiff-Bending Soft Driveshaft," *Proceedings of the 39th Annual Conference*, Reinforced Plastics/Composites Institute, Society of the Plastics Industry, Jan. 16–19, 1984.

Volterra, E., 1952, "Bending of a Circular Beam Resting on an Elastic Foundation," ASME JOURNAL OF APPLIED MECHANICS, Vol. 19, pp. 1–4.

Mode III Crack Tip Plastic Zone Solution for Work Hardening Solid Using Dislocation Motion

J. Weertman[2]

The stress and strain field solutions for the stationary mode III crack in small-scale yielding is obtained from a direct physical picture in which the plastic strain is produced by the motion of infinitesimal dislocations. The analysis is based on a shifting center, cylindrical coordinate system. The nonredundant dislocation density is determined. The ratio of nonredundant to redundant dislocation density within the plastic zone may be a useful measure for placing cracks into a brittle class, a ductile class and semibrittle to semiductile classes.

1 Introduction

Rice obtained a fairly general solution to the stationary mode III crack in a work hardening solid (Rice, 1967). A more physically direct way to this solution uses the motion of infinitesimal screw dislocations and stepped stress-strain curves (Weertman, 1986). A solution is presented here which eliminates the need of a stepped stress-strain curve. The method of solution makes use of the fact that a stress field which satisfies the equilibrium condition contains, except in the elastic case, a dislocation density field. Plastic strain is produced by dislocation motion down the stress trajectories of the stress field. If the stress trajectories, on increasing the applied stress intensity factor, K, remain fixed in space, the strain can be found from an integration down a stress trajectory of the dislocation density.

2 Basic Equations

Let the nonredundant dislocation density be represented by $\mathfrak{B}$, expressed as total Burgers vector of infinitesimal screw dislocations in a unit area. (See Nabarro (1967) for a review of nonredundant dislocations.) The elastic-plastic stress law is assumed to be one which satisfies $d\sigma_{rz}/d\sigma_{\theta z} = d\epsilon_{rz}/d\epsilon_{\theta z}$ and $d\sigma_{xz}/d\sigma_{yz} = d\epsilon_{xz}/d\epsilon_{yz}$, where σ_{ij} and ϵ_{ij} are the usual stress and strain components. In addition, it is assumed that the stress magnitude, which is equal to $\sigma = (\sigma_{rz}^2 + \sigma_{\theta z}^2)^{1/2} = (\sigma_{xz}^2 + \sigma_{yz}^2)^{1/2}$, is a function of only the strain magnitude $\epsilon = (\epsilon_{rz}^2 + \epsilon_{\theta z}^2)^{1/2} = (\epsilon_{xz}^2 + \epsilon_{yz}^2)^{1/2}$.

Let the stress vector be defined to be $\boldsymbol{\sigma} = \sigma_{\theta z}\mathbf{i}_r - \sigma_{rz}\mathbf{i}_\theta = \sigma_{yz}\mathbf{i}_x - \sigma_{xz}\mathbf{i}_y$. *The screw dislocations move in the direction of the stress vector when the stress vector is defined this way.* (The screw dislocations move at right angles to the Rice defined stress vector.) The strain vector is given by $\boldsymbol{\epsilon} = \epsilon_{\theta z}\mathbf{i}_r - \epsilon_{rz}\mathbf{i}_\theta = \epsilon_{yz}\mathbf{i}_x - \epsilon_{xz}\mathbf{i}_y$. The total strain vector $\boldsymbol{\epsilon}$ is the sum of the elastic $\boldsymbol{\epsilon}^e$ and the plastic $\boldsymbol{\epsilon}^p = \sigma/G$ parts (G is the shear modulus). The equation of static equilibrium is $\nabla \times \boldsymbol{\sigma} = 0$.

The dislocation density $\mathfrak{B}$ is given by the equation (Weertman, 1989)

$$\mathfrak{B} = -\nabla \cdot \boldsymbol{\epsilon}^p = (\nabla \cdot \boldsymbol{\sigma})/G. \quad (1)$$

Let a shifting center, cylindrical coordinate system r, θ be used in the analysis that is defined by the equations: $x = r\cos\theta + c(r,\theta)$; $y = r\sin\theta$. The crack tip is at $x = y = 0$. The origin of the shifting center, cylindrical coordinate system is on the crack plane at the point c ahead of the crack tip. In this coordinate system it is possible to show that the ∇ operator is given by (where $c' = \partial c/\partial r$ and $b' = \partial c/\partial\theta$).

$$\nabla = \{1/[r(1 + c'\cos\theta) - b'\sin\theta]\}\{[1 + (r - b'\sin\theta)(\partial/\partial r) + c'\cos\theta + c'\sin\theta(\partial/\partial\theta)]\mathbf{i}_r + [(1 + c'\cos\theta)(\partial/\partial\theta) - b'\cos\theta(\partial/\partial r) - c'\sin\theta]\mathbf{i}_\theta\}. \quad (2)$$

3 Solution

It is obvious by inspection that stress vector

$$\boldsymbol{\sigma} = \sigma(r)[\cos(\theta/2)\mathbf{i}_r - \sin(\theta/2)\mathbf{i}_\theta] \quad (3)$$

satisfies the static equilibrium equation ($\nabla \times \boldsymbol{\sigma} = 0$), if $d\sigma/dr = -(\sigma/2r)(1 - c')$. The shifting center coordinate system is used with $c' \neq 0$ and $b' = 0$. (In the elastic region: $\sigma(r) = K/(2\pi r)^{1/2}$. The elastic-plastic boundary occurs at $r = r_0 = K^2/2\pi\sigma_0^2$, where σ_0 is the yield stress. The elastic strain at yield is $\epsilon_0 = \sigma_0 = G$.)

The stress vector field given by equation (3) contains the dislocation density:

$$\mathfrak{B} = \cos(\theta/2)[2r(d\sigma/dr) + \sigma(1 + c')]/[2Gr(1 + c'\cos\theta)]$$

$$= c'\sigma\cos(\theta/2)/Gr(1 + c'\cos\theta). \quad (4)$$

The plastic strain ϵ^p can be found with the aid of Fig. 1 *when the stress and dislocation trajectories in the plastic zone do not shift their positions when the applied stress is increased.* This figure shows two closely-spaced dislocation–stress trajectories. Let ds represent an incremental

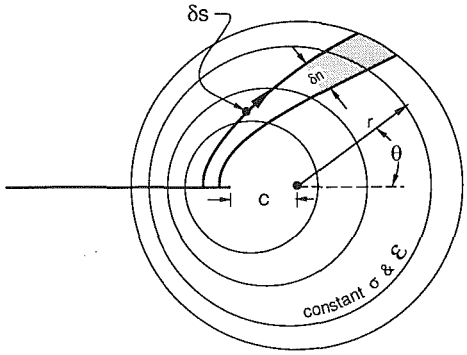


Fig. 1 Closely-spaced dislocation (and stress) trajectories

[2]Department of Materials Science and Engineering, Department of Geological Sciences, Northwestern University, Evanston, IL 60208.

Manuscript received by the ASME Applied Mechanics Division, October 21, 1988; final revision, March 6, 1989.

Copyright © 1989 by ASME

Downloaded 03 May 2010 to 171.66.16.31. Redistribution subject to ASME license or copyright; see http://www.asme.org/terms/Terms_Use.cfm

distance along a trajectory. The plastic strain ϵ^p is equal to the total Burgers vector of the dislocation between the (shaded region) trajectories beyond the position s divided by the separation of the trajectories at the place where the strain is found. (The function $f(s)$ is a measure of the trajectory separation.) Thus,

$$\epsilon^p = [1/\delta n_0 f(s)] \int_s^{s_{ep}} \mathcal{B}\delta n_0 f(s) ds \tag{5}$$

where s_{ep} is the value of s at the elastic-plastic boundary. Differentiating gives $\mathcal{B} = -\partial\epsilon^p/\partial s - [(\epsilon^p/f(s)](df/ds)$. Equations (1) give $\mathcal{B}(1/G)\partial\sigma/\partial s + (1/G)[(\sigma/f(s)](df/ds) = \partial\epsilon^e/\partial s + [(\epsilon^e/f(s)](df/ds)$. Eliminating $\mathcal{B}$ from these two expressions produces $\partial\epsilon/\partial s = -[(\epsilon/f(s)](df/ds)$. Thus $f(s) = \epsilon(0)/\epsilon(s)$. The dislocation density, therefore, is equal to

$$G\mathcal{B} = \partial\sigma/\partial s - (\sigma/\epsilon)(d\epsilon/ds) = (\partial\sigma/\partial s)[1 - (\sigma/\epsilon)(d\epsilon/d\sigma)]. \tag{6}$$

The stress trajectories of the stress vector (3) are given by the equation $dr/d\theta = -\cot(\theta/2)[r/(1-c')]$. The derivative ds/dr along a trajectory is given by $ds/dr = \{[1 + c'\cos\theta]^2 + [r(d\theta/dr) - c'\sin\theta]^2\}^{1/2} = (1 + c'\cos\theta)/\cos(\theta/2)$. Combining these results:

$$2c'/(1-c') = -[1 - (\sigma/\epsilon)(d\epsilon/d\sigma)]. \tag{7}$$

The equations above lead to

$$r = \int_\epsilon^\infty [r/c'\epsilon]d\epsilon - \int_\sigma^\infty [r/c'\sigma]d\sigma;$$

$$c = \int_\epsilon^\infty [r/\epsilon]d\epsilon - \int_\sigma^\infty [r/\sigma]d\sigma. \tag{8}$$

Substitution of equation (7) into the expression given earlier for $d\sigma/dr$, followed by integration, gives

$$r = r_0(\epsilon_0\sigma_0/\epsilon\sigma) = r_0(\sigma_0^2/\epsilon\sigma G) = K^2/2\pi\epsilon\sigma G. \tag{9}$$

If equation (9) is placed into equation (8), the result is

$$c = (K^2/2\pi G)\left\{\int_\epsilon^\infty (1/\epsilon^2\sigma)d\epsilon - \int_\sigma^\infty (1/\sigma^2\epsilon)d\sigma\right\}. \tag{10}$$

It is not difficult to show if the stress and dislocation trajectories are not to shift their positions in the plastic zone as K is increased that the ratio c/r must be a constant. If c' is a constant the stress-strain curve is either that of a power-law hardening material ($c/r = (1-n)/(1+n)$, $n \neq 0$, 1); or a perfectly-plastic solid ($c/r = 1$, $n = 0$); or an elastic solid ($c/r = 0$, $n = 1$). For a power-law work hardening material the stress trajectory equation is $r/r^* = [1/\sin(\theta/2)]^{(1+n)/n}$. In the elastic region the stress trajectory is given by the usual equation $r = \text{const.}/\sin^2(\theta/2)$.

For the power-law material the dislocation density $\rho_N = \mathcal{B}/b$ of nonredundant discrete dislocations (where the discrete Burgers vector length is b) is $\rho_N = (\sigma_0/brG)[r_0/r]^{n/(1+n)}\{(1 - n)/[1 + n + (1 - n)\cos\theta]\}\cos(\theta/2)$. The redundant dislocation density ρ_R generally is considered to be equal to $\alpha(\sigma/Gb)^2$, where α is a constant of order of magnitude 1. (Redundant discrete dislocations have a net Burgers vector of zero in any cross-section.) Thus ρ_N/ρ_R is equal to $\rho_N/\rho_R = (bG/\alpha r_0\sigma_0)[r_0/r]^{(1 - n)/(1 + n)}\{(1 - n)/[1 + n + (1 - n)\cos\theta]\}\cos(\theta/2)$. Near the crack tip $\rho_N >> \rho_R$. It is very questionable, of course, whether the conventional work hardening stress-strain curve is still valid once $\rho_N >> \rho_R$. This is why we suggested that cracks might be classified to the degree that nonredundant dislocations dominate the immediate crack tip region.

4 Summary

The stress-strain field of the crack tip plastic zone is linked directly with the physical picture in which the plastic strain is produced by the motion of infinitesimal dislocations down stress trajectories. The stress field itself is self evident when a shifting center, cylindrical coordinate system is used. Just as a problem with cylindrical geometry demands a cylindrical coordinate system for its analysis, rather than a cartesian one, although it may be solvable in the latter, the mode III crack problem wants a shifting center, cylindrical coordinate system rather than a fixed center one. The stress-strain field is the same one given earlier. This result is not new. The method by which the answer is reached enables the nonredundant dislocation density to be found readily. This is not true of the older, stress-potential based solution. This result is new. The use of nonredundant dislocations in the analysis is not just a matter of physical description convenience. Redundant and nonredundant dislocations can be identified in electron microscope examinations of samples. The nonredundant dislocation density given in the equations can, therefore, be subjected to experimental verification.

Acknowledgments

This research was supported by the National Science Foundation under NSF Grant DMR-86-07896.

References

Nabarro, F. R. N., 1967, *Theory of Crystal Dislocations*, Clarendon Press, Oxford, pp. 42–52.

Rice, J. R., 1967, "Stress Due to a Sharp Notch in a Work Hardening Elastic Plastic Material Loaded by Longitudinal Shear," ASME JOURNAL OF APPLIED MECHANICS, Vol. 34, pp. 287–298.

Weertman, J., 1986, "Dislocation Emission into a Mode III Crack Tip Plastic Zone," *Scripta Metallurgica*, Vol. 20, pp. 1483–1488.

Weertman, J., 1989, "The Analytical Solution of a Growing Steady-State Mode III Crack in an Elastic-Perfectly Plastic Solid Through an Electrical Analogy," *Proceedings of the Royal Society, London*, in press.

The Singularity at the Apex of a Rigid Wedge After Partial Separation

J. M. Duva[3]

1 Introduction

In a previous paper (Duva, 1988), the singularity at the apex of a square, rigid wedge embedded in a nonlinear material deforming in-plane strain was investigated. The aim of that analysis was to describe, in terms of the strength of the dominant singularity, the deformation at the (square) end of a relatively stiff, circular cylindrical fiber surrounded by plastically-deforming material. It was assumed that the deforming material (forming a 270 deg wedge) was perfectly bonded to the rigid material. In this note we consider that the wedge of deforming material has come away from the rigid material on one face. Such a situation is depicted in Fig. 1, which shows the voids formed at the end of a silicon carbide fiber in an aluminium matrix that has been subjected to tension in the direction of the fiber axis (Nutt and Duva, 1986). The plane-strain configuration we will analyze is shown in Fig. 2, including the plane polar coordinate system centered at the apex and the angle δ that gives the size of the wedge of deforming material. We will assume that in the vicinity of the apex the

[3]Department of Applied Mathematics, University of Virginia, Charlottesville, VA 22903. Assoc. Mem. ASME.

Manuscript received and accepted by the ASME Applied Mechanics Division, January 23, 1989.

Downloaded 03 May 2010 to 171.66.16.31. Redistribution subject to ASME license or copyright; see http://www.asme.org/terms/Terms_Use.cfm

distance along a trajectory. The plastic strain ϵ^p is equal to the total Burgers vector of the dislocation between the (shaded region) trajectories beyond the position s divided by the separation of the trajectories at the place where the strain is found. (The function $f(s)$ is a measure of the trajectory separation.) Thus,

$$\epsilon^p = [1/\delta n_0 f(s)] \int_s^{s_{ep}} \mathcal{B}\delta n_0 f(s) ds \tag{5}$$

where s_{ep} is the value of s at the elastic-plastic boundary. Differentiating gives $\mathcal{B} = -\partial\epsilon^p/\partial s - [(\epsilon^p/f(s)](df/ds)$. Equations (1) give $\mathcal{B}(1/G)\partial\sigma/\partial s + (1/G)[(\sigma/f(s))](df/ds) = \partial\epsilon^e/\partial s + [(\epsilon^e/f(s))](df/ds)$. Eliminating $\mathcal{B}$ from these two expressions produces $\partial\epsilon/\partial s = -[(\epsilon/f(s))](df/ds)$. Thus $f(s) = \epsilon(0)/\epsilon(s)$. The dislocation density, therefore, is equal to

$$G\mathcal{B} = \partial\sigma/\partial s - (\sigma/\epsilon)(d\epsilon/ds) = (\partial\sigma/\partial s)[1 - (\sigma/\epsilon)(d\epsilon/d\sigma)]. \tag{6}$$

The stress trajectories of the stress vector (3) are given by the equation $dr/d\theta = -\cot(\theta/2)[r/(1-c')]$. The derivative ds/dr along a trajectory is given by $ds/dr = \{[1 + c'\cos\theta]^2 + [r(d\theta/dr) - c'\sin\theta]^2\}^{1/2} = (1 + c'\cos\theta)/\cos(\theta/2)$. Combining these results:

$$2c'/(1-c') = -[1 - (\sigma/\epsilon)(d\epsilon/d\sigma)]. \tag{7}$$

The equations above lead to

$$r = \int_\epsilon^\infty [r/c'\epsilon]d\epsilon - \int_\sigma^\infty [r/c'\sigma]d\sigma;$$

$$c = \int_\epsilon^\infty [r/\epsilon]d\epsilon - \int_\sigma^\infty [r/\sigma]d\sigma. \tag{8}$$

Substitution of equation (7) into the expression given earlier for $d\sigma/dr$, followed by integration, gives

$$r = r_0(\epsilon_0\sigma_0/\epsilon\sigma) = r_0(\sigma_0^2/\epsilon\sigma G) = K^2/2\pi\epsilon\sigma G. \tag{9}$$

If equation (9) is placed into equation (8), the result is

$$c = (K^2/2\pi G)\left\{\int_\epsilon^\infty (1/\epsilon^2\sigma)d\epsilon - \int_\sigma^\infty (1/\sigma^2\epsilon)d\sigma\right\}. \tag{10}$$

It is not difficult to show if the stress and dislocation trajectories are not to shift their positions in the plastic zone as K is increased that the ratio c/r must be a constant. If c' is a constant the stress-strain curve is either that of a power-law hardening material ($c/r = (1-n)/(1+n)$, $n \neq 0$, 1); or a perfectly-plastic solid ($c/r = 1$, $n = 0$); or an elastic solid ($c/r = 0$, $n = 1$). For a power-law work hardening material the stress trajectory equation is $r/r^* = [1/\sin(\theta/2)]^{(1+n)/n}$. In the elastic region the stress trajectory is given by the usual equation $r = \text{const.}/\sin^2(\theta/2)$.

For the power-law material the dislocation density $\rho_N = \mathcal{B}/b$ of nonredundant discrete dislocations (where the discrete Burgers vector length is b) is $\rho_N = (\sigma_0/brG)[r_0/r]^{n/(1+n)}\{(1 - n)/[1 + n + (1 - n)\cos\theta]\}\cos(\theta/2)$. The redundant dislocation density ρ_R generally is considered to be equal to $\alpha(\sigma/Gb)^2$, where α is a constant of order of magnitude 1. (Redundant discrete dislocations have a net Burgers vector of zero in any cross-section.) Thus ρ_N/ρ_R is equal to $\rho_N/\rho_R = (bG/\alpha r_0\sigma_0)[r_0/r]^{(1 - n)/(1 + n)}\{(1 - n)/[1 + n + (1 - n)\cos\theta]\}\cos(\theta/2)$. Near the crack tip $\rho_N >> \rho_R$. It is very questionable, of course, whether the conventional work hardening stress-strain curve is still valid once $\rho_N >> \rho_R$. This is why we suggested that cracks might be classified to the degree that nonredundant dislocations dominate the immediate crack tip region.

4 Summary

The stress-strain field of the crack tip plastic zone is linked directly with the physical picture in which the plastic strain is produced by the motion of infinitesimal dislocations down stress trajectories. The stress field itself is self evident when a shifting center, cylindrical coordinate system is used. Just as a problem with cylindrical geometry demands a cylindrical coordinate system for its analysis, rather than a cartesian one, although it may be solvable in the latter, the mode III crack problem wants a shifting center, cylindrical coordinate system rather than a fixed center one. The stress-strain field is the same one given earlier. This result is not new. The method by which the answer is reached enables the nonredundant dislocation density to be found readily. This is not true of the older, stress-potential based solution. This result is new. The use of nonredundant dislocations in the analysis is not just a matter of physical description convenience. Redundant and nonredundant dislocations can be identified in electron microscope examinations of samples. The nonredundant dislocation density given in the equations can, therefore, be subjected to experimental verification.

Acknowledgments

This research was supported by the National Science Foundation under NSF Grant DMR-86-07896.

References

Nabarro, F. R. N., 1967, *Theory of Crystal Dislocations*, Clarendon Press, Oxford, pp. 42–52.

Rice, J. R., 1967, "Stress Due to a Sharp Notch in a Work Hardening Elastic Plastic Material Loaded by Longitudinal Shear," ASME JOURNAL OF APPLIED MECHANICS, Vol. 34, pp. 287–298.

Weertman, J., 1986, "Dislocation Emission into a Mode III Crack Tip Plastic Zone," *Scripta Metallurgica*, Vol. 20, pp. 1483–1488.

Weertman, J., 1989, "The Analytical Solution of a Growing Steady-State Mode III Crack in an Elastic-Perfectly Plastic Solid Through an Electrical Analogy," *Proceedings of the Royal Society, London*, in press.

The Singularity at the Apex of a Rigid Wedge After Partial Separation

J. M. Duva[3]

1 Introduction

In a previous paper (Duva, 1988), the singularity at the apex of a square, rigid wedge embedded in a nonlinear material deforming in-plane strain was investigated. The aim of that analysis was to describe, in terms of the strength of the dominant singularity, the deformation at the (square) end of a relatively stiff, circular cylindrical fiber surrounded by plastically-deforming material. It was assumed that the deforming material (forming a 270 deg wedge) was perfectly bonded to the rigid material. In this note we consider that the wedge of deforming material has come away from the rigid material on one face. Such a situation is depicted in Fig. 1, which shows the voids formed at the end of a silicon carbide fiber in an aluminium matrix that has been subjected to tension in the direction of the fiber axis (Nutt and Duva, 1986). The plane-strain configuration we will analyze is shown in Fig. 2, including the plane polar coordinate system centered at the apex and the angle δ that gives the size of the wedge of deforming material. We will assume that in the vicinity of the apex the

[3]Department of Applied Mathematics, University of Virginia, Charlottesville, VA 22903. Assoc. Mem. ASME.

Manuscript received and accepted by the ASME Applied Mechanics Division, January 23, 1989.

Copyright © 1989 by ASME

Downloaded 03 May 2010 to 171.66.16.31. Redistribution subject to ASME license or copyright; see http://www.asme.org/terms/Terms_Use.cfm

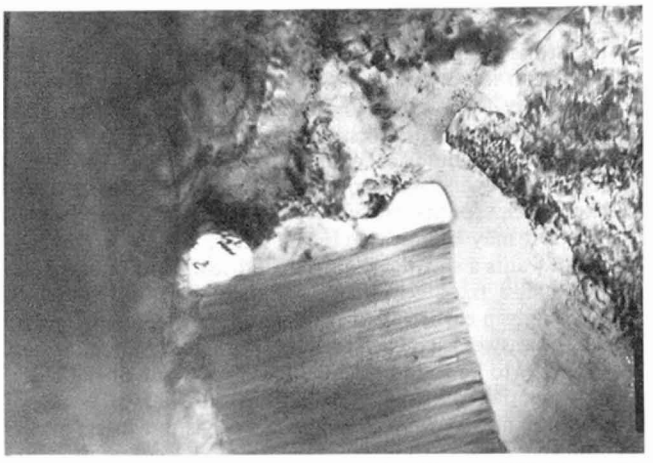


Fig. 1 Voids (white) formed at the end of a silicon carbide fiber in an aluminium matrix that has been subjected to tension in the fiber direction

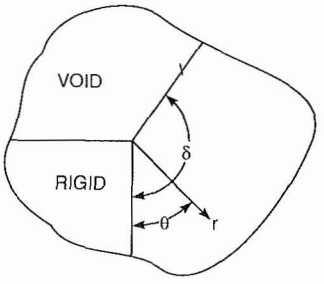


Fig. 2 Material wedge geometry with polar coordinates

stresses can be written in the form r^s times some unknown function of θ, as was done by Williams (1952) and many investigators since. Doing so leads to a nonlinear eigenvalue problem for s. We seek the smallest value of s greater than -1 as this represents the strongest admissible singularity.

2 Problem Formulation and Solution Procedure

The governing equations are the equilibrium equations

$$(r\sigma_{rr})_{,r} + \sigma_{r\theta,\theta} - \sigma_{\theta\theta} = 0, \tag{1a}$$

$$(r\sigma_{r\theta})_{,r} + \sigma_{\theta\theta,\theta} + \sigma_{r\theta} = 0, \tag{1b}$$

the linear strain-displacement equations

$$\epsilon_{rr} = \frac{\partial u}{\partial r}, \tag{2a}$$

$$\epsilon_{\theta\theta} = \frac{1}{r}\frac{\partial v}{\partial \theta} + \frac{u}{r}, \tag{2b}$$

$$\epsilon_{r\theta} = \frac{1}{2}\left(\frac{1}{r}\frac{\partial u}{\partial \theta} + \frac{\partial v}{\partial r} - \frac{v}{r}\right), \tag{2c}$$

where u and v are the radial and circumferential components of displacement, respectively, and the constitutive relation

$$\epsilon_{ij} = \frac{3}{2}\epsilon_0\left(\frac{\sigma_e}{\sigma_0}\right)^{n-1}\frac{s_{ij}}{\sigma_0}. \tag{3}$$

In this last equation, n, ϵ_0, and σ_0 are material parameters, s_{ij} is the stress deviator, and $\sigma_e = (3/2 s_{ij}s_{ij})^{1/2}$ is the effective stress. The power-law constitutive relation can be regarded as a nonlinear elastic relation or as a deformation theory plasticity relation giving the plastic strains for σ_e in excess of σ_0. In this study only an incompressible power-law material is considered. Incompressibility and the plane-strain constraint give some reason to expect real values of s; the similar interface crack and rough punch configurations have real, nonoscillating singularities under these conditions.

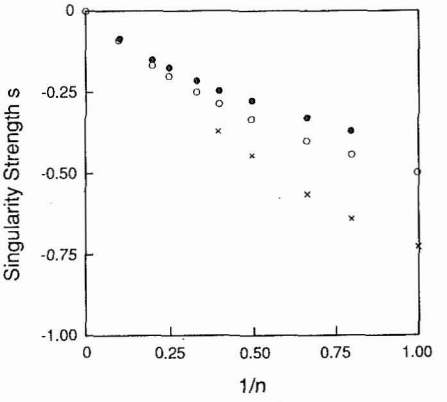


Fig. 3 Singularity strength s versus n^{-1} for wedge angles of $\delta = \pi/2$ (solid circles), $\delta = \pi$ (open circles), and $\delta = 3\pi/2$ (crosses)

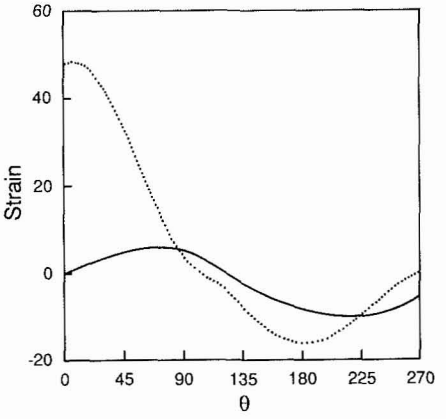


Fig. 4 Strain distributions $\epsilon_{rr} = \epsilon_{\theta\theta}$ (solid) and $\epsilon_{r\theta}$ (dotted) as a function of circumferential position θ, normalized with respect to $3/2\ \epsilon_0(r^s y(0)/\sigma_0)^n$

In order to imposed the mixed boundary conditions it is convenient, following Ponte (1987), to write

$$u = r^{sn+1}w(\theta), \quad v = r^{sn+1}x(\theta), \tag{4a}$$

$$\sigma_{rr} = r^s t(\theta),\ \sigma_{\theta\theta} = r^s y(\theta),\ \sigma_{r\theta} = r^s z(\theta),\ \sigma_{zz} = r^s p(\theta). \tag{4b}$$

Substitution into the governing equations (1), (2), and (3) and imposition of the plane-strain condition results in a coupled system of four first-order ordinary differential equations (for w, x, y, and z), and two algebraic equations. The equations are easily reproduced and not reported for the sake of brevity. This system composes a nonlinear eigenvalue problem for the parameter s, and was solved using a fourth-order Runge-Kutta integration scheme in conjunction with the shooting method (see Keller (1976)). A value of $y(0)$ was selected arbitrarily and values of s and $z(0)$ were adjusted until $z(\delta)$ and $y(\delta)$ were less than 10^{-4}.

3 Results and Discussion

Figure 3 shows results for s as a function of n for wedge angles of $\pi/2$, π and $3\pi/2$. This range was chosen because the wedge angle δ can be no larger than $3\pi/2$, given the geometry of the fiber end, and because the stresses are not singular for any value of n for $\delta < \pi/4$. The results for $n = 1$ agree in all cases with results reported by Dempsey and Sinclair (1981) and Atkinson et al. (1982). For a given value of n, the severity of the singularity increases with δ.

Downloaded 03 May 2010 to 171.66.16.31. Redistribution subject to ASME license or copyright; see http://www.asme.org/terms/Terms_Use.cfm

Figure 4 shows the (normalized) distribution of strain as a function of θ for the case $\delta = 3\pi/2$ and $n = 2.5$. Note that the relatively large shear strains at $\theta = 0$, though perhaps not surprising, are in qualitative agreement with finite element calculations performed by Nutt and Needleman (1987).

The efficacy of the numerical procedure depends both on δ and n. The first difficulty is the accurate solution of the algebraic equation for $t(\theta)$ at each step of the numerical integration of the system of differential equations. As n grows large this becomes increasingly time-consuming. The second difficulty is that the matrix used to improve the current estimates of s and $z(0)$ at each stage of the calculation can be very nearly singular, depending on whether or not the solution for the parameter values of interest is *isolated*. This feature is evident in the computation for $n = 1$ and $\delta = \pi/2$. If the solution is not well-behaved, not only is the process very sensitive to errors (such as those introduced in the calculation of $t(\theta)$ or in the numerical integration), but the process converges equadratically only in a very small neighborhood of the solution. The generation of solutions in these instances is very time-consuming. Finally, the large shear strains near the clamped boundary of the deforming wedge grow more severe with n and δ. These large gradients inhibit accurate numerical calculation.

The alert reader may have noticed that the numerical scheme is unnecessary if $\delta = \pi$. For this particular δ, an argument put forward by Hutchinson (1968) and Rice and Rosengren (1968) involving the path independence of the J-integral can be used to prove

$$s = \frac{-1}{n+1}.$$

This argument requires that there be no contribution to the integral from any portion of the integral path lying along the wedge flanks; the contribution is *not* zero for other angles. We note that the numerical scheme does reproduce the correct results in this case, subject to the limitations just described.

With an asymptotic expansion of the governing equations in powers of n^{-1}, it is easily shown that $s \to 0$ as $n^{-1} \to 0$. Thus, to complete the estimates of the singularity strengths, lines could be sketched in Fig. 3 connecting the last data point for each δ to the origin. The slope of these lines is available from the asymptotic analysis as well, but this first-order term is difficult to extract because second-order quantities are involved in the equations through the term $\sigma_e^{(1/n^{-1})-1}$.

References

Atkinson, C., Avila, J., Betz, E., and Smelser, R. E., 1982, "The Rod Pullout Problem, Theory and Experiment," *J. Mech. Phys. Sol.*, Vol. 30, No. 3, pp. 97–120.

Dempsey, J. P., and Sinclair, G. B., 1981, "On the Singular Behavior at the Vertices of a Bi-Material Wedge," *J. Elasticity*, Vol. 11, No. 3, pp. 317–327.

Duva, J. M., 1988, "The Singularity at the Apex of a Rigid Wedge Embedded in a Nonlinear Material," ASME JOURNAL OF APPLIED MECHANICS, Vol. 55, pp. 361–364.

Hutchinson, J. W., 1968, "Singular Behavior at the End of a Tensile Crack in a Hardening Material," *J. Mech. Phys. Sol.*, Vol. 16, No. 1, pp. 13–31.

Keller, H. B., 1976, "Numerical Solution of Two Point Boundary Value Problems," *Regional Conference Series in Applied Mathematics*, No. 24, SIAM, Philadelphia, PA.

Nutt, S. R., and Duva, J. M., 1986, "A Failure Mechanisms in Al-SiC Composites," *Scripta Met.*, Vol. 20, pp. 1055–1058.

Nutt, S. R., and Needleman, A., 1987, "Void Nucleation at Fiber Ends in Al-SiC Composites," *Scripta Met.*, Vol. 21, pp. 705–710.

Ponte Castañeda, P., 1987, "Asymptotic Fields in Steady Crack Growth with Linear Strain Hardening," *J. Mech. Phys. Sol.*, Vol. 35, No. 2, pp. 227–268.

Rice, J. R., and Rosengren, G. F., 1968, "Plain Strain Deformation Near a Crack Tip in a Power-Law Hardening Material," *J. Mech. Phys. Sol.*, Vol. 16, No. 1, pp. 1–12.

Williams, M. L., 1952, "Stress Singularities Arising From Various Boundary Conditions in Angular Corners of Plates in Extension," ASME JOURNAL OF APPLIED MECHANICS, Vol. 19, pp. 526–528.

Effect of the Coupling Between the Longitudinal and Transverse Displacements on the Dynamics of Rotating Curved Beams

Da-chih Chen[4] and A. A. Shabana[5]

1 Introduction

In most of the research on the dynamics of flexible mechanical systems, it is assumed that the undeformed flexible component is a geometrically perfect (straight) elastic link. In many industrial applications, however, it is impossible to achieve this perfection. Small initial curvature of the beams may result from manufacturing processes, and/or assembly when pretwist is required. Sanders and Tesar (1978) studied, both analytically and experimentally, the vibration response of systems composed of link members of realistic proportions. They concluded that links with significant curvature will develop more internal moment and larger longitudinal deformations than straight links due to axial periodic loads. Furthermore, the effect of both the increase in internal moment and larger longitudinal deformations may result in a "weak" link in the system. The effect of initial curvature on the vibration response of beams is also examined by Reddy and Singh (1981), Badlani and Midha (1982), Rosen and Rand (1985), and Dickinson (1980). In most of these investigations, mode shapes of straight beams are used, using classical approximation techniques, to describe the deformation of curved beams. In the mode shapes of straight beams, however, there is no kinematic coupling between the longitudinal and transverse displacements.

In this investigation, the effect of the neglect of the coupling between the longitudinal and transverse displacements in the assumed mode shapes of rotating curved beams is examined. A comparative study is presented to compare between the use of classical approximation techniques and the finite element method (Bartolone and Shabana, 1989; Chen, 1989) in the dynamics of initially-curved beams that undergo finite rotations.

2 Kinematic Relationships for Large Displacements

The global location of an arbitrary point p_i on the deformable curved beam i can be expressed in terms of the set of generalized coordinates of this beam as (Bartolone and Shabana, 1989; Chen, 1989)

$$\mathbf{r}^i = \mathbf{R}^i + \mathbf{A}^i \bar{\mathbf{u}}^i \tag{1}$$

where $\mathbf{r}^i$ is the global location of point p^i, $\mathbf{R}^i$ is the global location of the origin of the curved beam coordinate system, $\mathbf{A}^i$ is the transformation matrix from the beam coordinate system $(\bar{x}^i, \bar{y}^i)$ to the global coordinate system (x, y), and $\bar{\mathbf{u}}^i$ is the local position of point p^i defined in the beam coordinate system.

Taking into account the effects of both flexibility and initial curvature of the beam i, $\bar{\mathbf{u}}^i$ may be expressed as

$$\bar{\mathbf{u}}^i = \bar{\mathbf{u}}_o^i + \bar{\mathbf{u}}_f^i + \bar{\mathbf{u}}_c^i \tag{2}$$

where $\bar{\mathbf{u}}_o^i$ is the position vector of point p^i without initial curvature in the undeformed state, $\bar{\mathbf{u}}_f^i$ is the vector of elastic deformation of the beam, and $\bar{\mathbf{u}}_c^i$ is the change in the position vector due to the small initial curvature. These vectors are defined as

[4,5]Department of Mechanical Engineering, University of Illinois at Chicago, Chicago, IL 60680.

[5]Assoc. Mem. ASME.

Manuscript received by the ASME Applied Mechanics Division, March 3, 1989; final revision, April 13, 1989.

Downloaded 03 May 2010 to 171.66.16.31. Redistribution subject to ASME license or copyright; see http://www.asme.org/terms/Terms_Use.cfm

Figure 4 shows the (normalized) distribution of strain as a function of θ for the case $\delta = 3\pi/2$ and $n = 2.5$. Note that the relatively large shear strains at $\theta = 0$, though perhaps not surprising, are in qualitative agreement with finite element calculations performed by Nutt and Needleman (1987).

The efficacy of the numerical procedure depends both on δ and n. The first difficulty is the accurate solution of the algebraic equation for $t(\theta)$ at each step of the numerical integration of the system of differential equations. As n grows large this becomes increasingly time-consuming. The second difficulty is that the matrix used to improve the current estimates of s and $z(0)$ at each stage of the calculation can be very nearly singular, depending on whether or not the solution for the parameter values of interest is *isolated*. This feature is evident in the computation for $n = 1$ and $\delta = \pi/2$. If the solution is not well-behaved, not only is the process very sensitive to errors (such as those introduced in the calculation of $t(\theta)$ or in the numerical integration), but the process converges equadratically only in a very small neighborhood of the solution. The generation of solutions in these instances is very time-consuming. Finally, the large shear strains near the clamped boundary of the deforming wedge grow more severe with n and δ. These large gradients inhibit accurate numerical calculation.

The alert reader may have noticed that the numerical scheme is unnecessary if $\delta = \pi$. For this particular δ, an argument put forward by Hutchinson (1968) and Rice and Rosengren (1968) involving the path independence of the J-integral can be used to prove

$$s = \frac{-1}{n+1}.$$

This argument requires that there be no contribution to the integral from any portion of the integral path lying along the wedge flanks; the contribution is *not* zero for other angles. We note that the numerical scheme does reproduce the correct results in this case, subject to the limitations just described.

With an asymptotic expansion of the governing equations in powers of n^{-1}, it is easily shown that $s \to 0$ as $n^{-1} \to 0$. Thus, to complete the estimates of the singularity strengths, lines could be sketched in Fig. 3 connecting the last data point for each δ to the origin. The slope of these lines is available from the asymptotic analysis as well, but this first-order term is difficult to extract because second-order quantities are involved in the equations through the term $\sigma_e^{(1/n^{-1})-1}$.

References

Atkinson, C., Avila, J., Betz, E., and Smelser, R. E., 1982, "The Rod Pullout Problem, Theory and Experiment," *J. Mech. Phys. Sol.*, Vol. 30, No. 3, pp. 97–120.

Dempsey, J. P., and Sinclair, G. B., 1981, "On the Singular Behavior at the Vertices of a Bi-Material Wedge," *J. Elasticity*, Vol. 11, No. 3, pp. 317–327.

Duva, J. M., 1988, "The Singularity at the Apex of a Rigid Wedge Embedded in a Nonlinear Material," ASME JOURNAL OF APPLIED MECHANICS, Vol. 55, pp. 361–364.

Hutchinson, J. W., 1968, "Singular Behavior at the End of a Tensile Crack in a Hardening Material," *J. Mech. Phys. Sol.*, Vol. 16, No. 1, pp. 13–31.

Keller, H. B., 1976, "Numerical Solution of Two Point Boundary Value Problems," *Regional Conference Series in Applied Mathematics*, No. 24, SIAM, Philadelphia, PA.

Nutt, S. R., and Duva, J. M., 1986, "A Failure Mechanisms in Al-SiC Composites," *Scripta Met.*, Vol. 20, pp. 1055–1058.

Nutt, S. R., and Needleman, A., 1987, "Void Nucleation at Fiber Ends in Al-SiC Composites," *Scripta Met.*, Vol. 21, pp. 705–710.

Ponte Castañeda, P., 1987, "Asymptotic Fields in Steady Crack Growth with Linear Strain Hardening," *J. Mech. Phys. Sol.*, Vol. 35, No. 2, pp. 227–268.

Rice, J. R., and Rosengren, G. F., 1968, "Plain Strain Deformation Near a Crack Tip in a Power-Law Hardening Material," *J. Mech. Phys. Sol.*, Vol. 16, No. 1, pp. 1–12.

Williams, M. L., 1952, "Stress Singularities Arising From Various Boundary Conditions in Angular Corners of Plates in Extension," ASME JOURNAL OF APPLIED MECHANICS, Vol. 19, pp. 526–528.

Effect of the Coupling Between the Longitudinal and Transverse Displacements on the Dynamics of Rotating Curved Beams

Da-chih Chen[4] and A. A. Shabana[5]

1 Introduction

In most of the research on the dynamics of flexible mechanical systems, it is assumed that the undeformed flexible component is a geometrically perfect (straight) elastic link. In many industrial applications, however, it is impossible to achieve this perfection. Small initial curvature of the beams may result from manufacturing processes, and/or assembly when pretwist is required. Sanders and Tesar (1978) studied, both analytically and experimentally, the vibration response of systems composed of link members of realistic proportions. They concluded that links with significant curvature will develop more internal moment and larger longitudinal deformations than straight links due to axial periodic loads. Furthermore, the effect of both the increase in internal moment and larger longitudinal deformations may result in a "weak" link in the system. The effect of initial curvature on the vibration response of beams is also examined by Reddy and Singh (1981), Badlani and Midha (1982), Rosen and Rand (1985), and Dickinson (1980). In most of these investigations, mode shapes of straight beams are used, using classical approximation techniques, to describe the deformation of curved beams. In the mode shapes of straight beams, however, there is no kinematic coupling between the longitudinal and transverse displacements.

In this investigation, the effect of the neglect of the coupling between the longitudinal and transverse displacements in the assumed mode shapes of rotating curved beams is examined. A comparative study is presented to compare between the use of classical approximation techniques and the finite element method (Bartolone and Shabana, 1989; Chen, 1989) in the dynamics of initially-curved beams that undergo finite rotations.

2 Kinematic Relationships for Large Displacements

The global location of an arbitrary point p_i on the deformable curved beam i can be expressed in terms of the set of generalized coordinates of this beam as (Bartolone and Shabana, 1989; Chen, 1989)

$$\mathbf{r}^i = \mathbf{R}^i + \mathbf{A}^i \bar{\mathbf{u}}^i \tag{1}$$

where $\mathbf{r}^i$ is the global location of point p^i, $\mathbf{R}^i$ is the global location of the origin of the curved beam coordinate system, $\mathbf{A}^i$ is the transformation matrix from the beam coordinate system $(\bar{x}^i, \bar{y}^i)$ to the global coordinate system (x, y), and $\bar{\mathbf{u}}^i$ is the local position of point p^i defined in the beam coordinate system.

Taking into account the effects of both flexibility and initial curvature of the beam i, $\bar{\mathbf{u}}^i$ may be expressed as

$$\bar{\mathbf{u}}^i = \bar{\mathbf{u}}_o^i + \bar{\mathbf{u}}_f^i + \bar{\mathbf{u}}_c^i \tag{2}$$

where $\bar{\mathbf{u}}_o^i$ is the position vector of point p^i without initial curvature in the undeformed state, $\bar{\mathbf{u}}_f^i$ is the vector of elastic deformation of the beam, and $\bar{\mathbf{u}}_c^i$ is the change in the position vector due to the small initial curvature. These vectors are defined as

[4,5] Department of Mechanical Engineering, University of Illinois at Chicago, Chicago, IL 60680.

[5] Assoc. Mem. ASME.

Manuscript received by the ASME Applied Mechanics Division, March 3, 1989; final revision, April 13, 1989.

Copyright © 1989 by ASME

Downloaded 03 May 2010 to 171.66.16.31. Redistribution subject to ASME license or copyright; see http://www.asme.org/terms/Terms_Use.cfm

$$\tilde{\mathbf{u}}_o^i = (\tilde{u}_{ox}^i \;\; \tilde{u}_{oy}^i)^T \tag{3}$$

$$\tilde{\mathbf{u}}_f^i = (\tilde{u}_{fx}^i \;\; \tilde{u}_{fy}^i)^T = \mathbf{S}_f^i \mathbf{q}_f^i \tag{4}$$

$$\tilde{\mathbf{u}}_c^i = (\tilde{u}_{cx}^i \;\; \tilde{u}_{cy}^i)^T = \mathbf{S}_c^i \epsilon^i \tag{5}$$

where $\mathbf{S}_f^i$ is the matrix of shape functions of beam i, $\mathbf{q}_f^i$ is the vector of elastic coordinates, $\mathbf{S}_c^i$ is the shape matrix of the curved beam i in the undeformed state, and ϵ^i is the amplitude of the curvature function.

3 Kinetic Energy

The kinetic energy of the curved beam i is defined as

$$T^i = \frac{1}{2}\int_{V^i} \rho^i \dot{\mathbf{r}}^{iT} \dot{\mathbf{r}}^i dV^i \tag{6}$$

where ρ^i and V^i are, respectively, the mass density and volume of the beam and $\mathbf{r}^i$ is the velocity vector. Substituting the velocity vector into equation (6), one obtains

$$T^i = \frac{1}{2}\dot{\mathbf{q}}^{iT} \mathbf{M}^i \dot{\mathbf{q}}^i \tag{7}$$

where

$$\dot{\mathbf{q}}^i = \begin{bmatrix} \dot{\mathbf{R}}^i \\ \dot{\theta}^i \\ \dot{\mathbf{q}}_f^i \end{bmatrix}$$

and

$$\mathbf{M}^i = \int_{V^i} \rho^i \begin{bmatrix} \mathbf{I} & \mathbf{A}_\theta^i \tilde{\mathbf{u}}^i & \mathbf{A}^i \mathbf{S}_f^i \\ & \tilde{\mathbf{u}}^{iT} \tilde{\mathbf{u}}^i & \tilde{\mathbf{u}}^{iT} \tilde{\mathbf{I}} \mathbf{S}_f^i \\ \text{sym} & & \mathbf{S}_f^{iT} \mathbf{S}_f^i \end{bmatrix} dV^i \tag{8}$$

in which

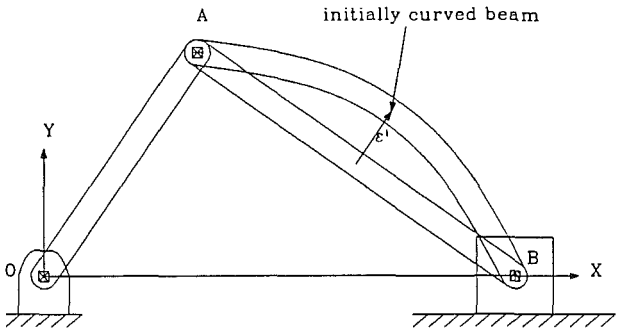


Fig. 1 Slider-crank mechanism

$$\mathbf{A}_\theta^i = \frac{\partial \mathbf{A}^i}{\partial \theta^i}, \qquad \tilde{\mathbf{I}} = \begin{bmatrix} 0 & 1 \\ -1 & 0 \end{bmatrix}.$$

One can verify that the nonlinear mass matrix of equation (8) can be expressed in terms of the following invariants that depend on the assumed displacement field as well as the initial curvature of the beam (Bartolone and Shabana, 1989).

$$\left.\begin{aligned}
&\mathbf{J}_1^i = \int_{V^i} \rho^i \tilde{\mathbf{u}}_o^i dV^i \qquad \mathbf{J}_5^i = \int_{V^i} \rho^i \tilde{\mathbf{u}}_o^{iT} \mathbf{S}_f^i dV^i \qquad \mathbf{J}_9^i = \int_{V^i} \rho^i \mathbf{S}_f^{iT} \mathbf{S}_c^i dV^i \\
&\mathbf{J}_2^i = \int_{V^i} \rho^i \mathbf{S}_f^i dV^i \qquad \mathbf{J}_6^i = \int_{V^i} \rho^i \mathbf{S}_f^{iT} \mathbf{S}_f^i dV^i \qquad \mathbf{J}_{10}^i = \int_{V^i} \rho^i \tilde{\mathbf{u}}_o^{iT} \tilde{\mathbf{I}} \mathbf{S}_f^i dV^i \\
&\mathbf{J}_3^i = \int_{V^i} \rho^i \mathbf{S}_c^i dV^i \qquad J_7^i = \int_{V^i} \rho^i \tilde{\mathbf{u}}_o^{iT} \mathbf{S}_c^i dV^i \qquad \mathbf{J}_{11}^i = \int_{V^i} \rho^i \mathbf{S}_f^{iT} \tilde{\mathbf{I}} \mathbf{S}_c^i dV^i \\
&J_4^i = \int_{V^i} \rho^i \tilde{\mathbf{u}}_o^{iT} \tilde{\mathbf{u}}_o dV^i \qquad J_8^i = \int_{V^i} \rho^i \mathbf{S}_c^{iT} \mathbf{S}_c^i dV^i \qquad \mathbf{J}_{12}^i = \int_{V^i} \rho^i \mathbf{S}_c^{iT} \tilde{\mathbf{I}} \mathbf{S}_f^i dV^i
\end{aligned}\right\} \tag{9}$$

By using the finite element method, one can show that the number of invariants can be significantly reduced to three. In this case, the three invariants are given by (Bartolone and Shabana, 1989)

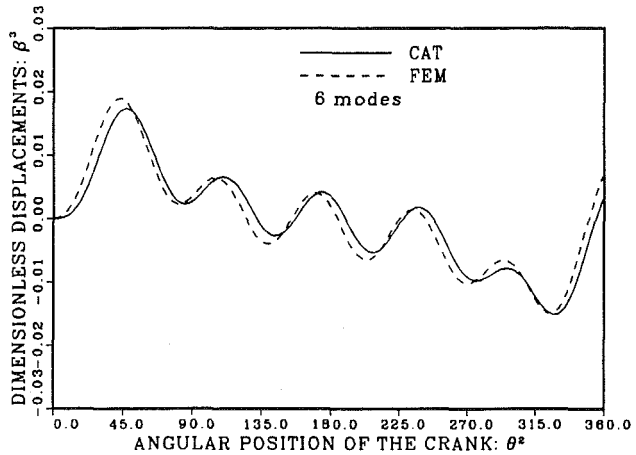


Fig. 3 Midpoint transverse deflection of the connecting rod without coupling in the mode shapes, $\epsilon = 3.048$ mm

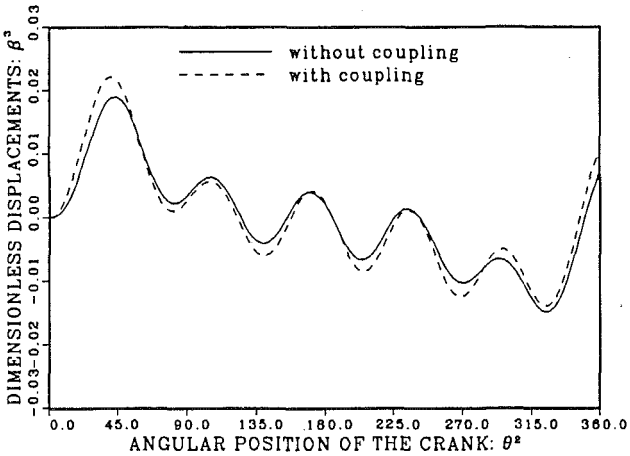


Fig. 2 Midpoint transverse deflection of the connecting rod; 2 modes, 8 elements of FEM, $\epsilon = 6.096$ mm

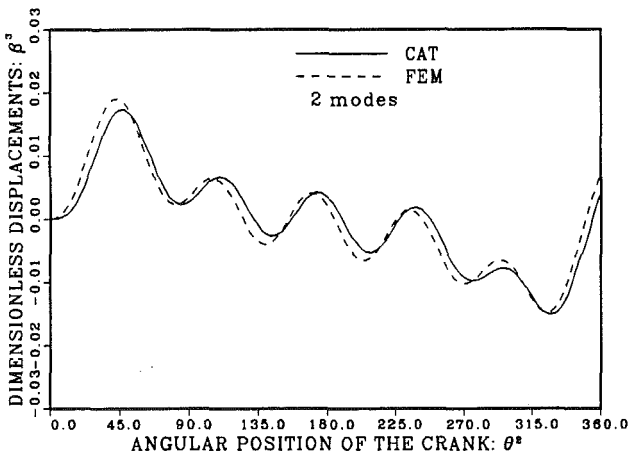


Fig. 4 Midpoint transverse deflection of the connecting rod without coupling in the mode shapes, $\epsilon = 6.096$ mm

Downloaded 03 May 2010 to 171.66.16.31. Redistribution subject to ASME license or copyright; see http://www.asme.org/terms/Terms_Use.cfm

$$\left.\begin{aligned}\mathbf{J}_1^{ij} &= \int_{V^{ij}} \rho^{ij}\mathbf{S}^{ij}dV^{ij}\\ \mathbf{J}_2^{ij} &= \int_{V^{ij}} \rho^{ij}\mathbf{S}^{ij\mathrm{T}}\mathbf{S}^{ij}dV^{ij}\\ \mathbf{J}_3^{ij} &= \int_{V^{ij}} \rho^{ij}\mathbf{S}^{ij\mathrm{T}}\tilde{\mathbf{I}}\mathbf{S}^{ij}dV^{ij}\end{aligned}\right\} \quad (10)$$

where ρ^{ij} and V^{ij} are, respectively, the mass density and volume of element j on beam i and $\mathbf{S}^{ij}$ is the shape function of the element.

4 Numerical Example

In this section, a multibody system is used to demonstrate the use of the dynamic formulation developed in the preceding sections. The slider-crank mechanism, which contains an initially-curved deformable connecting rod and is commonly used by other researchers, is chosen in order to examine the effect of the coupling between the longitudinal and transverse displacements on the dynamic response of curved beams. The assumed curvature used in this investigation is represented by a one-half sine wave function written as

$$\bar{y}^i = \epsilon^i \sin\frac{\pi\bar{x}^i}{l^i} \quad (11)$$

where ϵ^i and l^i are, respectively, the amplitude of the curvature function and the length of the beam. Figure 1 shows the slider-crank mechanism (Chen, 1989) which consists of a rigid crank OA, flexible connecting rod AB of uniform cross-section, and a sliding block located at B. All links are made of steel. The crankshaft and the connecting rod have length 0.1524 m and 0.3048 m, respectively. The diameter of the two links is 0.00635 m. The connecting rod is divided into eight two-dimensional beam elements. The connecting rod is assumed to have a small initial curvature defined by the curvature function of equation (11) and simply supported at the ends by pins. Different values for the amplitude, ϵ^i, of the curvature function are used in this investigation. These values are 0.01 and 0.02 of the length of the connecting rod. Both transverse and longitudinal deformations of the connecting rod will be allowed by considering the first six modes of vibration. Transverse deflection of the center of the initially curved beam is used as a measure of the beam deformation. The dimensionless parameter β obtained by dividing the actual deflection of the connecting rod by its length is used in this numerical study. The crankshaft of the slider-crank mechanism is assumed to rotate with a constant angular velocity of $\omega = 150$ rad/sec.

Kinematic Coupling Between Longitudinal and Transverse Deformation: In the Euler-Bernoulli theory for straight beams, it is assumed that there is no coupling between the longitudinal and transverse displacement in the linear elastic analysis. The mode shapes obtained define either transverse or longitudinal displacements. In many previous investigations mode shapes of straight beams are used to describe the deformation of curved beams. It was shown, however, by Bartolone and Shabana (1989), that the mode shapes of curved beams include coupling between the longitudinal and transverse displacements. Figure 2 shows the effect of this coupling on the dynamic response of the slider crank mechanism. Two cases are considered. In the first case, the mode shapes of the curved beams that contain the coupling terms are used. In the second case, the mode shapes of straight beams which contain no coupling terms are used. It is clear from these figures that the effect of the kinematic coupling terms on the dynamic response of the beam is significant.

Classical Approximation Methods: Another alternative for using the finite element method (FEM) is to use the classical approximation methods (CAT). In this investigation, the first five bending eigenfunctions and the first axial eigenfunction of the straight beam are used to introduce the elastic coordinates of the curved beam. Clearly in this case there is no coupling between the longitudinal and transverse displacements in the assumed displacement field. Dynamic coupling, however, as the result of the finite rotation does exist. In this section we compare the solution obtained using classical approximation methods with the solutions obtained from the finite element method in both cases where there is and there is no coupling in the mode shapes. Figures 3 and 4 show the numerical results, which indicate that the classical approximation solution agrees well with the finite element solution in the case where the mode shapes of straight beams, which include no coupling are used. Discrepancies, however, are observed between the results of the classical approximation methods and the finite element method when the kinematic coupling is considered in the finite element mode shapes.

Acknowledgment

This research was supported, in part, by the U. S. Army Research Office, Research Triangle Park, N. C.

References

Badlani, M., and Midha, A., 1982, "Member Initial Curvature Effects on the Elastic Slider-crank Mechanism Response," *Journal of Mechanical Design*, Vol. 104, pp. 159–167.

Bartolone, D. F., and Shabana, A. A., 1989, "Effect of Beam Initial Curvature on the Dynamics of Deformable Multibody Systems," *Mechanism and Machine Theory*, to appear.

Chen, D. C., 1989, "Effects of the Coupling Between Axial and Bending Displacements of Curved Beams," Master Thesis, Dept. of Mechanical Engineering, University of Illinois at Chicago, Chicago, IL.

Dickinson, S. M., 1980, "The Lateral Vibration of Slightly Bent Slender Beams Subject to Prescribed Axial End Displacement," *Journal of Sound and Vibration*, Vol. 68, No. 4, pp. 507–514.

Reddy, J. N., and Singh, I. R., 1981, "Large Deflection and Large Amplitude Free Vibrations of Straight and Curved Beams," *International Journal of Numerical Methods in Engineering*, Vol. 17, pp. 829–852.

Rosen, A., and Rand, O., 1985, "A General Model of the Dynamics of Moving and Rotating Rods," *Computers and Structures*, Vol. 21, No. 3, pp. 543–561.

Sanders, J. R., and Tesar, D., 1978, "The Analytical and Experimental Evaluation of Vibration Oscillations in Realistically Proportional Mechanisms," *Journal of Mechanical Design*, Vol. 100, pp. 762–768.

The Cylindrical Crack

T. N. Farris,[6] K. Kokini,[7] and I. Demir[8]

1 Introduction

The initiation and growth of a cylindrically-shaped crack along an interface (see Fig. 1) is one mode of failure for structures made of multiple materials containing an interface of cylindrical shape. The cylindrical interface crack between two isotropic solids was first analyzed by Erdogan and Ozbek (1969) and Ozbek and Erdogan (1969). The cylindrical crack in a homogeneous transversely-isotropic solid was analyzed by

[6]School of Aeronautics and Astronautics, Purdue University, West Lafayette, IN 47907. Assoc. Mem. ASME.

[7]School of Mechanical Engineering, Purdue University, West Lafayette, IN 47907. Mem. ASME.

[8]School of Aeronautics and Astronautics, Purdue University, West Lafayette, IN 47907.

Manuscript received by the ASME Applied Mechanics Division, July 20, 1988; final revision, January 16, 1989.

Downloaded 03 May 2010 to 171.66.16.31. Redistribution subject to ASME license or copyright; see http://www.asme.org/terms/Terms_Use.cfm

$$\left.\begin{aligned} \mathbf{J}_1^{ij} &= \int_{V^{ij}} \rho^{ij}\mathbf{S}^{ij}dV^{ij} \\ \mathbf{J}_2^{ij} &= \int_{V^{ij}} \rho^{ij}\mathbf{S}^{ij}\mathbf{S}^{ij}dV^{ij} \\ \mathbf{J}_3^{ij} &= \int_{V^{ij}} \rho^{ij}\mathbf{S}^{ij}\tilde{\mathbf{I}}\mathbf{S}^{ij}dV^{ij} \end{aligned}\right\} \quad (10)$$

where ρ^{ij} and V^{ij} are, respectively, the mass density and volume of element j on beam i and $\mathbf{S}^{ij}$ is the shape function of the element.

4 Numerical Example

In this section, a multibody system is used to demonstrate the use of the dynamic formulation developed in the preceding sections. The slider-crank mechanism, which contains an initially-curved deformable connecting rod and is commonly used by other researchers, is chosen in order to examine the effect of the coupling between the longitudinal and transverse displacements on the dynamic response of curved beams. The assumed curvature used in this investigation is represented by a one-half sine wave function written as

$$\bar{y}^i = \epsilon^i \sin \frac{\pi \bar{x}^i}{l^i} \quad (11)$$

where ϵ^i and l^i are, respectively, the amplitude of the curvature function and the length of the beam. Figure 1 shows the slider-crank mechanism (Chen, 1989) which consists of a rigid crank OA, flexible connecting rod AB of uniform cross-section, and a sliding block located at B. All links are made of steel. The crankshaft and the connecting rod have length 0.1524 m and 0.3048 m, respectively. The diameter of the two links is 0.00635 m. The connecting rod is divided into eight two-dimensional beam elements. The connecting rod is assumed to have a small initial curvature defined by the curvature function of equation (11) and simply supported at the ends by pins. Different values for the amplitude, ϵ^i, of the curvature function are used in this investigation. These values are 0.01 and 0.02 of the length of the connecting rod. Both transverse and longitudinal deformations of the connecting rod will be allowed by considering the first six modes of vibration. Transverse deflection of the center of the initially curved beam is used as a measure of the beam deformation. The dimensionless parameter β obtained by dividing the actual deflection of the connecting rod by its length is used in this numerical study. The crankshaft of the slider-crank mechanism is assumed to rotate with a constant angular velocity of $\omega = 150$ rad/sec.

Kinematic Coupling Between Longitudinal and Transverse Deformation: In the Euler-Bernoulli theory for straight beams, it is assumed that there is no coupling between the longitudinal and transverse displacement in the linear elastic analysis. The mode shapes obtained define either transverse or longitudinal displacements. In many previous investigations mode shapes of straight beams are used to describe the deformation of curved beams. It was shown, however, by Bartolone and Shabana (1989), that the mode shapes of curved beams include coupling between the longitudinal and transverse displacements. Figure 2 shows the effect of this coupling on the dynamic response of the slider crank mechanism. Two cases are considered. In the first case, the mode shapes of the curved beams that contain the coupling terms are used. In the second case, the mode shapes of straight beams which contain no coupling terms are used. It is clear from these figures that the effect of the kinematic coupling terms on the dynamic response of the beam is significant.

Classical Approximation Methods: Another alternative for using the finite element method (FEM) is to use the classical approximation methods (CAT). In this investigation, the first five bending eigenfunctions and the first axial eigenfunction of the straight beam are used to introduce the elastic coordinates of the curved beam. Clearly in this case there is no coupling between the longitudinal and transverse displacements in the assumed displacement field. Dynamic coupling, however, as the result of the finite rotation does exist. In this section we compare the solution obtained using classical approximation methods with the solutions obtained from the finite element method in both cases where there is and there is no coupling in the mode shapes. Figures 3 and 4 show the numerical results, which indicate that the classical approximation solution agrees well with the finite element solution in the case where the mode shapes of straight beams, which include no coupling are used. Discrepancies, however, are observed between the results of the classical approximation methods and the finite element method when the kinematic coupling is considered in the finite element mode shapes.

Acknowledgment

This research was supported, in part, by the U. S. Army Research Office, Research Triangle Park, N. C.

References

Badlani, M., and Midha, A., 1982, "Member Initial Curvature Effects on the Elastic Slider-crank Mechanism Response," *Journal of Mechanical Design*, Vol. 104, pp. 159–167.

Bartolone, D. F., and Shabana, A. A., 1989, "Effect of Beam Initial Curvature on the Dynamics of Deformable Multibody Systems," *Mechanism and Machine Theory*, to appear.

Chen, D. C., 1989, "Effects of the Coupling Between Axial and Bending Displacements of Curved Beams," Master Thesis, Dept. of Mechanical Engineering, University of Illinois at Chicago, Chicago, IL.

Dickinson, S. M., 1980, "The Lateral Vibration of Slightly Bent Slender Beams Subject to Prescribed Axial End Displacement," *Journal of Sound and Vibration*, Vol. 68, No. 4, pp. 507–514.

Reddy, J. N., and Singh, I. R., 1981, "Large Deflection and Large Amplitude Free Vibrations of Straight and Curved Beams," *International Journal of Numerical Methods in Engineering*, Vol. 17, pp. 829–852.

Rosen, A., and Rand, O., 1985, "A General Model of the Dynamics of Moving and Rotating Rods," *Computers and Structures*, Vol. 21, No. 3, pp. 543–561.

Sanders, J. R., and Tesar, D., 1978, "The Analytical and Experimental Evaluation of Vibration Oscillations in Realistically Proportional Mechanisms," *Journal of Mechanical Design*, Vol. 100, pp. 762–768.

The Cylindrical Crack

T. N. Farris,[6] K. Kokini,[7] and I. Demir[8]

1 Introduction

The initiation and growth of a cylindrically-shaped crack along an interface (see Fig. 1) is one mode of failure for structures made of multiple materials containing an interface of cylindrical shape. The cylindrical interface crack between two isotropic solids was first analyzed by Erdogan and Ozbek (1969) and Ozbek and Erdogan (1969). The cylindrical crack in a homogeneous transversely-isotropic solid was analyzed by

[6]School of Aeronautics and Astronautics, Purdue University, West Lafayette, IN 47907. Assoc. Mem. ASME.

[7]School of Mechanical Engineering, Purdue University, West Lafayette, IN 47907. Mem. ASME.

[8]School of Aeronautics and Astronautics, Purdue University, West Lafayette, IN 47907.

Manuscript received by the ASME Applied Mechanics Division, July 20, 1988; final revision, January 16, 1989.

Copyright © 1989 by ASME

Downloaded 03 May 2010 to 171.66.16.31. Redistribution subject to ASME license or copyright; see http://www.asme.org/terms/Terms_Use.cfm

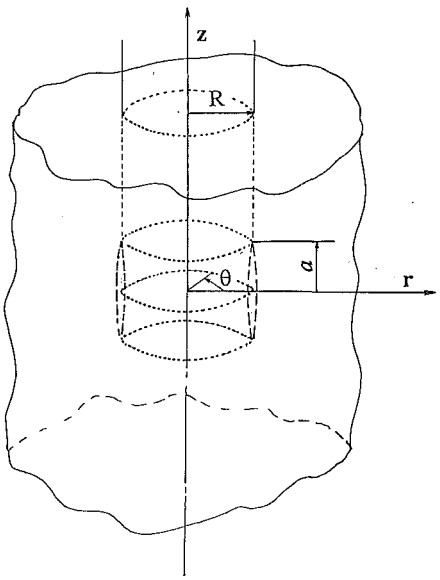


Fig. 1 Cylindrical crack and coordinate system

Kasano et al. (1984). Later Kasano et al. (1986) analyzed the cylindrical interface crack between anisotropic solids.

In this note the reduced problem of an infinite elastic body containing a cylindrical crack subjected to internal pressure is analyzed. The solution procedure reduces the elasticity boundary value problem to a system of integral equations whose solution is the dislocation densities. The integral equations are integrated using numerical quadrature and the Mode I and Mode II stress intensity factors are calculated directly from the dislocation densities. It is shown that for cracks that are long compared to their radius, the problem is self-similar and the crack driving force is independent of the crack length. A simple model based on Lame's solution for a pressurized cylinder is developed that describes this self-similar crack problem.

2 Axisymmetric Elastic Formulation

An infinite elastic body contains a cylindrically-shaped crack of radius R and length $2a$. The crack is loaded by internal pressure of magnitude p causing axisymmetric deformation. The boundary conditions appropriate for this problem are given next along with conditions for continuity between regions $1(r<R)$ and $2(r>R)$:

$$\sigma_r^1(R,z)=\sigma_r^2(R,z), \quad \sigma_{rz}^1(R,z)=\sigma_{rz}^2(R,z), \quad -\infty<z<\infty \tag{1}$$

$$\sigma_r^1(R,z)=-p, \quad \sigma_{rz}^1(R,z)=0, \quad -a<z<a \tag{2}$$

$$u^1(R,z)=u^2(R,z), \quad w^1(R,z)=w^2(R,z), \quad |z|>a \tag{3}$$

where σ represents the components of stress in cylindrical coordinates (Fig. 1), u is the radial (r) displacement, w is the axial (z) displacement, and the superscripts refer to regions 1 and 2.

Following Erdogan and Ozbek (1969), the stresses and displacements are written in terms of inverse Fourier transforms in the z-direction. After satisfying the continuity of tractions (equation (1)) and the appropriate conditions for $r\to 0$ and $r\to\infty$, there remain two unknown functions in the transform domain. The continuity of displacements, equation (3), is satisfied by writing the jump in the displacement across the crack in terms of the dislocation densities, B_1 and B_2, as

$$-\frac{\partial}{\partial z}\left[u^2(R,z)-u^1(R,z)\right]=B_1(z)H(a-|z|) \tag{4}$$

$$-\frac{\partial}{\partial z}\left[w^2(R,z)-w^1(R,z)\right]=B_2(z)H(a-|z|) \tag{5}$$

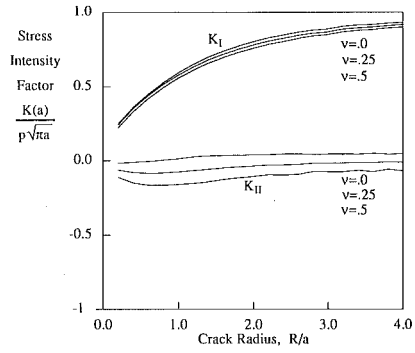


Fig. 2(a)

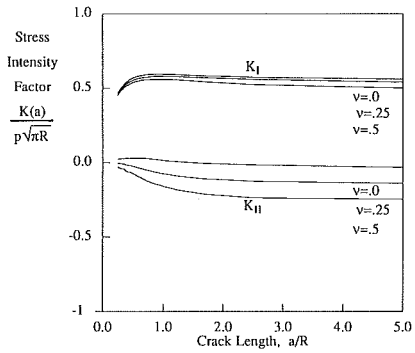


Fig. 2(b)

Fig. 2 Mode I and Mode II stress intensity factors; (a) normalized by $p\sqrt{\pi a}$, (b) normalized by $p\sqrt{\pi R}$

where H is the Heaviside step function equal to unity for positive argument and zero for negative argument. The traction boundary conditions, equations (2), are now written as

$$-\int_{-a}^{a}\frac{B_1(s)ds}{s-z}+\int_{-a}^{a}B_1(s)L_1(s,z)ds$$

$$-\int_{-a}^{a}B_2(s)L_2(s,z)ds=-\frac{4\pi(1-\nu^2)p}{E}, \quad -a<z<a \tag{6}$$

$$-\int_{-a}^{a}\frac{B_2(s)ds}{s-z}+\int_{-a}^{a}B_1(s)L_2(s,z)ds$$

$$-\int_{-a}^{a}B_2(s)L_3(s,z)ds=0, \quad -a<z<a \tag{7}$$

where the kernels L_1, L_2, and L_3 are given in the Appendix, E is Young's modulus, and ν is Poisson's ratio. The continuity of displacements outside the crack requires that the net dislocation is zero given

$$\int_{-a}^{a}B_1(s)ds=0, \quad \int_{-a}^{a}B_2(s)ds=0. \tag{8}$$

It is noted in passing that σ_z is continuous outside the crack but undergoes a jump across the faces of the crack.

The problem is reduced to inverting the system of integral equations, equations (6)–(8), for the unknown dislocation densities. The square root singularity in the dilocation densities is treated explicitly and the regular portion of B_1 and B_2 is approximated as piecewise quadratic leading to a system of linear equations which is inverted numerically. The Mode I and Mode II stress intensity factors are then calculated directly from the regular portion of the dislocation densities.

The stress intensity factors normalized by $\bar{K}_I$ for a plane-strain crack of length $2a$ subjected to internal pressure p, $\bar{K}_I=p\sqrt{\pi a}$, are shown in Fig. 2(a) as a function of R/a and ν. The value for K_I is the same for each crack tip and $K_{II}(a)=-K_{II}(-a)$. For large R/a, K_I approaches $\bar{K}_I$ and K_{II}

Downloaded 03 May 2010 to 171.66.16.31. Redistribution subject to ASME license or copyright; see http://www.asme.org/terms/Terms_Use.cfm

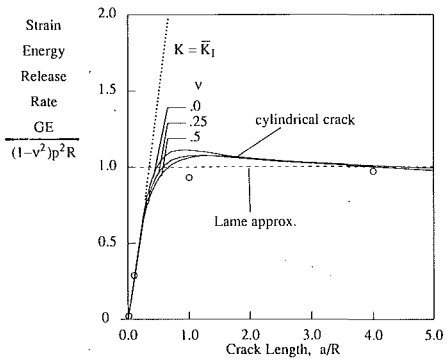


Fig. 3 Comparison of energy release rates: The solid lines are the cylindrical crack analysis; the dotted line is a plane-strain crack of length 2a in an infinite body; the dashed line is the Lamé approximation; and the circles are from Kasano et al. (1984) for $\nu = 0.3$

goes to zero. As the radius decreases, K_I reduces relative to its value for a plane-strain crack of the same length and K_{II} first increases then decreases in absolute value. Figure 2(*b*) shows K_I and K_{II} normalized by $p\sqrt{\pi R}$. For large values of a/R, $K_I/p\sqrt{\pi R}$ and $K_{II}/p\sqrt{\pi R}$ become approximately horizontal lines. This fact is discussed further in the Lamé Solution section.

3 Lamé Solution

Next, an approximate calculation of the strain energy release rate for plane strain,

$$G = \frac{1-\nu^2}{\mathrm{E}}\,(K_I^2 + K_{II}^2), \tag{9}$$

is outlined. The approximate calculation ignores the strain energy caused by deformation in the regions $|z| > a$ and is a more appropriate approximation for large values of a/R. That is, for large values of a/R the crack faces are constrained to open parallel to each other and only near the tips of the crack is the profile curved. Also, the self-similar crack profile near the tips is governed only by the crack radius R.

Region 1 is treated as a solid cylinder of length $2a$ and radius R subjected to external pressure p. Region 2 is treated as an infinite elastic body containing a circular hole of radius R, subjected to internal pressure p. The ends of the cylinder are constrained leading to plane-strain conditions. The total strain energy is calculated as

$$U = 2\pi a R^2\,\frac{p^2}{\mathrm{E}}\,[(1-\nu) - 2\nu^2 + (1+\nu)] = 4\pi a R^2\,\frac{p^2}{\mathrm{E}}\,(1-\nu^2) \tag{10}$$

where the term corresponding to $(1+\nu)$ between the equal signs describes region 2 while the remaining term describes region 1.

The strain energy release rate is defined in terms of the total strain energy as

$$G = \frac{\partial U}{\partial A} = \frac{(1-\nu^2)}{\mathrm{E}}\,p^2 R \tag{11}$$

where A is the area of the crack surfaces and self-similar growth (R constant) is assumed. For comparison, the energy release for a plane-strain crack of length $2a$ in an infinite body subjected to internal pressure p is

$$G = \frac{(1-\nu^2)}{\mathrm{E}}\,p^2 \pi a. \tag{12}$$

Equations (9), (11), and (12) for G are shown in Fig. 3. The Lamé approximation works well for $a/R > 2$ while the plane-strain value of G is appropriate for small a/R.

References

Erdogan, F., and Ozbek, T., 1969, "Stresses in Fiber-Reinforced Composites With Imperfect Bonding," ASME JOURNAL OF APPLIED MECHANICS, Vol. 36, pp. 865–869.

Kasano, H., Matsumoto, H., and Nakahara, I., 1984, "A Torsion-Free Axisymmetric Problem of a Cylindrical Crack in a Transversely Isotropic Body," *Bulletin of JSME*, Vol. 27, pp. 1323–1332.

Kasano, H., Matsumoto, H., and Nakahara, I., 1986, "A Cylindrical Interface Crack in a Nonhomogeneous Anisotropic Elastic Body," *Bulletin of JSME*, Vol. 29, pp. 1973–1981.

Ozbek, T., and Erdogan, F., 1969, "Some Elasticity Problems in Fiber-Reinforced Composites with Imperfect Bonds," *Int. J. Engng. Sci.*, Vol. 7, pp. 931–946.

APPENDIX

The continuous portion of the integral equation kernels are given by

$$L_1(s,z) = 2\int_0^\infty \left\{\left[2\xi R(K_1I_1 - K_0I_0) + (3-2\nu)(K_0I_1 - K_1I_0) + \xi^2R^2(K_0I_1 - K_1I_0) + \frac{4(1-\nu)}{\xi R}\,K_1I_1\right] + \frac{1}{2}\right\}\sin[\xi(s-z)]d\xi \tag{A1}$$

$$L_2(s,z) = 2\int_0^\infty [\xi R(K_0I_1 - K_1I_0) + \xi^2R^2(K_1I_1 - K_0I_0) + 2(1-\nu)K_1I_1] \times \cos[\xi(s-z)]d\xi \tag{A2}$$

$$L_3(s,z) = 2\int_0^\infty \left\{\xi^2R^2(K_1I_0 - K_0I_1) - \frac{1}{2}\right\}\sin[\xi(s-z)]d\xi \tag{A3}$$

where $I_0 = I_0(\xi R)$, $I_1 = I_1(\xi R)$, $K_0 = K_0(\xi R)$, and $K_1 = K_1(\xi R)$ are the Modified Bessel Functions. These integrals are evaluated numerically using Filon's Method.

A Note on Microbuckling in Unidirectional Fibrous Composites

Timothy M. Minahen[9] and Wolfgang G. Knauss[10]

1 Introduction

This note addresses the buckling of a fiber embedded in an elastic matrix of infinite extent. Specifically, we are interested in elucidating the difference in the buckling strength for two fiber/matrix interface conditions: (1) perfect fiber/matrix adhesion and (2) loss of adhesion, such that shear transfer is eliminated between matrix and fiber. For illustrative purposes we deal with the two-dimensional counterpart of the problem.

It has long been recognized (Rosen, 1965) that a prevalent mode of failure in composites under compression results from microbuckling of the fibers. Coordinated microbuckling of an ensemble of fibers causes interlaminar forces that tend to spread the laminas and thus give rise to the beginning of delaminations; such a mechanism operates directly in stress concentrations (Waas, 1987). The desire to account for this buckling phenomenon has been as long-standing as its recognition, as demonstrated by Rosen's analysis of two

[9]Graduate Research Assistant, Department of Aeronautics, Graduate Aeronautical Laboratories, California Institute of Technology, Pasadena, CA 91125.

[10]Professor of Aeronautics and Applied Mechanics, Graduate Aeronautical Laboratories, California Institute of Technology, Pasadena, CA 91125, Mem. ASME.

Manuscript received by the ASME Applied Mechanics Division, July 13, 1988; final revision, May 22, 1989.

Downloaded 03 May 2010 to 171.66.16.31. Redistribution subject to ASME license or copyright; see http://www.asme.org/terms/Terms_Use.cfm

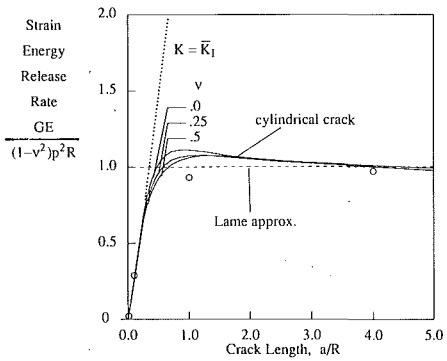


Fig. 3 Comparison of energy release rates: The solid lines are the cylindrical crack analysis; the dotted line is a plane-strain crack of length 2a in an infinite body; the dashed line is the Lamé approximation; and the circles are from Kasano et al. (1984) for $\nu = 0.3$

goes to zero. As the radius decreases, K_I reduces relative to its value for a plane-strain crack of the same length and K_{II} first increases then decreases in absolute value. Figure 2(*b*) shows K_I and K_{II} normalized by $p\sqrt{\pi R}$. For large values of a/R, $K_I/p\sqrt{\pi R}$ and $K_{II}/p\sqrt{\pi R}$ become approximately horizontal lines. This fact is discussed further in the Lamé Solution section.

3 Lamé Solution

Next, an approximate calculation of the strain energy release rate for plane strain,

$$G = \frac{1-\nu^2}{\mathrm{E}}\,(K_I^2 + K_{II}^2), \tag{9}$$

is outlined. The approximate calculation ignores the strain energy caused by deformation in the regions $|z| > a$ and is a more appropriate approximation for large values of a/R. That is, for large values of a/R the crack faces are constrained to open parallel to each other and only near the tips of the crack is the profile curved. Also, the self-similar crack profile near the tips is governed only by the crack radius R.

Region 1 is treated as a solid cylinder of length $2a$ and radius R subjected to external pressure p. Region 2 is treated as an infinite elastic body containing a circular hole of radius R, subjected to internal pressure p. The ends of the cylinder are constrained leading to plane-strain conditions. The total strain energy is calculated as

$$U = 2\pi aR^2\,\frac{p^2}{\mathrm{E}}\,[(1-\nu) - 2\nu^2 + (1+\nu)] = 4\pi aR^2\,\frac{p^2}{\mathrm{E}}\,(1-\nu^2) \tag{10}$$

where the term corresponding to $(1+\nu)$ between the equal signs describes region 2 while the remaining term describes region 1.

The strain energy release rate is defined in terms of the total strain energy as

$$G = \frac{\partial U}{\partial A} = \frac{(1-\nu^2)}{\mathrm{E}}\,p^2 R \tag{11}$$

where A is the area of the crack surfaces and self-similar growth (R constant) is assumed. For comparison, the energy release for a plane-strain crack of length $2a$ in an infinite body subjected to internal pressure p is

$$G = \frac{(1-\nu^2)}{\mathrm{E}}\,p^2\pi a. \tag{12}$$

Equations (9), (11), and (12) for G are shown in Fig. 3. The Lamé approximation works well for $a/R > 2$ while the plane-strain value of G is appropriate for small a/R.

References

Erdogan, F., and Ozbek, T., 1969, "Stresses in Fiber-Reinforced Composites With Imperfect Bonding," ASME JOURNAL OF APPLIED MECHANICS, Vol. 36, pp. 865–869.

Kasano, H., Matsumoto, H., and Nakahara, I., 1984, "A Torsion-Free Axisymmetric Problem of a Cylindrical Crack in a Transversely Isotropic Body," *Bulletin of JSME*, Vol. 27, pp. 1323–1332.

Kasano, H., Matsumoto, H., and Nakahara, I., 1986, "A Cylindrical Interface Crack in a Nonhomogeneous Anisotropic Elastic Body," *Bulletin of JSME*, Vol. 29, pp. 1973–1981.

Ozbek, T., and Erdogan, F., 1969, "Some Elasticity Problems in Fiber-Reinforced Composites with Imperfect Bonds," *Int. J. Engng. Sci.*, Vol. 7, pp. 931–946.

APPENDIX

The continuous portion of the integral equation kernels are given by

$$L_1(s,z) = 2\int_0^\infty \left\{\left[2\xi R(K_1I_1 - K_0I_0) + (3-2\nu)(K_0I_1 - K_1I_0) + \xi^2R^2(K_0I_1 - K_1I_0) + \frac{4(1-\nu)}{\xi R}\,K_1I_1\right] + \frac{1}{2}\right\}\sin[\xi(s-z)]d\xi \tag{A1}$$

$$L_2(s,z) = 2\int_0^\infty [\xi R(K_0I_1 - K_1I_0) + \xi^2R^2(K_1I_1 - K_0I_0) + 2(1-\nu)K_1I_1] \times \cos[\xi(s-z)]d\xi \tag{A2}$$

$$L_3(s,z) = 2\int_0^\infty \left\{\xi^2R^2(K_1I_0 - K_0I_1) - \frac{1}{2}\right\}\sin[\xi(s-z)]d\xi \tag{A3}$$

where $I_0 = I_0(\xi R)$, $I_1 = I_1(\xi R)$, $K_0 = K_0(\xi R)$, and $K_1 = K_1(\xi R)$ are the Modified Bessel Functions. These integrals are evaluated numerically using Filon's Method.

A Note on Microbuckling in Unidirectional Fibrous Composites

Timothy M. Minahen[9] and Wolfgang G. Knauss[10]

1 Introduction

This note addresses the buckling of a fiber embedded in an elastic matrix of infinite extent. Specifically, we are interested in elucidating the difference in the buckling strength for two fiber/matrix interface conditions: (1) perfect fiber/matrix adhesion and (2) loss of adhesion, such that shear transfer is eliminated between matrix and fiber. For illustrative purposes we deal with the two-dimensional counterpart of the problem.

It has long been recognized (Rosen, 1965) that a prevalent mode of failure in composites under compression results from microbuckling of the fibers. Coordinated microbuckling of an ensemble of fibers causes interlaminar forces that tend to spread the laminas and thus give rise to the beginning of delaminations; such a mechanism operates directly in stress concentrations (Waas, 1987). The desire to account for this buckling phenomenon has been as long-standing as its recognition, as demonstrated by Rosen's analysis of two

[9]Graduate Research Assistant, Department of Aeronautics, Graduate Aeronautical Laboratories, California Institute of Technology, Pasadena, CA 91125.

[10]Professor of Aeronautics and Applied Mechanics, Graduate Aeronautical Laboratories, California Institute of Technology, Pasadena, CA 91125, Mem. ASME.

Manuscript received by the ASME Applied Mechanics Division, July 13, 1988; final revision, May 22, 1989.

Copyright © 1989 by ASME

Downloaded 03 May 2010 to 171.66.16.31. Redistribution subject to ASME license or copyright; see http://www.asme.org/terms/Terms_Use.cfm

distinct fiber coordination modes: One mode considers parallel fibers supported by an elastic matrix to deform sinusoidally with the same phase, while the other mode consists of fibers deforming alternatively with the same wavelength, but 180 deg out of phase. Similarly, Steif (1987) considers this problem for incompressible, time-dependent material properties, treating matrix and fiber as two-dimensional continua.

The problem discussed here is that of a single elastic fiber bounded by an infinite elastic matrix, though the method used is readily extended to a periodic two-dimensional array of fibers. The boundary value problem development follows that of Waas (1987), who considered a two-dimensional array. The fiber is modeled as an elastic Euler-Bernoulli beam while the matrix is assumed to be a two-dimensional (plane stress) elastic continuum. This configuration is subjected to compressive loading and the bifurcation problem of fiber buckling is analyzed.

The buckling load is found to be sensitive to the interface condition between the fiber and matrix. This is shown by examining two problems: The first requires the displacement field to be continuous across the fiber/matrix interface and the second eliminates shear transfer through the interface. These two problems would seem to span the possible interface conditions and should give the range in which microbuckling need be of concern.

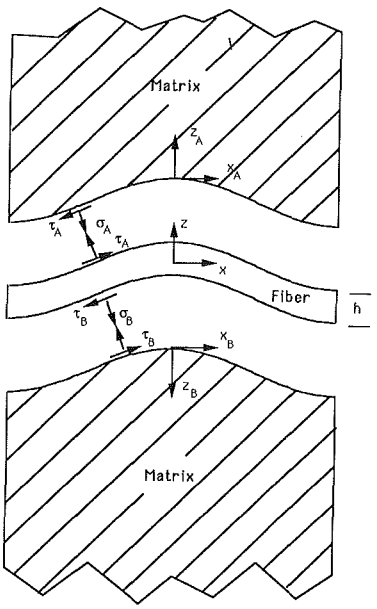


Fig. 1 Buckled geometry

2 Field Equations

The field equations are developed under the assumption that $E_m/E_f \ll 1$ (where the subscripts, m and f, refer to the matrix and fiber, respectively). If this is true, then it may be assumed that the matrix influence is felt only after bifurcation. Consider the fiber equilibrium as shown in Fig. 1.

For small displacements and rotations, the in-plane and bending problems of the fiber may be superposed. Then, if $u_o(x)$ and $w_o(x)$ are the deformations of the fiber neutral axis in the thrust and lateral directions, respectively, one has for the axial load, P, and the bending moment, M,

$$P = E_f h \frac{du_o}{dx}, \quad M = -\frac{E_f h^3}{12}\frac{d^2 w_o}{dx^2}. \tag{1a,b}$$

In the absence of body forces, fiber equilibrium requires

$$E_f h \frac{d^2 u_o}{dx^2} + \tau_A - \tau_B = 0 \tag{2}$$

$$\frac{E_f h^3}{12}\frac{d^4 w_o}{dx^4} - (\sigma_A - \sigma_B) - P\frac{d^2 w_o}{dx^2} - \frac{h}{2}\left(\frac{d\tau_A}{dx} + \frac{d\tau_B}{dx}\right) = 0. \tag{3}$$

The plane-stress problem of the equilibrium for the supporting medium, with $u_m(x,z)$ and $w_m(x,z)$ denoting the displacements in the x and z-directions, is (Sokolnikoff, 1956)

$$2\frac{\partial^2 u_m}{\partial x^2} + (1+\nu_m)\frac{\partial^2 w_m}{\partial x \partial z} + (1-\nu_m)\frac{\partial^2 u_m}{\partial z^2} = 0 \tag{4}$$

$$2\frac{\partial^2 w_m}{\partial z^2} + (1+\nu_m)\frac{\partial^2 u_m}{\partial x \partial z} + (1-\nu_m)\frac{\partial^2 w_m}{\partial x^2} = 0. \tag{5}$$

Requiring the displacements in the far field to be bounded yields solutions of the form, with α and B_i as yet undetermined constants

$$u_m(x,z) = \left[\frac{(3-\nu_m)}{\alpha(1+\nu_m)}B_2 - B_1 - B_2 z\right]e^{-\alpha z}\cos\alpha x \tag{6}$$

$$w_m(x,z) = (B_1 + B_2 z)e^{-\alpha z}\sin\alpha x. \tag{7}$$

This solution is valid for both matrix half-spaces by virtue of

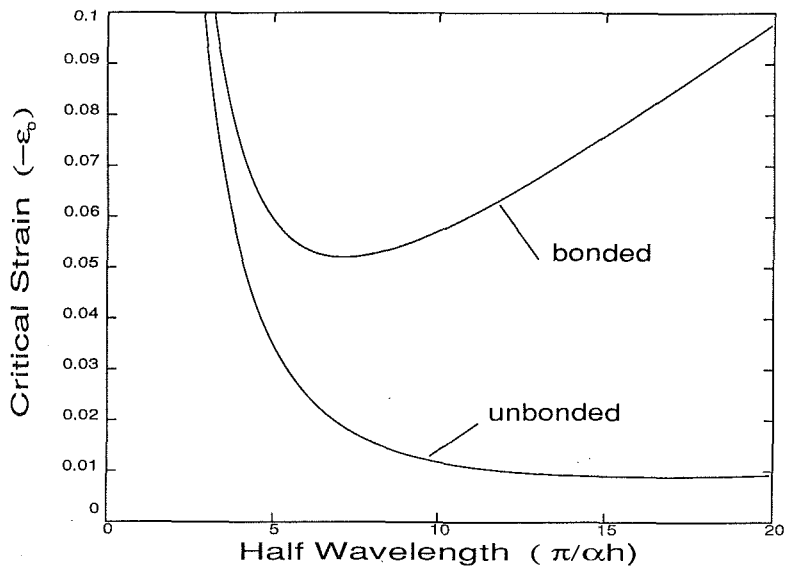


Fig. 2 Microbuckling of T300/BP907

Downloaded 03 May 2010 to 171.66.16.31. Redistribution subject to ASME license or copyright; see http://www.asme.org/terms/Terms_Use.cfm

the coordinate choices in Fig. 1. Requiring displacement continuity at fiber/matrix interface A (subscript A), and using

$$u_{mA}(x,0) = U\cos\alpha x, \quad w_{mA}(x,0) = W\sin\alpha x, \qquad (8a,b)$$

yields

$$B_1 = W \quad B_2 = \frac{\alpha(1+\nu_m)}{3-\nu_m}(U+W). \qquad (9a,b)$$

The linearly elastic constitutive assumption then allows expression of the interface stresses at A as

$$\sigma_{zA}(x,0) = -\frac{\alpha E_m}{(1+\nu_m)(3-\nu_m)}[2W-(1-\nu_m)U]\sin\alpha x \qquad (10)$$

$$\tau_{xzA}(x,0) = 2\alpha G_m\left(\frac{1-\nu_m}{3-\nu_m}W - \frac{2}{3-\nu_m}U\right)\cos\alpha x. \qquad (11)$$

Similar expressions apply at interface B.

Referring to Fig. 1, it is evident that

$$\sigma_{mA}(x,0) = \sigma_A, \quad \tau_{mA}(x,0) = \tau_A \qquad (12a,b)$$

$$\sigma_{mB}(x,0) = \sigma_B, \quad \tau_{mB}(x,0) = -\tau_B. \qquad (13a,b)$$

In the case where the displacement field is continuous across the interface one has, upon using kinematic assumption of Euler-Bernoulli beam theory,

$$u_{mA}(x,0) = u_o(x) - \frac{h}{2}\frac{dw_o}{dx}, \quad w_{mA}(x,0) = w_o(x) \qquad (14a,b)$$

$$u_{mB}(x,0) = u_o(x) - \frac{h}{2}\frac{dw_o}{dx}, \quad w_{mB}(x,0) = -w_o(x). \qquad (15a,b)$$

Substituting equations (10)–(15) into the fiber equilibrium equations (2), (3) results in $u_o(x) = 0$. Thus, the bifurcation takes place without additional axial deformation. Further, the lateral deformation of the fiber is $w(x) = A\sin\alpha x$, where α must satisfy the cubic equation

$$\rho^3 + \frac{12\mu}{(3-\nu_m)(1+\nu_m)}\rho^2 + 12\left[\epsilon_o + \frac{2(1-\nu_m)\mu}{(3-\nu_m)(1+\nu_m)}\right]\rho + \frac{48\mu}{(3-\nu_m)(1+\nu_m)} = 0. \qquad (16)$$

The nondimensional quantities $\mu = E_m/E_f$ and $\rho = \alpha h$ have been introduced and ϵ_o represents the uniform axial strain at bifurcation.

A similar analysis for the problem with zero shear transfer across the interface requires $\tau_A = \tau_B = 0$ and yields

$$W = \frac{2}{1-\nu_m}U. \qquad (17)$$

Using continuity in $w(x,z)$ at the fiber/matrix interfaces and solving for the normal stresses σ_A and σ_B allows solution of the fiber equilibrium equations. The wavelength of the buckled fiber must now satisfy the cubic equation

$$\rho^3 + 12\epsilon_o\rho + \mu = 0. \qquad (18)$$

3 Example Problem

The following example illustrates the influence of the fiber/matrix interface condition on the bifurcation load. The system analyzed simulates Thornel-300 graphite fibers preimpregnated with American Cyanamide BP907 epoxy resin which has a fiber-to-matrix elastic modulus ratio of 74.2. Figure 2 shows the buckling load as a function of wavelength for the two cases considered. The vertical axis represents the compressive strain at bifurcation while along the horizontal axis is plotted the nondimensional half-wavelength $\pi/\alpha h$. The label "bonded" refers to the case with complete displacement continuity through the interface. "Unbonded" refers to the case when no shear is transmitted across the interface and only the z-displacement field is continuous at the interface.

It is seen that the interface condition greatly influences the microbuckling load and wavelength. In the two extreme cases analyzed the critical strain, and thus load, drops by more than a factor of five when the displacement constraint at the interface is released. Experimental evidence (Hahn and Williams, 1986) indicates "bonded" two-dimensional arrays overpredict the buckling strain. The lower "unbonded" buckling strains, which compare more favorably with experimental results, indicate a strong dependence of the microbuckling process on the interface condition. In reality the condition of the interface bond will lie somewhere between these cases and will evolve, most likely, from a simultaneous interface failure during the buckling process.

References

Hahn, T., and Williams, J. G., 1986, "Compression Failure Mechanisms in Unidirectional Composites," *Composite Materials; Testing and Design*, (7th Conference) ASTM Spec. Techn. Publ. 893, J. M. Whitney, ed., pp. 115–139.

Rosen, B. W., 1965, "Mechanics of Composite Strengthening," *Fiber Composite Materials*, Chap. 3, ASM, Metals Park, Ohio.

Sokolnikoff, I. S., 1956, *Mathematical Theory of Elasticity*, Krieger, pp. 254.

Steif, P. S., 1987, "An Exact Two-Dimensional Approach to Fiber Micro-Buckling," *Int. Journal of Solids and Structurs*, Vol. 23, No. 9, pp. 1235–1246.

Waas, A. M., 1987, "Compressive Failure of Fibrous Laminated Composites in the Presence of Stress Gradients: Experiment and Analysis," *PhD. Thesis, Department of Aeronautics, California Institute of Technology, Pasadena, CA.*

Downloaded 03 May 2010 to 171.66.16.31. Redistribution subject to ASME license or copyright; see http://www.asme.org/terms/Terms_Use.cfm

Journal of Applied Mechanics

Book Reviews

Continuum Mechanics of Electromagnetic Solids, by Gerard A. Maugin. North Holland, Amsterdam, 1988. 598 pages, Price: $184.25.

REVIEWED BY A. C. ERINGEN[1]

With the development of nonlinear continuum mechanics in the 1960s, attention of engineering scientists was turned to the electromechanical theories of continua. During the following two decades some mechanicians have reopened research fields of continuum electrodynamics, which were considered to be closed by physicists. The present book is a culmination of several aspects of this research. The book consists of seven chapters and four short appendices.

Chapter 1 introduces various elementary concepts such as dielectrics, ionic crystals, ferroelectricity and piezoelectricity. Some divergences are made into the microscopic origin of different phenomenon, e.g., origin of magnetism, different types of magnetic materials, conduction of electricity, and electromagnetic waves. In this way the stage is set for the mathematical development of various interacting fields. Chapter 2 is a review of continuum mechanics. Concepts of strain, strain rates, balance laws, and constitutive equations are discussed and applied to thermoelasticity and some problems in elastic waves. Literature contains many excellent books and treatises on these topics. Therefore, one wonders why the author has devoted some 86 pages to continuum mechanics.

With Chapter 3 the main goal of this book begins. Here balance laws and Maxwell's equations are introduced both in integral and differential forms. Jump conditions at a discontinuity surface are obtained. Electromagnetic stress tensors, momenta, and energy are discussed and a principle of virtual power is formulated.

Chapter 4 is concerned with dielectrics and piezoelectricity. Nonlinear field and constitutive equations are developed. Voigt's linear theory of piezoelectricity is given and applied to the solutions of several problems which include piezoelectically-excited vibrations of plates, piezoelectric Rayleigh and Bleustein-Gulyaew waves.

Chapter 5 is devoted to elastic conductors. After the development of constitutive equations several problems are solved. Magnetothermoelastic waves, shock waves, simple waves, and a magnetoelastic piston problem are among these.

In Chapter 6 the author presents a recent theory on elastic ferromagnets. Because of the spin degree-of-freedom, balance laws and constitutive equations require extensions to include magnetic gyroscopic effects and the interactions of spin and lattice continua. Magnetoacoustic resonance, the Faraday effect, attenuation of magnetoacoustic waves, surface spin waves, Bloch and Neel walls, solitary waves, and buckling and vibrations of magnetoelastic plates are discussed expertly.

Chapter 7 deals with elastic ionic crystals, ferroelectricity, and ceramics. By means of principle of virtual power, two sets of field equations are obtained involving the usual Cauchy's equations of motion and polarization inertia. Constitutive equations include electric and polarization tensors which have been introduced previously by others. The theory is used to solve problems concerning free surfaces, capacitance of thin films, the acoustic activity of ionic crystals, surface, solitary, and shock waves. Some of the investigations, e.g., magnetoacoustic resonance, solitary waves in Chapter 6, and the discussion of waves in ferroelectrics in Chapter 7 are based on the work of the author and his collaborators. While they are sound mathematically, the results do not possess time-honored status and they must await experimental investigations. All chapters contain ample references, but they lack exercises for students.

The price of $184.25 for the book is excessive for student affordability. While the typing is excellent, because of the reduction in size, it requires good lighting and eye sight.

This reviewer became aware of Maugin's book only when he was asked recently to critique it. It is regrettable that nowhere in the book does the author make reference to the two-volume book (now in press) on electrodynamics of continua, which has been in preparation since 1976 under the joint authorship of A.C. Eringen and the author. Major parts of Chapters 1, 2, and 3 (excluding sections 3.6 to 3.8) and those of Chapters 4 and 6 (in total approximately one-third of the book) contain material and organization similar to that of the Eringen-Maugin manuscript, the precursor of this book. This is objectionable.

On the positive side, this book has dense coverage of a variety of contemporary theories of continuum mechanics of electromagnetic solids. It is well written by an author who has been actively involved in research. It should be on the shelves for research workers in the field.

The Nonlinear Theory of Elastic Shells: One Spatial Dimension, by A. Libai and J. G. Simmonds. Academic Press, Inc., 1988. 412 pages. Price: $49.50.

REVIEWED BY J. L. SANDERS, JR.[2]

This is not a textbook or an introduction to the subject for the uninitiated. It is a carefully written treatise on a limited part of the subject of shell theory authored by two experts in the field who have themselves contributed significantly to the literature. A second volume on the general theory (two spatial

[1]Department of Civil Engineering and Operations Research, Princeton University, Princeton, N.J. 08540.

[2]Professor, Division of Engineering and Applied Physics, Harvard University, Cambridge, Mass. 02138.

Copyright © 1989 by ASME

Downloaded 03 May 2010 to 171.66.16.31. Redistribution subject to ASME license or copyright; see http://www.asme.org/terms/Terms_Use.cfm